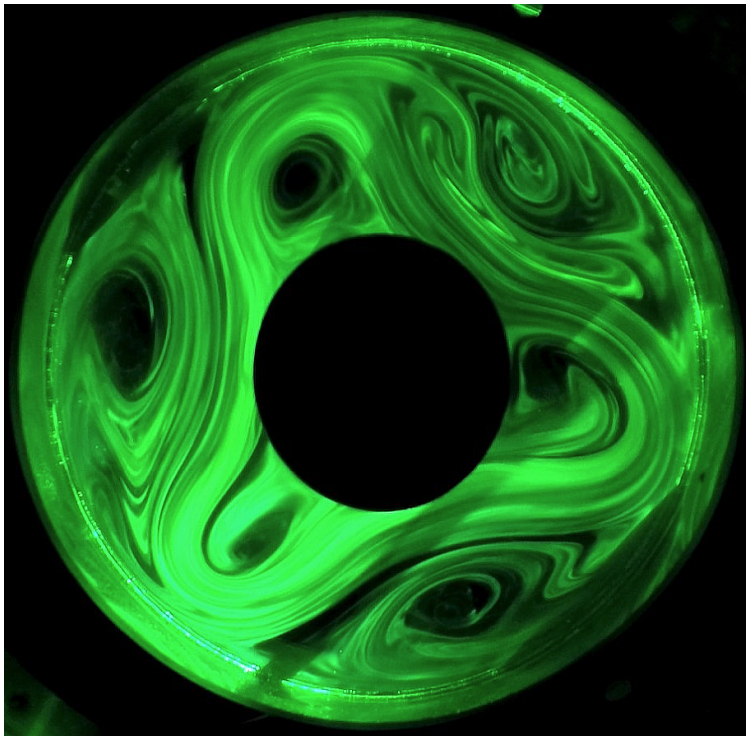
Comptes Rendus
de l'Académie des sciences

Physique



Volume 25, Special Issue S3, 2024

Special issue / *Numéro spécial*

Geophysical and astrophysical fluid dynamics in the laboratory / *Dynamique des fluides géophysiques et astrophysiques au laboratoire*

Guest editors / *Rédacteurs en chef invités*

Stephan Fauve, Michael Le Bars

ACADÉMIE DES SCIENCES
INSTITUT DE FRANCE

Académie des sciences — Paris

ISSN: 1878-1535 (electronic)

CENTRE MERSENNE

Comptes Rendus

Physique

Objective of the journal

Comptes Rendus Physique is an international peer-reviewed electronic journal, covering all areas of physics and astrophysics.

It publishes thematic issues, original research articles, review articles, historical perspectives, pedagogical texts or conference proceedings, of unlimited length, in English or in French and in as flexible a format as necessary (figures, associated data, etc.).

Comptes Rendus Physique has been published since 2020 with the centre Mersenne pour l'édition scientifique ouverte (Mersenne Center for open scientific publishing), according to a virtuous Diamond Open Access policy, free for authors (no author processing charges nor publishing fees) as well as for readers (immediate and permanent open access).

Editorial director: Étienne Ghys.

Editors-in-chief: Daniel Estève, Stephan Fauve.

Guest editors: Stephan Fauve and Michael Le Bars

Editorial board: Jacqueline Bloch, Hélène Bouchiat, Alexandre Bouzdine, Yves Bréchet, Françoise Combes, Jean Dalibard, Michel Davier, Pierre Fayet, Frédérique de Fornel, Maurice Goldman, Denis Gratias, Guy Laval, Chaouqi Misbah, Jean-Yves Ollitrault, Nathalie Palanque-Delabrouille.

Scientific secretary: Isabelle Vallet.

About the journal

Comptes Rendus Physique is published exclusively in electronic format.

All information on the journal, as well as the full text of all articles, is available on its website at: https://comptes-rendus.academie-sciences.fr/physique/.

Author enquiries

For any inquiries about submitting a manuscript, please refer to the journal's website: https://comptes-rendus.academie-sciences.fr/physique/.

Contact

Académie des sciences
23 quai de Conti
75006 Paris (France)
cr-physique@academie-sciences.fr



The articles in this journal are published under the license Creative Commons Attribution 4.0 International (CC-BY 4.0) https://creativecommons.org/licenses/by/4.0/deed.en

Comptes Rendus
Physique
2024, 25, nº S3

Contents / *Sommaire*

Michael Le Bars, Stephan Fauve
Foreword to the special issue: Geophysical and astrophysical fluid dynamics in the laboratory 1-4

Gabriel Hadjerci, Vincent Bouillaut, Benjamin Miquel, Sébastien Aumaître, Basile Gallet
Radiatively driven convection: diffusivity-free regimes of geophysical and astrophysical flows in the laboratory 5-20

Alban Pothérat, Susanne Horn
Seven decades of exploring planetary interiors with rotating convection experiments 21-75

Andreas Tilgner
Experiments on double diffusive convection 77-94

Sabrina Carpy, Michael Berhanu, Martin Chaigne, Sylvain Courrech du Pont
Fingerprints of surface flows on solid substrates ablated by phase change: from laboratory experiments to planetary landscapes 95-142

Ludovic Huguet, Quentin Kriaa, Thierry Alboussière, Michael Le Bars
Solid–liquid phase change in planetary cores 143-181

Jérémie Vidal, Jérôme Noir, David Cébron, Fabian Burmann, Rémy Monville, Vadim Giraud, Yoann Charles
Geophysical flows over topography, a playground for laboratory experiments 183-234

Marie Poulain-Zarcos, Nimish Pujara, Gautier Verhille, Matthieu J. Mercier
Laboratory experiments related to marine plastic pollution: a review of past work and future directions 235-266

Philippe Claudin, Sylvain Courrech du Pont, Clément Narteau
From lab to landscape-scale experiments for the morphodynamics of sand dunes ... 267-295

Pierre Philippe, Nadia Benahmed
Quantifying soil surface erosion 297-332

Renaud Deguen, Ludovic Huguet, Maylis Landeau, Victor Lherm, Augustin Maller, Jean-Baptiste Wacheul
Fluid dynamics of planetary differentiation 333-377

Uwe Harlander , Michael V. Kurgansky, Kevin Speer, Miklos Vincze
Baroclinic instability from an experimental perspective 379-426

Peter Read, Yakov Afanasyev, Jonathan Aurnou, Daphné Lemasquerier
Eddy-driven Zonal Jet Flows in the Laboratory 427-477

Adrien Lefauve
Geophysical stratified turbulence and mixing in the laboratory 479-507

Sylvain Joubaud, Samuel Boury, Philippe Odier
Internal gravity waves versus inertial waves in the laboratory 509-535

Pierre-Philippe Cortet, Nicolas Lanchon
Turbulence of internal gravity waves in the laboratory 537-556

Benoît Semin, François Pétrelis
Quasi-biennial oscillation: laboratory experiments 557-581

Christophe Gissinger
Laboratory modeling of MHD accretion disks 583-610

François Pétrélis
Experimental dynamos: from models to applications to the geodynamo 611-627

Frank Stefani , Sten Anders, Sven Eckert, Nico Freyer, Gunter Gerbeth, André Giesecke, Thomas Gundrum, Peter Kaever, Vivaswat Kumar, Federico Pizzi, Dirk Räbiger, Ján Šimkanin, Christian Steglich, Tobias Vogt, Nicole Wagner, Gerald Wedel
The DRESDYN precession experiment 629-647

ACADÉMIE DES SCIENCES
INSTITUT DE FRANCE

Comptes Rendus. Physique
2024, Vol. 25, Special issue S3, p. 1-4
https://doi.org/10.5802/crphys.253

Foreword / *Avant-propos*

Geophysical and astrophysical fluid dynamics in the laboratory / *Dynamique des fluides géophysiques et astrophysiques au laboratoire*

Foreword to the special issue: Geophysical and astrophysical fluid dynamics in the laboratory

Avant-propos du numéro spécial : Dynamique des fluides géophysiques et astrophysiques au laboratoire

Michael Le Bars [*, a] **and Stephan Fauve** [b]

[a] CNRS, Aix Marseille Univ, Centrale Marseille, IRPHE, Marseille, France

[b] Laboratoire de Physique de l'École Normale Supérieure, ENS, Université PSL, CNRS, Sorbonne Université, Université de Paris, 75005 Paris, France

E-mails: michael.le-bars@cnrs.fr (M. Le Bars), stephan.fauve@phys.ens.fr (S. Fauve)

Abstract. This special issue brings together 19 review articles addressing a broad range of problems in geophysical and astrophysical fluid dynamics, reflecting both the current state of the art and ongoing research, with a special focus on the contribution of laboratory experiments. This foreword outlines the general context and key challenges of the field, and places the individual contributions in perspective.

Résumé. Ce numéro spécial réunit 19 articles de revue couvrant un large spectre de problématiques en dynamique des fluides géophysiques et astrophysiques, reflétant à la fois l'état de l'art et les recherches en cours, avec un accent particulier sur l'apport des expériences en laboratoire. Cette préface présente le contexte général et les principaux défis du domaine, et met en perspective les différentes contributions.

Keywords. Geophysical fluid dynamics, Astrophysical fluid dynamics, Laboratory experiments.

Mots-clés. Dynamique des fluides géophysiques, Dynamique des fluides astrophysiques, Expériences de laboratoire.

Manuscript received and accepted 20 May 2025.

1. Introduction

Geophysical and Astrophysical Fluid Dynamics (GAFD) encompasses all types of flows occurring in any natural system, from Earth's atmosphere and oceans to the interiors of planets and stars, and even toastrophysical structures such as accretion disks. These systems involve a wide

* Corresponding author

range of fluids—air, water, liquid metals, plasmas—and span extensive spatial and temporal scales. Despite this diversity, GAFD research is unified by a common set of governing equations and a shared methodological framework: the construction of simplified models that isolate fundamental physical mechanisms. This special issue explores how laboratory experiments contribute to advancing our understanding of these generic mechanisms.

GAFD often involves extreme flow regimes and complex coupled physics that challenge numerical and theoretical approaches. While computational tools have advanced rapidly, particularly with the emergence of data-driven techniques, laboratory experiments remain indispensable. They give direct access to real systems, inherently including all physical effects, boundary conditions, and spatial and temporal scales, without relying on parameterizations or closure models. Laboratory experiments allow systematic exploration of parameter space and sustained operation in extreme regimes, thereby yielding statistically converged data. Laboratory flows emerge directly from the fundamental equations with no a priori, and can thus reveal rare, serendipitous and unexpected behaviors. These strengths coexist with inherent drawbacks: quantitative measurements are always challenging and limited, and experiments are constrained by practical restrictions on e.g. geometry, scale separation, and working fluid properties.

2. Topics overview

This special issue provides an overview of the state of the art and ongoing research in experimental GAFD. The 19 review articles highlight the breadth of physical processes accessible in the lab and underline the universality of the mechanisms across planetary and astrophysical contexts. The contributions demonstrate that progress stems from both large-scale experimental platforms and small-scale analog models.

Convection is a classical and long-standing research topic in fluid mechanics, with particular features in GAFD. Natural systems are often expected to operate in so-called ultimate regimes, where diffusive effects become negligible. While the existence of such a regime remains a subject of debate in the context of Rayleigh–Bénard convection, a radiatively driven convection setup has recently demonstrated an ultimate regime in a novel configuration [1]. Rotation plays a dominant role in GAFD, and its influence on convection has been studied experimentally for over seventy years, remaining a very active area of research [2]. Furthermore, many natural systems—including oceans, gas giants, and stellar interiors—feature multiple buoyancy sources, leading to complex double-diffusive convection regimes that are especially prone to laboratory investigation [3].

Phase-change dynamics are fundamental across planetary layers but remain challenging to parameterize due to complex interactions between fluid mechanics and out-of-equilibrium thermodynamics. Laboratory investigations address phenomena ranging from planetary surface ablation [4] to core crystallization processes [5]. The resulting solid boundary topographies, spanning multiple scales, increase the complexity of GAFD flows and offer a valuable platform for controlled experimental studies [6].

Multiphase flows pose major challenges for numerical modeling and are ubiquitous in natural systems. Experimental studies target applications ranging from marine plastic transport [7] and dune morphodynamics [8] to soil erosion [9] and metal-silicate differentiation during planetary accretion [10].

Stratification and rotation are fundamental components of GAFD, driving instabilities such as baroclinic modes [11]. They govern complex flow regimes including jet dynamics [12] and mixing in stratified turbulence [13]. They also sustain internal waves—gravity and inertial, respectively—that share many characteristics but exhibit key differences [14]. Internal waves play a central role in geophysical and astrophysical dynamics, particularly through their nonlinear interactions

that sustain wave turbulence [15] and generate mean flow oscillations, exemplified by the quasi-biennial oscillation [16].

Magnetohydrodynamics (MHD) is a central component of GAFD, yet remains particularly challenging to investigate experimentally. Ambitious laboratory setups, often pushing the limits of current technology, have been developed to explore MHD phenomena. The dynamics of accretion disks has been a subject of intense experimental effort [17]. Dynamo action remains a long-standing goal, with several past attempts yielding limited success. Nonetheless, notable progress includes the laboratory-scale observation of magnetic field reversals [18]. New experimental platforms are now entering the arena offering new opportunities for exploration [19].

3. Conclusion

This special issue is intended for researchers in GAFD, scientists from adjacent disciplines, and early-career or prospective students. It also aims to foster dialogue across traditionally compartmentalized fields—including atmospheric sciences, oceanography, deep geophysics, planetology, astrophysics, fluid mechanics, and nonlinear physics. Finally, it highlights the role of experimental GAFD as a powerful tool for education and outreach, thanks to accessible and illustrative setups that make complex processes tangible for students and the broader public.

In conclusion, laboratory experiments remain a cornerstone of GAFD. They complement observations, theory, and numerical simulations, providing unique access to physical insight. This role is increasingly critical as we seek to understand the changing dynamics of our planet and the surprising behaviors emerging from newly explored planetary and stellar systems.

References

[1] G. Hadjerci, V. Bouillaut, B. Miquel, S. Aumaître and B. Gallet, "Radiatively driven convection: diffusivity-free regimes of geophysical and astrophysical flows in the laboratory", *C. R. Phys.* **25** (2024), no. S3, pp. 5–20.

[2] A. Pothérat and S. Horn, "Seven decades of exploring planetary interiors with rotating convection experiments", *C. R. Phys.* **25** (2024), no. S3, pp. 21–75.

[3] A. Tilgner, "Experiments on double diffusive convection", *C. R. Phys.* **25** (2024), no. S3, pp. 77–94.

[4] S. Carpy, M. Berhanu, M. Chaigne and S. C. du Pont, "Fingerprints of surface flows on solid substrates ablated by phase change: from laboratory experiments to planetary landscapes", *C. R. Phys.* **25** (2024), no. S3, pp. 95–142.

[5] L. Huguet, Q. Kriaa, T. Alboussière and M. L. Bars, "Solid–liquid phase change in planetary cores", *C. R. Phys.* **25** (2024), no. S3, pp. 143–181.

[6] J. Vidal, J. Noir, D. Cébron, F. Burmann, R. Monville, V. Giraud and Y. Charles, "Geophysical flows over topography, a playground for laboratory experiments", *C. R. Phys.* **25** (2024), no. S3, pp. 183–234.

[7] M. Poulain-Zarcos, N. Pujara, G. Verhille and M. J. Mercier, "Laboratory experiments related to marine plastic pollution: a review of past work and future directions", *C. R. Phys.* **25** (2024), no. S3, pp. 235–266.

[8] P. Claudin, S. C. du Pont and C. Narteau, "From lab to landscape-scale experiments for the morphodynamics of sand dunes", *C. R. Phys.* **25** (2024), no. S3, pp. 267–295.

[9] P. Philippe and N. Benahmed, "Quantifying soil surface erosion", *C. R. Phys.* **25** (2024), no. S3, pp. 297–332.

[10] R. Deguen, L. Huguet, M. Landeau, V. Lherm, A. Maller and J.-B. Wacheul, "Fluid dynamics of planetary differentiation", *C. R. Phys.* **25** (2024), no. S3, pp. 333–377.

[11] U. Harlander, M. V. Kurgansky, K. Speer and M. Vincze, "Baroclinic instability from an experimental perspective", *C. R. Phys.* **25** (2024), no. S3, pp. 379–426.

[12] P. Read, Y. Afanasyev, J. Aurnou and D. Lemasquerier, "Eddy-driven zonal jet flows in the laboratory", *C. R. Phys.* **25** (2024), no. S3, pp. 427–477.

[13] A. Lefauve, "Geophysical stratified turbulence and mixing in the laboratory", *C. R. Phys.* **25** (2024), no. S3, pp. 479–507.

[14] S. Joubaud, S. Boury and P. Odier, "Internal gravity waves versus inertial waves in the laboratory", *C. R. Phys.* **25** (2024), no. S3, pp. 509–535.

[15] P.-P. Cortet and N. Lanchon, "Turbulence of internal gravity waves in the laboratory", *C. R. Phys.* **25** (2024), no. S3, pp. 537–556.

[16] B. Semin and F. Pétrelis, "Quasi-biennial oscillation: laboratory experiments", *C. R. Phys.* **25** (2024), no. S3, pp. 557–581.
[17] C. Gissinger, "Laboratory modeling of MHD accretion disks", *C. R. Phys.* **25** (2024), no. S3, pp. 583–610.
[18] F. Pétrélis, "Experimental dynamos: from models to applications to the geodynamo", *C. R. Phys.* **25** (2024), no. S3, pp. 611–627.
[19] F. Stefani, S. Anders, S. Eckert, et al., "The DRESDYN precession experiment", *C. R. Phys.* **25** (2024), no. S3, pp. 629–647.

ACADÉMIE DES SCIENCES
INSTITUT DE FRANCE

Comptes Rendus. Physique
2024, Vol. 25, Special issue S3, p. 5-20
https://doi.org/10.5802/crphys.207

Review article / *Article de synthèse*

Geophysical and astrophysical fluid dynamics in the laboratory / *Dynamique des fluides géophysiques et astrophysiques au laboratoire*

Radiatively driven convection: diffusivity-free regimes of geophysical and astrophysical flows in the laboratory

La convection engendrée par forçage radiatif, ou comment reproduire en laboratoire les régimes « ultimes » des écoulements géo- et astrophysiques

Gabriel Hadjerci [a], Vincent Bouillaut [b], Benjamin Miquel [c], Sébastien Aumaître [a] and Basile Gallet [*, a]

[a] Université Paris-Saclay, CNRS, CEA, Service de Physique de l'Etat Condensé, 91191 Gif-sur-Yvette, France

[b] Onera Châtillon, 92320, Châtillon, France

[c] Univ Lyon, CNRS, Ecole Centrale de Lyon, INSA Lyon, Université Claude Bernard Lyon 1, LMFA, UMR5509, 69130, Ecully, France

E-mail: basile.gallet@cea.fr (B. Gallet)

Abstract. We consider the turbulent heat transport induced by thermal convection. The widespread belief is that the transport properties of the turbulent flow should be independent of the tiny molecular diffusivities for asymptotically strong driving, but the associated "ultimate" scaling regime proves challenging to observe experimentally using standard convection cells (Rayleigh–Bénard geometry). We thus recently introduced an alternate experimental setup where convection is driven radiatively, with internal heating within the lower region of the body of fluid. This setup naturally leads to the ultimate regime of thermal convection. We then discuss how adding global rotation to the experimental setup has led to the first laboratory observation of the diffusivity-free regime of rapidly rotating turbulent convection, also known as the "geostrophic turbulence" scaling regime.

Résumé. Cet article traite du transport turbulent de chaleur engendré par convection thermique. Si la croyance dominante est que les propriétés de transport de l'écoulement turbulent sont asymptotiquement indépendantes des diffusivités moléculaires du fluide, ce régime dit « ultime » semble difficile à mettre en évidence dans les expériences traditionnelles de laboratoire (dispositif de Rayleigh–Bénard). Nous avons donc récemment développé un dispositif de convection par chauffage radiatif, dans lequel le fluide est chauffé en volume dans sa partie inférieure. Nous montrerons comment ce dispositif conduit naturellement à l'observation du régime ultime de convection thermique en laboratoire. Nous décrirons ensuite l'ajout

* Corresponding author

d'une rotation globale à ce dispositif expérimental, ingrédient important des écoulements géophysiques et astrophysiques. Nous montrerons en particulier comment ce dispositif a permis la première observation expérimentale du régime ultime de convection en rotation rapide, dit régime de « turbulence géostrophique ».

Keywords. turbulent convection, geophysical and astrophysical fluid dynamics, rotating turbulence.

Mots-clés. convection turbulente, dynamique des fluides géophysiques et astrophysiques, turbulence en rotation.

Funding. This research is supported by the European Research Council under grant agreement FLAVE 757239.

Manuscript received 24 May 2024, revised 12 September 2024, accepted 13 September 2024.

Thermal convection is a key driver of geophysical and astrophysical flows, be it in stellar and planetary interiors, in exoplanetary atmospheres, in the Earth ocean and in the oceans of outer solar system satellites [1–7]. In these various contexts the convective flow is typically strongly turbulent. A standard modeling assumption thus consists in assuming that the zeroth-law of turbulence applies [8]: the large-scale quantities should be related in a way that does not involve the tiny molecular diffusivities (of momentum, heat, or tracer concentration).

The vast majority of the physics literature on thermal convection focuses on the Rayleigh–Bénard (RB) convection setup, where a layer of fluid is sandwiched between a hot bottom plate and a cool top one. While arguably the simplest setup from a theoretical point of view, RB convection appears to be a questionable model for geophysical and astrophysical flows. Indeed, the diffusivity-free argument above suggests that the turbulent heat flux should be related to the temperature difference between the two plates in a way that does not involve the molecular diffusivities. As discussed in Section 1, this corresponds to the Nusselt number Nu (dimensionless heat flux) increasing with the Rayleigh number Ra (dimensionless temperature difference) as $Nu \sim Ra^{\gamma}$, with $\gamma = 1/2$. While the precise value of the exponent γ remains debated for the highest Ra achieved in laboratory experiments, all measured values lie in the range $0.26 \leq \gamma \leq 0.38$ [9–15], that is, the measured exponent is always strictly less than $1/2$ (restricting attention to smooth top and bottom plates, see below).

The lower value for the exponent γ results from the boundary layers adjacent to the top and bottom plates, which throttle the heat flux throughout the entire cell. Based on this observation, several alternate setups have been designed to mitigate the role of the boundary layers and observe diffusivity-free convection in the laboratory: convection in tall vertical channels [16–20], Rayleigh–Bénard convection with rough boundaries [21–27], and radiatively driven convection [28–30]. After briefly reviewing the results obtained using the first two experimental setups, we discuss radiatively driven convection in greater detail, with an emphasis on its ability to reproduce various diffusivity-free regimes of geophysical and astrophysical relevance.

In Section 1 we introduce standard RB convection together with the standard theoretical predictions for the exponent γ, before briefly reviewing results obtained in tall channel experiments and in RB experiments with rough boundaries. We introduce the radiatively driven convection setup in Section 2, focusing first on the observation of the diffusivity-free regime of non-rotating convection. In Section 3 we discuss the influence of rapid global rotation and the laboratory realization of the geostrophic turbulence scaling regime – the diffusivity-free or "ultimate" regime of rapidly rotating convection – using a rotating radiatively driven convection experiment. We conclude in Section 4.

1. A primer on Rayleigh–Bénard convection

The RB setup is sketched in Figure 1(a): a layer of fluid of height H lies between a warm bottom plate maintained at temperature $T_0 + \Delta T$ and a cool top plate maintained at temperature T_0. At the theoretical level, the layer can be considered infinite or periodic in the horizontal directions.

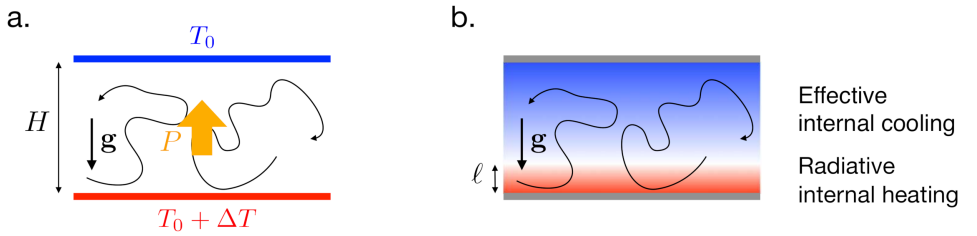


Figure 1. Rayleigh–Bénard convection (a) consists of a layer of fluid sandwiched between a hot bottom plate and a cool top one, the plates being kept at fixed temperatures. One typically measures the emergent heat flux. By contrast, radiatively driven convection (b) is powered by radiative heating and effective internal cooling, the boundaries being thermally insulated. One typically measures the emergent vertical temperature drop.

The density depends linearly on temperature T, $\rho = \rho_0[1 - \alpha(T - T_0)]$. Following the traditional Boussinesq approximation, the other coefficients characterizing the fluid's properties are independent of temperature: kinematic viscosity ν, thermal diffusivity κ, thermal expansion coefficient α, specific heat capacity C, etc. One can also show that, for small enough temperature drop ΔT, the density variations need only be included in the expression of the weight of the fluid element [31], while the velocity field can be considered incompressible (divergence-free).

There are two dimensionless control parameters for such Boussinesq RB convection. The Rayleigh number,

$$Ra = \frac{\alpha g \Delta T H^3}{\kappa \nu}, \tag{1}$$

characterizes the intensity of the thermal driving as compared to diffusive effects. The Prandtl number,

$$Pr = \frac{\nu}{\kappa}, \tag{2}$$

characterizes the relative importance of viscosity and thermal diffusion. To some extent, Pr can be considered constant for a given fluid: $Pr \simeq 7$ for water around room temperature, $Pr \simeq 3 \times 10^{-2}$ for liquid metals, $Pr \ll 1$ in typical astrophysical settings.

At low Rayleigh number the fluid remains motionless, with warm fluid sitting below heavier cooler fluid and heat diffused from the bottom to the top plate. However, this situation becomes unstable at stronger driving amplitude, that is, above a threshold value Ra_c of the Rayleigh number. Cellular motion arises, the system trying to reach the lower-potential-energy state where heavy fluid lies below lighter fluid. After reaching saturation, the flow is typically steady slightly above threshold and destabilizes at higher values of Ra through secondary instabilities. At very high Ra the flow is turbulent. As compared to the diffusive state, convective motion greatly enhances the heat transport from the bottom to the top plate. Indeed, fluid elements receive heat near the bottom plate, rise, and eventually deposit the heat at the cool top plate. Such convective transport is very efficient and greatly dominates over diffusive transport for large Rayleigh number, $Ra \gg Ra_c$. The overall efficiency of the heat transport can be characterized using the mean heat flux P transferred across any horizontal surface $z = \text{const.}$ in statistically steady state. Non-dimensionalizing this heat flux P with the diffusive heat flux of the steady motionless state leads to the Nusselt number:

$$Nu = \frac{PH}{\rho_0 C \kappa \Delta T}. \tag{3}$$

The heat flux P is a central quantity of the convection system, related to most other global quantities of interest. The heat flux P is directly proportional to the rate of mechanical energy input into the system, which in statistically steady state is balanced by viscous dissipation. The heat flux P is also related to the input of buoyancy variance into the system, the latter being balanced by turbulent mixing. A significant fraction of the research on thermal convection has thus been devoted to the determination of the scaling behavior of Nu as a function of Ra and Pr in controlled laboratory experiments and numerical simulations. The goal is to determine the behavior of Nu at asymptotically large Ra, and one typically seeks a power-law of the form $Nu \sim Ra^{\gamma} Pr^{\chi}$. However, two competing theoretical predictions have been put forward for the values of the exponents γ and χ.

1.1. *"Classical" scaling regime*

The classical theory is based on the observation that the temperature is almost homogeneous in the interior of high-Ra RB convection, with sharp gradients located within the boundary layers adjacent to the top and bottom plates. The interpretation is that the bulk turbulent flow efficiently mixes temperature, hence the isothermal profile in the interior of the domain. However, fluid hardly moves (in the vertical direction) near the top and bottom plates, hence the existence of boundary layers connecting the isothermal interior with the boundary values of the temperature field. Because the fluid hardly moves near the boundaries, heat transfer is dominated by diffusion in the boundary layers. Assuming that diffusive transfer across the boundary layers throttles the overall heat flux, we estimate P as

$$P \sim \frac{\rho_0 C \kappa \Delta T}{\delta} \tag{4}$$

where δ denotes the thickness of the thermal boundary layer. The boundary layer thickness δ can be deduced from a marginal stability argument initally articulated by Howard [32]: the Rayleigh number based on δ is comparable to the threshold Rayleigh number for thermal convection,

$$Ra^{(\delta)} = \frac{\alpha g \Delta T \delta^3}{\kappa \nu} \simeq Ra_c \,. \tag{5}$$

The rationale is the following: if δ were much thinner than (5), the boundary layer could grow diffusively. However, if δ were greater than the estimate (5), the boundary layer itself would become convectively unstable. The boundary layer would then spontaneously erode and δ would decrease. The conclusion is that, in statistically steady state, the boundary layer thickness δ is given by (5), where Ra_c is a constant number, typically of the order of 10^3. Substituting the estimate (5) for δ into equation (4) yields, after multiplication by $H/(\rho_0 C \kappa \Delta T)$:

$$Nu \sim \frac{H}{\delta} \sim Ra^{1/3} \,, \tag{6}$$

that is, $\gamma = 1/3$ and $\chi = 0$.

1.2. *Diffusivity-free or "ultimate" scaling regime*

The competing theoretical prediction, attributed to Spiegel and Kraichnan [33–35], is based on the zeroth law of turbulence. In a loose sense, the law states that large-scale quantities in a turbulent flow are related in a way that does not involve the tiny molecular diffusivities. In the present situation, one seeks a scaling relation between P and ΔT that does not involve κ nor ν. Start from the general scaling relation:

$$Nu \sim Ra^{\gamma} Pr^{\chi} \,. \tag{7}$$

Demanding that P and ΔT be related in a way that does not involve ν leads to $\chi = \gamma$ so that:

$$Nu \sim (Ra \times Pr)^{\gamma} . \tag{8}$$

Remembering that κ appears at the denominator of Nu, the only way for P and ΔT to be related in a way that does not involve κ is to have the right-hand side of (8) be inversely proportional to κ. We conclude that:

$$Nu \sim \sqrt{Ra \times Pr}, \tag{9}$$

that is, $\gamma = \chi = 1/2$. The scaling relation (9) is sometimes attributed to E.A. Spiegel [33,34], who is said to have put forward the idea in an astrophysical context without publishing it. In the meantime, his then postdoc advisor R.H. Kraichnan published a similar prediction, up to logarithmic corrections [35]. Kraichnan's approach consists in arguing that the boundary layers of the classical theory above should become turbulent at sufficiently high Rayleigh number. He assumes that a turbulent velocity boundary layer arises at large Ra, and that this turbulent boundary layer resembles those of standard shear flow turbulence, with a logarithmic layer and a viscous sublayer in the immediate vicinity of the boundary. This structure for the boundary layer leads to the prediction (9) divided by a logarithmic correction in Rayleigh number. In the physics and fluid dynamics community the scaling-law (9) is often referred to as the "ultimate" scaling regime of convection, possibly because according to Kraichnan the velocity boundary layers should ultimately become turbulent as Ra increases. In the astrophysics community, (9) is referred to as the mixing-length scaling-law and is believed to be the relevant scaling-law for the extreme parameter regimes of astrophysical flows.

1.3. *Non-standard RB setups to achieve the diffusivity-free regime*

As discussed above, for standard RB convection the measured heat transport exponent γ is significantly smaller than 1/2 as a result of the throttling effect of the boundary layers. Insightful alternate experimental setups were therefore designed to mitigate the role of the boundary layers.

Among the different strategies that have been deployed, one option consists in studying convection in a narrow vertical channel connecting two large reservoirs of cool and warm fluid at top and bottom, respectively. The goal is to have a tall enough channel for the system to be considered virtually infinite in the vertical direction. One then seeks a relation between the heat flux and the bulk vertical temperature *gradient*. One difficulty is then to identify the relevant lengthscale to define the associated dimensionless numbers. In early experiments, Gibert et al. [16] employed a mixing-length based on the ratio of the temperature fluctuations to the temperature gradient. With this definition, the resulting Nusselt number increases with the square root of the resulting Rayleigh number, indicating diffusivity-free scaling. However, it was further shown in Ref. [19,20] that the mixing-length scales as the width L of the domain: as a consequence, the turbulent heat flux in tall vertical channels is related to the vertical temperature gradient in a way which does not involve the molecular diffusivities, but which explicitly involves the width L of the domain. While such a diffusivity-free regime is a significant achievement at the fundamental level, this strong dependence on lateral width makes the setup ill-suited as a model of geophysical or astrophysical flows. Indeed, the latter flows typically correspond the limit $L \to \infty$ for fixed height H, opposite to the limit considered in tall vertical channels. As an alternative, one may try to reach this $L \to \infty$ regime while avoiding the top and bottom boundary layers by simulating thermal convection numerically using periodic boundary conditions in the vertical direction. However, in such numerical simulations the heat flux diverges as a result of the emergence of "elevator" modes. The conclusion seems to be that convective flows in the horizontally infinite plane layer are always aware of the height H of the layer.

An alternative strategy to disrupt the throttling effect of the boundaries consists in replacing the smooth top and bottom boundaries by rough plates. This approach leads to an increased value for the exponent γ. The latter reaches $1/2$ in some experiments, the precise value of the exponent and of the prefactor depending on details of the roughness elements (see e.g. Refs. [22,27]). The exponent was observed to revert to a more modest value at higher Rayleigh number in some experiments and idealized numerical simulations [27,36,37], with a high-Ra value close to $1/3$, when the thin boundary layer follows the roughness elements. Multiscale roughness (a fractal boundary) may be a way to disrupt the boundary layers up to arbitrarily high Rayleigh number [38].

Additionally, in other experiments with regular roughness elements the exponent remains close to $1/2$ up to the highest Ra achieved experimentally [24]. It could be that the relaxation to $\gamma = 1/3$ occurs at even higher Ra, or that the roughness has helped the system transition to an ultimate scaling regime. As compared to Kraichnan's theory, this ultimate regime would be characterized by a prefactor that depends on details of the roughness of the two plates.

In the following section we discuss radiative heating as an alternate way to observe diffusivity-free thermal convection, in a way that survives the limit $L \to \infty$. As compared to the use of rough plates, radiative heating comes with its own advantages and challenges. For instance, rough plates are much simpler to implement in a pre-existing RB experiment than radiative heating. On the other hand, radiative heating is arguably simpler to handle at the theoretical level: in contrast to rough-plate convection, radiatively driven convection is amenable to linear stability analysis with a well-defined threshold Rayleigh number for the emergence of convection. Additionally, the high-Ra exponent does not depend on the details of the structure of a rough boundary. In particular, radiatively driven convection is easily simulated numerically using high-accuracy pseudo-spectral solvers [39].

2. Radiatively driven convection

2.1. *An experimental setup to bypass the boundary layers*

One way to mitigate the throttling effect of the boundary layers is to input the heat predominantly beyond the latter, directly into the bulk turbulent flow as represented in Figure 1(b). We put this idea into practice by employing radiative heating in the experimental setup described thereafter and sketched in Figure 2. A cylindrical tank of radius 10cm with a transparent bottom plate contains a mixture of water and carbon-black dye. A powerful spotlight shines at the tank from below, and the absorption of light by the dye induces radiative heating. Following Beer–Lambert's law, the light intensity decreases exponentially with height z measured from the bottom of the tank, over an e-folding absorption scale ℓ, and so does the internal heat source. The absorption length ℓ is easily tuned through the concentration of the dye. For large dye concentration the heat source is localized in the immediate vicinity of the bottom plate, with ℓ much smaller than the thickness of the velocity and temperature boundary layers. Such a heat source is similar to an imposed bottom heat flux; we thus expect a throttling effect associated with the presence of the bottom boundary layer, in a similar fashion to RB convection. By contrast, using lower dye concentration, ℓ can be made much thicker than the boundary layers. The heat is then directly input into the bulk turbulent flow, bypassing the high thermal impedance of the boundary layers.

Achieving a clean exponentially decreasing heat source inside the tank requires a few precautions. The light emitted by the spotlight first travels through a water-cooled water tank which efficiently filters out infrared radiation. In addition, we use carbon-black dye, which absorbs visible light at the same rate regardless of wavelength. Assuming a horizontally homogeneous light flux, the internal radiative heat source inside the tank reads $(P/\ell)\, e^{-z/\ell}$, where P denotes the energy

flux radiated by the spotlight in the form of visible light (P is expressed in units of W.m^{-2}). Describing the experiment within the framework of the Boussinesq approximation, the governing equation for the temperature $T(x,y,z,t)$ inside the tank reads [28]:

$$\partial_t T + \mathbf{u}\cdot\nabla T = \kappa\nabla^2 T + \frac{P}{\rho_0 C\ell} e^{-z/\ell}, \tag{10}$$

where $\mathbf{u}(x,y,z,t)$ denotes the velocity field.

2.2. *Secular heating and effective internal cooling*

Cooling the fluid through the top surface would necessarily introduce boundary layers, which would negate the careful efforts deployed to bypass these layers on the heating side [40]. Instead, we resort to secular heating as an analog to internal cooling. Assuming adiabatic boundary conditions, one can average equation (10) over space to obtain the evolution equation for the spatially averaged temperature $\overline{T}(t)$:

$$\frac{\mathrm{d}\overline{T}}{\mathrm{d}t} = \frac{P}{\rho_0 CH}\left(1 - e^{-H/\ell}\right) \simeq \frac{P}{\rho CH}, \tag{11}$$

where H denotes the height of fluid and we have assumed $\ell \ll H$ to obtain the last equality. Equation (11) indicates that the mean temperature inside the tank increases linearly with time, because heat is supplied at a constant rate. To investigate the internal temperature structure

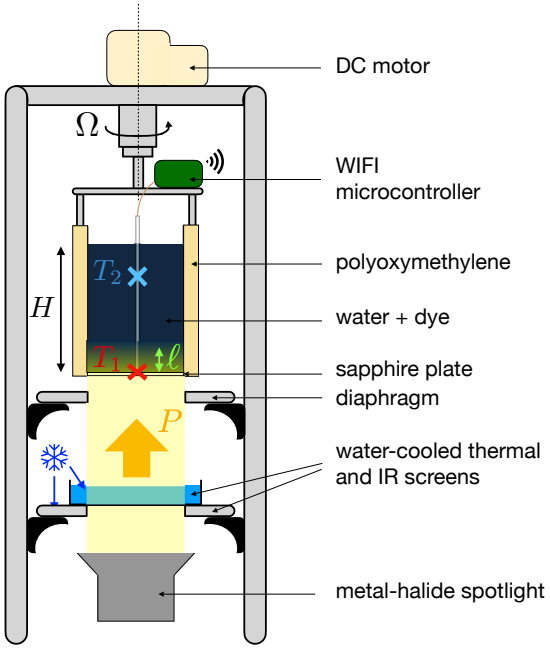


Figure 2. Radiatively driven convection in the laboratory. A powerful spotlight shines from below at a mixture of water and dye. The resulting internal heat source decreases exponentially with height over the absorption length ℓ, delivering a total heat flux P. With the goal of studying both rotating and non-rotating convection, the cylindrical tank is attached from above to a DC motor. Two thermocouples T_1 and T_2 measure the vertical temperature drop.

within the fluid, one can introduce the variable $\theta(x,y,z,t) = T(x,y,z,t) - \overline{T}(t)$ which represents the temperature fluctuations around the spatial average and obeys:

$$\partial_t \theta + \mathbf{u}\cdot\nabla\theta = \kappa\Delta\theta + \frac{P}{\rho_0 C}\left(\frac{e^{-z/\ell}}{\ell} - \frac{1}{H}\right). \tag{12}$$

In the parentheses is the radiative heat source, together with an effective uniform heat sink that balances the heat source over space average. Secular heating thus induces an effective uniform internal cooling in equation (12), offering a way to avoid any boundary layer on the cooling side. As for the traditional Boussinesq set of equations, equation (12) is coupled to the incompressible Navier–Stokes equation, the latter including a buoyancy term proportional to θ. Solutions to this set of equations reach a statistically steady state in the long time limit, which we wish to characterize. To wit, we measure a first temperature $T_1(t)$ using a thermocouple touching the bottom plate of the tank, and a second temperature $T_2(t)$ using second probe placed in the bulk of the fluid volume (at $z = H/2$ for non-rotating experiments and at $z = 3H/4$ for rotating experiments). At the outset of an experiment we fill the tank up to a height H with cold water mixed with carbon-black dye, before turning on the spotlight. While the two temperature signals drift with time as a result of secular heating, after an initial transient phase the temperature drop $T_1(t) - T_2(t)$ reaches a statistically steady state. We denote as ΔT the resulting time-averaged temperature drop, measured in the statistically steady phase. Examples of timeseries $T_1(t)$ and $T_2(t)$ can be found in Refs. [28,30]. Because of the large body of fluid, the rise of the mean temperature is fairly slow. This allows for an extended statistically steady state lasting many turnover times, while having a mean temperature that remains close to room temperature. The Boussinesq approximation is very well satisfied in this quasi-stationary state (as further confirmed by the good agreement with numerical simulations in Refs. [28,30]).

The knowledge of both the flux and the temperature drop gives us access to the Rayleigh number Ra and Nusselt number Nu. While these two parameters allow for a clear comparison with the RB literature, none of them is a true control parameter of our experiment. We thus also define the flux-based Rayleigh number Ra_P as:

$$Ra_P = Nu \times Ra = \frac{\alpha g P H^4}{\rho C \kappa^2 \nu}. \tag{13}$$

Although not independent from Ra and Nu, the flux-based Rayleigh number Ra_P is a true control parameter of the experiment, in the sense that it does not depend on the response of the flow and hence can be specified at the outset of an experimental run.

2.3. *Experimental observation of the ultimate scaling regime*

A suite of experiments typically consists in fixing the value of the dimensionless absorption length ℓ/H and performing experimental runs for various heights H of fluid. Lepot et al. [28] initially focused on two limiting situations of interest: $\ell/H < 10^{-4}$, where the heating is similar to fixed flux RB convection, and $\ell/H = 0.05$, which is sufficient to bypass the boundary layers. The resulting plots Nu versus Ra clearly confirm the intuition discussed above: $\ell/H < 10^{-4}$ leads to the classical regime of convection, with a best-fit exponent $\gamma = 0.31$, close to 1/3. By contrast, $\ell/H = 0.05$ leads to a best-fit exponent $\gamma = 0.54$, very close to the prediction 1/2 of the ultimate scaling regime. The experiment thus provides an efficient way to bypass the boundary layers and observe ultimate scaling regimes of convection in the laboratory.

The transition between the two regimes was further characterized by Bouillaut et al. [29], who performed additional experiments for various values of ℓ/H. The resulting dataset is shown in the (Ra, Nu) plane in Figure 3. Low ℓ/H data are compatible with the classical scaling regime, while high ℓ/H data are compatible with the ultimate or diffusivity-free scaling prediction.

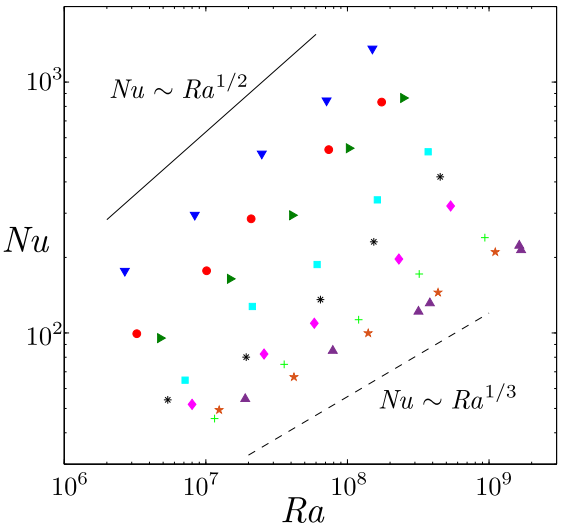


Figure 3. Nusselt number as a function of the Rayleigh number for various values of the absorption length ℓ. At fixed Ra, the Nusselt number increases with ℓ/H. Symbols are $\triangle$: $\ell/H = 5\times10^{-6}$ m; $\star$: $\ell/H = 0.0052$; $+$: $\ell/H = 0.0030$; $\Diamond$: $\ell/H = 0.0060$; $*$: $\ell/H = 0.012$; $\square$: $\ell/H = 0.024$; $\triangleright$: $\ell/H = 0.048$; $\bigcirc$: $\ell/H = 0.05$; $\triangledown$: $\ell/H = 0.096$. The solid and dashed lines are eyeguides.

Additionally, one observes that the prefactor of the scaling law depends on the dimensionless absorption length ℓ/H. Bouillaut et al. [29] introduce a simple "roll" model to predict the dependence of Nu on ℓ/H. The main idea consists of following the trajectory of a fluid element traveling at the periphery of the large-scale roll-shaped mean circulation of the turbulent flow. The fluid heats up as it travels within the radiatively heated region near the bottom of the tank, subsequently sharing that excess heat as it rises into the bulk region (see Ref. [29] for a detailed description of the model). Assuming that the speed of the mean circulation scales as a free-fall velocity, Bouillaut et al. [29] conclude that the Nusselt number should be proportional to ℓ/H for fixed Ra in the diffusivity-free regime. One thus expects data points pertaining both to the classical scaling regime and the ultimate scaling regime to collapse onto a single master curve when plotting $Nu(\ell/H)^2$ as a function of $Ra(\ell/H)^6$. Indeed, the classical scaling regime $Nu \sim Ra^{1/3}$corresponds to $Nu(\ell/H)^2 \sim [Ra(\ell/H)^6]^{1/3}$, while the ultimate scaling regime $Nu \sim (\ell/H)Ra^{1/2}$ corresponds to $Nu(\ell/H)^2 \sim [Ra(\ell/H)^6]^{1/2}$. As shown in Figure 4, this representation indeed leads to a good collapse of the data onto a single master curve, which provides a validation of the dependence of Nu on ℓ/H predicted by Bouillaut et al. [29].

For large enough $Ra(\ell/H)^2$ the boundary layers are bypassed. However, there is still a sub-dominant amount of heat that is directly input into the boundary layers. As inferred by Bouillaut et al. [29] through a refinement of their roll model and further confirmed using numerical simulation in Ref. [41], this process affects the high-Prandtl-number regime with no-slip boundary conditions, whereas it is negligible for low Prandtl number or stress-free boundary conditions (regardless of Pr).

2.4. *Maximal heat transport efficiency?*

The quest for the ultimate regime of thermal convection is deeply connected to the conjecture that turbulent convection may self-organize to maximize the heat transport. This idea, initially

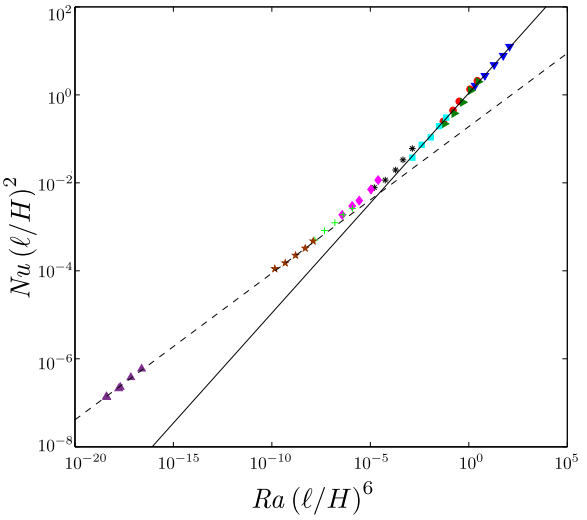


Figure 4. Rescaled Nusselt number as a function of the rescaled Rayleigh number, for various values of the absorption length ℓ (same symbols as Figure 3). The data indicate a clear transition from an exponent $\gamma = 1/3$ (dashed line) to an exponent $\gamma = 1/2$ (solid line).

put forward by Malkus [42], was addressed at a more mathematical level by Howard [32], who solved the associated variational problem and obtained an upper bound on the Nusselt number of the form $Nu \simeq Ra^{1/2}$, that is, $\gamma \leq 1/2$ (see also Refs. [43,44]). This bound only holds for the RB setup, however, and it turns out that radiatively driven convection allows for higher values of the exponent γ. Specifically, an analytical high-Rayleigh-number asymptotic solution to convection driven by internal heat sources and sinks was derived in Ref. [45]. The asymptotic solution achieves heat transport beyond the ultimate scaling regime, with $Nu \sim Ra$. While this asymptotic solution is observed in 2D DNS of radiatively driven convection with suitable boundary conditions [45], it is not realized in 3D DNS nor is it realized in the above-mentioned laboratory experiments. Instead, as intuition suggests, the high-Reynolds-number experimental flow is strongly turbulent and does not realize the idealized laminar flow solution computed by [45]. Spurred by this observation, the bounding procedure was subsequently refined in Ref. [46] by distinguishing between laminar versus turbulent branches of solutions (the bounding procedure was also extended to arbitrary distributions of heat sources and sinks, see Ref. [47]). The authors of Ref. [46] show that, for branches of flow solutions that obey the zeroth-law of turbulence (viscous energy dissipation rate independent of viscosity), the scaling exponent γ is bounded from above by $1/2$ at asymptotically high Ra (in other words, only non-turbulent flows can achieve $\gamma > 1/2$). Because the experimental data reviewed above are compatible with $\gamma = 1/2$, one concludes that radiatively driven convection maximizes the heat transport over turbulent flow solutions [46].

3. Radiatively driven rotating convection: observation of the diffusivity-free scaling regime

Radiatively driven convection is an appealing experimental setup to include the various additional ingredients of geophysical and astrophysical flows, such as global rotation or magnetic

field. The goal is to achieve the diffusivity-free regimes that are typically invoked when modeling geophysical and astrophysical convective flows, but remain out of reach of RB experiments [48–50] (see Ref. [51] for the rotating version of the "classical" scaling regime discussed in Section 1.1). As compared to RB convection using plates with regular roughness, an appealing aspect of radiatively-driven convection is that it comes with no preferred scale in the horizontal directions. This feature is particularly desirable when convection is subject to rotation or magnetic field, because these two ingredients tend to select a specific horizontal scale. The competition between the roughness scale of the plate and the preferred scale of rotating/magnetic convection may then complicate the analysis (see the careful studies in Refs. [52,53]). At the numerical level, rotating convection with periodic boundary conditions in the vertical direction [54] is also subject to "elevator modes" (see e.g. Ref. [55] for a discussion).

3.1. *Rapid rotation: the geostrophic turbulence scaling regime*

We consider convection subject to global rotation around the vertical axis z, restricting attention to astro- and geophysically relevant cases where centrifugal effects are negligible. Rotation then enters the governing equations through the addition of the Coriolis term in the Navier–Stokes equation. The rotation rate Ω is an additional dimensional control parameter of the system, its dimensionless counterpart being the Ekman number $E = \nu/(2\Omega H^2)$. The Nusselt number is a function of the three control parameters of the system:

$$Nu = \mathscr{F}(Ra_P, Pr, E)\,, \tag{14}$$

where $\mathscr{F}$ generically denotes the existence of some scaling relation. Due to the presence of an additional dimensionless parameter as compared to the non-rotating case, one cannot derive scaling predictions solely based on the dimensional analysis arguments introduced in Section 1.

Additional progress can be made by focusing on the rapidly rotating regime, $E \ll 1$. In this asymptotic regime, the critical (flux-based) Rayleigh number for the emergence of convection increases as $Ra_P^{(c)} \sim E^{-4/3}$. Crucially, Julien and Knobloch performed an asymptotic reduction of the rotating Boussinesq system [56,57]. The resulting reduced model was extensively studied by means of numerical simulations [58,59]. Most importantly, the reduced model indicates that, in the asymptotic regime of rapid rotation, the control parameter is the supercriticality $Ra_P/Ra_P^{(c)} \sim Ra_P E^{4/3}$. That is, instead of Ra_P, Pr and E appearing independently in the equations, only Pr and the grouping $Ra_P E^{4/3}$ arise in the reduced set of equations describing the asymptotic rapidly rotating regime. The Nusselt number thus depends only on these two control parameters:

$$Nu = \mathscr{F}(Ra_P E^{4/3}, Pr)\,, \tag{15}$$

provided rotation is fast enough. The next step consists in combining equation (15) with the dimensional analysis arguments put forward in Section 1. Specifically, assuming the existence of a diffusivity-free regime of rapidly rotating convection amounts to demanding that the function $\mathscr{F}$ in (15) be such that κ and ν can be crossed out on both sides of the equation. This leads to the "geostrophic turbulence" (GT) scaling regime of rapidly rotating convection [58]:

$$Nu \sim Ra_P^{3/5} E^{4/5} Pr^{-1/5}\,. \tag{16}$$

To our knowledge, this scaling prediction was initially put forward in Ref. [1] based on phenomenological arguments. In the context of rapidly rotating RB convection, it is more often cast in terms of the standard temperature-based Rayleigh number. Substituting $Ra_P = Nu \times Ra$ into (16):

$$Nu \sim Ra^{3/2} E^2 Pr^{-1/2}\,. \tag{17}$$

3.2. *Experimental realization*

As reported in Ref. [30], the radiatively driven convection setup can be adapted to include global rotation, allowing for an experimental realization of the insightful but somewhat academic numerical setup considered in Ref. [60]. Because no cooling is required and radiative heating is contactless, one can simply attach the tank from above to a motor and spin it around the vertical axis, see Figure 2. We perform the temperature measurements in the rotating frame, using thermocouples located on the axis of the cylinder and connected to a microcontroller. The tank is filled with cool water before rotation is turned on at a constant rate Ω. After a waiting phase of at least ten minutes, allowing for the fluid to settle in solid body rotation, we turn on the spotlight. The dimensional control parameters are varied in the range $H \in [10, 25]$cm and $\Omega \leq 85$rpm, to avoid centrifugal effects. Specifically, suites of experiments were performed in Ref. [30] with fixed height H of fluid and various values of the rotation rate Ω, for two values of the dimensionless absorption length, $\ell/H = 0.024$ and $\ell/H = 0.048$ (see Ref. [30] and the associated supplementary information for tables of parameter values and estimates of the negligible centrifugal effects).

A convenient way to plot the resulting dataset consists in introducing diffusivity-free parameters. The diffusivity-free flux-based Rayleigh number is defined as $\mathscr{R} = Ra_P E^3/Pr^2$, while the diffusivity-free Nusselt number is defined as $\mathscr{N} = NuE/Pr$. These two dimensionless combinations do not involve κ nor ν. If the system indeed achieves diffusivity-free convection, then the entire dataset should collapse onto a master curve in the $(\mathscr{R}, \mathscr{N})$ plane. Additionally, if this diffusivity-free regime is the GT regime (16), then the master curve must be a power-law $\mathscr{N} \sim \mathscr{R}^{3/5}$ (as obtained by substituting $Nu = \mathscr{N} Pr/E$ and $Ra_P = \mathscr{R} Pr^2/E^3$ into (16)).

The entire dataset collected by [30] is shown in Figure 5 in the $(\mathscr{R}, \mathscr{N})$ plane. The dataset does collapse onto a master curve, with two distinct power-law behaviors. For larger values of $\mathscr{R}$, the master curve agrees well with a power-law $\mathscr{N} \sim \mathscr{R}^{1/3}$, which corresponds to the ultimate regime of non-rotating convection (9) recast in terms of $\mathscr{N}$ and $\mathscr{R}$. By contrast, for lower values or $\mathscr{R}$ (say for $\mathscr{R} \lesssim 3 \times 10^{-7}$) the data agrees well with the GT scaling prediction $\mathscr{N} \sim \mathscr{R}^{3/5}$. We conclude that radiatively driven convection transitions from the ultimate regime of non-rotating convection to the ultimate regime of rapidly rotating convection as rotation increases. To facilitate comparison with numerical studies [58,60–62], Hadjerci et al. [63] show that the transition value $\mathscr{R} \simeq 3 \times 10^{-7}$ to enter the GT regime corresponds to a transition value of approximately 0.03 for the convective Rossby number, within the expected range [64]. That being said, the scatter around the master curve is arguably greater in the crossover region between the two asymptotic regimes, which suggests the possible existence of an intermediate regime involving the diffusivities.

Beyond the sole heat transfer, the GT regime comes with scaling predictions for the temperature fluctuations, the flow speed and the horizontal scale of the flow [64]. Radiatively driven rotating convection was recently shown to obey these additional scaling predictions based on further processing of the experimental data from Ref. [30], together with a suite of Direct Numerical Simulations of rotating radiatively driven convection using the solver Coral [63].

4. Conclusion

Radiatively driven convection provides an efficient way to achieve diffusivity-free convection in the laboratory. At the theoretical level, radiatively driven convection in the horizontally infinite plane layer is well-suited for theoretical studies, from linear stability analysis to upper-bound theory. This relative simplicity also makes radiatively driven convection well-suited to include the additional physical ingredients encountered in geophysical and astrophysical contexts, such as rotation or magnetic field. As an example, the rapidly rotating radiatively driven convection experiment has led to the first experimental observation of the diffusivity-free GT regime of

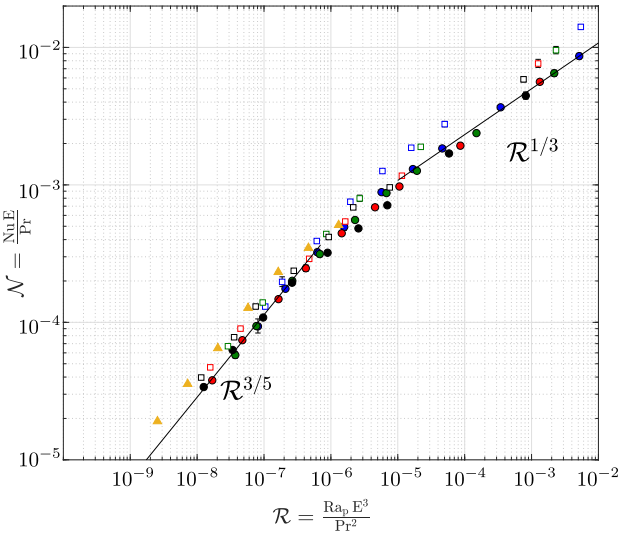


Figure 5. Diffusivity-free Nusselt number $\mathscr{N}$ as a function of the diffusivity-free flux-based Rayleigh number $\mathscr{R}$ for various fluid heights: blue, $H = 10$ cm, $Ra_P \simeq 2.5.10^{10}$; green, $H = 15$ cm, $Ra_P \simeq 1.3.10^{11}$; red, $H = 20$ cm, $Ra_P \simeq 3.5.10^{11}$; black, $H = 25$ cm, $Ra_P \simeq 9.10^{11}$. The dimensionless absorption length is $\ell/H = 0.024$ (filled circles) or $\ell/H = 0.048$ (open squares). The triangles are DNS data for $Ra_P = 10^{12}$, $Pr = 7$, and $\ell/H = 0.048$ (see Ref. [30]). In the rapidly rotating regime $\mathscr{R} \lesssim 3.10^{-7}$, the master curve agrees closely with the geostrophic turbulence scaling prediction $\mathscr{N} \sim \mathscr{R}^{3/5}$, shown as an eye guide. Experimental and numerical error bars are visible when larger than the symbol size.

rapidly rotating convection. Magnetic field could be the next ingredient to add, for instance by designing a radiatively driven liquid metal convection experiment driven by induction heating.

While we believe radiatively driven convection is interesting in itself, independently of RB convection, an intriguing question is whether the two systems can be related at the quantitative level. Can one infer the asymptotic behavior of the latter setup based on measurements performed using the former setup? Is there any link between the diffusivity-free regimes potentially arising in both systems? We are currently investigating this issue further and hope to report on it soon.

Declaration of interests

The authors do not work for, advise, own shares in, or receive funds from any organization that could benefit from this article, and have declared no affiliations other than their research organizations.

References

[1] D. J. Stevenson, "Turbulent thermal convection in the presence of rotation and a magnetic field: A heuristic theory", *Geophys. Astrophys. Fluid Dyn.* **12** (1979), no. 1, pp. 139–169.

[2] J. Marshall and F. Schott, "Open-ocean convection: Observations, theory, and models", *Rev. Geophys.* **37** (1999), no. 1, pp. 1–64.

[3] J. M. Aurnou, M. A. Calkins, J. S. Cheng, et al., "Rotating convective turbulence in Earth and planetary cores", *Phys. Earth Planet. Inter.* **246** (2015), pp. 52–71.

[4] M. F. De Jong and L. De Steur, "Strong winter cooling over the Irminger Sea in winter 2014–2015, exceptional deep convection, and the emergence of anomalously low SST", *Geophys. Res. Lett.* **43** (2016), no. 13, pp. 7106–7113.

[5] K. M. Soderlund, "Ocean dynamics of outer solar system satellites", *Geophys. Res. Lett.* **46** (2019), no. 15, pp. 8700–8710.

[6] B. W. Hindman, N. A. Featherstone and K. Julien, "Morphological Classification of the Convective Regimes in Rotating Stars", *Astrophys. J.* **898** (2020), no. 2, p. 120.

[7] S. Bire, W. Kang, A. Ramadhan, J.-M. Campin and J. Marshall, "Exploring ocean circulation on icy moons heated below", *J. Geophys. Res. Planets* **127** (2022), no. 3, article no. e2021JE007025.

[8] U. Frisch, *Turbulence: The Legacy of A.N. Kolmogorov*, Cambridge University Press, 1995.

[9] B. Castaing, G. Gunaratne, F. Heslot, et al., "Scaling of hard thermal turbulence in Rayleigh–Bénard convection", *J. Fluid Mech.* **204** (1989), pp. 1–30.

[10] S. Cioni, S. Ciliberto and J. Sommeria, "Strongly turbulent Rayleigh—Bénard convection in mercury: comparison with results at moderate Prandtl number", *J. Fluid Mech.* **335** (1997), pp. 111–140.

[11] A. Naert, T. Segawa and M. Sano, "High-Reynolds-number thermal turbulence in mercury", *Phys. Rev. E* **56** (1997), no. 2, R1302–R1305.

[12] X. Chavanne, F. Chillà, B. Chabaud, B. Castaing and B. Hébral, "Turbulent Rayleigh-–Bénard convection in gaseous and liquid He", *Phys. Fluids* **13** (2001), no. 5, article no. 1300.

[13] P.-E. Roche, F. Gauthier, R. Kaiser and J. Salort, "On the triggering of the Ultimate Regime of convection", *New J. Phys.* **12** (2010), no. 8, article no. 085014.

[14] X. He, D. Funfschilling, H. Nobach, E. Bodenschatz and G. Ahlers, "Transition to the Ultimate State of Turbulent Rayleigh–Bénard Convection", *Phys. Rev. Lett.* **108** (2012), no. 2, article no. 024502.

[15] C. R. Doering, "Absence of Evidence for the Ultimate State of Turbulent Rayleigh–Bénard Convection", *Phys. Rev. Lett.* **124** (2020), no. 22, article no. 229401.

[16] M. Gibert, H. Pabiou, F. Chillà and B. Castaing, "High-Rayleigh-Number Convection in a Vertical Channel", *Phys. Rev. Lett.* **96** (2006), no. 8, article no. 084501.

[17] M. Gibert, H. Pabiou, J.-C. Tisserand, B. Gertjerenken, B. Castaing and F. Chillà, "Heat convection in a vertical channel: Plumes versus turbulent diffusion", *Phys. Fluids* **21** (2009), no. 3, article no. 035109.

[18] J.-C. Tisserand, M. Creyssels, M. Gibert, B. Castaing and F. Chillà, "Convection in a vertical channel", *New J. Phys.* **12** (2010), no. 7, article no. 075024.

[19] M. R. Cholemari and J. H. Arakeri, "Axially homogeneous, zero mean flow buoyancy-driven turbulence in a vertical pipe", *J. Fluid Mech.* **621** (2009), pp. 69–102.

[20] S. S. Pawar and J. H. Arakeri, "Two regimes of flux scaling in axially homogeneous turbulent convection in vertical tube", *Phys. Rev. Fluids* **1** (2016), no. 4, article no. 042401.

[21] Y. Shen, P. Tong and K.-Q. Xia, "Turbulent Convection over Rough Surfaces", *Phys. Rev. Lett.* **76** (1996), no. 6, pp. 908–911.

[22] S. Ciliberto and C. Laroche, "Random Roughness of Boundary Increases the Turbulent Convection Scaling Exponent", *Phys. Rev. Lett.* **82** (1999), no. 20, pp. 3998–4001.

[23] Y.-B. Du and P. Tong, "Turbulent thermal convection in a cell with ordered rough boundaries", *J. Fluid Mech.* **407** (2000), pp. 57–84.

[24] P.-E. Roche, B. Castaing, B. Chabaud and B. Hébral, "Observation of the 1/2 power law in Rayleigh–Bénard convection", *Phys. Rev. E* **63** (2001), no. 4, article no. 045303.

[25] X.-L. Qiu, K.-Q. Xia and P. Tong, "Experimental study of velocity boundary layer near a rough conducting surface in turbulent natural convection", *J. Turbul.* **6** (2005), article no. N30.

[26] J.-C. Tisserand, M. Creyssels, Y. Gasteuil, H. Pabiou, M. Gibert, B. Castaing and F. Chillà, "Comparison between rough and smooth plates within the same Rayleigh—Bénard cell", *Phys. Fluids* **23** (2011), no. 1, article no. 015105.

[27] E. Rusaouën, O. Liot, B. Castaing, J. Salort and F. Chillà, "Thermal transfer in Rayleigh-–Bénard cell with smooth or rough boundaries", *J. Fluid Mech.* **837** (2018), pp. 443–460.

[28] S. Lepot, S. Aumaître and B. Gallet, "Radiative heating achieves the ultimate regime of thermal convection", *Proc. Natl. Acad. Sci. USA* **115** (2018), no. 36, pp. 8937–8941.

[29] V. Bouillaut, S. Lepot, S. Aumaître and B. Gallet, "Transition to the ultimate regime in a radiatively driven convection experiment", *J. Fluid Mech.* **861** (2019), article no. R5.

[30] V. Bouillaut, B. Miquel, K. Julien, S. Aumaître and B. Gallet, "Experimental observation of the geostrophic turbulence regime of rapidly rotating convection", *Proc. Natl. Acad. Sci. USA* **118** (2021), no. 44, article no. e2105015118.

[31] E. A. Spiegel and G. Veronis, "On the Boussinesq approximation for a compressible fluid", *Astrophys. J.* **131** (1960), pp. 442–447.

[32] L. N. Howard, "Heat transport by turbulent convection", *J. Fluid Mech.* **17** (1963), no. 3, pp. 405–432.

[33] E. A. Spiegel, "A Generalization of the Mixing-Length Theory of Turbulent Convection.", *Astrophys. J.* **138** (1963), pp. 216–225.

[34] E. A. Spiegel, "Convection in Stars I. Basic Boussinesq Convection", *Annu. Rev. Astron. Astrophys.* **9** (1971), no. 1, pp. 323–352.
[35] R. H. Kraichnan, "Turbulent Thermal Convection at Arbitrary Prandtl Number", *Phys. Fluids* **5** (1962), no. 11, pp. 1374–1389.
[36] Y.-C. Xie and K.-Q. Xia, "Turbulent thermal convection over rough plates with varying roughness geometries", *J. Fluid Mech.* **825** (2017), pp. 573–599.
[37] X. Zhu, R. J. A. M. Stevens, R. Verzicco and D. Lohse, "Roughness-facilitated local 1/2 scaling does not imply the onset of the ultimate regime of thermal convection", *Phys. Rev. Lett.* **119** (2017), no. 15, article no. 154501.
[38] S. Toppaladoddi, A. J. Wells, C. R. Doering and J. S. Wettlaufer, "Thermal convection over fractal surfaces", *J. Fluid Mech.* **907** (2021), article no. A12.
[39] B. Miquel, "Coral: a parallel spectral solver for fluid dynamics and partial differential equations", *J. Open Source Softw.* **6** (2021), no. 65, article no. 2978.
[40] S. Kazemi, R. Ostilla-Mónico and D. Goluskin, "Transition between boundary-limited scaling and mixing-length scaling of turbulent transport in internally heated convection", *Phys. Rev. Lett.* **129** (2022), no. 2, article no. 024501.
[41] B. Miquel, V. Bouillaut, S. Aumaître and B. Gallet, "On the role of the Prandtl number in convection driven by heat sources and sinks", *J. Fluid Mech.* **900** (2020), article no. R1.
[42] W. V. R. Malkus, "The heat transport and spectrum of thermal turbulence", *Proc. R. Soc. Lond., Ser. A* **225** (1954), no. 1161, pp. 196–212.
[43] C. R. Doering and P. Constantin, "Variational bounds on energy dissipation in incompressible flows. III. Convection", *Phys. Rev. E* **53** (1996), no. 6, pp. 5957–5981.
[44] F. H. Busse, "On Howard's upper bound for heat transport by turbulent convection", *J. Fluid Mech.* **37** (1969), pp. 457–477.
[45] B. Miquel, S. Lepot, V. Bouillaut and B. Gallet, "Convection driven by internal heat sources and sinks: Heat transport beyond the mixing-length or 'ultimate' scaling regime", *Phys. Rev. Fluids* **4** (2019), no. 12, article no. 121501.
[46] V. Bouillaut, B. Flesselles, B. Miquel, S. Aumaître and B. Gallet, "Velocity-informed upper bounds on the convective heat transport induced by internal heat sources and sinks", *Philos. Trans. R. Soc. Lond., Ser. A* **380** (2022), no. 2225, article no. 20210034.
[47] B. Song, G. Fantuzzi and I. Tobasco, "Bounds on heat transfer by incompressible flows between balanced sources and sinks", *Phys. D: Nonlinear Phenom.* **444** (2023), article no. 133591.
[48] E. M. King, S. Stellmach, J. Noir, U. Hansen and J. M. Aurnou, "Boundary layer control of rotating convection systems", *Nature* **457** (2009), no. 7227, pp. 301–304.
[49] R. P. J. Kunnen, "The geostrophic regime of rapidly rotating turbulent convection", *J. Turbul.* **22** (2021), no. 4-5, pp. 267–296.
[50] L. Terrien, B. Favier and E. Knobloch, "Suppression of wall modes in rapidly rotating Rayleigh–Bénard convection by narrow horizontal fins", *Phys. Rev. Lett.* **130** (2023), no. 17, article no. 174002.
[51] E. M. King, S. Stellmach and J. M. Aurnou, "Heat transfer by rapidly rotating Rayleigh—Bénard convection", *J. Fluid Mech.* **691** (2012), pp. 568–582.
[52] P. Joshi, H. Rajaei, R. P. J. Kunnen and H. J. H. Clercx, "Heat transfer in rotating Rayleigh–Bénard convection with rough plates", *J. Fluid Mech.* **830** (2017), R3.
[53] V. K. Tripathi and P. Joshi, "Regimes in rotating Rayleigh– Bénard convection over rough boundaries", *J. Fluid Mech.* **982** (2024), article no. A15.
[54] F. Toselli, S. Musacchio and G. Boffetta, "Effects of rotation on the bulk turbulent convection", *J. Fluid Mech.* **881** (2019), pp. 648–659.
[55] C. Liu, M. Sharma, K. Julien and E. Knobloch, "Fixed-flux Rayleigh—Bénard convection in doubly periodic domains: generation of large-scale shear", *J. Fluid Mech.* **979** (2024), article no. A19.
[56] K. Julien, E. Knobloch and J. Werne, "A New Class of Equations for Rotationally Constrained Flows", *Theor. Comput. Fluid Dyn.* **11** (1998), no. 3-4, pp. 251–261.
[57] K. Julien, E. Knobloch, R. Milliff and J. Werne, "Generalized quasi-geostrophy for spatially anisotropic rotationally constrained flows", *J. Fluid Mech.* **555** (2006), pp. 233–274.
[58] K. Julien, E. Knobloch, A. M. Rubio and G. M. Vasil, "Heat Transport in Low-Rossby-Number Rayleigh–Bénard Convection", *Phys. Rev. Lett.* **109** (2012), no. 25, article no. 254503.
[59] K. Julien, A. M. Rubio, I. Grooms and E. Knobloch, "Statistical and physical balances in low Rossby number Rayleigh-–Bénard convection", *Geophys. Astrophys. Fluid Dyn.* **106** (2012), no. 4-5, pp. 392–428.
[60] A. J. Barker, A. M. Dempsey and Y. Lithwick, "Theory and simulations of rotating convection", *Astrophys. J.* **791** (2014), no. 1, article no. 13.
[61] S. Stellmach, M. Lischper, K. Julien, et al., "Approaching the asymptotic regime of rapidly rotating convection: boundary layers versus interior dynamics", *Phys. Rev. Lett.* **113** (2014), no. 25, article no. 254501.

[62] J. Song, O. Shishkina and X. Zhu, "Scaling regimes in rapidly rotating thermal convection at extreme Rayleigh numbers", *J. Fluid Mech.* **984** (2024), article no. A45.

[63] G. Hadjerci, V. Bouillaut, B. Miquel and B. Gallet, "Rapidly rotating radiatively driven convection: experimental and numerical validation of the 'geostrophic turbulence' scaling predictions", *J. Fluid Mech.* **998** (2024), article no. A9.

[64] J. M. Aurnou, S. Horn and K. Julien, "Connections between nonrotating, slowly rotating, and rapidly rotating turbulent convection transport scalings", *Phys. Rev. Res.* **2** (2020), no. 4, article no. 043115.

ACADÉMIE DES SCIENCES
INSTITUT DE FRANCE

Comptes Rendus. Physique
2024, Vol. 25, Special issue S3, p. 21-75
https://doi.org/10.5802/crphys.233

Review article / *Article de synthèse*

Geophysical and astrophysical fluid dynamics in the laboratory / *Dynamique des fluides géophysiques et astrophysiques au laboratoire*

Seven decades of exploring planetary interiors with rotating convection experiments

Sept décennies d'exploration des intérieurs de planètes par les expériences de convection en rotation

Alban Pothérat [*, a] **and Susanne Horn** [a]

[a] Centre for Fluid and Complex Systems, Coventry University, Mile Lane, CV1 2NL Coventry, UK

E-mails: alban.potherat@coventry.ac.uk (A. Pothérat), susanne.horn@coventry.ac.uk (S. Horn)

Abstract. The interiors of all the planets in the solar system consist of layers, most of which are made out of fluids. When these layers are subject to superadiabatic temperature or compositional gradients, turbulent convection takes place that transports heat and momentum. In addition, planets are fast rotators. Thus, the key process that underpins planetary evolution, the existence of dynamo action or lack thereof, the observable flow patterns, and much more, is rotating convection. Because planetary interiors are remote and inaccessible to direct observation, experiments offer crucial, physically consistent models capable of guiding our understanding and complementing numerical simulations. If we can fully understand the fluid dynamics of the laboratory model, we may eventually fully understand the original. Experimentally reproducing rotating thermal convection relevant to planetary interiors comes with very specific challenges, in particular, modelling the central gravity field of a planet that is parallel to the temperature gradient. Three distinct classes of experiments have been developed to tackle this challenge. One approach consists of using an alternative central force field such as the electric one. This comes with the caveat that these forces are typically weaker than gravity and require going to space. Another method entails rotating the device fast enough so that the centrifugal force exceeds and effectively supersedes Earth's gravity. This mimics the equatorial and lower latitude regions of a planet. Lastly, insight into the polar and higher latitude regions is gained by using the actual lab gravity aligned with the rotation axis. These experiments have been continuously refined during the past seven decades. Here, we review their evolution, from the early days of visualising the onset patterns of convection, over central force field experiments in spacecraft, ultrasound velocity measurements in liquid metals, to the latest optical velocity mapping of rotating magnetoconvection in sulphuric acid inside high-field magnets. We show how innovative experimental design coupled with emerging experimental techniques has advanced our understanding of planetary interiors and helped us paint a more realistic, detailed picture of them, including Earth's liquid metal outer core.

Résumé. Les intérieurs de toutes les planètes du système solaire sont constitués de couches internes, dont la plupart sont fluides. Quand ces couches sont sujettes à un gradient de température ou de composition chimique super-adiabatiques, un écoulement convectif s'installe qui transporte chaleur et moment angulaire.

* Corresponding author

De plus, les planètes tournent extrêment vite. Ainsi, le processus-clé qui sous-tend l'évolution des planètes est la convection en rotation. Alors que les intérieurs de planètes sont eloignés et impropres à l'observation directe, les expériences de laboratoire présentent des modèles cohérents à même de guider notre compréhension et de complémenter les simulations numériques. Si nous parvenons à comprendre la mécanique des fluides des modèles de laboratoire, nous finirons peut-être par comprendre l'original complètement. Cependant, reproduire expérimentalement une convection en rotation pertinente pour les intérieurs de planètes présente une gageure en soi, ne serait-ce qu'au niveau de la modélisation de la gravité centrale d'une planète et de son gradient de température parallèle. Trois classes d'expériences distinctes sont apparues pour relever ce défi. Une première approche consiste à utiliser une autre force centrale, telle que la force de Coulomb. L'inconvénient est que ces forces sont typiquement plus faibles que la gravité ambiante et nécessitent donc d'aller dans l'espace. Une autre méthode implique de faire tourner le dispositif suffisamment vite pour que la force centrifuge dépasse et même remplace la gravité terrestre. Cette technique imite les conditions des regions équatoriales et à faible latitude d'une planète. Finalement, utiliser la véritable gravité terrestre alignée avec l'axe de rotation nous renseigne sur les régions polaires et à haute latitude. Ces expériences ont été perfectionnées au cours de plus de sept décenies. Nous parcourons ici leur évolution, depuis les premières visualisations des motifs au départ de la convection, en passant par les expériences à gravité centrale conduites à bord d'engins spatiaux, l'avènement de la vélocimétrie à ultrasons dans le métaux liquides, jusqu'aux dernières cartographies de champs de vitesse par méthodes optiques dans des écoulements de magnoconvection en rotation dans de l'acide sulfurique à l'intérieur d'aimants à champs fort. Nous montrons comment des concepts expérimentaux innovants couplés aux techniques expérimentales émergentes ont poussé notre compréhension des intérieurs de planètes et nous ont aidé à en dépeindre une image toujours plus détaillée et plus réaliste, en particulier du cœur liquide de la Terre.

Keywords. Rotating convection, Experimental fluid mechanics, Measurement techniques, Planetary interiors, Turbulent convection.

Mots-clés. Convection en rotation, Méchanique des fluides exprérimentale, Techniques de mesure, Intérieurs de planètes, Convection turbulente.

Funding. EPSRC (grant nos. EP/X010937/1 and EP/V047388/1), Leverhulme Trust (grant no. RPG-2017-366), European Research Council (ERC) (grant no. EP/X034402/1).

Manuscript received 7 September 2024, revised and accepted 13 January 2025.

1. Introduction

In 1906, Oldham [1], wrote

> Of all regions of the earth none invites speculation more than that which lies beneath our feet, and in none is speculation more dangerous: yet, apart from speculation, it is little that we can say regarding the constitution of the interior of the earth. [...] The central substance of the earth has been supposed to be fiery, fluid, solid, and gaseous in turn, till geologists have turned in despair from the subject, and become inclined to confine their attention to the outermost crust of the earth, leaving its centre as a playground for mathematicians.

Then the seismograph changed geophysics forever. Oldham analysed earthquake data and was indeed able to see inside the Earth. He concluded that the Earth had a mantle and core based on different travelling behaviours of seismic waves. In 1936, Inge Lehmann further proved seismologically that there was an inner solid core [2].

Seismology provides us with an accurate measure of the core-mantle and inner core boundaries (CMB, ICB) and unequivocal evidence that the outer core is liquid. Recent advanced seismological techniques have been revealing the detailed structure of Earth's mantle and inner core. They also complement other approaches, e.g. numerical simulations, high-pressure experiments or mineral physics modelling [3–8]. The outer core is a very different story. Its liquid nature makes it less amenable to seismology-based constraints. The main reason lies in the outer core's comparatively low viscosity and subsequent lack of shear strength. The outer core has a viscosity of about $\nu_{oc} \approx 10^{-6}$ m^2/s, which is about 10^{24} and 10^{16} times lower than those of the mantle [9] and the inner core [10], respectively.

The low viscosity of Earth's outer core has another crucial consequence: Rotation matters. The relative importance of rotation is expressed through the Ekman number, $Ek = \nu/(2\Omega H^2)$, where ν is the viscosity, H is the layer thickness, and Ω is the rotation rate. Earth's rotation rate is about $\Omega_E = 7.27 \times 10^{-5}$ rad/s, and the mantle, outer core and inner core have respective thicknesses of $H_\mathrm{m} = 2885$ km, $H_\mathrm{oc} = 2270$ km, and $H_\mathrm{ic} = 1216$ km. This gives $Ek_\mathrm{m} \approx 10^9$, $Ek_\mathrm{oc} \approx 10^{-15}$ and $Ek_\mathrm{ic} \approx 47$, respectively. Throughout the entire interior of the Earth, convection drives motion and transports heat and momentum. But the high Ek in the mantle and inner core means convection in those two regions is practically unaffected by rotation, whereas the low Ek in the outer core implies that convection there is strongly constrained by rotation [11–14]. Another distinct feature of the outer core is that it is both made of electrically conducting metal and liquid. Because of it, convection is vigorous enough to power dynamo action and so generates and sustains Earth's magnetic field.

In short, the outer core is dynamically very different compared to the mantle or the inner core. It is the layer of the Earth that is least accessible through conventional means, in particular, seismology. Hence, the outer core is still largely a "*playground*" for mathematicians, numericists, and, importantly, experimentalists. This by no means implies that it is all mere speculation or that we should not study the problem. Instead, to account for the large uncertainties on the actual conditions in Earth's interior, we need to create models that are rigorously built upon the known principles of mathematics, physics, and most crucially fluid dynamics. But as Willis puts it [15], "[...] it is less difficult to imitate one of nature's processes than to understand either the imitation or, through it, the original". In the study of outer core dynamics, it is experiments that most reliably ensure that our understanding is built on firm ground, and shall be the focus of this review.

We first discuss briefly the theoretical framework that is used to understand both the laboratory experiments and the planetary core processes these experiments aim to "*imitate*". Then, we give an overview of the major design principles and their historical development. In the main part, we review individual experiments, the challenges involved in experimental endeavours and the engineering strategy to tackle them. We shall also see how boldly extrapolating these models to the Earth as well as other planets encourages further exploration along this path while flagging up its limitations at the same time.

1.1. *Governing equations and control parameters*

To understand the challenges in bringing planetary physics to life in a small contraption at a laboratory scale, we shall start by summarising the main theoretical ingredients that both are usually assumed to share, i.e. rotating thermal convection. The most common and simplest framework describing rotating convection experiments exploring planetary interiors is that of the Navier–Stokes equations complemented by the transport equation for temperature T. The basic configuration is the Rayleigh–Bénard convection (RBC) one [16,17], made of a fluid layer, heated from below and cooled from above (in the sense of gravity) with a superadiabatic temperature gradient. The fluid in planetary cores modelled by lab experiments is usually assumed to be Newtonian and to be described within the Oberbeck–Boussinesq approximation [18–20]. Thus, its material properties, kinematic viscosity ν and thermal diffusivity κ are homogeneous, temperature- and pressure-independent. The density is approximated as a Taylor expansion around $T = T_\mathrm{m}$ up to the first order, i.e. it is assumed to be linearly dependent on the temperature,

$$\rho = \rho_\mathrm{m}(1 - \alpha(T - T_\mathrm{m})), \tag{1}$$

with α being the constant isobaric expansion coefficient, $\alpha \equiv -(1/\rho)\partial_T \rho|_p$. The subscript m denotes the reference value, typically, the arithmetic mean temperature between the top and bottom boundary temperatures, $T_\mathrm{m} = (T_\mathrm{t} + T_\mathrm{b})/2$, and $\rho_\mathrm{m} = \rho(T_\mathrm{m})$. The second term in the density is small except in the gravitational and centrifugal buoyancy terms [21–25]. The temperature is

the actual temperature in experiments and the superadiabatic part of the temperature when considering planetary interiors [26]. Planetary rotation is assumed constant, $\Omega\hat{\boldsymbol{e}}_z$, and the origin is placed at the centre of the planet. The governing equations in dimensional form under these assumptions are:

$$\nabla\cdot\boldsymbol{u} = 0, \tag{2}$$

$$D_t\boldsymbol{u} = \nu\nabla^2\boldsymbol{u} - \nabla p + 2\Omega\boldsymbol{u}\times\hat{\boldsymbol{e}}_z - \Omega^2 r\alpha(T-T_{\rm m})\hat{\boldsymbol{e}}_r + g\alpha(T-T_{\rm m})\hat{\boldsymbol{e}}_g, \tag{3}$$

$$D_t T = \kappa\nabla^2 T. \tag{4}$$

The unit vector $\hat{\boldsymbol{e}}_g$ points in the opposite direction of gravity, e.g. opposite to the spherical radial direction in spherical geometries or opposite to the vertical direction in plane geometries, such as cylinders or annuli; $\hat{\boldsymbol{e}}_r$ is the cylindrical radial unit vector perpendicular to the direction of rotation $\hat{\boldsymbol{e}}_z$.

These equations are more meaningful in nondimensional form. Choosing as reference quantities, the fluid layer thickness H, the temperature difference between the hot and cold boundary, in the case of Earth, the inner core boundary (ICB) and core-mantle boundary (CMB), Δ, the free-fall velocity $U_{\rm ff} = \sqrt{g\alpha H\Delta}$, and the corresponding time and pressure scales, $H/U_{\rm ff}$ and $\rho_{\rm m}U_{\rm ff}^2$, we have:

$$\nabla\cdot\boldsymbol{u} = 0, \tag{5}$$

$$D_t\boldsymbol{u} = \sqrt{\frac{Pr}{Ra}}\nabla^2\boldsymbol{u} - \nabla p + \sqrt{\frac{Pr}{RaEk^2}}\,\boldsymbol{u}\times\hat{\boldsymbol{e}}_z - \frac{Fr}{\gamma}Tr\,\hat{\boldsymbol{e}}_r + T\hat{\boldsymbol{e}}_z, \tag{6}$$

$$D_t T = \sqrt{\frac{1}{RaPr}}\nabla^2 T. \tag{7}$$

In this form, the problem is governed by the following nondimensional control parameters: the Ekman number, which expresses the ratio of viscous to Coriolis forces, the Rayleigh number, which is the ratio of buoyancy to viscous forces, the Prandtl number, which is the ratio of viscous to thermal diffusivities, the Froude number, which is the ratio of centrifugal to gravitational forces, and the radius-to-height aspect ratio (or alternatively, the diameter-to-height aspect ratio)

$$Ek = \frac{\nu}{2\Omega H^2}, \quad Ra = \frac{\alpha g\Delta H^3}{\nu\kappa}, \quad Fr = \frac{\Omega^2 R}{g}, \quad \gamma = \frac{R}{H}, \quad \Gamma = \frac{2R}{H}. \tag{8}$$

The form of Equations (5)–(7) brings out three further classical parameters, the free-fall-based Reynolds, Rossby, and Péclet numbers,

$$Re = \sqrt{\frac{Ra}{Pr}}, \quad Ro = \sqrt{\frac{RaEk^2}{Pr}}, \quad Pe = \sqrt{RaPr}. \tag{9}$$

This Rossby number is often referred to as the convective Rossby number to distinguish it from the output parameter. Similarly, also the Reynolds and Péclet numbers can be output parameters when defined with measured velocities [14].

1.2. *Main physical processes*

The Equations (3) and (6) include both the centrifugal and the standard gravitational buoyancy terms. Both act in a very similar way, that is, denser (colder) fluid moves in the direction of $\hat{\boldsymbol{e}}_r$ and $-\hat{\boldsymbol{e}}_g$, and lighter (warmer) fluid moves in the direction of $-\hat{\boldsymbol{e}}_r$ and $\hat{\boldsymbol{e}}_g$, respectively. Specifically, in a plane geometry, cold fluid moves radially outwards and downwards and warm fluid moves radially inwards and upwards. The Froude number expresses which of the buoyancy terms is dominant [22–25,27]. In experiments, Fr is always non-zero and in some experiments, it is the design principle that $Fr \gg 1$ such that the centrifugal acceleration supersedes the gravitational one and so becomes the effective gravity (see Section 3).

In most theoretical and numerical studies, Fr is set to zero. This is justified in most planetary settings where centrifugal buoyancy is negligible at the largest scale, e.g. for Earth's outer core $Fr \simeq 1.72 \times 10^{-3}$. In this case, the main effect of the Coriolis force on convective and other flows can be seen by considering the limit of fast rotation $Ek \to 0$, $Ro \to 0$ in the governing equations: away from boundary layers, the main balance is *geostrophic*, i.e. between the Coriolis force and the pressure gradient, so the curl of Equation (6) imposes that

$$\partial_z \boldsymbol{u} = \mathcal{O}(Ek, Ro) \to 0, \tag{10}$$

$$\nabla_{r\phi} \cdot \boldsymbol{u} = \mathcal{O}(Ek, Ro) \to 0, \tag{11}$$

where ϕ is the azimuthal coordinate and $\nabla_{r\phi}$ is the two-dimensional divergence in the r–ϕ plane. Hence, at the leading order, the Coriolis force makes the flow quasi-two-dimensional and quasi-horizontally solenoidal, a result known as the Taylor–Proudman Constraint (TPC) [28–30]. It implies that a cylindrical fluid parcel must conserve its height through motion, or equivalently, that the flow must follow surfaces of constant height along the rotation direction, called *geostrophic surfaces*. Since the TPC restricts possible fluid motions, the onset of stationary convection occurs at higher critical Rayleigh numbers Ra_c than without rotation. In a plane Rayleigh–Bénard configuration, $Ra_c \sim Ek^{-4/3}$, and the non-rotating convection cells at onset give way to much thinner spiral cells, of length scale $\ell_c \sim Ek^{1/3}$ [27]. Importantly, in low Prandtl number fluids ($Pr < 0.68$) such as liquid metals, the onset modes are oscillatory [27,31–36]. The critical Rayleigh number and length scales are then Pr-dependent, namely, $Ra_c \sim (Ek/Pr)^{-4/3}$ and $\ell_c \sim (Ek/Pr)^{1/3}$. These plane layer onset scalings hold asymptotically also in spherical and annular geometries [25,37–39].

At higher criticality, the TPC loosens, and the cellular structures turn into convective Taylor columns, and then plumes and geostrophic turbulence (see e.g. the recent reviews by Kunnen [11] and Ecke and Shishkina [40]). More generally, whenever inertia antagonises the effect of rotation, i.e. when the Rossby number based on the measured velocity Ro_U is finite, the TPC is partly violated and flow structures become anisotropic with a ratio of their axial to transverse length scale governed by the balance between Coriolis and inertia forces $l_z/l_\perp \sim Ro_U^{-1/3}$ [41–43], see the reviews by Godeferd and Moisy [44] and Biferale [45] on how anisotropy determines rotating turbulence.

The Coriolis force may, however, have another important effect. It can lead, at least locally, to a misalignment of the time-averaged temperature gradient and gravity and therefore the main pressure gradient. The misalignment drives a baroclinic flow (see the review by Harlander within this special issue [46]). For example, in Earth's core outside the polar region, baroclinic flows naturally arise as the TPC aligns the flow with rotation rather than gravity [47,48]. Similarly, in an experimental context or on a local planetary scale when $Fr > 0$, there is a flow even at arbitrarily low imposed temperature gradients. The Coriolis force constrains the baroclinic motion into an azimuthal wind u_ϕ which is controlled by the *thermal wind balance*. In cylindrical coordinates, and using the previous non-dimensionalisation, it reads

$$\partial_z u_\phi = Ro\left(\partial_r T + \frac{Fr}{\gamma} r \partial_z T\right) \tag{12}$$

and derives from the curl of Equation (3). The two examples mentioned above are illustrations of the first and second terms on the RHS of Equation (12), respectively, being significant.

1.3. *Planetary and experimental peculiarities*

In the planetary context, the spherical shell geometry constrains the expression of these processes. Since planets are extremely fast rotators, the flow tends to follow geostrophic contours

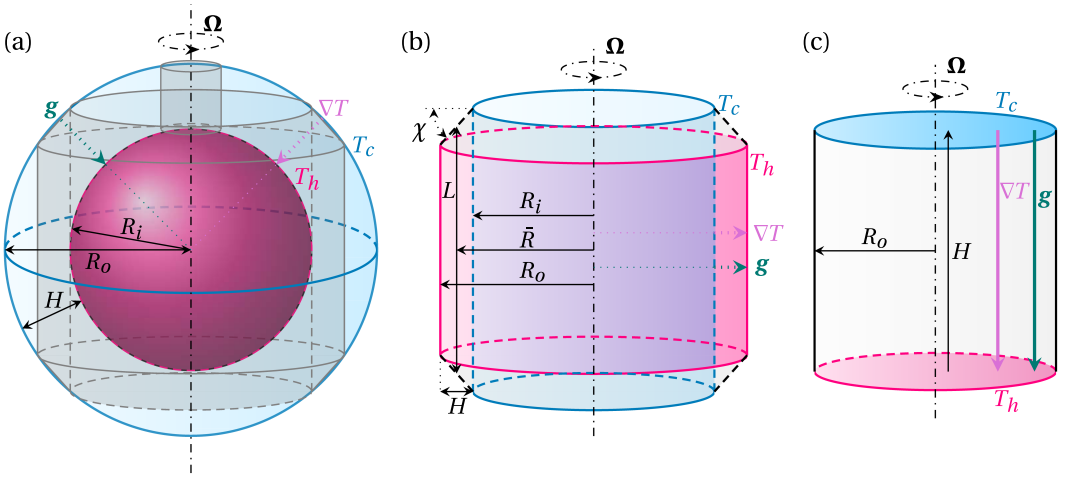


Figure 1. Sketches of the fundamental geometries used for the study of rotating convection in planetary core convection. The gravitational acceleration (or any proxy) $\boldsymbol{g}$ and the temperature gradient ∇T and their respective directions are indicated by dark green and lavender arrows. The angular rotation is assumed to be vertical, $\boldsymbol{\Omega} = \Omega \hat{\boldsymbol{e}}_z$, and the axis of rotation is marked by the vertical black dash-dotted line. The boundaries are demarcated by blue for the cold boundary T_c and pink for the hot boundary T_h. (a) Spherical shell; R_i is the inner radius, R_o is the outer radius, and $H = R_\mathrm{o} - R_\mathrm{i}$ is the spherical shell gap width. The grey cylinder of radius R_i is the tangent cylinder (TC). The grey annulus is detailed in (b), and the small grey cylinder in the polar region is detailed in (c). (b) *Busse annulus*; R_i is the inner radius, R_o is the outer radius, $H = R_\mathrm{o} - R_\mathrm{i}$ is the annulus gap width, $\bar{R} = R_\mathrm{i} + H/2 = R_\mathrm{o} - H/2$ is the mean radius, L is the mean height, and χ is the sloping angle of the endwalls. The endwalls are typically thermally insulating. (c) Cylinder; R_o is the radius, H is the height of the cylinder. The sidewalls are typically thermally insulating.

because of the TPC. Spherical shells being axisymmetric, these geostrophic contours are cylinders aligned with the rotation axis, so radial motions are impeded whereas azimuthal flows are favoured by rotation. One of these contours plays a particularly important role: the so-called tangent cylinder (TC) extruded from the equatorial boundary of the inner solid core along the rotation separates polar regions located below the poles from equatorial regions (see Figure 1a). If a fluid parcel was to cross the TC, it would see either a doubling or a halving of the domain's height along $\hat{\boldsymbol{e}}_z$, which the TPC strongly opposes. Hence the TC acts as a mechanical boundary between the polar and equatorial regions. For the same reason, radial motion near the equatorial plane is very strongly suppressed by the jump in domain height there. Thus, because of the Earth's solid inner core, the liquid outer core is split into two regions with different types of rotating convection [48,49].

In the equatorial region outside the TC, the gravity is rather perpendicular to the rotation. Near the equatorial plane, the gravity and temperature gradients drive motion in the plane, and therefore perpendicular to $\Omega\hat{\boldsymbol{e}}_z$. This motion is therefore not as strongly opposed by the TPC. Instead the rotation tends to elongate these cells along $\hat{\boldsymbol{e}}_z$ and so forms quasi-geostrophic columns extending across the entire northern and southern hemispheres, named *Busse columns*, after Busse's pioneering experimental work with the *Busse annulus* represented in Figure 1(b) [50]. The variation in domain height in the equatorial region and in the Busse annulus incurs a lin-

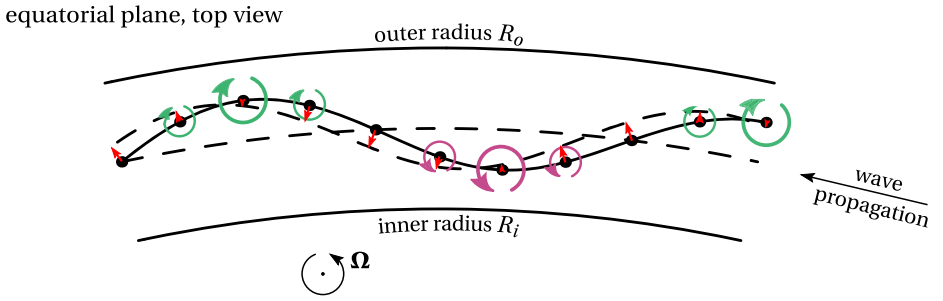


Figure 2. Sketch of the general propagating behaviour of (incompressible) Rossby waves, adapted from Ref. [55]. Visualised is part of the equatorial plane of a rotating spherical shell. Initially, a series of fluid columns is at rest and aligned along the mid-radius. If these columns are displaced in a sinusoidal manner, then the vortices that move outwards (indicated by the green arrows) must reduce in length to conserve mass, thus, they get squashed and acquire retrograde vorticity to conserve potential vorticity. Similarly, the vortices that move inwards (indicated by the purple arrows) must extend in length, they get stretched and acquire prograde vorticity. The effect on the neighbouring columns is that the columns to the west are pushed away from the rotation axis and the columns to the east are pushed towards the rotation axis (red arrows). This results in the phase of the initial sinusoidal pattern propagating westwards (prograde) which is known as the Rossby wave.

ear damping on the geostrophic structures called β-effect [30,51]. The reduced domain height at low latitudes prevents Busse columns from entering that region so they tend to remain close to the inner core. Nevertheless, the β-effect incurred by the sloping outer boundary forces Busse columns to oscillate radially and form *thermal Rossby waves*, as sketched in Figure 2. Hindman and Jain [52] offer an elegant explanation of their basic mechanism: Considering a column of height L,

> If a spinning column near the equator is pushed toward the rotation axis, the column grows in height as the chord length of the column's axis increases. In an incompressible fluid, this vortex stretching is accompanied by a commensurate narrowing of the column to conserve mass. Subsequently, as the column compresses laterally, the column must spin faster to conserve angular momentum about its own axis [25,53]. [...] This conservation principle is enforced by the constancy of the potential vorticity. As L increases, [the vorticity component aligned with the rotation axis] must also increase. The resulting induced vorticity causes the neighbouring column to the west to be pushed outward, away from the rotation axis, and the column to the east to be pushed inward, toward the rotation axis. These newly pushed columns conserve their own potential vorticity (i.e., angular momentum) and induce spinning columns further down the belt to also move inward and outward. The result is a prograde-propagating Rossby wave where the spinning columns dance back and forth, toward and away from the rotation axis.

One of the main design challenges in imitating this phenomenology arises out of the vertical direction of gravity in the lab, which makes it difficult to reproduce equatorial convection in experiments using Earth's gravity. Here the centrifugal forces comes to the experimentalist's rescue. Since the region outside the TC is annular, it can be simulated by rotating an annulus with sloping endwalls sufficiently fast for the centrifugal force to exert an apparent radial gravity. This was the essence of Busse's revolutionary idea [54].

In the polar regions inside the TC, the temperature gradient, the gravity and the rotation are mostly aligned, and topographic effects are minor: the convection there is expected to develop somewhat similarly to rotating RBC (RRBC). Experimentally, one would expect to capture its main

features by rotating a vertical cylindrical vessel around its axis at a sufficiently large speed for the Coriolis force to dominate, as in Figure 1(c). Unfortunately, at the scale of the laboratory, the centrifugal force becomes important at rapid rotation, and even more so for cylinders of low aspect ratios $\Gamma = 2R_o/H$ [22]. Such a cylinder may represent the entire TC or a smaller, concentric cylinder inside it, see Figure 1(a,c). A further issue arises from the nature of the TC: while it may be legitimate to model it with a rigid boundary, the thermal boundary condition there is both unknown and crucial: if adiabatic, isothermal surfaces remain horizontal all the way across the cylinder, whereas if isothermal, very strong baroclinicity drive a flow near the cylinder side wall [47,48,56]. Since there is no reason to think that either of these ideal cases applies to planetary cores, actual TCs must be reproduced in experiments.

Besides topographic effects, solid boundaries in planets and rotating experiments give rise to viscous boundary layers. Along boundaries perpendicular to the rotation axis, Ekman layers, of thickness $\mathcal{O}(Ek^{1/2})$ result from the balance between the viscous and the Coriolis force [30,57]. They become extremely thin in regimes of rotation relevant to planets, and fully resolving them curtails the range of Ekman numbers accessible to numerical simulations. One of their most distinctive property is that wall friction within the layer occurs at an angle with the bulk velocity. This results from the progressive deflection of the flow by the Coriolis force through the layer forming the so-called *Ekman spiral*. The second remarkable property of Ekman layers is that local axial vorticity in the bulk ω_z pulls a local mass flux out of the layer $u_z \simeq (1/2)\omega_z Ek^{1/2}$. This secondary flow, called *Ekman pumping* is driven by the imbalance between the radial pressure gradient induced in the Ekman layer by rotation in the bulk, and the reduced centrifugal force due to low velocities within the layer. This phenomenology even persists in the presence of planetary or laboratory magnetic fields but follows different scalings [58–60].

Boundary layers along vertical boundaries are *Stewartson layers* [30,61]. They exhibit a sandwiched structure made of two layers. A layer of thickness $\mathcal{O}(E^{1/4})$ arises from the balance between the Coriolis force and viscous friction in planes perpendicular to the rotation, while a thinner $\mathcal{O}(E^{1/3})$ is driven by secondary flows in planes meridional to the rotation axis. Kunnen et al. [62] offer a detailed analysis of their structure in the context of rotating Rayleigh–Bénard convection.

Vertical boundaries are also associated with specific convective structures called *wall modes*, with an onset at lower Rayleigh numbers than the bulk modes [32,33,63–68]. It is argued that their existence may be connected to that of boundary zonal flows [36,69–71]. These modes are robust to changes in the shape of the vertical boundary [72,73] and since they compete with bulk modes relevant to planets, and efficiently carry heat, their presence complicates the interpretation of experimental results in geophysical context.

Finally, a key question that arises when experimentally modelling either region is the choice of the working fluid, a choice that is closely linked to the envisaged measurement techniques and the specific aims pursued in building such devices. The Earth's outer core is mostly made of liquid iron, whose physical properties can be estimated from Iron's melting point [74,75], and high-pressure experiments [76–79] $\rho \simeq 10^4$ kg/m^3, $\nu \simeq 7\times10^{-6}$ m^2/s, $\kappa \simeq 4\times10^{-6}$ m^2/s, $\alpha \simeq 10^{-5}$ K^{-1}, so $0.1 \leq Pr \leq 1$ [80]. Liquid metals would therefore seem the obvious choice but have only been used in a handful of experiments. The main issue with liquid metals besides their direct or indirect costs, toxicity, and chemical reactivity is that they are opaque and so preclude any direct optical visualisation or any of the convenient LASER-based techniques used in transparent fluids to map velocity and temperature fields. For these reasons, high Pr fluids such as water, but also silicon oils and a few more exotic fluids, appear as cheap and attractive alternatives to understand the interplay between convection and rotation in planetary geometries. For the purpose of studying the effect of magnetic fields, however, liquid metals are usually the fluid of choice. However, neither liquid metals nor the high Prandtl fluids mentioned above afford the combination of electromagnetic effects with the advantage of optical visualisation. Sulphuric

acid recently emerged as a solution to do just that [56,81–83].

1.4. *Historical evolution through four classes of experiments*

The constraints imposed by terrestrial gravity led to four fundamental classes of rotating convection experiments that explore planetary interiors. However, with an outer core thickness of $H \simeq 2.26 \times 10^6$ m, a rotation of one revolution per (Earth) day, a mid-thickness gravity of $g \simeq 7$ m/s^2 [80], the regimes of the outer core of Earth are too extreme for any laboratory experiment: $Ek \simeq 10^{-15}$, $Ra \simeq 10^{22}$ to 10^{30}, $Ro \in [10^{-6}, 10^{-3}]$, $Re \in [10^{11}, 3 \times 10^{15}]$ and $Pe \in [10^{21}, 10^{31}]$. Other planets offer no solace either as they operate in just as extreme regimes [13,80]. Hence, experiments first focused on understanding the fundamentals of convection (onset, regimes, heat flux) to later extrapolate them to these extreme regimes, and incorporate some of the more complex specifics of the Earth (inhomogeneities, magnetic field). A timeline summarising the history of about seven decades of experiments (1953–2024) is given in Figure 3, and a large A3 version of it is provided as Supplementary Material. Representations of the regimes of parameters in (Ra, Ek) and in $(Ra/Ra_c, Ek)$ spaces spanned by all four types of experiments are shown in Figure 4 along with projected Earth's regimes. The details of dimensional and non-dimensional parameters for experiments conducted by each team identified in the chronological diagram of Figure 3 is reported in Tables 1 and 2, respectively.

In the following, we give a brief overview of the four fundamental classes of rotating convection experiments.

Central force field. It is extremely hard to produce self-gravitating spheres in miniature form within a terrestrial laboratory environment, thus, proxy-gravitational forces have so far been the only way to generate central force fields similar to Earth's gravity and suitable for studying rotating convection. Examples are the dielectrophoretic force which was utilised in two space experiments (GFFC, 1985–1999 [84] and GeoFlow, 2008–2020 [85]) and very recently the pycnoclinic acoustic radiation force which also works on Earth (Los Angeles, 2023 [86]). These experiments are detailed in Section 2.

Cylindrical radial gravity. This class of experiments simulates the regions outside the TC. Since gravity is mostly cylindrical-radial there, these experiments use annular vessels of various shapes: spherical, hemispherical, cylindrical and variations thereupon, detailed in Section 3. Guided by these constraints, the first experiments were pioneered by Busse in the 1970s in a rotating annulus, with slanted endwalls reproducing the β-effect and focussed mostly on the onset of convection [54]. Simpler cylindrical annuli with flat endwalls were later used to study inhomogeneous heat flux [87] and ultimate convection [88]. The first and only experiment in a full sphere in 1986 is due to Chamberlain [89]. Aside of this, spherical annuli became the geometry of choice for groups in Los Angeles [50], Cambridge [89], Bayreuth [90], Baltimore [91,92], Grenoble [74] and Maryland [93]. The mid-2000s mark the appearance of experiments on rotating magnetoconvection in spherical annuli in Grenoble [94] and Maryland [93], using gallium and sodium, respectively.

Axial gravity. Experiments relevant to the polar region started within the convection community, rather than with geophysicists. The combination of axial gravity and rotation, with the geometry of the geostrophic contour, makes cylindrical vessels the obvious choice for this type of experiment. Indeed the very first experiment on rotating convection was conducted on the 20th of November 1953 in Chicago by Fultz, Nakagawa, and Frenzen [95]. Since then, cylinders have remained the experimentalists' favourite to study rotating convection with axial gravity. A very brief summary of the numerous experiments of this type is given in Section 4.

Tangent cylinder. The radial and axial strands met in 2003 when Aurnou et al. [96] built the first experiment dedicated to studying the TC, with a raised heater inside a hemispherical dome filled with water. It wasn't until 2014 that this idea was pushed when Aujogue et al. used electrically conducting sulphuric acid and the availability of high magnetic fields up to 10 T to produce the study of magneto-rotating convection with PIV visualisations in a configuration directly relevant to planets [47,56,83,97]. This was followed by a much-improved rebuild using a cylinder instead of a hemisphere [48] (see Section 4).

2. Central force field: outer space and elsewhere

2.1. *Outer space: the geophysical fluid flow cell (GFFC) and the GeoFlow experiments*

Spherical geometries with a central force field may at first glance be essential for creating a laboratory model of Earth's outer core, and other geophysical and astrophysical systems. Unfortunately, on the ground, the terrestrial gravitational potential prevents such a setup. Thus, realistic experiments where the angle between the Coriolis and buoyancy force varies, are not straightforwardly realisable. We first focus on the two experiments that went to space to escape the terrestrial limitations: the Geophysical Fluid Flow Cell (GFFC) [84,98,100,163] and the GeoFlow experiment [85,101–106], shown in Figure 5. Neither experiment specifically aimed at understanding Earth's core, but both constitute unique laboratory experiments of (hemi-)spherical rotating convection.

The main underlying principle of both the space experiments is that if an electric potential is applied to a dielectric fluid, the neutral non-charged molecules are polarised, and a force acts in the direction of the strongest electric field region [85,98]. The idea was originally suggested by Smylie [164,165] but Hart et al. [84] later independently realised it for the first time in a spherical experiment. These polarisation forces are also known as dielectrophoretic forces and are density- and permittivity-dependent. They act in a very similar manner to traditional buoyancy forces resulting from either the gravitational or centrifugal potential, but here the potential is $\boldsymbol{E}\cdot\boldsymbol{E}$, with $\boldsymbol{E}$ being the electric field. The key advantage is that in spherical geometries these forces act effectively like a central gravity. Hence, in a rotating experiment, the angle between the electro-hydrodynamic "gravity" vector and the rotation vector vary latitudinally in a similar manner as in planetary and stellar interiors.

More specifically, one can approximate the functional dependence of the permittivity to the first order, as for the density in the Oberbeck–Boussinesq approximation (1):

$$\epsilon = \epsilon_{\mathrm{m}}(1-\gamma(T-T_{\mathrm{m}})), \tag{13}$$

where ϵ_{m} is the ambient permittivity and γ is the dielectric variability. The values for the different fluids used in the space experiment are given in Table 3. Since in all fluids $\gamma \approx \alpha$, the resulting system can be treated with an equivalent version of the Oberbeck–Boussinesq approximation [18,19]. Further, if the electrical field $\boldsymbol{E}$ behaves like a spherical capacitor [104], we have

$$\boldsymbol{E}(\boldsymbol{r}) = \frac{R_{\mathrm{i}}R_{\mathrm{o}}}{R_{\mathrm{o}}-R_{\mathrm{i}}}\frac{1}{r^2}V_{\mathrm{rms}}\hat{\boldsymbol{e}}_r, \tag{14}$$

where V_{rms} is the applied AC voltage to the shells. The resulting electro-hydrodynamic "gravity" is then

$$\boldsymbol{F}_e = g_e\gamma T\hat{\boldsymbol{e}}_r \quad \text{with } g_e(r) = \frac{2\epsilon_{\mathrm{m}}V_{\mathrm{rms}}^2}{\rho_{\mathrm{m}}}\left(\frac{R_{\mathrm{i}}R_{\mathrm{o}}}{R_{\mathrm{o}}-R_{\mathrm{i}}}\right)^2\frac{1}{r^5}. \tag{15}$$

Thus, gravity varies radially but falls off much steeper with $1/r^5$ compared to planetary gravities, closer to r or $1/r^2$. This, however, is argued to be only of secondary importance [98] even though the inner boundary gravity is much stronger than at the outer boundary, i.e. $g_{\mathrm{i}} \gg g_{\mathrm{o}}$. These values

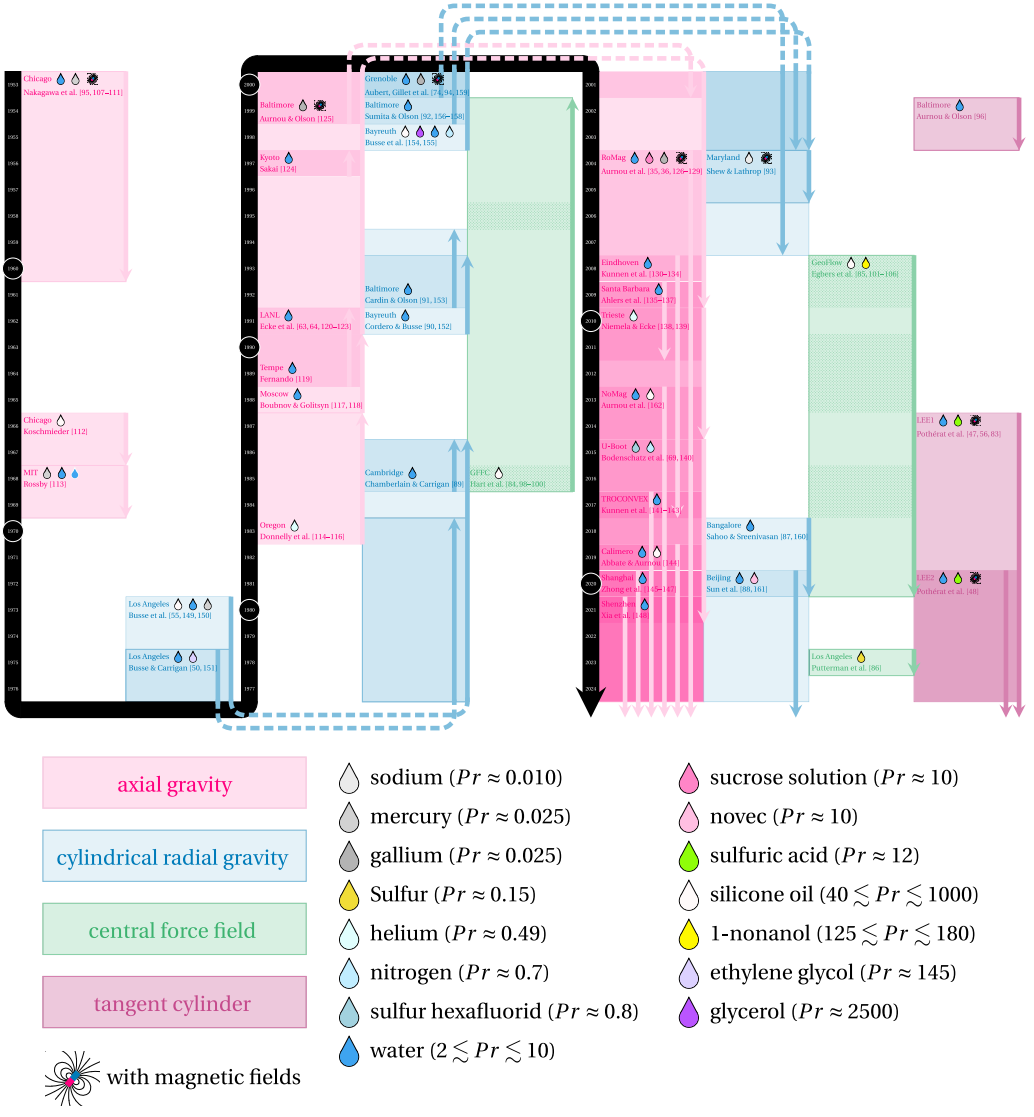


Figure 3. Timeline of the laboratory experiments relevant for planetary core convection from 1953 till 2024. As starting point the year of the date of submission of the first publication, or, where available, the date of the first experimental run is used, the endpoint is the year of the publication of the last publication of the experimental data. The experiments are either referred to by the name of the device or by the place they were conducted if the experimentalists were less creative with their naming convention than with the experimental design. The main experimentalist(s) are also given together with a selection of the relevant publications. The background colours indicate the class of experiment: pink—axial gravity, i.e. either cylinder or cuboid; blue—cylindrical radial gravity, i.e. cylindrical or spherical annulus, hemispherical or spherical shell; green—central force fields, i.e. sphere and hemisphere (the dotted areas indicate when the space missions took place); purple—tangent cylinder geometry. The working fluids in the experiments are indicated by the different droplets. If rotating magnetoconvection experiments were performed, a magnet symbol is added. An A3-scale version of the figure is also provided as a Supplementary File.

Table 1. Rotation rate Ω, temperature difference Δ, inner radius R_i (heater radius in TC geometries), outer radius R_o (corresponds to radius, i.e. half the diameter D in cylinders, outer vessel radius in TC geometries), height H (corresponds to gap width in spherical and other annulus experiments). No parameters are given in Busse and Carrigan [50]. The parameters for the experiments by Putterman et al. [86] are based on acoustic values.

Experiment	Ω (rad/s)	Δ (K)	R_i (cm)	R_o (cm)	H (cm)
			Central force field		
Hart et al. (GFFC) [84,98–100]	[0.03, 3.14]	[0.2, 20]	2.402	3.300	0.908
Egbers et al. (GeoFlow) [85,101–106]	{0.05, 5, 10}	[0.1, 10]	1.35	2.70	1.35
Putterman et al. [86]	106.8	-	-	3	3
			Axial gravity		
Nakagawa et al. [107–111]	0.52, 1.05	n/a	-	7.25, 10.5, 12.5	3, 5
Nakagawa et al. [95]	$[0.26, \pi]$	n/a	-	7	[4, 8]
Koschmieder [112]	$[\pi/2, 2\pi]$	[1.25, 2.5]	-	10.5	3
Rossby [113]	[0.1, 4.83]	n/a	-	11.1125	0.5, 1, 2, 3.5
Donnelly et al. [114–116]	[0.11, 1.981]	[2.1, 3.6]	0.81, 1.25	0.16, 0.25	
Boubnov and Golitsyn [117,118]	$[0.1, 2\pi]$	-	-	8.5	[2, 24]
Fernando [119]	[0.07, 1]	-	-	30 (cube)	50
Ecke et al. [63,64,120–123]	$[\pi/50, 4.9]$	n/a	-	5, 6.35, 3.65 (square)	5, 12.7, 9.4 (square)
Sakai [124]	[0.52, 2.1]	n/a	-	10	3, 6, 9
Aurnou and Olson [125]	$[7.3 \times 10^{-3}, \pi]$	n/a	-	7.6 (square)	1.85, 2.5
Aurnou et al. (RoMag) [35,36,126–129]	[0.7, 3.1]	[0.4, 60]	-	20	{5, 10, 20, 50}
Kunnen et al. [130–134]	[0.01, 4.1]	n/a	-	10, 11.5, 12.5	10, 11.5, 12.5
Ahlers et al. [135–137]	n/a	n/a	-	24.8	24.8, 49.5
Niemela and Ecke [138,139]	[0.03, 0.2]	[0.03, 0.2]	-	50	100
Niemela and Ecke [138,139]	[0.05, 1.8]	[0.4, 25]	-	{20, 60}	{10, 20, 40, 80, 180}
Bodenschatz et al. (U-Boot) [69,140]	[0.002, 1.3]	[1, 10.6]	-	110	{110, 220}

(continued on next page)

Table 1. (continued)

Experiment	Ω (rad/s)	Δ (K)	R_i (cm)	R_o (cm)	H (cm)
Kunnen et al. (TROCONVEX) [141–143]	[0.15, 2.2]	[1, 25]	-	40	{80, 200, 300, 400}
Abbate and Aurnou (Calimero) [144]	$[8.4\times10^{-2}, 3.7]$	[2, 55]	-	9.64	{19.05, 38.10, 80.01}
Zhong et al. [145–147]	n/a	n/a	-	12	[6.3, 60]
Xia et al. [148]	[0.63, 6.1]	[1, 34]	-	9.8	9.8
			Cylindrical radial gravity		
Busse et al. [54,149,150]	n/a	n/a	n/a	n/a	n/a
Busse and Carrigan [50,151]	n/a	n/a	n/a	n/a	n/a
Chamberlain and Carrigan [89]	[16, 80]	7	0	7.51	7.51
Cordero and Busse [90,152]	17.80, 19.89	[0.7, 3.7]	5	6.35, 8.94	1.35, 2.94
Cardin and Olson [91,153]	[26.2, 41.9]	[0, 10]	5	15	10
Busse et al. [154,155]	n/a	n/a	n/a	n/a	n/a
Sumita and Olson [92,156–158]	21.57	[0, 10]	5	15	10
Aubert et al. (Water) [74]	[20.9, 83.8]	[0, 25]	4	11	7
Aubert et al. (Gallium) [74]	[41.8, 83.8]	[0, 30]	4	11	7
Gillet et al. (Water) [159]	[20.9, 83.8]	[8, 33]	4	11	7
Gillet et al. (Gallium) [94,159]	[20.9, 83.8]	[8, 33]	4	11	7
Sahoo and Sreenivasan [87,160]	31.31	-	0.051	0.142	0.092
Sun et al. [88,161]	[12, 74]	n/a	12	12	12
			Tangent cylinder		
Aurnou and Olson [96]	$[4\times10^{-2}, 19.5]$	-	5	15.2	[11.6, 15.2]
Pothérat et al. (LEE1) [47,56,83]	[1.52, 6.28]	[0.3, 25]	5	13.8, 14.25	12
Pothérat et al. (LEE2) [48]	0, [0.75, 6.28]	[0.3, 23]	7.75	14.3	11

Table 2. Prandtl number $Pr = \nu/\kappa$, Rayleigh number, Ekman number $Ek = \nu/(2\Omega H^2)$, Froude number $Fr = \Omega^2 R_o/g$ (where $R_o = D/2$ in cylindrical geometries), and the (convective) Rossby number $Ro = \sqrt{Ek^2 Ra/Pr}$. The aspect ratio $\Gamma = R_i/(R_o - R_i)$ for spheres and $\Gamma = 2R_o/H$ for cylinders. Note that Pr, Ra, Ek, Fr, Ro are only approximate due to the temperature-dependence of the material properties. For terrestrial gravity we use $g = 9.8$ m/s^2. Most values for cylindrical geometries were taken from the review by Cheng et al. [141]. No parameters are given in Busse and Carrigan (1976). In the experiments by Boubnov and Golitsyn [117,118], Fernando [119] and Sahoo and Sreenivasan [87,160] convection is driven by imposing a heat flux instead of a temperature difference. Not all values in this table are taken from the original papers, some are estimated and may not represent actual measurement points

Experiment	Pr	Ra	Ek	Fr	Ro	Γ
Hart et al. (GFFC) [84,98–100]	8.4	$[4.1\times10^3, 4.3\times10^5]$	$[1.3\times10^{-3}, 1.5\times10^{-1}]$	$[1.7\times10^{-5}, 0.26]$	[0.03, 33]	2.65
Egbers et al. (GeoFlow) [85,101–106]	{64, 125, 178}	$[5.6\times10^2, 2.2\times10^5]$	$[2.6\times10^{-3}, 7.6\times10^{-3}]$	$[5.1\times10^{-5}, 2.55]$	[0.07, 3.1]	[17, 75.0]
Putterman et al. [86]	0.15	3×10^6	6×10^{-4}	0.026	2.7	-
Nakagawa et al. (mercury) [95,107,109–111]	0.024	$[10^4, 1.27\times10^{11}]$	$[10^{-6}, 3.46\times10^{-4}]$	$[0.36, 8.1]\times10^{-3}$	[0.13, 1.2]	2.8, 2.9
Nakagawa et al. (water) [108]	6.4	$[10^5, 9\times10^8]$	$[7\times10^{-6}, 10^{-3}]$	$[7\times10^{-3}, 1]$	$[6.24\times10^{-4}, 8.32\times10^{-2}]$	[1.66, 15]
Koschmieder [112]	881	$[9.9, 20]\times10^2$	$[1.34, 5.38]\times10^{-2}$	[0.025, 0.4]	$[1.4, 8.1]\times10^{-2}$	20.6
Rossby [113]	[0.025, 200]	$[2\times10^3, 6\times10^6]$	$[1.6\times10^{-5}, 1.8\times10^{-2}]$	$[1.1\times10^{-4}, 0.26]$	$[5\times10^{-5}, 283]$	6.4, 11.1, 22.2, 44.5
Donnelly et al. [114–116]	[0.49, 0.76]	$[10^3, 4\times10^6]$	$[0.03, 1.7\times10^{-4}]$	$[9.2\times10^{-5}, 3.36]$	[0.016, 4.28]	3.2, 4.9, 7.8
Ecke et al. [63,64,120–123]	[3, 7]	$[2\times10^3, 5\times10^8]$	$0, [0.1, 1.4\times10^{-5}]$	$[1.1\times10^{-5}, 0.66]$	$[1.17\times10^{-4}, 8.9]$	1, 2, 5, 0.78 (square)
Sakai [124] (square vessel)	6.4	$[10^6, 10^9]$	$[1.4\times10^{-5}, 1.1\times10^{-3}]$	$[2.8\times10^{-1}, 0.1]$	$[1.1\times10^{-2}, 0.44]$	2.2, 3.3, 6.7
Aurnou and Olson [125]	0.023	$[1.5\times10^3, 2.9\times10^4]$	$[3.2\times10^{-3}, 3.2\times10^{-2}]$	$[4.15\times10^{-7}, 7.6\times10^{-2}]$	[0.11, 8.1]	4 (square)
Aurnou et al. (RoMag) [35,36,126–129]	0.025	$[1.4\times10^4, 2.1\times10^9]$	$[2.3\times10^{-7}, 1\times10^{-4}]$	$[10^{-2}, 0.2]$	$[1.7\times10^{-4}, 3.0]$	{0.4,1,2,4}
Kunnen et al. [130–134]	[5.68, 7.85]	$[1.28\times10^8, 3.5\times10^9]$	$[1.17\times10^{-6}, 8.7\times10^{-4}]$	$[1.17\times10^{-6}, 0.56]$	[0.023, 11.5]	1
Ahlers et al. [135–137]	[4.38, 6.26]	$[2.37\times10^8, 7.2\times10^{10}]$	$[10^{-6}, 3.36\times10^{-3}]$	$[3.3\times10^{-7}, 0.05]$	[0.06, 22.2]	0.5, 1, 2
Niemela and Ecke [138,139]	0.7	$[4\times10^9, 4\times10^{11}]$	$[2\times10^{-7}, 3\times10^{-5}]$	$[4.6\times10^{-5}, 2.0\times10^{-3}]$	[0.07, 5.0]	0.5

(continued on next page)

Table 2. (continued)

Experiment	Pr	Ra	Ek	Fr	Ro	Γ
Aurnou et al. (NoMag) [162]	[4, 7]	$[10^5, 10^{13}]$	$[10^{-8}, 10^{-2}]$	$[5.1\times10^{-5}, 0.20]$	$[10^{-6}, 10^3]$	{0.11, 0.25, 0.33, 0.5, 0.75, 1.5, 2, 3, 6}
Bodenschatz et al. (U-Boot) [69,140]	0.8	$[8\times10^9, 8\times10^{14}]$	$[1\times10^{-8}, 3\times10^{-5}]$	$[4.48\times10^{-7}, 0.19]$	[0.07, 42]	{0.5, 1}
Kunnen et al. (TROCONVEX) [141–143]	[2, 7]	$[1\times10^{10}, 7\times10^{13}]$	$[5\times10^{-9}, 3\times10^{-6}]$	$[9.2\times10^{-4}, 0.20]$	$[2\times10^{-4}, 30]$	{0.1, 0.13, 0.2, 0.5}
Abbate and Aurnou (Calimero) [144]	{6, 41, 206, 993}	$[10^8, 10^{12}]$	$[10^{-7}, 10^{-4}]$	$\{6.9\times10^{-5}, 0.13\}$	[0.02, 2.5]	{0.24, 0.51, 1.0}
Zhong et al. [145–147]	4.38	$[1.4\times10^7, 2.9\times10^{11}]$	$[2\times10^{-7}, 1.3\times10^{-4}]$	[0.005, 0.31]	$[1.2\times10^{-6}, 6.94]$	0.4, 0.5, 1, 2, 3.8
Xia et al. [148]	4.34	$[2.8\times10^8, 9.5\times10^9]$	$[1.4\times10^{-6}, 1.4\times10^{-5}]$	[0.004, 0.363]	[0.025, 1]	1
Chamberlain and Carrigan [89]	6.5	$[3.3\times10^5, 2.6\times10^6]$	$[10^{-6}, 5.0\times10^{-6}]$	[2.0, 49]	$[2.3\times10^{-4}, 3.2\times10^{-3}]$	1
Cordero and Busse [90,152]	6.2	$[5.3\times10^5, 5.1\times10^6]$	$3.3\times10^{-6}, 5.6\times10^{-6}$	2.1, 3.6	$9.5\times10^{-4}, 5.1\times10^{-3}$	1.7, 3.7
Cardin and Olson [91,153]	7	4.5×10^9	$[1.2\times10^{-6}, 1.9\times10^{-6}]$	[11, 24]	$\leq4.8\times10^{-2}$	0.5
Sumita and Olson [92,156–158]	7	$[4.5\times10^8, 1.2\times10^9]$	2.4×10^{-6}	7.0	$[1.9\times10^{-2}, 3.8\times10^{-2}]$	0.5
Aubert et al. (water) [74]	7	$[2.9\times10^7, 8.6\times10^9]$	$[1.2\times10^{-6}, 4.9\times10^{-6}]$	[4.9, 79]	$[0, 1.7\times10^{-1}]$	0.64
Aubert et al. (gallium) [74]	0.025	$[1.2\times10^7, 2.6\times10^8]$	$[3.6\times10^{-7}, 7.2\times10^{-7}]$	[20, 79]	$[0, 7.4\times10^{-2}]$	0.64
Gillet et al. (water) [159]	7	$[3.3\times10^8, 9.1\times10^9]$	$[1.2\times10^{-6}, 4.9\times10^{-6}]$	[4.9, 79]	$[8.4\times10^{-3}, 1.8\times10^{-1}]$	0.64
Gillet et al. (gallium) [94,159]	0.025	$[2.4\times10^7, 2.3\times10^8]$	$[4.9\times10^{-7}, 1.5\times10^{-6}]$	[4.9, 79]	$[1.5\times10^{-2}, 1.4\times10^{-1}]$	0.64
Sun et al. [88,161]	4.34	$[10^6, 3.7\times10^{12}]$	$[6.7\times10^{-7}, 2.4\times10^{-2}]$	$[5\times10^{-8}, 80]$	$[2.5\times10^{-3}, 100]$	1
Aurnou and Olson [96]	7	$[3\times10^6, 3\times10^{10}]$	$[10^{-5}, 9\times10^{-4}]$	$[1.5\times10^{-5}, 4.8\times10^{-2}]$	$[6.6\times10^{-3}, 59]$	[0.66, 0.86] (0.33)
Pothérat et al. (LEE1) [47,56,83]	{7, 12}	$[1.4\times10^7, 2.9\times10^9]$	$[1.3\times10^{-6}, 4.5\times10^{-5}]$	$[2.8\times10^{-2}, 0.44]$	$[3.2\times10^{-2}, 0.58]$	0.8 (0.35)
Pothérat et al. (LEE2) [48]	6.4	$[2.1\times10^7, 1.1\times10^9]$	$[3.5\times10^{-6}, 4.2\times10^{-5}]$	$0, [3.1\times10^{-3}, 0.44]$	$[6.3\times10^{-3}, 0.29]$	1.1

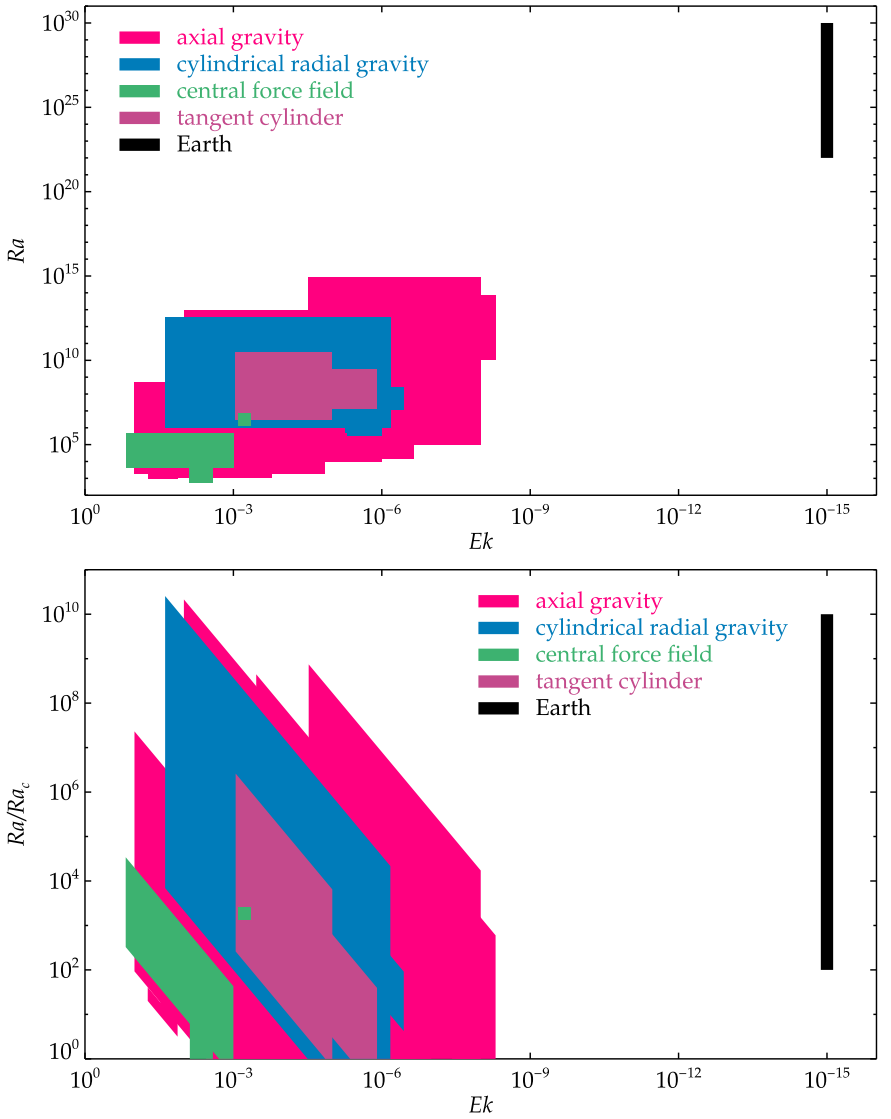


Figure 4. Parameter space spanned by the four types of experiments modelling rotating convection in the Earth's outer liquid core, and parameter range where the actual Earth's outer core is currently believed to operate. While in (Ra, Ek) space, all experiments sit very far from realistic geophysical regimes, especially, in terms of Rayleigh numbers, their levels of criticality Ra/Ra_c may well reach the Earth's. The data represented here is given in Tables 1 and 2.

are given in Table 3. Ra is the usual Rayleigh number but is defined using the outer value g_o. The typical values of g_o are much smaller than Earth's gravity. This demands microgravity and severely constrains rotation rates and vessel sizes to small values.

The Geophysical Fluid Flow Cell (GFFC) flew to space for the first time on the 29th of April 1985 together with two squirrel monkeys, 24 rats and seven astronauts [84,98,163]. The principal investigator was John Hart of the University of Colorado at Boulder, it was managed by NASA's Marshall Space Flight Center. The experiment was conducted in the Spacelab, a microgravity

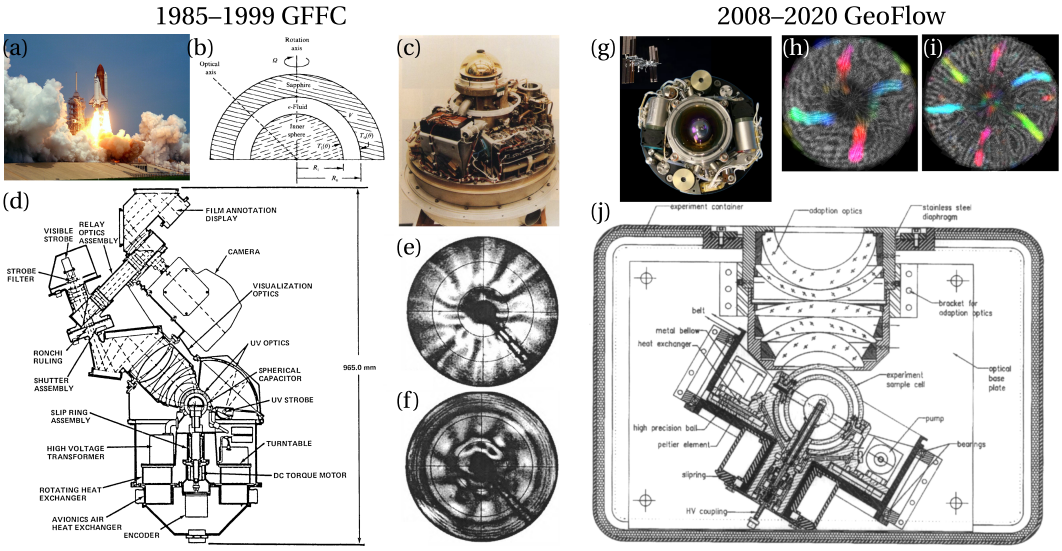


Figure 5. Left panels (a–f): the Geophysical Fluid Flow Cell (GFFC) experiment; (a) Space Shuttle Challenger with Spacelab 3 that flew GFFC to space; (b) sketch of the cross-section of the GFFC test cell [98]; (c) rotating turntable with power supply, circulation pumps, test cell, and associated circuitry [98]; (d) the full GFFC experiment including optical imaging system [163]; (e,f) unwrapped convection planforms showing banana cells and pronounced polar disturbances, the tangent cylinder is at 43°, (e) shows north–south fringes (sensitive to latitudinal temperature gradients) and (f) shows east–west fringes (sensitive to longitudinal temperature gradients) [99]. Right panels (g–j): the GeoFlow experiment; (g) photo of the experimental setup with the International Space Station (ISS), image by ESA; (h,i) Wollaston Shearing Interferometry which visualises the thermal gradients based on the changes of the temperature-dependent refractive index, the columnar cells are coloured using automatic pattern recognition [106], (h) spiralling columnar cells and (i) almost straight cells; (j) the full GeoFlow experiment with adaption optics and rotary tray [101].

Table 3. Material properties used in the space experiments, ρ_m is the mean density, ϵ_m the mean permittivity, α the expansion coefficient, γ the dielectric variability, V_rms the (maximum) applied a.c. voltage, and g_o and g_i the values of the electro-hydrodynamic "gravity" at the outer and inner radius of the (hemi)spherical shell, respectively. The silicone oil Dow Corning 0.65 cSt 200 Fluid was used in the GFFC experiment, silicone oil M5 in the GeoFlow I experiments, and 1-nonanol at different mean temperatures during the GeoFlow II experiments. Note that $\epsilon_0 = 8.854 \times 10^{-12}$ CV^{-1}·m^{-1} is the vacuum permittivity. Taken from Refs. [98] and [104,105].

Fluid	ρ_m (kg/m^3)	ϵ_m	α (K^{-1})	γ (K^{-1})	V_rms (kV)	g_o (m/s^2)	g_i (m/s^2)
Silicone oil DC 0.65 cs	760	$2.5\epsilon_0$	1.34×10^{-3}	1.29×10^{-3}	10	1.13	5.55
Silicone oil M5	920	$2.70\epsilon_0$	1.08×10^{-3}	1.07×10^{-3}	10	0.26	8.54
1-nonanol (20.0 °C)	820	$8.60\epsilon_0$	9.45×10^{-4}	2.95×10^{-3}	6.5	0.40	12.76
1-nonanol (30.5 °C)	822	$8.33\epsilon_0$	9.45×10^{-4}	2.46×10^{-3}	6.5	0.39	12.32

laboratory developed by ESA and flown by the NASA space shuttle Challenger. The specific mission was Spacelab 3 (STS 51-B; 29 April 6–May 6, 1985), the first in which a strict low-gravity environment was maintained in orbit, here in a low Earth orbit of 400 km altitude. GFFC's second space flight in 1995 was with the US Microgravity Laboratory-2 (USML-2) on board the space shuttle Columbia (STS-73; 20 October–5 November 1995) [99,100]. The first mission provided about 110 h of experimental data mainly in the form of about 50,000 film images. During the second mission, 29 separate 6-h runs (174 h in total) were carried out.

The set-up itself is a spherical shell rotating at up to 3 rad/s, but only its northern hemisphere was used in the experiment, as depicted in Figure 5. The inner shell was made of polished nickel of radius $R_\mathrm{i} = 2.402$ cm and the outer northern hemispherical shell of radius $R_\mathrm{o} = 3.300$ cm was a 1 cm thick transparent sapphire dome, with electrically conducting coating on the inner side acting as an electrode. An AC voltage $V_\mathrm{rms} = 10\ \mathrm{kV} \pm 0.5\%$ at 300 Hz was applied across the gap. This ensured the absence of conductive electric currents that may lead to other and undesired fluid instabilities, as the associated period was short compared to the charges' relaxation time of the working fluid. The southern hemisphere was filled with Teflon to avoid the effect of non-radial electric fields occurring in the vicinity of the inner sphere's mechanical support. The working fluid was a dielectric silicone oil Dow Corning with $Pr = 8.4$. The inner sphere was heated and the outer sphere was cooled with a computer-regulated temperature gradient of up to $20\ \mathrm{K} \pm 0.1\ \mathrm{K}$. Individual heater elements also allowed to study differential, latitudinally varying heating, and several experiments were run with a hotter north pole (a cooler pole would have obscured visualisations). During the second flight, problems with the temperature regulation led to a temperature drift of about 10% to 20% and overheating occurred. This limited the data interpretability, especially for the planned different latitudinal heating scenarios. As optical techniques shadowgraph and back-focus Schlieren visualisations were used, which give information about the temperature structures. Successive images from the fixed camera only allowed flow reconstruction in weakly time-dependent flows but not for more chaotic and turbulent flows. During the second flight, an additional video camera was installed, but it failed at the 19th run. Originally, it was also planned to use spiropyrane, a photochromic dye that is activated by UV light, as a flow tracer for velocity measurements during the Spacelab 3 mission. However, the dye degraded over the time of 1.5 years when it was not accessible during integration into the space module, thus, not permitting the extraction of accurate velocity data.

The GeoFlow experiment was very similar in conception, and was integrated into the Fluid Science Laboratory of the European Columbus module on the International Space Station (ISS). This crucial difference allowed for much longer, extensive campaigns with more than 2500 h of scientific run time [85,101–106]. It allowed daily data transfer from the orbit and thereby almost real-time data analysis. The GeoFlow experiment went to space for the first time on 7 August 2008 and stayed there until January 2009 (GeoFlow I), with three follow-up missions (March 2011–May 2012; December 2012–May 2013; November 2016–February 2017; (GeoFlow II, IIb, IIc). The head of the GeoFlow Team was Christoph Egbers from the Brandenburg University of Technology Cottbus-Senftenberg. Unlike GFFC, GeoFlow was a full sphere with inherent limitations due to the heating supply shaft at the south pole [85,101]. The device had an inner radius of $R_\mathrm{i} = 1.35$ cm and an outer radius of $R_\mathrm{o} = 2.70$ cm with the possible rotation rates of $\Omega = 63$ rad/s. The working fluid of GeoFlow I was the silicone oil M5 with $Pr = 64$. For GeoFlow II, the team improved the olfactory aspect and used the alcohol 1-nonanol, known in the cosmetics industry for its lemon fragrance, with $Pr = 125$ and $Pr = 178$. Most of the results were for very slow rotation rates that were mainly there to ensure the visualisation of the full latitudinal direction and more relevant to mantle convection [102–105]. Only the GeoFlow IIc experiment focused on rotating convection with parameters comparable to the GFFC experiment, with a minimum $Ek = 2.64 \times 10^{-3}$, and maximum $Ra = 1.59 \times 10^5$. The fluid 1-nonanol also allowed them to study both convection

induced by the temperature difference between the spherical shells and due to the internal dielectric heating [106]. The flow visualisation technique used was Wollaston prism shearing interferometry which showed only projections of the thermal structure since safety and weight limitations did not permit the use of tracer particles or larger optical systems [106]. Exemplar pictures are shown in Figure 5.

Both experiments, GFFC and GeoFlow studied the stability properties, the formation of patterns and the transition between states, including chaos and turbulence. Many of the results had rather high values of Ek and Ro, as well as low values of Ra, thus, they are practically in a rotation-unaffected regime [11,12,14]. These flows show a tessellated pattern, also found in more recent numerical simulations of non-rotating convection [166,167]. The GeoFlow experiments also show mantle-like plumes influenced by non-Oberbeck–Boussinesq effects [102–104,168].

In the rotating regime, the main result was the confirmation of the existence of columnar convection in radial gravity ("banana cells" [25]) in the equatorial region. Experiments also captured their drifting in the prograde direction, illustrated in Figure 5 [84,98,106]. In both experiments, columnar convection was very robust, likely because of the relatively high Prandtl number [11,144,169–172]. The experiments, especially GFFC, also showed that at higher supercriticalities, retrograde mid-latitude convection modes develop, the TC becomes convectively active, and later on these mid-latitude and polar modes become unstable. Likely, there were two effects at play here, a loosening of the rotational constraint, i.e. moving closer to the non-rotating regime expected at higher supercriticality [48]. The unique specificity of GFFC was that they could also observe the interactions of the columnar equatorial cells with the retrograde-propagating mid-latitude convection modes, which can only be captured with spherical radial gravity. These interactions initially caused a wavering, and finally the erosion of the columnar equatorial cells. They also found that the virtual boundary of the tangent cylinder broke down, with columnar convection only within 20° of the equator whereas the tangent cylinder extended up to 43°. The no-slip boundary conditions (in addition to the not-very-extreme control parameters) were likely the reason for not observing any zonal flows. However, these boundary conditions are arguably also more relevant for Earth's core than for gas giants. Many of the results are indeed reminiscent of more modern numerical spherical simulations of rotating thermal convection [167,173,174]. They further also showed that spherical shell thermal convection may be hysteretic, finding sometimes the same and sometimes different flow patterns depending on whether they increased or decreased Ra [99,100]. The GFFC experiment also explored latitudinal inhomogeneous heating. They observed spiralling convection when the north pole was heated, which was interpreted as evidence for baroclinic waves. They showed that with increased differential heating, the interaction of the equatorial columnar cells with mid-latitude waves leads to triangular waves and ultimately, with turbulent structures moving downward from the pole to full turbulence.

2.2. … *and elsewhere: Kelvin forces and pycnoclinic acoustic gravity*

The main limitations of the space experiments' applicability to planetary core convection are the relatively low Ra and high Ek required to minimise centrifugal effects. Their other shortcoming is that the poor electric conductivity of dielectric materials renders the study of MHD effects practically infeasible.

Having said that, it may be worthwhile to embrace Coriolis-centrifugal convection, and so thanks to the combination of $\Omega^2\boldsymbol{r}$ and $\boldsymbol{g}$, spot tornado-like vortices as they occur in planetary and stellar atmospheres [22,23,145,175–178].

Ferrofluids offer an alternative route to creating a central force field, with the benefit that some of them are also electrically conducting. Experiments of this kind have been conducted in

non-rotating thermo-magnetic convection where spherical gravity is mimicked using permanent magnets as an inner core, and a ferrofluid fills the outer core [179,180]. However, neither rotating convection nor magnetoconvection have so far been realised. The idea is here that a magnetised fluid is attracted towards higher magnetic fields. This attracting body force is referred to as Kelvin force and mimics buoyancy. The magnetisation depends on both the magnetic field and the temperature, a colder fluid is attracted more strongly than a warmer fluid. This is expressed through the pyromagnetic coefficient which plays the role of the expansion coefficient.

Acoustic gravity is another clever way of creating thermal rotating convection with a central force field in an Earth-bound laboratory setting [86]: Sound, when averaged over many cycles, exerts a force on density gradients in a gas. The so-called pycnoclinic acoustic radiation force $-\langle v_{\rm ac}^2\rangle\nabla\bar{\rho}/2$ yields an acoustic gravity of $\boldsymbol{g}_{\rm ac} = \nabla\langle v_{\rm ac}^2\rangle/2$ [181,182]. Here, $\bar{\rho}$ is the time-averaged density and $v_{\rm ac}$ is the acoustic velocity. Koulakis et al. [86] use a rotating spherical plasma bulb with a radius of 1.5 cm filled with a weakly ionized sulfur gas. The gas is heated volumetrically by microwaves. The rotation is essential to guarantee quiescent conditions of the plasma. Then, the amplitude modulation of the microwave power generates a high amplitude, spherically symmetric acoustic standing wave. This creates an acoustic gravity that can briefly reach values of up to 1000 times Earth's gravity, so centrifugal effects become negligible. Gravity changes sign roughly at half the bulb radius, so confining the convective zone to the outer region, as in stars and Earth's core. While the parameters are only slightly more extreme than the space experiments, density differences of a factor of about two make it possible to study compressible rotating spherical convection too.

3. Cylindrical radial gravity

Given the difficulties in modelling spherical rotating thermal convection with central force fields, geophysicists, planetary scientists and fluid dynamicists had to resort to alternative means to model planetary core convection. A very successful branch of laboratory research in this regard relied on centrifugal buoyancy to mimic equatorial and low-latitude convection.

3.1. *The Busse annulus*

The cylindrical annulus geometry was first conceptualised as a laboratory device with direct application to Earth's core by Busse in 1970 [25]. The underlying idea here is to use the cylindrically radially outward-directed centrifugal force and then cool the inner boundary and heat the outer one. This ensures that buoyancy acts in the right direction, as sketched in Figure 1. Only the product of gravity and temperature gradient matters physically. Busse let the centrifugal acceleration exceed Earth's gravity by a factor of two or three [55] and envisioned slanted boundaries, where the height varies with cylindrical radial distance from the vertical rotation axis. The resulting β-effect creates slowly drifting columnar thermal Rossby waves. These are nowadays also known as *Busse* columns and have been argued to exist in planetary cores [25]. Busse first derived a simple analytical model for the onset Rayleigh number, drift frequency and wave number in the small gap approximation with asymptotically small endwall slopes. He then materialised his theoretical ideas into an innovative laboratory setup [54]. The concept of the *Busse annulus* turns the arduous three-dimensional spherical problem into a tractable two-dimensional one and offers simple access to the spherical rotating convection problem.

Busse (and collaborators) subsequently fleshed out the original idea [54,149,150,154,155,183–188], including the application to magnetoconvection [189,190] and the geodynamo [191] (see also the reviews [55,192–194] and Section 3.2 on the spherical geometry). The *Busse Annulus* has been subject to many theoretical and numerical studies up to recent days [38,195–199]. In

particular, Calkins et al. [199] lifted the original restriction to small slopes and near-criticality. He introduced an asymptotically reduced three-dimensional set of equations for quasi-geostrophic convection, thus, establishing a closer connection to spheres and spherical shells.

Here, we focus on the experimental aspects of the *Busse Annulus* [54,149,150,154,193]. A sketch of the first laboratory realisation [54] is shown in Figure 6(a). Two concentric cylinders were mounted on two circular end plates. The outer cylinder was heated through a circulating thermostatically controlled reservoir enclosed in an outer nearly cubical Plexiglas box. The inner cylinder was cooled by circulating water through two centred hollow shafts mounted on the end plates, and ball-and-socket couplings connected the stainless steel shaft to the cooling tubes. Baffles at the inside of the end plates ensured an efficient distribution towards the inner annulus wall. The shafts also served as rotation axis, and rotation rates of up to 400 rpm (41.9 rad/s) were achieved. The temperature difference was measured using a thermocouple in each of the water baths. Since the experiment concerned the onset of convection, typical temperature differences were less than 1 K. The inner cylinder was made of aluminium and three different sizes were used, $R_\mathrm{i} = \{13.34\ \mathrm{cm}, 3.81\ \mathrm{cm}, 3.18\ \mathrm{cm}\}$. The outer cylinder was made of acrylic plastic (Plexiglas) to allow for optical access, and the outer Plexiglas cube helped to avoid optical distortions. The used radii were $R_\mathrm{o} = \{13.94\ \mathrm{cm}, 4.775\ \mathrm{cm}, 4.74\ \mathrm{cm}\}$. The endwalls were made of Teflon and three different sloping angles were used: $\chi = 0$ (corresponding to horizontal plates) and $\chi = 22.5°$ and 45°. The mean heights were $L = \{28.6\ \mathrm{cm}, 6.97\ \mathrm{cm}, 6.69\ \mathrm{cm}, 1.96\ \mathrm{cm}, 0.95\ \mathrm{cm}, 0.45\ \mathrm{cm}\}$. The working fluids were silicon-oil and water. Small amounts of Kalliroscope were used for flow visualisation. These are nearly neutrally buoyant particles that align with the shear. Stroboscopic light was used to make the shear patterns visible and to measure the rotation rate. The onset of convection was determined visually.

Quantitative measurements involved measuring a buoyancy parameter B versus an inverse Ekman number $Ek = \nu/(\Omega L^2)$ (bar the factor 2 in both cases). In modern terminology, their buoyancy parameter is in fact the square of the (convective) Rossby number. This can be seen by recalling that $Ro = \tau_\mathrm{rot}/\tau_\mathrm{buoy}$, i.e. the ratio of a rotational time scale, $\tau_\mathrm{rot} = 1/\Omega$ and the buoyancy time scale, $\tau_\mathrm{buoy} = H/\sqrt{\alpha\Delta\Omega^2\bar{R}H}$, defined in analogy to the usual free-fall time scale, with the temperature difference $\Delta = T_h - T_c$, $\Omega^2\bar{R}$ being used as centrifugal gravity, and the characteristic length scale being the gap width H. Thus, we have

$$Ro^2 = B = \frac{\tau_\mathrm{rot}^2}{\tau_\mathrm{buoy}^2} = \frac{\alpha\Delta\Omega^2\bar{R}H}{H^2\Omega^2} = \frac{\alpha\Delta\bar{R}}{H}. \tag{16}$$

At the onset of convection, Busse and Carrigan saw the first experimental evidence of the retrograde drifting columns that were slightly tilted and helical. Their results showed decent agreement with the small gap linear theory [25]. Qualitatively, it was also found that the wavelength of the instability decreased with increasing rotation rate in the sloping endwall cases. The instabilities in this case were typically the superposition of several waves and the columns showed beating phenomena. Dedicated experiments sought hysteresis and subcritical convection but found none of them. The β-effect arising out of the interplay of the Coriolis force with the top and bottom conical endwalls was found to inhibit the convective instability compared to the flat case that develops columns, see Figure 6(b). At high rotation rates the experiment strikingly exhibits geostrophic columns, in agreement with the TPC, which imposes that the flow be z-independent in these regimes.

Zonal flows. For the observations of zonal flows, Busse and Hood modified the Busse annulus ($L = 12.6$ cm, $H = 2.46$ cm, $\bar{R} = 3.51$ cm) to include radial curvature of top and bottom boundaries, either convex or concave [149]. The mean flow was measured by releasing electrolytic dye into

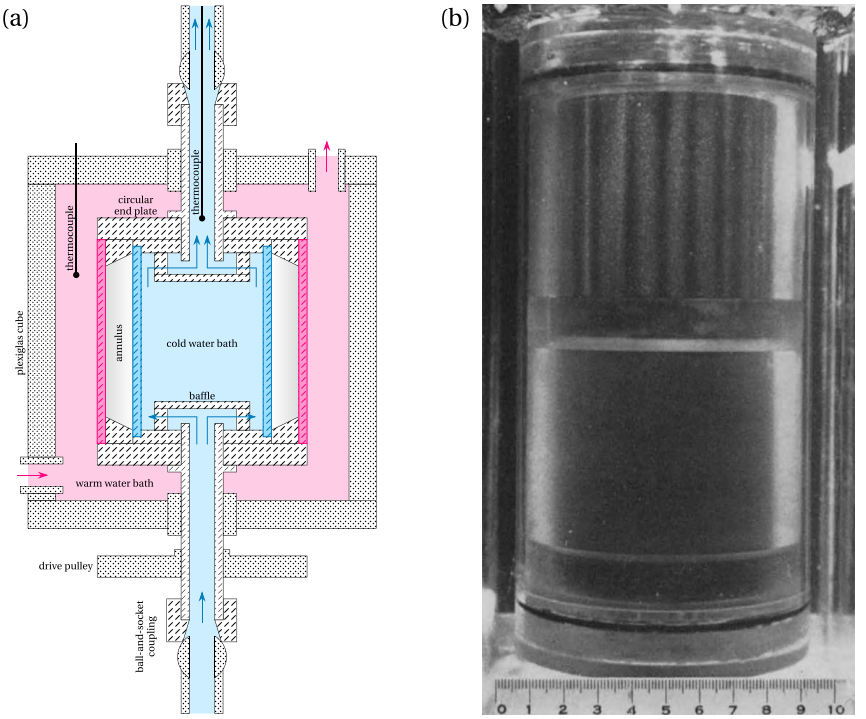


Figure 6. (a) Schematic vertical cross-section of Busse and Carrigan's original annulus apparatus, adapted from Ref. [54]. The northeast lines pattern indicates the rotating parts and the crosshatch dotted pattern indicates the non-rotating parts, in particular, the Plexiglas cube. The radius and height of the inner and outer cylinders were adaptable and varied during the experimental campaigns. (b) Photograph of two annuli stacked on top of each other, scale is in cm, adapted from Ref. [54]. The upper part shows an annulus with constant height, showing strong convection columns. The lower part shows an annulus with conical endwalls, that results in an axisymmetric flow at the same parameters. The working fluid was water at 30 °C and Kalliroscope was used for visualisation.

the working fluid (water) by frequent pulsed currents, following a method devised by Baker [200], and taking photographs at intervals of 10 s.

A similar experiment by Azouni et al. [150] used mercury and water as as working fluids. The outer cylinder was replaced by anodized aluminium to avoid the thermal loss through the acrylic sidewall ($L = 14.48$ cm, $\tilde{R} = 3.917$ cm, $H = 3.917$ cm and $\chi = 47.4°$). They measured drift rates and amplitudes of the convection columns by combining and correlating five thermistor probes in the equatorial plane and spaced in azimuth. Three were embedded in the inner cylinder flush with the outer surface, two others were glued to the outer cylinder.

Earth's gravity creates a thermal wind and a meridional circulation scaling as Ω^{-1} and $\Omega^{-1/2}$, respectively. The thermal wind is antisymmetric relative to the equatorial plane, being retrograde in the lower part and prograde in the upper part, thus, it does not affect the dye injected in the equatorial plane too much. The meridional circulation is noticeable, on the other hand. It leads to an upflow near the hot outer wall and a downflow near the cold inner wall, thus, there is an additional prograde zonal flow at the outer wall and a retrograde flow at the inner one.

Both experiments confirmed the existence of a mean zonal flow. The main differential rotation was argued to stem from a mean flow instability due to Reynolds stresses generated through

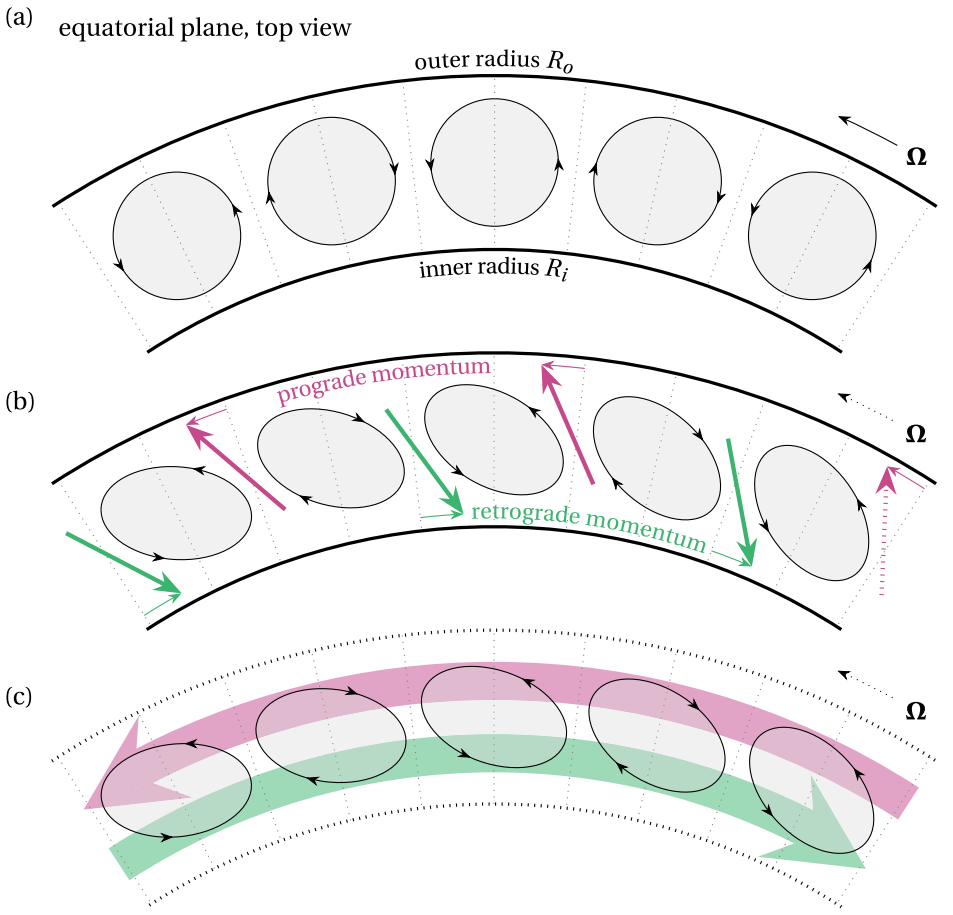


Figure 7. Creation of mean zonal flows in spherical shell and annuli geometries. (a) Convective columns, initially at rest; (b) columns get tilted, here in the prograde direction, e.g. by small fluctuations which create Reynolds stresses. Prograde momentum (purple arrows) is carried outwards and retrograde momentum (green arrows) is transported inwards. (c) Resulting prograde flow at the outer boundary and retrograde flows at the inner boundary increases the initial tilt leading to a feedback process sustaining a mean flow.

strong mean zonal shear, shown schematically in Figure 7. The convective columns in Figure 7(a) get slightly tilted, e.g. by small fluctuations. This creates Reynolds stresses $\langle u'_r u'_\phi \rangle$, where u'_r and u'_ϕ are the fluctuating part of the radial and azimuthal velocity component, respectively. Depending on the initial tilt, either direction of the evolving mean flow is possible. If tilted in the prograde direction, Figure 7(b), then prograde momentum (purple arrows) is carried outwards and retrograde momentum (green arrows) is transported inwards. Thus, the flow is retrograde at the inner boundary and prograde at the outer boundary. The resulting flow increases the initial tilt leading to a feedback process sustaining a mean flow, Figure 7(c). Thus, there is a differential rotation in which the outer fluid rotates faster than the inner one. If the columns are tilted in the opposite direction, the mean flow direction is reversed. For similar reasons, for convex endwalls, thermal Rossby waves propagate faster on the outside than on the inside, thus, the columns spiral outwards and the mean flow is retrograde at the inner boundary and prograde on the outer boundary. The opposite happens for concave endwalls [55,149]. Viscous stresses

oppose the differential rotation and lead to an equilibrium. The differential rotation was argued to be rather insensitive to the cylindrical annulus sidewall, and, hence should also be found in spherical shells [55]. Azouni et al. [150] found drift rates in agreement with Busse's simplified theory, whereas the amplitudes decreased with increasing Rayleigh number.

More recent developments. Busse continued investigating flows in the *Busse annulus*. He and his collaborators found quasi-geostrophic chaotic states in air [193]. They also devised an elegant method to visualise convective patterns using thermochromatic liquid crystals in high-Pr fluids [154]. At such high Pr, the effects of rotation were much lower. They found different types of patterns, such as knots and hexaroll, which are predicted theoretically [188], but also patterns that still lack a theoretical description such as oblique rolls.

The *Busse annulus* without sloping endwalls was later replicated by Jiang et al. [88,161]; they rediscovered the centrifugal force as a proxy for gravity and called it supergravity. Their achievable parameters were comparable to Busse's original design, with rotation rates between 211 rpm to 705 rpm, focussing on the strongly supercritical regime. While they also rediscovered the mean flow instability, the constant radial height does not permit e.g. Rossby waves and thus, makes the experiment less geophysically relevant.

3.2. *Spheres, spherical annuli and hemispherical shells*

Spherical geometries are a natural improvement of the *Busse annuli*, as they capture a more realistic β-effect and, in some setups, the Stewartson layers wrapped around the TC [30,62]. Here too, centrifugal gravity is used to mimic the gravitational field in the equatorial region, still at the expense of the polar regions. As for the *Busse annulus*, since the centrifugal gravity points outwards, the temperature difference has to be reversed with the outer spherical wall held at constant hot temperature using either water [151] or air [153].

In spherical shell geometries, the radial temperature gradient is controlled by cold fluid (water, or even Kerosene [93]) circulating through the inner sphere. A solid shaft must be fitted to connect the inner sphere to the cooling circuit and to hold the solid sphere at the centre of the outer sphere. This, however, finalises the sacrifice of the polar regions. Because of this shaft, we refer to setups of this category as the *spherical annulus* configuration. Another non-planetary feature of the spherical shells is the misalignment of the temperature gradient and gravity that increases with latitude. This source of baroclinicity combined with the Coriolis force incurs an artificial azimuthal wind, and results must therefore be interpreted keeping its influence in mind [151].

Several experiments were built on this principle with variants trying to address some of its shortcomings. These experiments are classics of geophysical rotating convection and have been extensively reviewed [201–203]. We shall only recall their main outcomes and highlight some specificities of the experimental approach itself.

Experiments at moderate *Pr*: water and oil. The first spherical annulus experiment was designed by Busse and Carrigan [50,151], whose original sketch is reproduced in Figure 8(a). The working fluids were water and ethylene glycol and the inner core radius was varied by using different inner spheres. High rotations up to 1000 rpm ensured the gravity was effectively cylindrical radial. The outer sphere (inner radius 10 cm) was made of transparent plastic and heated by a temperature-controlled water bath. The flow was diagnosed by seeding the fluid with reflective platelets that align with the shear and taking snapshots through the outer sphere. From these visualisations, the authors were able to detect the onset of convection and characterise the size of the onset structures. They mostly recovered Busse's linear theory for the onset of convection in a rotating shell with central gravity in the small-gap limit and identified the onset structures as being Rossby waves originating near the inner sphere, at $Ra_c \sim Ek^{-4/3}$, see original visualisations in

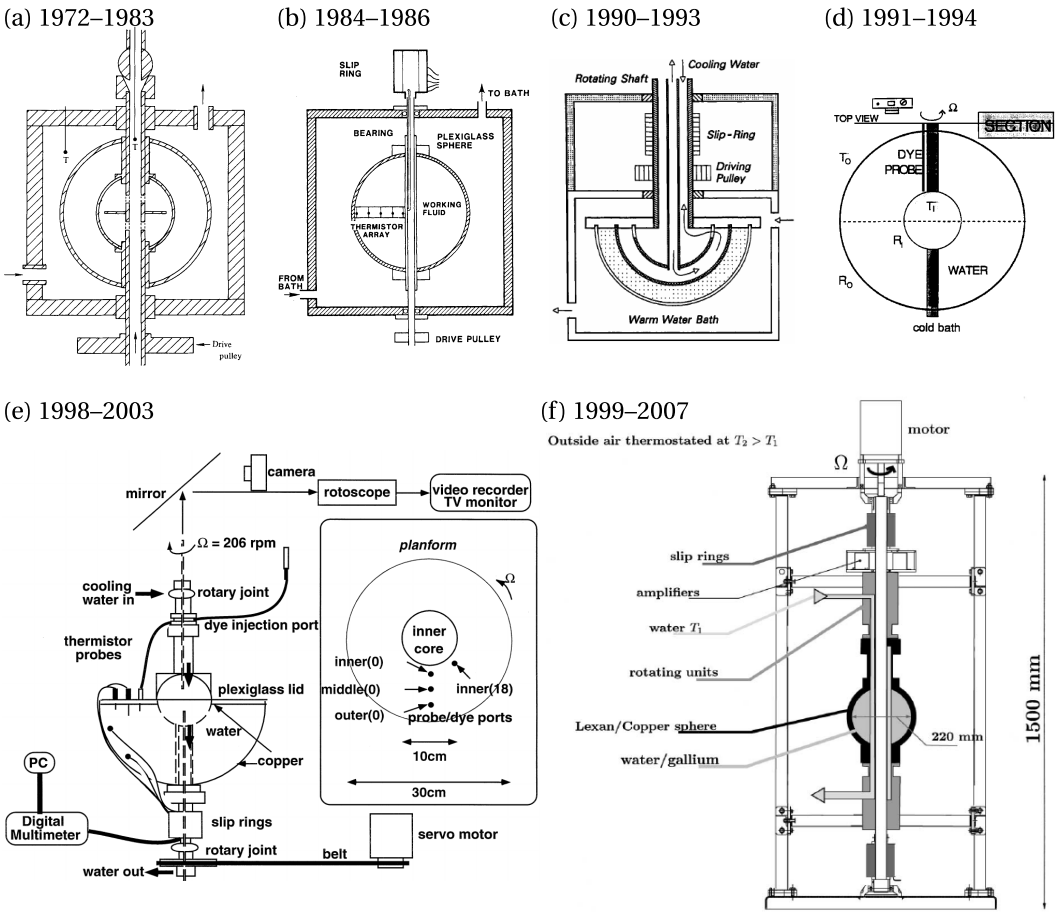


Figure 8. Evolution of the spherical shell experiments since 1976: (a) 1972–1983: Busse and Carrigan's original spherical shell convection device with spherical inner cold boundary [50,151], (b) 1984–1986: Chamberlain and Carrigan's modification of Carrigan and Busse's original setup, with no inner sphere and linearly increasing outer wall temperature [89], (c) 1990–1993: Cordero and Busse's hemispherical experiment [90], (d) 1001–1994: Cardin and Olson (1994)'s air-cooled setup [153], (e) 1999–2003: Sumita and Olson's modified version of Cardin and Olson's setup with a hemispherical annulus [92,156–158], (f) 1999–2007: Aubert and collaborators' water and liquid metal experiment [74,159].

Figure 9(a). The critical wavenumber of the Rossby waves follows the theoretical scaling law but with a lower prefactor. A discrepancy between the experiment and the small gap theory arises due to the presence of Stewartson layers developing along the TC. The Stewartson layers tend to stabilise the Rossby waves because they are precisely located where the waves originate. This effect becomes negligible in the limit $Ek \to 0$.

Chamberlain and Carrigan [89] later modified the setup, by removing the inner sphere and thereby the Stewartson layers [89], see Figure 8(b). The outer bath temperature was controlled to increase linearly in time to maintain a constant temperature gradient in the absence of inner cooling. After a short transient, the lag in the temperature response of the fluid inside the sphere leads to a constant temperature gradient there. The radial temperature profile is then the same as if the heat source was distributed in volume, up to a background temperature linearly increasing

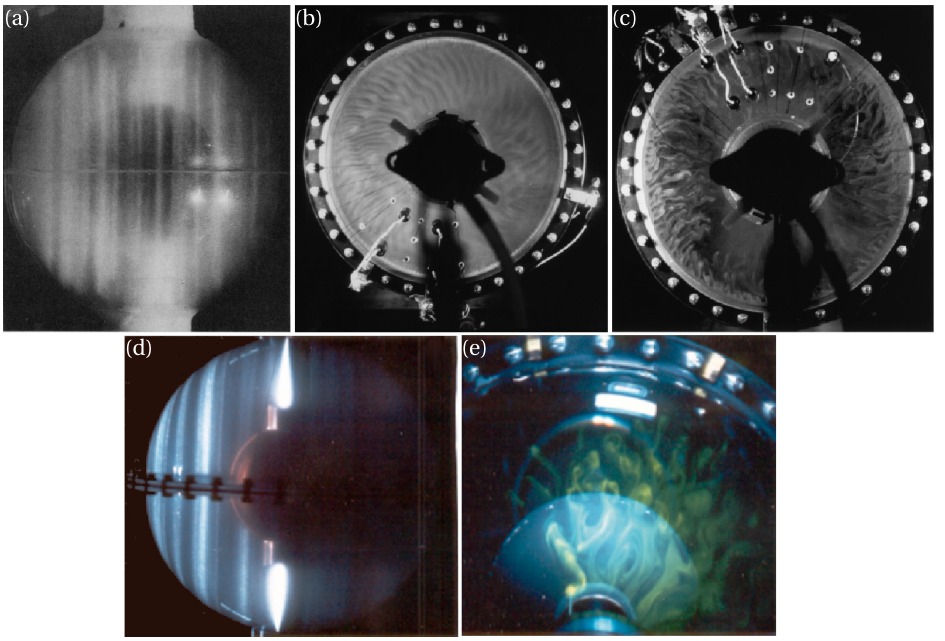


Figure 9. Patterns of rotating convection in a spherical gap by order of criticality: (a) Rossby waves at the onset of convection originally observed by Busse and Carrigan (side view) [50], (b) spiralling columns at $\widetilde{Ra} = 5.9$ (top view through the transparent top lid of the hemispherical vessel) [156], (c) dual convection at $\widetilde{Ra} = 19.3$ (top view as for (b)) [156], (d) chaotic convection at $\widetilde{Ra} = 50$ (side view) [153], (e) same as (d), but top view.

in time. This radial temperature profile was monitored by radially aligned temperature probes. The critical Rayleigh numbers were found in better agreement with Robert's linear theory for an internally heated sphere [37] than Busse's small-gap linear theory [25]. As in the previous experiment, however, the centrifugal wind incurred by the high-latitude baroclinicity prevented the authors from observing the retrograde drift of the Rossby waves. This led them to suggest experiments using a cylindrical annulus to eliminate that effect as Busse and collaborators did [149,150].

The first measurement of the drift of Rossby waves with a spherical geometry came from Cordero and Busse [90] using a hemispherical shell. Baroclinic effects were minimised by rotating the hemisphere at a speed where the sum of gravity and centrifugal forces produced an apparent gravity with parabolic iso-values nearly parallel to the curvature of the sphere. The outer sphere was made of glass and heated by an external thermostatically-controlled bath of water. The inner sphere was made of brass with an internal water-cooling circuit. Using the same visualisation method as in spherical experiments [50] and thermistors, the authors captured the variations of the decay of the drift velocity with the Rayleigh number as well as the appearance of secondary rolls of larger wavelength near the outer sphere.

The next series of spherical annulus experiments was initiated by Cardin and Olson [91,153], see Figure 8(c). They also used water but with a slightly larger outer sphere of radius 15 cm. Unlike previous spherical annuli, the outer temperature was thermostatically controlled at room temperature by the air current induced by the sphere's rotation. The rotation up to 400 rpm was somewhat lower than in Carrigan and Busse's experiment, so the proxy-gravity was not entirely cylindrical-radial but also had a significant vertical component. A new visualisation system relied on snapshots synchronised with a strobe light illuminating vertical planes and

a fluid seeded with rheoscopic flakes to identify the structures. In the horizontal planes, the flow was visualised by releasing dye at the inner sphere. The new visualisation system made it possible to investigate the regimes beyond the onset of convection. They found that for moderate and higher supercriticality, the classical Rossby waves give way to a chaotic columnar regime. The flow is quasi-geostrophic, made of irregularly distributed columns extending over the entire shell height. Its basic pattern is made of retrograde vortices produced at the inner core boundary extending outward into prograde spiralling streets of retrograde vortices (see Figure 9(d)). This regime is consistent with equatorial mirror-symmetry [204] and non-periodic magnetic flux [205] inferred from geomagnetic data. Scaling up experimental velocities in this regime to Earth parameters yields estimates of 0.1 cm/s for the convective velocity, consistent with estimates from geomagnetic variations [206]. However, the extrapolated column size of 20 km-radius columns is unobservable and inconsistent with the large-scale geomagnetic data. Cardin and Olson attributed this discrepancy to the action of the Lorentz force in the core.

The transition to the chaotic regime and the fully developed stages of convection were further investigated by Sumita and Olson [156]. They modified Cardin and Olson's setup into a lower hemisphere, with copper inner and outer boundaries, closed at the equatorial plane with a transparent Plexiglas lid. The copper parts enabled a better control of the temperature with a more homogenous distribution at the boundary. The lid offered a better visualisation window and its near-thermally insulating properties left the mostly radial conducting thermal gradient unaffected. The temperature was monitored by thermistors inserted at adjustable depths through the lid. They rotated the experiment at a fixed speed of 206 rpm to generate a parabolic gravity iso-potential, with radial gravity seven times greater at the equator than at the pole. Under these conditions, Sumita and Olson observed the progressive filling of the gap by Rossby waves drifting in the retrograde direction for $\widetilde{Ra} = Ra/Ra_c \leq 8$, see Figure 9(b), as well as a radial increase in their azimuthal wave number: the effect is driven by the increasing slope enforcing an ever stronger TPC suppressing radial motion. At higher forcing $\widetilde{Ra} > 8$, this effect splits the flow into a turbulent inner region and strongly suppressed motion in the outer region where Rossby waves are expelled, a regime they coined *dual convection*, illustrated in Figure 9(c).

Further experiments in the same setup using silicon oil and water as working fluid enabled Sumita and Olson to explore much higher levels of supercriticality, up to $\widetilde{Ra} = 612$ [158]. In these regimes, the turbulent convection homogenises the temperatures to a nearly isothermal state with a thin boundary layer near the inner boundary and the heat transfer follows a scaling law of the form $Nu \sim Ra^{0.4}$. This law, and a comparison of experimental thermal fluctuations to theory [153] led the authors to identify this regime as geostrophically turbulent.

Experiments at low *Pr*: liquid metals. The advent of Ultrasound Doppler Velocimetry (UDV) [36,207,208], which unlike the name suggests does not rely on the Doppler effect [209], made it possible to measure velocities in the bulk flow of core fluid-like liquid metals.

Aubert and collaborators [74] took advantage of this technology to perform experiments in a spherical annulus geometry with a thick central shaft, and no inner sphere, see Figure 8(f). The shaft provided cooling through a central cylindrical copper wall, so in planetary terms, Aubert et al.'s experiment had a cylindrical core and a solid, impermeable TC. They performed experiments both in water and gallium. With water, direct visualisations with Kalliroscope were obtained through the outer sphere made of transparent plastic and maintained at thermostated room temperature by air currents as in Cardin and Olson's experiment [153]. With gallium, optical visualisation is not possible and the outer sphere was replaced by a copper sphere heated by a resisting wire wrapped around it. They measured velocities in both fluids across the gap with two probes along two directions within the equatorial plane. From these two measurements, they are able to reconstruct radial (convective) and azimuthal (zonal) velocities. For both fluids, the

maximum convective velocity in the turbulent regime scales as $u_r \sim (\alpha g Q/\rho C_p \Omega^3 (R_o - R_i)^4)^{2/5}$, a law that can be recovered by assuming a triple balance between Coriolis, inertia and the Archimedean (buoyancy) force, called CIA balance. Here, Q is the heat flux, and C_p is the heat capacity at constant pressure of the fluid. Velocities rescaled by this law are higher in gallium than water for the same criticality. The reason is the two-order-of-magnitude lower Pr of gallium. These high velocities drive a strong zonal flow, which forms as the condensate of an inverse energy cascade fed by the convective scales [159]. The condensate materialises at Rhines' scale, which results from the balance between the β-effect and Reynolds stresses [210]. Energy dissipation at this scale and for the larger scales of turbulence occurs by Ekman friction. However, bold extrapolation of this phenomenology to Earth leads to overestimated velocities by an order of magnitude and too small scales, compared to geomagnetic data. The authors attributed the mismatch, again, to the absence of a magnetic field in their experiments.

Gillet and collaborators conducted further experiments with the same setup up to $\widetilde{Ra} = 80$ focusing on the zonal flow [159]. In the viscous regime of water experiments, the zonal flow scales with the onset convective scales. In the inertial regime reached with gallium, by contrast, they recovered the phenomenology of Aubert et al. [74] with a zonal flow scaling as Rhines' scale. Based on this phenomenology, they showed that at these larger criticalities, the average zonal flow $\overline{U}_\phi$ scales with the *rms* radial convective flow $\widetilde{U}_r$ as $\overline{U}_\phi \sim \widetilde{U}_r^{4/3}$. Unlike early experiments at low criticality in water, where the zonal flow expected from the drift of Rossby waves is weak, the zonal flow observed in this regime is at least an order of magnitude faster than the parasitic thermal wind incurred by the misalignment of temperature gradients and gravity. Hence, in these turbulent regimes at low Pr, the spherical annulus produces a more geophysically relevant zonal flow than most of the water experiments.

Zonal flows controlled by the Rhines scales were also recovered in the *Coraboloid* experiment recently conducted at UCLA [211]: the β-effect was obtained by rotating water in a 37.25 cm diameter cylindrical tank with a free surface. Rotations speeds of 35 rpm, 50 rpm and 60 rpm lead to a parabolic deformation of the free surface. Convection in this "paraboloid core" was driven by a cold 10.2 cm cylinder placed at the centre of the tank spanning the entire fluid height. Zonal flows form in all cases but are more stable at 60 rpm. The Rhines scale varies little between 50 rpm and 60 rpm but centrifugal buoyancy only dominates vertical buoyancy at 60 rpm. The authors concluded that centrifugal buoyancy stabilised the zonal flow, which is consistent with Gillet et al.'s [159] experiments in liquid metal. The properties of jets in a geophysical context are extensively reviewed by Read et al. [212].

Lastly, Shew and Lathrop [93] built a large spherical annulus (external diameter), $D = 60$ cm with magnetic runs and dynamo applications in mind. A much larger setup was later built more specifically to create a dynamo, which is still under development [213]. However, the Shew and Lathrop experiment remains to date the only rotating convection experiment running with liquid sodium. Measurements rely on thermocouples immersed within the fluid, and velocities are obtained by correlating neighbouring thermocouples and using Taylor's hypothesis. They focussed on the turbulent regime and observed small-scale convective motions with a strong, large-scale retrograde azimuthal flow. The local intensity of the zonal flow intensity fits a scaling of $u_\theta \simeq 3.5\Omega\alpha D\Delta$ obtained from a simple balance between Buoyancy and the Coriolis force. As one would expect, they observe developed turbulence with weak convective heat transport and a near-diffusive temperature profile. They measured Reynolds numbers in the range $Re \sim 10^3$–10^4, and a total radial heat flux following a $Nu \sim Ek^{-1/3}Ra$ scaling, indicating a rotation-dominated heat transfer [11,40]. Extrapolating these measurements to Earth leads to an estimated Rayleigh number of $Ra \sim 10^{23}$ and convective velocities comparable to the azimuthal flow of $\simeq 2 \times 10^{-4}$ m/s, from which they estimated the magnetic Reynolds number in the equatorial regions of the Earth to be $Rm \simeq 2 \times 10^2$. They identified a "knee" in the energy

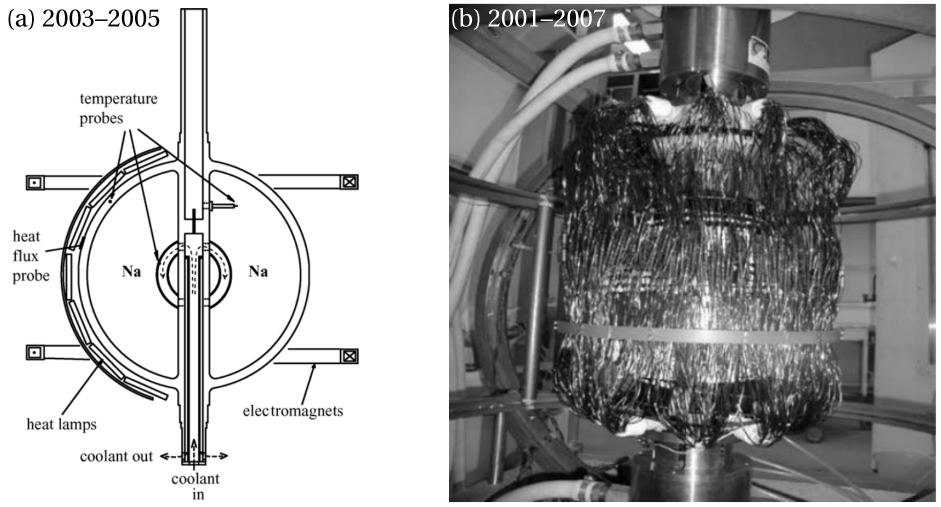


Figure 10. Liquid metal experiments: (a) 2003–2005: Shew and Lathrop's sodium experiment with a Helmholtz coil generating an axial magnetic field [93], (b) 2001–2007: Gillet et al.'s Gallium experiment with their "hairy magnet" made of a long toroidal wire wrapped around the shell, generating an azimuthal magnetic field of up to 0.03 T [94].

spectra where energy was injected by convection into the flow, which, extrapolated to Earth, corresponds to a turnover time of 30 days, and a size of 1 km, again well below any observable scale. They also derived an estimate for the Joule dissipation in the Earth's core in the range of 10 GW to 10 TW.

3.3. *Rotating magnetoconvection in spherical annulus experiments*

Extrapolating rotating convection experiments to Earth yields estimates that are inconsistent with geomagnetic data, for which the Lorentz force usually takes the blame. It was therefore natural for rotating magnetoconvection experiments to emerge. There are essentially three strategies to go about these experiments: letting the fluid motion itself generate its own magnetic field, putting a magnet around the experiment, or bringing the experiment to a magnet.

The first strategy, dynamo experiments, however, poses such a challenge on its own that no working concept of a convective dynamo experiment has been put forward yet. There are even claims that such experiments are impossible at laboratory scale [214]. Time will tell...

The second strategy has been pursued to date by only two magnetoconvection experiments with a spherical geometry by Shew and Lathrop and Gillet et al. [93,94], both represented on Figure 10. These experiments rely on the rotating convection devices previously built by the Maryland and Grenoble groups [74,93,94]. The main drawback of this strategy is that only relatively weak magnets can be transported and fitted around existing setups, and thus, deliver limited magnetic fields. In the geophysical context, the Lorentz force is typically assessed relative to the Coriolis force by the Elsasser number $\Lambda = \sigma B_0^2/(2\rho\Omega)$, which for the Earth is deemed to lie between 0.1 and 100 [13,80,153,215,216]. Shew and Lathrop [93] placed a 3 mT Helmholtz coil around their spherical annulus providing $\Lambda \leq 1.9 \times 10^{-4}$ and saw a global decrease in heat flux with increasing magnetic field. Gillet and collaborators [94], created a "hairy magnet", see Figure 10, by wrapping 444 turns of a wire around meridional planes and through the central shaft of their spherical annulus to generate an azimuthal field of up to 0.03 T, and $\Lambda \leq 9.94 \times 10^{-2}$. They found a zonal flow following the non-magnetic phenomenology [94], but with larger azimuthal

length scales and magnetically controlled zonal velocity scaling as $\bar{U} \sim (\widetilde{U}_r \widetilde{U}_\theta)^{2/3} \sim \widetilde{U}_r (l_\theta / l_\beta)^{2/3}$. Hence, both experiments showed the stabilising effect predicted at low Λ [217,218]. Their relevance to the Earth is, however, questionable considering the Lorentz force may become destabilising at greater values of Λ around unity [27,216,217,219–221].

Finally, the third strategy, and the power of large magnets it affords, has only been exploited in set-ups targeting the polar region, namely LEE1 and LEE2, which took advantage of fields up to 10 T. These are discussed in Section 5.

3.4. *Experiments with inhomogeneous heating*

In most experiments, great efforts are deployed to keep homogeneous temperature boundary conditions, so as to preserve the ideal character and to make the results universal. Yet, there is evidence that large-scale magnetic flux anomalies are driven by large-scale inhomogeneities at the CMB [222–224] and that they may drive magnetic field reversals [225–231]. Heat flux heterogeneity at the CMB may thus play a role in the interior dynamics. Hart [99,100] made the first attempt at studying them but suffered from limitations inherent to space experiments, when the heat source failed, as discussed in Section 2. Since then, two experiments studied their effect on rotating convection systematically.

Sumita and Olson [92,157] adapted their experiment [156,158] and created a local thermal inhomogeneity with a small rectangular heater attached to the outer boundary. Its size and latitudinal position were varied. This extra heating models a local cold anomaly of the Earth's CMB where the outward heat flux locally is higher since the temperature gradient in the experiment is reversed compared to the Earth's outer core. The total heat flux was monitored by comparing the inlet and outlet temperatures of the inner sphere's cooling shaft. The intensity of the anomaly was quantified by the ratio of excess heat flux at the rectangular heater q_h to the flux at the inner boundary Q, $Q^* = q_h/Q$. The heterogeneity drives a local prograde (eastwards) flow. Two different regimes exist: For $Q^* < 0.7$, in the so-called *local locking* regime, this flow remains localised near the outer boundary. For stronger inhomogeneities, in the *global locking* regime, a large-scale spiral with a sharp front develops across the whole gap, see Figure 11. The front separates warm and cold regions and is accompanied by a thin jet linking the outer and inner boundaries, which is responsible for an increase in global heat flux and large inhomogeneities at the inner boundary. The regimes are practically independent of the size of the heater but depend on its latitudinal position: at low latitudes, the prograde flow forms but does not develop into a front, whereas at higher latitudes, the front enters a regime of periodic formation and destruction. Sumita and Olson estimated the heat flux beneath East Asia to be $Q^* \simeq 2$, based on the CMB temperature and its variations [232–234] and seismic models [235]. For this value, global locking is possible, so they proposed that "the existence of this front in the core may explain the Pacific quiet zone in the secular variation of the geomagnetic field and the longitudinally heterogeneous structure of the solid inner core."

Sahoo and Sreenivasan [87,160] built a cylindrical annulus filled with water (height 37 cm, inner/outer radii 5 cm/14.2 cm), with flat, thermally insulating top and bottom boundaries, mostly radial centrifugal force and PIV in horizontal planes [87,160]. At the inner boundary the temperature is imposed, while at the outer boundary, the heat flux is imposed by the heater fitted around the annulus. Unlike Sumita and Olson's experiment, the inhomogeneity is not local but takes the form of an azimuthal variation of boundary heat flux controlled by dividing the external heater into four independently controlled $\pi/2$ sectors. The system spanned inhomogeneities in the range $0 \leq Q^* \leq 2$. Here q_h is the amplitude of the azimuthal flux variation.

Experiments were conducted with alternating high and low fluxes every π (one-fold symmetry) and every $\pi/2$ (two-fold symmetry). Both configurations lead to a slight reduction of the

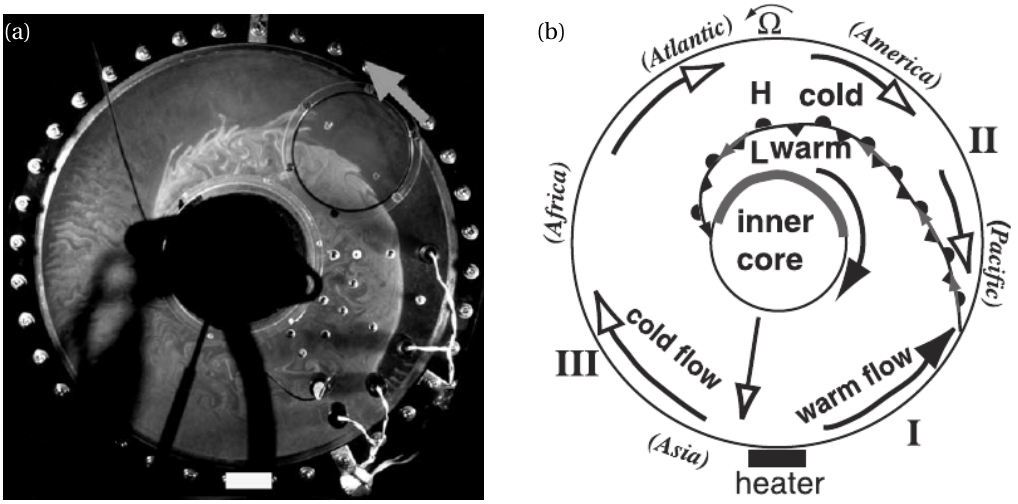


Figure 11. Flow patterns produced by localised heating of the outer boundary of a hemispherical shell [157]. (a) Inner core spiral developing in the global locking mechanism as a result of localised heating at the outer hemisphere, visualised by injection of dye [157]. (b) The front forming the spiral results from the collision of the eastward and westward jets originating at the heating anomaly, a mechanism suspected to take place in the Earth's core (right).

critical flux-based Rayleigh number for the onset of convection. Examples of vorticity fields are represented on Figure 12. The flow consists of counter-rotating vortex pairs separated by thin downwellings similar to Sumita and Olson. These large scales are accompanied by small-scale motion. With a two-fold variation, the flow becomes homogeneous above about 30 times the critical Rayleigh number, most likely as a result of the strong azimuthal flow that exists in this regime. Homogenisation was not observed with a one-fold variation as convection in the low-flux sector is not able to transport motion across it. Sahoo and Sreenivasan interpreted the magnetic field inhomogeneities as signatures of CMB inhomogeneities to estimate that $Q^* > 2$ for the Earth, implying regions of subadiabatic heat flux. Achieving these in the experiments, would, however, require adding active cooling to the outer wall. Nevertheless, such inhomogeneities in the Earth's magnetic field suggest that homogenisation does not take place in the equatorial regions of the core. This offers a potential method to constrain the Rayleigh number in the Earth's outer core.

4. The default setup for axial gravity: cylinders

Experiments in geometries where the natural terrestrial gravity, the temperature gradient and the imposed rotation are aligned (Figure 1(c)) capture the part of the planet that the experiments with cylindrical radial gravity neglected—the polar region. The default set-up is a straight cylinder, the shape that naturally arises in rapidly rotating systems. Only three experiments were conducted in box geometries [117,119,124] which creates the undesired issue of developing corner flows that have no planetary equivalent. These Cartesian geometries, however, ease visual access in experiments.

Convection in rotating spherical convection onsets in the equatorial region and thus was initially thought to be the most relevant for planetary interiors. Nowadays, it is, however, clear that the polar region is at least equally important in the more supercritical regimes where planets

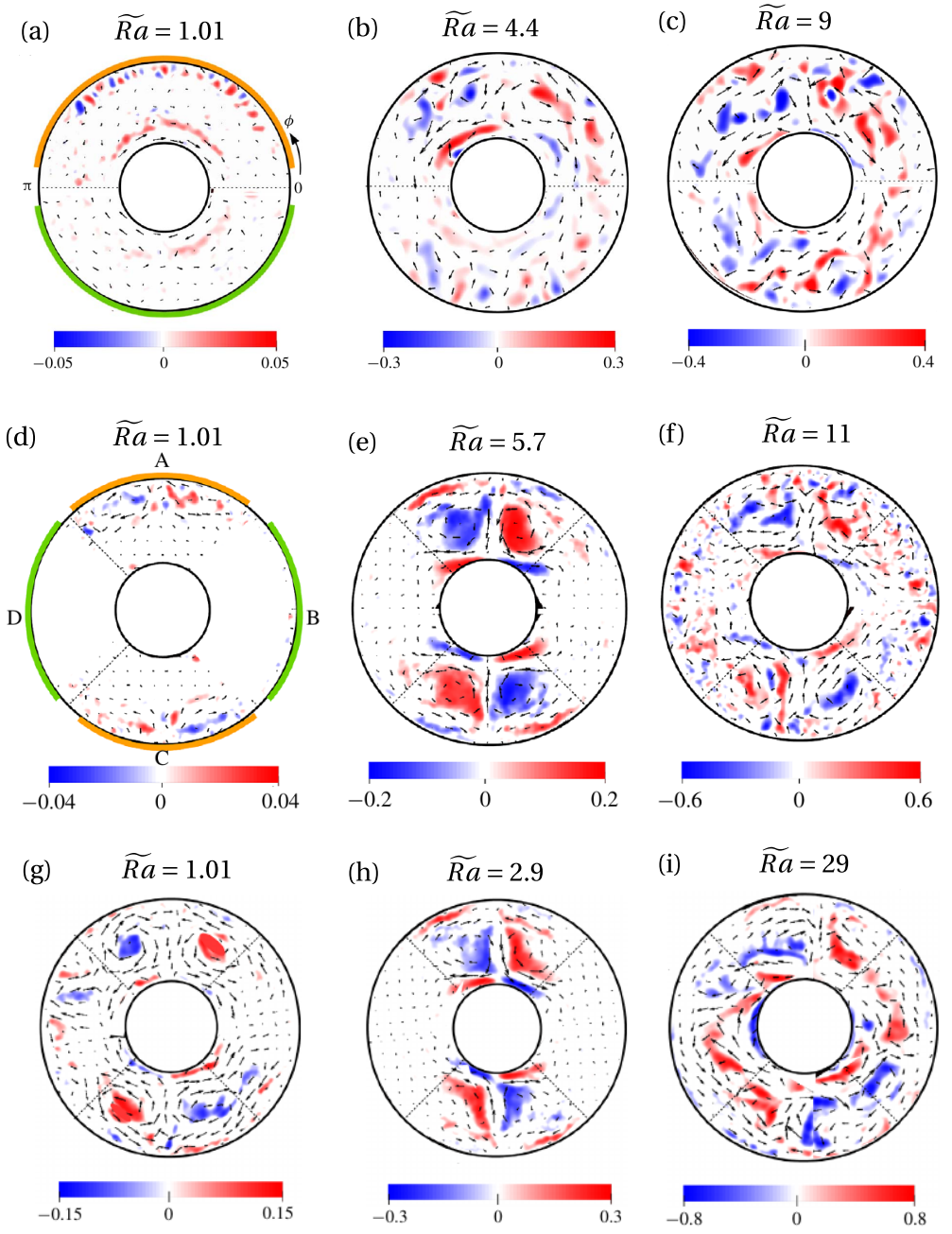


Figure 12. Horizontal velocity vectors (arrows) and shaded contours of axial vorticity (s^{-1}) in horizontal planes of Sahoo and Sreenivasan's experiment [87] in an annulus with a heated outer boundary with two or four sectors of independently adjustable heat flux (yellow and green colours indicate regions or high and low heat flux respectively). Plots are averaged in time, and shown for different levels of supercriticality $\widetilde{Ra}$. (a–c) One-fold variations with $Q^* = 0.7$, (d–f) two-fold variation at $Q^* = 1$ showing regionalisation of convection, (g–i) two-fold variation with $Q^* = 2$, homogenisation of convection takes place at sufficiently high forcing under the effect of the azimuthal flow.

reside [49,236]. Thus, the importance of some of the classical rotating convection experiments with axial gravity to geophysical processes is sometimes only emphasised more strongly in hindsight [128,215,216,237,238]. Nonetheless, as visualised in Figure 3, this configuration has been the most common and enduring one since the beginning of rotating convection experiments and shows no signs of losing its popularity. There are several recent thorough reviews detailing the experiments, their results and more [11,13,40,141] so that here we keep the discussion very brief.

Arguably the first systematic and quantitative experiments of rotating convection was a series of mercury experiments conducted by Fultz, Nakagawa, Frenzen and Goroff in the years 1953 to 1960 at the University of Chicago [95,107–111], the first one conducted on the 20 November 1953 as shown in Figure 13(a). (A few earlier rotating experiments were also conducted by Nakagawa and Fultz at the University of Tokyo and Chicago, respectively, in water and air, however, the upper surface was cooled by evaporation which is a slightly different fluid dynamics problem from the Rayleigh–Bénard-like set-up we consider throughout this review [108].) These seminal experiments were very comprehensive. Since they were conducted in a liquid metal with $Pr \approx 0.025$, oscillatory convection was naturally included. Moreover, Nakagawa had access to an electromagnet of a discarded 36.5 in cyclotron which had been reconditioned at the Enrico Fermi Institute for Nuclear Studies at the University of Chicago with a field strength of up to 1.3 T, shown in Figure 13(b) [239]. This allowed him to also study rotating magnetoconvection. These experiments were mainly concerned with the flow behaviour close to the onset of convection and the validation of linear stability results derived by Chandrasekhar and Elbert [27,216,237].

The focus on relatively low supercriticalities remained until the end of the last century. The most common working fluid was water [63,64,113,117–121,123,124] which allows direct optical access and visualisation, but prohibits oscillatory convection. The same applies to silicone oil as tested by Koschmieder [112] and Rossby [113]. These earlier experiments established the formation of regular cell patterns and convective Taylor columns as the typical structures of steady bulk convection, see Figure 13(c), but also found irregular vortex patterns; an example is shown Figure 13(d). Also, the heat transport and its scaling with the control parameters were investigated, especially in the few visually opaque experiments (either due to the fluid or by design) by Rossby in mercury [113], Donnelly and collaborators in cryogenic helium-I [114–116], and Aurnou and Olson in gallium [125]. None of the experiments was likely extreme enough to capture the geostrophic turbulent heat transport scaling one may expect in Earth's outer core or planetary interior, though.

Likely the most crucial finding in that period, however, was the discovery of wall modes by Ecke and collaborators, shown in Figure 13(e) [63,64,68]. Wall modes explained why the onset of convection as determined e.g. by heat transport measurements did not agree with Chandrasekhar's predictions but was indeed at lower Ra. The destabilising effect of the wall and the breaking of the symmetry results in structures that travel along the periphery of the rotating convection vessel and exponentially decay towards its centre. Initially thought to be mainly an onset phenomenon and an experimental restriction, wall modes are now known to be much more persistent and transform non-linearly into a boundary-zonal flow affecting also strongly supercritical settings [36,69,70,72,73,240–242]. Moreover, they may also exist along the virtual boundary of the tangent cylinder in Earth's outer core, as we will discuss in the next Section 5.

In our current 21st century, the goal has changed and is now rather to push turbulent rotating convection to the extreme, such as in the TROCONVEX experiment in Figure 13(f) [11,142]. The most popular working fluid is still water [122,126,127,130–137,141–143,145–148], but also cryogenic helium [138,139], silicone oils [144], sucrose solution [126], gallium [35,36,128,129], and

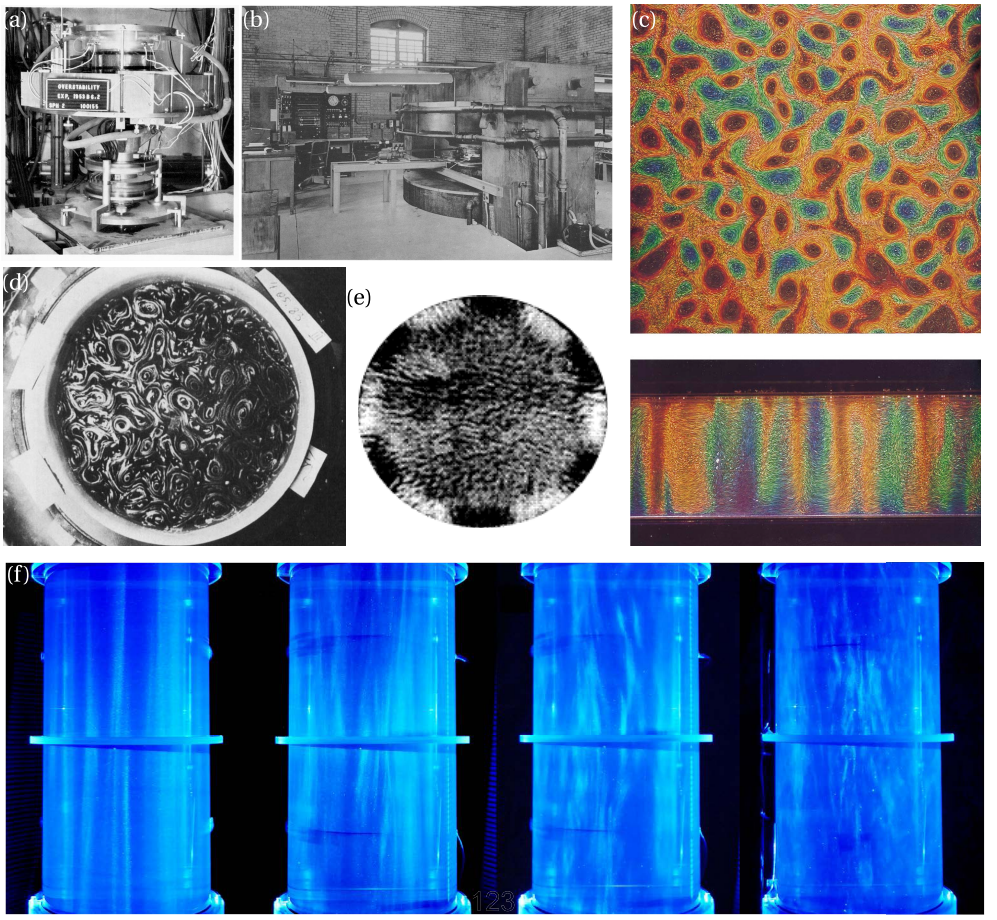


Figure 13. (a) The first experiment of rotating convection in Chicago on the 20 November 1953 [95]. (b) The hydromagnetic laboratory at the University of Chicago where Nakagawa did his seminal rotating convection experiments [239]. (c) Visualisation of columns in rotating convection in water using thermotropic liquid-crystal capsules by Sakai, top and side view (top/bottom) [124]. (d) Visualisation of chaotic vortices in rotating convection in water using aluminium powder on the top surface by Boubnov and Golitsyn [117]. (e) Visualisation of wall modes in water using shadowgraph by Zhong et al. [63]. (f) Visualisation of the flow regimes in turbulent rotating convection in water using rheoscopic particles and illumination with a vertical light sheet; left to right: convective Taylor columns, plumes, geostrophic turbulence, rotationally influenced turbulence by Cheng et al. [142].

pressurised SF_6 [69,140]. The connection to geophysics and planetary physics is sought much more explicitly, in particular, in the Calimero (Californian Model of Earth's Rotation), NoMag, RoMag (all three in Los Angeles, Aurnou and collaborators [126,144,162]) and TROCONVEX (Eindhoven, Kunnen and collaborators [141]) experiments. Notably, RoMag, is the only operative liquid metal rotating magnetoconvection experiment with thus, the closest resemblance to planetary core fluid. Thus, this meant establishing the possible regimes of geostrophic convection (see Figure 13(e), convective Taylor columns, plumes, geostrophic turbulence, rotationally influenced turbulence), testing various scalings for the heat and momentum transport, length scales, the importance of centrifugal effects and much more. Several of these experiments in

China, the USA and The Netherlands, are still active and running and producing results (see Figure 3), thus, we may expect more to come that will enrich our understanding of the polar physics in planetary interiors in the future.

5. Tangent cylinder dynamics

Rotating convection in cylinders, reviewed in Section 4, may represent the dynamics in the polar regions. However, those experiments do likely not fully capture the entirety of the polar region that extends up to the virtual tangent cylinder (TC) boundary, see Figure 1(a). The sidewall boundary conditions in cylindrical experiments are usually impermeable and adiabatic. The boundary conditions of planetary tangent cylinders are, however, likely neither. The most recent data from the SWARM mission clearly shows a strong jet wrapped around the TC and, importantly, meandering in and out of the TC [243]. Similarly, dynamo simulations at extreme enough parameters show flows across the TC [236].

Thus, several major questions arise: First, under which conditions can the Taylor–Proudman constraint (TPC, see Section 1.2) be violated such that the TC boundary becomes permeable? Second, how much heat is transferred between the polar and equatorial regions across the TC? Finally, given such drastic differences in boundary conditions, how well do the experiments in cylinders truly represent polar convection?

5.1. *Aurnou et al.'s TC: what's new in Baltimore?*

Aurnou and collaborators [96] undertook the first attempt at addressing these questions in their Baltimore lab. They built a setup with a hemispherical vessel (15.2 cm diameter) filled with water, sitting in a cylindrical bath also filled with water ensuring a cold, approximately homogeneous temperature at its outer boundary (Figure 14(a)). A heater shaped like a hockey puck (10 cm-diameter, 3.6 cm high) rested at the flat bottom of the hemisphere. The heater achieved two functions: first, it delivered a constant heat flux q into the fluid. Second, the outer edge of the puck formed a discontinuity in the height of the fluid domain in the same way as a planetary solid core does. The choice of a puck shape for the heater, instead of a spherical one was motivated by the difference in gravitational fields between the Earth and the experiment: in the experiment, the axial gravity would misalign with a spherical boundary of near-constant temperature and drive unwanted baroclinic flows in its vicinity. By contrast, the flat upper surface of the heater is everywhere perpendicular to the gravity, and so eliminates that problem. Hence, in the lab, pucks are a better representation of the Earth's inner core than spheres.

Aurnou and collaborators used dye visualisation and thermistors embedded near the heater surface to measure heat fluxes and velocities. They identified five successive regimes based on the flow structure observed as the thermal forcing ramps up during a transient experiment. These regimes map to those in cylindrical vessels but for specificities inherent to the TC geometry. At low thermal forcing, no convection is detected inside or outside the TC but non-vertical residual thermal gradients drive a very weak thermal wind that suppresses convection and thus increases the critical Rayleigh number for the onset of convection inside the TC. Increasing the thermal forcing leads to a ring of vortices attached to the outside of the TC. These vortices result from baroclinic instability and remain confined outside the TC due to the TPC. Inside the TC, convection is still absent. At higher thermal forcing, convection sets in within the TC at a slightly higher critical Rayleigh number than in cylindrical vessels with adiabatic sidewalls because of the weak thermal wind. The onset structures are helical, prograde near the heater and retrograde near the top. They ignite near the TC boundary and their motion is confined within the TC by the TPC as visualised during a transient experiment in Figure 15(b). Further increasing the thermal

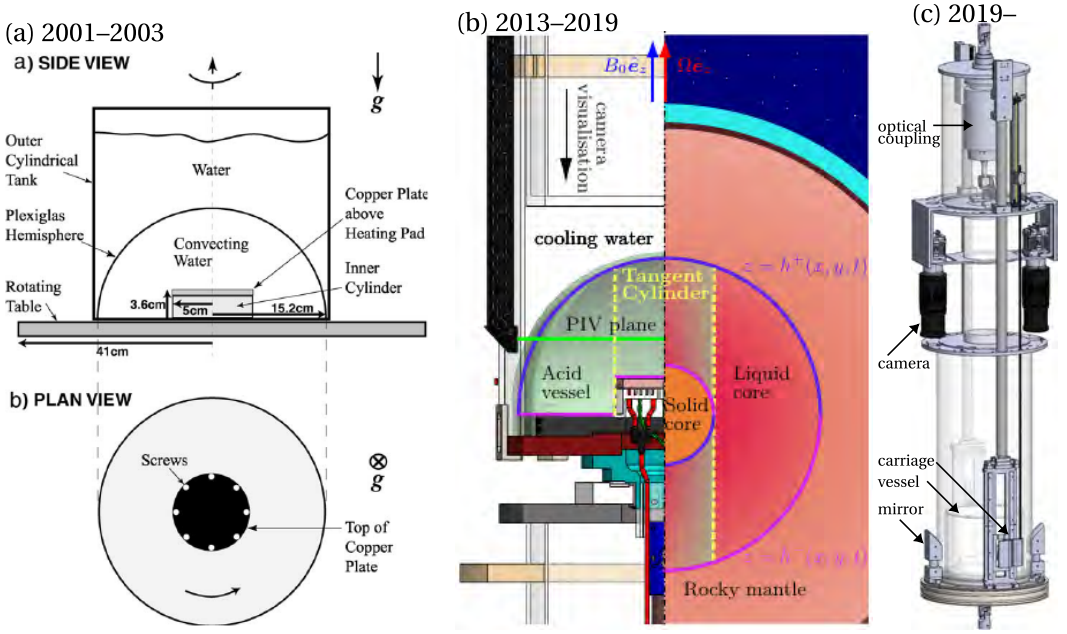


Figure 14. Sketches of the three experiments reproducing the TC geometry: (a) 2001–2003: rotating vessel of Aurnou et al. showing the puck-shaped heater inside the hemispherical dome filled with water [96], (b) 2013–2019: rotating part and static support of LEE1 set against a section of the Earth illustrating how the inner core, ICB and CMB are modelled in the experiment [47,56,83], (c) 2019–: rotating part of LEE2, with cameras, mirrors and optical slip ring, where the fluid vessel is now cylindrical instead of hemispherical. The two large black cameras near the top and the two mirrors fitted at the bottom are part of the PIV system for vertical planes. The vertically travelling carriage near the bottom holds the lens generating the horizontal LASER plane for PIV in horizontal planes of adjustable height [48].

forcing, but keeping strong rotation, the helical structures fill the entire TC, in a regime that would nowadays be referred to as "rotation-dominated columnar regime" [11,169]. When rotation is less dominant over buoyancy, the flow structures do not extend over the full height of the volume but remain strongly affected by rotation [11,169].

The presence of baroclinicity in background rotation drives a strong azimuthal wind with maximum velocity $U_\phi^{\max}$ near the inner TC boundary. The scaling of its intensity with the convective buoyancy flux $q_B = \alpha g q/(\rho C_p)$, as $U_\phi^{\max} \sim 2.05(q_B/\Omega)^{0.52\pm0.03}$ confirms this mechanism. The authors suggest that this mechanism and its confinement to polar regions within the TC may explain the polar vortices inferred there from the 1980 Magsat and 2000 Oersted satellite missions [244]. Extrapolation of their experimental observation to Earth leads to estimates of a few km for the diameter of columnar vortices within the TC and a flux Rayleigh number of the order of 10^{31}. They do stress however that testing this thermal wind scaling for the Earth would require incorporating such effects as the Lorentz force, compressibility and other possible effects.

5.2. *Little Earth experiment I (LEE1)*

Pothérat and collaborators used design ideas similar to Aurnou et al. [96] in the Little Earth Experiment (LEE1), a hemispherical dome of diameter 28.5 cm, and a puck-shaped heater 2.25 cm in

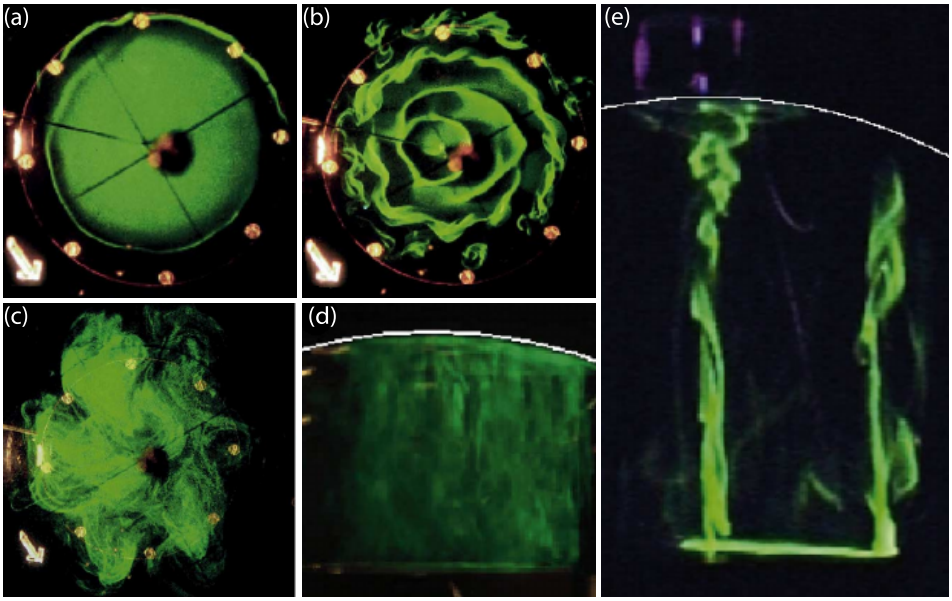


Figure 15. Dye visualisations showing the regimes of rotating convection inside a TC during the instationary phase following the ignition of thermal forcing from a state of solid body rotation by Aurnou et al. [96]. Top view of (a) the onset of convection and (b) helical plumes at $Ra = 9.01 \times 10^9$; $Ek = 9.65 \times 10^{-5}$, (c) side view of baroclinic instability developing across the TC boundary, (d) side view of fully developed convection inside the TC before the onset of baroclinic instability at ($Ra = 1.10 \times 10^{10}$, $Ek = 4.11 \times 10^{-5}$). Arrows indicate the direction of rotation. (e) Plumes arising near the TC boundary at the onset of convection ($Ra = 4.44 \times 10^9$, $Ek = 4.26 \times 10^{-5}$).

height and 10 cm in diameter. They introduced two novelties with drastic consequences for the experimental realisation (Figure 14(b)). First, they incorporated PIV measurements to capture the detail of the time-dependent velocity field in horizontal planes and in one meridional plane. Second, LEE1 targeted magnetostrophic regimes with an Elsasser number of $\Lambda \sim 1$ [47,56,83].

Combining optical methods and strong MHD effects requires a working fluid that is both transparent and electrically conducting. The fluid with the highest electrical conductivity satisfying these constraints is sulphuric acid at 30% mass concentration, of conductivity $\sigma = 86$ S/m, i.e. 10^4 times less than a typical liquid metal. Luckily, sulphuric acid is also the least dangerous amongst potential candidates (hydrofluoric acid, ionic liquids etc.). Since sulphuric acid is typically 5 to 10 times less dense than a liquid metal, it is easy to see that to reach $\Lambda \sim 1$ at $Ek \sim 10^{-6}$, magnetic fields of the order of 10 T are needed. To complicate matters, the magnetic field must pervade a sufficiently large volume to host a fluid dynamics experiment with its instrumentation i.e. a cylindrical volume of about 30 cm diameter over about 1 m. At the time of LEE1's operation, only one magnet in the world was capable of delivering such a magnetic field: the 12 MW M10 magnet of the Grenoble High Magnetic Field Laboratory (LNCMI-G) with up to 10 T in a 376 mm-diameter/2 m-long warm bore (Nowadays, LNCMI-G offers up to 18 T in their new hybrid magnet [245]). Using such a large magnet meant that only one strategy was reasonably possible for the design of LEE1 out of the three outlined in Section 3.3: LEE1 had to be built to fit into the existing magnet. This imposed further severe constraints on the design. Materials rotating within the bore had to be non-conducting to avoid Foucault currents, and those in contact with the working fluid had to possess long-term resistance to highly concentrated acids. Electronic

equipment and electric motors cannot operate in high magnetic fields and have to be deported either far above or far below the magnet. The space between the vessel and the inner wall of the magnet bore is only a few cm. Thus, visualisation from the side had to rely on small concave mirrors providing sufficient angular access to capture the entire height of the TC. Finally, LEE1's motor was located about 0.5 m underneath the bottom of the magnet. The acquisition system (camera, laptop controlling PIV LASERS and recording thermocouple signals) was placed on a rotating platform about 2 m above the top of the magnet. In total, LEE1 was approximately 4.5 m in height and linked by a structure mostly made of different plastics.

The heater was made of a plastic heat exchanger circulated by ethylene–glycol heated in the static frame. The top of the heater delivering heat to the acid was made of SHAPAL, a heat-conducting, electrically insulating and acid-resistant ceramic. This design avoided electric parts but its thermal inertia prevented any feedback control of the temperature difference.

Non-magnetic rotating convection. LEE1 was first operated in water to focus on non-magnetic rotating convection in the TC. In the entire range of parameters investigated, the flow was mostly confined within the TC, i.e. the TPC was sufficiently well satisfied for the TC boundary to be practically impermeable, with only some weak motion detected outside the TC, see Figure 16(a,d,g). The onset of convection follows similar laws to the onset of planar layer convection, but with slightly different prefactors: close for the critical Rayleigh number $Ra_c = (32.3 \pm 4)Ek^{-1.29\pm0.05}$, but lower for the critical wavenumber $k_c = (0.58 \pm 0.08)Ek^{-0.32\pm0.05}$. Past the onset, both wall modes and bulk modes are observed, which implies that the TC boundary acts as a solid impermeable wall in conditions relatively close to onset [32]. Unlike in cylindrical tanks, however, wall modes were not detected below the onset of bulk convection. A possible explanation is that the TPC does not erect a boundary when the flow is still. In other words, below the onset of convection, the TC does not exist as a wall, so neither do wall modes. With increasing supercriticality, the flow follows a complex sequence of patterns to arrive at a state dominated by a single retrograde vortex for $\widetilde{Ra} \simeq 10$. At high latitude, this vortex is associated with a retrograde thermal wind located *inside* the TC, whose intensity follows a scaling nearly identical to that found by Aurnou et al. [96] $Ro = (5.33 \pm 0.3)(NuRaEk^3Pr^{-2})^{0.51\pm0.04}$. The heat flux shows a clear transition between regimes of rotation-dominated convection scaling as $Nu \simeq 0.38Ek^2Ra^{1.58}$ and buoyancy-dominated convection with $Nu \simeq 0.2Ek^{0.33}$ which resembles convection in cylinders and plane layers [11,40].

Magneto-rotating convection. Unlike liquid planetary cores, LEE1 operates in the quasi-static MHD regime where the feedback of the flow onto the magnetic field is negligible, so the magnetic field is imposed, and constant, and dynamo processes are excluded [246]. The acid's low conductivity also precludes the occurrence of Alfvén waves or magneto-Coriolis waves, even though these can exist a low magnetic Reynolds numbers in liquid metals [247,248] and bear relevance to those in planetary cores [249,250]. Hence, LEE1 focuses on capturing the feedback of the magnetic field on convection rather than the reverse.

The magnetic regimes differ from the nonmagnetic ones in a number of ways, see Figure 16. At the most fundamental level, the Coriolis force now competes with the Lorentz force, so the TPC no longer applies. Instead, a Magnetic Taylor–Proudman constraint (MTPC) imposes a kinematic relation between the flow along the TC boundary (u_ϕ) and the flow through it (u_r):

$$\Delta_{rz}\langle u_r\rangle_{t,\phi} + \Lambda\partial^2_{zz}\langle u_\phi\rangle_{t,\phi} = 0. \tag{17}$$

This theory is confirmed using PIV in two horizontal planes at low and high latitudes showing that a meridional flow through the TC boundary follows the MTPC [83]. As a result of this reorganisation of the flow, the azimuthal flow does not follow the thermal wind scaling and increases significantly with Λ. Applying the MTPC to the Earth would require a more general

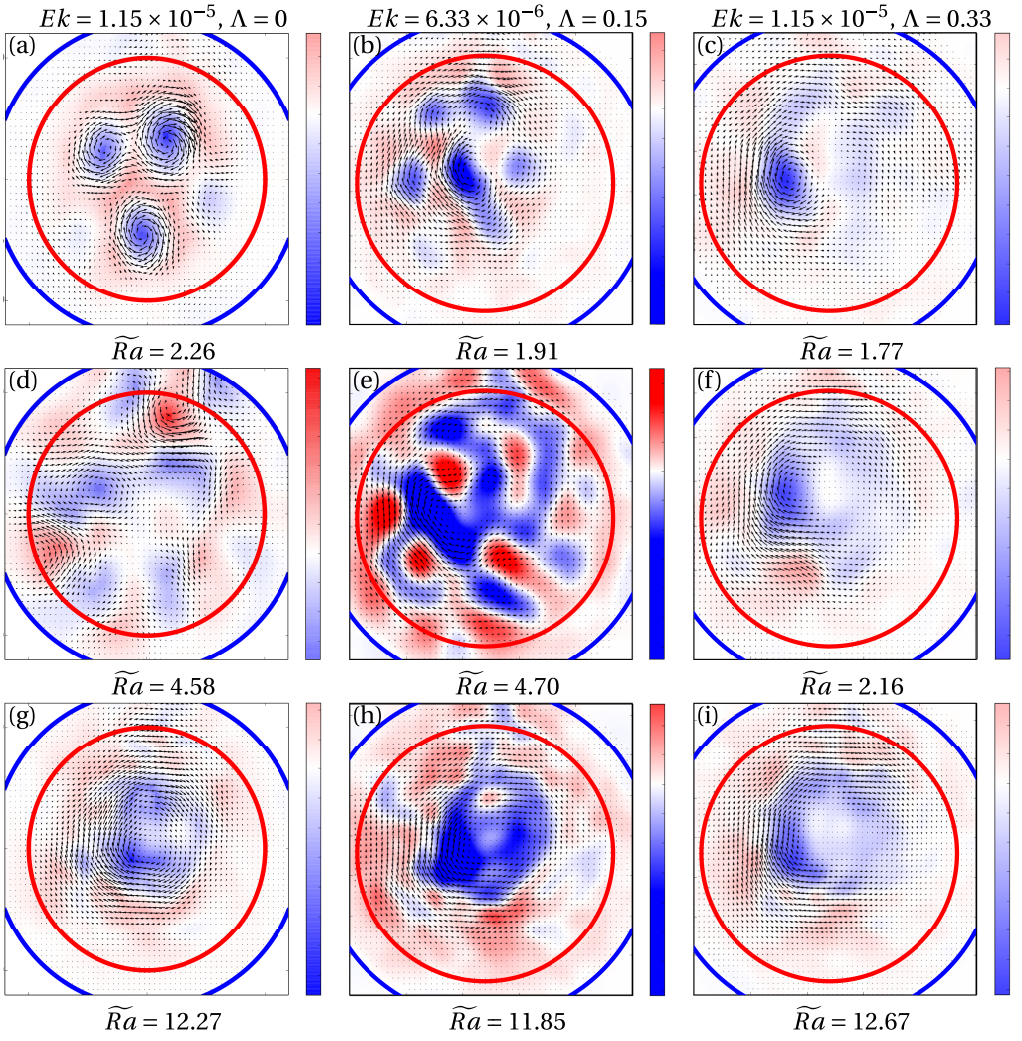


Figure 16. PIV visualisation of the non-magnetic and MHD flow patterns inside the TC in LEE1 [47,97] showing vorticity (blue denotes negative vorticity, red positive vorticity) and velocity (arrows) averaged in time in a plane located at 51° latitude (i.e. just below the point where the TC meets the hemispherical vessel wall). Values of $\widetilde{Ra}$ are calculated with respect to the critical Rayleigh number for $\Lambda = 0$, even for cases where $\Lambda > 0$. The red circle indicates the position of the TC boundary whereas the blue circle corresponds to the vessel wall. The non-magnetic case (a,d,g) exhibits large, merged columns in the weakly supercritical regime. For higher criticality, wall modes are visible and for the highest criticality, a large central retrograde vortex exists at the centre. At $\Lambda = 0.15$ (b,e,h), the effect of the magnetic field is not pronounced and the flow patterns resemble those at $\Lambda = 0$. For $\Lambda = 0.33$ (c,f,i), a large off-centre retrograde structure forms a much lower criticality, with a zero-vorticity "eye" in its centre.

form to incorporate the complex geometry of the Earth's magnetic field. Nonetheless, the MTPC provides at least a plausible mechanism to account for the meandering of the zonal flow in and out of the TC inferred from the SWARM data [243], and previous simulations suggesting that the

TPC was broken at the TC boundary [236,251].

The main effect of the Lorentz force inside the TC is a suppression of heat transfer. At $\Lambda > 0.2$, Nusselt numbers are systematically much lower than their counterparts at $\Lambda = 0$, but scale with a greater power of Ra (up to 1). Unlike in the non-magnetic case, the highest thermal forcing available, $Ra \sim 10^9$, is insufficient to reach a transition to a buoyancy-dominated regime [97]. This does not imply, however, that the presence of a magnetic field always suppresses heat transfer in general. In spherical shells for example, dynamo simulations at $Pr = 1$ show enhancement of heat transfer at $Ek \lesssim 10^{-5}$ [252] and the trend observed in LEE1 does not exclude that the imposed magnetic field could lead to heat transfer enhancement in the TC at higher Rayleigh numbers than accessible in the experiment. This just goes to show how much is left to understand the basics of rotating magneto-convection. Detecting the onset of rotating magneto-convection inside the TC would require far more magnet time than possible in M10 but several states of convection are detected when increasing the thermal forcing. Near the onset of convection within the TC, both bulk and wall modes display similar structures to the non-magnetic case. As the thermal forcing is increased these are progressively replaced by a large retrograde vortex occupying the middle of the TC, consistent with the very strong azimuthal flows observed there, see Figure 16. This structure however appears at comparably lower thermal forcing, and much higher intensity than in the non-magnetic case and displays off-centre maximum vorticity [97]. These results suggest that the axial magnetic field favours the emergence of a large polar vortex, again a plausible, if not directly applicable mechanism for the emergence of polar vortices in the Earth's outer core [244].

5.3. *Little Earth experiment II*

LEE2 is a complete rebuild of LEE1 with much greater control of both the rotation and heating, reduced vibrations and a 10-fold increase in PIV resolution. Its new vessel focuses on the TC itself so the heater diameter was increased and the outer dome was replaced by a cylinder of diameter 22 cm with a puck-shaped heater of diameter 15 cm and yielding a TC height of $H = 14.3$ cm. Thus, the region outside the TC is now a rather thin rectangular annulus. The outer wall is still cooled by a bath of water at a constant temperature, which imposes a cold temperature along the top and its side walls, i.e. only 3.5 cm away from the TC boundary. This creates a much greater source of baroclinicity there than in LEE1 to potentially break away from the TPC, and so attain regimes of higher inertia that would otherwise require higher thermal forcing.

Inside the new heater, the fluid heat exchanger was replaced by two resistive wires joined together in a spiral shape, and fed with opposite currents to cancel out the total Lorentz force due to the heating current inside the high magnetic field. This made it possible to implement a feedback control loop on the heater to control the temperature difference between any pair of thermistors placed inside the device. Four were located at the top of the heater surface. Two pairs were placed inside and outside of the side wall and the top wall. Measurement inside the vessel provided a more accurate input for the control of the temperature drop within the fluid. With this system, the axial temperature difference between the top of the heater and the underside of the top wall could be kept constant for longer periods of time and controlled to ± 0.1 K. The two thermistor pairs also measured the local heat flux across the outer cylinder top and side walls.

The new PIV system benefited from a movable vertical LASER plane whose axial position could be remotely controlled during operation, without having to restart the experiment: this made it possible to scan the flow using several PIV planes during the same run. All signals were passed to the static frame via an optical slip ring capable of absorbing the bandwidth of the PIV cameras. These were located further away from the bore than in LEE1 to be able to operate at fields up to 12 T. These changes made LEE2 considerably heavier, so the new, more powerful motor too had

to be placed further away from the magnet and the total height of the device reached 6.5 m. LEE2 could also be operated outside M10 in a shorter non-magnetic configuration (2.5 m tall).

LEE2's high PIV resolution made it possible to map the regimes of convection against the classification established for classical rotating RBC during the 2010's [11,169]. By order of criticality, the flow starts with a regime without convection within the TC, but with a weak toroidal flow in the outer annulus driven by baroclinicity. At slightly higher forcing, the outer flow becomes unstable to baroclinic instabilities and exhibits a ring of co-rotating vortices similar to the "rim instabilities" identified by Aurnou et al. [96], and visible in Figure 17(a). Since this region has a constant height, these vortices are not Rossby waves, which they nevertheless resemble. Convection in the TC sets in at approximately the critical Rayleigh number for plane layer rotating RBC and displays the same cellular regime at the onset with the same length scale (Figure 17(b)). For slightly higher thermal forcing, the cellular network breaks into quasi-geostrophic columns with a symmetric spiral structure of prograde vorticity near the bottom (hot) wall and retrograde vorticity at the top (cold) wall. The structure is surrounded by a sheath of opposite vorticity (Figure 17(c)). Up to this point, the TC boundary acts essentially as an impermeable wall separating the flow inside and outside the TC with the exception of thin jets induced by baroclinic vortices locally traversing the TC boundary near the top, where baroclinicity is strongest. Further increasing the thermal forcing, convection within the TC enters a plume regime, where columns become three-dimensional, and lose their outer sheath of opposite vorticity. More jets cross the TC near the top and the TC boundary becomes locally permeable over practically the whole height but a small region near the bottom (Figure 17(d)). Even higher forcing disrupts the plumes and the flow displays turbulent features with a wide range of scales from small, 3D scales to a small number (two to four) of large vortices. The global balance of force suggests these may still be quasi-geostrophic (QG). However, they appear to be driven by strong baroclinic jets originating outside the TC. In this regime, the TPC is broken over the entire cylinder height but a strong zonal flow persists at its location (Figure 17(e)).

These regimes broadly follow those found in classical rotating RBC [11,40]. A key feature of the TC geometry is that these regimes become more and more distorted by baroclinically-induced inertia, which progressively loosens the TPC. The breakup of the TC boundary also enables the heat flux to escape laterally, and thus to bypass the suppression of axial heat transfer by rotation within the TC. As a result, the transition between them takes place at significantly lower thermal forcing. A further effect of the strong baroclinicity at the TC boundary is the suppression of wall modes which, unlike in cylindrical vessels appear in none of these regimes. The absence of wall modes and the fact that transitions take place over a narrower range of critical Rayleigh numbers implies that QG turbulence and large-scale vortices [169,253–256] are more easily reachable in TC geometries with strong baroclinicity.

These results suggest that inertia induced by baroclinicity, or otherwise, near the TC boundary in the Earth or other planets may favour the emergence of large structures at lower levels of criticality. This could potentially explain the large scales observed in the polar regions. Hence, inertia such as that induced by baroclinicity offers a second possible route for the breakup of the TC besides magnetic effects. This mechanism too could favour the meandering of zonal flows in and out of the TC. LEE2 is poised to examine the competition between these mechanisms in detail with future campaigns in high magnetic fields at LNCMI-G.

6. Discussion

In the end, what does the evolution of experiments modelling rotating convection in planetary interiors over the last 70 years tell us? For sure, experiments are hard, cumbersome, and inherently limited by the abysmal gap that separates the relative comfort of the laboratory from

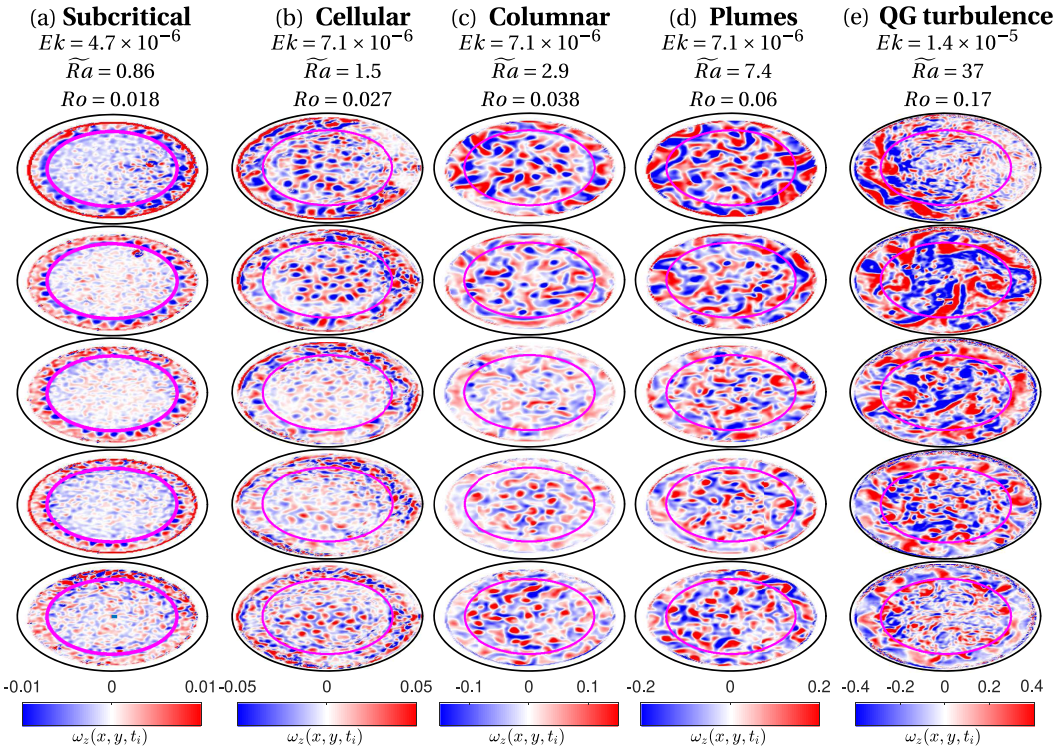


Figure 17. Snapshots of axial vorticity obtained from non-simultaneous PIV measurements in LEE2 at $z = H/6$, $H/3$, $H/2$, $2H/3$, $5H/6$ (from bottom to top) [48]. The pink circle marks the location of the TC boundary. Regimes encountered by order of criticality $\widetilde{Ra}$ are similar to those encountered in rotating convection in a cylinder with a solid sidewall. However, the transitions between them take place at lower criticality because of inertia incurred by the baroclinic flow outside the TC. In particular, quasi-geostrophic turbulence appears at $\widetilde{Ra} = 37$ versus $\widetilde{Ra} \simeq 80$ in Aguirre-Guzman et al.'s work [253]. The baroclinic flow incurs a local breakup of the TPC visible through structures straddling the TC boundary as low as $\widetilde{Ra} = 2.9$ (in the plane at $z = 5/6H$).

realistic planetary conditions: the gravity points in the wrong direction, the fluids are either too viscous or too opaque, the experiments are of the wrong shape, cannot rotate fast enough, reliable measurements are extremely difficult to obtain and the list goes on… Yet, none of these hurdles have deterred the ingenuity of experimentalists. From Nakagawa's early experiments in cylinders [108–110], to modelling equatorial regions with an annulus [54] and the solid core with a hockey puck [96] and the more recent mapping velocity fields in vessels with a tangent cylinder [47,56,83], they have kept focussing on targeted aspects of planetary interiors: they isolated equatorial and polar regions to obtain Earth-like gravity at least locally, they worked with transparent fluids to reveal the first flow patterns of the outer core [50], be it at expense of some of the low-Pr convection patterns [35], they simulated radial gravity in space at the cost of limited ranges of parameters [84,98,100], etc. None of these experiments is a realistic representation of the Earth's outer core, but each of them has revealed key bits of knowledge, which accumulated, and confronted with geophysical data, simulations and mathematical models, have, little by little, shaped our current understanding of planetary cores. The key to their success is that however incomplete, experiments are the best proxy for actual physical processes taking place in planetary

interiors, provided the relevant processes can be identified and characterised.

Yet, at a time when numerical simulations have become so accessible and so powerful, and when "realistic" or "Earth-like" simulations are emerging [257], it is worth asking whether there is still a place for cumbersome laboratory experiments. The answer lies in the respective merits of both approaches: simulations in extreme regimes will remain time-intensive, at least as costly as experiments and not easily repeatable for the foreseeable future. Unlike experiments, they do offer access to the entire time-dependent field of variables. Unlimited accessibility to an ocean of data is only useful when knowing where to look, and experiments on more targeted processes covering wide parameter ranges are ideally placed to point in the right direction. So are the analysis of real geophysical data and simple mathematical theories. Furthermore, even when simulations are perfectly resolved at all scales and all time scales, a very hard condition to meet, the results are still only as good as the mathematical model they are solving. Experiments, on the other hand, are no facsimile: they return the real physics of all the processes they incorporate and so provide a real-life test of the mathematical and numerical models. So the answer is yes, experiments are crucial and will continue to improve, just like numerical simulations, and just like the oldest methods in the field: geophysical observation and simple mathematical theories. None of these approaches work anywhere near as well in isolation as when they can draw on the progress and feedback of the other three.

The main issue faced by experimentalists and theoreticians alike is that of the extrapolation of their results to the Earth or other planets. Given the limitations of numerics and experiments and the large uncertainties on the actual conditions in planetary interiors, attempting a precise model combining all potentially relevant processes would certainly be in vain. Stevenson finds solace in an elegant way out of this conundrum [258], citing a similar point made by Urey about the chemical composition of planets [259]:

> What Urey is doing is giving a license to study ill-posed problems. By ill-posed, I mean that the issue can be stated with precision but the knowledge needed to settle the issue is not yet entirely adequate. [...] The important lesson that we learn is this: It is not so important that you get the right answer: it is most important that you ask the right question.

In this spirit, the question we may be able to ask may not concern so much the exact nature of the convection in planetary interiors but rather: "What processes arising from the interplay of convection and rotation may we expect to play a role there?". Seven decades of exploring planetary interiors with experiments on rotating convection have certainly provided a wealth of answers to that question but by no means all of them.

So what lies ahead for experiments? The colossal progress of experiments certainly owes to the audacious ideas of their creators, but not only. They also constantly drew on technological and scientific advances from other fields: from the dawn of spacecraft in the 1960s it became possible to escape lab gravity twenty years later [84]. LASERs and digital signal processing led to the advent of optical velocity mapping, ultrasound velocimetry made it possible to measure velocity profiles in opaque metals [94,207,208]. At the same time, experimental design has incorporated more and more complex aspects of outer core dynamics: cylinders became slanted annuli, then spheres, then spheres with a puck. Heating became inhomogeneous, internal [89,106,260] and now magnetic fields are becoming an increasingly important part of the mix.

What is next is certainly found at the crossing of what is currently missing or insufficiently explored in terms of physical processes and what is becoming technologically possible. It is the biased view of the authors that the greatest scope for progress may lie in incorporating MHD effects in the rotating convection experiments. Certainly, the dynamo problem has been the focus of significant experimental endeavours, whose main focus was to find under which conditions a flow could spontaneously generate a magnetic field. The physical processes reproduced in these experiments are largely inspired by potential mechanisms thought to be driv-

ing them in planets and stars. Convection is the best candidate for the Earth and all planets of the Solar system but tidal forces exerted by the Earth and precession of the Moon's rotation axis may have driven a past dynamo on the Moon [261,262]. For Ganymede, iron snow produced by compositional precession is a possible dynamo mechanism [263]. Yet, successful dynamos to date are all mechanically driven: the Karlsruhe dynamo forces a flow through pipes shaped to guarantee the dynamo [264]. In the Riga dynamo, a turbine produces a double helix flow structure [265], and in the Von Kárman Sodium (VKS) dynamo, magnetised counter-rotating impellers generate an unstable von Kárman flow and produce the dynamo [266,267]. The upcoming DRESDYN dynamo project in Dresden will spin a 8 m^3 cylinder filled with Sodium along two axes to produce a precession-driven dynamo [268,269]. This will potentially be the first dynamo driven by the same process as a geophysical or astrophysical dynamo. Hence, the generic character of this question and the magnitude of the challenge involved in building experimental dynamos have pushed aside the question of how actual planetary dynamos work [270]. So understandably, none of the dynamo experiments directly model actual planetary dynamos and the playground of understanding planetary dynamos has been occupied by numericists [225,236]. For planets, the question is to find which flow within the outer core produces a magnetic field consistent with observations. Crucially, the associated Lorentz force due to the magnetic field may drastically alter the answers to that question. In fact, the effects of the Earth's field are often invoked when extrapolating rotating convection experiments to Earth [74,96,153]. Yet, the Lorentz force is still subject to debate: proponents of the geostrophic scenario argue that it remains much smaller than the Coriolis force [271,272], while others argue that a magnetostrophic scenario where both forces are comparable is required to explain the flow patterns inferred from geomagnetic data [216,273]. Here the availability of large electromagnets offers scope for experiments in magnetorotating convection to advance these questions. These possibilities are only starting to be explored: fields up to 18 T in sufficiently large volumes to host laboratory experiments [245] even make it possible to reach extreme regimes where Alfvén waves may interact with convection [248,274]. Such experiments may also benefit from decades of accumulated knowledge on liquid metal MHD turbulence [275–281] and MHD convection tracing back to Nakagawa's first experiments [108,125,282,283]. Such large magnets combined with measurement techniques developed for transparent electrolytes [81,82,284,285] now even offer the possibility of mapping velocity and pressure fields in magnetorotating convection at similar Ek to non-MHD experiments but with Elsasser numbers within the range expected for the Earth (between 0.1 and 10) [56,83]. So perhaps now is the time for Hide's 1958 wisdom to finally come true [286]:

> Now it is clear that extensions in several directions, especially into hydromagnetics, will have to be made if results of any geomagnetic interest are to be obtained.

Other, non-MHD processes that have been well investigated outside the context of convection in the outer core can be integrated into rotating convection experiments to capture essential elements of the outer core dynamics: solidification and re-melting of the inner core releases or absorbs lighter elements into/from the liquid outer core, and so incurs significant compositional buoyancy [287]. Only one experiment focused on compositional convection in the context of the inner core [91]. It is sometimes dismissed on the ground that the large Schmidt numbers associated with it justify mimicking convection there with high Prandtl number thermal convection. This analogy may not capture well the crucial conditions at the core boundaries, and even less the interplay between thermal and compositional convection.

Variations of physical properties too may play several roles. In gas giants, they can lead to compressibility effects or to a radial regionalisation of convection forming layers with strongly differentiated convective patterns [288–292]. While less significant in the liquid core of Earth-like planets, density variations and the variation of other physical properties may still produce local stratification capable of locally suppressing convection: the presence of such a stratified layer has indeed been theorised near the core-mantle boundary [293].

The role of the centrifugal force is somewhat less obvious: it remains very small at the scale

of planetary cores, but may act at the scale of crucial convection patterns forming there[23]: tornadoes forming in the Sun offer a reminder not to discard the centrifugal force too quickly in large systems[175,177].

Another seven decades will surely tell which of these, or other avenues convection experiments will travel along, but there is little doubt that even then, they will still be advancing in the journey to the outer core of the Earth.

Declaration of interests

The authors do not work for, advise, own shares in, or receive funds from any organization that could benefit from this article, and have declared no affiliations other than their research organizations.

Funding

AP is supported by EPSRC (grant EP/X010937/1) and the Leverhulme Trust (grant RPG-2017-366). SH is supported by the UKRI Horizon Europe guarantee, selected by the European Research Council (ERC), grant no. EP/X034402/1 (MAGNADO). SH further received funding from EPSRC, grant no. EP/V047388/1.

Acknowledgements

We would like to thank John Brothold for his inspiring talk at the 18th SEDI conference at Great Barrington, MA. The authors acknowledge the relaxed atmosphere around the time of the XXXIIIrd Zappanale in Bad Doberan, Germany, which allowed them to fully focus on this review, and perhaps sipped into some of the wording therein, thusly prompting the question: "*Does humour belong in* [Science]?".

Supplementary data

Supporting information for this article is available on the journal's website under https://doi.org/10.5802/crphys.233 or from the author.

References

[1] R. D. Oldham, "The constitution of the interior of the Earth, as revealed by earthquakes", *Quart. J. Geol. Soc.* **62** (1906), no. 1–4, pp. 456–475.

[2] I. Lehmann, "P'", *Publications du Bureau central séismologique international. Série A: Travaux scientifiques* **14** (1936), pp. 87–115.

[3] M. I. Billen, "Modeling the dynamics of subducting slabs", *Annu. Rev. Earth Planet. Sci.* **36** (2008), no. 1, pp. 325–356.

[4] T. M. Olugboji and J. Park, "Structures of the oceanic lithosphere-asthenosphere boundary: Mineral-physics modeling and seismological signatures", *Geochem. Geophys. Geosyst.* **14** (2013), no. 4, pp. 880–901.

[5] S. Mukhopadhyay and R. Parai, "Noble gases: A record of Earth's evolution and mantle dynamics", *Annu. Rev. Earth Planet. Sci.* **47** (2019), no. 1, pp. 389–419.

[6] M. D. Long, "Constraints on subduction geodynamics from seismic anisotropy", *Rev. Geophys.* **51** (2013), no. 1, pp. 76–112.

[7] L. Stixrude and C. Lithgow-Bertelloni, "Geophysics of chemical heterogeneity in the mantle", *Annu. Rev. Earth Planet. Sci.* **40** (2012), no. 1, pp. 569–595.

[8] J. P. Brodholt, "Pressure-induced changes in the compression mechanism of aluminous perovskite in the Earth's mantle", *Nature* **407** (2000), no. 6804, pp. 620–622.

[9] C. Normand, Y. Pomeau and M. G. Velarde, "Convective instability: a physicist's approach", *Rev. Mod. Phys.* **49** (1977), no. 3, pp. 581–624.

[10] R. Jeanloz and H.-R. Wenk, "Convection and anisotropy of the inner core", *Geophys. Res. Lett.* **15** (1988), no. 1, pp. 72–75.

[11] R. P. J. Kunnen, "The geostrophic regime of rapidly rotating turbulent convection", *J. Turbul.* **22** (2021), no. 4–5, pp. 267–296.

[12] R. E. Ecke and O. Shishkina, "Turbulent rotating Rayleigh–Bénard convection", *Annu. Rev. Fluid Mech.* **55** (2023), pp. 603–638.

[13] J. M. Aurnou, M. A. Calkins, J. S. Cheng, K. Julien, E. M. King, D. Nieves, K. M. Soderlund and S. Stellmach, "Rotating convective turbulence in Earth and planetary cores", *Phys. Earth Planet. Inter.* **246** (2015), pp. 52–71.

[14] J. M. Aurnou, S. Horn and K. Julien, "Connections between nonrotating, slowly rotating, and rapidly rotating turbulent convection transport scalings", *Phys. Rev. Res.* **2** (2020), no. 4, article no. 043115.

[15] B. Willis, *The Mechanics of Appalachian Structure*, US Government Printing Office: Washington, 1894.

[16] H. Bénard, "Les tourbillons cellulaires dans une nappe liquide", *Revue Gen. Sci. Pure Appl.* **11** (1900), pp. 1261–1271.

[17] L. Rayleigh, "On convection currents in a horizontal layer of fluid, when the higher temperature is on the under side", *Lond. Edinb. Dubl. Philos. Mag. J. Sci.* **32** (1916), no. 192, pp. 529–546.

[18] A. Oberbeck, "Ueber die Wärmeleitung der Flüssigkeiten bei Berücksichtigung der Strömungen infolge von Temperaturdifferenzen", *Ann. Phys.* **243** (1879), no. 6, pp. 271–292.

[19] J. V. Boussinesq, *Théorie analytique de la chaleur*, Gauthier-Villars: Paris, 1903.

[20] D. D. Gray and A. Giorgini, "The validity of the Boussinesq approximation for liquids and gases", *Int. J. Heat Mass Transfer* **19** (1976), no. 5, pp. 545–551.

[21] F. Marques, I. Mercader, O. Batiste and J. M. Lopez, "Centrifugal effects in rotating convection: axisymmetric states and three-dimensional instabilities", *J. Fluid Mech.* **580** (2007), pp. 303–318.

[22] S. Horn and J. M. Aurnou, "Regimes of Coriolis-centrifugal convection", *Phys. Rev. Lett.* **120** (2018), article no. 204502.

[23] S. Horn and J. M. Aurnou, "Tornado-like vortices in the quasi-cyclostrophic regime of Coriolis-centrifugal convection", *J. Turbul.* **22** (2021), no. 4–5, pp. 297–324.

[24] S. Horn and J. M. Aurnou, "Rotating convection with centrifugal buoyancy: Numerical predictions for laboratory experiments", *Phys. Rev. Fluids* **4** (2019), no. 7, article no. 073501.

[25] F. H. Busse, "Thermal instabilities in rapidly rotating systems", *J. Fluid Mech.* **44** (1970), no. 3, pp. 441–460.

[26] F. H. Busse, "Is low Rayleigh number convection possible in the Earth's core?", *Geophys. Res. Lett.* **29** (2002), no. 7, pp. 9-1–9-3.

[27] S. Chandrasekhar, *Hydrodynamic and Hydromagnetic Stability*, Clarendon Press, Oxford University Press: Oxford, 1961.

[28] W. Thomson, "LII. On the stability of steady and of periodic fluid motion", *Lond. Edinb. Dubl. Philos. Mag. J. Sci.* **23** (1887), no. 144, pp. 459–464.

[29] J. Proudman, "On the motion of solids in a liquid possessing vorticity", *Proc. R. Soc. Lond. A* **92** (1916), no. 642, pp. 408–424.

[30] H. P. Greenspan, *The Theory of Rotating Fluids*, Cambridge University Press: Cambridge, 1969.

[31] T. Clune and E. Knobloch, "Pattern selection in rotating convection with experimental boundary conditions", *Phys. Rev. E* **47** (1993), no. 4, pp. 2536–2550.

[32] H. F. Goldstein, E. Knobloch, I. Mercader and M. Net, "Convection in a rotating cylinder. Part 1. Linear theory for moderate Prandtl numbers", *J. Fluid Mech.* **248** (1993), pp. 583–604.

[33] H. F. Goldstein, E. Knobloch, I. Mercader and M. Net, "Convection in a rotating cylinder. Part 2. Linear theory for low Prandtl numbers", *J. Fluid Mech.* **262** (1994), pp. 293–324.

[34] S. Horn and P. J. Schmid, "Prograde, retrograde, and oscillatory modes in rotating Rayleigh–Bénard convection", *J. Fluid Mech.* **831** (2017), pp. 182–211.

[35] J. M. Aurnou, V. Bertin, A. M. Grannan, S. Horn and T. Vogt, "Rotating thermal convection in liquid gallium: multi-modal flow, absent steady columns", *J. Fluid Mech.* **846** (2018), pp. 846–876.

[36] T. Vogt, S. Horn and J. M. Aurnou, "Oscillatory thermal–inertial flows in liquid metal rotating convection", *J. Fluid Mech.* **911** (2021), article no. A5.

[37] P. H. Roberts, "On the thermal instability of a rotating-fluid sphere containing heat sources", *Philos. Trans. R. Soc. Lond. A Math. Phys. Sci.* **263** (1968), no. 1136, pp. 93–117.

[38] A. Barik, S. A. Triana, M. Calkins, S. Stanley and J. Aurnou, "Onset of convection in rotating spherical shells: Variations with radius ratio", *Earth Space Sci.* **10** (2023), no. 1, article no. e2022EA002606.

[39] E. Dormy, A. M. Soward, C. A. Jones, D. Jault and P. Cardin, "The onset of thermal convection in rotating spherical shells", *J. Fluid Mech.* **501** (2004), pp. 43–70.

[40] R. E. Ecke and O. Shishkina, "Turbulent rotating Rayleigh–Bénard convection", *Annu. Rev. Fluid Mech.* **55** (2023), no. 1, pp. 603–638.

[41] J. Brons, T. P. Thomas and A. Pothérat, "Transition between advection and propagation of inertial waves in rotating turbulence", *J. Fluid Mech.* **886** (2020), article no. A22.

[42] J. Brons, T. P. Thomas and A. Pothérat, "Mean flow anisotropy without waves in rotating turbulence", *J. Fluid Mech.* **889** (2020), article no. A37.

[43] P. Billant, "Is the Taylor–Proudman theorem exact in unbounded domains? Case study of the three-dimensional stability of a vortex pair in a rapidly rotating fluid", *J. Fluid Mech.* **920** (2021), article no. R1.

[44] F. S. Godeferd and F. Moisy, "Structure and dynamics of rotating turbulence: a review of recent experimental and numerical results", *Appl. Mech. Rev.* **67** (2015), no. 3, article no. 030802.

[45] L. Biferale, "Rotating turbulence", *J. Turbul.* **22** (2021), no. 4–5, pp. 232–241.

[46] U. Harlander, M. V. Kurgansky, K. Speer and M. Vincze, "Baroclinic instability from an experimental perspective", *C. R. Phys.* **25** (2024), no. S3, pp. 379–426.

[47] K. Aujogue, A. Pothérat, B. Sreenivasan and F. Debray, "Experimental study of the convection in a rotating tangent cylinder", *J. Fluid Mech.* **843** (2018), pp. 355–381.

[48] R. Agrawal, M. Holdsworth and A. Pothérat, *Regimes of rotating convection in a tangent cylinder*, Preprint, ArXiv, 2024, 2408.07837.

[49] T. Gastine and J. M. Aurnou, "Latitudinal regionalization of rotating spherical shell convection", *J. Fluid Mech.* **954** (2023), article no. R1.

[50] F. H. Busse and C. R. Carrigan, "Laboratory simulation of thermal convection in rotating planets and stars", *Science* **191** (1976), no. 4222, pp. 81–83.

[51] J. Pedlosky, *Geophysical Fluid Dynamics*, Springer Verlag: New York, Heidelberg, Berlin, 1987.

[52] B. W. Hindman and R. Jain, "Radial trapping of thermal Rossby waves within the convection zones of low-mass stars", *Astrophys. J.* **932** (2022), no. 1, article no. 68.

[53] R. Hide, "Free hydromagnetic oscillations of the earth's core and the theory of the geomagnetic secular variation", *Philos. Trans. R. Soc. Lond. A Math. Phys. Sci.* **259** (1966), no. 1107, pp. 615–650.

[54] F. H. Busse and C. R. Carrigan, "Convection induced by centrifugal buoyancy", *J. Fluid Mech.* **62** (1974), no. 3, pp. 579–592.

[55] F. H. Busse and R. D. Simitev, *Convection in rotating spherical fluid shells*, Preprint, ArXiv, 2009, 0906.1124.

[56] K. Aujogue, A. Pothérat, I. Bates, F. Debray and B. Sreenivasan, "Little Earth experiment: An instrument to model planetary cores", *Rev. Sci. Instrum.* **87** (2016), article no. 084502.

[57] V. W. Ekman, "On the influence of the earth's rotation on ocean-currents", *Arkiv for Matematik, Astronomi Och Fysik* **2** (1905), no. 11, pp. 1–53.

[58] D. J. Acheson and R. Hide, "Hydromagnetics of rotating fluids", *Rep. Progr. Phys.* **36** (1973), no. 2, pp. 159–221.

[59] A. Pothérat, J. Sommeria and R. Moreau, "An effective two-dimensional model for MHD flows with tranverse magnetic field", *J. Fluid Mech.* **424** (2000), pp. 75–100.

[60] P. A. Davidson and A. Pothérat, "A note on Bodewadt–Hartmann layers", *Eur. J. Mech. B Fluids* **21** (2002), no. 5, pp. 545–559.

[61] K. Stewartson, "On almost rigid rotations", *J. Fluid Mech.* **3** (1957), no. 1, pp. 17–26.

[62] R. P. J. Kunnen, H. J. H. Clercx and G. J. F. Van Heijst, "The structure of sidewall boundary layers in confined rotating Rayleigh–Bénard convection", *J. Fluid Mech.* **727** (2013), pp. 509–532.

[63] F. Zhong, R. Ecke and V. Steinberg, "Asymmetric modes and the transition to vortex structures in rotating Rayleigh–Bénard convection", *Phys. Rev. Lett.* **67** (1991), no. 18, pp. 2473–2476.

[64] F. Zhong, R. E. Ecke and V. Steinberg, "Rotating Rayleigh–Bénard convection: asymmetric modes and vortex states", *J. Fluid Mech.* **249** (1993), pp. 135–159.

[65] J. Herrmann and F. H. Busse, "Asymptotic theory of wall-attached convection in a rotating fluid layer", *J. Fluid Mech.* **255** (1993), pp. 183–194.

[66] E. Y. Kuo and M. C. Cross, "Traveling-wave wall states in rotating Rayleigh–Bénard convection", *Phys. Rev. E* **47** (1993), no. 4, article no. R2245.

[67] K. Zhang and X. Liao, "The onset of convection in rotating circular cylinders with experimental boundary conditions", *J. Fluid Mech.* **622** (2009), pp. 63–73.

[68] R. E. Ecke, "Rotating Rayleigh–Bénard convection: bits and pieces", *Phys. D: Nonlinear Phenom.* **444** (2023), article no. 133579.

[69] X. Zhang, D. P. Van Gils, S. Horn, et al., "Boundary zonal flow in rotating turbulent Rayleigh–Bénard convection", *Phys. Rev. Lett.* **124** (2020), no. 8, article no. 084505.

[70] X. Zhang, R. E. Ecke and O. Shishkina, "Boundary zonal flows in rapidly rotating turbulent thermal convection", *J. Fluid Mech.* **915** (2021), article no. A62.

[71] R. E. Ecke, X. Zhang and O. Shishkina, "Connecting wall modes and boundary zonal flows in rotating Rayleigh–Bénard convection", *Phys. Rev. Fluids* **7** (2022), no. 1, article no. L011501.

[72] X. M. de Wit, W. J. Boot, M. Madonia, A. J. Aguirre Guzmán and R. P. Kunnen, "Robust wall modes and their interplay with bulk turbulence in confined rotating Rayleigh–Bénard convection", *Phys. Rev. Fluids* **8** (2023), no. 7, article no. 073501.

[73] L. Terrien, B. Favier and E. Knobloch, "Suppression of wall modes in rapidly rotating Rayleigh–Bénard convection by narrow horizontal fins", *Phys. Rev. Lett.* **130** (2023), no. 17, article no. 174002.

[74] J. Aubert, D. Brito, H.-C. Nataf, P. Cardin and J.-P. Masson, "A systematic experimental study of rapidly rotating spherical convection in water and liquid gallium", *Phys. Earth Planet. Inter.* **128** (2001), no. 1, pp. 51–74.

[75] F. D. Stacey, *Physics of the Earth*, Brookfield Press: Brisbane, 1992.

[76] F. Xu, G. Morard, N. Guignot, et al., "Thermal expansion of liquid Fe-S alloy at high pressure", *Earth Planet. Sci. Lett.* **563** (2021), article no. 116884.

[77] G. Morard, J. Siebert, D. Andrault, N. Guignot, G. Garbarino, F. Guyot and D. Antonangeli, "The Earth's core composition from high pressure density measurements of liquid iron alloys", *Earth Planet. Sci. Lett.* **373** (2013), pp. 169–178.

[78] L. E. González and D. J. González, "Structure and dynamics in liquid iron at high pressure and temperature. A first principles study", *J. Geophys. Res.: Solid Earth* **128** (2023), no. 2, article no. e2022JB025119.

[79] M. Pozzo, C. Davies, D. Gubbins and D. Alfe, "Thermal and electrical conductivity of iron at Earths core conditions", *Nature* **485** (2012), no. 7398, pp. 355–358.

[80] G. Schubert and K. M. Soderlund, "Planetary magnetic fields: Observations and models", *Phys. Earth Planet. Inter.* **187** (2011), no. 3, pp. 92–108.

[81] O. Andreev, Y. Kolesnikov and A. Thess, "Visualization of the Ludford column", *J. Fluid Mech.* **721** (2013), pp. 438–453.

[82] B. Moudjed, A. Pothérat and M. Holdsworth, "PIV mapping of pressure and velocity fields in the plane magnetohydrodynamic Couette flow", *Exp. Fluids* **61** (2020), no. 12, article no. 255.

[83] A. Pothérat, K. Aujogue and F. Debray, "Magnetic Taylor–Proudman constraint explains flows into the Tangent cylinder", *Phys. Rev. Lett.* **133** (2024), no. 18, article no. 184101.

[84] J. E. Hart, J. Toomre, A. E. Deane, et al., "Laboratory experiments on planetary and stellar convection performed on Spacelab 3", *Science* **234** (1986), no. 4772, pp. 61–64.

[85] C. Egbers, W. Brasch, B. Sitte, J. Immohr and J.-R. Schmidt, "Estimates on diagnostic methods for investigations of thermal convection between spherical shells in space", *Meas. Sci. Technol.* **10** (1999), no. 10, pp. 866–877.

[86] J. P. Koulakis, Y. Ofek, S. Pree and S. Putterman, "Thermal convection in a central force field mediated by sound", *Phys. Rev. Lett.* **130** (2023), no. 3, article no. 034002.

[87] S. Sahoo and B. Sreenivasan, "Convection in a rapidly rotating cylindrical annulus with laterally varying boundary heat flux", *J. Fluid Mech.* **883** (2020), article no. A1.

[88] H. Jiang, X. Zhu, D. Wang, S. G. Huisman and C. Sun, "Supergravitational turbulent thermal convection", *Sci. Adv.* **6** (2020), no. 40, article no. eabb8676.

[89] J. A. Chamberlain and C. R. Carrigan, "An experimental investigation of convection in a rotating sphere subject to time varying thermal boundary conditions", *Geophys. Astrophys. Fluid Dyn.* **35** (1986), no. 1–4, pp. 303–327.

[90] S. Cordero and F. H. Busse, "Experiments on convection in rotating hemispherical shells: Transition to a quasi-periodic state", *Geophys. Res. Lett.* **19** (1992), no. 8, pp. 733–736.

[91] P. Cardin and P. Olson, "An experimental approach to thermochemical convection in the Earth's core", *Geophys. Res. Lett.* **19** (1992), no. 20, pp. 1995–1998.

[92] I. Sumita and P. Olson, "A laboratory model for convection in Earth's core driven by a thermally heterogeneous mantle", *Science* **286** (1999), no. 5444, pp. 1547–1549.

[93] W. L. Shew and D. P. Lathrop, "Liquid sodium model of geophysical core convection", *Phys. Earth Planet. Inter.* **153** (2005), no. 1–3, pp. 136–149.

[94] N. Gillet, D. Brito, D. Jault and H.-C. Nataf, "Experimental and numerical studies of magnetoconvection in a rapidly rotating spherical shell", *J. Fluid Mech.* **580** (2007), pp. 123–143.

[95] D. Fultz, Y. Nakagawa and P. Frenzen, "An instance in thermal convection of Eddington's "Overstability"", *Phys. Rev.* **94** (1954), no. 6, pp. 1471–1472.

[96] J. Aurnou, S. Andreadis, L. Zhu and P. Olson, "Experiments on convection in Earths core tangent cylinder", *Earth Planet. Sci. Lett.* **212** (2003), no. 1–2, pp. 119–134.

[97] K. Aujogue, *Little Earth experiment: a journey towards the Earth's tangent cylinder*, PhD thesis, Coventry University, 2016.

[98] J. E. Hart, G. A. Glatzmaier and J. Toomre, "Space-laboratory and numerical simulations of thermal convection in a rotating hemispherical shell with radial gravity", *J. Fluid Mech.* **173** (1986), pp. 519–544.

[99] J. E. Hart, D. Ohlsen, S. Kittelman, N. Borhani, F. Leslie and T. Miller, *The geophysical fluid flow cell experiment*, tech. rep., NASA Marshall Space Flight Center, 1999.

[100] J. E. Hart, "Experiments on thermal convection in rotating spherical shells with radial gravity: The geophysical fluid flow cell", in *Third Microgravity Fluid Physics Conference*, 1996.

[101] C. Egbers, W. Beyer, A. Bonhage, R. Hollerbach and P. Beltrame, "The geoflow-experiment on ISS (part I): Experimental preparation and design of laboratory testing hardware", *Adv. Space Res.* **32** (2003), no. 2, pp. 171–180.

[102] B. Futterer, C. Egbers, N. Dahley, S. Koch and L. Jehring, "First identification of sub-and supercritical convection patterns from "GeoFlow", the geophysical flow simulation experiment integrated in Fluid Science Laboratory", *Acta Astronaut.* **66** (2010), no. 1–2, pp. 193–200.

[103] B. Futterer, N. Dahley, S. Koch, N. Scurtu and C. Egbers, "From isoviscous convective experiment "GeoFlow I" to temperature-dependent viscosity in "GeoFlow II" – Fluid physics experiments on-board ISS for the capture of convection phenomena in Earth's outer core and mantle", *Acta Astronaut.* **71** (2012), pp. 11–19.

[104] B. Futterer, A. Krebs, A.-C. Plesa, F. Zaussinger, R. Hollerbach, D. Breuer and C. Egbers, "Sheet-like and plume-like thermal flow in a spherical convection experiment performed under microgravity", *J. Fluid Mech.* **735** (2013), pp. 647–683.

[105] F. Zaussinger, A. Krebs, V. Travnikov and C. Egbers, "Recognition and tracking of convective flow patterns using Wollaston shearing interferometry", *Adv. Space Res.* **60** (2017), no. 6, pp. 1327–1344.

[106] F. Zaussinger, P. Haun, P. S. Szabo, V. Travnikov, M. Al Kawwas and C. Egbers, "Rotating spherical gap convection in the GeoFlow International Space Station (ISS) experiment", *Phys. Rev Fluids* **5** (2020), no. 6, article no. 063502.

[107] D. Fultz and Y. Nakagawa, "Experiments on over-stable thermal convection in mercury", *Proc. R. Soc. Lond. A. Math. Phys. Sci.* **231** (1955), no. 1185, pp. 211–225.

[108] Y. Nakagawa and P. Frenzen, "A theoretical and experimental study of cellular convection in rotating fluids", *Tellus* **7** (1955), no. 1, pp. 2–21.

[109] Y. Nakagawa, "Experiments on the instability of a layer of mercury heated from below and subject to the simultaneous action of a magnetic field and rotation", *Proc. R. Soc. Lond. A. Math. Phys. Sci.* **242** (1957), no. 1228, pp. 81–88.

[110] Y. Nakagawa, "Experiments on the instability of a layer of mercury heated from below and subject to the simultaneous action of a magnetic field and rotation. II", *Proc. R. Soc. Lond. A. Math. Phys. Sci.* **249** (1959), no. 1256, pp. 138–145.

[111] I. R. Goroff, "An experiment on heat transfer by over stable and ordinary convection", *Proc. R. Soc. Lond. A. Math. Phys. Sci.* **254** (1960), no. 1279, pp. 537–541.

[112] E. L. Koschmieder, "On convection of a uniformly heated plane", *Beitrage zur Physik der Atmosphäre* **39** (1967), pp. 216–225.

[113] H. T. Rossby, "A study of Bénard convection with and without rotation", *J. Fluid Mech.* **36** (1969), no. 2, pp. 309–335.

[114] P. G. J. Lucas, J. M. Pfotenhauer and R. J. Donnelly, "Stability and heat transfer of rotating cryogens. Part 1. Influence of rotation on the onset of convection in liquid 4He", *J. Fluid Mech.* **129** (1983), pp. 251–264.

[115] J. M. Pfotenhauer, P. G. J. Lucas and R. J. Donnelly, "Stability and heat transfer of rotating cryogens. Part 2. Effects of rotation on heat-transfer properties of convection in liquid He", *J. Fluid Mech.* **145** (1984), pp. 239–252.

[116] J. M. Pfotenhauer, J. J. Niemela and R. J. Donnelly, "Stability and heat transfer of rotating cryogens. Part 3. Effects of finite cylindrical geometry and rotation on the onset of convection", *J. Fluid Mech.* **175** (1987), pp. 85–96.

[117] B. M. Boubnov and G. S. Golitsyn, "Experimental study of convective structures in rotating fluids", *J. Fluid Mech.* **167** (1986), pp. 503–531.

[118] B. M. Boubnov and G. S. Golitsyn, "Temperature and velocity field regimes of convective motions in a rotating plane fluid layer", *J. Fluid Mech.* **219** (1990), pp. 215–239.

[119] H. J. Fernando, R.-R. Chen and D. L. Boyer, "Effects of rotation on convective turbulence", *J. Fluid Mech.* **228** (1991), pp. 513–547.

[120] Y. Liu and R. E. Ecke, "Heat transport scaling in turbulent Rayleigh–Bénard convection: effects of rotation and Prandtl number", *Phys. Rev. Lett.* **79** (1997), no. 12, pp. 2257–2260.

[121] L. Ning and R. E. Ecke, "Rotating Rayleigh–Bénard convection: Aspect-ratio dependence of the initial bifurcations", *Phys. Rev. E* **47** (1993), no. 5, pp. 3326–3333.

[122] Y. Liu and R. E. Ecke, "Heat transport measurements in turbulent rotating Rayleigh–Bénard convection", *Phys. Rev. E* **80** (2009), no. 3, article no. 036314.

[123] P. Vorobieff and R. E. Ecke, "Transient states during spin-up of a Rayleigh–Bénard cell", *Phys. Fluids* **10** (1998), no. 10, pp. 2525–2538.

[124] S. Sakai, "The horizontal scale of rotating convection in the geostrophic regime", *J. Fluid Mech.* **333** (1997), pp. 85–95.

[125] J. M. Aurnou and P. L. Olson, "Experiments on Rayleigh–Bénard convection, magnetoconvection and rotating magnetoconvection in liquid gallium", *J. Fluid Mech.* **430** (2001), pp. 283–307.

[126] E. M. King, S. Stellmach, J. Noir, U. Hansen and J. M. Aurnou, "Boundary layer control of rotating convection systems", *Nature* **457** (2009), no. 7227, pp. 301–304.

[127] J. S. Cheng, S. Stellmach, A. Ribeiro, A. Grannan, E. M. King and J. M. Aurnou, "Laboratory-numerical models of rapidly rotating convection in planetary cores", *Geophys. J. Int.* **201** (2015), no. 1, pp. 1–17.

[128] E. M. King and J. M. Aurnou, "Turbulent convection in liquid metal with and without rotation", *Proc. Natl. Acad. Sci. USA* **110** (2013), no. 17, pp. 6688–6693.

[129] A. M. Grannan, J. S. Cheng, A. Aggarwal, E. K. Hawkins, Y. Xu, S. Horn, J. Sánchez-Álvarez and J. M. Aurnou, "Experimental pub crawl from Rayleigh–Bénard to magnetostrophic convection", *J. Fluid Mech.* **939** (2022), article no. R1.

[130] R. P. J. Kunnen and H. J. H. Clercx, "Breakdown of large-scale circulation in turbulent rotating convection", *Europhys. Lett.* **84** (2008), no. 2, article no. 24001.

[131] R. P. J. Kunnen, B. J. Geurts and H. J. H. Clercx, "Experimental and numerical investigation of turbulent convection in a rotating cylinder", *J. Fluid Mech.* **642** (2010), pp. 445–476.

[132] H. Rajaei, P. Joshi, K. M. Alards, R. P. Kunnen, F. Toschi and H. J. Clercx, "Transitions in turbulent rotating convection: A Lagrangian perspective", *Phys. Rev. E* **93** (2016), no. 4, article no. 043129.

[133] P. Joshi, H. Rajaei, R. P. Kunnen and H. J. Clercx, "Effect of particle injection on heat transfer in rotating Rayleigh–Bénard convection", *Phys. Rev. Fluids* **1** (2016), no. 8, article no. 084301.

[134] H. Rajaei, R. P. Kunnen and H. J. Clercx, "Exploring the geostrophic regime of rapidly rotating convection with experiments", *Phys. Fluids* **29** (2017), no. 4, article no. 45105.

[135] J. Q. Zhong, R. J. Stevens, H. J. Clercx, R. Verzicco, D. Lohse and G. Ahlers, "Prandtl-, Rayleigh-, and Rossby-number dependence of heat transport in turbulent rotating Rayleigh–Bénard convection", *Phys. Rev. Lett.* **102** (2009), no. 4, article no. 044502.

[136] S. Weiss, R. Stevens, J.-Q. Zhong, H. J. Clercx, D. Lohse and G. Ahlers, "Finite-size effects lead to supercritical bifurcations in turbulent rotating Rayleigh–Bénard convection", *Phys. Rev. Lett.* **105** (2010), no. 22, article no. 224501.

[137] S. Weiss and G. Ahlers, "Heat transport by turbulent rotating Rayleigh–Bénard convection and its dependence on the aspect ratio", *J. Fluid Mech.* **684** (2011), pp. 407–426.

[138] J. J. Niemela, S. Babuin and K. R. Sreenivasan, "Turbulent rotating convection at high Rayleigh and Taylor numbers", *J. Fluid Mech.* **649** (2010), pp. 509–522.

[139] R. E. Ecke and J. J. Niemela, "Heat transport in the geostrophic regime of rotating Rayleigh–Bénard convection", *Phys. Rev. Lett.* **113** (2014), no. 11, article no. 114301.

[140] M. Wedi, D. P. Van Gils, E. Bodenschatz and S. Weiss, "Rotating turbulent thermal convection at very large Rayleigh numbers", *J. Fluid Mech.* **912** (2021), article no. A30.

[141] J. S. Cheng, J. M. Aurnou, K. Julien and R. P. Kunnen, "A heuristic framework for next-generation models of geostrophic convective turbulence", *Geophys. Astrophys. Fluid Dyn.* **112** (2018), no. 4, pp. 277–300.

[142] J. S. Cheng, M. Madonia, A. J. Aguirre Guzmán and R. P. Kunnen, "Laboratory exploration of heat transfer regimes in rapidly rotating turbulent convection", *Phys. Rev. Fluids* **5** (2020), no. 11, article no. 113501.

[143] R. P. Kunnen, "The geostrophic regime of rapidly rotating turbulent convection", *J. Turbul.* **22** (2021), no. 4–5, pp. 267–296.

[144] J. A. Abbate and J. M. Aurnou, "Rotating convective turbulence in moderate to high Prandtl number fluids", *Geophys. Astrophys. Fluid Dyn.* **117** (2023), no. 6, pp. 1–40.

[145] S.-S. Ding, K. L. Chong, J.-Q. Shi, G.-Y. Ding, H.-Y. Lu, K.-Q. Xia and J.-Q. Zhong, "Inverse centrifugal effect induced by collective motion of vortices in rotating thermal convection", *Nat. Commun.* **12** (2021), no. 1, article no. 5585.

[146] H.-Y. Lu, G.-Y. Ding, J.-Q. Shi, et al., "Heat-transport scaling and transition in geostrophic rotating convection with varying aspect ratio", *Phys. Rev. Fluids* **6** (2021), no. 7, article no. L071501.

[147] J.-Q. Shi, H.-Y. Lu, S.-S. Ding and J.-Q. Zhong, "Fine vortex structure and flow transition to the geostrophic regime in rotating Rayleigh–Bénard convection", *Phys. Rev. Fluids* **5** (2020), no. 1, article no. 011501.

[148] Y.-B. Hu, Y.-C. Xie and K.-Q. Xia, "On the centrifugal effect in turbulent rotating thermal convection: onset and heat transport", *J. Fluid Mech.* **938** (2022), article no. R1.

[149] F. H. Busse and L. L. Hood, "Differential rotation driven by convection in a rapidly rotating annulus", *Geophys. Astrophys. Fluid Dyn.* **21** (1982), no. 1–2, pp. 59–74.

[150] M. A. Azouni, E. W. Bolton and F. H. Busse, "Convection driven by centrifugal bouyancy in a rotating annulus", *Geophys. Astrophys. Fluid Dyn.* **34** (1986), no. 1–4, pp. 301–317.

[151] C. R. Carrigan and F. H. Busse, "An experimental and theoretical investigation of the onset of convection in rotating spherical shells", *J. Fluid Mech.* **126** (1983), pp. 287–305.

[152] S. Cordero, "Experiments on convection in a rotating hemispherical shell: transition to chaos", *Geophys. Res. Lett.* **20** (1993), no. 23, pp. 2587–2590.

[153] P. Cardin and P. Olson, "Chaotic thermal convection in a rapidly rotating spherical shell: consequences for flow in the outer core", *Phys. Earth Planet. Inter.* **82** (1994), no. 3–4, pp. 235–259.

[154] M. Jaletzky and F. H. Busse, "New patterns of centrifugally driven thermal convection", *Proc. Natl. Acad. Sci. USA* **97** (2000), no. 10, pp. 5060–5064.

[155] M. Westerburg and F. H. Busse, "Centrifugally driven convection in the rotating cylindrical annulus with modulated boundaries", *Nonlinear Process. Geophys.* **10** (2003), no. 3, pp. 275–280.

[156] I. Sumita and P. Olson, "Laboratory experiments on high Rayleigh number thermal convection in a rapidly rotating hemispherical shell", *Phys. Earth Planet. Inter.* **117** (2000), no. 1, pp. 153–170.

[157] I. Sumita and P. Olson, "Rotating thermal convection experiments in a hemispherical shell with heterogeneous boundary heat flux: Implications for the Earth's core", *J. Geophys. Res.: Solid Earth* **107** (2002), no. B8, article no. ETG-5.

[158] I. Sumita and P. Olson, "Experiments on highly supercritical thermal convection in a rapidly rotating hemispherical shell", *J. Fluid Mech.* **492** (2003), pp. 271–287.

[159] N. Gillet, D. Brito, D. Jault and H. C. Nataf, "Experimental and numerical studies of convection in a rapidly rotating spherical shell", *J. Fluid Mech.* **580** (2007), pp. 83–121.

[160] S. S. Sahoo and B. Sreenivasan, "Response of Earth's magnetic field to large lower mantle heterogeneity", *Earth Planet. Sci. Lett.* **549** (2020), article no. 116507.

[161] H. Jiang, D. Wang, S. Liu and C. Sun, "Experimental evidence for the existence of the ultimate regime in rapidly rotating turbulent thermal convection", *Phys. Rev. Lett.* **129** (2022), no. 20, article no. 204502.

[162] E. K. Hawkins, J. S. Cheng, J. A. Abbate, T. Pilegard, S. Stellmach, K. Julien and J. M. Aurnou, "Laboratory models of planetary core-style convective turbulence", *Fluids* **8** (2023), no. 4, article no. 106.

[163] C. K. Hill, U. S. N. Aeronautics, S. Administration and G. C. M. S. F. Center, *Spacelab Mission 3 Experiment Descriptions*, NASA Technical Memorandum, National Aeronautics, Space Administration, Scientific, and Technical Information Branch, 1982.

[164] D. E. Smylie, "Thermal convection in dielectric liquids and modelling in geophysical fluid dynamics", *Earth Planet. Sci. Lett.* **1** (1966), no. 5, pp. 339–340.

[165] B. Chandra and D. E. Smylie, "A laboratory model of thermal convection under a central force field", *Geophys. Fluid Dyn.* **3** (1972), no. 3, pp. 211–224.

[166] T. Gastine, J. Wicht and J. M. Aurnou, "Turbulent Rayleigh–Bénard convection in spherical shells", *J. Fluid Mech.* **778** (2015), pp. 721–764.

[167] N. A. Featherstone and B. W. Hindman, "The emergence of solar supergranulation as a natural consequence of rotationally constrained interior convection", *Astrophys. J. Lett.* **830** (2016), no. 1, article no. L15.

[168] S. Horn, O. Shishkina and C. Wagner, "On non-Oberbeck–Boussinesq effects in three-dimensional Rayleigh–Bénard convection in glycerol", *J. Fluid Mech.* **724** (2013), pp. 175–202.

[169] K. Julien, A. M. Rubio, I. Grooms and E. Knobloch, "Statistical and physical balances in low Rossby number Rayleigh–Bénard convection", *Geophys. Astrophys. Fluid Dyn.* **106** (2012), no. 4–5, pp. 392–428.

[170] R. J. A. M. Stevens, H. J. H. Clercx and D. Lohse, "Optimal Prandtl number for heat transfer in rotating Rayleigh–Bénard convection", *New J. Phys.* **12** (2010), no. 7, article no. 075005.

[171] S. Horn and O. Shishkina, "Rotating non-Oberbeck–Boussinesq Rayleigh–Bénard convection in water", *Phys. Fluids* **26** (2014), no. 5, article no. 055111.

[172] S. Horn and O. Shishkina, "Toroidal and poloidal energy in rotating Rayleigh–Bénard convection", *J. Fluid Mech.* **762** (2015), pp. 232–255.

[173] T. Gastine, J. Wicht and J. Aubert, "Scaling regimes in spherical shell rotating convection", *J. Fluid Mech.* **808** (2016), pp. 690–732.

[174] N. A. Featherstone, E. H. Anders, K. C. Augustson, et al., "The puzzling structure of solar convection: Window into the dynamo", in *Heliophysics 2024 Decadal Whitepapers*, 2023. Online at https://api.semanticscholar.org/CorpusID:258686768. (accessed 25 February 2025).

[175] M. Luna, F. Moreno-Insertis and E. Priest, "Are tornado-like magnetic structures able to support solar prominence plasma?", *Astrophys. J. Lett.* **808** (2015), no. 1, article no. L23.

[176] S. Horn and J. M. Aurnou, "Rotating convection with centrifugal buoyancy: Numerical predictions for laboratory experiments", *Phys. Rev. Fluids* **4** (2019), no. 7, article no. 073501.

[177] H. Kuniyoshi, M. Shoda, H. Iijima and T. Yokoyama, "Magnetic tornado properties: A substantial contribution to the solar coronal heating via efficient energy transfer", *Astrophys. J.* **949** (2023), no. 1, article no. 8.

[178] K. Tziotziou, E. Scullion, S. Shelyag, et al., "Vortex motions in the solar atmosphere: Definitions, theory, observations, and modelling", *Space Sci. Rev.* **219** (2023), no. 1, article no. 1.

[179] R. E. Rosensweig, J. Browaeys, J.-C. Bacri, A. Zebib and R. Perzynski, "Laboratory study of spherical convection in simulated central gravity", *Phys. Rev. Lett.* **83** (1999), no. 23, pp. 4904–4907.

[180] W.-G. Früh, "Using magnetic fluids to simulate convection in a central force field in the laboratory", *Nonlinear Process. Geophys.* **12** (2005), no. 6, pp. 877–889.

[181] J. P. Koulakis, S. Pree, A. L. Thornton and S. Putterman, "Trapping of plasma enabled by pycnoclinic acoustic force", *Phys. Rev. E* **98** (2018), no. 4, article no. 043103.

[182] J. P. Koulakis and S. Putterman, "Convective instability in a stratified ideal gas containing an acoustic field", *J. Fluid Mech.* **915** (2021), article no. A25.
[183] M. Schnaubelt and F. H. Busse, "Convection in a rotating cylindrical annulus part 3. Vacillating and spatially modulated flows", *J. Fluid Mech.* **245** (1992), pp. 155–173.
[184] F. H. Busse and A. C. Or, "Convection in a rotating cylindrical annulus: thermal Rossby waves", *J. Fluid Mech.* **166** (1986), pp. 173–187.
[185] F. H. Busse, "Asymptotic theory of convection in a rotating, cylindrical annulus", *J. Fluid Mech.* **173** (1986), pp. 545–556.
[186] A. C. Or and F. H. Busse, "Convection in a rotating cylindrical annulus. Part 2. Transitions to asymmetric and vacillating flow", *J. Fluid Mech.* **174** (1987), pp. 313–326.
[187] J. Tao, "Thermal convection in a rotating cylindrical annulus and its mean zonal flows", *J. Fluid Mech.* **552** (2006), pp. 73–82.
[188] M. Auer, F. H. Busse and R. M. Clever, "Three-dimensional convection driven by centrifugal buoyancy", *J. Fluid Mech.* **301** (1995), pp. 371–382.
[189] F. H. Busse and F. Finocchi, "The onset of thermal convection in a rotating cylindrical annulus in the presence of a magnetic field", *Phys. Earth Planet. Inter.* **80** (1993), no. 1–2, pp. 13–23.
[190] E. Kurt, W. Pesch and F. H. Busse, "Pattern formation in the rotating cylindrical annulus with an azimuthal magnetic field at low Prandtl numbers", *J. Vib. Control* **13** (2007), no. 9–10, pp. 1321–1330.
[191] F. H. Busse, "A model of the geodynamo", *Geophys. J. Int.* **42** (1975), no. 2, pp. 437–459.
[192] F. H. Busse, "Convection driven zonal flows and vortices in the major planets", *Chaos: Interdiscip. J. Nonlinear Sci.* **4** (1994), no. 2, pp. 123–134.
[193] F. H. Busse, G. Hartung, M. Jaletzky and G. Sommermann, "Experiments on thermal convection in rotating systems motivated by planetary problems", *Dyn. Atmos. Oceans* **27** (1997), no. 1–4, pp. 161–174.
[194] F. H. Busse, "Convective flows in rapidly rotating spheres and their dynamo action", *Phys. Fluids* **14** (2002), no. 4, pp. 1301–1314.
[195] A. P. Bassom and A. M. Soward, "Localised rotating convection induced by topography", *Physica D* **97** (1996), no. 1–3, pp. 29–44.
[196] J. S. Oishi, K. J. Burns, J. B. Marston and S. M. Tobias, "Direct statistical simulation of the Busse annulus", *J. Fluid Mech.* **949** (2022), article no. R1.
[197] R. J. Teed, C. A. Jones and R. Hollerbach, "On the necessary conditions for bursts of convection within the rapidly rotating cylindrical annulus", *Phys. Fluids* **24** (2012), no. 6, article no. 066604.
[198] J. Wicht, M. French, S. Stellmach, N. Nettelmann, T. Gastine, L. Duarte and R. Redmer, "Modeling the interior dynamics of gas planets", in *Magnetic Fields in the Solar System: Planets, Moons and Solar Wind Interactions*, Springer International Publishing: Cham, 2018, pp. 7–81.
[199] M. A. Calkins, K. Julien and P. Marti, "Three-dimensional quasi-geostrophic convection in the rotating cylindrical annulus with steeply sloping endwalls", *J. Fluid Mech.* **732** (2013), pp. 214–244.
[200] D. J. Baker, "A technique for the precise measurement of small fluid velocities", *J. Fluid Mech.* **26** (1966), no. 3, pp. 573–575.
[201] P. Olson, "Laboratory experiments on the dynamics of the core", *Phys. Earth Planet. Inter.* **187** (2011), no. 3–4, pp. 139–156.
[202] P. Olson, "Experimental dynamos and the dynamics of planetary cores", *Annu. Rev. Earth Planet. Sci.* **41** (2013), pp. 153–181.
[203] P. Cardin and P. Olson, "8.13 - Experiments on core dynamics", in *Treatise on Geophysics*, 2nd edition (G. Schubert, ed.), Elsevier: Amsterdam, Boston, Heidelberg, London, New York, Oxford, Paris, San Diego, San Francisco, Singapore, Sydney, Tokyo, 2015, pp. 317–339.
[204] G. Hulot, J.-L. Le Mouël and D. Jault, "The flow at the core-mantle boundary symmetry properties", *J. Geomagn. Geoelec.* **42** (1990), no. 7, pp. 857–874.
[205] D. Gubbins and J. Bloxham, "Morphology of the geomagnetic field and implications for the geodynamo", *Nature* **325** (1987), no. 6104, pp. 509–511.
[206] J. Bloxham, D. Gubbins and A. Jackson, "Geomagnetic secular variation", *Philos. Trans. R. Soc. Lond. A Math. Phys. Sci.* **329** (1989), no. 1606, pp. 415–502.
[207] D. Brito, H.-C. Nataf, P. Cardin, J. Aubert and J.-P. Masson, "Ultrasonic doppler velocimetry in liquid gallium", *Exp. Fluids* **31** (2001), no. 6, pp. 653–663.
[208] N. T. Baker, A. Pothérat, L. Davoust and F. Debray, "Controlling the dimensionality of MHD turbulence at low Rm", *Exp. Fluids* **58** (2017), no. 7, article no. 79.
[209] S. Processing, *2D/3D Ultrasonic velocimetry*. Online at https://signal-processing.com/udv-md/. (accessed 25 February 2025).
[210] P. B. Rhines, "Waves and turbulence on a beta-plane", *J. Fluid Mech.* **69** (1975), no. 3, pp. 417–443.

[211] T. L. Lonner, A. Aggarwal and J. M. Aurnou, "Planetary core-style rotating convective flows in paraboloidal laboratory experiments", *J. Geophys. Res.: Planets* **127** (2022), no. 10, article no. e2022JE007356.
[212] P. Read, Y. Afanasyev, J. Aurnou and D. Lemasquerier, "Eddy-driven zonal jet flows in the laboratory", *C. R. Phys.* **25** (2024), no. S3, pp. 427–477.
[213] D. P. Lathrop and C. B. Forest, "Magnetic dynamos in the lab", *Phys. Today* **64** (2011), no. 7, pp. 40–45.
[214] A. Tilgner, "Towards experimental fluid dynamos", *Phys. Earth Planet. Inter.* **117** (2000), no. 1–4, pp. 171–177.
[215] P. H. Roberts and E. M. King, "On the genesis of the Earth's magnetism", *Rep. Prog. Phys.* **76** (2013), no. 9, article no. 096801.
[216] S. Horn and J. M. Aurnou, "The Elbert range of magnetostrophic convection. I. Linear theory", *Proc. R. Soc. A* **478** (2022), no. 2264, article no. 20220313.
[217] D. R. Fearn, "Thermal and magnetic instabilities in a rapidly rotating fluid sphere", *Geophys. Astrophys. Fluid Dyn.* **14** (1979), no. 1, pp. 103–126.
[218] A. M. Soward, "Convection driven dynamos", *Phys. Earth Planet. Inter.* **20** (1979), no. 2–4, pp. 134–151.
[219] I. A. Eltayeb, "Hydromagnetic convection in a rapidly rotating fluid layer", *Proc. R. Soc. Lond. A Math. Phys. Sci.* **326** (1972), no. 1565, pp. 229–254.
[220] I. A. Eltayeb, "Overstable hydromagnetic convection in a rotating fluid layer", *J. Fluid Mech.* **71** (1975), no. 01, pp. 161–179.
[221] K. Aujogue, A. Pothérat and B. Sreenivasan, "The onset of plane rotating magnetoconvection at low Ekman number", *Phys. Fluids* **27** (2015), no. 10, article no. 106602.
[222] D. Gubbins and M. Richards, "Coupling of the core dynamo and mantle: thermal or topographic?", *Geophys. Res. Lett.* **13** (1986), no. 13, pp. 1521–1524.
[223] J. Bloxham and D. Gubbins, "Thermal core–mantle interactions", *Nature* **325** (1987), no. 6104, pp. 511–513.
[224] C. L. Johnson and C. G. Constable, "Persistently anomalous Pacific geomagnetic fields", *Geophys. Res. Lett.* **25** (1998), no. 7, pp. 1011–1014.
[225] G. A. Glatzmaier, R. S. Coe, L. Hongre and P. H. Roberts, "The role of the Earth's mantle in controlling the frequency of geomagnetic reversals", *Nature* **401** (1999), no. 6756, pp. 885–890.
[226] C. Kutzner and U. R. Christensen, "Simulated geomagnetic reversals and preferred virtual geomagnetic pole paths", *Geophys. J. Int.* **157** (2004), no. 3, pp. 1105–1118.
[227] J. Wicht and A. Tilgner, "Theory and modeling of planetary dynamos", in *Planetary Magnetism*, Springer: New York, 2010, pp. 501–542.
[228] P. Olson and H. Amit, "Magnetic reversal frequency scaling in dynamos with thermochemical convection", *Phys. Earth Planet. Inter.* **229** (2014), pp. 122–133.
[229] J. Wicht and D. G. Meduri, "A Gaussian model for simulated geomagnetic field reversals", *Phys. Earth Planet. Inter.* **259** (2016), pp. 45–60.
[230] F. Terra-Nova and H. Amit, "Regionally-triggered geomagnetic reversals", *Sci. Rep.* **14** (2024), no. 1, article no. 9639.
[231] J. A. Tarduno, M. K. Watkeys, T. N. Huffman, R. D. Cottrell, E. G. Blackman, A. Wendt, C. A. Scribner and C. L. Wagner, "Antiquity of the South Atlantic Anomaly and evidence for top-down control on the geodynamo", *Nat. Commun.* **6** (2015), no. 1, article no. 7865.
[232] R. Boehler, "High-pressure experiments and the phase diagram of lower mantle and core materials", *Rev. Geophys.* **38** (2000), no. 2, pp. 221–245.
[233] J. C. Castle, K. C. Creager, J. P. Winchester and R. D. van der Hilst, "Shear wave speeds at the base of the mantle", *J. Geophys. Res.: Solid Earth* **105** (2000), no. B9, pp. 21543–21557.
[234] E. J. Garnero, "Heterogeneity of the lowermost mantle", *Annu. Rev. Earth Planet. Sci.* **28** (2000), no. 1, pp. 509–537.
[235] R. D. van der Hilst and H. Kárason, "Compositional heterogeneity in the bottom 1000 kilometers of Earth's mantle: Toward a hybrid convection model", *Science* **283** (1999), no. 5409, pp. 1885–1888.
[236] N. Schaeffer, D. Jault, H.-C. Nataf and A. Fournier, "Turbulent geodynamo simulations: a leap towards Earths core", *Geophys. J. Int.* **211** (2017), no. 1, pp. 1–29.
[237] S. Horn and J. M. Aurnou, "The Elbert range of magnetostrophic convection. II. Comparing linear theory to nonlinear low-*Rm* simulations", *Proc. R. Soc. A* (2025). (in press).
[238] E. M. King and J. M. Aurnou, "Magnetostrophic balance as the optimal state for turbulent magnetoconvection", *Proc. Natl. Acad. Sci. USA* **112** (2015), no. 4, pp. 990–994.
[239] S. Chandrasekhar, "Thermal convection", *Daedalus* **86** (1957), no. 4, pp. 323–339.
[240] M. Wedi, V. M. Moturi, D. Funfschilling and S. Weiss, "Experimental evidence for the boundary zonal flow in rotating Rayleigh–Bénard convection", *J. Fluid Mech.* **939** (2022), article no. A14.
[241] O. Shishkina, "Tenacious wall states in thermal convection in rapidly rotating containers", *J. Fluid Mech.* **898** (2020), article no. F1.

[242] B. Favier and E. Knobloch, "Robust wall states in rapidly rotating Rayleigh–Bénard convection", *J. Fluid Mech.* **895** (2020), article no. R1.
[243] C. C. Finlay, N. Gillet, J. Aubert, P. W. Livermore and D. Jault, "Gyres, jets and waves in the Earths core", *Nat. Rev. Earth Environ.* **4** (2023), pp. 377–392.
[244] G. Hulot, C. Eymin, B. Langlais, M. Mandea and N. Olsen, "Small-scale structure of the geodynamo inferred from Oersted and Magsat satellite data", *Nature* **416** (2002), no. 6881, pp. 620–623.
[245] P. Pugnat, R. Barbier, C. Berriaud, et al., "43+T grenoble hybrid magnet: From final assembly to commissioning of the superconducting outsert", *IEEE Trans. Appl. Supercond.* **32** (2022), no. 6, pp. 1–7.
[246] P. H. Roberts, *Introduction to Magnetohydrodynamics*, Longmans: London, 1967.
[247] D. Schmitt, T. Alboussière, D. Brito, P. Cardin, G. D., D. Jault and H.-C. Nataf, "Rotating spherical Couette flow in a dipolar magnetic field: Experimental study of magneto-inertial waves", *J. Fluid Mech.* **604** (2008), pp. 175–197.
[248] S. Lalloz, L. Davoust, F. Debray and A. Pothérat, "Alfvén waves at low Magnetic Reynolds number: transitions between diffusion, dispersive Alfvén waves and nonlinear propagation", *J. Fluid Mech.* **1003** (2025), article no. A19.
[249] N. Gillet, D. Jault, E. Canet and A. Fournier, "Fast torsional waves and strong magnetic field within the Earths core", *Nature* **465** (2010), pp. 74–77.
[250] N. Gillet, F. Gerick, D. Jault, T. Schwaiger, J. Aubert and M. Istas, "Satellite magnetic data reveal interannual waves in Earth's core", *Proc. Natl. Acad. Sci. USA* **119** (2022), no. 13, article no. e2115258119.
[251] H. Cao, R. K. Yadav and J. M. Aurnou, "Geomagnetic polar minima do not arise from steady meridional circulation", *Proc. Natl. Acad. Sci. USA* **115** (2018), no. 44, pp. 11186–11191.
[252] R. K. Yadav, T. Gastine, U. R. Christensen, L. D. Duarte and A. Reiners, "Effect of shear and magnetic field on the heat-transfer efficiency of convection in rotating spherical shells", *Geophys. J. Int.* **204** (2016), no. 2, pp. 1120–1133.
[253] A. J. Aguirre Guzmán, M. Madonia, J. S. Cheng, R. Ostilla-Mónico, H. J. H. Clercx and R. P. J. Kunnen, "Force balance in rapidly rotating Rayleigh–Bénard convection", *J. Fluid Mech.* **928** (2021), article no. A16.
[254] B. Favier, L. J. Silvers and M. R. Proctor, "Inverse cascade and symmetry breaking in rapidly rotating Boussinesq convection", *Phys. Fluids* **26** (2014), no. 9, article no. 096605.
[255] C. Guervilly, D. W. Hughes and C. A. Jones, "Large-scale vortices in rapidly rotating Rayleigh–Bénard convection", *J. Fluid Mech.* **758** (2014), pp. 407–435.
[256] S. Stellmach, M. Lischper, K. Julien, G. Vasil, J. S. Cheng, A. Ribeiro, E. M. King and J. M. Aurnou, "Approaching the asymptotic regime of rapidly rotating convection: boundary layers versus interior dynamics", *Phys. Rev. Lett.* **113** (2014), no. 25, article no. 254501.
[257] J. Aubert, "State and evolution of the geodynamo from numerical models reaching the physical conditions of Earths core", *Geophys. J. Int.* **235** (2023), no. 1, pp. 468–487.
[258] D. J. Stevenson, "Cosmochemistry and structure of the giant planets and their satellites", *Icarus* **62** (1985), no. 1, pp. 4–15.
[259] H. C. Urey, *The Planets, Their Origin and Development*, Yale Universith Press: New Haven, 1952.
[260] V. Bouillaut, B. Miquel, K. Julien, S. Aumaître and B. Gallet, "Experimental observation of the geostrophic turbulence regime of rapidly rotating convection", *Proc. Natl. Acad. Sci. USA* **118** (2021), no. 44, article no. e2105015118.
[261] E. K. Shea, B. P. Weiss, W. S. Cassata, D. L. Shuster, S. M. Tikoo, J. Gattacceca, T. L. Grove and M. D. Fuller, "A long-lived lunar core dynamo", *Science* **335** (2012), no. 6067, pp. 453–456.
[262] C. Stys and M. Dumberry, "A past lunar dynamo thermally driven by the precession of its inner core", *J. Geophys. Res.: Planets* **125** (2020), no. 7, article no. e2020JE006396.
[263] U. R. Christensen, "Iron snow dynamo models for Ganymede", *Icarus* **247** (2015), pp. 248–259.
[264] R. Stieglitz and U. Müller, "Experimental demonstration of a homogeneous two-scale dynamo", *Phys. Fluids* **13** (2001), no. 3, pp. 561–564.
[265] A. Gailitis, O. Lielausis, S. Dement'ev, et al., "Detection of a flow induced magnetic field eigenmode in the Riga dynamo facility", *Phys. Rev. Lett.* **84** (2000), no. 19, pp. 4365–4368.
[266] R. Monchaux, M. Berhanu, M. Bourgoin, et al., "Generation of a magnetic field by dynamo action in a turbulent flow of liquid sodium", *Phys. Rev. Lett.* **98** (2007), no. 4, article no. 044502.
[267] M. Berhanu, R. Monchaux, S. Fauve, et al., "Magnetic field reversals in an experimental turbulent dynamo", *Europhys. Lett.* **77** (2007), no. 5, article no. 59001.
[268] F. Stefani, A. Gailitis, G. Gerbeth, A. Giesecke, T. Gundrum, G. Rüdiger, M. Seilmayer and T. Vogt, "The DRESDYN project: liquid metal experiments on dynamo action and magnetorotational instability", *Geophys. Astrophys. Fluid Dyn.* **113** (2019), no. 1–2, pp. 51–70.
[269] F. Stefani, S. Anders, S. Eckert, et al., "The DRESDYN precession experiment", *C. R. Phys.* **25** (2024), no. S3, pp. 629–647.

[270] F. Pétrélis, "Experimental dynamos: from models to applications to the geodynamo", *C. R. Phys.* **25** (2024), no. S3, pp. 611–627.
[271] T. Schwaiger, T. Gastine and J. Aubert, "Force balance in numerical geodynamo simulations: a systematic study", *Geophys. J. Int.* **219** (2019), S101–S114.
[272] J. Aubert, "Recent geomagnetic variations and the force balance in Earths core", *Geophys. J. Int.* **221** (2020), no. 1, pp. 378–393.
[273] E. Dormy, "Strong-field spherical dynamos", *J. Fluid Mech.* **789** (2016), pp. 500–513.
[274] P. H. Roberts and K. Zhang, "Thermal generation of Alfvén waves in oscillatory magnetoconvection", *J. Fluid Mech.* **420** (2000), pp. 201–223.
[275] A. Alemany, R. Moreau, P. Sulem and U. Frisch, "Influence of an external magnetic field on homogeneous MHD turbulence", *J. Méc.* **18** (1979), no. 2, pp. 277–313.
[276] K. Messadek and R. Moreau, "An experimental investigation of MHD quasi-two-dimensional turbulent shear flows", *J. Fluid Mech.* **456** (2002), pp. 137–159.
[277] T. Alboussière, V. Uspenski and R. Moreau, "Quasi-2D MHD turbulent shear layers", *Exp. Therm. Fluid Sci.* **20** (1999), no. 20, pp. 19–24.
[278] S. Eckert, G. Gerbeth, W. Witke and H. Langenbrunner, "MHD turbulence measurements in a sodium channel exposed to a transverse magnetic field", *Int. J. Heat Fluid Flow* **22** (2001), no. 3, pp. 358–364.
[279] A. Pothérat and R. Klein, "Why, how and when MHD turbulence at low *Rm* becomes three-dimensional", *J. Fluid Mech.* **761** (2014), pp. 168–205.
[280] A. Pothérat and R. Klein, "Do magnetic fields enhance turbulence at low magnetic Reynolds number?", *Phys. Rev. Fluids* **2** (2017), no. 6, article no. 063702.
[281] N. Baker, A. Pothérat, L. Davoust and F. Debray, "Inverse and direct energy cascades in three-dimensional magnetohydrodynamic turbulence at low magnetic Reynolds number", *Phys. Rev. Lett.* **120** (2018), article no. 224502.
[282] L. Davoust, M. D. Cowley, R. Moreau and R. Bolcato, "Buoyancy-driven convection with a uniform magnetic field. Part 2. Experimental investigation", *J. Fluid Mech.* **400** (1999), pp. 59–90.
[283] T. Vogt, W. Ishimi, T. Yanagisawa, Y. Tasaka, A. Sakuraba and S. Eckert, "Transition between quasi-two-dimensional and three-dimensional Rayleigh–Bénard convection in a horizontal magnetic field", *Phys. Rev. Fluids* **3** (2018), no. 1, article no. 013503.
[284] O. Andreev, A. Thess and C. Haberstroh, "Visualization of magnetoconvection", *Phys. Fluids* **15** (2003), no. 12, pp. 3886–3889.
[285] A. Alferenok, A. Pothérat and U. Lüdtke, "Optimal magnet configuration for Lorentz Force Velocimetry in low conductivity fluids", *Meas. Sci. Technol.* **24** (2013), no. 6, article no. 065303.
[286] R. Hide, "An experimental study of thermal convection in a rotating liquid", *Philos. Trans. R. Soc. Lond. A Math. Phys. Sci.* **250** (1958), no. 983, pp. 441–478.
[287] T. Alboussière, R. Deguen and M. Melzani, "Melting-induced stratification above the Earths inner core due to convective translation", *Nature (London)* **466** (2010), pp. 744–747.
[288] J. Leconte and G. Chabrier, "A new vision of giant planet interiors: Impact of double diffusive convection", *Astron. Astrophys.* **540** (2012), article no. A20.
[289] T. Gastine and J. Wicht, "Stable stratification promotes multiple zonal jets in a turbulent Jovian dynamo model", *Icarus* **368** (2021), article no. 114514.
[290] K. M. Moore, A. Barik, S. Stanley, et al., "Dynamo simulations of Jupiter's magnetic field: The role of stable stratification and a dilute core", *J. Geophys. Res.: Planets* **127** (2022), no. 11, article no. e2022JE007479.
[291] J. R. Fuentes, B. W. Hindman, A. E. Fraser and E. H. Anders, "Evolution of semiconvective staircases in rotating flows: Consequences for fuzzy cores in giant planets", *Astrophys. J. Lett.* **975** (2024), no. 1, article no. L1.
[292] S. Horn, *Oscillatory thermal-inertial layer formation in the outer molecular region of gas giants*, 2024. In preperation.
[293] B. A. Buffett and C. T. Seagle, "Stratification of the top of the core due to chemical interactions with the mantle", *J. Geophys. Res.: Solid Earth* **115** (2010), no. B4, article no. B04407.

ACADÉMIE DES SCIENCES
INSTITUT DE FRANCE

Comptes Rendus. Physique
2024, Vol. 25, Special issue S3, p. 77-94
https://doi.org/10.5802/crphys.194

Research article / *Article de recherche*

Geophysical and astrophysical fluid dynamics in the laboratory / *Dynamique des fluides géophysiques et astrophysiques au laboratoire*

Experiments on double diffusive convection

Expériences sur la convection doublement diffusive

Andreas Tilgner [a]

[a] Institute of Astrophysics and Geophysics, University of Göttingen, Friedrich-Hund-Platz 1, 37077 Göttingen, Germany

E-mail: andreas.tilgner@phys.uni-goettingen.de

Abstract. Double diffusive convection is a form of convection that was studied in the past mostly for its application in oceanography and which receives increasing attention in the context of planetary cores. This review will focus on measurements of transport properties of double diffusive convection which were performed in two types of experiments: the experiments either start from two layers separated by a sharp interface, or they investigate convection within uniform gradients. The most recent experiments were done on the finger regime in which the slowly diffusing component drives the motion while the rapidly diffusing component stabilizes the fluid and this review is restricted to this configuration.

Résumé. La convection doublement diffusive est une forme de convection qui a été étudiée dans le passé surtout pour son application océanographique et qui reçoit de plus en plus d'attention dans le contexte de la convection dans les noyaux planétaires. Cette revue est consacrée aux mesures des propriétés de transport de la convection doublement diffusive qui ont été effectuées dans deux types d'expériences: soit l'expérience démarre de deux couches séparées par une discontinuité, soit elle étudie la convection à l'intérieur de gradients uniformes. Les expériences les plus récentes ont été réalisées dans le régime des doigts de salinité dans lequel la composante qui diffuse lentement entraîne le mouvement alors que la composante qui diffuse rapidement stabilise le fluide et cette revue se concentre sur cette configuration.

Keywords. convection, double diffusive convection, salt fingers, double diffusive instability, layering.

Mots-clés. convection, convection double diffusive, doigts de sel, instabilité double diffusive, couches de mélange.

Funding. The author is supported by DFG project Ti 243/15.

Manuscript received 13 February 2024, revised 4 July 2024, accepted 10 July 2024.

1. Introduction

Double diffusive convection is concerned with convection in fluids whose density depends on two ingredients or components. The most prominent example is ocean water with a density determined by both temperature and salinity. This combination is at the origin of the term "thermohaline convection" as synonym for "double diffusive convection" or "two component convection". Peculiar effects arise in ocean water convection because of the widely different diffusion constants for heat and salt ions, which explains the emphasis on double diffusion in

the name “double diffusive convection”. Similar effects must be expected in the Earth’s core if both temperature and chemical composition contribute to density variations in the outer core. Other applications of double diffusive convection appear in geology such as in magma chambers.

The most spectacular effects arise when one of the components contributes to a stable stratification of the medium while the other component on its own leads to unstable stratification. The discrepancy in diffusion rates allows for a mechanism which permits convective motion despite a stable stratification of total density. The form of this motion depends on whether the fast or the slowly diffusing component is driving the motion. The latter case leads to convection in narrow elongated structures as for example in Figures 1 and 2, called “finger convection”, while the former case shows less distinctive structures and is usually called the “diffusive regime”, except that astrophysicists tend to call it “semiconvection”. Both types of double diffusive convection lead to layer formation, so called “staircases”. They consist in the finger regime of vertically stacked layers with every second layer filled with fingers, while large scale overturning convection occurs in the intervening layers as demonstrated for example by the visualizations in Ref. [1].

Numerical computations struggle to simulate double diffusive convection in the parameter regimes one is generally interested in. It helps numerical simulations that the important phenomena occur both in 2D and in 3D so that much can be learned from 2D simulations. But it remains challenging to simulate staircases with their coexisting convection rolls, which extend over a large width, and fingers, which require a high resolution. Numerical methods also struggle to cope with a large ratio of diffusivity constants. State of the art methods use two different grids, one for every component of the double diffusive system. Presumably the most advanced numerical method and simulations at the most extreme parameters accessible today are presented in Refs. [2,3].

This review will regard double diffusive convection as an extension of the more familiar Rayleigh–Bénard convection problem which inquires the vertical heat transport through a layer in between horizontal boundaries with controlled temperatures. This does not do full justice to the richness of double diffusive effects studied in the laboratory. For example, a simple rising plume is a non trivial object of surprising shape in a double diffusive environment [4,5] and the phenomenon of lateral intrusion [6,7] does not exist in single component convection. However, the vertical flux through a stratified layer is the most fundamental problem and deserves special attention.

The existence of staircases motivates experiments in which one attempts to isolate a single finger layer between two convecting layers. This is done by starting from two layers initially separated by a sharp interface as described in Section 3. The experiments on transport between fixed horizontal boundaries more akin to Rayleigh–Bénard convection will appear in Section 5.

A key observable in all types of convection is the flux of heat or salinity across the convective layer. It is of interest to compare the advances made in this respect for double diffusive convection versus Rayleigh–Bénard convection. Experiments in the 1960’s throughout the 1980’s on double diffusive convection were contemporaneous with experiments on Rayleigh–Bénard convection using very much the same techniques, frequently performed by the same researchers. They used cells a few tens in centimeters in size filled with standard working fluids such as water or air. The activity on Rayleigh–Bénard convection gained new momentum in later decades through innovative set ups using more exotic working fluids such as cryogenic gas [8] or compressed gas [9]. In addition, there was a race towards ever larger facilities [10,11]. One of the rewards of all this activity was a large database for the heat flux in turbulent convection in a gas in dependence of the Rayleigh number, in which the Rayleigh number spans many orders of magnitude. These data showed that the reasoning leading to the celebrated $4/3$-law of double diffusive convection to be discussed below is not valid for all Rayleigh numbers in Rayleigh–Bénard convection. It is still not known with certainty how the heat flux scales with Rayleigh number at

extreme parameters, which motivates further and further experiments [12].

Experimental research on double diffusive convection stagnated in comparison and advanced at a much slower pace, at least in as far as quantitative flux measurements are concerned on which this review will focus. If the example of Rayleigh–Bénard convection is any indication, we must expect that measurements over an extended range of parameters in double diffusive convection will also give new impetus to the subject and call into question current theories. This paper will review the experimental techniques employed so far.

The behaviour of double diffusive convection depends very much on the sign of the gradients of the two components involved, leading to either finger convection or the diffusive regime. However, any experimental apparatus can usually study both regimes and easily switch from one type of double diffusive convection to the other. It is therefore sufficient for the purpose of this review to focus on one of the two regimes. Only the literature on finger convection will be cited because the most recent experiments were restricted to this regime. Many reviews of double diffusive convection have appeared in the past, the most complete of which is certainly the book by Radko [13]. The present paper will review aspects that are too technical or too experimentally minded to have been mentioned before. There will also be a special focus on fluxes as they are the most important and most accurately measured quantities, and visualizations or other less quantitative results will receive less attention.

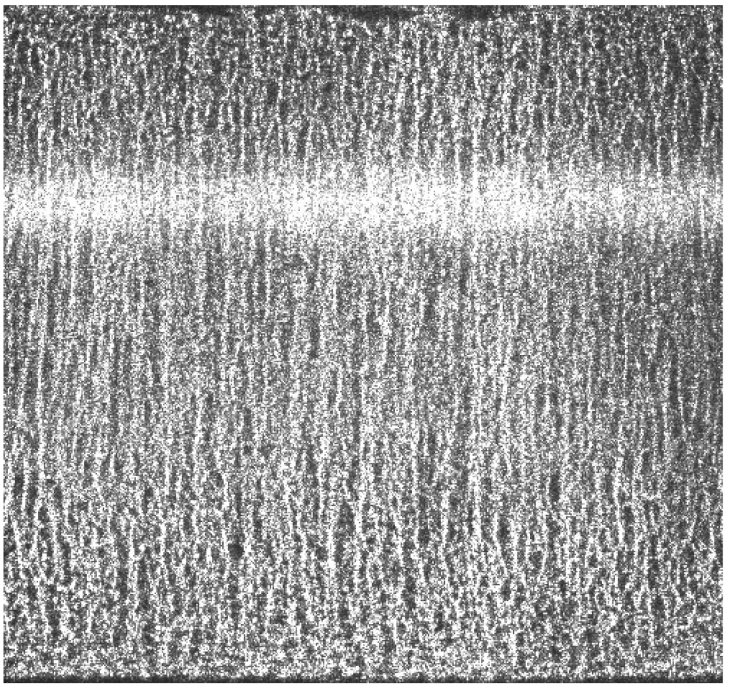


Figure 1. Shadowgraph picture of finger convection for $Ra_c = 1.15 \times 10^{11}$ and $Ra_T = -9.70 \times 10^7$. The bright horizontal bar is an artefact of the illumination. This picture is taken from Ref. [14].

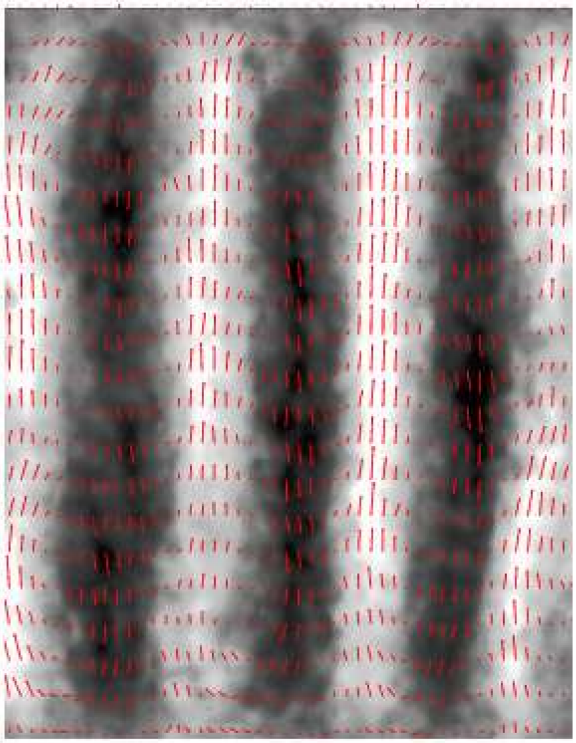


Figure 2. Velocity field obtained from particle image velocimetry at $Ra_c = 1.05 \times 10^9$ and $Ra_T = -3.81 \times 10^5$. The red lines indicate direction and velocity of the flow, the shade of gray depends on the vertical component of velocity. This figure is taken from Ref. [14].

2. Finger convection basics

2.1. *Fingers and layers*

The two components governing the density of the convecting fluid are commonly called temperature and salinity even if two other physical quantities are responsible for the density variations. Temperature just stands for the rapidly diffusing component, and salinity for the slowly diffusing one. For instance, it is experimentally convenient to use sugar and salt dissolved in water, in which case the salt concentration as the more rapidly diffusing variable plays the role of temperature and "salinity" stands for sugar concentration.

For a start, let us think of a water volume consisting initially of two layers with a sharp interface, with a layer of cold fresh water underlying a layer of warm salty water. Let us assume that the combinations of temperature and salinity are such that the top layer is less dense than the bottom layer so that there is no reason for a large scale overturning motion. How will this system evolve? The interface will of course thicken by diffusion. A more efficient vertical transport arises from a possible instability. Assume that a particle from the top layer is displaced into the bottom layer. If there was no diffusion, this particle would return to the top layer because of its small density. In the presence of diffusion, however, the particle exchanges heat with its environment, and more so than it exchanges salinity because of the different diffusion constants. In a thought experiment going to the extremes, imagine temperature diffusing instantaneously and salinity not diffusing at all. The lowered particle then immediately loses its temperature contrast with the other fluid at the same height while retaining its salinity so that this particle is now more dense than the

other fluid in the bottom layer and it will continue to sink. The identical reasoning holds for a particle lifted from the bottom to the top layer that continues to rise. The two layer system is therefore prone to a convection instability. The horizontal wavelength of the instability must be small enough so that the temperature in for example every down flow quickly equilibrates by diffusion with the neighboring up flows. The convection rolls will tend to be slender and look like fingers. At the same time, fingers cannot be too narrow either to prevent a too rapid exchange of salinity between neighboring fingers, and also of momentum by viscous friction. This instability mechanism is obviously not limited to an initially sharp interface but may operate in smooth gradients as well.

The fingering instability must saturate at some point. The fingers can only grow to some finite length before they will become unstable themselves, just like the plume of smoke rising from a cigarette. It is at present not clear what the most potent instability mechanism for fingers is. A much debated candidate is a collective instability [15,16] in which an internal gravity wave is excited by the finger flow and which prevents any further lengthening of the fingers. Once the fingers have reached their maximum length, they transport salty water from the top layer to the base of the fingers within the bottom layer. This increases the density there, so that the bottom layer below the fingers is unstable to global overturning. Likewise, the up going fingers pump fresh water to the bottom of the top layer which creates an unstable density stratification within the top layer, too. The finger instability thus leads from top to bottom to overturning convection in relatively warm salty water in the top layer, a finger layer in the middle, and overturning convection in relatively cold fresh water in the bottom layer. This state will last if temperature and salinity at some top and bottom boundaries can be controlled and maintained. Otherwise, the motion will end once temperature and salinity differences are used up.

A modification of this system helps to understand why layering frequently occurs spontaneously in double diffusive systems, at least transiently. Replace in the two layer system considered so far the bottom layer with fresh water that is itself stably stratified because its temperature increases with height, but the density of the top layer is still smaller than the density of the topmost fluid in the bottom layer. How is the system going to evolve from these modified initial conditions? The ideas exposed above still apply in the beginning: Fingers develop because of the rapid lateral diffusion of heat compared with the slow lateral diffusion of salinity, the fingers stop growing in length because of some instability, the fingers pump salty water to their base and fresh water to the top. The difference with the previous system is that now the bottom layer is not globally unstable, but only down to the depth at which the bottom layer has the same density as the fluid that accumulates at the bottom of the fingers. This starts an overturning motion of finite depth which mixes salinity and temperature within large scale convection rolls. The bottom of these rolls qualitatively recreates the same conditions that characterized the interface we started from: Relatively warm and salty water overlying stably stratified fresh water. We therefore expect a second layer of fingers to form at the bottom of the motion considered so far, followed by a second overturning layer. If only the water layer extends deep enough, we can expect more and more layers to form as deeper and deeper strata start to move.

The subsequent fate of the these layers is less clear. For these layers to survive in a stationary state, one needs of course to supply fluxes of salinity and heat at the top and bottom of the system, but in addition, the flow needs to be able to adjust so that the fluxes through each finger layer equals the fluxes through each overturning layer. Whether such a state is reached, and what the flow characteristics in such a state are, is part of the questions laboratory experiments seek to answer.

2.2. *Equation and parameters*

We need to introduce the relevant parameters which allow us to compare different experiments among each other and to compare experiments with situations in nature. The experiments are always parametrized within the Boussinesq approximation which linearizes the dependence of density ρ on temperature T and salinity or ion concentration c as

$$\rho(T,c) = \rho_0 \left\{1 - \alpha(T - T_0) + \beta(c - c_0)\right\} \tag{1}$$

where T_0 and c_0 are the temperature and ion concentration of a reference state at which the density is ρ_0, so that $\rho(T_0, c_0) = \rho_0$. The signs in eq. (1) are chosen such that the expansion coefficients α and β are both positive. The Boussinesq approximation assumes that density variations need only be retained in the buoyancy term in the momentum equation and that all other material properties are constant. This leads to the following equations of evolution for the temperature and concentration fields $T(\boldsymbol{r}, t)$ and $c(\boldsymbol{r}, t)$, the velocity $\boldsymbol{v}(\boldsymbol{r}, t)$ and the pressure $p(\boldsymbol{r}, t)$:

$$\frac{\partial}{\partial t}\boldsymbol{v} + (\boldsymbol{v}\cdot\nabla)\boldsymbol{v} = -\frac{1}{\rho}\nabla p + \nu\nabla^2\boldsymbol{v} + g\alpha T\hat{\boldsymbol{z}} - g\beta c\hat{\boldsymbol{z}} \tag{2}$$

$$\nabla\cdot\boldsymbol{v} = 0 \tag{3}$$

$$\frac{\partial}{\partial t}T + \boldsymbol{v}\cdot\nabla T = \kappa\nabla^2 T \tag{4}$$

$$\frac{\partial}{\partial t}c + \boldsymbol{v}\cdot\nabla c = D\nabla^2 c \tag{5}$$

where $\hat{\boldsymbol{z}}$ denotes a unit vector in the vertical direction. The diffusivities for heat and salt are κ and D, the kinematic viscosity of the fluid is ν, and the gravitational acceleration is g.

To find the parameters that help comparing different situations, we remove dimensions from these equations. We first select a length L, typically the total height of an experimental cell, and express the position vector $\boldsymbol{r}$ in terms of the non dimensional vector $\boldsymbol{r}'$ as $\boldsymbol{r} = \boldsymbol{r}'L$. Likewise, we may rewrite time as $t = t'L^2/D$ and the various fields as $\boldsymbol{v} = \boldsymbol{v}'D/L$, $p = p'\rho D^2/L^2$, $c = c'\Delta c$, and $T = T'\Delta T$ where Δc and ΔT are typical concentration and temperature differences occurring in the system. These might be the differences between the top and bottom layers in the experiment started from two layers as described above, or it could be the difference between top and bottom boundaries imposed by controlled boundary conditions as in Sections 5.2 and 5.3. With these choices, one arrives at equations of evolution containing four non dimensional parameters. Two of them are combinations of material properties, namely the Schmidt and Lewis numbers Sc and Le defined as $Sc = \nu/D$ and $Le = \kappa/D$. The other two parameters quantify the buoyancy forces and are the thermal and chemical Rayleigh numbers Ra_T and Ra_c defined by

$$Ra_T = \frac{g\alpha\Delta T L^3}{\kappa\nu}, \quad Ra_c = \frac{g\beta\Delta c L^3}{D\nu}. \tag{6}$$

There are therefore four independent control parameters, but there is no universal agreement on which parameters exactly are the most revealing. Apart from trivial changes of notation (the chemical Rayleigh number is frequently called the salinity Rayleigh number Ra_S), a reliable source of confusion resides in the sign conventions. Most papers study either finger convection or the diffusive regime and define the Rayleigh numbers such that they are positive for the system under consideration. A more systematic notation uses negative Rayleigh numbers to signal the stabilizing component. Finger convection then occurs in the quadrant $Ra_T < 0$, $Ra_c > 0$. This convention requires Δc and ΔT to be defined as

$$\Delta T = T_{\text{bottom}} - T_{\text{top}}, \quad \Delta c = c_{\text{top}} - c_{\text{bottom}}. \tag{7}$$

Certain combinations and variations of the four control parameters above are in widespread use. For example, one often sees the "diffusivity ratio" τ which is nothing but the inverse Lewis number, $\tau = 1/Le$. Another popular combination of material properties is the Prandtl number Pr with $Pr = \nu/\kappa = Sc/Le$. All the experiments discussed in this review were done in aqueous solution. With the help of various solutes and temperatures, Pr can then be varied from approximately 5 to 10. If the two components taking part in the double diffusive convection are heat and ion concentration, then $Le \approx 100$. The exact value depends on the ion species and temperature. If on the other hand the two components are concentrations of salt and sugar, then $Le \approx 3$.

The two Rayleigh numbers are frequently combined to the so called density ratio, denoted by R_ρ or Λ and defined as

$$\Lambda = \frac{Ra_T}{Ra_c}\frac{Sc}{Pr} = \frac{\alpha\Delta T}{\beta\Delta c}. \tag{8}$$

Sign conventions again matter in this definition. With the convention adopted in this review, $\Lambda < 0$ for finger convection. However, most papers adapt their definitions in order to obtain a positive Λ for their specific application. The diffusivity ratio is an intuitive parameter because it compares the buoyancy due to temperature variations with the buoyancy due to salinity variations. Double diffusive effects are necessary for any motion in the finger regime if $|\Lambda| > 1$ so that the stabilizing thermal buoyancy overwhelms the destabilizing chemical buoyancy and the layer is density stable. Global overturning is naively expected for $|\Lambda| < 1$. If $|\Lambda|$ is too large, the fluid becomes linearly stable and the stabilizing thermal gradient is strong enough to prevent any motion, even finger convection. In the model of uniform gradients in an infinitely extended fluid, $|\Lambda|$ needs to be less than Le for finger convection to occur according to linear stability analysis. The density ratio directly measures the distance to the intuitive limits of the finger regime.

The quantities one desires to measure are chiefly the thermal and salinity fluxes, $\boldsymbol{j}_T$ and $\boldsymbol{j}_c$, defined by rewriting eqs. (4), (5) as $\frac{\partial}{\partial t}T + \nabla\cdot\boldsymbol{j}_T = 0$ and $\frac{\partial}{\partial t}c + \nabla\cdot\boldsymbol{j}_c = 0$ which implies $\boldsymbol{j}_T = \boldsymbol{v}T - \kappa\nabla T$ and $\boldsymbol{j}_c = \boldsymbol{v}c - D\nabla c$. Only averaged fluxes are usually accessible experimentally. Let us denote the average over time and the entire fluid volume by angular brackets. The ratio of the averaged heat flux divided by the heat transport by diffusion alone in a state of rest is called the Nusselt number Nu. If the temperature difference is imposed between two horizontal planes the distance L apart and if z denotes an axis pointing upwards, Nu is given by (note the definition of ΔT above):

$$Nu = \frac{F_T}{\kappa(-\Delta T)/L} \tag{9}$$

where $F_T = \langle j_{T,z}\rangle$ is the global vertical thermal flux. The analogous quantity for salinity, based on the vertical ion flux $F_c = \langle j_{c,z}\rangle$, is called the Sherwood number Sh in the chemical literature and we will adopt this name here:

$$Sh = \frac{F_c}{D\Delta c/L}. \tag{10}$$

Another quantity determined in many experimental papers is the flux ratio γ, which is defined as $\gamma = (\alpha F_T)/(\beta F_c)$, with the usual precautions concerning sign conventions.

There is a simple idea almost every paper compares it results to which is the 4/3-law. Let us try to determine the Sherwood number as a function of four control parameters which we choose to be Ra_c, Λ, Pr and Sc and let us assume that Sh depends as a power law on Ra_c so that $Sh \propto Ra_c^q f(\Lambda, Pr, Sc)$ with a possibly complicated function f. How can the exponent q be determined? It is plausible to assume that the salinity flux should be independent of L because fingers evolve according to the heat and salinity exchange between neighboring fingers which are spaced by a distance much less than L. One may also argue that the thickness of the concentration boundary layer near one plate should not be influenced by the presence of another

distant boundary, which again implies that the salinity flux must be independent of L and which leads to $Sh \propto Ra_c^{1/3} f(\Lambda, Pr, Sc)$ and in dimensional variables to $F_c \propto \Delta c^{4/3}$.

3. The two layer system

A whole series of experiments studied the system described in Section 2.1. Start from two layers separated by a sharp interface with warm salty water lying over cold fresh water (or any other combination of slow and fast diffusers) and let the system evolve. These experiments face two major challenges: How to set up the initial conditions and how to diagnose the evolution. This section will review some milestones in chronological order.

An early experiment dates back to Turner [17] who actually used the combination of heat and salt. The experiment was started by filling a $25 \times 25 \times 45\, cm^3$ tank halfway with light fluid and by then adding dense fluid through a pipe at the bottom of the tank. The fluid volume is thereby stably stratified at all times and tolerates some mechanical disturbance without immediately mixing both layers. Nonetheless, this filling procedure is the more reliable the stronger the density contrast between the two layers, so that the density ratio cannot be made too small (it ranged from 2 to 10 in these experiments). One also wants to prevent fingers from already forming during the filling. This is why the tank was initially filled with warm and cold fresh water, and salt was added to the top only once the tank was filled. Two rectangular grids were mounted in the tank, one in each layer. The two layers were initially homogenized by oscillating the grids up and down. The stirring must be gentle enough in order not to destroy the interface, yet rigorous enough to homogenize the layers. After a few minutes, the stirring was stopped and the state thus obtained constituted the starting point for the double diffusive convection.

The vertical temperature profile in the tank was monitored with moveable thermistors. The main idea of the experiment was to set the grids into motion anew after a certain time to mix each layer again, withdraw samples from each layer and determine their salinity with a conductivity probe together with their temperature. This technique allowed to determine heat and salinity fluxes. The experiment can of course not be run longer than the time it takes to deplete the salinity and temperature contrast between the two initial layers.

Stern and Turner [18] chose to investigate the salt-sugar system. In this case, salt is the fast diffuser. The large sugar molecules have a diffusivity smaller than that of salt by a factor of 3. The choice of salt and sugar dissolved in water as opposed to the more oceanographically minded salinity in hot or cold water is mainly motivated by the concern that lateral heat losses might influence the measurements. Stern and Turner used two different filling procedures. They either first filled half of the tank with dense salty water and carefully poured less dense sugary water on top by pouring on a thin piece of wood floating on the water, or they used what they called the dam break method. With this method, a vertical wall is introduced in the tank and each side of the tank is filled with one or the other of the two types of fluid. The wall is then removed and the lighter fluid flows on top of the denser fluid. This sounds like a rather brutal method but the authors report that internal waves generated by the dam break method died out quickly and that the resulting two layers were a useful initial condition for the subsequent finger formation. The observations relied on visualizations with dye and aluminum flakes.

Linden [19] used the combination of heat and sugar to drive double diffusive convection. The main reason for this choice was the desire to measure velocity with the thymol blue technique [20]. To use this technique, one dissolves the pH-indicator thymol blue at concentrations of typically 10^{-4} per weight in the water and titrates the solution with HCl and $NaOH$ just to the acid side of the end point of the indicator so that the solution appears orange yellow. If a current is sent through two electrodes sticking into the fluid, H^+ ions are drawn towards the negative electrode where they react to H_2 which locally increases the pH. If the increase is large enough,

the color switches to dark blue. The darkened fluid gets carried away from the electrode by the flow and can be followed for as long as it takes for the pH of the darkened drop to return to its original value by diffusion with the environment. This technique works well if there are no other positive ions than H^+ to transport current, and this is why Linden [19] avoided a salty solution. In the modern days of particle image velocimetry, there is presumably no space left for this elegant visualization technique.

Schmitt [21] returned to the heat-salt system but in a tank larger than those used previously with a height of $98cm$ and a cross section of $19 \times 19\,cm^2$. The convection in a larger tank leads to more vigorous flow which can be relied upon to well mix the fluid outside the finger layer and which obviates the need for a stirring device as used by Turner [17]. A larger tank also accommodates larger flow structures so that more bulky probes can be inserted into the flow without disturbing it. The experiment was equipped not only with a moveable thermistor, but also with a salinity probe. Apart from the rig that held the probe, the mechanically obstructing part of the salinity probe was a platinum electrode of radius $0.25\,mm$ which sampled conductivity in a volume approximately ten times this size. Another in situ salinity probe appeared in Ref. [22].

The filling procedure used by Schmitt [21], or later by McDougall and Taylor [23] involved a mechanical barrier between the two layers. This was a propylene sheet in the case of McDougall and Taylor [23] which was carefully removed once the two layers were set up to allow finger formation to start.

A very convenient visual detection of fingers is by a shadowgraph either with a vertical or a horizontal plane of view. The experiments in this section do not require top and bottom boundaries with special properties, so that they can be made transparent. One can then take shadowgraph pictures along a vertical line of sight as was done by Shirtcliffe and Turner [24] who observed fingers with square cross section in the sugar-salt system.

Let us now turn to the results of these experiments. There are three issues that nearly every experiment on the two layer system addresses. These are the salinity flux, the heat flux or equivalently the flux ratio, and the thickness of the finger zone. The results concerning the last of these topics is usually framed in terms of a Stern number A defined as

$$A = \frac{\alpha F_T - \beta F_c}{\nu\left(\alpha \frac{\partial}{\partial_z}\overline{T} - \beta \frac{\partial}{\partial_z}\overline{c}\right)} \tag{11}$$

where F_T and F_c are the thermal and ion fluxes introduced in the previous section and $\overline{T}$ and $\overline{c}$ are the horizontal averages of temperature and ion concentration. The collective instability of fingers [15,16] sets in if the Stern number exceeds a threshold value of 1. While experiments with the heat-salt system are broadly in agreement with this criterion, Ref. [25] found a Stern number on the order of 10^{-3} in the saturated fingers in the sugar-salt system, so that the Stern number does not seem to yield a universally valid measure for finger lengths.

All the flux measurements are compatible with the 4/3-law. However, the data within each data set extends over barely one order of magnitude in Ra_c so that the exponent in the flux law is poorly constrained and the results are not a definitive confirmation of the 4/3-law. Concerns have been voiced over variations of the prefactor in the 4/3-law from one experiment to another which might call into question the validity of the 4/3-law [26]. Considering the data compilations provided by Refs. [22] and [27] which show variations of up to almost a factor of 2 in either this prefactor or the flux ratio and a comparable scatter in the data obtained from every individual apparatus, one simply has to admit that the data on the two layer system lack the accuracy for definitive conclusions. The experiments on the two layer system investigate the transient of a system whose initial conditions are not well controlled. It would be rather surprising to find perfect agreement between the results obtained from one filling procedure and another. It is presumably impossible to run measurements on the two layer system of the same quality

as we grew accustomed to from other fluid dynamic experiments in the past two decades or so. The experiments described in this section had the merit of launching the subject and of providing indications of relevant mechanisms, but other set ups must provide the stringent tests for quantitative theories.

4. Educational experiments

The experiments of the previous section use low cost equipment, offer pleasing visualization and demonstrate basic physics. They are ideally suited for student labs. Ref. [28] assembles a gratifying combination of methods and parameters of a two layer system for a student exercise. They employ a method not mentioned so far in this review which speaks in favor of sugar as one of the two components: Sugar is optically active and rotates the direction of polarization of polarized light traversing a sugar solution. This effect yields a non invasive method for measuring sugar concentration profiles.

A collection of material properties useful for double diffusive systems involving water, temperature, salt and sugar, including optical activity, is compiled in Ref. [29].

Another set of experimental instructions worth mentioning realizes a salt fountain which is a concept introduced in Ref. [30] that predates the discovery of salt fingering (albeit one may argue about when exactly salt fingers were discovered. For a nice account of the early history of salt finger experiments, see [31].). A salt fountain is essentially a single finger. Imagine a vertically oriented pipe whose walls are made of a good thermal conductor lowered into a part of the ocean in which warm salty water lies over comparatively cold and fresh water with a small length of the pipe protruding out of the water. If the water inside the pipe is given a push upwards, it will continue to rise for the reasons given in Section 2.1 to explain the existence of fingers. In the present case, the pipe walls prohibit any lateral salt diffusion whatsoever. One obtains a perpetual outflow at the upper end of the pipe which looks like a fountain. Ref. [30] contains a succinct description of a laboratory demonstration of such a fountain, and Heavers [32] gives more detailed instructions.

5. Gradient systems

We noted in Section 3 that the two layer system is sensitive to initial conditions which vary from apparatus to apparatus because different filling procedures start the experiment from one or the other non zero velocity field. In addition, the interface between the two layers has thickened by diffusion and mixing by the time the experiment properly speaking starts. The two layer system is an unsatisfactory system from the experimental point of view and it seems preferable to start finger formation from uniform temperature and salinity gradients, or even better, maintain these gradients as long as desired so that the fingers can reach a statistically stationary state.

This section will discuss three types of experiments. The first type sets up uniform gradients, lets fingers evolve, and runs until the gradients are consumed by convection. These experiments again investigate a transient and share in principle the same problem as encountered in the two layer system, but in alleviated form because the initial conditions do not contain a sharp gradient. The second type of experiments maintains solute gradients with semi permeable membranes, while the third type achieves the same goal in an electrochemical cell. The last two classes of experiments are therefore of a similar design as Rayleigh–Bénard convection, in the sense that a gradient is imposed across a cell and the transport through the cell can be accurately measured in a statistically stationary state.

5.1. *Run down experiments*

A variation of the two layer experiment by Turner [17] was used by Taylor [33] to produce a uniform gradient. Two layers with warm salt water over cold fresh water were prepared at first. Fingers started to form at the interface. Then, a grid was dropped through the tank which destroyed the fingers and partially mixed the two layers to create a transition zone with a continuous gradient in which new fingers formed. Dye was mixed into the water in the initial upper layer to visualize motions, and the tank was equipped with thermistors and conductivity probes moveable both in vertical and horizontal directions. The main result of this investigation was that individual fingers did not extend throughout the entire gradient zone. The finger layer rather looked like a disorganized ensemble of elongated blobs. According to the spatial spectra deduced from the probes moving across the tank, the fingers were only approximately twice as long as wide for density ratios between 2 and 5.

Stern and Turner [18] report about two different run down experiments with preconfigured gradients. The first one realizes one of the initial conditions considered in Section 2.1 with a uniform stabilizing temperature gradient in fresh water with a layer of warm and salty water on top. For this experiment, the tank was first filled with stratified water with the commonly used two bucket method: The tank is filled through a tube with its outlet at the bottom of the tank. This tube is connected to a reservoir (or bucket) full of warm water, which itself is connected to a second reservoir full of cold water. The second connection ensures that the water levels in both reservoirs is at the same height at all times. As the first reservoir empties into the tank, water flows from the second reservoir into the first where it is mixed with the water already present. The temperature of the water exiting the first reservoir is therefore decreasing linearly as a function of the delivered volume which results in the stably stratified layer in the tank.

For the configuration discussed in Section 2.1, one needs in addition to prepare some warm salty water of density less than that of the water at the top of the stably stratified layer and carefully pour that water into the tank from the top. Following this procedure, Stern and Turner [18] observed fingers and an increasing number of layers if the stabilizing gradient was increased, as expected from the discussion in Section 2.1. In a second experiment, Stern and Turner filled the two buckets with either a salt or a sugar solution of identical temperature to fill the tank with a uniform layer with a stabilizing salt and a destabilizing sugar gradient. Finger formation already started during filling with this procedure so that measurements on the subsequent transients are again sensitive to details of how the experiment was started. Stern and Turner used this feature to make an interesting observation: If the tank was filled slowly and carefully, fingers developed that extended through the entire tank. Rapid filling or filling at an increasing rate led to a layer with large scale convection patterns that was not replaced by fingers later on, even though it was sandwiched between two finger layers. If on the contrary the authors locally stirred the tank full of extended fingers, the flow quickly returned to vertical fingers. Later experiments explored in greater detail the robustness of salt fingers created by the two bucket method against mechanical perturbations such as periodic shear [34], localized stirring [35] or intermittent turbulence [36].

5.2. *Membranes as boundaries*

Krishnamurti [1] was the first to build an experiment in which differences in temperature and salinity between top and bottom boundaries could be maintained over long periods of time for the sugar-salt system. The convection cell itself had a cross section of $30cm \times 10cm$ and heights varying from $30cm$ to $183cm$. The central idea of the apparatus was to place a reservoir filled with sugar solution above and another reservoir filled with salt solution below the convection cell, and

to introduce between the reservoirs and the cell a membrane that lets salt and sugar pass from one fluid volume to the next, but which is impermeable to fluid flow. Each reservoir was $30cm$ deep.

The feasibility of the experiment depends on whether one finds membranes with the desired properties. In a preliminary experiment, Krishnamurti and Zhu [37] test the properties of their membranes by comparing measurements to results of linear stability calculations and other analytical solutions and find good agreement. The combination of membrane and reservoir acts like a Dirichlet boundary condition by which salt or sugar concentrations at the top and bottom boundaries are fixed. However, there will be flow through the membranes if enough pressure head is present so that certain precautions were necessary during the operation of the apparatus as described now.

The top and bottom reservoirs were mechanically mixed to guarantee homogeneous concentration within each tank. With the help of additional tanks, each reservoir could be flushed and its contents be replaced with freshly prepared solution with the prescribed concentrations. The outflow of each reservoir was collected and its composition determined which allowed to measure the vertical fluxes of salt and sugar. The concentrations in each tank were kept at nearly constant levels by flushing the two reservoirs in turn and at regular intervals, but never simultaneaously. All the connections to one reservoir need to be closed while the other is flushed to prevent possible pressure differences from pushing water through the membranes. It is also important that there be no air bubbles within the working fluid, which is why several bubble traps were part of the set up.

A later experiment [38] simplified the apparatus by forgoing the flushing, so that the concentrations in each reservoir changed, but hopefully slowly enough compared with the dynamics in the convection cell. The measurements of the fluxes must then be done by taking samples from the reservoirs to determine their concentrations.

In addition to flux measurements, the double diffusive convection was diagnosed by particle image velocimetry and particle tracking velocimetry. Vertical profiles of sugar and salt concentrations were determined by sending a horizontal beam of polarized light through the cell and by measuring both the angle by which the polarization direction was rotated and the deflection angle of the beam (from which the refractive index was deduced).

As one could have expected, Krishnamurti's idea of a novel experimental system led to a whole series of new observations. These concerned first of all qualitative descriptions inspired by visualizations. In addition to straight fingers, Krishnamurti [1] mentions "lumpy" and "wavy" fingers. The largest convection tank could accommodate a record number of up to 15 layers (8 finger layers and 7 overturning layers). A remark in [1, Section 4.3] reads: "The junction between the convection layer and the finger layer fluctuated so rapidly that the image of the laser beams made the fluid appear to be "boiling" and reliable measurements were difficult to obtain here." Fast fluctuations of this type were never reported before. In addition, the overturning could have an unusual structure and consist of many disorganized small scale plumes but lacking a large scale circulation [38].

On the quantitative side, the flux measurements point at a difficulty if one attempts to express the fluxes in terms of power laws or a sum of several power laws as we are used to from Rayleigh–Bénard convection, because every time a new convection or finger layer appears, the flux through the cell decreases discontinuously. Thanks to the measurements of the vertical profile of salt and sugar concentrations, it was also possible to compare the flux law through a finger layer in a staircase with the flux laws obtained from the two layer system in Section 3. The fingers within the staircase did not fit well the 4/3-law but instead followed the relation $F_c \propto \Delta c^a$ with a between 0.18 and 0.19.

5.3. *Electrochemical cells*

The second system we know of that allows us to study double diffusive convection in a statistically stationary state is an electrochemical cell. This system is a variation of the one introduced in Ref. [39] as a model system to study Rayleigh–Bénard convection at high Prandtl number. Imagine a cell bounded by two horizontal copper electrodes filled with aqueous solution of $CuSO_4$. If a current is sent through this cell, copper ions detach from one electrode and deposit on the other. The behaviour of such an electrolytic cell is textbook material in electrochemistry [40]. A non uniform spatial distribution of copper ions develops which may lead to convection instability. The variable copper ion concentration is responsible for the variations of density. However, the electrolytic cell really becomes useful for convection studies only after one adds a supporting electrolyte like H_2SO_4 to the solution. The sulfuric acid does not participate in any reaction at the electrodes, but the electric field due to the potential difference applied between the two electrodes separates the ions of the sulfuric acid which accumulate near the electrodes within layers whose thickness is on the order of a Debye length. These microscopically thin layers screen the bulk of the cell from the electric field. For a sufficient concentration of H_2SO_4, the bulk is nearly field free and the copper ions diffuse and are advected by macroscopic fluid flow, but they do not drift in any electric field. If c denotes the copper ion concentration, then its equation of evolution is given by eq. (5).

The next step is to find a way to control the Rayleigh number. This is done with the help of the limiting current, a phenomenon common to all electrolytic cells [40]. The cell is initially filled with a solution of known copper concentration c_0. Let us consider the variations of the electric current through the cell as a function of the applied voltage. The current increases with voltage as long as the voltage is small. A copper concentration gradient must build up near each electrode because only diffusion can transport ions in the proximity of the boundaries. With increasing voltage, the current and the gradients increase until the copper concentration near the cathode drops to zero. This is when the limiting current is reached, because a further increase of the voltage cannot increase the current any more. Since the bulk concentration is c_0 and the concentration at the cathode is zero, the only way to increase the concentration gradient at the cathode is to reduce the thickness of the concentration boundary layer. This would require a higher advection velocity in the bulk to carry away the larger current, which is only possible if the buoyancy forces increase, which necessitates larger concentration differences. However, the concentration drop at the cathode is already at its maximum value, so that a further increase of the current is impossible. Because the average concentration is c_0 and the concentration at the cathode is down to zero, we must by symmetry have a concentration of $2c_0$ at the anode. With the applied voltage set such that the limiting current flows through the cell, we know the concentration difference between top and bottom boundaries and can thus compute the chemical Rayleigh number.

Such an electrochemical cell was used in Ref. [39] to study Rayleigh–Bénard convection (with further technical details given in Ref. [41]) and Hage and Tilgner [14] modified it simply by regulating the temperature of the two copper electrodes so that double diffusive convection could be investigated. The ion flux is very conveniently determined in this system from the electric current flowing through the cell, and particle image velocimetry allows to measure both convection velocities and the size of salinity fingers.

The most remarkable finding in Ref. [14] was that finger convection occurs for $|\Lambda| < 1$ when the density stratification is top heavy and large scale overturning convection could occur according to linear stability analysis (even though it is in competition with narrow fingers for $0.9 < |\Lambda| < 1$, see Ref. [42]), but finger convection nonetheless prevails. Almost all measurements in Ref. [14] were taken for $|\Lambda| < 1$ to explore this unexpected form of convection. The main observables were

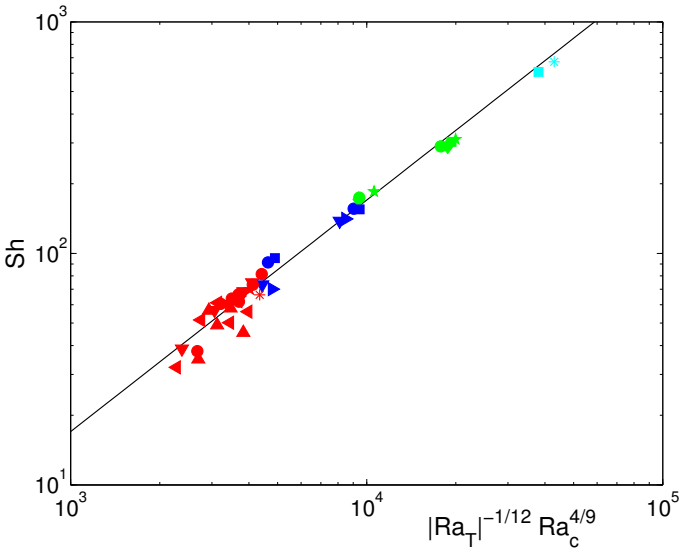


Figure 3. The Sherwood number as a function of $|Ra_T|^{-1/12}Ra_c^{4/9}$ obtained from measurements in an electrochemical cell. The symbol shapes vary according to the magnitude of the adverse temperature gradient and the symbol color according to the cell height. The original figure appeared in Ref. [14].

found to obey scaling laws in terms of the two Rayleigh numbers, and the exponents obtained from the best least square fits agreed with the following simple picture: The dynamics of long and narrow fingers should not be affected by distant boundaries, so that the height L of the cell should not matter. The fluid inside the fingers retains the ion concentration of the boundary they started from with little loss due to diffusion during the journey from one electrode to the other, while temperature quickly diffuses horizontally so that the fluid in the bulk only probes the local temperature gradient but is insensitive to the temperature at the boundaries. The dynamics of the fingers should therefore depend on Δc and $\Delta T/L$, but not on L. Scaling laws for the finger thickness d, the convection velocity v and the thickness of the concentration boundary layer λ may involve powers of Δc and $\Delta T/L$, but none of L alone. The Sherwood number is given by $Sh = L/(2\lambda)$. The 4/3-law is of course compatible with this reasoning as explained in Section 2.2 and reads $Sh \propto Ra_c^{1/3} f(\Lambda, Pr, Sc)$ if expressed for Sh. The best fit in Ref. [14] actually yielded $Sh \propto |Ra_T|^{-1/12} Ra_c^{4/9}$. However, this is identical to $Sh \propto Ra_c^{1/3}|\Lambda|^{-1/12} Ra_c^{1/36}$, so that apart from a virtually undetectable factor $Ra_c^{1/36}$, this expression conforms with the 4/3-law. These experiments used rectangular cells of cross section $20 \times 20\,cm^2$ and heights varying from $2\,cm$ to $20\,cm$, so that Ra_c varied by more than three orders of magnitude. These measurements (shown in Figure 3) are as of today the most precise test of the 4/3-law.

A later experiment with the same cell focussed on the transition from finger convection to overturning convection [44]. This study showed that the ion flux can actually be increased by an adverse temperature gradient. The maximal ion transport at a given Ra_c is observed at the Ra_T at which the transition from fingers to convection rolls occurs. The fingers are slower than the convection rolls, but they fill the entire fluid volume with a velocity field with a large vertical component, whereas convection rolls contain large cores which contribute little to vertical transport.

Kellner and Tilgner [44] identified as a possible criterion for the transition from fingers to convection rolls the condition that the time it takes fluid in fingers to travel across the cell may

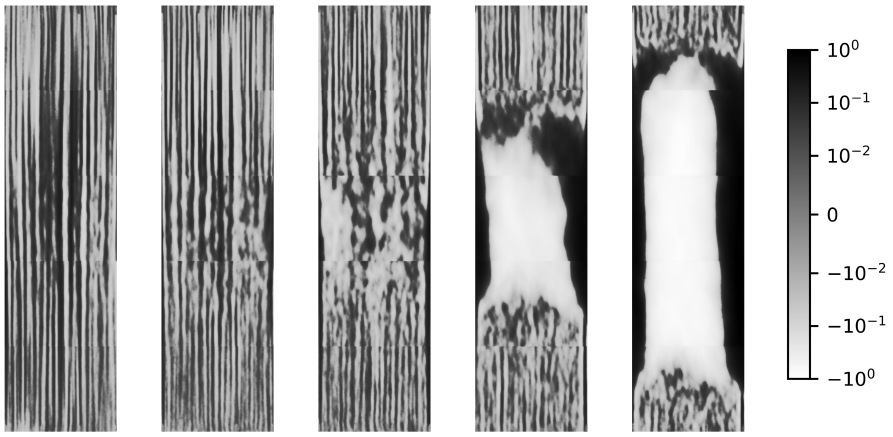


Figure 4. Grey scale maps of the vertical velocity normalized by the maximal absolute value of vertical velocity for $Ra_c = 1.12 \times 10^{13}$ and, from left to right, $Ra_T = -1.22 \times 10^{11}$, -1.01×10^{11}, -4.97×10^{10}, -2.44×10^{10} and -1.23×10^{10}. This figure is taken from Ref. [43].

not be shorter than the time it takes heat to diffuse across a finger, because the heat diffusion is central to the finger forming mechanism explained in Section 2.1. This criterion was confirmed by later experiments [43].

Ref. [43] used a cell of up to $80\,cm$ height in the hope of finding staircases made of several layers. An overturning layer in between two finger layers could indeed be observed for $Ra_c > 10^{12}$ and Ra_T in the right range. For $|Ra_T|$ too small, there simply is a single roll layer as in Rayleigh–Bénard convection, and for $|Ra_T|$ too large, fingers extend straight from top to bottom. At intermediate $|Ra_T|$, one observes fingers which are thicker in the center than near the boundaries, or overturning layers within a staircase whose thickness increases with decreasing $|Ra_T|$ as shown in Figure 4.

6. Conclusion and outlook

Single component or Rayleigh–Bénard convection has been studied for well over a century. The fact that this problem still attracts interest is certainly for the most part due to the charming simplicity of the boundary conditions, the governing equations and the underlying physics which nonetheless give rise to very complex behavior. Double diffusion adds another layer of complexity to the flow. The experimental study of the double diffusive version of the problem is very immature compared with the single component case. The data coverage is limited, as shown in Figure 5. What is more, the results from the different experiments do not combine well to a coherent picture. For example, Stern and Turner [18] mention a dependence on initial conditions in that convective layers, once formed, are not easily replaced by fingers. Other experiments on gradient systems do not report a similar effect, even though the authors of Ref. [43] made an effort to find a dependence on initial conditions or a hysteresis and did not find any.

Another point concerns the short fingers discovered by Taylor [33]. This feature is spectacular enough to be easily detectable in any visualization, and yet, it did not show in the experiments of Ref. [14] at nearby parameters. Flux measurements also raise questions. Krishnamurti [1] found from best fits to her measurement of fluxes through finger layers within staircases a relation different from the 4/3-law, while the results of Ref. [43] were compatible with the 4/3-law.

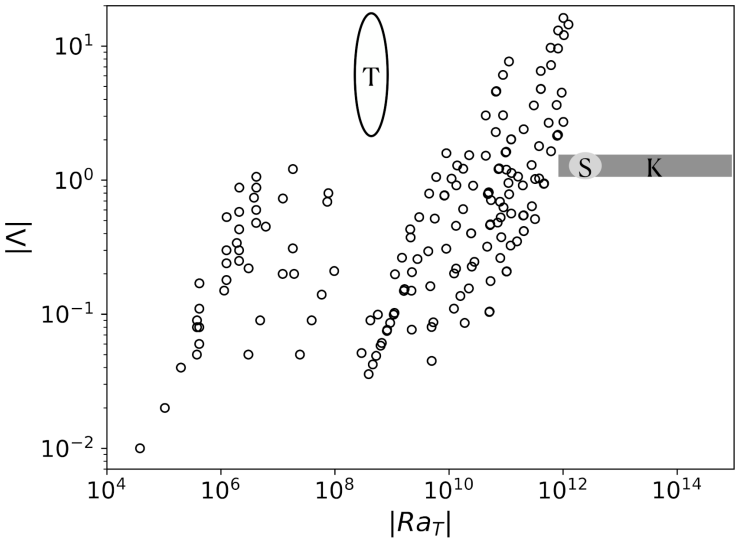


Figure 5. Overview of the parameters of the experiments on gradient systems. The many circles show data points obtained with the electrochemical cells, and the oval labeled T shows the experiment by Taylor [33]. The grey shaded regions correspond to experiments on the sugar-salt system. The light shaded region labeled S is covered by Stern and Turner [18] and the dark shaded region labeled K by Krishnamurti [1].

None of these observations constitutes an outright contradiction for the moment, either because the measured quantities are not exactly comparable, or because the control parameters in the different experiments do not overlap, or because experimental uncertainties do not allow firm conclusions. Nonetheless, the collection of these observations raises questions and these points certainly need closer inspection as part of a more complete investigation of the parameter space.

The limited survey in Figure 5 also implies that we presently do not know well the dependence of salinity and heat transport on the control parameters. The situation could be notably improved by fully exploiting the tools we already have. But new ideas for experimental systems capable of controlling an applied salinity and temperature gradient would certainly also be of great benefit to the field. No matter which system is used, there remains a lot of data collection to be done.

Declaration of interests

The authors do not work for, advise, own shares in, or receive funds from any organization that could benefit from this article, and have declared no affiliations other than their research organizations.

References

[1] R. Krishnamurti, “Double-diffusive transport in laboratory thermohaline staircases”, *J. Fluid Mech.* **483** (2003), pp. 287–314.

[2] Y. Yang, R. Verzicco and D. Lohse, “Scaling laws and flow structures of double diffusive convection in the finger regime”, *J. Fluid Mech.* **802** (2016), pp. 667–689.

[3] J. Li and Y. Yang, “On the wall-bounded model of fingering double diffusive convection”, *J. Fluid Mech.* **973** (2023), article no. A37.

[4] A. B. Tsinober, Y. Yahalom and D. J. Shlien, "A point source of heat in a stable salinity gradient", *J. Fluid Mech.* **135** (1983), pp. 199–217.

[5] R. W. Griffiths and A. A. Bidokhti, "Interleaving intrusions produced by internal waves: a laboratory experiment", *J. Fluid Mech.* **602** (2008), pp. 219–239.

[6] B. R. Ruddick and J. S. Turner, "The vertical length scale of double-diffusive intrusions", *Deep-Sea Res., Part A* **26** (1979), no. 8, pp. 903–913.

[7] R. Krishnamurti, "Double-diffusive interleaving on horizontal gradients", *J. Fluid Mech.* **558** (2006), pp. 113–131.

[8] F. Heslot, B. Castaing and A. Libchaber, "Transitions to turbulence in helium gas", *Phys. Rev. A* **36** (1987), no. 12, pp. 5870–5873.

[9] A. Belmonte, A. Tilgner and A. Libchaber, "Boundary layer length scales in thermal turbulence", *Phys. Rev. Lett.* **70** (1993), pp. 4067–4070.

[10] J. J. Niemela, L. Skrbek, K. R. Sreenivasan and R. J. Donnelly, "Turbulent convection at very high Rayleigh numbers", *Nature* **404** (2000), pp. 837–840.

[11] R. DuPuits, C. Resagk, A. Tilgner, F. H. Busse and A. Thess, "Structure of thermal boundary layers in turbulent Rayleigh–Bénard convection", *J. Fluid Mech.* **572** (2007), pp. 231–254.

[12] P.-E. Roche, "The ultimate state of convection: a unifying picture of very high Rayleigh numbers experiments", *New J. Phys.* **22** (2020), no. 7, article no. 073056.

[13] T. Radko, *Double-Diffusive Convection*, Cambridge University Press, 2013.

[14] E. Hage and A. Tilgner, "High Rayleigh number convection with double diffusive fingers", *Phys. Fluids* **22** (2010), article no. 076603.

[15] M. E. Stern, "Collective instability of salt fingers", *J. Fluid Mech.* **35** (1969), pp. 209–218.

[16] J. Y. Holyer, "On the collective instability of salt fingers", *J. Fluid Mech.* **110** (1981), pp. 195–207.

[17] J. S. Turner, "Salt fingers across a density interface", *Deep-Sea Res.* **14** (1967), pp. 499–611.

[18] M. E. Stern and J. S. Turner, "Salt fingers and convecting layers", *Deep-Sea Res., Part A* **16** (1969), no. 5, pp. 497–511.

[19] P. F. Linden, "On the structure of salt fingers", *Deep-Sea Res.* **20** (1973), pp. 325–340.

[20] D. J. Baker, "A technique for the precise measurement of small fluid velocities", *J. Fluid Mech.* **26** (1966), pp. 573–575.

[21] R. W. Schmitt, "Flux measurements on salt fingers at an interface", *J. Mar. Res.* **37** (1979), no. 3, pp. 419–436.

[22] J. Taylor and P. Bucens, "Laboratory experiments on the structure of salt fingers", *Deep-Sea Res.* **36** (1989), no. 11, pp. 1675–1704.

[23] T. J. McDougall and J. R. Taylor, "Flux measurements across a finger interface at low values of the stability ratio", *J. Mar. Res.* **42** (1984), pp. 1–14.

[24] T. G. L. Shirtcliffe and J. S. Turner, "Observations of the cell structure of salt fingers", *J. Fluid Mech.* **41** (1970), pp. 707–719.

[25] R. B. Lambert and J. W. Demenkow, "On the vertical transport due to fingers in double diffusive convection", *J. Fluid Mech.* **54** (1972), no. 4, pp. 627–640.

[26] J. R. Taylor and G. Veronis, "Experiments on double-diffusive sugar-salt fingers at high stability ratio", *J. Fluid Mech.* **321** (1996), pp. 315–333.

[27] C. Y. Shen, "Heat-salt finger fluxes across a density interface", *Phys. Fluids* **5** (1993), no. 11, pp. 2633–2643.

[28] R. M. Heavers and L. A. Colucci, "Sugar Fingers and Double-Diffusive Convection", *J. Chem. Educ.* **86** (2009), no. 11, article no. 1326.

[29] B. R. Ruddick and T. G. L. Shirtcliffe, "Data for double diffusers: Physical properties of aqueous salt-sugar solutions", *Deep-Sea Res., Part A* **26** (1979), no. 7, pp. 775–787.

[30] H. Stommel, A. B. Arons and D. Blanchard, "An oceanographical curiosity: the perpetual salt fountain", *Deep-Sea Res.* **3** (1956), no. 2, pp. 152–153.

[31] R. W. Schmitt, "The Salt Finger Experiments of Jevons (1857) and Rayleigh (1880)", *J. Phys. Oceanogr.* **25** (1995), no. 1, pp. 8–17.

[32] R. M. Heavers, "The salt fountain", *Phys. Teach.* **32** (1994), no. 9, pp. 524–525.

[33] J. R. Taylor, "Anisotropy of Salt Fingers", *J. Phys. Oceanogr.* **23** (1993), no. 3, pp. 554–565.

[34] M. G. Wells, R. W. Griffiths and J. S. Turner, "Generation of density fine structure by salt fingers in a spatially periodic shear", *J. Geophys. Res. Oceans* **106** (2001), no. C4, pp. 7027–7036.

[35] M. G. Wells and R. W. Griffiths, "Localized stirring in a field of salt-fingers", *Dyn. Atmos. Oceans* **35** (2002), no. 4, pp. 327–350.

[36] M. G. Wells and R. W. Griffiths, "Interaction of salt finger convection with intermittent turbulence", *J. Geophys. Res. Oceans* **108** (2003), no. C3, article no. 25.

[37] R. Krishnamurti and Y. Zhu, "Double-diffusive convection with imposed vertical mass flux", *J. Mar. Res.* **48** (1990), pp. 89–108.

[38] R. Krishnamurti, "Heat, salt and momentum transfer in a laboratory thermohaline staircase", *J. Fluid Mech.* **638** (2009), pp. 491–506.

[39] R. J. Goldstein, H. D. Chiang and D. L. See, "High-Rayleigh-number convection in a horizontal enclosure", *J. Fluid Mech.* **213** (1990), pp. 111–126.

[40] R. F. Probstein, *Physicochemical Hydrodynamics. An introduction*, John Wiley & Sons, 1994.

[41] H. D. Chiang and R. J. Goldstein, "Application of the Electrochemical Mass Transfer Technique to the study of Bouyancy-driven Flows", in *Transport Phenomena in Heat and Mass Transfer* (J. A. Reizes, ed.), Elsevier, 1992, pp. 1–25.

[42] R. W. Schmitt, "Thermohaline convection at density ratios below one: A new regime for salt fingers", *J. Mar. Res.* **69** (2011), pp. 779–795.

[43] A. Rosenthal, K. Lüdemann and A. Tilgner, "Staircase formation in unstably stratified double diffusive finger convection", *Phys. Fluids* **34** (2022), article no. 116605.

[44] M. Kellner and A. Tilgner, "Transition to finger convection in double-diffusive convection", *Phys. Fluids* **26** (2014), article no. 094103.

ACADÉMIE DES SCIENCES
INSTITUT DE FRANCE

Comptes Rendus. Physique
2024, Vol. 25, Special issue S3, p. 95-142
https://doi.org/10.5802/crphys.230

Review article / *Article de synthèse*

Geophysical and astrophysical fluid dynamics in the laboratory / *Dynamique des fluides géophysiques et astrophysiques au laboratoire*

Fingerprints of surface flows on solid substrates ablated by phase change: from laboratory experiments to planetary landscapes

De l'échelle du laboratoire aux paysages planétaires, quelles sont les empreintes laissées par des écoulements de surface sur des substrats solides en ablation soumis à des changements de phase ?

Sabrina Carpy [a,*], **Michael Berhanu** [b], **Martin Chaigne** [b] **and Sylvain Courrech du Pont** [b]

[a] LPG (Laboratoire de Planétologie et Géosciences), Nantes Université, CNRS (UMR 6112), 44322 Nantes, France

[b] MSC (Matière et Systèmes Complexes), Université Paris Cité, CNRS (UMR 7057), 75013 Paris, France

E-mail: sabrina.carpy@univ-nantes.fr (S. Carpy)

Abstract. Physical or chemical phase changes in ablation, such as sublimation, melting or dissolution, are studied in physics for their many engineering applications. At solid/fluid interfaces, the interaction between a phase change and a flow can lead to pattern formation. In this case, the fluid mechanics associated with such phase changes play a key role in the evolution of terrestrial and planetary landscapes, observed by probes orbiting planets and moons. On Earth, sea ice, glaciers and karst plateaus extend over meters or kilometers. The scale of these landscapes contrasts with the scale of the physical mechanisms that govern their evolutionary dynamics. Indeed, it is the typical size of atmospheric boundary layers or melt-water/vapor/solute films that constrain the heat/concentration transfer at the phase change/dissolution interface, and hence the rate of solid ablation. In many situations, these layers are controlled by fluid flow, either natural or forced convection. In the former case, the flow may be buoyancy driven by the melting/dissolution/sublimation itself, resulting in density stratification caused by, for example, temperature/concentration gradients. This stratification may be stable or unstable. In the second case, the flow forced by winds or slopes can be considered as a flow of an infinite height or of a finite height, such as shallow water flow. In all cases, the mass flux modifies topography, which in turn affects the boundary layer flows and

* Corresponding author

thus the ablation rate in a retroactive way. In nature, the positive feedback between geometry and mass transfer drives the spontaneous formation of characteristic patterns at different scales. These patterns are not just geological curiosities, such as Zen stones or dirt cones but markers of the hydrodynamic processes at work. Many landscapes are shaped by regular, repeated patterns, whether sharp-edged, scalloped, parallel-crested, or stepped. By experimentally investigating different modes of flow transport on solid substrates undergoing physical or chemical phase change, this review aims to highlight the role of the flow transport mode in the diversity of patterns observed on analogous materials. Understanding the diversity of these patterns is key to assessing the environmental conditions under which they form on planets such as Mars or Pluto, where phase changes play a very important geomorphological role.

Résumé. Les processus en ablation, tels que les changements de phase, physiques (sublimation/fusion) ou chimiques (dissolution), sont étudiés dans de nombreuses applications techniques en physique. Pour les interfaces solide/fluide, l'interaction entre un changement de phase et un écoulement peut conduire à la formation de motifs topographiques. Dans ce cas, la mécanique des fluides associée à de tels changements de phase joue un rôle primordial dans l'évolution des paysages terrestres et planétaires, observés par les sondes en orbite autour des planètes et des lunes. Sur Terre, la glace de mer, les glaciers et les plateaux karstiques s'étendent sur des mètres ou des kilomètres. L'échelle de ces paysages contraste avec l'échelle des mécanismes physiques qui régissent leur dynamique évolutive. C'est en effet la taille typique des couches limites atmosphériques ou des films d'eau de fonte/soluté qui limite le transfert de chaleur/concentration à l'interface de changement de phase/dissolution, et donc le taux d'ablation du solide. Dans de nombreuses situations, ces couches sont contrôlées par l'écoulement du fluide, de type convection naturelle ou forcée. Dans le premier cas, la flottabilité de la fonte/dissolution elle-même, entraîne une stratification en densité causée par des gradients de température/concentration, qui peut être stable ou instable. Dans le second cas, l'écoulement forcé par des vents ou des pentes peut être considéré comme un écoulement de hauteur infinie ou finie, tels que les écoulements à surface libre. Dans tous les cas, le flux de masse modifie la topographie, qui en retour impacte les écoulements de couches limites (fines ou épaisses) et donc le taux d'ablation de manière rétroactive. Dans la nature, la rétroaction positive entre la géométrie et le transfert de masse entraîne la formation spontanée de formes caractéristiques à différentes échelles. Ces formes ne sont pas seulement des curiosités géologiques, comme le sont par exemple les « Zen stones », ces pierres sur un piédestal de glace ou encore les cônes de poussière, mais des marqueurs des processus hydrodynamiques en jeu. De nombreux paysages sont façonnés selon des motifs réguliers et répétés, qu'ils soient pointus, en forme de cupules, à ligne de crêtes parallèles entre elles ou encore en marches d'escaliers. Dans ce papier de synthèse, nous recensons les études expérimentales dédiées à l'étude des motifs générés par différents modes de transport des flux sur des substrats solides soumis à des changements de phase physiques ou chimiques. Nous souhaitons ainsi mettre en avant le rôle du mode de transport des flux dans la diversité des motifs observés sur des matériaux analogues. Comprendre la diversité de ces motifs est essentiel pour évaluer les conditions environnementales dans lesquelles ils se forment, notamment sur des planètes comme Mars ou Pluton sur lesquelles les changements de phase jouent un rôle géomorphologique majeur.

Keywords. Sublimation, Melting, Dissolution, Natural solid bedforms, Experimental analogues, Pattern formation, Classification.

Mots-clés. Sublimation, Fusion, Dissolution, Motifs solides naturels, Analogues expérimentaux, Formation de motifs, Classification.

Funding. French Research Council (SHERPAS ANR-23-CE49-0006 and PhysErosion ANR-22-CE30-0017).

Manuscript received 9 July 2024, revised 18 December 2024, accepted 20 December 2024.

1. Ablation by mass transfer on solid substrate submitted to phase change

In engineering applications, mass transfer techniques such as dissolution or sublimation have been used to constrain fluid/structure interactions. Naphthalene sublimation is a process that has been widely used in aerodynamics in a broad range of topics such as pollutant dispersion in urban areas [1] or ablation processes in space capsules [2]. Ablation patterns may appear during the descent phase of an atmospheric space capsules [3,4], similar to meteorites' regmaglypts [5], due to the laminar–turbulent transition of the flow. Other solid substrates such as bitumen, copper, brass, aluminum or magnetite, when subjected to liquid water flow, develop ablation patterns [6], which are similar to those appearing on molten ice subjected to water flow or

sublimated ice subjected to wind flow. Whether the phase change is a solid–gas phase transition (sublimation), a solid–liquid phase transition (melting) or a dissolution phenomenon, substrate ablation is strongly linked to a feedback between the fluid flow and the underlying topography, which generally leads to the emergence of patterns. Hereafter, we will refer as solid bedforms to these periodic patterns that are induced by mass transfer built up at the interface between a moving fluid and a solid surface. Although previous experimental works have observed the emergence of solid bedforms, their morphology and dynamics were not the main focus of these engineering applications.

Interest in solid bedforms has been renewed by space missions exploration that have revealed many surprising landscapes, such as the spiral troughs on the north polar cap of Mars, interpreted as cyclic steps [7] and the bladed terrain of Pluto, interpreted as *penitentes* [8]. Sublimation of ice combined with surface flows like wind could be a major geomorphic agent in explaining these planetary landscapes [9]. On Earth water ice on its solid phase represents 2.4% of the global volume of water, but covers 14% of the Earth' surface [10]. Water ice on Earth is subjected to melting and sublimation processes at its surface. However, for most planetary bodies, excluding Earth and Titan, environmental conditions (pressure, temperature) at the surface do not allow the existence of three phases of their exotic ice. N_2, CH_4, CO_2, NH_3 ices [11], are subjected to surface sublimation that prevails in the solar system. Soluble rocks on Earth also present solid bedforms such as scallops or *rillenkarrens* that could be found on limestone, gypsum and salt [12,13]. Solid bedforms therefore have a wide variety of compositions, environments, shapes and physical phenomena involved.

The apparent regularity of these solid bedforms is surprising, given the complexity of the mechanisms behind their formation [14]. Lab-scale experiments contribute significantly to our understanding of their formation and dynamic processes. It requires constant control of experimental parameters (pressure, temperature, partial pressure/humidity, acidity) to reproduce natural cases. Often, analogues substrates are selected to accelerate process kinetics to experimentally more feasible times. So, experimental approaches that simulate rock dissolution with the aim of creating *rillenkarren* [15–17], scallops and *flutes*, rely on the use of plaster [18–20] or even caramel [21], for example. In many situations, fluid dynamic instabilities [14] (e.g. the *Rayleigh Plateau*, *Kelvin Helmholtz*, *Rayleigh Taylor* or *Rayleigh Bénard* instabilities) explain the emergence of natural patterns with a characteristic scale. For example, the growth of transverse patterns (perpendicular to the mean flow), like the dissolution waves on limestone walls in the laminar–turbulent regime [22], or the ripples and cyclic steps on ice due to run-off flows [23,24], have been explained as a positive feedback between the topography, the thickness of the turbulent boundary layer and the ablation rate. Moreover, longitudinal patterns (parallel to the mean flow), like the *Rillenkarren* formed by run-off flows on limestone, could be explained by a linear stability study of the coupled system of equations involving mass transfer and fluid motion, that affect the topography of the bed [17,25,26] under specific boundary conditions.

What environmental conditions are required for the formation of these very large natural solid bedforms? What physical parameters control their size, shape and spatial distribution? How can we explain the fact that the same patterns are found in rock and ice on Earth, but also on other icy planetary surfaces, when the phase changes at work are not always the same? In order to understand the mechanisms responsible for the formation of solid bedforms subjected to a surface flow, and to deduce the links between their shape, dimensions and the characteristics of the environment in which they develop, we describe some experimental results and if any, the scaling laws that describe the development of these solid bedforms during the dissolution [17,20,22,27–29], the melting [30,31] and the sublimation [32] processes. Since the time scales involved for the formation of natural bedforms are too large, experimental models are used to test formation hypotheses over realistic experimental timescales, in order to reconstruct

the formation history of these patterns and the environmental conditions under which they emerged.

The morphological similarities between some solid bedforms resulting from different ablation processes [6,33] in the case of ice sublimation, ice melting and rock dissolution will be described in Section 2 for: sharp patterns; polygonal depression; crested bedforms parallel or perpendicular to the flow; stepped patterns; and debris-covered ice structures. In Section 3, we explore the positive feedback that influence the evolution of the solid/fluid interface by identifying the relevant equations of the problem (hydrodynamic–morphodynamic coupling) with a jump condition at the interface. We will only explore cases where one mechanism is dominant over the other (e.g. double diffusion is out of the scope of this paper). Analogous modeling presented in Section 4 can then be used to constrain the role of fluid mechanics in the evolution of these forms and test hypothesis. The diversity of these patterns is reinforced by the complexity of the flows that carry a passive scalar such as temperature or concentration: a change in density in a natural convection flow would give rise to buoyancy instabilities; a disturbance to the topography in an advective flow can lead to space modulations of concentration. On a large scale, these mechanisms are responsible for the formation of surprising landscapes when hydrodynamic surface flows drain through karst environments, or when katabatic winds descend the slopes of terrestrial and extraterrestrial glaciers. The discussion in Section 5 focuses on the genetic link between the type of flow and the bedfoms that could be helpful in the classification process. We propose to discuss the effect of non-linearity on the resulting bedforms and the perspective to use some scaling laws in a planetological context.

2. Diversity of natural solid bedforms by phase change on solid substrate

There are a wide variety of natural bedforms carved out of ice or soluble rock. These forms are fascinating in their uniqueness or repetitiveness. Examples include stones that look as if they have been placed on a pedestal of ice, blade-like shapes made of ice or soluble rock, steps of ice or soluble rock in streams of water, gullies that incise the soluble rock with spiky crests, or gentle undulations on expanses of blue ice, which can take the form of scallops on cave walls. All these forms are subject to phase changes, whether liquid/solid or solid/vapor for ice, or dissolution for soluble rock. This section highlights the similarities in shape despite the differences in mass transfer mechanisms, and lists the natural forms that have been observed. Experimental studies have been carried out to explain some of these shapes, which we review in Section 4.

2.1. *Sharp patterns*

First described by Charles Darwin in Chile in 1835, *penitentes* are shapes formed by sublimation in old, compact ice/snow, either as spikes or as blades pointing skywards (Figure 1(a)). On Earth, *penitentes* are mainly located in high altitudes: they have been particularly well described in the Santiago Highlands, where all snow and icy surfaces above 4000 m are covered with them; on the summit and flanks of the Tutupaca volcano in Peru [34]; on the Quelccaya Ice Cap in Peru [35]; and on the Tapado Glacier in northern Chile [35]. But similar forms have also been observed at very low altitudes such as Greenland [36]. Given the climatic conditions that favour their formation, *penitentes* are generally found in regions where humidity and temperature are low, on downslopes where the wind is very weak but sunshine is intense. As a result, similar patterns on the icy surfaces of other Solar System bodies have been interpreted as *penitentes*, such as the Bladed Terrain Deposit of Pluto's *Tartarus Dorsa* region [8,37]. It has been suggested that *penitentes* as high as 15 m may exist on Europa's surface [38], although the resolution of currently available images of Europa's surface is insufficient to verify this, but this hypothesis is debated

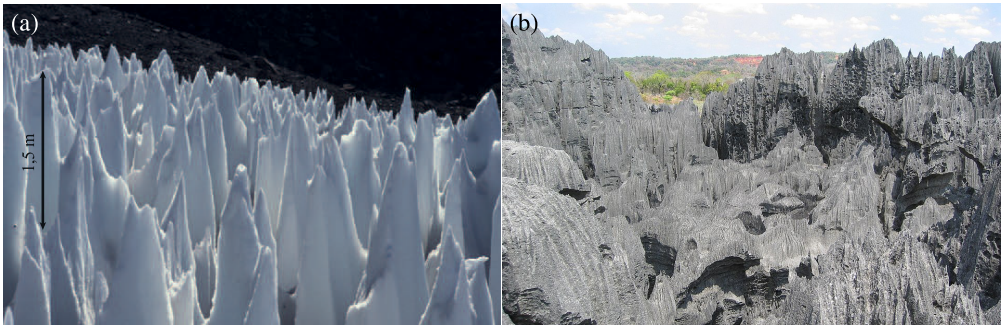


Figure 1. *Penitentes* and *Tsingy*. (a) *Penitentes* (Rio Blanco, Central Andes of Argentina). Crédits: P. Dubuc, Arvaki, CC BY-SA 3.0 license. (b) *Tsingy* of Bemaraha [47,48]. Credits: A. S. Maloney, CC BY-SA 3.0 license.

because of the low atmospheric pressure on Europa [39,40]. From base to tip, these spikes can reach heights of a few centimetres [39] to several metres [41], depending on environmental conditions. The cross-section of the *penitentes* is rather lenticular, tapering towards the pointed summit, and their blades are parallel to the sunlight at midday. The horizontal spacing is of the same order of magnitude as the height of the tips [42]. The orientation of the *penitentes* in terms of azimuth is linked to the local geometry of the insulation [43]. In particular, Matthes et al. [44] observes an inclination of the *penitentes* following the elevation of the midday sun. For geometric reasons, sublimation is more effective in hollows. Illumination plays a key role [45], as do heat transport in the ice and the transport of vapor from the ice [46]. The bedforms detected on the surface of icy substrates, even if their formation is induced by sublimation, can be interpreted in different ways. Knowledge of the mechanism of formation of the different sublimation induced shapes can help to classify solid bedforms between *penitentes* and other bedforms, such as scallops (Figure 2(a)) or transverse linear waves (Figure 3(a)).

Pointed shapes can also be found in the dissolution of rocks, in karst. In that case, the limestone substrate is rigid and not very porous. One of the most intriguing sharp-edged landscapes formed by rock dissolution are limestone forests, found at tropical locations such as in the western part of Madagascar in the area called *Tsingy* [47,52], in Malaysia [53] or in south China [54]. Spectacular sharp and vertical pinnacles, tens of meters high, rise from the surface of a horizontal *Karst* plateau (Figure 1(b)). The general shape is needle-shaped, with a slope of 15° to 20°, which remains even when the material has been strongly dissolved. These sharp-edged *karren* forms, which develop in groups, have several degrees of evolution: from dragon teeth to sharp-edged pinnacles before evolving to *Tsingy* [55]. The smallest in size belong to the *lappies*' family (2–3 m) and the largest, by one order of magnitude, belong to the *mega-lappies*' family (20–30 m). On their slopes, centimeter scale *rillenkarren* (see Section 2.4) can be observed. Because the material is pure and not porous, dissolution remains on the surface, not in the bulk. Formation of the limestone forests appears to be complex, but is believed to be caused by a dissolution process under the run-off caused by tropical heavy rain. The rainfalls channelized by large scale fractures are collected into an underground cave network. Subjected to run-off flow, soluble rock are less dissolved as it flows along the slope, such as the layer gain in concentration. This could preserve the homothetic character of these forms (recession of these faces parallel to itself). If the material is porous, such as dolomite, then the shape is not sharp-edged, but resembles a mushroom. In very seldom locations, in very arid area like the Atacama desert in Chile or the banks of the Dead Sea in Israel, salt pinnacles of few ten centimeters can be observed on salt deposit [56].

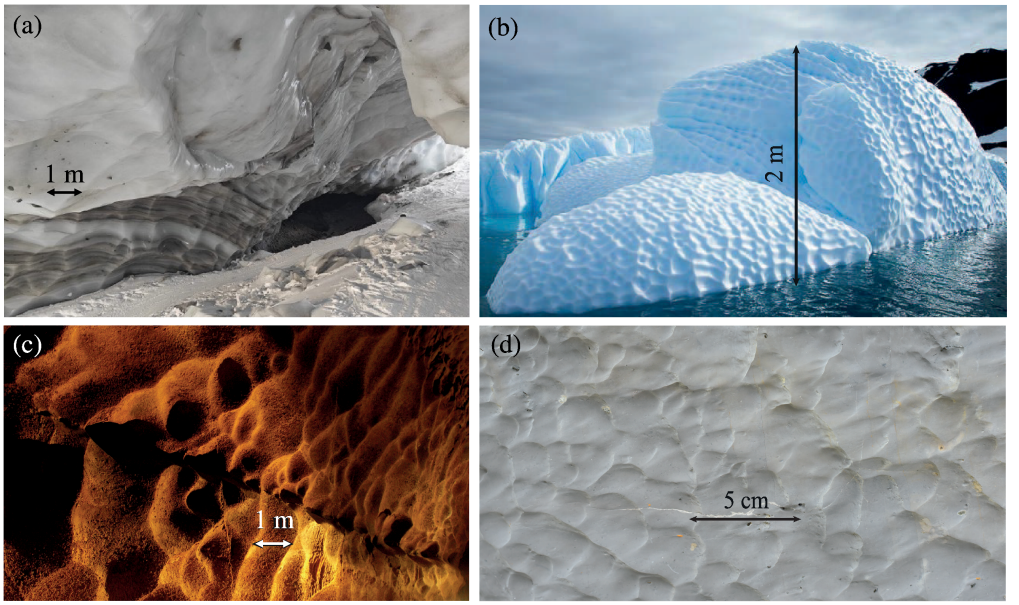


Figure 2. Scallops on different substrates. (a) Icy scallops formed by sublimation (French Alps). Credits: A. Mounier. (b) Icy scallops formed by melting on an overturned iceberg (Paulet Island, Antarctique). Credits: P. Colla. (c) Limestone scallops formed by dissolution (Grotte de Saint-Marcel d'Ardèche, France). Credits: M. Bordiec/S. Carpy/O. Bourgeois, reprinted with permission from [49]. (d) Limestone scallops by dissolution (Moulin de Vogüé, France). Credits: M. Bordiec/S. Carpy/O. Bourgeois, reprinted with permission from [49].

2.2. *Polygonal depression*

Suncups and ablation hollows are bowl-shaped, circular or oval in plan, and parabolic or tapered in vertical section, and occur on ice and snow. In comparison to *penitentes* on Earth, they are located at lower altitudes, where the ambient temperature is generally higher (e.g. in the Alps [45]), and in areas more exposed to winds than those where *penitentes* develop. With amplitudes ranging from a few centimetres to half a metre, they do not reach heights comparable to those of the *penitentes*, although they are also controlled by solar radiation and influenced by albedo and the amount of dust in the ice/snow [45,57]; the role of wind is not clearly excluded. Suncups could constitute a surface texture found particularly on the North Polar Cap of Mars [9,58–61] and on the Sputnik plain of Pluto [62]. Similar shapes appear on the walls of ice caves [63–65] and are known as "scallops". Ice caves, although they represent only a tiny fraction of the Earth's cryosphere, exist on every continent outside the tropics and are defined as rock caves containing ice, in seasonal or perennial form [12]. Conceptual models of the climate prevailing in these ice caves have been built from measurement campaigns conducted over several decades [66], in particular in the *Eisriesenwelt* cave (Salzburg, Austria) [65], which is one of the largest known ice caves in the world, with its more than 40 km of galleries. In winter, the temperature of this cave is below 0 °C and the air is dry [32], which favors episodes of sublimation, enhanced by cold, dry air that is blown and circulates through the cave, at speeds not exceeding 0.2 $m{\cdot}s^{-1}$ [63,65,67]. In most ice caves, the temperature of the ice surface remains relatively stable throughout the year, with varying rates of sublimation depending on the geometry of the cave. For example, although ablation is restricted to the winter months when sublimation is most

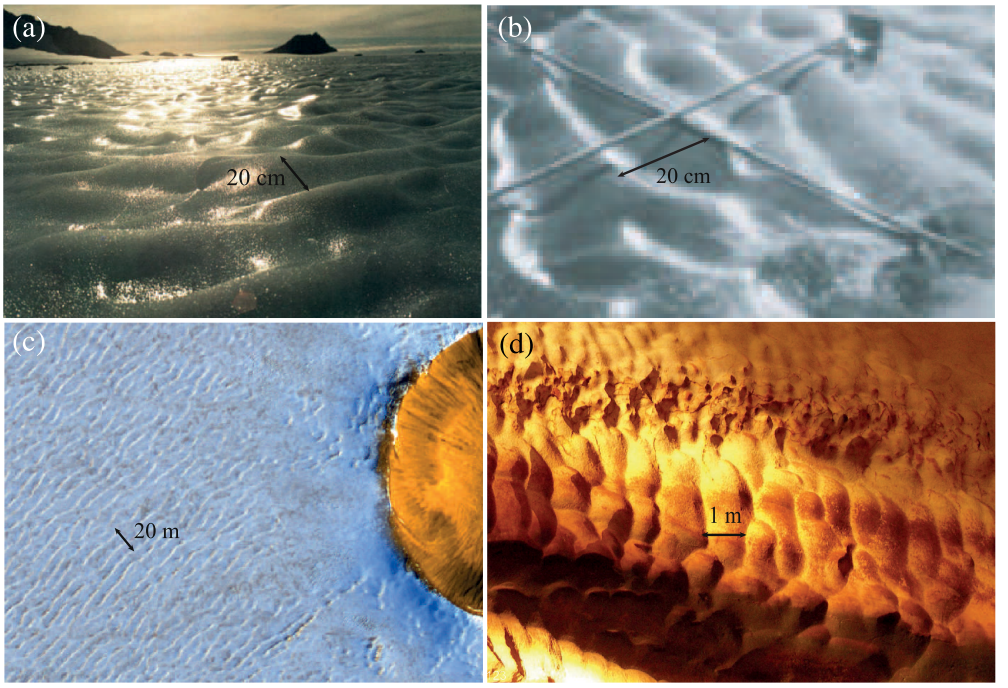


Figure 3. Ripple-like bedforms over different substrates submitted to mass transfer: (a) by sublimation (blue ice ripples in *Svea*, Antarctica adapeted from [50]. Copyright 1999 by the American Geophysical Union). (b) By melting, Rivière St-Croix ice ripples, Wisconsin, USA [51]. (c) By sublimation, martian North polar Cap, reprinted with permission from [49]. *HiRISE* PSP_009689_2645. (d) By dissolution, *Coups de Gouge*, Grotte de Saint-Marcel d'Ardèche, France. Credits: M. Bordiec/S. Carpy/O. Bourgeois, reprinted with permission from [49].

effective, the annual ablation rate in ice caves ranges from 3 mm·year^{-1} [68] to 35 mm·year^{-1} [64], resulting in sublimation rates of between 3.8×10^{-10} m·s^{-1} and 4.5×10^{-9} m·s^{-1}.

Scallops are widespread polygonal depression patterns, both on ice [63,64] (Figure 2(a–b)) and on soluble rock walls [12,55] (Figure 2(c–d)), and on many other substrates [6]. By analogy, Meakin and Jamtveit [69] suggest that these shapes can be likened to those observed on certain meteorites [5], on corroding metal pipe surfaces [70] and cohesive surfaces in fluvial systems [71]. The characteristic sizes of scallops range from centimetres to metres. They are shell-shaped, ablation-induced depressions. When they cover a surface, they exhibit uniformity in terms of size, shape and spacing (Figure 2). They are formed when solid surfaces are immersed in a fluid different from their composition when subjected to mass transfer induced ablation. The scallops are asymmetrical compared to suncups, which are circular depressions. They are oriented with respect to the flow: the downstream side forms a sharp shape and the upstream side is steeper in longitudinal section (Figure 2(d)). Similarly, scallops have sometimes been assimilated to shapes transverse to the flow direction [6,22], although they differ from ripples and flutes, which are transverse waves (Figure 3), which are considered to be special cases of scallops [20] (see Section 2.3). Due to the complexity of flows and possible variations in the conditions that lead to the formation of these solid bedforms, the understanding of their development is not completely acquired [69].

2.3. *Crested patterns perpendicular to the flow direction*

Transverse linear waves (Figure 3) form and develop on the surface of icy substrates (by sublimation or melting) or soluble rocks (by dissolution), and they are known as "sublimation waves", "ices ripples", "fluted scallops", "flutes" or "solution ripples" in karstology. Their crests are regularly spaced and parallel, oriented perpendicular to the flow [12,55]. The waves are likely to migrate in the direction of flow over time. Their cross-sectional profile in relation to the direction of flow is slightly asymmetrical (Figure 3(b)), with a downstream slope greater than the upstream slope [20,72]. They exist on all types of solid substrates, such as salt [73] and ice, immersed in liquid water [23,31], in ice caves [67] or on Antarctic ice surfaces exposed to strong winds [74]. If dissolution forms are naturally very common in limestone caves [19,67,71] with a range of wavelengths from a few centimetres to several metres (Figure 3(d)), measurements of the flow characteristics responsible for their formation are rare in these natural environments. Sublimation waves (Figure 3(a)) are periodic, linear and transverse bedforms of different scales (from centimetres to metres) depending on their dry windy environment [74,75]. On Earth, Blue Ice Areas that cover 1% of Antarctica reveal the presence of sublimation ice ripples [4], about 10 cm in wavelength that emerge in ~2 month and migrate at 2 cm/month. The difficulties of field campaigns in such remote places with uncontrolled environmental conditions explain the very few field measurements collected on sublimation waves. The compilation of documented natural examples of sublimation waves has revealed a real lack of morphological and kinetic data related to the development of these solid bedforms [32]. Shapes on the North Polar Cap of Mars (Figure 3(c)) and certain shapes on the surface of Pluto (plain *Sputnik Planitia*) can also be interpreted as sublimation waves [11].

2.4. *Crested patterns parallel to the flow direction*

The term *Karren* designates the dissolution patterns, which are created by the run-off flows on denuded rock walls [12,55,76]. We focus here on the patterns, which are caused by the flows of water driven by gravity along the bare slope and originated from rain and snow falls. Some effects of seepage are possible for slightly porous and fractured rocks and can affect the morphologies. The *Karren* patterns occur mainly by dissolution of limestone and dolomite, but they can also appear on gypsum and salt (Halite) [56]. In view of the wide variety of shapes and front, a specific terminology has been defined to classify the different types [76]. Among the most important examples, *Rillenkarren* are adjacent grooves or small channels directed along the main slope [76,77] (Figure 4(a–d)). In cross-section, their profiles are parabolic, separated by sharp ridge lines. Viewed from above, these lines are remarkably parallel and spatially regular, typically 1.5 to 2.5 cm wide and 2 to 6 mm deep in limestone. However, the typical size can be significantly larger than the centimeter, like for the *Rillenkarren* found on Madre de Dios Island in Chile (Figure 4(c)). In the field, the flow creating these patterns is a thin film of water that runs down the slope. The run-off flow is fed by the impact of droplets and the role of the droplet impact remains an open question [15]. Moreover, *Rillenkarren* grooves are preferentially observed on the sloped wall (typically 45°) above a smooth area, where the water film is thicker [15]. The *Wandkarren* are a special case of the *Rillenkarren* and occurs on nearly vertical walls created by large rock fractures. The *Rinnenkarren* or Runnels are dissolution channels of larger size, which are formed once the water has been channelized in a rivulet. *Rundkarren* are similar to *Rinnenkarren*, but the ridges between the channels are rounded by subsoil dissolution [76] or maybe by snow cover. *Meanderkarren* are *Rinnenkarren* with meanders. The flow dynamics of water channelized in *Rinnenkarren* systems have been studied on the field and in laboratory reproduction with non soluble materials [47].

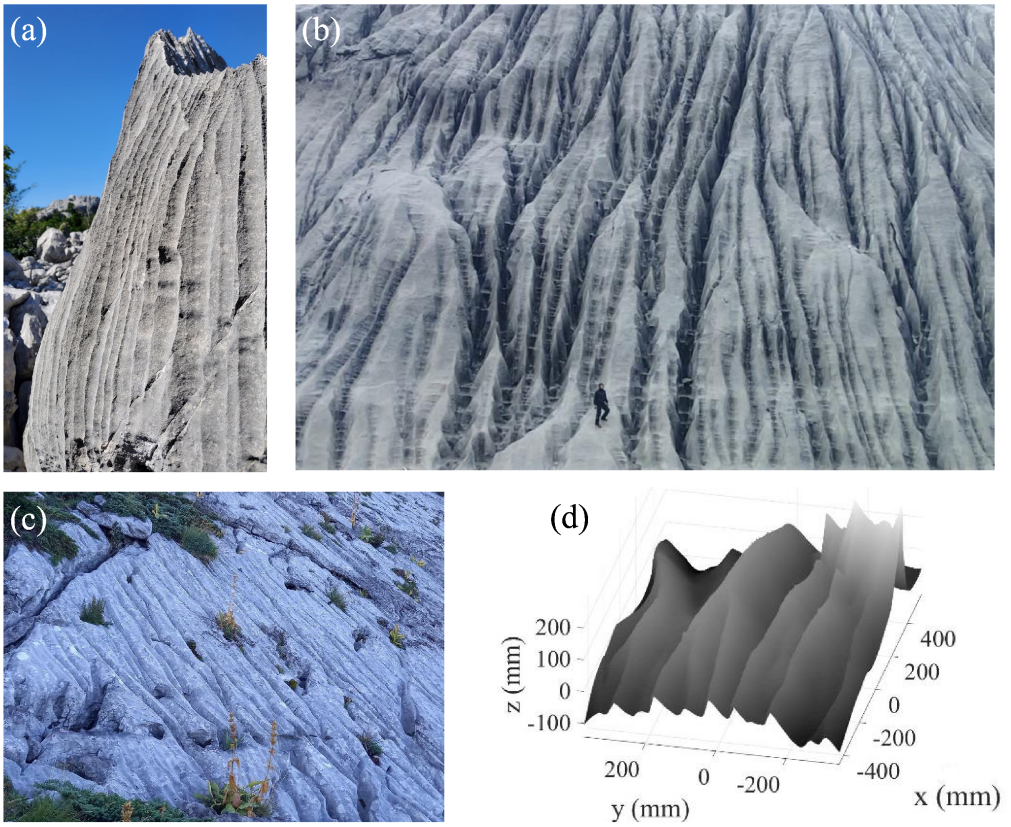


Figure 4. (a) Nearly vertical *Rillenkarren* on limestone. The photo was taken in Velebit (Croatia). The typical groove width is about 1 cm. Credits S. Courrech du Pont. (b) *Rillenkarren* of the order of one meter on Madre de Dios Island in Chile, Ultima Patagonia expedition, *Centre Terre*. Note the human at the bottom of the picture, to get an idea of the characteristic scale. From Tourte et al. [78]. (c) Inclined limestone pavement or *Lapiaz* at the site *Combe Oursière* near Lans en Vercors, France. Rounded *Rillenkarren* are directed along the main slope of about 45° inclination. Credits M. Berhanu, M. Chaigne and J. Derr. (d) 3D reconstruction of *Rillenkarren* on the previous field site at small scale using a structured light scanner. The slope is aligned along the x axis. Sharp ridges can be seen.

2.5. *Stepped bedforms*

Cyclic steps are bedforms that are shaped like a succession of steps, moving against the flow [79]. These steps are associated with hydraulic jumps at the free surface. Cyclic steps occur at the bottom of *bedières* (Figure 5(a)). They have been studied experimentally on sloping ice over which liquid water flows [24]. Cyclic steps have also been described on solid rock substrates over which rivers flow [80]. In the case of sublimation, the spirals of the North Cap of Mars have been interpreted as cyclic steps of several kilometers in wavelength, influenced by jumps of katabatic origin [7].

There are also stepped, regular undulations known as *trittkarrens*, *stepkarrens* or *heelprint karrens* (Figure 5(b)), which are observed in dissolving rocks with a gentle slope. They are perpendicular to the sharp ridge lines of the *rillenkarrens* described in Section 2.4 and therefore

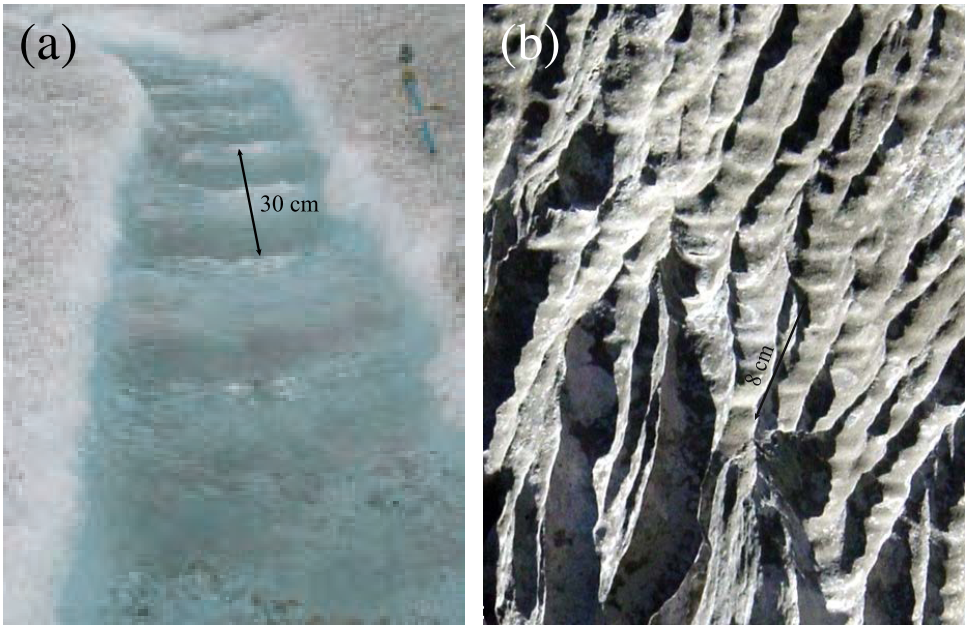


Figure 5. (a) Cyclic steps by melting in *Bédières*. Crédit: L. Karlstrom, adpated from [80] with permission of John Wiley and Sons. (b) *Trittkarrens* steps perpendicular to the crests of *Rillenkarrens*. Crédit: L. Perrella, CC BY-SA 3.0 license.

perpendicular to the flow. They are small-scale *karrens* (on the order of centimetres) that can form on various dissolving rocks, such as limestone and gypsum [81]. Morphologically, they are described by Ford & Williams [12] as arched-front forms with a flat floor, 10 to 30 cm in diameter, which are open at the end of the downslope. Mottershead [81] characterizes them more by their "stepped shape" in cross-section and the presence of a slight gradient.

2.6. *Debris-covered ice structures*

Natural pattern can also form because an object changes boundary conditions. Rock or debris covering the ice can insulate the underlying ice or increase the melting rate. The resulting differential melting forms characteristic structures observed on glaciers such as glacier tables, dirt cones or ice sails as shown in Figure 6 [82–86]. Glacier tables are large rocks standing on an ice foot (Figure 6 top), dirt cones are ice cones covered by a layer of debris (Figure 6 bottom left), and ice sails (or ice pyramids) are clean ice structures protruding from the debris-covered surface (Figure 6 bottom right).

Many glaciers are covered by a layer of debris, which modifies the melting rate of the ice. Several field measurements have shown that the melting rates initially increases with the thickness of debris cover, reaches a maximum for a thickness of about 2 cm, and then decreases with debris thickness [87–89]. Debris insulate the underlying ice, which explains the decrease in melting rate with the thickness of debris. The initial increase with thickness is ascribed to the patchiness of the debris coverage, which gradually changes the albedo of the surface as the coverage proportion increases and to a wind-shielding effect of the cover; the wind velocity at the ice/debris interface rapidly decreases with debris thickness [89]. This decrease in wind velocity reduces the rate of evaporation of the melt water and the consumption of energy in latent heat (for evaporation), which increases the energy available for melting [89].

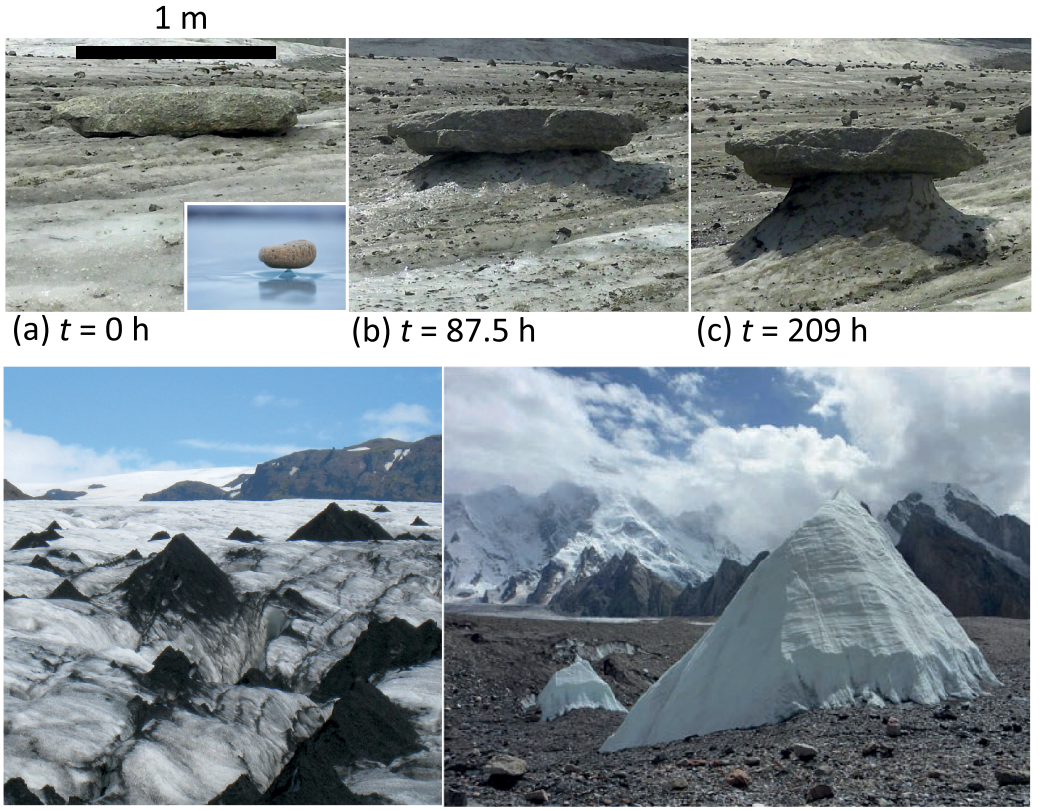


Figure 6. Melting and sublimation structures due to debris or rock cover. Top: Glacier table (rock supported by a pillar of ice) forming on the *Mer de Glace* glacier in the French Alps from Hénot et al. [85]. Inset: Zen stone (stone supported by a pillar of ice) on Lake Baikal, southern Siberia. Credits: Olga Zima. Glacier tables and zen stones form at different scales and by slightly different mechanisms (Section 4.3), figure adapted under the CC BY 4.0 license. Bottom left: Dirt cones (ice cones covered by a layer of grains) on Sólheimajökull Glacier, Iceland. Credits: Patagonier, CC BY-SA 3.0 license. Bottom right: Ice Sails on the Baltoro Glacier (Karakoram mountain range, Pakistan), from Evatt et al., 2017 [82]. Credits: C. Mayer, 2011, under the CC BY 4.0 license.

3. Modelization of phase change dynamics in presence of a flow

The natural bedforms reviewed in Section 2 emerge when there are heterogeneities in the ablation velocity of a bed, which can result from a coupling between the rate of phase change (dissolution, sublimation or melting) and a flow. Here we introduce the equations that allow to model these processes occurring at the solid/fluid interface. Solidification, condensation and precipitation are not discussed in this review, but in some natural examples deposition and ablation effects may be intertwined [69]. The set of equations which will be found for melting, sublimation or dissolution will also be valid for solidification, condensation or precipitation.

During a phase change of a solid, the chemical bonds between the particles constituting the solid are broken to form a liquid phase or gaseous phase depending on the thermodynamic

conditions, usually the temperature and the pressure. A phase is a region of material in which the chemical and physical properties are locally homogeneous at the molecular scale. Thermodynamics determines the equilibrium state, with the occurrence of one or another specific phase, or even the coexistence of several phases. The dynamics of the phase transition, the rate of phase change from one phase to another, is an out of thermodynamic equilibrium phenomenon.

In some cases, the dynamics is set by kinetic effects at the molecular scale associated to chemical bonds breaking and formation. However, when these processes are "fast", the limiting mechanism that determines the dynamics of the phase change is a transport mechanism that either transfers the energy necessary for the phase change, or removes chemical species to maintain the interface in a non-equilibrium state, or even a combination of both phenomena. For example, the melting of ice in salty (NaCl) water could be limited either by the heat transport or by the salt transport to the ice through the melt water, because the melting temperature depends on the salt concentration. In the absence of flow, these transfers occur by thermal diffusion or by chemical species diffusion. In the presence of a flow in the fluid phase, they are generally greatly enhanced by advection phenomena. The modeling of phase change dynamics can be thus often described as an advection–diffusion problem in the fluid phase, where the rate of phase change is expressed as a boundary condition.

3.1. *Boundary conditions at an evolving interface*

We consider the phase transition between a solid and a fluid phase, liquid or gas. For simplicity, we focus on the melting of a pure substance, the dissolution of a homogeneous solid in a fluid phase composed of a solvent and a solute and the sublimation of a solid in a gaseous phase containing a small proportion of the vapor generated by the phase change. In the second case, the solute molecules are produced by the dissolution of the solid and in the third cases, the vapor molecules are produced by the sublimation of the solid. These two cases are formally equivalent. Dissolution patterns can therefore have analogous counterparts for sublimation.

3.1.1. *Kinetics of the phase change*

At the solid/fluid interface, the rate of detachment of the molecules and atoms constituting the solid is modeled by the chemical kinetics of phase change. In a first approximation, this rate can be taken to be proportional to the distance to thermodynamic equilibrium [90,91].

Melting. For the melting/solidification, except for the rapid phase change of metastable materials such as supercooled water, the kinetic molecular effects are usually negligible [92]. In this case, the solid/interface can be considered locally at the thermodynamic equilibrium. This means that the pressure and the temperature at the interface belong to the coexistence curve for two phases at thermodynamic equilibrium. If the pressure is imposed externally, then the temperature is the corresponding melting temperature T_{m}, which can be determined by the Clapeyron relation [93]. For example, when ice melts at atmospheric pressure on Earth, the melting temperature during the phase change is equal to 0 °C. The melting temperature also decreases with the local curvature of the interface due to Gibbs–Thomson effect [90], as the local environment differs when a molecule on the solid is located at a tip. This effect, which is important for crystal growth, is often negligible for melting at macroscopic scales. Under these conditions, the melting rate is determined by the thermal energy input (see Section 3.1.3).

Dissolution. In contrast, in the case of dissolution, kinetic effects are often considered relevant [91]. We consider the case of a pure solid in contact with a liquid phase constituted of a solvent and a solute, whose molecules or ions are the same as those in the solid phase. The

proportion of solute particles in the solution is quantified by the mass solute concentration field $c(\mathbf{x}, t)$, i.e. the local mass of solute per unit volume. This case corresponds for example to the dissolution of solid salt (NaCl, halite crystal), which decomposes into the ions sodium Na^+ and chloride Cl^- in water. Due to electroneutrality, the concentrations of positive and negative ions are equal at the macroscopic scale and the solute concentration is numerically equal to the sum of the concentrations of positive and negative ions. For example the mass solute concentration of NaCl: the mass of solute per unit volume is equal to the mass concentration of ions Na^+ plus the mass concentration of ions Cl^-. The saturation concentration c_{sat} is the solute concentration when the solid and the liquid phases are at thermodynamic equilibrium. The attachment and detachment rates of ions are then equal. As a thermodynamic parameter, c_{sat} depends on the temperature, the pressure, the presence of other chemical species and also on the local curvature by a phenomenon analogous to the Gibbs–Thomson effect [94]. This last effect is relevant for scales below the micron and is neglected in the remainder. For small concentrations, the chemical activities can be assimilated to concentrations.

Sublimation. In the case of sublimation of a solid (e.g. water ice), the concentration of the volatile substance (e.g. water vapor), is usually expressed in terms of the partial vapor pressure. According to the ideal gas law, which holds for diluted gases, the partial pressure is proportional to the mass concentration, i.e. $p_x = c_x RT/M_x$, where M_x is the molar mass of the specie x and R is the universal gas constant. Similarly, when the interface between the atmosphere and the sublimating solid is at thermodynamic equilibrium, the partial pressure is equal to the saturation vapor pressure p_{sat}. This quantity can vary strongly as a function of the temperature according to the Clapeyron relation [93].

3.1.2. *Relationship between phase change rate and kinetic effects*

Dissolution and sublimation rates can be related to the rate of the chemical reaction $\mathscr{R}$, which corresponds to the breaking of the chemical bonds in the solid phase. We define $\mathscr{R}$ as the solute mass flux for dissolution or the vapor mass flux for sublimation. $\mathscr{R}$ is homogeneous to a mass per time and surface unit. The simplest models for dissolution/sublimation processes assume that $\mathscr{R}$ is proportional to the distance to equilibrium expressed in terms of concentrations, $c_{\text{i}} - c_{\text{sat}}$, where c_{i} is the solute or vapor concentration at the solid interface. We call α, the proportionality coefficient, which expresses the speed of the chemical reaction. This linear relationship can be justified by more rigorous considerations of chemical kinetics [95] or gas kinetics [96–98].

If $c_{\text{i}} < c_{\text{sat}}$, the solid recedes by dissolution (sublimation) and vice versa if $c_{\text{i}} > c_{\text{sat}}$, the solid grows by precipitation (condensation). Writing the conservation of solute mass, the mass flux $\mathscr{R}$ is also equal to the product of the density (mass per unit volume) and the velocity of the interface. The following equation then relates the velocity of the interface, i.e. the rate of phase change, to the speed of chemical reaction in the laboratory reference frame for a motionless solid phase, at a point of the interface:

$$\mathscr{R}(\mathbf{x}, t) = \alpha(c_{\text{sat}} - c_{\text{i}}) = -\rho_{\text{s}}\, \mathbf{v}_{\text{i}}(\mathbf{x}, t) \cdot \mathbf{n}, \tag{1}$$

where ρ_{s} is the solid density and $\mathbf{v}_{\text{i}}$ is the interface velocity (or dissolution/sublimation velocity) and $\mathbf{n}$ is the vector normal to the interface pointing outwards the solid surface.

To summarize, the mass flux for the two ablation processes, sublimation and dissolution, actually share a common formulation, in the sense that the existence of the transfer and the direction in which it takes place are conditioned by a concentration, either in the atmosphere or in the solution. For dissolution and sublimation, α is a positive coefficient expressing the speed of the chemical reaction and is homogeneous to a velocity. α qualitatively translates the finite time required to break and create chemical bonds in the dissolution and sublimation processes. The

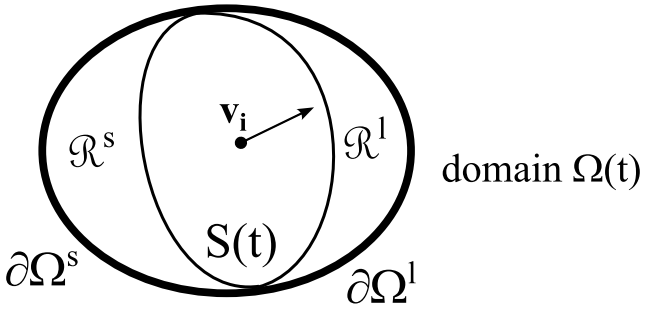


Figure 7. Scheme for determining the jump conditions at the evolving interface $S(t)$ separating two phases, for example a solid $\mathscr{R}^s$ and a liquid $\mathscr{R}^l$. We consider an infinitesimal spatial domain $\Omega(t)$ on either side of the interface $S(t)$. $\mathbf{v}_i$ is the velocity field of displacement of the interface. The outer boundary of the domain is denoted by $\partial\Omega(t)$, which is composed of $\partial\Omega^s$ and $\partial\Omega^l$ for the part in contact with $\mathscr{R}^s$ and $\mathscr{R}^l$, respectively.

interface velocity can vary along the solid surface and its heterogeneity causes pattern formation. For sublimation, using the theory of gas kinetics, the coefficient α for vacuum or very tenuous atmospheres is the product of a thermal velocity of the gas molecules times a dimensionless adsorption coefficient ε on the surface [96–98]:

$$\alpha = \varepsilon\sqrt{\frac{RT_s}{2\pi M_s}}. \tag{2}$$

α is thus a function of the surface temperature of the solid T_s and depends on the molar mass of sublimated molecules M_s.

3.1.3. *Moving interface*

In Equation (1), the concentration at the interface, c_i, must be determined to solve the dissolution or sublimation problems. Therefore, to determine the phase change rate $\mathbf{v}_i$, in addition to these kinetic considerations, it is necessary to take into account the balance equations through the continuity equation, the solute (or vapor) mass equation and the energy equation, in the presence of a moving interface. In melting problems, kinetic effects are usually negligible, so the interface temperature is the melting temperature T_m given by the thermodynamics, and the melting rates are in most cases determined by the balance equations.

The Kotchine's theorem or jump relations [92,99] provides an elegant method to derive the conservation relations in three dimensions. We consider a quantity $f(\mathbf{x}, t)$ obeying to a local conservation equation with no source or sink term

$$\frac{\partial f(\mathbf{x}, t)}{\partial t} + \nabla \cdot (\mathbf{J_f}(\mathbf{x}, t)) = 0, \tag{3}$$

where $\mathbf{J_f}(\mathbf{x}, t)$ is the incoming flux of the scalar quantity f, which can be mass, concentration or temperature and $\nabla \cdot (s)$ is the divergence operator. By applying the Reynolds transport theorem for the quantity $f(\mathbf{x}, t)$ to the infinitesimal domain $\Omega(t)$ shown in Figure 7, where the two phases considered are the solid (s) and the liquid (l), the Kotchine's theorem gives:

$$(f^l - f^s)(\mathbf{v}_i \cdot \mathbf{n}) = (\mathbf{J}^l - \mathbf{J}^s) \cdot \mathbf{n}. \tag{4}$$

This relation gives the boundary condition that relates the interface velocity $\mathbf{v}_i$ to the quantities on each side of the interface: f^l and f^s, and the flux of f, i.e. $\mathbf{J}^l$ and $\mathbf{J}^s$, where $\mathbf{n}$ is the vector normal to the interface pointing outwards the solid surface. This theorem can be applied to any physical quantity following a local conservation Equation (3).

Mass balance. The mass flux corresponds to an advection term $\mathbf{J_f}(\mathbf{x}, t) = \rho\mathbf{u}$ of the density field $f(\mathbf{x}, t) = \rho$ by the velocity field $\mathbf{u}$. Substituting this into the Equation (3) gives the conservation of mass, in three dimensions:

$$\frac{\partial \rho}{\partial t} + \nabla \cdot (\rho \mathbf{u}) = 0. \tag{5}$$

Considering an evolving interface $S(t)$ of local velocity $\mathbf{v}_\mathrm{i}$ between a liquid phase and a solid phase (subscripts l and s, respectively), Figure 7, the jump relation, Equation (4) gives:

$$(\rho_\mathrm{i} - \rho_\mathrm{s})(\mathbf{v}_\mathrm{i} \cdot \mathbf{n}) = (\rho_\mathrm{i}\mathbf{u}_\mathrm{i} \cdot \mathbf{n} - \rho_\mathrm{s}\mathbf{u}_\mathrm{s} \cdot \mathbf{n}) \tag{6}$$

$\mathbf{u}_\mathrm{i}$ and ρ_i are the velocity and the density in the liquid phase at the position of the interface. $\mathbf{u}_\mathrm{s}$ is the velocity in the solid phase, which is zero (no advection in the solid) and ρ_s is the density of the solid, supposed homogeneous.

By generalizing to any type of fluid, this jump relation determines the normal fluid velocity at the evolving interface:

$$\mathbf{u}_\mathrm{i} \cdot \mathbf{n} = (\mathbf{v}_\mathrm{i} \cdot \mathbf{n}) \left(1 - \frac{\rho_\mathrm{s}}{\rho_\mathrm{i}}\right). \tag{7}$$

This condition for the normal velocity in the fluid translates the non penetration of the liquid phase in the solid. It must be completed by an expression for the velocity tangential to the interface in the liquid. Here, the tangential velocity of the fluid is zero at the dissolving boundary, as usual for a viscous fluid in contact with a solid wall, which reads $\mathbf{u} \wedge \mathbf{n} = \mathbf{0}$.

Balance of solute or vapor concentration. The local conservation relation (Equation (3)) applied to the mass solute concentration $c(\mathbf{x}, t)$ reads:

$$\frac{\partial c}{\partial t} + \nabla \cdot (\mathbf{J_c}) = 0 \quad \text{with } \mathbf{J_c} = c\mathbf{u} - D\nabla c, \tag{8}$$

where ∇ is the gradient operator. As an example of the incoming flux $\mathbf{J_c}$, we consider a volume element including the solid/liquid interface (see Figure 7) in dissolution. The chemical species can be transported by advection and diffusion. According to the Fick's law, the diffusive flux is proportional to the solute gradient: $\mathbf{J_c} = -D\nabla c$, where D is the solute diffusion coefficient. Applied to an incompressible flow and homogeneous diffusion coefficient, this equation identifies with the classical advection–diffusion equation for the concentration (solute or vapor):

$$\frac{\partial c}{\partial t} + \mathbf{u} \cdot \nabla c = D\nabla^2 c. \tag{9}$$

When considering a pure solid phase (i.e., concentration and density in the solid are equal) of the same chemical specie as the solute, specifying the fluxes in Equation (4) for the concentration gives:

$$(c_\mathrm{i} - \rho_\mathrm{s})(\mathbf{v}_\mathrm{i} \cdot \mathbf{n}) = c_\mathrm{i}\mathbf{u}_\mathrm{i} \cdot \mathbf{n} - D\nabla c|_\mathrm{i} \cdot \mathbf{n} - \rho_\mathrm{s}\mathbf{u}_\mathrm{s} \cdot \mathbf{n}. \tag{10}$$

The diffusive flux $-D\nabla c|_\mathrm{i}$ at the solid interface depends on the concentration gradient at the interface in the fluid. After simplification by assuming that the solid phase is immobile ($\mathbf{u}_\mathrm{s} = \mathbf{0}$), one finds:

$$\rho_\mathrm{s}\mathbf{v}_\mathrm{i} \cdot \mathbf{n} = c_\mathrm{i}(\mathbf{v}_\mathrm{i} \cdot \mathbf{n} - \mathbf{u}_\mathrm{i} \cdot \mathbf{n}) + D(\nabla c|_\mathrm{i} \cdot \mathbf{n}). \tag{11}$$

Substituting the value of $\mathbf{u}_\mathrm{i} \cdot \mathbf{n}$ from Equation (7) into this expression gives a general boundary condition for the interface velocity $\mathbf{v}_\mathrm{i}$:

$$(\mathbf{v}_\mathrm{i} \cdot \mathbf{n})\rho_\mathrm{s} \left(1 - \frac{c_\mathrm{i}}{\rho_\mathrm{i}}\right) = D(\nabla c|_\mathrm{i} \cdot \mathbf{n}). \tag{12}$$

Moreover, the interface velocity is also related to the mass solute flux $\mathscr{R}$ given by Equation (1).

Heat balance. Finally, we express the conservation of energy. Similarly, the spatial variation of the temperature in the solid and fluid phases leads to thermal diffusion according to the Fourier's law. The heat flux due to conduction is equal to $-\lambda\nabla T$, where T is the temperature field and λ is the thermal conductivity (different for solid and liquid phases). The enthalpy h per unit mass is $h = (1/2)\,\mathbf{u}^2 + c_\mathrm{p}\,T$ where c_p is the specific heat capacity at constant pressure (different for each phases) and T is the temperature. In absence of source term, negligible fluid dissipation and for an incompressible flow, the heat balance is [100]:

$$\frac{\partial(\rho c_\mathrm{p} T)}{\partial t} + \nabla\cdot(\rho c_\mathrm{p} T\mathbf{u}) = \nabla\cdot(\lambda\nabla T), \tag{13}$$

where λ is the thermal conductivity. The heat transport by diffusion is modeled using the Fourier law, $\mathbf{J_T} = -\lambda\nabla T$, where $\mathbf{J_T}$ is the heat flux. It has the dimension of a power per surface unit. If the properties of the fluid (ρ, c_p and λ) are homogeneous, this last equation resumes to the classic advection–diffusion equation for the temperature field:

$$\frac{\partial T}{\partial t} + \mathbf{u}\cdot\nabla T = \kappa\nabla^2 T, \tag{14}$$

where $\kappa = \lambda/(\rho c_\mathrm{p})$ is the thermal diffusivity.

In general, a phase change reaction leads to an energy variation due to the breaking of molecular bonds. If a mass m_x has experienced a phase change from a phase 1 to 2 at constant temperature and pressure, the difference of enthalpy reads: $\Delta H = m_x h_\mathrm{r}$, where h_r is the reaction enthalpy per mass unit. For condensed phases (liquid or solid), the reaction enthalpy reads as a function of the heat capacity per unit mass c_p:

$$h_\mathrm{r} = c_{\mathrm{p},2}\,T_\mathrm{i} - c_{\mathrm{p},1}\,T_\mathrm{i}, \tag{15}$$

where T_i is the interface temperature. For the melting of a pure substance at constant temperature, T_i and h_r identify to the melting temperature T_m and to the latent heat L_m. The melting is an endothermic process and L_m is always positive, as well as in sublimation. In contrast the reaction enthalpy for dissolution can be positive (e.g. salt NaCl or sucrose) or negative (e.g. like caustic soda NaOH) [101].

Applying Kotchine's theorem to energy conservation (Equation (13)) gives:

$$[\rho_\mathrm{i} c_{\mathrm{p,l}} T_\mathrm{i} - \rho_\mathrm{s} c_{\mathrm{p,s}} T_\mathrm{m}]\mathbf{v}_\mathrm{i}\cdot\mathbf{n} = [\rho_\mathrm{l} c_{\mathrm{p,l}} T_\mathrm{i}\mathbf{u}_\mathrm{i} - \lambda_\mathrm{l}\nabla T|_{\mathrm{l,i}} + \lambda_\mathrm{s}\nabla T|_{\mathrm{s,i}}]\cdot\mathbf{n}. \tag{16}$$

where subscript l and s, stand for liquid and solid phase, respectively. Using Equation (7) for the expression of $\mathbf{u}_\mathrm{i}\cdot\mathbf{n}$ gives:

$$\left[\rho_\mathrm{i} c_{\mathrm{p,l}} T_\mathrm{m}\left[1 - \left(1 - \frac{\rho_\mathrm{s}}{\rho_\mathrm{i}}\right)\right] - \rho_\mathrm{s} c_{\mathrm{p,s}} T_\mathrm{i}\right]\mathbf{v}_\mathrm{i}\cdot\mathbf{n} = [-\lambda_\mathrm{l}\nabla T|_{\mathrm{l,i}} + \lambda_\mathrm{s}\nabla T|_{\mathrm{s,i}}]\cdot\mathbf{n}. \tag{17}$$

Using the definition of the reaction enthalpy Equation (15), where 2 and 1, stands for liquid and solid, subscripts l and s, respectively we obtain the following relation, which identifies to the classic Stefan condition, when $T_\mathrm{i} = T_\mathrm{m}$ and $h_\mathrm{r} = L_\mathrm{m}$:

$$\rho_\mathrm{s} h_\mathrm{r}\mathbf{v}_\mathrm{i}\cdot\mathbf{n} = [-\lambda_\mathrm{l}\nabla T|_{\mathrm{l,i}} + \lambda_\mathrm{s}\nabla T|_{\mathrm{s,i}}]\cdot\mathbf{n}. \tag{18}$$

This last equation determines the rate of phase change of a pure substance, which is controlled by the difference of thermal energy flux on both sides of the interface.

Mass transfer versus heat transfer processes. The same formalism apply to dissolution/sublimation and to the melting of multi-component systems. In both cases, the combination of Equations (1), (12) and (18) are coupled because the fluid physical properties (densities, diffusion coefficient, the saturation concentration, the latent heat, the heat capacity, ...) are function of the temperature or of the composition. The combined resolution of the three equations is not addressed in the literature, to our knowledge, for ablation problems. However, with the hypothesis of local thermodynamic equilibrium (fast kinetics), the phase change of binary or multi-components systems can be modeled, using energy conservation and mass conservation of each specie [102].

Nevertheless, in most practical cases, the interface motion is governed by one limiting process, either the temperature or the solute transport. For example, for dissolution, the phase change rate is assumed to be not controlled by the energy input, but by the concentration field at the interface [91,95,103]. Similarly, for the melting of pure ice into salt water, the local salt modifies the melting temperature, which can lead to complex phenomena, where the hypothesis of thermodynamic equilibrium is not valid [90,92]. In some conditions, the phase change can be controlled by the salt concentration and the ice melting problem is closer to a dissolution problem [104]. In this review, we do not address in details the case of melting of pure water ice in salt water, which is a rich topic with a large variety of phenomena. This topic of crucial environmental importance on Earth is covered by recent reviews [105–107].

In many natural dissolution phenomena, the temperature can be considered constant and set by the external conditions, i.e. the heat transport is fast enough to compensate the dissolution reaction enthalpy [108]. In this case, the rate of phase change is given by Equations (1) and (12). Combining these two equations leads to the boundary condition for the dissolving interface:

$$\rho_s \mathbf{v}_i = -\alpha(c_{sat} - c_i)\mathbf{n} = \frac{1}{1 - c_i/\rho_i} D(\nabla c|_i \cdot \mathbf{n})\mathbf{n}. \tag{19}$$

This boundary condition combines the concentration value c_i and the concentration gradient $\nabla c|_i$ at the interface. By introducing the typical length scale δ_c of the concentration gradient, i.e. $\nabla c \sim (c_b - c_i)/\delta_c$ where c_b is the far field concentration, we can define the Damköhler number

$$Da = (\alpha \delta_c)/D, \tag{20}$$

which compares the relative importance of the chemical reaction (middle-hand side of Equation (19)) to the diffusive transport (right-hand side of Equation (19)). In the case of natural rocks, for which $c_i \ll \rho_i$, the interfacial concentration is given by $c_i = c_b/(1 + Da) + c_{sat} Da/(1 + Da)$ [109]. If the chemical reaction rate is the limiting process at low values of Da compared to one, then $c_i \sim c_b + Da\, c_{sat}$. This corresponds to the case of slow dissolution reaction, valid for most weakly soluble minerals, as the low values of α correspond often to small values of c_{sat} [110]. In contrast, large values of Da give $c_i \approx c_{sat}$ and correspond to fast dissolution regime. This occurs for very soluble substances like salt or sugar in water. In this case, the advection–diffusion equation (Equation (9)) is thus solved with the boundary conditions $c_i = c_{sat}$ and Equation (12), which relates the normal concentration gradient to the interface velocity.

Finally, we remark, that the previous boundary conditions determine the normal projection of the interface velocity ($\mathbf{v}_i \cdot \mathbf{n}$) and do not constrain the tangential part. We assume thus, that the interfacial velocity is directed along the local normal to the interface $\mathbf{n}$. This condition has important geometric consequences in the evolution of interfaces undergoing phase changes [111].

3.2. *Models for melting, dissolution and sublimation*

For an evolving interface undergoing a phase change, the interface velocity $\mathbf{v}_\mathrm{i}$ is thus coupled by boundary conditions to advection–diffusion equations, which set the transport of the solute concentration field and/or of the temperature field, by the velocity field $\mathbf{u}(\mathbf{x},t)$ in the fluid phase. To close the problem, the determination of the velocity field is given by the Navier–Stokes equations, which express the local conservation of momentum. However, the spatial variations in composition due to the solute concentration and temperature affect the fluid properties. The density, the fluid viscosity, the diffusion coefficient, the diffusivity, the latent heat then vary spatially. The heterogeneity of the properties makes the question difficult to address theoretically. For sake of simplicity, we assume hereafter weak solute concentrations and weak variations of fluid properties with temperature. The density variations, which depend on concentration and temperature, are only taken into account when multiplied by the gravitational term (Boussinesq hypothesis). This is true for small variations in concentration and temperature. Finally, we assume that the properties of the fluid are homogeneous.

3.2.1. *Melting/solidification of a pure substance*

In these conditions, the model describing the melting/solidification of a pure substance in presence of a flow in the liquid phase is given by the following set of partial equations:

$$\frac{\partial T}{\partial t} = \kappa_\mathrm{s}\nabla^2 T \quad \text{(solid phase)} \tag{21}$$

$$\frac{\partial T}{\partial t} + \mathbf{u}\cdot\nabla T = \kappa_\mathrm{l}\nabla^2 T \quad \text{(liquid phase)} \tag{22}$$

$$\nabla\cdot\mathbf{u} = 0 \quad \text{(liquid phase)} \tag{23}$$

$$\rho_{\mathrm{l},0}\frac{\partial \mathbf{u}}{\partial t} + \rho_{\mathrm{l},0}(\mathbf{u}\cdot\nabla)\mathbf{u} = -\nabla P + \mu\nabla^2\mathbf{u} + \rho_{\mathrm{l},0}(1-\beta(T-T_0))\mathbf{g} \quad \text{(liquid phase)}. \tag{24}$$

Balance in total energy, mass, and momentum are described by the heat transport equation (Equations (21) and (22) in solid and liquid phases, respectively), by the continuity equation for an incompressible flow (Equation (23)) and the Navier–Stokes equations (Equation (24)) for a viscous flow. β is the thermal expansion coefficient (for example $\beta = 2.06\times10^{-4}$ K^{-1} for liquid water at 20 °C), P is the pressure field, $\boldsymbol{g}$ is the gravity acceleration and μ the dynamic viscosity of the liquid phase (the kinematic viscosity ν is equal to μ/ρ). κ_s and κ_l are the thermal diffusivities in the solid and liquid phase, respectively. The liquid density $\rho_{\mathrm{l},0}$ is assumed to be homogeneous and constant in the Navier–Stokes equation (Equation (24)) according to the Boussinesq approximation, where the density is only slightly modified in the gravitational term. T_0 is the temperature for which $\rho_\mathrm{l}(T_0) = \rho_{\mathrm{l},0}$. Note that the coefficient β corresponds to a linearization of the equation of state in the liquid phase, whose knowledge is required to solve the Navier–Stokes equation.

These equations must be associated to the following boundary conditions at the melting interface, whose velocity is $\mathbf{v}_\mathrm{m}$:

$$\mathbf{u}\cdot\mathbf{n} = v_\mathrm{m}\left(1-\frac{\rho_\mathrm{s}}{\rho_\mathrm{i}}\right) \tag{25}$$

$$\mathbf{u}\wedge\mathbf{n} = \mathbf{0} \tag{26}$$

$$T_\mathrm{i} = T_\mathrm{m} \tag{27}$$

$$\rho_\mathrm{s}L_\mathrm{m}\mathbf{v}_\mathrm{m}\cdot\mathbf{n} = -\lambda_\mathrm{l}\nabla T|_{\mathrm{l,i}}\cdot\mathbf{n} + \lambda_\mathrm{s}\nabla T|_{\mathrm{s,i}}\cdot\mathbf{n}. \tag{28}$$

Table 1. List of relevant dimensionless numbers for melting phenomena

Melting	Definition	Interpretation
Stefan number	$St = L_\mathrm{m}/(c_\mathrm{p}\,\Delta T)$	Competition of the latent heat with the stored thermal energy One Stefan number for each phase
Prandtl number	$Pr = \nu/\kappa$ $Pr \sim 10$ (water)	Momentum transport by viscosity versus heat diffusion
Density ratio	$r_\rho = \rho_\mathrm{l}/\rho_\mathrm{s}$ $r_\rho \sim 1.09$ (water)	Ratio liquid phase density to solid phase density at the interface
Reynolds number	$Re = (\delta_U\, U)/\nu$	Competition between flow advection and the viscous diffusion
Thermal Péclet number	$Pe_\mathrm{T} = (\delta_U\, U)/\kappa = Pr\,Re$	Competition between flow advection and the temperature diffusion
Thermal Rayleigh number	$Ra = \dfrac{\beta \Delta T\, g \delta_T^3}{\kappa\nu}$	Competition between buoyancy driven advection and diffusion phenomena
Interface motion number	$r_{\mathrm{m},U} = \dfrac{\kappa T_\mathrm{m}}{\rho_\mathrm{s} L_\mathrm{m} \delta_T U}$	Ratio of the melting interface velocity to the typical flow velocity

δ_U is the characteristic length scale of the flow, either the typical scale of velocity gradient or the thickness of a viscous boundary layer. δ_T is the characteristic scale of the temperature field (such as the thickness of a boundary layer). Note that the Stefan number may be defined differently in the literature.

For the other interfaces, the relevant boundary conditions depend on the considered problem, like for example cancellation of the velocity field on solid walls and of thermal gradient for insulating walls. The pressure field depends also on the external boundary conditions.

Moreover, as the solid/fluid interface evolves the domain of each phases as a function of time, the interface evolution introduces thus geometrical non-linearities by domain variation and induces computational challenges for direct resolutions.

Relevant dimensionless numbers can be introduced to define flow and melting regimes, see Table 1. The density ratio $\rho_\mathrm{i}/\rho_\mathrm{s}$, where ρ_i is taken at the melting temperature, determines the normal velocity at the melting interface. For each phase, we can define a Stefan number $St = L_\mathrm{m}/(c_\mathrm{p}\Delta T)$, with ΔT the typical temperature variation in the problem. This number compares the latent heat to the stored thermal energy, the lower the St value, the higher the melting speed. Note that the inverse definition of the Stefan number is also commonly used in the literature. The Prandtl number, $Pr = \nu/\kappa_\mathrm{l} = \mu/(\rho\kappa_\mathrm{l})$ is the ratio of kinematics viscosity to thermal diffusivity. Pr for water is about 13.5 at 0 °C and 6.99 (smaller) at 20 °C, because the fluid viscosity decreases with temperature, whereas the thermal conductivity increases. The momentum transport is thus faster than the heat transport, but without a clear separation of scales. For the hydrodynamics, we can introduce the Reynolds number $Re = (\delta_U U)/\nu$, where δ_U is a characteristic length and the thermal Rayleigh number $Ra_\mathrm{T} = (\Delta\rho\, g \delta_T^3)/(\mu\kappa_\mathrm{l})$ with $\Delta\rho = \rho_0 \beta \Delta T$, where δ_T is a characteristic scale of the temperature field. δ_T and δ_U depend on the considered system and flow conditions. The thermal Péclet number $Pe_\mathrm{T} = (\delta_U U)/\kappa_\mathrm{l} = Pr\,Re$ compares in Equation (22) the heat advection to the heat diffusion. For sufficiently large Rayleigh numbers and unstable density stratification, the liquid can move by thermal convection: the onset of convection (Rayleigh–Bénard instability)

between two horizontal solid plates maintained at constant temperatures, is predicted for a Rayleigh number above a critical value equal to 1707.8 [100].

3.2.2. *Dissolution/precipitation of a solid in a solvent*

For the dissolution/precipitation of a solid in a liquid phase (solution) consisting of a solvent and a solute of concentration c, the set of equations to solve in the liquid phase is, with the previous simplifying hypotheses:

$$\nabla \cdot \mathbf{u} = 0 \tag{29}$$

$$\frac{\partial c}{\partial t} + \mathbf{u} \cdot \nabla c = D\nabla^2 c \tag{30}$$

$$\rho_{\mathrm{l},0} \frac{\partial \mathbf{u}}{\partial t} + \rho_{\mathrm{l},0}(\mathbf{u} \cdot \nabla)\mathbf{u} = -\nabla P + \mu \nabla^2 \mathbf{u} + \rho_{\mathrm{l}} \mathbf{g}. \tag{31}$$

Equations (29) and (31) are again the incompressible Navier–Stokes equation in the Boussinesq approximation, the fluid density is assumed homogeneous and equal to the mean value $\rho_{\mathrm{l},0}$, except for the gravity term. The equation of state of the liquid phase relates the local density to the temperature and the chemical composition (here the solute concentration). For negligible temperature variations, the liquid density is related to the concentration by the relation: $\rho_{\mathrm{l}} = c(\rho_{\mathrm{sat}} - \rho_{\mathrm{l},0})/(c_{\mathrm{sat}}) + \rho_{\mathrm{l},0}$, where ρ_{sat} is the saturation liquid density. This linear dependency of density with concentration is valid for most solutes. The increase in density with c leads to buoyancy effects through the term $\rho_{\mathrm{l}}\mathbf{g}$. The boundary conditions at the solid/liquid interface are:

$$\mathbf{u} \cdot \mathbf{n} = v_{\mathrm{i}} \left(1 - \frac{\rho_{\mathrm{s}}}{\rho_{\mathrm{i}}}\right) \tag{32}$$

$$\mathbf{u} \wedge \mathbf{n} = \mathbf{0} \tag{33}$$

$$\rho_{\mathrm{s}} \mathbf{v}_{\mathrm{i}} = -\alpha(c_{\mathrm{sat}} - c_{\mathrm{i}})\mathbf{n} \tag{34}$$

$$\rho_{\mathrm{s}} \mathbf{v}_{\mathrm{i}} \left(1 - \frac{c_{\mathrm{i}}}{\rho_{\mathrm{i}}}\right) = D(\nabla c|_{\mathrm{i}} \cdot \mathbf{n})\mathbf{n}, \tag{35}$$

where α is the chemical dissolution rate coefficient.

To close the set of equation, like for melting, additional boundary conditions are required at non dissolving interfaces of the domain. Then, the dissolution velocity v_{i} at each point of the interface can be in principle computed to predict the erosion rate and a possible pattern emergence. Several dimensionless numbers are relevant to distinguish the hydrodynamic and dissolution regimes, see Table 2. We have already introduced the Damköhler number $Da = \alpha\delta/D$, which compares the chemical kinetics of the dissolution reaction with the diffusion transport at the solid/liquid interface. The Schmidt number $Sc = \nu/D = \mu/(\rho D)$ is the ratio of the momentum diffusion due to viscosity to the solute diffusion. Note that for the dissolution of ions or organics substances in liquid water, the Schmidt number is always of the order of 1000, i.e. the particle diffusion is always slow compared to the momentum diffusion. Consequently, the concentration boundary layers are usually significantly thinner than the viscous boundary layers, because on a given time scale momentum diffuses farther than solute $\delta_c \sim (DT)^{1/2}$, $\delta_\nu \sim (\nu T)^{1/2}$ and $D \ll \nu$. In addition, the ratios $c_{\mathrm{sat}}/\rho_{\mathrm{sat}} \approx c_{\mathrm{sat}}/\rho_{\mathrm{i}}$ and $\rho_{\mathrm{i}}/\rho_{\mathrm{s}}$ are also useful to define the weak concentration regime and the density jump at the interface, respectively. To characterize the hydrodynamics, the Reynolds number $Re = \delta_U U/\nu$ evaluates the importance of the nonlinear term in the Navier–Stokes equation (velocity field advection) in front of the viscosity term, where δ_U and U are the characteristic length and velocity of the flow. Using δ_c the characteristic scale for the concentration field, usually small in front of δ_U, we can define the solutal Rayleigh number $Ra = [(\rho_{\mathrm{i}} - \rho_b) g \delta_c^3]/(\mu D)$, where ρ_b is the liquid density of the "bath" i.e., far from

Table 2. List of relevant dimensionless numbers for dissolution phenomena

Dissolution	Definition	Interpretation
Damkhöler number	$Da = \alpha\delta_c / D$	Competition between chemical reaction rate and diffusive transport
Schmidt number	$Sc = \nu / D$ $Sc \sim 1000$ (ions in water)	Momentum transport by viscosity versus solute diffusion
Density ratio	$r_\rho = \rho_{\text{sat}} / \rho_{\text{s}}$ $r_\rho \sim 0.55$ (solid and saturated water)	Ratio liquid phase density (solute + solvant) to solid phase density of a soluble body
Concentration number	$r_c = c_{\text{sat}} / \rho_{\text{sat}}$ $r_c \sim 0.2$ (salt)	Ratio of the saturation concentration to the saturation liquid density. Determine the condition of weak concentration
Reynolds number	$Re = (\delta_U U) / \nu$	Competition between flow advection and the viscous diffusion
Péclet number	$Pe = (\delta_U U) / D = Sc\,Re$	Competition between transport due to flow advection and the concentration diffusion.
Solutal Rayleigh number	$Ra = \dfrac{(\rho_{\text{sat}} - \rho_b) g \delta_c^3}{D\mu}$	Competition between buoyancy driven advection and diffusion phenomena
Interface motion number	$r_{d,U} = \dfrac{D c_{\text{sat}}}{\rho_{\text{s}} \delta_c U}$	Ratio of the dissolving interface velocity to the typical flow velocity

δ_U is a characteristic scale of the flow, either the typical scale of the velocity gradient or the thickness of a viscous boundary layer, and δ_c is the characteristic scale of the concentration field.

the dissolving interface. Like the thermal Rayleigh number we introduce in Section 3.2.1, the solutal Rayleigh number determines the condition of appearance of convective motion by a hydrodynamic instability mechanism [21,109,112]. Finally, the Péclet number $Pe = (\delta_U U)/D$ compares advection with diffusion. The Péclet number is directly related to the Reynolds and Schmidt numbers $Pe = Sc\,Re$.

3.2.3. *Sublimation/condensation between a solid and a gas phase*

The hydrodynamic and mass transfer equations for the sublimation of a solid in an incompressible fluid whose composition is different from that of the sublimating material (sublimation of water ice in air for exemple) are identical to Equations (29) and (31). The fluid is subject to small temperature variations (constant $\rho_{\text{l},0}$). The transport of the ablated species within the fluid is treated as a passive scalar, satisfying an advection/diffusion equation for the concentration (Equation (30)). The boundary conditions (34)–(35) are identical to those for dissolution, with α representing the sublimation reaction rate coefficient. The sublimation velocity will be influenced by the type of flow (natural or forced convection) and the nature of the flow (laminar or turbulent). Special attention must therefore be paid to the turbulence

Table 3. List of relevant dimensionless numbers for sublimation phenomena

Sublimation	Definition	Interpretation
Damkhöler number for sublimation	$Da_s = \alpha\delta_s/D$	Competition between sublimation reaction rate and diffusive transport
Schmidt number	$Sc = \nu/D$ $Sc \sim 1$ (for gas)	Momentum transport by viscosity versus molecular diffusion
Density ratio	$r_\rho = \rho_{sat}/\rho_s$	Ratio gaseous phase density (gas + sublimated specie) to solid phase density of a soluble body
Relative humidity	$RH = \dfrac{p_{vap}}{p_{sat}}$ $RH < 1$ sublimation	Determine the conditions favorable to sublimation of the specie
Reynolds number	$Re = (\delta_U U)/\nu$	Competition between flow advection and the viscous diffusion
Péclet number	$Pe = (\delta_U U)/D = Sc\,Re$	Competition between flow advection and the concentration diffusion
Mass Rayleigh number	$Ra = \dfrac{(\rho_{sat} - \rho_b) g \delta_s^3}{D\mu}$	Competition between buoyancy driven advection and and diffusion phenomena
Interface motion number	$r_{s,U} = \dfrac{Dc_{sat}}{\rho_s \delta_s U}$	Ratio of the sublimating interface velocity to the typical flow velocity

δ_U is a characteristic scale of the flow, either the typical scale of the velocity gradient or the thickness of a viscous boundary layer. δ_s is the characteristic scale of the concentration field.

models used. As with dissolution, dimensionless numbers for phase change in sublimation are defined in Table 3. The Damkhöler number for sublimation, $Da_s = \alpha\delta_s/D$, is used to compare sublimation kinetics with diffusion transport at the gas/solid interface. The Schmidt number is the ratio of momentum diffusion to viscosity and molecular diffusion in the gas. For gases, this number is often close to 1, i.e. 1000 times lower than for dissolution, meaning that molecular diffusion is comparable to momentum diffusion. In this case, the velocity and concentration boundary layers are of the same order of magnitude. In the case of sublimation, the $r_\rho = \rho_{sat}/\rho_s$ ratio is very small, indicating a concentration jump at the interface. Temperature and pressure of the environment control the value of p_{sat}. Heat can come from radiation, which would add a source term in volume in the heat equation that has to be solved. To ensure a weak concentration regime, in the case of sublimation we are interested in the specific humidity, $RH = p_{vap}/p_{sat}$, where p_{vap} is the vapor pressure of the specie and p_{sat} the saturated pressure of the specie. A low value of this number corresponds to a dry atmosphere (and therefore favorable to sublimation). As in the case of dissolution, the Reynolds number is used to assess the competition between viscous diffusion and advection by the flow and the combination of *Sc* and *Re* gives the *Pe* number, which compares concentration transport by flow advection and diffusion. If buoyancy forces are driving the flow, the same Rayleigh number *Ra* as in the dissolution case can be used to estimate the relative strength of buoyancy due to concentration/density variations and diffusion.

3.2.4. *Melting, dissolution and sublimation. Analogies and differences*

The dissolution/sublimation velocity is set by the normal to the surface component of the concentration gradient (Equation (12)) and the concentration field in the fluid phase is found by solving an advection diffusion equation for the concentration. As seen previously, for large values of the Damköhler number *Da*, the concentration at interface is close to the saturation concentration ($c_i = c_{sat}$). The problem becomes thus mathematically identical to the melting situation in case of negligible temperature diffusion in the solid (often valid for large Stefan number $St = L_m/(Cp\Delta T)$), where the advection–diffusion equation of the temperature is solved with the boundary conditions $T_i = T_m$. In that case, Equation (18) relates the interface velocity to the normal temperature gradient. In both cases, the kinetics of the molecular mechanisms (attachment and detachment) is assumed fast enough to be neglected and the interface state corresponds to the thermodynamics equilibrium, when the coexistence between two phases occurs. The motion of the interface is yet an out-of-equilibrium process caused by the difference of fluxes on each side of the interface. Therefore, dissolution and melting patterns can often be paralleled [69], as they arise qualitatively by the same mechanisms. Nevertheless, some of dimensionless numbers have always very different orders of magnitude. The Schmidt number *Sc* is about 1000 for dissolution, whereas the Prandtl number *Pr* is about 10, meaning that the heat diffuses faster than the concentration and that the diffusion of both quantities is less efficient than momentum diffusion. Typically, the sizes of the concentration structures like plumes, eddies, boundary layers are smaller than those corresponding to the temperature.

Another important difference, is related to the external boundary conditions of the problem. Despite the mathematical analogy, the saturation concentration does not play the same role than the melting temperature in practical cases. Usually in dissolution experiments in a closed domain, the process stops, when the liquid concentration reaches the saturation value, due to accumulation of the solute. Providing fresh water for concentration is the most suitable way to avoid this effect. For melting examples, an energy input is externally supplied to sustain the phase change and if it is maintained constant, the melting continues until the solid has completely disappeared. However, it can also stop if the system is closed without loss of energy, allowing it to reach equilibrium temperature. In both case, for the ablation process to be effective, the system must be out of equilibrium.

For dissolution, the kinetics effects are often considered more relevant that for melting. For most low solubility minerals, such as quartz and other silicates [91], the rate of dissolution is often considered to be limited by the chemical kinetics. For minerals of intermediate solubility, such as limestone and gypsum, the interaction between transport and reaction has been addressed in a recent review [113] of dissolution in porous media, wormhole formation and fracture growth by dissolution. The reaction seems to be confined to a small distance necessary to reach conditions close to saturation. In addition, the role of the reaction in the presence of a flow, and thus of the coefficient α in the dissolution rate, has only been directly shown in very few experiments. Using a microfluidic flow experiment combined to dedicated numerical simulations, Dutka et al. [114] find an intermediate situation ($Da \sim 3$) for dissolution of gypsum samples. In this example, the dissolution rate is mainly limited by diffusion, but is significantly influenced by the reaction rate coefficient α. For very soluble materials like salt (NaCl) or sucrose, to our knowledge, in macroscopic experiments the role of the reaction is not perceptible for dissolution dynamics and pattern formation [21,109,112]. Therefore, most macroscopic dissolution experiments belong to the diffusion limited regime, i.e. large *Da*. The case of the generation of meter scale natural conduits in limestone caves is debatable and could depends if the dissolution occurs in acid conditions (large *Da*) or in alkaline conditions (small *Da*) [115].

Then, according to Equation (1), the kinetics define a maximal dissolution velocity $v_{d,max} = \alpha c_{sat}/\rho_s$. Although, the values of α are not always well determined experimentally, the

order of magnitude of the maximal dissolution velocity, $v_{d,\max}$, is of the order of 10^{-5} m/s, for fast dissolving materials like salt [103]. Consequently in the presence of a flow at a macroscopic scale, the interface velocity is usually very small in front of the hydrodynamic velocity, in the case of dissolution or sublimation. The evolution of the interface and of the hydrodynamic acts thus with two separated time scales. For the melting of a pure substance in extreme situations, the separation of time scales is not always guaranteed. A dimensionless number to quantify this time scale separation can be defined as the ratio between the interface velocity to the typical flow velocity: $r_{d,U} = Dc_{\mathrm{sat}}/(\rho_{\mathrm{s}}\delta_c U)$ for dissolution and $r_{\mathrm{m},U} = \kappa T_{\mathrm{m}}/(\rho_{\mathrm{s}} L_{\mathrm{sat}}\delta_T U)$ for melting respectively. These numbers are usually very small compared to one, but must be evaluated in each situation.

We note also an important analogy between dissolution/sublimation and melting in the context of erosion processes. Once thermodynamic equilibrium is broken, the flow in the fluid phase always affects the rate of phase change. At a melting interface, an increase of the local flow velocity increases the shear rate in the thermal boundary layer or the concentration boundary layer. The thickness of boundary layers decreases and the local phase change rate increases. Contrary to mechanical erosion, for which erosion occurs when the shear stress overcomes a threshold, there is no such threshold for dissolution or melting. An infinitesimally weak velocity can thus participate to the emergence of a dissolution/sublimation or melting pattern.

Finally, as we pointed out before, the sublimation of a solid in a atmosphere, where the sublimated vapor is in small proportion is formally analogous to the dissolution of a solid in a solvent. As the theoretical description is identical, the same dimensionless numbers arise naturally, by considering the concentration field of vapor in the atmosphere (the index $_{\mathrm{l}}$ (liquid phase) by $_{\mathrm{g}}$ (gas phase)). However, the physical properties of the liquid and gas phases differ strongly, leading to different orders of magnitude for the physical coefficients c_{p}, ν, κ, $D, \ldots$ In addition, because the heat capacity of gases is smaller, the coupling between concentration and temperature fields is stronger. Sublimation is usually modeled by addressing the vapor transport and taking into account the temperature variations, which change in turn the saturation vapor pressure, with the hypothesis of local equilibrium of the interface [116]. As the molecular mechanisms at the origin of diffusion and viscosity are similar in gas (which is not the case for liquids), the Schmidt number and the Prandtl numbers are of order one ($Sc = 0.63$ for water vapor in air and $Pr = 0.7$ for air) [101]. Compressibility effects can also become significant, modifying the hydrodynamic description.

3.3. *Choice of analog material for an experiment*

As many natural patterns created by a phase change often occur in complex situations with intermittent conditions and entangled physical mechanisms, model laboratory experiments are useful to identify their formation mechanism and dynamics. However, the timescales in which they appear and evolve are often very long compared to human time scales. It is therefore necessary to accelerate the phenomenon in order to carry out experiments within a manageable time, typically one hour. The question is then whether the physics studied for fast evolution is qualitatively similar to the natural case, and whether the laboratory results can be extrapolated to the field, by examining the relevant dimensionless number. A list of these dimensionless numbers are summarized in the Tables 1–3.

For melting experiments by a fluid flow, most of experiments are performed with ice in contact with water. The melting/solidification temperature of 0 °C is relatively close to ambient temperature compared to other common pure materials and is accessible using standard laboratory equipment. The melting rate can be conveniently adjusted by varying the temperature of the water flow. Ice can also be used to mimic the melting of minerals or materials at high

temperatures. This has been done in an experiment where an impinging jet of molten material hits a solid wall [117]. Organic phase change materials are also used to investigate the interaction between phase change and melting, like cyclohexane [118] (T_m = 6.38 °C), hexadecane [119] (T_m = 17.7 °C) or polyethylene glycol wax [120] (T_m = 19 °C). The latent heat and thermal parameters are of a similar order of magnitude, but the organic liquid are much more viscous and less thermally conductive. Consequently the Prandtl number $Pr = \nu/\kappa$ is large compared to one and of order 1000 instead of about 10 with water. Fluid mechanics experiments with phase change material have been also performed with liquid metals like gallium [121] (T_m = 29.7 °C), which have larger densities and allow to reach small values of the Prandtl numbers (about 2×10^{-2}).

For phase changes by dissolution, the three most important types of soluble rocks are salt (Halite or sodium chloride, NaCl), gypsum ($CaSO_4{\cdot}2H_2O$) and limestone (Calcite, $CaCO_3$), whose solubility (approximately the saturation concentration) in water are around 360 g/L, 2.0 g/L and 15 mg/L, respectively. The solubility of limestone is strongly dependent on carbon dioxide concentration and the acidity, which is measured with the pH scale. These three rock examples belong respectively to three mineral families with similar chemical and physical properties, the halides, the sulfates and the carbonates, respectively. In general, the dissolution parameters, c_{sat} and α will have similar value for components belonging to the same family.

The chemical dissolution/precipitation reactions are:

$$(NaCl)_s \leftrightarrows Na^+ + Cl^-$$

for salt (sodium chloride) and:

$$(CaSO_4{\cdot}2H_2O)_s \leftrightarrows Ca^{2+} + SO_4^{2-} + 2H_2O$$

for gypsum (dihydrated calcium sulfate).

They are described by simple dissolution/precipitation reaction. Limestone is the most common and important case, due to the large distribution all over the continents of regions shaped by the hydrochemical erosion of limestone called Karsts [122]. The chemical reactions for removal or deposition of the calcite are quite complex with several elementary steps [91,123]. However, they can be summarized in a single chemical equation:

$$CaCO_3 + CO_2 + H_2O \leftrightarrows Ca^{2+} + 2HCO_3^-$$

Note that the reaction involves CO_2 as a gas dissolved in the aqueous phase, whose presence in the solution acidifies the water. Therefore, the rate at which calcite dissolves depends on exposure to the atmosphere and pH. To simplify, the limestone dissolves at low pH (acid) with the consumption of CO_2 and precipitates at high pH (basic) with the production of CO_2 especially for acid enough water, erosion is often assumed to be controlled by solute transport rather than dissolution kinetics [91]. The values of the relevant experimental parameters for the most common soluble materials are given in Table 4 for a temperature of about 20 °C. We note that the dissolution rate α conveying the chemical kinetics, is not well known, especially for fast dissolving materials, because the hydrodynamic methods (like the rotating sample one) depends on a laminar model for the boundary layer and could suffer from biases [124]. In absence of external flow, the use of a holographic method to follow the evolution of the density profile by diffusion provides a consistent method to measure α for gypsum [95]. As mentioned previously, dissolution of a gypsum sample in a microfluidic cell allows to measure α [114]. The obtained values are compatible with the holographic measurement without flow motion. Nevertheless, it appears that in general the largest values of α are associated to large saturation concentration, as it has been tested for the dissolution of some organic substances [110]. Sugar (sucrose) and similar organic compound like glucose or benzoic acid are convenient to perform dissolution experiments [21,125,126], because they can be molded to the prescribed shape after thermal

Table 4. Characteristic parameters for dissolution in fresh water at a temperature of about 20 °C

	Solid density ρ_s (kg·m^{-3})	Saturation concentration c_{sat} (kg·m^{-3})	Saturation density ρ_{sat} (kg·m^{-3})	Dissolution rate α (m·s^{-1})	Diffusion coefficient D (min|max) (m^2·s^{-1})	Dynamic viscosity μ (min|max) (Pa·s)
Limestone $CaCO_3$	2711	0.312	997.432	3×10^{-6}	1.4×10^{-9}	1.002×10^{-3}
Gypsum $CaSO_4{\cdot}2H_2O$	2320	2.04	999.16	2.7×10^{-6}	1.0×10^{-9}	1.002×10^{-3}
Salt NaCl	2170	317.5	1200	5.0×10^{-4}	1.5×10^{-9} 1.6×10^{-9}	1.00×10^{-3} 1.99×10^{-3}
Sugar $C_{12}H_{22}O_{11}$ Sucrose	1540	887	1327	$\gtrsim 5 \times 10^{-6}$	5.2×10^{-10} 7.1×10^{-11}	1.00×10^{-3} 0.212

The density of fresh water is $\rho_0 = 997.12$ kg·m^{-3} and its dynamic viscosity $\mu_0 = 1.002 \times 10^{-3}$ Pa·s [101]. Limestone, data from Kaufmann et al. [127] at high carbon dioxide pressure. For limestone, c_{sat} is strongly dependent on the carbon dioxide pressure and on the pH. This value is particularly high, $c_{sat} \approx 0.015$ kg·m^{-3} under standard conditions. Gypsum, data from Colombani et al. [95]. Salt, data from Alkattan et al. [103] and from the Handbook [101]. Sucrose, data from Cohen et al. [21], and others [128,129] and from the Handbook [101].

melting. However, viscosity increases by several orders of magnitude with concentration, which is not the case for mineral rocks, and some of the observations may not be relevant for soluble rocks. Plaster has the same chemical composition than gypsum. It has an intermediate solubility between salt and limestone and can be easily molded. This is why plaster has been used in several important studies of dissolution in water flows within a matter of hours [15,17,20]. Yet, the obtained samples are often porous, which may influence the surface patterning and the measured erosion rates. Furthermore, some experiments can be performed with synthetic large salt crystals (like NaCl, KCl or KBr), but the samples are expensive and limited to a few centimeters. Then, mineralogical samples from mines and quarries can be also used in experiments. However, they often show defects in composition if they contain impurities, and in mechanical properties due to grain boundaries or fractures.

Finally, we now consider the case of sublimation of a solid. Sublimation technique [130] has been used to obtain informations about heat transfer in experiments. Analogies have been made between mass and heat transfer. Naphthalene ($C_{10}H_8$), with its high sublimation rate at room temperature [131], has been used as sublimating substrate for its good casting and machining properties but it is considered carcinogenic and to our knowledge has not been used to study bedforms. Camphor has already been used to test the influence of material surface roughness on the triggering of the laminar–turbulent transition when objects coming from space enter the atmosphere. However, it requires high temperatures for sublimation [132]. Water ice under controlled cold and dry atmospheres appears to be the most obvious substrate. The use of water ice as the substrate for sublimation experiment has some advantages over the previous ones: it is not toxic, it requires less extreme temperatures, the material is inexpensive to produce and can be shaped in any desired manner. But here the duration of experiments can be a problem. For a fixed ambient and partial pressure, the saturation margin $p_{sat} - p_{vap}$ determines the sublimation velocity (see Table 5). Thus, water–ice experiments would have to run for weeks to achieve the same depth of ablation that a CO_2–ice experiment can achieve in hours. Under similar

Table 5. Characteristic parameters for sublimation in N_2 atmosphere

	Solid density ρ_s ($kg{\cdot}m^{-3}$)	Saturation pressure p_{sat} (Pa)	Vapor pressure p_{vap} Pa (min|max)	Sublimation velocity v_s ($m{\cdot}s^{-1}$)	Diffusion coefficient D ($m^2{\cdot}s^{-1}$)	Kinematic viscosity ν ($m^2{\cdot}s^{-1}$)
Svéa, Antartica H_2O	865	336	100–166	3×10^{-9}	2.9×10^{-5}	1.5×10^{-5}
Nantes, wind tunnel CO_2	1560	1.4×10^{5}	40	1.4×10^{-6}	1.5×10^{-5}	1.5×10^{-5}

Kinematic viscosities are computed from Sutherland's law for the viscosity of gases. In both cases, sublimation velocities are estimated in the absence of wind. Water ice data from Bintanja [50] with $RH\sim0.3$, CO_2 ice data with $RH\ll1$ from Bordiec et al. [32].

environmental conditions, water ice will always sublime about three orders of magnitude slower than CO_2 ice.

4. Dissolution, melting and sublimating patterns in experiments

Pattern can be shaped by an instability of the flow, be periodic with a characteristic wavelength, but recognizable shapes can also be driven by specific boundary conditions. Here, we have chosen to classify experiments as a function of the external forcing and boundary conditions, which, we believe, modify the coupling processes described in Section 3 that drive pattern formation. Because diffusion tends to homogenize concentration and temperature fields, it cannot drive the spatial variation of the concentration/temperature field that leads to pattern formation (but when associated with specific boundary conditions); a flow is required. This flow can be buoyancy driven by the phase change itself or externally driven (or both). When externally driven, the flow can be deep, as in caves or oceans, or shallow and possibly interacting with the free surface, which is the usual case of a surface exposed to rainfall. Riverbeds can be subject to both deep and shallow flows.

4.1. *Buoyancy driven flow and associated bedforms*

Melting or dissolution of a body in quiescent water leads to density stratification at the eroding surface, either because the solution density depends on temperature or on solute concentration. This density stratification may be stable or unstable with respect to gravity. In either case, this density stratification drives a buoyant flow (but in the singular case of an infinite and perfectly flat surface). Experiments usually consist of simply following the dissolution of a block of sugar (glucose, sucrose, or a mixture) [21,48,108,133,134], salt (NaCl), or plaster [21], or the melting of an icy block in a tank of water [135].

4.1.1. *Stable density stratification*

The dissolution of axisymmetric sugar bodies in quiescent water has been studied experimentally by Pegler and Davies Wykes [108] and by Huang et al. [48] for the case of stable density stratification (Figure 8). In this case, the erosion creates a thin convective boundary layer of concentration that grows while flowing along the body surface. These experiments show that an initial upright cylinder sharpens with time while receding [48] whereas an initial cone blunts with time [108]; the erosion dynamics depends on the initial shape [108]. The erosion dynamics and shapes are well described by a boundary layer model derived by Acrivos [136], in the limit of

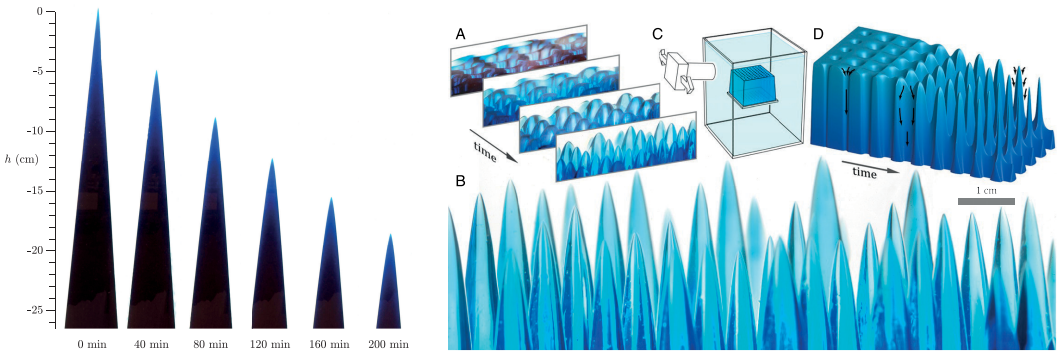


Figure 8. Left: dissolution of a candy cone (from Pegler and Davies Wykes [108]). Copyright Cambridge University Press 2020. The cone slowly blunts with time and the receding velocity slowly decreases with time. Right: A block seeded with vertical pores dissolves and form an array of sharp pinnacles (from Huang et al. [48]), under the CC BY 4.0 license.

high Schmidt number, i.e., the concentration boundary layer is within the viscous layer [108,137]. They have shown in particular that in this 2D-model convex upward shapes sharpen with time with a receding rate that increases with time, whereas triangles and concave upward shapes blunt with time with a receding rate that decreases with time [137]. For simple shapes, self similar solutions exist but no asymptotic, stationary shape [108,137]. Huang et al. also interestingly "speculate that this mechanism contributes to the formation of pinnacles in nature", such as tsingys or stone forests [48], the *sharp patterns* described in Section 2.1, Figure 1(b). Weady et al. studied the melting of initial vertical cylinder in a tank of water at different temperature T_∞ [135]. These cylinders sharpen to form upward pinnacles when $T_\infty \gtrsim 7$ °C and downward pinnacles when when $T_\infty \lesssim 5$ °C, because water density is maximum around 4 °C [135]. At intermediate temperatures, scallop-like patterns form at the ice surface. Authors explain these patterns as imprints of a Kelvin–Helmholtz instability between the rising fluid near the surface and the sinking outer flow [135].

4.1.2. *Unstable density stratification*

If the density stratification induced by the dissolution or melting of an object is unstable rather than stable, i.e. if the density gradient is opposed to the gravity direction, the results are significantly different, both at the global scale and at a smaller scale, where patterns appear. The first observations of this phenomenon date back to at least the beginning of the 20th century, when Schürr described the appearance of "convection stripes" on the surface of immersed soluble crystals in 1904 [138,139]. The appearance of patterns on the surface of solids under the effect of convection flow generated by their dissolution [140,141] or melting [142,143] was subsequently observed, but the first quantitative studies of patterning date from the late 1990s. Drawing an analogy with turbulent thermal convection, Sullivan et al. proposed that a solutal Rayleigh–Bénard instability determines the thickness of the concentration boundary layer, and therefore the dissolution rate, but also the characteristic size of the patterns. It proved to be in good agreement with experiments conducted on horizontal salt crystals [112,144,145].

This can be explained with the schematic in Figure 9. When a soluble solid is brought into contact with water, a boundary layer of concentration is created around it, which grows initially by diffusion. At downward facing surfaces, the boundary layer eventually destabilises when buoyancy overcomes diffusion in concentration transport, i.e., a solutal Rayleigh–Bénard

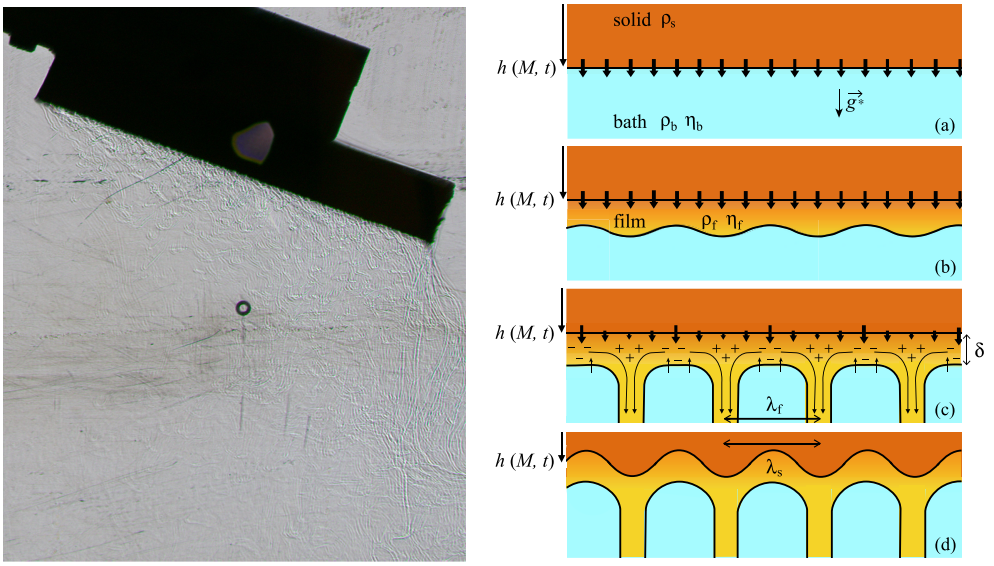


Figure 9. Left: Shadowgraph of a plaster block in water showing the sinking plumes of the solutal convection. The bottom surface is 20 cm long. Credits: Martin Chaigne. Right: Sketch of the solutal Rayleigh–Bénard instability and its imprint on the block (from Cohen et al. [21], with the permission of the American Physical Society).

instability happens, analogous to the thermal Rayleigh–Bénard instability. The instability threshold is given by a criterion involving the solutal Rayleigh number:

$$\frac{\Delta\rho g\delta_c^3}{\rho_b \nu D} = Ra_c, \tag{36}$$

with $\Delta\rho$ the difference in density between the saturated fluid and the fluid in the bath, η the dynamic viscosity of the fluid, D the diffusion coefficient of the solute in the fluid, and Ra_c a critical value of the solutal Rayleigh number. Using the values in Table 4 and taking $Ra_c = 1101$, which is the theoretical value for the onset of the Rayleigh–Bénard instability with mixed slip and no-slip boundary conditions [100], we find that the thickness δ_c is of the order of 0.1 mm for salt, 0.4 mm for gypsum and between 0.7 and 2 mm for limestone. Experimental values of the dissolution rate rather suggest $Ra_c \simeq 100$ [112,144], which modifies the estimated thickness of the boundary layer by a factor of 2. The nonlinear evolution of the destabilized boundary layer then leads to the emission of thin plumes of solute-laden fluid. Their typical thickness is that of the boundary layer, while the typical spacing between two plumes is of the order of a few boundary layer thicknesses [21,144]. In Figure 9, they are visualised using the shadowgraph technique under a block of plaster suspended in water at an angle of 20° to the horizontal. From the time the first plumes are emitted, the flow enters a quasi-permanent regime during which the boundary layer remains, in average, marginally stable.

At a large scale, the boundary layer therefore has a constant thickness that leads to a constant dissolution rate. At a smaller scale, however, the convection flow induces a spatially variable dissolution rate: the boundary layer is thicker (and therefore the dissolution rate lower) vertically across a plume than between two plumes, where it is thinned by the arrival of fresh water rising from the bottom. These local variations in the dissolution rate then imprint on the soluble solid, all the more so as the emergence of a topography locks the position of the plumes [21]. Under a horizontal surface, this leads to the appearance of a pattern of cavities surrounded by

sharp crests reminiscent of scallops [111,112,145], the size of which reflects the wavelength of the hydrodynamic instability.

If the surface is inclined, the patterns obtained are qualitatively different. The dissolution flow tends to follow the inclination of the block as observed on the shadowgraph in Figure 9. This flow causes a spatial coherence of flow structures along the block and leads to the appearance of parallel stripes in the direction of gravity [21,133]. It can be seen in Figure 10, which shows photos at different time intervals of the underside of a block of plaster dissolving in water. The block of plaster was suspended in an aquarium of fresh water at room temperature, frequently replenished so that the concentration of solute remained far from saturation. Stripes appear, becoming deeper and wider, until they form grooves with very sharp edges. These same stripes can be observed on inclined caramel plates immersed in water, as shown in Figure 11. In this case, however, the initial pattern of stripes is itself unstable. The stripes rapidly cross to form chevrons and then asymmetrical concave, open at the bottom, scallop-like patterns, which run up the block in the opposite direction to the flow while widening [21,133]. The same succession of patterns can be seen on salt blocks. Figure 12 shows the (transverse) pattern, made up of cavities surrounded by sharp crests. The propagation of the patterns in the opposite direction to the flow can be explained by the fact that the plumes of solute-laden water detach at the crests (Figure 12). Thus, the dissolution rate is greater immediately downstream of a crest than upstream, causing it to propagate upstream [21]. Cohen et al. suggest that differential upstream velocities could explain transversalization of the initial stripe pattern because solute flow channelize on crests. Yet the precise mechanism explaining why this initial pattern destabilises in caramel and salt to form propagating scallops, which is not observed in plaster, remains to be elucidated. One of the major differences between the two cases is that the large differences in density between pure water and water saturated with salt or sugar ($\Delta\rho/\rho_0 = 0.2$ for salt and 0.33 for sugar) lead to highly turbulent convection flows, with typical velocities of the order of a few cm/s, much larger than for plaster, for which $\Delta\rho/\rho_0 = 1.7 \times 10^{-3}$. For limestone, the density differences are even smaller ($\Delta\rho/\rho_0 < 3 \times 10^{-4}$), which makes it difficult to extrapolate these experimental results directly to the natural case. Although Cohen et al. point out the morphological similarity between the scallops appearing on blocks of salt or caramel and those adorning the walls of limestone caves [21,133], the possibility that solutal convection plays a role in the formation of the latter remains an open question, all the more so when an externally imposed flow is present. Underground rivers flowing in cave conduits can indeed reach typical velocities of the order of 1 m/s, much larger than the typical velocities induced by solutal convection. How such flows might influence the convection instability and the associated pattern formation is unclear. It is more likely, however, that the natural convection instability is at the origin of the large arrays of scallops observed on the immersed walls of icebergs, which melt in the polar oceans (see Figure 2(b)). Similar pattern formation is indeed expected when melting induces thermal or solutal convection. Cohen et al. [133] reported the formation of scallops at the top face of an ice block of fresh water melting in a bath of (densier) salt water. Between fresh water and seawater, the relative density difference $\Delta\rho/\rho_0$ equal to 0.025.

On a much larger scale, the average thickness of the boundary layer is fixed by the balance between diffusion and buoyancy (Equation (36)). For a flat surface inclined downwards, the dissolution rate is therefore constant over time and globally uniform along the surface. This was verified by Davies Wykes et al., who showed that sugar cones or prisms suspended upside down in an aquarium of water retain their shape [134]. The authors found no significant variation in erosion rate as a function of surface inclination angle, in contrast to Cohen et al. who found that erosion rate decreases with the inclination of the block. They argue that inclination should be taken into account in the gravity term, which predicts a dissolution rate proportional to $\cos(\theta)^{1/3}$, in agreement with their measurements [21]. This dependency of angle only becomes significant

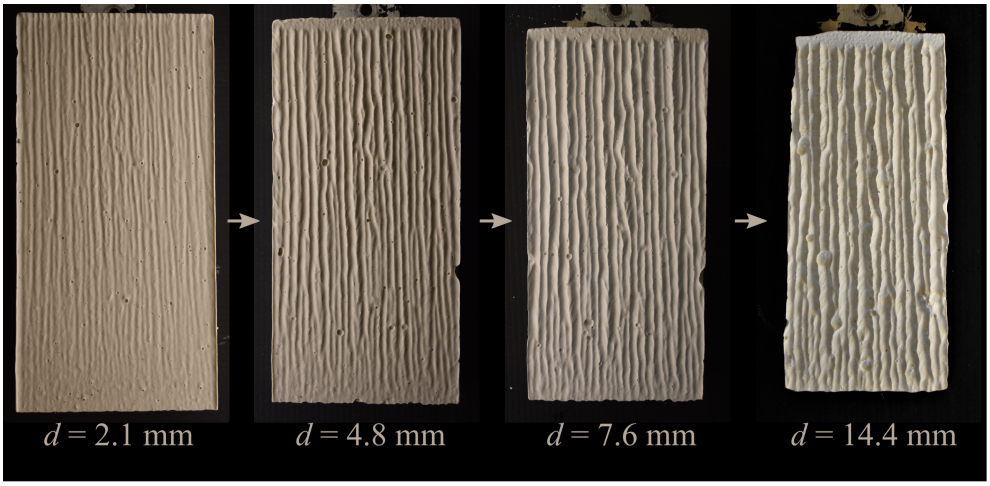


Figure 10. Patterning of the bottom surface of a plaster block immersed in tap water at an angle of 20° from the horizontal. The water was at room temperature, between 17 °C and 21 °C. The plaster block was regularly removed from the tank to take photographs of the surface and to record the topography. The scale is the same for each photograph. The block on the left is 20 cm long. Gravity points downward. d is the mean eroded thickness of the bottom surface. From left to right, photographs were taken after 148, 343, 541, and 928 h of immersion. Credits: Martin Chaigne.

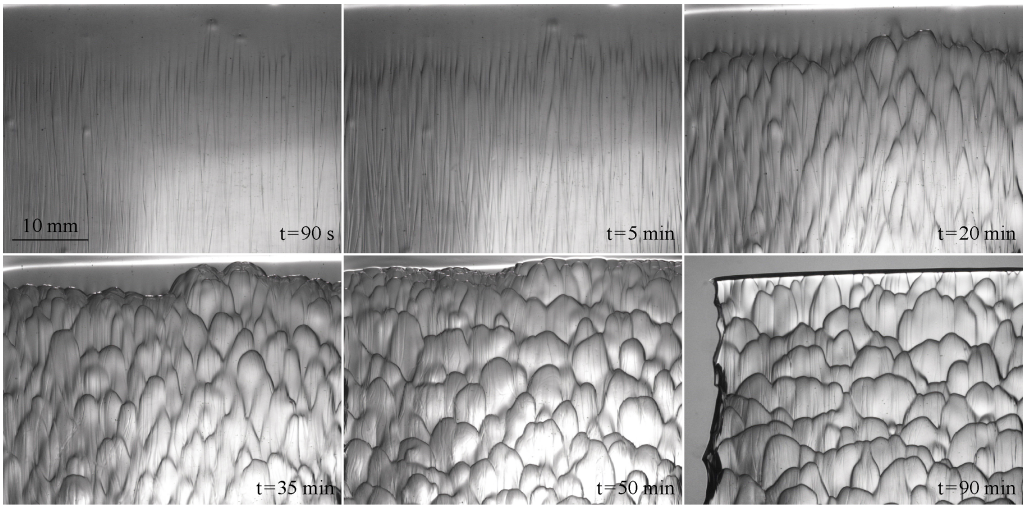


Figure 11. Patterning of the bottom surface of a caramel block immersed in tap water (20 °C) at an angle of 60° from the horizontal (from Cohen et al. [21], with the permission of the American Physical Society).

for large inclination, which may explain why Davies Wykes et al. did not observe it. We can therefore expect that an object of arbitrary shape dissolving from below will not always retain its shape. The large-scale convection can also shape cavities in confined geometries. By injecting water at a low flow rate into a cylindrical hole dug in salt, Gechter et al. observed that, due to the convective instability, the ceiling dissolved much faster than the sides and floor [146].

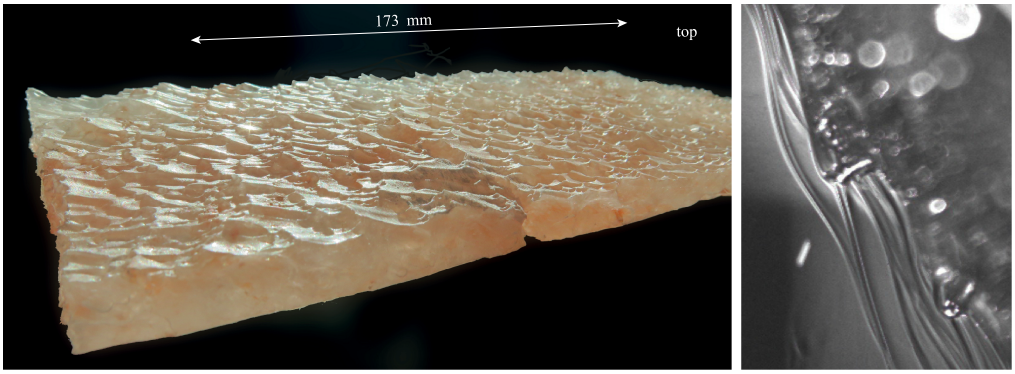


Figure 12. Left: Bottom surface of a salt block after immersion for 1 h in tap water (20 °C) at an angle of 60° from the horizontal. Right: Detail showing plumes of solute-laden fluid detaching from the crests of a caramel block. Both images are from Cohen et al. [21], with the permission of the American Physical Society.

The initially circular profile deforms to become, over time, a triangular prism with a vertical ceiling. Sharma et al. obtained a similar shape by studying the formation of alcoves from defects on horizontal sugar walls dissolving in water [147].

4.2. *Forced surface flows and associated bedforms*

In the case of wind over sublimating surface or river current under a melting or dissolving surface, the velocity of the flow can be much larger than the velocity of the ablation process. In that case, two boundary conditions for convective flows have to be considered: the deep flow and the shallow water flow. Experiments should therefore be considered with care, ensuring that the wavelength of the patterns is either small in front of the flow thickness or much greater than it, respectively. To this end, the dimensionless number $k\delta_U$ has to be considered, where k is the wave number and δ_U, the thickness of the fluid layer under consideration. This thickness corresponds to the height of the boundary layer thickness in atmospheric wind tunnels or in a closed water channel and to the height of the flow in a free surface flow. If $k\delta_U > 2\pi$, then deep flow condition should be considered, and if not, shallow water.

4.2.1. *Deep flows*

The patterning in response to a unidirectional water flow at high Reynolds number has been mainly investigated in deep flow regime for the dissolution of plaster plates, which have the same chemical composition than gypsum. By imposing a flow velocity of order the meter per second, several studies [18,19,70,148,149] report after about a hundred hours the formation of a scallop pattern, similar to *the polygonal depressions* observed in the nature and previously described in Section 2.2, Figure 2(c–d). In experiments, the typical scallop size and the surface roughness increase in time. In particular Allen [18,71] studies the temporal evolution of the pattern and the emergence of the scallops and pointed out the crucial role of initial defects, which are unavoidable with plaster due to its slight porosity. Defects larger than a critical size (about the centimeter) depending on the hydrodynamics give rise to “heel-shaped hollows of parabolic plan called flutes”. The subsequent pattern evolution generates an assemblage of scallops (Figure 13(c)). Smaller defects in contrast, grow mainly in length to produce narrow grooves parallel to the flow and of width about the centimeters. These patterns correspond to

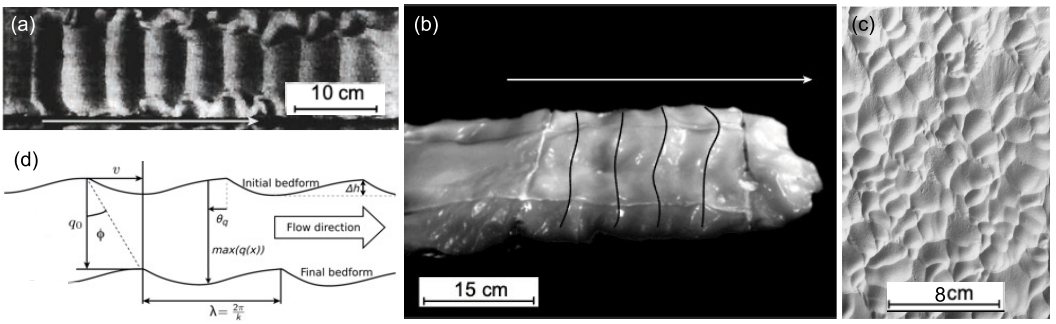


Figure 13. Deep flow conditions experiments. (a) Dissolution waves from Blumberg and Curl [20], copyright Cambridge University Press 1974 and (b) sublimation waves from Bordiec et al. [32], with permission from Elsevier. (c) Scallops from Allen [18] by dissolution of plaster. Copyright Cambridge University Press 1971. (d) Schematic of the parameters used in the scaling laws: wavelength λ, amplitude Δh, propagation angle ϕ and ablation rates q_0, adapted from Blumberg and Curl [20], copyright Cambridge University Press 1974.

the *crested patterns parallel to the flow direction* described in Section 2.4, but are surprisingly generated rather in deep flow regime, whereas the natural examples correspond mostly to thin film flows. Allen proposed that these dissolution structures may be related to structures of the wall turbulence, the streaks. However, these grooves can generate for longer flow exposure in a second step, flutes and finally a scallop assemblage.

Regularly spaced crests, parallel to each other and oriented perpendicular to the turbulent overlaying flow (Section 2.3, Figure 3) are known to be formed under deep flow conditions. We will show in the remainder, that they have been reproduced in dissolution, sublimation and melting experiments. The mass transfer at work, coupled with the flow, induces a modulation of the surface on which transverse linear waves appear. In Blumberg and Curl [20] experiment, dissolution waves are reproduced on a plaster block as an analogous material of soluble rock (Figure 13b). Their morphodynamic study revealed wavelengths, amplitudes, propagation angles and dissolution rates defined in Figure 13(d) as a function of flow velocity and the ratio between fluid viscosity and diffusion coefficient, a dimensionless quantity known as the Schmidt number (see Table 2). By comparing the flow velocity with the ablation rate (typically 1 m·s^{-1} and 0.5 µmm·s^{-1}), these experiments are well placed in a quasi-static interface evolution, i.e. $r_{d,U} \ll 1$ (see Table 2). The boundary layer of this flow $\delta_U \simeq 7.6$ cm is imposed by the water tunnel geometry. This height must be greater than the wavelength of the patterns. Depending on the set of parameters, that we can reduce here to the dependence on two dimensionless numbers (Schmidt and Reynolds), dissolution waves have wavelengths between 2–5 cm. They have a millimetric amplitude and migrate at different speeds (1–3.2 $\times 10^{-7}$ m·s^{-1}) in the direction of flow.

The aim of this approach is to understand the process of dissolution wave formation in a qualitative way, and help to enrich a database. It highlights a regime of appearance of this undulating surface roughness formed by dissolution in a transition regime, by considering a dimensionless number, the Reynolds number (see Table 2), based on the wavelength over the viscous length (i.e. the kinematic viscosity of the fluid ν over the friction velocity u_*). The friction velocity used for the velocity scale [150] is based on the wall shear stress such as $u_* = (\tau_w/\rho_f)^{1/2}$ with ρ_f, the fluid density. However, this approach does not allow the exact determination of the growth time of the patterns, which in this case do not emerge from an initially perfectly flat surface. In order to promote the appearance of patterns, the authors dug grooves transverse to

the flow at regular intervals to disrupt the flow. Nevertheless, according to the authors, these initial disturbances to the topography did not appear to affect either the wavelengths or the final profiles, as demonstrated by the tests they were able to carry out by varying the distance between intervals for the same set of parameters. The patterns obtained evolved gradually by increasing or decreasing the wavelength initially imposed by the grooves, in response to hydrodynamic instability.

A correlation has been established between dissolution waves (Figure 13(b)) and sublimation waves observed in the field (Figure 3(a)) and the analog sublimation experiment on CO_2 ice performed in an atmospheric wind tunnel [32] (Figure 13(c)). This theoretical study [11] is based on a 2D linear stability analysis of the coupled system between turbulent flow and mass transfer, following on from pioneer work [22,32,151]. It highlights the unstable wavelength range for solid bedforms by varying the Schmidt number, showing the dependence on it of the parameters involved in the dispersion relations (wavenumber λ, growth rate σ, angular frequency ω). The growth rate and angular frequency are functions of the wavelength-based Reynolds number ($Re_\lambda = \lambda u_* / 2\pi\nu = (k\nu/u_*)^{-1} = k_+^{-1}$), and a positive growth rate is found in the transitional near-wall regime, whereas modes in the turbulent or laminar regime decay due to their negative growth rate in the deep flow condition. The critical mode is the mode with the strongest positive growth rate, meaning that with time it will become the dominant wavelength visible on the ice surface. The dimensionless values of this critical growth rate, wave number and angular frequency are found numerically, and can be dimensionalised to give rise to three scaling laws:

$$\lambda_c = \frac{\nu}{u_*} \frac{2\pi}{k^+_{c,\mathrm{ref}}} Sc^{1/5} \tag{37}$$

$$v_c = \frac{\omega^+_{c,\mathrm{ref}}}{k^+_{c,\mathrm{ref}}} \frac{q_0}{\rho_\mathrm{s}} \tag{38}$$

$$t_c = \frac{1}{\sigma^+_{c,\mathrm{ref}}} \frac{\rho_\mathrm{s}}{q_0} \frac{\nu}{u_*} Sc^{1/6} \tag{39}$$

with $k^+_{c,\mathrm{ref}} = 6.7 \times 10^{-3}$, $\omega^+_{c,\mathrm{ref}} = 0.013 \times 10^{-3}$, $\sigma^+_{c,\mathrm{ref}} = 8.9 \times 10^{-3}$ where reference values are given for $Sc = 1$ [11]. The first scaling law links the friction velocity to the critical wavelength that correspond to the most amplified mode. The second scaling law links the migration velocity to the ablation rate. The third scaling law combines the ablation rate and friction velocity estimated before into formation timescale, allowing to constrain the age of the surface.

Similar work could be carried out to extend the database in order to include melting bedforms [30,31,152,153]. Experimental works showed that under turbulent flow conditions, ice-water ripple patterns developed in response to an initial perturbation in the ice interface. While the topography was initially disturbed in previous experiments from Gilpin et al. [153], recent experimental work form Bushuk et al. [154] shows that the waves can develop from an initially flat bed with millimeter-scale imperfections but observes the formation of these patterns in the same flow regime known as laminar–turbulent transition based on Re_λ. These two-dimensional ice waves, which develop perpendicularly to the direction of flow, migrate in the direction of flow, indicating that the maximum mass flux is not found in the troughs, but slightly upstream from the creation of these patterns (see Figure 13(a)). These patterns can then evolve into three-dimensional structures, known as ice-scallops. They identify 3 stages of the evolution, starting from the flat bed to the scalloped interface. Recirculating 3D effects could induce reinforcing feedback due to turbulence redistribution for the three component of the kinetic energy due to wall effect. They identify a length of the shear production zone that could

constrain the wavelength of the scalloped bedforms. Finally, we note that the understanding of the evolution of an initial flat bed by melting or dissolution remains an open question. The conditions of the flow and of the bed, which will give rise either to wavy bedforms perpendicular to the flow or to straight patterns parallel to the flow, are not known. The initial defects or bed preparation seem to play a crucial role. Yet, further experimental and theoretical studies seem necessary to elucidate the question.

4.2.2. *Shallow flow*

In shallow water, the flow may strongly depend on the thickness of the flow and may couple with channel shape or free surface deformation, which can promote the growth of specific patterns. The case of melting/dissolution in presence of shallow water has been mainly investigated experimentally in creeping flow regime in the context of fracture dissolution and in the context of wormhole formation in a soluble porous medium. We refer to the recent review of Ladd and Szymczak [113] for more information on the subject. In transport controlled regime, the fracture aperture in gypsum decreases with the distance [155]. However, especially in experiments with NaCl the general shape and small scale pattern formation occurs in presence of buoyancy instabilities [156–158], which have been already discussed in Section 4.1. For faster flows, the shallow water situation corresponds often to the case of thin films flows, which occur in the nature as the run-off caused by the rainfalls. In this case the water free-surface dynamics may affect the pattern emergence and its evolution with time.

To our knowledge, among the diversity of *Karren* patterns (see Section 2.4) only the generation of *Rillenkarren* has been reported in quantitative experiments. Around 1980, Glew and Ford [15] applied artificial rain with an intensity about 35 mm/h upon molded plaster blocks of various inclination, leading to film flows about 100 μm depth. After several hundred hours an array of parabolic centimeters wide grooves were obtained. Their cross sections are well approximated by parabola. Sharp ridges separate the rills. The grooves disappear at the bottom of the blocks, when the film thickness exceeds approximately 150 μm. The obtained morphology resembles thus well to natural *Rillenkarren* reported on limestone. The authors estimate that an important condition to generate these pattern consists in the impact of the rain droplets on the water film, which may generate small scale turbulence and efficient solute mixing in the film. With a similar protocol, some morphological difference on the rain flutes development are found as a function of the water temperature (24 °C and 45 °C) [16]. More recently, Guerin et al. [17] demonstrate that dissolution grooves appear without drop impacts, by subjecting inclined soluble plates to runoff water flows. For flowing film of homogeneous thickness of order 200 μm, nearly parallel rills of similar width appear after few minutes on pink salt plates and after few hours on plaster plates (see Figure 14). Their width and depth increase linearly with time by pattern coarsening, until their crests emerge and channelize the flow, leading a slower increase of channel width. The initial typical channel width (of order 0.5 mm) appears to be proportional to the water film thickness, which is set by the hydrodynamic conditions. By rescaling the measured channel width and depth by the film thickness, the experimental points obtained for different flow parameters values and during all the experiment duration (few 10 h for plaster) gather on one master curve. Two formation scenarios have been proposed, a bed instability mechanism and an imprint of flow structures. In the first case, a locally greater fluid depth corresponds to a higher flow velocity, which increases the local dissolution rate. Any perturbation is thus amplified, leading to a linear instability of the bed. In the second scenario, a streamwise modulation of the flow velocity would produce a modulation of the dissolution rate, which could explain the linear growth of pattern amplitude with time. Recent theoretical studies [25,26] investigate more thoroughly the first scenario. The spontaneous emergence of rills is confirmed. The initial pattern wavelength selection arises from a balance between the film flattening at large scale by gravity and capillarity

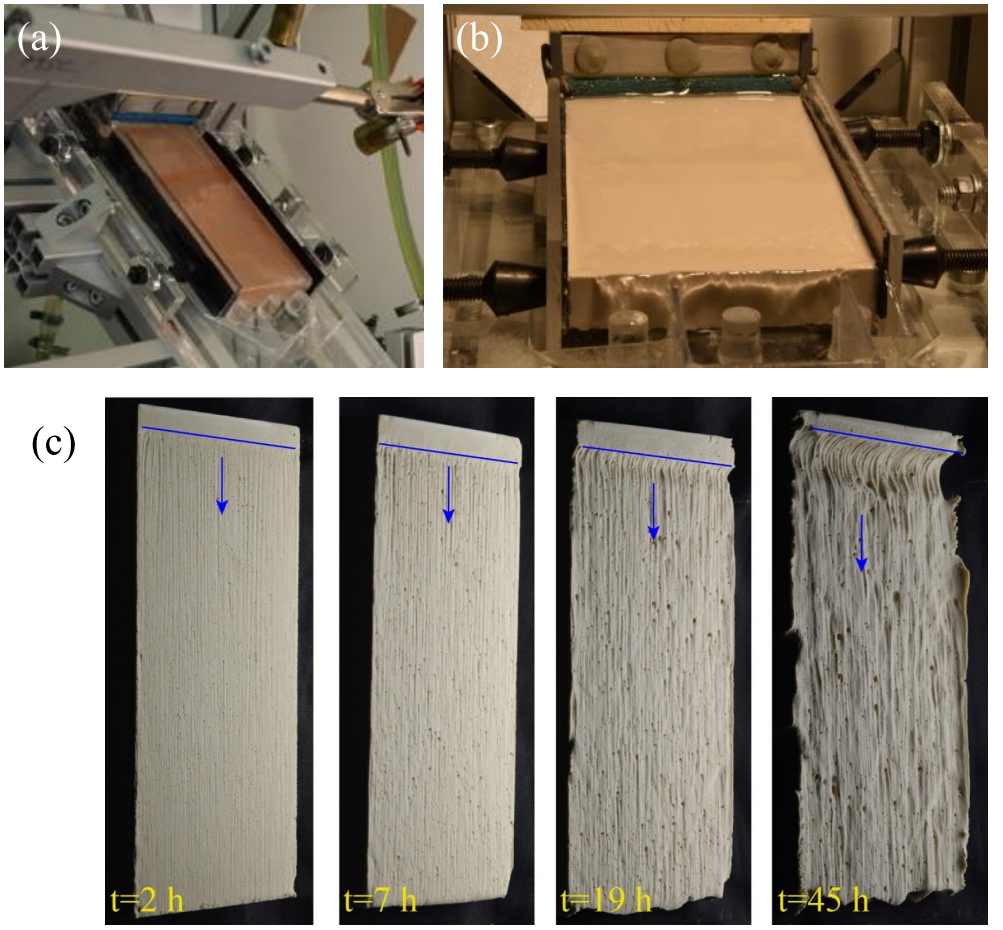


Figure 14. (a) Side view of the experimental setup of Guerin et al. [17] with a block of pink Himalayan salt. (b) Front view. A homogeneous film of streaming water flows on a plaster block. (c) Evolution of the surface of a plaster block subjected to a runoff water film in the experiment. Flow rate 2.8 L/min, inclination 39°, average velocity 0.84 m/s. A pattern of dissolution grooves develops progressively in the direction of flow. Reproduced by permission of the American Physical Society.

and the viscosity that acts as a low-pass space filter for small scale perturbations. However, the comparison with experiments and the field remains challenging, because once the pattern becomes noticeable with naked eye, its amplitude is likely large enough to perturb the flow hydrodynamics of the thin film. The regime of validity of the linear instability analysis would be limited to short times. Finally, we note that in the field, the age of the *Karren* are not precisely known, as well as the meteorological conditions that accompanied their formation. Further experimental and numerical studies are required to identify the mechanisms explaining the emergence of *Rillenkarren* and their long term evolution.

Although less investigated in the literature, dissolution patterns emerging from runoff flows have also some counterparts generated by melting. In particular, at the surface of glaciers, the meltwater is channelized into liquid water streams [159]. The flow in these channels may increase the heat exchange and thus their depths by enhancing melting. Mantelli et al. [160] proposed an

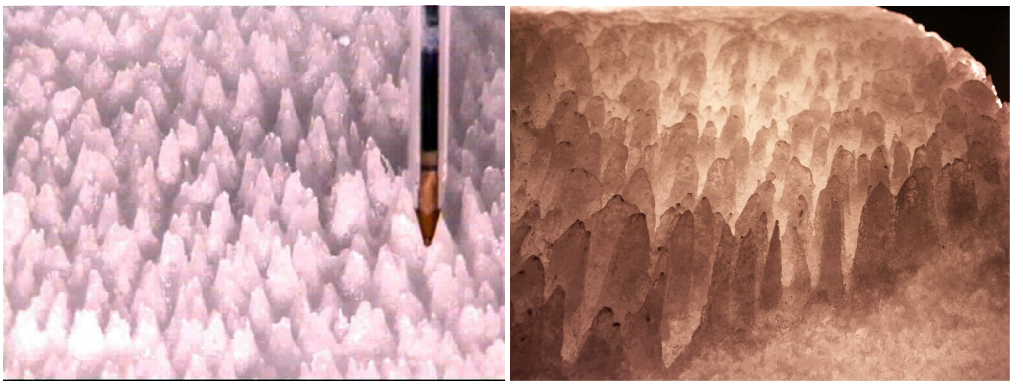


Figure 15. *Penitentes* in a laboratory scale experiment (from Bergeron et al. [161], reproduced by permission of the American Physical Society).

explanation of the regular spacing between the ice streams by a linear stability analysis coupling the bed topography, the water flow and the heat transport. To our knowledge, no laboratory experiments have been reported in the literature. Finally, we note that the ice streams are an equivalent of the *Rinnenkarren* for dissolution. An analog of *Rillenkarren* is missing. Arrays of adjacent parallel grooves on steep slopes do not seem indeed commonly observed. The reason of this statement deserves also further studies.

4.3. *Pattern formation stimulated by radiation*

The heat required for melting or sublimation can come largely from the absorption of light, which is often the case in glaciers under sublimation conditions or where the ambient temperature is low. Then, modulation in albedo, or exposure to light, plays an important role in the formation of patterns such as penitentes (Figure 1(a)), glacier tables or dirt cones (Figure 6).

Penitentes have been reproduced in a laboratory scale experiment by Bergeron et al. [161]. A block of snow was kept in a chamber with a plexiglas cover at low temperature in a dried air environment (relative humidity was typically between 5 and 10%) and illuminated from above with a 120 W lamp, disposed outside the chamber. In sublimation conditions, for temperature between −10 and −20 °C, penitentes appeared after two hours of irradiation with a characteristic of a few millimeters (Figure 15). In melting conditions, above −4 °C, no structures were observed. In sublimation condition, under −35 °C, no penitentes formed after irradiation time as long as ten hours. Authors suggest that the block may be saturated in water vapor because vapor pressure of water rapidly decreases with temperature below 0 °C. They also report that a breeze of 2.5 m/s above the snow prevents penitentes formation. Authors propose that initial pattern are the smallest possible ablation structures, which are limited by the optical extinction length (characteristic length on which light is absorbed in the snow) [42,161]. The optical extinction length depends on particle radius and ice volume fraction in the snow, and is estimated to be of the order of 1 mm in their experiment [161].

Pattern formation is generally ascribed to a geometric coupling between light absorption and topography: light absorption is greater at troughs than at peaks [41,42,162,163]. Claudin et al. did a linear stability analysis and found two driving mechanisms: the above mentioned geometric effect but also a Mullins–Sekerka type mechanism [46,164]. Since the light is absorbed by the snow (or ice) on a given distance from the interface, and the temperature of the interface is held at

the (cold) ambient air temperature, the temperature increases with depth in the snow. This drives a heat flux in the snow toward the interface, which is greater at troughs than at peaks. In their calculation, the balancing stabilizing effect comes from vapor diffusion, which authors arbitrarily limit to a boundary layer of finite thickness, thereby providing the characteristic wavelength of the instability and pattern formation [46]. Authors suggest that this characteristic thickness could be set by wind, forcing turbulent mixing above a certain height above the snow. However, this seems to be challenged by the observation of Bergeron et al. [161]. Cohen et al. proposed that this length scale could be set by a solutal Rayleigh–Bénard instability, because density of water vapor is less than density of air [21]. This instability in the buoyancy-driven vapor flow would prevail over other mechanisms in initiating the pattern and selecting the wavelength of formation.

Patterns are not exclusively shaped by instabilities. Recognizable structures can also be formed by differential ablation due to specific boundary conditions, such as the interaction with a non-melting (or less eroding) cover. This is the case for fairy chimneys (also named hoodoo), glacier tables, dirt cones, and zen stone, for example (Figure 6). Here we review recent laboratory experimental works that have addressed the formation of glacier tables, dirt cones, and zen stone described in Section 2.6, Figure 6.

Hénot et al. have studied the formation of glacier tables and, in particular, the conditions for their formation [84]. They followed the melting of an ice sheet partially covered by a cylindrical cap made of different materials and with different height-to-radius aspect ratios. The ice melts at room temperature (25 °C) due to infrared radiation from the walls (at room temperature) and convection in the air (because cold air at the ice interface is denser than the air at room temperature). They found that, depending on the cap material, the cap may sink into the ice sheet or a glacier table may form, which corresponds to the ice under the cap melting faster or slower than the surrounding sheet, respectively (Figure 16). They explained the onset of table formation by the competition between two effects. On the one hand, the cap insulates the underlying ice because the cap temperature is higher than the ice temperature, which decreases the infrared radiative influx (and increases the infrared radiative outflux) and the convective flux. On the other hand, the cap exposes a larger area to the incoming heat than the covered (contact) area, which may increase the (conductive) heat flux to the covered ice. The relative weight of these two effects depends on the thermal conductivity of the cap the material. The conductive flux (from the cap to the ice) decreases and the cap temperature (and insulation) increases as the thermal conductivity decreases, which is favorable for table formation. This modeling proved to be predictive in the field [85].

Hénot et al. used the same approach to study the formation of dirt cones: they followed the melting at room temperature of an ice sheet partially covered with a pile of plastic grains [86]. Differential melting resulted in the formation of an ice cone covered by a granular layer. The authors explain the formation of dirt cones (Section 2.6, Figure 6), not directly by the dependence of the melting rate on the debris thickness [89], but by the same mechanisms as for glacier tables with the additional coupling to the granular medium: as the cone forms, the exposed capped area increases and the shape can reach a steady state [86,165].

Taberlet and Plihon have studied the formation of zen stones by ice (differential) sublimation in a lyophilizer [166]. The initial flat ice sheet is partially covered with a 3 cm-diameter 5 mm-thick disk. Using various metals for the covering disk, they showed that the material conductivity is of little importance in the formation of zen stone. They observed the formation of a zen stone for aluminum, grooved aluminium, and copper disks. They conclude that the main mechanism is an umbrella effect, the covering disk shields the ice from external radiations [166].

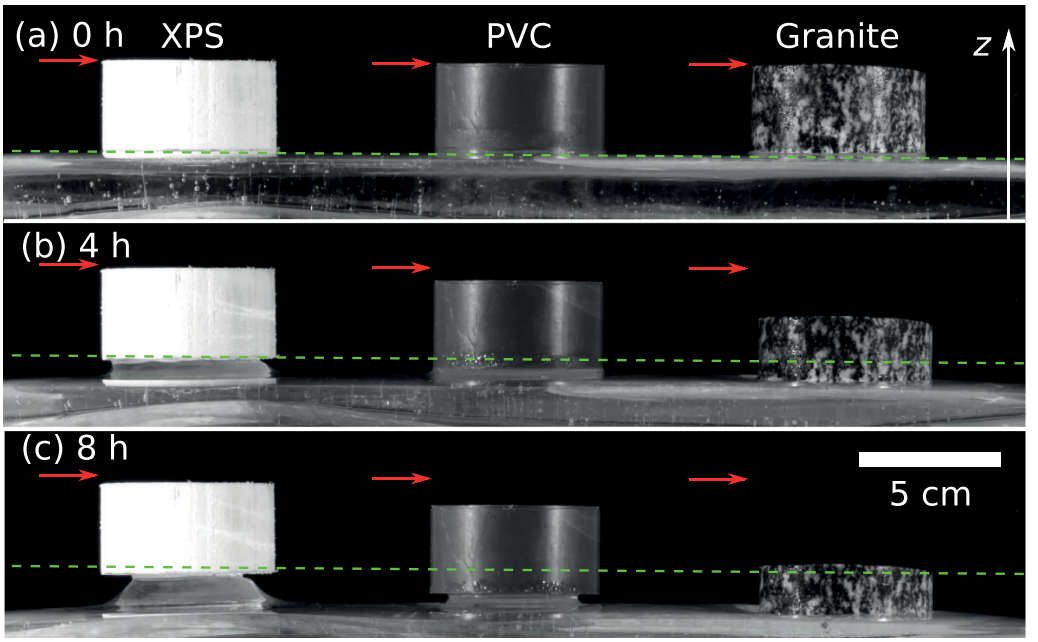


Figure 16. Ice underlying cylindrical caps melts faster or slower than the surrounding ice sheet depending on the cap material (from Hénot et al. [84], reproduced by permission of the American Physical Society).

5. Discussion and conclusions

5.1. *Solid bedforms as imprint of flow structures*

The objectives of this review paper were: (i) to examine the natural bedforms induced by phase change that occur at the solid surface of Earth and of planets and (ii) to demonstrate how laboratory experiments can contribute to a better understanding of the pattern formation and their evolution. These bedforms are produced largely by the combined action of a flow and a phase change, which may be melting, dissolution, or sublimation. Although the phase changes at work are not the same, the natural objects inventoried in this study have similar shapes, whether the substrate is rock or ice. We proposed a classification of patterns in the field, based on morphologic indicators, into 6 categories: sharp patterns, polygonal depression, crested bedforms perpendicular or parallel to the flow, stepped patterns, and structures due to capping. Then, we presented the theoretical framework for modeling the interaction between a flow and a phase change, with the objective of elucidating the evolution of the solid/fluid interface and the emergence of patterns. Subsequently, a review of the previous experimental studies in the literature reporting bedforms was conducted, and a classification of experiments has been established based on the type of flow (flow generated by the phase change or imposed externally) or boundary conditions.

To be able to relate the classification of these shapes to that of the type of flow (forced and natural convection) and boundary conditions, it is necessary to consider whether some of these shapes form part of a continuum or not. For example, by experimentally reproducing in a controlled environment ice scallops in a water-tunnel under unidirectional turbulent flow [153], 2D structures similar to the sublimation ripples observed in blue ice-areas in Antarctica, were

initially obtained, some of which subsequently evolved into 3D structures. There could therefore be a continuum between these forms, which would explain why they all line up with the curve proposed by Thomas [6]. In addition, these scallops exist in both forced and natural convection flows, and one can ask if there is a morphometric parameter that could provide insight into the competition between inertia and buoyancy? The dynamic nature of these objects, which propagate downstream (forced convection) or upstream (natural convection), should help to refine the processes involved and better understand the environments in which they were formed.

5.2. *Effect of non-linearities on the resulting bedform*

Among the solid bedforms in ablation, some of them are generated by instabilities of the flow or of the bed that can initiate a characteristic scale related to the parameters of the flow. However, as the pattern amplitude grows several effects must be taken into account to explain its shape at a given time, and these often cannot be analyzed linearly. Firstly, geometric coarsening occurs when the small structures are absorbed by the large ones. By this merging process, the characteristic wavelength increases with time. A measured pattern size must be put in relation with the pattern age. This effect has been particularly evidenced in laboratory experiments [17] and interface evolution models [111]. In addition, other geometric focusing effects can lead to crest formations by normal ablation. This phenomenon initially proposed by A. Lange in the fifties to explain the scallop shapes in limestone wall [167] has been recently revisited by Chaigne et al. [111]. They have shown that any ablation process on an interface displaying sign changes of curvatures will show in finite time emergence of singularities, i.e. discontinuities of the gradient. This effect can explain, why the sinusoidal patterns predicted by linear instability mechanism evolve generically to structures with sharp tips and crests. Although the singularities are regularized at small scale by material properties or the boundary layer hydrodynamics, this concept describes well the qualitative shape of a solid surface undergoing an ablation process like melting, dissolution or sublimation.

Once a pattern has reached a sufficient size, it can retroact on the flow that created it. In the case of the patterns emerging from a bed instability like for the mechanisms proposed for scallops [22] in turbulent flows or for Rillenkarren by run-off [17,25,26], this mechanism is a part of the instability mechanism. The pattern amplitude increases the flow modulation, which amplifies in turn the pattern growth. However, the saturation of the instability relies often on nonlinear mechanisms, which may involve higher order terms in amplitude equations [168]. Physically, a nonlinear feedback can decrease the flow modulation, once the pattern amplitude exceeds a characteristic scale, typically the boundary layer thickness of the relevant field (temperature, solute concentration, vapor concentration), the free-surface in thin films or the system size. For patterns emerging by an instability of the flow like those created by from Rayleigh–Bénard convection [21,112,133], the hydrodynamic feedback is more complex. In linear regime, the surface is a fingerprint of the flow structures. However, we noted the need of plumes position locking to explain the emergence of coherent dissolution [21] or melting patterns [169]. These effects are currently not well addressed quantitatively and deserve further study.

Hydrodynamic focusing constitutes a more specific situation of feedback of the pattern topography on the flow. For example, in a free-surface flow, once separated channels have been formed, they will collect more water, until a drainage network emerges. This phenomenon is more described for rivers carved by erosion, but analogous cases occur by dissolution like the *Rinnenkarren* [55] on limestone pavements or by melting like the ice streams on Glacier [160].

The nonlinear study of ablation pattern in nature could constitute the next step of future researches.

5.3. *On the use of scaling laws for planetary applications*

Because of the large timescale required to form natural solid bedforms, the choice of analogous materials that enable to sustain experimental timescale is a real challenge. In this context, experiments on the dissolution of plaster, caramel, sugar or salt have provided an opportunity to explore a wide range of natural bedforms under different flow conditions (deep flow, free surface flow, buoyancy driven flow with or without stable stratification). It is then possible to reproduce most of the natural shapes identified, such as sharp-edged, crested bedforms parallel or perpendicular to the flow, and scalloped. To our knowledge, stepped bedforms have not yet been reproduced in dissolution, to date just in melting [24]. For cyclic steps (Section 2.5, Figure 5), therefore, modelling and comparing models with laboratory experiments has only been tackled to a limited extent. Other experimental studies in melting concern crested bedforms parallel to the flow and scallops [153,154]. Experiments in sublimation are difficult to implement, requiring highly constrained environments (temperature, humidity, hygrometry). As a result, they only exist for penitentes and crested bedforms perpendicular to the flow, without any systematic exploration of the parameters involved.

However, sublimation dominates on many icy surfaces of planetary bodies. Therefore, complementary phase change studies would provide additional databases that could be useful for validating scaling laws that are commonly used in planetology. Further work is needed both on modeling and on comparative analogue studies between different phase changes to confirm some of these scaling laws. A first step in this direction has been initiated by Carpy et al. [11], in the case of crested waves perpendicular to the flow direction, considering dissolution and sublimation. They use sublimation and dissolution database to validate scaling laws obtained theoretically on the basis of a linear stability analysis of the coupled system of equations between mass transfer and the turbulent boundary layer in a deep flow case. Further development is required to include melting database. These scaling laws link the friction velocity to the critical wavelength and the critical migration velocity to the sublimation rate. The third scaling law that combines the sublimation rate and friction velocity estimated before into a sublimation wave formation timescale, allowing to constrain the age of the ice surface has yet to be validated. Before applying scaling laws to planetary surfaces, it is necessary to bear in mind the constraints on the use of these laws, independently of the non-linear effects discussed in the previous paragraph (5.2). In the case of *penitentes* (Section 2.1, Figure 1(a)), new experiments (and models) are needed to understand the role of fluid flow in their formation in order to ascertain if buoyancy-driven vapor flow plays a role in their formation as suggested by Cohen et al. [21].

5.4. *Concluding remarks*

Although geomorphology and planetology have been the main motivation for the experimental studies reported here, they raise fundamental questions that combine several fields, including hydrodynamics, thermodynamics, materials science, nonlinear physics, and morphogenesis. Laboratory-scale experiments are key to understanding the role of flows in the formation processes and dynamics of these solid bedforms undergoing ablation phase change. Since experiments take place over shorter timescales, forcings and boundary conditions can be tested. As we have seen from the various experiments collected, these solid bedforms correspond to imprints of the flow, driven either by boundary conditions, by instabilities intrinsic to the flow, or by instabilities associated with a perturbation of the topography at the interface. This is an important distinction. However, the non-linear pattern dynamics and geometric effects result in a time evolution of the pattern, with a typical slow increase in characteristic length scales through coarsening and the occurrence of sharp structures. In some specific cases, in particular when the

pattern emergence can be explained by a linear instability mechanism of the interface, scaling laws can be derived relating the typical bedform length to hydrodynamic parameters.

Comparing phase changes with each other provides a better understanding of the processes occurring at the interface, and allows to investigate the large dimensionless numbers and different scales involved. Due to the complex nature of the flow or the complicated boundary conditions, as well as the geometric shapes of natural objects, numerical simulations are limited, so experiments play a key role. Many natural pattern shapes have not yet been addressed, which could lead to new experimental projects. In addition, further experimental studies are required to address some pending questions, such as the evolution of a flat, dissolving or melting bed in the presence of a turbulent flow. Similar work could be carried out on accumulation patterns (solidification, precipitation, condensation). In this case, will the change in the sign of the transfer lead to a "photo negative", or will this have an effect on the shape, size and diversity of the patterns obtained? This question opens up new experimental perspectives to be explored. Improving models through the laboratory experiments could help predict landscape evolution or infer past conditions from patterns.

Declaration of interests

The authors do not work for, advise, own shares in, or receive funds from any organization that could benefit from this article, and have declared no affiliations other than their research organizations.

Funding

SC is supported by French Research Council project through grant *SHERPAS ANR-23-CE49-0006*. MB, MC and SCdP are supported by French Research Council project through grant *PhysErosion ANR-22-CE30-0017*. We thank M. Bordiec and O. Bourgeois for scientific discussion on natural examples.

References

[1] F. Pascheke, J. F. Barlow and A. Robins, "Wind-tunnel modelling of dispersion from a scalar area source in urban-like roughness", *Bound.-Layer Meteorol.* **126** (2008), no. 23, pp. 103–124.

[2] C. Combs, N. T. Clemens and P. M. Danehy, "Development of naphthalene PLIF for visualizing ablation products from a space capsule heat shield", in *52nd Aerospace Sciences Meeting*, American Institute of Aeronautics and Astronautics: Reston, 2014. AIAA 2014-1152. Online at https://arc.aiaa.org/doi/10.2514/6.2014-1152 (accessed January 31, 2025).

[3] G. Hochrein and G. Wright Jr., "Analysis of the TATER nosetip boundary layer transition and ablation experiment", in *14th Aerospace Sciences Meeting*, American Institute of Aeronautics and Astronautics: Reston, 1976. AIAA 1976-167. Online at https://arc.aiaa.org/doi/abs/10.2514/6.1976-167 (accessed January 31, 2025).

[4] S. P. Schneider, "Laminar-turbulent transition on reentry capsules and planetary probes", *J. Spacecr. Rockets* **43** (2006), no. 6, pp. 1153–1173.

[5] T. C. Lin and P. Qun, "On the formation of regmaglypts on meteorites", *Fluid Dyn. Res.* **1** (1987), no. 3-4, pp. 191–199.

[6] R. M. Thomas, "Size of scallops and ripples formed by flowing water", *Nature* **277** (1979), pp. 281–283.

[7] I. B. Smith, J. W. Holt, A. Spiga, A. D. Howard and G. Parker, "The Spiral troughs of Mars as cyclic steps", *J. Geophys. Res.: Planets* **118** (2013), no. 9, pp. 1835–1857.

[8] J. E. Moores, C. L. Smith, A. D. Toigo and S. D. Guzewich, "Penitentes as the origin of the bladed terrain of Tartarus Dorsa on Pluto", *Nature* **541** (2017), no. 7636, pp. 188–190.

[9] N. Mangold, "Ice sublimation as a geomorphic process: A planetary perspective", *Geomorphology* **126** (2011), no. 1-2, pp. 1–17.

[10] A. Ohmura, "Cryosphere during the twentieth century", *Geophys. Monogr. Ser.* **150** (2004), pp. 239–257.

[11] S. Carpy, M. Bordiec and O. Bourgeois, "Scaling laws for ablation waves formed by ice sublimation and rock dissolution: applications to the Earth, Mars and Pluto", *Front. Astron. Space Sci.* **10** (2023), article no. 1176158.
[12] D. Ford and P. D. Williams, *Karst Hydrogeology and Geomorphology*, John Wiley & Sons, Springer: Netherlands, 2007.
[13] M. T. Kozary, J. C. Dunlap and W. E. Humphrey, "Incidence of saline deposits in geologic time", in *Saline Deposits: A Symposium based on Papers from the International Conference on Saline Deposits, Houston, Texas, 1962* (R. B. Mattox, W. T. Holser, H. Ode, W. L. McIntire, N. M. Short, R. E. Taylor and D. C. Van Siclen, eds.), Geological Society of America: New York, 1968, pp. 43–57.
[14] F. Gallaire and P. T. Brun, "Fluid dynamic instabilities: Theory and application to pattern forming in complex media", *Philos. Trans. R. Soc. A: Math. Phys. Eng. Sci.* **375** (2017), no. 2093, pp. 1–44.
[15] J. R. Glew and D. C. Ford, "A simulation study of the development of Rillenkarren", *Earth Surf. Process.* **5** (1980), no. 1, pp. 25–36.
[16] T. Slabe, A. Hada and M. Knez, "Laboratory modeling of karst phenomena and their rock relief on plaster, subsoil karren, rain flutes karren and caves", *Acta Carsologica* **45** (2016), no. 2, pp. 187–204.
[17] A. Guérin, J. Derr, S. Courrech du Pont and M. Berhanu, "Streamwise dissolution patterns created by a flowing water film", *Phys. Rev. Lett.* **125** (2020), no. 19, article no. 194502.
[18] J. R. L. Allen, "Bed forms due to mass transfer in turbulent flows: a kaleidoscope of phenomena", *J. Fluid Mech.* **49** (1971), no. 1, pp. 49–63.
[19] M. F. Goodchild and D. C. Ford, "Analysis of scallop patterns by simulation under controlled conditions", *J. Geol.* **80** (1972), no. 1, pp. 121–122.
[20] P. N. Blumberg and R. L. Curl, "Experimental and theoretical studies of dissolution roughnesses", *J. Fluid Mech.* **65** (1974), no. 4, pp. 735–751.
[21] C. Cohen, M. Berhanu, J. Derr and S. Courrech du Pont, "Buoyancy driven dissolution of inclined blocks: Erosion rate and pattern formation", *Phys. Rev. Fluids* **5** (2020), article no. 053802.
[22] P. Claudin, O. Durán and B. Andreotti, "Dissolution instability and roughening transition", *J. Fluid Mech.* **832** (2017), no. R2, pp. 1–14.
[23] C. Camporeale and L. Ridolfi, "Ice ripple formation at large Reynolds numbers", *J. Fluid Mech.* **694** (2012), pp. 225–251.
[24] M. Yokokawa, N. Izumi, K. Naito, G. Parker, T. Yamada and R. Greve, "Cyclic steps on ice", *J. Geophys. Res. F: Earth Surf.* **121** (2016), no. 5, pp. 1023–1048.
[25] M. B. Bertagni and C. Camporeale, "The hydrodynamic genesis of linear karren patterns", *J. Fluid Mech.* **913** (2021), article no. A34.
[26] S. Djambov and F. Gallaire, "Boundary-layer approach to the linear karren instability", *J. Fluid Mech.* **977** (2023), article no. R3.
[27] C. B. Thorsness and T. J. Hanratty, "Stability of dissolving or depositing surfaces", *AIChE J.* **25** (1979), no. 4, pp. 697–701.
[28] P. Y. Chan and N. Goldenfeld, "Steady states and linear stability analysis of precipitation pattern formation at geothermal hot springs", *Phys. Rev. E* **76** (2007), no. 4, pp. 1–11.
[29] C. Camporeale and L. Ridolfi, "Hydrodynamic-driven stability analysis of morphological patterns on stalactites and implications for cave paleoflow reconstructions", *Phys. Rev. Lett.* **108** (2012), no. 23, pp. 1–5.
[30] G. D. Ashton and J. F. Kennedy, "Ripples on the underside of river ice covers", *J. Hydraul Eng.* **98** (1972), pp. 1603–1624.
[31] G. D. Ashton, "Turbulent heat transfer to wavy boundaries", in *Proceedings of the Heat Transfer and Fluid Mechanics Institute*, 1972, pp. 200–213.
[32] M. Bordiec, S. Carpy, O. Bourgeois, et al., "Sublimation waves: Geomorphic markers of interactions between icy planetary surfaces and winds", *Earth-Sci. Rev.* **211** (2020), article no. 103350.
[33] J. R. L. Allen (ed.), *Sedimentary Structures, Their Character and Physical Basis*, Developments in Sedimentology, Elsevier: Amsterdam, Oxford, New York, 1982, p. 592.
[34] G. C. Amstutz, "On the formation of snow penitentes", *J. Glaciol.* **3** (1958), no. 24, pp. 304–311.
[35] K. E. Sinclair and S. MacDonell, "Seasonal evolution of penitente glaciochemistry at Tapado Glacier, Northern Chile", *Hydrol. Process.* **30** (2016), no. 2, pp. 176–186.
[36] N. E. Odell, "Ablation at high altitudes and under high solar incidence", *Am. J. Sci.* **239** (1941), no. 5, pp. 379–382.
[37] J. M. Moore, A. D. Howard, O. M. Umurhan, et al., "Bladed Terrain on Pluto: Possible origins and evolution", *Icarus* **300** (2018), pp. 129–144.
[38] D. E. J. Hobley, J. M. Moore, A. D. Howard and O. M. Umurhan, "Formation of metre-scale bladed roughness on Europa's surface by ablation of ice", *Nat. Geosci.* **11** (2018), no. 12, pp. 901–904.
[39] K. P. Hand, D. Berisford, T. Daimaru, J. Foster, A. E. Hofmann and B. Furst, "Penitente formation is unlikely on Europa", *Nat. Geosci.* **13** (2020), no. 1, pp. 17–19.

[40] D. E. J. Hobley, J. M. Moore, A. D. Howard and O. M. Umurhan, "Reply to: Penitente formation is unlikely on Europa", *Nat. Geosci.* **13** (2020), no. 1, pp. 20–21.
[41] L. Lliboitry, "The origin of penitents", *J. Glaciol.* **2** (1954), no. 15, pp. 331–338.
[42] M. D. Betterton, "Theory of structure formation in snowfields motivated by penitentes, suncups, and dirt cones", *Phys. Rev. E* **63** (2001), no. 5, article no. 056129.
[43] S. Hastenrath and B. Koci, "Micro-morphology of the snow surface at the Quelccaya ice cap, Peru", *J. Glaciol.* **27** (1981), no. 97, pp. 423–428.
[44] F. E. Matthes, "Ablation of snow-fields at high altitudes by radiant solar heat", *Trans. Am. Geophys. Union* **15** (1934), article no. 380.
[45] M. D. Betterton, "Theory of structure formation in snowfields motivated by penitentes, suncups, and dirt cones", *Phys. Rev. E* **63** (2001), no. 5, pp. 1–12.
[46] P. Claudin, H. Jarry, G. Vignoles, M. Plapp and B. Andreotti, "Physical processes causing the formation of penitentes", *Phys. Rev. E* **92** (2015), no. 3, article no. 033015.
[47] M. Veress, Z. Zentai, K. Péntek, Z. Mitre, G. Deák and S. Samu, "Flow dynamics and shape of rinnenkarren systems", *Geomorphology* **198** (2013), pp. 115–127.
[48] J. M. Huang, J. Tong, M. Shelley and L. Ristroph, "Ultra-sharp pinnacles sculpted by natural convective dissolution", *Proc. Natl. Acad. Sci. USA* **117** (2020), no. 38, pp. 23339–23344.
[49] M. Bordiec, *Formation d'ondes topographiques par transfert de masse et diffusion dans un écoulement turbulent : analyse d'exemples naturels terrestres et planétaires et modélisations*, PhD thesis, Nantes Université, 2020.
[50] R. Bintanja, "On the glaciological, meteorological, and climatological significance of Antarctic Blue Ice areas", *Rev. Geophys.* **37** (1999), no. 3, pp. 337–359.
[51] K. L. Carey, "Observed configuration and computed roughness of the underside of rive ice, St. Croix River, Wisconsin", *US Geol. Survey Prof. Pap.* **550** (1966), B192–B198.
[52] J. N. Salomon, "The tsingy karrenfields of Madagascar", in *Karst Rock Features: Karren Sculpturing* (A. Ginés, M. Knez, T. Slabe and W. Dreybrodt, eds.), Karst Research Institute, Založba ZRC, 2009, pp. 411–422.
[53] M. Day and T. Waltham, "The pinnacle karrenfields of Mulu", in *Karst Rock Features. Karren Sculpturing* (A. Ginés, M. Knez, T. Slabe and W. Dreybrodt, eds.), Karst Research Institute, Založba ZRC, 2009, pp. 423–432.
[54] M. Knez and T. Slabe, "Lithologic and morphological properties and rock relief of the Lunan stone forests", in *Karst Rock Features. Karren Sculpturing* (A. Ginés, M. Knez, T. Slabe and W. Dreybrodt, eds.), Karst Research Institute, Založba ZRC, 2002, pp. 259–266.
[55] A. Ginés, "Karrenfield Landscapes and Karren Landforms", in *Karst Rock Features, Karren Sculpturing* (A. Ginés, M. Knez, T. Slabe and W. Dreybrodt, eds.), Karst Research Institute, Založba ZRC, 2009, pp. 13–24.
[56] A. Frumkin, "Salt karst", in *Treatise on Geomorphology*, Academic Press: San Diego, CA, 2013, pp. 407–424.
[57] J. J. Rhodes, R. L. Armstrong and S. G. Warren, "Mode of formation of "ablation hollows" controlled by dirt content of snow", *J. Glaciol.* **33** (1987), no. 114, pp. 135–139.
[58] M. C. Malin and K. S. Edgett, "Mars global surveyor Mars orbiter camera: Interplanetary cruise through primary mission", *J. Geophys. Res.* **106** (2001), no. E10, pp. 23429–23570.
[59] S. Milkovich, "Surface textures of Mars' north polar layered deposits: A framework for interpretation and future exploration", *Mars J.* **2** (2006), pp. 21–45.
[60] M. E. Banks, S. Byrne, K. Galla, et al., "Crater population and resurfacing of the Martian north polar layered deposits", *J. Geophys. Res. E: Planets* **115** (2010), no. 8, pp. 1–11.
[61] M. Massé, O. Bourgeois, S. Le Mouélic, C. Verpoorter, L. Le Deit and J. P. Bibring, "Martian polar and circumpolar sulfate-bearing deposits: Sublimation tills derived from the North Polar Cap", *Icarus* **209** (2010), no. 2, pp. 434–451.
[62] M. W. Telfer, E. J. R. Parteli, J. Radebaugh, et al., "Dunes on Pluto", *Science* **360** (2018), no. 6392, pp. 992–997.
[63] P. Bella, "Morphology of ice surfaces in the Dobšiná Ice Cave", in *Proceedings of the 2nd International Workshop on Ice Caves* (S. Turri and J. Zelinka, eds.), Slovak Caves Administration: Liptovský Mikulá, 2006, pp. 15–23. Online at http://www.ssj.sk/en/user_files/IWIC_2_15.pdf (accessed January 31, 2025).
[64] A. Persoiu and S.-E. Lauritzen (eds.), *Ice Caves*, Elsevier Inc.: Amsterdam, Oxford, Cambridge, 2018, p. 752.
[65] F. Obleitner and C. Spötl, "The mass and energy balance of ice within the Eisriesenwelt cave, Austria", *Cryosphere* **5** (2011), no. 1, pp. 245–257.
[66] A. Perşoiu, B. P. Onac and I. Perşoiu, "The interplay between air temperature and ice mass balance changes in Scărişoara Ice Cave, Romania", *Acta Carsologica* **40** (2011), no. 3, pp. 445–456.
[67] R. L. Curl, "Scallops and flutes", *Trans. Cave Res. Group of Great Britain* **7** (1966), no. 2, pp. 121–160.
[68] P. Marshall and M. C. Brown, "Ice in Coulthard Cave, Alberta", *Canad. J. Earth Sci.* **11** (1974), no. 4, pp. 510–518.
[69] P. Meakin and B. Jamtveit, "Geological pattern formation by growth and dissolution in aqueous systems", *Proc. R. Soc. A: Math. Phys. Eng. Sci.* **466** (2010), no. 2115, pp. 659–694.
[70] B.-P. Villien, Y. Zheng and D. H. Lister, "The scalloping phenomenon and its significance in flow-assisted corrosion", in *Proceedings of the Twenty Sixth Annual CNS-CNA Student Conference*, Canadian Nuclear Society:

Toronto, 2001, pp. 1–10. Online at https://www.nuceng.ca/univcomm/studconf2001/S16.PDF (accessed January 31, 2025).

[71] J. R. Allen, "Transverse erosional marks of mud and rock: their physical basis and geological significance", *Sediment. Geol.* **5** (1971), no. 3-4, pp. 167–385.

[72] O. Hammer, S. E. Lauritzen and B. Jamtveit, "Stability of dissolution flutes under turbulent flow", *J. Cave Karst Studies* **73** (2011), no. 3, pp. 181–186.

[73] I. Karcz and I. Zak, "Bedforms in salt deposits of the Dead sea brines", *J. Sediment. Res.* **57** (1987), no. 4, pp. 723–735.

[74] R. Bintanja, C. H. Reijmer and S. J. M. H. Hulscher, "Detailed observations of the rippled surface of Antarctic blue-ice areas", *J. Glaciol.* **47** (2001), no. 158, pp. 387–396.

[75] G. Weller, "The heat and mass balance of snow dunes on the central Antarctic plateau", *J. Glaciol.* **8** (1969), no. 53, pp. 277–284.

[76] M. Veress, "The KARREN and KARREN formation of bare slopes", *Earth-Sci. Rev.* **188** (2019), pp. 272–290.

[77] J. Lundberg and A. Ginés, "Rillenkarren", in *Karst Rock Features, Karren Sculpturing*, Karst Research Institute, Zalozba ZRC, 2009, pp. 185–210.

[78] B. Tourte, F. Chenu, L. Morel, et al., "Ruissellement et dissolution dun bassin versant lapiazé des karsts de Patagonie, île Tarlton, archipel de Madre de Dios (Chili)", *Collection EDYTEM. Cahiers de géographie* **19** (2017), no. 1, pp. 137–146. Included in a thematic issue: Monitoring en milieux naturels. Retours d'expériences en terrains difficiles.

[79] J. F. Kennedy, "The formation of sediment ripples, dunes, and antidunes", *Annu. Rev. Fluid Mech.* **1** (1969), pp. 147–168.

[80] N. Izumi, M. Yokokawa and G. Parker, "Incisional cyclic steps of permanent form in mixed bedrock-alluvial rivers", *J. Geophys. Res.: Earth Surf.* **122** (2017), no. 1, pp. 130–152.

[81] D. Mottershead, "Identification and mapping of rock weathering surface forms and features", *Zeitschrift für Geomorphologie Supplementband* **120** (2000), pp. 5–22.

[82] G. W. Evatt, C. Mayer, A. Mallinson, I. D. Abrahams, M. Heil and L. Nicholson, "The secret life of ice sails", *J. Glaciol.* **63** (2017), no. 242, pp. 1049–1062.

[83] A. C. Fowler and C. Mayer, "The formation of ice sails", *Geophys. Astrophys. Fluid Dyn.* **111** (2017), no. 6, pp. 411–428.

[84] M. Hénot, N. Plihon and N. Taberlet, "Onset of glacier tables", *Phys. Rev. Lett.* **127** (2021), no. 10, article no. 108501.

[85] M. Hénot, V. J. Langlois, J. Vessaire, N. Plihon and N. Taberlet, "Formation of glacier tables caused by differential ice melting: field observation and modelling", *Cryosphere* **16** (2022), no. 6, pp. 2617–2628.

[86] M. Hénot, V. J. Langlois, N. Plihon and N. Taberlet, "How dirt cones form on glaciers: Field observation, laboratory experiments, and modeling", *Phys. Rev. E* **107** (2023), no. 3, article no. 034905.

[87] G. Östrem, "Ice melting under a thin layer of moraine, and the existence of ice cores in moraine ridges", *Geografiska Annaler* **41** (1959), no. 4, pp. 228–230.

[88] L. E. Mattson, "Ablation on debris covered glaciers: an example from the Rakhiot Glacier, Punjab, Himalaya", *Snow Glacier Hydrol.* **218** (1993), pp. 289–296.

[89] G. W. Evatt, I. D. Abrahams, M. Heil, C. Mayer, J. Kingslake, S. L. Mitchell, A. C. Fowler and C. D. Clark, "Glacial melt under a porous debris layer", *J. Glaciol.* **61** (2015), no. 229, pp. 825–836.

[90] M. G. Worster, "Solidification of fluids", in *Perspectives in Fluid Dynamics - A Collective Introduction to Current Research* (G. K. Batchelor, H. K. Moffatt and M. G. Worster, eds.), Cambridge University Press: Cambridge, 2000, pp. 393–446. Online at http://www.itg.cam.ac.uk/people/grae/44.pdf (accessed January 31, 2025).

[91] S. L. Brantley, in *Kinetics of Water–Rock Interaction* (S. L. Brantley, J. D. Kubicki and A. F. White, eds.), Springer: New York, 2008.

[92] V. Alexiade and A. D. Solom, *Mathematical Modeling of Melting and Freezing Processes*, Hemisphere Publishing Corporation, Taylor & Francis: Washington DC, 1993.

[93] H. B. Callen, *Thermodynamics and An Introduction to Thermostatistics*, John Wiley & Sons: New York, Chichester, Brisbane, Toronto, Singapore, 1985.

[94] H. B. Aaron and G. R. Kotler, "The effects of curvature on the dissolution kinetics of spherical precipitates", *Metal Sci. J.* **4** (1970), no. 1, pp. 222–225.

[95] J. Colombani and J. Bert, "Holographic interferometry study of the dissolution and diffusion of gypsum in water", *Geochim. Cosmochim. Acta* **71** (2007), no. 8, pp. 1913–1920.

[96] I. W. Eames, N. J. Marr and H. Sabir, "The evaporation coefficient of water: a review", *Int. J. Heat Mass Transfer* **40** (1997), no. 12, pp. 2963–2973.

[97] C. Mas, *Modélisation physique du procédé de découpe de métaux par laser*, PhD thesis, 2003. Online at https://api.semanticscholar.org/CorpusID:169339509.

[98] K. J. Kossacki and J. Leliwa-Kopystynski, "Temperature dependence of the sublimation rate of water ice: Influence of impurities", *Icarus* **233** (2014), pp. 101–105.
[99] C. Truesdell and R. Toupin, "The classical field theories", in *Principles of Clasical Mechanics and Field Theory* (S. Flügge, ed.), Encyclopedia of Physics, Springer: New York, 1960.
[100] S. Chandrasekhar, *Hydrodynamic and Hydromagnetic Stability*, Clarendon Press: Oxford, 1961.
[101] D. R. Lide (ed.), *The Handbook of Chemistry and Physics*, CRC Press: Boca Raton, FL, 2004.
[102] S. Carpy and H. Mathis, "Modeling binary alloy solidification by a random projection method", *Numer. Methods Partial Differ. Equ.* **35** (2019), no. 2, pp. 733–760.
[103] M. Alkattan, E. H. Oelkers, J.-L. Dandurand and J. Schott, "Experimental studies of halite dissolution kinetics, 1 The effect of saturation state and the presence of trace metals", *Chem. Geol.* **137** (1997), no. 8, pp. 201–219.
[104] A. W. Woods, "Melting and dissolving", *J. Fluid Mech.* **239** (1992), pp. 429–448.
[105] A. Malyarenko, A. J. Wells, P. J. Langhorne, N. J. Robinson, M. J. Williams and K. W. Nicholls, "A synthesis of thermo-dynamic ablation at ice–ocean interfaces from theory, observations and models", *Ocean Model.* **154** (2020), article no. 101692.
[106] A. L. McCutchan and B. A. Johnson, "Laboratory experiments on ice melting: a need for understanding dynamics at the ice–water interface", *J. Marine Sci. Eng.* **10** (2022), no. 8, article no. 1008.
[107] C. Cenedese and F. Straneo, "Icebergs melting", *Annu. Rev. Fluid Mech.* **55** (2023), pp. 377–402.
[108] S. S. Pegler and M. S. Davies Wykes, "Shaping of melting and dissolving solids under natural convection", *J. Fluid Mech.* **900** (2020), article no. A35.
[109] J. Philippi, M. Berhanu, J. Derr and S. Courrech du Pont, "Solutal convection induced by dissolution", *Phys. Rev. Fluids* **4** (2019), article no. 103801.
[110] M. Nicklasson and A. Brodin, "The relationship between intrinsic dissolution rates and solubilities in the water–ethanol binary solvent system", *Int. J. Pharm.* **18** (1984), no. 1-2, pp. 149–156.
[111] M. Chaigne, S. Carpy, M. Massé, J. Derr, S. Courrech du Pont and M. Berhanu, "Emergence of tip singularities in dissolution patterns", *Proc. Natl. Acad. Sci. USA* **120** (2023), no. 48, article no. e2309379120.
[112] T. S. Sullivan, Y. Liu and R. E. Ecke, "Turbulent solutal convection and surface patterning in solid dissolution", *Phys. Rev. E* **54** (1996), no. 1, article no. 486.
[113] A. J. C. Ladd and P. Szymczak, "Reactive flows in porous media: challenges in theoretical and numerical methods", *Annu. Rev. Chem. Biomol. Eng.* **12** (2021), no. 1, pp. 543–571.
[114] F. Dutka, V. Starchenko, F. Osselin, S. Magni, P. Szymczak and A. J. C. Ladd, "Time-dependent shapes of a dissolving mineral grain: Comparisons of simulations with microfluidic experiments", *Chem. Geol.* **540** (2020), article no. 119459.
[115] M. D. Covington, "Calcite dissolution under turbulent flow conditions: a remaining conundrum", *Acta Carsologica* **43** (2014), no. 1, pp. 195–202.
[116] J. Chittenden, V. Chevrier, L. Roe, K. Bryson, R. Pilgrim and D. Sears, "Experimental study of the effect of wind on the stability of water ice on Mars", *Icarus* **196** (2008), no. 2, pp. 477–487.
[117] A. Lecoanet, F. Payot, C. Journeau, N. Rimbert and M. Gradeck, "Classification of ablation mode during impact of hot liquid jet on a solid", *Int. J. Heat Mass Transfer* **181** (2021), article no. 121883.
[118] S. H. Davis, U. Müller and C. Dietsche, "Pattern selection in single-component systems coupling Bénard convection and solidification", *J. Fluid Mech.* **144** (1984), pp. 133–151.
[119] J. Noel, C. Metivier, S. Becker and S. Leclerc, "Natural convection in phase change material: experimental study", *Int. J. Heat Mass Transfer* **183** (2022), article no. 122047.
[120] A. M. Leitch, "Analog experiments on melting and contamination at the roof and walls of magma chambers", *J. Volcanol. Geotherm. Res.* **129** (2004), no. 1, pp. 173–197.
[121] C. Gau and R. Viskanta, "Melting and solidification of a pure metal on a vertical wall", *J. Heat Transfer* **108** (1986), no. 1, pp. 174–181.
[122] G. Kaufmann, "Modelling karst geomorphology on different time scales", *Geomorphology* **106** (2009), pp. 62–77.
[123] R. Vesipa, C. Camporeale and L. Ridolfi, "Thin-film induced morphological instabilities over calcite surfaces", *Proc. R. Soc. A* **471** (2015), no. 2176, article no. 20150031.
[124] J. Colombani, "Measurement of the pure dissolution rate constant of a mineral in water", *Geochim. Cosmochim. Acta* **72** (2008), no. 23, pp. 5634–5640.
[125] E. Nakouzi, R. E. Goldstein and O. Steinbock, "Do dissolving objects converge to a universal shape?", *Langmuir* **31** (2014), no. 14, pp. 41145–41150.
[126] J. M. Huang, M. N. Moore and L. Ristroph, "Shape dynamics and scaling laws for a body dissolving in fluid flow", *J. Fluid Mech.* **765** (2015), pp. 1–10.
[127] G. Kaufmann and W. Dreybrodt, "Calcite dissolution kinetics in the system $CaCO_3$–H_2O–CO_2 at high undersaturation", *Geochim. Cosmochim. Acta* **71** (2007), no. 6, pp. 1398–1410.
[128] A. C. English and M. Dole, "Diffusion of sucrose in supersaturated solutions", *J. Am. Chem. Soc.* **72** (1950), no. 7, pp. 3261–3267.

[129] J. K. Gladden and M. Dole, "Diffusion in supersaturated solutions. II. Glucose solutions", *J. Am. Chem. Soc.* **75** (1953), no. 16, pp. 3900–3904.
[130] P. S. Mendes, "The naphthalene sublimation technique", *Exp. Therm. Fluid Sci.* **4** (1991), no. 5, pp. 510–523.
[131] T. K. Sherwood and C. Johannes, "The maximum rate of sublimation of solids", *AIChE J.* **8** (1962), no. 5, pp. 590–593.
[132] M. J. O'Neil, *The Merck Index: An Encyclopedia of Chemicals, Drugs, and Biologicals*, Royal Society of Chemistry: Great Britain, 2013.
[133] C. Cohen, M. Berhanu, J. Derr and S. Courrech du Pont, "Erosion patterns on dissolving and melting bodies (2015 Gallery of Fluid motion)", *Phys. Rev. Fluids* **1** (2016), article no. 050508.
[134] M. S. Davies Wykes, J. M. Huang, G. A. Hajjar and L. Ristroph, "Self-sculpting of a dissolvable body due to gravitational convection", *Phys. Rev. Fluids* **3** (2018), article no. 043801.
[135] S. Weady, J. Tong, A. Zidovska and L. Ristroph, "Anomalous convective flows carve pinnacles and scallops in melting ice", *Phys. Rev. Lett.* **128** (2022), no. 4, article no. 044502.
[136] A. Acrivos, "Mass transfer in laminar–boundary-layer flows with finite interfacial velocities", *AIChE J.* **6** (1960), no. 3, pp. 410–414.
[137] S. S. Pegler and M. S. Davies Wykes, "The convective Stefan problem: Shaping under natural convection", *J. Fluid Mech.* **915** (2021), article no. A86.
[138] J. Schürr, "Sur la vitesse de dissolution des sels dans leurs solutions aqueuses", *J. Phys. Théor. Appl.* **4** (1905), no. 1, pp. 17–26.
[139] J. Schürr, "Recherches sur la vitesse de dissolution des sels dans leurs solutions aqueuses", *J. Chim. Phys. Phys.-Chim. Biol.* **2** (1904), pp. 245–306.
[140] H. Grijseels, D. J. A. Crommelin and C. J. De Blaey, "Hydrodynamic approach to dissolution rate", *Int. J. Clin. Pharm.* **3** (1981), pp. 129–144.
[141] F. Dacheng and A. Hellawell, "The surface morphology of crystals melting under solutions of different densities", *J. Cryst. Growth* **92** (1988), no. 3-4, pp. 364–370.
[142] R. C. Kerr, "Melting driven by vigorous compositional convection", *J. Fluid Mech.* **280** (1994), pp. 255–285.
[143] Y.-C. Yen, "Onset of convection in a layer of water formed by melting ice from below", *Phys. Fluids* **11** (1968), no. 6, pp. 1263–1270.
[144] T. S. Sullivan, W. J. Brown, M. D. Kerkel and R. E. Ecke, "Turbulent convection and surface patterning in solid dissolution", *Phys. Lett. A* **206** (1995), pp. 49–53.
[145] Y. Liu, L. Ning and R. E. Ecke, "Dynamics of surface patterning in salt-crystal dissolution", *Phys. Rev. E* **53** (1996), no. 6, pp. 5572–5575.
[146] D. Gechter, P. Huggenberger, P. Ackerer and H. N. Waber, "Genesis and shape of natural solution cavities within salt deposits", *Water Resour. Res.* **44** (2008), no. 11, article no. W11409.
[147] R. S. Sharma, M. Berhanu and A. Kudrolli, "Alcove formation in dissolving cliffs driven by density inversion instability", *Phys. Fluids* **34** (2022), no. 5, article no. 054118.
[148] B. Villien, Y. Zheng and D. Lister, "Surface dissolution and the development of scallops", *Chem. Eng. Commun.* **192** (2005), no. 1, pp. 125–136.
[149] D. Wang, D. Ewing and C. Y. Ching, "Time evolution of surface roughness in pipes due to mass transfer under different Reynolds numbers", *Int. J. Heat Mass Transfer* **103** (2016), pp. 661–671.
[150] H. Schlichting, *Boundary-Layer Theory*, 7th edition, McGraw Hill: New York, 1979.
[151] T. J. Hanratty, "Stability of surfaces that are dissolving or being formed by convective diffusion", *Annu. Rev. Fluid Mech.* **13** (1981), no. 1, pp. 231–252.
[152] K.-S. Hsu, F. A. Locher and J. F. Kennedy, "Forced-convection heat transfer from irregular melting wavy boundaries", *J. Heat Transfer* **101** (1979), pp. 598–602.
[153] R. R. Gilpin, T. Hirata and K. C. Cheng, "Wave formation and heat transfer at an ice–water interface in the presence of a turbulent flow", *J. Fluid Mech.* **99** (1980), pp. 619–640.
[154] M. Bushuk, D. M. Holland, T. P. Stanton, A. Stern and C. Gray, "Ice scallops: a laboratory investigation of the ice–water interface", *J. Fluid Mech.* **873** (2019), pp. 942–976.
[155] W. Li, J. T. Germaine and H. H. Einstein, "Transport-controlled dissolution in an evolving fracture: The extended Purday solution and fracture flow tests", *Water Resour. Res.* **57** (2021), no. 3, article no. e2020WR029166.
[156] C. Oltean, F. Golfier and M. A. Bués, "Numerical and experimental investigation of buoyancy-driven dissolution in vertical fracture", *J. Geophys. Res.: Solid Earth* **118** (2013), no. 5, pp. 2038–2048.
[157] R. Hu, K. Li, C.-X. Zhou, T. Wang, Z. Yang and Y.-F. Chen, "On the role of gravity in dissolving horizontal fractures", *J. Geophys. Res.: Solid Earth* **128** (2023), no. 3, article no. e2022JB025214.
[158] W. Guo, R. Hu, C.-X. Zhou, Z. Yang and Y.-F. Chen, "Dissolution regimes of a horizontal channel in a gravity field", *Phys. Rev. Fluids* **8** (2023), no. 12, article no. 123902.
[159] L. H. Pitcher and L. C. Smith, "Supraglacial streams and rivers", *Annu. Rev. Earth Planet. Sci.* **47** (2019), pp. 421–452.

[160] E. Mantelli, C. Camporeale and L. Ridolfi, "Supraglacial channel inception: Modeling and processes", *Water Resour. Res.* **51** (2015), no. 9, pp. 7044–7063.
[161] V. Bergeron, C. Berger and M. D. Betterton, "Controlled irradiative formation of penitentes", *Phys. Rev. Lett.* **96** (2006), no. 9, article no. 098502.
[162] T. Bartels-Rausch, V. Bergeron, J. H. E. Cartwright, et al., "Ice structures, patterns, and processes: A view across the icefields", *Rev. Modern Phys.* **84** (2012), no. 2, pp. 885–944.
[163] L. M. Cathles, D. S. Abbot and D. R. MacAyeal, "Intra-surface radiative transfer limits the geographic extent of snow penitents on horizontal snowfields", *J. Glaciol.* **60** (2014), no. 219, pp. 147–154.
[164] W. W. Mullins and R. F. Sekerka, "Stability of a planar interface during solidification of a dilute binary alloy", *J. Appl. Phys.* **35** (1964), no. 2, pp. 444–451.
[165] D. J. Drewry, "A quantitative assessment of dirt-cone dynamics", *J. Glaciol.* **11** (1972), no. 63, pp. 431–446.
[166] N. Taberlet and N. Plihon, "Sublimation-driven morphogenesis of Zen stones on ice surfaces", *Proc. Natl. Acad. Sci. USA* **118** (2021), no. 40, article no. e2109107118.
[167] A. L. Lange, "Introductory notes on the changing geometry of cave structures", *Cave Stud.* **11** (1959), pp. 69–90.
[168] S. Fauve, "Pattern forming instabilities", in *Hydrodynamics and Nonlinear Instabilities* (C. Godrèche and P. Manneville, eds.), Cambridge University Press: Cambridge, 2005.
[169] B. Favier, J. Purseed and L. Duchemin, "Rayleigh–Bénard convection with a melting boundary", *J. Fluid Mech.* **858** (2019), pp. 437–473.

ACADÉMIE DES SCIENCES
INSTITUT DE FRANCE

Comptes Rendus. Physique
2024, Vol. 25, Special issue S3, p. 143-181
https://doi.org/10.5802/crphys.216

Review article / *Article de synthèse*

Geophysical and astrophysical fluid dynamics in the laboratory / *Dynamique des fluides géophysiques et astrophysiques au laboratoire*

Solid–liquid phase change in planetary cores

Changement de phase dans les noyaux planétaires

Ludovic Huguet[*,a], **Quentin Kriaa**[b], **Thierry Alboussière**[c] and **Michael Le Bars**[d]

[a] ISTerre, Université Grenoble Alpes, Université Savoie Mont Blanc, CNRS, IRD, Université Gustave Eiffel, 38000 Grenoble, France

[b] Physics of Fluids Group, Max Planck Center for Complex Fluid Dynamics, and J. M. Burgers Centre for Fluid Dynamics, University of Twente, P.O. Box 217, 7500AE Enschede, The Netherlands

[c] Université de Lyon, ENSL, UCBL, UJM, CNRS, Laboratoire LGL-TPE, France

[d] CNRS, Aix Marseille Univ, Centrale Marseille, IRPHE, Marseille, France

Current address: School of Earth and Environment, University of Leeds, Leeds LS2 9JT, UK (L. Huguet)

E-mails: l.g.huguet@leeds.ac.uk (L. Huguet), quentinkriaa@gmail.com (Q. Kriaa), thierry.alboussiere@ens-lyon.fr (T. Alboussière), michael.le-bars@univ-amu.fr (M. Le Bars)

Abstract. The ubiquitous phenomena of crystallization and melting occur in various geophysical contexts across many spatial and temporal scales. In particular, they take place in the iron core of terrestrial planets and moons, profoundly influencing their dynamics and magnetic field generation. Crystallization and melting entail intricate multiphase flows, buoyancy effects, and out-of-equilibrium thermodynamics, posing challenges for theoretical modeling and numerical simulations. Besides, due to the inaccessible nature of the planetary deep interior, our understanding relies on indirect data from seismology, mineral physics, geochemistry, and magnetism. Consequently, phase-change-driven flows in planetary cores constitute a compelling yet challenging area of research. This paper provides an overview of the role of laboratory fluid dynamics experiments in elucidating the solid–liquid phase change phenomena occurring thousands of kilometers beneath our feet and within other planetary depths, along with their dynamic repercussions. Drawing parallel with metallurgy, it navigates through all scales of phase change dynamics, from microscopic processes (nucleation and crystal growth) to macroscopic consequences (solid–liquid segregation and large-scale flows). The review delves into the two primary planetary solidification regimes, top-down and bottom-up, and elucidates the formation of mushy and/or slurry layers in the various relevant configurations. Additionally, it outlines remaining challenges, including insights from ongoing space missions poised to unveil the diverse planetary regimes.

* Corresponding author

Résumé. Les phénomènes de cristallisation et de fusion se produisent dans divers contextes géophysiques à diverses échelles spatiales et temporelles. Ils prennent notamment place dans le noyau en fer des planètes telluriques et des lunes, où ils jouent un rôle primordial dans leur dynamique et dans la génération de leur champ magnétique. La cristallisation et la fusion se caractérisent par des écoulements multiphasiques complexes, des effets de flottabilité et une thermodynamique hors équilibre, difficilement accessibles à la modélisation théorique et aux simulations numériques. De plus, les profondeurs planétaires demeurent inaccessibles aux observations directes, et notre compréhension repose sur des données indirectes provenant de la sismologie, de la physique minérale, de la géochimie et du magnétisme. Par conséquent, les écoulements induits par un changement de phase dans les noyaux planétaires constituent un domaine de recherche à la fois passionnant et stimulant. Cet article donne un aperçu du rôle qu'ont les expériences de laboratoire en dynamique des fluides pour élucider des phénomènes de changement de phase solide-liquide se produisant à des milliers de kilomètres sous nos pieds ou dans d'autres planètes, ainsi que de leurs conséquences dynamiques. En établissant des parallèles avec la métallurgie, cet article navigue à travers toutes les échelles de la dynamique du changement de phase, des processus microscopiques (nucléation et cristallisation) à leurs conséquences macroscopiques (ségrégation solide-liquide et écoulements de grande échelle). Nous décrivons en détail les deux principaux régimes de solidification planétaire, descendant et ascendant, ainsi que la formation de couches de solides interconnectées ("mush") ou dispersées ("slurry") dans les diverses configurations pertinentes. Enfin, cette revue décrit les défis restants, notamment dans le cadre de missions spatiales en cours qui dévoileront sans aucun doute la diversité des régimes planétaires.

Keywords. Crystallization, Phase change, Two-phase flows, Planetary cores, Magnetic field.

Mots-clés. Cristallisation, Changement de phase, Écoulements diphasiques, Noyaux planétaires, Champ magnétique.

Funding. European Research Council (ERC) (grant number 716429), Labex OSUG@2020 (ANR10 LABX56), Programme National de Planétologie (PNP) of CNRS-INSU co-funded by CNES.

Manuscript received 15 April 2024, revised 10 October 2024, accepted 11 October 2024.

1. Introduction

Crystallization and melting are ubiquitous in various geophysical settings across large ranges of spatial and temporal scales. In most instances, solidification and melting are associated with subsequent buoyancy effects with profound dynamical consequences, leading to stable stratification or intense convective motions. Indeed, beyond latent heat and heat transfers, solidification and melting in geophysical settings are often intricately linked with species segregation due to the heterogeneity of the considered fluids. For instance, on our planet, the crystallization of ice at the poles increases the concentration of salt into the ocean water, hence playing a pivotal role in climate by driving part of the global ocean circulation. Diving towards the planetary deep, the significance of the local solid–liquid phase change of the mantle is revealed through volcanic activity. Partial melting within the lithosphere also shapes the composition of the crust and contributes to the formation of stable continents. In the early epochs of Earth's history, more substantial melting occurred within the mantle, driven by the energetic processes of accretion and the presence of short-lived radiogenic elements, resulting in a partial or global magma ocean setting the initial thermochemical state of today's solid mantle. Still going deeper, the inner part of the Earth's core has been solidifying over the last billion years or so, sustaining the Earth's magnetic field generation. Similar phase changes involving water, silicate, and iron are actually ubiquitous on all terrestrial planets and icy moons.

1.1. *Phase change and planetary magnetic fields*

The planet of reference for magnetic field production is the Earth, whose magnetic field is most likely produced by dynamo in its liquid core. This process describes how the motions of an

electrically conducting fluid produce a magnetic field. The coupling between magnetism and fluid motions leads to the presence of electrical currents that feed the magnetic field but are constantly subject to ohmic dissipation. As a result, dynamo action can be sustained only as long as the electromotive action of the flow is sufficiently large compared to ohmic dissipation, which translates as a condition on the magnetic Reynolds number (e.g., [1])

$$Re_m = \frac{UL}{\eta_m} \gg 1, \tag{1}$$

where U and L are respectively the characteristic velocity scale and length scale of the flow, and η_m is the magnetic diffusivity. This necessary yet insufficient requirement places constraints on the vigor of the flow. Then, a burning question when observing a dynamo-generated magnetic field is: how do planetary cores sustain fluid motions that drive a dynamo?

Three contributions are usually mentioned that participate in sustaining the Earth's magnetic field: *thermal convection* due to the secular cooling of the planet, and possibly to internal heating through radioactive decay; *crystallization* of the core at the center that leads to chemical segregation between pure iron (that solidifies on the solid inner core) and lighter elements that rise in the liquid outer core, feeding compositional convection; *latent heat* release during crystallization that warms the fluid near the inner core, hence boosting the thermal convection. These three elements have proven important in driving the Earth's dynamo, and the last two of them are directly related to core crystallization. Earth's energy budget makes it very unlikely to sustain a dynamo without contribution from crystallization, hence questioning the model of a convective Earth dynamo before the start of the inner core growth (e.g., [2]). In addition to these three sources, mechanical driving processes (libration, precession, tidal deformation) can provide an alternative source of energy for generating magnetic fields in planetary cores [3–7].

Some small Earth-like planets show evidence of past (Mars, Moon) or present (Ganymede, Mercury) global magnetic field (e.g., [8] or [9] for interior structure). These observations have questioned the scientific community, as long-term, global magnetic fields seem difficult to sustain in such small cores. In contrast to the Earth's bottom-up core crystallization, a regime of top-down crystallization might take place on small planets. Associated flows may sustain a dynamo, but their complexity has been up-to-now only remotely tackled.

Planetary cores are very particular geophysical objects, as no direct observation can be made. Our knowledge of the deepest part of planets relies on indirect observations from geochemistry (for composition), geodesy and gravity measurements (for internal structure, mass, moment of inertia, libration), seismology (for internal structure, density, velocity, and state), and magnetism. Since the early 20th century, the image of the Earth's core seen by the seismology shows stratified layers (E′ layer and F-layer) [10, 11] acting against the well-mixed state of the liquid core. Seismological studies have also revealed a complex structure inside the Earth's inner core, including east-west hemispheric dichotomy, innermost inner core, radial or lateral variation of elastic anisotropy, and attenuation [11, 12]. Planetary seismology on the Moon [13–15] and on Mars [16–18] have also demonstrated the presence of a liquid core and some partially solid part at the top of the core or the bottom. The advance of satellite observations and planetary space missions has enabled us to better constrain the structure, intensity, and secular variation of planetary magnetic fields. The precision of geomagnetic measurements has even allowed us to infer the dynamics at the top of Earth's core, which provides key information on the state and the velocity of the fluid iron motions. However, in contrast with atmospheric and oceanic observations, the lack of direct measurements challenges our knowledge of the state and dynamics of planetary cores and makes it necessary to challenge the output of phase-change experiments and models with the available data.

1.2. *From the casting industry to planetary cores*

This review focuses on solid–liquid phase change within planetary cores and its dynamic consequences. In this context, the phase change is envisaged through its planetary, large-scale significance. But its intricate nature, encompassing both macroscopic and microscopic scales, is always present. At the atomic or molecular level, energy barriers must be overcome to induce a change in atomic arrangement. Diffusion processes operating at microscale influence the morphology of the liquid–solid interface, resulting in the formation of isolated crystals or dendritic structures, possibly modified by convection. The thickness of the region undergoing crystallization then represents the mesoscale, potentially involving compaction and other associated effects. While most studies focus on specific scales, it remains challenging to integrate all of them into a single numerical model. Consequently, experimental approaches hold significant value as they naturally capture all the complexity of phase change, albeit with the challenge of disentangling the individual contributions.

Many of our ideas on crystallization in planetary cores originate from the study of metallurgy (e.g., [19, 20]). Yet the conditions are very different: the expected growth rate of crystallization of the inner core—$V \sim 10^{-10}$ m·s^{-1}—is unseen in the iron casting where the mm·s^{-1} is more typical. Similarly, the temperature gradient in the core—$G \sim 10^{-3}$ K·m^{-1}—is much smaller than usual values in metallurgy. A consequence is that heuristic laws valid in metallurgy may not apply to the core. Fortunately, we can still rely on laws based on physical arguments. For instance, the primary dendrite spacing is found to scale proportionally to $V^{-1/4}G^{-1/2}$, based on diffusion length scales and the radius of curvature of the tips of the dendrites. This kind of scaling has been applied to obtain estimates of dendrite spacing and grain size in the inner core, reaching orders of magnitude of tens of meters [21], well beyond day-to-day experience.

Many factors in the planetary interiors do not have their counterparts in metallurgy. Compaction due to the deformation of crystallizing material under its weight or other stresses is a key factor in cores but is hardly studied in material processing. The effects of rotation and a background magnetic field are also potentially very important in planetary interiors. Magnetic fields have been investigated in the framework of steel casting, but not in the same view. They have been used to stir the fluid (traveling magnetic fields) or to brake fluid motion (DC magnetic fields), depending on the configuration and the desired final properties. At the scale of a solidifying zone, in the presence of a temperature gradient, thermoelectric currents can develop at the liquid–solid interface, acting as a short-circuited thermocouple. These currents have been measured using small electric potential probes [22]. When a constant magnetic field is applied, the thermoelectric currents produce Lorentz forces and drive a flow that can compete and reverse the flow induced by compositional buoyancy [23, 24]. All the ingredients for similar effects exist in metallic cores but have received little attention so far in this context.

1.3. *Outline*

This review is organized as follows. In Section 2, we first describe the state-of-the-art of our thermodynamical understanding of planetary cores' phase change and the variety of solidification regimes. This leads us to define two main scenarios, whose dynamics are described in depth in the following sections: the formation of a mushy layer detailed in Section 3, and the formation of a slurry layer detailed in Section 4, respectively. Mushy layers correspond to situations where the solid forms a continuous, yet possibly porous matrix attached to a boundary. Slurry layers correspond to mixtures of fluid and detached grains in suspension, no matter what their concentration. The final Section 5 details the main remaining open questions and the upcoming challenges related to ongoing space missions. It also briefly describes phase change applications in other planetary settings, which could be each the subject of a long review.

2. Crystallization in planetary cores

2.1. *Composition and state*

The solidification scenario of a planetary core depends on its liquidus temperature (also referred to as the solidification temperature or the melting temperature) and on its effective temperature profile (geotherm), which both depend on the pressure profile and core composition.

Planetary cores are primarily composed of iron[1], plus some light elements which could include sulfur, oxygen, silicon, hydrogen, and carbon [8, 25]. Mineralogical studies of these various iron alloys under the pressure and temperature conditions of planetary cores allow for the determination of their density, melting temperature, thermal conductivity, and compressibility, depending on their composition and whether they are in a solid or liquid state. The melting temperature and thermal conductivity help determine when the first solid will form due to the thermal evolution of the core. The liquid compressibility and the slope of the liquidus determine whether crystallization will begin at the core's center or surface. The density difference between the liquid and the solid (positive or negative) determines the dynamics of liquid/solid segregation. All these parameters have been measured in various experimental studies for different alloys, such as Fe–Si [26], Fe–S [27, 28], Fe–S–O [29, 30], Fe–Si–H [31], Fe–Ni–S [32, 33], Fe–Ni–Si [34, 35], and Fe–Ni–H [36].

In the canonical framework, the core is assumed to be well-mixed during its accretion, leading to a uniform bulk composition before the crystallization starts [37]. The liquid mixture is then described by a Fe–X alloy where the element X stands for a light element. In addition, a partition coefficient equal to 0 is usually considered, meaning that the iron solid phase is pure. In that case, the state of the core is described by the typical binary phase diagram sketched in Figure 1. Such a diagram is given for a constant pressure, hence for a fixed depth in the core. Mineral physics studies provide the eutectic composition and temperature, and the Clayperon slope for a wide pressure range. Parameterized equations of state are built to determine which phase exists for all compositions, temperatures, and pressures. Over time, the core cools down, so the state of the core is generally expected to go from fully liquid to partially solid and, ultimately, fully solid. It is apparent in Figure 1 that the bulk X mass fraction in the fully liquid state controls the composition of the crystals that form. Cores on the iron-rich side of the eutectic (hypo-eutectic) $c_{\mathrm{X}} < c_{\mathrm{X,e}}$ form pure iron crystals; on the opposite, the X-rich cores (hyper-eutectic) $c_{\mathrm{X}} > c_{\mathrm{X,e}}$ form $\mathrm{Fe}_a\mathrm{X}_b$ crystals, which are generally considered positively buoyant.

2.2. *Dynamical scenarios of solidification*

Figure 1 offers a simple, local picture of core crystallization solely based on thermodynamics. But in practice, core crystallization is a dynamic process due to the presence of buoyancy effects. Since the liquid Fe–X mixture contains a light element, pure iron crystals are denser than the liquid, and are therefore negatively buoyant, while $\mathrm{Fe_aX_b}$ crystals are positively buoyant. The segregation of the newly solid phase and the remaining liquid phase determines the dynamical evolution of the cores, including the growth of a solid layer. Moreover, this segregation may lead to the formation of convective or stably stratified fluid zones. Fluid motions driven by buoyant parcels of fluid or by buoyant crystals are thought to generate enough energy to sustain a dynamo action [38–40].

The pathways of crystallization and segregation depend on two aspects. First, it depends on how the density of the crystals compares with that of the ambient. Second, crystal migration depends on exactly where solidification happens. For illustration purposes, we focus here on

[1] More specifically, of an iron-nickel alloy.

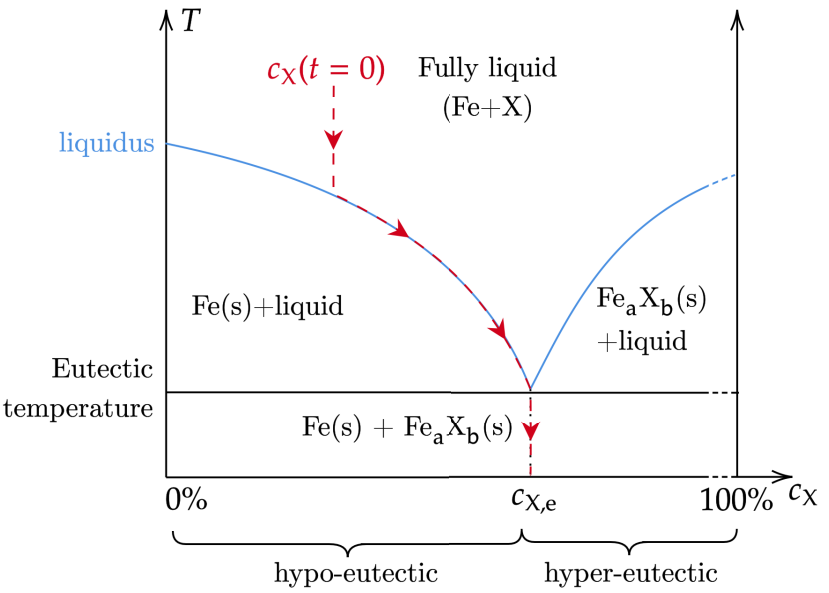


Figure 1. Simplified sketch of the binary phase diagram of iron (Fe) and a light element denoted "X", showing the state of the core as a function of the X mass fraction c_X and of temperature. The solid blue line corresponds to the liquidus, and the solid dark line is the solidus. The composition of the eutectic is denoted $c_{X,e}$. The integers a and $b \neq 0$ in subscript parameterize the composition of the solid forming on the X-rich side of the eutectic. For simplicity, we focus in Section 2.2 on a core lying on the iron-rich side of the eutectic (hypo-eutectic). In that case, the dashed red line shows a typical evolution of the state of the liquid core assuming thermodynamic equilibrium, for an initial mass fraction $c_X(t=0) < c_{X,e}$ and an initial temperature above the liquidus.

an iron-sulfur core on the iron-rich side of the eutectic, i.e. with a sulfur concentration $c_S < c_{S,e}$ and we describe two scenarios corresponding respectively to the evolution of the Earth and of a small Earth-like planet (or moons) like Ganymede. More crystallization scenarios can be found in [8]. In all scenarios, the ultimate state of the core is to be entirely solid (for small cores such as asteroids) or partially solid (for larger cores such as those of the Moon, Mercury, and Earth).

Figure 2a shows the typical bottom-up regime of solidification of the Earth [41]. As the core cools down, its temperature eventually crosses the liquidus curve at its center because the slope of the core temperature is steeper than the liquidus. Consequently, solid crystals first appear at the planet center, as sketched by red circles. At the bottom of the crystallizing region, an iron solid layer grows by the formation of a solid matrix or by the accumulation of free iron crystals (see Section 2.3). In the meantime, the residual liquid depleted in iron is lighter than the bulk Fe–S mixture, so it rises in the core and nourishes compositional convection above the solid layer (gray arrows in Figure 2a).

Consider now the top-down freezing of small Earth-like planets like Ganymede [42], as sketched in Figure 2b. In such planets, studies [28, 43–46] suggest that the slope of the liquidus as a function of depth is either steeper than the core temperature or even negative [45, 46]. Therefore, as the core cools down its temperature profile first crosses the liquidus at the core periphery, where the first crystals appear [8, 47, 48] (see the red circles in Figure 2b). Iron crystals might grow from the core-mantle boundary or spontaneously nucleate freely in the bulk. The formation

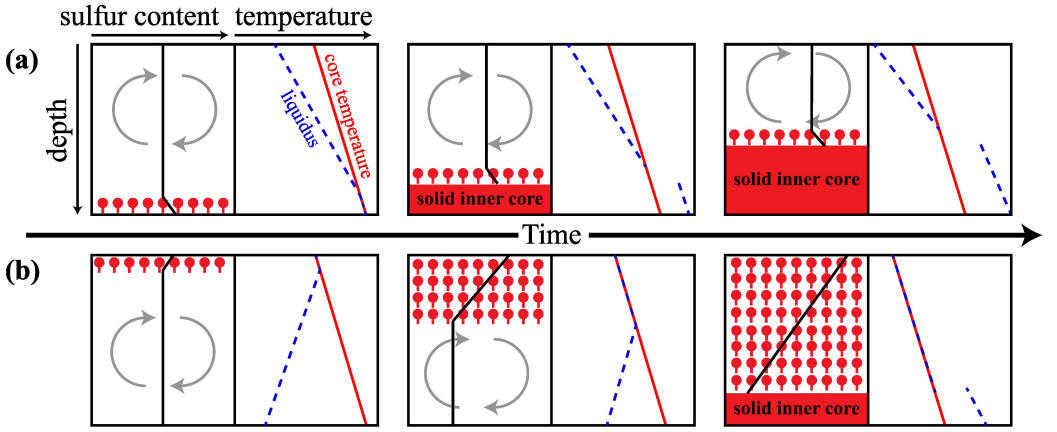


Figure 2. Two dynamical scenarios of solidification of an iron-rich, sulfur hypo-eutectic core: (a) bottom-up solidification in an Earth-like planet; (b) top-down solidification in a smaller Earth-like planet. Figure adapted with permission from Breuer et al. [8], under the CC BY 4.0 license.

of the first crystals on the surface or in the bulk will depend on physical properties (wettability, roughness, nucleation rate [49]), and dynamical processes (growth rate, constitutional supercooling layer [21], collisional breeding [50]). We will deepen the conditions of crystallization in the Sections 2.3 and 2.4. As they are denser than the ambient liquid, both cases end up with unstable crystals that settle due to gravity. The remaining light-element-rich liquid is lighter than the ambient, so it rises. The crystallization region extends from the core-mantle boundary to a lower limit where the crystals remelt because of the increasing ambient temperature. As a first-order estimate, this location is given by the core temperature matching the liquidus [8,47,48]. This region of solidification is called the snow zone, and the whole phenomenon of crystallization-settling-remelting is often referred to as iron snow. This snow zone is often thought to be at thermodynamic equilibrium, leading to the assumptions of fast crystallization and remelting compared to the crystal dynamics [40]. For the sake of simplicity, the departure from equilibrium in the snow zone is assumed to be negligible, even though supercooling can modify the snow dynamics in some experiments [51] (see Section 4.2.1). However, quantifying the departure from equilibrium requires releasing the previous hypotheses, making the theoretical model complex to handle [52,53]. At the lower edge of the snow zone, the molten snowflakes form a liquid mixture that is richer in iron than the ambient liquid, all the more as it is concentrated in molten snowflakes, all the less as it dilutes with the ambient. This molten snow is therefore negatively buoyant, so it sinks towards the center of the core and nourishes compositional convection—see [54] for a numerical study. Eventually, the core temperature becomes lower than the liquidus everywhere, so that snowflakes accumulate at the core center and pile up as a growing inner core.

Both scenarios described here are based on sketches and idealized hypotheses: they now need to be confronted with the reality of lab experiments.

2.3. *Mushy or slurry layers*

During the crystallization of a binary mixture, the equilibrium temperature at the interface between the solid and liquid is equal to the liquidus temperature. However, the growth of the solid by crystallization requires a slight departure from this equilibrium, leading to the formation of

supercooled regions ahead of the solidification front (i.e. the liquid temperature is below the freezing point). In addition, the composition of the liquid and the solid differ in terms of a light element composition depending on its solubility (generally very small for light elements (S, C, H, O), except for Si). Near the solidification front, the liquid is enriched in light elements, leading to the formation of a compositional gradient. Therefore, the fluid ahead of the front of solidification is often in a constitutionally supercooled state [55]. The morphological stability of the interface, which depends on both the temperature and composition gradients, has been extensively examined theoretically and experimentally [20, 56]. In the conditions of planetary crystallization, the pressure gradient also plays a major role in the front stability, as the core and liquidus temperatures are pressure-dependent [21, 57] (Figure 2). If the interface is morphologically unstable, the front of solidification will encounter cellular growth, dendritic growth, or equiaxed crystal growth when considering an increasingly large zone of the constitutional supercooled layer [20, 58] (Figure 3). In planetary cores, the stability of the front of solidification depends on the liquidus and Clapeyron slope (Figure 3). The liquidus slope $\partial T_m/\partial c|_P$ is negative or positive depending on whether the liquid composition is hypo-eutectic or hyper-eutectic (Figure 1). The Clapeyron slope $\partial T_m/\partial P|_c$ is mainly positive for iron alloys at high pressure, yet, for Fe–S at an intermediate pressure, the Clapeyron slope is negative [30, 33, 59]. In addition, the solidification rate and advective transport of the solute in the liquid play a key role in controlling the structure of the thermal and chemical fields near the solidification front. While crystallization is very slow and is of the order of one millimeter a year [37, 60], advective transport in the liquid can be several orders of magnitude larger [61]. For the Earth, the theoretical analysis of the stability of the solidification front, at the conditions of the inner core boundary, suggests an unstable front of solidification [21, 57, 62].

Figure 4 shows two experiments of equiaxed and dendritic crystallization using analog material, like metallurgy studies. Equiaxed crystal growth leads to the formation of a two-phase region in which free crystals nucleate and grow, and the surrounding liquid can be convectively stable or unstable: this is a so-called *slurry layer* (Figure 4a). Alternatively, dendritic growth leads to the formation of a two-phase region in which dendrites coexist with an interstitial liquid that can also be stable or unstable: a so-called *mushy layer* (Figure 4b). In a mushy layer, primary dendrites grow mainly in the same direction. Both regimes can co-exist for the same conditions; mushy layers preferentially grow from a substrate, and slurry layers exist if enough nucleation sites are present. Hence, by analogy with metallurgy, the crystallization conditions at the inner core boundary may lead to the formation of a mushy layer [21, 57, 61, 62] or of a slurry layer [57, 63]. The presence of a slurry layer depends on the thickness of the constitutional supercooled layer [57], and the ability to produce nucleation sites in the bulk of this layer (see Section 2.4) [57, 64]. The stability of the front of solidification in other planetary cores remains poorly known even though the presence of dendrite crystallization has been suggested in asteroids based on observations in metallic meteorites [65, 66], and the presence of an iron snow regime (slurry layer) has been suggested at the top of the core of small moons or planets [42, 47] (see Figure 2b).

2.4. *Nucleation paradox*

Crystallization has been extensively studied in the literature (e.g., [20]), given its importance in industrial processes (metallurgy, casting, ...). It is divided into two steps: nucleation followed by crystal growth. While the second step has also been widely studied in the context of planetary cores, the nucleation step has been largely ignored [37, 57]. For liquid metals, classical nucleation theory [20, 58] requires either a very large supercooling in a homogeneous environment or a wettable surface reducing the supercooling. Experiments in various pure metals or alloys [58, 69–71]

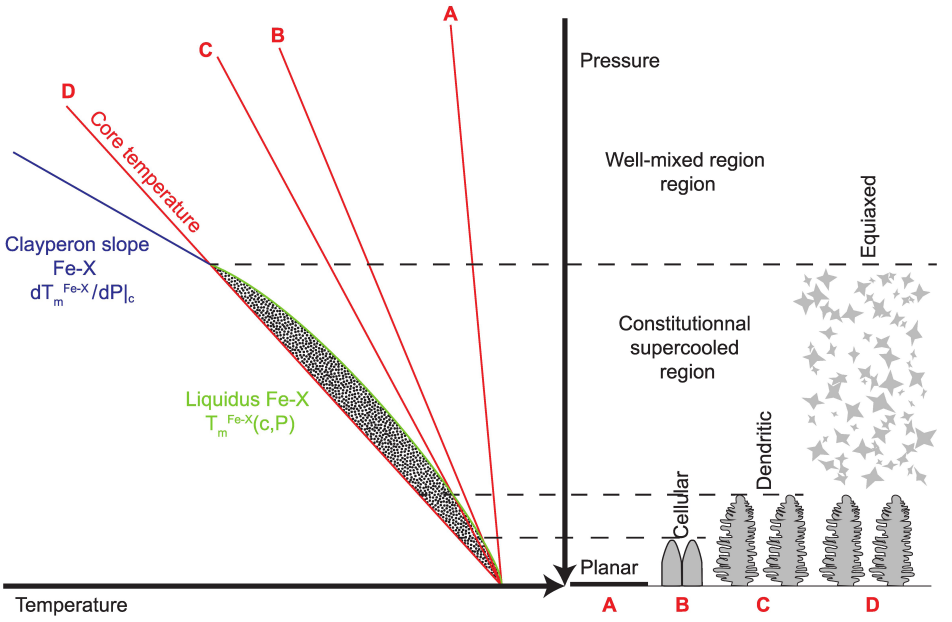


Figure 3. Schematic view (for the Earth's core) of the core temperature profile (very close to the adiabatic profile), liquidus profile, and Clayperon slope, associated with a stable (A) or unstable (B–D) solidification front. An unstable front of solidification will encounter cellular (B), dendritic (C), or equiaxed growth (D). The thickness of the constitutional supercooled region (black dashed lines) depends on the core temperature and the liquidus profile, which both depend on the growth rate and composition.

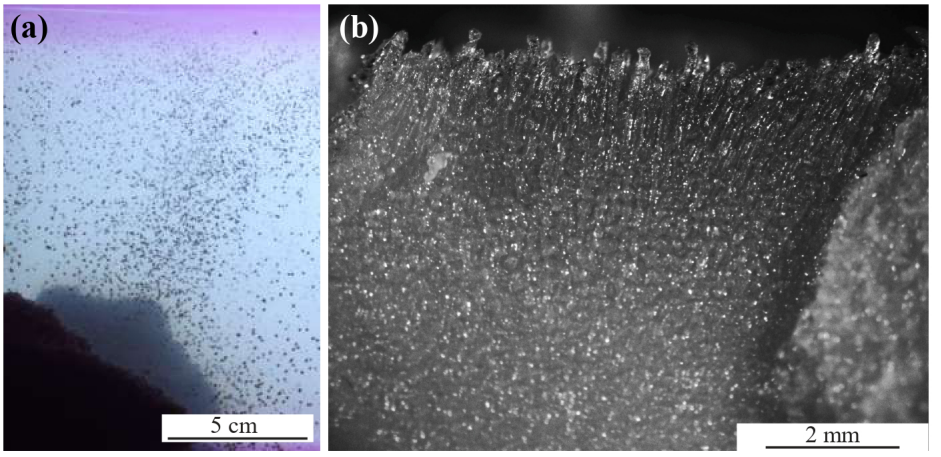


Figure 4. (a) A slurry layer in a tank cooled from above. Equiaxed crystals form near the top boundary, settle, and accumulate at the bottom of the tank. (b) Mushy layer with dendrites growing from the bottom of a tank cooled from below [61, 67]. Both cases used ammonium chloride solutions as an analog to the Fe–X mixture [68].

have shown that the critical supercooling is quite large compared to the melting temperature, i.e. about 20% of T_m. To explain the stability of the supercooled metals, Frank suggested that local structures exist in supercooled liquids [72]. This hypothesis was later confirmed by identifying atomic structures with a degree of icosahedral short-range order in experiments in alloys [73] or in iron [74–76]. These icosahedral short-range order structures may lead to the formation of stable or metastable quasi-crystals [77], which would preferentially grow instead of crystalline phase [73]. The undercoolability (meaning the ability to remain stable for a supercooled liquid) of metal alloys then depends on the stability of these local structures in the supercooled liquid, which would ultimately depend on the presence of other phases than the iron [78]. These short-range order structures have been suspected to play a major role in determining the melting temperature and the viscosity of high-pressure liquids [79]. However, the experimental detection of such structure in a supercooled liquid at high pressure and temperature is extremely difficult. Still, the detection of footprints, such as the twining of dendrites in Al alloys [80], might be plausible. One may think that the advance of electromagnetic levitation containerless experiments [81] in various environments including microgravity [82,83] along with laser shock experiments [84,85], which already provide physical properties of iron at high-pressure, may be able to determine the degree of supercooling for iron alloys at the high pressure and high temperature, which up-to-now remains unknown.

Recently, Huguet et al. [49] extrapolated the theory and results from the classical nucleation theory to planetary core conditions. They also investigated plausible causes of deviation from the canonical theory. They revealed that the nucleation barrier is likely to be very high even at the center of the Earth's core. The Earth's inner core nucleation paradox arises from the incompatibility between the slow cooling rate of the Earth's core and the high energetic barrier for homogeneous nucleation. While heterogeneous nucleation seems to be unlikely at the center of the Earth's core [49] (it is located thousands of kilometers away from any solid surface), the presence of the solid surface at the core-mantle boundary should ease the nucleation in a top-down scenario of crystallization [86].

Motivated by this work, several studies have attempted to resolve the paradox using molecular dynamics simulations [87–90]. The presence of light elements can either reduce or increase the nucleation barrier [87]. In a two-step scenario of nucleation, Sun et al. [89] found that the body-centered cubic (bcc) phase of iron has a lower nucleation barrier than the stable hexagonal close-packed (hcp) phase. However, the nucleation barrier remains significantly high even considering light elements or complex pathways of nucleation. This energetic barrier might be particularly significant for the existence of a slurry layer since the latter requires nucleation sites in the bulk: the origin of these nucleation sites remains a matter of speculation in planetary cores [64], especially for bottom-up solidification in which no solid phase is initially present [49]. The recent molecular dynamic [87] and geodynamical studies [91] further highlight the importance of the nucleation process in the crystallization of planetary cores, which remains a subject of active research.

We will now describe in more detail the dynamics of a mushy, and then of a slurry layer in the context of planetary cores. We will highlight fluid dynamics or crystallization experiments that unravel the dynamics of such layers in cores.

3. Mushy layer

Here we present the growth of a mushy layer and its dynamics in the context of planetary cores. Mushy layers have been considerably studied through theoretical, numerical, and experimental approaches because of their importance in industrial casting and sea ice dynamics (see e.g., [92–94]). Experiments have used metallic alloys or salt solutions [61,95–100] (see Figures 4b and 5).

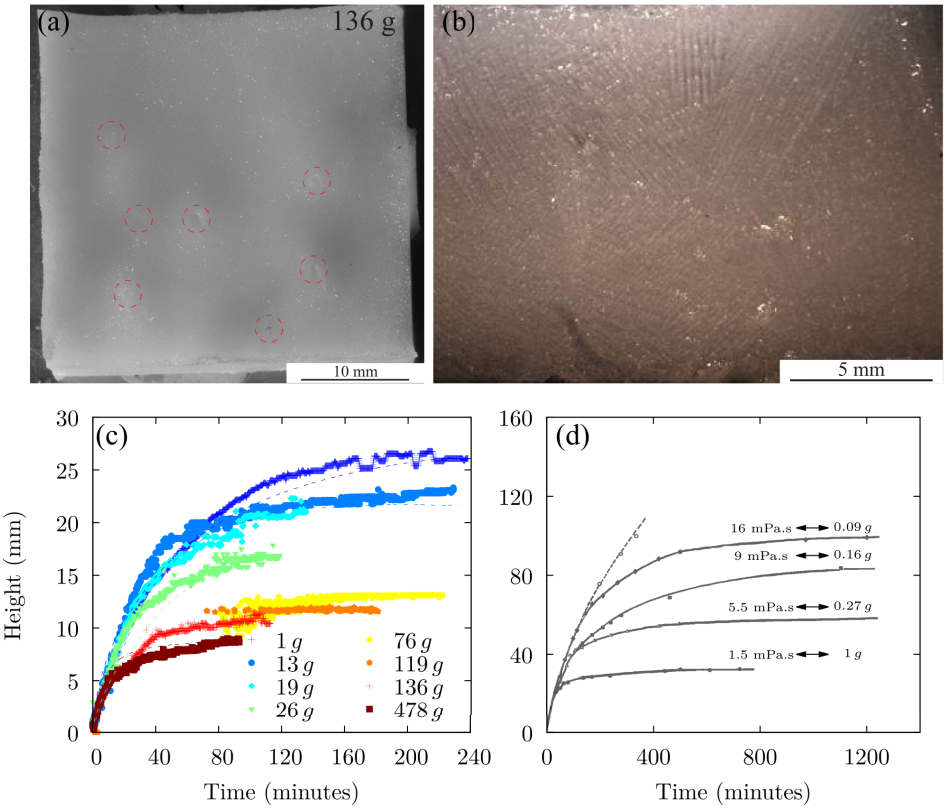


Figure 5. (a) Top view of a mushy layer growing under high gravity level (136 g) [61, 67]. Red circles denote the chimneys, which are evidence of mushy layer convection. (b) Side view of the mushy layer consisting of ammonium chloride dendrites. Dendrites formed grains with different preferential orientations [67]. (c) The thickness of the mushy layer as a function of time for different apparent gravities. Squares are the experimental results and dashed lines are predictions from the evolution model [61]. (d) Same as (c) for different viscosities, which correspond to different gravity levels given as an indication [98]. Panels (a,b) and (c,d) adapted with permission from Huguet [67] and Huguet et al. [61], respectively.

Ammonium chloride and sodium chloride solutions have proven good analogs for studying the solidification of metals [68]. Following these works, dedicated experimental studies have been performed to unravel the effect of convection [61, 101] and magnetic field [102] on the structure of the Earth's inner core. Note that a core mushy layer differs in terms of structure and evolution compared to the classical casting case: while the dendrites are canonically seen as a steady solid matrix growing from a surface, large planetary dendrites might flow under their weight, melt due to external forces, and sink into the liquid core.

3.1. *State of a mushy layer growing at the Earth's inner core*

Crystallization of the inner core is a major source of energy for convection in the outer core, which generates the Earth's magnetic field. Reciprocally, convection alters the transfer of light elements to the inner core's surface, significantly impacting crystallization. Fearn et al. [62]

showed that the inner core boundary conditions lead to the formation of dendrites [103]. Based on thermodynamic arguments, they demonstrated that this dendritic mushy layer might extend down to the center of the Earth's core [62]. The mushy zone can be subject to convective instabilities [104]: the boundary layer mode and the mushy layer mode. The first mode would be unstable in the inner core since the solute released upon solidification is lighter than the ambient [61]. The mushy layer mode of convection is controlled by the mushy layer Rayleigh number R_m [105–108] written as:

$$R_m = \frac{\beta^\star \Delta C g \Pi(\Phi) h}{\nu \kappa}, \tag{2}$$

where $\beta^\star = \beta - \Gamma\alpha$ is the expansion coefficient due to temperature and concentration changes (β is the solute expansion coefficient, α is the thermal expansion coefficient, Γ is the liquidus slope), ΔC is the difference of composition across the height of the mushy layer, ν and κ are the viscosity and thermal diffusivity of the interstitial liquid. In contrast with the classical Rayleigh number definition, the mushy layer Rayleigh number is proportional to the thickness h of the layer. The permeability $\Pi(\Phi)$ depends on the solid fraction Φ and is described by the Kozeny-Carman equation [109]

$$\Pi(\Phi) = \frac{\lambda_1^2}{4} \frac{(1-\Phi)^3}{k_0 \Phi}, \tag{3}$$

where λ_1 is the primary interdendritic spacing which is set by the morphological instability of the front of solidification [98]. The parameter k_0 is a constant (usually taken equal to 5 for directional solidification) but depends on the mean flow direction [110]. The mushy layer mode is unstable when the critical Rayleigh number is above 25 [98]. The effective Rayleigh number is limited by permeability, as vigorous convection induces more crystallization which increases the solid fraction and so decreases the permeability [61]. This second mode of convection would usually lead to the formation of chimneys as the iron-depleted liquid may dissolve iron dendrites in regions of upwelling [104]. The formation of chimneys is well documented by theoretical [93, 107, 108, 111] and experimental works in metallurgy [95, 96, 102, 112]. Based on observations in experiments and evidence from meteorites [113], Bergman et al. [102] suggest that the chimneys could be several hundreds of meters large at the inner core boundary. But in the presence of a magnetic field, the convection may take a different form than the chimneys-mode [114]. A strong enough magnetic field might suppress chimney convection [115], even if the mushy layer is convectively unstable.

The particular conditions at the inner core boundary are different from those in the canonical metallurgy literature, due to the simultaneous presence of vigorous convection in the outer core and a very slow inner core growth. Most of the experimental studies [61, 101] on the mushy layer at the inner core boundary have explored the effect of the convection in and above the mushy layer on its internal structure (solid fraction, size of the dendrites, or presence of chimneys). To investigate the effect of the vigor of this convection, several experimental studies have been performed by increasing or decreasing the Rayleigh number R_m (see Equation (2)) [61, 98]. Tait and Jaupart [98] used a viscosifier to decrease the Rayleigh number. Huguet et al. [61] increased the apparent gravity g to increase the Rayleigh number R_m. Figure 5 shows the time evolution of the thickness of a growing mushy layer. Since all other controlling parameters (composition and heat flux) are similar between the experiments, the final thickness of the mushy layer is a proxy of the solid fraction as a function of the Rayleigh number. The solid fraction is significantly increased by the vigorous convection of the liquid in and above it. Extrapolated to the inner core conditions, Huguet et al. [61] suggested that the inner core mushy layer has a solid fraction very close to one, meaning that the remaining liquid is very sparse.

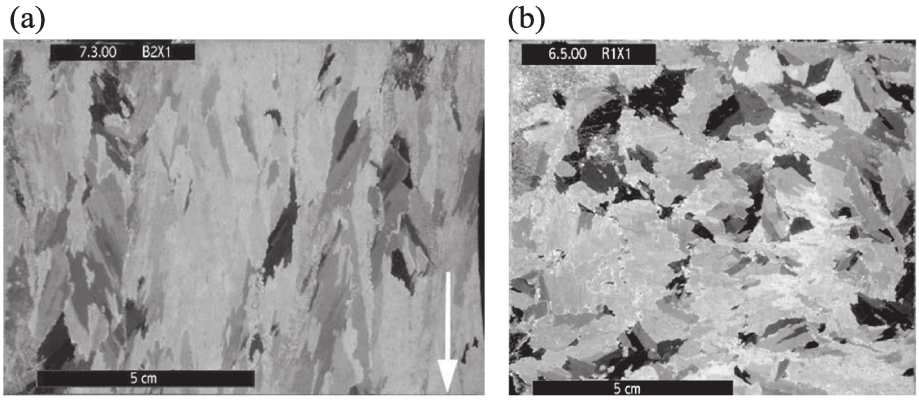


Figure 6. Transverse thin section of sea ice crystals with a mean flow parallel to the front of solidification (a) and with no mean flow (b). The white arrow in (a) shows the direction of convective flow near the interface. Panels (a and b) adapted from Bergman et al. [121] with permission of John Wiley and Sons.

At the inner core boundary, the heat flux extracted by the convection induces a directional solidification of the mushy layer, which produces a preferred orientation of the crystals [20, 116, 117]. Their orientation is determined by the crystal lattice, which depends on pressure, temperature, and crystal composition. For example, iron has a body-centered cubic lattice at ambient pressure (1 bar), but at high pressure, the most stable lattice for iron is still debated, between a hexagonal-closed package lattice [118] and body-centered cubic [119, 120]. Analog materials commonly used in mushy layer studies, such as ammonium chloride have a body-centered cubic lattice, and ice growing from salty water has a hexagonal closed package lattice. However, Bergman et al. [121] showed that in directional solidification experiments with hexagonal close-packed crystals, the fluid motions above the mushy layer force the crystals to have a preferred orientation parallel to the flow (Figure 6). With a laboratory model of the inner core growth, Bergman et al. [101] showed that the convective patterns in the liquid induce a texturing of the mushy layer, which might explain the structure of the inner core as seen by seismological studies [11, 12].

The typical length scale of the iron crystals (dendrites or equiaxed crystals) is controlled by crystallization at the inner core boundary. The primary spacing between dendrites (related to the grain width) is proportional to the growth rate and the chemical and temperature gradients [20]. Based on morphological analysis [21] and experimental studies [122, 123], the typical size of the dendrites in the Earth's core is thought to be between 10^{-1} and 10^{2} m. Experiments with high apparent gravity have also shown that the interdendritic spacing and grain size decrease with the vigor of convection [61]. Besides, at the length and time scales of laboratory experiments [61, 101, 102], the network of dendrites is seen as a fixed matrix in the mushy layer. But in planetary cores, dendrites can also compact under their weight on a very long timescale [124]. Theoretical and numerical works [91, 124] show that the compaction of a mushy layer will depend on the viscosity of the solid, the mush permeability (related to the solid fraction), and the growth rate of the solid. At the inner core conditions, Shimizu et al. [124] predict that the mushy layer will compact on the length scale of a few kilometers.

In conclusion, the Earth's inner core mushy layer, if it exists at all, is likely very thin and very depleted in liquid, with strong lateral heterogeneity of crystal orientation as fluid flow and magnetic field induce localized preferred orientation. The presence of an initial supercooled

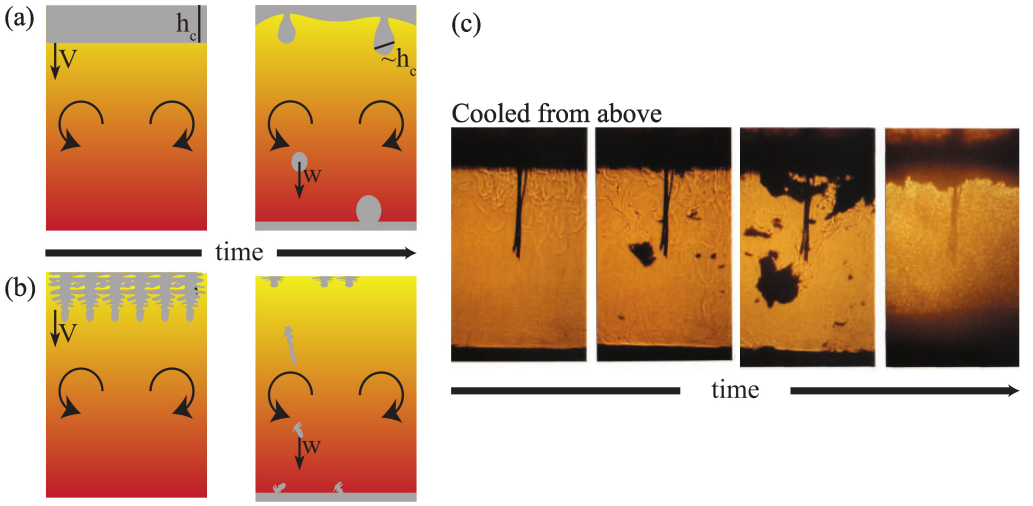


Figure 7. (a,b) Schematic view of the destabilization of a growing mushy layer (with a growth rate V) at the top of the core of a small planet [86,126]. (a) Rayleigh–Taylor instability of the iron layer. The wavelength of the instability is about the thickness of the layer h_c [126]. (b) Necking of independent dendrites. The typical dendrite size depends on the iron's rheology [86]. In (a) and (b) iron crystals fall into the liquid core (with a falling velocity w) and remelt or accumulate at the bottom. (c) Photos of an experiment using ammonium chloride aqueous solution cooled from above [127]. A large chunk of the mushy layer falls into the liquid and produces the crystallization of tiny equiaxed crystals. A temperature probe is inserted into the middle of the tank. Panel (c) adapted with permission from Chen [127].

layer, as suggested by the nucleation paradox [49], may imply a phase of rapid growth that changes the structure of the mushy layer. Therefore, the history of the crystallization of the mushy layer is hidden in the layering of the Earth's inner core [91].

3.2. *Mushy zone at the top of planetary cores*

In Section 3.1, we discussed the state of the mush growing from the center of the Earth's core, but as we saw in Section 2.2, crystallization can occur from the core-mantle boundary. While many studies argue in favor of the formation of a slurry layer (snow layer) in this regime of crystallization [42, 47] (see Section 4), other studies for small planetary cores suggest that iron crystals grow from the core-mantle boundary [66, 86, 125, 126] (Figure 7).

Based on the observation of metallic meteorite samples, Haack and Scott [65] suggested that dendrite can inwardly grow attached to the core-mantle boundary. Such a mushy layer may differ from the one at the inner core boundary as composition, temperature, and pressure conditions are quite different. The existence of a mushy layer at the top of a core depends on the morphological stability of the interface. Deguen [128] suggests that conditions at the core-mantle boundary of the asteroid might be compatible with an unstable interface and, therefore the formation of a mushy layer.

In a mushy layer composed of iron solid dendrite and a hypo-eutectic liquid, growing from the top will lead to a stably stratified interstitial liquid and unstable dendrites (as they are denser than the surrounding liquid [61,126]). The absence of convection and the slow growth rate in the mush

induce a highly porous mushy layer, in contrast to the highly compact mushy layer at the inner core boundary [61]. Therefore, the mushy layer can be seen as a solid interconnected matrix layer with viscosity depending on the porosity [126] (Figure 7a), or as independent dendrites growing towards the center [86] (Figure 7b). A mushy layer will be subjected to Rayleigh–Taylor instability [126]. The length and time scales of the delamination of the mushy layer depend on the rheology and the solid fraction, which are controlled by the strain, rate, temperature, and composition.

Experimental studies of unstable mushy layers [127, 129] have shown that large chunks of a mushy layer, with a typical size ranging between the interdendritic spacing and the mush thickness, can fall into the liquid (Figure 7c). However, the rheology of salt or ice dendrites is in the brittle regime. The fragmentation of dendrites is often observed in experiments due to the vigorous convection and strong strain rate applied to secondary or tertiary arms of dendrites [68, 130, 131]. In planetary cores, the rheology of iron at high pressure and temperature is still poorly known [132] and the strain rate is likely to be small (for example, the typical convective velocity for the Earth's core is of the order of mm/s).

On another end, independent dendrites attached to the core-mantle boundary can be seen as slab necking under gravity during the subduction process in the Earth's mantle [133–135]. The necking and delamination of dendrites could produce a large range of crystal sizes falling into the liquid core [86, 126]. Moreover, the fragmentation of dendrites induces the formation of equiaxed crystals through the production of secondary nucleation sites [68, 130]. It is also well-known that stronger convection will produce more fragments resulting in a larger amount of equiaxed crystals in the bulk [131].

Laboratory experiments and theoretical studies applied to the growth of the top-down mushy layer are missing to determine which destabilization mode dominates. One might suggest that the existence of an iron snow might result from the growth of a thin mushy layer producing a high quantity of small crystals falling into the liquid cores, as further described in Section 4. The existence of such a regime would solve the paradoxical existence of a large nucleation barrier for homogeneous nucleation since primary dendrites would grow from the core-mantle boundary and secondary nucleation would provide sites for the iron snow [136].

3.3. *Melting of a mushy layer at the inner core boundary*

Finally, Earth's seismology has highlighted the existence of the transition region between the outer core and the inner core [137, 138]. This region, the so-called F-layer, is characterized by the observation of slower P-waves than predicted by the Preliminary Reference Earth Model (PREM) [139], which assumes a well-mixed outer core. Therefore, the F-layer is expected to be a denser and stably stratified fluid layer. Its origin is still debated but one explanation comes from the melting of the inner core. Melting of the inner core would release a denser liquid enriched in iron, sitting at the base of the outer core. Several studies have examined mechanisms for such melting including a translation convection mode of the inner core [140, 141] and a heterogeneous heat flux at the inner core boundary [142]. A model experiment was set up in Alboussière et al. [140] to mimic the phase changes induced by the translation of the inner core (Figure 8). One hemisphere crystallizes and releases light elements, while the other melts and releases dense liquid iron with few light elements. This was modeled in a volume of salted water, injecting fresh (light) water on the right side of the bottom surface through a porous surface, while more salted water was injected on the left side. Overall, the buoyancy flux of light elements exceeded slightly that of heavy elements to account for the slow net crystallization of the inner core. Then, a dense layer started to grow from the bottom, providing a mechanism for the existence of the F-layer. Light plumes could still cross that dense layer and drive a convective flow throughout

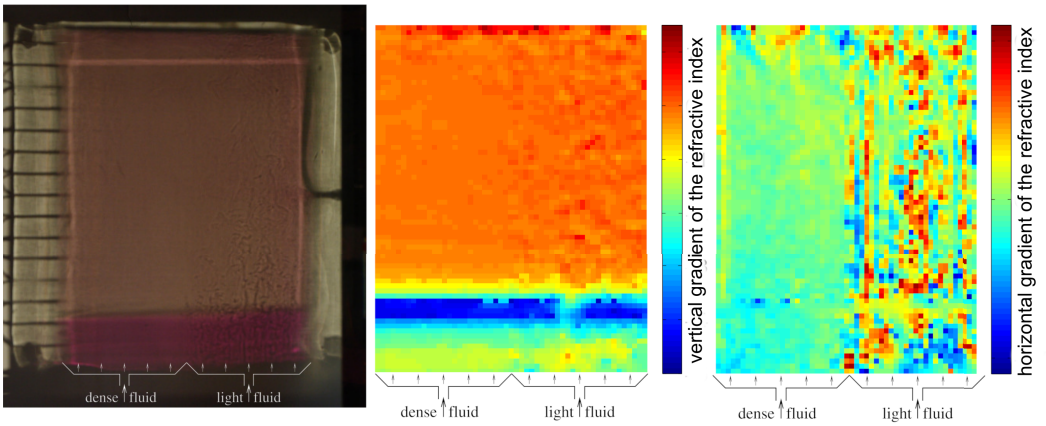


Figure 8. Convection experiment with light and dense fluid released from the bottom and formation of an F-layer [140]. The shadowgraph on the left shows the dense fluid (with purple dye) and light fluid rising through. Using a synthetic Schlieren method, the vertical gradient (in the middle) and the horizontal gradient (on the right) of the refractive index reveal the dense layer and the convective plume, respectively. Figure adapted with permission from Alboussière et al. [140].

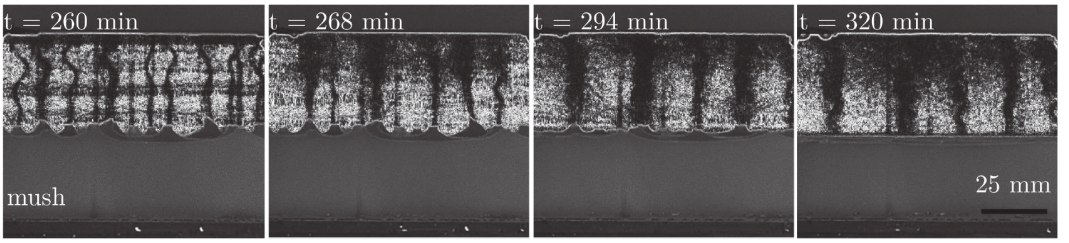


Figure 9. Heating and melting from above of a growing mushy layer [61]. The crystallization and convection inside the mushy layer induce the formation of chimneys and meandering plumes (t = 260 min). Note that double-diffusive convection occurs in the liquid layer as seen in other experiments [146]. Once heating and melting start, chimneys melt and mushy layer convection becomes stronger, as evidenced by the turbulent plumes (t = 268, 294, 320 min). Figure adapted with permission from Huguet et al. [61].

the whole volume. The corresponding flow necessarily exists in the Earth's core, at least to drive the geodynamo.

Several experiments using a reactive porous medium or a mushy layer have shown that the melting implies a change in the structure of the matrix and the liquid composition [61, 143–145]. Moreover, melting induces an enhanced crystallization in a deeper part of the mushy layer [61, 145] as heavy melt drives stronger compositional convection and recrystallization (Figure 9). This leads to a higher solid fraction inside the mush [61, 145], the formation of a dense layer above the mush, and the disappearance of cones of chimneys [61] (Figure 9).

4. Slurry layer

In Section 2, we show that the crystallization of a planetary core can lead to the formation of free crystals in a slurry layer. Here, we examine the fluid dynamics and the phase change of crystals in such a particle-laden environment. A key ingredient of the slurry dynamics is the difference of density between the crystals and the interstitial fluid. When crystals are sufficiently concentrated, this density difference manifests as an effective buoyancy on the ambient fluid, through which crystals may collectively force a large-scale flow beyond the scale of a single crystal. Despite the existence of studies on such flows in other geophysical contexts (landslides [147], turbidity currents [148, 149], snow avalanches [150]), the planetary situation of crystals settling in a bulk liquid is much different and fewer experiments have been performed to model this phenomenon. In addition, crystal formation and remelting are two complex ingredients that must be included to model core evolution. With an incremental approach, the next subsections first describe the collective dynamics of inert particles (Section 4.1) before adding the additional complexity of phase change (Section 4.2).

4.1. *Collective motion of inert particles*

4.1.1. *What numbers control the motion of particles?*

Suppose a suspension of particles settles in an infinite domain. The motion of a single particle depends on its radius r_p, the local gravity g, the particle density ρ_p, and finally the fluid density ρ_a and kinematic viscosity ν_a. The motion of multiple particles depends on their local volume fraction ϕ, and if the ambient fluid is moving, it also depends on the ambient fluid velocity U_a. According to the Vaschy–Buckingham theorem, four dimensionless numbers can be used to characterize the motion of a suspension in a moving ambient: the density ratio $\Pi_\rho \equiv \rho_p/\rho_a$ quantifies the particles' inertia; the volume fraction ϕ controls the collective behavior of particles and their forcing on the fluid; the particle Reynolds number $Re_p \equiv 2w_s r_p/\nu_a$ characterizes the regime of the flow past a single particle. It depends on the terminal settling velocity w_s of a single particle, which is usually implicitly defined as a function of Re_p. A classical expression for $Re_p < 800$ is [151]:

$$w_s = \frac{w_s^{\text{Stokes}}}{1 + 0.15 Re_p^{0.687}}, \tag{4}$$

where the Stokes velocity is defined as

$$w_s^{\text{Stokes}} = \frac{2 g r_p^2 (\rho_p - \rho_a)}{9 \nu_a \rho_a}. \tag{5}$$

Finally, the Rouse number $\mathscr{R} \equiv w_s/U_a$ quantifies how fast particles gravitationally drift with respect to ambient fluid motions. This can be shown from the momentum equation of a single small particle settling in a moving fluid: for a sufficiently small particle with low inertia (see [152] for details), the buoyancy of this particle balances its drag that is proportional to the difference between the local fluid velocity $\boldsymbol{v}_a$ and the local particle velocity $\boldsymbol{v}_p$. This readily gives $\boldsymbol{v}_p = \boldsymbol{v}_a - w_s \boldsymbol{e}_r$ where $\boldsymbol{e}_r$ is the radial unit vector pointing outward from the core center. Such a small particle follows the ambient flow and constantly drifts in the direction of gravity with a velocity w_s; the Rouse number quantifies the relative gravitational drift between the particle and the local fluid motions with $|\boldsymbol{v}_p - \boldsymbol{v}_a|/|\boldsymbol{v}_a| = w_s/|\boldsymbol{v}_a| = \mathscr{R}$. This 4D parameter space is a reference to characterise the dynamics of inert monodisperse particles with a locally uniform volume volume fraction ϕ. Additional ingredients of relevance for planetary interiors (e.g. heterogeneities of concentration, phase change, polydispersity…), that would largely expand the size of this parameter space, are incrementally considered in the next sections.

The difficulty in resolving the particulate dynamics in large-scale turbulent geophysical flows has led many experimentalists to model slurries as a fluid whose effective density (and viscosity) differs from the ambient—for example using salt water instead of a dense suspension of particles. Such an approximation corresponds to the limits $Re_p \to 0$ and $\mathscr{R} \to 0$. We show below some experimental works that revealed the need to refine the description of the particles' dynamics.

To gain understanding on the dynamics of settling-driven convection, two different approaches can be found: some authors focus on the fundamental building blocks that nourish this convection at a local scale—continuous releases of buoyancy in *particle-laden plumes*, and instantaneous releases of buoyancy in *particle clouds* or particle-laden thermals—while other authors investigate the slurry dynamics directly as a whole with a global approach. Numerical simulations and models of core evolution usually adopt this second vision and consider slurry layers like the snow zone as a uniform region with quasi-steady dynamics (e.g., [47]). Yet, Section 2.4 suggests that the slurry dynamics is neither steady nor uniform in the snow zone. Therefore, the motions produced in the snow zone might be described as a sum of localized releases of snowflakes in different locations and at different times. How should these releases be parameterized in terms of crystal sizes, concentrations, distance in space, and delay in time between two bursts of crystals? Should these releases be instantaneous or have a finite duration? In this regard, studies of local convective structures bring some light on the dynamics that might be at play in slurry layers. Both the local and global approaches are addressed respectively in Sections 4.1.2 and 4.1.3. Since we are interested in large-scale flows in liquid iron that has a low viscosity 10^{-6} $\mathrm{m}^2{\cdot}\mathrm{s}^{-1}$, these flows are likely turbulent, which is why we restrict the description to such flows.

4.1.2. *Modelling convection with a local approach*

Particle-laden plumes are often studied in a steady state with the "filling box" technique (see the illustration with a one-phase plume in Figure 10a): from an inlet at the center of the top wall of the tank, a first source feeds a negatively buoyant plume with a volume flux Q_p; in the meantime, a second source feeds a volume flux Q_{in} that nourishes a downward displacement flow in the whole tank; finally, a sink lets a volume flux Q_{out} spill from the tank, thus maintaining a constant volume of fluid in the tank. This setup is particularly relevant to quantify the plume entrainment which characterizes its coupling with the ambient fluid. McConnochie et al. [153] recently used this technique with particle plumes. They revealed that particles modify the entrainment rate of such steady plumes when they settle in opposite directions to the initial volume flux, e.g., when downward-settling particles rain out from an upward-oriented plume. Other experiments by Zurner et al. [154] focused more precisely on the coupling between the particulate motion and the flow. In their experiments, particles were continuously sieved from the top of an injection column and formed a steady settling-driven plume—see Figure 10b. By measuring both the local fluid velocities through PIV and the velocity of each particle through PTV, the authors quantified the energy transfer from the particles to the fluid. Their results show that particles of low particle Reynolds number are more efficient at transferring energy to the flow than particles of large particle Reynolds number. This was interpreted as a consequence of the difference in near-field flow around particles.

In both experiments [153, 154], the particulate nature of the buoyancy forcing directly affects the particle plume, modifying its coupling with the ambient and, if multiple plumes are driving large-scale convection, with other particle plumes. It points to the importance of the density and size of crystals in solidifying cores.

The transient settling of particle clouds reveals some additional physics that depends on the cloud Reynolds number based on its radius and bulk velocity. Several studies have focused on

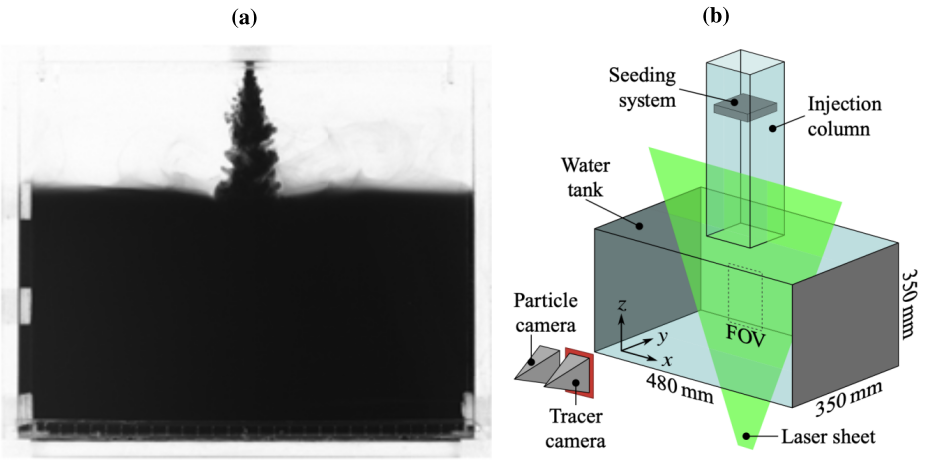


Figure 10. (a) Steady-state reached in a "filling box" experiment with a dyed salty plume generated in fresh water. (b) Experimental setup used by Zürner et al. [154] to generate a central settling-driven plume from the injection column into the water tank. Panels (a) adapted from Dadonau et al. [155], (b) adapted from Zürner et al. [154], with permission of the Cambridge University Press and the American Physical Society, respectively.

clouds of large cloud Reynolds number (e.g., [156–163]). They are typically generated in the lab by releasing some buoyant material from the inlet of an injector that is located above water [159], exactly at the free surface [157, 158, 161] or submerged [157, 160, 161, 163]. In most experiments, the injector is initially sealed by a membrane that keeps the buoyant material until it is ruptured (see Figure 11a). After rupturing the membrane, the buoyant mixture rolls up and a large-scale turbulent cloud forms in which the particles swirl as long as the cloud falls faster than the settling speed of an individual crystal (see snapshots one and two in Figure 11b); as the cloud dilutes, it decelerates and particles rain out of the cloud when the latter is as slow as their settling speed [164] (see the third snapshot in Figure 11b); after this separation, particles settle almost vertically with a constant velocity (see the fourth snapshot in Figure 11b). The larger the Rouse number, the earlier the separation (compare Figures 11b and 11c). It means that a given buoyancy anomaly released from a fixed initial cloud size gradually loses its ability to produce large-scale fluid motions as the particle size is increased, due to the decoupling between eddies and the particles that gravitationally drift with respect to the flow—in other words, the flow experiences transitions that are bound to the particulate nature of the buoyant material. The entrainment of particle clouds is also affected by the particles' properties: in [163] the authors showed that particle clouds have a maximum growth rate and hence dilute the fastest for a finite particle size, 75% faster than first-order estimates that disregard the particulate nature of the buoyancy forcing.

To sum up, these experiments with plumes and clouds show that the particle size, through Re_p, $\mathscr{R}$ and ϕ, affects the efficiency of the collective drag, the decoupling of particles from fluid motions, and the entrainment capacity of these local flows. Therefore, it controls the ability of the slurry to generate a large-scale flow, with consequences for dynamo generation. The next section confirms this conclusion and addresses another key question: when no length scale nor velocity scale is imposed by plumes and particle clouds, how does a slurry layer evolve and what is its spatial structure?

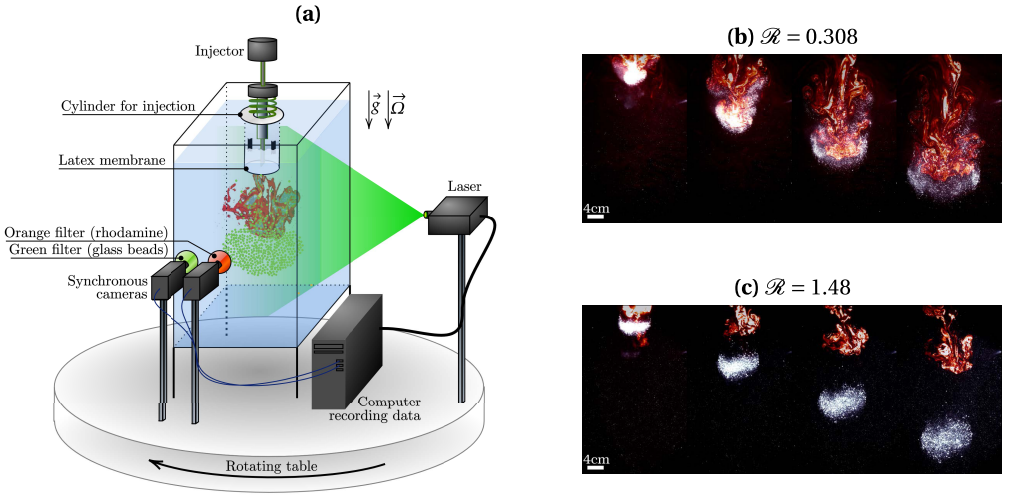


Figure 11. (a) Experimental setup used in Kriaa et al. [163]. A cylinder partly immersed below the free surface is initially sealed by a latex membrane; after rupturing the membrane with a needle, glass spheres settle in fresh water, reflect the green light from the vertical laser sheet, and their motion is recorded by the camera with the green filter. The orange coloring (rhodamine B) is initially present with particles in the cylinder; as particles fall, this dye is tracked by the camera with an orange filter. The influence of background rotation can be studied since the setup is entirely mounted on a rotating table. (b,c) Snapshots show, in the absence of background rotation, the gradual separation between particles (in white) and the released dye (in orange), all the faster as the Rouse number $\mathscr{R}$ increases from (b) to (c). Time intervals Δt between snapshots are (b) $\Delta t = 3.0s$ and (c) $\Delta t = 1.2s$. Panels (a) and (b) adapted from Kriaa et al. [163] with the permission of the American Physical Society.

4.1.3. *A global approach of convection*

Besides the local analysis of convection through its building blocks, some experiments directly analyze the behavior of a whole layer of particles settling in an initially quiescent fluid. The simplest approach is to consider this layer uniform, settling above another layer of clear lighter fluid. This configuration has been investigated in experiments to analyze the onset of the fluid motions at the interface between the two layers through a Rayleigh–Taylor-like instability [165–167], typically after sliding a gate open. For example, Fries et al. [167] let a mixture of water and particles settle above slightly denser sugary water, with a motivation to study the settling and deposition of ash from warm volcanic clouds. Other authors let dense particles settle in the air down a settling column until they penetrate in a tank of constant [166, 168] or piecewise linear [169] density profile, and they analyze the particle instabilities that develop near the free surface. Some studies in a Hele-Shaw cell (see Figure 12 extracted from Harada et al. [170]) or in numerical simulations [171] have shown that particles behave collectively when the interparticle distance of a uniform suspension, proportional to $r_p\phi^{-1/3}$, is sufficiently small for the hydrodynamic perturbations of neighboring particles to overlap, enabling them to collectively drag the interstitial fluid. A paramount consequence is that the collective settling of particles considerably accelerates their fall compared to the individual settling velocity of isolated particles.

These previous studies mainly focus on the transient formation of the Rayleigh–Taylor-like instability and essentially analyze the propagation of the front of particles without analyzing the

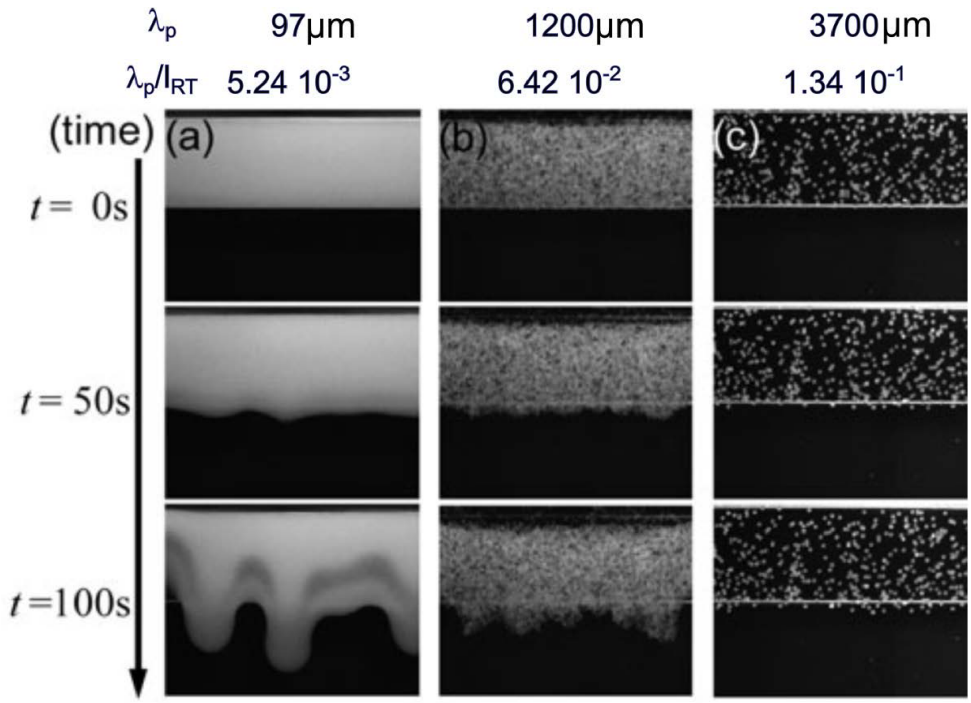


Figure 12. Snapshots of experiments where a suspension of white particles settles above the clear fluid in a narrow cell. From left to right the inter-particle distance λ_p increases (it is respectively equal to 97 μm, 1200 μm and 3700 μm), leading to a transition from a collective fluid-like behavior (particles undergo a Rayleigh–Taylor-like fluid instability) to individual particle-like behavior (particles essentially settle vertically). This transition to individual behavior is reflected by the ratio of the inter-particle distance λ_p over the expected width of the Rayleigh–Taylor mushrooms l_{RT}, which equals 5.24×10^{-3}, 6.42×10^{-2} and 1.34×10^{-1} from left to right. Figure extracted from Harada et al. [170] with permission from Springer Nature.

fluid motions that ensue at larger times. If crystals continuously settle in a snow zone, what would be the dynamics of this layer over timescales larger than necessary for crystals to cross through the whole layer? Insight can be gained from experiments of bubble-driven convection: some bubbles are continuously injected at the bottom of a water tank, over the entire cross-section of the tank. Several of these studies focused on the formation of rolls in 2D tanks having a narrow gap between two of their side walls, as observed in experiments of Kimura [172] (Figure 13a) and in numerical simulations by Climent and Magnaudet [173] (Figure 13b). The experiments showed that the rate of injection of bubbles affects the aspect ratio of these rolls, while the size of bubbles controls their ability to couple with fluid motions and cross through the cells when they are sufficiently large [172]. However, such two-dimensional studies have evidenced very different behaviors compared to observations in 3-D flows. Different regimes exist depending on the bubble injection rate [174], and while 2D bubble columns tend to show well-structured stacks of rolls, experiments in 3D columns are more chaotic [175]. Experiments of Iga and Kimura [176] with a uniform flux of bubbles injected at the bottom of a water tank with a 24 cm × 24 cm cross-section have shown that the bubble-driven convection leads to irregular 3D patterns that do not reach a steady state, as shown in Figure 13c.

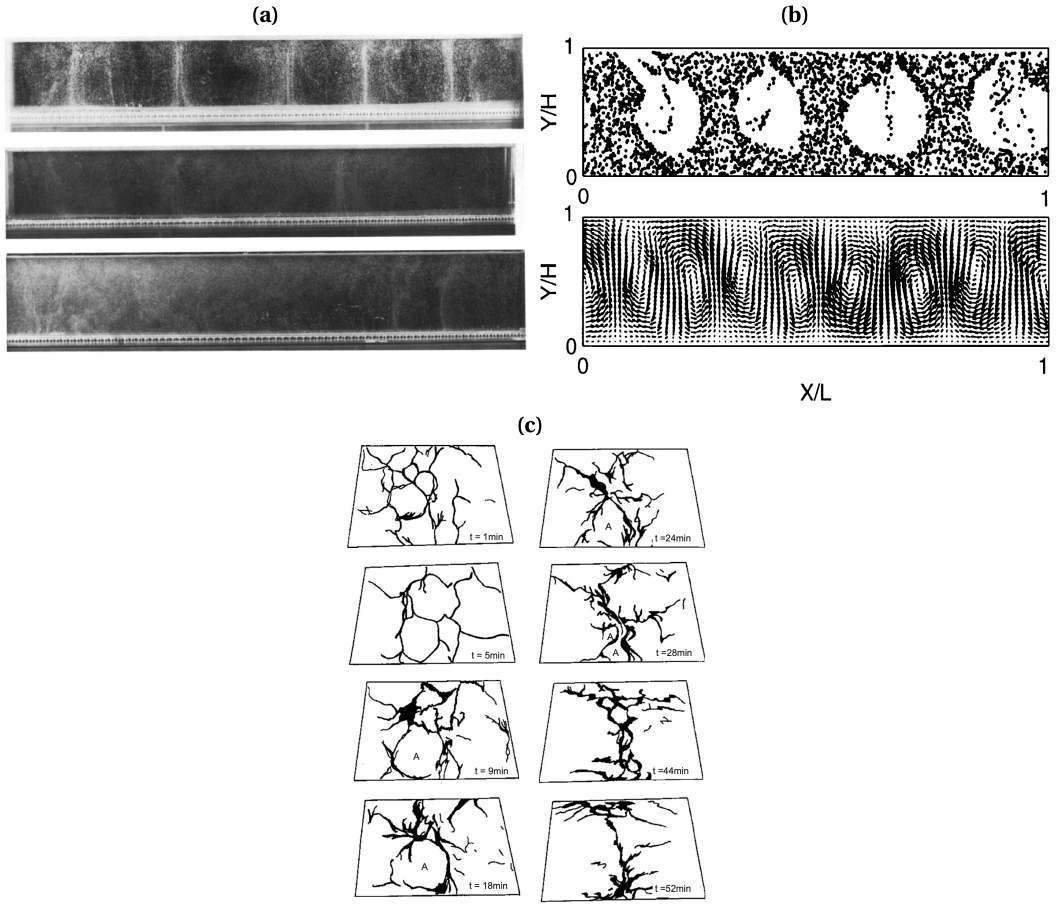


Figure 13. (a) Steady convective cells produced in a narrow 2D water tank by a constant injection of bubbles. The whiter the regions are the more concentrated in bubbles. The injection rate of bubbles increases from the first to the third row. (b) Similar observations in numerical simulations: black dots denote the bubble on the first row, while the second row shows the velocity field. Results were obtained for an aspect ratio $L/H = 4$ and a Rayleigh number of 2.07×10^5. (c) Sketches of the evolution of a 3D bubble-laden as seen from above, with the time origin corresponding to the start of bubble injection. The dark regions are laden with bubbles. Figure (a) and Figure (c) are respectively adapted from Kimura [172] and Iga and Kimura [176] ©The Japan Society of Fluid Mechanics and IOP Publishing Ltd and reproduced by permission of IOP Publishing. All rights reserved. Figure (b) is adapted from Climent et al. [173] with the permission of the American Physical Society.

Although bubbles differ from solid crystals by their ability to deform and the possible existence of a slip velocity at their interface, such bubble-driven flows provide valuable information. They support the idea that the motion of crystals in the slurry layer has little chance of being uniform and steady, even when disregarding issues due to bulk crystallization.

These studies confirm the order-of-magnitude impact that collectivity can have on the timescale of crystal segregation in the core and on the estimates of convective velocities that may or may not drive a dynamo. Unfortunately, collective effects are still poorly understood, difficult to investigate experimentally, and challenging to model numerically. Further experiments

are required to gain more understanding of these aspects, especially in the context of a global settling-driven convection of solid particles over large timescales, for which the parameter space (Π_ρ, ϕ, Re_p and $\mathscr{R}$) remains largely unexplored.

4.2. *Influence of phase change in slurry layers*

4.2.1. *Crystallization*

Slurry layers involve the crystallization of free crystals when rising or falling. In metallurgy, the formation of equiaxed crystals above the front of solidification is associated with the convective motion of the fluid [177]. Experiments of equiaxed crystal solidification (with analog material) have shown the complexity of the multiphase flow associated with crystal growth, as a slurry layer encounters processes of nucleation, fragmentation, sedimentation, and convective fluid motion [92, 177, 178]. These experiments [177] and early numerical simulations [92, 179, 180] have shown that the microscale dynamics (nucleation, grain growth, sedimentation) cannot be disregarded for an understanding of the macroscale segregation in industrial casting [181]. These dynamics can be modeled only at a small scale or with a few crystals. In the most recent numerical studies, the growth of equiaxed crystals with fluid motions can be modeled using the phase-field method and lattice Boltzmann methods in small computational domains, but with the presence of up to a few hundreds of crystals [182–184]. Other experiments with equiaxed crystals have investigated the growth rate of individual falling crystals as a function of the surrounding constitutional supercooling [185, 186], or the production rate of crystals through fragmentation of dendrites via convective motion [130, 187, 188]. However, despite the existence of recent techniques to track particles in multiphase flows [129, 189], the fluid motions that naturally emerge in slurry layers make it challenging to perform quantitative measurements, especially in large fluid domains. In planetary cores, the formation of a slurry layer (the Earth's F-layer or a snow layer in small cores) is thought to be accompanied by a stably stratified layer due to the release of light elements upon crystal growth and the sinking of dense crystal [42, 53, 190]. Following the seminal studies done by Loper and Roberts [191] and Loper [52], theoretical one-dimensional models have been developed [53, 190] for the Earth's F-layer. They showed that the bulk crystallization of iron crystals and their sedimentation are compatible with the existence of a stratified layer at the bottom of the Earth's core. Numerical models of the thermal evolution of Ganymede or Mars core in a regime of iron snow led to the same conclusion [40, 48]. However, even with several assumptions made (one-dimensional and two-phase flow, Boussinesq approximation), the most advanced model for such a slurry layer requires at least 8 equations and 14 input parameters [53].

Only a few experiments have been developed to investigate the dynamic of crystallization of a slurry layer in the configuration of iron snow [51, 129]. Huguet et al. [51] recently investigated the solidification of free ice crystals, their sedimentation, and their melting in a hotter layer (Figure 14). A cyclic pattern was observed of alternating bursts of crystallization and quiet periods with no crystallization (Figure 14a). The bursts of crystallization were due to the formation of large numbers of crystals in a supercooled layer by fragmentation of dendrites. The ice crystals then melted as they rose in hotter regions of the tank. Quiet periods were due to the inhibition of crystallization as the supercooling was reduced in the tank, caused by the release of latent heat of solidification, and the convection induced by the motions of crystals. These experiments revealed the wide range of crystal sizes formed upon solidification in the slurry layer, as shown in Figure 14b. Crystallization in slurry is thought to produce a polydisperse distribution of crystals, which will have consequences on their fall and melting in the iron snow regime.

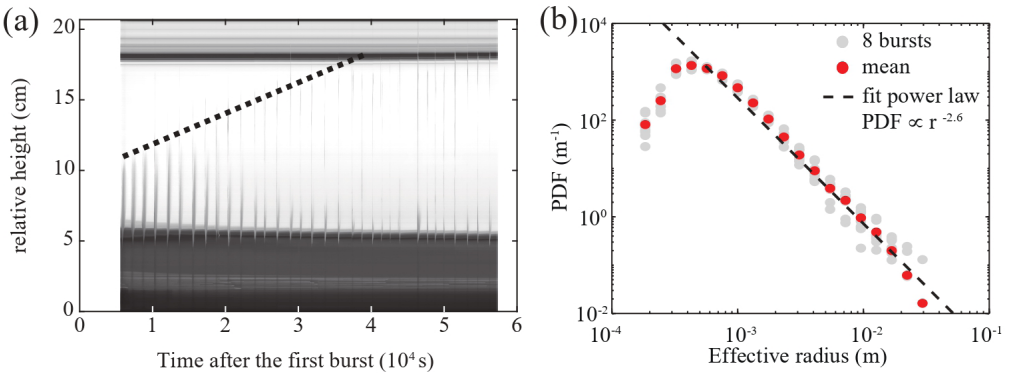


Figure 14. Experimental study of the homogeneous crystallization of a tank of water cooled from below. (a) Shows a space-time diagram from a vertical cross-section in the middle of the tank: darker regions correspond to ice. The dynamics exhibit clear alternative behaviors with periods of intense upward snow followed by quiet periods. The black dashed line denotes the maximum height of rising ice crystal i.e. the height of the liquidus. (b) Shows the measured probability distribution function of rising snow particle radius, highlighting the large distribution. Panels (a,b) adapted with permission from Huguet et al. [51].

4.2.2. *Crystals remelting*

According to the simplistic vision of iron snow previously introduced in Section 2.2, the bottom of the snow zone is delimited by the location where the local temperature is equal to the liquidus temperature; below this position, the temperature is larger than the liquidus and snowflakes remelt. Models of the thermal evolution of small Earth-like planets have time steps of order 10^6 yrs [47, 48], which is insufficient to resolve settling and remelting of snowflakes. Therefore, these processes are considered instantaneous, and all snowflakes are assumed to remelt right at the lower edge of the snow zone. In practice, particles have a finite melt rate, and they travel a finite distance before disappearing there exists a "*remelting layer*" between the snow zone and the zone of compositional convection.

The remelting layer is usually disregarded. Therefore, models of compositional convection in the deeper core are fully liquid models in which the whole buoyancy is of a fluid nature. As shown in Figure 15a, Olson et al. [192] designed an experiment where drops of aqueous solution rained out from a shower head into quiescent air, penetrated through a first layer of silicone oil in which the drops settled—the analog of the snow zone—, and finally penetrated through a second layer of pure water—the analog of the convective zone—where convection developed depending on the buoyancy flux of raindrops, see Figure 15b. By relating the Rayleigh number which quantifies the convective forcing, to the Reynolds number based on the average velocity of plumes propagating down the second convective layer, the authors showed that this plume velocity verifies an inertial scaling that is independent of viscosity and diffusivity. This observation led Olson et al. [192] to use diffusion-free dynamo scalings to analyze whether a dynamo could be sustained by precipitation-driven convection on Earth, Mercury, or Ganymede; the details for each case can be found in [192].

Few studies include phase change and particle settling in a large-scale flow. Large-scale studies consider either a fully fluid convection or a settling-driven convection of inert particles. From the physicist and mathematician's viewpoints, melting and dissolving are equivalent [193–195], so information can be found in the literature on individual particles melting or dissolving as they settle. Most studies have tried to measure and predict the trajectory and shrinking of a

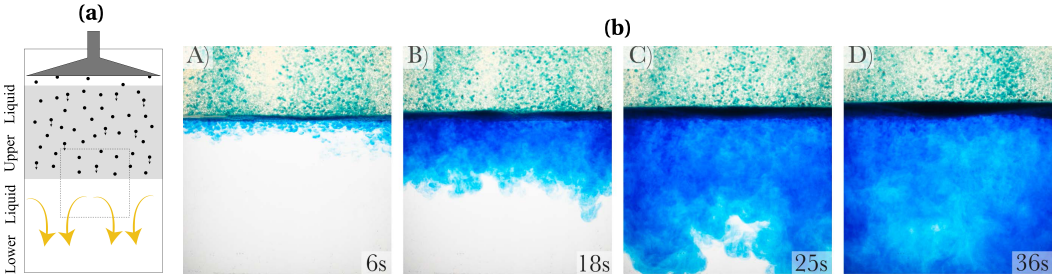


Figure 15. (a) Sketch of the setup used by Olson et al. [192] to model precipitation-driven dynamos. The light grey top layer contains silicone oil and typically stands for the snow zone; the white bottom layer contains fresh water and stands for the convective zone. The dyed aqueous drops that are continuously injected represent settling crystals. (b) Time series of the compositional convection that develops in the lower convective layer. The width of every snapshot is 18 cm. We thank Olson et al. for providing panels (a) and (b) which correspond to the experiments used in [192].

single solid sphere falling and dissolving in a homogeneous ambient [196–199]. Recently, Huguet et al. [200] studied a settling sphere of $Re_p \sim 10^3$–10^4. They showed that when the particle melts, its trajectory has a lower amplitude of oscillation and a drag coefficient almost twice larger than when it is inert. Aligning with the work of [201], Huguet et al. [200] conjecture that is it due to enhanced mixing in the sphere's wake due to the melt's buoyancy. These observations are important for the timescale of crystal segregation in the core; future experiments could clarify the role of the melt liquid by using other materials whose melt liquid is neutrally buoyant, as done in [202]. The experiments in [200] also revealed that when a melting sphere falls in a stratified ambient, it excites internal waves that contain ~1% of the initial potential energy of the sphere for a Brunt-Väisälä frequency $N \sim 0.1$–0.2 Hz. How the waves of several crystals might combine in the snow zone, and how they would couple with the crystals' motion remain open questions that require further investigation.

Recent experiments were conducted that include the collective aspect of the particles' dynamics while they dissolve (see Chapter 4 in [203]). To do so, homemade dyed sugar grains of controlled size were sieved with a constant mass rate over a cylindrical water tank. A plume of dissolving sugar grains formed over a wide surface area, and a vertical laser sheet enabled to visualize the flow in the midplane. The sugar grains were visible in the laser sheet because they reflected the laser light. In addition, the sugar was cooked like caramel and doped with Rhodamine B, hence the wakes of dissolved sugar were visible in the flow (see Figure 16a,b). By aligning with the usual assumptions of models of core thermal evolution—a uniform and constant mass flux of monodisperse particles is fed through the bottom of the snow zone (in experiments, through the water-free surface)—these experiments revealed the importance of the remelting layer and how the size of grains hugely affects its dynamics. First, for an identical mass rate, varying the diameter of sugar grains from 45 μm to 363 μm controls a flow transition, from a laminar plume that gains intensity over a long transient when forced by the rectilinear fall of large grains (Figure 16a), to a turbulent lazy plume that emerges faster when forced by fast-dissolving small grains (Figure 16c). This flow transition is determined by the enhanced forcing imposed by smaller grains, and their ability to nourish a Rayleigh–Taylor-like instability at the plume onset—both because smaller grains behave more collectively and hardly decouple from fluid motions. Second, the plume velocity explicitly depends on the size of grains through their settling velocity which controls how dilute the grains are in the plume. For these two reasons, the size of grains imprints

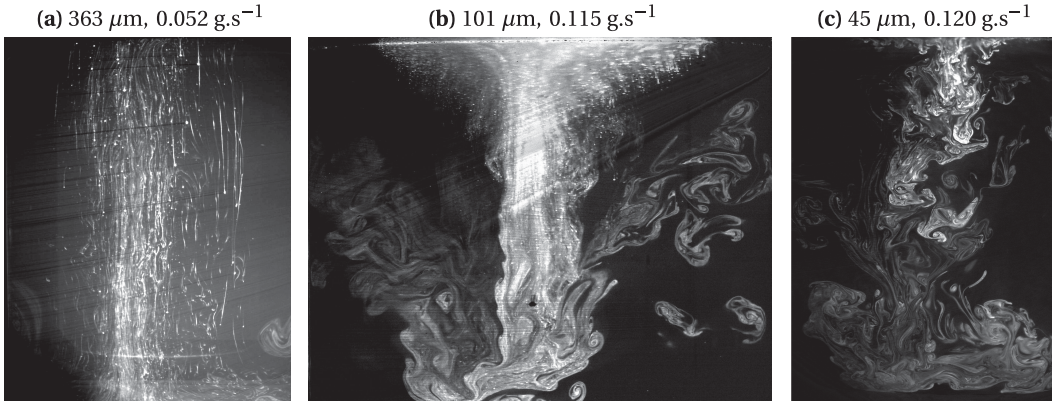


Figure 16. Snapshots of sugar plumes of different sugar radii and similar mass rates (see above snapshots). The vertical extent of each snapshot is (a) 38 cm, (b) 23 cm, (c) 38 cm. Snapshots of the experiments presented in Chapter 4 of Kriaa [203].

a lasting signature on the plume, even after full dissolution/melting. Third, the thickness of the remelting layer depends both on the mass flux imposed and on the size of grains (for a mass rate of 0.1 g/s, grains of radius $r_p = 45$ µm dissolve over a few centimeters whereas grains of radius $r_p = 363$ µm dissolve deeper than the tank height of 38 cm). Since the mass flux of crystals depends on the dynamics of the snow zone that feeds the melting layer with crystals, it reinforces the need to accurately model the fluid motions and the crystal sedimentation in the snow zone.

If crystals are sufficiently large, they may get deep in the core before remelting. As long as they remain large enough for their settling velocity to largely exceed the surrounding flow velocity ($\mathscr{R} \gg 1$), crystals are expected to settle radially inward irrespective of the ambient fluid motions and to inject their buoyancy deep in the core. Only when crystals are sufficiently small can they be entrained in ambient flows? Here again, constraints on the size of crystals are paramount to better model the core evolution and where compositional convection might take place. We mentioned in Section 4.2.1 that polydisperse distributions are expected; it remains an open question to know how polydisperse experiments behave compared to these experiments with monodisperse distributions. Crystals of different sizes settle with different velocities; therefore, they might collide, form clusters, and shield one another from the ambient fluid (see such effects in [204]), thus delaying phase change, as already observed in the monodisperse experiments.

Such idealized experiments show that many open questions remain, even before addressing the geophysically relevant effects of compressibility and magnetism. Such effects will be difficult to tackle experimentally. Yet, to account for the very complex physics involved in phase-change-driven convection, including out-of-equilibrium thermodynamics and crystal size distribution that are inaccessible to Direct Numerical Simulations, laboratory experiments are, at the very least, necessary to test parameterization schemes and to benchmark numerical models that will then address planetary mysteries.

5. Implications and limitations

5.1. *Consequences for observations*

A better understanding and modelling of phase-change driven flows in planetary cores is especially relevant in the current context of new observations from recent (e.g., Bepi Colombo) and

upcoming (e.g., Juice, Europa Clipper, Psyche) space missions, which will help to unravel the evolution of planetary cores. The dynamics of internal flows will remain inaccessible to observations on many planets, at least within the foreseeable future. The challenge of lab experiments on solidification and melting is therefore to provide large-scale signatures that are closely linked to the microscale physics at play in the core, so as to constrain the core dynamics from planetary-scale observations.

5.1.1. *Dynamo and magnetic observations*

A better understanding of crystal migration could help guide future magnetic observations. The crystals' size affects how they force the flow, decouple from it, and how deep they remelt, thus affecting the characteristic flow velocity U and the size of the convective zone L. If they are sufficiently large, the magnetic Reynolds number $Re_m = UL/\eta_m$ can exceed the minimum value required for dynamo action. The more turbulent the flow, the more high-order multipoles can be excited and therefore the more multipolar the magnetic field might be.

However, magnetic observations at the surface of a planet do not only depend on the inner core dynamics. For the same Re_m, the magnetic multipoles produced by a deep convective zone (scenario of top-down freezing) decay over a large distance before being measured at the planet's surface, favoring the predominance of the magnetic dipole; conversely, the magnetic field produced by a convective zone near the core-periphery decays over a smaller distance and is prone to show higher-order multipoles [48]. In addition, solidification can lead to stratification, as expected in Ganymede where top-down freezing leads to the rejection of a sulfur-rich residual liquid rising to the core's top [47, 48]. Such a stratification filters the magnetic field, reducing higher-order multipoles relative to the magnetic dipole [54]. So far, the existence of such a stratification has been deduced from thermodynamical arguments (see e.g., [48]). Aspects of fluid dynamics remain to be investigated, like the possible erosion of the stratification by the underlying convection, the two-way coupling between the stratification and the flow produced by the settling crystals, and the transport of crystals by inertio-gravity as observed in other astrophysical contexts in astrophysical fluid dynamics [205].

5.1.2. *Seismic observation of the Earth's inner core*

Seismological studies of the Earth's inner core have revealed large and small-scale heterogeneities of the seismic properties (attenuation, anisotropy, or wave velocity), which are thought to be consequences of the evolution of the inner core and then of its crystallization pathway [11, 12]. Radial and regional variations of anisotropy are related to the principal orientation of the crystals and their intrinsic properties. Several studies modeling traveling waves in the complex medium have attempted to understand the seismic observations [206–208] and their link to the history of solidification [207].

As shown in the Section 3, the structure of the mushy layer originates from the dynamic of the crystallization (growth rate, crystal alignment, chimneys, remelting). Beyond experimental works of crystallization, several experimental studies have attempted to correlate seismic observations to crystallization and dynamics of the Earth's inner core [61, 209, 210], using ultrasonic waves as analog to seismic waves. Solidification texturing of the mushy layer [122] can cause the apparent elastic anisotropy [209] as crystal elongation aligns with heat flux. A model has been proposed involving convective translation of the inner core [140]: this would produce crystallization in one hemisphere and melting in the other. Huguet et al. [61] have shown that the melting of a mushy layer lowers its attenuation and have argued that the western hemisphere of the inner core melts as it has a weak attenuation. The translation, as such, does not explain the anisotropy nor the innermost inner core. But pre-existing texture [210] or post-solidification deformation [124, 211] of the solid mushy layer might alter the solidification texturing, which can perhaps explain

anisotropy variation in the inner core or a different structure in the innermost part of the inner core. With the increase in the number and quality of seismic observations, the relation between the mushy layer structure and its seismic properties will deserve more investigation, guided by experimental results to identify the evolution of the Earth's inner core.

5.2. *Additional questions to address*

On a very long timescale, a growing mushy layer might deform under its weight. Few theoretical and numerical studies with 1D models of compaction [91, 124] have shown that the length-scale of compaction is relatively small compared to the size of the inner core and that a significant amount of liquid in a compacted mushy layer can be trapped. However, the complexity of extending these models to 2D or 3D renders an experimental approach highly valuable. Compaction in porous medium has been extensively studied through experiments and numerical simulations [212–214], but not in regard to a mushy layer growing at the inner core boundary. The next set of experiments may investigate the compaction using "soft" material like paraffin or lead and applying external compression force or high apparent gravity. We have already seen how convection in a mush increases its solid fraction, without deformation of the solid structure. It would be interesting to see in experiments the second phase of compaction, where the solid fraction increases further because of solid deformation.

Experiments on the crystallization of a core have been performed in many configurations and with different materials (ice, analog salt solution, metals). However, only a few studies have been performed in the configuration of a snow layer [51, 129] or of a top-down mushy layer [127, 129]. Future experiments would have to focus on the stability of a top-down mushy layer and its interaction with the top cooling boundary. In the slurry layer, the processes of crystal growth and fragmentation can be investigated experimentally to predict the size distribution of iron crystals in the snow layer, which is until now unknown. Indeed, a slurry layer has little chance of being monodisperse: if crystals form anywhere in the bulk, upward or downward settling enables crystals of many sizes to meet and interact in the core; if large pieces of solid iron are delaminated from the core-mantle boundary, they might trigger nucleation in a supercooled ambient, especially if their detachment results in the dispersal of smaller fragments. As we have seen, the crystal size has a drastic influence on convection. Hence, although experiments with monodisperse particle distributions are a necessary step to fully comprehend the physics at play, it is unclear how their results would be affected when moving on to polydisperse distributions. Disentangling all the effects that are coupled might require keeping track of the space-and-time evolution of the size distribution in the flow. Two types of experimental hurdles must be overcome. First, surface tension plays a much stronger role in experiments compared to planetary scales. Secondly, deforming solid materials in experiments is difficult, as the available stress is limited by the size of the setup.

The dynamical consequences of planetary rotation remain largely unexplored in experiments. Some studies have considered its influence on miscible plumes [215–218], bubble-laden plumes (e.g., [219]) or particle clouds [163, 220–222], always in the configuration where the rotation axis and gravity are aligned hence corresponding to flows inside the tangent cylinder. While rotation tends to constrain flow structures to align with and be invariant along the rotation axis, the buoyancy force tends to constrain radial motions. How these constraints compete with one another when gravity and rotation are not aligned, and how the spherical geometry of the core shapes convection, remain two challenging questions for experimentalists.

The influence of magnetic field on the two-phase flow in mushy or slurry layer has only been sparsely investigated by experiments and theoretical work [115, 223]. Experimental studies usually require metallic phases, which are opaque, making two-phase flow tracking very difficult.

Magnetohydrodynamics can be also experimentally studied with a transparent material such as a water-electrolyte solution and an extremely intense magnetic field [224,225]. One might think the solidification of such a water-electrolyte solution makes it possible to have direct visualization of two-phase flows affected by a magnetic field.

5.3. *Similar questions in other fields*

Many more communities share common challenges with core dynamicists, starting with geoscientists studying the cooling of magma reservoirs. Crystallizing magmatic flows are prodigiously complex. Crystals can form in the bulk or on the walls [226, 227] of, for example, a magma chamber—a competition that is challenging to model and unravel from geological samples [228, 229]. Since crystal growth injects latent heat, changes the local fluid composition, and modifies its rheology, the fluid properties and buoyancy hugely depend on the distribution and dynamics of crystals [227, 229, 230]. The resulting convection is reflected in the zonation of rocks on the walls and the alignment of crystals with the flow [228, 229], which depend on the exact convective patterns and chamber geometry [226]. Yet, even from the sole point of view of microphysical processes, the interpretation of geological samples is complex: the porous crystals can temporarily retain liquid or move in a saturated environment [227, 230], which affects their phase change and possibly their density; with polydispersity [231] and aggregation [228], all these ingredients modify crystal migration, with direct feedback on magma heterogeneity and rheology.

In watercourses, basins, or coasts of cold regions (e.g., [136, 232, 233]), water can be supercooled, leading to the formation of sub-millimetric to millimetric ice crystals called *frazil ice* in turbulent streams. In this context as well, the large number of crystals forming in the turbulent flow cannot be resolved numerically, which is why parameterizations (e.g., [234, 235]) or continuum models (e.g., [236]) are used to model the crystals. Despite numerous laboratory and field studies on frazil ice, the exact nucleation mechanism for crystals remains unknown. Additional questions remain to be solved concerning the influence on frazil growth and aggregation of, notably, initial supercooling, thermal evolution of the water column, turbulence intensity, and double-diffusive mixing in saline waters. In-situ observations (e.g., [136]) and laboratory experiments (e.g., [237]) have provided valuable information on the morphology of frazil crystals. Yet, despite the careful analyses of ice samples in thin sections or CAT-SCANS [238], a lot remains to be investigated on their aggregation in anchor ice, whether the latter essentially grow in situ or by collecting frazil crystals, what controls the ability of frazil ice to stick to pebbles or vegetation, and how frazil aggregates manage to trap sediments, pollutants or organisms in grease ice (for a review, see [239]).

A field sharing many challenges with those of the present paper is cloud dynamics, and how it is coupled to cloud microphysics. Although hydrometeors are widely modeled as a continuum in analog experiments (e.g., [167, 240, 241]) and simulations (e.g., [149, 236, 242–244]), the mathematical grounds of the continuum approach are regularly violated due to excessive particle dilution [245, 246]. Disregarding the particulate nature of the hydrometeors, which imposes a spatially-discretized coupling between the air and the particles [170, 247], leads to persistent shortcomings to model how the particle-scale dynamics are coupled to the cloud macrophysics [246, 248]: hydrometeors only drag air in their vicinity and they release or absorb latent heat locally. Since drag and rates of phase change depend crucially on the size of hydrometeors [249–251], cloud microphysics directly affects latent heating and evaporative cooling in stratocumuli, altering cloud convection and stability, with a direct consequence on cloud coverage and hence cloud feedback [252]. Through precipitation, microphysics also hugely affects cloud aggregation which “remains one of the largest sources of uncertainty in climate models and thus

for reliable projections of climate change" [253]: during extreme precipitation events, the simultaneous fall and evaporation of hydrometeors can cause violent downbursts that spread on the floor as cold winds, favoring the ascent of warm updrafts above them, leading to cloud aggregation near the downbursts [254, 255].

These questions are equally relevant on other planets, for example, concerning helium rains due to H-He demixing in Jupiter (e.g., [256, 257]). Convective storms are common in the gas giants of our solar system [258]. The influence of microphysics on their atmosphere dynamics has been mentioned to explain the heterogeneity of ammonia in Jupiter's atmosphere through the formation of ammonia-rich hailstones [259, 260], as expected during some long-lasting evaporatively-driven downdrafts in the deep Jovian atmosphere [258]. More work is also required to model clouds on exoplanets. Taking the example of tidally-locked hot Jupiters, the huge temperature contrast between the sub-stellar point and the night side strongly constrains their atmospheric dynamics [261, 262]. This creates a planetary-scale 3D flow that affects the dispersal and stability of tracers through vertical mixing, with consequences on cloud coverage if cold traps deplete the atmosphere of some chemicals through precipitation [261]. Here again, the size of the meteors greatly affects the outcome of the scenarios that have been modeled [261], but the huge amount of chemicals involved further complexify the picture [262], notably due to the possible change in composition of the particles as they simultaneously grow and migrate in the atmosphere [262, 263].

Declaration of interests

The authors do not work for, advise, own shares in, or receive funds from any organization that could benefit from this article, and have declared no affiliations other than their research organizations.

Funding

LH is supported by the European Research Council (ERC) under the European Unions Horizon 2020 research and innovation programme (grant number 716429). ISTerre is part of Labex OSUG@2020 (ANR10 LABX56). MLB and TA are supported by the Programme National de Planétologie (PNP) of CNRS-INSU co-funded by CNES.

References

[1] U. Christensen, P. Olson, G. Glatzmaier, "Numerical modelling of the geodynamo: a systematic parameter study", *Geophys. J. Int.* **138** (1999), p. 393-409.

[2] M. Landeau, A. Fournier, H.-C. Nataf, D. Cébron, N. Schaeffer, "Sustaining Earth's magnetic dynamo", *Nat. Rev. Earth Environ.* **3** (2022), no. 4, p. 255-269.

[3] R. R. Kerswell, W. V. R. Malkus, "Tidal instability as the source for Io's magnetic signature", *Geophys. Res. Lett.* **25** (1998), no. 5, p. 603-606.

[4] M. Le Bars, M. A. Wieczorek, Ö. Karatekin, D. Cébron, M. Laneuville, "An impact-driven dynamo for the early Moon", *Nature* **479** (2011), no. 7372, p. 215-218.

[5] C. A. Dwyer, D. J. Stevenson, F. Nimmo, "A long-lived lunar dynamo driven by continuous mechanical stirring", *Nature* **479** (2011), no. 7372, p. 212-214.

[6] M. Le Bars, D. Cébron, P. Le Gal, "Flows driven by libration, precession, and tides", *Annu. Rev. Fluid Mech.* **47** (2015), no. 1, p. 163-193.

[7] M. Le Bars, A. Barik, F. Burmann, D. P. Lathrop, J. Noir, N. Schaeffer, S. A. Triana, "Fluid dynamics experiments for planetary interiors", *Surv. Geophys.* **43** (2022), no. 1, p. 229-261.

[8] D. Breuer, T. Rueckriemen, T. Spohn, "Iron snow, crystal floats, and inner-core growth: modes of core solidification and implications for dynamos in terrestrial planets and moons", *Prog. Earth Planet. Sci.* **2** (2015), no. 1, article no. 39.

[9] D. Breuer, T. Spohn, T. Van Hoolst, W. van Westrenen, S. Stanley, N. Rambaux, "Interiors of Earth-like planets and satellites of the solar system", *Surv. Geophys.* **43** (2022), no. 1, p. 177-226.
[10] J. C. E. Irving, S. Cottaar, V. Lekić, "Seismically determined elastic parameters for Earth's outer core", *Sci. Adv.* **4** (2018), no. 6, article no. eaar2538.
[11] L. Waszek, J. Irving, T.-S. Pham, H. Tkalvcić, "Seismic insights into Earth's core", *Nat. Commun.* **14** (2023), no. 1, article no. 6029.
[12] A. Deuss, "Heterogeneity and anisotropy of Earth's inner core", *Annu. Rev. Earth Planet. Sci.* **42** (2014), no. 1, p. 103-126.
[13] R. C. Weber, P.-Y. Lin, E. J. Garnero, Q. Williams, P. Lognonne, "Seismic detection of the lunar core", *Science* **331** (2011), no. 6015, p. 309-312.
[14] R. F. Garcia, J. Gagnepain-Beyneix, S. Chevrot, P. Lognonné, "Very preliminary reference Moon model", *Phys. Earth Planet. Inter.* **188** (2011), no. 1, p. 96-113.
[15] R. F. Garcia, A. Khan, M. Drilleau *et al.*, "Lunar seismology: An update on interior structure models", *Space Sci. Rev.* **215** (2019), p. 1-47.
[16] S. C. Stähler, A. Khan, W. B. Banerdt *et al.*, "Seismic detection of the martian core", *Science* **373** (2021), no. 6553, p. 443-448.
[17] H. Samuel, M. Drilleau, A. Rivoldini *et al.*, "Geophysical evidence for an enriched molten silicate layer above Mars's core", *Nature* **622** (2023), no. 7984, p. 712-717.
[18] J. C. E. Irving, V. Lekić, C. Durán *et al.*, "First observations of core-transiting seismic phases on Mars", *Proc. Natl. Acad. Sci. USA* **120** (2023), no. 18, article no. e2217090120.
[19] M. C. Flemings, "Solidification processing", *Metall. Mater. Trans. B* **5** (1974), p. 2121-2134.
[20] W. Kurz, D. J. Fisher, M. Rappaz, *Fundamentals of Solidification*, 5th ed., Trans Tech Publications, 2023.
[21] R. Deguen, T. Alboussière, D. Brito, "On the existence and structure of a mush at the inner core boundary of the Earth", *Phys. Earth Planet Inter.* **164** (2007), no. 1, p. 36-49.
[22] O. Lielausis, A. Mikelsons, E. Shcherbinin, Y. Gelfgat, "Electric currents in molten metals and their interaction with a magnetic field", in *Proceedings of the I.U.T.A.M. Symposium "Metallurgical Applications of MHD"*, 1982, p. 234-245.
[23] T. Alboussière, R. Moreau, D. Camel, "Influence of a magnetic field on the solidification of metallic alloys", *C. R. Acad. Sci. Paris* **313** (1991), p. 749-755.
[24] P. Lehmann, R. Moreau, D. Camel, R. Bolcato, "Modification of interdendritic convection in directional solidification by a uniform magnetic field", *Acta Mater.* **46** (1998), no. 11, p. 4067-4079.
[25] K. Hirose, S. Labrosse, J. Hernlund, "Composition and state of the core", *Annu. Rev. Earth Planet. Sci.* **41** (2013), p. 657-691.
[26] J. S. Knibbe, W. van Westrenen, "The thermal evolution of Mercury's Fe–Si core", *Earth Planet. Sci. Lett.* **482** (2018), p. 147-159.
[27] G. Morard, C. Sanloup, G. Fiquet, M. Mezouar, N. Rey, R. Poloni, P. Beck, "Structure of eutectic Fe–FeS melts to pressures up to 17 GPa: implications for planetary cores", *Earth Planet. Sci. Lett.* **263** (2007), no. 1–2, p. 128-139.
[28] A. S. Buono, D. Walker, "The Fe-rich liquidus in the Fe–FeS system from 1 bar to 10 GPa", *Geochim. Cosmochim. Acta* **75** (2011), no. 8, p. 2072-2087.
[29] A. L. Edgington, L. Vovcadlo, L. Stixrude, I. G. Wood, D. P. Dobson, E. Holmström, "The top-down crystallisation of Mercury's core", *Earth Planet. Sci. Lett.* **528** (2019), article no. 115838.
[30] A. Pommier, V. Laurenz, C. J. Davies, D. J. Frost, "Melting phase relations in the Fe–S and Fe–SO systems at core conditions in small terrestrial bodies", *Icarus* **306** (2018), p. 150-162.
[31] K. Hikosaka, S. Tagawa, K. Hirose, Y. Okuda, K. Oka, K. Umemoto, Y. Ohishi, "Melting phase relations in Fe–Si–H at high pressure and implications for Earth's inner core crystallization", *Sci. Rep.* **12** (2022), no. 1, article no. 10000.
[32] J. Liu, J. Li, "Solidification of lunar core from melting experiments on the Fe–Ni–S system", *Earth Planet. Sci. Lett.* **530** (2020), article no. 115834.
[33] A. Pease, J. Li, "Liquidus determination of the Fe–S and (Fe, Ni)–S systems at 14 and 24 GPa: Implications for the Mercurian core", *Earth Planet. Sci. Lett.* **599** (2022), article no. 117865.
[34] D. Ikuta, E. Ohtani, N. Hirao, "Two-phase mixture of iron–nickel–silicon alloys in the Earth's inner core", *Commun. Earth Environ.* **2** (2021), no. 1, article no. 225.
[35] T. Komabayashi, G. Pesce, R. Sinmyo *et al.*, "Phase relations in the system Fe–Ni–Si to 200 GPa and 3900 K and implications for Earth's core", *Earth Planet. Sci. Lett.* **512** (2019), p. 83-88.
[36] Y. Shibazaki, H. Terasaki, E. Ohtani, R. Tateyama, K. Nishida, K. I. Funakoshi, Y. Higo, "High-pressure and high-temperature phase diagram for Fe0.9Ni0.1–H alloy", *Phys. Earth Planet. Inter.* **228** (2014), p. 192-201, High-Pressure Research in Earth Science: Crust, Mantle, and Core.
[37] F. Nimmo, "8.02—Energetics of the core", in *Treatise on Geophysics* (G. Schubert, ed.), Elsevier, Oxford, second ed., 2015, p. 27-55.
[38] S. J. Braginsky, "Structure of the F layer and reasons for convection in the Earth's core", *Doklady Akad. Nauk SSSR* **149** (1963), p. 8-10.

[39] J. R. Lister, B. A. Buffett, "The strength and efficiency of thermal and compositional convection in the geodynamo", *Phys. Earth Planet. Inter.* **91** (1995), no. 1–3, p. 17-30.
[40] C. J. Davies, A. Pommier, "Iron snow in the Martian core?", *Earth Planet. Sci. Lett.* **481** (2018), p. 189-200.
[41] J. A. Jacobs, "The Earth's inner core", *Nature* **172** (1953), no. 4372, p. 297-298.
[42] S. A. Hauck, J. M. Aurnou, A. J. Dombard, "Sulfur's impact on core evolution and magnetic field generation on Ganymede", *J. Geophys. Res.* **111** (2006), no. E9, p. 2156-2202.
[43] Y. Fei, C. M. Bertka, L. W. Finger, "High-pressure iron-sulfur compound, Fe3S2, and melting relations in the Fe–FeS system", *Science* **275** (1997), no. 5306, p. 1621-1623.
[44] L. Chudinovskikh, R. Boehler, "Eutectic melting in the system Fe–S to 44 GPa", *Earth Planet. Sci. Lett.* **257** (2007), no. 1, p. 97-103.
[45] A. Rivoldini, T. Van Hoolst, O. Verhoeven, A. Mocquet, V. Dehant, "Geodesy constraints on the interior structure and composition of Mars", *Icarus* **213** (2011), no. 2, p. 451-472.
[46] M. Dumberry, A. Rivoldini, "Mercury's inner core size and core-crystallization regime", *Icarus* **248** (2015), p. 254-268.
[47] T. Rückriemen, D. Breuer, T. Spohn, "The Fe snow regime in Ganymede's core: a deep-seated dynamo below a stable snow zone", *J. Geophys. Res. Planets* **120** (2015), p. 1095-1118.
[48] T. Rückriemen, D. Breuer, T. Spohn, "Top-down freezing in a Fe–FeS Core and Ganymede's present-day magnetic field", *Icarus* **307** (2018), p. 172-196.
[49] L. Huguet, J. A. Van Orman, S. A. Hauck, M. A. Willard, "Earth's inner core nucleation paradox", *Earth Planet. Sci. Lett.* **487** (2018), p. 9-20.
[50] U. Svensson, A. Omstedt, "Simulation of supercooling and size distribution in frazil ice dynamics", *Cold Reg. Sci. Technol.* **22** (1994), no. 3, p. 221-233.
[51] L. Huguet, M. Le Bars, R. Deguen, "A laboratory model for iron snow in planetary cores", *Geophys. Res. Lett.* **50** (2023), no. 24, article no. e2023GL105697.
[52] D. Loper, "A nonequilibrium theory of a slurry", *Continuum Mech. Thermodyn.* **4** (1992), no. 3, p. 213-245.
[53] F. Wilczyński, C. J. Davies, C. A. Jones, "A two-phase pure slurry model for planetary cores: one-dimensional solutions and implications for Earth's F-layer", *J. Fluid Mech.* **976** (2023), article no. A5.
[54] U. R. Christensen, "Iron snow dynamo models for Ganymede", *Icarus* **247** (2015), p. 248-259.
[55] J. W. Rutter, B. Chalmers, "A prismatic substructure formed during solidification of metals", *Can. J. Phys.* **31** (1953), no. 1, p. 15-39.
[56] W. W. Mullins, R. F. Sekerka, "Stability of a planar interface during solidification of a dilute binary alloy", *J. Appl. Phys.* **35** (1964), p. 444-451.
[57] H. Shimizu, J. P. Poirier, J. L. Le Mouël, "On crystallization at the inner core boundary", *Phys. Earth Planet. Inter.* **151** (2005), no. 1, p. 37-51.
[58] J. W. Christian, *The Theory of Transformations in Metals and Alloys*, Elsevier, Newnes, 2002.
[59] B. Chen, J. Li, S. A. Hauck II, "Non-ideal liquidus curve in the Fe–S system and Mercury's snowing core", *Geophys. Res. Lett.* **35** (2008), no. 7, article no. L07201.
[60] S. Labrosse, J.-L. Poirier, J.-L. LeMouël, "The age of the inner core", *Earth Planet. Sci. Lett.* **190** (2001), p. 111-123.
[61] L. Huguet, T. Alboussière, M. I. Bergman, R. Deguen, S. Labrosse, G. Lesœur, "Structure of a mushy layer under hypergravity with implications for Earth's inner core", *Geophys. J. Int.* **204** (2016), no. 3, p. 1729-1755.
[62] D. R. Fearn, D. E. Loper, P. H. Roberts, "Structure of the Earth's inner core", *Nature* **292** (1981), p. 232-233.
[63] J. Wong, C. J. Davies, C. A. Jones, "A regime diagram for the slurry F-layer at the base of Earth's outer core", *Earth Planet. Sci. Lett.* **560** (2021), article no. 116791.
[64] P. H. Roberts, D. E. Loper, "Towards a theory of the structure and evolution of a dendrite layer", in *Stellar and Planetary Magnetism*, Gordon & Breach Science Publishers Ltd, 1983, ISBN-10: 0677164300, ISBN-13: 978-0677164304.
[65] H. Haack, E. R. D. Scott, "Asteroid core crystallization by inward dendritic growth", *J. Geophys. Res.* **97** (1992), no. E9, p. 14727-14734.
[66] N. L. Chabot, H. Haack, *Evolution of Asteroidal Cores*, University of Arizona Press, 2006, 747-771 pages.
[67] L. Huguet, *Cristallisation et convection sous hyper-gravité*, Phd thesis, Ecole Normale Supérieure de Lyon, 2014.
[68] K. Jackson, J. Hunt, D. Uhlmann, T. Seward, "On origin of equiaxed zone in castings", *Trans. Metall. Soc. AIME* **236** (1966), no. 2, p. 149-158.
[69] D. Turnbull, "Formation of crystal nuclei in liquid metals", *J. Appl. Phys.* **21** (1950), no. 10, p. 1022-1028.
[70] D. W. Gomersall, S. Y. Shiraishi, R. G. Ward, "Undercooling phenomena in liquid metal droplets", *J. Aust. Inst. Metals* **10** (1965), no. 3, p. 220-222.
[71] J. Schade, A. McLean, W. Miller, "Surface tension measurements on oscillating droplets of undercooled liquid metals and alloys", in *Undercooled Alloy Phases* (E. W. Collings, C. C. Koch, eds.), The Metall. Soc. AIME, 1987, p. 233-248.
[72] F. C. Frank, "Supercooling of liquids", *Proc. R. Soc. Lond. A.* **215** (1952), no. 1120, p. 43-46.
[73] K. F. Kelton, G. W. Lee, A. K. Gangopadhyay, R. W. Hyers, T. J. Rathz, J. R. Rogers, M. B. Robinson, D. S. Robinson, "First

X-ray scattering studies on electrostatically levitated metallic liquids: demonstrated influence of local icosahedral order on the nucleation barrier", *Phys. Rev. Lett.* **90** (2003), no. 19, article no. 195504.
[74] T. Schenk, D. Holland-Moritz, V. Simonet, R. Bellissent, D. M. Herlach, "Icosahedral short-range order in deeply undercooled metallic melts", *Phys. Rev. Lett.* **89** (2002), no. 7, article no. 075507.
[75] P. Ganesh, M. Widom, "Ab initio simulations of geometrical frustration in supercooled liquid Fe and Fe-based metallic glass", *Phys. Rev. B* **77** (2008), no. 1, article no. 014205.
[76] M. Inui, K. Maruyama, Y. Kajihara, M. Nakada, "Icosahedral ordering in liquid iron studied via x-ray scattering and Monte Carlo simulations", *Phys. Rev. B* **80** (2009), no. 18, article no. 180201.
[77] D. Shechtman, I. Blech, D. Gratias, J. W. Cahn, "Metallic phase with long-range orientational order and no translational symmetry", *Phys. Rev. Lett.* **53** (1984), no. 20, article no. 1951.
[78] D. Holland-Moritz, T. Schenk, V. Simonet, R. Bellissent, P. Convert, T. Hansen, D. M. Herlach, "Short-range order in undercooled metallic liquids", *Mater. Sci. Eng.: A* **375** (2004), p. 98-103.
[79] R. Boehler, M. Ross, "2.22—Properties of rocks and minerals, high-pressure melting", in *Treatise on Geophysics* (G. Schubert, ed.), Elsevier, Oxford, 2nd ed., 2015, p. 573-582.
[80] G. Kurtuldu, P. Jarry, M. Rappaz, "Influence of Cr on the nucleation of primary Al and formation of twinned dendrites in Al–Zn–Cr alloys: Can icosahedral solid clusters play a role?", *Acta Mater.* **61** (2013), no. 19, p. 7098-7108.
[81] K. F. Kelton, A. K. Gangopadhyay, G. W. Lee *et al.*, "X-ray and electrostatic levitation undercooling studies in Ti–Zr–Ni quasicrystal forming alloys", *J. Non-Cryst. Solids* **312** (2002), p. 305-308.
[82] A. K. Gangopadhyay, M. E. Sellers, G. P. Bracker *et al.*, "Demonstration of the effect of stirring on nucleation from experiments on the International Space Station using the ISS-EML facility", *NPJ Microgravity* **7** (2021), no. 1, article no. 31.
[83] D. M. Matson, L. Battezzati, P. K. Galenko *et al.*, "Electromagnetic levitation containerless processing of metallic materials in microgravity: rapid solidification", *NPJ Microgravity* **9** (2023), no. 1, article no. 65.
[84] J. Li, Q. Wu, J. Li *et al.*, "Shock melting curve of iron: A consensus on the temperature at the Earth's inner core boundary", *Geophys. Res. Lett.* **47** (2020), no. 15, article no. e2020GL087758.
[85] R. G. Kraus, R. J. Hemley, S. J. Ali *et al.*, "Measuring the melting curve of iron at super-Earth core conditions", *Science* **375** (2022), no. 6577, p. 202-205.
[86] L. Huguet, S. A. Hauck, J. A. Van Orman, Z. Jing, "Implications of the homogeneous nucleation barrier for top-down crystallization in Mercury's Core", in *Mercury: Current and Future Science of the Innermost Planet*, vol. 2047, Lunar and Planetary Institute, 2018, p. 6101.
[87] A. J. Wilson, D. Alfè, A. M. Walker, C. J. Davies, "Can homogeneous nucleation resolve the inner core nucleation paradox?", *Earth Planet. Sci. Lett.* **614** (2023), article no. 118176.
[88] A. J. Wilson, A. M. Walker, D. Alfè, C. J. Davies, "Probing the nucleation of iron in Earth's core using molecular dynamics simulations of supercooled liquids", *Phys. Rev. B* **103** (2021), no. 21, article no. 214113.
[89] Y. Sun, F. Zhang, M. I. Mendelev, R. M. Wentzcovitch, K.-M. Ho, "Two-step nucleation of the Earth's inner core", *Proc. Natl. Acad. Sci. USA* **119** (2022), no. 2, article no. e2113059119.
[90] C. J. Davies, M. Pozzo, D. Alfè, "Assessing the inner core nucleation paradox with atomic-scale simulations", *Earth Planet. Sci. Lett.* **507** (2019), p. 1-9.
[91] M. Lasbleis, M. Kervazo, G. Choblet, "The fate of liquids trapped during the earth's inner core growth", *Geophys. Res. Lett.* **47** (2020), no. 2, article no. e2019GL085654.
[92] C. Beckermann, C. Y. Wang, "Multiphase/-scale modeling of alloy solidification", *Annu. Rev. Heat Transfer* **6** (1995), p. 115-198.
[93] M. G. Worster, "Convection in mushy layers", *Annu. Rev. Fluid Mech.* **29** (1997), no. 1, p. 91-122.
[94] D. L. Feltham, N. Untersteiner, J. S. Wettlaufer, M. G. Worster, "Sea ice is a mushy layer", *Geophys. Res. Lett.* **33** (2006), no. 14, article no. L14501.
[95] S. M. Copley, A. F. Giamei, S. M. Johnson, M. F. Hornbecker, "The origin of freckles in unidirectionally solidified castings", *Metall. Trans.* **1** (1970), no. 8, p. 2193-2204.
[96] J. R. Sarazin, A. Hellawell, "Channel formation in Pb–Sb, Pb–Sn, and Pb–Sn–Sb alloy ingots and comparison with the system NH_4Cl–H_2O", *Metall. Trans. A* **19** (1988), no. 7, p. 1861-1871.
[97] C. F. Chen, F. Chen, "Experimental study of directional solidification of aqueous ammonium chloride solution", *J. Fluid Mech.* **227** (1991), p. 567-586.
[98] S. Tait, C. Jaupart, "Compositional convection in a reactive crystalline mush and melt differentiation", *J. Geophys. Res.* **97** (1992), no. B5, p. 6735-6756.
[99] M. G. Worster, R. C. Kerr, "The transient behaviour of alloys solidified from below prior to the formation of chimneys", *J. Fluid Mech.* **269** (1994), p. 23-44.
[100] M. G. Worster, J. S. Wettlaufer, "Natural convection, solute trapping, and channel formation during solidification of saltwater", *J. Phys. Chem. B* **101** (1997), no. 32, p. 6132-6136.
[101] M. I. Bergman, M. Macleod-Silberstein, M. Haskel, B. Chandler, N. Akpan, "A laboratory model for solidification

of Earth's core", *Phys. Earth Planet. Inter.* **153** (2005), no. 1–3, p. 150-164, Studies of the Earth's Deep Interior SEDI 2004.
[102] M. I. Bergman, D. R. Fearn, J. Bloxham, M. C. Shannon, "Convection and channel formation in solidifying Pb–Sn alloys", *Metall. Mater. Trans. A* **28** (1997), no. 3, p. 859-866.
[103] D. E. Loper, P. H. Roberts, "A study of conditions at the inner core boundary of the Earth", *Phys. Earth Planet. Inter.* **24** (1981), no. 4, p. 302-307.
[104] M. G. Worster, "Instabilities of the liquid and mushy regions during solidification of alloys", *J. Fluid Mech.* **237** (1992), p. 649-669.
[105] A. J. Wells, J. S. Wettlaufer, S. A. Orszag, "Maximal potential energy transport: A variational principle for solidification problems", *Phys. Rev. Lett.* **105** (2010), no. 25, article no. 254502.
[106] A. J. Wells, J. S. Wettlaufer, S. A. Orszag, "Brine fluxes from growing sea ice", *Geophys. Res. Lett.* **38** (2011), no. 4, article no. L04501.
[107] A. J. Wells, J. S. Wettlaufer, S. A. Orszag, "Nonlinear mushy-layer convection with chimneys: stability and optimal solute fluxes", *J. Fluid Mech.* **716** (2013), p. 203-227.
[108] D. W. Jones, M. G. Worster, "Fluxes through steady chimneys in a mushy layer during binary alloy solidification", *J. Fluid Mech.* **714** (2013), p. 127-151.
[109] P. C. Carman, *Flow of Gases Through Porous Media*, Academic Press, 1956.
[110] T. Takaki, S. Sakane, M. Ohno, Y. Shibuta, T. Aoki, "Permeability prediction for flow normal to columnar solidification structures by large–scale simulations of phase–field and lattice Boltzmann methods", *Acta Mater.* **164** (2019), p. 237-249.
[111] M. G. Worster, "Natural convection in a mushy layer", *J. Fluid Mech.* **224** (1991), p. 335-359.
[112] R. J. McDonald, J. D. Hunt, "Convective fluid motion within the interdendritic liquid of a casting", *Metall. Mater. Trans. B* **1** (1970), no. 6, p. 1787-1788.
[113] K. H. Esbensen, V. F. Buchwald, "Planet(oid) core crystallisation and fractionation-evidence from the Agpalilik mass of the Cape York iron meteorite shower", *Phys. Earth Planet. Inter.* **29** (1982), no. 3, p. 218-232.
[114] M. I. Bergman, D. R. Fearn, "Chimneys on the Earth's inner-outer core boundary?", *Geophys. Res. Lett.* **21** (1994), no. 6, p. 477-480.
[115] M. I. Bergman, D. R. Fearn, J. Bloxham, "Suppression of channel convection in solidifying Pb–Sn alloys via an applied magnetic field", *Metall. Mater. Trans. A* **30** (1999), no. 7, p. 1809-1815.
[116] A. Hellawell, P. M. Herbert, "The development of preferred orientations during the freezing of metals and alloys", *Proc. R. Soc. Lond.. Series A. Math. Phys. Sci.* **269** (1962), no. 1339, p. 560-573.
[117] S. Corrsin, "Further generalization of Onsager's cascade model for turbulent spectra", *Phys. Fluids* **7** (1964), p. 1156-1159.
[118] S. Tateno, K. Hirose, Y. Ohishi, Y. Tatsumi, "The structure of iron in Earth's inner core", *Science* **330** (2010), no. 6002, p. 359-361.
[119] L. Vovcadlo, I. G. Wood, M. J. Gillan, J. Brodholt, D. P. Dobson, G. D. Price, D. Alfè, "The stability of bcc-Fe at high pressures and temperatures with respect to tetragonal strain", *Phys. Earth Planet. Inter.* **170** (2008), no. 1–2, p. 52-59.
[120] A. B. Belonoshko, T. Lukinov, J. Fu, J. Zhao, S. Davis, S. I. Simak, "Stabilization of body-centred cubic iron under inner-core conditions", *Nat. Geosci.* **10** (2017), no. 4, p. 312-316.
[121] M. I. Bergman, D. M. Cole, J. R. Jones, "Preferred crystal orientations due to melt convection during directional solidification", *J. Geophys. Res.: Solid Earth* **107** (2002), no. B9, article no. ECV-6.
[122] M. I. Bergman, "Measurements of electric anisotropy due to solidification texturing and the implications for the Earth's inner core", *Nature* **389** (1997), no. 6646, p. 60-63.
[123] M. I. Bergman, "Estimates of the Earth's inner core grain size", *Geophys. Res. Lett.* **25** (1998), no. 10, p. 1593-1596.
[124] I. Sumita, S. Yoshida, M. Kumazawa, Y. Hamano, "A model for sedimentary compaction of a viscous medium and its application to inner-core growth", *Geophys. J. Int.* **124** (1996), no. 2, p. 502-524.
[125] A. Scheinberg, L. T. Elkins-Tanton, G. Schubert, D. Bercovici, "Core solidification and dynamo evolution in a mantle-stripped planetesimal", *J. Geophys. Res.* **121** (2016), no. 1, p. 2-20.
[126] J. A. Neufeld, J. F. J. Bryson, F. Nimmo, "The top-down solidification of iron asteroids driving dynamo evolution", *J. Geophys. Res.* **124** (2019), no. 5, p. 1331-1356.
[127] F. Chen, "Stability analysis on convection in directional solidification of binary solutions (invited review paper)", *Proc.-Nat. Sci. Council Republic of Chin. Part a Phys. Sci. Eng.* **25** (2001), no. 2, p. 71-83.
[128] R. Deguen, *Dynamique de la cristallisation de la graine: expériences et modèles*, Phd thesis, Université Joseph-Fourier-Grenoble I, 2009.
[129] S. Anders, D. Noto, Y. Tasaka, S. Eckert, "Simultaneous optical measurement of temperature and velocity fields in solidifying liquids", *Exp. Fluids* **61** (2020), p. 1-19.
[130] T. Campanella, C. Charbon, M. Rappaz, "Grain refinement induced by electromagnetic stirring: A dendrite fragmentation criterion", *Metall. Mater. Trans. A* **35** (2004), p. 3201-3210.
[131] M. Stefan-Kharicha, A. Kharicha, M. Wu, A. Ludwig, "On the coupling mechanism of equiaxed crystal generation

with the liquid flow driven by natural convection during solidification", *Metall. Mater. Trans. A* **49** (2018), p. 1708-1724.
[132] S. Ritterbex, T. Tsuchiya, "Viscosity of hcp iron at Earth's inner core conditions from density functional theory", *Sci. Rep.* **10** (2020), no. 1, article no. 6311.
[133] V. Regard, C. Faccenna, O. Bellier, J. Martinod, "Laboratory experiments of slab break-off and slab dip reversal: insight into the Alpine Oligocene reorganization", *Terra Nova* **20** (2008), no. 4, p. 267-273.
[134] T. Duretz, S. M. Schmalholz, T. V. Gerya, "Dynamics of slab detachment", *Geochem. Geophys. Geosyst.* **13** (2012), no. 3, article no. Q03020.
[135] D. Bercovici, G. Schubert, Y. Ricard, "Abrupt tectonics and rapid slab detachment with grain damage", *Proc. Natl. Acad. Sci. USA* **112** (2015), no. 5, p. 1287-1291.
[136] S. F. Daly, Cold Regions Research and Engineering Laboratory (U.S.), *Frazil Ice Dynamics*, vol. 84, US Army Corps of Engineers, Cold Regions Research & Engineering Laboratory, 1984.
[137] A. Souriau, G. Poupinet, "The velocity profile at the base of the liquid core from PKP(BC+Cdiff) data: An argument in favour of radial inhomogeneity", *Geophys. Res. Lett.* **18** (1991), no. 11, p. 2023-2026.
[138] T. Ohtaki, S. Kaneshima, "Independent estimate of velocity structure of Earth's lowermost outer core beneath the northeast Pacific from PKiKP- PKPbc differential traveltime and dispersion in PKPbc", *J. Geophys. Res.: Solid Earth* **120** (2015), no. 11, p. 7572-7586.
[139] A. M. Dziewonski, D. L. Anderson, "Preliminary reference Earth model", *Phys. Earth Planet. Inter.* **25** (1981), no. 4, p. 297-356.
[140] T. Alboussière, R. Deguen, M. Melzani, "Melting-induced stratification above the Earth's inner core due to convective translation", *Nature* **466** (2010), no. 7307, p. 744-747.
[141] M. Monnereau, M. Calvet, L. Margerin, A. Souriau, "Lopsided growth of Earth's inner core", *Science* **328** (2010), no. 5981, p. 1014-1017.
[142] D. Gubbins, B. Sreenivasan, J. Mound, S. Rost, "Melting of the Earth's inner core", *Nature* **473** (2011), no. 7347, p. 361-363.
[143] M. A. Hallworth, H. E. Huppert, A. W. Woods, "Crystallization and layering induced by heating a reactive porous medium", *Geophys. Res. Lett.* **31** (2004), no. 13, article no. L13605.
[144] M. A. Hallworth, H. E. Huppert, A. W. Woods, "Dissolution-driven convection in a reactive porous medium", *J. Fluid Mech.* **535** (2005), p. 255-285.
[145] J. Yu, M. I. Bergman, L. Huguet, T. Alboussière, "Partial melting of a Pb–Sn mushy layer due to heating from above, and implications for regional melting of Earth's directionally solidified inner core", *Geophys. Res. Lett.* **42** (2015), p. 7046-7053.
[146] F. Chen, "Formation of double-diffusive layers in the directional solidification of binary solution", *J. Cryst. Growth* **179** (1997), no. 1–2, p. 277-286.
[147] H. M. Fritz, F. Mohammed, J. Yoo, "Lituya Bay landslide impact generated mega-tsunami 50 th Anniversary", in *Tsunami Science Four Years after the 2004 Indian Ocean Tsunami: Part II: Observation and Data Analysis*, Birkhäuser, Basel, 2009, p. 153-175.
[148] F. Necker, C. Härtel, L. Kleiser, E. Meiburg, "High-resolution simulations of particle-driven gravity currents", *Int. J. Multiphase Flow* **28** (2002), no. 2, p. 279-300.
[149] R. Ouillon, E. Meiburg, B. R. Sutherland, "Turbidity currents propagating down a slope into a stratified saline ambient fluid", *Environ. Fluid Mech.* **19** (2019), no. 5, p. 1143-1166.
[150] A. Köhler, J. N. McElwaine, B. Sovilla, "GEODAR data and the flow regimes of snow avalanches", *J. Geophys. Res.: Earth Surf.* **123** (2018), no. 6, p. 1272-1294.
[151] C. T. Crowe, J. D. Schwarzkopf, M. Sommerfeld, Y. Tsuji, *Multiphase Flows with Droplets and Particles*, vol. 2, CRC Press, Boca Raton, 2011.
[152] Q. Kriaa, B. Favier, M. Le Bars, "Two-way coupling Eulerian numerical simulations of particle clouds settling in a quiescent fluid", *Phys. Rev. Fluids* **8** (2023), no. 7, article no. 074302.
[153] C. D. McConnochie, C. Cenedese, J. N. McElwaine, "Entrainment into particle-laden turbulent plumes", *Phys. Rev. Fluids* **6** (2021), no. 12, article no. 123502.
[154] T. Zürner, C. Toupoint, D. De Souza, D. Mezouane, R. Monchaux, "Settling of localized particle plumes in a quiescent water tank", *Phys. Rev. Fluids* **8** (2023), no. 2, article no. 024301.
[155] M. Dadonau, J. L. Partridge, P. F. Linden, "The effect of double diffusion on entrainment in turbulent plumes", *J. Fluid Mech.* **884** (2020), article no. A6.
[156] H. Rahimipour, D. Wilkinson, "Dynamic behaviour of particle clouds", in *11th Australasian Fluid Mechanics Conference University of Tasmania, Hobart, Australia*, 1992.
[157] G. J. Ruggaber, *Dynamics of sediment clouds related to open-water sediment disposal*, Phd thesis, MIT, 2000.
[158] J. W. M. Bush, B. A. Thurber, F. Blanchette, "Particle clouds in homogeneous and stratified environments", *J. Fluid Mech.* **489** (2003), p. 29-54.

[159] B. Zhao, A. W. K. Law, E. Eric Adams, D. Shao, Z. Huang, "Effect of air release height on the formation of sediment thermals in water", *J. Hydraul. Res.* **50** (2012), no. 5, p. 532-540.
[160] A. C. H. Lai, B. Zhao, A. W.-K. Law, E. E. Adams, "Two-phase modeling of sediment clouds", *Environ. Fluid Mech.* **13** (2013), no. 5, p. 435-463.
[161] M. Landeau, R. Deguen, P. Olson, "Experiments on the fragmentation of a buoyant liquid volume in another liquid", *J. Fluid Mech.* **749** (2014), p. 478-518.
[162] P. Peñas, O. R. Enríquez, J. Rodríguez-Rodríguez, "Bubble-laden thermals in supersaturated water", *J. Fluid Mech.* **924** (2021), article no. A31.
[163] Q. Kriaa, E. Subra, B. Favier, M. Le Bars, "Effects of particle size and background rotation on the settling of particle clouds", *Phys. Rev. Fluids* **7** (2022), no. 12, article no. 124302.
[164] R. Deguen, P. Olson, P. Cardin, "Experiments on turbulent metal-silicate mixing in a magma ocean", *Earth Planet. Sci. Lett.* **310** (2011), no. 3, p. 303-313.
[165] G. Boffetta, A. Mazzino, "Incompressible Rayleigh–Taylor turbulence", *Annu. Rev. Fluid Mech.* **49** (2017), no. 1, p. 119-143.
[166] S. Carey, "Influence of convective sedimentation on the formation of widespread tephra fall layers in the deep sea", *Geology* **25** (1997), no. 9, p. 839-842.
[167] A. Fries, J. Lemus, P. A. Jarvis, A. B. Clarke, J. C. Phillips, I. Manzella, C. Bonadonna, "The influence of particle concentration on the formation of settling-driven gravitational instabilities at the base of volcanic clouds", *Front. Earth Sci.* **9** (2021), article no. 640090.
[168] M. Mizukami, R. N. Parthasarathy, G. M. Faeth, "Particle-generated turbulence in homogeneous dilute dispersed flows", *Int. J. Multiph. Flow* **18** (1992), no. 3, p. 397-412.
[169] V. Manville, C. J. N. Wilson, "Vertical density currents: a review of their potential role in the deposition and interpretation of deep-sea ash layers", *J. Geol. Soc.* **161** (2004), no. 6, p. 947-958.
[170] S. Harada, T. Mitsui, K. Sato, "Particle-like and fluid-like settling of a stratified suspension", *Eur. Phys. J. E* **35** (2012), no. 1, article no. 1.
[171] Y. Yamamoto, F. Hisataka, S. Harada, "Numerical simulation of concentration interface in stratified suspension: continuum–particle transition", *Int. J. Multiph. Flow* **73** (2015), p. 71-79.
[172] R. Kimura, "Cell formation in the convective mixed layer", *Fluid Dyn. Res.* **3** (1988), no. 1, p. 395-399.
[173] E. Climent, J. Magnaudet, "Large-scale simulations of bubble-induced convection in a liquid layer", *Phys. Rev. Lett.* **82** (1999), no. 24, p. 4827-4830.
[174] Y. Mezui, M. Obligado, A. Cartellier, "Buoyancy-driven bubbly flows: scaling of velocities in bubble columns operated in the heterogeneous regime", *J. Fluid Mech.* **952** (2022), article no. A10.
[175] R. F. Mudde, "Gravity-driven bubbly flows", *Annu. Rev. Fluid Mech.* **37** (2005), no. 1, p. 393-423.
[176] K. Iga, R. Kimura, "Convection driven by collective buoyancy of microbubbles", *Fluid Dyn. Res.* **39** (2007), no. 1, p. 68-97.
[177] C. Beckermann, C. Y. Wang, "Equiaxed dendritic solidification with convection: Part III. Comparisons with NH_4Cl–H_2O experiments", *Metall. Mater. Trans. A* **27** (1996), no. 9, p. 2784-2795.
[178] A. Kharicha, M. Stefan-Kharicha, A. Ludwig, M. Wu, "Simultaneous observation of melt flow and motion of equiaxed crystals during solidification using a dual phase particle image velocimetry technique. Part I: Stage characterization of melt flow and equiaxed crystal motion", *Metall. Mater. Trans. A* **44** (2013), p. 650-660.
[179] R. S. Rerko, H. C. de Groh, C. Beckermann, "Effect of melt convection and solid transport on macrosegregation and grain structure in equiaxed Al–Cu alloys", *Mater. Sci. Eng.: A* **347** (2003), no. 1–2, p. 186-197.
[180] M. Wu, A. Ludwig, "Modeling equiaxed solidification with melt convection and grain sedimentation-I: Model description", *Acta Mater.* **57** (2009), no. 19, p. 5621-5631.
[181] C. Beckermann, "Modelling of macrosegregation: applications and future needs", *Int. Mater. Rev.* **47** (2002), no. 5, p. 243-261.
[182] S. Sakane, T. Takaki, M. Ohno, Y. Shibuta, T. Aoki, "Two-dimensional large-scale phase-field lattice Boltzmann simulation of polycrystalline equiaxed solidification with motion of a massive number of dendrites", *Comput. Mater. Sci.* **178** (2020), article no. 109639.
[183] N. Yamanaka, S. Sakane, T. Takaki, "Multi-phase-field lattice Boltzmann model for polycrystalline equiaxed solidification with motion", *Comput. Mater. Sci.* **197** (2021), article no. 110658.
[184] T. Takaki, "Large-scale phase-field simulations for dendrite growth: A review on current status and future perspective", in *IOP Conference Series: Materials Science and Engineering*, vol. 1274, IOP Publishing, 2023.
[185] B. Appolaire, V. Albert, H. Combeau, G. Lesoult, "Experimental study of free growth of equiaxed NH4Cl crystals settling in undercooled NH_4Cl–H_2O melts", *ISIJ Int.* **39** (1999), no. 3, p. 263-270.
[186] A. Badillo, D. Ceynar, C. Beckermann, "Growth of equiaxed dendritic crystals settling in an undercooled melt, Part 1: Tip kinetics", *J. Cryst. Growth* **309** (2007), no. 2, p. 197-215.
[187] A. Hellawell, S. Liu, S. Lu, "Dendrite fragmentation and the effects of fluid flow in castings", *Jom* **49** (1997), no. 3, p. 18-20.

[188] A. Ludwig, M. Stefan-Kharicha, A. Kharicha, M. Wu, "Massive formation of equiaxed crystals by avalanches of mushy zone segments", *Metall. Mater. Trans. A* **48** (2017), p. 2927-2931.
[189] S. Anders, D. Noto, M. Seilmayer, S. Eckert, "Spectral random masking: a novel dynamic masking technique for PIV in multiphase flows", *Exp. Fluids* **60** (2019), p. 1-6.
[190] J. Wong, C. J. Davies, C. A. Jones, "A Boussinesq slurry model of the F-layer at the base of Earth's outer core", *Geophys. J. Int.* **214** (2018), no. 3, p. 2236-2249.
[191] D. E. Loper, P. H. Roberts, "On the motion of an iron-alloy core containing a slurry: I. General theory", *Geophys. Astrophys. Fluid Dyn.* **9** (1977), no. 1, p. 289-321.
[192] P. Olson, M. Landeau, B. H. Hirsh, "Laboratory experiments on rain-driven convection: implications for planetary dynamos", *Earth Planet. Sci. Lett.* **457** (2017), p. 403-411.
[193] A. J. Wells, M. G. Worster, "Melting and dissolving of a vertical solid surface with laminar compositional convection", *J. Fluid Mech.* **687** (2011), p. 118-140.
[194] L. Gagliardi, O. Pierre-Louis, "Thin film modeling of crystal dissolution and growth in confinement", *Phys. Rev. E* **97** (2018), no. 1, article no. 012802, https://arxiv.org/abs/1801.02552.
[195] B. Favier, J. Purseed, L. Duchemin, "Rayleigh–Bénard convection with a melting boundary", *J. Fluid Mech.* **858** (2019), p. 437-473.
[196] R. G. Rice, P. J. Jones, "Complete dissolution of spherical particles in free-fall", *Chem. Eng. Sci.* **34** (1979), no. 6, p. 847-852.
[197] R. G. Rice, "Transpiration effects in solids dissolution", *Chem. Eng. Sci.* **37** (1982), no. 10, p. 1465-1469.
[198] T. Elperin, A. Fominykh, "Mass and heat transfer during solid sphere dissolution in a non-uniform fluid flow", *Heat Mass Transf.* **41** (2005), no. 5, p. 442-448.
[199] R. G. Rice, D. D. Do, "Dissolution of a solid sphere in an unbounded, stagnant liquid", *Chem. Eng. Sci.* **61** (2006), no. 2, p. 775-778.
[200] L. Huguet, V. Barge-Zwick, M. Le Bars, "Dynamics of a reactive spherical particle falling in a linearly stratified fluid", *Phys. Rev. Fluids* **5** (2020), no. 11, article no. 114803.
[201] J. Zhang, M. J. Mercier, J. Magnaudet, "Core mechanisms of drag enhancement on bodies settling in a stratified fluid", *J. Fluid Mech.* **875** (2019), p. 622-656.
[202] N. He, Y. Cui, D. W. Q. Chin, T. Darnige, P. Claudin, B. Semin, "Sedimentation of a single soluble particle at low Reynolds and high Péclet numbers", *Phys. Rev. Fluids* **9** (2024), no. 4, article no. 44502.
[203] Q. Kriaa, *Flows induced by the settling and phase change of particles: iron rain and iron snow in planetary interiors*, Phd thesis, Aix-Marseille Universite, 2023.
[204] R. C. Kerr, "Convective crystal dissolution", *Contrib. Mineral. Petrol.* **121** (1995), no. 3, p. 237-246.
[205] N. Magnan, T. Heinemann, H. N. Latter, "A physical picture for the acoustic resonant drag instability", *Mont. Not. R. Astron. Soc.* **529** (2024), no. 1, p. 688-701.
[206] V. F. Cormier, "Texture of the uppermost inner core from forward-and back-scattered seismic waves", *Earth Planet. Sci. Lett.* **258** (2007), no. 3, p. 442-453.
[207] V. F. Cormier, J. Attanayake, "Earth's solid inner core: Seismic implications of freezing and melting", *J. Earth Sci.* **24** (2013), no. 5, p. 683-698.
[208] A. Lincot, P. Cardin, R. Deguen, S. Merkel, "Multiscale model of global inner-core anisotropy induced by hcp alloy plasticity", *Geophys. Res. Lett.* **43** (2016), no. 3, p. 1084-1091.
[209] M. I. Bergman, L. Giersch, M. Hinczewski, V. Izzo, "Elastic and attenuation anisotropy in directionally solidified (hcp) zinc, and the seismic anisotropy in the Earth's inner core", *Phys. Earth Planet. Inter.* **117** (2000), no. 1, p. 139-151.
[210] D. Brito, D. Elbert, P. Olson, "Experimental crystallization of gallium: ultrasonic measurements of elastic anisotropy and implications for the inner core", *Phys. Earth Planet. Inter.* **129** (2002), no. 3–4, p. 325-346.
[211] R. Deguen, "Structure and dynamics of Earth's inner core", *Earth Planet. Sci. Lett.* **333** (2012), p. 211-225.
[212] F. Guillard, P. Golshan, L. Shen, J. R. Valdes, I. Einav, "Dynamic patterns of compaction in brittle porous media", *Nat. Phys.* **11** (2015), no. 10, p. 835-838.
[213] C. David, T.-f. Wong, W. Zhu, J. Zhang, "Laboratory measurement of compaction-induced permeability change in porous rocks: Implications for the generation and maintenance of pore pressure excess in the crust", *Pure Appl. Geophys.* **143** (1994), p. 425-456.
[214] T. W. Barraclough, J. R. Blackford, S. Liebenstein, S. Sandfeld, T. J. Stratford, G. Weinländer, M. Zaiser, "Propagating compaction bands in confined compression of snow", *Nat. Phys.* **13** (2017), no. 3, p. 272-275.
[215] H. J. S. Fernando, R.-r. Chen, B. A. Ayotte, "Development of a point plume in the presence of background rotation", *Phys. Fluids* **10** (1998), no. 9, p. 2369-2383.
[216] J. C. Goodman, G. C. Collins, J. Marshall, R. T. Pierrehumbert, "Hydrothermal plume dynamics on Europa: Implications for chaos formation", *J. Geophys. Res.* **109** (2004), no. E3, article no. E03008.
[217] D. Frank, J. R. Landel, S. B. Dalziel, P. F. Linden, "Anticyclonic precession of a plume in a rotating environment", *Geophys. Res. Lett.* **44** (2017), no. 18, p. 9400-9407.

[218] B. R. Sutherland, Y. Ma, M. R. Flynn *et al.*, "Plumes in rotating fluid and their transformation into tornados", *J. Fluid Mech.* **924** (2021), article no. A15.
[219] D. Frank, J. R. Landel, S. B. Dalziel, P. F. Linden, "Effects of background rotation on the dynamics of multiphase plumes", *J. Fluid Mech.* **915** (2021), article no. A2.
[220] B. A. Ayotte, H. J. S. Fernando, "The motion of a turbulent thermal in the presence of background rotation", *J. Atmos. Sci.* **51** (1994), no. 13, p. 1989-1994.
[221] K. R. Helfrich, "Thermals with background rotation and stratification", *J. Fluid Mech.* **259** (1994), p. 265-280.
[222] Q. Kriaa, M. Landeau, M. Le Bars, "Influence of planetary rotation on metal-silicate mixing and equilibration in a magma ocean", *Phys. Earth Planet. Inter.* **352** (2024), article no. 107168.
[223] D. Bercovici, E. Mulyukova, "Two-phase magnetohydrodynamics: Theory and applications to planetesimal cores", *Phys. Earth Planet. Inter.* **300** (2020), article no. 106432.
[224] K. Aujogue, A. Pothérat, I. Bates, F. Debray, B. Sreenivasan, "Little earth experiment: an instrument to model planetary cores", *Rev. Sci. Instrum.* **87** (2016), no. 8, article no. 084502.
[225] K. Aujogue, A. Pothérat, B. Sreenivasan, F. Debray, "Experimental study of the convection in a rotating tangent cylinder", *J. Fluid Mech.* **843** (2018), p. 355-381.
[226] J. S. Turner, I. H. Campbell, "Convection and mixing in magma chambers", *Earth-Sci. Rev.* **23** (1986), no. 4, p. 255-352.
[227] R. S. J. Sparks, H. E. Huppert, J. S. Turner, "The fluid dynamics of evolving magma chambers", *Philos. Trans. R. Soc. Lond.. Ser. A, Math. Phys. Sci.* **310** (1997), no. 1514, p. 511-534.
[228] M. B. Holness, R. Farr, J. A. Neufeld, "Crystal settling and convection in the Shiant Isles main sill", *Contrib. Mineral. Petrol.* **172** (2017), article no. 7.
[229] M. B. Holness, M. J. Stock, D. Geist, "Magma chambers versus mush zones: constraining the architecture of sub-volcanic plumbing systems from microstructural analysis of crystalline enclaves", *Philos. Trans. R. Soc. A: Math. Phys. Eng. Sci.* **377** (2019), no. 2139, article no. 20180006.
[230] O. Namur, M. C. S. Humphreys, M. B. Holness, "Crystallization of interstitial liquid and latent heat buffering in solidifying gabbros: skaergaard intrusion, greenland", *J. Petrol.* **55** (2014), no. 7, p. 1389-1427.
[231] J. Klein, S. P. Mueller, J. M. Castro, "The influence of crystal size distributions on the rheology of magmas: new insights from analog experiments", *Geochem. Geophys. Geosyst.* **18** (2017), no. 11, p. 4055-4073.
[232] M. A. Morales Maqueda, A. J. Willmott, N. R. T. Biggs, "Polynya dynamics: a review of observations and modeling", *Rev. Geophys.* **42** (2004), no. 1, article no. RG1004.
[233] S. Martin, "Frazil ice in rivers and oceans", *Annu. Rev. Fluid Mech.* **13** (1981), no. 13, p. 379-397.
[234] Y. Matsumura, K. I. Ohshima, "Lagrangian modelling of frazil ice in the ocean", *Ann. Glaciol.* **56** (2015), no. 69, p. 373-382.
[235] D. W. Rees Jones, A. J. Wells, "Frazil-ice growth rate and dynamics in mixed layers and sub-ice-shelf plumes", *The Cryosphere* **12** (2018), no. 1, p. 25-38.
[236] A. Herman, M. Dojczman, K. Świszcz, "High-resolution simulations of interactions between surface ocean dynamics and frazil ice", *The Cryosphere* **14** (2020), no. 11, p. 3707-3729.
[237] S. Ushio, M. Wakatsuchi, "A laboratory study on supercooling and frazil ice production processes in winter coastal polynyas", *J. Geophys. Res.: Oceans* **98** (1993), no. C11, p. 20321-20328.
[238] M. Dubé, B. Turcotte, B. Morse, "Inner structure of anchor ice and ice dams in steep channels", *Cold Reg. Sci. Technol.* **106–107** (2014), p. 194-206.
[239] P. D. Barrette, "Understanding frazil ice: the contribution of laboratory studies", *Cold Reg. Sci. Technol.* **189** (2021), article no. 103334.
[240] S. S. Shy, R. E. Breidenthal, "Turbulent stratified interfaces", *Phys. Fluids A: Fluid Dyn.* **3** (1991), no. 5, p. 1278-1285.
[241] E. Kruger, *Dynamics of downdraughts and cold pools: an experimental and numerical study*, Phd thesis, University of Cambridge, 2020.
[242] G. Boffetta, A. Celani, F. D. Lillo, S. Musacchio, "The Eulerian description of dilute collisionless suspension", *Europhys. Lett.* **78** (2007), no. 1, article no. 14001.
[243] J. F. Reali, P. Garaud, A. Alsinan, E. Meiburg, "Layer formation in sedimentary fingering convection", *J. Fluid Mech.* **816** (2017), p. 268-305.
[244] J. Lemus, A. Fries, P. A. Jarvis, C. Bonadonna, B. Chopard, J. Lätt, "Modelling settling-driven gravitational instabilities at the base of volcanic clouds using the lattice boltzmann method", *Front. Earth Sci.* **9** (2021), article no. 713175.
[245] Y.-J. Chou, Y.-C. Shao, "Numerical study of particle-induced Rayleigh–Taylor instability: effects of particle settling and entrainment", *Phys. Fluids* **28** (2016), no. 4, article no. 043302.
[246] J. P. Mellado, B. Stevens, H. Schmidt, N. Peters, "Two-fluid formulation of the cloud-top mixing layer for direct numerical simulation", *Theoret. Comput. Fluid Dyn.* **24** (2010), no. 6, p. 511-536.
[247] Y. Yamamoto, "Numerical simulation of concentration interface in stratified suspension: continuum–particle transition", *Int. J. Multiphase Flow* **73** (2015), p. 71-79.

[248] J. P. Mellado, "Cloud-top entrainment in stratocumulus clouds", *Annu. Rev. Fluid Mech.* **49** (2017), no. 49, p. 145-169.
[249] V. G. Levich, *Physicochemical Hydrodynamics*, Prentice-Hall International Series in the Physical and Chemical Engineering Sciences, Prentice-Hall, Englewood Cliffs, NJ, 1962.
[250] W. Q. Fu, "Radiative transfer", in *Atmospheric Science* (J. M. Wallace, P. V. Hobbs, eds.), Academic Press, San Diego, 2nd ed., 2006, p. 113-152.
[251] H. R. Pruppacher, J. D. Klett, in *Microphysics of Clouds and Precipitation*, Atmospheric and Oceanographic Sciences Library, vol. 18, Springer, Netherlands, Dordrecht, 2010.
[252] R. Wood, "Stratocumulus Clouds", *Mon. Weather Rev.* **140** (2012), no. 8, p. 2373-2423.
[253] M. Beniston, "Grand challenges in climate research", *Front. Environ. Sci.* **1** (2013), article no. 1.
[254] S. Malardel, "Atmospheric buoyancy-driven flows", in *Buoyancy-Driven Flows* (C. Cenedese, E. P. Chassignet, J. Verron, eds.), Cambridge University Press, Cambridge, 2012, p. 312-337.
[255] C. Muller, D. Yang, G. Craig *et al.*, "Spontaneous aggregation of convective storms", *Annu. Rev. Fluid Mech.* **54** (2022), no. 1, p. 133-157.
[256] D. J. Stevenson, E. E. Salpeter, "The phase diagram and transport properties for hydrogen-helium fluid planets", *Astrophys. J. Suppl. Ser.* **35** (1977), p. 221-237.
[257] N. Nettelmann, J. J. Fortney, K. Moore, C. Mankovich, "An Exploration of double diffusive convection in Jupiter as a result of Hydrogen–Helium phase separation", *Mont. Not. R. Astron. Soc.* **447** (2015), no. 4, p. 3422-3441.
[258] S. Markham, T. Guillot, C. Li, "Rainy downdrafts in abyssal atmospheres", *Astron. Astrophys.* **674** (2023), article no. A177.
[259] R. Hueso, T. Guillot, A. Sánchez-Lavega, "Convective storms and atmospheric vertical structure in Uranus and Neptune", *Philos. Trans. R. Soc. A: Math. Phys. Eng. Sci.* **378** (2020), no. 2187, article no. 20190476.
[260] T. Guillot, D. J. Stevenson, S. K. Atreya, S. J. Bolton, H. N. Becker, "Storms and the depletion of ammonia in Jupiter: I. Microphysics of "Mushballs"", *J. Geophys. Res.: Planets* **125** (2020), no. 8, article no. e2020JE006403.
[261] V. Parmentier, A. P. Showman, Y. Lian, "3D mixing in hot Jupiters atmospheres—I. Application to the day/night cold trap in HD 209458b", *Astron. Astrophys.* **558** (2013), article no. A91.
[262] C. Helling, "Exoplanet clouds", *Annu. Rev. Earth Planet. Sci.* **47** (2019), p. 583-606.
[263] M. S. Marley, A. S. Ackerman, J. N. Cuzzi, D. Kitzmann, "Clouds and hazes in exoplanet atmospheres", *Comp. Climatol. Terr. planets* **1** (2013), p. 367-391.

ACADÉMIE DES SCIENCES
INSTITUT DE FRANCE

Comptes Rendus. Physique
2024, Vol. 25, Special issue S3, p. 183-234
https://doi.org/10.5802/crphys.219

Review article / *Article de synthèse*

Geophysical and astrophysical fluid dynamics in the laboratory / *Dynamique des fluides géophysiques et astrophysiques au laboratoire*

Geophysical flows over topography, a playground for laboratory experiments

Écoulements géophysiques en présence de topographie, un terrain de jeu pour la modélisation expérimentale

Jérémie Vidal [a], Jérôme Noir [*, b], David Cébron [a], Fabian Burmann [b], Rémy Monville [a], Vadim Giraud [b] and Yoann Charles [b, c]

[a] Université Grenoble Alpes, CNRS, ISTerre, 38000 Grenoble, France

[b] Institut für Geophysik, ETH Zürich, Sonneggstrasse 5, Zürich 8092, Switzerland

[c] Development of Advanced Engineering Solutions (DAES), Avenue des Grandes-Communes 8, Petit-Lancy 1213, Switzerland

E-mails: jeremie.vidal@univ-grenoble-alpes.fr (J. Vidal), jerome.noir@eaps.ethz.ch (J. Noir), david.cebron@univ-grenoble-alpes.fr (D. Cébron), fabian.burmann@eaps.ethz.ch (F. Burmann), remy.monville@univ-grenoble-alpes.fr (R. Monville), vadim.giraud@eaps.ethz.ch (V. Giraud)

Abstract. Physicists face major challenges in modelling multi-scale phenomena that are observed in geophysical flows (e.g. in the Earth's oceans and atmosphere, or liquid planetary cores). In particular, complexities arise because geophysical fluids are rotating and subject to density variations, but also because the fluid boundaries have complex geometries (e.g. the ocean floor) with wavelengths ranging from metres to thousands of kilometres. Dynamical models of planetary fluid layers are thus often constrained by observations, whose interpretation necessitates a comprehensive understanding of the underlying physics. To this end, geophysical studies often combine cutting-edge experiments across a wide range of parameters, together with theory and numerical simulations, to derive predictive scaling laws applicable for planetary settings. In this review, we discuss experimental efforts that have contributed to our understanding of geophysical flows with topography. More specifically, we focus on (i) the flow response to mechanical (orbital) forcings in the presence of a large-scale (ellipsoidal) topography, (ii) some effects of small-scale topography onto bulk flows and boundary-layer dynamics, and (iii) the interaction between convection and roughness. The geophysical context is briefly introduced for each case, and some experimental perspectives are drawn.

Résumé. Les écoulements géophysiques, par exemple dans les océans ou les noyaux planétaires liquides, présentent souvent une turbulence caractérisée par une multitude d'échelles de temps et d'espace. Celles-ci résultent notamment des effets de rotation globale et de stratification en densité, mais aussi des effets de paroi qui sont souvent irréguliers (e.g. la bathymétrie du plancher océanique). Ainsi, peu d'études ont considéré la modélisation des écoulements géophysiques avec rotation, stratification en densité et effets topographiques. En pratique, la meilleure approche consiste souvent à combiner des expériences de

* Corresponding author

laboratoire sur une large gamme de paramètres, ainsi que des travaux théoriques et/ou numériques, pour ensuite extrapoler les résultats aux conditions géophysiques. Dans cet article de revue, nous discutons les travaux principalement expérimentaux qui ont permis de mieux comprendre la dynamique des écoulements géophysiques avec des effets topographiques de paroi. Premièrement, nous détaillons les écoulements engendrés par les forçages orbitaux (e.g. la marée ou la précession) pour un fluide contenu dans un ellipsoïde. Ensuite, nous illustrons les effets d'une topographie de petite échelle sur certains écoulements en volume et de couche limite. Enfin, nous discutons l'influence d'une paroi non lisse sur les écoulements engendrés par la convection.

Keywords. Topography, Rotation, Stratification, Geophysical flows, Planetary cores, Subsurface oceans.

Mots-clés. Topographie, Rotation, Stratification, Écoulements géophysiques, Noyaux planétaires, Océans de subsurface.

Funding. European Research Council (ERC) (grant agreement No 847433, THEIA project), ETH grant #ETH-04 22-1, European Research Council (ERC) (grant agreement No 833848, UEMHP project), French Academy of Sciences, Electricité de France, Labex OSUG@2020 (ANR10 LABX56).

Manuscript received 3 May 2024, revised and accepted 17 October 2024.

1. Introduction

Fluid dynamics enjoys great popularity among geophysicists and planetary scientists, which is not surprising considering the ubiquity of fluid phenomena in the universe. Many rocky planets possess shallow thin fluid layers (e.g. oceans or atmospheres), as well as thicker ones in depth (e.g. liquid cores or subsurface oceans in icy moons). From a physicist's perspective, geophysical fluid dynamics serves as both an applied and pure science. It is applied because we observe and predict the effects of geophysical flows in our daily life (such as weather forecasting, climate evolution, or Earth's magnetic field variations). Yet, it is also pure because most geophysical flows involve fundamental fluid dynamics processes (like waves, hydrodynamic instabilities, and turbulence) that are still not fully understood.

Indeed, several scientific questions currently challenge our geophysical flow models, such as the origin of the ancient magnetic fields on Earth [1] and the Moon [2]. Similarly, controversies persist regarding estimates of heat transport by turbulent convection, which is key for understanding the long-term evolution of natural systems over billions of years. Actually, these questions arise because the internal dynamics of planetary bodies remains barely known. In the middle of the nineteenth century, Hopkins [3] proposed that one could probe planets' interiors from the variations of their rotation. Indeed, if a planet or a moon has a hidden fluid layer, it could be inferred by looking at the planet's response to orbital perturbations, such as precession or nutations. This pioneering idea found many applications in the twentieth century, such as the confirmation of the liquidity of the Earth's outer core [4], or the existence of a molten core in Mercury [5] and in the Earth's moon [6]. Nowadays, the increasing accuracy of the Earth's and moon's rotations provides a unique opportunity to go beyond the detection of their liquid cores to address the question of their internal dynamics. Meanwhile, space missions like the ESA mission JUICE or the NASA mission CLIPPER, which are dedicated to the icy moons of Jovian planets, will provide unprecedented data to probe their subsurface oceans. However, global models based on Earth-like oceanic circulation are unlikely to be directly applicable to these envelopes [7]. Specific models are thus still missing to properly model the fluid dynamics within such moons.

Therefore, understanding the dynamics of planets' and moons' fluid envelopes remains a central question in contemporary geophysics and planetary sciences. Before discussing recent progress on this topic, we shall first establish the fundamental physical components necessary for modelling these fluid envelopes.

1.1. *The key ingredients of geophysical fluid models*

Planetary fluid envelopes are unique by their large size, but also because of the physical mechanisms governing their dynamics. Notably, they often experience the effects of global rotation. The Earth is currently rotating at an angular velocity $\Omega_s \simeq 7.3 \times 10^{-5}$ rad·s^{-1}, and was even rotating faster in the past [8]. Global rotation is dynamically important if, first, the dynamics is in a low-viscosity regime (i.e. with a rotation time scale much smaller than the viscous time scale). This leads to the definition of the Ekman number E given by

$$E = \frac{\nu}{\Omega_s L^2}, \tag{1}$$

where ν is the kinematic viscosity of the fluid, and L is the typical length scale of the system. The low-viscosity regime is thus defined by $E \ll 1$. Moreover, geophysical turbulence also depends on the relative strength of the nonlinearities in the system. We introduce the Rossby number Ro (comparing the rotation and nonlinear advection time scales), which is related to the classical Reynolds number Re (which compares the viscous and nonlinear advection time scales) as $Ro = ReE\,(L/\ell)^2$ with

$$Ro = \frac{u_\ell}{\Omega_s \ell}, \quad Re = \frac{\ell u_\ell}{\nu}, \tag{2a,b}$$

where u_ℓ is the typical amplitude of the velocity at the flow length scale ℓ. The dynamics ignores rotation when $Ro \gg 1$, whereas it is strongly shaped by rotational effects when $Ro \ll 1$. Note that the length scale ℓ introduced above is still undefined. Actually, since geophysical systems exhibit many length scales in the range $0 < \ell \leq L$, different dynamical regimes can be expected as a function of the length scale (e.g. [9] for liquid planetary cores). In practice, the Rossby number can have values from $Ro \ll 1$ at large scales to $Ro \gtrsim 1$ at smaller scales. The transition between these regimes is expected to be controlled by the Zeman length scale defined as [10]

$$\ell_z \sim \left(\frac{\epsilon}{\Omega_s^3}\right)^{1/2}, \tag{3}$$

where ϵ is the mean energy dissipation rate per unit of mass. Turbulent structures with length scales $\ell \gg \ell_z$ are modified by global rotation and anisotropic, whereas the turbulence is unaffected by rotation and nearly isotropic when $\ell \ll \ell_z$ [11, 12]. If we consider the largest scales (assuming $\ell \sim L$), typical values are $Ro \sim 10^{-7} - 10^{-6}$ for the Earth's liquid core with $E \sim 10^{-15}$ (assuming $u_\ell \sim$ 1–10 km·y^{-1} for core flows driven by convection [13], and the core radius ~3480 km). This indicates that the Earth's liquid core is in a regime where viscous and advection effects are much smaller than rotational ones. Note also that a typical value for the Reynolds number is then $Re \sim 10^8$ for the largest scales. The later example clearly illustrates a common difficulty in geophysical modelling, namely obtaining turbulent flows with $Re \gg 1$ in the regime $Ro \ll 1$, which is only accessible by considering low enough values of E.

Second, geophysical flows are often subject to buoyancy effects and density stratification. The latter is usually characterised by the Brunt–Väisälä (BV) frequency, denoted below by N. For a compressible fluid, the square of the BV frequency is given by [14]

$$N^2 = \frac{\boldsymbol{g}}{\rho} \cdot \left(\nabla\rho - \frac{\rho}{c_s^2}\boldsymbol{g}\right), \tag{4}$$

where $\boldsymbol{g}$ is the gravity field, ρ is the fluid density, and c_s is the speed of sound. The BV frequency measures the departure of the actual density gradient to the adiabatic (isentropic) density gradient (given by $\rho\boldsymbol{g}/c_s^2$ in hydrostatic equilibrium). As such, stably stratified fluids (e.g. a light fluid over a dense one in laboratory conditions) are characterised by $N^2 > 0$, whereas convection can occur for unstable stratification with $N^2 < 0$. For example, the Earth's oceans are known to be stably stratified in density. There is some variability as a function of the location and

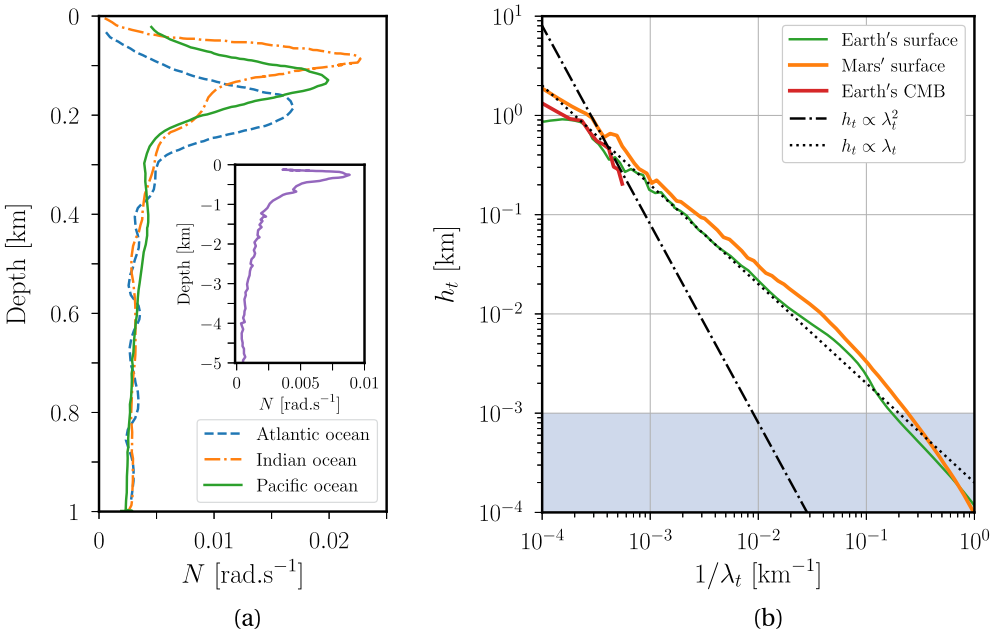


Figure 1. (a) Illustrative profiles of the Brunt–Väisälä frequency N, as a function of depth, in the Earth's oceans (adapted from [19]). Inset shows a typical profile in the deep ocean in the western North Pacific (adapted from figure 3.6 in [20]). (b) Spatial spectra of topography, where h_t is the height of the topography at wavelength λ_t. Spectra deduced from the RMS of the observed power spectrum at the Earth's and Mars' surface [21], and a seismological model of the Earth's CMB (obtained from body waves) is also shown [22]. Blue region shows the (laminar) Ekman boundary layer, of typical thickness $\mathcal{O}(\sqrt{\nu/\Omega_s})$, at the Earth's CMB or at the bottom of the surface oceans (which have the same viscosity $\nu \approx 10^{-6}$ m^2·s^{-1}). Empirical law $h_t \propto 2\times10^{-4}\,\lambda_t$ (dash-dot line) for the RMS height at the surface [23], and $h_t \propto 8\times10^{-8}\,\lambda_t^2$ (dotted line) for the CMB (from gravity RMS spectrum [24]).

the seasons [15], but typical values are $N \sim 10^{-3}$–10^{-2} rad·s^{-1} in the upper ocean and $N\sim10^{-5}$–10^{-4} rad·s^{-1} in the deep ocean (Figure 1a). On the contrary, the Earth's liquid core is convecting in bulk [13] (which implies $N^2 \sim 0$), but it might be either weakly stratified with $N/\Omega_s \leq \mathcal{O}(1)$ [16,17] or strongly stratified with $N/\Omega_s \gg 1$ [18] in a thin layer near the core-mantle boundary[1] (CMB). Therefore, the two dynamical regimes should be investigated.

Both global rotation and stratification give rise to peculiar linear and turbulent flows, which make geophysical systems so unique and interesting. Yet, we can also draw some analogies between these two kinds of dynamics [25]. For instance, they can both sustain wave motions in the form of inertial waves with angular frequencies bounded by $2\Omega_s$ for rotating fluids [26], or as internal (gravity) waves with angular frequencies bounded by N for stably stratified fluids [27]. In the Earth's atmosphere, internal gravity waves emitted over mountains carry energy from the surface to the upper atmosphere, and participate in mixing processes [28] and angular momentum exchange between the atmosphere and the solid Earth [29]. Similarly, the radiation of internal (gravity) waves over the sea floor bathymetry contributes to ocean mixing and tidal energy dissipation [30]. For the dynamics, rotating and stratified flows are also often separated into bulk and thin boundary-layer regions. Finally, the associated turbulence is strongly anisotropic

[1] This is the interface between the liquid core made of molten iron, and the mantle made of silicate rocks.

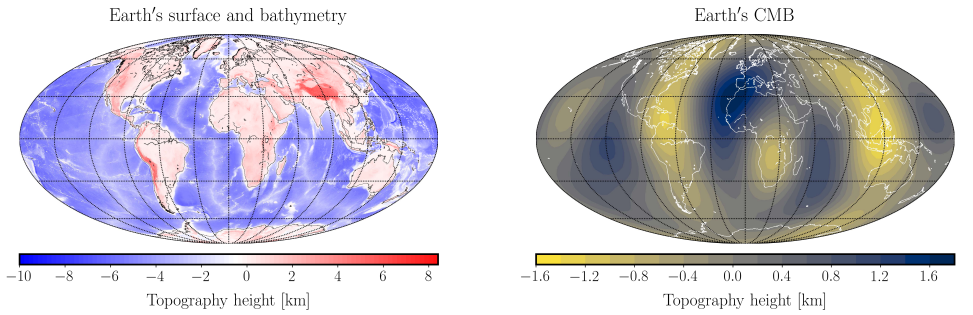


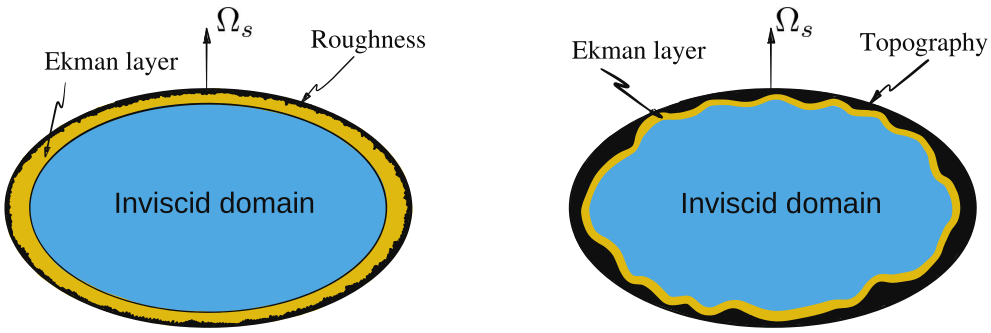
Figure 2. Landscape of topographies affecting geophysical flows. Colour bar shows the topography height (in km) on a map using a Mollweide projection. (a) ETOPO1 global relief model of the Earth's surface, integrating continents' topography and oceans' bathymetry. Data provided in [42]. (b) Meso-scale topography at the Earth's CMB. Mean model obtained from seismological studies using body-wave and normal-mode inversions. Only the largest-scale components with spherical harmonics degree ≤ 6 are shown. Data provided in [22].

(e.g. with rotation [31] and stratification [32,33]), which is very different from the classical picture of isotropic Kolmogorov turbulence.

1.2. *The shape of planetary fluid envelopes*

To complete our picture of geophysical fluid envelopes, it is often needed to account for boundary effects. Planets' and moons' fluid envelopes are near-spherical bodies, on which a broad spectrum of topography wavelengths is superimposed (see Figure 1b at the Earth's surface and CMB). At the leading order, the departure from the global spherical geometry is elliptical due to the combined action of centrifugal distortion and tides (as qualitatively expected from the theory of equilibrium figures for rotating fluid masses [34]). For the Earth's core, a typical value for polar ellipticity is ∼1/400 (as estimated from LOD variations [35] and the nutations [36]). Similarly, the equatorial ellipticity due to the lunar tides has the typical amplitude $\sim 10^{-7}$–10^{-6} over geologic time scales, as estimated from hydrostatic tidal theory [8]. Contemplating the Earth's surface and oceans' floor (Figure 2a), we observe that topographic features exist at all scales ranging from a few kilometres to a few hundred metres (i.e. meso-scales), but sub-metres structures are also present (i.e. roughness, not shown here). Meanwhile, mantle dynamics and global seismology suggest the presence of bumps and ridges at the Earth's CMB, with heights of a few kilometres and with horizontal extents of 1–10^3 km (Figure 2b), as well as small-scale roughness (e.g. due to thermo-chemical interactions between the liquid core and the solid mantle [37, 38]). Fewer data are available for the ocean's floor or bottom ice layer of Jovian satellites. Nonetheless, while they are insufficient to derive a precise picture, they all suggest that the interface is not smooth [39–41].

In the context of this review paper, we define thin-layer systems (e.g. the Earth's oceans and atmosphere) as fluid envelopes with a depth much smaller than the mean planetary radius, and thick-layer ones (e.g. planetary liquid cores and subsurface oceans) as envelopes whose depth is a large fraction of the radius. Let us finally introduce the concept of roughness and meso-scale topography (Figure 3). We refer below to roughness as small-wavelength topographies with height of the order of (or smaller than) the boundary-layer thickness. The latter is typically ∼0.1–10 m for a laminar viscous boundary layer in the Earth's oceans or in the Earth's core. On the



(a) Roughness (b) Meso-scales

Figure 3. Illustration of the concept of (a) roughness and (b) meso-scale topography in a planetary context.

contrary, meso-scales are defined as topographies with small to intermediate wavelengths, whose height is large with respect to the Ekman-layer thickness but smaller than the large length scale L (e.g. 100 m to 100 km).

1.3. *Geophysical modelling, a challenge for numerics and experiments*

Flows in geophysical fluid envelopes are mostly driven by two kinds of forcings, namely thermal-solutal convection [13] or mechanical forcings through coupling with a rigid boundary (e.g. at a CMB, or an icy crust in Jovian moons). In geophysical systems, mechanical forcings typically result from orbital perturbations such as precession, librations, or tides [43]. Convective flows in geophysical contexts are often characterised by slow time scales, while orbitally driven dynamics usually occur on time scales comparable to the planetary rotation time scale. This contrast gives rise to distinct regimes of geophysical turbulence. Rapidly rotating convection is expected to be quasi two-dimensional (2-D) in the planetary regime $Ro \ll 1$ [9]. In contrast, mechanical forcings can sustain anisotropic turbulence combining three-dimensional (3-D) flows (e.g. waves) and quasi 2-D ones (e.g. mean zonal flows). Since these phenomena are often simultaneously present in natural systems, geophysical flows often exhibit a wide range of time and length scales. Moreover, geophysical systems are often characterised by rather extreme parameters (Figure 4). One of the difficulties in geophysical studies is thus to account for such diverse phenomena, and to approach the appropriate range of parameters. In particular, modelling high-Re turbulent flows in the low-Ro regime is very challenging, as it requires lowering E as much as possible. To this end, numerical and experimental approaches can be employed, and their pros and cons are summarised below.

Numerics. Direct numerical simulations (DNS) usually offer a great flexibility to model flows in global geometries, or to account for phenomena that are difficult to control in laboratory conditions (e.g. dynamo action or thermal effects). However, the main disadvantage is that probing the low-viscosity and rapidly rotating regime of geophysical flows is beyond the capabilities of any DNS, even for the most advanced ones available today. For instance, the largest simulation of core convection struggled to consistently reach the value $E \sim 10^{-7}$ [46]. Moreover, it often takes months to only model a few turnover time scales, such that the long time scale of the flow remains currently out of reach in DNS. Fortunately, the expected almost 2-D nature of rapidly rotating convection [9] allows developing reduced models that can efficiently probe the low-Ro turbulent regime [44, 45]. Yet, we cannot easily adopt such an alternative route with topography.

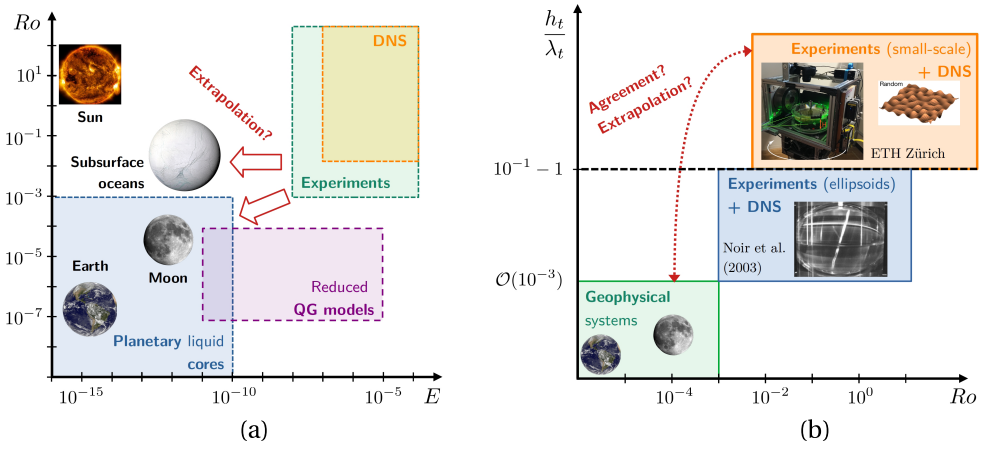


Figure 4. Schematic regime diagrams for the dynamics of thick-layer fluid systems. (a) Parameter space as a function of the Rossby number Ro and the Ekman number E. It shows the huge gap between parameters characterising geophysical systems, and those that are accessible to experimental works and DNS in global geometries. Reduced QG models refer to models of rapidly rotating convection in spherical geometries [44, 45], in which the flow is assumed quasi-invariant along the rotation axis. (b) Parameter space depending on h_t/λ_t (where h_t is the topography amplitude at the wavelength λ_t, see Figure 1b) and Ro.

Indeed, the numerical challenge is more pronounced when incorporating topographic effects into the models. Despite efforts to develop efficient numerical methods capable of modelling topography (e.g. spectral-element methods), there remains a significant disparity of many orders of magnitude from geophysical values (e.g. with $E \sim 10^{-5}$ for the most turbulent flows in global ellipsoidal geometries [47, 48]).

Experiments. As stated by K. S. Thorne and R. D. Blandford in their textbook *Modern Classical Physics* [49], fluid dynamics is historically an experimental science. Given the aforementioned limitations of DNS for rapidly rotating flows with topography, experiments still appear as a valuable alternative nowadays. In short, experiments do not suffer from the difficulty of resolving a broad range of time and spatial scales, and they are not limited to weakly nonlinear regimes. Typically, a metre-size experiment using water and rotating up to 60 RPM corresponds to the values $E \sim 10^{-7}$ and $Ro \sim 10^{-3}$–10. Another benefit of experiments is that very different shapes can be chosen for the fluid container. For that reason, they have proven invaluable to investigate ellipsoidal geometries or cavities with topographical features. Briefly speaking, experiments must be designed with care in order to (i) ensure that the desired physical processes to investigate do control the dynamics, and (ii) provide sufficient quantitative information to test the models or derive scaling laws. Both aspects are paramount to successful experimental investigations, and they must be well-designed from the very beginning of the experimental development. A detailed discussion of experimental techniques is beyond the scope of the present review, but we can outline for the non-expert readers what is achievable by using non-intrusive measurements. There are different techniques to measure the velocity, pressure, temperature, or density. They all provide partial views of the system, in contrast with DNS giving access to all quantities in the fluid domain. For instance, routinely used optical techniques in recent experiments [50, 51], such as Particle Image Velocimetry (PIV), typically allow recovering 2-D maps of the velocity fields with certain spatial and temporal resolutions. With a typical mid-range setup, we can expect to measure velocities $u_\ell \sim 10^{-3}$–1 m·s^{-1}, with a resolution of a few millimetres over a

view field of tens of centimetres at a sampling frequency $\sim 10^2$ Hz. Dedicated highly customised PIV systems, which are much more costly, can only marginally extend this range by a factor ~10. In some peculiar experimental setups, 3-D reconstructions are also possible but difficult to perform (especially in rapidly rotating experiments). In opaque fluids (e.g. liquid metal), acoustic techniques must be employed, such as Ultrasonic Doppler Velocimetry (UDV) [52] or time of flight [53], which only offer 1-D profiles of a single velocity component (with roughly the same resolution range and slightly lower sampling frequency). Temperature, density, or pressure are often limited to point measurements. More elaborated techniques, such as Laser Induced Fluorescence (LIF) [54] or synthetic Schlieren [55, 56], can provide 2-D maps but at the expense of a complex setup that is not always possible to mount on rotating devices.

Contrary to non-rotating regimes (i.e. $Ro \to \infty$), for which laboratory experiments are miles ahead of DNS for turbulent modelling, it appears that DNS and experiments are rather close in terms of accessible parameters for rotating flows. Since the high-Re and low-Ro regimes are still largely unexplored, both numerical and experimental approaches are worth considering. Moreover, since the extreme parameters relevant to planetary fluid envelopes are (and will remain) out of reach of both DNS and experiments, we must resort to dimensional arguments and scaling laws for geophysical applications. This requires a systematic exploration of the parameter space and, then, the results must be extrapolated using asymptotic laws constrained by the available data. To this end, experiments are well suited to explore more complex small-wavelength geometries and, sometimes, extreme dynamical regimes than DNS, but at the expense of limited quantitative information (in particular at low forcing). On the other hand, DNS are suitable to study global geometries in laminar and less turbulent regimes, but with well-controlled physics and with access to all resolved quantities in the entire volume. Consequently, they often allow exploring different regimes in the parameter space (Figure 4), which makes the two approaches complementary to infer robust scaling laws for geophysical applications.

1.4. *Outline of the paper*

Motivated by some applications discussed above, we will describe experimental works that have significantly contributed to our understanding of geophysical flows with topography. We will only describe DNS and theory when required for interpreting laboratory experiments. Nonetheless, we point out that numerical and theoretical works remain essential to make progress in our understanding of these geophysical questions. As such, they would deserve an independent review. It is only through the combination of all three approaches that we shall gain insights into the geophysical dynamics of thick fluid envelopes.

The manuscript is divided as follows. We first describe in Section 2 the effects of large-scale ellipsoidal topographies on the flow dynamics driven by mechanical (orbital) forcings. Next, we discuss in Section 3 how a small-wavelength topography can modify rotating flows, with a particular focus on spin-up experiments with meso-scale topographies and the transition to turbulent (Ekman) boundary layers. We then consider turbulent convection with small-wavelength topography in Section 4. We briefly discuss in Section 5 why density stratification is challenging to account for with global rotation in experimental conditions, before ending the manuscript in Section 6.

2. Flow dynamics with a large-scale (ellipsoidal) topography

We first consider the effects of large-wavelength topographies on the flow dynamics of thick-layer envelopes. Given the broad range of the subject, we have chosen to focus on flows driven by mechanical (orbital) forcings in liquid-filled ellipsoids without wall roughness, and we also

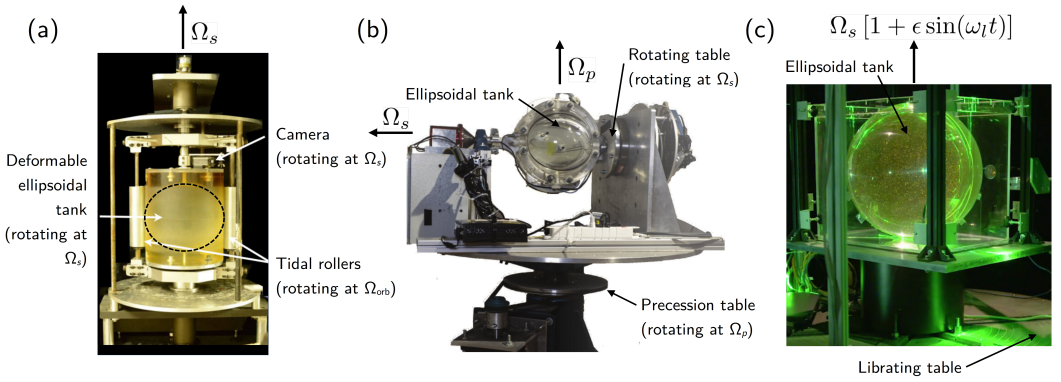


Figure 5. Illustrative experiments of mechanically driven flows in water-filled ellipsoids, which can go down to $E \sim 10^{-6}$ and $Ro \sim 10^{-2}$. (a) Tidal forcing. The fluid cavity, rotating at the angular velocity Ω_s, is elliptically deformed by the action of two rollers rotating at $\Omega_{\rm orb}$. Adapted from [48]. (b) Precession. The ellipsoidal cavity is rotating around its z-axis at the angular velocity $\Omega_s \mathbf{1}_z$, which it is itself rotating at $\mathbf{\Omega}_p$ around another axis that is fixed in the inertial frame. The two axes are tilted by the precession angle α (here at $\pi/2$). Adapted from [61]. (c) Longitudinal librations. The cavity is rotating at the angular velocity $\Omega_s\,[1+\epsilon\sin(\omega_l t)]$, where Ω_s is the angular velocity of the fluid, ϵ is the libration amplitude, and ω_l is the libration (angular) frequency. Adapted from [51].

discuss the case of spherical containers when appropriate (as the flow properties can be similar, e.g. for precession). For geophysical applications, the mechanical forcings that have been mainly considered in the literature are

- tidal forcing,
- precession (i.e. a fluid-filled cavity whose axis of rotation is itself rotating around a secondary axis, which is fixed in the inertial frame),
- librations (i.e. oscillations of the figure axes of an object with respect to a fixed, mean rotation axis), which can be either in longitude (i.e. an azimuthal harmonic modulation of the rotation rate of the cavity) or in latitude.

As discussed below, these forcings are capable of driving flow instabilities and (possibly) anisotropic turbulence in the bulk of the cavity, through either topographic or viscous couplings at the boundary. Hence, they are worth considering for geophysical applications.

Investigating turbulent flows in ellipsoidal or spherical geometries is still very challenging, especially in the low-viscosity regime relevant to most geophysical systems (Figure 4a). Starting with the seminal work of Malkus [57], flows driven in ellipsoids by orbital forcings have received increasing attention, especially using experimental and theoretical approaches. Most studies have considered water-filled ellipsoids (Figure 5), but a few have also employed a liquid metal to explore hydromagnetic effects [58, 59]. A detailed discussion of all these studies is beyond the scope of the present paper. We refer the readers to [43] for an exhaustive review of the particularities of every forcing, and to [60] for a summary of the different experiments. Here, we first emphasise that experimental studies of mechanically driven flows in full ellipsoids (i.e. without an inner core) share some common points that can be understood in light of theoretical progress. Secondly, we discuss whether the experimental results can be extrapolated to planetary conditions, and outline some experimental perspectives to build more realistic models.

2.1. *The full ellipsoid, a playground for joint experimental and theoretical works*

2.1.1. *Inertial modes, a cornerstone to understand rotating flows*

Rotating flows are often shaped by the action of inertial waves, whose restoring effect is global rotation [26]. In a bounded geometry, these waves can admit counterparts known as inertial modes. We assume that the fluid is neutrally buoyant (i.e. $N = 0$), and co-rotating with the rigid surrounding envelope at the steady angular velocity $\Omega_s \mathbf{1}_\Omega$ (where $\mathbf{1}_\Omega$ is a unit vector). In the rotating frame, the fluid boundary is an ellipsoid given in Cartesian coordinates (x, y, z) by $(x/a)^2 + (y/b)^2 + (z/c)^2 = 1$, where (a, b, c) are the semi-major axes of the ellipsoid. In this rotating frame, an inertial mode is an inviscid solution of the eigenvalue problem given by

$$\mathrm{i}\omega_i \boldsymbol{u}_i + 2\Omega_s(\mathbf{1}_\Omega \times \boldsymbol{u}_i) = -\nabla\Phi_i, \quad \nabla \cdot \boldsymbol{u}_i = 0, \quad \boldsymbol{u}_i \cdot \mathbf{1}_n|_{\partial V} = 0, \tag{5a–c}$$

where $0 \leq |\omega_i| < 2\Omega_s$ is the eigenvalue of the ith normal mode, $\boldsymbol{u}_i$ is the eigenvector for the velocity (respectively Φ_i for the pressure), and where $\mathbf{1}_n$ is the unit vector normal to the boundary ∂V. Note that the degenerate solutions with $\omega_i = 0$ are referred to geostrophic modes. They satisfy the Taylor–Proudman theorem

$$\boldsymbol{\Omega} \cdot \nabla \boldsymbol{u}_i = \mathbf{0}, \tag{6}$$

showing that they are invariant along the rotation axis. Inertial modes were first evidenced by the pioneering experiment of Aldridge and Toomre [62], who considered a full sphere subject to longitudinal librations (as in Figure 5c). Indeed, some inertial modes can be excited by librations when the libration frequency ω_l is close to some eigenvalues ω_i (Figure 6a). Theoretical analysis later showed that such inertial modes can be excited because of viscous effects in the Ekman boundary layer [63–65]. Other mechanisms can also sustain inertial waves or modes (after multiple reflections), such as boundary-layer instabilities [66] or bulk forcings [67–69].

Next, we may wonder how inertial modes are modified when the sphere is deformed into an ellipsoid. Insight into this question can be gained by looking at the two simplest inertial modes, called the spin-over modes. They are associated with a uniform vorticity along the equatorial x- or y-axes. Their eigenvalues ω_{so} are given by [72]

$$\omega_{\mathrm{so}}(a, b, c) = \pm 2\Omega_s \frac{ab}{\sqrt{a^2 + c^2}\sqrt{b^2 + c^2}}. \tag{7}$$

The ellipsoidal deformation is thus responsible for a shift in frequency of the spherical eigenvalue $\omega_{\mathrm{so}}(1, 1, 1) = \Omega_s$. Similar effects exist for higher-order inertial modes, which are more or less pronounced depending on the modes' complexity. Therefore, detecting some inertial modes could be a way to probe the ellipticity of a fluid envelope (which is linked to Hopkins' original idea [3]). Figure 6(b) illustrates a more subtle effect of the large-scale ellipsoidal topography. As proved in [71], the frequency distribution of the eigenvalues is different in a sphere and an ellipsoid. The probability density function is uniform in a sphere, but non-uniform in an ellipsoid. For instance, low-frequency modes with $|\omega_i| \to 0$ are favoured when the ellipsoid is strongly elongated with $c/a \gg 1$, whereas high-frequency modes with $|\omega_i| \to 2\Omega_s$ are enhanced in flattened ellipsoids with $c/a \ll 1$. Consequently, this effect likely weakens the physical relevance of the oldest works, which employed strongly deformed ellipsoids to overcome diffusive effects, for modelling the wave-driven dynamics of geophysical flows in weakly deformed spheres.

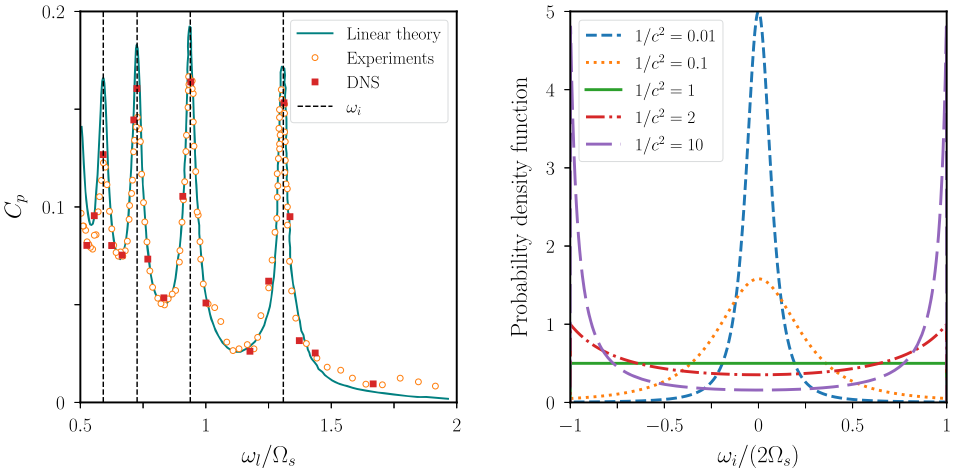


Figure 6. Inertial modes in a rapidly rotating sphere or ellipsoid. (a) Time average of the normalised pressure difference C_p between the centre and the pole of a water-filled sphere subject to longitudinal librations (as in Figure 5c), where $\epsilon = \tilde{\epsilon}\omega_l/\Omega_s$ is the libration amplitude with $\tilde{\epsilon} = 8°$, for the Reynolds number $Re_\omega = \omega_l a^2/\nu = 6.2 \times 10^4$ (with the radius $a = 10$ cm of the sphere). Comparison between experiments, DNS, and theoretical predictions. Adapted from figure 3 in [62] and figure 2 in [70]. (b) Asymptotic distribution of the normalised eigenvalues $\omega_i/(2\Omega_s)$ in the interval $[-1, 1]$, in a spheroid with $a = b = 1$ rotating along the $z-$axis, as a function of $1/c^2$. Adapted from figure 2 in [71].

Finally, a key property of inertial modes in an ellipsoid is that any divergenceless and square-integrable[2] velocity $\boldsymbol{v}$ can be sought as a combination of the inviscid eigenvectors (including the geostrophic ones) as [71, 73]

$$\boldsymbol{v}(\boldsymbol{r}, t) = \sum_{i=1}^{\infty} \gamma_i(t)\boldsymbol{u}_i(\boldsymbol{r}), \tag{8}$$

where $\boldsymbol{r}$ is the position vector and $\{\gamma_i(t)\}_i$ are arbitrary time-dependent coefficients. Therefore, many experimental results have been interpreted by using theories based upon inertial modes. So far, several phenomena have been experimentally observed, and the interplay with theory has allowed us to understand a somehow generic flow response in an ellipsoid (Figures 7–10).

2.1.2. *Forced (laminar) flows, the first brick*

Beyond inertial modes or waves, mechanical forcings often drive a (laminar) basic flow. It can involve in Equation (8) either a single modal component (in the case of a perfect resonance, as in Figure 6a) or a superposition of few large-scale modes. In the particular case of precession, the forced basic flow is close to a uniform-vorticity flow (even with viscosity [76, 81]), which is essentially a tilted rotation with an irrotational strain to satisfy the non-penetration at the boundary [82, 83]. Such uniform-vorticity flows, which are often referred to as Poincaré flows, are the only ones to carry angular momentum in an ellipsoid [84, 85]. As such, they are often expected to play a particular role in the rotational dynamics of the whole planet [86]. Depending on the frequency of the forcing, the forced flow can exhibit direct resonances (Figure 7a), whose amplitude is smoothed out by viscosity in experiments [74, 83, 85].

[2] i.e. any incompressible flow, either viscous or not, but with a finite value of the volume-averaged kinetic energy.

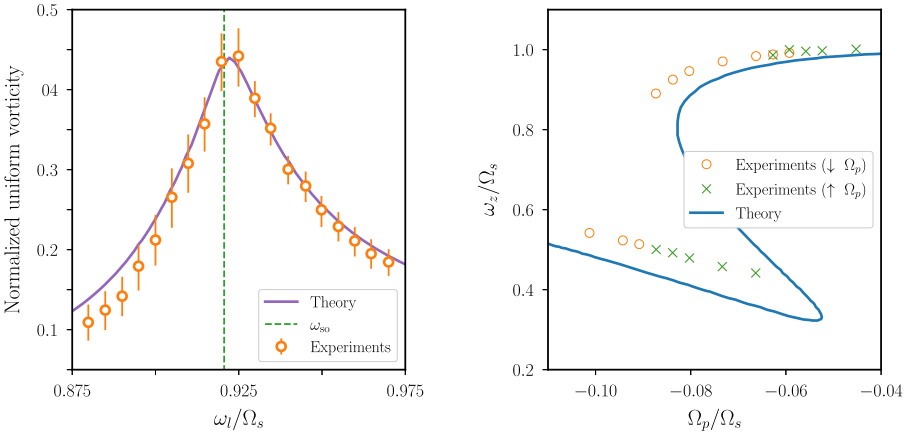


Figure 7. Laminar uniform vorticity flows, as obtained in experiments and predicted by theory. (a) Direct resonance for latitudinal librations. Triaxial ellipsoid with $a = 0.078$ m, $b = 0.125$ m and $c = 0.1042$ m, subject to librations at $E = 1.57 \times 10^{-5}$. Vertical dashed line shows the value of ω_{so} given by Equation (7) for this geometry. Experimental values obtained using Ultrasonic-Doppler-Velocimetry (UDV) measurements, and the theory is given by a uniform-vorticity model [74]. See further details in [75]. (b) Vertical component of the fluid rotation vector ω_z/Ω_s, as a function of Ω_p/Ω_s, in a spheroid with $c/a \simeq 0.847$. Precession forcing with $E = 2.3 \times 10^{-5}$ and a precession angle of 15°. Experimental values obtained using PIV measurements. Hysteresis is found by either gradually decreasing (∘) or increasing (×) the value of *Po*. Theory obtained from [76]. Adapted from figure 4 in [77].

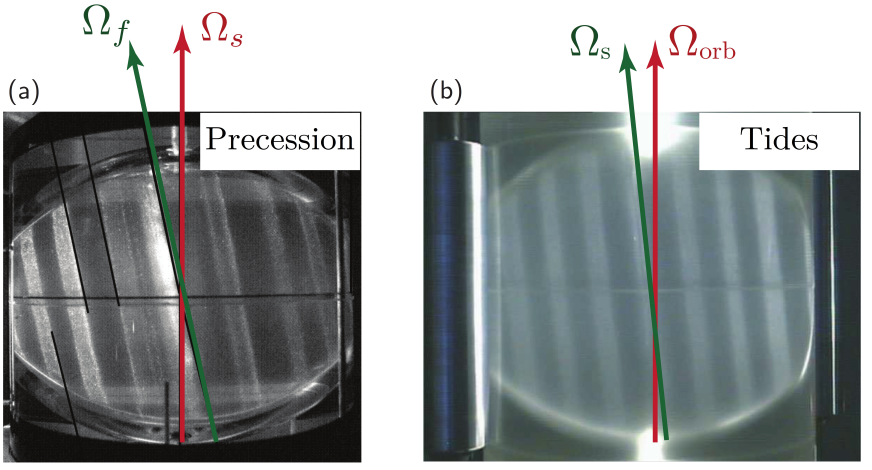


Figure 8. Similarities of mean (laminar) flows observed in ellipsoids subject to mechanical forcings. Visualisations in a meridional plane using Kalliroscope flakes. (a) Precession in a spheroid with $c/a = 0.96$. Experiment performed at $E = 2.24 \times 10^{-6}$ and $\Omega_p/\Omega_s = -0.01$, for a precession angle of 20°. $\mathbf{\Omega}_f$ is the axis of rotation of the fluid, which is tilted from the mantle spin axis along Ω_s. Adapted from [78]. (b) Tidal flow in an ellipsoid. Experiment performed at $E = 10^{-5}$. Here, the orbital angular velocity along Ω_{orb} (enforced by the two rollers) is inclined by an angle of 5° from the spin axis along Ω_s (which is aligned with $\mathbf{\Omega}_f$). Adapted from [67].

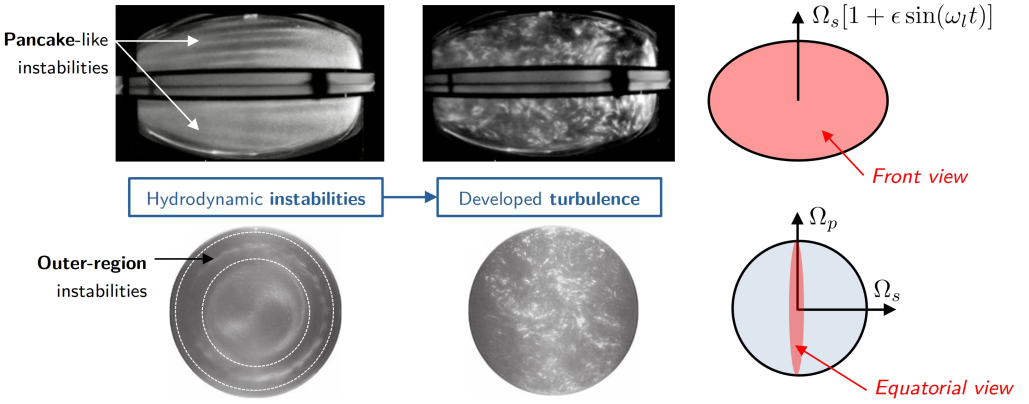
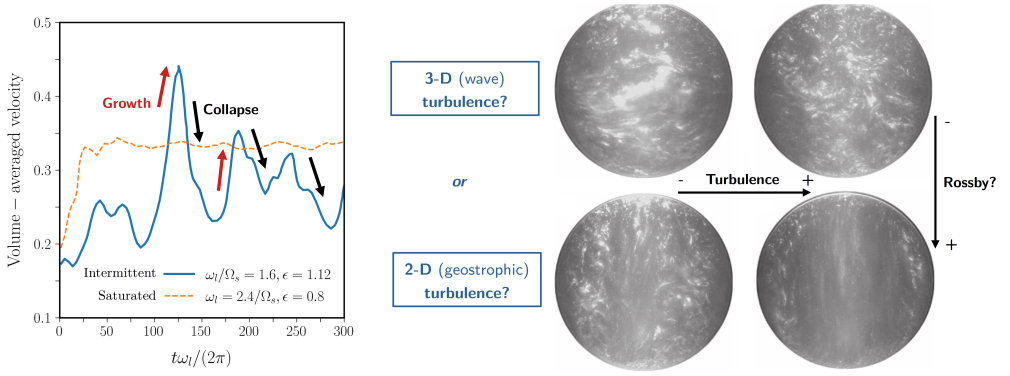


Figure 9. Schematic flow response in ellipsoids subject to mechanical forcings. Top: Front visualisations of libration-driven flows in an ellipsoid at $E \simeq 2.7 \times 10^{-5}$. Adapted from figure 3 in [48]. Bottom: Equatorial visualisations (using reflective flakes) of precession-driven flows in a sphere (with orthogonal spin and precession axes) at $E \simeq 1.25 \times 10^{-5}$. Adapted from Figures 5 and 13 in [79].



(a) (b)

Figure 10. (a) Different turbulent regimes of libration-driven flows in an ellipsoid at $E \simeq 2 \times 10^{-5}$. Vertical axis shows the volume-averaged velocity (measured from equatorial PIV in the experiment), which is also averaged in time using four points per libration cycle to only retain the long-term time scales of the flow. Adapted from figure 6 in [80]. (b) 3-D (wave) turbulence versus 2-D (geostrophic) turbulence. Equatorial visualisations (using reflective flakes) of precession-driven turbulence in a sphere (with orthogonal spin and precession axes) at $E \simeq 1.25 \times 10^{-5}$. Adapted from figure 5 in [79].

Despite their apparent simplicity, laminar basic flows in ellipsoids can have a rather complicated evolution in the parameter space. For instance, the uniform-vorticity flow in a precessing cavity can be non-unique for a broad range of precession rates (Figure 7b), as found in experiments [61, 77] and in agreement with prior theory [76, 87]. Some viscously driven flows can also be important ingredients to build a complete model, such as the oblique shear layers generated by the breakdown of the oscillatory Ekman layer at the critical latitudes [52, 88], or laminar mean flows resulting from nonlinear interactions in the Ekman boundary layer (as reported in experiments for all three forcings [48, 70, 89, 90]) or from self-interactions of wave motions

(as predicted [91–93] and experimentally observed [67]). It is interesting to note the similarity of the mean (zonal) flows obtained in both tidally-driven and precession-driven flows (Figure 8). In both cases, the tilted rotation of the fluid (directly forced for precession, but resulting from a triadic instability for tidal forcing, see below) generates an almost identical pattern of zonal flows, which have yet to be fully understood.

2.1.3. *The long route to rotating turbulence*

The forced laminar flow is usually linearly unstable to small-amplitude perturbations. As outlined in Figure 9, we often observe the following route to turbulence in experiments, from the onset of hydrodynamic instabilities (when the forcing amplitude is strong enough to overcome diffusive effects) to anisotropic turbulence.

(1) Instabilities. Linear stability theory suggests that triadic (parametric) instabilities are often triggered by mechanical forcings. In diffusionless fluids, these triadic (parametric) instabilities obey the generic resonance condition given by

$$\omega_0 = \omega_1 \pm \omega_2, \tag{9}$$

where ω_0 is the angular frequency of the forced Poincaré flow viewed in the frame rotating with the fluid (e.g. ω_l for longitudinal librations as in Figure 5c), and $\omega_{1,2}$ are the angular frequencies of two (free) inertial modes of the inviscid fluid. A triadic (parametric) instability can only grow upon the basic flow if its diffusionless growth rate σ is larger than the diffusive damping effects in the system. For an ellipsoidal boundary without roughness, the leading-order dissipative mechanism in a hydrodynamic experiment is provided by the friction within the Ekman layer [26]. For a laminar Ekman layer, the onset criterion for triadic instabilities is thus given by

$$\sigma > \mathcal{O}(E^{1/2}). \tag{10}$$

For the mechanical forcings listed above, the diffusionless growth rate σ of the flow instabilities is often proportional to the ellipsoidal deformation (at the leading order). If so, criterion (10) means that the ellipsoidal deformation must be greater than the thickness of the Ekman layer (typically ~0.1–1 m in core conditions for a laminar Ekman layer) for the onset of instabilities. Other damping mechanisms, such as an enhanced spin-up because of meso-scale topographies or roughness (see Section 3), could thus naturally affect the viability of such instability mechanisms. The most famous example of such instabilities is the elliptical instability [94], which can be driven by tidal forcing or librations in experiments [48, 51, 58, 59, 80, 95, 96]. For precession, various triadic instabilities are expected in inviscid ellipsoids [97], but their clear identification remains difficult given the accessible range of parameters in experiments [61, 77, 98]. Indeed, current experiments using water-filled ellipsoids are usually limited to $E \sim \mathcal{O}(10^{-6})$ (see Tables 1 and 2 in [60]). Another parametric instability of interest for precession is the so-called conical shear instability (CSI). It results from triadic interactions between two inertial modes and the viscous conical shear layer, such that this instability can be observed in spherical geometries [99, 100]. The CSI was probably present in the seminal experiments of Malkus [57] and Vanyo [101], but the unambiguous experimental observation only came later using a spheroid [102]. Note that the above parametric instabilities can also coexist with other hydrodynamic instabilities, such as the viscous shear-driven instability for tides [103], or boundary-layer instabilities for precession [100, 104] and librations [66, 105].

(2) Rotating turbulence. Next, anisotropic turbulent flows are usually observed in experiments (Figure 9). The different mechanisms of linear hydrodynamic instability are rather well understood now. On the contrary, our understanding of the route to turbulence is still incomplete. Theoretical works suggest that such a transition could occur through nonlinear saturation of the

primary flows, or because of various mechanisms involving inertial waves or modes [51,106,107]. Determining the relevant turbulent regimes, which may be forcing-dependent, is still an open question. As illustrated in Figure 10(a), experiments have shown that the mechanically driven turbulence can be either intermittent [48,80,90] (e.g. with successive chaotic cycles made of resonant growth, saturation, collapse and relaminarisation), or sustained [51, 79, 108, 109]. Moreover, the developed anisotropic turbulence could be either 3-D or quasi 2-D (Figure 10b). These two regimes have been observed in experiments, such as for precession [79] or librations [51]. Finally, strong turbulence can be obtained if the forcing amplitude is large enough, which may be relevant for engineering applications [110, 111].

2.2. *Unanswered questions for future experiments*

Experimental (and theoretical) works have allowed us to get satisfactory physical insight into the flow response of liquid-filled ellipsoids to mechanical forcings, from the generation of laminar flows to the transition to turbulence (Figures 7–10). However, the story is not over and there is room for developing new experiments to attack some unsolved problems. As outlined below, obtaining a better fundamental understanding of the various turbulent states is crucial, in particular to extrapolate the results to geophysical conditions safely.

2.2.1. *Insight from turbulence studies*

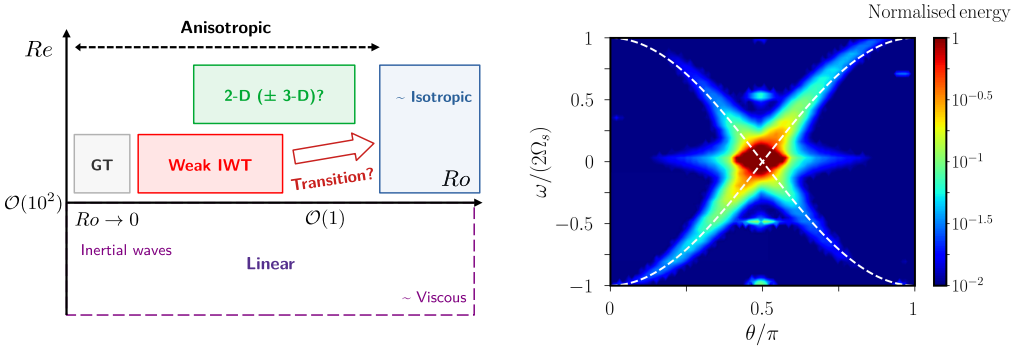
The ability of mechanically driven flows to exhibit different states of rotating anisotropic turbulence (Figure 10b) is really fascinating. Indeed, it echoes the fundamental problem of rotating turbulence in low-Ro flows [31]. As sketched in Figure 11(a), different regimes of rotating turbulence can be obtained as a function of Ro and Re. For instance, rotating turbulence can be in a quasi 2-D regime in which energy is concentrated in the form of quasi-geostrophic flows (i.e. with flows almost invariant along the rotation axis). Since rapidly rotating convection is known to sustain low-frequency and quasi 2-D flows when $Ro \ll 1$ (e.g. [44, 45] in spherical geometries), the regime of quasi-geostrophic turbulence is widely studied in the geophysical community [9]. However, when Ro is not vanishingly small, 3-D inertial waves can also take part in the anisotropic turbulence and transfer energy to smaller scales through a direct energy cascade. Some experiments have indeed shown the key role played by inertial waves [112–116], which can still coexist with quasi 2-D columnar motions and an inverse cascade [117–119]. Note that different theories or scaling laws have been proposed for rotating turbulence, for instance using phenomenological arguments [120–122], various closure models [123–125] or from DNS [126, 127]. They often yield different predictions, against which experimental results can be tested. Currently, most rotating experiments are designed in the light of weak Inertial Wave Turbulence (IWT). The latter is indeed of great interest for turbulence modelling because it provides, in the asymptotic regime $Ro \ll 1$, a natural closure of the turbulent equations [128].

Weak IWT considers weakly nonlinear interactions (when $Ro \ll 1$) of plane inertial waves, which satisfy the plane-wave dispersion relation given by

$$\omega(\boldsymbol{k}) = \pm 2\Omega_s \frac{k_\parallel}{|\boldsymbol{k}|} \tag{11}$$

from Equations (5a,b), where $\boldsymbol{k}$ is the wave vector with $k_\parallel = \boldsymbol{k} \cdot \mathbf{1}_\Omega$ and the perpendicular wave vector $\boldsymbol{k}_\perp = \boldsymbol{k} \times \mathbf{1}_\Omega$ of norm $k_\perp$. In the theory, the weak nonlinearities take the form of three-wave interactions. For wave-vector triads $[\boldsymbol{k}, \boldsymbol{p}, \boldsymbol{q}]$ satisfying the resonance conditions given by

$$\boldsymbol{k} + \boldsymbol{p} + \boldsymbol{q} = \mathbf{0}, \quad \omega(\boldsymbol{k}) + \omega(\boldsymbol{p}) + \omega(\boldsymbol{q}) = 0, \tag{12a,b}$$



(a) (b)

Figure 11. (a) Schematic regime diagram for rotating turbulence as a function of *Re* and *Ro*. Adapted from figure 1 in [31]. GT: Geostrophic Turbulence. IWT: Inertial Wave Turbulence. (b) Experimental observation of inertial wave turbulence, adapted and modified from [112]. The experimental set-up is a rotating cylinder of 90 cm in height and 80 cm in diameter, which is rotating at $\Omega_s = 4\pi$ rad·s^{-1}. Colour bar shows the normalised density energy (in logarithmic scale), measured for the entire wave number range in the experiment, as a function of the frequency ω and the angle θ between the rotation axis and the wave vector (measured from the rotation axis). White dashes curves show dispersion relation (11) of plane inertial waves, along which the energy is concentrated. The strongest energy is near $\theta \approx \pi/2$, which evidences a strong geostrophic component.

(weak) IWT is governed by a Wave Kinetic Equation (WKE) written in symbolic form as [129]

$$\partial_t \mathcal{N}(\boldsymbol{k}) = Ro^2 \mathcal{T}(\boldsymbol{k}), \tag{13}$$

where $\mathcal{N}(\boldsymbol{k}) = \mathcal{E}_a(k_\perp, k_\parallel)/\omega(\boldsymbol{k})$ is the wave action with the axisymmetric kinetic energy spectrum[3] $\mathcal{E}_a(k_\perp, k_\parallel)$, and where $\mathcal{T}(\boldsymbol{k})$ is a collision integral (defined over the wave vectors satisfying the above triadic conditions). The solution of the WKE with a steady non-zero $\mathcal{N}(\boldsymbol{k})$, known as the Kolmogorov–Zakharov (KZ) spectrum, has received much interest in the turbulence community. Finding an explicit KZ solution of the general WKE is a difficult task but, here, the problem is considerably simplified in the anisotropic limit $k_\parallel \ll k_\perp$. In this regime, the WKE admits the anisotropic KZ solution given by [123, 130]

$$\mathcal{E}_a(k_\perp, k_\parallel) \sim \sqrt{\epsilon \Omega_s} k_\perp^{-5/2} k_\parallel^{-1/2}. \tag{14}$$

The KZ solution predicts a net direct energy cascade within an inertial range, where the rate of spectral energy transfer is assumed to be equal to the mean energy dissipation rate per unit of mass ϵ. First experimental observations [112] did find that rotating turbulence can exhibit energy along the inertial-wave dispersion relation (Figure 11b), which was then obtained in some DNS [107, 131]. Later on, dedicated experiments [116] and simulations [132, 133] confirmed the main spatial properties of anisotropic KZ spectrum (14). Moreover, formula (14) predicts that the one-dimensional spectrum should scale as $|\boldsymbol{k}|^{-2}$ at large scales (for which we might assume $k_\perp \sim k_\parallel$), which is consistent with early experimental [134] and numerical findings [125, 127].

It has been proposed that mechanically driven flows in ellipsoids could sustain IWT in geophysical conditions (e.g. for tidal flows [51, 107]). Despite IWT is appealing from a

[3] It is defined as $\mathcal{E}_a(k_\perp, k_\parallel) = 2\pi k_\perp \mathcal{E}(\boldsymbol{k})$ with the kinetic energy spectrum $\mathcal{E}(\boldsymbol{k})$, such that the total kinetic energy is $\propto \int^\infty \mathcal{E}_a(k_\perp, k_\parallel)\, \mathrm{d}k_\perp \mathrm{d}k_\parallel$.

fundamental viewpoint, its relevance for mechanically driven turbulence in ellipsoids is currently not obvious. Indeed, it is unclear if the underlying assumptions of IWT are satisfied or not in geophysical conditions. In particular, we remind the reader that IWT is a local turbulence theory, which is valid for homogeneous flows (i.e. unbounded) when $Ro \ll 1$. First, mechanically driven flows in ellipsoids likely occur in the low-Ro regime, but this regime could only be valid at large scales (e.g. $Ro \sim 10^{-6}$ for planetary liquid cores with $l \sim L$). Indeed, at smaller scales, the local Rossby number is expected to increase as $\ell \to \ell_z$ (assuming that u_ℓ/ℓ increases as ℓ decreases, e.g. $u_\ell/\ell \sim \epsilon^{1/3}\ell^{-2/3}$ for a Kolmogorov cascade [9]). Second, rotating turbulence is often shaped by spatial inhomogeneities. The latter notably manifest in the form of inertial modes at large scales, as discussed for ellipsoids in Section 2.1, but which are also found in other geometries [135–137]. Therefore, it would be necessary to extend the WT theory to account for finite-size geometrical effects to assess the validity of the WT predictions for the largest scales characterised by $Ro \ll 1$. The continuous dispersion relation given by Equation (11) should then be replaced by a discrete one in bounded geometries, which often prevents the occurrence of many triadic interactions. For IWT, DNS in periodic domains [138] showed that discretisation effects become non-negligible when $Ro \lesssim 10^{-3}$. Consequently, it is still unclear whether the KZ spectrum can properly describe the low-Ro regime at rather large scales in bounded geophysical systems. Note that a first extension of the IWT theory has been done by considering a rotating channel that is infinite in the horizontal directions perpendicular to the rotation axis [139]. Yet, the fully bounded case remains to be considered theoretically and, then, compared to new experiments.

2.2.2. 2-*D or not* 2-*D? That is another question*

Another weakness of IWT is that it does not account for geostrophic flows,which are associated with $k_\parallel = 0$ in Equation (11). Indeed, there is no direct resonant triad satisfying Equations (12a,b) that can transfer energy from 3-D waves to the geostrophic component at the leading asymptotic order in $Ro \ll 1$ [126]. Actually, this results is also valid for any inviscid flow in a bounded geometry in the low-Ro regime [140]. If energy were only supplied to the 3-D waves, then geostrophic structures would not be excited and no inverse cascade of energy could occur in the dynamics. However, the preferred regime of rapidly rotating turbulence could be that of quasi-geostrophic turbulence when $Ro \to 0$. This may result from the anisotropic properties of the inertial-wave dispersion relation [141, 142], but also because the geostrophic manifold could be a global attractor of the rotating flows when $Ro \to 0$ [143]. If true, this could thus challenge the validity of the WT theory for geophysical flows with $Ro \ll 1$. Moreover, most experiments and DNS of rotating turbulence are only performed for moderately small values of Ro (Figure 4). For such values, nearly geostrophic components are often observed (e.g. [51, 107] for tidal flows). Therefore, it is essential to understand the mechanisms feeding and sustaining geostrophic flows from a fundamental viewpoint, but also for geophysical applications.

So far, the transition between these 2-D and 3-D regimes is not fully understood. Indeed, the dominant mechanisms sustaining geostrophic flows may be forcing-dependent and Ro-dependent. Moreover, they may also be distinct in forced and decaying turbulence. Nonetheless, two canonical nonlinear mechanisms are usually put forward to explain the growth of geostrophic components [126]. The first one involve near-resonant triadic interactions [144], for which triads $[\boldsymbol{k}, \boldsymbol{p}, \boldsymbol{q}]$ satisfy the detuned resonance conditions given by

$$\omega(\boldsymbol{k}) + \omega(\boldsymbol{p}) + \omega(\boldsymbol{q}) = \mathcal{O}(Ro), \tag{14a,b}$$

together with $k_\parallel = 0$ and $p_\parallel = -q_\parallel$. This is the scenario investigated in [145–147], which can lead to the onset of geostrophic flows with a growth rate $\propto (kRo)^2$ when $kRo \ll 1$ or $\propto kRo$

when $kRo \gtrsim 1$ [147]. The second mechanism involves quartetic interactions (or four-wave interactions) [126]. For primary triads $[\boldsymbol{k},\boldsymbol{p},\boldsymbol{q}]$ satisfying conditions (12), we can find quaterts $[\boldsymbol{p},\boldsymbol{q},\boldsymbol{r},\boldsymbol{s}]$ satisfying the quatertic resonance conditions given by

$$\underbrace{\boldsymbol{p}+\boldsymbol{q}}_{=-\boldsymbol{k}}+\boldsymbol{r}+\boldsymbol{s}=\boldsymbol{0}, \quad \underbrace{\omega(\boldsymbol{p})+\omega(\boldsymbol{q})}_{=-\omega(\boldsymbol{k})}+\omega(\boldsymbol{r})+\omega(\boldsymbol{s})=0, \tag{15a,b}$$

with $s_\parallel = 0$. We refer the reader to Appendix B in [126] for a detailed example. This mechanism, which also predicts a growth rate $\propto (kRo)^2$, was observed numerically [106] and experimentally [148]. Note that other mechanisms have also been invoked such as various interactions with eddies [149–152], and the shape of the fluid domain could also play a role [153].

Back to geophysical flows, nearly 2-D turbulence is unambiguously the preferred regime for rapidly rotating convective flows [9]. On the contrary, it is unclear which regime is preferred for mechanically-driven turbulence in geophysical (i.e. $Ro \ll 1$ and $E \to 0$) or experimental conditions (with finite values of Ro and E). Fortunately, future experiments could shed new light on this controversial question. For a new-generation experiment with a metre-size ellipsoid filled with water at room temperature, it seems very difficult to lower the Ekman number below $E \sim 10^{-7}$ with a typical value $\Omega_s \sim 10$ rad·s^{-1} for the angular velocity of currently used rotating tables. Nonetheless, this may be sufficient to start disentangling the various mechanisms and turbulent regimes in an ellipsoid. Finally, it would also be worth extending the theory to account for ellipsoidal (or spherical) boundaries for a better quantitative comparison with the experiments. Indeed, since geostrophic flows have very different properties in unbounded and bounded systems (e.g. due to the beta effect [26]), the finite-size geometry could quantitatively affect the predictions previously obtained in either unbounded or cylindrical geometries.

2.2.3. *Towards geophysical extrapolation*

In addition to the fundamental and enthralling question of the properties of rotating turbulence, we also have to obtain scaling laws to correctly extrapolate the experimental results to geophysical conditions (which are still out of reach). Some scaling laws, which have been proposed for linear and nonlinear features of mechanically driven flows, are gathered in Table 1. For instance, scaling laws are crucial if we want to estimate the contribution of mechanically driven flows to tidal dissipation in the subsurface oceans of some icy moons [154, 155], or to assess their viability to sustain planetary magnetic fields (to go beyond prior numerical studies [100, 156, 157]). In the latter case, dimensional analysis tells us that the typical magnetic field strength B driven by dynamo action could be given at the fluid surface by [158]

$$B \propto \sqrt{\mu \rho_m}\,(L\mathscr{P})^{1/3}, \tag{16}$$

where μ is the fluid magnetic permeability, ρ_m is the mean fluid density, and $\mathscr{P}$ is the mean energy production rate per unit of mass. Moreover, on the long time scales characterising dynamo action, we may also expect the dynamics to be close to a steady state yielding $\mathscr{P} \sim \epsilon$ from the energy balance, where ϵ is the mean energy dissipation rate per unit of mass. Hence, finding a quantitative estimate of ϵ is often a cornerstone in turbulence theory and for geophysical extrapolation. Direct measurements of ϵ are difficult because they require a well-resolved velocity field. Since we have $\epsilon = \epsilon(u_\ell, \ell)$ by dimensional analysis, a first and accessible step towards geophysical extrapolation is therefore to estimate the typical strength u_ℓ of mechanically driven turbulent flows (e.g. Table 1). Yet, not all the predictions have been quantitatively validated with experiments. Moreover, another pitfall is that prior laws were obtained without a clear understanding

Table 1. Proposed scaling laws for the diffusionless growth rate σ and the flow amplitude u_ℓ for precession and tidal forcings in ellipsoids. The proposed numerical prefactors can be found in the original works. $\eta_e = |a^2 - b^2|/(a^2 + b^2)$ is the equatorial ellipticity of the ellipsoid with semi-major axes (a, b, c), and η_p its polar flattening. $\Delta\omega$ is the differential rotation between the fluid and the mantle due to precession. EI: elliptical instability, VSDI: Viscous shear-driven instability, CSI: conical shear instability, SI: Shear instability

Forcing	Tides		Precession	
mechanism	EI	VSDI	CSI	KSI
Growth rate σ	$\mathcal{O}(\eta_e\lvert\Omega_s - \Omega_{\rm orb}\rvert)$	-	$\mathcal{O}(\lvert\Delta\omega\rvert E^{1/5})$	$\mathcal{O}(\lvert\Delta\omega\rvert\eta_p)$
Turbulence amplitude u_ℓ	$\mathcal{O}(\eta_e\lvert\Omega_s - \Omega_{\rm orb}\rvert a)$	$\mathcal{O}(\eta_e^2\Omega_s a E^{-\chi})$	$\mathcal{O}(\lvert\Delta\omega\rvert E^{2/5} a)$	$\mathcal{O}(\lvert\Delta\omega\rvert\eta_p a)$
References	[48, 159, 160]	[103]	[85, 99]	[85, 97, 161]

of the underlying rotating turbulence regime. As an example, the energy dissipation law is expected to be given from formula (14) by [123]

$$\epsilon \sim \frac{u_\ell^4 l_\parallel}{\Omega_s l_\perp^3} \tag{17}$$

with $\ell_\perp \sim 1/k_\perp$ and $\ell_\parallel \sim 1/k_\parallel$, which differs from the usual scaling $\epsilon \sim u_\ell^3/\ell$ in isotropic Kolmogorov turbulence. Since these dissipation scalings would yield different estimates from Equation (16), new experiments are required to validate the scaling laws for the different regimes.

Additional physical ingredients would also be worth including in new experiments, such as a shell geometry (i.e. with an inner core). Prior experimental works [154, 162] showed that the flow response to mechanical forcings in a shell is qualitatively similar to that in a full ellipsoid, even if the mathematical theory of inertial modes is very different in a shell geometry [163]. This similarity should thus be further investigated using future experiments. Including density stratification (with $N^2 > 0$) would also be of great importance for other geophysical systems. For example, there are (nearly) isolated and lenticular vortices in the oceans [164] or Jovian planets [165], whose dynamics (from birth to death) could affect mixing processes. Dedicated experiments could be useful to model the dynamics inside [166, 167] and outside [168] such geophysical eddies, which can be modelled by ellipsoidal vortices [169–171]. Investigating the flow response in an ellipsoid with coupled global rotation and density stratification is currently very challenging (see Section 5), but it may be amenable to experimental work in the future. Finally, the ongoing (and future) space missions will likely shed new light on turbulent flows in Jovian planets. Therefore, the flow compressibility may be worth considering in next-generation experiments to model the dynamics of gas giants in a global geometry (e.g. following a pioneering experimental work [172]).

3. Slowly varying flows over meso-scale and rough topographies

We now consider how small-wavelength topographies (i.e. meso-scale and roughness) can affect rotating flows. Several phenomena well studied in non-rotating but possibly stratified fluids, such as the drag due to an obstacle or wall-driven turbulence, remain poorly quantified for rotating flows. Moreover, small-wavelength topography could also inhibit the growth of bulk (turbulent) flows driven by orbital mechanical forcings (as discussed in Section 2), by enhancing the dissipation in Equation (10). For all these reasons, it is key to assess the effects of small-wavelength topographies on rotating flows. We discuss in Section 3.1 how meso-scale topographies and roughness affect bulk rotating flows in thick-layer systems, and we investigate how a turbulent boundary layer (BL) is modified by roughness in Section 3.2.

3.1. *Bulk flows over meso-scale topographies and roughness*

3.1.1. *Meso-scale topography*

Flows interacting with topographical features have garnered interest within the oceanographic and atmospheric research communities, benefiting from the abundance of data available to study both the dynamics of the flows and the characteristics of the topography. For atmospheric and oceanic applications (i.e. thin-layer systems), it is customary to solve the dynamics using the f-plane approximation, that is to only retain the component of the planet's rotation vector $\mathbf{\Omega}$ onto the local direction of gravity by introducing the Coriolis parameter $f = 2\Omega_s \cos\theta$, where θ is the colatitude in spherical coordinates. In the context of stratified fluids with $0 < |f| < N$, where N is the BV frequency as defined above in Equation (4), energy transfer and dissipation is well captured by the propagation and breaking of Lee waves (i.e. internal gravity waves emitted over mountains), thereby promoting efficient vertical mixing processes [28]. Experimental investigations have revealed the existence of various flow regimes, ranging from linear wave radiation to blocked flows. They depend on the relationship between the potential energy acquired by a fluid parcel as it traverses from the base of a valley to the summit of a topographic feature, and the kinetic energy available within the background flow (as quantified by a Froude number). In scenarios characterised by low values of the Froude number, linear and weakly nonlinear Lee waves propagate in the ocean, radiating energy away from the topography. Conversely, when the Froude number is large, the available kinetic energy is not sufficient to transport parcels over the topography. This leads to the emergence of blocked flows and regimes of wave emission, but with an effective wavelength larger than that of the topographical features. A more detailed description of flows over topography in stratified fluids can be found in [28].

In thick-layer fluid systems, the departures from a strictly adiabatic density gradient (i.e. when $N^2 \neq 0$) are expected but undocumented. Hence, the flow dynamics with weak or without stratification (i.e. either weakly stable or neutral) also deserves consideration for such geophysical applications. However, such dynamical regimes have gained much less attention relative to strongly stratified regimes. Let us delve into the simplest scenario of an incompressible, neutrally buoyant fluid in rapid rotation steadily passing a single obstacle. As described below, the observed flows are contingent upon the obstacle's aspect ratio and the fluid velocity.

Single bump. For isolated bumps, defined as objects with a comparable horizontal extent L in both the stream-wise and cross-stream directions, Taylor columns (i.e. flow structures that are almost invariant along the rotation axis) dominate the flow when $HRo/L \ll 1$ (where H is the total fluid column height). Physically, it means that the vertical travel time of inertial waves over the whole fluid column above the bump, which is given by $H/(\Omega_s L)$ for inertial waves with the same wavelength as the topography, must be much shorter than the typical time it takes to horizontally translate the obstacle by a distance L. Conversely, a wake of inertial waves predominates when $HRo/L \gg 1$. These phenomena have been validated in experiments employing various shapes of obstacles, such as elevated straight cylinders/bumps [173–175] or cylindrical depressions [176].

Single ridge. For elongated obstacles like ridges, the dynamics additionally hinges on the cross-sectional shape. It has been demonstrated that the formation of Taylor columns is inhibited for elongated and non-slender objects of vertical (h) and horizontal stream-wise ($L_\parallel$) dimensions with $h \gtrsim L_\parallel$, and with significant cross-stream dimensions (i.e. $L_\perp \gg L_\parallel$, see Figure 12a). In such cases, the flow manifests purely as a wake of inertial waves [177, 178] (even at vanishingly small values of Ro). This was recently confirmed by laboratory experiments [179], where an elongated cylinder is steadily towed in a rotating square tank for small to moderate values of Ro. As shown in Figure 13, bulk flows dominated by 3-D inertial waves are observed in such experiments. Conversely, experiments conducted with slender elongated obstacles (i.e. $h \ll L_\parallel \ll L_\perp$, see

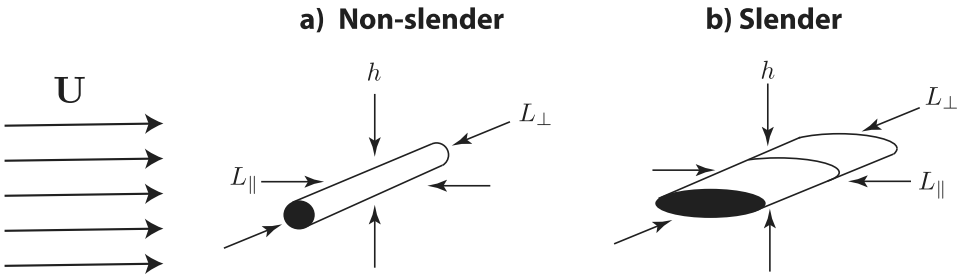


Figure 12. Illustration of the concept of (a) a non-slender obstacle with $h \gtrsim L_\parallel$ and (b) a slender obstacle with $h \ll L_\parallel$, where h is the obstacle's thickness, $L_\parallel$ is its stream-wise dimension (i.e. along the direction of the velocity $\boldsymbol{U}$), and $L_\perp$ is its cross-stream dimension. In the two cases, the obstacle is elongated with $L_\perp \gg L_\parallel$.

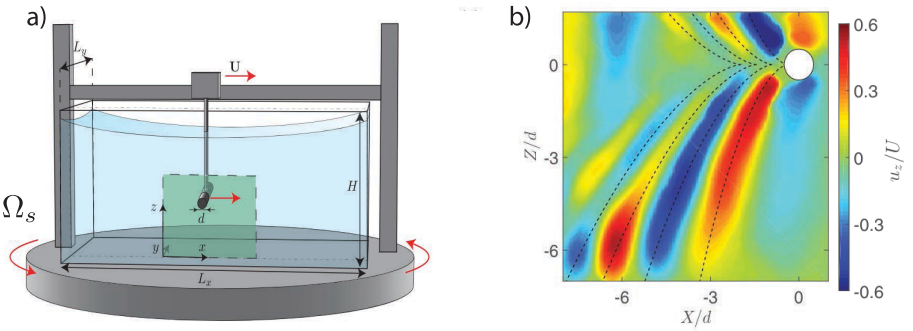


Figure 13. Inertial waves radiated by an elongated (non-slender) cylinder steadily towed in a rotating tank. Adapted from [179]. (a) Sketch of the experimental setup. (b) Cross-section showing the vertical velocity from PIV normalised by the towing speed. In the experiment, the Rossby number is small and the obstacle Reynolds number is less than 10^3.

Figure 12b) showed geostrophic dominated dynamics of blocked flows at low values of *Ro*, and distorted zonal circulations at larger values of *Ro* [180].

2-D topography. Considerably less attention has been devoted to spatially more intricate topographies in neutrally buoyant fluid (e.g. arrangements of multiple hills), particularly concerning angular momentum transfer and energy dissipation within the fluid. This issue was recently tackled experimentally [181], by investigating the impact of meso-scale bottom topography on the spin-up time, that is the time required for the fluid's rotation to realign with that of the container after a sudden increase. This time is a proxy for the rate of angular momentum exchange. In the experiment, the bottom of a straight circular cylinder was paved with a chessboard-like array of square blocks with varying horizontal extents and fixed height (Figure 14). The decay rate of the mean kinetic energy was monitored in horizontal cross-sections, using PIV velocity fields. The evolution of the mean energy is exponential, and the spin-up time is defined as the e-folding time. Topographic effects yield a significantly shorter spin-up time, up to 10 times for a specific horizontal length scale of the blocks, meaning that in this experiment the axial torque can be up to 10 times larger with a topography than for a flat cylinder. In the canonical flat end walls case, the spin-up time follows a scaling law $\tau \propto E^{-1/2}$ [26]. With topography, this scaling is altered with an exponent decreasing with the wavelength. At the smallest wavelength considered in this study, it is almost independent of E. In addition, the authors observed a vertical propagation

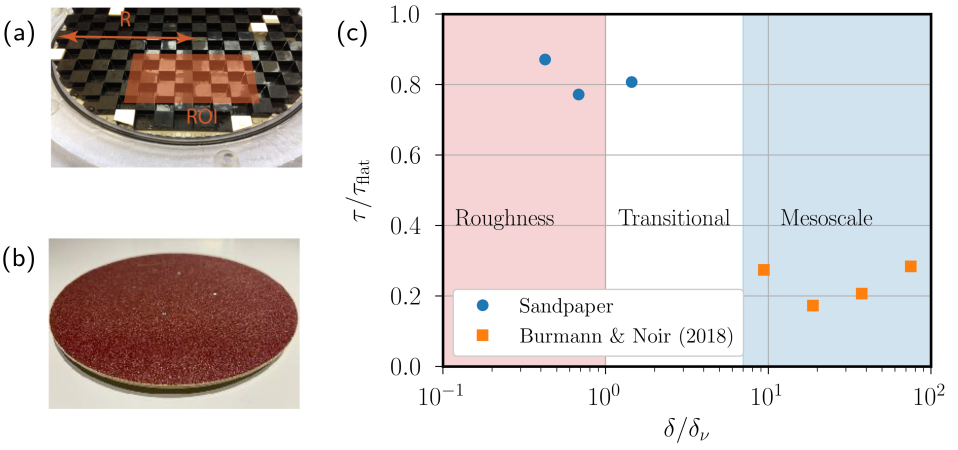


Figure 14. (a) Meso-scale topography at the bottom of a cylinder (of radius R) in spin-up experiments [181]. ROI: Region of Interest considered in the original paper. (b) Roughness in spin-up experiments with rough end walls conducted at ETH Zürich. (c) Spin-up time τ (scaled by that of a flat end wall cylinder $\tau_{\rm flat}$) as a function of the horizontal length of topography δ (scaled by the thickness δ_ν of the Ekman layer). Red shaded and blue shaded areas indicate roughness and meso-scale topography, respectively.

of inertial waves generated near the bottom topography, with a typical wavelength comparable to (or smaller than) the topographic blocks. These observations suggest that the mechanism by which the BL communicates with the bulk has evolved from a large-scale Ekman circulation for a flat cylinder to a more efficient inertial wave radiation-dominated regime with topography. This process is similar to the dissipation of tidal energy by the emission of Lee waves in the bottom ocean [28]. A spin-up time independent of Ekman at the smaller wavelength suggests that the initial transfer of angular momentum from the surface to the fluid is governed by strong non-linear dynamics near the bottom topography, which ultimately radiates energy in the bulk via inertial waves. This scenario for small-wavelength topography at small (but finite) values of *Ro* requires further investigation, including a more detailed flow visualisation near the topography.

While such experiments represented an initial step to get insights into the effects of complex topography patterns on fluid dynamics (and its interaction with the surrounding solid), several unresolved questions remain. In particular, a detailed characterisation of the flow near the topography, and the development of a model to forecast torque and energy dissipation, deserve further consideration.

3.1.2. *Rough surfaces, a challenge for experimental approach*

Roughness, that is topography embedded in the BL, is also likely to be present in geophysical systems (e.g. at the Earth's CMB [37, 38], Earth's surface and ocean floor). Its presence will affect the dissipation processes and transfer of angular momentum. Accounting for roughness in numerical models is also difficult, and it often entails solving the large-scale flows using DNS in which the effects of the roughness are parameterised using models of boundary layers dynamics (see for instance Section 3.2 below for turbulent boundary layers). Controlled experiments do not suffer from the limitations of DNS and can be used to validate the idealised models of rough end-walls. In a typical laboratory experiment, employing water at room temperature in a tank of typical size $L \sim 50$ cm rotating at the angular velocity $\Omega_s \sim 2\pi$ rad·s^{-1}, the Ekman number is of order $E \sim 10^{-6}$. This results in a viscous BL thickness of approximately $\delta_\nu \sim 50$–100 µm.

This entails employing textured walls, with a typical height and wavelength on the order of $\delta \sim 1$–100 μm. The primary challenge in such experiments lies in controlling the roughness. Indeed, at such sub-millimetre scales, constructing consistently rough walls that remain flat and statistically homogeneous on the small scales of the roughness ($\delta \sim 1$–100 μm) is non-trivial. We present in Figure 14 previously unpublished experimental data from a preliminary experiment on spin-up with rough end walls, conducted at ETH Zürich[4]. Here, sandpaper of varying grain sizes is affixed to the end walls of a cylinder, and the azimuthal velocity within the fluid bulk is measured using Laser Doppler Velocimetry (LDV). The spin-up time is determined as the e-folding time of the decay in the amplitude of the azimuthal circulation. Not surprisingly, these initial findings suggest that the spin-up time is shortened when the roughness is embedded within the Ekman layer. Once the grain size exceeds the BL thickness, a shift in dynamics occurs, still associated with an enhanced coupling but not as significant. In all cases, the increase of the torque by the roughness with respect to a flat wall is merely of the order of 20%, much less than that of a meso-scale topography in the same range of Rossby and Ekman numbers. A speculative scenario at low values of *Ro* posits that the roughness enhances angular momentum exchange and energy dissipation within the BL itself, while the spin-up is still communicated to the bulk through large-scale Ekman pumping, less efficient than the wave radiation with meso-scale topography. This preliminary data suggest that further experiments are worth considering, in particular to characterise the large scale circulation.

3.1.3. *Experimental perspectives*

Extensive research has been devoted to exploring the impact of meso-scale topography on the dynamics of geophysical fluids within the oceanic and atmospheric communities. However, these findings often lack direct applicability to thick-layer fluid systems. Due to the inherent challenges of flows over topography for DNS (particularly in nonlinear regimes), experiments are indispensable to fill the gap between the numerically accessible regimes and the inaccessible regimes of planets and moons. Meanwhile, the observed pivotal role of inertial waves suggests the potential development of linear and weakly nonlinear wave drag models to estimate the torque and energy dissipation (alike that of Lee waves in the Earth's oceans and atmosphere [28]), or reduced quasi-geostrophic models as in the recent works on flows over rough seafloors [182, 183]. Experiments over a broad range of parameters and topography shapes will be necessary to test those models, and extend them beyond the weakly nonlinear limit. This would entail using challenging velocity measurements near the topography, together with measures of global quantities such as the torque exerted by the fluid on the solid boundaries.

Finally, the interaction between the large-scale flows driven by an oscillatory mechanical forcing (as the ones discussed in Section 2) and small-wavelength topography remains unexplored. Ever since it was proposed by Hopkins [3] in the middle of the nineteenth century that one could probe the internal structure of planets from their rotation, the role of the topographic torque between cores or subsurface oceans and their surrounding shells has been debated (e.g. at the Earth's CMB [86, 184]). In contrast to the steady flows discussed above, the mechanically driven flows are oscillatory with periods close to the rotation period. The interaction of oscillating flows with topography in neutrally buoyant fluids remains inadequately documented, especially within thick-layer fluid systems. While canonical problems in ellipsoidal geometries have received extensive attention, the modification of inertial waves or modes, and their nonlinear couplings with topography, remains largely unexplored even in the simplest scenarios involving single bumps or ridges. Further experimental work is thus needed to elucidate the mechanisms of energy dissipation and angular momentum transfer for such geophysical applications.

[4] Conducted during the graduate internship of Y. Charles.

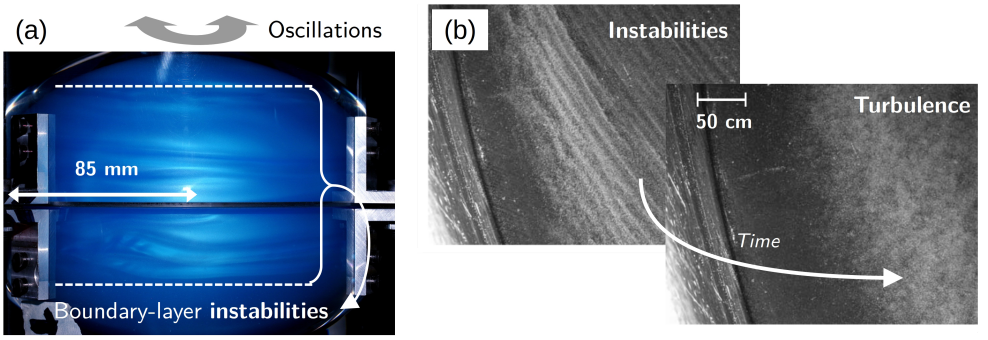


Figure 15. Transition from laminar to turbulent Ekman boundary layers (BLs). (a) BL instabilities driven by longitudinal librations in a sphere at $Re_\delta \sim 100$ and $E \simeq 5\times10^{-5}$. Flow visualisation using Kalliroscope flakes (which make the volume of fluid opaque, except for the first mm below the boundary). Adapted from [105]. (b) Ekman BL instabilities (in the form of rolling waves [187], here oriented with an angle of about 20° from the geostrophic flow), and turbulence triggered during the spin-down of a rotating tank. Visualisation using particle-streak photographs. Adapted from figure 3 in [50].

3.2. *Turbulent boundary layers with flat and rough end-walls*

Like in the Earth's atmosphere [185], the Ekman boundary layer (BL) could be turbulent in thick fluid envelopes. For that, the local Reynolds number must be much larger than the critical values 55–150 for the onset of boundary-layer instabilities [186–188]. For instance, the mechanical (orbital) forcings discussed in Section 2 can sustain some boundary-layer instabilities in experimental conditions (e.g. for librations [105], see Figure 15a), but also in some geophysical conditions (e.g. at the Moon's CMB, where the local Reynolds number is $\sim10^4$–10^5 because of precession-driven flows [100]). Similarly, a transition to turbulent BLs is also commonly observed in laboratory experiments during spin-down of a rotating tank (Figure 15b). A description of turbulent Ekman BLs is interesting for geophysical modelling. For instance, wall friction is enhanced by a turbulent BL (compared to the classical $E^{1/2}$ scaling for a laminar Ekman BL), such that wall-driven turbulence could weaken or inhibit the growth of the mechanically driven bulk flows discussed in Section 2. However, obtaining a turbulent BL dynamics is challenging using global DNS, in which the boundary layers are often laminar because of the numerical difficulty to resolve for both the largest scales of the flows and the smaller ones associated with turbulent BLs. Therefore, it is worth obtaining mathematical parametrisations for turbulent Ekman BLs, which could be later implemented in global numerical models (or used for geophysical extrapolation).

In practice, the ultimate goal is often to obtain an estimate of the drag coefficient $\tau_\star/(\rho U^2)$ in geophysical conditions, where $\tau_\star$ is the surface shear stress on the wall, ρ is the density (which is constant for an incompressible fluid), and U is the amplitude of the geostrophic velocity far enough from the wall. Initially motivated by atmospheric applications, the turbulent Ekman BL forced by a steady geostrophic flow on a plane has been studied using experiments, DNS and theory, complemented by more than a hundred years of meteorological data [189, 190]. Classical similarity theory provides asymptotic laws for the velocity in a turbulent Ekman BL [191–193], which is often in good agreement with measurements. First, we remind the readers the basics of the similarity theory for a highly turbulent Ekman BL with roughness, and we discuss its usual simplified version for smooth boundaries. Constraints obtained from experimental works are later discussed and, finally, we outline some remaining open questions for geophysical modelling and future experimental works.

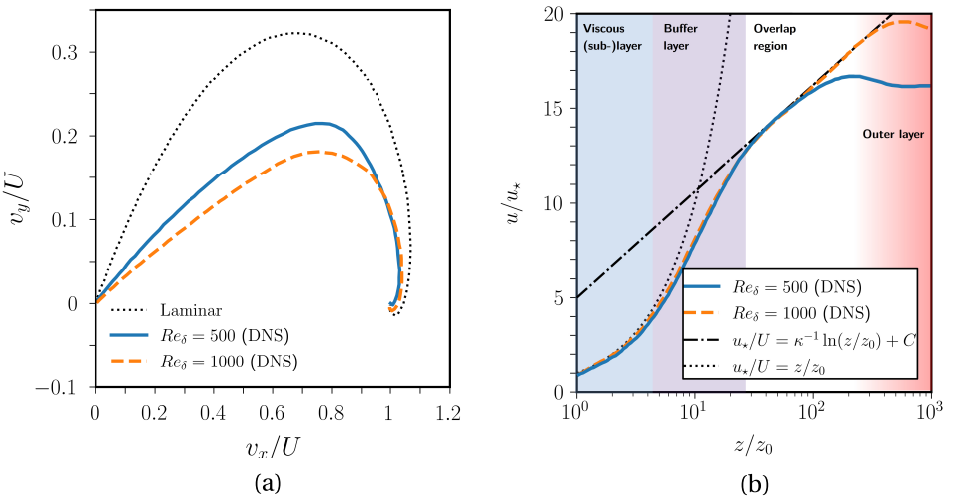


Figure 16. Neutral turbulent Ekman BL over a smooth plane boundary, for a geostrophic (bulk) flow U in the x direction. Adapted from figure 2 in [195]. (a) Hodograph showing the modification of the Ekman spiral (obtained for a laminar BL) as a function of Re_δ for a turbulent Ekman BL. (v_x, v_y) are the Cartesian components of the mean velocity in the coordinate system aligned with the geostrophic flow $\boldsymbol{U}$. The surface veering angle β is given by the slope near the origin. (b) Normalised mean velocity $u/u_\star$ as a function of the normalised distance z/z_0 to the wall. In the DNS, $u_\star$ is estimated from $u_\star^2 = \nu\partial_z Q$ with $Q = (u^2 + v^2)^{1/2}$. The linear law $u/u_\star = z/z_0$ (in the viscous sub-layer), and law-of-the-wall (23a) with $\kappa = 0.41$ and $C = 5$ (i.e. the $y-$intercept at $z/z_0 = 1$), are also shown.

3.2.1. *Theoretical considerations for turbulent Ekman BLs*

We consider the mean (free-stream) geostrophic velocity $\boldsymbol{U} = U\mathbf{1}_x$ in the bulk, which flows over a smooth or rough planar boundary. We introduce the local Reynolds number as

$$Re_\delta = \frac{U\delta_\nu}{\nu} \quad \text{with } \delta_\nu = \sqrt{\frac{2\nu}{f}}, \tag{18a,b}$$

where δ_ν is the laminar BL thickness, and $f = 2\Omega_s$ is the Coriolis parameter in experimental conditions. If $Re_\delta \geq 200$–300, a turbulent Ekman BL can be established above the boundary. When the Reynolds number is large enough, turbulent BLs are often assumed to be described by universal laws, such as the law-of-the-wall that is expected to be valid for any wall-driven turbulent flows (e.g. for channel flows). Such descriptions are thus cornerstones in the theory of turbulence [194], as many turbulent models are calibrated to reproduce them for simple flows. However, there is a noticeable difference between non-rotating and rotating flows. The wall shear stress is expected to be along the direction of the background flow for non-rotating flows, whereas the stress is tilted from the geostrophic flow $\boldsymbol{U}$ with rotation (Figure 16a). Indeed, laminar and turbulent Ekman BLs display a spiral structure as a function of the distance $|z|$ from the wall and, close to the wall, the boundary shear stress is tilted from the free-stream velocity with the veering angle β. As Re_δ increases, turbulence tends to reduce the veering angle from its laminar value of 45°. Hence, the theory has to be slightly modified to work with coordinates defined from the stress direction.

To do so, we denote by u the mean shear-wise velocity (i.e. in the wall-stress direction) departing from the bulk flow $\boldsymbol{U}$, and by v the (mean) cross-shear velocity. The veering angle

is thus given by $\beta = \arctan(v/u)$ at the wall. It is then postulated that, away from the wall, the velocity decrease from the geostrophic bulk flow is independent of viscosity and is represented by the so-called velocity-defect-law. The latter is given from dimensional analysis by [191, 192]

$$\frac{u-U_g}{u_\star} = G_1\left(\frac{fz}{u_\star}\right), \quad \frac{v-V_g}{u_\star} = G_2\left(\frac{fz}{u_\star}\right), \tag{19a,b}$$

where U_g is the component of the geostrophic bulk flow $\boldsymbol{U}$ in the shear-wise direction (respectively V_g in the cross-shear direction), $u_\star$ is the friction velocity estimated from the mean wall-stress $\tau_\star = \rho u_\star^2$, and (G_1, G_2) are some universal functions. On the contrary, near the wall, the average velocity is expected to be given by the law-of-the-wall as

$$\frac{u}{u_\star} = F_1\left(\frac{z}{z_r}\right), \quad \frac{v}{u_\star} = 0, \tag{20a,b}$$

where z_r is an adjustable constant, and F_1 is a universal function. Finally, it is assumed that there is an overlap region in which the velocity law-of-the-wall can be matched with the velocity-defect law (as originally proposed for turbulent flows in channels and circular tubes [196]). Admissible solutions are obtained by similarity analysis [191, 192], which shows that (F_1, G_1) are logarithmic functions and G_2 is constant. Notably, we obtain the usual form of the law-of-the-wall as

$$\frac{u}{u_\star} = \frac{1}{\kappa}\ln\left(\frac{z}{z_r}\right), \quad \frac{v}{u_\star} = 0, \tag{21a,b}$$

where κ is the von Kármán constant, and z_r is a scale height (sometimes called the roughness length). Finally, the matching between Equations (19b) and (20b) in the overlap region provides the wall stress through[5]

$$\frac{U\cos(\vartheta)}{u_\star} = \frac{1}{\kappa}\ln\left(\frac{\delta_\star}{z_r}\right) + B, \quad \sin(\vartheta) = A\frac{u_\star}{U}, \quad \vartheta = \beta + C_5\frac{z_r}{\delta_\star}, \tag{22a–c}$$

with $\delta_\star = u_\star/f$, and where β is the veering angle between the boundary (shear) stress vector and $\boldsymbol{U}$ is the free-stream geostrophic velocity. Note that the basic theory states that $C_5 = 0$ [191, 192], but the C_5-correction has been later proposed to have a better agreement with DNS when $Re_\delta <$ 5000 for smooth boundaries [193].

As illustrated in Figure 16(b), turbulent Ekman BLs are characterised by different sub-layers in agreement with the aforementioned analysis. First, there is a viscous sub-layer close to the wall in which $u_\star/U$ varies almost linearly with the distance from the wall [194]. Far enough from the wall, there is the overlap region in which $u/u_\star$ approximately obeys the law-of-the-wall, before reaching the outer layer (i.e. the last sub-layer before the bulk free-stream flow). Between the viscous and overlap sub-layers, there is a transition zone (the buffer layer) in which the mean velocity is neither linear nor logarithmic.

3.2.2. *Adjustable constants and boundary stress*

The above analysis is often assumed to be a universal feature of wall-driven turbulence [194], but there is a kind of black magic to estimate which results are independent of the turbulence mechanism. For instance, there are no universally accepted values for κ. Proposed values for non-rotating BLs are $\kappa = 0.36$–0.45 [199], and fitted values range between 0.36 and 0.59 for turbulent Ekman BLs [200]. However, the standard value is often chosen to be $\kappa \simeq 0.41$. Without roughness, it is generally assumed that $z_r \propto \nu/u_\star$ [185, 201], such that the law-of-the-wall is generally rewritten as

$$\frac{u}{u_\star} = \frac{1}{\kappa}\ln\left(\frac{z}{z_0}\right) + C, \quad z_0 = \frac{\nu}{u_\star}. \tag{23a,b}$$

In this case, the value of C is also not consensual. Traditional estimates for non-rotating BLs put it between 4.9 and 5.1, but values from 4 to 10 may also be acceptable [199]. For turbulent

[5] Note the retraction [197] of the more recently proposed logarithmic law with shifted origin [198].

Ekman BLs, very different values $C = 0.2$–0.4 [200] and $C = 5$–5.5 [50, 193] have been proposed in the literature. The rough case has received much less consideration for Ekman layers [202], but has been investigated without global rotation with various roughnesses [203, 204]. For roughness of height h_r, such works have shown that deviations from the smooth regime occur when $u_\star h_r/\nu > 2$–15, and a fully rough regime is reached when $u_\star h_r/\nu > 25$–90. In the fully rough state, data for sand roughness suggested that $z_r \approx h_r/30$. Note that the higher-order C_5-term has not been tested yet with roughness.

In addition to the von Kármán constant κ and z_r, there are also three unknown constants (A, B, C_5) that appear in Equations (22a–c) to complete the theory. It is natural to try estimating their values using DNS, as it is possible to design numerical models that are very close to the theoretical assumptions of the turbulence model. These adjustable parameters are also assumed to have the same values for rough and smooth walls [193]. Hence, some works have attempted to obtain their values using smooth boundaries with DNS. To do so, it is customary [205] to introduce the local Reynolds number given by Equation (18a) such that $\delta_\star/z_0 = Re_\delta^2 (u_\star/U)^2/2$ [185]. Next, Equations (22a–c) can be rewritten as [201, 206]

$$\frac{U}{u_\star}\cos(\vartheta) + \frac{2}{\kappa}\ln\left(\frac{U}{u_\star}\right) = \frac{2}{\kappa}\ln(Re_\delta) - \frac{\ln(2)}{\kappa} + B, \quad \sin(\vartheta) = A\frac{u_\star}{U}, \quad \vartheta = \beta + \frac{2C_5}{Re_\delta^2}\left(\frac{U}{u_\star}\right)^2. \tag{24a–c}$$

For consistency, note that there is an inconsequential typo in the sign of $\kappa^{-1}\ln(2)$ in [207]. Typically, it is found that $C_5 \approx -52$ [185,201,207,208] when $Re_\delta < 5000$, with for instance the mean values $(5.91, 1.35)$ when $2000 \leq Re_\delta \leq 4000$ [205]. Note that different values are obtained when C_5 is set to zero or not. For instance, it has been proposed that $(6.9, -0.35)$ when $C_5 = 0$ or $(5.4, 0.26)$ when $C_5 \approx -52$ [201], but the others values $(7.1, -0.73)$ with $C_5 = 0$ or $(5.1, 0)$ with $C_5 \approx -52$ could also be acceptable [185]. The similarity theory has also been compared with measurements of the atmospheric boundary layer [189, 190], showing a broad agreement, but with variations of (A, B) as a function of the latitude. This strongly suggests that, for turbulent Ekman BLs, the different coefficients do not have universal values in the similarity theory.

Finally, we can use the above theory to estimate the drag coefficient for geophysical applications. The wall stress being $\rho u_\star^2 \cos(\beta)$ in the $\boldsymbol{U}$ direction, the friction coefficient between the fluid and a rigid wall can be estimated as $k_f = (u_\star/U)^2\cos(\beta)$. For precession-driven flows, the Ekman BL theory with either $C_5 = 0$ [77, 100] or $C_5 \approx -52$ [206] has been used. Note that the simpler non-rotating limit with $\vartheta = \beta = 0$ has also been employed (e.g. for Venus [209], sometimes together with $B = \kappa^{-1}\ln(2\kappa)$ as in [210]), which simplifies further to a constant $U/u_\star$ if $\delta_\star/z_0$ is imposed. For instance, the constant value $(u_\star/U)^2 = k_f = 0.002$ was used to model the friction at the Moon's CMB [6].

3.2.3. *Experimental investigations*

Only a few experimental works have explored the Ekman BL turbulence. Two kinds of experiments have been designed, using either annular rotating wind tunnels [200, 202, 211] or water-filled tanks mounted on a turntable [50, 212, 213]. Contrary to DNS, the comparison between experimental results and the similarity theory is more complicated. First, there is an influence of the vortical nature of the geostrophic flow in the interior, whereas the imposed flow is rectilinear in the theory. This effect can be quantified by introducing the apparatus Rossby number $Ro_a = U/(rf)$, where r is the radius of the observation point. Typical experimental values are $Ro_a \sim 0.1$–1 in [200, 211] and $Ro_a \sim 0.48$–2.36 [50], whereas we have $Ro_a \to 0$ in the theory. A large enough turntable should thus be employed to approach the theoretical regime. For instance, as stated in [202], a wind tunnel with a radius of approximately 11 m should be used to avoid significant curvature effects. To weaken such effects, recent experiments [50,212,213] have been carried out on the CORIOLIS table, which is the largest turntable worldwide with a tank whose

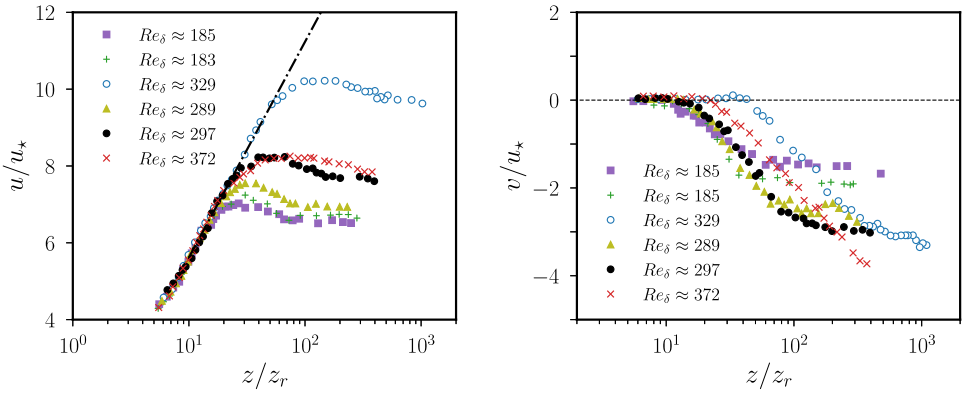


Figure 17. Turbulent Ekman BLs in the pioneering experiments of Kreider [211]. (a) Normalised shear-wise velocity $u/u_\star$ as a function of z/z_r. Dash-dot line shows law-of-the-wall (21a) with $\kappa \approx 0.41$. (b) Normalised cross-shear velocity $v/u_\star$ as a function of z/z_r. Dashed line shows law-of-the-wall (21b) for the cross-shear velocity.

diameter is 13 m. Another difficulty comes from the experimental measurements. The friction velocity $u_\star$ has been obtained using wall-stress sensors [200] (requiring difficult calibration and alignment procedures), by using linear regression of law-of-the-wall (21) [202, 211], or from the rate of change of the angular momentum during spin-up or spin-down processes [50]. The comparison suggests that the two latter techniques are the more accurate ones [50, 200]. For the velocity profiles, the oldest studies used hot-wire anemometry [200, 202, 211], whereas the most recent ones employed PIV techniques [50, 212, 213].

Given the intrinsic experimental difficulties, it is a tour de force that experiments have managed to confirm the similarity theory. The first experimental results, obtained at $Re_\delta \sim 600$–2000 [200], indeed showed a broadly good agreement with the similarity theory when $z/z_r > 10^2$. Yet, all the theoretical predictions were not confirmed at that time. For instance, the shear-wise velocity-defect-law (19a) was not fully obtained in [200], as well as a vanishing cross-shear velocity as expected from law-of-the-wall (21b) in the overlap region. The experimental confirmation of such predictions was later given by Kreider [211], as illustrated in Figure 17 where we have digitised some of his results. In particular, we observe that the measurements of the cross-shear velocity roughly vanish when $z/z_r \lesssim 20$, as expected from law-of-the-wall (21b) in the overlap region. Another striking observation is that these old measurements are already in good agreement with the similarity theory, even for the moderate values $Re_\delta \sim 150$–400. More recent experiments [50, 212] did further confirm the robustness of the similarity theory for smooth boundaries with cleaner measurements, but, quantitatively, the different studies slightly disagree. For instance, the constants (A, B) were found to be $(7.32, -2.67)$ in [50] and $(6.01, 0.018)$ in [200], which typically gives a friction about 15–20% higher in [200] than reported in [50]. Such differences have been attributed to roughness by [50], which was not well controlled in [200].

So far, there is only one study that investigated roughness effects on turbulent Ekman BLs [202]. The experimental setup is illustrated in Figure 18(a). Various kinds of bottom roughness were employed, namely a coarse grained sandpaper, a textured paint, bare duct floor coated with clear varnish, and an artificial celanese turf (usually used for indoor-outdoor carpeting). However, note that these experiments only allowed exploring the regime with $0.2 \leq u_\star z_r/\nu \leq 4.6$. A simple way to explore the effects of roughness on the Ekman layer is to look at the veering angle β and the drag coefficient. As shown in Figure 18(b), we observe that the rough points are

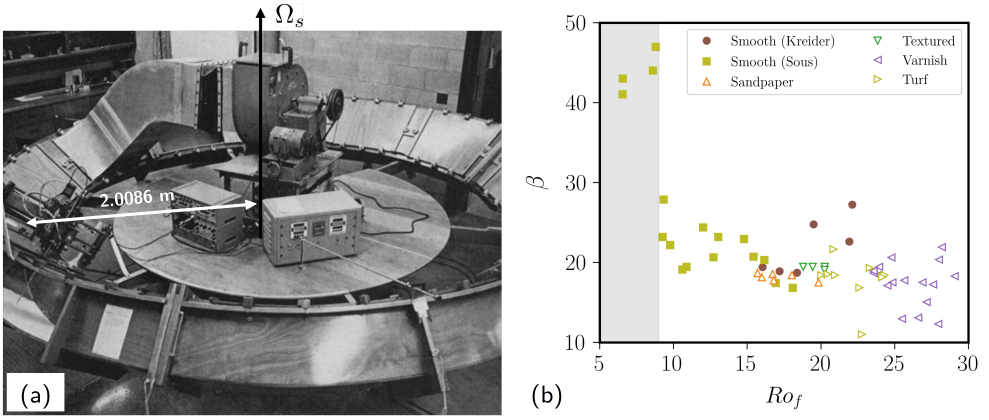


Figure 18. (a) Experimental setup to investigate a turbulent Ekman BL with roughness [202]. Annular rotating wind tunnel with a duct in wood, whose floor is inclined from an angle of 45° to the horizontal. The duct has a width of 45.72 cm and a height of 30.48 cm. (b) Veering angle β (in degrees) as a function of the modified Rossby number $Ro_f = u_\star/\sqrt{f'\nu}$, where $f' \approx f + U/r$ is the modified Coriolis parameter [50]. Measurements for smooth [50, 211] rough boundaries [202] are shown. The transition from a laminar to a turbulent Ekman BL occurs at $Ro_f \simeq 9$ [50], corresponding to a BL instability at a local (boundary layer) Reynolds number of $Re_\delta \approx 150$ [50, 187].

very close to the smooth points (as expected in this regime). However, the roughness height z_r is found to have more influence on the friction velocity (Figure 19a). Indeed, $u_\star/U$ increases when the dimensionless roughness height z_r/H increases (where H is defined as the geostrophic height above which the angular deflection of the velocity vector no longer changes in magnitude). Moreover, all the data collapse on a master curve, suggesting that roughness has somehow universal effects. As shown in the inset, the rough points are well predicted by law (22a) with $\kappa \approx 0.41$ and $B \approx -5.87$. Finally, to compare the results with [202] and without [200, 211] roughness on a single plot, we show in Figure 19(b) the evolution of the geostrophic drag coefficient $u_\star^2/U^2$ as a function of the surface Rossby number $Ro_s = U/(f z_r)$. We find that all the rough points seem to collapse on a power law of the form $u_\star^2/U^2 \propto Ro_s^{-0.4}$, whose exponent is larger than that predicted by a prior eddy-viscosity model yielding $u_\star^2/U^2 \propto Ro_s^{-0.238}$ [214]. Note that the smooth and rough points also almost collapse on a single curve, which seems to be well described by a nonlinear eddy-viscosity model [189, 215]. Moreover, we see that the geostrophic drag coefficient estimated from [211] is larger than that estimated with roughness [202]. This is somehow unexpected, but this may suggest that roughness was present but not reported in the experiment [211]. Future experimental studies could thus start reproducing these points to elucidate the origin of this puzzling observation, before exploring other rough regimes with larger values of $u_\star z_r/\nu$.

3.2.4. *Remaining open questions and experimental perspectives*

The similarity theory outlined above was derived for high-Re_δ turbulent Ekman BLs above planar boundaries, but experiments and DNS showed that it is also quite robust for moderately large values $Re_\delta \sim 200$–1000. Yet, all these works show that the constants in the theory are not as universal as initially expected, as they can significantly vary in the different configurations. Therefore, this calls for dedicated studies for each application. Another challenge is to properly assess the validity of the similarity theory with roughness, to go beyond the pioneering experiments presented in [202]. Indeed, roughness is expected in many geophysical systems (e.g. at a

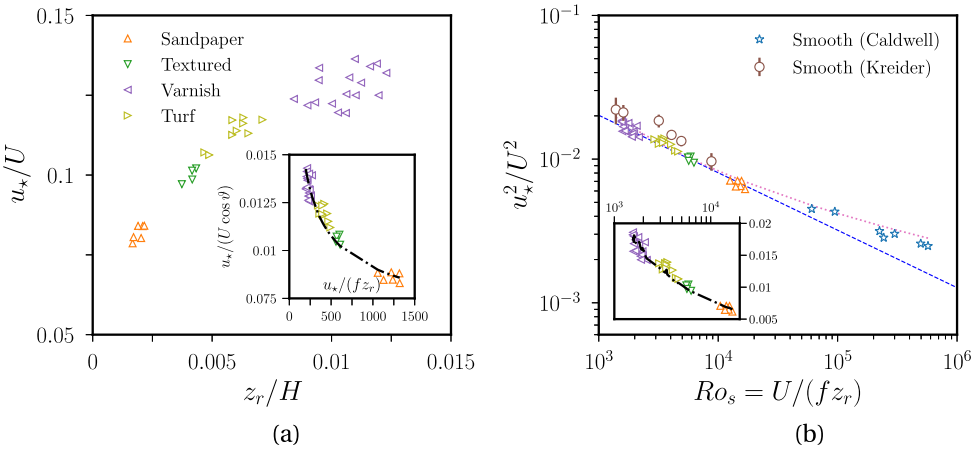


Figure 19. Effects of roughness of turbulent Ekman BLs from [202]. Common symbols are used in the two panels. (a) Dimensionless friction velocity $u_\star/U$ as a function of z_r/H. H is the geostrophic height above which the angular deflection of the velocity vector no longer changes in magnitude. Inset shows the comparison between the rough points and law (22a) with the fitted parameters $\kappa \approx 0.41$ and $B \approx -5.87$ assuming $C_5 = 0$. (b) Geostrophic drag coefficient $(u_\star/U)^2$ as a function of the surface Rossby number $Ro_s = U/(fz_r)$. Experimental points for smooth boundaries from [187,211]. Dashed (blue) line shows the empirical power law $u_\star/U \propto Ro_s^{-0.2}$, which is close from the nonlinear law $u_\star/U = \alpha_1/(\log_{10}(Ro_s) - \alpha_2)$ obtained from a nonlinear eddy-viscosity model [189,215] with the fitted parameter $\alpha_1 = 0.2238$ and $\alpha_2 \approx 1.542$ (dotted pink line). Inset shows, using the same axes, the comparison between the rough points and law (22a) with the fitted parameters $\kappa \approx 0.41$ and $B \approx -5.87$ assuming $C_5 = 0$.

planet's CMB [37,38]). In particular, next-generation experiments should investigate the different regimes as a function of the roughness height z_r, to properly quantify the enhancement of the friction by roughness. Another limitation is that, in the similarity theory, the turbulent Ekman BL is forced by a steady geostrophic flow. However, the orbital forcings discussed in Section 2 can sustain oscillatory and non-geostrophic large-scale flows (e.g. equatorial rotation with a nearly diurnal frequency in the rotating frame for precession [83]), which may lead to turbulent Ekman BLs [100]. So far, a numerical study proposed the fitted values $(A, B, C_5) = (5.74, 1.55, -25)$ for the precession-driven flow oscillating at $f/2$ over a smooth boundary [206], which lead to smaller values of $u_\star$ and β compared to those obtained with a steady flow. Therefore, it would be worth pursuing in this direction by considering the effects of oscillatory flows on turbulent Ekman BLs in future works (e.g. to assess the effects of the flow frequency). In particular, previous experimental works on oscillatory turbulent BLs [216,217], which used oscillatory-flow water tunnels, could be revisited by including global rotation.

For geophysical applications to thick-layer fluid systems, we may also question the validity of the similarity theory with curvature effects. It is well-known that the laminar BL solution fails to be valid at the so-called critical latitudes [26], where the laminar BL thickness diverges. Hence, we may also anticipate some issues for the similarity theory at these critical latitudes. Indeed, a prior numerical work [206] showed that it is not straightforward to properly extrapolate such local laws for turbulent Ekman BLs to a global near-spherical geometry. Moreover, the Ekman BL could be turbulent at some latitudes and laminar at others (e.g. near the pole and the critical latitudes, respectively). The proper extrapolation of the similarity theory to this case,

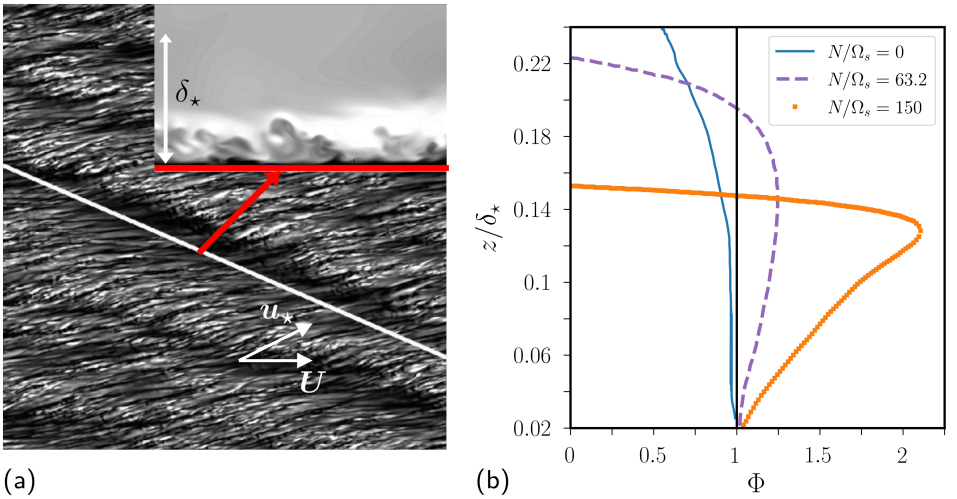


Figure 20. Turbulent Ekman BL with stratification in DNS. (a) Instantaneous visualisation of wall shear stress. Colour coded from black (low) to white (high). White arrows indicate the orientation of bulk geostrophic flow $\boldsymbol{U}$ and that of $u_\star$. Tilted white line indicates a large-scale structure in the flow. Inset shows a vertical cross-section of $u/|\boldsymbol{U}|$ along the red arrow, with colour coded from black to white in the range $[0.12, 1.11]$. DNS for a turbulent BL at $Re_\delta \simeq 500$ in the intermediate stratified regime, adapted from Figures 9 and 11 in [195]. (b) Deviations from law-of-the-wall (23) measured by the quantity $\Phi = (\kappa z/u_\star)\,\partial_z Q$ with $\kappa = 0.41$, as a function of the ratio N/Ω_s. DNS (using a large-eddy-simulation approximation) at $Re_\delta \simeq 5\times10^7$ and $Pr \sim 5$–10, adapted from figure 9 in [221].

where the mass fluxes at each latitude are interconnected (e.g. by the Ekman pumping), remains to be found. Moreover, the turbulent theory may not be valid in the presence of meso-scale topographies, which deserves further investigation. If the meso-cale topography has slender or non-slender bumps, we may preserve or disrupt the viscous sub-layer. It is also known that wall-driven turbulence is affected by the convexity of meso-scale topography [218]. Another limitation of the above turbulent theory is that some thick-layer systems may only be at the margin of turbulence. For instance, the expected values of the BL Reynolds number $Re_\delta \sim 100$–500 due to precession-driven flows at the Earth's CMB [219, 220] might be large enough to sustain wall-driven instabilities, but not to obtain a fully turbulent BL. Since experimental works clearly show some deviations from the similarity theory when Re_δ is not large enough, the similarity theory may not give accurate enough predictions for such applications.

Note that turbulent Ekman BLs can also be affected by density variations. In particular, buoyancy effects deserve consideration to understand the interplay between turbulent BLs and convective flows. Temperature should be governed by a similar law-of-the-wall [222], but the validity of a universal law-of-the-wall for temperature was also questioned [223]. The interaction between rotating convection and turbulent Ekman BLs remains to be studied, but the non-rotating case has already been considered. It could indeed be key for elucidating the transition between the different regimes of turbulent convection (see in Section 4), or for estimating basal melting of ice shelves [224]. The stably stratified regime is also of paramount importance for some geophysical applications. As illustrated in Figure 20(a), stratified Ekman BLs have some similarities with unstratified Ekman BLs (e.g. a friction velocity $u_\star$ tilted from the bulk geostrophic flow). However, strong departures from the law-of-the-wall can be obtained depending on the value of N/Ω_s (even for high-Re_δ BLs, see Figure 20b). Different

turbulent regimes can be identified as a function of the strength of stratification [195], from weakly stratified Ekman BLs (similar to neutral ones) to strongly stratified Ekman BLs (which can exhibit global intermittency and turbulent collapse, as for non-rotating stratified BLs [225]). Except in the weakly stratified regime, the standard law-of-the-wall fails to describe the observed turbulence with stratification [195, 221]. A quantitative understanding of stratified turbulent Ekman BLs is thus considerably more difficult than without stratification. Other similarities theories have been proposed to go beyond the classical log-law theory (e.g. Monin-Obukhov [226, 227] or Perlin [221, 228] theories), but their range of validity remains to be carefully determined. Finally, wave motions can also be emitted by the turbulent dynamics in stratified Ekman BLs [207, 221, 229], and be radiated away in the bulk. The vertical energy flux associated with such waves is likely negligible compared to the turbulent friction in the BL, but these waves could affect entrainment and mixing processes in the near-wall region (e.g. without global rotation [230–232]).

To finish with, we have pointed out that turbulent Ekman BLs are far from being fully understood. As such, it calls for new experimental (and numerical) studies before conducting geophysical extrapolation of the results. Such works should explore the BL dynamics for low to medium values of Re_δ to understand the route to wall-driven turbulence, as well as high-Re_δ BLs to characterise the properties of the fully turbulent regimes and to assess the validity of the turbulence theories.

4. Convection-driven flows with topography

Many geophysical systems are subject to thermal convection (e.g. the Earth's liquid core [13], subsurface oceans [7], or the Sun [233]). It is thus natural to seek physical insight into turbulent convection using experiments. Experimental setups have mainly considered variations around the classical configuration of Rayleigh–Bénard convection (RBC), for which convection is driven by the temperature difference ΔT between a bottom plate and a top one at the distance L. As illustrated in Figure 21, RBC is well suited to experimentally model the local properties of turbulent convection of a thick-layer fluid system (even with rotation, as suggested by a recent numerical work [234]).

In the following, we assume that convection can be described using the Oberbeck–Boussinesq (OB) approximation (i.e. with constant physical properties, except its density that varies with temperature in the buoyancy force). Despite the restricted range of validity of the OB approximation [236, 237], it is often employed in theoretical works and usually offers a good (qualitative) understanding of most experimental results. RBC is then controlled by the Rayleigh number Ra, the Prandtl number Pr, and the convective Rossby number Ro_c (which is a proxy of the Rossby number based on L). They are defined by

$$Ra = \frac{\alpha g \Delta T L^3}{\nu \kappa}, \quad Pr = \frac{\nu}{\kappa}, \quad Ro_c = E\left(\frac{Ra}{Pr}\right)^{1/2}, \tag{25a–c}$$

where α is the thermal expansion coefficient of the fluid, g is the acceleration of ambient gravity, ν is the kinematic viscosity of the fluid, and κ is the thermal diffusivity. Convection is affected by global rotation when $Ro_c \ll 1$ and, in contrast, is barely modified by rotation when $Ro_c \geq 1$.

One of the difficulties in convection modelling is to reach the extreme parameters characterising geophysical systems (Table 2). For a water-filled tank with $\Delta T \sim 100$ K (at maximum), it is difficult to obtain high-Ra convection given the thermal expansion coefficient of water $\alpha \sim 10^{-4}$ K^{-1} (which does not efficiently convert temperature differences into density variations to explore high-Ra convection). This effect can be partly balanced by increasing the height L of the tank (e.g. with $L \sim 4$ m in the TROPOCONVEX experiment [238]), but there are then some mechanical and

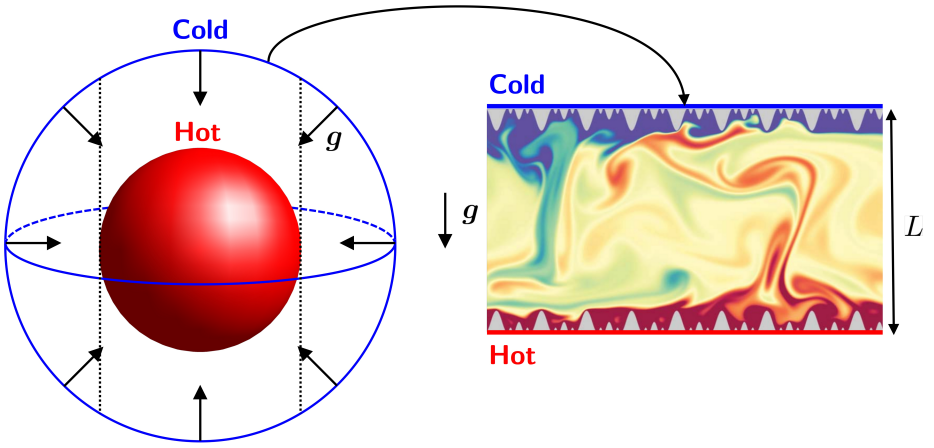


Figure 21. Thermal convection in a thick-layer envelope (e.g. with radial gravity $\boldsymbol{g}$ in a spherical shell), as modelled by Rayleigh–Bénard convection (RBC) in experiments (with axial gravity). Visualization of temperature variations with multiple-scale topography on top and bottom planes is also illustrated (adapted from figure 2 in [235]).

Table 2. Typical values of the Rayleigh number Ra, the Prandtl number Pr, the Ekman number E, and the convective Rossby number Ro_c in natural (turbulent) systems and in laboratory experiments

	Ra	Pr	E	Ro_c
Earth's core [13]	10^{20}–10^{30}	10^{-2}–1	10^{-15}	$\ll 1$
Fully molten silicate layers [240,241]	10^{25}–10^{30}	1–10^{4}	10^{-13}	10^{-2}–10^{2}
Sun [233,242]	10^{19}–10^{24}	10^{-7}–10^{-4}	$\leq 10^{-14}$	≥ 1
Experiments [239,243]	$\leq 10^{15}$	10^{-2}–10^{3}	5×10^{-9}–∞	10^{-4}–∞

thermal constraints (e.g. it is difficult to ensure thermal insulation on the lateral walls). Therefore, water-filled experiments are typically limited to $Ra \sim 10^{12}$–10^{13}, and most experiments probing more vigorous convection use other fluids with $0.6 \leq Pr \leq 7$ [239] (e.g. He or SF_6).

A detailed account of the fundamental aspects of convective flows is available elsewhere for non-rotating [239, 244] and rotating [243] convection, so we will not discuss them here. Instead, we will briefly discuss experimental (and numerical) works dedicated to the interplay between turbulent convection and small-wavelength topography. The effects of a topographic β-plane, as well as of global spherical-like geometries, are also beyond the scope of the following review (although they are directly relevant for modelling thick-layer systems). We refer the interested reader to [245, 246] for geophysically motivated descriptions of such convection experiments. We first discuss the interplay between small-wavelength topography and RBC (both without and with rotation), and then we outline some experimental perspectives.

4.1. *Non-rotating (and rotating) RBC with small-scale topography*

We first consider the limit case of non-rotating RBC (i.e. $Ro_c \to \infty$), which is appropriate for the dynamics of slowly rotating convective systems (e.g. solar convection, and possibly molten silicate layers). In particular, estimating the efficiency of heat transport by convection is key for understanding the heat budget of these systems and their long-term thermal evolution over

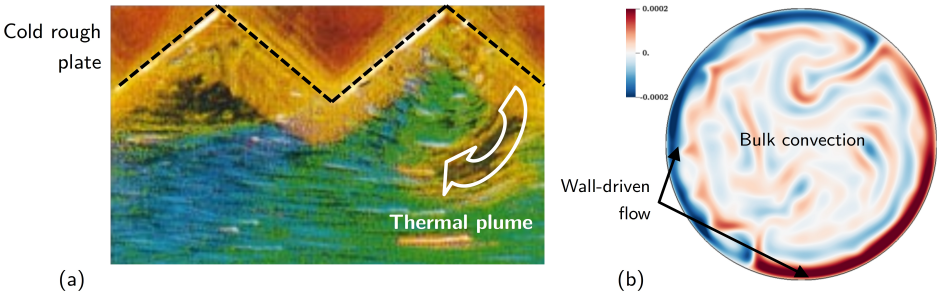


Figure 22. (a) Observation of topography-driven flows in an experiment of RBC with rough plates at $Ra \simeq 2.6 \times 10^9$ and $Pr \simeq 5.4$. Visualization of the flow (streak image of the fluid, seeded with thermochromic liquid crystal spheres) near the upper rough (cold) plate. Wall-driven (cold) eruptions are in brown, and warmer flow structures are in green and blue. Adapted from figure 4 in [264]. (b) Observation of wall-driven mode in rotating RBC. Numerical simulation in a cylinder at $Ra = 5 \times 10^{10}$, $Pr = 5.2$ and $E = 10^{-7}$. Colour bar shows the vertical velocity in the mid-plane of the cylinder. Adapted from figure 5 in [274].

billions of years. Convective heat transport is usually characterised by the Nusselt number Nu given by $Nu = QL/(k\Delta T)$, where k is the thermal conductivity (in $\mathrm{W{\cdot}m^{-1}{\cdot}K^{-1}}$), and Q is the heat flux per unit of area with convection (in $\mathrm{W{\cdot}m^{-2}}$). There is still a long-standing controversy about the asymptotic scaling law $Nu \sim f(Ra, Pr)$ for turbulent convection in the asymptotic high-Ra regime. Indeed, classical theory predicts $Nu \sim Ra^{1/3}$ [247], whereas the ultimate theory states that $Nu \sim Ra^{1/2}Pr^{1/2}$ (at least for $Pr \leq 1$) when convection operates in a diffusion-free regime [248, 249]. Actually, in the theory, the ultimate regime of RBC is expected to be linked to the existence of turbulent BLs. A few studies have thus investigated the nature of the BLs in high-Ra convection. It was first conjectured that BL turbulence would occur when the local friction Reynolds number is greater than ~200 in non-rotating RBC [250]. Later on, some experiments [251, 252] and DNS [253–257] did confirm that the viscous and thermal BLs become turbulent and can be described by similar laws-of-the-wall when the friction Reynolds number is large enough. Yet, some local departures from the law-of-the-wall have also been documented in the presence of large-scale plumes [253–255]. Moreover, despite the presence of turbulent BLs, contradictory results were found for the scaling of Nu with Ra [254, 255]. Whether very high-Ra RBC with smooth plates is governed by the classical theory or falls into the ultimate regime is still thus unknown in experimental conditions, and it remains the subject of active research [239,244].

This fundamental problem has been revisited by using topographic effects for a few years. Indeed, small-scale topography can favour wall-driven flows [258,259], such as thermal plumes and wall-driven turbulence (see Figure 22a). As such, it could possibly favour the transition to the ultimate regime [260]. Different experiments of RBC with small-scale topography on the walls have thus been conducted, using topography with different shapes and heights [235, 261–269]. Most studies employed either water or another fluid with $Pr \geq 1$, but a few used an air-filled experiment [258, 270]. These studies did find that small-scale topography can often enhance heat transport by turbulent convection, with either an exponent larger than 1/3 or with a higher numerical prefactor. Scaling laws with exponents close to 1/2 have even been experimentally reported in some studies [271, 272]. This suggests that turbulent convection might reach a diffusion-free regime in the presence of wall-driven turbulence (at least for the considered values of Ra). However, topography does not always enhance heat transport. By further increasing the value of Ra, the 1/2 scaling can be lost [273], which can depend on the chosen topographies [235].

Finally, contrary to the non-rotating case, the interaction between rotating RBC and small-scale topography has only received scant attention [275,276]. Further work is thus required to get insight into the effects of topography on RBC. Rotating RBC is also often impacted by the presence of (zonal) wall modes along the lateral boundaries (Figure 22b). Their presence is largely indifferent to the bulk convection [277, 278], and they may have a non-trivial topological origin [274, 279]. From an experimental viewpoint, these modes can affect heat flux measurements in the bulk, and reduce our ability to precisely study the regimes of bulk turbulence [243]. A recent theoretical work [280] showed that such wall-driven flows can be strongly weakened by including well-chosen topographic defaults on the lateral walls, which paves the way for future experimental applications.

4.2. *Experimental perspectives*

Characterising heat transport of RBC with small-scale topography in the presence (or absence) of wall-driven turbulence is key from a fundamental viewpoint, but it could also be important for engineering [281] and geophysical applications. For instance, the BL Reynolds number due to convection may have the typical value 100–1000 at the Earth's CMB [13], which could be sufficient for the onset of BL instabilities and wall-driven turbulence. Further experimental work, together with joint theoretical and numerical studies, may therefore help to make progress on this fundamental question For rotating RBC, including topographic defaults on lateral walls seems key to weaken the strength of wall-driven flows in future experiments [280]. Finally, we could naturally wonder how much the various convection scaling laws remain valid in the presence of non-Oberbeck–Boussinesq (NOB) effects (i.e. non-uniform material properties of the fluid due to temperature variations) or compressibility. Such effects can be important in some experimental conditions (e.g. a gas near its saturated vapor curve [282] to explore high-Ra convection, or a gas subject to extreme rotation rates [283]), but also in some geophysical systems (e.g. for mantle convection in super-Earth [284], or in gas giants). As for incompressible RBC [285], theory shows that the Nusselt number in non-rotating compressible (anelastic) convection remains bounded by $Ra^{1/2}$ [286]. Hence, the ultimate regime of non-rotating RBC might also exist with compressibility. As such, the interplay between small-scale topography and compressible convection would certainly deserve consideration in the future.

Finally, exploring the effects of meso-scale topographies on rapidly rotating convection in planetary-core geometries would be worth considering. Indeed, the low-frequency dynamics of planetary-core convection is strongly shaped by global rotation, which tends to sustain columnar motions that are nearly invariant along the rotation axis of the fluid. However, prior theoretical [287–289] and experimental [290] works in the cylindrical annulus geometry showed that this low-frequency dynamics can be modified in the presence of sinusoidal deformations on top and bottom walls (e.g. in trapping columnar motions near bumps, or in sustaining low-frequency Rossby waves). Similar effects were found in DNS using a quasi-geostrophic approximation, in a rotating spherical shell with a non-slender meridional ridge [291]. The convective flow was dominated by zonal circulation when Ra is large enough and, at low values of Ro, blocked flows were reported (as in [180] for slender obstacles). Moreover, it was observed that topography can transfer energy from large-scale (convective) flows to smaller-scale flows in the form of Rossby waves (whose amplitude scales as $Ro^{1/2}$). Future experiments could build upon such prior works to explore these effects, such as in the idealised annulus geometry that is amenable to experimental investigation (where Earth's gravity is replaced by centrifugal gravity [246]).

5. Brief discussion of rotating stratified flows

Beyond neutrally buoyant fluids and convection, understanding the dynamics of rotating and stratified flows with topography is also crucial for some geophysical applications (e.g. the wave-driven drag over a topography, wave-driven mixing processes in rotating stratified ellipsoids, or the turbulence in stratified Ekman BLs). The effects of density stratification have not been reviewed in the previous sections, as they deserve specific review articles. We refer the interested reader to the two reviews in this special issue on different regimes of stratified turbulence without topography [32, 33], and to [28, 292] for theoretical descriptions of topographic effects in stratified flows. However, rotating experiments with stratification and topography are not very common [293, 294]. In brief, these experimental works have mainly explored the regime $N/\Omega_s \sim \mathcal{O}(1)$, and often considered the low-frequency dynamics (e.g. to investigate spin-up processes, or the quasi-geostrophic dynamics). In the following, we explain why it is still very difficult to study rotating stratified flows in the laboratory. Indeed, there are intrinsic difficulties that need to be overcome in future experimental works before answering unsolved geophysical questions.

5.1. *Accessible experimental regimes*

Since the strength of stratification is subject to strong uncertainties for geophysical applications, exploring the dynamics for a broad range of values of N/Ω_s would be desirable. We can estimate BV frequency (4) for an incompressible fluid from $N^2 \sim (g/\ell_V)|\Delta\rho|/\rho$ in laboratory conditions, where ℓ_V is the height of the container (in metres), $g \simeq 9.81$ m·s^{-2} is the value of Earth's gravity, and $|\Delta\rho|/\rho$ is the relative density anomaly. For salty (NaCl) water, the density anomaly can vary from 0 to ~ 0.3 (at most) by changing the salt concentration. As such, the values of N that are accessible in a water-filled experiment are limited (Figure 23a). Typically, for a metre-size tank (which is required to lower the value of E), we cannot impose an initial stratification with a BV frequency greater than $N \sim 1.7$ rad·s^{-1}. For a rotating table with a rotation rate Ω_s between 0.1–10 rad·s^{-1}, the maximum value would be $N/\Omega_s \sim 10$–20. Beyond the regime $N/\Omega_s \leq 1$, stratified regimes with $N/\Omega_s \geq 1$ could also be considered in experiments, but a first technical difficulty is to impose the initial stratification profile. The standard approach (known as the double-bucket method) does not offer great flexibility to impose arbitrary stratification, but other strategies have been proposed [295]. Another difficulty would also result from the velocity measurements. To probe the low-*Ro* dynamics with $Ro \sim 10^{-3}$–10^{-2} in a metre-size experiment, the velocity would have a typical amplitude $u_\ell \sim 10^{-4}$–10^{-1} m·s^{-1} for an angular velocity $\Omega_s \sim 0.1$–10 rad·s^{-1}, which could be below the detection level of the different velocimetry techniques. Therefore, it seems difficult to simultaneously explore low-*Ro* and strongly stratified regimes with currently available experiments.

Rapidly rotating regimes with $N/\Omega_s \leq 1$ would also be difficult to probe because of centrifugal effects. Indeed, if global rotation is strong enough, centrifugal gravity will deform the initial vertical stratification. To maintain a vertical stratification with negligible centrifugal effects, as well as small viscous ones with $E \ll 1$, a large tank with a relatively moderate rotation is required. This can be estimated by the ratio between centrifugal forces to Earth's gravity given by $\Delta_g = \Omega^2 \ell_H / g$ (where ℓ_H is the horizontal length scale of the tank, where centrifugal gravity is maximum). Assuming that the tank has a typical aspect ratio $\ell_H/\ell_V \sim 1$, we can introduce the Ekman number E such that $\Delta_g = \nu^2/(E^2 \ell_H^3 g)$. For a fixed value of Δ_g, the maximum value of ℓ_H is thus given by

$$\ell_H \sim \left(\frac{\nu^2}{g \Delta_g E^2} \right)^{1/3}, \tag{26}$$

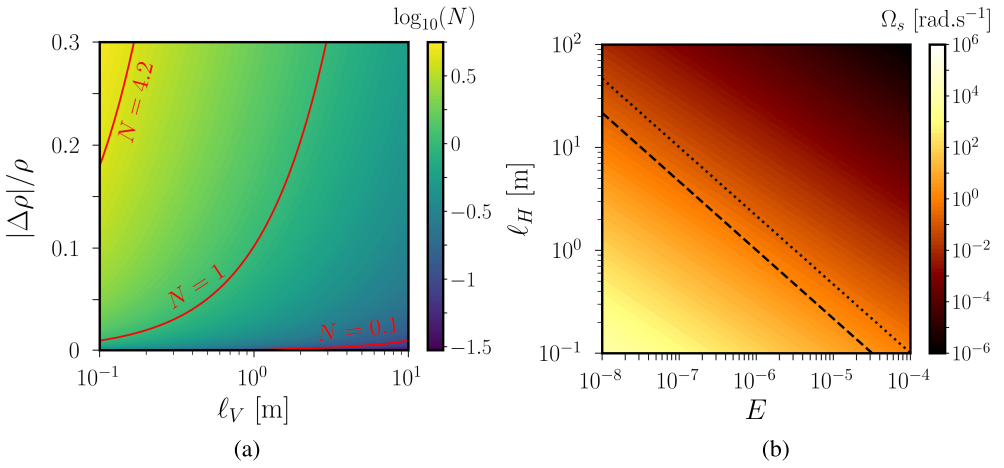


Figure 23. (a) Typical values (in logarithmic scale) of the BV frequency $N \sim \sqrt{(g/\ell_V)|\Delta\rho|/\rho}$ (in rad·s^{-1}) in a water-filled experiment at room temperature, where ℓ_V is the height of the fluid container (in metres), $g \simeq 9.81$ m·s^{-2} is the acceleration of gravity, and $|\Delta\rho|/\rho$ is the (relative) density anomaly. The water density can be changed by varying the salt concentration (from 0 to approximately 300 kg·m^{-3}). Red curves show the values $N \in [0.1, 1, 4.2]$ rad·s^{-1}. (b) How to keep centrifugal gravity under control in a rotating experiment. Colour bar shows the rotation rate Ω_s (in rad·s^{-1}) required to reach the Ekman number E for a water-filled experiment with equal horizontal and vertical length scales $\ell_H \sim \ell_V$. Dashed line (respectively, dotted line) shows the length scale ℓ_H given by Equation (26) such that $\Delta_g = 10^{-1}$ (respectively, $\Delta_g = 10^{-2}$).

where $g \simeq 9.81$ m·s^{-2} is the value of Earth's gravity, and $\nu = 10^{-6}$ m^2·s^{-1} is the kinematic viscosity of water at ambient temperature. Formula (26) shows that when Δ_g is reduced (i.e. the more centrifugal gravity is negligible), then the horizontal length scale ℓ_H increases. As shown in Figure 23(b), to reach a value $E = 10^{-6}$ with a rotation rate $\Omega_s \sim 1$ rad·s^{-1}, we must use a tank with $\ell_H \sim 1$ m if $\Delta_g = 10^{-1}$ (or $\ell_V \sim 4$ m if $\delta_g = 10^{-2}$). For a value of the Ekman number $E \sim 10^{-8}$, we would instead need a much larger tank with $\ell_H \sim 20$ m. Therefore, the dynamics of rotating stratified fluids with $E < 10^{-6}$ cannot be probed with a metre-size tank. The only alternative would be to change the aspect ratio of the tank. While keeping $\ell_H \sim 1$ m to weaken wall-driven flows, we could increase ℓ_V up to 4–5 m (e.g. as in the TROPOCONVEX convection experiment) but at the expense of a smaller value of the BV frequency (according to Figure 23a).

5.2. *Specific properties of inertia-gravity waves in experimental conditions*

Inertial waves and modes have proven useful to characterise the flow response of rotating fluids with large-scale ellipsoidal topographies (see Section 2), but also with small-wavelength topographies (see Section 3). When global rotation and density stratification are coupled, inertia-gravity waves (IGWs) could be expected to play a similar role. IGWs are mixed waves that are sustained by Coriolis force and gravity. Let us discuss their properties in the case of a fine-tuned experiment, in which rotation is aligned with gravity and centrifugal effects are negligible. We consider a fluid that is stratified in density with a constant BV frequency $N > 0$ along Earth's gravity $\boldsymbol{g} = -g\mathbf{1}_z$ (where g is a constant), and rotating along the same axis at the

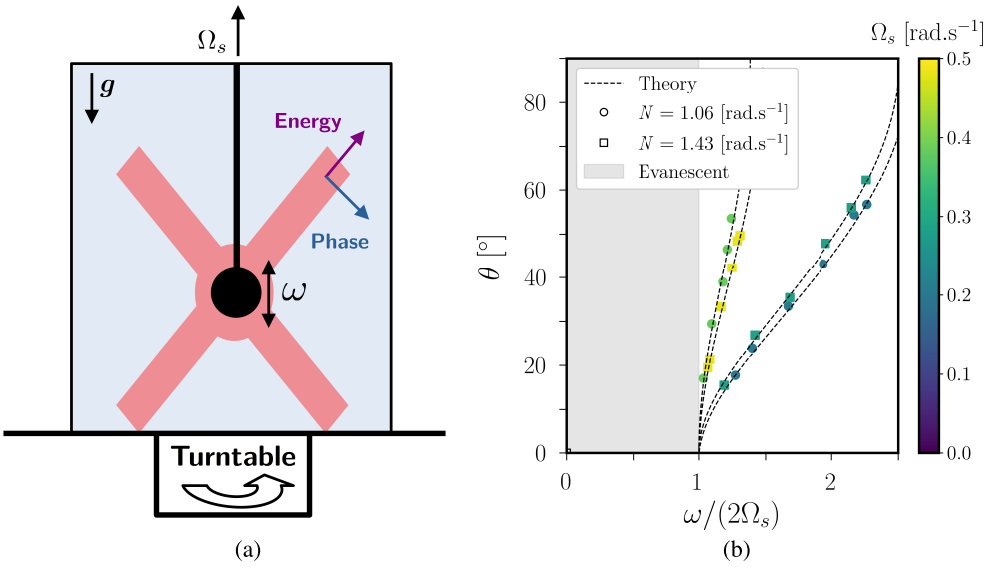


Figure 24. Experimental investigation of inertia-gravity waves (IGWs), for a rotating stratified fluid with aligned global rotation $\boldsymbol{\Omega} = \Omega_s \mathbf{1}_z$ and gravity $\boldsymbol{g} = -g\mathbf{1}_z$ in the regime $N/\Omega_s > 2$. Adapted from [296]. (a) Sketch of the experimental setup. A solid sphere, which is embedded in the fluid, oscillates at the angular frequency ω. The oscillation generates IGWs, which manifest in the form of wave beams (red regions, in which the phase and group velocities are orthogonal). (b) Angle θ (in degrees) between the wave vector $\boldsymbol{k}$ and gravity in dispersion relation (28). Excellent agreement is found between the experimental results and theory. No waves were reported when $|\omega| \leq 2\Omega_s < N$.

angular velocity $\boldsymbol{\Omega} = \Omega_s \mathbf{1}_z$. In the rotating frame, IGWs satisfy the eigenvalue problem given by [167]

$$-\omega_i^2 \boldsymbol{u}_i + \mathrm{i}\omega_i (2\boldsymbol{\Omega} \times \boldsymbol{u}_i) + N^2 (\boldsymbol{u}_i \cdot \mathbf{1}_z)\mathbf{1}_z = -\mathrm{i}\omega_i \nabla \Phi_i, \quad \nabla \cdot \boldsymbol{u}_i = 0, \tag{27a,b}$$

where ω_i is the angular frequency of the wave, and $\boldsymbol{u}_i$ is the eigenvector for the wave velocity (respectively Φ_i for the pressure). It turns out that Equation (27a) is a mixed hyperbolic-elliptic equation, whose nature changes as a function of ω_i only (i.e. the equation is either entirely hyperbolic in the fluid volume for a given value of ω_i, or is entirely elliptic in the volume). As such, it can be shown (using a plane-wave analysis) that local IGWs can only exist when $\min(2\Omega_s, N) \leq |\omega_i| \leq \max(2\Omega_s, N)$. In this interval, ω_i satisfies the dispersion relation given by

$$\omega_i^2 \boldsymbol{k}^2 = N^2 |\mathbf{1}_z \times \boldsymbol{k}|^2 + 4\Omega_s^2 (\mathbf{1}_z \cdot \boldsymbol{k})^2, \tag{28}$$

where $\boldsymbol{k}$ is the (local) wave vector of the plane wave. As illustrated in Figure 24, the local analysis agrees very well with experimental results [296]. In the other interval $0 < |\omega_i| \leq \min(2\Omega_s, N)$, the equation is elliptic such that there are no wave motions (i.e. plane waves are evanescent, as for high-frequency disturbances without stratification [297]). However, if the entire fluid is forced in volume (not like in [296], where the oscillatory forcing was only local in space), then some low-frequency eigenmodes can exist in this frequency interval [167,298]. Such 3-D modes, which appear similar to the low-frequency Kelvin waves in oceanography, owe their existence to the presence of lateral (vertical) walls [299].

The existence of a frequency gap in experimental conditions has annoying consequences, as it hampers our ability to safely extrapolate experimental results to thick-layer systems. Indeed, a

frequency gap implies that an oscillatory forcing (e.g. a velocity flowing over a small-wavelength topography) will not be able to excite (locally) propagating waves for some frequencies in experimental conditions (but it may excite evanescent disturbances, as found without stratification [297]). However, such a frequency gap is not globally expected in a thick-layer fluid system in which gravity is radial [300, 301]. In such systems, for a given value of ω_i, the fluid volume is indeed separated into regions in which waves can propagate, and other regions in which wave motions are locally evanescent. Therefore, at different latitudes, the same oscillatory forcing could excite or not waves in thick-layer fluid systems (contrary to the experimental setup). The mathematical properties of IGWs are thus drastically different in experimental models and in geophysical systems, such that experimental results should be extrapolated with care to thick fluid envelopes.

6. Concluding remarks

6.1. *A common need for new experiments*

This paper enlightens the critical role of experimental studies in advancing our understanding of topographic effects in geophysical fluid dynamics. One key aspect discussed is the need to bridge the gap between numerically accessible regimes, and the often inaccessible flow regimes encountered in geophysical fluid envelopes. Given the inherent challenge of simulating flows over topography with DNS, we have here emphasised the importance of experiments in complementing theoretical and numerical works. These problems have been extensively studied in the context of thin-layer systems (e.g. stratified oceans and atmospheres) using experiments, DNS or theory. However, those results are not directly relevant for thick-layer systems, such as planetary cores and subsurface oceans. Those have received comparatively less attention from theoretical and experimental viewpoints, partly because of the scarcity of direct observations. Meanwhile, indirect observations (e.g. the accurate measurements of the Earth's and Moon rotation, or the measurements of the upcoming space missions to Jovian satellites) require a better understanding of the role of topography for mixing, angular momentum transfer, or magnetic field generation. Density stratification is also not well-constrained in such hidden layers, such that all possible situations should be considered (including neutral regimes, weak or strong stable stratifications, or convection).

Since the most advanced DNS are limited in the accessible range of parameters, but also in the geometries they can simulate, experiments have thus played a crucial role in making progress in this field. For instance, they often allow us to validate asymptotic theoretical models or derive (empirical) scaling laws, which can be extrapolated to the out-of-reach range of parameters of geophysical bodies. However, particular attention must be given to the regimes in which the experiments operate (i.e. are they already governed by the dynamics prevailing at planetary conditions?). An illustrative example is the debate about the expected rotating turbulence regime driven by mechanical (orbital) forcings. Indeed, experiments conducted at moderately small values of the Ekman and Rossby numbers likely operate in a different turbulent regime from that in geophysical conditions.

We have also identified some key points that would help to pave the way for future experiments. Firstly, it appears quite clear that we should consider larger experimental devices. This is required to reduce the value of the Ekman number to probe high-*Re* turbulence while keeping the Rossby number small enough, but also to allow measurements in BLs and in the vicinity of topographical features. Such measurements are indeed currently too challenging using submetre size experiments. If we target a typical value $E \sim 10^{-8}$, it would be achievable with a two-metre size experiment rotating at 60 RPM, and using water at ambient temperature as a working fluid. Few devices of this class exist, such as the Big Sister three-metre sodium experiment

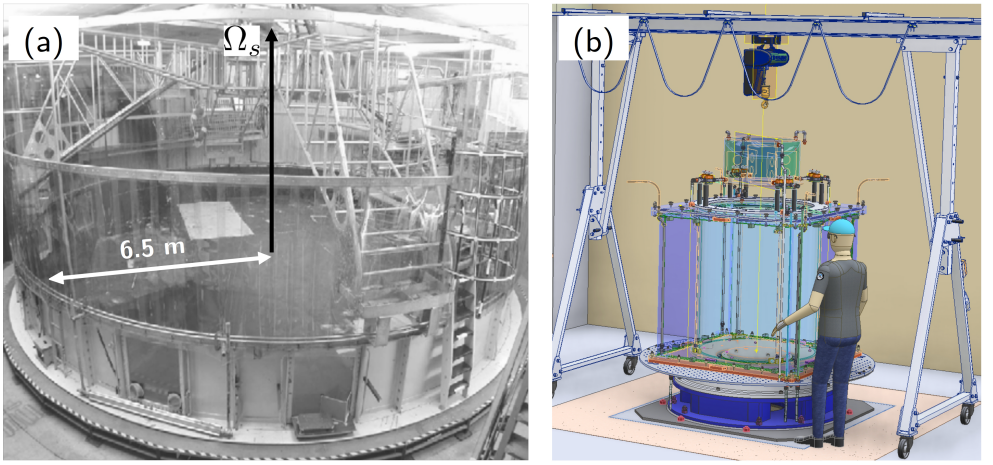


Figure 25. (a) CORIOLIS experimental facility in LEGI laboratory (Grenoble, France). This is the largest turntable worldwide, with a diametre of 13 m and a height of 1 m, rotating at 6 RPM at maximum. It has notably been used to investigate the dynamics of Ekman layers [50, 188, 212, 213]. (b) THEIA experimental facility, currently under construction in ISTERRE laboratory (Grenoble, France). It will be dedicated to the study of rotating flows with topography. The turntable will be capable of embarking tanks with a diameter of ~1 m and a height of ~2 m, rotating at a maximum rotation frequency of 10 RPM.

in Maryland [302, 303] or the forthcoming two-metre DRESDYN device [304]. While the targeted low-E values are accessible with such experiments, they are dedicated to specific forcing and focus on hydromagnetic flows. Hence, they do not offer enough flexibility to address the questions discussed here. It may be more desirable to think of the next-generation experiments as an experimental platform that would allow investigating a broader range of problems, similar to the unique CORIOLIS facility hosted in the LEGI laboratory (Figure 25a). This is an open tank with a diameter of 13 m, rotating at 6 RPM and embarking a fluid layer with a maximum height of one metre (resulting in an Ekman number $E \sim 10^{-6}$). This unique instrument is well suited to model thin-layer dynamics with stratification at the cost of a moderate Ekman number. Yet, it is not ideal to investigate the flow dynamics in closed containers representative of thick-layer systems.

Another benefit of large experiments would be to investigate the combined effects of stratification and rotation when $N \lesssim \Omega_s$, in contrast with the existing studies dedicated to oceanic dynamics that mainly explored the other regimes with $N \gg \Omega_s$. As shown in Figure 23, it would be possible to perform experiments in the weakly stratified regimes at low Ekman numbers, and possibly in the more strongly stratified regime $1 \leq N/\Omega_s \leq 10$. Finally, a larger device would also allow us to investigate the same range of Ekman numbers as we currently do with sub-metre size experiments, but using higher viscosity fluids (10–100 times) in order to increase the Ekman BL thickness by a factor 3 to 10. Detailed investigations of the effect of roughness in such a device would be achievable with topographic features, ranging from a few microns to several millimetres.

6.2. *Larger experiments, a realistic prospect?*

We have argued that substantial advancement in the field of rapidly rotating geophysical fluid dynamics is contingent upon the development of new large-scale facilities. A few laboratories have already acquired large-capacity turntables capable of embarking experiments of 1–2 m in

size, such as the ones used in [179, 305] or the upcoming THEIA experimental facility in Grenoble (Figure 25b). Even if they cannot reach low-E regimes with $E \ll 10^{-8}$, these facilities pave the way for the development of even more ambitious devices. However, there will be some unavoidable difficulties when working with large-scale devices at small Ekman numbers. As anticipated from stability analyses, such rapidly rotating flows will be prone to instability for much smaller-amplitude perturbations than in the current devices. It is therefore essential to pay close attention to the potential adverse effects, including small temperature fluctuations across the tank, the rotation of the Earth that will prevent from achieving perfect solid-body rotation [306, 307], or any deviation from the intended geometry exceeding some characteristic length scales (e.g. the BL thickness). Another challenge inherent to a unique apparatus is the repeatability and validation of the results. It has become standard practice in the computational fluid dynamics community to conduct periodic benchmark studies on canonical problems, which allow testing and validating the different algorithms (e.g. [308, 309] for the geodynamo). The development of a similar approach, based on well-understood simple problems (e.g. the resonances of eigenmodes, or linear spin-up/down), would be particularly important in the context of unique devices aimed at achieving unprecedented ranges of parameters.

In our opinion, developing such new large-scale facilties should only be undertaken within the context of an open-access collaborative project (e.g. as in astronomy with the large telescopes, or in particule physics with the CERN). As outlined below, it is essential that the collaborative structure in question fulfils some fundamental conditions.

(1) Motivations. It should be driven by common interests, identified by a broad scientific community (e.g. the needs for a better understanding of the rapidly rotating fluid dynamics and related phenomena, which are shared among all geophysical sciences).

(2) Accessibility. It should provide *easy access* to the facility for all users (e.g. similar to astronomical observatories or supercomputers).

(3) Scientific recognition. While open access to publications is becoming a standard practice in academia, technical solutions or inconclusive results are rarely acknowledged and never rewarded. To maintain a culture of risk-taking and ambitious project development, it is essential to recognise the significant time, energy and creativity required. This may not always result in a peer-reviewed publication, but it is nevertheless a crucial aspect of academic endeavour. A collaborative platform involving recognised experts should offer an alternative to the classical publication scheme to share this unconventional outcomes, for instance in the form of open access repositories (as done by the CERN).

(4) Scientific commitment. The success of such an enterprise is contingent upon the dedication of senior scientists who are past the stage of developing their careers. This would allow them to assume the risks inherent to these high-risk and high-gain projects. Moreover, it would be worth incorporating early-career and intermediate-career scientists into the management structure (to stimulate creativity and to ensure the continuity of the legacy).

(5) Long-term funding and legacy. It is not feasible to obtain financial support for a collaborative platform through the conventional grant schemes, which are constrained by temporal limitations. To achieve this, a host institution must demonstrate a long-term commitment, while national and international institutions must pledge sustainable financial support. Finally, given the likelihood of more rigorous financial constraints in the near future, a shared financial support would be the most optimal management strategy to secure such ambitious research activities.

For all these reasons, we believe that the experimental geophysical fluid dynamics community would greatly benefit from large collaborative projects rather than individual incentives. While

already done in other fields (e.g. in astronomy or particle physics), this seems however at odds with the current research organisation that tends to reward individuals rather than consortiums.

Declaration of interests

The authors do not work for, advise, own shares in, or receive funds from any organization that could benefit from this article, and have declared no affiliations other than their research organizations.

Funding

JV, RM and DC are supported by the European Research Council (ERC) under the European Union's Horizon 2020 research and innovation programme (grant agreement No 847433, THEIA project). JN and VG are supported by ETH grant #ETH-04 22-1. FB received funding from the European Research Council (ERC) under the European Union's Horizon 2020 research and innovation program (grant agreement No 833848, UEMHP project). DC acknowledges the French Academy of Sciences, Electricité de France, Labex OSUG@2020 (ANR10 LABX56).

Acknowledgements

The authors thank S. Fauve and M. Le Bars for the opportunity to write this review article. DC thanks the French Academy of Science and Electricité de France for granting their 'Ampére Prize' to the ISTerre 'Geodynamo' team. JV acknowledges Y. Colin de Verdière for fruitful discussions about waves in rotating and stratified fluids. DC and RM thank D. Jault for discussions on topographic effects in planetary cores. DC thanks M. Solazzo for his valuable help and his engineering work on rotating experiments with topographic effects. The authors would like to dedicate the paper to Stijn Vantieghem, who made major contributions in our field but passed away in 2023 at the age of 39.

References

[1] M. Landeau, A. Fournier, H.-C. Nataf, D. Cébron, N. Schaeffer, "Sustaining Earth's magnetic dynamo", *Nat. Rev. Earth Environ.* **3** (2022), no. 4, p. 255-269.
[2] M. A. Wieczorek, B. P. Weiss, D. Breuer *et al.*, "Lunar magnetism", *Rev. Mineral. Geochem.* **89** (2023), no. 1, p. 207-241.
[3] W. Hopkins, "On the phenomena of precession and nutation, assuming the fluidity of the interior of the Earth", *Philos. Trans. R. Soc. Lond. A* **129** (1839), p. 381-423.
[4] H. Jeffreys, R. O. Vicente, "The theory of nutation and the variation of latitude", *Mon. Not. R. Astron. Soc.* **117** (1957), no. 2, p. 142-161.
[5] J.-L. Margot, S. J. Peale, R. F. Jurgens, M. A. Slade, I. V. Holin, "Large longitude libration of Mercury reveals a molten core", *Science* **316** (2007), no. 5825, p. 710-714.
[6] C. F. Yoder, "The free librations of a dissipative Moon", *Philos. Trans. R. Soc. A* **303** (1981), no. 1477, p. 327-338.
[7] K. M. Soderlund, M. Rovira-Navarro, M. Le Bars, B. E. Schmidt, T. Gerkema, "The physical oceanography of ice-covered moons", *Annu. Rev. Mar. Sci.* **16** (2024), p. 25-53.
[8] M. Farhat, P. Auclair-Desrotour, G. Boué, J. Laskar, "The resonant tidal evolution of the Earth-Moon distance", *Astron. Astrophys.* **665** (2022), article no. L1.
[9] H.-C. Nataf, N. Schaeffer, "Dynamic regimes in planetary cores: τ–ℓ diagrams", *C. R. Géosci.* **356** (2024), no. G1, p. 1-30.
[10] O. Zeman, "A note on the spectra and decay of rotating homogeneous turbulence", *Phys. Fluids* **6** (1994), no. 10, p. 3221-3223.
[11] P. D. Mininni, D. Rosenberg, A. Pouquet, "Isotropization at small scales of rotating helically driven turbulence", *J. Fluid Mech.* **699** (2012), p. 263-279.

[12] A. Delache, C. Cambon, F. Godeferd, "Scale by scale anisotropy in freely decaying rotating turbulence", *Phys. Fluids* **26** (2014), no. 2, article no. 025104.
[13] C. A. Jones, "8.05 - Thermal and compositional convection in the outer core", in *Treatise on Geophysics* (G. Schubert, ed.), Elsevier, Oxford, 2nd ed., 2015, p. 115-159.
[14] E. Chaljub, B. Valette, "Spectral element modelling of three-dimensional wave propagation in a self-gravitating Earth with an arbitrarily stratified outer core", *Geophys. J. Int.* **158** (2004), no. 1, p. 131-141.
[15] W. J. Emery, W. G. Lee, L. Magaard, "Geographic and seasonal distributions of Brunt-Väisälä frequency and Rossby radii in the North Pacific and North Atlantic", *J. Phys. Oceanogr.* **14** (1984), no. 2, p. 294-317.
[16] B. Buffett, "Geomagnetic fluctuations reveal stable stratification at the top of the Earth's core", *Nature* **507** (2014), no. 7493, p. 484-487.
[17] T. Gastine, J. Aubert, A. Fournier, "Dynamo-based limit to the extent of a stable layer atop Earth's core", *Geophys. J. Int.* **222** (2020), no. 2, p. 1433-1448.
[18] B. A. Buffett, "Chemical stratification at the top of Earth's core: constraints from observations of nutations", *Earth Planet. Sci. Lett.* **296** (2010), no. 3-4, p. 367-372.
[19] P. R. Gent, J. R. Luyten, "How much energy propagates vertically in the equatorial oceans?", *J. Phys. Oceanogr.* **15** (1985), no. 7, p. 997-1007.
[20] L. D. Talley, G. L. Pickard, W. J. Emery, J. H. Swift, *Descriptive Physical Oceanography: An Introduction*, 6th ed., Academic Press, London, 2011.
[21] M. Rexer, C. Hirt, "Ultra-high-degree surface spherical harmonic analysis using the Gauss-Legendre and the Driscoll/Healy quadrature theorem and application to planetary topography models of Earth, Mars and Moon", *Surv. Geophys.* **36** (2015), no. 6, p. 803-830.
[22] P. Koelemeijer, "Toward consistent seismological models of the core–mantle boundary landscape", in *Mantle Convection and Surface Expressions*, American Geophysical Union, Hoboken, 2021, ISBN 9781119528609, Chapter 9, p. 229-255.
[23] A. I. Ermakov, R. S. Park, B. G. Bills, "Power laws of topography and gravity spectra of the solar system bodies", *J. Geophys. Res. Planets* **123** (2018), no. 8, p. 2038-2064.
[24] M. Puica, V. Dehant, M. Folgueira, T. Van Hoolst, J. Rekier, "Analytical computation of total topographic torque at the core–mantle boundary and its impact on tidally driven length-of-day variations", *Geophys. J. Int.* **234** (2023), no. 1, p. 585-596.
[25] G. Veronis, "The analogy between rotating and stratified fluids", *Annu. Rev. Fluid Mech.* **2** (1970), no. 1, p. 37-66.
[26] H. P. Greenspan, *The Theory of Rotating Fluids*, Cambridge University Press, Cambridge, 1968.
[27] D. E. Mowbray, B. S. H. Rarity, "A theoretical and experimental investigation of the phase configuration of internal waves of small amplitude in a density stratified liquid", *J. Fluid Mech.* **28** (1967), no. 1, p. 1-16.
[28] S. Legg, "Mixing by oceanic Lee waves", *Annu. Rev. Fluid Mech.* **53** (2021), p. 173-201.
[29] M. G. Wurtele, R. D. Sharman, A. Datta, "Atmospheric Lee waves", *Annu. Rev. Fluid Mech.* **28** (1996), no. 1, p. 429-476.
[30] O. Richet, J.-M. Chomaz, C. Muller, "Internal tide dissipation at topography: triadic resonant instability equatorward and evanescent waves poleward of the critical latitude", *J. Geophys. Res. Oceans* **123** (2018), no. 9, p. 6136-6155.
[31] F. S. Godeferd, F. Moisy, "Structure and dynamics of rotating turbulence: a review of recent experimental and numerical results", *Appl. Mech. Rev.* **67** (2015), no. 3, article no. 030802.
[32] P.-P. Cortet, N. Lanchon, "Turbulence of internal gravity waves in the laboratory", *C. R. Phys.* **25** (2024), no. S3, p. 537-556.
[33] A. Lefauve, "Geophysical stratified turbulence and mixing in the laboratory", *C. R. Phys.* **25** (2024), no. S3, p. 479-507.
[34] S. Chandrasekhar, *Ellipsoidal Figures of Equilibrium*, Dover Publications, New York, 1987.
[35] C. J. Davies, D. R. Stegman, M. Dumberry, "The strength of gravitational core-mantle coupling", *Geophys. Res. Lett.* **41** (2014), no. 11, p. 3786-3792.
[36] V. Dehant, S. A. Campuzano, A. De Santis, W. van Westrenen, "Structure, materials and processes in the Earth's core and mantle", *Surv. Geophys.* **43** (2022), no. 1, p. 263-302.
[37] C. Narteau, J.-L. Le Mouël, J.-P. Poirier, E. Sepúlveda, M. Shnirman, "On a small-scale roughness of the core–mantle boundary", *Earth Planet. Sci. Lett.* **191** (2001), no. 1-2, p. 49-60.
[38] J.-L. Le Mouël, C. Narteau, M. Greff-Lefftz, M. Holschneider, "Dissipation at the core-mantle boundary on a small-scale topography", *J. Geophys. Res. Solid Earth* **111** (2006), no. B4, p. 1-10.
[39] H. A. Zebker, B. Stiles, S. Hensley, R. Lorenz, R. L. Kirk, J. Lunine, "Size and shape of Saturn's moon Titan", *Science* **324** (2009), no. 5929, p. 921-923.
[40] L. Iess, N. J. Rappaport, R. A. Jacobson, P. Racioppa, D. J. Stevenson, P. Tortora, J. W. Armstrong, S. W. Asmar, "Gravity field, shape, and moment of inertia of Titan", *Science* **327** (2010), no. 5971, p. 1367-1369.

[41] F. Nimmo, B. G. Bills, "Shell thickness variations and the long-wavelength topography of Titan", *Icarus* **208** (2010), no. 2, p. 896-904.
[42] C. Amante, B. W. Eakins, "ETOPO1, Global 1 arc-minute global relief model: procedures, data sources and analysis", 2009, NOAA Tech. Memo. NESDIS NGDC-24, 19.
[43] M. Le Bars, D. Cébron, P. Le Gal, "Flows driven by libration, precession, and tides", *Annu. Rev. Fluid Mech.* **47** (2015), p. 163-193.
[44] C. Guervilly, P. Cardin, N. Schaeffer, "Turbulent convective length scale in planetary cores", *Nature* **570** (2019), no. 7761, p. 368-371.
[45] O. Barrois, T. Gastine, C. C. Finlay, "Comparison of quasi-geostrophic, hybrid and 3-D models of planetary core convection", *Geophys. J. Int.* **231** (2022), no. 1, p. 129-158.
[46] N. Schaeffer, D. Jault, H.-C. Nataf, A. Fournier, "Turbulent geodynamo simulations: a leap towards Earth's core", *Geophys. J. Int.* **211** (2017), no. 1, p. 1-29.
[47] B. Favier, A. M. Grannan, M. Le Bars, J. M. Aurnou, "Generation and maintenance of bulk turbulence by libration-driven elliptical instability", *Phys. Fluids* **27** (2015), no. 6, article no. 066601.
[48] A. M. Grannan, B. Favier, M. Le Bars, J. M. Aurnou, "Tidally forced turbulence in planetary interiors", *Geophys. J. Int.* **208** (2017), no. 3, p. 1690-1703.
[49] K. S. Thorne, R. D. Blandford, *Modern Classical Physics: Optics, Fluids, Plasmas, Elasticity, Relativity, and Statistical Physics*, Princeton University Press, Princeton, 2017.
[50] D. Sous, J. Sommeria, D. Boyer, "Friction law and turbulent properties in a laboratory Ekman boundary layer", *Phys. Fluids* **25** (2013), no. 4, article no. 046602.
[51] T. Le Reun, B. Favier, M. Le Bars, "Experimental study of the nonlinear saturation of the elliptical instability: inertial wave turbulence versus geostrophic turbulence", *J. Fluid Mech.* **879** (2019), p. 296-326.
[52] J. Noir, D. Brito, K. Aldridge, P. Cardin, "Experimental evidence of inertial waves in a precessing spheroidal cavity", *Geophys. Res. Lett.* **28** (2001), no. 19, p. 3785-3788.
[53] F. Burmann, J. Noir, S. Beetschen, A. Jackson, "Low-cost solutions for velocimetry in rotating and opaque fluid experiments using ultrasonic time of flight", *Exp. Tech.* **46** (2022), no. 3, p. 429-439.
[54] V. Lherm, R. Deguen, T. Alboussière, M. Landeau, "Rayleigh–Taylor instability in impact cratering experiments", *J. Fluid Mech.* **937** (2022), article no. A20.
[55] B. R. Sutherland, S. B. Dalziel, G. O. Hughes, P. F. Linden, "Visualization and measurement of internal waves by synthetic schlieren. Part 1. Vertically oscillating cylinder", *J. Fluid Mech.* **390** (1999), p. 93-126.
[56] S. Dalziel, G. O. Hughes, B. R. Sutherland, "Whole-field density measurements by synthetic schlieren", *Exp. Fluids* **28** (2000), no. 4, p. 322-335.
[57] W. V. R. Malkus, "Precession of the Earth as the cause of geomagnetism: experiments lend support to the proposal that precessional torques drive the Earth's dynamo", *Science* **160** (1968), no. 3825, p. 259-264.
[58] L. Lacaze, W. Herreman, M. Le Bars, S. Le Dizes, P. Le Gal, "Magnetic field induced by elliptical instability in a rotating spheroid", *Geophys. Astrophys. Fluid Dyn.* **100** (2006), no. 4-5, p. 299-317.
[59] W. Herreman, M. Le Bars, P. Le Gal, "On the effects of an imposed magnetic field on the elliptical instability in rotating spheroids", *Phys. Fluids* **21** (2009), no. 4, article no. 046602.
[60] M. Le Bars, A. Barik, F. Burmann, D. P. Lathrop, J. Noir, N. Schaeffer, S. A. Triana, "Fluid dynamics experiments for planetary interiors", *Surv. Geophys.* **43** (2022), no. 1, p. 229-261.
[61] F. Burmann, J. Noir, "Experimental study of the flows in a non-axisymmetric ellipsoid under precession", *J. Fluid Mech.* **932** (2022), article no. A24.
[62] K. D. Aldridge, A. Toomre, "Axisymmetric inertial oscillations of a fluid in a rotating spherical container", *J. Fluid Mech.* **37** (1969), no. 2, p. 307-323.
[63] K. Zhang, K. H. Chan, X. Liao, J. M. Aurnou, "The non-resonant response of fluid in a rapidly rotating sphere undergoing longitudinal libration", *J. Fluid Mech.* **720** (2013), p. 212-235.
[64] D. Cébron, J. Vidal, N. Schaeffer, A. Borderies, A. Sauret, "Mean zonal flows induced by weak mechanical forcings in rotating spheroids", *J. Fluid Mech.* **916** (2021), article no. A39.
[65] Y. Lin, R. Hollerbach, J. Noir, S. Vantieghem, "Resonant and non-resonant flows in longitudinally and latitudinally librating spheres", *Phys. Fluids* **35** (2023), no. 7, article no. 076612.
[66] A. Sauret, D. Cébron, M. Le Bars, "Spontaneous generation of inertial waves from boundary turbulence in a librating sphere", *J. Fluid Mech.* **728** (2013), article no. R5.
[67] C. Morize, M. Le Bars, P. Le Gal, A. Tilgner, "Experimental determination of zonal winds driven by tides", *Phys. Rev. Lett.* **104** (2010), no. 21, article no. 214501.
[68] K. Zhang, X. Liao, *Theory and Modeling of Rotating Fluids: Convection, Inertial Waves and Precession*, Cambridge University Press, Cambridge, 2017.
[69] Y. Lin, "Triadic resonances driven by thermal convection in a rotating sphere", *J. Fluid Mech.* **909** (2021), article no. R3.

[70] A. Sauret, D. Cébron, C. Morize, M. Le Bars, "Experimental and numerical study of mean zonal flows generated by librations of a rotating spherical cavity", *J. Fluid Mech.* **662** (2010), p. 260-268.
[71] Y. Colin de Verdière, J. Vidal, "The spectrum of the Poincaré operator in an ellipsoid", *J. Spectr. Theory* (2024), p. 1-22 (to appear) arXiv:2305.01369.
[72] S. Vantieghem, "Inertial modes in a rotating triaxial ellipsoid", *Proc. R. Soc. A* **470** (2014), no. 2168, article no. 20140093.
[73] G. Backus, M. Rieutord, "Completeness of inertial modes of an incompressible inviscid fluid in a corotating ellipsoid", *Phys. Rev. E* **95** (2017), no. 5, article no. 053116.
[74] S. Vantieghem, D. Cébron, J. Noir, "Latitudinal libration driven flows in triaxial ellipsoids", *J. Fluid Mech.* **771** (2015), p. 193-228.
[75] Y. Charles, *Flows driven by librations in latitude in triaxial ellipsoids*, Phd thesis, ETH Zurich, 2018.
[76] F. H. Busse, "Steady fluid flow in a precessing spheroidal shell", *J. Fluid Mech.* **33** (1968), no. 4, p. 739-751.
[77] C. Nobili, P. Meunier, B. Favier, M. Le Bars, "Hysteresis and instabilities in a spheroid in precession near the resonance with the tilt-over mode", *J. Fluid Mech.* **909** (2021), article no. A17.
[78] J. Noir, *Ecoulements d'un fluide dans une cavité en précession: approches numérique et expérimentale,* Phd thesis, Université Joseph-Fourier Grenoble I, 2000.
[79] S. Goto, A. Matsunaga, M. Fujiwara, M. Nishioka, S. Kida, M. Yamato, S. Tsuda, "Turbulence driven by precession in spherical and slightly elongated spheroidal cavities", *Phys. Fluids* **26** (2014), no. 5, article no. 055107.
[80] A. M. Grannan, M. Le Bars, D. Cébron, J. M. Aurnou, "Experimental study of global-scale turbulence in a librating ellipsoid", *Phys. Fluids* **26** (2014), no. 12, article no. 126601.
[81] S. Kida, "Steady flow in a rapidly rotating spheroid with weak precession: I", *Fluid Dyn. Res.* **52** (2020), no. 1, article no. 015513.
[82] P. H. Roberts, C.-C. Wu, "On flows having constant vorticity", *Phys. D* **240** (2011), no. 20, p. 1615-1628.
[83] J. Noir, D. Cébron, "Precession-driven flows in non-axisymmetric ellipsoids", *J. Fluid Mech.* **737** (2013), p. 412-439.
[84] D. Ivers, "Enumeration, orthogonality and completeness of the incompressible Coriolis modes in a tri-axial ellipsoid", *Geophys. Astrophys. Fluid Dyn.* **111** (2017), no. 5, p. 333-354.
[85] J. Vidal, D. Cébron, "Precession-driven flows in stress-free ellipsoids", *J. Fluid Mech.* **954** (2023), article no. A5.
[86] J. Rekier, B. F. Chao, J. Chen, V. Dehant, S. Rosat, P. Zhu, "Earth"s rotation: observations and relation to deep interior", *Surv. Geophys.* **43** (2022), no. 1, p. 149-175.
[87] D. Cébron, "Bistable flows in precessing spheroids", *Fluid Dyn. Res.* **47** (2015), no. 2, article no. 025504.
[88] S. Kida, "Steady flow in a rapidly rotating sphere with weak precession", *J. Fluid Mech.* **680** (2011), p. 150-193.
[89] S. T. Suess, "Viscous flow in a deformable rotating container", *J. Fluid Mech.* **45** (1971), no. 1, p. 189-201.
[90] J. Noir, D. Cébron, M. Le Bars, A. Sauret, J. M. Aurnou, "Experimental study of libration-driven zonal flows in non-axisymmetric containers", *Phys. Earth Planet. Int.* **204** (2012), p. 1-10.
[91] A. Tilgner, "Zonal wind driven by inertial modes", *Phys. Rev. lett.* **99** (2007), no. 19, article no. 194501.
[92] S. Le Dizès, "Reflection of oscillating internal shear layers: nonlinear corrections", *J. Fluid Mech.* **899** (2020), article no. A21.
[93] Y. Lin, J. Noir, "Libration-driven inertial waves and mean zonal flows in spherical shells", *Geophys. Astrophys. Fluid Dyn.* **115** (2021), no. 3, p. 258-279.
[94] R. R. Kerswell, "Elliptical instability", *Annu. Rev. Fluid Mech.* **34** (2002), no. 1, p. 83-113.
[95] M. Le Bars, L. Lacaze, S. Le Dizes, P. Le Gal, M. Rieutord, "Tidal instability in stellar and planetary binary systems", *Phys. Earth Planet. Int.* **178** (2010), no. 1-2, p. 48-55.
[96] L. Lacaze, P. Le Gal, S. Le Dizes, "Elliptical instability in a rotating spheroid", *J. Fluid Mech.* **505** (2004), p. 1-22.
[97] R. R. Kerswell, "The instability of precessing flow", *Geophys. Astrophys. Fluid Dyn.* **72** (1993), no. 1-4, p. 107-144.
[98] F. Burmann, L. Kira, J. Noir, "Precessing non-axisymmetric ellipsoids: bi-stability and fluid instabilities", *J. Fluid Mech.* **997** (2024), article no. A52.
[99] Y. Lin, P. Marti, J. Noir, "Shear-driven parametric instability in a precessing sphere", *Phys. Fluids* **27** (2015), no. 4, article no. 046601.
[100] D. Cébron, R. Laguerre, J. Noir, N. Schaeffer, "Precessing spherical shells: flows, dissipation, dynamo and the lunar core", *Geophys. J. Int.* **219** (2019), no. Supplement 1, p. S34-S57.
[101] J. Vanyo, P. Wilde, P. Cardin, P. Olson, "Experiments on precessing flows in the Earth's liquid core", *Geophys. J. Int.* **121** (1995), no. 1, p. 136-142.
[102] Y. Horimoto, A. Katayama, S. Goto, "Conical shear-driven parametric instability of steady flow in precessing spheroids", *Phys. Rev. Fluids* **5** (2020), no. 6, article no. 063901.
[103] A. Sauret, M. Le Bars, P. Le Gal, "Tide-driven shear instability in planetary liquid cores", *Geophys. Res. Lett.* **41** (2014), no. 17, p. 6078-6083.
[104] S. Lorenzani, A. Tilgner, "Fluid instabilities in precessing spheroidal cavities", *J. Fluid Mech.* **447** (2001), p. 111-128.
[105] J. Noir, F. Hemmerlin, J. Wicht, S. M. Baca, J. M. Aurnou, "An experimental and numerical study of librationally driven flow in planetary cores and subsurface oceans", *Phys. Earth Planet. Int.* **173** (2009), no. 1-2, p. 141-152.

[106] R. R. Kerswell, "Secondary instabilities in rapidly rotating fluids: inertial wave breakdown", *J. Fluid Mech.* **382** (1999), p. 283-306.
[107] T. Le Reun, B. Favier, A. J. Barker, M. Le Bars, "Inertial wave turbulence driven by elliptical instability", *Phys. Rev. Lett.* **119** (2017), no. 3, article no. 034502.
[108] Y. Horimoto, S. Goto, "Sustaining mechanism of small-scale turbulent eddies in a precessing sphere", *Phys. Rev. Fluids* **2** (2017), no. 11, article no. 114603.
[109] Y. Horimoto, G. Simonet-Davin, A. Katayama, S. Goto, "Impact of a small ellipticity on the sustainability condition of developed turbulence in a precessing spheroid", *Phys. Rev. Fluids* **3** (2018), no. 4, article no. 044603.
[110] P. Meunier, "Geoinspired soft mixers", *J. Fluid Mech.* **903** (2020), article no. A15.
[111] S. Goto, Y. Horimoto, T. Kaneko *et al.*, "Precessing cylinder as high-shear-rate mixer: application to emulsification", *Phys. Fluids* **35** (2023), no. 3, article no. 035139.
[112] E. Yarom, E. Sharon, "Experimental observation of steady inertial wave turbulence in deep rotating flows", *Nat. Phys.* **10** (2014), no. 7, p. 510-514.
[113] A. Campagne, B. Gallet, F. Moisy, P.-P. Cortet, "Disentangling inertial waves from eddy turbulence in a forced rotating-turbulence experiment", *Phys. Rev. E* **91** (2015), no. 4, article no. 043016.
[114] E. Yarom, A. Salhov, E. Sharon, "Experimental quantification of nonlinear time scales in inertial wave rotating turbulence", *Phys. Rev. Fluids* **2** (2017), no. 12, article no. 122601.
[115] A. Salhov, E. Yarom, E. Sharon, "Measurements of inertial wave packets propagating within steady rotating turbulence", *Europhys. Lett.* **125** (2019), no. 2, article no. 24003.
[116] E. Monsalve, M. Brunet, B. Gallet, P.-P. Cortet, "Quantitative experimental observation of weak inertial-wave turbulence", *Phys. Rev. Lett.* **125** (2020), no. 25, article no. 254502.
[117] M. Duran-Matute, J.-B. Flór, F. S. Godeferd, C. Jause-Labert, "Turbulence and columnar vortex formation through inertial-wave focusing", *Phys. Rev. E* **87** (2013), no. 4, article no. 041001.
[118] A. Campagne, B. Gallet, F. Moisy, P.-P. Cortet, "Direct and inverse energy cascades in a forced rotating turbulence experiment", *Phys. Fluids* **26** (2014), no. 12, article no. 125112.
[119] O. Shaltiel, A. Salhov, O. Gat, E. Sharon, "Direct measurement of energy transfer in strongly driven rotating turbulence", *Phys. Rev. Lett.* **132** (2024), no. 22, article no. 224001.
[120] Y. Zhou, "A phenomenological treatment of rotating turbulence", *Phys. Fluids* **7** (1995), no. 8, p. 2092-2094.
[121] S. V. Nazarenko, A. A. Schekochihin, "Critical balance in magnetohydrodynamic, rotating and stratified turbulence: towards a universal scaling conjecture", *J. Fluid Mech.* **677** (2011), p. 134-153.
[122] Y. B. Baqui, P. A. Davidson, "A phenomenological theory of rotating turbulence", *Phys. Fluids* **27** (2015), no. 2, article no. 025107.
[123] S. Galtier, "Weak inertial-wave turbulence theory", *Phys. Rev. E* **68** (2003), no. 1, article no. 015301.
[124] C. Cambon, R. Rubinstein, F. S. Godeferd, "Advances in wave turbulence: rapidly rotating flows", *New J. Phys.* **6** (2004), no. 1, article no. 73.
[125] F. Bellet, F. S. Godeferd, J. F. Scott, C. Cambon, "Wave turbulence in rapidly rotating flows", *J. Fluid Mech.* **562** (2006), p. 83-121.
[126] L. M. Smith, F. Waleffe, "Transfer of energy to two-dimensional large scales in forced, rotating three-dimensional turbulence", *Phys. Fluids* **11** (1999), no. 6, p. 1608-1622.
[127] M. Thiele, W.-C. Müller, "Structure and decay of rotating homogeneous turbulence", *J. Fluid Mech.* **637** (2009), p. 425-442.
[128] S. Galtier, "A multiple time scale approach for anisotropic inertial wave turbulence", *J. Fluid Mech.* **974** (2023), article no. A24.
[129] S. Galtier, *Physics of Wave Turbulence*, Cambridge University Press, Cambridge, 2022.
[130] A. A. Gelash, V. S. L'vov, V. E. Zakharov, "Complete Hamiltonian formalism for inertial waves in rotating fluids", *J. Fluid Mech.* **831** (2017), p. 128-150.
[131] P. Clark Di Leoni, P. J. Cobelli, P. D. Mininni, "The spatio-temporal spectrum of turbulent flows", *Eur. Phys. J. E* **38** (2015), p. 1-10.
[132] T. Le Reun, B. Favier, M. Le Bars, "Evidence of the Zakharov–Kolmogorov spectrum in numerical simulations of inertial wave turbulence", *Europhys. Lett.* **132** (2020), no. 6, article no. 64002.
[133] N. Yokoyama, M. Takaoka, "Energy-flux vector in anisotropic turbulence: application to rotating turbulence", *J. Fluid Mech.* **908** (2021), article no. A17.
[134] C. N. Baroud, B. B. Plapp, Z.-S. She, H. L. Swinney, "Anomalous self-similarity in a turbulent rapidly rotating fluid", *Phys. Rev. Lett.* **88** (2002), no. 11, article no. 114501.
[135] G. P. Bewley, D. P. Lathrop, L. R. M. Maas, K. R. Sreenivasan, "Inertial waves in rotating grid turbulence", *Phys. Fluids* **19** (2007), no. 7, article no. 071701.
[136] C. Lamriben, P.-P. Cortet, F. Moisy, L. R. M. Maas, "Excitation of inertial modes in a closed grid turbulence experiment under rotation", *Phys. Fluids* **23** (2011), no. 1, article no. 015102.

[137] J. Boisson, C. Lamriben, L. R. M. Maas, P.-P. Cortet, F. Moisy, "Inertial waves and modes excited by the libration of a rotating cube", *Phys. Fluids* **24** (2012), no. 7, article no. 076602.
[138] L. Bourouiba, "Discreteness and resolution effects in rapidly rotating turbulence", *Phys. Rev. E* **78** (2008), no. 5, article no. 056309.
[139] J. F. Scott, "Wave turbulence in a rotating channel", *J. Fluid Mech.* **741** (2014), p. 316-349.
[140] H. P. Greenspan, "On the non-linear interaction of inertial modes", *J. Fluid Mech.* **36** (1969), no. 2, p. 257-264.
[141] P. A. Davidson, P. J. Staplehurst, S. B. Dalziel, "On the evolution of eddies in a rapidly rotating system", *J. Fluid Mech.* **557** (2006), p. 135-144.
[142] P. J. Staplehurst, P. A. Davidson, S. B. Dalziel, "Structure formation in homogeneous freely decaying rotating turbulence", *J. Fluid Mech.* **598** (2008), p. 81-105.
[143] B. Gallet, "Exact two-dimensionalization of rapidly rotating large-Reynolds-number flows", *J. Fluid Mech.* **783** (2015), p. 412-447.
[144] F. P. Bretherton, "Resonant interactions between waves. The case of discrete oscillations", *J. Fluid Mech.* **20** (1964), no. 3, p. 457-479.
[145] L. M. Smith, Y. Lee, "On near resonances and symmetry breaking in forced rotating flows at moderate Rossby number", *J. Fluid Mech.* **535** (2005), p. 111-142.
[146] P. Clark di Leoni, P. D. Mininni, "Quantifying resonant and near-resonant interactions in rotating turbulence", *J. Fluid Mech.* **809** (2016), p. 821-842.
[147] T. Le Reun, B. Gallet, B. Favier, M. Le Bars, "Near-resonant instability of geostrophic modes: beyond Greenspan's theorem", *J. Fluid Mech.* **900** (2020), article no. R2.
[148] M. Brunet, B. Gallet, P.-P. Cortet, "Shortcut to geostrophy in wave-driven rotating turbulence: the quartetic instability", *Phys. Rev. Lett.* **124** (2020), no. 12, article no. 124501.
[149] P. D. Mininni, A. Alexakis, A. Pouquet, "Scale interactions and scaling laws in rotating flows at moderate Rossby numbers and large Reynolds numbers", *Phys. Fluids* **21** (2009), no. 1, article no. 015108.
[150] L. Bourouiba, D. N. Straub, M. L. Waite, "Non-local energy transfers in rotating turbulence at intermediate Rossby number", *J. Fluid Mech.* **690** (2012), p. 129-147.
[151] M. Buzzicotti, H. Aluie, L. Biferale, M. Linkmann, "Energy transfer in turbulence under rotation", *Phys. Rev. Fluids* **3** (2018), no. 3, article no. 034802.
[152] H. Lam, A. Delache, F. S. Godeferd, "Supply mechanisms of the geostrophic mode in rotating turbulence: interactions with self, waves and eddies", *J. Fluid Mech.* **971** (2023), article no. A10.
[153] A. van Kan, A. Alexakis, "Critical transition in fast-rotating turbulence within highly elongated domains", *J. Fluid Mech.* **899** (2020), article no. A33.
[154] D. Lemasquerier, A. M. Grannan, J. Vidal, D. Cébron, B. Favier, M. Le Bars, J. M. Aurnou, "Libration-driven flows in ellipsoidal shells", *J. Geophys. Res. Planets* **122** (2017), no. 9, p. 1926-1950.
[155] A. Wilson, R. R. Kerswell, "Can libration maintain Enceladus's ocean?", *Earth Planet. Sci. Lett.* **500** (2018), p. 41-46.
[156] K. S. Reddy, B. Favier, M. Le Bars, "Turbulent kinematic dynamos in ellipsoids driven by mechanical forcing", *Geophys. Res. Lett.* **45** (2018), no. 4, p. 1741-1750.
[157] J. Vidal, D. Cébron, N. Schaeffer, R. Hollerbach, "Magnetic fields driven by tidal mixing in radiative stars", *Mon. Not. R. Astron. Soc.* **475** (2018), no. 4, p. 4579-4594.
[158] P. A. Davidson, "Scaling laws for planetary dynamos", *Geophys. J. Int.* **195** (2013), no. 1, p. 67-74.
[159] A. J. Barker, Y. Lithwick, "Non-linear evolution of the tidal elliptical instability in gaseous planets and stars", *Mon. Not. R. Astron. Soc.* **435** (2013), no. 4, p. 3614-3626.
[160] J. Vidal, D. Cébron, A. ud Doula, E. Alecian, "Fossil field decay due to nonlinear tides in massive binaries", *Astron. Astrophys.* **629** (2019), article no. A142.
[161] A. J. Barker, "On turbulence driven by axial precession and tidal evolution of the spin–orbit angle of close-in giant planets", *Mon. Not. R. Astron. Soc.* **460** (2016), no. 3, p. 2339-2350.
[162] L. Lacaze, P. Le Gal, S. Le Dizes, "Elliptical instability of the flow in a rotating shell", *Phys. Earth Planet. Int.* **151** (2005), no. 3-4, p. 194-205.
[163] M. Rieutord, B. Georgeot, L. Valdettaro, "Wave attractors in rotating fluids: a paradigm for ill-posed Cauchy problems", *Phys. Rev. Lett.* **85** (2000), no. 20, p. 4277-4280.
[164] I. Bashmachnikov, F. Neves, T. Calheiros, X. Carton, "Properties and pathways of Mediterranean water eddies in the Atlantic", *Prog. Oceanogr.* **137** (2015), p. 149-172.
[165] P. S. Marcus, "Jupiter's Great Red Spot and other vortices", *Annu. Rev. Astron. Astrophys.* **31** (1993), no. 1, p. 523-569.
[166] J. Labarbe, O. N. Kirillov, "Diffusive instabilities of baroclinic lenticular vortices", *Phys. Fluids* **33** (2021), no. 10, article no. 104108.
[167] J. Vidal, Y. Colin de Verdière, "Inertia-gravity waves in geophysical vortices", *Proc. R. Soc. A* **480** (2024), no. 2285, article no. 20230789.
[168] M. Le Bars, "Numerical study of the McIntyre instability around Gaussian floating vortices in thermal wind balance", *Phys. Rev. Fluids* **6** (2021), no. 9, article no. 093801.

[169] O. Aubert, M. Le Bars, P. Le Gal, P. S. Marcus, "The universal aspect ratio of vortices in rotating stratified flows: experiments and observations", *J. Fluid Mech.* **706** (2012), p. 34-45.
[170] H. M. De la Rosa Zambrano, A. Cros, R. C. Gómez, M. Le Bars, P. Le Gal, "A laboratory study of floating lenticular anticyclones", *Eur. J. Mech. B Fluids* **61** (2017), p. 1-8.
[171] D. Lemasquerier, G. Facchini, B. Favier, M. Le Bars, "Remote determination of the shape of Jupiter's vortices from laboratory experiments", *Nat. Phys.* **16** (2020), no. 6, p. 695-700.
[172] S. Su, D. Cébron, H.-C. Nataf, P. Cardin, J. Vidal, M. Solazzo, Y. Do, "Acoustic spectra of a gas-filled rotating spheroid", *Eur. J. Mech. B Fluids* **84** (2020), p. 302-310.
[173] G. I. Taylor, "Experiments on the motion of solid bodies in rotating fluids", *Proc. R. Soc. Lond. A* **104** (1923), no. 725, p. 213-218.
[174] R. Hide, A. Ibbetson, "An experimental study of Taylor columns", *Icarus* **5** (1966), no. 1-6, p. 279-290.
[175] R. Hide, A. Ibbetson, M. J. Lighthill, "On slow transverse flow past obstacles in a rapidly rotating fluid", *J. Fluid Mech.* **32** (1968), no. 2, p. 251-272.
[176] D. L. Boyer, P. A. Davies, W. R. Holland, "Rotating flow past disks and cylindrical depressions", *J. Fluid Mech.* **141** (1984), p. 67-95.
[177] K. E. Heikes, T. Maxworthy, "Observations of inertial waves in a homogeneous rotating fluid", *J. Fluid Mech.* **125** (1982), p. 319-345.
[178] E. R. Johnson, "The effects of obstacle shape and viscosity in deep rotating flow over finite-height topography", *J. Fluid Mech.* **120** (1982), p. 359-383.
[179] N. Machicoane, V. Labarre, B. Voisin, F. Moisy, P.-P. Cortet, "Wake of inertial waves of a horizontal cylinder in horizontal translation", *Phys. Rev. Fluids* **3** (2018), no. 3, article no. 034801.
[180] E. R. Weeks, Y. Tian, J. S. Urbach, K. Ide, H. L. Swinney, M. Ghil, "Transitions between blocked and zonal flows in a rotating annulus with topography", *Science* **278** (1997), no. 5343, p. 1598-1601.
[181] F. Burmann, J. Noir, "Effects of bottom topography on the spin-up in a cylinder", *Phys. Fluids* **30** (2018), no. 10, article no. 106601.
[182] T. Radko, "A generalized theory of flow forcing by rough topography", *J. Fluid Mech.* **961** (2023), article no. A24.
[183] T. Radko, "The sandpaper theory of flow–topography interaction for homogeneous shallow-water systems", *J. Fluid Mech.* **977** (2023), article no. A9.
[184] V. Dehant, R. Laguerre, J. Rekier, A. Rivoldini, S. A. Triana, A. Trinh, T. Van Hoolst, P. Zhu, "Understanding the effects of the core on the nutation of the Earth", *Geod. Geodyn.* **8** (2017), no. 6, p. 389-395.
[185] G. N. Coleman, "Similarity statistics from a direct numerical simulation of the neutrally stratified planetary boundary layer", *J. Atmos. Sci.* **56** (1999), no. 6, p. 891-900.
[186] D. K. Lilly, "On the instability of Ekman boundary flow", *J. Atmos. Sci.*. **23** (1966), no. 5, p. 481-494.
[187] D. R. Caldwell, C. W. Van Atta, "Characteristics of Ekman boundary layer instabilities", *J. Fluid Mech.* **44** (1970), no. 1, p. 79-95.
[188] D. Aelbrecht, G. Chabert D'Hieres, D. Renouard, "Experimental study of the Ekman layer instability in steady or oscillating flows", *Cont. Shelf Res.* **19** (1999), no. 15-16, p. 1851-1867.
[189] G. D. Hess, J. R. Garratt, "Evaluating models of the neutral, barotropic planetary boundary layer using integral measures: Part I. Overview", *Bound.-Layer Meteorol.* **104** (2002), p. 333-358.
[190] G. D. Hess, J. R. Garratt, "Evaluating models of the neutral, barotropic planetary boundary layer using integral measures: Part II. Modelling observed conditions", *Bound.-Layer Meteorol.* **104** (2002), no. 3, p. 359-369.
[191] G. Csanady, "On the "resistance law" of a turbulent Ekman layer", *J. Atmos. Sci.* **24** (1967), no. 5, p. 467-471.
[192] A. K. Blackadar, H. Tennekes, "Asymptotic similarity in neutral barotropic planetary boundary layers", *J. Atmos. Sci.* **25** (1968), no. 6, p. 1015-1020.
[193] P. R. Spalart, "Theoretical and numerical study of a three-dimensional turbulent boundary layer", *J. Fluid Mech.* **205** (1989), p. 319-340.
[194] S. B. Pope, *Turbulent Flows*, Cambridge University Press, New York, 2000.
[195] C. Ansorge, J. P. Mellado, "Global intermittency and collapsing turbulence in the stratified planetary boundary layer", *Bound.-Layer Meteorol.* **153** (2014), no. 1, p. 89-116.
[196] C. B. Millikan, "A critical discussion of turbulent flows in channels and circular tubes", in *Proceedings of the Fifth International Congress for Applied Mechanics, Cambridge*, 1938, p. 386-392.
[197] P. R. Spalart, G. N. Coleman, R. Johnstone, "Retraction: "Direct numerical simulation of the Ekman layer: A step in Reynolds number, and cautious support for a log law with a shifted origin" [Phys. Fluids 20, 101507 (2008)]", *Phys. Fluids* **21** (2009), no. 10, article no. 109901.
[198] P. R. Spalart, G. N. Coleman, R. Johnstone, "Direct numerical simulation of the Ekman layer: a step in Reynolds number, and cautious support for a log law with a shifted origin", *Phys. Fluids* **20** (2008), no. 10, article no. 101507.
[199] W. K. George, "Is there a universal log law for turbulent wall-bounded flows?", *Philos. Trans. R. Soc. Lond. A* **365** (2007), no. 1852, p. 789-806.

[200] D. R. Caldwell, C. W. Van Atta, K. N. Helland, "A laboratory study of the turbulent Ekman layer", *Geophys. Astrophys. Fluid Dyn.* **3** (1972), no. 2, p. 125-160.
[201] K. Shingai, H. Kawamura, "A study of turbulence structure and large-scale motion in the Ekman layer through direct numerical simulations", *J. Turbul.* **5** (2004), no. 1, article no. 013.
[202] G. C. Howroyd, P. R. Slawson, "The characteristics of a laboratory produced turbulent Ekman layer", *Bound.-Layer Meteorol.* **8** (1975), p. 201-219.
[203] M. R. Raupach, R. A. Antonia, S. Rajagopalan, "Rough-wall turbulent boundary layers", *Appl. Mech. Rev.* **44** (1991), no. 1, p. 1-25.
[204] M. Kadivar, D. Tormey, G. McGranaghan, "A review on turbulent flow over rough surfaces: fundamentals and theories", *Int. J. Thermofluids* **10** (2021), article no. 100077.
[205] L. Braun, B. A. Younis, B. Weigand, "A turbulence closure study of the flow and thermal fields in the Ekman layer", *Bound.-Layer Meteorol.* **175** (2020), p. 25-55.
[206] S.-A. Shih, S. A. Triana, J. Rekier, V. Dehant, "Turbulent dissipation in the boundary layer of precession-driven flow in a sphere", *AIP Adv.* **13** (2023), no. 7, article no. 075025.
[207] E. Deusebio, G. Brethouwer, P. Schlatter, E. Lindborg, "A numerical study of the unstratified and stratified Ekman layer", *J. Fluid Mech.* **755** (2014), p. 672-704.
[208] G. N. Coleman, J. H. Ferziger, P. R. Spalart, "A numerical study of the turbulent Ekman layer", *J. Fluid Mech.* **213** (1990), p. 313-348.
[209] C. F. Yoder, "Venus' free obliquity", *Icarus* **117** (1995), no. 2, p. 250-286.
[210] J. G. Williams, D. H. Boggs, C. F. Yoder, J. T. Ratcliff, J. O. Dickey, "Lunar rotational dissipation in solid body and molten core", *J. Geophys. Res. Planets* **106** (2001), no. E11, p. 27933-27968.
[211] J. F. Kreider, *A laboratory study of the turbulent Ekman layer*, Phd thesis, University of Colorado, Boulder, 1973.
[212] E. Ferrero, A. Longhetto, L. Montabone *et al.*, "Physical simulations of neutral boundary layer in rotating tank", *Il Nuovo Cimento* **28** (2005), p. 1-17.
[213] D. Sous, J. Sommeria, "A Tsai's model based S-PIV method for velocity measurements in a turbulent Ekman layer", *Flow Meas. Instrum.* **26** (2012), p. 102-110.
[214] L. Prandtl, W. Tollmien, "Die Windverteilung über dem Erdboden, errechnet aus den Gesetzen der Rohrströmung", *Z. Geophys.* **1** (1924), p. 47-55.
[215] E. C. Kung, "On the momentum exchange between the atmosphere and earth over the northern hemisphere", *Mon. Weather Rev.* **96** (1968), no. 6, p. 337-341.
[216] I. G. Jonsson, "A new approach to oscillatory rough turbulent boundary layers", *Ocean Eng.* **7** (1980), no. 1, p. 109-152.
[217] J. Sleath, "Turbulent oscillatory flow over rough beds", *J. Fluid Mech.* **182** (1987), p. 369-409.
[218] M. Méndez, M. S. Shadloo, A. Hadjadj, A. Ducoin, "Boundary layer transition over a concave surface caused by centrifugal instabilities", *Comput. Fluids* **171** (2018), p. 135-153.
[219] B. A. Buffett, "Conditions for turbulent Ekman layers in precessionally driven flow", *Geophys. J. Int.* **226** (2021), no. 1, p. 56-65.
[220] B. Sikdar, M. Dumberry, "The differential precession of Earth's fluid and solid cores", *Phys. Earth Planet. Int.* **339** (2023), article no. 107022.
[221] J. R. Taylor, S. Sarkar, "Stratification effects in a bottom Ekman layer", *J. Phys. Oceanogr.* **38** (2008), no. 11, p. 2535-2555.
[222] P. G. Huang, P. Bradshaw, "Law of the wall for turbulent flows in pressure gradients", *AIAA J.* **33** (1995), no. 4, p. 624-632.
[223] P. Bradshaw, G. P. Huang, "The law of the wall in turbulent flow", *Proc. R. Soc. Lond. A* **451** (1995), no. 1941, p. 165-188.
[224] M. G. Rosevear, B. Gayen, B. K. Galton-Fenzi, "The role of double-diffusive convection in basal melting of Antarctic ice shelves", *Proc. Natl. Acad. Sci. USA* **118** (2021), no. 6, article no. e2007541118.
[225] L. Mahrt, "Stably stratified atmospheric boundary layers", *Annu. Rev. Fluid Mech.* **46** (2014), p. 23-45.
[226] A. S. Monin, "The atmospheric boundary layer", *Annu. Rev. Fluid Mech.* **2** (1970), no. 1, p. 225-250.
[227] A. M. Obukhov, "Turbulence in an atmosphere with a non-uniform temperature", *Bound.-Layer Meteorol.* **2** (1971), no. 1, p. 7-29.
[228] A. Perlin, J. N. Moum, J. M. Klymak, M. D. Levine, T. Boyd, P. M. Kosro, "A modified law-of-the-wall applied to oceanic bottom boundary layers", *J. Geophys. Res. Oceans* **110** (2005), no. C10, p. 1-9.
[229] J. R. Taylor, S. Sarkar, "Internal gravity waves generated by a turbulent bottom Ekman layer", *J. Fluid Mech.* **590** (2007), p. 331-354.
[230] P. F. Linden, "The deepening of a mixed layer in a stratified fluid", *J. Fluid Mech.* **71** (1975), no. 2, p. 385-405.
[231] E. Xuequan, E. J. Hopfinger, "On mixing across an interface in a stably stratified fluid", *J. Fluid Mech.* **166** (1986), p. 227-244.

[232] J. R. Munroe, B. R. Sutherland, "Internal wave energy radiated from a turbulent mixed layer", *Phys. Fluids* **26** (2014), no. 9, article no. 096604.
[233] S. Hanasoge, L. Gizon, K. R. Sreenivasan, "Seismic sounding of convection in the Sun", *Annu. Rev. Fluid Mech.* **48** (2016), p. 191-217.
[234] T. Gastine, J. M. Aurnou, "Latitudinal regionalization of rotating spherical shell convection", *J. Fluid Mech.* **954** (2023), article no. R1.
[235] X. Zhu, R. J. A. M. Stevens, O. Shishkina, R. Verzicco, D. Lohse, "$Nu \sim Ra^{1/2}$ scaling enabled by multiscale wall roughness in Rayleigh–Bénard turbulence", *J. Fluid Mech.* **869** (2019), article no. R4.
[236] E. A. Spiegel, G. Veronis, "On the Boussinesq approximation for a compressible fluid", *Astrophys. J.* **131** (1960), p. 442-447.
[237] D. D. Gray, A. Giorgini, "The validity of the Boussinesq approximation for liquids and gases", *Int. J. Heat Mass Transf.* **19** (1976), no. 5, p. 545-551.
[238] J. S. Cheng, M. Madonia, A. J. Aguirre Guzmán, R. P. J. Kunnen, "Laboratory exploration of heat transfer regimes in rapidly rotating turbulent convection", *Phys. Rev. Fluids* **5** (2020), no. 11, article no. 113501.
[239] P.-E. Roche, "The ultimate state of convection: a unifying picture of very high Rayleigh numbers experiments", *New J. Phys.* **22** (2020), no. 7, article no. 073056.
[240] V. Solomatov, "9.04 - Magma oceans and primordial mantle differentiation", in *Treatise on Geophysics* (G. Schubert, ed.), Elsevier, Oxford, 2nd ed., 2015, p. 81-104.
[241] Y. Zhang, N. Zhang, M. Tian, "Internal dynamics of magma ocean and its linkage to atmospheres", *Acta Geochim.* **41** (2022), no. 4, p. 568-591.
[242] J. Schumacher, K. R. Sreenivasan, "Colloquium: Unusual dynamics of convection in the Sun", *Rev. Mod. Phys.* **92** (2020), no. 4, article no. 041001.
[243] R. E. Ecke, O. Shishkina, "Turbulent rotating Rayleigh–Bénard convection", *Annu. Rev. Fluid Mech.* **55** (2023), p. 603-638.
[244] D. Lohse, O. Shishkina, "Ultimate Rayleigh–Bénard turbulence", *Rev. Mod. Phys.* **96** (2024), no. 3, article no. 035001.
[245] P. Cardin, P. Olson, "8.13 - Experiments on core dynamics", in *Treatise on Geophysics* (G. Schubert, ed.), Elsevier, Oxford, 2nd ed., 2015, p. 317-339.
[246] A. Pothérat, S. Horn, "Seven decades of exploring planetary interiors with rotating convection experiments", *C. R. Phys.* **25** (2024), no. S3, p. 21-75.
[247] W. V. R. Malkus, "The heat transport and spectrum of thermal turbulence", *Proc. R. Soc. Lond. A* **225** (1954), no. 1161, p. 196-212.
[248] E. A. Spiegel, "A generalization of the mixing-length theory of turbulent convection", *Astrophys. J.* **138** (1963), p. 216-225.
[249] R. H. Kraichnan, "Turbulent thermal convection at arbitrary Prandtl number", *Phys. Fluids* **5** (1962), no. 11, p. 1374-1389.
[250] J. Schumacher, V. Bandaru, A. Pandey, J. D. Scheel, "Transitional boundary layers in low-Prandtl-number convection", *Phys. Rev. Fluids* **1** (2016), no. 8, article no. 084402.
[251] G. Ahlers, E. Bodenschatz, D. Funfschilling, S. Grossmann, X. He, D. Lohse, R. J. A. M. Stevens, R. Verzicco, "Logarithmic temperature profiles in turbulent Rayleigh–Bénard convection", *Phys. Rev. Lett.* **109** (2012), no. 11, article no. 114501.
[252] G. Ahlers, E. Bodenschatz, X. He, "Logarithmic temperature profiles of turbulent Rayleigh–Bénard convection in the classical and ultimate state for a Prandtl number of 0.8", *J. Fluid Mech.* **758** (2014), p. 436-467.
[253] E. P. Van Der Poel, R. Ostilla-Mónico, R. Verzicco, S. Grossmann, D. Lohse, "Logarithmic mean temperature profiles and their connection to plume emissions in turbulent Rayleigh–Bénard convection", *Phys. Rev. Lett.* **115** (2015), no. 15, article no. 154501.
[254] X. Zhu, V. Mathai, R. J. A. M. Stevens, R. Verzicco, D. Lohse, "Transition to the ultimate regime in two-dimensional Rayleigh–Bénard convection", *Phys. Rev. Lett.* **120** (2018), no. 14, article no. 144502.
[255] J.-C. He, Y. Bao, X. Chen, "Turbulent boundary layers in thermal convection at moderately high Rayleigh numbers", *Phys. Fluids* **36** (2024), no. 2, article no. 025140.
[256] J. D. Scheel, J. Schumacher, "Predicting transition ranges to fully turbulent viscous boundary layers in low Prandtl number convection flows", *Phys. Rev. Fluids* **2** (2017), no. 12, article no. 123501.
[257] A. Blass, P. Tabak, R. Verzicco, R. J. A. M. Stevens, D. Lohse, "The effect of Prandtl number on turbulent sheared thermal convection", *J. Fluid Mech.* **910** (2021), article no. A37.
[258] O. Liot, J. Salort, R. Kaiser, R. Du Puits, F. Chillà, "Boundary layer structure in a rough Rayleigh–Bénard cell filled with air", *J. Fluid Mech.* **786** (2016), p. 275-293.
[259] O. Liot, Q. Ehlinger, É. Rusaouën, T. Coudarchet, J. Salort, F. Chillà, "Velocity fluctuations and boundary layer structure in a rough Rayleigh–Bénard cell filled with water", *Phys. Rev. Fluids* **2** (2017), no. 4, article no. 044605.
[260] S. Toppaladoddi, S. Succi, J. S. Wettlaufer, "Roughness as a route to the ultimate regime of thermal convection", *Phys. Rev. Lett.* **118** (2017), no. 7, article no. 074503.

[261] Y. Shen, P. Tong, K.-Q. Xia, "Turbulent convection over rough surfaces", *Phys. Rev. Lett.* **76** (1996), no. 6, p. 908.
[262] Y.-B. Du, P. Tong, "Enhanced heat transport in turbulent convection over a rough surface", *Phys. Rev. Lett.* **81** (1998), no. 5, p. 987-990.
[263] S. Ciliberto, C. Laroche, "Random roughness of boundary increases the turbulent convection scaling exponent", *Phys. Rev. Lett.* **82** (1999), no. 20, p. 3998-4001.
[264] Y.-B. Du, P. Tong, "Turbulent thermal convection in a cell with ordered rough boundaries", *J. Fluid Mech.* **407** (2000), p. 57-84.
[265] J.-C. Tisserand, M. Creyssels, Y. Gasteuil, H. Pabiou, M. Gibert, B. Castaing, F. Chillà, "Comparison between rough and smooth plates within the same Rayleigh–Bénard cell", *Phys. Fluids* **23** (2011), no. 1, article no. 015105.
[266] J. Salort, O. Liot, E. Rusaouen, F. Seychelles, J.-C. Tisserand, M. Creyssels, B. Castaing, F. Chillà, "Thermal boundary layer near roughnesses in turbulent Rayleigh–Bénard convection: flow structure and multistability", *Phys. Fluids* **26** (2014), no. 1, article no. 015112.
[267] P. Wei, T.-S. Chan, R. Ni, X.-Z. Zhao, K.-Q. Xia, "Heat transport properties of plates with smooth and rough surfaces in turbulent thermal convection", *J. Fluid Mech.* **740** (2014), p. 28-46.
[268] Y.-C. Xie, K.-Q. Xia, "Turbulent thermal convection over rough plates with varying roughness geometries", *J. Fluid Mech.* **825** (2017), p. 573-599.
[269] E. Rusaouën, O. Liot, B. Castaing, J. Salort, F. Chillà, "Thermal transfer in Rayleigh–Bénard cell with smooth or rough boundaries", *J. Fluid Mech.* **837** (2018), p. 443-460.
[270] R. du Puits, "Thermal boundary layers in turbulent Rayleigh–Bénard convection with rough and smooth plates: A one-to-one comparison", *Phys. Rev. Fluids* **9** (2024), no. 2, article no. 023501.
[271] P.-E. Roche, B. Castaing, B. Chabaud, B. Hébral, "Observation of the 1/2 power law in Rayleigh–Bénard convection", *Phys. Rev. E* **63** (2001), no. 4, article no. 045303.
[272] X. Zhu, R. A. Verschoof, D. Bakhuis, S. G. Huisman, R. Verzicco, C. Sun, D. Lohse, "Wall roughness induces asymptotic ultimate turbulence", *Nat. Phys.* **14** (2018), no. 4, p. 417-423.
[273] X. Zhu, R. J. A. M. Stevens, R. Verzicco, D. Lohse, "Roughness-facilitated local 1/2 scaling does not imply the onset of the ultimate regime of thermal convection", *Phys. Rev. Lett.* **119** (2017), no. 15, article no. 154501.
[274] B. Favier, E. Knobloch, "Robust wall states in rapidly rotating Rayleigh–Bénard convection", *J. Fluid Mech.* **895** (2020), article no. R1.
[275] P. Joshi, H. Rajaei, R. P. J. Kunnen, H. J. H. Clercx, "Heat transfer in rotating Rayleigh–Bénard convection with rough plates", *J. Fluid Mech.* **830** (2017), article no. R3.
[276] V. K. Tripathi, P. Joshi, "Regimes in rotating Rayleigh–Bénard convection over rough boundaries", *J. Fluid Mech.* **982** (2024), article no. A15.
[277] X. Zhang, D. P. M. Van Gils, S. Horn *et al.*, "Boundary zonal flow in rotating turbulent Rayleigh–Bénard convection", *Phys. Rev. Lett.* **124** (2020), no. 8, article no. 084505.
[278] X. M. de Wit, W. J. M. Boot, M. Madonia, A. J. Aguirre Guzmán, R. P. J. Kunnen, "Robust wall modes and their interplay with bulk turbulence in confined rotating Rayleigh–Bénard convection", *Phys. Rev. Fluids* **8** (2023), no. 7, article no. 073501.
[279] F. Zhang, J.-H. Xie, "Non-Hermitian Chern number in rotating Rayleigh–Bénard convection", *J. Fluid Mech.* **999** (2024), article no. A65.
[280] L. Terrien, B. Favier, E. Knobloch, "Suppression of wall modes in rapidly rotating Rayleigh–Bénard convection by narrow horizontal fins", *Phys. Rev. Lett.* **130** (2023), no. 17, article no. 174002.
[281] A. García, J. P. Solano, P. G. Vicente, A. Viedma, "The influence of artificial roughness shape on heat transfer enhancement: corrugated tubes, dimpled tubes and wire coils", *Appl. Therm. Eng.* **35** (2012), p. 196-201.
[282] P. Urban, P. Hanzelka, T. Králík, M. Macek, V. Musilová, L. Skrbek, "Elusive transition to the ultimate regime of turbulent Rayleigh–Bénard convection", *Phys. Rev. E* **99** (2019), no. 1, article no. 011101.
[283] R. Menaut, Y. Corre, L. Huguet *et al.*, "Experimental study of convection in the compressible regime", *Phys. Rev. Fluids* **4** (2019), no. 3, article no. 033502.
[284] Y. Ricard, T. Alboussière, "Compressible convection in super-Earths", *Phys. Earth Planet. Int.* **341** (2023), article no. 107062.
[285] C. R. Doering, P. Constantin, "Variational bounds on energy dissipation in incompressible flows. III. Convection", *Phys. Rev. E* **53** (1996), no. 6, p. 5957-5981.
[286] T. Alboussière, Y. Ricard, S. Labrosse, "Upper bound of heat flux in an anelastic model for Rayleigh–Bénard convection", *J. Fluid Mech.* **999** (2024), article no. A94.
[287] P. I. Bell, A. M. Soward, "The influence of surface topography on rotating convection", *J. Fluid Mech.* **313** (1996), p. 147-180.
[288] J. Herrmann, F. H. Busse, "Stationary and time dependent convection in the rotating cylindrical annulus with modulated height", *Phys. Fluids* **10** (1998), no. 7, p. 1611-1620.
[289] A. P. Bassom, A. M. Soward, "Localised rotating convection induced by topography", *Phys. D* **97** (1996), no. 1-3, p. 29-44.

[290] M. Westerburg, F. H. Busse, "Centrifugally driven convection in the rotating cylindrical annulus with modulated boundaries", *Nonlinear Process. Geophys.* **10** (2003), no. 3, p. 275-280.
[291] M. A. Calkins, J. Noir, J. D. Eldredge, J. M. Aurnou, "The effects of boundary topography on convection in Earth's core", *Geophys. J. Int.* **189** (2012), no. 2, p. 799-814.
[292] P. G. Baines, *Topographic Effects in Stratified Flows*, Cambridge University Press, Cambridge, 2022.
[293] D. L. Boyer, P. A. Davies, "Laboratory studies of orographic effects in rotating and stratified flows", *Annu. Rev. Fluid Mech.* **32** (2000), no. 1, p. 165-202.
[294] K. D. Stewart, C. J. Shakespeare, "On stratified flow over a topographic ridge in a rotating annulus", *Geophys. Astrophys. Fluid Dyn.* **118** (2024), no. 1, p. 25-70.
[295] M. Economidou, G. R. Hunt, "Density stratified environments: the double-tank method", *Exp. Fluids* **46** (2009), p. 453-466.
[296] T. Peacock, P. Weidman, "The effect of rotation on conical wave beams in a stratified fluid", *Exp. Fluids* **39** (2005), p. 32-37.
[297] Ž. Nosan, F. Burmann, P. A. Davidson, J. Noir, "Evanescent inertial waves", *J. Fluid Mech.* **918** (2021), article no. R2.
[298] S. Friedlander, W. L. Siegmann, "Internal waves in a contained rotating stratified fluid", *J. Fluid Mech.* **114** (1982), p. 123-156.
[299] Y. Colin de Verdière, J. Vidal, "On gravito-inertial surface waves", preprint, 2024, p. 1–14, https://arxiv.org/abs/2402.12992.
[300] S. Friedlander, W. L. Siegmann, "Internal waves in a rotating stratified fluid in an arbitrary gravitational field", *Geophys. Astrophys. Fluid Dyn.* **19** (1982), no. 3-4, p. 267-291.
[301] B. Dintrans, M. Rieutord, L. Valdettaro, "Gravito-inertial waves in a rotating stratified sphere or spherical shell", *J. Fluid Mech.* **398** (1999), p. 271-297.
[302] D. S. Zimmerman, S. A. Triana, D. P. Lathrop, "Bi-stability in turbulent, rotating spherical Couette flow", *Phys. Fluids* **23** (2011), no. 6, article no. 065104.
[303] D. S. Zimmerman, S. A. Triana, H.-C. Nataf, D. P. Lathrop, "A turbulent, high magnetic Reynolds number experimental model of Earth's core", *J. Geophys. Res. Solid Earth* **119** (2014), no. 6, p. 4538-4557.
[304] F. Stefani, A. Gailitis, G. Gerbeth, A. Giesecke, T. Gundrum, G. Rüdiger, M. Seilmayer, T. Vogt, "The DRESDYN project: liquid metal experiments on dynamo action and magnetorotational instability", *Geophys. Astrophys. Fluid Dyn.* **113** (2019), no. 1–2, p. 51-70.
[305] D. Lemasquerier, B. Favier, M. Le Bars, "Zonal jets at the laboratory scale: hysteresis and Rossby waves resonance", *J. Fluid Mech.* **910** (2021), article no. A18.
[306] J. Boisson, D. Cébron, F. Moisy, P.-P. Cortet, "Earth rotation prevents exact solid-body rotation of fluids in the laboratory", *Europhys. Lett.* **98** (2012), no. 5, article no. 59002.
[307] S. A. Triana, D. S. Zimmerman, D. P. Lathrop, "Precessional states in a laboratory model of the Earth's core", *J. Geophys. Res. Solid Earth* **117** (2012), article no. B04103.
[308] U. R. Christensen, J. Aubert, P. Cardin *et al.*, "A numerical dynamo benchmark", *Phys. Earth Planet. Int.* **128** (2001), no. 1-4, p. 25-34.
[309] P. Marti, N. Schaeffer, R. Hollerbach *et al.*, "Full sphere hydrodynamic and dynamo benchmarks", *Geophys. J. Int.* **197** (2014), no. 1, p. 119-134.

ACADÉMIE DES SCIENCES
INSTITUT DE FRANCE

Comptes Rendus. Physique
2024, Vol. 25, Special issue S3, p. 235-266
https://doi.org/10.5802/crphys.217

Review article / *Article de synthèse*

Geophysical and astrophysical fluid dynamics in the laboratory / *Dynamique des fluides géophysiques et astrophysiques au laboratoire*

Laboratory experiments related to marine plastic pollution: a review of past work and future directions

Expériences de laboratoire en lien avec la pollution plastique océanique : une revue des travaux passés et directions futures

Marie Poulain-Zarcos [a], Nimish Pujara [b], Gautier Verhille [c] and Matthieu J. Mercier [*, d]

[a] Ecole Centrale de Lyon, CNRS, Universite Claude Bernard Lyon 1, INSA Lyon, LMFA, UMR5509, 69130, Ecully, France

[b] Department of Civil & Environmental Engineering, University of Wisconsin-Madison, Madison, WI 53706, USA

[c] Aix Marseille Univ, CNRS, Centrale Med, IRPHE, Marseille, France

[d] Institut de Mécanique des Fluides de Toulouse (IMFT) - UMR 5502, CNRS, Université de Toulouse, Toulouse INP, Université Paul Sabatier UT3, Toulouse, France

E-mails: marie.poulain-zarcos@ec-lyon.fr (M. Poulain-Zarcos), npujara@wisc.edu (N. Pujara), gautier.verhille@cnrs.fr (G. Verhille), matthieu.mercier@imft.fr (M. Mercier)

Abstract. Plastic pollution is a very active research topic for a wide variety of scientific disciplines. While existing reviews of plastic pollution in the ocean cover the topic from different disciplinary and interdisciplinary viewpoints, this review addresses the contributions from laboratory experiments towards the geophysical processes important in marine plastic pollution research. We review the laboratory research on the transport, transformations, and origin and fate of marine plastic pollution with recommendations for future research.

Résumé. La pollution plastique mondiale est un sujet d'étude très actif pour de nombreuses communautés des sciences géophysiques. Un certain nombre de revues bibliographiques ont déjà abordé la pollution plastique des océans selon différents points de vue, avec des perspectives ciblées ou bien interdisciplinaires. Nous passons ici en revue les contributions récentes d'études expérimentales en laboratoire abordant certains aspects spécifiques de la pollution plastique marine. Plus précisément, nous avons considéré tous les processus basés sur la physique pour décrire l'origine, le devenir et le transport des particules plastiques dans les océans.

* Corresponding author

Keywords. plastic pollution, ocean dynamics, laboratory approaches.
Mots-clés. pollution plastique, dynamique océanique, expérience de laboratoire.
Manuscript received 16 April 2024, revised 8 October 2024, accepted 11 October 2024.

1. General considerations

1.1. *Overview*

Oceanic plastic pollution, also called marine plastic litter, is a global challenge for society and the actions to monitor, assess, or prevent its impacts have been identified in the Sustainable Development Goals by the United Nations Organization (#14 "Life below water") [1]. Marine litter in general encompasses materials other than plastic (i.e., glass, ceramics, metal, wood), but plastic pollution is the dominant fraction [2]. Marine plastic pollution research is currently focused on improving understanding and modelling tools of transport processes, fluxes, origin and the final fate of the global plastic odyssey [3].

A consensus is emerging on the physical oceanography of *floating* plastics, as summarized in a recent review [4] and illustrated in Figure 1. The dynamics of floating plastic is intricately coupled to many geophysical flows covering all spatiotemporal scales, from basin-scale long-lived gyres to wind- and wave-driven transport at the local scale. This is due to the persistence of plastic particles, which also span a wide size range from large debris ($O(1)$ m) to microplastics of $O(1)$ mm, and smaller. The large-scale open ocean flows (process A in Figure 1), which are driven by a balance between surface winds and geostrophy, are responsible for the main accumulation zones of plastic pollution, often referred to as the "7^{th} continent" or "garbage patch".

Plastics also enter the deep marine environment due to *settling* or *accumulation* processes as illustrated in Figure 2. The physical oceanography of deep sea plastics is less known, but field observations have provided clues to relate it to many geophysical processes related to the thermo-haline circulation and submarine sediments dynamics [5].

1.2. *Mass budget*

Assessing the mass budget of marine plastics sea is still a debated point, however it is an important milestone in order to close the gap between production and the global inventory of marine plastics. Estimates for marine plastic litter entering the oceans are based on population density and waste management, suggesting that between 4.8 and 12.7 million tonnes of plastic debris per year enter the ocean [7]. Considering the cumulative effects, including the accumulation of uncertainties over the years, it is estimated that the oceans would have accumulated between 75 to 200 million tonnes by 2015 [1]. We can assess these figures with the values obtained from modelling and observations for the three main vertical regions of the oceans: surface waters, ocean bottom, and the water column.

The most recent estimates for the mass of floating marine plastic are 0.13 between 3.8 million tonnes [8], compared to previous estimates that were lower with larger uncertainties, in the range 0.14 to 236 thousands of tonnes [9–11]. The first estimates of plastics in the deep sea sediments span from 3 million tonnes [12] and 170 million tonnes [13], but these are based on field samples covering only a few percent of the seafloor. Within the water column, microplastics particles smaller than 0.5 mm have been found throughout the oceans, with estimates for the global ocean in the range between 11.6 and 21.1 million tonnes [14].

Recently, the most complete global model gave a consistent view of the plastic cycle in the ocean, based on data assimilation and 3D transport models [15]. After re-evaluating sources and plastic concentrations from all the various marine reservoirs and sinks, the model based on

different scenarios for various sizes of particles gives coherent values for the mass budget to be adequately described without evoking a "missing" plastic sink. While this is an encouraging step forward in the global plastic mass budget, it is worth noting that this model (and in models in general) only account for macro-plastics (larger than 200 mm), meso-plastics (5 – 200 mm), and large micro-plastics (1 – 5 mm). Small micro-plastics (1 – 1000 μm) and nano-plastic (less than 1 μm) are not considered, which have a smaller contribution to the overall mass budget, but are of great importance in terms of eco-toxicological effects [1]. These size classifications, although slightly unusual for describing particle motion in oceanic environments, is a common approach in plastic pollution research.

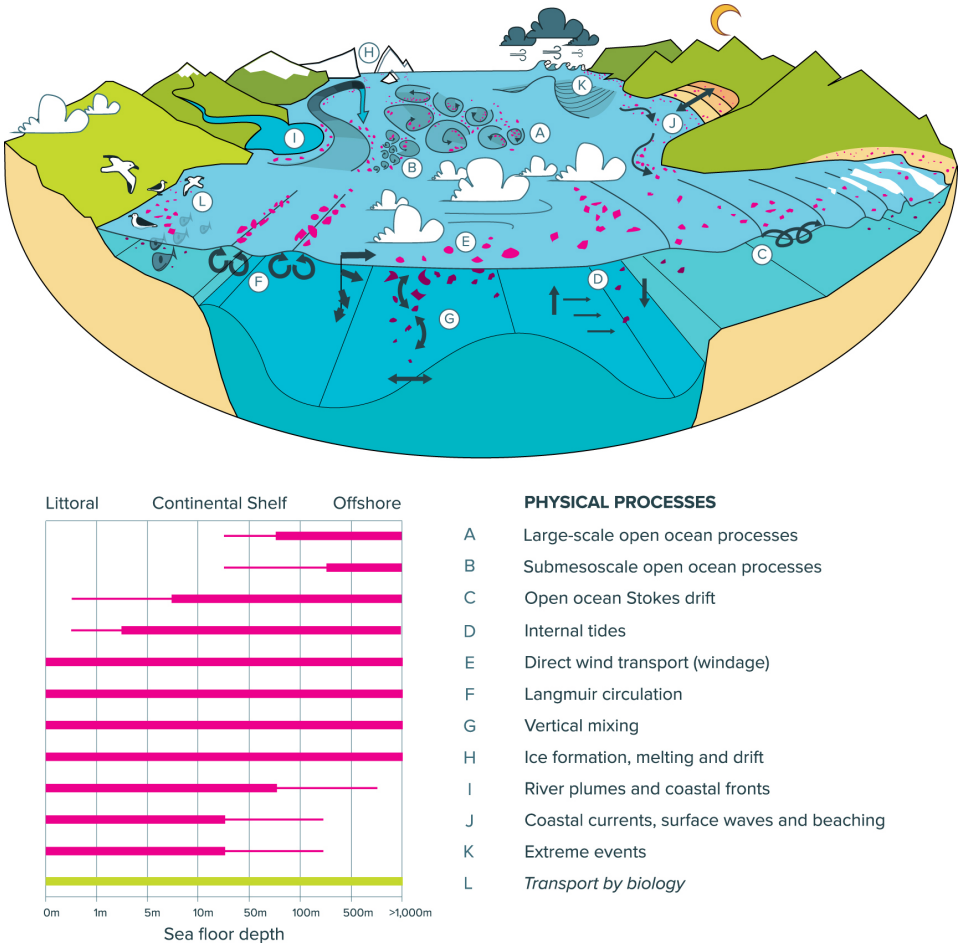


Figure 1. Schematic from [4] of the physical processes that affect plastic transport in the ocean (top panel). The table identifies the regions in which different processes are important (bottom panel). Thick pink lines indicate the process is amongst the most important in that region while thin pink lines indicate the process is of secondary importance. Transport by organisms is represented with a green line since it is not a physical process.

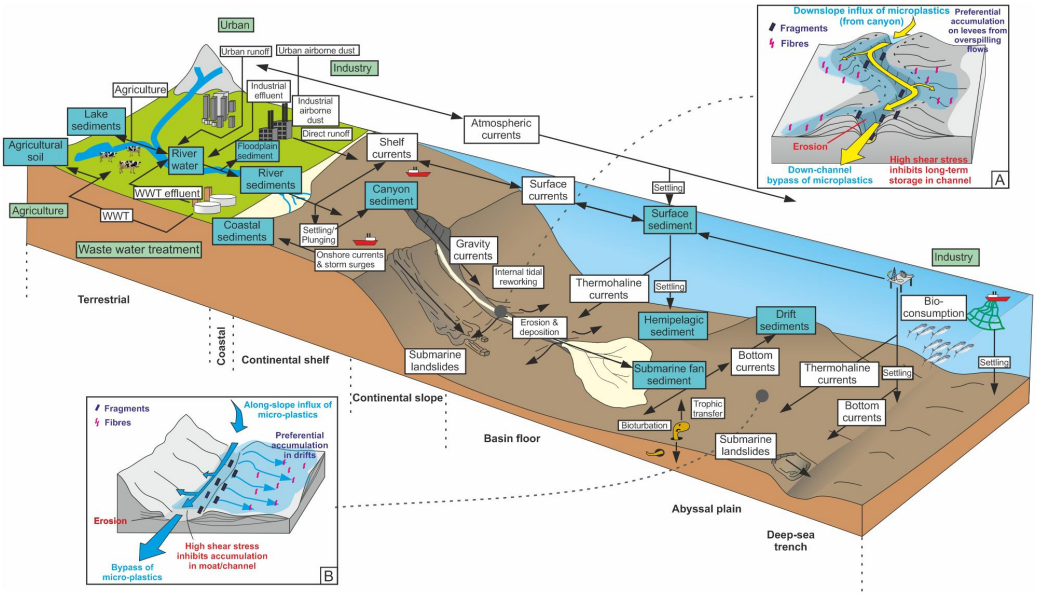


Figure 2. Microplastic sources, fluxes, and sinks from [5] modified and extended to the marine environment from [6]. Green boxes represent primary sources, blue boxes represent temporary and permanent sinks, white boxes represent transport mechanisms with arrows representing fluxes. Insets show the potential distribution and fluxes in (A) a channel-levee system and (B) a bottom current moat and drift system. WWT refers to waste water treatment plants.

1.3. *Scope and key parameters*

For marine plastics throughout the oceans, a far better understanding of transport processes and fate is required to properly assess the overall plastic mass budget. The Physics and Mechanics research communities can provide this improved understanding by adequately parameterizing all the relevant processes in the plastic cycle. Ultimately, this will allow modelling approaches to improve their ability to predict plastic pollution distributions, a key tool for political and public actions [1].

In this review, we are focused on reviewing research that seeks to parameterize geophysical processes using laboratory experiments. We address transport processes in § 2 (separated into horizontal and vertical transport, including processes B,C,E,G and J in Figure 1), transformation processes in § 3 (e.g., biofouling, fragmentation, and aggregation), and origin and fate processes in § 4 (exchanges of plastics in the ocean with benthic sediments, coastlines). In addition to reviewing existing research, we attempt to anticipate where future breakthroughs are likely or required. Terrestrial and atmospheric plastic pollution [16], although related to marine plastic pollution, are out-of-scope of this review.

Other recent reviews have also addressed the importance of physics-based research for plastic pollution. These include a focus on solute and particle transport on nearshore and shelf processes [17], plastic dynamics in coastal [18] and estuarine [19] environments, and a survey on fluid dynamical challenges related to plastic pollution [20]. We recommend the interested reader to consult these reviews alongside ours in order to benefit from complementary points-of-view, particularly on the description of the physical properties of plastic particles in the oceans, and on the role of tidal flows.

Table 1. Dimensional (resp. non-dimensional) in black (resp. color) physical parameters describing the fluid and plastic particles.

Symbol	Definition / Name	Typical values (when relevant)
ρ_i	particle (subscript p) or fluid (subscript f) density	$\rho_p \in [0.8, 2.3]$ g/cm^3, $\rho_f \in [1.00, 1.03]$ g/cm^3
ν	kinematic viscosity of the fluid	$\sim 10^{-6}$ m^2/s (20°C)
ℓ_p	characteristic length of the particle	[~ 1 μm, ~ 1 m]
ϕ_p	porosity of the particle	[0, 1[(solid VS highly porous)
E	Young modulus of the particle	~ 1 GPa
$\lambda = \ell_{p,\max}/\ell_{p,\min}$	aspect ratio of the particle	$\lambda \ll 1$ (fragments), $\lambda = O(1)$ (beads), $\lambda \gg 1$ (fibers)
$G_M(x,y,z)/\ell_{p,max}$	non-dimensional center of mass of the particle	$[-0.5, 0.5]$
δ_R/ℓ_p	non-dimensional roughness of the particle	$< 10^{-8}$(smooth pellets) up to 10^{-1}(fragments)
Φ_v	volumetric concentration	$\Phi_v < 0.01$
D_{10}, D_{50}, D_{90}	sizes related to percentiles (10%, 50%, and 90%) of the particles size cumulative distribution.	

Table 2. Dimensional (resp. non-dimensional) in black (resp. color) dynamic parameters describing the properties of the fluid-plastic coupling. An * indicates a general definition, with a more precise definition dependent on the specifics of the problem.

Symbol	Definition / Name	Sections where it appears
ℓ_f	characteristic length scale of the flow*	§ 2–4
τ_f	characteristic timescale of the flow*	§ 2–4
τ_p	relaxation time scale of the particle*	§ 2–4
U	slip velocity of the particle relative to flow*	§ 2–4
K_h, K_v	horizontal and vertical eddy diffusivities*	§ 2
$\gamma = \rho_p/\rho_f$	density ratio	§ 2–4
$\mathrm{Re} = U\ell_p/\nu$	Reynolds number	§ 2.1, § 2.2
$\mathrm{Ga} = \left((\gamma-1)g\ell_p^3\right)^{1/2}/\nu$	Galileo number	§ 2.2
$\mathrm{Sz} = \ell_p/\ell_f$	Size number, the ratio of particle-to-fluid length scales	§ 2.1, § 2.2, § 3.2
$\mathrm{St} = \tau_p/\tau_f$	Stokes number	§ 2.1, § 2.2
$\mathrm{Sd} = \tau_w/\left(\left(\rho_p-\rho_f\right)g\ell_p\right)$	Shields number (with τ_w the wall-shear-stress)	§ 4.1
$\mathrm{Sv} = U_s/U_f$	settling/rising number (also known as Dean/Rouse number)	§ 2.2, § 4.2
$\mathrm{Sc}_t = \nu_t/K_{v\text{ or }h}$	turbulent Schmidt number (with ν_t the eddy viscosity)*	§ 2.2

The properties of plastic particles are a rich set since they have range of complex various shapes, cover a large range of length scales, and density values usually near the one of water although they are not neutrally buoyant. The coupling of marine plastics with the fluid motion covers a large range of different scenarios, from tracers for very small plastic particles to inertial, floating and/or settling particles. Additionally, plastic at sea is subject to physical, biological, and chemical transformations of its physical and mechanical properties. Given this large range of possibilities, we list the important parameters related to physics-based modelling of marine plastic pollution at the outset. Table 1 lists the dimensional and non-dimensional parameters that describes the physical properties of marine plastic pollution, and Table 2 lists the dynamical parameters associated with the transport, transformation and fate of plastic pollution in a fluid. The typical values indicated in Table 1 are extracted from previous review papers focusing on the description of plastic particles as pollutants [18,21] or sediments [22]. Extra parameters could be considered, such as a shape descriptor or a class for angularity for instance, but that are not uniquely defined hence we did not included them for simplicity. Along the manuscript, plastic pollution is described either as solid particles, for instance as a new class of sediment [23] as discussed in § 4.1, but also as a dispersed phase estimating its concentration for continuous modelling (in § 2.2 for instance), often used for eco-toxicological concerns or global approaches.

Finally, it shall be noted that achieving similarity with respect to the non-dimensional parameters presented before, in the context of marine plastic litter, is apparently easier than with natural sediments. Indeed, the density ratio γ being close to 1, it can be easily adjusted to match the other parameters such as the Reynolds/Galileo number or Schields number. The scaling of the particles dynamics with respect to the flow is not the only constraint for laboratory approaches, the appropriate scaling of the geophysical flows of interest remains.

2. Transport

To date, there have been two broad approaches to describe plastic transport in geophysical flows. The first one focuses on horizontal distribution of plastics in the two-dimensional surface flows of the oceans, usually considering only the large scale features. The second approach describes the vertical transport of plastic, and predicts concentration profiles based on a flux equilibrium formalized by an advection-diffusion equation. In this section, we briefly review these two approaches using two complementary descriptions of particle transport in fluids, i.e. the Lagrangian vs. Eulerian formalisms. Examples of laboratory experiments designed to improve the reliability of plastic transport modelling are also discussed.

2.1. *Horizontal transport*

The study of horizontal transport of plastics was initially carried out to determine where plastics end up after being released into the environment. The aim was to highlight areas of accumulation on the ocean surface (assuming that the majority of plastics float on the ocean/sea surface). These models are called ocean global circulation models (OGCMs), and combine Eulerian and Lagrangian approaches. In these models, plastics are modeled as tracers whose transport is computed using a stochastic differential equation [24]. More precisely, their trajectory as a function of time, $\mathbf{X}(t)$, is obtained from information on the Eulerian velocity field of the fluid, $\mathbf{v}(\mathbf{x},\tau)$, as

$$\mathbf{X}(t+\Delta t) = \mathbf{X}(t) + \int_t^{t+\Delta t} \left[\mathbf{v}(\mathbf{x},\tau) + \mathbf{v}_{\text{subgrid}}(\mathbf{x},\tau)\right] d\tau. \tag{1}$$

The velocity field $\mathbf{v}_{\text{subgrid}}(\mathbf{x},\tau)$ is used to describe the physics at the subgrid-scale of OGCMs, which can correspond to local processes such as submesoscale eddies, wind or wave-induced

Stokes drift [25]. When this subgrid modelling is neglected compared to large-scale open ocean flows (process A in Figure 1), OGCMs are still successful in identifying the continuous accumulation zones of plastic pollution, often referred to as the "7$^{\text{th}}$ continent" or "garbage patch" [11]. But, there are a number of pathways that lead to non-homogeneous plastics surface concentrations [26,27]. In practice, $\mathbf{v}_{\text{subgrid}}(\mathbf{x},\tau)$ encompasses all unresolved physics, including stochastic terms to model particle dispersion [24].

In this framework, plastic particle properties such as density, size, deformability, porosity are usually ignored. To address this, approaches for computing inertial plastic particle motion based on the 'Maxey–Riley–Gatignol' modelling framework coupled to geophysical flows have attempted to include the unresolved physics as explicitly computed forces acting on the particles [28]; this in order to include the influence of relevant parameters such as the Stokes and particle Reynolds number. Laboratory experiments in a controlled environment are also dedicated to the study of the impact of the various aspects mentioned above (particle and flow properties) on particle transport with the aim of providing more realistic modelling in OGCMs. The paragraphs below discuss various aspects related to this aim.

Wave-induced transport by Stokes drift (U_{SD})

The Stokes drift is the difference between the wave-averaged velocity of the particle (Lagrangian point of view) and the mean Eulerian fluid velocity in a stationary reference frame [29,30]. Laboratory measurement of Stokes drift as predicted from irrotational wave theory in a closed laboratory wave tank has been the source of much confusion due to the presence of mean Eulerian currents and viscous boundary layers that are specific to each laboratory setup [30]. Laboratory confirmation of the classical Stokes drift theory was finally provided by van den Bremer et al. [31] (see also [32]), who showed good agreement between theoretical predictions based on irrotational wave theory and laboratory experiments using transient wave groups. The difficulties and subtleties involved in confirming the classical Stokes drift demonstrate that laboratory data of horizontal plastic transport due to Stokes drift should be interpreted with care. For regular (or harmonic) wave forcing, the Eulerian-mean flows must be either explicitly measured or indirectly inferred from measurements of the drift of small floating particles. Alternatively, transient waves or wave groups may also be used to understand how the drift of plastic particles differs from that of ideal tracers. Laboratory experiments have been carried out to study the influence of the plastic properties on their horizontal drift in wave flume experiments. The open questions tackled are related to the different behaviors of plastics with various sizes, shapes, and buoyancy.

The wave-induced transport of plastic particles under harmonic wave forcing has been studied in a large-scale facility [33]. It must be noted that such configurations are weakly influenced by the rigid flat bottom, with intermediate water depths ($0.3 < kh < 3$, with h the water depth and k the wave number) [33]. The authors considered spherical particles with diameters up to 1.4 % of the wavelength, i.e. small particles. However, the authors played with the particle buoyancy through the particle to fluid ratio, γ, to compare the transport of negatively (> 1) and positively (< 1) buoyant particles. For information, the Stokes number St, which compares the characteristic response time of the transported species to changes in the surrounding fluid velocity with the wave angular frequency, is about 10^{-2} in this study. Therefore, the particles are assumed to be weakly inertial although the particle density differs from that of the fluid by around 30 %. As the particle Reynolds number is also used to characterize particle dynamics, we additionally provide its range in this study: $100 < \text{Re} < 3000$. In the context of plastic pollution, these particles can be used as models for meso-plastics.

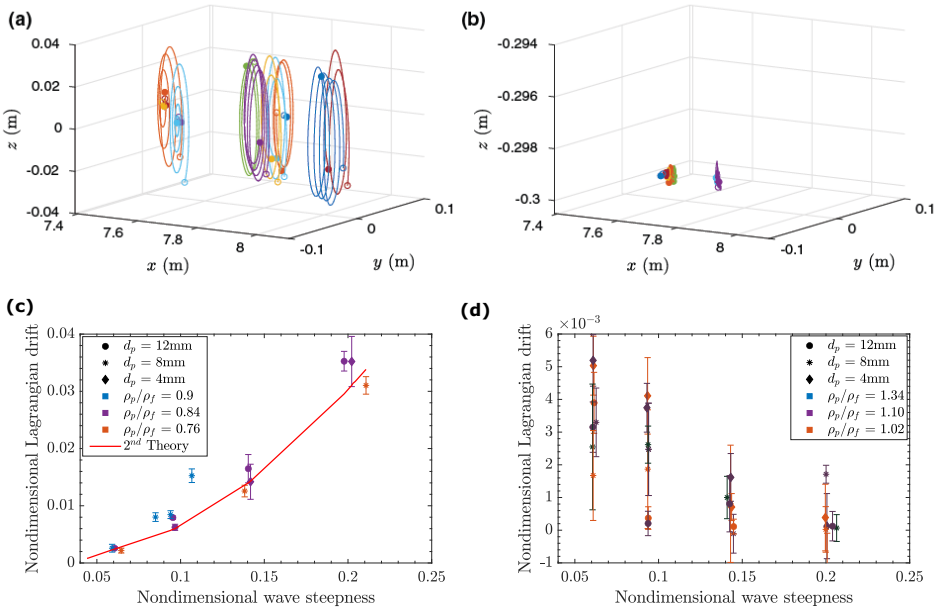


Figure 3. Examples of Lagrangian trajectories for (a) buoyant and (b) non-buoyant particles. Note the different z scales. Nondimensional Lagrangian drift measured over different steepness for (c) buoyant and (d) non-buoyant particles with varying size and densities. Solid line represents the theoretical second order solution. Results from [33].

The wave characterization was performed thanks to resistance-type wave gauges placed in a mobile frame to ensure a large spatial resolution of the wave field without any particles. Particle trajectories, over a large field of view (around 0.3×1 m^2), were measured using a Particle Tracking Velocimetry system involving two cameras. Examples of trajectories for buoyant (resp. non-buoyant) particles are shown on Figure 3 (a) (reps. Figure 3 (b)). First, the trajectories of non-buoyant particles are shorter than the ones of buoyant particles which exhibit orbital motion. However, depending on the wave height and wavelength ratio, the non-buoyant particles can move faster than in conditions presented in Figure 3 (b). Second, the authors showed that buoyant particles with different sizes and densities have a positive (shoreward) drift which increases when the wave steepness increases (Figure 3 (c)), the latter being defined as Ak with A the wave amplitude.

This increase is well predicted by classical second-order Stokes drift theory (solid line in Figure 3 (c)). Furthermore, particle size and density appear to have no influence on the Lagrangian drift of buoyant particles as long as the particle size does not exceed 1.5 % of the wavelength (Sz $\ll$ 1), which is in agreement with [34]. Finally, for non-buoyant particles staying near the flume bottom, a positive Lagrangian drift is also observed (Figure 3 (d)). However, this is one order of magnitude less than the Lagrangian drift of buoyant particles, meaning that the particles move essentially with the bottom orbital velocity. A reduction in drift with particle size and density is also suggested, although the uncertainty in the experimental data is too high to identify it with certainty. More interestingly, the Lagrangian drift of non-buoyant particles decreases when the wave steepness increases. These observations are in opposition with previous studies [35] and cannot be predicted by a single drift formulation. The authors explained this due to a larger influence of bottom orbital velocity in their experiments. Therefore, in this case, a modified

"Maxey–Riley–Gatignol" formulation is needed.

Recently, similar laboratory experiments [36] than previously described have investigated the influence of the size and shape under deep-water-wave conditions ($kh > 3$), extending the results presented for spherical plastic particles with $Sz \ll 1$. Spheres and anisotropic objects ($\lambda \neq 1$) such as discs, bottle caps, plates or net fragments are considered, with Sz varying between 0.003 and 0.2. The authors have summarized their observations by defining an amplification factor for the Stokes drift of a finite-size object compared to the one for an infinitely small one. The discs have shown the strongest amplification of the drift, increasing by $5-6\%$ for a relative increase of size of 1%, while spheres experienced an increase of 3% for the same increase of size. Results for spheres have shown reasonable agreement with numerical/theoretical predictions [34]. An increase in Stokes drift has also been predicted due to the rise in particle buoyancy (related to the enhancement of particle size). In the numerical study, the authors also mention an influence of the ratio of particle to fluid density, γ. This could not be validated experimentally, however, due to the wide dispersion of γ in the experimental measurements.

In conclusion, the main parameters that control the horizontal wave-induced transport (Stokes drift) are the ratio of particle to fluid density γ, the wave steepness Ak and the non-dimensional water depth kh, in good agreement with theoretical predictions. This drift can be enhanced for particles having at least one dimension not too small compared to the wavelength of the wave (Sz > 0.1); the amplification due to size effects being stronger for anisotropic particles than spheres, although the influence of λ has not been quantified. The results are valid for a large range of values for the Reynolds number (10 < Re < 3000), and small values of the Stokes number (St < 0.01). It should be noted that wave-induced transport is only involved in the transport of meso (and larger) plastics. Smaller plastics (microplastics typically smaller than 10 cm), due to their low buoyancy, are easily suspended in the water column and are more subject to vertical transport (see § 2.2). Consequently, as Isobe et al. [37] suggest, the larger plastics, due to net shoreward drift, remain in the coastal region, while the smaller ones, depending on their vertical position, move seaward. Large objects are also sensitive to wind-induced drift, which is discussed in the next paragraph.

Transport due to winds and currents

The influence of wind forcing at the air-water interface on the transport of plastic particles relates to the more general problem of the relative importance of water currents and winds in determining the drift of floating objects [38]. This well-known phenomenon has been thoroughly investigated recently [38] to provide a complete description of the wind factor $(U-U_w)/U_a$, which compares the drift velocity of an object U (with respect to the current velocity U_w) to the near-surface wind velocity U_a. The dominant forces at play are the inertial drag in the fluid and the air, and inertia. Various limits can be considered depending on the density of the object with respect to water, γ, and on its aspect ratio λ. Slender bodies (membrane-like), with $\lambda > 10^4$, are all drifting in a similar manner whatever γ with a wind factor being approximately 0.03. This value is due to the dominant influence of the 'skin' drag (both in air and in water) in the drag forces, hence the wind factor is nearly equal to $\sqrt{\rho_a/\rho_f}$ in this case, with ρ_a the air density. For objects with moderate values of the aspect ratio, typically $\lambda \leq 10^2$, the wind factor is controlled by the comparison of the form drag in air and water, which is related to the position of the waterline. Hence, depending on γ, its value is in the range 0.015 (for iceberg) to 0.08 (for cork).

The results in [38] have been obtained experimentally for a large range of the parameters. Additional data from mangroves to iceberg observations have validated the theoretical results for objects smaller than $\ell_p \sim 1$ km, the limit at which the influence of the Coriolis force must also be considered in the forces at play. For most object commonly found floating in the oceans, the wind factor remains very small, between 0.02 and 0.04.

Other unresolved processes

When modelling the horizontal transport of floating plastic litter using eq. (1), other "coherent" flow features would require similar laboratory interest to discriminate the specificity of plastic models with respect to the transport of other more commonly studied objects (plankton, pollution, etc.). One can mention specifically the meso-scale eddies [26], the Langmuir cells [39], or thermal fronts [40], that have been specifically identified to influence local surface concentration estimates of plastic. In general, the velocity $\mathbf{v}(\mathbf{x},\tau)$ does not include sub-surface phenomena influencing surface dynamics [41]. Neverthelss, this "near-surface" physics is of importance for proper modelling. Van der Mheen et al [42] showed, based on field measurements, that the horizontal distribution of drogued drifters (15 m below the surface) and undrogued drifters (at the surface) can differ. In particular, they showed a high concentration in the western part of the Indian Ocean, while undrogued drifters are more dispersed.

Finally, another challenging aspect is the rich nature of open-ocean wave climate. Wave packets for instance have been studied to refine classic modeling for more realistic scenarios [31]. However, validation from laboratory experiments remains uncertain. Stokes drift due to random waves forcing is often considered more simply modelled as a diffusive process [30], hence this approach relates to the other processes described hereafter. Others contributions involving more complex (open-ocean wave climate) and turbulent features can be modeled by a diffusion process, typically using a diffusion tensor $\mathbf{K_h}$, or by modifying eq. (1) into a "Fokker–Planck" equation. In its simplest form, the stochastic horizontal transport can be modeled by a white-noise of constant value amplitude added to the trajectory described in eq. (1) [24]. No specific laboratory experiments have investigated the particular case of plastic particles evolving in two-dimensional turbulence, although they appear to be well-suited tools for some pioneer work on Lagrangian transport in "chaotic" flows [43].

2.2. *Vertical transport*

The study of vertical transport was first initiated to understand the depth concentration profile, $n_p(z)$, of plastic collected at the sea surface. Knowledge of the depth concentration profile makes it possible to (i) correct surface sampling by eliminating the influence of meteorological conditions during sampling, and (ii) reduce the proportion of plastic missing from the environment [14,44]. Vertical transport of plastics is described by a balance between a buoyant flux and a turbulent one. From the mass conservation equation (see [45–47] for calculation details), this balance can be written as the advection-diffusion equation

$$\frac{\partial n_p(t,z)}{\partial t} + W_p \frac{\partial n_p(t,z)}{\partial z} - \frac{\partial}{\partial z}\left[K_z(z)\frac{\partial n_p(t,z)}{\partial z}\right] = 0, \tag{2}$$

where W_p is the plastics rise velocity and K_z is the vertical eddy diffusivity. On the one hand, the depth concentration profile depends on particle shape, density and size via W_p, as recently demonstrated by field measurements [48]. On the other hand, this transport depends on the features of the turbulence, through the eddy diffusivity (numerical study of [49]). Therefore W_p and K_z have to be chosen carefully. Note that we generally consider a stationary problem, meaning that $n_p(t,z)$ is taken as $n_p(z)$, the first term is thus removed in eq. (2).

This 1D modelling was formulated first by Kukulka et al. [50] in the context of plastic pollution, by analogy with air pollution [51], oceanography (temperature and salinity profiles) [52] and sediment transport [47,53]. The main difference between atmospheric/oceanic applications and plastic/sediment transport applications is the inertia of the species transported. This is characterized by the Stokes number St, which compares the characteristic response time of the transported species to changes in the surrounding fluid velocity with the dissipative time scale

of the flow. In atmospheric/oceanic applications, the transport of tracers is modeled (St $\ll$ 1), whereas in the case of sediments or plastics transport, particles are in general no longer tracers (St > 1).

In the context of plastics pollution, the Stokes number falls in an intermediate regime not classically studied in particle dynamics field. In addition, we have to consider a combined effect of both finite size (with respect to the Kolmogorov scale) and buoyancy. If we can consider to first order that the density of plastics is close to the density of water, leading to $\gamma \sim 1$, it was shown that the behavior of particles with slightly positive buoyancy differs greatly from that of tracers and from that of particles with slightly negative buoyancy, even for particles size close to the Kolmogorov scale and therefore for particles with small and intermediate St [54]. As previously mentioned in the literature [55,56], the use of St based on the Kolmogorov scale is not the only relevant parameter to describe the vertical transport of floating particles such as plastics: γ must also be taken into account. Therefore, plastics transport opens up a new range of parameters for predicting both W_p and K_z.

Vertical settling/rising speed

Firstly, to predict vertical transport (and deduce the depth concentration profile), studies to date have used the rise velocity of an isolated particle in a fluid at rest to set W_p [57]. In recent years, a considerable effort has been made to provide an estimate of the rise velocity of an isolated particle in a quiescent fluid, based on real plastics [58,59] or on regular shapes based on plastic sizes [60]. Based on the classic balance between buoyancy and drag forces, the relevant parameters to set W_p for a given plastic are γ, ℓ_p, Re (or Ga) and a shape factor. The influence of non-homogeneous density distribution, leading to a center of mass not collocated with the center of buoyancy, on the settling dynamics has been recently investigated for spheres [61], cylinders ($1 < \lambda < 4$) [62] or fibers ($\lambda \gg 1$) [63], leading to a moderate changes in the settling/rising speed induced by changes in the wake dynamics, for high enough values of the Galileo/Reynolds numbers (Ga/Re).

As a remark, the volume fraction of plastics in the ocean is very diluted (few pieces/m^3, [58]) and therefore modulations of W_p due to collective effects observed at high volume fractions [64,65] are not expected. However, even for low volume fractions, experiments and direct numerical simulations on particles denser than the surrounding fluid have shown that turbulence modulates the vertical velocity of the particles [66,67]. When turbulence intensity is high (i.e. Sv < 1), W_p is greater than the particle velocity in a quiescent fluid and it evolves linearly with characteristic velocity of the flow, U_f [66,67]. However, when U_f is less than W_p (i.e. Sv > 1), W_p becomes less than the velocity in a quiescent fluid [66,67]. Again for dense particles, this effect is sharpen as γ decreases and approaches 1 [68]. In addition, the vertical velocity modulation was also observed in wavy flows. For spherical particles, the flow increases W_p relative to the particle velocity in a quiescent fluid, this effect being all the more evident the larger the particles [69]. To date, to the author's knowledge, there is no model for predicting W_p in turbulent flow for plastics (and also finite size and/or inertial particles), W_p is generally considered to be the velocity in a fluid at rest.

Free-surface turbulence

Secondly, to model the vertical dynamics of plastics, the eddy diffusivity is required. K_z is the capacity of turbulence to transport particles. It depends on the properties of the particles and the turbulence. Due to technical limitations in (i) simulating finite sizes and buoyant particles in geophysical flows and/or (ii) tracking large quantities of particles in geophysical flows in time and space, eddy diffusivity for plastic litter has never been measured directly, at least to the author's

knowledge. One possibility is to reproduced similar approaches proposed for other transported quantities in geophysical flows (sediment, plankton, etc.), and to approximate it as

$$K_z(z) = \frac{\nu_t(z)}{Sc_t}, \tag{3}$$

with $\nu_t(z)$ the vertical profile of the eddy viscosity, and Sc_t the turbulent Schmidt number. While eddy viscosity is determined using classical turbulent models such as $k-\epsilon$ or $k-\omega$, the turbulent Schmidt number is still debated, with values ranging from 0.1 to 7 [70–72]. To date, there is no law to predict its value according to particle size, concentration and the nature of the flow [70,72,73]. Therefore, it must be determined from laboratory experiments for each flow configuration and particle type. In the context of plastic pollution, the aim is to reproduce both the vertical characteristics of turbulence (anisotropy and inhomogeneity) and the properties of particles (finite size and buoyancy).

We describe below one of the laboratory experiments carried out to study vertical particle transport induced by wind and waves in the context of plastic pollution [71].

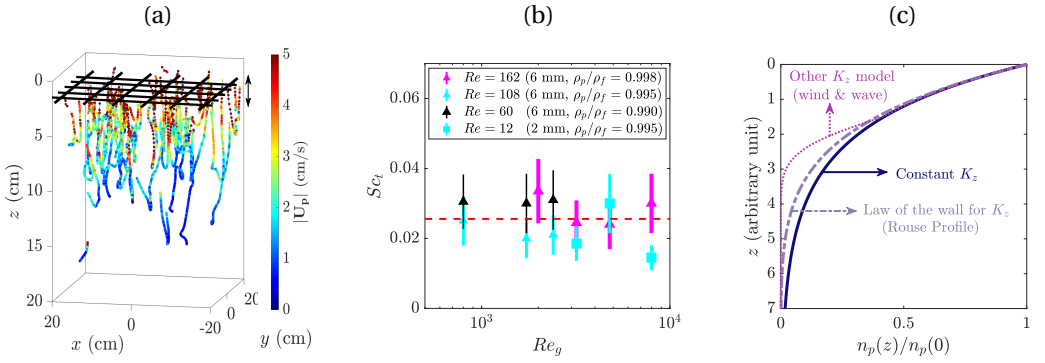


Figure 4. (a) Example of trajectories of 6 mm particles in the oscillating grid system. The color bar is the velocity norm. (b) Estimated turbulent Schmidt number as a function of the grid Reynolds number. The legend indicate the particle Reynolds number, the particle diameter and the density ratio with respect to the fluid. The red dash line is the mean value. (c) Normalised depth concentration profiles for a microplastic of 0.1 mm size. The profiles are obtained by integrating eq. (2) using different laws for eddy diffusivity, K_z (constant [50], law of the wall [74], wind and waves [75]). The z has an arbitrary unit because, for each model of K_z, certain parameters are still unknown for plastic pollution, making it impossible to predict the exact depth at which plastics may be found.

In this study, microplastics are modeled by 2 and 6 mm diameter spheres with γ between 0.99 and 1, to represent the upper range of buoyant microplastics densities [18]. They are placed in oscillating grid turbulence (Figure 4 (a)). Indeed, this flow is known to reproduce the same decay laws of wind- and wave-induced turbulence at the ocean surface for dissipation rate and fluctuating velocities [75–78]. Note that in the case of anisotropic and inhomogeneous turbulence, such as oceanic turbulence or oscillating grid turbulence, the Kolmogorov scale varies in space. This is why, in what follows, we use the particle Reynolds number based on the particle rise velocity and the particle diameter instead of St. For information, in [71], St is always of $O(1)$. Optical techniques (Particle Tracking and Particle Image Velocimetry) allowed to measure (i) the rise velocity of the particles, W_p (ii) the depth concentration profiles, $n_p(z)$ and (iii) the vertical profile of $\nu_t(z)$ (see [75] for more details and [79] for extension to oceanic applications).

Firstly, a reduction in W_p of around 60 % is observed over the entire turbulence intensity range investigated. This reduction is of the same order of magnitude as that expected in the literature [66,68]. Secondly, the turbulent Schmidt number for microplastics was estimated to be around 0.03, using an inverse problem approach from the experimental profiles ν_t and n_p (Figure 4 (b)). It depends neither on particle size nor on the ratio of particle density to fluid density, although this is still under debate [72,73]. This finding may be due to the small range of St investigated in this study. Furthermore, for microplastics pollution, the turbulent Schmidt number appears to be constant with respect to turbulence intensity (Figure 4 (b)). However, the value of 0.03 is outside the range of previous values estimated for sediments and tracers, between 0.1 and 7 [70,72,73]. This could be explained by the new range of parameters studied: nearly-buoyant particles of finite size and low volume fraction (between 10 and 1000 times lower than the volume fraction in previous studies) [47,70,73].

Note that another approach is also used to deduce $n_p(z)$, again largely inspired by work on sediment transport in rivers: the Rouse/Einstein approach [74]. It predicts the evolution of the depth concentration profile assuming the so-called law of the wall, an empirical law predicting a linear decrease in eddy diffusivity as a function of distance from the turbulence source (sediment bed or sea surface according to the application). The use of this law in eq. (2) leads to $n_p(z) \propto z^{\mathrm{Sv}}$ (Rouse profile). In this case, Sv is the so-called Rouse number defined as W_p/u_*^w with u_*^w the frictional velocity of the water on the sediment bed/sea surface. An example of Rouse profile is shown in Figure 4 (c) (dashed line) for a microplastic around 0.1 mm size and a sea state corresponding to Beaufort 2 (moderate winds). The advantages of Rouse profile are the reduced number of parameters and the prediction of profile shape as a function of the Rouse number [53,80]. However, for a given Rouse number, the profile shape (and therefore the maximum depth reached by particles) of plastics collected at sea differs from that expected for sediments [48]. To date, the parameters (γ, St, type of flow plus wave influence in the case of floating plastics, etc.) explaining this difference have not been identified. However, if we go back to the original definition of the Rouse number, it appears that it depends on the turbulent Schmidt number, which could explain the disagreements between studies [74]. Indeed, Sc_t is usually set to 1 in the context of plastic pollution [81], while we have shown it could differ from 1 as discussed above.

In Figure 4 (c), depth profiles obtained with other parametric laws for K_z are also shown for comparison (constant eddy diffusivity which has been used historically [50] and another one for wind and waves turbulence from oscillating grid turbulence [75]). As a remark, the z as no unit because, for convenience and due to the debate on the turbulent Schmidt number depending on both particle and flow properties, we consider $\mathrm{Sc}_t = 1$ to plot the three profiles. To date, the question of the "exact" profile to describe turbulent diffusivity remains open. Indeed, depending on the plastic buoyancy, it may be transported by different oceanic processes (See [4, Table 1]) with specific turbulence variations with depth [82–85]. In rivers, the same question arises for the K_z profile, particularly in relation to soil roughness (sand, vegetation, etc.) [86].

In conclusion, the main parameters that control the plastics vertical dynamics using Eulerian description are W_p, implicitly dependant on Re and shape, and $K_z(z)$. These parameters, in the context of plastic pollution, do not solely depend on the Stokes number, which alone does not allow to decouple the effects of finite size (with respect to the Kolmogorov scale), buoyancy and fluid-particle coupling.

Particle settling in wavy flows

Negatively buoyant particles introduced in a wavy flow experience both horizontal and vertical drifts (where we use the term drift to differentiate the long-time transport over many wave periods from the leading order wave-induced oscillatory motion, analogous to Stokes drift for

tracer particles in an irrotational wavy flow). A number of studies have considered this problem theoretically [87–91] and in laboratory experiments [69,92,93], with Sv $\ll 1$. In this case, Sv is defined using U_{SD} (see § 2.1). In the viscous regime (small, slowly settling particles), the particle motion can be modelled as the sum of the fluid velocity and the (orientation-dependent) particle settling velocity. For spheres in this regime, the effective settling is expected to be enhanced by a kinematic effect that is the vertical analogue to the horizontal Stokes drift [88,91]. For small (inertia-less) spheroidal particles, waves result in a preferential particle orientation that is the angular analogue of the horizontal Stokes drift and only a function of the particle aspect ratio λ. This orientation can be predicted by theory [90,92] and observed in experiments even if the particles are inertial [92]. Further, the preferential orientation modifies particle drift, reducing the effective settling relative to random orientation [89,90] and introducing a horizontal drift in the opposite direction to wave propagation [90].

The "Maxey–Riley–Gatignol" equations [94] are a popular choice for modelling inertial spherical particle motion in waves [87–91], but there are several discrepancies and gaps between this choice of model and laboratory experiments. First, the equations are applied without inclusion of the history force though its importance may not be negligible since the unsteady wavy flow produces fluid and particle accelerations that are large (up to approximately 10 % of gravity in experiments). Second, the equation is often applied outside its range of validity with respect to the particle Reynolds number. While the equation is valid for small particle Reynolds number based on the slip velocity, the settling of many plastics (including microplastics) violates this assumption. Last, the relative importance of inertial effects due to the fluid such as wakes for instance (characterized by the particle Reynolds number), and due to the particle (characterized by the Stokes number) are not clearly understood. In experiments where the flow field and particle motion are simultaneously measured, it is found that the particle motion is well described by the simple model where the particle velocity is the sum of the fluid velocity and the particle settling velocity, whether that is in waves [93] or cellular flow [95], at least for both small Re and St. This is in contrast to what is predicted from Stokes number expansions of the "Maxey–Riley–Gatignol" equations. On a related note, the predicted enhancement of the settling velocity in waves if the particle velocity is taken to be the sum of the fluid velocity and the particle settling velocity, is much smaller from theory (approximately 0-2 % [87,88,91]) compared to what is reported in experiments (approximately 20-50 % [69,93]). The experimental results even show that this increase of the settling velocity is larger for particles with small values of the Reynolds number, and also increases with another dimensionless parameter, the so-called wave parameter (H/gT^2, where H and T are the wave height and period respectively).

Given that there is well-developed theory for the behavior of particles in the viscous limit and that there are discrepancies between theory and experiments for inertial particles, future laboratory experiments should seek to carry out further investigations of both small particles whose behavior is characterized by a small Reynolds number and large particles whose behavior is characterized by non-negligible Stokes number and different particle Reynolds numbers. Together with investigating the effects of particle shape, this would clarify whether the effects predicted for small particles are observable and how to correctly model the behavior of larger particles.

Other unresolved processes

Some open questions related to more complex scenarios for vertical transport seem at reach of the current laboratory approaches. The influence of biofilm on the vertical transport has been identified as an important element for near surface dynamics [96], with a model that evidences an oscillating vertical behavior of plastics due to biofilm formation and degradation, this is discussed in § 3.1. The influence of aggregation processes is also mentioned, with or without

influenced of biofilm, leading to different vertical dynamics depending on the nature of the partner in the hetero-aggregation, phytoplankton or sediments [97]. All theses objects are to be studied in turbulent flow conditions.

3. Transformations

3.1. *Buoyancy changes (biofouling and aggregation)*

Since plastic particles have a density similar to water ($\gamma \sim 1$), it is important to consider processes that can alter their density. Biofouling, the process by which a layer of marine biota attaches to the surface of plastics, is one such process. It modifies the density by inducing volume and composition changes, and was observed fairly early on [98], but its characterization is far from obvious and raises a number of questions. Indeed, it is a complex phenomenon influenced by a wide range of parameters (i.e., geographic location, climate, water temperature, nutriments, substrate) [99]. Although never observed, either experimentally or in the field, time-oscillating vertical transport related to life and death of biofilms is used in predictions of plastic pollution transport [96]. Note that the efficiency of biofouling for small microplastics is still under debate as they might be too small for multicellular organisms to attach [100]. If the biofouling plays an important role in the evolution of plastic in the ocean, it has not been tackled yet by physicists mainly as it involves several mechanisms which are not well understood: the growth of the film that depends on the quantity of nutrient available, the hydrodynamical constraint which can erode the film, the quantity of light received by the organisms, etc.

Flocculation (or aggregation) can also change the apparent density of plastic particles. This complex process naturally occurring for small enough particles (typically $\ell_p \leq 100\mu$m) is of similar nature for plastics and natural fine sediments. Due to their polymer nature, plastic particles have the possibility to form homogeneous aggregates as well as heterogeneous aggregates with living organisms, sediments, metal oxides, proteins, etc [101]. Several experiments have revealed that microplastics can rapidly coagulate with biogenic particles [102–104], when in weak concentrations compared to biogenic one. Indeed, biofilm leads also to a reduction in hydrophobicity, which could increase the aggregation rate of the particle with phytoplankton [100,105], ultimately leading to the alteration of the settling properties of flocs or marine snow [97]. In this case, one consider the marine snow to be altered by plastic particles. It remains challenging to quantify the modifications at the scale of the particle (most important for small microplastics), but this biologically-induced flocculation is due to the suppression of repulsive forces for coated particles with biofilms [106].

The alteration of the specific properties of hetero-aggregates (i.e., size, density, porosity and rising/settling velocity) are also influenced by the presence of suspended sediment and salinity gradients [107]. Hetero-aggregates of plastic particles with suspended sediments are a more recent experimental observations that can occurred for nanoplastics with larger particles (nanoplastics of 0.1μm and sediment smaller than 100μm) [108], for particles of similar sizes (microplastics in the range $63-125\mu$m and clay finer than 20μm) [109]. It can also occur for much larger plastic particles than sediment (microplastics in the range $63-125\mu$m with kaolin smaller than 2μm), favored by the presence of surfactants in water and leading to a change from floating to sinking behavior of small microplastics [110].

Although homo-aggregates are also possible for plastic particles in suspension, they remain highly unlikely as plastic pollution is highly diluted in most aquatic environments ($\Phi_v \ll 0.1\,\%$). Nevertheless, some specific configurations lead to this process which is influence strongly by water properties, such as salinity concentrations or even gradients [111]. The influence of the shape of microplastics still needs to be clarified, although it has been shown important at smaller

scales [112]. The global importance of flocculation processes involving plastics is also uncertain, since they mainly influence the dynamics of small microplastics and nanoplastics. The temporal evolution of the properties of aggregates is rarely discussed, although it is of importance for modelling approaches.

Overall, modifications of γ for bio-fouled or agglomerated particles can lead to radical changes in their vertical dynamics (from rising to sinking § 2.2), the changes in their dynamics due to size effects remaining less important (Sz related to the vertical speed mainly). The homo and hetero-agglomerates containing plastic particles are porous particles that are more complex to characterize. Their occurrence is very sensitive to the forces of interactions that can be altered by environmental conditions. This is of importance for interactions with sediments at depth (§ 4.1) or at the coastlines (§ 4.2) as well.

3.2. *Fragmentation*

We saw in previous sections that the mechanical properties of microplastics, such as size, shape and density, play important roles on their dynamics in oceanic flows. Contrary to classical problem in particle laden flows, these mechanical features evolve with time for plastic litters. For instance weathering, erosion and/or fragmentation lead to the formation of smaller and smaller particles with arbitrary shape. In the remaining of this section we will focus on another key ingredient to understand the evolution of the plastic litters in the ocean: the fragmentation process. Indeed the large majority of collected samples floating at sea are fragments [113]. Then a reliable parameterization of the dynamics of microplastics in the ocean cannot neglect the size evolution to reach reliable prediction [114].

Overall mechanism

Microplastic fragmentation is a two-step mechanism. The first step is the degradation of plastic properties by UV, salt, ozone, living organisms, etc. [115]. This leads to an increase of the brittleness of the plastic through a shortening of the polymer chain and the creation of crack into the material [116]. As chemistry is mainly involved in this process, it will not be discussed in details here. However, several aspects of the weathering involved physical mechanisms partly discussed in previous sections. For instance, the quantity of UV absorbed by a microplastic depends on its depth and on its orientation, or the thickness of the layer of biofilm enveloping the particles depends on the shear experienced by the particle, etc. To our knowledge, there is no clear modelling of the timescale of the brittleness evolution of plastic in natural environment based on laboratory experiments, although some recent results for polyethylene are promising [117]. The second step is the fragmentation of the particle in smaller fragments. Several groups have investigated the size distribution of fragments floating at the surface of the ocean by sampling them (see legend in Figure 5 (a)). Several parameters have been investigated like the shape, colors, material, sizes, etc. Here we will focus on this last parameter. Several fragment size distributions measured in different locations are shown in Figure 5 (a). They all have the same shape: a heavy tail for large fragment which can be approximated by a power law proportional to $L^{-\alpha}$ with $\alpha \sim 5/2$ and a rapid decay for particle smaller than $\ell_c \sim 1$ mm. Note that the evolution of the size distribution for plastics smaller than 500 μm is still unclear as it depends on the mesh size of the net used to collect them [118,119]. These smaller particles are also more sensitive to vertical mixing, as we saw previously in § 2, this might induce another bias during the collect. Moreover, the age of the each sampled plastic is not known as it can either have been produced in the 1970s, when the mass production of plastic started, or much more recently. A last remark is as the different timescales involved in the fragmentation processes are unknown [120] and that the measurements of the size distribution is quite recent, there is no clue that the size

distribution reached a stationary regime or is still in a transient one. The plastic length scales have to be compared with the Kolmogorov length scale, η_K (the smallest length scale of the turbulent flow), encountered in the ocean which can be less than 100 μm [121]. Therefore, fragmentation mainly concerns object whose length lies in the inertial range $\mathrm{Sz} = \ell/\eta_K > 1$. The apparent universality of the pdf suggests that a single mechanism is at play for the plastic fragmentation whatever the location on the globe, although the power α is not universal [122]. It should then be possible to model the fragment size distribution and the timescale of fragmentation.

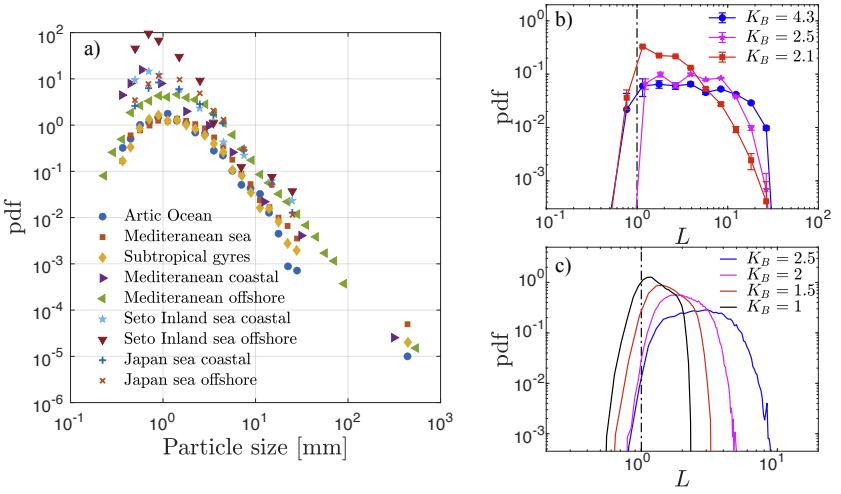


Figure 5. a) Compilation of the fragment size distribution measured at different locations around the world by different teams, data from [113] and [123]. The vertical dispersion is only due to the choice of the normalization of the distribution made by the authors. Experimental b) and numerical c) fragment size distribution of brittle fibers broken in turbulent flow for different brittleness, from [124].

So far two scenarios have been investigated: fragmentation in the swash zone due to breaking waves and fragmentation in the open ocean during storms. The first case has been mainly investigated experimentally by oceanographers. In these experiments, plastics are suspended in a tank filled with water and pebbles or sand grains. The mechanical action of breaking waves is reproduced either by the rotation of an inclined container partially filled [125,126] or by a sloshing experiment where a box containing sand, water and some plastics are set alternatively to a given inclination with respect to gravity [127]. In all these experiments, microplastics are made from the abrasion and the breakup of larger objects and the efficiency of these two mechanisms is not discussed in the interpretation of the data. Moreover, all these studies focused mainly on the global fragmentation rate by measuring the mass/number of microplastics produced from a macro object. They all find an increase of the fragmentation rate with the wave energy and that increasing the grain sizes enhances the fragmentation up to a certain point. Finally, if plastic degradation, mainly due to UV in their experiments, increases the fragmentation rate, it is not required to break plastic litters into microplastics. If these studies highlight the role of breaking waves in the swash zone in the production of microplastics, no theoretical modelling relating the wave energy, the brittleness of the plastic and the grain/pebble size to the fragmentation rate has been developed. This prevents a direct use of these results to predict quantitatively the evolution of the plastic size distribution in the coastal environment.

Fragmentation of brittle plastic

The fragmentation of plastics in open ocean has been investigated recently by physicists. The initial motivation was the modelling of the fragment size distribution which has been measured the first time by [9]. The fat tails was interpreted as a continuous breaking in smaller pieces where an object is broken in n smaller fragments, then each fragment is broken in n smaller fragments, etc [9]. This recursive scenario was inspired by a study on the fragmentation of plastic ball colliding at high speed [128]. The observed cut-off for small fragment sizes cannot be modelled with this approach and new theory is requested to interpret the behavior of the fragment size distribution for small fragments. Similar theoretical approach has been used to predict numerically the evolution of plastics in the ocean [123]. However, the continuous breaking scenario is unlikely to occur in the ocean. Indeed, from a mechanical point of view, breaking smaller and smaller objects requires more and more force or a continuous embrittlement of the particles. If the embrittlement timescale is longer than the fragmentation one, a cut-off length ℓ_c, which depends on the Young modulus E and the shape of the object, and also on the fluid density, kinematic viscosity and the intensity of turbulence [129], might be easily understood with mechanical argument: the probability that a plastic larger than ℓ_c breaks is high whereas plastic smaller than ℓ_c have a very low probability to break [124,130].

This scenario has been investigated experimentally by [124]. They studied the fragmentation of thin glass fiber immersed in a turbulent von Kármán flow driven by the counter rotation of two opposite impellers facing each other. Such flows have been used in several studies in geophysical research as it allows to generate very high Reynolds number in a relatively small facility [131,132] and have some interesting properties for the dynamo instability [133]. The use of glass, a brittle material, allows to use simple model for the fracture mechanism: the material breaks if the constraint is higher than a threshold. They measure the time evolution of the fragment size distribution for different brittleness and compare their results with numerical simulations. In both cases, the size distribution converges toward a peaked distribution with a most probable fragment size of the order of the typical elastic length ℓ_c [129]. They were able to have a quantitative description of the time evolution of the size distribution using the statistics of the deformations for flexible fibers in turbulent flows (Figures 5 (b) and (c)), in good agreement with field data (Figure 5 (a)). One possible refinement could be the continuous input of plastics in the system. Indeed, in their study, the total mass of plastics is fixed contrary to the environmental application, where the flux of plastics entering the ocean is expected to scale with their global production. The modification of the fragment size distribution in that case has recently been investigated theoretically and fits the data relatively well [134]. A second refinement is the time evolution of the brittleness of the particle to capture the ageing of the plastic in the ocean. One important assumption in this model is that the particle length is in the inertial range so larger than the Kolmogorov length. This approximation is valid for microplastics as the smallest lengthscale of the flow can be of the order of 50 μm during breaking wave events [121]. However, this approximation may not be valid for nanoplastics whose length can be smaller than 1 μm. The formation of these nanoplastics may be either due to abrasion of larger objects which have been embrittled by UV radiation or directly by the breaking of particle smaller than the Kolmogorov length. If the former scenario has not been tackled yet, the latter has been investigated numerically. At scales smaller than the Kolmogorov length, the flow is smooth and can be approximated by a linear gradient evolving randomly in time. Bending is then very unlikely. However, depending on the orientation of the particles with the eigenvectors of the rate of strain tensor and of its intensity, the fiber can buckle and break in several fragments [135]. If this scenario might be at the origin of nanoplastics, no quantitative comparison between this model and the measurements on nanoplastics has been done yet.

So far, experiments on the modelling of the formation of microplastic have been focused on the evolution of the fragment size distribution. If this work has been successful, it remains to model the fragmentation rate for particle larger than the Kolmogorov length. Indeed, the fragmentation rates estimated experimentally in non exactly homogeneous and isotropic turbulence (von Kármán flow) and the one estimated numerically in numerical simulation using idealized flow (kinematic simulation) differs from several orders of magnitude [124]. This discrepancy has still to be understood. For particle smaller than the Kolmogorov length, the timescale is determined by the probability that a particle has the right orientation with the gradient of the velocity field and whose amplitude is high enough [135]. This different timescales have then to be compared with the ageing timescale by chemical or biological degradation of plastic to determine if both timescales have to be considered or if the dynamics of the system is governed by only one timescale which is much longer than the other one.

4. Origin and Fate

There are a great variety of sources and sinks for plastic litter in the oceans [136]. Sources (inputs) for plastic can be terrestrial (mismanaged waste [7] entering via rivers [137], estuaries [19], coastlines), offshore (i.e. fishing, shipping), or atmospheric [16,138]. Plastic pollution also exits the ocean environment through a variety of sinks, including beaching or grounding at coastlines, ejection into atmosphere, settling to seafloor and being buried in benthic sediments, or ingestion by biological organisms. One can notice that many environmental compartments play a dual role (source and sink). Here, we focus on some specific sources and sinks that have been investigated both in the laboratory and the field.

4.1. *Plastics in (and as) sediments*

Microplastics in sediments have been observed in many locations for decades, although variability in sampling techniques and analysis has made it difficult to estimate the true extent and impact of microplastics in benthic sediments [139]. The more recent efforts to study plastic litter in deep sediments over the last fifteen years have allowed for better coverage and concentration/mass estimation. Various global estimates have been presented according to statistical analysis of samples based on size and type of locations. Estimates are between 3 and 170 megatonnes with most likely values in the range between 3 and 25 megatonnes [12,13,140]. Most of this deep pollution is accumulated along slopes, more than 60 % of the total being between 200 m and 2000 m with a majority of pieces smaller than 2.5 cm.

Recently, an interdisciplinary approach to describe plastic particles as a specific type of sediment has been discussed, with the key research goals of this framework identified [23,141]. Such an approach has the potential to accelerate progress on modelling the fate and transport of plastic pollution by leveraging the vast existing research on sediment. An important goal, then, is to identify the similarities and differences between the fate and transport of plastics compared with sediments and to start using methods to describe plastic particles that were originally devised for sediments. For example, new conventions for the description of plastics found in the environment would include: plastic class ranges with grades or size ranges based on transport properties; texture or shape descriptions; detailed distribution of sizes using histograms or classical metrics such as the median diameter (d_{50}). Another important goal is to identify the differences between the fate and transport of plastics compared with sediments. The main difference is related to the particle density ρ_p. Whereas the value of 2.6 g/cm^3 is often used for natural sediment particles, with sediment aggregates or flocs spanning a narrow range of

$1-1.4$ g/cm^3, the density of plastics spans a wider range with values both above and below the water density ρ_f, typically covering values such that γ is in the range $[0.03-2]$.

Another important goal is to consider the differences in terms of transport of plastic particles. Since plastic particles are solid objects in a fluid, the various modes of transport for sediments are encountered (bedload, saltation, suspended transport) as well as surface transport (discussed in § 2). The relevant parameter to characterize the different regimes for sediment motion is the Shields number, Sd as defined in Table 2, which is a comparison of the fluid forces on a particle (drag and lift) with its buoyancy. However in the context of plastic particles, due to their low density values compared to ρ_f, bedload transport shall be revisited. More specifically, two processes play an important role: the erosion and deposition behaviors and the corresponding threshold values for the shear stresses at the sediment bed. The first experimental evaluation of the plastic-specific erosion thresholds were obtained for samples collected at sea with $d_{50} \sim 4$ mm [142], more comprehensive studies have covered a wide range of plastic/sediment properties [59,143]. It is clear that much lower critical thresholds values are needed to initiate motion of plastic particles compared to sediment of the same size, and the influence of the shape and size is also of importance. The rationalization of the measured values should include the particle Reynolds number Re, the aspect ratio λ or some shape influence, as well as some description of the size differences between sediment and plastic, in a similar manner than classically made for mixed-size sediments [144], with a hiding-exposure function. Additionally, the influence of the difference in static friction for sediment and plastic has to be considered as well as local forces at play for attractive as well as repulsive interactions, as already discussed when discussing their aggregation in § 3.1. Although the description start to be well-posed, a complete understanding of the physical properties is not yet achieved. Finally, in the context of the specific type of bedload transport called dune migrations, a recent experimental study has described new processes when combining fine sediments and plastic objects covering a very large range of sizes (always larger than the value of d_{50} for the sediments) [145]. The main observations described are changes in dunes morphology due to fast transport of individual or (collective) patches of plastic items that enhances sediment transport as well. Even for dilute concentrations ($\Phi_\nu < 0.1\,\%$), the coupling between poly-disperse sediments with very different erosion/deposition thresholds is important to consider here.

Plastic litter in turbidity currents

We now turn to the specific case of plastic particles that are transported as a very dilute phase along with sediments put in suspensions and flowing as turbidity currents. As presented in a recent review [5], such flows which convey sediments as well as organic matter to the deep ocean are likely to entrain plastic litter as well. Plastic reaching deep sediments are originating from the surface (natural or biologically-induced settling), from the coastal riverine inputs evolving in turbidity currents or are transported by deep flows such as thermo-haline circulation, bottom currents or internal tides dynamics along continental slopes or in canyons. Submarine canyons and ocean trenches are regions of greater concentrations of plastic items. More specifically, canyons have specific topographic and dynamics features that are associated to a funneling effect for turbidity currents, and are often connected to a river input, which altogether make them obvious accumulation zones as confirmed by observations [146].

Nevertheless, it is not straightforward to quantify how much plastic is accumulating there. When plastic particles are suspended in turbidity currents, either by being already present at sources or by erosion of previous inputs in the canyons, some key open questions are to be answered. Where are plastics suspended in the currents? How do they deposit and where are they likely to end in the deposit? One can anticipate that the influence of plastic properties can induce a sorting/differentiation with depth, but also influence the total distance travelled,

etc. Due to the differences in nature of plastic and sediments, one expects a different behavior of plastic than for "classic" polydisperse turbidity currents [5]. Figure 6(a) is an example of setup designed to address those questions [147]. A large reservoir is made of suspended quartz sand (density 2.65 g/cm^3) with grain-size range similar to that encountered in natural turbidite systems ($d_{10} = 35\,\mu$m, $d_{50} = 133\,\mu$m, $d_{90} = 214\,\mu$m) at a volume fraction of 15 %. The resulting current density is 1.25 g/cm^3. The microplastics added to the suspension at a volume fraction $\Phi_v \leq 10^{-4}$ are of two types. Melamine fragments have densities of 1.5 g/cm^3 and a median size of $250 \pm 50\,\mu$m, and polyester fibers have densities of 1.38 g/cm^3, a length of 6 mm and a diameter of 12.5 μm. The injection rate (fixed at 12.5 m^3/h here) and angle of the channel are set to be in hydrodynamic similarity for sediment mobility. Experiments performed at an angle of 8° do not generate a deposit but can be sampled vertically using siphon tubes, whereas deposits can build up for an angle of 4°, but the siphon sampling cannot be reliably done. The experimental setup is nearly two-dimensional, the lateral extent of the tank being 0.2 m.

After a careful analysis of the siphon or deposit samples, the main results from this study, presented in Figure 6(b), are that fibers and fragments have very different behaviors in the turbidity currents and deposits.

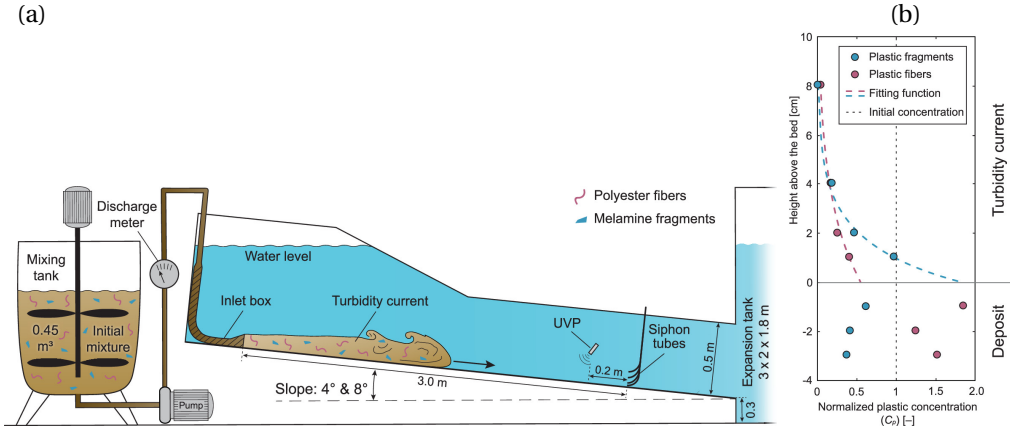


Figure 6. From [147]. (a) Experimental setup used for experiments. (b) Concentration of melamine fragments and polyester fibers in the turbidity current and in the deposits. Values are normalized with the initial concentrations in the mixing tank.

The concentrations profiles for fibers and fragments within the current are similar to the sediment concentration profile (not shown here), with an exponential decay with increasing depth from the bottom. A similar comment can be made for the vertical structure of the deposit, with no clear trends to decipher. Only the relative abundance are different, with fragments dominating over fiber in the suspension, and the reverse order in the deposit.

In [148], additional complexity has been added to this problem by considering a similar experiment but with a more diverse distribution of sediments in suspension, with the mass percentages being 65% quartz sand, 17.5 % silt, 7.5 % clay (all these classes have a density of 2.6 g/cm^3) and 5% Garnet sand (3.90 g/cm^3). The main interest here is to reproduce typical mass and size distributions observed in field studies of turbidity currents. The microplastics particles (1.50 g/cm^3) remain as a dilute phase, since its mass percentage is less than 2.5 % [148]. The experiment is also performed in a more realistic geometry in a wider tank than previously described ($11 \times 6 \times 1.2$ m^3), with levees on a slope to funnel the current, followed by a flat basin filled with fine sand for the deposit to develop in a three-dimensional manner. By analysing

the samples collected at various locations in the deposit from several cumulative injections, the authors have shown that plastic particles are more likely to be observed in levees (inner and outer parts) than in the center of the channel. They are also transported further downstream in the basin plain. These results are in agreement with observations from accumulation zones such as canyons [146].

If the influence of shape has been clearly identified in a simple configuration for turbidity currents, more quantitative studies are still required to investigate the influence of various other factors related to size comparison between plastic and sediments. These results have implications for sediments sampling strategies and analysis. The likeliness of trapping fibers more efficiently has still to be clarified but at least this is confirmed by recent observations [149]. The vertical profiles for plastic should also be related to the turbulent vertical transport described in § 2. The combined erosion/deposition processes in more realistic scenario are also only emerging, the parameter space to cover for relevant values of Shields and particle Reynolds numbers being quite large.

4.2. *Particles at coastlines*

On geophysical scales, the fate and transport of plastic pollution in the coastal environment is controlled by a multitude of physical processes, including winds, internal and surface gravity waves, diurnal heating/cooling, river plumes and estuarine circulations, stratification of the water column, and mean flow and turbulence in the surf and swash zones; these processes are described in more detail in recent reviews [4,17,150–154]. Considering how these processes influence plastic transport, the coastal environment can be a significant source, sink, and/or reservoir for the ocean plastic pollution budget.

Tracking of surface drifters in the ocean as they become beached (or grounded) has allowed for investigating how macroplastics could become beached, showing, for example, that mid-latitude islands may be particularly prone to debris accumulation [155], drifters in estuaries tend to be beached locally within a small number tidal cycles [156], and that the beaching process can be modelled as a diffusion process due to submesoscale eddies [157,158]. Field observations from a plastic spill [159] have shown how physical properties of plastic nurdles can change due to fire (intemperi or inceneration) and interaction with the marine environment, and possibly alter the beaching location. A number of studies have also conducted numerical modelling of plastic fate and transport at geophysical scales informed by field data, showing the importance of considering the coastline as a source, sink, or reservoir. For example, plastic beaching is a significant part of the plastics mass balance, with up to 75 % of all plastics washed up on beaches [85], but the mean beaching time for plastics near coastlines showing some discrepancy with field data [160–162]. For microplastics, there is a prevalence of field data on the plastic concentrations in beach sediments showing the distribution of plastics deposited at coastlines to be highly variable along any particular stretch of a coastline and over time (i.e. [163–168] amongst many others), though the lack of standardisation in field sampling techniques continues to pose challenges for comparing across studies [136].

In the field-based studies using measurements and modelling at geophysical scales, the primary focus is the roles of wind and ocean currents in predicting the transport of plastics. The role of wave-driven processes is often assumed to be subsumed by the wind speed, which ignores the complexities of Stokes drift and surf and swash zone processes mentioned above. Another common simplification is that of the coastline being either a permanent sink for plastics that are beached or a simple source, even if it is recognized that the coastline is a dynamic reservoir that can act both as a source and a sink. In other words, while some plastics can become buried sufficiently deep that they are effectively permanently removed from the ocean environment,

other plastics may become beached and then later resuspended. Note, permanent removal from the ocean environment can also occur due to human action via beach clean-ups or due to animals via ingestion. Finally, it is recognized that, much like sediment, plastics can also be transported along the coastline, but that this is not accurately accounted for in current models or field observations.

Laboratory studies of how plastics interact with a coastline, including investigations of coastlines acting as a source, sink, and/or reservoir, are relatively rare compared to the larger body of research on plastic pollution transport in the open ocean. However, as noted above, the mechanisms of plastic beaching and resuspension are some of the largest uncertainties and unknowns in predictions of the plastics budget at geophysical scales.

Laboratory studies on the coastal sink for plastic pollution (i.e. [33,169–175]) typically track the motion of plastic particles in a physical simulated coastal environment within a wave tank. The focus on wave-driven flow is due to the fact that waves are the primary drivers of flow near coastlines, though the effects of wind and oceanic currents can also be important. Not surprisingly, laboratory studies find that the biggest change in the beaching process for plastic particles is related to whether the particles are positively buoyant or negatively buoyant. Positively buoyant particles ($\gamma < 1$) are biased to be positioned near the top of the water column, which favors onshore motion in wave-driven flow that results in particles having a greater tendency to reach the shoreline and accumulate near the furthest onshore reach of wave run-up. Most studies discuss the likelihood of beaching in the swash zone qualitatively, likely because particle beaching is particularly sensitive to the water level oscillations and circulations particular to each wave tank as well as the beach profile shape and sediment. Larsen et al. [173] performed a more quantitative analysis of beaching by quantifying the beaching time for different plastic particles dropped at different locations along the wave tank. The influence of particle size and shape, coupled with its buoyancy, is brought in via the Sv number based on the particle's terminal rising velocity and the fluid velocity scale. In coastal engineering literature, this dimensionless quantity is called the Dean number (see explanation of the Dean number in, for example, [176]) and it was originally developed to provide a heuristic explanation of the cross-shore motion of sand grains. While these experiments have taken into account the surf zone dynamics, they do not necessarily give a detailed picture of the mechanics of beaching in the swash zone. Davidson et al. [174] filled this gap by using a transient wave to generate a single swash event that carried plastic particles up the beach during the run-up and deposited some of them while returning others to the water. They provide a model to explain their results that includes the introduction of a swash zone Stokes number, where τ_f is based on an experimentally validated model of swash flow [177].

Negatively buoyant particles are biased to be positioned lower in the water column, where the flow is biased to be in different directions depending on the cross-shore location. While there is an onshore directed bias outside the surf zone (albeit smaller than the Stokes drift [33]), there is an offshore directed bias in the surf and swash zones [169], which overall results in particles having a tendency to accumulate near the wave breaker zone at the outer edge of the surf zone. Thus, the dynamics of negatively buoyant plastics has a greater correlation with the dynamics of coastal sediments. As before, the influence of particle size and shape, coupled with its buoyancy, is brought in via the Sv number. While a number of such studies were conducted with a fixed beach profile and without sediment, Guler et al. [171] performed experiments where the beach was made of loose sediment and the beach profile was allowed to evolve while the positions of plastic particles were tracked at specific intervals. They found that the particle shape, size relative to beach sediment, and the shape of the beach profile can all influence the cross-shore location of where negatively buoyant particles accumulate due to factors such as the hydrodynamics of individual plunging wave crests, surf zone flow and turbulence, and the particle's angularity and ability to roll.

As noted above, laboratory experiments are well suited to investigate the interaction of plastics with coastlines. The wave-driven flows that dominate in the coastal environment are usually unresolved in geophysical models and are resolvable in laboratory wave tank facilities. While a number of laboratory studies have investigated how wave-driven coastal dynamics can allow a coastline to act as a sink for plastics, there are a number of questions that remain before to bridge the gaps between the lab and geophysical scales. Existing work obviously shows negatively buoyant and positively buoyant particles have qualitatively different cross-shore dynamics, but a clear understanding of the dominant processes that determine the fate (beaching or burial location) and transport (Stokes drift, turbulent transport, undertow effects) has yet to emerge with different frameworks proposed in different studies (see § 2). It is possible that the cross comparisons between studies are hampered by differences in geomorphic features of the coastline (i.e. beach profile [171]) and the lack of understanding of particle resuspension, as discussed in § 4.1. Relatedly, it may be worth noting that while "microplastics" are defined as plastics whose size is smaller than 5 mm, that definition needs to be reevaluated carefully in the lab so that there is not an outsized influence of inertial effects in plastic particle dynamics (defined via suitable Stokes and Reynolds numbers). Small particles may be significantly influenced by particle and fluid inertia in the shallow depths of swash zone flow in the lab, for instance. Thus, laboratory experiments are well placed to provide a better understanding plastic resuspension (shown to be important in the related problem of resurfacing of unexploded munitions that are buried in beach sediments [178]), alongshore transport and accumulation of plastic debris (analogous to alongshore transport of other debris [179]), and debris interactions with the complexities of coastal canopies such as vegetation and coral [172].

5. Outlook

Laboratory studies presented all along this review have provided significant inputs to the global modelling of plastic marine litter fate and transport. With a slight personal perspective, we want to emphasize here on some specific points that represent significant breakthroughs in the recent years. The influence of shape on plastic behavior in turbidity currents have been clearly identified as very important (§ 4.1) whereas it is not the dominant factor for Stokes drift horizontal transport (§ 2). The influence of vertical velocity (related to γ, smaller or larger than 1, and the size) is the most important parameter to consider in beaching processes (§ 4.2) as well as for vertical transport (§ 2). Finally, there is a clear connection between plastic size distribution and the characteristic length for plastic object to break due to the fluid turbulent agitation (§ 3.2).

Although marine plastic pollution is at first sight associated with solid particles moving in the ocean, we consider of great importance to make new estimates of non-dimensional parameters specific to solid transport with respect to plastic such as the Dean number for beaching, the Shields parameter for erosion, the turbulent Schmidt number for turbulent transport. These parameters based on complex physics already for sediments, are not easy to predict and can lead to unexpected values. This could prevent from misleading guesses having strong influence when extrapolated at the global scale. Across this article, we have often referred to the list of relevant parameters for the description and modelling of marine plastic litter dynamics, described in Tables 1 and 2. We anticipated that some of them shall be influential, such as unbalanced mass distribution [62] or porous particles [180], but to the authors knowledge, these specific issues for plastic pollution still need to be addressed.

Discussions at the end of each section have already emphasized on open questions related to the isolated processes described. To a certain extent, the influence of combining those processes together is also an important path towards a more realistic parameterization of these processes. For instance, one expects the influence of particles aggregation to alter their turbulent vertical

transport and the estimation of the corresponding Schmidt number; a similar comment should hold for the combined horizontal and vertical transport occurring in meso-scale geophysical turbulent flows. The motion of particles at depth in the oceans is also confronted to changes in water properties and the presence of salinity/temperature/density stratification that affect the vertical speed in a complex manner [181]. However, observations [44] have reported the presence of microplastics up to 1000 meters below the surface. Experimental laboratory studies could provide valuable insights into all these processes.

Finally, some new processes for the marine plastic cycle are starting to be investigated but are still in their premises, requiring additional laboratory studies. Atmospheric transport of plastic particles has been identified as a fast route for microplastics, which can travel thousands of kilometers, between countries and over oceans, in a relatively short time (days to weeks) in the atmospheric boundary layer[16,182]. The fluxes at the ocean/atmosphere interface remain hard to estimate, and the first experimental values obtained for particles exiting the ocean have showed an increase of aerosolization with increasing plastic concentration in water and decreasing size [183]. The trapping of plastic particles in Artic sea ice has also been identified as an important "temporary" sink [184] for marine plastic litter. Even if the sources for these microplastic particles are not well identified, it seems essential to understand the trapping mechanism in the phase change of water into ice. Recent experiments have identified the influence of size on the trapping process (micro vs. nano-plastics) [185], the important role of air bubbles at the surface of trapped plastics has also recently been discussed [186]. On a more original aspect, the marine environment with important biological activity is often considered as mucus-rich, with elevated concentrations of exopolymers that modify the rheological properties of sea water. These non-Newtonian fluid-regions have been documented as prone to unusual dynamics of plastic particles [187], with changes in orientation of complex-shaped plastics. Modification of the aggregation processes is also anticipated.

As a final note, we would like to highlight that all the efforts from the research community at large to improve our understanding of marine plastic pollution contribute to revisit and improve our knowledge of some complex geophysical processes. Similar comments could hold for other objects of interest, such as algae, phytoplankton, jellyfish patches, marine snow, etc. However for marine plastic pollution, as already stressed in [4], it is the paradoxical benefit society has gained from a massive pollution it created.

Acknowledgements

The authors thank S. Blosse, M. Mrokowska, A. Pradel, C. Russel and two anonymous reviewers for discussions and suggested corrections on this manuscript, as well as the editors of this thematic issue on "Laboratory models of astrophysical and geophysical fluid dynamical processes" for offering the opportunity to discuss marine plastic pollution.

Declaration of interests

The authors do not work for, advise, own shares in, or receive funds from any organization that could benefit from this article, and have declared no affiliations other than their research organizations.

References

[1] J. McGlade, S. Fahim, I. Green, et al., *From Pollution to Solution: A global assessment of marine litter and plastic pollution (Nairobi)*, tech. rep., United Nations Environment Programme, 2021. Online at https://www.unep.org/resources/pollution-solution-global-assessment-marine-litter-and-plastic-pollution.

[2] C. Morales-Caselles, J. Viejo, E. Martí, et al., "An inshore–offshore sorting system revealed from global classification of ocean litter", *Nat. Sustain.* **4** (2021), no. 6, pp. 484–493.
[3] C. M. Rochman and T. Hoellein, "The global odyssey of plastic pollution", *Science* **368** (2020), no. 6496, pp. 1184–1185.
[4] E. Van Sebille, S. Aliani, K. L. Law, et al., "The physical oceanography of the transport of floating marine debris", *Environ. Res. Lett.* **15** (2020), article no. 023003.
[5] I. A. Kane and M. A. Clare, "Dispersion, Accumulation, and the Ultimate Fate of Microplastics in Deep-Marine Environments: A Review and Future Directions", *Front. Earth Sci.* **7** (2019), pp. 41–42.
[6] A. A. Horton and S. J. Dixon, "Microplastics: An introduction to environmental transport processes", *WIREs Water* **5** (2018), no. 2, article no. e1268.
[7] J. R. Jambeck, R. Geyer, C. Wilcox, T. R. Siegler, M. Perryman, A. Andrady, R. Narayan and K. L. Law, "Plastic waste inputs from land into the ocean", *Science* **347** (2015), no. 6223, pp. 768–771.
[8] Y. Zhang, P. Wu, R. Xu, et al., "Plastic waste discharge to the global ocean constrained by seawater observations", *Nat. Commun.* **14** (2023), no. 1, article no. 1372.
[9] A. Cózar, F. Echevarria, J. I. Irigoien, et al., "Plastic debris in the open ocean", *P. Natl. Acad. Sci. USA* **111** (2014), no. 28, pp. 10239–10244.
[10] M. Eriksen, L. C. M. Lebreton, H. S. Carson, et al., "Plastic Pollution in the World's Oceans: More than 5 Trillion Plastic Pieces Weighing over 250,000 Tons Afloat at Sea", *PLoS ONE* **9** (2014), no. 12, article no. e111913.
[11] E. Van Sebille, C. Wilcox, L. Lebreton, et al., "A global inventory of small floating plastic debris", *Environ. Res. Lett.* **10** (2015), no. 12, article no. 124006.
[12] P. T. Harris, T. Maes, K. Raubenheimer and J. P. Walsh, "A marine plastic cloud – Global mass balance assessment of oceanic plastic pollution", *Cont. Shelf Res.* **255** (2023), article no. 104947.
[13] C. Martin, C. A. Young, L. Valluzzi and C. M. Duarte, "Ocean sediments as the global sink for marine micro- and mesoplastics", *Limnol. Oceanogr. Lett.* **7** (2022), no. 3, pp. 235–243.
[14] K. Pabortsava and R. S. Lampitt, "High concentrations of plastic hidden beneath the surface of the Atlantic Ocean", *Nat. Commun.* **11** (2020), no. 1, article no. 4073.
[15] M. L. A. Kaandorp, D. Lobelle, C. Kehl, H. A. Dijkstra and E. Van Sebille, "Global mass of buoyant marine plastics dominated by large long-lived debris", *Nat. Geosci.* **16** (2023), no. 8, pp. 689–694.
[16] D. Allen, S. Allen, S. Abbasi, et al., "Microplastics and nanoplastics in the marine-atmosphere environment", *Nat. Rev. Earth Environ.* **3** (2022), no. 6, pp. 393–405.
[17] M. Moulton, S. H. Suanda, J. C. Garwood, N. Kumar, M. R. Fewings and J. M. Pringle, "Exchange of Plankton, Pollutants, and Particles Across the Nearshore Region", *Ann. Rev. Mar. Sci.* **15** (2022), pp. 167–202.
[18] I. Chubarenko, E. Esiukova, A. Bagaev, et al., "Microplastics particles in coastal zone: Approach of physical oceanography", in *Microplastic Contamination in Aquatic Environments*, second edition, Elsevier, 2024, pp. 249–310.
[19] I. Jalón-Rojas, S. Defontaine, M. Bermúdez and M. Díez-Minguito, "2.15 – Transport of microplastic debris in estuaries", in *Treatise on Estuarine and Coastal Science (Second Edition). Volume 2: Physical Aspects*, second edition (D.-. Baird and M. Elliott, eds.), Academic Press Inc., 2024, pp. 368–409.
[20] B. R. Sutherland, M. DiBenedetto, A. Kaminski and T. van den Bremer, "Fluid dynamics challenges in predicting plastic pollution transport in the ocean: A perspective", *Phys. Rev. Fluids* **8** (2023), no. 7, article no. 070701.
[21] A. A. Koelmans, P. E. Redondo-Hasselerharm, N. H. M. Nor, V. N. de Ruijter, S. M. Mintenig and M. Kooi, "Risk assessment of microplastic particles", *Nat. Rev. Mater.* **7** (2022), no. 2, pp. 138–152.
[22] S. Rohais, J. J. Armitage, M.-F. Romero-Sarmiento, et al., "A source-to-sink perspective of an anthropogenic marker: A first assessment of microplastics concentration, pathways, and accumulation across the environment", *Earth-Sci. Rev.* **254** (2024), article no. 104822.
[23] C. E. Russell, F. Pohl and R. Fernández, "Plastic as a Sediment – A Universal and Objective practical solution to growing ambiguity in plastic litter classification schemes", *Earth-Sci. Rev.* (2024), article no. 104994. submission.
[24] E. Van Sebille, S. M. Griffies, R. Abernathey, et al., "Lagrangian ocean analysis: Fundamentals and practices", *Ocean Model.* **121** (2018), pp. 49–75.
[25] V. Onink, D. Wichmann, P. Delandmeter and E. Van Sebille, "The role of Ekman currents, geostrophy, and stokes drift in the accumulation of floating microplastic", *J. Geophys. Res. Oceans* **124** (2019), no. 3, pp. 1474–1490.
[26] L. Brach, P. Deixonne, M.-F. Bernard, et al., "Anticyclonic eddies increase accumulation of microplastic in the North Atlantic subtropical gyre", *Mar. Pollut. Bull.* **126** (2018), pp. 191–196.
[27] C. Maes, N. Grima, B. Blanke, E. Martinez, T. Paviet-Salomon and T. Huck, "A surface 'superconvergence' pathway connecting the South Indian Ocean to the subtropical South Pacific gyre", *Geophys. Res. Lett.* **45** (2018), no. 4, pp. 1915–1922.
[28] F. J. Beron-Vera, "Nonlinear dynamics of inertial particles in the ocean: from drifters and floats to marine debris and Sargassum", *Nonlinear Dyn.* **103** (2021), no. 1, pp. 1–26.
[29] G. G. Stokes, "On the theory of oscillatory waves", *Trans. Camb. Philos. Soc.* **8** (1847), pp. 441–455.

[30] T. S. van den Bremer and Ø. Breivik, "Stokes drift", *Philos. Trans. R. Soc. Lond., Ser. A* **376** (2018), no. 2111, article no. 20170104.

[31] T. S. van den Bremer, C. Whittaker, R. Calvert, A. Raby and P. H. Taylor, "Experimental study of particle trajectories below deep-water surface gravity wave groups", *J. Fluid Mech.* **879** (2019), pp. 168–186.

[32] S. G. Monismith, "Stokes drift: theory and experiments", *J. Fluid Mech.* **884** (2020), article no. F1.

[33] J. M. Alsina, C. E. Jongedijk and E. Van Sebille, "Laboratory Measurements of the Wave-Induced Motion of Plastic Particles: Influence of Wave Period, Plastic Size and Plastic Density", *J. Geophys. Res. Oceans* **125** (2020), no. 12, article no. e2020JC016294.

[34] R. Calvert, M. McAllister, C. Whittaker, A. Raby, A. Borthwick and T. Van Den Bremer, "A mechanism for the increased wave-induced drift of floating marine litter", *J. Fluid Mech.* **915** (2021), article no. A73.

[35] W. M. Kranenburg, J. S. Ribberink, R. E. Uittenbogaard and S. J. M. H. Hulscher, "Net currents in the wave bottom boundary layer: On waveshape streaming and progressive wave streaming", *J. Geophys. Res. Earth Surf.* **117** (2012), no. F3, article no. F03005.

[36] R. Calvert, A. Peytavin, Y. Pham, et al., "A Laboratory Study of the Effects of Size, Density, and Shape on the Wave-Induced Transport of Floating Marine Litter", *J. Geophys. Res. Oceans* **129** (2024), article no. e2023JC020661.

[37] A. Isobe, K. Kubo, Y. Tamura, E. Nakashima, N. Fujii, et al., "Selective transport of microplastics and mesoplastics by drifting in coastal waters", *Mar. Pollut. Bull.* **89** (2014), no. 1-2, pp. 324–330.

[38] T. J. W. Wagner, I. Eisenman, A. M. Ceroli and N. C. Constantinou, "How Winds and Ocean Currents Influence the Drift of Floating Objects", *J. Phys. Oceanogr.* **52** (2022), no. 5, pp. 907–916.

[39] K. Brunner, T. Kukulka, G. Proskurowski and K. L. Law, "Passive buoyant tracers in the ocean surface boundary layer: 2. Observations and simulations of microplastic marine debris", *J. Geophys. Res. Oceans* **120** (2015), no. 11, pp. 7559–7573.

[40] E. A. D'Asaro, A. Y. Shcherbina, J. M. Klymak, et al., "Ocean convergence and the dispersion of flotsam", *P. Natl. Acad. Sci. USA* **115** (2018), no. 6, pp. 1162–1167.

[41] M. Chamecki and T. Chor, "Effects of Turbulence on the Transport of Positively Buoyant Particles in the Ocean Mixed Layer", *Bulletin of the American Physical Society* **67** (2022), article no. T02.00002.

[42] M. Van der Mheen, C. Pattiaratchi and E. Van Sebille, "Role of Indian Ocean dynamics on accumulation of buoyant debris", *J. Geophys. Res. Oceans* **124** (2019), no. 4, pp. 2571–2590.

[43] N. T. Ouellette, P. J. J. O'Malley and J. P. Gollub, "Transport of Finite-Sized Particles in Chaotic Flow", *Phys. Rev. Lett.* **101** (2008), no. 17, article no. 174504.

[44] X. Chen, X. Xiong, X. Jiang, H. Shi and C. Wu, "Sinking of floating plastic debris caused by biofilm development in a freshwater lake", *Chemosphere* **222** (2019), pp. 856–864.

[45] H. Rouse, "Modern conceptions of the mechanics of fluid turbulence", *Transactions of the American Society of Civil Engineers* **102** (1937), no. 1, pp. 463–505.

[46] B. P. Greimann, M. Muste and F. M. Holly Jr, "Two-phase formulation of suspended sediment transport", *J. Hydraul. Res.* **37** (1999), no. 4, pp. 479–500.

[47] J. Chauchat, "A comprehensive two-phase flow model for unidirectional sheet-flows", *J. Hydraul. Res.* **56** (2018), no. 1, pp. 15–28.

[48] M. H. DiBenedetto, J. Donohue, K. Tremblay, E. Edson and K. L. Law, "Microplastics segregation by rise velocity at the ocean surface", *Environ. Res. Lett.* **18** (2023), no. 2, article no. 024036.

[49] K. Enders, R. Lenz, C. A. Stedmon and T. G. Nielsen, "Abundance, size and polymer composition of marine microplastics ≥10 μm in the Atlantic Ocean and their modelled vertical distribution", *Mar. Pollut. Bull.* **100** (2015), pp. 70–81.

[50] T. Kukulka, G. Proskurowski, S. Morét-Ferguson, D. W. Meyer and K. L. Law, "The effect of wind mixing on the vertical distribution of buoyant plastic debris", *Geophys. Res. Lett.* **39** (2012), no. 7, article no. L07601.

[51] Y. Tominaga and T. Stathopoulos, "Turbulent Schmidt numbers for CFD analysis with various types of flowfield", *Atmos. Environ.* **41** (2007), no. 37, pp. 8091–8099.

[52] L. Umlauf and H. Burchard, "A generic length-scale equation for geophysical turbulence models", *J. Mar. Res.* **61** (2003), no. 2, pp. 235–265.

[53] H. Michallet and M. Mory, "Modelling of sediment suspensions in oscillating grid turbulence", *Fluid Dyn. Res.* **35** (2004), no. 2, article no. 87.

[54] V. Mathai, V. N. Prakash, J. Brons, C. Sun and D. Lohse, "Wake-driven dynamics of finite-sized buoyant spheres in turbulence", *Phys. Rev. Lett.* **115** (2015), no. 12, article no. 124501.

[55] M. Bourgoin and H. Xu, "Focus on dynamics of particles in turbulence", *New J. Phys.* **16** (2014), no. 8, article no. 085010.

[56] H. R. S. Salmon, L. J. Baker, J. L. Kozarek and F. Coletti, "Effect of shape and size on the transport of floating particles on the free surface in a natural stream", *Water Resour. Res.* **59** (2023), no. 10, article no. e2023WR035716.

[57] K. L. Law, S. E. Morét-Ferguson, D. S. Goodwin, E. R. Zettler, E. DeForce, T. Kukulka and G. Proskurowski, "Distribution of surface plastic debris in the eastern Pacific Ocean from an 11-year data set", *Environ. Sci. Technol.* **48** (2014), no. 9, pp. 4732–4738.

[58] M. Poulain, M. J. Mercier, L. Brach, et al., "Small microplastics as a main contributor to plastic mass balance in the North Atlantic subtropical gyre", *Environ. Sci. Technol.* **53** (2018), no. 3, pp. 1157–1164.

[59] K. Waldschläger and H. Schüttrumpf, "Effects of particle properties on the settling and rise velocities of microplastics in freshwater under laboratory conditions", *Environ. Sci. Technol.* **53** (2019), no. 4, pp. 1958–1966.

[60] K. D. Goral, H. G. Guler, B. E. Larsen, et al., "Settling velocity of microplastic particles having regular and irregular shapes", *Environ. Res.* **228** (2023), article no. 115783.

[61] J. B. Will and D. Krug, "Rising and Sinking in Resonance: Mass Distribution Critically Affects Buoyancy-Driven Spheres via Rotational Dynamics", *Phys. Rev. Lett.* **126** (2021), no. 17, article no. 174502.

[62] B. R. Angle, M. J. Rau and M. L. Byron, "Settling of nonuniform cylinders at intermediate Reynolds numbers", *Phys. Rev. Fluids* **9** (2024), no. 7, article no. 070501.

[63] A. Roy, R. J. Hamati, L. Tierney, D. L. Koch and G. A. Voth, "Inertial torques and a symmetry breaking orientational transition in the sedimentation of slender fibres", *J. Fluid Mech.* **875** (2019), pp. 576–596.

[64] S. J. Bennett, J. F. Atkinson, Y. Hou and M. J. Fay, "Turbulence modulation by suspended sediment in a zero mean-shear geophysical flow", in *Coherent Flow Structures at Earth's Surface*, John Wiley & Sons, 2013, pp. 309–321.

[65] W. Fornari, S. Zade, L. Brandt and F. Picano, "Settling of finite-size particles in turbulence at different volume fractions", *Acta Mech.* **230** (2019), pp. 413–430.

[66] P. Nielsen, "Turbulence effects on the settling of suspended particles", *J. Sediment. Res.* **63** (1993), no. 5, pp. 835–838.

[67] G. H. Good, P. J. Ireland, G. P. Bewley, E. Bodenschatz, L. R. Collins and Z. Warhaft, "Settling regimes of inertial particles in isotropic turbulence", *J. Fluid Mech.* **759** (2014), article no. R3.

[68] W. Fornari, F. Picano, G. Sardina and L. Brandt, "Reduced particle settling speed in turbulence", *J. Fluid Mech.* **808** (2016), pp. 153–167.

[69] A. De Leo, L. Cutroneo, D. Sous and A. Stocchino, "Settling velocity of microplastics exposed to wave action", *J. Mar. Sci. Eng.* **9** (2021), no. 2, article no. 142.

[70] C. Gualtieri, A. Angeloudis, F. Bombardelli, S. Jha and T. Stoesser, "On the values for the turbulent Schmidt number in environmental flows", *Fluids* **2** (2017), no. 2, article no. 17.

[71] M. Poulain-Zarcos, *Étude de la distribution verticale de particules plastiques dans l'océan: caractérisation, modélisation et comparaison avec des observations*, PhD thesis, INPT, Toulouse, France, 2020.

[72] J. Chauchat, D. Hurther, T. Revil-Baudard, Z. Cheng and T.-J. Hsu, "Controversial turbulent Schmidt number value in particle-laden boundary layer flows", *Phys. Rev. Fluids* **7** (2022), no. 1, article no. 014307.

[73] M. Son, J. Byun, S. U. Kim and E.-S. Chung, "Effect of particle size on calibration of Schmidt number", *J. Coast. Res.* **3** (2016), no. 75, pp. 148–152.

[74] H. Rouse, "Experiments on the mechanics of sediment suspension", in *Proceedings of the fifth international congress for applied mechanics*, 1938, pp. 550–554.

[75] M. Poulain-Zarcos, M. J. Mercier and A. ter Halle, "Global characterization of oscillating grid turbulence in homogeneous and two-layer fluids, and its implication for mixing at high Peclet number", *Phys. Rev. Fluids* **7** (2022), no. 5, article no. 054606.

[76] P. D. Craig and M. L. Banner, "Modeling wave-enhanced turbulence in the ocean surface layer", *J. Phys. Oceanogr.* **24** (1994), no. 12, pp. 2546–2559.

[77] S. M. Thompson and J. S. Turner, "Mixing across an interface due to turbulence generated by an oscillating grid", *J. Fluid Mech.* **67** (1975), no. 2, pp. 349–368.

[78] E. J. Hopfinger and J.-A. Toly, "Spatially decaying turbulence and its relation to mixing across density interfaces", *J. Fluid Mech.* **78** (1976), no. 1, pp. 155–175.

[79] V. Onink, E. Van Sebille and C. Laufkötter, "Empirical Lagrangian parametrization for wind-driven mixing of buoyant particles at the ocean surface", *Geosci. Model Dev.* **15** (2022), no. 5, pp. 1995–2012.

[80] N. Gratiot, H. Michallet and M. Mory, "On the determination of the settling flux of cohesive sediments in a turbulent fluid", *J. Geophys. Res. Oceans* **110** (2005), no. C6, article no. C06004.

[81] M. P. Born, C. Brüll, D. Schaefer, G. Hillebrand and H. Schüttrumpf, "Determination of Microplastics' Vertical Concentration Transport (Rouse) Profiles in Flumes", *Environ. Sci. Technol.* **57** (2023), no. 14, pp. 5569–5579.

[82] W. G. Large, J. C. McWilliams and S. C. Doney, "Oceanic vertical mixing: A review and a model with a nonlocal boundary layer parameterization", *Rev. Geophys.* **32** (1994), no. 4, pp. 363–403.

[83] J. C. McWilliams and P. P. Sullivan, "Vertical mixing by Langmuir circulations", *Spill Sci. Technol. Bull.* **6** (2000), no. 3-4, pp. 225–237.

[84] J. C. McWilliams and E. Huckle, "Ekman layer rectification", *J. Phys. Oceanogr.* **36** (2006), no. 8, pp. 1646–1659.

[85] V. Onink, C. E. Jongedijk, M. J. Hoffman, E. Van Sebille and C. Laufkötter, "Global simulations of marine plastic transport show plastic trapping in coastal zones", *Environ. Res. Lett.* **16** (2021), article no. 064053.
[86] Y. Li, L. Xie and T. C. Su, "Profile of suspended sediment concentration in submerged vegetated shallow water flow", *Water Resour. Res.* **56** (2020), no. 4, article no. e2019WR025551.
[87] I. Eames, "Settling of particles beneath water waves", *J. Phys. Oceanogr.* **38** (2008), no. 12, pp. 2846–2853.
[88] F. Santamaria, G. Boffetta, M. Martins Afonso, A. Mazzino, M. Onorato and D. Pugliese, "Stokes drift for inertial particles transported by water waves", *Eur. Phys. Lett.* **102** (2013), article no. 14003.
[89] M. H. DiBenedetto, N. T. Ouellette and J. R. Koseff, "Transport of anisotropic particles under waves", *J. Fluid Mech.* **837** (2018), pp. 320–340.
[90] N. Pujara and J.-L. Thiffeault, "Wave-averaged motion of small particles in surface gravity waves: Effect of particle shape on orientation, drift, and dispersion", *Phys. Rev. Fluids* **8** (2023), article no. 074801.
[91] M. H. DiBenedetto, L. K. Clark and N. Pujara, "Enhanced settling and dispersion of inertial particles in surface waves", *J. Fluid Mech.* **936** (2022), article no. A38.
[92] M. H. DiBenedetto, J. R. Koseff and N. T. Ouellette, "Orientation dynamics of nonspherical particles under surface gravity waves", *Phys. Rev. Fluids* **4** (2019), no. 3, article no. 034301.
[93] L. K. Clark, M. H. DiBenedetto, N. T. Ouellette and J. R. Koseff, "Settling of inertial nonspherical particles in wavy flow", *Phys. Rev. Fluids* **5** (2020), no. 12, article no. 124301.
[94] M. R. Maxey and J. J. Riley, "Equation of motion for a small rigid sphere in a nonuniform flow", *Phys. Fluids* **26** (1983), pp. 883–889.
[95] L. Bergougnoux, G. Bouchet, D. Lopez and É. Guazzelli, "The motion of solid spherical particles falling in a cellular flow field at low Stokes number", *Phys. Fluids* **26** (2014), article no. 093302.
[96] M. Kooi, E. H. van Nes, M. Scheffer and A. A. Koelmans, "Ups and downs in the ocean: effects of biofouling on vertical transport of microplastics", *Environ. Sci. Technol.* **51** (2017), no. 14, pp. 7963–7971.
[97] P. Möhlenkamp, A. Purser and L. Thomsen, "Plastic microbeads from cosmetic products: an experimental study of their hydrodynamic behaviour, vertical transport and resuspension in phytoplankton and sediment aggregates", *Elem. Sci. Anth.* **6** (2018), article no. 61.
[98] E. R. Zettler, T. J. Mincer and L. A. Amaral-Zettler, "Life in the 'plastisphere': microbial communities on plastic marine debris", *Environ. Sci. Technol.* **47** (2013), no. 13, pp. 7137–7146.
[99] F. M. C. Fazey and P. G. Ryan, "Biofouling on buoyant marine plastics: An experimental study into the effect of size on surface longevity", *Environ. Pollut.* **210** (2016), pp. 354–360.
[100] L. A. Amaral-Zettler, E. R. Zettler, T. J. Mincer, M. A. Klaassen and S. M. Gallager, "Biofouling impacts on polyethylene density and sinking in coastal waters: a macro/micro tipping point?", *Water Res.* **201** (2021), article no. 117289.
[101] M. Yan, L. Wang, Y. Dai, H. Sun and C. Liu, "Behavior of Microplastics in Inland Waters: Aggregation, Settlement, and Transport", *Bull. Environ. Contam. Toxicol.* **107** (2021), no. 4, pp. 700–709.
[102] M. Long, B. Moriceau, M. Gallinari, C. Lambert, A. Huvet, J. Raffray and P. Soudant, "Interactions between microplastics and phytoplankton aggregates: Impact on their respective fates", *Mar. Chem.* **175** (2015), pp. 39–46.
[103] J. Michels, A. Stippkugel, M. Lenz, K. Wirtz and A. Engel, "Rapid aggregation of biofilm-covered microplastics with marine biogenic particles", *Proc. R. Soc. Lond., Ser. B* **285** (2018), no. 1885, article no. 20181203.
[104] A. Porter, B. P. Lyons, T. S. Galloway and C. Lewis, "Role of Marine Snows in Microplastic Fate and Bioavailability", *Environ. Sci. Technol.* **52** (2018), no. 12, pp. 7111–7119.
[105] J. D. Zardus, B. T. Nedved, Y. Huang, C. Tran and M. G. Hadfield, "Microbial biofilms facilitate adhesion in biofouling invertebrates", *Biol. Bull.* **214** (2008), no. 1, pp. 91–98.
[106] J. Zhang, Q. Zhang, J. P.-Y. Maa, et al., "Effects of organic matter on interaction forces between polystyrene microplastics: An experimental study", *Sci. Total Environ.* **844** (2022), article no. 157186.
[107] F. Mendrik, R. Fernández, C. R. Hackney, C. Waller and D. R. Parsons, "Non-buoyant microplastic settling velocity varies with biofilm growth and ambient water salinity", *Commun. Earth Environ.* **4** (2023), no. 1, article no. 30.
[108] Y. Li, X. Wang and a. Fu W. others, "Interactions between nano/micro plastics and suspended sediment in water: Implications on aggregation and settling", *Water Res.* **161** (2019), pp. 486–495.
[109] T. J. Andersen, S. Rominikan, I. S. Olsen, K. H. Skinnebach and M. Fruergaard, "Flocculation of PVC Microplastic and Fine-Grained Cohesive Sediment at Environmentally Realistic Concentrations", *Biol. Bull.* **240** (2021), no. 1, pp. 42–51.
[110] B. R. Sutherland, M. S. Dhaliwal, D. Thai, Y. Li, M. Gingras and K. Konhauser, "Suspended clay and surfactants enhance buoyant microplastic settling", *Commun. Earth Environ.* **4** (2023), no. 1, article no. 393.
[111] Z. Venel, H. Tabuteau, A. Pradel, et al., "Environmental Fate Modeling of Nanoplastics in a Salinity Gradient Using a Lab-on-a-Chip: Where Does the Nanoscale Fraction of Plastic Debris Accumulate?", *Environ. Sci. Technol.* **55** (2021), no. 5, pp. 3001–3008.

[112] C. Veclin, C. Desmet, A. Pradel, et al., "Effect of the Surface Hydrophobicity–Morphology–Functionality of Nanoplastics on Their Homoaggregation in Seawater", *ACS EST Water* **2** (2022), no. 1, pp. 88–95.

[113] A. Cózar, E. Martí, C. M. Duarte, et al., "The Arctic Ocean as a dead end for floating plastics in the North Atlantic branch of the Thermohaline Circulation", *Sci. adv.* **3** (2017), article no. e1600582.

[114] V. Onink, M. L. A. Kaandorp and C. Van Sebille E.and Laufkötter, "Influence of Particle Size and Fragmentation on Large-Scale Microplastic Transport in the Mediterranean Sea", *Environ. Sci. Technol.* **56** (2022), pp. 15528–15540.

[115] B. Singh and N. Sharma, "Mechanistic implications of plastic degradation", *Polym. Degrad. Stabil.* **93** (2008), pp. 561–584.

[116] A. ter Halle, L. Ladirat, X. G. Goudounèche, et al., "Understanding the fragmentation pattern of marine plastic debris", *Environ. Sci. Technol.* **50** (2016), no. 11, pp. 5668–5675.

[117] R. Okubo, A. Yamamoto, A. Kurima, T. Sakabe, Y. Ide and A. Isobe, "Estimation of the age of polyethylene microplastics collected from oceans: Application to the western North Pacific Ocean", *Mar. Pollut. Bull.* **192** (2023), article no. 114951.

[118] P. K. Lindeque, M. Cole, R. L. Coppock, et al., "Are we underestimating microplastic abundance in the marine environment? A comparison of microplastic capture with nets of different mesh-size", *Environ. Pollut.* **265** (2020), article no. 114721.

[119] M. George and P. Fabre, "Floating plastics in oceans: A matter of size", *Curr. Opin. Green Sustain. Chem.* **32** (2021), article no. 100543.

[120] R. C. Thompson, W. Courtene-Jones, S. Phal, K. Raubenheimer and A. A. Koelmans, "Twenty years of microplastics pollution research—what have we learned?", *Science* **386** (2024), no. 6720, article no. eadl2746.

[121] J. R. Gemmrich and D. M. Farmer, "Near-Surface Turbulence in the Presence of Breaking Waves", *J. Phys. Oceanogr.* **34** (2004), no. 5, pp. 1067–1086.

[122] M. Kooi, S. Primpke, S. M. Mintenig, C. Lorenz, G. Gerdts and A. A. Koelmans, "Characterizing the multidimensionality of microplastics across environmental compartments", *Water Res.* **202** (2021), article no. 117429.

[123] M. L. A. Kaandorp, H. A. Dijkstra and E. Van Sebille, "Modelling size distributions of marine plastics under the influence of continuous cascading fragmentation", *Environ. Res. Lett.* **16** (2021), article no. 054075.

[124] C. Brouzet, R. Guiné, M.-J. Dalbe, B. Favier, N. Vandenberghe, E. Villermaux and G. Verhille, "Laboratory model for plastic fragmentation in the turbulent ocean", *Phys. Rev. Fluids* **6** (2021), article no. 024601.

[125] I. Efimova, M. Bagaeva, A. Bagaev, A. Kileso and I. P. Chubarenko, "Secondary Microplastics Generation in the Sea Swash Zone With Coarse Bottom Sediments: Laboratory Experiments", *Front. Mar. Sci.* **5** (2018), article no. 313.

[126] I. Chubarenko, I. Efimova, M. Bagaeva, A. Bagaev and I. Isachenko, "On mechanical fragmentation of single-use plastics in the sea swash zone with different types of bottom sediments: Insights from laboratory experiments", *Mar. Pollut. Bull.* **150** (2020), article no. 110726.

[127] M. P. Born, C. Brüll and H. Schüttrumpf, "Implications of a New Test Facility for Fragmentation Investigations on Virgin (Micro)plastics", *Environ. Sci. Technol.* **57** (2023), pp. 10393–10403.

[128] G. Timár, J. Blömer, F. Kun and H. J. Herrmann, "New Universality Class for the Fragmentation of Plastic Materials", *Phys. Rev. Lett.* **104** (2010), no. 9, article no. 095502.

[129] C. Brouzet, G. Verhille and P. Le Gal, "Flexible Fiber in a Turbulent Flow: A Macroscopic Polymer", *Phys. Rev. Lett.* **112** (2014), no. 7, article no. 074501.

[130] K. Aoki and R. Furue, "A model for the size distribution of marine microplastics: A statistical mechanics", *PLoS ONE* **16** (2021), no. 11, article no. e0259781.

[131] S. Douady, Y. Couder and M. E. Brachet, "Direct observation of the intermittency of intense vorticity filaments in turbulence", *Phys. Rev. Lett.* **67** (1991), no. 8, pp. 983–986.

[132] S. Klein, M. Gibert, A. Bérut and E. Bodenschatz, "Simultaneous 3D measurement of the translation and rotation of finite-size particles and the flow field in a fully developed turbulent water flow", *Meas. Sci. Technol.* **24** (2013), article no. 024006.

[133] R. Monchaux, M. Berhanu, M. Bourgoin, et al., "Generation of a Magnetic Field by Dynamo Action in a Turbulent Flow of Liquid Sodium", *Phys. Rev. Lett.* **98** (2007), article no. 044502.

[134] M. George, F. Nallet and P. Fabre, "A threshold model of plastic waste fragmentation: New insights into the distribution of microplastics in the ocean and its evolution over time", *Mar. Pollut. Bull.* **199** (2024), article no. 116012.

[135] S. Allende, C. Henry and J. Bec, "Dynamics and fragmentation of small inextensible fibers in turbulence", *Philos. Trans. R. Soc. Lond., Ser. A* **378** (2020), no. 2175, article no. 20190398.

[136] K. L. Law, "Plastics in the Marine Environment", *Ann. Rev. Mar. Sci.* **9** (2017), pp. 205–229.

[137] L. Weiss, W. Ludwig, S. Heussner, et al., "The missing ocean plastic sink: Gone with the rivers", *Science* **373** (2021), no. 6550, pp. 107–111.

[138] M. Trainic, J. M. Flores, I. Pinkas, et al., "Airborne microplastic particles detected in the remote marine atmosphere", *Commun. Earth Environ.* **1** (2020), article no. 64.
[139] L. Van Cauwenberghe, L. Devriese, F. Galgani, J. Robbens and C. R. Janssen, "Microplastics in sediments: A review of techniques, occurrence and effects", *Mar. Environ. Res.* **111** (2015), pp. 5–17.
[140] J. Barrett, Z. Chase, J. Zhang, et al., "Microplastic Pollution in Deep-Sea Sediments From the Great Australian Bight", *Front. Mar. Sci.* **7** (2020), article no. 576170.
[141] K. Waldschläger, M. Z. M. Brückner, B. Carney Almroth, et al., "Learning from natural sediments to tackle microplastics challenges: A multidisciplinary perspective", *Earth-Sci. Rev.* **228** (2022), article no. 104021.
[142] A. Ballent, S. Pando, A. Purser, M. F. Juliano and L. Thomsen, "Modelled transport of benthic marine microplastic pollution in the Nazaré Canyon", *Biogeosciences* **10** (2013), no. 12, pp. 7957–7970.
[143] K. D. Goral, H. G. Guler, B. E. Larsen, S. Carstensen, E. D. Christensen, N. B. Kerpen, T. Schlurmann and D. R. Fuhrman, "Shields Diagram and the Incipient Motion of Microplastic Particles", *Environ. Sci. Technol.* **57** (2023), no. 25, pp. 9362–9375.
[144] P. R. Wilcock, "Methods for estimating the critical shear stress of individual fractions in mixed-size sediment", *Water Resour. Res.* **24** (1988), no. 7, pp. 1127–1135.
[145] C. E. Russell, R. Fernández, D. R. Parsons and S. E. Gabbott, "Plastic pollution in riverbeds fundamentally affects natural sand transport processes", *Commun. Earth Environ.* **4** (2023), no. 1, article no. 255.
[146] M. Pierdomenico, A. Bernhardt, J. T. Eggenhuisen, et al., "Transport and accumulation of litter in submarine canyons: a geoscience perspective", *Front. Mar. Sci.* **10** (2023), article no. 1224859.
[147] F. Pohl, J. T. Eggenhuisen, I. A. Kane and M. A. Clare, "Transport and Burial of Microplastics in Deep-Marine Sediments by Turbidity Currents", *Environ. Sci. Technol.* **54** (2020), no. 7, pp. 4180–4189.
[148] D. Bell, E. L. Soutter, Z. A. Cumberpatch, R. A. Ferguson, Y. T. Spychala, I. A. Kane and J. T. Eggenhuisen, "Flow-process controls on grain type distribution in an experimental turbidity current deposit: Implications for detrital signal preservation and microplastic distribution in submarine fans", *Depositional Rec.* **7** (2021), no. 3, pp. 392–415.
[149] I. A. Kane, M. A. Clare, E. Miramontes, R. Wogelius, J. J. Rothwell, P. Garreau and F. Pohl, "Seafloor microplastic hotspots controlled by deep-sea circulation", *Science* **368** (2020), no. 6495, pp. 1140–1145.
[150] F. Feddersen, "Scaling surf zone turbulence", *Geophys. Res. Lett.* **39** (2012), article no. L18613.
[151] W. R. Geyer and P. MacCready, "The Estuarine Circulation", *Annu. Rev. Fluid Mech.* **46** (2014), pp. 175–197.
[152] A. R. Horner-Devine, R. D. Hetland and D. G. MacDonald, "Mixing and Transport in Coastal River Plumes", *Annu. Rev. Fluid Mech.* **47** (2015), no. 1, pp. 569–594.
[153] P. Chardón-Maldonado, J. C. Pintado-Patiño and J. A. Puleo, "Advances in swash-zone research: Small-scale hydrodynamic and sediment transport processes", *Coast. Eng.* **115** (2016), pp. 8–25.
[154] T. Aagaard, J. Brinkkemper, D. F. Christensen, M. G. Hughes and G. Ruessink, "Surf Zone Turbulence and Suspended Sediment Dynamics—A Review", *J. Mar. Sci. Eng.* **9** (2021), article no. 1300.
[155] R. Lumpkin, N. Maximenko and M. Pazos, "Evaluating Where and Why Drifters Die", *J. Atmos. Ocean. Technol.* **29** (2012), pp. 300–308.
[156] Z. Chen, M. Bowen, G. Li, G. Coco and B. Hall, "Retention and dispersion of buoyant plastic debris in a well-mixed estuary from drifter observations", *Mar. Pollut. Bull.* **180** (2022), article no. 113793.
[157] J. Meyerjürgens, T. H. Badewien, S. P. Garaba, J.-O. Wolff and O. Zielinski, "A State-of-the-Art Compact Surface Drifter Reveals Pathways of Floating Marine Litter in the German Bight", *Front. Mar. Sci.* **6** (2019), article no. 58.
[158] R. Pawlowicz, "The Grounding of Floating Objects in a Marginal Sea", *J. Phys. Oceanogr.* **51** (2021), pp. 537–551.
[159] A. de Vos, L. Aluwihare, S. Youngs, et al., "The *M/V X-Press Pearl* Nurdle Spill: Contamination of Burnt Plastic and Unburnt Nurdles along Sri Lanka's Beaches", *ACS Environ. Au* **2** (2022), pp. 128–135.
[160] K. Critchell, A. Grech, J. Schlaefer, F. P. Andutta, J. Lambrechts, E. Wolanski and M. Hamann, "Modelling the fate of marine debris along a complex shoreline: Lessons from the Great Barrier Reef", *Estuar. Coast. Shelf Sci.* **167** (2015), pp. 414–426.
[161] M. L. A. Kaandorp, H. A. Dijkstra and E. Van Sebille, "Closing the Mediterranean marine floating plastic mass budget: Inverse modeling of sources and sinks", *Environ. Sci. Technol.* **54** (2020), pp. 11980–11989.
[162] M. L. A. Kaandorp, S. L. Ypma, M. Boonstra, H. A. Dijkstra and E. Van Sebille, "Using machine learning and beach cleanup data to explain litter quantities along the Dutch North Sea coast", *Ocean Science* **18** (2022), pp. 269–293.
[163] M. A. Browne, T. S. Galloway and R. C. Thompson, "Spatial Patterns of Plastic Debris along Estuarine Shorelines", *Environ. Sci. Technol.* **44** (2010), pp. 3404–3409.
[164] A. Turra, A. B. Manzano, R. J. S. Dias, M. M. Mahiques, L. Barbosa, D. Balthazar-Silva and F. T. Moreira, "Three-dimensional distribution of plastic pellets in sandy beaches: shifting paradigms", *Sci. Rep.* **4** (2014), article no. 4435.
[165] M. Zbyszewski, P. L. Corcoran and A. Hockin, "Comparison of the distribution and degradation of plastic debris along shorelines of the Great Lakes, North America", *J. Gt. Lakes Res.* **40** (2014), pp. 288–299.

[166] C. Eriksson, H. Burton, S. Fitch, M. Schulz and J. van den Hoff, "Daily accumulation rates of marine debris on sub-Antarctic island beaches", *Mar. Pollut. Bull.* **66** (2013), pp. 199–208.

[167] M. Compa, C. Alomar, M. Morató, E. Álvarez and S. Deudero, "Spatial distribution of macro-and micro-litter items along rocky and sandy beaches of a Marine Protected Area in the western Mediterranean Sea", *Mar. Pollut. Bull.* **178** (2022), article no. 113520.

[168] B. Davidson, K. Batista, S. Samrah, L. M. Rios Mendoza and N. Pujara, "Microplastic contamination of sediments across and within three beaches in western Lake Superior", *J. Gt. Lakes Res.* **48** (2022), pp. 1563–1572.

[169] P. L. Forsberg, D. Sous, A. Stocchino and R. Chemin, "Behaviour of plastic litter in nearshore waters: First insights from wind and wave laboratory experiments", *Mar. Pollut. Bull.* **153** (2020), article no. 111023.

[170] N. B. Kerpen, T. Schlurmann, A. Schendel, J. Gundlach, D. Marquard and M. Hüpgen, "Wave-Induced Distribution of Microplastic in the Surf Zone", *Front. Mar. Sci.* **7** (2020), article no. 590565.

[171] H. G. Guler, B. E. Larsen, O. Quintana, et al., "Experimental study of non-buoyant microplastic transport beneath breaking irregular waves on a live sediment bed", *Mar. Pollut. Bull.* **181** (2022), article no. 113902.

[172] N. B. Kerpen, B. E. Larsen, T. Schlurmann, et al., "Microplastic retention in marine vegetation canopies under breaking irregular waves", *Sci. Total Environ.* **912** (2024), article no. 169280.

[173] B. E. Larsen, M. A. A. Al-Obaidi, H. G. Guler, et al., "Experimental investigation on the nearshore transport of buoyant microplastic particles", *Mar. Pollut. Bull.* **187** (2023), article no. 114610.

[174] B. Davidson, J. Brenner and N. Pujara, "Beaching model for buoyant marine debris in bore-driven swash", *Flow* **3** (2023), article no. E35.

[175] P. Núñez, A. Romano, J. García-Alba, G. Besio and R. Medina, "Wave-induced cross-shore distribution of different densities, shapes, and sizes of plastic debris in coastal environments: A laboratory experiment", *Mar. Pollut. Bull.* **187** (2023), article no. 114561.

[176] R. G. Dean and R. A. Dalrymple, *Coastal Processes with Engineering Applications*, Cambridge University Press, 2004.

[177] N. Pujara, P. L. F. Liu and H. Yeh, "The swash of solitary waves on a plane beach: flow evolution, bed shear stress and run-up", *J. Fluid Mech.* **779** (2015), pp. 556–597.

[178] D. Cristaudo and J. A. Puleo, "Observation of munitions migration and burial in the swash and breaker zones", *Ocean Eng.* **205** (2020), article no. 107322.

[179] E. Murphy, I. Nistor, A. Cornett, A. Rayner, S. Baker and J. Stolle, "Application of an optical tracking technique to characterize nearshore wave-driven transport and dispersion of model driftwood", *Coast. Eng.* **189** (2024), article no. 104481.

[180] A. Emadzadeh and Y.-M. Chiew, "Settling velocity of porous spherical particles", *J. Hydraul. Eng.* **146** (2020), no. 1, article no. 04019046.

[181] J. Magnaudet and M. J. Mercier, "Particles, Drops, and Bubbles Moving Across Sharp Interfaces and Stratified Layers", *Annu. Rev. Fluid Mech.* **52** (2020), pp. 61–91.

[182] J. Brahney, N. Mahowald, M. Prank, G. Cornwell, Z. Klimont, H. Matsui and K. A. Prather, "Constraining the atmospheric limb of the plastic cycle", *Proc. Natl. Acad. Sci. USA* **118** (2021), no. 16, article no. e2020719118.

[183] C. Harb, N. Pokhrel and H. Foroutan, "Quantification of the Emission of Atmospheric Microplastics and Nanoplastics via Sea Spray", *Environ. Sci. Technol. Letters* **10** (2023), no. 6, pp. 513–519.

[184] I. Peeken, S. Primpke, B. Beyer, et al., "Arctic sea ice is an important temporal sink and means of transport for microplastic", *Nat. Commun.* **9** (2018), no. 1, article no. 1505.

[185] A. Pradel, M. Gautier, D. Bavay and J. Gigault, "Micro- and nanoplastic transfer in freezing saltwater: implications for their fate in polar waters", *Environ. Sci.: Processes Impacts* **23** (2021), no. 11, pp. 1759–1770.

[186] I. Chubarenko, I. Bocherikova, E. Esiukova, I. Isachenko, A. Kupriyanova, O. Lobchuk and S. Fetisov, "Microplastics in sea ice: A fingerprint of bubble flotation", *Sci. Total Environ.* **892** (2023), article no. 164611.

[187] M. M. Mrokowska and A. Krztoń-Maziopa, "Settling of microplastics in mucus-rich water column: The role of biologically modified rheology of seawater", *Sci. Total Environ.* **912** (2024), article no. 168767.

ACADÉMIE DES SCIENCES
INSTITUT DE FRANCE

Comptes Rendus. Physique
2024, Vol. 25, Special issue S3, p. 267-295
https://doi.org/10.5802/crphys.203

Review article / *Article de synthèse*

Geophysical and astrophysical fluid dynamics in the laboratory / *Dynamique des fluides géophysiques et astrophysiques au laboratoire*

From lab to landscape-scale experiments for the morphodynamics of sand dunes

Des expériences depuis l'échelle du laboratoire à celle du terrain pour la morphodynamique des dunes de sable

Philippe Claudin [*, a], **Sylvain Courrech du Pont** [b] **and Clément Narteau** [c]

[a] Physique et Mécanique des Milieux Hétérogènes, CNRS – ESPCI – PSL Research Univ. – Sorbonne Univ. – Univ. Paris Cité, Paris, France

[b] Laboratoire Matière et Systèmes Complexes, Univ. Paris Cité, CNRS, Paris, France

[c] Institut de Physique du Globe de Paris, Univ. Paris Cité, CNRS, Paris, France

E-mails: philippe.claudin@espci.fr (P. Claudin), sylvain.courrech@u-paris.fr (S. Courrech du Pont), narteau@ipgp.fr (C. Narteau)

Abstract. We review the main processes that drive the morphodynamics of dunes, i.e. their growth in height, migration and elongation, and emphasise the contribution of experiments to the understanding of these mechanisms. The main control parameters are the sediment flux Q and the saturation length L_{sat} associated with the spatial relaxation of the flux towards the transport capacity. The other relevant quantities are essentially dimensionless: fluid response to a bed perturbation, dune geometry (orientation, aspect ratio), transport ratios under multi-directional wind regimes. We argue that laboratory experiments dealing with sedimentary bedforms in water flows are good analogues to study the morphodynamics of aeolian dunes at reduced length and time scales, as L_{sat} and L_{sat}^2/Q are expected to be smaller for subaqueous bedload. Besides, dune shape and dynamics are mainly governed by flow and boundary conditions, independent of the transport mode. We discuss different experimental set-ups and results, especially concerning dune pattern orientation and dune interaction. Under natural wind regimes in terrestrial deserts, we show the potential of field experiments in which the control of initial and boundary conditions allows for the quantification of all the relevant mechanisms involved in dune growth. We emphasise the general agreement between observations, measurements and theoretical predictions, which indicates a robust comprehension of the underlying processes. This understanding can serve as a foundation for further investigations, including the interpretation of dune landscapes and the resolution of inverse problems.

Résumé. Nous passons en revue les principaux processus qui déterminent la morphodynamique des dunes, c'est-à-dire leur croissance en hauteur, leur migration et leur élongation, et nous mettons en avant la contribution des expériences pour la compréhension de ces mécanismes. Les principaux paramètres de contrôle sont le flux sédimentaire Q et la longueur de saturation L_{sat} associée à la relaxation spatiale du flux vers sa valeur à saturation homogène et stationnaire. Les autres quantités pertinentes sont essentiellement sans dimension : réponse du fluide à une perturbation du lit, géométrie des dunes (orientation, rapport d'aspect),

* Corresponding author

rapports entre les taux de transport sous des régimes de vent multidirectionnels. Nous expliquons que les expériences de laboratoire portant sur les formes de lit sédimentaires sous l'eau sont de bons analogues pour étudier la morphodynamique des dunes éoliennes à des échelles de longueur et de temps réduites, car L_{sat} et L_{sat}^2/Q sont typiquement plus petits pour le transport par charriage. En outre, la forme et la dynamique des dunes sont principalement gouvernées par les régimes d'écoulement et les conditions aux limites, indépendamment du mode de transport. Nous discutons différents montages expérimentaux et résultats, en particulier ceux qui concernent l'orientation des dunes et leur interactions. Pour les régimes de vents naturels dans les déserts terrestres, nous montrons le potentiel des expériences de terrain pour lesquelles le contrôle des conditions initiales et aux limites permet de quantifier tous les mécanismes pertinents impliqués dans la croissance des dunes. Nous soulignons le bon accord général entre les observations, les mesures et les prédictions théoriques, ce qui montre une bonne compréhension des processus qui sont à l'œuvre. Cette compréhension peut servir de base à d'autres recherches, comme par exemple l'interprétation des paysages dunaires et à la résolution de problèmes inverses.

Keywords. dune shape and dynamics, growth, orientation.

Mots-clés. forme et dynamique des dunes, croissance, orientation.

Funding. CN acknowledges the financial support of the French National Research Agency through grants ANR-18-IDEX-0001, and ANR-23-CE56-0008.

Manuscript received 2 June 2024, revised 29 August 2024, accepted 4 September 2024.

1. Introduction

Aeolian sand dunes display magnificent sedimentary patterns in various environments [1–3]: terrestrial deserts [4] and coastal areas [5], but also planetary surfaces such as those of Mars [6–8], Titan [9–11], Venus [12–14], Pluto [15] and comet 67P [16]. The shape, size and orientation of these dunes are determined by various factors, including the prevailing wind regime and the availability of sediment, as well as the hydrodynamic regimes [17]. On Earth, individual dunes span length scales from 10 to 10^3 m, and they can interact with each other in dune fields of hundreds of kilometres [4]. Small dunes emerge or react quickly to consistent winds over a few days, while large dunes and dune fields integrate wind regimes over long times. This integrative behaviour allows for a rich variety of shapes and makes it difficult to interpret a dune landscape in all its complexity. Dunes are thus witnesses of past winds and they have been used to constrain global climate models on the planetary bodies where they are observed. Performing comparative planetology in dune geomorphology is also a challenge due to the significant variability in environmental parameters.

To study the fundamental processes at work in dune dynamics, field observations take advantage of remote sensing to explore vast areas, but they are limited to a narrow range of time scales and often lack of sufficiently idealised configurations to specify the initial condition or separate coupled effects. Here we discuss the contribution of experiments in the understanding of dune pattern development, and this paper is constructed as follows. A first theoretical section briefly reviews the growing mode in height associated with a bed instability, and an elongation process in multidirectional wind regimes (Section 2). Section 3 describes laboratory experiments, where, in order to cut down space and time scales of aeolian transport processes, dune dynamics is analogously studied in water tanks and channels, where the grains are moved by a water flow. Section 4 is devoted to landscape-scale experiments, i.e., dealing in the field with actual space and time scales of the dune under controlled initial and boundary conditions.

Importantly, sedimentary bedforms also naturally develop in subaqueous environments, such as rivers and sea floors. Although we do exploit here the (partial) analogy between aeolian and subaqueous sediment transport, we will not review the vast literature on sedimentary subaqueous pattern, which includes not only ripples and dunes, but also other types like anti-dunes,

chevrons and bars associated with specific geometries and regimes of free-surface channelised water flows [18–33]. Furthermore, we will not address in detail the sensitivity of sediment transport to environmental parameters (e.g., fluid and grain density, grain size distribution). Instead, we will abstract sediment transport into a few key quantities that control the main features of dune development in all these different environments. Finally, we will not consider cohesion between grains, nor the effect of vegetation. These aspects are mentioned in the conclusion as perspectives.

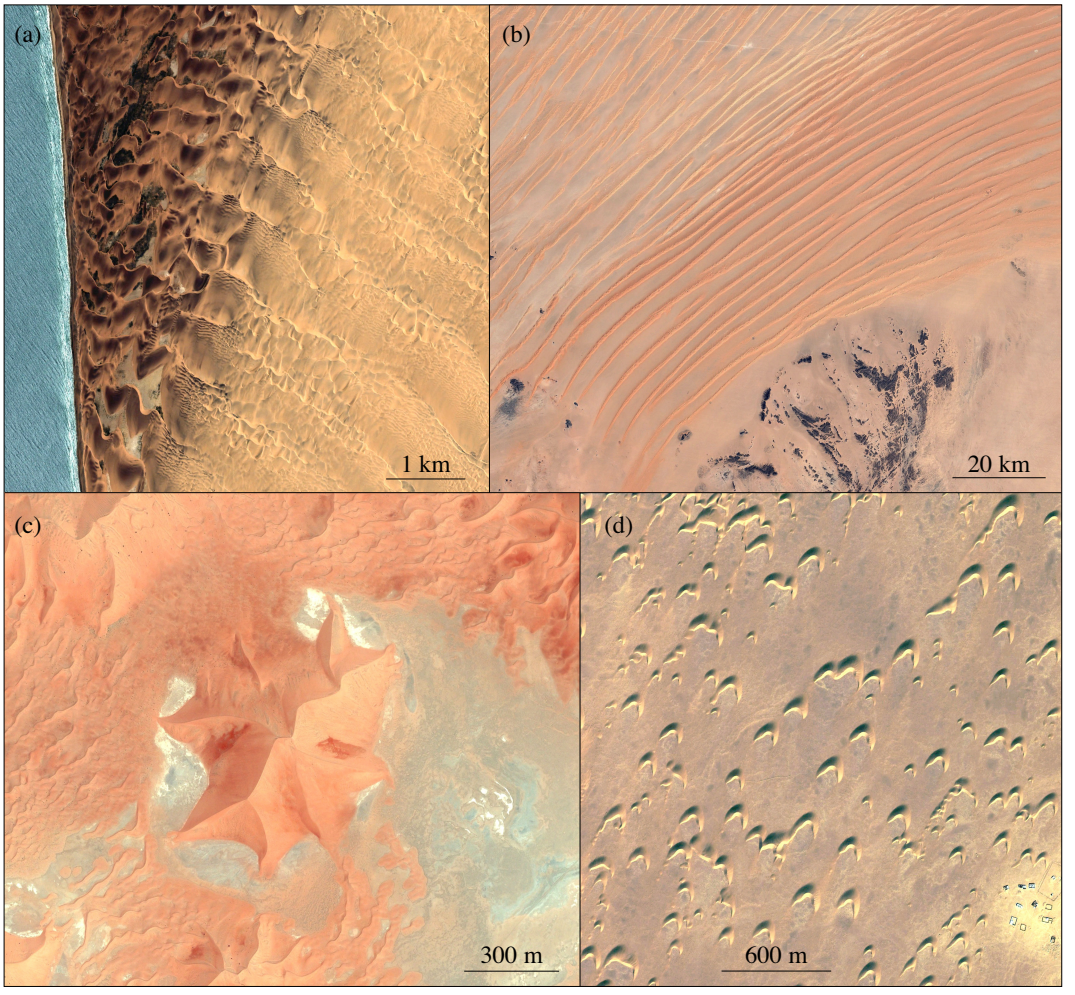


Figure 1. Various dune types on Earth. (a) Barchanoid ridges (left, along the coast) and transverse long-crested dunes (right, inland) in Angola (16.336° S, 11.836° E, November 2002, credit: Image Landsat / Copernicus). Dunes inland are transverse to the resultant direction [17]. (b) Linear dunes in the Rub al-Khali desert (16.817° N, 45.869° E, December 2010, credit: Image Landsat / Copernicus). (c) Star dune in the Rub al-Khali desert (20.388° N, 54.331° E, April 2007, credit: Maxar Technologie). (d) Field of barchan dunes in Occidental Sahara (27.20° N, 13.21° W, November 2022, credit: Maxar Technologies).

2. Dune theory

In order to present the general framework of dune pattern formation, it is first necessary to introduce the dimensionless numbers that concern sediment transport by a fluid flow over a granular bed [34–36]. We then review the instability mechanism by which dunes can emerge from a flat bed under a unidirectional flow [37–43]. We finally discuss the case of a multi-directional flow regime, especially where dunes can elongate over a consolidated substratum [44–47]. These theoretical considerations serve as a basis for the development and interpretation of the experiments, both in the laboratory and in the field.

2.1. *Key quantities for sediment transport*

A fluid flow over a granular surface can set the grains into motion when the shear stress it exerts on the bed exceeds a certain threshold. Three main dimensionless parameters controlling the corresponding sediment transport can be built [48]. Considering grains of bulk density ρ_p and diameter d in a fluid of density ρ_f and kinematic viscosity ν, we define the density ratio s, the Shields number Θ to rescale the bed shear stress $\rho_f u_*^2$, and the Galileo number $\mathcal{G}$ to rescale the viscosity. They write:

$$s = \rho_p/\rho_f, \qquad \Theta = u_*^2/u_g^2, \qquad \mathcal{G} = u_g d/\nu, \tag{1}$$

where g is the gravity acceleration, and $u_g = \sqrt{(s-1)gd}$ a reference velocity scale. As shown by numerical simulations [48], s essentially governs the transition from bedload (s of the order of a few units, the moving grains keep contact with the bed) to saltation (s larger than a few tens, the grains experience jumps and make dissipative rebounds when colliding with the bed). Θ quantifies the strength of the flow, especially with respect to the threshold value Θ_t below which transport vanishes. $\mathcal{G}$ distinguishes viscous ($\mathcal{G} < 1$) and turbulent ($\mathcal{G} > 1$) transport conditions, which affects particle drag and flow properties in general. Another important – yet not independent – quantity is the Reynolds number based on the grain size $\mathcal{R}_d = d u_*/\nu$. It tells whether the flow over this granular bed is in the smooth or rough regime [49,50].

Sediment transport can then be summarised into three key quantities. The first one is the already mentioned threshold Θ_t. The corresponding threshold velocity is then $u_t \propto u_g$. The second quantity is the saturated flux q_{sat} at given flow strength, i.e. the vertically integrated maximal amount of sediment that such a flow is capable to transport per unit time and width in the reference homogeneous and steady configuration. Defined as a volumic flux, its scaling factor is then $d u_g$. The actual flux q needs space to relax towards this saturated value if it changes (because wind speed increases for example). The length scale associated to this relaxation is the third quantity and is called the saturation length L_{sat} [37,38,51–54]. How u_t/u_g, $q_{\mathrm{sat}}/(d u_g)$ and L_{sat}/d vary with s, Θ and $\mathcal{G}$ is a current topic of research, especially in the context of sediment transport in planetary conditions [55–58]. However, the review of such studies is out of the scope of the present review. In fact, for the subject of this paper, generic behaviours are enough knowledge. For example, q_{sat} is an increasing function of Θ, typically linear in the case of aeolian (terrestrial) saltation: $q_{\mathrm{sat}} \propto d u_g(\Theta - \Theta_t)$ [55,59–63]. Also, the saturation length is significantly smaller for subaqueous bedload than for aeolian saltation, typically in proportion of s [52].

2.2. *Sand bed instability mechanism*

Here we briefly derive the linear stability analysis of a granular erodible bed submitted to a constant fluid flow, which contains the fundamental processes that contribute to the emergence and the growth of dunes [37,40,42]. We denote as $h(x,t)$ the bed elevation profile, which depends

on the direction of the flow x and time t. Bed elevation is related to the sediment flux q by mass conservation, which writes

$$\partial_t h + \vec{\nabla} \cdot \vec{q} = 0. \tag{2}$$

In the simple case of unidirectional flow considered here, the second term in Equation (2) reduces to $\partial_x q$. A flux increase ($\partial_x q > 0$) is associated with erosion ($\partial_t h < 0$), and inversely for flux decrease and sand deposition. As discussed in the previous subsection, q relaxes towards its saturated value $q_{\rm sat}$, and only the latter is an explicit function of the shear stress applied by the flow on the bed. A simple choice for this relaxation is to take it as a first order process, which we write [37]:

$$L_{\rm sat} \partial_x q = q_{\rm sat} - q, \tag{3}$$

but other options are possible [51,53,54].

Another piece of this analysis is the hydrodynamic response of the flow with respect to a perturbation of the bed elevation, in comparison to the reference case of a flat bed. This part writes simplest with a decomposition of the bed elevation profiles in Fourier modes. As we are interested in this subsection in the linear regime of the dune instability, we can consider the generic form for the bed perturbation (here in complex notation, real part is understood):

$$h(x,t) = \zeta e^{i(kx-\omega t)+\sigma t}, \tag{4}$$

where k is the wavenumber of the perturbation (or equivalently the wavelength $\lambda = 2\pi/k$), and ζ its amplitude. We will assume $k\zeta \ll 1$. The goal is to derive the dispersion relation that relates the growth rate σ and the phase velocity $c = \omega/k$ as a function of k. The bed shear stress in response to such a perturbation writes, at linear order in $k\zeta$:

$$\tau = \rho_f u_*^2 \left[1 + kh(\mathscr{A} + i\mathscr{B})\right], \tag{5}$$

where $\mathscr{A}$ and $\mathscr{B}$ are the in-phase and in-quadrature dimensionless shear stress coefficients. Experiments [64,65] and theoretical [39,66–70] analyses show that these coefficients are typically both positive, and of the order of unity. This means that the basal shear stress is in phase advance with respect to the bed elevation (Figure 2). In other words, the flow is maximum upstream of the ridge, by a distance $\sim \lambda\mathscr{B}/(2\pi\mathscr{A})$. Importantly, $\mathscr{A}$ and $\mathscr{B}$ are functions of $k\nu/u_*$, and also differ in the rough ($\mathscr{R}_d > 10$) and smooth ($\mathscr{R}_d < 1$) regimes in a range of wavenumbers around $10^3\, u_*/\nu$, associated with an anomalous response [42,49]. Here, for simplicity, we assume that $\mathscr{A}$ and $\mathscr{B}$ are constants, which essentially corresponds to the case of aeolian dunes in the rough regime.

The perturbation in shear stress (Equation (5)) can be transposed to the saturated flux for any given transport law relating $q_{\rm sat}$ to Θ, and a similar linear expression is obtained – strictly speaking, this is true when the transport threshold can be neglected, and things are slightly more complicated otherwise [42,71]. Importantly, τ and $q_{\rm sat}$ are in phase, but, as a consequence of the spatial relaxation (Equation (3)), q lags downstream of $q_{\rm sat}$ by $L_{\rm sat}$ (Figure 2). Assuming that $L_{\rm sat}$ is a constant [52], it is possible to solve these expressions in order to determine the growth rate of a bed perturbation of wavenumber k,

$$\sigma = \frac{Q}{L_{\rm sat}^2} (kL_{\rm sat})^2 \frac{\mathscr{B} - \mathscr{A}\, kL_{\rm sat}}{1 + (kL_{\rm sat})^2}, \tag{6}$$

where the reference flux $Q = \tau \partial_\tau q_{\rm sat}$ is here defined as the susceptibility of the saturated flux with respect to the shear stress [37,40,42,72]. The numerator of this function, which determines the sign of σ, reflects the competition between a hydrodynamic destabilising process associated with the upstream shift of the shear stress (positive contribution to σ, larger $\mathscr{B}/\mathscr{A}$) and a stabilising process associated with the downstream lag of the flux (negative contribution to σ, larger $L_{\rm sat}$). In particular, this function shows a cut-off length, or a minimal wavelength, below which all perturbations are stable: $\lambda_{\rm min} = 2\pi L_{\rm sat}\mathscr{A}/\mathscr{B}$. The most unstable wavelength is for $\lambda_{\rm max} \simeq 2\lambda_{\rm min}$.

A metre-scale value of the saturation length for aeolian saltation [52] gives $\lambda_{\max}$ on the order of 15–30 m, in good agreement with observations [72–75]. The typical growth time of the instability is $L_{\rm sat}^2/Q$, i.e. typically of the order of a few hours during a storm event [72], or on the order of a few weeks if we consider more regular intermittent wind conditions in terrestrial deserts [75].

Another important point is that this bed instability is convective, and one can also derive the velocity c of the bed perturbation of wavenumber k from the linear analysis. It reads:

$$c = \frac{Q}{L_{\rm sat}}\, kL_{\rm sat}\, \frac{\mathscr{A} + \mathscr{B} kL_{\rm sat}}{1 + (kL_{\rm sat})^2}\,. \tag{7}$$

For small values of $kL_{\rm sat}$, that is for large enough bed wavelength, $c \simeq Q\mathscr{A}k$, a scaling proportional to Q and inversely to bedform size that is recovered for developed dunes and sometimes named Bagnold's law for propagative dunes (barchan in particular) [76,77]. As seen below, the fact that larger dunes migrate slower is an important process for the transverse instability (Section 2.4).

Given the assumptions under which it has been derived, Equation (6) provides a theoretical dispersion relation that can be generalised to all environment according to few generic quantities, namely Q, $L_{\rm sat}$, $\mathscr{A}$ and $\mathscr{B}$. The transition from the meter scale of saturation length in a context of aeolian saltation to a millimetre scale (predicted, but yet unmeasured) for underwater bedload allows for a downscaling of pattern emergence from tens of meters and weeks in terrestrial deserts to centimetres and a tens of seconds in an underwater environment, while preserving the primary physical processes. These numbers are of course for the linear regime of the instability. Once the pattern grows in height, non-linearities soon appear. They are first associated with the hydrodynamic response relating τ to h [64,78], then with the development of an avalanche slip face on the downstream side of the bumps [75], and later to the coarsening dynamics characterised by the rearrangement/elimination of pattern defects [79] and interactions between bedforms behaving as individual objects [72,80–83]. However, the working hypothesis for the laboratory experiments is that the downscaling methodology remains valid for non-linear processes, including the long-term dynamics of dune fields.

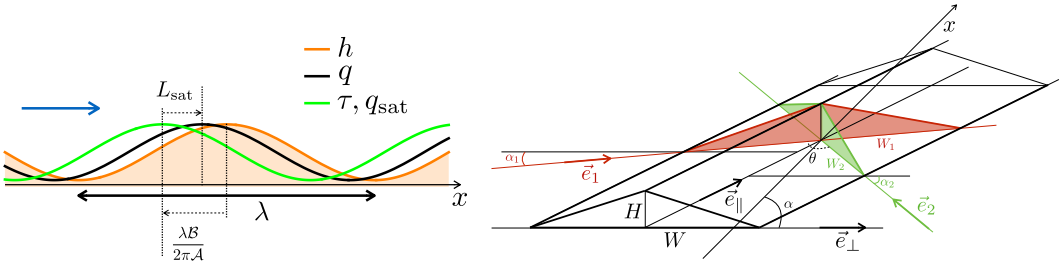


Figure 2. Left panel: Schematic illustration of the upstream shift $\sim \lambda\mathscr{B}/(2\pi\mathscr{A})$ of the basal shear stress τ with respect to the bed elevation profile h, and the spatial lag $L_{\rm sat}$ between the saturated flux $q_{\rm sat}$ and the actual flux q. Flow is from left to right, in the x-direction. Right panel: Schematics of two winds blowing alternately over a symmetric triangular dune of height H and width W. The normal- and parallel-to-crest directions are aligned with $\vec{e}_\perp$ and $\vec{e}_\parallel$, respectively. The primary wind 1 (resp. the secondary wind 2) blows along the direction $\vec{e}_1$ ($\vec{e}_2$), making an angle α_1 (α_2) with respect to $\vec{e}_\perp$. It sees an apparent dune width W_1 (W_2). The reference x-axis is along the bisector of the two winds, which make a divergence angle θ. The orientation α of the dune is defined as the angle made by $\vec{e}_\perp$ with respect to x.

2.3. *Multi-directional flow regime*

The above linear analysis can be generalised in the case of a multi-directional flow regime, which we discuss here for simplicity in the bidirectional case [71]. As schematised in Figure 2, the primary and secondary flows are associated with time duration $t_{1,2}$, reference fluxes $Q_{1,2}$ and directions along unitary vectors $\vec{e}_{1,2}$. We call θ the divergence angle between these two directions, take the x-axis as their bisector, and define the transport ratio $N = Q_1 t_1/(Q_2 t_2) > 1$ between the two flows [44,84–86]. The period of flow reorientation $t_1 + t_2$ is assumed to be small in comparison to the characteristic growth time of the dune. The existence of this time period associated with the flow change provides an additional length scale to the problem. We can define $W_R = \sqrt{Q_1 t_1}$. It sets the typical streamwise size below which a dune loses the memory of its past shape after the primary wind has blown, and thus does not integrate the entire wind regime. In what follows, we consider that $W > W_R$.

In this case, the most unstable mode not only selects a preferred wavelength $\lambda_{\max}$ but also an orientation angle $\alpha_{\max}$ of the dune pattern with respect to the x-direction. These two quantities depend of course on N and θ [71]. If N is close to one, $\alpha_{\max}$ shows a transition from an orientation roughly transverse to the resultant flux $\vec{q}_{\text{sat}}$ when $\theta < \pi/2$ (i.e., $\alpha_{\max}$ close to 0) to an orientation roughly aligned with the resultant flux when $\theta > \pi/2$ (i.e., $\alpha_{\max}$ close to $\pi/2$), see Figure 3. Both winds contribute to the dune elevation regardless of which dune side they blow on, which explains the change in dune orientation with θ. By contrast, $\lambda_{\max}$ is less dependent on N and θ.

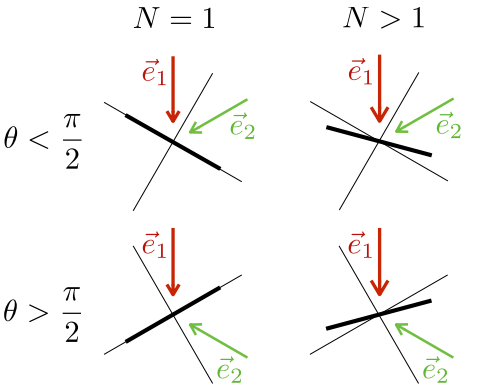


Figure 3. Schematics of the dune orientation when the wind divergence angle θ is smaller (upper row, dune mostly perpendicular to the resultant) or larger (lower row, dune mostly along the resultant) than $\pi/2$. The selected orientation tends to be more perpendicular to the dominant wind 1 as the transport ratio N increases (right column).

These results for dune orientation derived in the limit of emerging bedforms with a small aspect ratio ($k\zeta \ll 1$) [71] are consistent with those obtain by a geometric approach [44], which entirely reduces the role of hydrodynamics on the estimation of the flow speed-up at the crest [87], and neglects sediment transport relaxation (the spatial lag L_{sat}). For transverse dunes of width W and finite height H lying on a flat bed, the flux at the crest writes $q^c = Q(1+\gamma)$, where the flux-up factor γ is proportional to the dune aspect ratio H/W (a typical value $\gamma \simeq 1.7$ for an aspect ratio around $1/12$). In the linear analysis for a unidirectional wind, we can derive $\gamma \propto k\zeta\sqrt{\mathscr{A}^2 + \mathscr{B}^2}$, where $k\zeta$ is indeed proportional to the aspect ratio of the transverse bed perturbation. In the

considered bimodal flow regime, introducing the angle $\alpha_{1,2}$ between the flow and the normal-to-crest direction, the apparent dune width exposed to the flow is $W_{1,2} = W/\cos\alpha_{1,2}$, so that the flux at the crest is

$$\vec{q}^c_{1,2} = Q_{1,2}\left(1+\gamma\cos\alpha_{1,2}\right)\vec{e}_{1,2}. \tag{8}$$

Their contributions add up in

$$\vec{q}^c = \frac{t_1}{t_1+t_2}\vec{q}^c_1 + \frac{t_2}{t_1+t_2}\vec{q}^c_2 = \vec{q}^c_\perp + \vec{q}^c_\parallel, \tag{9}$$

where $\vec{q}^c_\perp$ and $\vec{q}^c_\parallel$ are the normal- and parallel-to-crest components of the mean transport rate, respectively. With the approximation that the growth rate associated with each flow is $\sigma_{1,2} \simeq q^c_{1,2}/(HW_{1,2})$, the most unstable mode corresponds to the dune orientation for which the sum $\sigma_1+\sigma_2$, i.e. $q^c_\perp$, is maximum – also referred to as the gross bedform-normal rule [44,84]. The resulting selected angle is in good agreement with the one obtained from the linear theory [71], emphasising the key process of dune growth in height by sand transport in the direction perpendicular to the crest.

2.4. *Elongation mechanism and migration on sediment-starved beds*

Dunes may also form on consolidated beds that are partially devoid of mobile sediment. This configuration is far from those for which the aforementioned linear stability analysis can be applied. Instead of a periodic dune pattern emerging as the result of erosion and deposition of a surface fully covered with sand, dunes develop as isolated objects on the non-erodible bed. As the variability of wind regimes increases, from a unimodal to a multimodal distribution of wind orientation, these dunes may take on a crescentic shape, such as barchans or asymmetric barchans, or a long shape, including linear and seif dunes [44–46,86,88–90] as well as the individual arms of star dunes [91]. The elongation of these arms or linear dunes is driven by the sediment transported along the crest ($q^c_\parallel > 0$), when the winds alternatively hit both sides of the crest. As seen from the above equations, this process, controlled by aspect ratios, is scale free. When these dunes do not migrate, their orientation is that of the main flux and the net flux perpendicular to the crest vanishes: $q^c_\perp = 0$, as well predicted by the geometric approach of [44]. As for the bed instability mechanism under multidirectional flow conditions (Section 2.3), elongation only occurs if the size of the dune is greater than W_R, in order to be able to integrate all flow contributions.

The elongation dynamics of a dune from a fixed sand source has been studied by numerical simulations, where the wind regime is bimodal and the sediment injection rate $J_{\min}$ is constant [47]. The dune grows from the source area without migrating. If $J_{\min}$ is large enough, the dune eventually reaches a steady state, with a roughly triangular cross-section of constant aspect ratio as width and height decrease linearly from the source area. The length of the dune is proportional to the ratio $J_{\min}/q_{\text{out}}$, where q_{out} is the outflux that escapes from the dune uniformly at all cross-sections. At the tip of the dune in the direction of elongation, the section is successively swept by flows impacting from either side of the crest. The authors of [47] suggest that the tip size is controlled by the its cut-off length $\lambda_{\min}$, i.e. related to L_{sat} again. Another possibility is that the dune ends where the transverse instability (see below) can break it, i.e. where its width is on the order of W_R. Elongating dunes are thus strongly linked to their sediment supply, and they often develop from large dunes or at the edge of sand seas. In these cases, the resulting dune field displays a typical spatial periodicity. Numerical simulations have shown that the corresponding wavelength can be inherited from the bed instability developing on the sediment layer, which serves as governing boundary or initial conditions [44,92].

A last generic configuration is that of dunes that are not attached to a source but can migrate over such a consolidated bed. The simplest case is that of a sand bar of height H transverse

to a unidirectional flow. Their migration velocity follows Bagnold's scaling in Q/H, associated with mass conservation at the downwind avalanche slipface [34,76]. The migration of the dunes induces an instability that tends to break the transverse structure into smaller dunes whose length and width are both of the order of H [93,94]. This instability, called transverse instability, results from the positive feedback loop between the migration rate of the longitudinal sections of the dune and the transverse sediment fluxes: lower sections tend to migrate faster than higher ones, curving the avalanche slipface, which redirects the sand towards the highest parts, thus amplifying the phenomenon. This is also what is likely to happen when dunes under multidirectional wind regimes are smaller than W_R, which prevents them to elongate.

3. Laboratory-scale experiments

The minimum size of aeolian dunes, on the order of 10 m in length on Earth, make them difficult to reproduce in laboratory-scale experiments. The alternative is to study subaqueous sedimentary bedforms, which can be downscaled to a length of about a centimetre. Increasing the fluid density (decreasing the density ratio s) lowers the threshold fluid velocity for grain entrainment and increases the fluid inertia relative to grain inertia, which consequently reduces the saturation length and the corresponding minimum size for bedforms under water compared to the aeolian case.

The details of sediment transport in subaqueous conditions, typically bedload when the Shields number is not too large, are of course different than those of aeolian saltation. But although the key parameters such as the saturation length L_{sat} and the reference sediment flux Q scale differently with respect to grain and fluid characteristics [48], the physical background of the dune theory (Section 2) is discussed without referring to any particular transport law. A caveat, however is that, as opposed to air flows over saltating grains for which the regime is typically rough, water flows over granular surfaces are more likely to be in the smooth regime, where, depending on grain size and bedform wavelength, a specific hydrodynamic response can occur, which affects the coefficients $\mathscr{A}$, $\mathscr{B}$ [42,49]. In this case, the viscous length ν/u_* comes as an additional relevant length scale for the minimum size for bedforms. Nevertheless, like aeolian dunes, these subaqueous sedimentary bedforms form from the positive feedback loop between the bed topography, the fluid flow, and the sediment transport, with analogous generic processes at play for their formation and dynamics.

As illustrated in this section, underwater experiments have proven useful in understanding sandy desert landscapes, especially regarding the shape of dunes in response to flow forcing and sand supply conditions, as well as interactions between dunes or with a fixed obstacle. The morphology and migration velocity of subaqueous barchans in experiments have been compared to aeolian barchan on Earth by several authors [95–97] and recently reviewed in [98]. For example, the aspect ratio of height to width is similar and, importantly, both aeolian and subaqueous barchans migrate at a velocity inversely proportional to their height $c \propto Q/H$. However, subaqueous barchans have a slightly larger ratio of width to length and a smaller ratio of horn length to length than aeolian barchans (see Figures 1 and 4 for photographs of barchans).

Noteworthy, in the context of fluvial or oceanographic geomorphology, periodic underwater bedforms of small wavelength (typically smaller than a few tenth of centimetres) are commonly referred to as ripples, whereas larger bedforms (larger than a few meters) are referred to as dunes [99]. Here we consider underwater bedform to be analogous to aeolian dunes with respect to the morphodynamical processes and we will indistinctly use the term "dune" for both of them. As these subaqueous dunes are smaller, the characteristic times associated with their evolution

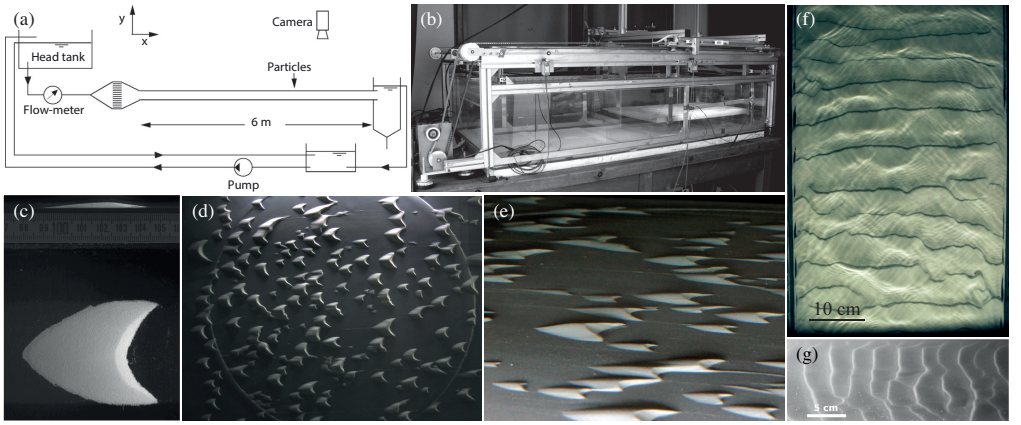


Figure 4. Different experimental setups, barchan (crescentic) and periodic transverse dunes in unidirectional flow. (a) Sketch of the closed water channel used in [100]. The flow is driven by gravity from the head tank. A convergent and honeycomb system eliminates large turbulent eddies. A tank at the end of the channel collects sand grains and a pump refills the head tank. The channel section is 12 cm wide and 6 cm high. (b) Photograph of the setup used in [86]. A tray (80 cm wide and 90 cm long, here on the right of the tank) oscillates in a water tank (2 m long, 1 m wide, and filled with 50 cm of water). The translation motion is asymmetric. (c) Barchan dune in setup (a) [100]. Flow is from left to right. A barchan dune has a characteristic crescent shape with two horns (or arms) pointing in the dowstream direction. It has a gentle slope (~ 0.1) on the upstream side and an avalanche face on the lee side. (d) & (e) Field of barchan dunes in setup (b) (Photo credit: S. Courrech du Pont). The disk is 70 cm wide. Flow is from left to right. (f) Periodic transverse dunes in an open (free surface) channel setup. Flow is upward. Photo credit: A. Valance and L. Guignier. (g) Periodic transverse dunes in a closed channel, from [27]. Flow is from right to left. In (f) and (g), dunes are fully developed and exhibit avalanche faces in the lee side. Early pattern is straighter.

are also smaller, allowing "long time ranges" to be observed in laboratory experiments. This is of particular interest because dunes can integrate flows for long periods of time.

3.1. *Experimental setups*

Subaqueous sand patterns have been studied in flumes, which are either pipes [28,101], open [85,102,103], or closed channels [27,100,104–107], or using an oscillating tray [44,80] (Figure 4). The confined pipe geometry is not ideal for studying dune morphodynamics as observed in natural environments, but grain or powder entrainment and pattern formation in such a configuration [28] are relevant to industry [101].

Water channel with a rectangular section is the most commonly used device. The flow can be driven by pumps, propellers, or by gravity, which does not produce noise as engines do. Divergent-convergent devices combined to honeycomb help to minimise turbulent eddies. In open channels, the flow can generate unwanted waves at the free surface. Closed channels seem more appropriate and facilitate the use of gravity to drive the flow. The flat top surface

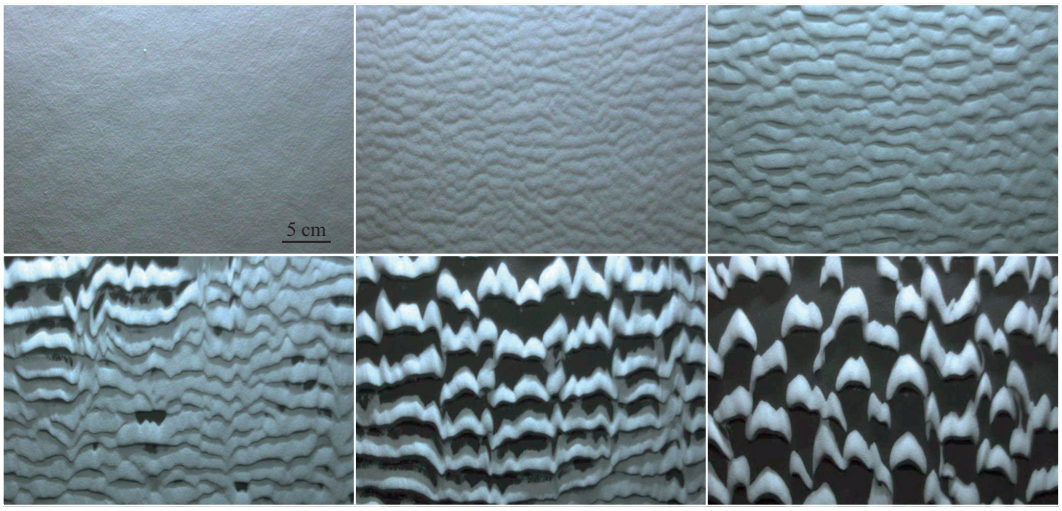


Figure 5. Sand bed of limited thickness subjected to a unidirectional flow. Flow is from top to bottom (translated tray setup). Images were taken after none, 40, 180, 410, 560, and 930 tray strokes. Experiment images are from [86].

also simplifies visualisation. With transparent walls, water channels enable PIV to characterise the flow with or without dunes [27,108] and to follow the paths of individual grains [109]. Some channels are intentionally narrow to study two-dimensional dunes [104,105,110]. These setups are appropriate to study the development of periodic dunes from the destabilisation of a sand bed or single isolated dunes in unidirectional flows. Regarding interactions between dunes, care must be taken when extrapolating results to three-dimensional dunes. Although some experiments have been conducted in large flumes [85], the width of the channel is typically between 10 and 20 cm in laboratory [27,100,103], which limits the number of dunes in the cross-section or the study of dunes in multidirectional flows, as is often the case in Earth deserts where wind directions change with seasons [43]. To study dunes in multidirectional flows, the sand bed is placed on a horizontal turntable that rotates to change the direction of the sand bed with respect to the water flow [86,89]. The width of the setup then limits the length of the dune field.

A way to increase the dimension of the field and to avoid the need for a large flow rate is to use an oscillating tray, which can also be a turntable [86,95]. The oscillating tray's back-and-forth motion is asymmetric, with acceleration and velocity above the transport threshold in one direction and below the threshold in the other. At the end of the fast motion, the tray slowly decelerates to avoid backflow in the tray's reference frame. The repetition of this oscillating motion simulates a unidirectional flow over the bed. The main advantage of this setup is the size of the field that can be studied, a disk of 70 cm in diameter in [86]. Since the tray is at rest twice during the motion cycle, this setup also facilitates controlled sand supply, which is an important parameter when studying dune fields. The main drawbacks are that these experiments take longer than in flumes, and that the intermittent flow and sand transport are difficult to characterise.

In all setups, grains are glass, zirconium, or ceramic beads of diameter ranging from 50 μm to 1 mm and flow velocities typically range from 20 to 70 cm/s. These values give dimensionless numbers on the order of $s \simeq 2$–7, $\Theta \simeq 0.5$–3 and $\mathscr{G} \simeq 1$–100.

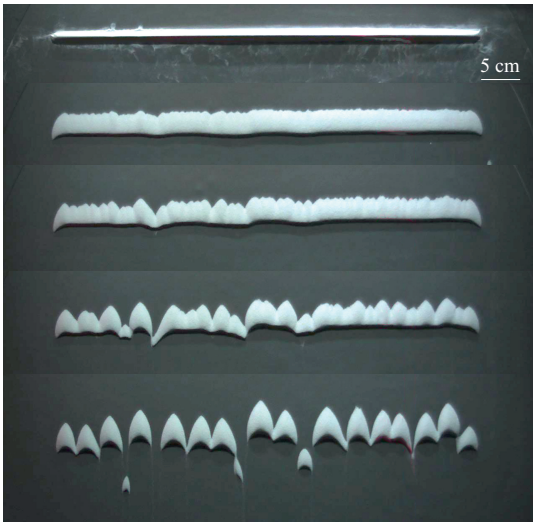


Figure 6. Instability of an isolated transverse ridge migrating on a starved bed. Flow is from top to bottom (translated tray setup). Images were taken after none, 40, 100, 200, 400, and 800 tray strokes. Images are from [86].

3.2. *Dune instability*

Experiments have shown that a fully sand covered bed, initially flat, destabilises into a periodic migrating pattern with a well-defined wavelength and velocity. In steady flow, the initial wavelength is about 15 mm for glass beads of 100 µm and friction velocity in between 15 and 20 mm/s [27]. With such small patterns, the three-step feed-back mechanism (topography / fluid friction velocity / sediment flux) described in Section 2.2 has not been directly verified in laboratory experiments – the corresponding thickness of the boundary layers and saturation length are too small. No linear regime is observed in the development of the instability (exponential growth of amplitude with a constant wavelength) in laboratory setups, probably because it is too short, but rather a coarsening of the pattern from the beginning [27,28,44,86]. A linear regime has however been observed during 150 s in a natural river with a bedform wavelength of about 9 cm for grain of diameter 0.3 mm and a shear velocity of 4 cm/s [70].

3.3. *Dunes in multidirectional flows and different sand supply conditions - the two dune growth mechanisms*

The relationship between wind regimes and dune type, shape and orientation is at the heart of dune studies, not least because dunes and their deposits are proxies for past winds. Most experimental studies focus on understanding equilibrium shapes and how dunes respond to changes in wind regime or sand supply conditions, the two main factors controlling free dune type (free dunes are dunes for which wind and sand transport are not constrained by other factors such as obstacles or vegetation [17,111–113]). Here we discuss a selection of experiments, which together with numerical simulations (e.g., [41,88,91,114]), have shown that dune shape is controlled by its dynamics, which can be decomposed in the three processes of growth in height, migration and elongation [17]. The relative balance of these three dynamics is mainly controlled by flow regime and sediment supply and availability [17].

Under unidirectional flow and on a fully covered sand bed, dunes grow continuously as periodic long ridges perpendicular to the flow direction (transverse dunes), from the excavation

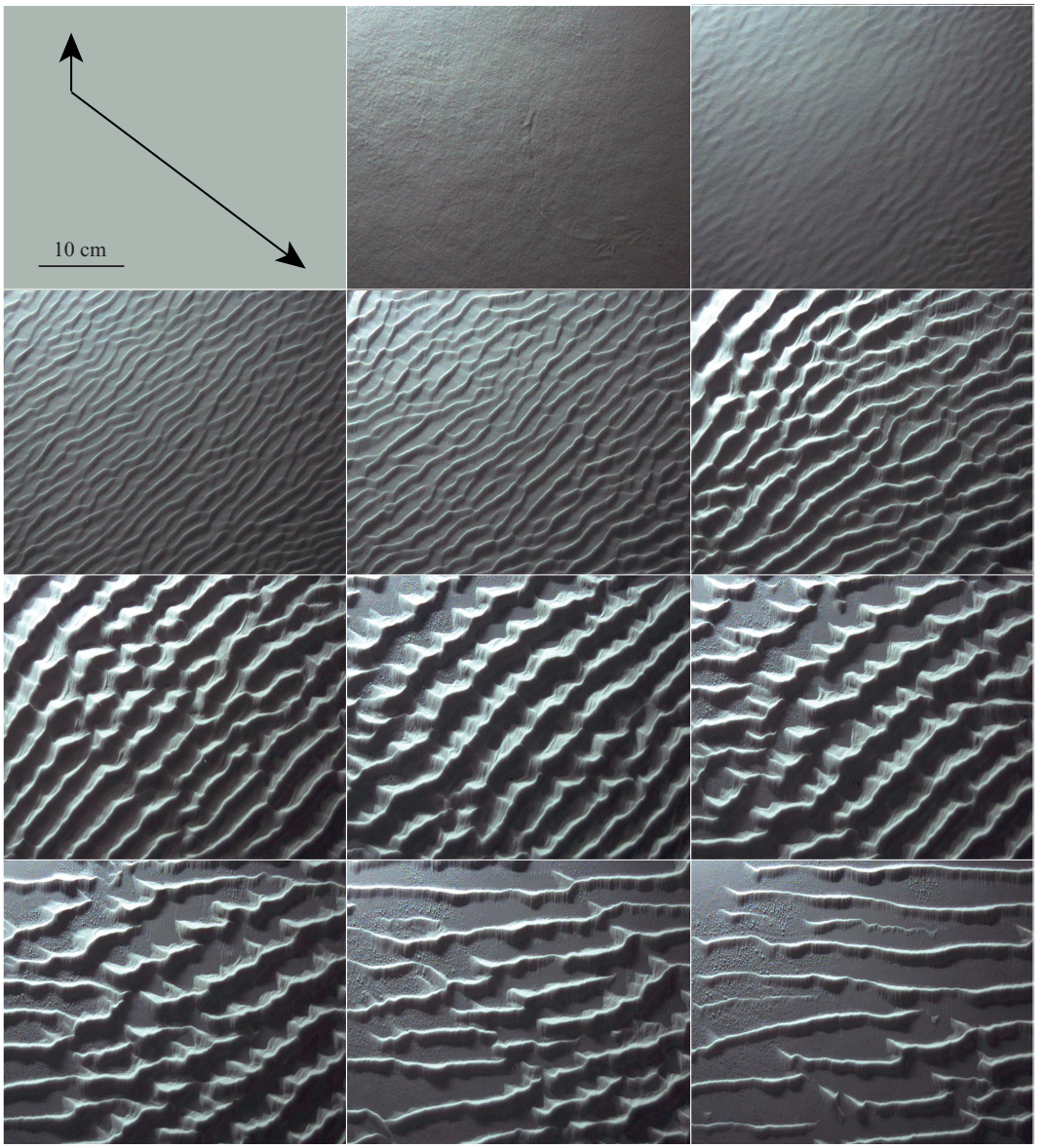


Figure 7. Sand bed of limited thickness subjected to a periodic bidirectional flow (translated tray setup). First panel shows the flow regime. The two flow directions form an angle $\theta = 130°$. The tray alternatively translates 10 times in the primary flow direction and 2 times in the secondary flow direction; the transport ratio N between the primary and the secondary flows equals 5. Images were taken at the end of the upward secondary flow after none, 1, 3, 7, 12, 16, 30, 40, 50, 65, and 85 cycles (one cycle counts $10 + 2 = 12$ tray strokes). Photo credit: S. Courrech du Pont, from experimental set-up of [44].

of the underlying substrate and coarsening. When the thickness of the sand bed is limited, the bed gets progressively starved and the transverse dunes break into rows of barchans (Figure 5, [86]). This change in dune morphology (long transverse dunes to barchans) corresponds to a change in dominant dynamics (growth in height to migration). On a starved bed, a perturbation

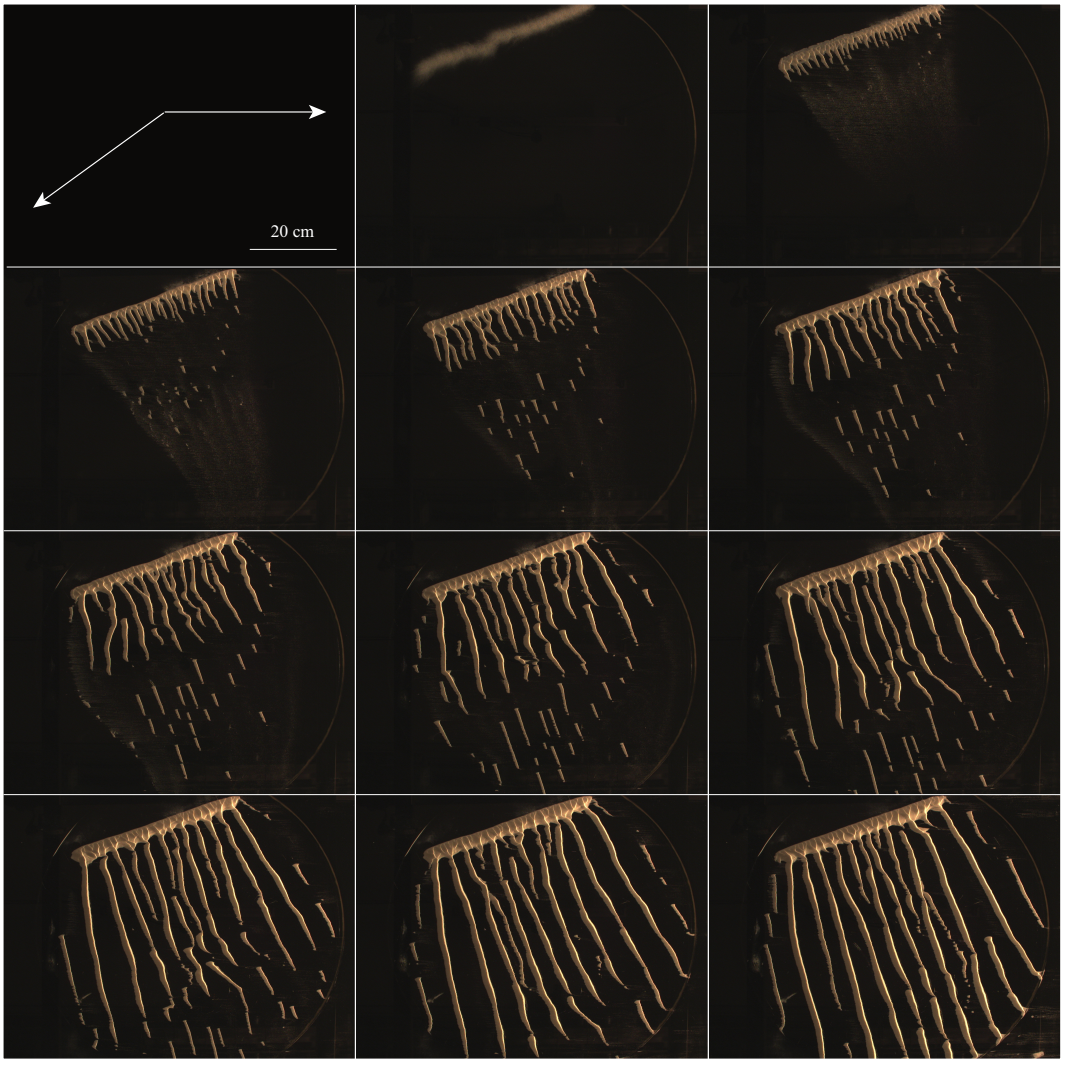


Figure 8. Dune growth and elongation from a line source of sand in a periodic bidirectional flow (translated tray setup). Sand is periodically supplied along a line (at top left). First panel shows the flow regime: the two flow directions form an angle $\theta = 144°$ and the transport ratio between the two flows is $N = 1$ (symmetric). Images were taken at the end of the rightward flow after none, 10, 20, 40, 60, 80, 120, 160, 200, 260, and 400 flow cycles (one cycle counts $3 + 3 = 6$ tray strokes). Photo credit: S. Courrech du Pont.

in dune height leads to a perturbation in migration velocity (lower parts migrate faster than higher ones). The subsequent sinuosity of the dune crest leads to lateral sediment fluxes that amplify the perturbation (Figure 6, [86,93,94]). Figure 1 (a) shows a spatial transition between dunes on completely covered and partially starved sand beds in the field.

In multidirectional flow regimes, dunes may integrate the different flow sequences (Section 2.3) and each of them may contribute to the development of the dune. Dunes on a fully covered bed in bidirectional flow regimes have been studied experimentally in a large flume by Rubin and Ikeda [85] (first experiments dealt with the orientation of impact ripples in bidirectional winds [84]) and later by Reffet et al. [86] and others [44] using the translated tray setup

(Figure 7). These experiments have shown that dune orientation maximises the gross bedform-normal transport, i.e., the rate of growth rate in height (Section 2.3). Subsequently, dunes can be transverse, oblique or longitudinal with respect to the mean sand flow direction. This major experimental result has allowed to quantitatively use dune orientation to constrain prediction of wind regimes [115–117].

In bidirectional flow regimes, when the bed becomes starved, the periodic dunes either break into barchans (which may be asymmetric [89]) or break and reconnect to form periodic dunes with a different orientation (Figure 7, [44]). These experiments show that long dunes and periodic patterns can have two different orientation depending on the bed condition (fully covered or starved), and that a mechanism stabilises long dunes on starved beds in multidirectional flow, which is dune elongation. This second growth mechanism (the first being growth in height) can generate long linear dunes on starved beds, a common pattern on Earth (Figure 1 (b) [44]) and probably on Titan [118]) from sand sources (Figure 8, [44]).

The space of parameters controlling the dune type has only been partially explored experimentally (in unidirectional or bidirectional flow regimes only), star dunes (Figure 1 (d)), for example, have not yet been reproduced in experiments. More complex flow regimes and varied boundary conditions need to be addressed in order to obtain the aimed phase diagram of dune patterns.

3.4. *Dune interaction and autogenic processes*

Dunes highly interact with their environment. Dune interactions can be divided into three categories: dune interaction with obstacles, dune interaction with each other, and dune interaction with vegetation. Experiments are particularly important for dune interactions because numerical models of dunes only partially reproduce the complexity of the flow and, in particular, the wake that develops downwind of the dune.

Barchan interactions with obstacles has recently been investigated by Assis et al. (Figure 9, [106]). In their study obstacles have sizes comparable to the size of dunes. They have shown that depending on the different aspect ratios between the dune and the obstacle, the different aspect ratios of the obstacle, and the flow velocity, the dune will either pass over the obstacle, bypass the obstacle, or get stuck and form an echo dune. During the process, sand may be trapped in the lee side of the obstacle and form a lee (or shadow) dune. These studies are particularly important for risk prevention and management of human infrastructure in desert environments.

Under a unidirectional wind, dunes on starved beds are migrating barchan dunes. Barchan dunes loose sand from their horns and can capture free sand flux. Numerical models have shown that the balance between gain and loss corresponds to an unstable equilibrium. The output flux depends little on the size of the dune and is nearly constant, whereas the gain is proportional to the width of the barchan if the free flux is homogeneously distributed [119]. An isolated barchan should either shrink or grow. In deserts, barchan are not isolated, but are numerous and interact (Figure 1 (d)). Their interactions appear to regulate their size and their arrangement within the field [72,76]. Two types of interactions have been identified corresponding to long-range and short-range sand exchange. (i) Sand lost by a barchan from its horn is captured by a barchan downstream, driving dune arrangement in echelon [76,77]. (ii) Smaller barchans migrate faster than larger ones, leading to dune collisions. Experiments have shown that dune collisions can result in dune merging, sand redistribution between the two dunes, or formation of new dunes, depending on the relative size and alignment between impacting and impacted dunes (Figure 9, [80,103,120]). Dunes merge if the impacting dune is much smaller than the impacted one. If the impacting dune is larger, the flow perturbation downstream the impacting dune locally increases the fluid velocity experienced by the impacted dune enough to cut it into pieces. The

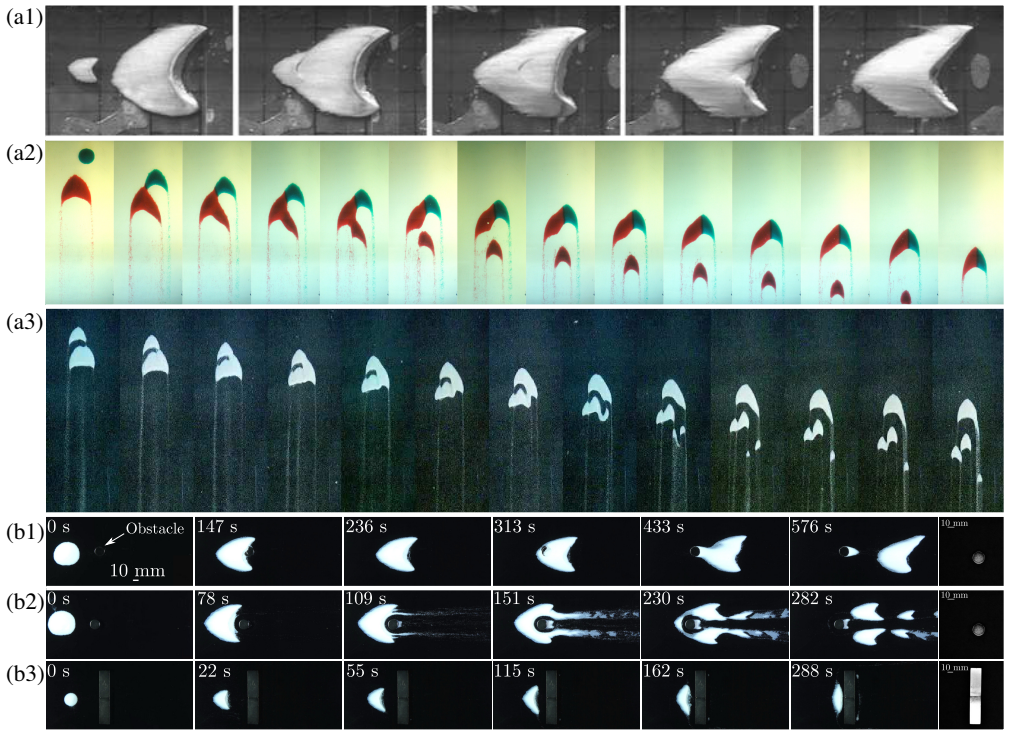


Figure 9. Barchan dune interactions. (a1-3) Time-lapses of barchan collisions. Depending on the size ratio and alignment between the two barchans, the two barchans merge (a1), sand is redistributed into two barchans (a2), or into a larger number of dunes (a3). (a1) Flume setup, flow is from left to right and view in images is 12 cm high, from [103]. (a2) Translated tray setup. Flow is from top to bottom, view in images is 19 cm wide, from [80]. (a3) Translated tray setup, flow is from top to bottom, view in images is 8 cm wide, credit: S. Courrech du Pont [43]. (b1-2) Barchan dunes interacting with an obstacle. The dune can either pass over the obstacle (b1), bypass the obstacle (b2), or get stuck (b3). The flow is from left to right (flume setup) and the obstacle is either a cylinder 18 mm in diameter and 2 mm high (b1), a cylinder 18 mm in diameter and 8 mm high (b2), or a rectangular block 1 cm high, 10 cm wide, and 2 cm long (in the flow direction). Note the sand trapped in the lee of the obstacle in (b1). (b1-3) figures are from [106].

impacting dune may merge with one or more of the newly formed dunes [80,103]. Dune splitting during collisions has been shown to regulate dune size using mean-field approaches [80,121]. Following the experimental identification of collision types and parameters, a more complete phase diagram of binary collisions was developed in numerical simulations [121,122]. These collision rules were then used to simulate the dynamics of large groups of barchans with agent models, demonstrating that barchan collisions can not only regulate the size of barchans, but also result in the self-organisation of the dune field in corridors [119,123–126].

The other important type of interaction is the interaction with vegetation. The coupling between sand transport, dunes, and vegetation is also dynamical. Vegetation can grow on dunes,and dunes can kill the vegetation, which remobilises the underlying sand [127–129]. This coupling is still a challenge for laboratory experiments, but is of primary importance because it is relevant for most coastal deserts and for vegetated dunes that cover large areas in China and Australia.

4. Landscape-scale experiments

The concept of landscape-scale experiments is a novel approach to geomorphology that differs from the usual field instrumentation or remote sensing analysis, and is particularly suited to modern issues in aeolian research and dune physics. Indeed, although the minimum size of the dunes and their migration rate remain beyond the operational capacity in wind tunnels, the temporal and spatial scales associated with dune growth mechanisms appear to be accessible in the field, enabling the validation and quantification of the processes that contribute to the formation of dune patterns in their natural environment. Given the extreme conditions typically encountered in arid deserts, along with the specific properties of wind regimes, these in-situ experiments necessitate the integration of logistical considerations for the acquisition of long-term measurements. These challenges have been met for 6 years in the Tengger Desert thanks to a Franco-Chinese collaboration combining theoretical approaches with field experience.

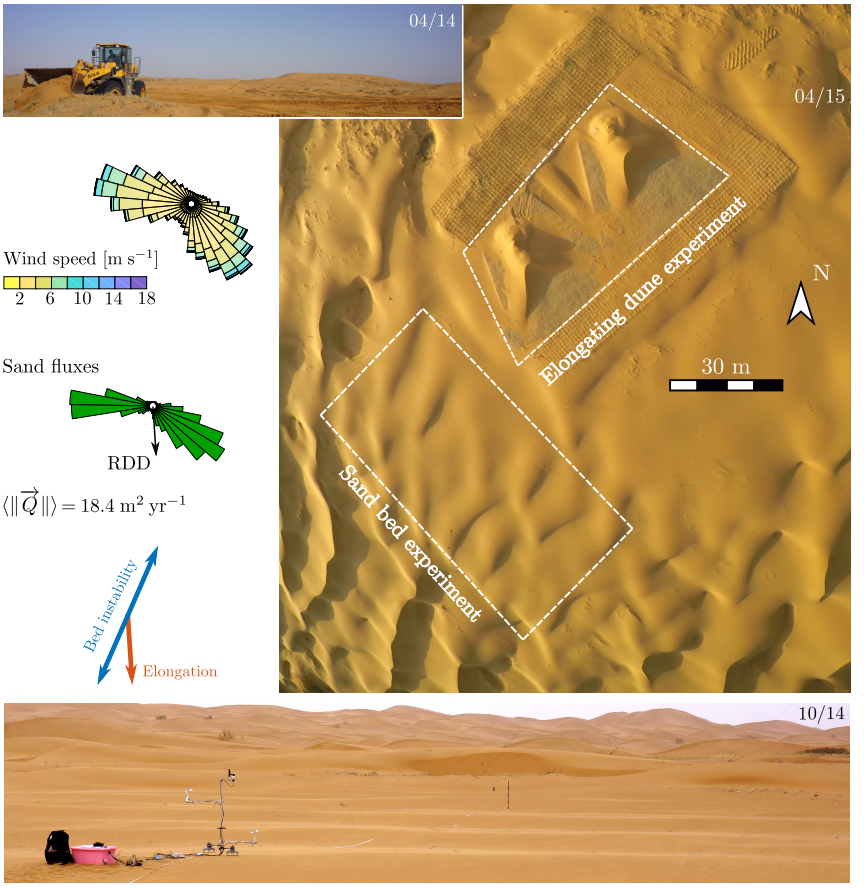


Figure 10. Landscape scale experiments in the Tengger Desert, China (37.560°N, 105.033°E). Two independent experiments are dedicated to the elongation and bed instability mechanisms. Wind and transport roses point in the direction of the flow. Arrows show dune orientations predicted from wind data. The bottom picture shows wind measurements at different heights along a wind-parallel transect during the development of the dune instability.

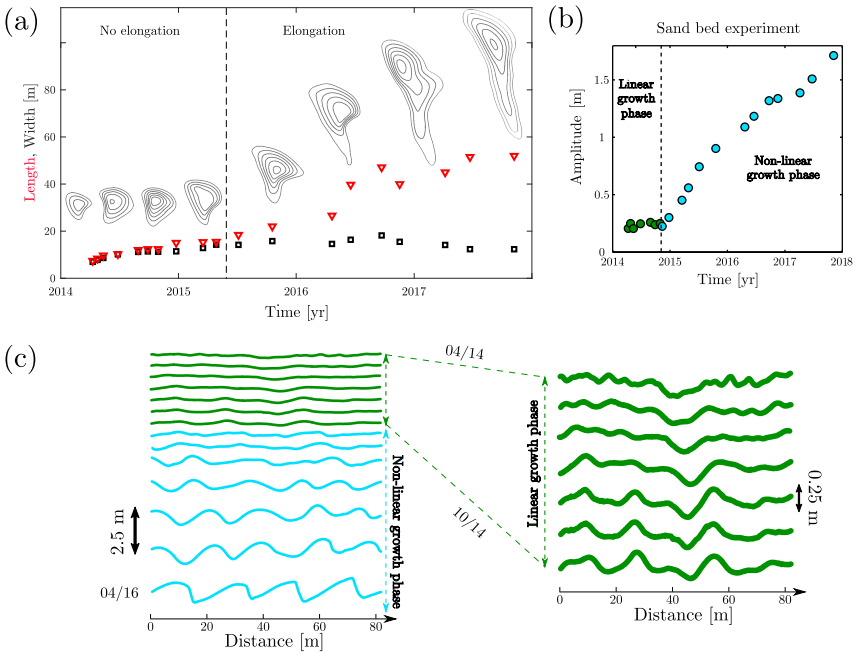


Figure 11. The evolution of bedforms in landscape scale experiments. (a) Length and width of the southwest dune in the elongating dune experiment with respect to time. Contour lines show the dune at different times. (b) Average amplitude of the topography variations $\delta h = 2\sqrt{2}(\langle h^2\rangle - \langle h\rangle^2)^{1/2}$ in the sand-bed experiment with respect to time. (c) Evolution of topography along a transect of the sand-bed experiment from the initial flattening. The colour distinguishes the linear (green) and non-linear (blue) regimes of dune growth.

4.1. *Experimental set-up in the field*

Working on surfaces large enough for elementary dunes to be observed, the main objective of the landscape-scale experiments is to quantitatively characterize the development of bedforms in a natural aeolian environment using controlled initial and boundary conditions as well as a continuous monitoring of the surface winds and climatic conditions that contribute to aeolian transport. Such control, inherent in laboratory experiments, is the main difference with field observations, and also helps to limit the impact of some of the heterogeneities (e.g., vegetation, grain-size distribution) often encountered in desert areas.

The experimental site is located in the southernmost border of the Gobi Desert, which has a typical continental monsoon climate with less than 180 mm of annual precipitation. The local wind regime is clearly bimodal (Figure 10), with a dominant wind in the southeast direction flowing mainly in spring when the Siberian-Mongolian high pressure cell weakens, and a secondary wind in the west direction flowing mainly in summer due to the East Asian monsoon. Figure 10 shows that this bimodal wind regime gives rise to a bimodal transport regime, which may be modeled by a divergence angle of $\theta \simeq 149^{\circ}$ and a transport ratio of $N \simeq 2$.

Field experiments have been continuously conducted over 4 years from October 2013 to November 2017. To focus on the bed instability and elongation mechanisms described in Sections 2.2 and 2.4, two main experiments have been performed (Figure 10). The elongating dune experiment started in October 2013 by placing two conical sand heaps 2.5 and 3 m high on a flat gravel bed isolated from the incoming sand by straw checkerboards. To allow for dunes

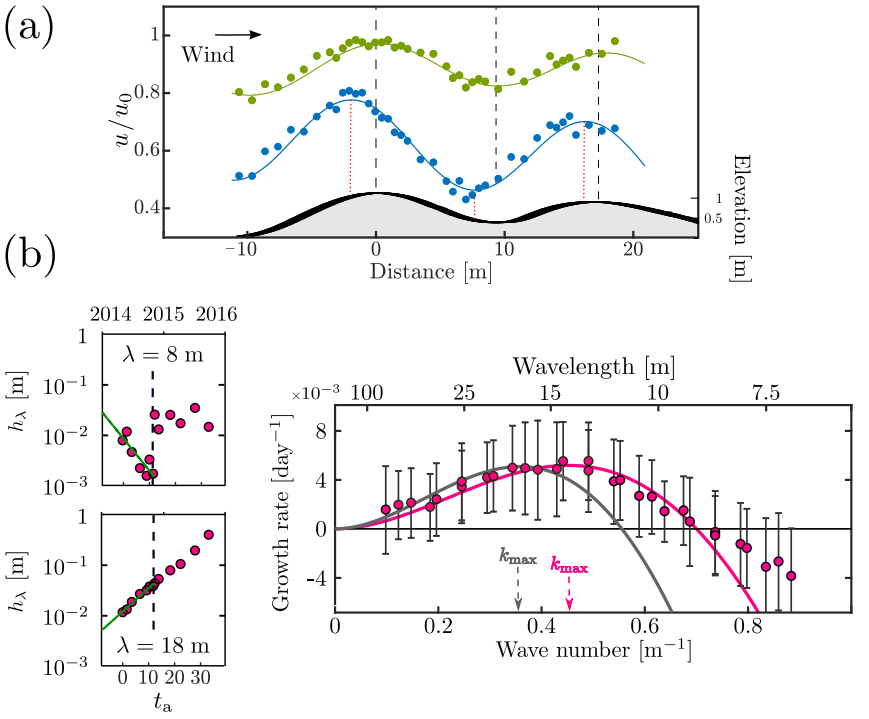


Figure 12. Experimental and theoretical dispersion diagrams from field data. (a) Elevation and normalised wind speed according to distance along a dune profile (blue and green for anemometers at 4 and 100 cm height, respectively). The wind speeds are normalised by a wind speed measured by a fixed reference anemometer. The average upwind shift gives $\mathscr{A} \simeq 3$ and $\mathscr{B} \simeq 1.5$. (b) Experimental dispersion relation for the linear regime of the dune instability (red points). It is derived from topographic data only, using the exponential variation of the amplitude of different wavelengths from 10 April to 30 October 2014 (see examples for wavelength of 8 and 18 m). Solid lines are dispersion relations using Equation (6) and the best fit to the data $\{L_{sat}, \mathscr{A}, \mathscr{B}\} = \{0.7\,\text{m}, 1.96, 0.96\}$ (red), or the same parameters measured independently in the field $\{L_{sat}, \mathscr{A}, \mathscr{B}\} = \{0.95\,\text{m}, 3, 1.5\}$ (gray). The most unstable wavelengths $\lambda_{max} = 2\pi/k_{max}$ are equal to 14.6 and 18.5 m, respectively.

to increase their size and compensate for their loss, sand has been added 10 times, from May 2014 to September 2016, always in the same places, to rebuild the original sand heaps. To the southwest of the elongating dune experiment, pre-existing dunes were also levelled by bulldozer in April 2014 to form a flat rectangular bed 100 m long and 75 m wide. The main axis of this sand bed experiment dedicated to the bed instability mechanism was aligned with the direction of the primary wind.

More than 20 ground-based laser scans were performed to regularly measure the evolution of surface elevation in the sand bed and the elongating dune experiments over 4 years. The point density varied from 470 to 2 370 points per m^2 with a centimetre height accuracy. Throughout the experiments, wind data from local meteorological towers and an airport located 10 km east from the experimental dune field are used to calculate the saturated sand flux on a flat sand bed and at the dune crests according to the formalism described in [44]. In the experimental area, the mean grain size is $d \simeq 190\ \mu$m and the threshold shear velocity for aerodynamic entrainment of sand grains is $u_t \simeq 0.23$m/s [75].

Additionally, a zone of bare sand has been preserved between the two sand heaps of the elongating dune experiment. There, a rectangular sand slab 12 m long, 3 m wide and 20 cm high was built downwind of the gravel bed and the straw checkerboard according to the direction of the prevailing wind. The changes in elevation of this sand berm before and after a wind event was used to estimate the saturation length L_{sat}. Finally, the wind response to topography, as encoded in the theory by means of coefficients $\mathscr{A}$ and $\mathscr{B}$ (Equation (5)), was measured with a anemometers moved along a known (and approximately sinusoidal) dune elevation profile (Figure 10).

4.2. *Characteristic length scales in landscape-scale experiments*

The initial volumes of the two sand heaps of the elongating dune experiment were insufficient to integrate the entire period of wind reorientation, and they rapidly took a dome dune shape under the effect of the first wind reversals [130]. Subsequently, seasonal winds reshaped the dunes, resulting in the formation of crescentic barchans with varying orientations (Figure 11 (a)). The regular sand supply combined with the exchange of sediments between the two piles led to the growth of the pile to the northeast. This pile developed a southeast-facing slip face, a longer southern arm, and gradual adopted an asymmetric barchan shape. Then, the width of the dune remained constant, while its southern arm continued to elongate at an angle of less than 10^{o} to the resulting sand flux in response to the alternating winds (Figure 10 (a)). This illustrates not only the dependence of dune shape on dune size, but also the existence of a threshold dune size for the elongation mechanism.

In the sand-bed experiment, the working surface of $7,500$ m^2 was initially flattened down to differences between minimum and maximum elevations of less than 25 cm, with an average residual variation around $\delta h \approx 20$ cm in April 2014 (Figure 11 (c, d)). Aeolian transport rapidly smoothed all traces left by the levelling process, and migrating bedforms of different wavelengths start to develop. While a dominant wavelength of approximately 15 m started to be visible in August 2014, it was only in October 2014 that the amplitude of these growing bedforms exceeded the initial δh and that slip faces oriented to the southeast began to emerge. The growth continued at a steady rate until the completion of the topographic surveys in October 2017, resulting in a clear periodic dune pattern in October 2016 as the amplitude of the dominant mode increases by almost a factor of five.

Taking advantage of this incipient growth, wind measurements were conducted to quantify the flow perturbation over low sinusoidal bedforms and estimate the aerodynamic coefficients $\mathscr{A}$ and $\mathscr{B}$ (Section 2.2). As predicted by the theory (Figure 2), Figure 12 (a) shows that the wind perturbation reflects the topography of the underlying incipient dunes. The amplitude of the wind speed perturbation decreases with height above the bed. Compared to the elevation profile, there is an upwind shift in wind speed for the bottom anemometers, but not for the top anemometers, in agreement with the existence of inner and outer layers [67]. In the near-surface region, here typically for heights of less than 15 cm (in the inner layer), the upwind shift (≈ 1 m) and the amplitude of the wind speed perturbation were used to get $\mathscr{A} = 3 \pm 1$ and $\mathscr{B} = 1.5 \pm 0.5$. These values are confirm theoretical expectations [42] as well as previous but less precise estimates [131]. Independently, the measurement of the saturation length, derived from the erosion of the sand berm during a storm event in April 2014, gave $L_{\mathrm{sat}} = 0.95$ m. These values allowed us to compute the theoretical dispersion relation of the dune instability (Equation (6), as displayed with the blue curve in Figure 12 (b)).

Using all topographic surveys of the sand-bed experiment, the elevation profile along different transect are used to estimate the evolution of the contribution of individual modes (i.e., wavelengths) to the overall topography. When expressed according to a dimensionless transport time

scale ($\Delta t_a = Q\Delta t/L_{sat}^2$), all the individual modes exhibit exponential variation over short times (Figure 12 (b)). Once again, abrupt changes in growth rate are observed in November 2014, a date at which the exponential rate is no longer ubiquitous. The results of the field experiment not only corroborate the dune instability theory with regard to the initial exponential growth of individual modes, but also identify the transition from the linear to the non-linear regime of dune growth, which occurs for remarkably low values of dune aspect ratio (≈ 0.03).

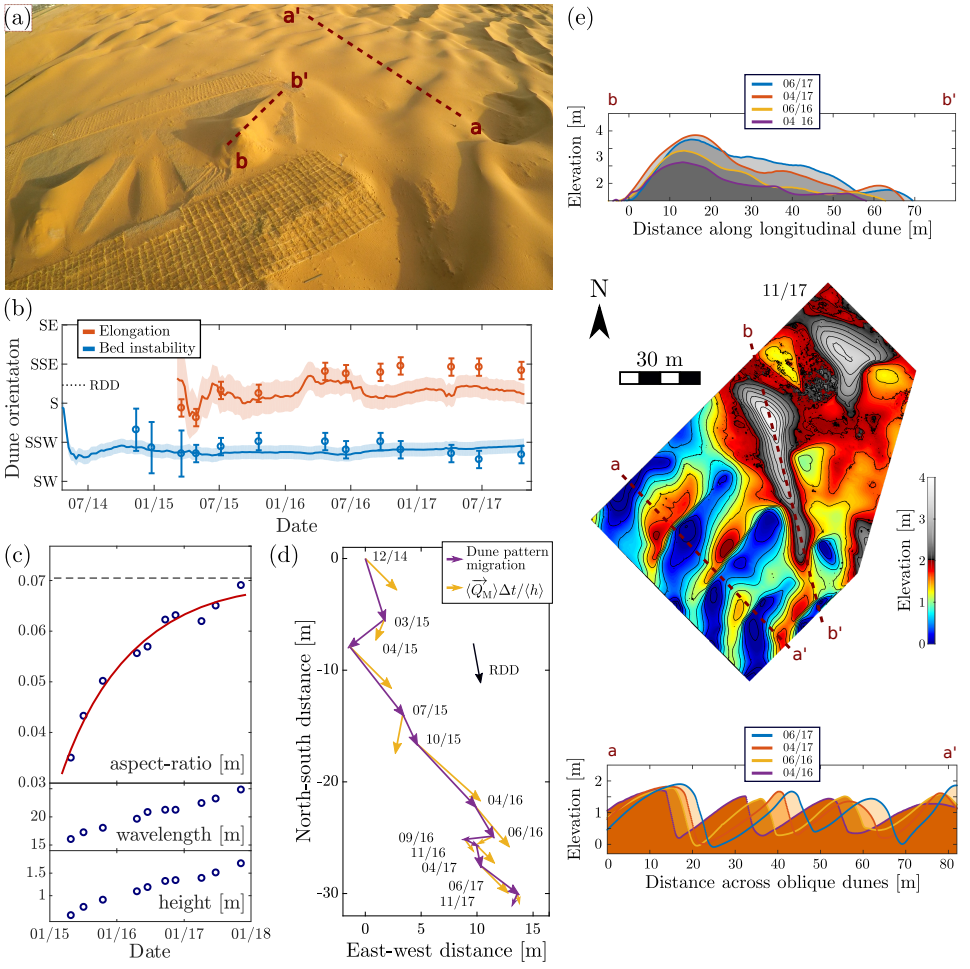


Figure 13. Dune dynamics in landscape scale experiments. (a) Direction along which migration and elongation are measured in the field (b) Observed (circles) and predicted (lines and shaded area) dune orientations for the dune instability (blue) and the elongation mechanisms (red). (c) Evolution of dune aspect-ratio, wavelength and amplitude in the sand-bed experiments. (d) Observed (purple) and predicted (yellow) dune migrations in the sand-bed experiments with respect to time. (e) Elongation (top) and migration (bottom) in the elongating and sand-bed experiments, respectively.

During the linear regime, from April to October 2014, the experimental dispersion relation of the dune instability was obtained by plotting the exponential growth rate of the different modes as a function of their wave number k (Figure 12 (b)). The growth rate is positive for large wavelengths and negative for small wavelengths, reaching a maximum value for an intermediate wavelength of approximately 15 m. The presence of clear maximum and the continuous trend from unstable (i.e., growing waves, $\sigma > 0$) to stable regimes (i.e., decaying waves, $\sigma < 0$) reflect most of the behaviours predicted by the theory during the linear phase of dune growth. This is demonstrated by the consistency between the experimental dispersion relation, derived exclusively from topographic data, and the theoretical relation, derived from the pertinent physical parameters that were independently measured in the field (Figure 12 (b)). Other studies confirmed the general agreement between observations and theoretical predictions for dune emergence [72,74,92], but, importantly, here it comes from measurements performed on a purposely prepared system, rather than "passive" observations.

4.3. *Dune dynamics in landscape-scale experiments*

In addition to the elementary processes associated with the emergence of dunes, landscape-scale experiments permit the analysis of the long-term dynamics of aeolian bedforms, including dune shape and orientation, as well as the rates at which they grow in height, migrate, and elongate (Figure 13).

At the time of each topographic survey, the mean transport rate at the crest of dunes can be computed using the wind data acquired in the field from the beginning of the experiments. This allows for a comparison of the observed and predicted (Sections 2.3, 2.4 and [44]) dune orientations, both for the migrating dunes in the sand-bed experiment and elongating dunes. Figure 13 (b) illustrates that these dune orientations are in good agreement with expectations, despite the simplifying assumptions inherent to the model (i.e., triangular dune, no crest reversal). As showed by [132], the periodic dune orientation in the zone of full sand availability validates the gross bedform-normal rule in the field, as they align with the direction in which the normal component of transport is maximum [84]. Since they form an angle of 34^{o} with the resultant sand flux, they may be described as oblique [133]. In contrast, the elongating dunes may be considered as longitudinal, since they diverge by only 10^{o} from the resultant sand flux [133].

During the non-linear phase of dune growth in the sand-bed experiment, Figure 13 (c) shows a constant increase in both dune height and wavelength. The dune aspect-ratio slowly converges toward a steady-state value of 0.07, the typical dune aspect-ratio observed in this area. As the periodic dunes grow in height, the entire pattern also migrates. The migration vectors can be derived from two successive elevation data sets by cross-correlation and compared to the model prediction by computing the sand flux at the crest for the specific time period and dune orientation (Figure 13 (d)). The observed vectors are consistent with the predicted vectors, both in terms of magnitude and direction, indicating that the model estimate accurately reflects the sand flux at the crest. In the sand bed experiment, dunes eventually reached a height of 2 m and migrated at an average speed of 5 $\mathrm{m\,yr^{-1}}$ from June 2016 to June 2017 (Figure 13 (e)). In the elongating dune experiment, the length of the longest dune increased by more than 10 m from April 2016 to June 2017, with a height profile which decreased almost linearly from the sand source area to the tip, in agreement with the numerical predictions of [47].

5. Conclusion and perspectives

The interpretation of dune landscapes, which result from complex interactions (superimposed bedforms, collisions) and integrate wind regimes over long times, can be achieved by identifying

the elementary physical processes at work and their associated scales. For this purpose, idealised and controlled experiments, both at laboratory and landscape scales, are an invaluable source of knowledge. A comprehensive range of dunes, encompassing a multitude of shapes and orientations, can be replicated and tracked over time, from their emergence to their interactions and coarsening dynamics. These experiments are also key to assess the models with which these processes are theoretically described, and to quantify their relevant parameters. In turn, the theory provides a framework for understanding the main controlling scales, in particular by analysing the extent to which the processes at work in the morphodynamics of subaqueous laboratory experiments dealing with bedload and centimetre-scale sedimentary bedforms can be analogous to those of large aeolian sand dunes generated by saltation.

This approach of dune dynamics based on processes and scales also gives a quantitative reference and building blocks for numerical models, such as agent-based and cellular automata, to simulate larger dune fields. In particular setting the values of the saturation length L_{sat} and the sand flux Q allows for a quantitative calibration of the results [41]. It also lays the physical foundation for the comparison of dunes in terrestrial and planetary environments [1,7,8,16,17,79,134,135], for which fluid and sediment characteristics can take values significantly different than those commonly in terrestrial deserts.

Given the central role of the saturation length in dune dynamics, further experiments are required to investigate how L_{sat} depends on environmental parameters, and to relate it to the properties of the fluid and the grains, the flow regime, and the structure of the transport layer. In particular, low pressure conditions (larges values of s, the density ratio between the particles and the gas), which are typical of planetary surfaces, must be further explored [57]. In this limit, one expects a smooth hydrodynamic regime to emerge associated with enhanced values of kinematic viscosity as well as a reduced drag force on the grains [16,17,135]. The same is true for the sediment flux Q and the transport threshold u_t. This knowledge is essential for using these dune patterns as observational tools to learn more about the flow and sediment properties in places where direct measurements are often difficult to implement. Planetary environments as diverse as those reported on Mars and Titan will thus continue to provide a wide range of dune patterns that will undoubtedly serve to guide the development of new experiments, as well as provide empirical constraints to improve the theoretical parametrisation and description of the processes.

When sufficiently large, dune flanks can destabilise like flat beds [72], explaining how a hierarchy of dune patterns develops, from the most unstable mode to the giant dune size, with different generations of dunes interacting with each other [82,136]. These primary and secondary structures are valuable sources of information on the properties of surface winds over different periods, from seasonal to millennial time scales. In areas where sediment availability varies spatially, the different growth mechanisms can also coexist [137,138], or the same mechanism can produce dunes with different orientations [91]. Experiments have not yet addressed superimposed patterns and complex shapes such as star dunes or raked dunes. Further long-term experimental studies are required to investigate dune interaction and coarsening processes in this context of superimposed patterns or for the spatial organisation of dune fields, such as barchan corridors [77]. Of particular interest is a better understanding of the dynamics by which dune fields eliminate or create defects in the dune pattern, in order to quantify how far from a possible equilibrium state the dune system is [79,139]. This long term evolution would also provide a set of constraints on the wind regimes that may have generated these dune patterns [140], making the inverse problem of characterising past winds from the shape and orientation of dunes potentially feasible [141].

Finally, dealing with vegetation is an important step for laboratory and landscape scale experiments dedicated to dune dynamics. Coastal zone studies and management over the last few

decades have generated a vast amount of data and observations, which have yet to be fully exploited [142]. All this information offers significant potential for the development of new field experiments under controlled conditions in the presence of vegetation [143]. Meanwhile, growing plants in the laboratory is a difficult time consuming task, and it remains to be determined what the best experimental analogue of vegetation is. A primary objective would be to ascertain some mechanical properties of plants that are relevant to sediment transport and dune morphodynamics. All these experimental efforts should be combined with studies investigating the role of cohesion (e.g., moisture, fine material, sintering, but also coupling to icy surfaces as on Mars), which introduces additional sources of interaction between bedforms, and can modify shear stress and sediment transport, eventually leading to possibly similar feedbacks of those involved by vegetation [144].

Acknowlegments

The authors would like to thank B. Andreotti, M. Baddock, S. Carpy, F. Charru, P. Delorme, S. Douady, O. Durán, H. Elbelrhiti, A. Fourrière, C. Gadal, X. Gao, M. Génois, A. Gunn, P. Hersen, J. Iversen, P. Jia, M. Lapôtre, M. Louge, P. Lü, A. Lucas, J. Merrison, B. Murray, J. Nield, O. Pouliquen, K. Rasmussen, E. Reffet, S. Rodriguez, O. Rozier, D. Rubin, G. Wiggs, D. Zhang and Y. Zhang for extensive discussions on ripples, dunes and sediment transport. We are grateful to A. Valance and E. Franklin for sharing images from their experiments.

Declaration of interests

The authors do not work for, advise, own shares in, or receive funds from any organization that could benefit from this article, and have declared no affiliations other than their research organizations.

References

[1] R. D. Lorenz and J. R. Zimbelman, *Dune Worlds: How Windblown sand shapes planetary landscapes*, Springer-Praxis Geophysical Sciences, Springer, 2014.

[2] S. Diniega, M. Kreslavsky, J. Radebaugh, S. Silvestro, M. W. Telfer and D. Tirsch, "Our evolving understanding of aeolian bedforms, based on observation of dunes on different worlds", *Aeolian Res.* **26** (2017), pp. 5–27.

[3] A. Gunn and D. J. Jerolmack, "Conditions for aeolian transport in the Solar System", *Nat. Astron.* **6** (2022), pp. 923–929.

[4] C. S. Breed and T. Grow, "Morphology and distribution of dunes in sand seas observed by remote sensing", in *A study of global sand seas* (E. D. McKee, ed.), U.S. Geological Survey, 1979, pp. 252–302.

[5] P. A. Hesp and I. J. Walker, "11.17 Coastal dunes", in *Treatise on Geomorphology*, Academic Press Inc., 2013, pp. 328–355.

[6] J. A. Cutts and R. S. U. Smith, "Eolian deposits and dunes on Mars", *J. Geophys. Res.* **78** (1973), pp. 4139–4154.

[7] M. C. Bourke, N. Lancaster, L. K. Fenton, E. J. R. Parteli, J. R. Zimbelman and J. Radebaugh, "Extraterrestrial dunes: An introduction to the special issue on planetary dune systems", *Geomorphology* **121** (2010), pp. 1–14.

[8] M. G. A. Lapôtre, R. C. Ewing, C. M. Weitz, K. W. Lewis, M. P. Lamb, B. L. Ehlmann and D. M. Rubin, "Morphologic diversity of Martian ripples: Implications for large-ripple formation", *Geophys. Res. Lett.* **45** (2018), pp. 10229–10239.

[9] R. D. Lorenz, S. Wall, J. Radebaugh, et al., "The sand seas of Titan: Cassini RADAR observations of longitudinal dunes", *Science* **312** (2006), pp. 724–727.

[10] J. Radebaugh, R. D. Lorenz, J. I. Lunine, et al., "Dunes on Titan observed by Cassini RADAR", *Icarus* **194** (2008), pp. 690–703.

[11] S. Rodriguez, A. Garcia, A. Lucas, et al., "Global mapping and characterization of Titan's dune fields with Cassini: Correlation between RADAR and VIMS observations", *Icarus* **230** (2014), pp. 168–179.

[12] R. Greeley, J. R. Marshall and R. N. Leach, "Microdunes and other aeolian bedforms on Venus: wind tunnel simulations", *Icarus* **60** (1984), pp. 152–160.

[13] A. T. Basilevsky, R. O. Kuzmin, O. V. Nikolaeva, et al., "The surface of Venus as revealed by the Venera landings: Part II", *GSA Bulletin* **96** (1985), pp. 137–144.
[14] C. M. Weitz, J. J. Plaut, R. Greeley and R. S. Saunders, "Dunes and microdunes on Venus: Why were so few found in the Magellan data?", *Icarus* **112** (1994), pp. 282–295.
[15] M. W. Telfer, E. J. R. Parteli, J. Radebaugh, et al., "Dunes on pluto", *Science* **360** (2018), pp. 992–997.
[16] P. Jia, B. Andreotti and P. Claudin, "Giant ripples on comet 67P/Churyumov–Gerasimenko sculpted by sunset thermal wind", *Proc. Natl. Acad. Sci. USA* **114** (2017), pp. 2509–2514.
[17] S. Courrech du Pont, D. M. Rubin, C. Narteau, et al., "Complementary classifications of aeolian dunes based on morphology, dynamics, and fluid mechanics", *Earth-Sci. Rev.* **255** (2024), article no. 104772.
[18] J. L. Best, "The fluid dynamics of river dunes: a review and some future research directions", *J. Geophys. Res.* **110** (2005), article no. F04S02.
[19] P. A. Carling, E. Golz, H. G. Orr and A. Radecki-Pawlik, "The morphodynamics of fluvial sand dunes in the River Rhine, near Mainz, Germany. I. Sedimentology and morphology", *Sedimentology* **47** (2000), pp. 227–252.
[20] D. R. Parsons, J. L. Best, O. Orfeo, R. J. Hardy, R. Kostaschuk and S. N. Lane, "Morphology and flow fields of three-dimensional dunes, Rio Paraná, Argentina: Results from simultaneous multibeam echo sounding and acoustic Doppler current profiling", *J. Geophys. Res.* **110** (2005), article no. F04S03.
[21] H. Ikeda, "Experiments on bedload transport, bedforms, and sedimentary structures using fine gravel in the 4-meter-wide flume", *Environ. Res. Center pap.* **2** (1983), pp. 1–78.
[22] S. E. Coleman and B. W. Melville, "Bed-form development", *J. Hydraul. Eng.* **120** (1994), pp. 544–560.
[23] S. E. Coleman and B. W. Melville, "Initiation of bed forms on a flat sand bed", *J. Hydraul. Eng.* **122** (1996), pp. 301–310.
[24] S. E. Coleman, J. J. Fedele and M. H. García, "Closed-conduit bed-form initiation and development", *J. Hydraul. Eng.* **129** (2003), pp. 956–965.
[25] J. H. Baas, "A flume study on the development and equilibrium morphology of current ripples in very fine sand", *Sedimentology* **41** (1994), pp. 185–209.
[26] J. G. Venditti, M. A. Church and S. J. Bennett, "Bed form initiation from a flat sand bed", *J. Geophys. Res.* **110** (2005), article no. F01009.
[27] V. Langlois and A. Valance, "Formation and evolution of current ripples on a flat sand bed under turbulent water flow", *Eur. Phys. J. E* **22** (2007), pp. 201–208.
[28] M. Ouriemi, P. Aussillous and E. Guazzelli, "Sediment dynamics. Part 2. Dune formation in pipe flow", *J. Fluid Mech.* **636** (2009), pp. 321–336.
[29] H. Y. Chang, D. B. Simons and D. A. Woolhiser, "Flume experiments on alternate bar formation", *J. Waterways Harbors Coast. Eng. Div.* **97** (1971), pp. 155–165.
[30] T. E. Lisle, H. Ikeda and F. Iseya, "Formation of stationary alternate bars in a steep channel with mixed-size sediment: a flume experiment", *Earth Surf. Process. Landf.* **16** (1991), pp. 463–469.
[31] S. Lanzoni, "Experiments on bar formation in a straight flume. 2. Uniform sediment", *Water Resour. Res.* **36** (2000), pp. 3351–3363.
[32] O. Devauchelle, L. Malverti, E. Lajeunesse, C. Josserand, P.-Y. Lagrée and F. Métivier, "Rhomboid beach pattern: a laboratory investigation", *J. Geophys. Res.* **115** (2010), article no. F02017.
[33] S. Rodrigues, E. Mosselman, N. Claude, C. L. Wintenberger and P. Juge, "Alternate bars in a sandy gravel bed river: generation, migration and interactions with superimposed dunes", *Earth Surf. Process. Landf.* **40** (2014), pp. 610–628.
[34] O. Durán, P. Claudin and B. Andreotti, "On aeolian transport: Grain-scale interactions, dynamical mechanisms and scaling laws", *Aeolian Res.* **3** (2011), pp. 243–270.
[35] A. Valance, K. R. Rasmussen, A. Ould El Moctar and P. Dupont, "The physics of aeolian sand transport", *Comptes Rendus. Physique* **16** (2015), pp. 105–117.
[36] T. Pähtz, A. H. Clark, M. Valyrakis and O. Durán, "The physics of sediment transport initiation, cessation, and entrainment across aeolian and fluvial environments", *Rev. Geophys.* **58** (2020), article no. e2019RG000679.
[37] B. Andreotti, P. Claudin and S. Douady, "Selection of dune shapes and velocities. Part 2: A two-dimensional modelling", *Eur. Phys. J. B, Condens. Matter Complex Syst.* **28** (2002), pp. 341–352.
[38] K. Kroy, S. Sauermann and H. J. Herrmann, "Minimal model for sand dunes", *Phys. Rev. Lett.* **88** (2002), article no. 054301.
[39] K. Kroy, S. Sauermann and H. J. Herrmann, "Minimal model for aeolian sand dunes", *Phys. Rev. E* **66** (2002), article no. 031302.
[40] P. Claudin and B. Andreotti, "A scaling law for aeolian dunes on Mars, Venus, Earth, and for subaqueous ripples", *Earth Planet. Sci. Lett.* **252** (2006), pp. 30–44.
[41] C. Narteau, D. Zhang, O. Rozier and P. Claudin, "Setting the length and time scales of a cellular automaton dune model from the analysis of superimposed bed forms", *J. Geophys. Res.* **114** (2009), article no. F03006.
[42] F. Charru, B. Andreotti and P. Claudin, "Sand ripples and dunes", *Annu. Rev. Fluid Mech.* **45** (2013), pp. 469–493.

[43] S. Courrech du Pont, "Dune morphodynamics", *Comptes Rendus. Physique* **16** (2015), pp. 118–138.
[44] S. Courrech du Pont, C. Narteau and X. Gao, "Two modes for dune orientation", *Geology* **42** (2014), pp. 743–746.
[45] X. Gao, C. Narteau, O. Rozier and S. Courrech du Pont, "Phase diagrams of dune shape and orientation depending on sand availability", *Sci. Rep.* **5** (2015), article no. 14677.
[46] A. Lucas, C. Narteau, S. Rodriguez, O. Rozier, Y. Callot, A. Garcia and S. Courrech du Pont, "Sediment flux from the morphodynamics of elongating linear dunes", *Geology* **43** (2015), pp. 1027–1030.
[47] O. Rozier, C. Narteau, C. Gadal, P. Claudin and S. Courrech du Pont, "Elongation and Stability of a Linear Dune", *Geophys. Res. Lett.* **46** (2019), pp. 14521–14530.
[48] O. Durán, B. Andreotti and P. Claudin, "Numerical simulation of turbulent sediment transport, from bed load to saltation", *Phys. Fluids* **24** (2012), p. 103306.
[49] P. Claudin, O. Durán and B. Andreotti, "Dissolution instability and roughening transition", *J. Fluid Mech.* **832** (2017), article no. R2.
[50] P. Jia, B. Andreotti and P. Claudin, "Hydrodynamic roughness induced by a multiscale topography", *J. Fluid Mech.* **974** (2023), article no. A16.
[51] S. Sauermann, K. Kroy and H. J. Herrmann, "Continuum saltation model for sand dunes", *Phys. Rev. Lett.* **64** (2001), article no. 031305.
[52] B. Andreotti, P. Claudin and O. Pouliquen, "Measurements of the aeolian sand transport saturation length", *Geomorphology* **123** (2010), pp. 243–248.
[53] M. Lämmel and K. Kroy, "Analytical mesoscale modeling of aeolian sand transport", *Phys. Rev. E* **96** (2017), article no. 052906.
[54] H. Selmani, A. Valance, A. Ould El Moctar, P. Dupont and R. Zegadi, "Aeolian sand transport in out-of-equilibrium regimes", *Geophys. Res. Lett.* **45** (2018), pp. 1838–1844.
[55] J. F. Kok, E. J. R. Parteli, T. I. Michaels and D. Bou Karam, "The physics of wind-blown sand and dust", *Rep. Prog. Phys.* **75** (2012), article no. 106901.
[56] D. Berzi, A. Valance and J. T. Jenkins, "The threshold for continuing saltation on Earth and other solar system bodies", *J. Geophys. Res.* **122** (2017), pp. 1374–1388.
[57] B. Andreotti, P. Claudin, J. J. Iversen, J. P. Merrison and K. R. Rasmussen, "A lower-than-expected saltation threshold at Martian pressure and below", *Proc. Natl. Acad. Sci. USA* **118** (2021), article no. e2012386118.
[58] T. Pähtz and O. Durán, "Scaling laws for planetary sediment transport from DEM-RANS numerical simulations", *J. Fluid Mech.* **963** (2023), article no. A20.
[59] J. E. Ungar and P. K. Haff, "Steady state saltation in air", *Sedimentology* **34** (1987), pp. 289–299.
[60] K. R. Rasmussen, J. D. Iversen and P. Rautahemio, "Saltation and wind-flow interaction in a variable slope wind tunnel", *Geomorphology* **17** (1996), pp. 19–28.
[61] B. Andreotti, "A two-species model of aeolian sand transport", *J. Fluid Mech.* **510** (2004), pp. 47–70.
[62] M. Creyssels, P. Dupont, A. Ould El Moctar, A. Valance, I. Cantat, J. T. Jenkins, J. M. Pasini and K. R. Rasmussen, "Saltating particles in a turbulent boundary layer: experiment and theory", *J. Fluid Mech.* **625** (2009), pp. 47–74.
[63] T. Pähtz and K. Tholen, "Aeolian sand transport: Scaling of mean saltation length and height and implications for mass flux scaling", *Aeolian Res.* **52** (2021), article no. 100730.
[64] D. P. Zilker, G. W. Cook and T. J. Hanratty, "Influence of the amplitude of a solid wavy wall on a turbulent flow. Part 1. Non-separated flows", *J. Fluid Mech.* **82** (1977), pp. 29–51.
[65] K. A. Frederick and T. J. Hanratty, "Velocity measurements for a turbulent nonseparated flow over solid waves", *Exp. Fluids* **6** (1988), pp. 477–486.
[66] T. B. Benjamin, "Shearing flow over a wavy boundary", *J. Fluid Mech.* **6** (1959), pp. 161–205.
[67] J. C. R. Hunt, S. Leibovich and K. J. Richards, "Turbulent shear flows over low hills", *Q. J. R. Meteorol. Soc.* **114** (1988), pp. 1435–1470.
[68] W. S. Weng, J. C. R. Hunt, D. J. Carruthers, A. Warren, G. F. S. Wiggs, I. Livingstone and I. Castro, "Air flow and sand transport over sand-dunes", in *Aeolian Grain Transport*, Acta Mechanica Supplementum, Springer, 1991, pp. 1–22.
[69] F. Charru and E. J. Hinch, "'Phase diagram' of interfacial instabilities in a two-layer Couette flow and mechanism of the long-wave instability", *J. Fluid Mech.* **414** (2000), pp. 195–223.
[70] A. Fourrière, P. Claudin and B. Andreotti, "Bedforms in a turbulent stream: formation of ripples by primary linear instability and of dunes by non-linear pattern coarsening", *J. Fluid Mech.* **649** (2010), pp. 287–328.
[71] C. Gadal, C. Narteau, S. Courrech du Pont, O. Rozier and P. Claudin, "Incipient bedforms in a bidirectional wind regime", *J. Fluid Mech.* **862** (2019), pp. 490–516.
[72] H. Elbelrhiti, P. Claudin and B. Andreotti, "Field evidence for surface-wave-induced instability of sand dunes", *Nature* **437** (2005), pp. 720–723.
[73] C. Gadal, C. Narteau, R. C. Ewing, A. Gunn, D. J. Jerolmack, B. Andreotti and P. Claudin, "Spatial and temporal development of incipient dunes", *Geophys. Res. Lett.* **47** (2020), article no. e2020GL088919.

[74] P. Delorme, G. F. S. Wiggs, M. C. Baddock, P. Claudin, J. M. Nield and A. Valdez, "Dune initiation in a bimodal wind regime", *J. Geophys. Res.* **125** (2020), article no. e2020JF005757.
[75] P. Lü, C. Narteau, Z. Dong, et al., "Direct validation of dune instability theory", *Proc. Natl. Acad. Sci. USA* **118** (2021), article no. e2024105118.
[76] R. A. Bagnold, *The physics of blown sand and desert dunes*, Chapman & Hall, London, 1941.
[77] H. Elbelrhiti, B. Andreotti and P. Claudin, "Barchan dune corridors: field characterization and investigation of control parameters", *J. Geophys. Res.* **113** (2008), article no. F02S15.
[78] J. Buckles, T. J. Hanratty and R. J. Adrian, "Turbulent flow over large-amplitude wavy surfaces", *J. Fluid Mech.* **140** (1984), pp. 27–44.
[79] M. Day and G. Kocurek, "Pattern similarity across planetary dune fields", *Geology* **46** (2018), pp. 999–1002.
[80] P. Hersen and S. Douady, "Collision of barchan dunes as a mechanism of size regulation", *Geophys. Res. Lett.* **32** (2005), article no. L21403.
[81] A. Valance, "Nonlinear sand bedform dynamics in a viscous flow", *Phys. Rev. E* **83** (2011), article no. 036304.
[82] X. Gao, C. Narteau and O. Rozier, "Development and steady states of transverse dunes: A numerical analysis of dune pattern coarsening and giant dunes", *J. Geophys. Res.* **120** (2015), pp. 2200–2219.
[83] P. A. Jarvis, K. A. Bacik, C. Narteau and N. M. Vriend, "Coarsening dynamics of 2D subaqueous dunes", *J. Geophys. Res.* **127** (2022), article no. e2021JF006492.
[84] D. M. Rubin and R. E. Hunter, "Bedform alignment in directionally varying flows", *Science* **237** (1987), pp. 276–278.
[85] D. M. Rubin and H. Ikeda, "Flume experiments on the alignment of transverse, oblique, and longitudinal dunes in directionally varying flows", *Sedimentology* **37** (1990), pp. 673–684.
[86] E. Reffet, S. Courrech du Pont, P. Hersen and S. Douady, "Formation and stability of transverse and longitudinal sand dunes", *Geology* **38** (2010), pp. 491–494.
[87] P. S. Jackson and J. C. R. Hunt, "Turbulent wind flow over a low hill", *Q. J. R. Meteorol. Soc.* **101** (1975), pp. 929–955.
[88] E. J. R. Parteli, O. Durán, H. Tsoar, V. Schwämmle and H. J. Herrmann, "Dune formation under bimodal winds", *Proc. Natl. Acad. Sci. USA* **106** (2009), pp. 22085–22089.
[89] K. Taniguchi, N. Endo and H. Sekiguchi, "The effect of periodic changes in wind direction on the deformation and morphology of isolated sand dunes based on flume experiments and field data from the Western Sahara", *Geomorphology* **179** (2012), pp. 286–299.
[90] H. Tsoar and E. J. R. Parteli, "Bidirectional winds, barchan dune asymmetry and formation of seif dunes from barchans: a discussion", *Environ. Earth Sci.* **75** (2016), article no. 1237.
[91] D. Zhang, C. Narteau, O. Rozier and S. Courrech du Pont, "Morphology and dynamics of star dunes from numerical modelling", *Nat. Geosci.* **5** (2012), pp. 463–467.
[92] C. Gadal, C. Narteau, S. Courrech du Pont, O. Rozier and P. Claudin, "Periodicity in fields of elongating dunes", *Geology* **48** (2020), pp. 343–347.
[93] E. J. R. Parteli, J. S. Andrade and H. J. Herrmann, "Transverse instability of dunes", *Phys. Rev. Lett.* **107** (2011), article no. 188001.
[94] L. Guignier, H. Niiya, H. Nishimori, D. Lague and A. Valance, "Sand dunes as migrating strings", *Phys. Rev. E* **87** (2013), article no. 052206.
[95] P. Hersen, S. Douady and B. Andreotti, "Relevant length scale of barchan dunes", *Phys. Rev. Lett.* **89** (2002), article no. 264301.
[96] N. Endo, T. Sunamura and H. Takimoto, "Barchan ripples under unidirectional water flows in the laboratory: formation and planar morphology", *Earth Surf. Process. Landf.* **30** (2005), pp. 1675–1682.
[97] E. M. Franklin and F. Charru, "Morphology and displacement of dunes in a closed-conduit flow", *Powder Technol.* **190** (2009), pp. 247–251.
[98] Y. Zhang, Y. Lin, N. He, X. Gao and B. Yang, "Local similarity between aeolian barchan dunes and their downsized subaqueous counterparts", *J. Geophys. Res.* **129** (2024), article no. e2023JF007617.
[99] J. G. Venditti, "9.10 Bedforms in Sand-Bedded Rivers", in *Treatise on Geomorphology* (J. F. Shroder, ed.), Academic Press Inc., 2013, pp. 137–162.
[100] E. M. Franklin and F. Charru, "Subaqueous barchan dunes in turbulent shear flow. Part 1. Dune motion", *J. Fluid Mech.* **675** (2011), pp. 199–222.
[101] S. Al-Lababidi, W. Yan, H. Yeung, P. Sugarman and C. P. Fairhurst, "Sand transport characteristics in water and two-phase air/water flows in pipelines", in *Proceedings of the Sixth North American Conference on Multiphase Technology*, BHR Group, 2008, pp. 159–174.
[102] P. A. Mantz, "Bedforms produced by fine, cohesionless, granular and flakey sediments under subcritical water flows", *Sedimentology* **25** (1978), pp. 83–103.
[103] N. Endo, K. Taniguchi and A. Katsuki, "Observation of the whole process of interaction between barchans by flume experiments", *Geophys. Res. Lett.* **31** (2004), article no. L12503.

[104] C. Groh, A. Wierschem, N. Aksel, I. Rehberg and C. A. Kruelle, "Barchan dunes in two dimensions: Experimental tests for minimal models", *Phys. Rev. E* **78** (2008), article no. 021304.
[105] K. A. Bacik, S. Lovett, C. P. Caulfield and N. M. Vriend, "Wake induced long range repulsion of aqueous dunes", *Phys. Rev. Lett.* **124** (2020), article no. 054501.
[106] W. R. Assis, D. S. Borges and E. M. Franklin, "Barchan Dunes Cruising Dune-Size Obstacles", *Geophys. Res. Lett.* **50** (2023), article no. e2023GL104125.
[107] Bin Yang, Y. Chong, Y. Lin, N. He, Y. Zhang and X. Gao, "Experimental study of the stability of crescent barchan shape in subaqueous dune evolution in unsteady water flow", *Eur. J. Mech. B Fluids* **103** (2024), pp. 246–258.
[108] F. Charru and E. M. Franklin, "Subaqueous barchan dunes in turbulent shear flow. Part 2. Fluid flow", *J. Fluid Mech.* **694** (2012), pp. 131–154.
[109] C. A. Alvarez and E. M. Franklin, "Birth of a subaqueous barchan dune", *Phys. Rev. E* **96** (2017), article no. 062906.
[110] T. Loiseleux, P. Gondret, M. Rabaud and D. Doppler, "Onset of erosion and avalanche for an inclined granular bed sheared by a continuous laminar flow", *Phys. Fluids* **17** (2005), article no. 103304.
[111] K. Pye and H. Tsoar, *Aeolian Sand And Sand Dunes*, Kluwer Academic Publishers, 1990.
[112] R. Cooke, A. Warren and A. Goudie, *Desert Geomorphology*, UCL Press, London, 1993.
[113] I. Livingstone and A. Warren, *Aeolian geomorphology: an introduction*, Addison Wesley Longman, 1996.
[114] O. Durán, E. J. R. Parteli and H. J. Herrmann, "A continuous model for sand dunes: Review, new developments and application to barchan dunes and barchan dune fields", *Earth Surf. Process. Landf.* **35** (2010), pp. 1591–1600.
[115] K. L. Anthonsen, L. B. Clemmensen and J. H. Jensen, "Evolution of a dune from crescentic to parabolic form in response to short-term climatic changes: Råbjerg Mile, Skagen Odde, Denmark", *Geomorphology* **17** (1996), pp. 63–77.
[116] L. K. Fenton, T. I. Michaels, M. Chojnacki and R. A. Beyer, "Inverse maximum gross bedform-normal transport 2: application to a dune field in Ganges Chasma, Mars and comparison with HiRISE repeat imagery and MRAMS", *Icarus* **230** (2014), pp. 47–63.
[117] R. C. Ewing, A.-P. B. Peyret, G. Kocurek and M. C. Bourke, "Dune field pattern formation and recent transporting winds in the Olympia Undae Dune Field, north polar region of Mars", *J. Geophys. Res.* **115** (2010), article no. E08005.
[118] B. Charnay, E. Barth, S. Rafkin, et al., "Methane storms as a driver of Titan's dune orientation", *Nat. Geosci.* **8** (2015), pp. 362–366.
[119] P. Hersen, K. H. Andersen, H. Elbelrhiti, B. Andreotti, P. Claudin and S. Douady, "Corridors of barchan dunes: Stability and size selection", *Phys. Rev. E* **69** (2004), article no. 011304.
[120] W. R. Assis and E. M. Franklin, "A comprehensive picture for binary interactions of subaqueous barchans", *Geophys. Res. Lett.* **47** (2020), article no. e2020GL089464.
[121] O. Durán, V. Schwämmle, P. G. Lind and H. J. Herrmann, "The dune size distribution and scaling relations of barchan dune fields", *Granul. Matter* **11** (2009), pp. 7–11.
[122] P. A. Jarvis, C. Narteau, O. Rozier and N. M. Vriend, "The probabilistic nature of dune collisions in 2D", *Earth Surf. Dyn.* **11** (2022), no. 4, pp. 803–815.
[123] M. Génois, S. Courrech du Pont, P. Hersen and G. Grégoire, "An agent-based model of dune interactions produces the emergence of patterns in deserts", *Geophys. Res. Lett.* **40** (2013), pp. 3909–3914.
[124] S. Worman, A. B. Murray, R. Littlewood, B. Andreotti and P. Claudin, "Modeling emergent large-scale structures of barchan dune fields", *Geology* **41** (2013), pp. 1059–1062.
[125] M. Génois, P. Hersen, S. Courrech du Pont and G. Grégoire, "Spatial structuring and size selection as collective behaviours in an agent-based model for barchan fields", *Eur. Phys. J. B, Condens. Matter Complex Syst.* **86** (2013), article no. 447.
[126] M. Génois, P. Hersen, E. Bertin, S. Courrech du Pont and G. Grégoire, "Out-of-equilibrium stationary states, percolation, and subcritical instabilities in a fully nonconservative system", *Phys. Rev. E* **94** (2016), article no. 042101.
[127] P. A. Hesp, "Foredunes and blowouts: initiation, geomorphology and dynamics", *Geomorphology* **48** (2002), pp. 245–268.
[128] O. Durán and H. J. Herrmann, "Vegetation against dune mobility", *Phys. Rev. Lett.* **97** (2006), article no. 188001.
[129] P. A. Hesp, "Conceptual models of the evolution of transgressive dune field systems", *Geomorphology* **199** (2013), pp. 138–149.
[130] X. Gao, C. Gadal, O. Rozier and C. Narteau, "Morphodynamics of barchan and dome dunes under variable wind regimes", *Geology* **46** (2018), pp. 743–746.
[131] P. Claudin, G. F. S. Wiggs and B. Andreotti, "Field evidence for the upwind velocity shift at the crest of low dunes", *Boundary-Layer Meteorol.* **148** (2013), pp. 195–206.
[132] L. Ping, C. Narteau, Z. Dong, Z. Zhang and S. Courrech du Pont, "Emergence of oblique dunes in a landscape-scale experiment", *Nat. Geosci.* **7** (2014), pp. 99–103.

[133] R. E. Hunter, B. M. Richmond and TAU Rho Alpha, "Storm-controlled oblique dunes of the Oregon coast", *Geol. Soc. Am. Bull.* **94** (1983), pp. 1450–1465.

[134] A. Lucas, S. Rodriguez, C. Narteau, et al., "Growth mechanisms and dune orientation on Titan", *Geophys. Res. Lett.* **41** (2014), pp. 6093–6100.

[135] O. Durán Vinent, B. Andreotti, P. Claudin and C. Winter, "A unified model of ripples and dunes in water and planetary environments", *Nat. Geosci.* **12** (2019), pp. 345–350.

[136] B. Andreotti, A. Fourrière, F. Ould-Kaddour, A. B. Murray and P. Claudin, "Giant aeolian dune size determined by the averaged depth of the atmospheric boundary layer", *Nature* **457** (2009), pp. 1120–1123.

[137] P. Lü, C. Narteau, Z. Dong, O. Rozier and S. Courrech du Pont, "Unravelling raked linear dunes to explain the coexistence of bedforms in complex dunefields", *Nat. Commun.* **8** (2017), article no. 14239.

[138] P. Lü, C. Narteau, Z. Dong, et al., "Coexistence of Two Dune Growth Mechanisms in a Landscape-Scale Experiment", *Geophys. Res. Lett.* **49** (2022), article no. e2021GL097636.

[139] M. C. Marvin, M. G. A. Lapôtre, A. Gunn, M. Day and A. Soto, "Dune interactions record changes in boundary conditions", *Geology* **51** (2023), pp. 947–951.

[140] C. Gadal, P. Delorme, C. Narteau, G. F. S. Wiggs, M. C. Baddock, J. M. Nield and P. Claudin, "Local wind regime induced by giant linear dunes: Comparison of ERA5-land reanalysis with surface measurements", *Boundary-Layer Meteorol.* **185** (2022), pp. 309–332.

[141] L. Fernandez-Cascales, A. Lucas, S. Rodriguez, X. Gao, A. Spiga and C. Narteau, "First quantification of relationship between dune orientation and sediment availability, Olympia Undae, Mars", *Earth Planet. Sci. Lett.* **489** (2018), pp. 241–250.

[142] B. Castelle, Q. Laporte-Fauret, V. Marieu, et al., "Nature-based solution along high-energy eroding sandy coasts: preliminary tests on the reinstatement of natural dynamics in reprofiled coastal dunes", *Water (Switz.)* **11** (2019), article no. 2518.

[143] Q. Laporte-Fauret, B. Castelle, R. Michalet, V. Marieu, S. Bujan and D. Rosebery, "Morphological and ecological responses of a managed coastal sand dune to experimental notches", *Sci. Total Environ.* **782** (2021), article no. 146813.

[144] V. Ralaiarisoa, P. Dupont, A. Ould El Moctar, F. Naaim-Bouvet, L. Oger and A. Valance, "Particle impact on a cohesive granular media", *Phys. Rev. E* **105** (2022), article no. 054902.

ACADÉMIE DES SCIENCES
INSTITUT DE FRANCE

Comptes Rendus. Physique
2024, Vol. 25, Special issue S3, p. 297-332
https://doi.org/10.5802/crphys.225

Review article / *Article de synthèse*

Geophysical and astrophysical fluid dynamics in the laboratory / *Dynamique des fluides géophysiques et astrophysiques aulaboratoire*

Quantifying soil surface erosion

Quantifier l'érosion de surface des sols

Pierre Philippe[*,a] **and Nadia Benahmed**[a]

[a] RECOVER, INRAE, Aix Marseille University, Aix-en-Provence, France

E-mails: pierre.philippe@inrae.fr (P. Philippe), nadia.benahmed@inrae.fr (N. Benahmed)

Abstract. This review first introduces the general context of soil erosion, an omnipresent natural process involving a wide variety of spatial and temporal scales. While this loss of solid matter induced by all kinds of fluid flows on the surface of soils is often a source of beauty in the landscapes that surround us, it also constitutes a major risk and poses growing threats in the context of global change as loss of agricultural soil fertility, decline in coastal ecosystems or increase in safety standards for flood protection structures. It is therefore essential to be able to predict future soil removal rates at multiple scales, in order to anticipate or mitigate their impacts. This requires experimental quantification of soil's vulnerability to erosion. In order to describe this type of measurement in deeper detail, we restricted the scope of our review to situations of concentrated surface erosion of homogeneous soils, on moderate spatial and temporal scales, as typically studied in the fields of civil or environmental engineering. Measuring erosion itself is challenging, both in terms of determining the rate of mass removal from a surface, and in terms of selecting and quantifying a relevant hydrodynamic quantity to reflect the strength exerted by the flow. A conceptual framework is then required to correctly define soil's erodibility, which is defined as an intrinsic property of the material through an empirical erosion law. In the most commonly accepted approach, this erodibility combines two distinct parameters: an erosion initiation threshold, generally chosen as a critical shear stress, and an erosion kinetic coefficient. The various types of erodimeters found in literature are then presented and compared, with a specific and more complete description of the three main devices used in geomechanics (EFA, HET and JET). Finally, before concluding and suggesting some perspectives on the topic, we outline the various advantages and applications of the erodibility values derived from experimental tests, while showing the limitations of the approach and the questions raised by them.

Résumé. Cet article de synthèse introduit tout d'abord le contexte général de l'érosion des sols, un processus naturel omniprésent impliquant des échelles spatio-temporelles extrèmement variées. Si cette perte de matière solide induite par toutes sortes d'écoulements fluides à la surface des sols est souvent source de beauté des paysages qui nous entourent, elle n'en constitue pas moins un risque majeur et fait peser des menaces croissantes dans le contexte du changement global comme la perte de fertilité des sols agricoles, le déclin des écosystèmes littoraux ou le besoin accru de sureté des ouvrages de protection contre les inondations. Par conséquent, il est essentiel de pouvoir prédire aux différentes échelles les niveaux futurs de retrait des sols afin de mettre en oeuvre de possibles mesures d'anticipation ou d'atténuation. Il convient pour cela de connaître la sensibilité à l'érosion d'un sol via une quantification expérimentale. Pour décrire plus en détail ce type de mesures, le choix est fait ici de restreindre le cadre considéré aux situations d'érosion

* Corresponding author

de surface concentrée de sols homogènes, sur des échelles spatiales et temporelles restant modérées, et telle que typiquement étudiée dans les domaines de l'ingénierie civile ou environnementale. La mesure de l'érosion en elle-même est délicate et complexe, aussi bien pour déterminer le taux de matière érodée à une surface que pour sélectionner et quantifier une grandeur hydrodynamique pertinente, capable de rendre compte de la force exercée par l'écoulement. Un cadre conceptuel est ensuite nécessaire pour définir correctement une érodabilité du sol, condidérée comme une propriété intrinsèque du matériau à travers une loi empirique d'érosion. Dans l'approche la plus communément acceptée, cette érodibilité regroupe deux paramètres distincts : un seuil d'initiation de l'érosion, généralement choisi comme une contrainte de cisaillement critique, et un coefficient cinétique. Les différents types d'érodimètres issus de la litérature sont ensuite présentés et comparés, avec un descriptif spécifique et plus complet sur les trois principaux dispositifs utilisés en géomécanique (EFA, HET et JET). Enfin, avant de conclure et de suggérer quelques perspectives futures sur la thématique, nous présentons les nombreux avantages et utilisations possibles des valeurs d'érodabilité issues de ces essais, tout en montrant les limites de l'approche et les questions que celles-ci soulèvent.

Keywords. Erosion, Measurement, Soil's erodibility.

Mots-clés. Erosion, Mesure, Erodabilité des sols.

Manuscript received 26 May 2024, revised 27 November 2024, accepted 2 December 2024.

1. Context of soil erosion and related issues

1.1. *A ubiquitous process on a variety of scales*

Quoting Wikipedia[1], *erosion is the action of surface processes (such as water flow or wind) that removes soil, rock, or dissolved material from one location on the Earth's crust and then transports it to another location where it is deposited.* Adopt this definition, which is already rather broad, nevertheless excludes several adjacent mechanisms likely to lead to the dislocation and crumbling of solid matter but which involve no motion, such as weathering [1, 2] or others physico-biological actions [3]. We therefore strictly define our object of study as being the erosion generated by the detachment and entrainment of solid matter from the surface of a soil under the action of a fluid flow. Soil is understood here as a geomaterial in the broadest sense, encompassing all types of soil, including clay, sand or silt, as well as coarser materials, from pebbles to boulders, or even snow. The variety is rather vast, with highly contrasting levels of internal cohesion between constituent particles that also vary greatly in size: from cohesion-less granular soils to coherent materials or soft rocks.

As defined above, the erosion of solid matter is difficult to dissociate from, and in fact includes, the subsequent transport induced by the eroding flow. This complementary removal process enabling the loosened soil to be evacuated, more or less rapidly, thereby allowing erosion to possibly continue. Thus, the major problems associated with soil erosion stem directly from the combination of conditions that initiate soil removal and enable its transport, wether over a few millimeters or thousands of kilometers. There is a wide variety of soil erosion types [4–6] and the main natural processes involved include: Sediment transport (in mountain streams, rivers, oceans, or deserts) [4,7–10]; Coastal erosion [11,12]; Rain splash and runoff erosion (including rill erosion, gullies, etc) on farmland or hill-slope [5,13,14], with essential role of plant covers [15,16]; Piping in natural soils [17, 18]; Scouring of riverbanks [19, 20] or bridge pier foundations [21, 22]; Internal and external erosion of earthen hydraulic structures [23–26]. From a geomorphological point of view, the different spatial scales involved vary tremendously, from a simple sand ripple to mountains, from a drop of water to the confluence of the Amazon. Similarly, the timescales of erosion range from a few seconds to several million years [27]! Mountains are thus erased or

[1] https://en.wikipedia.org/wiki/Erosion



Figure 1. Example of gullies sculpted by erosion in farmland as strikingly painted by Alexandre Hogue in "The crucified Land" (1939). Licence: CC BY-NC-SA 4.0.

valleys carved out on geological periods, while violent events such as a massive landslide may last a very short time.

As a result, erosion leaves its omnipresent imprint on relief and landscape, through riverbeds and deltas, cliffs and coastlines, or inspiring country fields (see for instance Figure 1) . . . We enjoy this imprint daily as we contemplate the exceptional beauty of nature. But we also endure it by living under the threat of natural events more or less directly responsible for various erosional processes, such as floods, landslides, coastal storms or torrential flows. Soil erosion thus has a feedback effect on our environment through the increasing construction of protective systems, as it poses a major hazard to many sensitive natural and man-made elements: beaches, dunes, farmland, building foundations, bridge piers, earthen engineering structures . . .

1.2. *A primary vector of risks*

Sediment transport is part of a natural geological cycle, based on land subduction balanced by gradual relief degradation and subsurface erosion. However this equilibrium is increasingly disrupted by human activity [6]. The global average rate of soil erosion by water is estimated to be somewhere between 0.1 and 0.15 mm/year, exhibiting significant local disparities [28,29], with a strong upward trend in erosion rate due to climate change, land use and other socio-economic factors [30–33]. In itself, this acceleration threatens the geological balance between formation and removal of natural soils, endangering both human food security and global ecosystem sustainability [28]. Soil erosion of agricultural fields, mainly due to rainfall and surface runoff, is another threat suspected of reducing agricultural potential, particularly fertility, or inducing soil thinning [34]. For instance, in the US, the Department of Agriculture (USDA) recommends a soil loss rate below 1 mm/year for soil conservation [29], but research work continues on this soil loss tolerance [35]. Agricultural erosion also has an impact on the global carbon cycle, but whose effect is still uncertain and debated [36–38].

As mentioned earlier, the erosion of sediments can lead to the transport of solid or dissolved matter over long distances, posing the risk of pollution through the dispersion of contaminants.



Figure 2. Photographs from an artistic perspective of Le Signal building (Soulac-sur-Mer, France). This construction, built between 1967 and 1970, was definitely abandoned in 2014 under the threat of coastal erosion and finally demolished in 2023. Credit: Le Signal@Olivier Crouzel (https://www.oliviercrouzel.fr).

These dangerous elements include radioactive particles [39], heavy metals [40, 41], or microplastics [42, 43], whose proliferation is of particular concern due to their notoriously harmful effects on virtually all ecosystems.

The desertification of entire regions, such as the Sahel and the Sahara, has been greatly intensified by anthropogenic climate change [44], and is partly induced by wind erosion and subsequent transport [10], which contribute to both the degradation of agricultural soils and the invasion of land through the displacement of large volumes of sand.

The sharp decline in coastline due to increased shoreline and beach erosion is also a cause for great concern [11, 12], particularly in the current and, above all, future context of rising sea levels and more frequent ocean storms [45, 46]. The main threats concern the coastal ecosystem and human activities, the sea, which is gradually moving closer to natural or anthropic habitats, as illustrated in Figure 2.

In addition, the safety of man-made structures in permanent or intermittent contact with water is constantly threatened by the erosion that can be generated by subsequent flows. This hazard seems to be growing, particularly in the alarming context of global change, which is very likely to lead to an intensification of extreme climatic events (storms, precipitation, flooding). Major concerns include scouring around rigid structures such as bridge piers [47] or concrete dikes, or direct water flow erosion of earthen hydraulic structures, such as flood defence works, earthen dams and levees, river and canal embankments [23–26].

1.3. *A need for predictive modeling*

Given these severe risks posed, directly and indirectly, by soil erosion, the human response cannot be solely focused on protection, although this is an essential element. For effective management, we should also be able to predict the effects of erosion over time as reliably as possible, which requires the development of models capable of incorporating to varying degrees the complexity of the processes involved. Before attempting any modeling, the scales to be considered must first be defined, both in terms of time and space. These scales are constrainted by the global dimensions of the system in question and the total duration targeted, and require the introduction of elementary time and space steps at the scale of the basic processes under consideration.

For example, erosion of the Earth's crust is a central feature of long-term landform modelling, combining tectonics and surface processes [27, 48]. However, many soil erosion models are built

on a catchment scale, focusing on shorter durations, typically decades, to assess over time both sediment production and transport capacity. In an extremely active field of research, a number of operational tools have been proposed [49, 50]. Such distributed models are specifically designed for a particular area, on a regional, national or continental scale, and include, among others: the European Soil Erosion Model EUROSEM [51], the Water Erosion Prediction Project WEPP [52], the Pan European Soil Erosion Risk Assessment PESERA coarse scale model [53], the (Revised) Universal Soil Loss Equation (R)USLE [32, 54] (see Figure 3 as an illustration), or else the Limburg Soil Erosion Model LISEM [55]. Empirical, conceptual and physical process-based approaches can be distinguished, all requiring a large number of input data explicitly accounting as much as possible for climate variation (rainfall, temperature, etc.) and vegetation characteristics. A highly critical parameter is land erodibility, mostly derived from soil characteristics [56, 57] and used as an integrated coefficient at the model mesh scale. However, despite significant progress in model spatial resolution, the elementary mesh incorporates a large number of heterogeneities and spatial variabilities in subsoil characteristics, remaining well above the micro-scale where a homogeneous material behavior can be found, known as Representative Elementary Volume (REV) in the field of soil mechanics [58]. Despite the obvious interest and need for these large-scale models, they still have significant limitations [57]. In particular, they suffer from the wide dispersion of available data and their usually limited calibration domain, with no effective validation outside of it [59].

Another approach consists in studying and modeling soil surface erosion at the representative material scale that is considerably smaller, typically on soil sections of a few hundred square centimetres. The number of input parameters for these models is significantly reduced, and calibration is generally simpler, often based on well-controlled laboratory experiments. This line of research was particularly initiated to analyze river erosion and sediment transport, especially in the case of granular (i.e. non-cohesive) sediments, for which an empirical modeling framework has long been established. This framework is essentially based on the dimensionless Shields number, which compares fluid stress and buoyancy weight for grains or pebbles at the riverbed interface. The Shields number governs the sediment transport and a specific curve empirically determining its critical value at the threshold of erosion initiation [9, 60, 61]. The case of cohesionless sediments corresponds to a straightforward situation where the physical origin of grain movement is clear. The understanding is much more complex for cohesive soils, where soil composition, grain size distribution and internal interactions within the material play major role, rendering the previous Shields'approach inadequate in most cases [62, 63]. Moreover an erosion threshold alone is not sufficient to describe the phenomenon, which has its own kinetics controlling the rate of soil removal once erosion has initiated. The mechanisms responsible for material entrainment appear obviously more complex and varied for cohesive soils, necessitating a better physical and physico-chemical understanding of the processes [64]. This is all the more true as the cohesion of a soil can have several possible origins: macroscopic expression of microscopic inter-molecular interactions within very fine soils, but also emerging property from the presence of binding agents between larger grains (partially saturated granular soils, cemented or bio-cemented soils, etc.). To the best of the authors' knowledge, it is currently impossible to present an exhaustive and coherent physical picture of the mechanisms of cohesive soil erosion, as understanding of the phenomenon is still very limited in the community concerned. A few fragments of theory do exist, often quite disconnected from each other, and will be mentioned in this article. Advances in numerical modeling have been much more significant, and a recent review article provides an up-to-date synthesis of modeling of soil surface erosion [65], but again with very few elements specific to cohesive soils. While awaiting a clearer understanding, developments mainly relied on empirical approaches, particularly through the formulation of erosion laws at material scale [66].

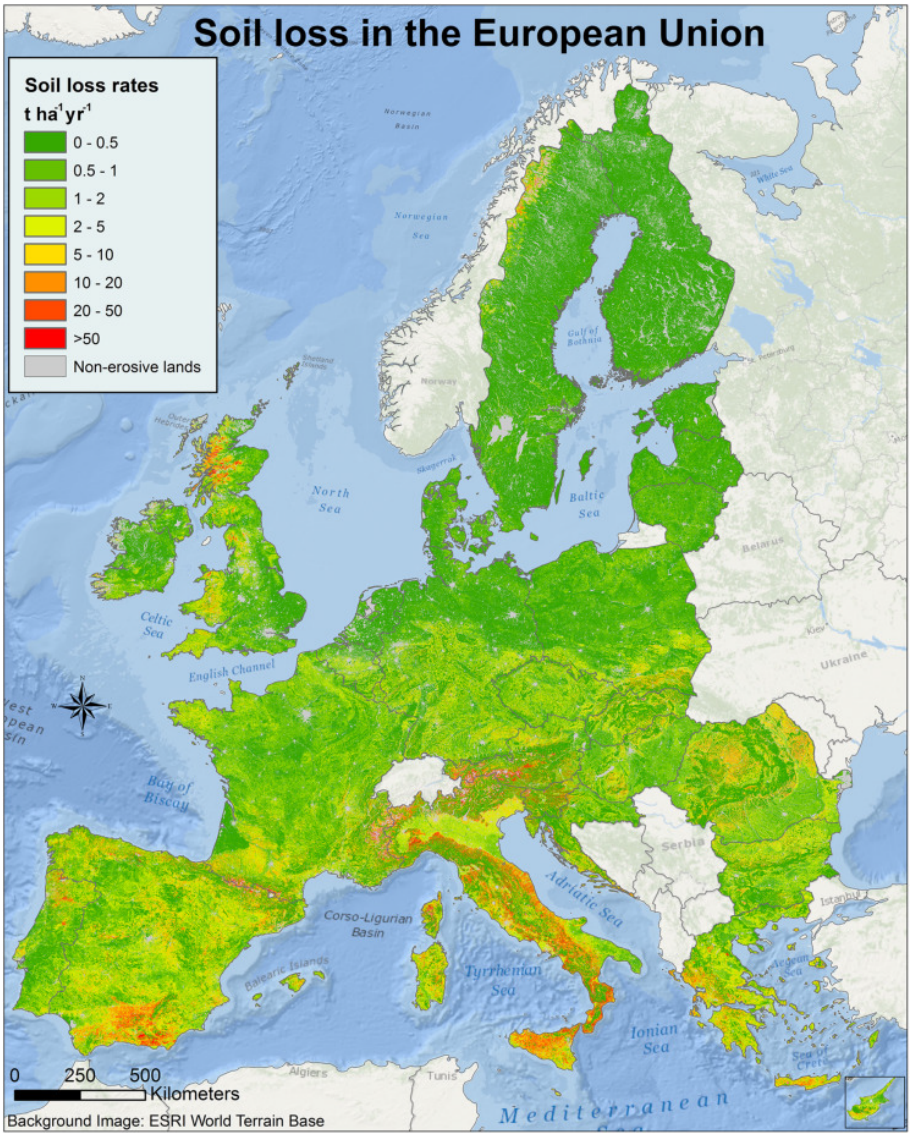


Figure 3. An example of results achievable with large-scale models is shown here with the map of soil loss rates in the European Union (for reference year 2010) based on RUSLE2015 [54].

Whatever the scale considered, modeling requires establishing a relationship between the quantity of soil eroded, typically described by an erosion rate or a sediment transport capacity, and the force exerted by the hydraulic flow. Such relationships effectively introduce parameters that account for the soil's resistance to concentrated water flow [66]. These parameters can be seen as integrated erodibility coefficients or indexes in large-scale models, deduced from many input parameters, by contrast with intrinsic soil properties at the material level. A critical aspect concerns the selection of a proxy indicator for the hydraulic strength [66]. For instance, runoff erosion intensity on a ground plot is generally expressed in terms of the transport capacity, as a function of shear stress [52, 67] or unit stream power [55, 68]. However, alternative choices exist,

such as flow rate, water head or Froude number [66]. These integrated or more local erosion laws are primarily empirical, with some being based on a conceptual framework [69], proposing a unified formulation [70, 71], or including a stochastic component [72, 73], as will be discussed further in Section 2.2.

However, as a prerequisite to any modeling, obtaining reliable and varied experimental data, both in field and from the lab, is essential for supplying, calibrating and validating the various types of erosion and transport models. With this objective in mind, and in order to build up the most reliable predictions possible, methodologies have been developed to measure soil and sediment erosion or, in other words, to determine the erodibility parameters of the material or elementary ground unit under consideration with maximum precision. Given the vast range of different mechanisms at the root of soil loss by water flow [13], adopting a global approach appears impractical and, as Knapen and co-authors have pointed out [66], *it is obvious that soil erosion should be considered as a process-specific concept with different erodibility indices*. The forward corollary is that specific measurement approaches are obviously needed for each of these erodibility quantifications.

1.4. *Scope of the present review*

In this review, we have chosen to focus on experimental methods developed to determine the resistance of consolidated cohesive soils against surface erosion, subject to submerged and concentrated flow conditions, over reduced time and space scales, excluding any additional impact of slope with respect to the horizontal in our discussion. The main practical applications concern scouring and interfacial erosion on coherent geomaterials such as seabed sediment, mostly constituted of sand-mud mixtures [8, 63] and subject in particular to intense and increasing coastal erosion [46], or compacted clayey soils in earthen hydraulic structures, typically levees or embankment dams [26]. In this particularly sensitive application, two types of erosion can occur: external erosion, where there is overflow on the face of the structure, and internal erosion, associated with mechanisms induced by infiltration flows within the structure and its foundations. These two causes are responsible, in nearly the same proportion, for almost 100% of reported earth dam failures [23, 24]. The mechanisms of internal erosion, which have been extensively studied over the last twenty years and are now well identified, involve, for some, zones within or below the structure where cohesive constituent soils can be superficially eroded by a head of water. This is notably the case for the so-called concentrated leak erosion, contact erosion or backward piping erosion in its development phase [26]. Within soils with a granular structure, there also exist internal erosion processes that occur not at the surface but within the volume of the material [74], although these will not be discussed here.

In what follows, we will present the different methods to assess, for a soil subjected to a concentrated submerged hydraulic flow along an initially flat and horizontal surface, the same parameters, hereinafter referred to as *erodibility*. These parameters will be defined conceptually in greater detail below.

2. Experimental determination of soil's erodibility

2.1. *Difficulties and challenges*

Developing a device and protocol adapted to the study of soil erosion is a major experimental challenge. It requires simultaneous and independent quantification of both the rate of solid matter loss and the hydrodynamic load exerted by the eroding flow. However, each of these measurements proved difficult to implement for several reasons.

The rate of erosion at the surface of a soil sample is straightforwardly defined as the mass of solid matter lost per unit of time and per unit of surface area. The most direct method of determining it would be to measure the gradual loss of mass over time for the sample under test but this, however, poses major practical difficulties. While weighing a given initial mass, it is necessary to detect very small variations in mass, particularly when identifying an erosion threshold. As a result, weighing accuracy is severely limited, especially considering significant noise expected due to the supplementary force generated by the water flow, usually in a turbulent regime with substantial hydrodynamic fluctuations. Consequently, the use of direct mass measurements for erosion monitoring remains marginal.

Assuming soil homogeneity and measuring the corresponding density, the change in mass of the eroded sample can be deduced from the change in volume and therefore, more directly, from the progressive deepening of the surface exposed to the flow. Since the long-existing point gauge measurements [75,76], the techniques used have become increasingly sophisticated, particularly with the use of 2D or 3D laser systems [77–79] and imaging processing methods such as digital photogrammetry [80] or light attenuation [81]. However, there are several major obstacles to accurately tracking the eroded area: the upper surface can rapidly develop a complex and evolving morphology; the rapid build-up of suspended matter in the flow makes the water turbid, preventing the use of certain probes, particularly optical ones, or even direct visualization; the presence of heterogeneity or defects at the scale being investigated compromises the validity of the approach.

In the end, the quantity of soil removal is often deduced from other complementary experimental data rather than being directly measured at the eroded area. The resulting sediment loss can be straightforwardly determined from the concentration in eroded material inside the flow emerging from the active zone. Erosion rate is then obtained through the conservation of solid matter exchanges. However, this procedure may suffer from a time lag induced by the distance imposed between the measurement zone and the erosion zone. The concentration of eroded material can be determined by regular sampling and weighing of the downward flow, but solely on a high periodicity basis, or, for fine sediment transported in suspension, by continuous time monitoring using a turbidimeter, which in practice requires prior calibration for each test. In an even more indirect manner, and subject to strong simplifying assumptions, the measurement of the flow-pressure relationship in the erosion zone can be used to estimate the soil removal rate, based on the increase in flow cross-section and therefore in the associated hydraulic radius [82]. However, this method is rather approximate and is also directly linked to hydrodynamic measurements of the eroding flow, unlike previous approaches.

Measuring soil erosion rates involves considering factors, including the history and aging of the soil being studied. There are typically two options for real soil assessment: conducting tests on-site using portable devices or collecting soil samples for laboratory testing. This second procedure generally enables more precise measurements under better-controlled conditions, with sophisticated equipment. However, in some cases, the original sampled soil cannot be tested intact, due to damage or the presence of interfering elements (large particles, roots, etc.). The soil is then reconstituted under the same conditions as those found on the site. However, this reconstituted soil may lose the memory it has gained from in situ consolidation and, as will be discussed later, its resistance to erosion tends to be consistently reduced. It should be noted that for specific comprehensive studies, model soil samples can be prepared on demand using the same methodology for systematic testing.

Linking erosion rate with flow intensity requires accurately measuring the flow and deriving appropriate and relevant characteristic quantities. This also poses a number of difficulties, firstly in selecting the flow features that closely reflect the physics of erosion, and, secondly, in implementing the accompanying measurements in practice, particularly considering that the

flow regime is most often turbulent. In such turbulent flow, the movement of fluid is chaotic, characterized by irregular fluctuations in velocity and pressure. This turbulence complicates the measurement process as traditional techniques may not capture all relevant flow features accurately.

Many competing quantities can be used to characterize a flow, generally presenting direct or semi-empirical relationships between them, with a strong dependence on the specificity of the hydrodynamic configuration considered, which can vary widely (flow in a channel, flow in a pipe with cross-sectional variation, submerged impact jet . . .). Classically accepted quantities for characterising flow include discharge, stream power, flow shear stress, or shear velocity [66]. As already mentioned, a key challenge lies in ensuring that the chosen hydrodynamic indicator adequately represents the erosion mechanisms which, by definition, take place at the interface between soil and water flow. A volume-averaged magnitude is therefore unlikely to be straightforwardly relevant for describing this type of superficial phenomenon and requires prior calibration to correlate with a more local characterization. In this respect, the bottom shear stress (or equivalently shear velocity) at the soil surface appears to be a flow predictor with significant potential. Consequently, it has often been selected, although it's not the most straightforward to determine, as will be discussed below.

Once a hydrodynamic reference variable has been selected, it is essential to consider whether its mean value is representative of the effective flow loads generating erosion. While this question does not arise in the case of a perfectly stationary ideal flow, the same is no longer true in more realistic situations where the hydrodynamic regime is generally turbulent, inducing more or less pronounced fluctuations within the flow [83, 84]. A moderate average value can therefore mask much higher extreme values, likely to induce localized erosion puffs. To take these fluctuations into account, it is then necessary to characterize the complete statistical distribution, particularly in the upper tail [73]. Note that a perfectly similar approach can be adopted in the presence of spatial variations in flow along the erosion surface [85]. Furthermore, variability in erosion does not solely arise from flow dynamics but also from the eroded material itself, which is rarely homogeneous, particularly in field conditions [86].

Monitoring basic hydrodynamic quantities involves measuring the overall discharge rate, using a suitable flowmeter, and the pressure difference between upstream and downstream of the erosion zone, using either two absolute pressure transducers or directly a differential pressure gauge. This standard instrumentation can be exceptionally accompanied by more sophisticated measurements, such as for calibration purposes, in particular to reconstruct the velocity field in space, whether using normal profiles at the interface of interest, 2D maps in the vertical plane, or even full 3D velocity fields. To achieve this, precision instruments are required, such as laser or acoustic Doppler velocimeter, particle image velocimetry systems, or hot-wire measurements [87–89]. Most interestingly, it is next possible to derive the time-averaged shear stress from this mean velocity profile using various correlation strategies with established laws [90, 91]. Direct measures of bottom shear stress are also available [91], either at a single point with a Preston tube [92, 93] or over a surface with MEMS-based, oil-film interferometry, floating element or hot wire techniques [94–96]. In all cases, the measurement of bottom shear stress relies on inferring it from another quantity, necessitating the use of these inventive and sometimes unexpected methods, such as for example shear-induced bioluminescence [97], electrochemical technique [84] or ferrofluid spike deformation [89]. It is important to note that high time resolution is crucial when fluctuations, rather than mean value, have to be obtained, especially in turbulent flow conditions where fluctuations play a major role in erosion process.

In practice, from the perspective of routinely carrying out tests to quantify soil erosion resistance, implementing high-tech measurement systems to tackle all the key issues raised above can be impractical. To circumvent this limitation, interpretation models, specific to each test and its

own hydraulic configuration, have been developed. Based on a number of simplified (or even oversimplified) and/or known empirical correlations, such models make it possible to propose reduced relationships between key hydrodynamic and geometric quantities, related to flow and erosion. This approach helps limit the number of input quantities that need to be measured, rendering testing more feasable in practical settings. Pre-calibration is also usually required. For example, in a test involving flow through a pipe, the lateral shear stress can be deduced from either overall head loss or discharge rate [82]. Similarly, in a test involving an impinging submerged jet, the tangential shear stress can be expressed as a function of both height and flow rate of the jet [75].

2.2. *Conceptual framework for intrinsic soil's erodibility*

Since knowledge of the elementary physics involved in the removal and transport of cohesive soils by flow is still limited to date, erosion laws, i.e. laws relating erosion rate to relevant hydrodynamic quantities, have primarily been formulated empirically. Several competing formulations have been proposed, mostly but not exclusively based on fluid shear stress [18,66,69–71,86, 98–104]. As the existence of a threshold for erosion is fairly widely accepted in the scientific community, although this is still open to debate [105], excess shear stress models are most frequently proposed, using as control variable the amount of shear stress exerted by the flow in excess with respect to a threshold indicative of the material's resistance. For simplicity's sake, these expressions take typically the form of power laws. This approach is reminiscent of long-established empirical laws describing solid transport, as initially suggested by Duboys [106] and later refined by Meyer-Peter Müller equation for the bedload of sand and gravel [7,8]. This type of law is also often proposed for the stream capacity in large-scale integrated approaches of landscape evolution models, as illustrated in [107].

Although there are a few other alternative formulations [18, 100, 102], the most common surface erosion law is generically expressed as:

$$E_{\mathrm{m,v}} = \begin{cases} K_{\mathrm{m,v}}(\tau - \tau_{\mathrm{c}})^n & \text{if } \tau \geq \tau_{\mathrm{c}} \\ 0 & \text{if } \tau < \tau_{\mathrm{c}} \end{cases} \tag{1}$$

where the erosion rate E_{m} (respectively E_{v}) is defined as the soil mass (respectively volume) loss by surface and time units (see previous Figure 4) while τ is the bottom shear stress exerted by the flow. The new parameters introduced in this formulation are: (i) the proportionality coefficient K (being equivalently K_{m} or K_{v}), called the coefficient of soil erosion, the detachment rate coefficient, the concentrated flow soil erodibility, or simply erodibility according to various authors; (ii) the stress threshold τ_{c}, which quantifies the soil's resistance to erosion and is commonly referred to as critical shear stress; (iii) the exponent n of the power law, where $n > 0$.

In practical terms, especially concerning the units of the proportionality coefficients, this erosion law can also be conveniently written in dimensionless form as follows:

$$E_{\mathrm{m,v}} = \begin{cases} E^*_{\mathrm{m,v}} \left(\frac{\tau}{\tau_{\mathrm{c}}} - 1 \right)^n & \text{if } \tau \geq \tau_{\mathrm{c}} \\ 0 & \text{if } \tau < \tau_{\mathrm{c}} \end{cases} \tag{2}$$

where $E^*_{\mathrm{m,v}} = K_{\mathrm{m,v}} \tau_{\mathrm{c}}^n$ appears as a standard (mass or volume) erosion rate, which coincides with the actual erosion rate obtained for a flow shear stress equal to twice the soil's critical threshold τ_{c}. This quantity is also occasionally referred to as the rate coefficient [108].

The exponent n of the power law is certainly of practical interest as it accounts for nonlinear relationship between erosion rate and excess stress, both for concave curvature ($0 < n < 1$) and convex curvature ($n > 1$). However, unlike the other two parameters, K and τ_{c}, which will be discussed just beyond, it is much more difficult to provide for n a straightforward physical

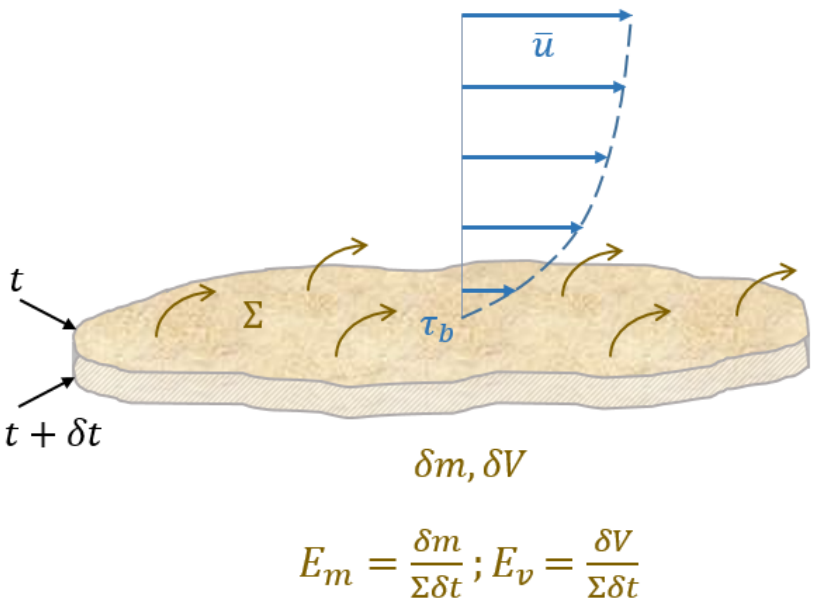


Figure 4. Sketch of a soil surface Σ subject to erosion by a flow characterised by a given mean velocity $\overline{u}$ profile and related bottom shear stress τ_b. The mass (respectively volume) loss is denoted δm (respectively δV) and the erosion rate E_m in mass (respectively E_v in volume) is directly derived.

interpretation, or even a more indirect one. While Walder proposed a generalized erosion law where $n = 7/4$ [71], other authors have shown that a value strictly greater than 1 leads to a divergence[2] in erosion kinetics and therefore appears non-physical [109]. Consequently, the linear excess-shear stress erosion law, where $n = 1$, is the one commonly used in practice. The preference for $n = 1$ is most likely due to several factors. Firstly, it offers conceptual simplicity. Additionnally, determining an exponent $n \neq 1$ that would be used as a free fitting parameter is challenging, given the wide dispersion frequently observed in most erosion rate measurements, as illustrated in Figure 5 by several examples involving natural or reference soils [110–113]. Note that selecting $n = 1$ also provides convenient units for K_m and K_v, which are $\mathrm{s{\cdot}m^{-1}}$ and $\mathrm{m^2{\cdot}s{\cdot}kg^{-1}}$, respectively.

In the simplified modelling of surface erosion, the physical interpretation of the K and τ_c parameters is relatively straightforward. Assuming there exists a threshold for initiating the erosion process, this threshold is directly reflected by τ_c in a bottom shear stress-based representation of hydrodynamic loading. From a phenomenological perspective, it is natural to introduce the excess shear stress $\tau - \tau_\mathrm{c}$ more precisely. Therefore, under constant imposed shear stress $\tau > \tau_\mathrm{c}$, the proportionality coefficient K will control the intensity of the erosion rate and thus directly the kinetics of the process. Each of these two parameters contributes to quantifying a soil's sensitivity to erosion, both in terms of resistance, with an initiation threshold that must not be exceeded if the risk of erosion is to be inhibited, and in terms of kinetics once the process has been initiated, in relation to the survival time of a structure in a crisis situation. In summary, K and τ_c collectively capture a soil's sensitivity to erosion, that is referred to as *soil's erodibility*. This conceptual framework, as defined by this local linear law, implicitly

[2] More precisely, in a pipe flow configuration assuming uniform radial extension by erosion, the authors of this study demonstrated that the pipe radius diverges in finite time if ever $n > 1$.

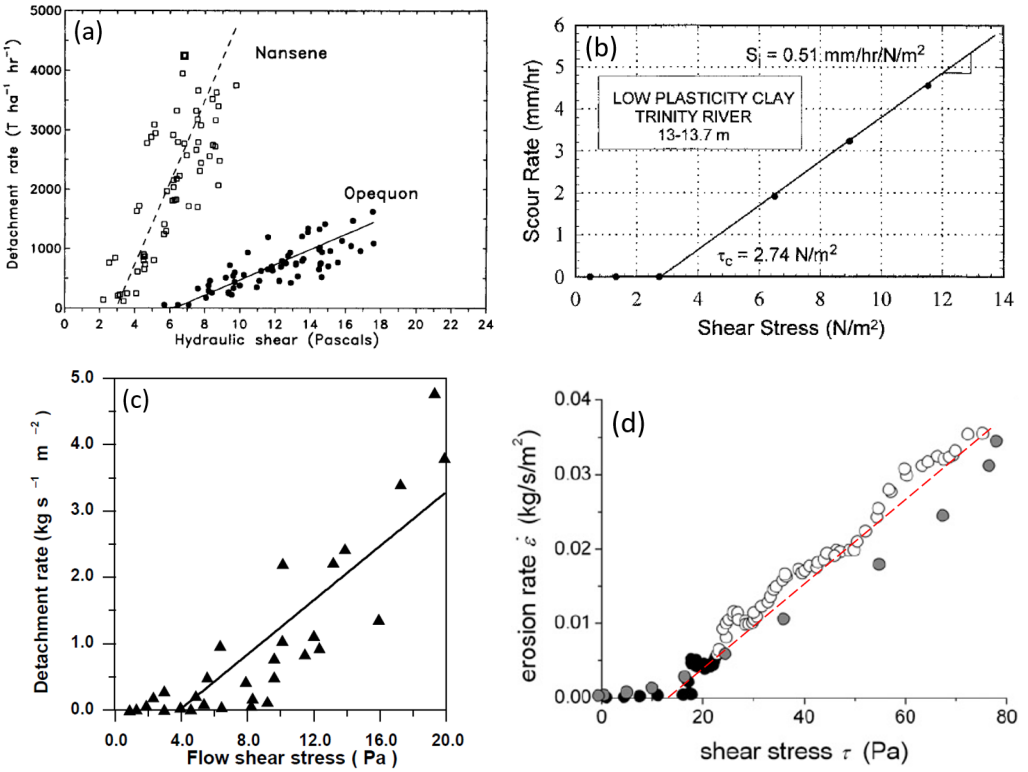


Figure 5. Some illustrative comparisons of the linear excess shear stress model with experimental data of either the mass E_m or volume E_v erosion rate obtained for: (a) cropland soils [110]; (b) low plasticity clay [111]; (c) sandy-clay silty soil [112]; (d) kaolinite-sand mixture [113].

assumes that the action exerted by the flow on the soil surface is fully described by the bottom shear stress alone, regardless of the hydrodynamic configuration generating the erosion. The corollary leads directly to considering the erodibility parameters K and τ_c as intrinsic material properties, independent of all other external influences. Undoubtedly, this question is highly debatable. While it is obvious that erodibility depends on soil properties [114, 115], it is by no means evident that it depends exclusively on them. In reality, there are likely other external factors that can influence erosion sensitivity, such as environmental conditions, vegetation cover, land use, variations in the hydraulic regime, etc. These external influences can interact with the properties of the soil to affect the erosion rates. Therefore, it may be more accurate to consider erodibility as a dynamic property that can vary depending on the specific conditions and context in which erosion occurs.

Despite the simplistic assumption of applying a minimalist model with a linear relationship between erosion rate and flow stress, the comparison with experimental measurements is generally acceptable and sometimes even very satisfactory, as demonstrated in previous Figure 5 with results from studies using a wide variety of devices and soils [110–113]. Considering in addition the broad to very broad dispersion almost systematically observed in these erosion data, the excess shear stress model appears to be reasonably acceptable. This explains why little effort has been made to complicate further the conceptual framework starting from this consistent although minimalist basis. However, there is a more sophisticated modeling approach in which this

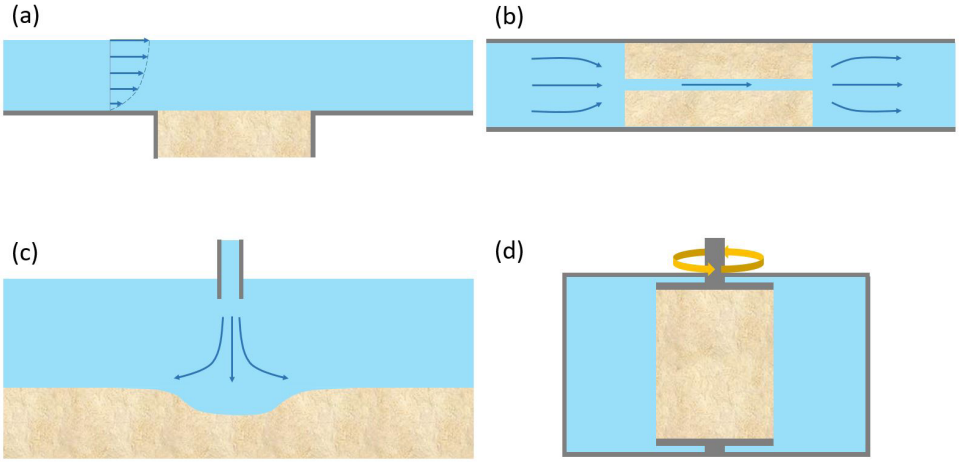


Figure 6. Sketches of the most typical flow configurations in erosion testing devices: (a) tangential flume flow; (b) through-pipe flow; (c) jet flow; (d) rotation flow.

excess shear stress law is used as part of a probabilistic description of soil erosion [73,82,85]. Such probabilistic approaches allow to consider substantial deviations from the average phenomenon represented by a unique mean field erosion law. This variability can be temporal and is particularly important with respect to flow stress in turbulent regimes. It can also occur in space, either due to intrinsic variability in soil properties, or if the eroding flow at the surface of the material is not uniform, as in the case of porous flow for instance [85]. In this case, this also means that there may be a dependence on the size of the eroded sample, as long as the latter is too small to fully reflect the whole range of variation of the key parameters. These probabilistic models enable for instance to address the structure scale [116] or to question the existence of a threshold on a macroscopic scale [82, 85, 105].

2.3. *Developments of a wide range of dedicated erodimeters*

The systematic evaluation of the two *erodibility* parameters, allowing quantification of the absolute value of erosion resistance and relative classification of soils, has driven the development of numerous specific erosion devices. These devices involve various types of flow, with the tested soil being submerged or not, and where the flow features can vary widely: free surface or confined flow, tangential or impingement flow, stationary or time evolving regime. The main hydrodynamic configurations of these erosion tests include longitudinal channels, annular flume, pipe flow, submerged impinging jet and, more seldom, rotating flow. For example, as suggested by [117] and sketched in Figure 6, these devices can be broadly classified into four different categories: flume erosion tests [63,77,98,100,111,118–132], through-pipe erosion tests [113,133–142], jet erosion tests [75, 76, 81, 143–147] and rotating apparatus tests [143, 148–151]. These different types of erosion tests offer a variety of experimental setups to study erosion processes under different hydrodynamic conditions. Each type of test has its advantages and limitations, and the choice of test method depends on the specific research objectives and conditions being studied.

Measurements of erosion and sediment transport in channels represent some of the first devices used to study these processes. Flows are generally free surface, although confined configurations also exist, especially for in-situ purpose as will be discussed later. Erosion occurs

at the bottom of the channel, either over a large area of sediment, or limited to the upper surface of one or more soil samples, which are generally cylindrical in shape and vertically oriented. In the latter case, the sample must be raised either manually or by a piston, as regularly as possible to ensure that its eroded top remains aligned with the rest of the floor. Depending on the device, this is achieved either by visual criteria (operator-dependent) or by more sophisticated feedback systems [77, 130]. These channels are usually straight and rectangular in cross section, with a flow rate regulated by a pump, within a recirculating closed-loop system [98,111,118,122,124,127,128,130,152] or not [63,77,120,121,123,125,126]. However, flow establishment length in such flumes can be relatively large, a condition which is not always met in practice or may require large dimensions for the device to achieve. From this perspective, another common geometry for studying erosion and sediment transport is the annular flume, where flow, confined or not, is generated from above using a speed-controlled rotation drive system, sometimes called carousel [119]. Symmetry (i.e., invariance by rotation) and the absence of a pump result in a periodic condition in the flow direction, as a replica of infinite river, enabling the investigation of long-time processes [100, 119, 120, 131, 132, 153]. However, this is of interest mainly for sediment transport issues, but less suitable for studying erosion alone.

As mentioned in previous Section 1.4, one of the main mechanisms of internal erosion in an earthen hydraulic structure is driven by concentrated flow along a through pipe creating a preferential path for erosion. To reproduce this phenomenon in the laboratory, the Pinhole test was the pioneer test for characterising qualitatively the soil dispersivity [133]. Afterwards, for quantitative assessment of erosion, the Drill Hole test was proposed [135]. Later, Wan and Fell developed the original version of the device referred to as Hole Erosion Test (HET) [137, 138]. In this type of test, a hole is first drilled longitudinally through a soil sample before immersion in water. Then, to generate erosion, a controlled flow is imposed along this pipe. The soil must possess specific cohesion properties to withstand the drilling of the hole and not subsequently collapse. To avoid this problem and, above all, to enable the erosion phenomenon to be visualized, few variants of the device have been proposed, with, instead of a pipe, a slot carved in the soil at the interface with a transparent wall, and called either Slot Erosion Test (SET) [137], viewable HET [141] or Groove test [142]. Intrinsically, all these test configurations based on a pipe across the sample induces a strong and immediate feedback between soil surface erosion and the eroding flow through the progressive geometric evolution of the pipe, or slot.

The impinging jet tests are inspired by the hydraulic configuration of scour as observed in field. These devices were mainly developed in North America [81, 143, 144], where significant advancements have been made, notably by Hanson's group with their Jet Erosion Test (JET) [75, 145, 154–156]. Generally speaking, these tests consist in completely submerging the soil zone or sample under study, then applying in the upper water column a downward jet flow of adjustable velocity impinging, usually perpendicular, on the surface to be eroded. A scour crater is thus gradually excavated and its dimensions regularly measured, requiring the jet to be temporarily stopped, or deflected, for measurement. The latter is difficult to achieve, and is often limited to the depth beneath the jet. Nevertheless, more sophisticated techniques have been developed to determine the overall shape of the scour crater [76, 81, 122]. However, the volume or mass of soil eroded can only be an estimate. In the same category of tests relying on jet flow perpendicular to the soil, is the Borehole Test [146, 157], which differs significantly from the other impinging tests in that the flow takes place through a vertical tube previously introduced into the soil. Last but not least, this cratering configuration is also highly relevant to the case of high-speed gas jets, particularly in the context of extraterrestrial landings (Moon, Mars) [158–160].

Devices based on rotating flows are relatively limited in number, probably due to their rather complex application. Two examples of such devices are the Rotating Cylinder Test (RCT) [143,149, 150] and the Rotating Erosion Testing Apparatus (RETA) [151]. In principle, a flow is generated

by an external rotating cylinder while a soil sample is placed at the center, around the axis. Shear stress at the soil surface is deduced from a direct or indirect measurement of the torque exerted on the sample, while erosion is assessed by weighing the remaining soil and/or the eroded soil, requiring regular pauses in the spinning system to make these measurements. While these devices offer a unique approach to studying erosion under rotating flow conditions, their complexity and the need for frequent interruptions in testing may limit their widespread use compared to other erosion testing methods.

There are several fundamental differences between these various devices and configurations. Apart from the variable degree of turbulence in the flows, they are distinguished by their permanent or evolving features. Flume configurations typically maintain a relatively constant flow throughout the test, with the eroded soil sample being continuously re-positioned at the bottom of the channel. In contrast, the other configurations involve a regular receding of the water–soil interface, leading to a gradual evolution of the flow geometry that may be more or less pronounced depending on the testing method, such as through-pipe or jet erosion compared to flume erosion. Flow control methods also differ among the configurations, with some using regulated discharge (by pump or rotary drive for carousel configuration) and others imposing constant pressure difference (in the case of pipe flow). The hydrodynamic configurations encountered present a variety of complexities, requiring different degrees of reliance on empirical laws to determine relevant flow quantities serving as input variables for the interpretation models (see Section 2). This is particularly the case with the impinging jet whose flow is slowed down on its axis and sharply deflected radially until it tangents the ground surface [161]. Combined with the additional dependence on several jet parameters (nozzle size and shape, distance from the soil surface, etc.), the direct determination of flow features is a real challenge, especially in the presence of a developing crater [162]. Furthermore, differing situations can be highlighted with regard to flow direction in relation to soil intrinsic anisotropy. This anisotropy, directly linked to a gradient of soil properties, results either from natural consolidation under gravity, or from static pressure or dynamic layer compaction during the soil sample reconstitution in the laboratory. Erosion resistance will therefore differ depending on whether the flow stress is exerted perpendicularly (i.e. flume tests) or tangentially (i.e. through-pipe and rotating tests) to the consolidation or compaction orientation of the soil. Additionally, there exist various methods in soil mechanics practice to prepare a specimen under predetermined conditions [163], and the choice made for an erosion test can have an impact on the erodibility values measured.

Conducting measurements on site is also a critical point, particularly in the context of submarine hydraulics, necessitating the development of in-situ devices that prioritize portability and robustness [86]. This is especially important when dealing with mechanically fragile or environmentally sensitive soils, such as soft/loose muds or soils subject to biological activity which may have a strengthening (bio-stabilization) or weakening (bio-turbation) effect on erosion [86, 108]. These on-site devices include the Jet Erosion Test [145], the In Situ Erosion Flume (ISEF) [122], the IFREMER erodimeter [63, 126], the Mobile Recirculating Flume (MORF) [164], the VIMS Sea Carousel [120], the Adjustable Shear Stress Erosion and Transport (ASSET) flume [165] and several versions of the Cohesive Strength Meter (CSM) [124, 166]. However, in the cases where soil cores can be extracted under good conditions and without risking material disturbance, there is an obvious advantage in carrying out erosion measurements in the laboratory, on a set-up that generally provides far better possibilities in terms of instrumentation, metrology and control of ambient conditions allowing for more precise and controlled experimentation. Additionally, aside from in-situ tests, it is worth noting that erosion tests can also be conducted on real structures or specific physical models of comparable size, particularly in overflowing or wave overtopping configurations [167–173].

To further illustrate some of these different types of erodimeters, the following section describes in more detail the three main erodimeter systems encountered in the field of geomechanics: Erosion Function Apparatus (EFA), Hole Erosion Test (HET), and Jet Erosion Test (JET).

3. Focus on principal erosion devices in geomechanics

3.1. *Erosion function apparatus (EFA)*

A well-known illustration of linear erosion channel (i.e. configuration of Figure 6a) is the Erosion Function Apparatus (EFA) developed in the early 1990's by Briaud and collaborators from Texas A&M University (College Station, Colorado, US) [111]. This apparus has been standardized and commercialized by a company specialized in construction materials testing equipment[3]. It has become widely used in geotechnical engineering research and soil erosion studies, providing valuable insights into erosion mechanisms and helping to inform engineering practices related to erosion control.

Typically, the soil sample to be tested is collected in the field using a Shelby tube and then placed in a circular opening at the bottom of the hydraulic flume. The latter, depicted in Figure 7a, is a rectangular channel with pump-driven re-circulation. In the setup illustrated in Figure 7b, it is crucial to maintain alignment between the top of the sample and the bottom of the channel. This alignment is achieved by regularly pushing up the Shelby tube with a piston, following as closely as possible the rate at which the sample erodes. A side window allows visual monitoring of the sample to determine when the piston should be raised incrementally, typically in 1 mm steps under manual control. The progression of the piston provides the volumetric erosion rate E_v. A global test protocol was developed and adapted for the critical visual detection step to ensure accurate monitoring of erosion progression. A flow-meter installed in the flume measures the average flow velocity, from which the bottom shear stress τ can be determined using the Moody's chart. The average velocity can be varied across a wide range, from 0.2 to 6 $\mathrm{m{\cdot}s^{-1}}$, enabling for multiple data points to be collected for a single sample in order to plot the relationship between erosion rate and either flow velocity or bottom shear stress. The test provides a classification of the soil's resistance to erosion, as detailed in forthcoming Section 4.1. Additionally, through regression analysis, quantitative values for the critical shear stress τ_c and erosion coefficient K_v can be determined.

3.2. *Hole erosion test (HET)*

There is no real standard for the Hole Erosion Test (HET), and several research teams have developed their own devices. All of them can be considered direct descendants of the original HET device developed by Wan and Fell at University of New South Wales (Sydney, Australia) in the early 2000's [137, 138]. Figure 8 shows pictures of the first HET device alongside several examples of later versions that incorporate various improvements. These improvements may include enhancements to the testing methodology, modifications to the setup for increased accuracy or efficiency, or adaptations to accommodate specific research requirements. Overall, these developments reflect ongoing efforts within the research community to refine and optimize erosion testing techniques for better understanding of soil erosion.

The distinctive feature of the HET test is the presence of a through-hole in the soil sample as sketched in Figure 6b. By imposing flow along this pipe, high stresses can be generated in a straightforward manner. However, the use of undisturbed soils is challenging since the drilling

[3] https://www.humboldtmfg.com/erosion-function-apparatus.html

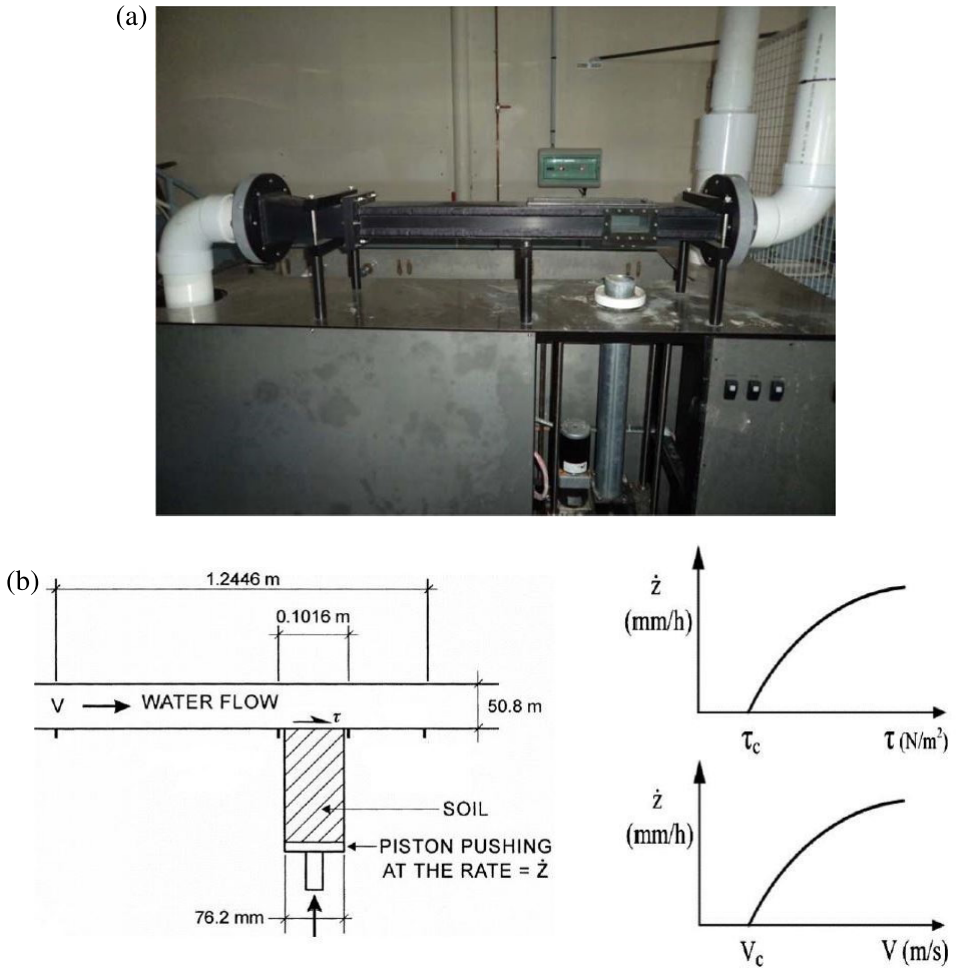


Figure 7. (a) Picture of the Erosion Function Apparatus in operation at ESTP (Paris) [174, 175]. (b) Sketch of the soil sample in the Shelby tube and of typical erosion curves from [176].

phase, even in a reconstituted soil specimen, is delicate, as some materials may be too fragile to withstand the drilled pipe, and may experience slaking either before or during the test [180]. Depending on the protocol, the initial diameter of the hole varies from 3 to 6 mm. Once the tube containing the soil sample is assembled with the rest of the device, the whole system is saturated and a flow is applied, either at a imposed flow rate or imposed pressure. As erosion occurs and the diameter of the hole increases with mass loss, interpolation laws are used to estimate its size at any time, assuming a cylindrical geometry and, the final diameter is measured or estimated post-test to refine the interpolation. The measured quantities typically include flow rate, downstream turbidity and pressure at various positions. The pressure measurements are particularly crucial for accurately determining the pressure drop induced by the flow through the pipe. This involves considering singular pressure losses at the pipe inlet and outlet. For instance, the HET-P device uses a Pitot static tube for local pressure measurement, positioned right at the exit of the hole [140, 181]. Interpretation models may vary among research teams, but all manage to derive the erosion rate and wall shear stress (in a hole geometry assumed to be

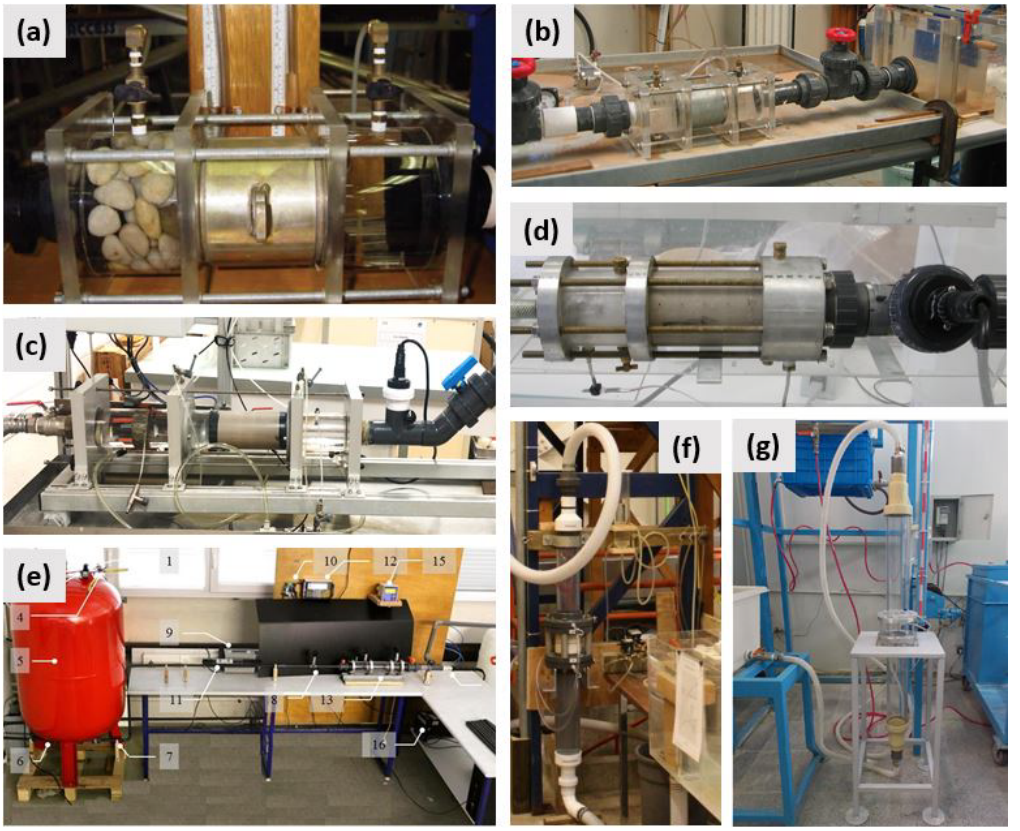


Figure 8. (a) Original HET by Wan and Fell at University of New South Wales (Sydney, Australia) [137]. (b) HET developed at US Bureau of Reclamation (Denver, Colorado, US) [177]. (c) HET developed at INRAE (Aix-en-Provence, France) [82, 175]. (d) HET developed at University Gustave Eiffel (Champs-sur-Marne, France) [113]. (e) HET developed at University of Lorraine (Nancy, France) [178]. (f) HET-P developed at University of British Columbia (Vancouver, Canada) [179]. (g) HET developed at Shiraz University of Technology (Shiraz, Iran) [140].

cylindrical) from measurements (pressure, flow rate and turbidity if available), in order to deduce the erodibility parameters τ_c and K by linear regression.

3.3. *Jet erosion test (JET)*

The Jet Erosion Test (JET) device is probably the most widely used erosion testing device due to its versatility for both laboratory and field experiments. Inspired by the practical case of soil scour, the JET device is the eponymous and certainly the best-known among the jet erosion tests. It was originally developed in the late 1980's by Hanson and his colleagues at the Agricultural Research Service Hydraulic Engineering Research Unit in Stillwater, Oklahoma, US. Since then, it has undergone a succession of upgrades and improvements [75, 145, 154]. The testing apparatus, as shown in Figure 9b, and its accompanying interpretation method are described in ASTM Standard D5852 (2003). Additionally, there are two field versions: the original one and a more compact mini-JET [155], as depicted in Figure 9b. These field versions allow for erosion testing

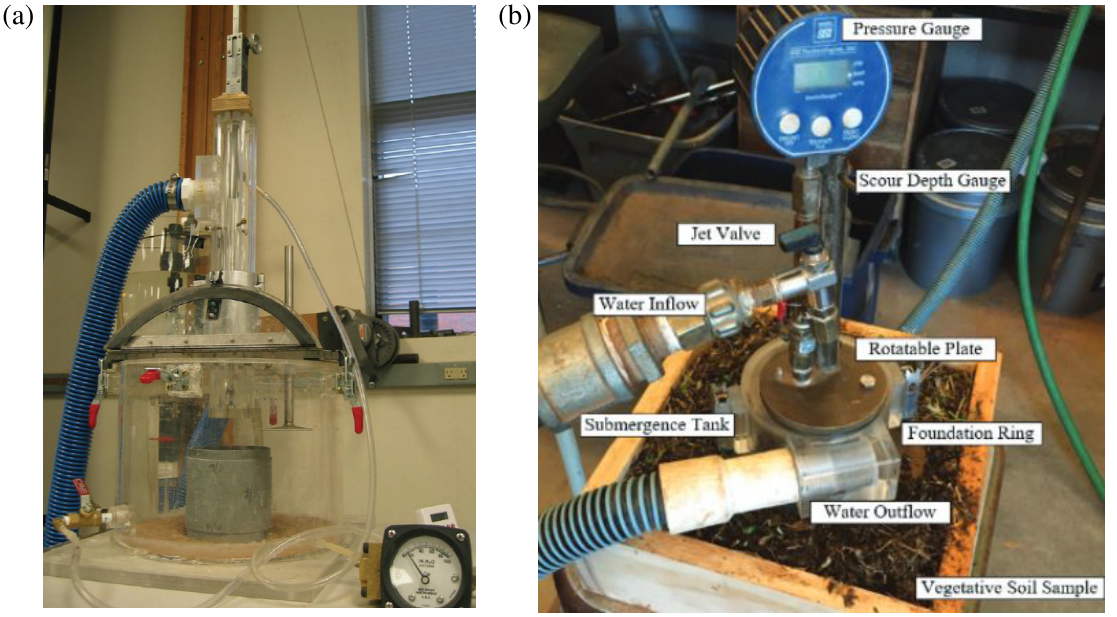


Figure 9. (a) Picture of the Jet Erosion Test at ESTP (Paris) [177]. (b) Picture of the mini-JET [182].

in real-world environments, providing valuable insights into soil erosion processes under natural conditions.

In practice, after full immersion of a soil sample or the ground area to be tested on site, a submerged jet is generated at the outlet of a delivery tube, positioned perpendicular to the soil surface, in the configuration shown in Figure 6c. The jet is supplied by a pump, either via an adjustable head tank or by direct connection when high stresses are required. The circular nozzle at the bottom of the tube is fixed at 6.4 mm, but the distance to the soil surface is adjustable. The estimated maximum erosion stress can thus be varied over a very wide range, from 4 to 1500 Pa. Variations in maximum bed scour depth are measured using a point gauge. The latter is tightly fitted to pass exactly through the nozzle, temporarily interrupting the flow while the measurement is being taken when the gauge comes into contact with the bottom of the erosion crater.

There have been several developments and improvements in the interpretation method for the JET, which ultimately provides the two expected parameters τ_c and K_v. However, despite using consistent input variables such as jet velocity, presumably constant during the test, and measured depth, there are significant disparities in the erodibility parameters obtained, depending on the method employed [183, 184]. This underscores the importance of refining interpretation methods and ensuring consistency in experimental procedures to obtain reliable and accurate results in soil erosion testing.

3.4. *Comparative analysis of the three erosion devices: EFA, HET, JET*

The comparison of the three erosion testing devices, JET, EFA, and HET, reveals various advantages and drawbacks in terms of their applicability, erosion rate measurement methods, and hydrodynamic complexities. This provides the following comparative overview [177, 185].

JET and EFA offer the possibility of testing all types of soil, even those that are weakly or even non-cohesive, although in the case of JET, the grains tend to fall back into the crater and may distort the scour depth measurement. On the other hand, HET, which requires hole drilling, cannot be implemented on soils that are not cohesive enough or are too soft, as they risk collapsing [26]. Similarly, swelling soils should be avoided. Even on resistant sample, drilling can cause some damage to the soil. Regarding erosion rate, it is measured directly with the EFA, but using a visual procedure that is thus operator-dependant and rather critical. In the other two devices, the erosion rate is simply deduced from other measurements, such as turbidity or scour depth, with varying degrees of accuracy. Indeed, assuming that the cylindrical geometry is maintained during the test, HET modelling enables volume loss to be quantified, whereas JET interpretation is limited to the cavity depth under the jet in a simplistic 1D approach. With regard to the possibility of testing natural soils, while the HET and EFA are only laboratory tests, the JET can also be used in-situ, on flat or inclined (and even vertical) surfaces, especially its compact version mini-JET that is easy-to-use and inexpensive. It should be noted, however, that unlike HET where soil samples generally have to be reconstituted, those tested at EFA can be preserved in conditions close to those on site, thanks to the use of a Shelby tube.

In terms of hydrodynamics, the three devices display very different flow configurations of increasing complexity. The simplest situation is clearly that of the EFA, which is based on a steady channel flow whose characteristics have long been known, even if they require the use of empirical laws for the friction factor. It should be noted, however, that the transition between the bottom of the channel and the flush surface of the soil sample can create local flow disturbances, which may compromise the assumption of flatness preservation on the eroded interface, as well as the critical visual detection controlling the 1 mm piston increment. The hydrodynamics of the HET are more complex, firstly because of the flow reduction and expansion at the inlet and outlet of the hole, which generate singular head losses and intensified erosion. Secondly, while flows in cylindrical pipes are also well known, this is an atypical case where the length is small and the radius grows during the test. As already mentioned, the modelling of the HET flow has been developed and perfected in great depth to take account of these different aspects, although it requires the assumption, which is therefore questionable, that the hole remains cylindrical. However, the experimental validation of analytical scaling laws definitely supports the interpretation model [109]. In contrast to the other two systems, it's also worth noting the ability to impose either flow or pressure hydraulic conditions. Finally, the JET configuration seems to be the most complex, from the initial situation of a jet impacting a flat surface, but even more so as the scouring crater develops. Approximate flow modelling therefore requires drastic simplifications, as is done for JET test interpretation.

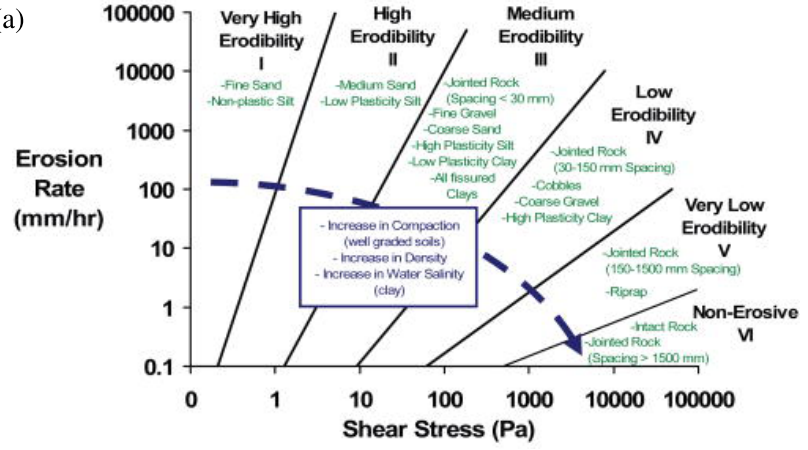
4. Benefits and limitations of quantifying soil erodibility

4.1. *Classification of soil's erodibility*

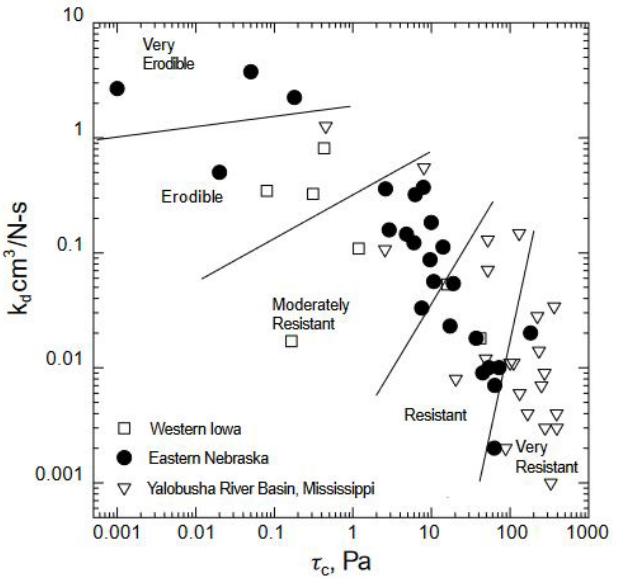
Several classification rules have been proposed, based on the extensive databases of experimental values of erodibility parameters that have been progressively built up with the results of erosion tests on a very wide range of soils with highly variable properties and compositions. Each classification rule likely offers insights into soil erosion behavior under specific testing conditions and may be tailored to different applications or soil types. Basically, there are three competing proposals, originating from EFA, JET and HET data, respectively.

Briaud's classification system, based on EFA tests carried out on a wide variety of soils, categorizes soils into six distinct categories of materials, ranging from non-erosive to very high erodibility [176]. As can be seen in Figure 10, this classification, with various soil categories,

(a)



(b)



(c)

Erosion rate index	Description
<2	Extremely rapid
2–3	Very rapid
3–4	Moderately rapid
4–5	Moderately slow
5–6	Very slow
>6	Extremely slow

Figure 10. The different charts for soil's erodibility classification: (a) Chart proposed by Briaud based on EFA test results [176]; (b) Chart proposed by Hanson based on JET tests [145]; (c) Erosion rate index based classification as suggested by Wan and Fell [138].

is developed using a log-log diagram displaying the rate of erosion as a function of stress, in some words the same type of representation as that of the erosion law. In this diagram, each test corresponds to multiple data points, with the eventually of straddling two categories, which can complicate classification. The boundaries between the categories are represented as linear, implying power law relationships between erosion rate E_v and exerted shear stress τ, with increasing exponent. This type of relationship is therefore substantially different from the linear excess shear stress erosion law of Equation (2) (with $n = 1$). It is also important to note that this classification may have limitations, particularly in cases where soils exhibit behavior that falls between two categories as already mentioned.

A second classification has been proposed by Hanson on the basis of the very large number of tests carried out with JET device, primarily through in-situ testing across various locations in the United States [75, 145, 156]. This classification is based on a log–log representation of the erosion coefficient K_v (here denoted k_d) as a function of critical shear stress τ_c, with each soil tested corresponding to a single point. As shown in Figure 10, the chart is divided into five zones by linear boundaries, representing power law relationships, which categorize soils from resistant to very erodible. It is noteworthy that K_v is expressed in unconventional units, in $cm^3 \cdot N^{-1} \cdot s^{-1}$.

Alternatively, Wan and Fell introduced the erosion rate index I_m, derived from HET test results, which is defined as $I_m = -\log(K_m)$ with K_m expressed in $s \cdot m^{-1}$ [138]. They proposed a classification into six categories for the expected soil erosion ranging from extremely rapid, for $I_m < 2$, to extremely slow, for $I_m > 6$ (See Figure 10).

Although these classifications are all derived from test-specific databases and established by rather arbitrary boundaries between soil categories, they appear reasonably applicable across various types of test. Overall, these classification systems provide a framework for categorizing soils based on their erosion characteristics, offering insights into their behavior under different stress conditions. They serve as practical tools for understanding and assessing soil erosion potential, aiding in the planning and management of erosion control measures.

4.2. *Erodibility parameters in practice*

The various erosion tests presented and discussed in previous Section 3 enable positioning a given soil in the various classifications proposed above, and hence, offer valuable tools for qualitatively assessing soil's resistance against erosion. By knowing the erosion characteristics of a soil, particularly one present on a construction site, engineers and researchers can position it within the classifications proposed earlier, which enables them to identify the soil's category in terms of erosion sensitivity. Therefore, they can make informed decisions regarding erosion risk management. This knowledge helps ensure that appropriate measures are taken to prevent erosion-related issues during and after the construction or repair of hydraulic structures.

From a more quantitative point of view, critical shear stress is the key parameter of interest as regards soil's resistance against erosion in civil engineering conception, including design and safety requirement. It serves as a crucial threshold, defining the maximum bottom shear stress that a soil can withstand before experiencing erosion. This parameter is essential for ensuring the stability and longevity of earthen structures subjected to hydraulic forces such as infiltration or overflow. The main difficulty lies in accurately estimating the actual stresses potentially generated by water flows on the surface and within the hydraulic structure under consideration.

On the other hand, erosion coefficient K becomes crucial in crisis situations or emergency scenarios, when erosion is occurring within an hydraulic structure. In fact, as a variable representative of the kinetics of soil removal, K controls the rate of pipe expansion by erosion. For example, in the case of a through pipe with constant upstream water level and continuous erosion, and considering that the soil's critical shear stress is virtually negligible compared to that exerted

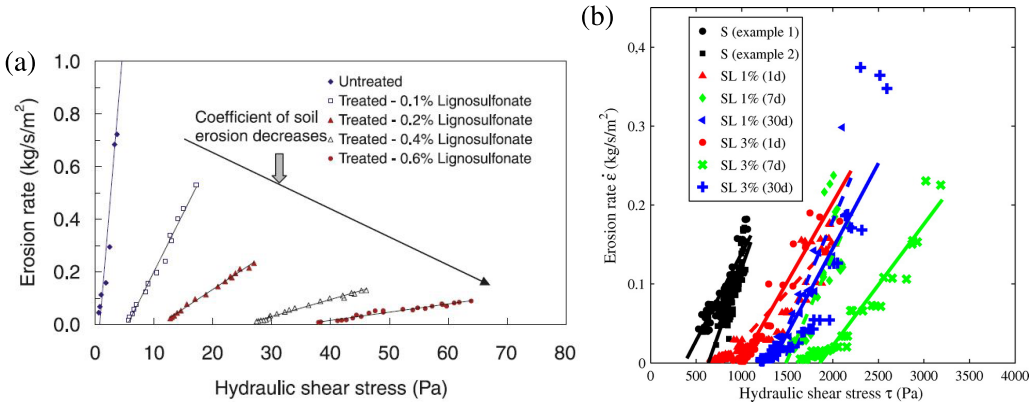


Figure 11. Examples of quantitative evidence of enhanced soil erosion resistance through (a) lignosulfonate treatment [189] and (b) lime treatment [178].

by the flow, the expansion rate of a through pipe can be shown to be highly dependent on the erosion index I_m. For instance, the time required for a pipe to expand from 25 mm to 1 m in diameter can vary over four orders of magnitude, from a few tens of minutes to several months depending on the value of I_m which ranges from 2 to 6 [186]. Going a step further, Bonelli and Benahmed proposed a simple model, with several mechanical quantities inferred from fourteen case studies, to estimate the remaining time until breaching for an earthen dam once a downstream leak due to piping flow erosion has been detected [82, 187]. From this model, the following relation was obtained:

$$\Delta t_c = t_c - t_d < \frac{2\rho_{dry}}{K_m \nabla P} \ln\left(\frac{H_{dam}}{2R_d}\right) \tag{3}$$

where Δt_c is the remaining time to dam roof collapse with t_d and t_c the time of initial leak detection and the time of ultimate collapse, ρ_{dry} is the soil's dry density, ∇P denotes the pressure gradient (assumed constant) through the pipe, H_{dam} is the dam height and R_d is the estimated radius of the pipe at detection. As the upper limit is inversely proportional to K_m, it potentially varies over 4 to 5 orders of magnitude. However, this variation may be less pronounced for soils that are sufficiently clay-rich and compacted during construction, such as those found in dams (through perhaps less so in a levee).

Erodibility parameters can also be useful indicators for validating and quantifying soil reinforcement achieved through various treatments, such as biocementing [188], chemical stabilization [189] and cement or lime addition [178, 190–192]. Figure 11 shows two illustrations of erodibility strengthening obtained by lignosulfonate [189] and lime [178] treatment with obvious critical shear stress increase in both cases while erosion coefficient substantially decreases as shown on the left graph. Another example depicted in Figure 12 shows the progressive increase in both critical shear stress τ_c and erosion index I_m during curing period after a lime treatment [191, 193]. These illustrations highlight the effectiveness of various soil treatments in enhancing resistance to erosion, as evidenced by changes in erodibility parameters.

4.3. *Lack of predictability from soil properties*

It is still a widely debated question whether there is a sufficiently conclusive connection between soil's susceptibility to erosion and usual properties, as commonly characterized in the laboratory (see e.g. in [163] for details on definitions and measurement methods for the usual characteristics

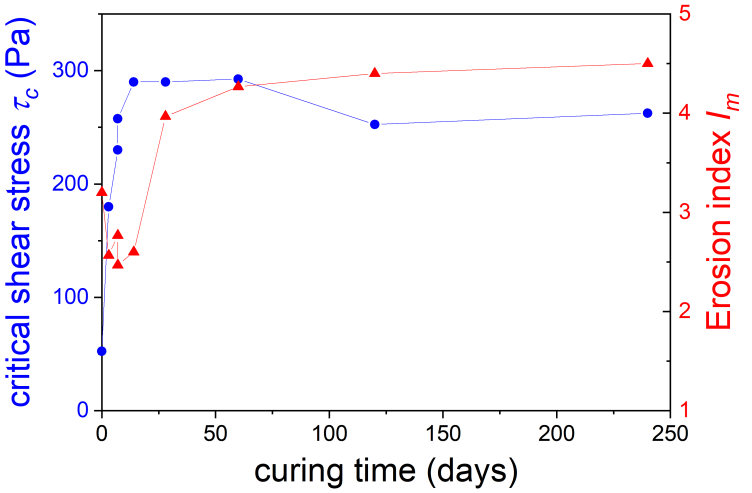


Figure 12. Example of gains in erodibility, i.e. critical shear stress τ_c and erosion index I_m, as a function of curing time during lime treatment of a Rhône river soil specimen (with $t = 0$ corresponding to untreated soil). Figure adapted from [191, 193].

of soils). All the more so since behind this issue is that of the intrinsic character of erodibility parameters, as postulated in the conceptual framework commonly proposed and which would be directly confirmed by such an immediate correlation with other inherent soil features.

Much effort has been devoted to finding quantifiable relationships, mostly on an empirical basis, between erodibility and the main measurable properties in natural soils, including particle size distribution, density, water content, plasticity index, consolidation time and many other quantities [63, 100, 108, 115, 185, 193–197]. A wide variety of empirical relationships have emerged in the literature, partially listed for instance by Winterwerp [64, 69], Grabowski [115] and Kimiaghalam [196], but further enriched since then. These relationships mainly concern the critical shear stress τ_c, with numerous correlations, more or less convincing, the essential ones of which have been synthesized by various authors [64, 115, 193, 197–199]. It is also a parameter for which theoretical approaches are frequently proposed, most often by extension of known results on the threshold for incipient motion of a purely frictional grain without cohesion or adhesion [62, 63, 199–201]. A power law with the plasticity index is also suggested [64, 69, 196]. By comparison, the kinetic erodibility parameter K has been less studied, which is most likely due to the greater experimental difficulty in determining it with confidence, particularly in-situ. Nonetheless, a theoretical model linking K to some consolidation parameters for fine soils can be reported [64] while some empirical or semi-empirical laws can be also mentioned [155, 183]. What all these studies have in common is the wide dispersion in erodibility data, which severely restricts the extent of the empirical relationships they attempt to support. The main reasons for this are undoubtedly the difficulties in measuring soil erosion already mentioned in Section 2.1, and the high degree of spatial variability in soil properties due to lack of uniformity, which is particularly acute for field measurements. A further consideration is the additional impact of ambient conditions such as temperature [202–204], for which an Arrhenius-type activation factor on erosion rate has been proposed and experimentally validated [202], or, more specifically for fine soils with clay fractions, salinity or pH [136, 202, 203, 205].

Independently of the investigation of direct relationships with other soil properties, some authors have also argued the existence of an underlying correlation between τ_c and K, thereby reducing the characterization of soil erodibility to the knowledge of a unique parameter, in line with

the previous classification by Wan and Fell [138], which is based solely on K_m (see Section 4.1). Thus, supported by many JET test results, Hanson was the first to suggest the existence of an inverse power relationship of the form $K \propto \tau_c^{-\gamma}$ with $\gamma \approx 0.5$ [145]. Interestingly, it turns out that such an exponent equal to 1/2 can be recovered by dimensional analysis [206]. However, a broader review of the literature reveals a much wider range of exponent values, from $\gamma \approx 0.4$ to $\gamma \approx 2.4$, as reported by several authors [20, 76, 183, 184, 190, 207, 208]. Together with the huge dispersion of the data almost systematically observed and the dependence of the erodibility parameters on the choice of protocol or interpretation model (at least for JET measurements) [183, 184, 209], it appears more than hazardous to make any attempt of generalization. Especially since some contradictory analyses seem to conclude that there is no universal correlation between τ_c and K [66]. All in all, it seems difficult to go beyond the simple qualitative observation that a soil with less (more) resistance in terms of critical shear stress τ_c generally undergoes higher (lower) erosion rates under equivalent hydrodynamic conditions, i.e. when exposed to the same excess shear stress, thus corresponding to a greater (lower) erosion coefficient K.

In short, the compilation of all these correlation analyses leads to the conclusion that there are no standardized relationships from a quantitative point of view, and only very few general trends from a more qualitative point of view.

4.4. *Ongoing questions, difficulties and limits*

Additionally to the lack of strong correlations, several results highlight problems and raise questions about some limitations of the proposed conceptual framework.

One of the first issues encountered is beyond the simple scope of laboratory erosion tests, and relates more broadly to the ability of a reconstituted soil sample to reflect the effective hydro-mechanical behavior of the same soil under its natural conditions on site, leading to significant discrepancies in erosion tests results. In particular, it is known that one key issue is the loss of strength exhibited by reconstituted soil sample compared with that measured on undisturbed state [210]. In the specific case of erosion, detachment rates of disturbed samples were measured to be more than an order of magnitude higher than those observed for natural soil [211], although approximately proportional, as shown in Figure 13. This discrepancy is illustrated in the same Figure where data by an extract from HET database of INRAE reveals in the previous Wan and Fell's classification that intact soils consistently placed in the most erosion-resistant soil categories, contrasting with reconstituted samples. Consequently, the observed disparity underscores the challenge of accurately assessing soil erodibility in laboratory settings, where reconstituted samples may not faithfully represent the behavior of soils in their natural state. As a result, the extrapolation of laboratory-derived erodibility parameters to real-world conditions may be subject to considerable uncertainty and may not capture the true erosion susceptibility of soils in the field.

The variability in erodibility parameters across different experimental devices presents another significant challenge in erosion testing. Studies have highlighted wide disparities in erodibility parameters such as critical shear stress and erosion coefficient when the same soil sample is tested using different devices [174, 175, 177, 180, 182, 193, 212, 213]. For instance, from a comparison of results obtained with the Rotating Cylinder and the Hole Erosion Test (HET), Lim (2006) has shown a clear correlation between the two sets of data, but without achieving equality between the respective values of critical shear stress and erosion coefficient [180]. This discrepancy was particularly pronounced when distinguishing between dispersive[4] and non-dispersive

[4] A dispersive soil is structurally unstable when exposed to water, and particularly susceptible to erosion, due to a high concentration of exchangeable sodium ions and a large specific surface area [214].

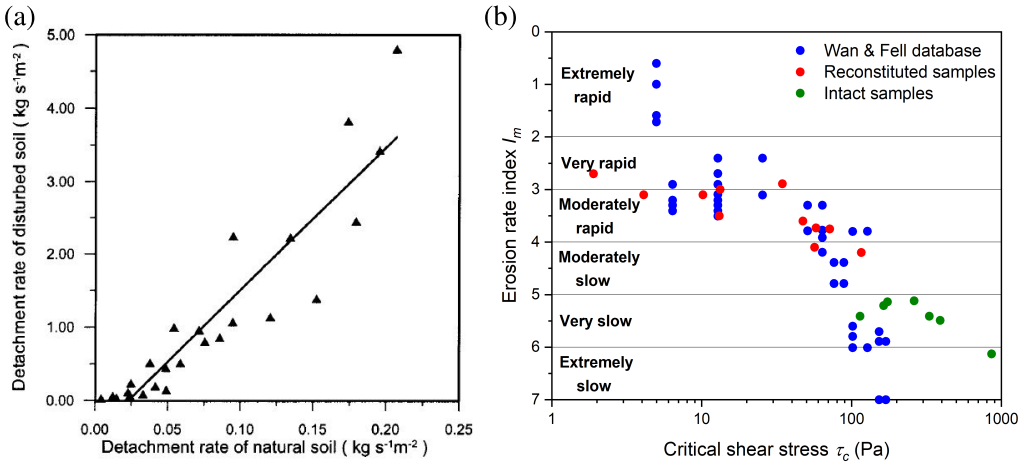


Figure 13. (a) Comparison of the erosion rates measured for disturbed and natural soil samples [211]. (b) Distinct ranking in Wan and Fell's chart according to the intact or reconstituted nature of several soil samples from INRAE's HET database.

soils. In cases involving non-dispersive soils, this work has shown that a much greater difference in erosion indexes I_m is observed for the second category, the erosion index I_m derived from the HET systematically yielded higher values as can be seen in Figure 14. Similarly, extensive analyses comparing JET and HET have consistently shown that HET tends to yield slower erosion rates K, or equivalently higher erosion indexes I_m, and larger critical shear stresses τ_c, up to more than an order of magnitude as observed in Figure 14, thus overestimating soil resistance to erosion compared to JET [177, 179, 193, 212]. Erdogan and collaborators (2008) found particularly large discrepancies for soils with heterogeneous structures, composed for example of clay aggregates while the difference is still significant, but much smaller, for more homogeneous materials [177]. It was suggested that the complex hydraulic configuration of the JET test, along with the simplifying assumptions required for interpretation, may contribute to the discrepancies observed. However, comparisons between mini-JET and flume erosion test suggest that variations are more moderate on average despite substantial dispersion, and perhaps a weaker correlation between erodibility values [182, 213]. In addition, a 2D axisymmetrical numerical modelling of surface erosion by a submerged turbulent impinging jet showed that there was no major inconsistency between measured erosion rates and those calculated on the basis of the erodibility parameters provided by the corresponding JET interpretation [215]. Furthermore, comparisons between HET and EFA have similarly indicated an overestimation of soil resistance, and therefore an underestimation of its erodibility, with the HET results [174, 175]. Note however that the same type of overall agreement between simulation and experiment is obtained for the HET configuration [216].

In conclusion, using the HET rather than another device therefore can lead to category changes in Fell's classification based on erodibility parameters, even though the relative position between two given soils may remain the same. However, note that a more global energy-based method enables identical categories to be found between HET and JET results [102]. Overall, as suggested by Mahalder and co-authors [213], τ_c and K estimates appear to be significantly influenced by the specific hydrodynamics induced by the testing device configuration. This raises a number of fundamental concerns. To be, or not to be intrinsic, that is the question for soil's erodibility if we are to paraphrase Shakespeare in light of these inconsistent comparative results! One may indeed wonder whether a unique and generic framework can effectively apply

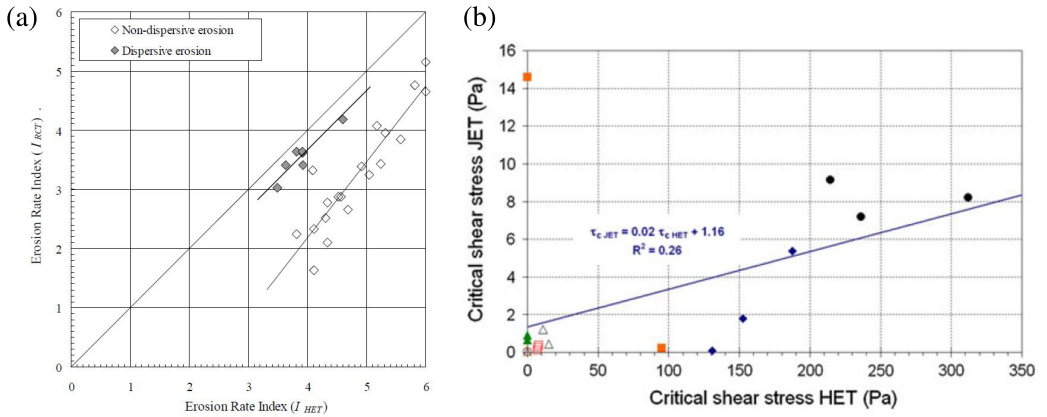


Figure 14. (a) Confrontation between the erosion indexes I_{m} obtained from HET and RCT tests, with distinction between non-dispersive and dispersive erosion [180]. (b) Confrontation between the critical shear stresses τ_{c} obtained from HET and JET tests [212].

for all types of soils and whatever the nature of the eroding flow at their exposed surface. The underlying question behind this line of thought is what erosion really is, particularly in terms of small-scale processes. There remains considerable exploration work to be continued, given the great variety of situations in terms of soil composition, physico-bio-chemical aspects and soil/runoff interactions, with widely varying lengths and characteristic times, including ageing.

5. Summary and perspectives

At a very broad scope, we can conclude that each disciplinary field has its own perception and definition of soil erosion, with quite specific scales of time and space. This vision derives organically from the object of study under consideration, the elementary mechanism of one discipline corresponding sometimes to the ultimate scale of another. In view of this vast spectrum of phenomena with many associated challenges and threats, we have chosen to emphasize the field of soil mechanics, i.e. for typical eroded soil surfaces of a few tens of centimetres with durations of minutes to hours.

Throughout this review, the reader has been able to appreciate the vast amount of work carried out on the subject, but also the intrinsic difficulties of soil erosion. The importance of quantifying the erosion resistance of soils has been demonstrated, in order to characterize their performance or predict topological changes in heterogeneous ground. We have shown how challenging it is to measure, both in terms of accurately determining the mass loss at an exposed soil interface, and in terms of correctly evaluating the most relevant quantities accounting for the load exerted by rather complex flows. Despite some limitations, the development of a conceptual framework for surface erosion has proved its worth and validity, enabling erodibility parameters to be defined explicitly for any coherent soil, for the purposes of own characterization, relative classification or even modeling. Yet questions remain as to the assumed intrinsic nature of this new material property. Finally, the description and comparison of the three leading erodimeters used in the field of soil mechanics, namely EFA, HET and JET, provided practical insights into these erodibility assessment tests.

From a purely fundamental point of view, a research perspective consists in improving our knowledge of the elementary processes involved in soil erosion, since this generic term actually covers different local mechanisms, some of which have already been identified but are still

poorly understood [217]. Accordingly, Winterwerp and Kesteren propose the existence of 4 erosion modes for cohesive marine sediments: entrainment, floc erosion, surface erosion and mass erosion [64]. This approach represents a major scientific bottleneck that precludes the development of non-empirical models or realistic scenarios to explain how, and through which successive steps, a fragment of soil is ultimately removed from the surface of a compact material under hydraulic stress of sufficient intensity and/or duration. These mechanisms should be able to provide us with valuable information on the size (or more likely the size distribution) of the elementary soil aggregates thereby eroded and on the characteristic time, or even on the hydraulic conditions, required for such a process. This effort needs to be based on theoretical approaches, but must also involve specific experimental investigations, which require a high degree of customization in order to explore small scales, particularly on natural geomaterials. An interesting alternative is to substitute real soils by purely artificial materials, specifically developed, whose key characteristics are well under control and capable of facilitating this local exploration [201, 217]. The contribution of numerical simulation could also be essential, particularly with the Discrete Element Method (DEM) integrating both microscopic laws modeling internal cohesion and coupling between fluid and grains, which requires significant methodological developments [218–220]. However, this raises the question of how representative such over simplified systems can be, given that erosion appears to be highly material-dependent, as revealed by the poor correlation between erodibility and soil properties.

From a more practical perspective, there is still room for further improvement in soil erodibility tests, both from a technical perspective and in terms of interpretation models, possibly by extending the conceptual framework used. Progress in this respect could hopefully address some of the questions raised in the preceding section. At the same time, it is essential to promote the implementation of routine tests of this kind in geotechnical and environmental engineering, particularly when safety considerations prevail. Beyond the usual properties associated with composition and structure of a soil, erodibility could then simply become an additional standard parameter for material identification, on an equal basis with other parameters such as shear strength or plasticity index. Many of the researchers involved in some of the works summarized in this review have been working towards this goal in their respective networks for several years, with notable advances and real prospects. Undoubtedly, erosion testing devices have proved their merits and are increasingly finding their place in the hydraulic engineering community. EFA is widely used, mainly in the United States, and notably played an important role in the post-crisis expertise carried out on New Orleans levees after Hurricane Katrina in 2005 [221]. JET also remains a very common test, particularly because of its ability to be conducted on site. A recent workshop brought together a large number of current operators to draw lessons and propose future prospects for this instrument [156]. As for HET, this device has undergone several improvements since its original version and is increasingly being used in civil engineering. In France, for example, several companies have licensed the version developed by INRAE, and a new standard on HET testing (PR XP P94-065[5]) has just been certified at the end of 2023, including soil sample preparation and testing protocol. Progress is definitely on the right course!

Declaration of interests

The authors do not work for, advise, own shares in, or receive funds from any organization that could benefit from this article, and have declared no affiliations other than their research organizations.

[5] https://www.boutique.afnor.org/fr-fr/norme/xp-p94065

References

[1] J. Gaillardet, B. Dupré, P. Louvat, C. Allègre, "Global silicate weathering and CO2 consumption rates deduced from the chemistry of large rivers", *Chem. Geol.* **159** (1999), no. 1, p. 3-30.

[2] P. A. Dinis, E. Garzanti, A. Hahn, P. Vermeesch, M. Cabral-Pinto, "Weathering indices as climate proxies. A step forward based on Congo and SW African river muds", *Earth-Sci. Rev.* **201** (2020), article no. 103039.

[3] A. B. Murray, M. A. F. Knaapen, M. Tal, M. L. Kirwan, "Biomorphodynamics: Physical-biological feedbacks that shape landscapes", *Water Resour. Res.* **44** (2008), article no. W11301.

[4] W. Merritt, R. Letcher, A. Jakeman, "A review of erosion and sediment transport models", *Environ. Model. Softw.* **18** (2003), p. 761-799.

[5] H. Aksoy, M. L. Kavvas, "A review of hillslope and watershed scale erosion and sediment transport models", *CATENA* **64** (2005), no. 2, p. 247-271, 25 Years of Assessment of Erosion.

[6] J. Poesen, "Soil erosion in the Anthropocene: research needs", *Earth Surf. Process. Landf.* **43** (2018), no. 1, p. 64-84.

[7] L. C. van Rijn, *Principles of Sediment Transport in Rivers, Estuaries and Coastal Seas*, vol. 1006, Aqua Publications, Amsterdam, 1993.

[8] R. Soulsby, *Dynamics of Marine Sands*, Thomas Telford Publishing, 1997.

[9] T. Pähtz, A. H. Clark, M. Valyrakis, O. Durán, "The physics of sediment transport initiation, cessation, and entrainment across aeolian and fluvial environments", *Rev. Geophys.* **58** (2020), no. 1, article no. e2019RG000679.

[10] Y. Shao, *Physics and Modelling of Wind Erosion*, Atmospheric and Oceanographic Sciences Library, vol. 37, Springer, 2009, 1-452 pages.

[11] L. Mentaschi, M. I. Vousdoukas, J.-F. Pekel, E. Voukouvalas, L. Feyen, "Global long-term observations of coastal erosion and accretion", *Sci. Rep.* **8** (2018), no. 1, article no. 12876.

[12] A. Williams, N. Rangel-Buitrago, E. Pranzini, G. Anfuso, "The management of coastal erosion", *Ocean Coast. Manag.* **156** (2018), p. 4-20.

[13] R. B. Bryan, "Soil erodibility and processes of water erosion on hillslope", *Geomorphology* **32** (2000), no. 3, p. 385-415.

[14] C. Castillo, J. Gómez, "A century of gully erosion research: urgency, complexity and study approaches", *Earth-Sci. Rev.* **160** (2016), p. 300-319.

[15] G. Gyssels, J. Poesen, E. Bochet, Y. Li, "Impact of plant roots on the resistance of soils to erosion by water: a review", *Prog. Phys. Geo.: Earth Environ.* **29** (2005), no. 2, p. 189-217.

[16] V. H. D. Zuazo, C. R. R. Pleguezuelo, "Soil-erosion and runoff prevention by plant covers: a review", in *Sustainable Agriculture* (E. Lichtfouse, M. Navarrete, P. Debaeke, S. Véronique, C. Alberola, eds.), vol. 2009, Springer, Netherlands, p. 785-811.

[17] A. Bernatek-Jakiel, J. Poesen, "Subsurface erosion by soil piping: significance and research needs", *Earth-Sci. Rev.* **185** (2018), p. 1107-1128.

[18] G. V. Wilson, R. Wells, R. Kuhnle, G. Fox, J. Nieber, "Sediment detachment and transport processes associated with internal erosion of soil pipes", *Earth Surf. Process. Landf.* **43** (2018), no. 1, p. 45-63.

[19] D. M. Lawler, "The measurement of river bank erosion and lateral channel change: A review", *Earth Surf. Process. Landf.* **18** (1993), no. 9, p. 777-821.

[20] J. P. Julian, R. Torres, "Hydraulic erosion of cohesive riverbanks", *Geomorphology* **76** (2006), no. 1, p. 193-206.

[21] C. Wang, X. Yu, F. Liang, "A review of bridge scour: mechanism, estimation, monitoring and countermeasures", *Nat. Hazards* **87** (2017), p. 1881-1906.

[22] K. Gao, C. Naito, M. T. Suleiman, "Erosion mitigation of bridge abutment backfill during flood events", *J. Perform. Constr. Facil.* **37** (2023), no. 6, article no. 04023054.

[23] M. Foster, R. Fell, M. Spannagle, "The statistics of embankment dam failures and accidents", *Can. Geotech. J.* **37** (2000), no. 5, p. 1000-1024.

[24] K. S. Richards, K. R. Reddy, "Critical appraisal of piping phenomena in earth dams", *Bull. Eng. Geol. Environ.* **66** (2007), p. 381-402.

[25] C. F. Wan, R. Fell, "Assessing the potential of internal instability and suffusion in embankment dams and their foundations", *J. Geotech. Geoenviron. Eng.* **134** (2008), no. 3, p. 401-407.

[26] S. Bonelli, *Erosion in Geomechanics Applied to Dams and Levees*, ISTE Ltd and John Wiley & Sons Inc, London, Hoboken, 2013.

[27] F. Ahnert, F. Ahnert, *Introduction to Geomorphology*, Hodder Arnold Publication, Arnold, 1998.

[28] D. Wuepper, P. Borrelli, R. Finger, "Countries and the global rate of soil erosion", *Nat. Sustain.* **3** (2020), p. 51-55.

[29] D. R. Montgomery, "Soil erosion and agricultural sustainability", *Proc. Natl. Acad. Sci. USA* **104** (2007), no. 33, p. 13268-13272.

[30] J. Boardman, J. Poesen, R. Evans, "Socio-economic factors in soil erosion and conservation", *Environ. Sci. Policy* **6** (2003), no. 1, p. 1-6.

[31] Z. Li, H. Fang, "Impacts of climate change on water erosion: a review", *Earth-Sci. Rev.* **163** (2016), p. 94-117.

[32] P. Borrelli, D. A. Robinson, L. R. Fleischer *et al.*, "An assessment of the global impact of 21st century land use change on soil erosion", *Nat. Commun.* **8** (2017), no. 1, article no. 2013.
[33] P. Borrelli, D. A. Robinson, P. Panagos, C. Ballabio, "Land use and climate change impacts on global soil erosion by water (2015–2070)", *Proc. Natl. Acad. Sci. USA* **117** (2020), no. 36, p. 21994-22001.
[34] P. V. G. Batista, D. L. Evans, B. M. Cândido, P. Fiener, "Does soil thinning change soil erodibility? An exploration of long-term erosion feedback systems", *SOIL* **9** (2023), no. 1, p. 71-88.
[35] L. Li, S. Du, L. Wu, G. Liu, "An overview of soil loss tolerance", *Catena* **78** (2009), no. 2, p. 93-99.
[36] K. V. Oost, T. A. Quine, G. Govers *et al.*, "The impact of agricultural soil erosion on the global carbon cycle", *Science* **318** (2007), no. 5850, p. 626-629.
[37] N. J. Kuhn, T. Hoffmann, W. Schwanghart, M. Dotterweich, "Agricultural soil erosion and global carbon cycle: controversy over?", *Earth Surf. Process. Landf.* **34** (2009), no. 7, p. 1033-1038.
[38] S. Doetterl, A. A. Berhe, E. Nadeu, Z. Wang, M. Sommer, P. Fiener, "Erosion, deposition and soil carbon: A review of process-level controls, experimental tools and models to address C cycling in dynamic landscapes", *Earth-Sci. Rev.* **154** (2016), p. 102-122.
[39] O. Evrard, J. P. Laceby, H. Lepage, Y. Onda, O. Cerdan, S. Ayrault, "Radiocesium transfer from hillslopes to the Pacific Ocean after the Fukushima Nuclear Power Plant accident: a review", *J. Environ. Radioact.* **148** (2015), p. 92-110.
[40] J. P. Brady, G. A. Ayoko, W. N. Martens, A. Goonetilleke, "Development of a hybrid pollution index for heavy metals in marine and estuarine sediments", *Environ. Monit. Assess.* **187** (2015), article no. 306.
[41] J. B. Kowalska, R. Mazurek, M. Gąsiorek, T. Zaleski, "Pollution indices as useful tools for the comprehensive evaluation of the degree of soil contamination—A review", *Environ. Geochem. Health* **40** (2018), p. 2395-2420.
[42] L. C. M. Lebreton, J. van der Zwet, J.-W. Damsteeg, B. Slat, A. Andrady, J. Reisser, "River plastic emissions to the world's oceans", *Nat. Commun.* **8** (2017), article no. 15611.
[43] H. Zhang, "Transport of microplastics in coastal seas", *Estuar. Coast. Shelf Sci.* **199** (2017), p. 74-86.
[44] A. L. Burrell, J. P. Evans, M. G. De Kauwe, "Anthropogenic climate change has driven over 5 million km^2 of drylands towards desertification", *Nat. Commun.* **11** (2020), article no. 3853.
[45] K. Zhang, B. C. Douglas, S. P. Leatherman, "Global warming and coastal erosion", *Clim. Change* **64** (2004), p. 41-58.
[46] T. Pang, X. Wang, R. A. Nawaz, G. Keefe, T. Adekanmbi, "Coastal erosion and climate change: A review on coastal-change process and modeling", *Ambio* **52** (2023), no. 12, p. 2034-2052.
[47] L. Brandimarte, P. Paron, G. D. Baldassarre, "Bridge pier scour: A review of processes, measurements and estimates", *Environ. Eng. Manag. J.* **11** (2012), p. 975-989.
[48] P. Bishop, "Long-term landscape evolution: linking tectonics and surface processes", *Earth Surf. Process. Landf.* **32** (2007), no. 3, p. 329-365.
[49] A. Pandey, S. K. Himanshu, S. Mishra, V. P. Singh, "Physically based soil erosion and sediment yield models revisited", *CATENA* **147** (2016), p. 595-620.
[50] P. Borrelli, C. Alewell, P. Alvarez *et al.*, "Soil erosion modelling: A global review and statistical analysis", *Sci. Total Environ.* **780** (2021), article no. 146494.
[51] R. P. C. Morgan, J. N. Quinton, R. E. Smith *et al.*, "The European Soil Erosion Model (EUROSEM): a dynamic approach for predicting sediment transport from fields and small catchments", *Earth Surf. Process. Landf.* **23** (1998), no. 6, p. 527-544.
[52] D. C. Flanagan, J. C. Ascough, M. A. Nearing, J. M. Laflen, "The Water Erosion Prediction Project (WEPP) model", in *Landscape Erosion and Evolution Modeling* (R. S. Harmon, W. W. Doe, eds.), Springer US, Boston, MA, 2001, p. 145-199.
[53] M. J. Kirkby, B. J. Irvine, R. J. A. Jones, G. Govers, P. team, "The PESERA coarse scale erosion model for Europe. I. – Model rationale and implementation", *Eur. J. Soil Sci.* **59** (2008), no. 6, p. 1293-1306.
[54] P. Panagos, P. Borrelli, J. Poesen, C. Ballabio, E. Lugato, K. Meusburger, L. Montanarella, C. Alewell, "The new assessment of soil loss by water erosion in Europe", *Environ. Sci. Policy* **54** (2015), p. 438-447.
[55] A. P. J. De Roo, C. G. Wesseling, C. J. Ritsema, "LISEM: A single-event physically based hydrological and soil erosion model for drainage basins. I: Theory, input and outpout", *Hydrol. Process.* **10** (1996), no. 8, p. 1107-1117.
[56] Y. Le Bissonnais, "Aggregate stability and assessment of soil crustability and erodibility: I. Theory and methodology", *Eur. J. Soil Sci.* **47** (1996), no. 4, p. 425-437.
[57] C. Alewell, P. Borrelli, K. Meusburger, P. Panagos, "Using the USLE: chances, challenges and limitations of soil erosion modelling", *Int. Soil Water Conserv. Res.* **7** (2019), no. 3, p. 203-225.
[58] R. Al-Raoush, A. Papadopoulos, "Representative elementary volume analysis of porous media using X-ray computed tomography", *Powder Technol.* **200** (2010), no. 1, p. 69-77.
[59] D. Favis-Mortlock, J. Boardman, V. MacMillan, "The limits of erosion modeling", in *Landscape Erosion and Evolution Modeling* (R. S. Harmon, W. W. Doe, eds.), Springer US, Boston, MA, 2001, p. 477-516.
[60] J. M. Buffington, "The legend of A. F. Shields", *J. Hydraul. Eng.* **125** (1999), no. 4, article no. 17211.
[61] S. Dey, S. Z. Ali, "Bed sediment entrainment by streamflow: State of the science", *Sedimentology* **66** (2019), no. 5, p. 1449-1485.

[62] M. Righetti, C. Lucarelli, "May the Shields theory be extended to cohesive and adhesive benthic sediments?", *J. Geophys. Res. Oceans* **112** (2007), article no. C10020.
[63] W. Jacobs, P. Le Hir, W. Van Kesteren, P. Cann, "Erosion threshold of sand-mud mixtures", *Cont. Shelf Res.* **31** (2011), no. 10, supplement, p. S14-S25, Proceedings of the 9th International Conference on Nearshore and Estuarine Cohesive Sediment Transport Processes.
[64] J. C. Winterwerp, W. G. M. van Kesteren, *Introduction to the Physics of Cohesive Sediment in the Marine Environment*, Developments in Sedimentology, vol. 56, Elsevier, Amsterdam, 2004, 121-159 pages.
[65] H. Feng, Z.-Y. Yin, M. Peng, Q. Guo, "State-of-the-art review of continuum mechanics-based modelling of soil surface erosion", *Archives Comput. Meth. Eng.* (2024).
[66] A. Knapen, J. Poesen, G. Govers, G. Gyssels, J. Nachtergaele, "Resistance of soils to concentrated flow erosion: a review", *Earth-Sci. Rev.* **80** (2007), no. 1, p. 75-109.
[67] G.-H. Zhang, Y.-M. Liu, Y.-F. Han, X. C. Zhang, "Sediment transport and soil detachment on steep slopes: II. Sediment feedback relationship", *Soil Sci. Soc. Am. J.* **73** (2009), no. 4, p. 1298-1304.
[68] G. Govers, G. Rauws, "Transporting capacity of overland flow on plane and on irregular beds", *Earth Surf. Process. Landf.* **11** (1986), no. 5, p. 515-524.
[69] J. C. Winterwerp, W. G. M. van Kesteren, B. van Prooijen, W. Jacobs, "A conceptual framework for shear flow–induced erosion of soft cohesive sediment beds", *J. Geophys. Res. Oceans* **117** (2012), no. C10, article no. 10020.
[70] L. P. Sanford, J. P.-Y. Maa, "A unified erosion formulation for fine sediments", *Mar. Geol.* **179** (2001), no. 1, p. 9-23.
[71] J. S. Walder, "Dimensionless erosion laws for cohesive sediment", *J. Hydraul. Eng.* **142** (2016), no. 2, article no. 04015047.
[72] A. Sidorchuk, "Stochastic components in the gully erosion modelling", *Catena* **63** (2005), no. 2, p. 299-317, Gully Erosion: A Global Issue.
[73] B. C. Van Prooijen, J. C. Winterwerp, "A stochastic formulation for erosion of cohesive sediments", *J. Geophys. Res. Oceans* **115** (2010), article no. C01005.
[74] S. Bonelli, *Erosion of Geomaterials*, ISTE Ltd and John Wiley & Sons Inc, London, Hoboken, 2012.
[75] G. J. Hanson, K. R. Cook, "Apparatus, test procedures, and analytical methods to measure soil erodibility in situ", *Appl. Eng. Agric.* **20** (2004), no. 4, p. 455-462.
[76] V.-N. Nguyen, J.-R. Courivaud, P. Pinettes, H. Souli, J.-M. Fleureau, "Using an improved jet-erosion test to study the influence of soil parameters on the erosion of a silty soil", *J. Hydraul. Eng.* **143** (2017), no. 8, article no. 04017018.
[77] O. Witt, B. Westrich, "Quantification of erosion rates for undisturbed contaminated cohesive sediment cores by image analysis", *Hydrobiologia* **494** (2003), no. 1–3, p. 271-276, 9th International Symposium on the Interactions between Sediments and Water, Banff, Canada, May 05–10, 2002.
[78] C. Lee, C. H. Wu, J. A. Hoopes, "Automated sediment erosion testing system using digital imaging", *J. Hydraul. Eng.* **130** (2004), no. 8, p. 771-782.
[79] E. Foti, I. C. Rabionet, A. Marini, R. E. Musumeci, A. Sánchez-Arcilla, "Experimental investigations of the bed evolution in wave flumes: performance of 2D and 3D optical systems", *Coast. Engng* **58** (2011), no. 7, p. 606-622.
[80] D. H. Rieke-Zapp, M. A. Nearing, "Digital close range photogrammetry for measurement of soil erosion", *Photogramm. Rec.* **20** (2005), no. 109, p. 69-87.
[81] B. R. Sutherland, S. Dalziel, "Bedload transport by a vertical jet impinging upon sediments", *Phys. Fluids* **26** (2014), no. 3, article no. 035103.
[82] S. Bonelli, R. Fell, N. Benahmed, "Concentrated leak erosion", in *Erosion in Geomechanics Applied to Dams and Levees*, John Wiley & Sons, Ltd, London, Hoboken, 2013, p. 271-341.
[83] N.-S. Cheng, A. W.-K. Law, "Fluctuations of turbulent bed shear stress", *J. Eng. Mech.* **129** (2003), no. 1, p. 126-130.
[84] L. Keirsbulck, L. Labraga, M. G. el Hak, "Statistical properties of wall shear stress fluctuations in turbulent channel flows", *Intl J. Heat Fluid Flow* **37** (2012), p. 1-8.
[85] R. Beguin, P. Philippe, Y.-H. Faure, "Pore-scale flow measurements at the interface between a sandy layer and a model porous medium: application to statistical modeling of contact erosion", *J. Hydraul. Eng.-ASCE* **139** (2013), no. 1, p. 1-11.
[86] T. J. Tolhurst, K. S. Black, D. M. Paterson, "Muddy sediment erosion: insights from field studies", *J. Hydraul. Eng.* **135** (2009), no. 2, p. 73-87.
[87] B. C. Khoo, Y. T. Chew, C. J. Teo, "Near-wall hot-wire measurements. Part II: turbulence time scale, convective velocity and spectra in the viscous sublayer", *Exp. Fluids* **31** (2001), no. 5, p. 494-505.
[88] W. Nimmo Smith, P. Atsavapranee, J. Katz, T. Osborn, "PIV measurements in the bottom boundary layer of the coastal ocean", *Exp. Fluids* **33** (2002), no. 6, p. 962-971.
[89] A. S.-A. Rosaria, E. Musumeci, V. Marletta, E. Foti, "A ferrofluid-based sensor to measure bottom shear stresses under currents and waves", *J. Hydraul. Res.* **56** (2018), no. 5, p. 630-647.
[90] H. Schlichting, K. Gersten, *Boundary-Layer Theory*, 8th ed., Springer-Verlag, Berlin, Heidelberg, 2000.
[91] J. Klewicki, W. Saric, I. Marusic, J. Eaton, "Wall-bounded flows", in *Springer Handbook of Experimental Fluid Mechanics* (C. Tropea, A. L. Yarin, J. F. Foss, eds.), Springer, Berlin, Heidelberg, 2007, p. 871-907.

[92] V. C. Patel, "Calibration of the Preston tube and limitations on its use in pressure gradients", *J. Fluid Mech.* **23** (1965), no. 1, p. 185-208.
[93] J. D. Ackerman, T. M. Hoover, "Measurement of local bed shear stress in streams using a Preston-static tube", *Limnol. Oceanogr.* **46** (2001), no. 8, p. 2080-2087.
[94] D. Sturzebecher, S. Anders, W. Nitsche, "The surface hot wire as a means of measuring mean and fluctuating wall shear stress", *Exp. Fluids* **31** (2002), no. 3, p. 294-301.
[95] J. W. Naughton, M. Sheplak, "Modern developments in shear-stress measurement", *Prog. Aerosp. Sci.* **38** (2002), no. 6, p. 515-570.
[96] W. J. Baars, D. T. Squire, K. M. Talluru, M. R. Abbassi, N. Hutchins, I. Marusic, "Wall-drag measurements of smooth- and rough-wall turbulent boundary layers using a floating element", *Exp. Fluids* **57** (2016), article no. 90.
[97] E. Foti, C. Faraci, R. Foti, G. Bonanno, "On the use of bioluminescence for estimating shear stresses over a rippled seabed", *Meccanica* **45** (2010), p. 881-895.
[98] E. Partheniades, "Erosion and deposition of cohesive soils", *J. Hydraul. Div.-ASCE* **91** (1965), no. 1, p. 105-139.
[99] R. Ariathurai, K. Arulanandan, "Erosion rates of cohesive soils", *J. Hydraul. Div.-ASCE* **104** (1978), no. 2, p. 279-283.
[100] T. M. Parchure, A. J. Mehta, "Erosion of soft cohesive sediment deposits", *J. Hydraul. Eng.-ASCE* **111** (1985), no. 10, p. 1308-1326.
[101] R. B. Krone, "Effects of bed structure on erosion of cohesive sediments", *J. Hydraul. Eng.* **125** (1999), no. 12, p. 1297-1301.
[102] D. Marot, P.-L. Regazzoni, T. Wahl, "Energy-based method for providing soil surface erodibility rankings", *J. Geotech. Geoenviron. Eng.* **137** (2011), no. 12, p. 1290-1293.
[103] A. R. Sharif, J. F. Atkinson, "Model for surface erosion of cohesive soils", *J. Hydraul. Eng.* **138** (2012), no. 7, p. 581-590.
[104] M. J. Bora, W. Cai, S. Pekkat, A. Garg, S. Sekharan, "Development of a simplified theoretical model to determine erodibility of compacted soil in hole erosion test based on fluid energy transformation", *Acta Geotech.* **18** (2023), no. 10, p. 5441-5455.
[105] J. W. Lavelle, H. O. Mofjeld, "Do critical stresses for incipient motion and erosion really exist?", *J. Hydraul. Eng.-ASCE* **113** (1987), no. 3, p. 370-385.
[106] P. Duboys, "Le Rhône et les rivières à lit affouillable", *Annales des Ponts et Chaussées* **18** (1879), p. 141-195.
[107] P. Davy, D. Lague, "Fluvial erosion/transport equation of landscape evolution models revisited", *J. Geophys. Res. Earth Surf.* **114** (2009), article no. F03007.
[108] K. Black, T. Tolhurst, D. Paterson, S. Hagerthey, "Working with natural cohesive sediments", *J. Hydraul. Eng.* **128** (2002), no. 1, p. 2-8.
[109] S. Bonelli, O. Brivois, "The scaling law in the hole erosion test with a constant pressure drop", *Int. J. Numer. Anal. Meth. Geomech.* **32** (2008), no. 13, p. 1573-1595.
[110] J. M. Laflen, W. J. Elliot, J. R. Simanton, C. S. Holzhey, K. D. Kohl, "WEPP - soil erodibility experiments for rangeland and cropland soils", *J. Soil Water Conserv.* **46** (1991), no. 1, p. 39-44.
[111] J. L. Briaud, F. C. K. Ting, H. C. Chen, Y. Cao, S. W. Han, K. W. Kwak, "Erosion function apparatus for scour rate predictions", *J. Geotech. Geoenviron. Eng.* **127** (2001), no. 2, p. 105-113.
[112] G. Zhang, B. Liu, M. A. Nearing, C. Huang, K. Zhang, "Soil detachment by shallow flow", *Trans. ASAE* **45** (2004), no. 2, p. 351-357.
[113] I. Haghighi, C. Chevalier, M. Duc, S. Guédon, P. Reiffsteck, "Improvement of hole erosion test and results on reference soils", *J. Geotech. Geoenviron. Eng.* **139** (2013), no. 2, p. 330-339.
[114] H. Mitchener, H. Torfs, "Erosion of mud/sand mixtures", *Coast. Engng* **29** (1996), no. 1, p. 1-25.
[115] R. C. Grabowski, I. G. Droppo, G. Wharton, "Erodibility of cohesive sediment: the importance of sediment properties", *Earth-Sci. Rev.* **105** (2011), no. 3, p. 101-120.
[116] M. Andreini, P. Gardoni, S. Pagliara, M. Sassu, "Probabilistic models for the erosion rate in embankments and reliability analysis of earth dams", *Reliab. Eng. Syst. Saf.* **181** (2019), p. 142-155.
[117] M. Z. Karim, S. E. Tucker-Kulesza, "Predicting soil erodibility using electrical resistivity tomography", *J. Geotech. Geoenviron. Eng.* **144** (2018), no. 4, article no. 04018012.
[118] A. Shaikh, J. F. Ruff, S. R. Abt, "Erosion rate of compacted NA-Montmorillonite soils", *J. Geotech. Eng.* **114** (1988), no. 3, p. 296-305.
[119] C. L. Amos, J. Grant, G. Daborn, K. Black, "Sea Carousel—A benthic, annular flume", *Estuar. Coast. Shelf Sci.* **34** (1992), no. 6, p. 557-577.
[120] J.-Y. Maa, L. Wright, C.-H. Lee, T. Shannon, "Vims Sea Carousel: a field instrument for studying sediment transport", *Mar. Geol.* **115** (1993), no. 3, p. 271-287.
[121] J. Mcneil, C. Taylor, W. Lick, "Measurements of erosion of undisturbed bottom sediments with depth", *J. Hydraul. Eng.* **122** (1996), no. 6, p. 316-324.
[122] E.-J. Houwing, L. C. van Rijn, "In Situ Erosion Flume (ISEF): determination of bed-shear stress and erosion of a kaolinite bed", *J. Sea Res.* **39** (1998), no. 3, p. 243-253.

[123] T. M. Ravens, P. M. Gschwend, "Flume measurements of sediment erodibility in boston harbor", *J. Hydraul. Eng.* **125** (1999), no. 10, p. 998-1005.
[124] T. Tolhurst, K. Black, D. Paterson, H. Mitchener, G. Termaat, S. Shayler, "A comparison and measurement standardisation of four in situ devices for determining the erosion shear stress of intertidal sediments", *Cont. Shelf Res.* **20** (2000), no. 10, p. 1397-1418.
[125] J. Aberle, V. Nikora, R. Walters, "Effects of bed material properties on cohesive sediment erosion", *Mar. Geol.* **207** (2004), no. 1, p. 83-93.
[126] P. L. Hir, P. Cann, B. Waeles, H. Jestin, P. Bassoullet, "Chapter 11 Erodibility of natural sediments: experiments on sand/mud mixtures from laboratory and field erosion tests", in *Sediment and Ecohydraulics* (T. Kusuda, H. Yamanishi, J. Spearman, J. Z. Gailani, eds.), Proceedings in Marine Science, vol. 9, Elsevier, Amsterdam, 2008, p. 137-153.
[127] R. W. Crowley, D. Bloomquist, J. R. Hayne, C. M. Holst, F. D. Shah, "Estimation and measurement of bed material shear stresses in erosion rate testing devices", *J. Hydraul. Eng.* **138** (2012), no. 11, p. 990-994.
[128] R. W. Crowley, D. Bloomquist, F. D. Shah, C. M. Holst, "The Sediment Erosion Rate Flume (SERF): a new testing device for measuring soil erosion rate and shear stress", *Geotech. Test. J.* **35** (2012), no. 4, p. 649-659.
[129] T. Sutarto, A. N. T. Papanicolaou, C. G. Wilson, E. J. Langendoen, "Stability analysis of semicohesive streambanks with CONCEPTS: coupling field and laboratory investigations to quantify the onset of fluvial erosion and mass failure", *J. Hydraul. Eng.* **140** (2014), no. 9, article no. 04014041.
[130] H. Shan, O. Wiblishauser, K. Kerenyi, M. Uhrig, C. Huang, "Efficient automated laboratory testing of erosion resistance forfine-grained soils", in *Proceedings of the 10th International Conference on Scour and Erosion, Arlington, VA, USA*, vol. 147, 2021.
[131] B. G. Krishnappan, "Review of a semi-empirical modelling approach for cohesive sediment transport in river systems", *Water* **14** (2022), no. 2, article no. 256.
[132] P. Yao, M. Su, Z. Wang, L. C. van Rijn, M. J. F. Stive, C. Xu, Y. Chen, "Erosion behavior of sand-silt mixtures: revisiting the erosion threshold", *Water Resour. Res.* **58** (2022), no. 9, article no. e2021WR031788.
[133] J. L. Sherard, L. P. Dunnigan, R. S. Decker, E. F. Steele, "Pinhole test for identifying dispersive soils", *J. Geotech. Eng. Div.* **102** (1976), no. 1, p. 69-85.
[134] E. I. Hjeldnes, B. V. Lavania, "Cracking, leakage, and erosion of earth dam materials", *J. Geotech. Eng. Div.* **106** (1980), no. 2, p. 117-135.
[135] G. Lefebvre, K. Rohan, S. Douville, "Erosivity of natural intact structured clay: evaluation", *Can. Geotech. J.* **22** (1985), no. 4, p. 508-517.
[136] L. N. Reddi, I.-M. Lee, M. V. S. Bonala, "Comparison of internal and surface erosion using flow pump tests on a sand-kaolinite mixture", *Geotech. Test. J.* **23** (2000), no. 1, p. 116-122.
[137] C. F. Wan, R. Fell, "Investigation of rate of erosion of soils in embankment dams", *J. Geotech. Geoenviron. Eng.* **130** (2004), no. 4, p. 373-380.
[138] C. F. Wan, R. Fell, "Laboratory tests on the rate of piping erosion of soils in embankment dams", *Geotech. Test. J.* **27** (2004), no. 3, p. 295-303.
[139] N. Benahmed, S. Bonelli, "Investigating concentrated leak erosion behaviour of cohesive soils by performing hole erosion tests", *Eur. J. Environ. Civil Eng.* **16** (2012), no. 1, p. 43-58.
[140] S. Fattahi, A. Soroush, P. Shourijeh, "The hole erosion test: a comparison of interpretation methods", *Geotech. Test. J.* **40** (2017), no. 3, p. 494-505.
[141] L. Xie, X. Liang, T.-C. Su, "Measurement of pressure in viewable hole erosion test", *Can. Geotech. J.* **55** (2018), no. 10, p. 1502-1509.
[142] I. Sharma, A. Thomas, "Experimental evaluation of internal erosion using groove erosion test", *Int. J. Geomech.* **22** (2022), no. 6, article no. 04022056.
[143] W. L. Moore, F. D. Masch Jr., "Experiments on the scour resistance of cohesive sediments", *J. Geophys. Res. (1896–1977)* **67** (1962), no. 4, p. 1437-1446.
[144] O. Aderibigbe, N. Rajaratnam, "Erosion of loose beds by submerged circular impinging vertical turbulent jets", *J. Hydraul. Res.* **34** (1996), no. 1, p. 19-33.
[145] G. J. Hanson, A. Simon, "Erodibility of cohesive streambeds in the loess area of the midwestern USA", *Hydrol. Process.* **15** (2001), no. 1, p. 23-38.
[146] J.-L. Briaud, M. Chedid, H.-C. Chen, A. Shidlovskaya, "Borehole erosion test", *J. Geotech. Geoenviron. Eng.* **143** (2017), no. 8, article no. 04017037.
[147] C. Dong, G. Yu, H. Zhang, M. Zhang, "Scouring by submerged steady water jet vertically impinging on a cohesive bed", *Ocean Eng.* **196** (2020), article no. 106781.
[148] K. Arulanandan, R. B. Krone, P. Loganathan, "Pore and eroding fluid influences on surface erosion on soil", *J. Geotech. Eng. Div.* **101** (1975), no. 1, p. 51-66.
[149] R. P. Chapuis, T. Gatien, "An improved rotating cylinder technique for quantitative measurements of the scour resistance of clays", *Can. Geotech. J.* **23** (1986), no. 1, p. 83-87.

[150] S. S. Lim, N. Khalili, "An improved rotating cylinder test design for laboratory measurement of erosion in clayey soils", *Geotech. Test. J.* **32** (2009), no. 3, p. 232-238.
[151] D. Bloomquist, D. Sheppard, S. Schofield, R. Crowley, "The rotating erosion testing apparatus (reta): a laboratory device for measuring erosion rates versus shear stresses of rock and cohesive materials", *Geotech. Test. J.* **35** (2012), no. 4, p. 641-648.
[152] F. Ternat, P. Boyer, F. Anselmet, M. Amielh, "Erosion threshold of saturated natural cohesive sediments: modeling and experiments", *Water Resour. Res.* **44** (2008), article no. W11434.
[153] B. G. Krishnappan, "Rotating circular flume", *J. Hydraul. Eng.* **119** (1993), no. 6, p. 758-767.
[154] G. J. Hanson, L. S. Hunt, "Lessons learned using laboratory JET method to measure soil erodibility of compacted soils", *Appl. Eng. Agric.* **23** (2007), no. 3, p. 305-312.
[155] A.-S. Al-Madhhachi, G. Hanson, G. Fox, A. Tyagi, R. Bulut, "Deriving parameters of a fundamental detachment model for cohesive soils from flume and jet erosion tests", *Trans. ASABE* **56** (2013), p. 489-504.
[156] G. A. Fox, L. Guertault, C. Castro-Bolinaga *et al.*, "Perspectives on the Jet Erosion Test (JET): lessons learned, challenges and opportunities in quantifying cohesive soil erodibility", *ASABE Papers* **65** (2022), no. 2, p. 197-207.
[157] A. Shidlovskaya, M. Bahmani, J.-L. Briaud, H.-C. Chen, "Improvements in test procedure and data reduction for the Borehole Erosion Test", *Geotech. Test. J.* **46** (2023), no. 2, p. 295-315.
[158] P. T. Metzger, C. D. Immer, C. M. Donahue, B. T. Vu, R. C. Latta III, M. Deyo-Svendsen, "Jet-induced cratering of a granular surface with application to lunar spaceports", *J. Aerosp. Eng.* **22** (2009), no. 1, p. 24-32.
[159] C. Q. LaMarche, A. Benavides Moran, B. van Wachem, J. S. Curtis, "Two-fluid modeling of cratering in a particle bed by a subsonic turbulent jet", *Powder Technol.* **318** (2017), p. 68-82.
[160] S. D. Guleria, D. V. Patil, "Experimental investigations of crater formation on granular bed subjected to an air-jet impingement", *Phys. Fluids* **32** (2020), article no. 053309.
[161] S. Beltaos, R. N., "Impinging circular turbulent jets", *J. Hudraul. Div.-ASCE* **100** (1974), no. HY10, p. 1313-1328.
[162] Z. Benseghier, P. Cuellar, L.-H. Luu, J.-Y. Delenne, S. Bonelli, P. Philippe, "Relevance of free jet model for soil erosion by impinging jets", *J. Hydraul. Eng.* **146** (2020), no. 1, article no. 04019047.
[163] K. Head, R. Epps, *Manual of Soil Laboratory Testing, Third Edition: Volume Two: Permeability, Shear Strength and Compressibility Tests*, Whittles Publishing, Caithness, 2011.
[164] K. Black, A. Cramp, "A device to examine the in situ response of intertidal cohesive sediment deposits to fluid shear", *Cont. Shelf Res.* **15** (1995), no. 15, p. 1945-1954.
[165] J. D. Roberts, R. A. Jepsen, S. C. James, "Measurements of sediment erosion and transport with the adjustable shear stress erosion and transport flume", *J. Hydraul. Eng.* **129** (2003), no. 11, p. 862-871.
[166] T. Tolhurst, K. Black, S. Shayler, S. Mather, I. Black, K. Baker, D. Paterson, "Measuring the in situ erosion shear stress of intertidal sediments with the Cohesive Strength Meter (CSM)", *Estuar. Coast. Shelf Sci.* **49** (1999), no. 2, p. 281-294.
[167] G. J. Hanson, K. R. Cook, S. L. Hunt, "Physical modeling of overtopping erosion and breach formation of cohesive embankments", *Trans. ASAE* **48** (2005), no. 5, p. 1783-1794.
[168] C. Thornton, S. Hughes, B. Scholl, "Full-scale testing of levee resiliency during wave overtopping", in *Proceedings from Annual Innovative Dam and Levee Design and Construction for Sustainable Water Management*, Elsevier, 2012, p. 721-735.
[169] T. Kakinuma, Y. Shimizu, "Large-scale experiment and numerical modeling of a riverine levee breach", *J. Hydraul. Eng.* **140** (2014), no. 9, article no. 04014039.
[170] F. S. R. D. Jan Olschewski, S. Cantré, R. Ossowski, "Overflowing tests at the Polish DredgDikes research dike – stability of the dike surface against erosion", *Eng. Struct. Technol.* **6** (2014), no. 4, p. 159-168.
[171] S. Cantré, J. Olschewski, F. Saathoff, "Full-scale flume experiments to analyze the surface erosion resistance of dike embankments made of dredged materials", *J. Water. Port, Coast. Ocean Eng.* **143** (2017), no. 3, article no. 04017001.
[172] S. Bonelli, S. Nicaise, G. Charrier, N. Chaouch, F. Byron, Y. Grémeaux, "Quantifying the erosion resistance of dikes with the overflowing simulator", in *Proceedings of the 3rd International Conference on Protection against Overtopping, 6–8 June 2018, Grange-over-Sands, United Kingdom*, 2018.
[173] C. Picault, F. Crampette, S. Bonelli *et al.*, "Field testing of the overflow erosion of rhone river levees", in *Proceedings of the 4th International Seminar on Dam Protections against Overtopping, 30 Nov 2 Dec 2012, Madrid, Spain*, 2023.
[174] A. Bennabi, T. Karoui, A. Benamar, H. Wang, "Some elements of comparison between two laboratory devices for soil erosion testing", in *Proceedings of the 6th International Conference on Scour and Erosion 27–31 August 2012, Paris, France*, 2012.
[175] S. Youssef, *Soil surface erosion: local law and influence of soil and flow properties on the erosion resistance of hydraulic structures*, Phd thesis, Aix Marseille University, 2023.
[176] J.-L. Briaud, A. V. Govindasamy, I. Shafii, "Erosion charts for selected geomaterials", *J. Geotech. Geoenviron. Eng.* **143** (2017), no. 10, article no. 04017072.
[177] Z. M. Erdogan, "Determining erosion indices of cohesive soils with the hole erosion test and jet erosion test", 2008, Report DSO-08-05, https://api.semanticscholar.org/CorpusID:52839129.

[178] A. Mehenni, O. Cuisinier, F. Masrouri, "Impact of lime, cement, and clay treatments on the internal erosion of compacted soils", *J. Mater. Civil Eng.* **28** (2016), no. 9, article no. 04016071.
[179] M. Lüthi, *A modified Hole Erosion test (HET-P) to study erosion characteristics of soil*, Phd thesis, University of British Columbia, 2011.
[180] S. S. Lim, *Experimental investigation of erosion in variably saturated clay soils*, Phd thesis, School of Civil and Environmental Engineering, The University of New South Wales, 2006.
[181] M. Lüthi, R. Fannin, R. Millar, "A modified hole erosion test (HET-P) device", *Geotech. Test. J.* **35** (2012), article no. 104336.
[182] B. Mcnichol, K. Kassa, G. Fox, R. Miller, L. Guertault, "Erodibility parameters derived from jet and flume erosion tests on root-permeated soils", *J. Contemp. Water Res. Educ.* **160** (2017), p. 119-131.
[183] E. R. Daly, G. A. Fox, A.-S. T. Al-Madhhachi, D. E. Storm, "Variability of fluvial erodibility parameters for streambanks on a watershed scale", *Geomorphology* **231** (2015), p. 281-291.
[184] M. Karamigolbaghi, S. M. Ghaneeizad, J. F. Atkinson, S. J. Bennett, R. R. Wells, "Critical assessment of jet erosion test methodologies for cohesive soil and sediment", *Geomorphology* **295** (2017), p. 529-536.
[185] Transportation Research Board and National Academies of Sciences, Engineering, and Medicine, *Relationship Between Erodibility and Properties of Soils*, The National Academies Press, Washington, DC, 2019.
[186] R. Fell, J.-J. Fry, "State of the art on the likelihood of internal erosion of dams and levees by means of testing", in *Erosion in Geomechanics Applied to Dams and Levees* (S. Bonelli, ed.), Civil Engineering and Geomechanics Series, John Wiley & Sons, Ltd, 2013, p. 1-99.
[187] S. Bonelli, N. Benahmed, "Piping flow erosion in water retaining structures", *Int. J. Hydrop. Dams* **18** (2011), no. 3, p. 94-99.
[188] N.-J. Jiang, K. Soga, M. Kuo, "Microbially induced carbonate precipitation for seepage-induced internal erosion control in sand–clay mixtures", *J. Geotech. Geoenviron. Eng.* **143** (2017), no. 3, article no. 04016100.
[189] B. Indraratna, T. Muttuvel, H. Khabbaz, "Modelling the erosion rate of chemically stabilized soil incorporating tensile force – deformation characteristics", *Can. Geotech. J.* **46** (2009), no. 1, p. 57-68.
[190] B. Indraratna, T. Muttuvel, H. Khabbaz, R. Armstrong, "Predicting the erosion rate of chemically treated soil using a process simulation apparatus for internal crack erosion", *J. Geotech. Geoenviron. Eng.* **134** (2008), no. 6, p. 837-844.
[191] G. Herrier, S. Bonelli, "Internal erosion resistance of soils treated with lime: an evolutive benefit", in *Scour and Erosion: Proceedings of the 7th International Conference on Scour and Erosion, Perth, Australia, 2–4 December 2014* (L. Cheng, S. Draper, H. An, eds.), CRC Press, London, 2014, p. 73-80.
[192] M. Konstadinou, G. Herrier, T. Stoutjesdijk, F. Losma, C. Zwanenburg, R. Dobbe, "Lime treatment: evaluation for use in dike applications in the Netherlands", *J. Mater. Civil Eng.* **35** (2023), no. 3, article no. 04022465.
[193] R. Fell, G. Hanson, G. Herrier, D. Marot, T. Wahl, "Relationship between the erosion properties of soils and other parameters", in *Erosion in Geomechanics Applied to Dams and Levees* (S. Bonelli, ed.), Civil Engineering and Geomechanics Series, John Wiley & Sons, Ltd, 2013, p. 343-381.
[194] M. H. C. Tarek, S. Mostafa, J. Imran, I. B. Kahn, "Erosion resistance of cohesive soils", *J. Hydraul. Res.* **46** (2008), no. 6, p. 777-787.
[195] P.-L. Regazzoni, D. Marot, "Investigation of interface erosion rate by Jet Erosion Test and statistical analysis", *Eur. J. Environ. Civil Eng.* **15** (2011), no. 8, p. 1167-1185.
[196] N. Kimiaghalam, S. P. Clark, H. Ahmari, "An experimental study on the effects of physical, mechanical, and electrochemical properties of natural cohesive soils on critical shear stress and erosion rate", *Int. J. Sediment Res.* **31** (2016), no. 1, p. 1-15.
[197] I. Shafii, Z. Medina-Cetina, A. Shidlovskaya, J.-L. Briaud, "Relationship between soil erodibility and soil properties", *J. Geotech. Geoenviron. Eng.* **149** (2023), no. 1, article no. 04022121.
[198] National Academies of Sciences, Engineering, and Medicine, *Relationship Between Erodibility and Properties of Soils*, The National Academies Press, Washington, DC, 2019.
[199] D. Chen, J. Zheng, C. Zhang, D. Guan, Y. Li, Y. Wang, "Critical shear stress for erosion of sand-mud mixtures and pure mud", *Front. Marine Sci.* **8** (2021), article no. 713039.
[200] D. Chen, Y. Wang, B. Melville, H. Huang, W. Zhang, "Unified formula for critical shear stress for erosion of sand, mud, and sand–mud mixtures", *J. Hydraul. Eng.* **144** (2018), no. 8, article no. 04018046.
[201] F. Brunier-Coulin, P. Cuéllar, P. Philippe, "Generalized shields criterion for weakly cohesive granular materials", *Phys. Rev. Fluids* **5** (2020), article no. 034308.
[202] R. Gularte, W. Kelly, V. Nacci, "Erosion of cohesive sediments as a rate process", *Ocean Engng* **7** (1980), no. 4, p. 539-551.
[203] S. Hoomehr, A. I. Akinola, T. Wynn-Thompson, W. Garnand, M. J. Eick, "Water temperature, pH, and road salt impacts on the fluvial erosion of cohesive streambanks", *Water* **10** (2018), no. 3, article no. 302.
[204] A. I. Akinola, T. Wynn-Thompson, C. G. Olgun, S. Mostaghimi, M. J. Eick, "Fluvial erosion rate of cohesive streambanks is directly related to the difference in soil and water temperatures", *J. Environ. Qual.* **48** (2019), no. 6, p. 1741-1748.

[205] V. Ravisangar, K. E. Dennett, T. W. Sturm, A. Amirtharajah, "Effect of sediment pH on resuspension of Kaolinite sediments", *J. Environ. Eng.* **127** (2001), no. 6, p. 531-538.
[206] B. Andreotti, Y. Forterre, O. Pouliquen, *Granular Media: Between Fluid and Solid*, Cambridge University Press, New York, 2013.
[207] A. L. Layzell, R. D. Mandel, "An assessment of the erodibility of Holocene lithounits comprising streambanks in northeastern Kansas, USA", *Geomorphology* **213** (2014), p. 116-127.
[208] R. W. Thoman, S. L. Niezgoda, "Determining erodibility, critical shear stress, and allowable discharge estimates for cohesive channels: case study in the powder river basin of Wyoming", *J. Hydraul. Eng.* **134** (2008), no. 12, p. 1677-1687.
[209] A. Khanal, G. A. Fox, A. T. Al-Madhhachi, "Variability of erodibility parameters from laboratory mini jet erosion tests", *J. Hydrol. Eng.* **21** (2016), no. 10, article no. 04016030.
[210] K. Høeg, R. Dyvik, G. Sandbækken, "Strength of undisturbed versus reconstituted silt and silty sand specimens", *J. Geotech. Geoenviron. Eng.* **126** (2000), no. 7, p. 606-617.
[211] G.-H. Zhang, B.-Y. Liu, G.-B. Liu, X.-W. He, M. A. Nearing, "Detachment of undisturbed soil by shallow flow", *Soil Sci. Soc. Am. J.* **67** (2003), no. 3, p. 713-719.
[212] P.-L. Regazzoni, D. Marot, "A comparative analysis of interface erosion tests", *Nat. Hazards* **67** (2013), no. 2, p. 937-950.
[213] B. Mahalder, J. S. Schwartz, T. M. Wynn-Thompson, A. M. Palomino, J. Zirkle, "Comparison of erodibility parameters for cohesive streambank soils between in situ jet test device and laboratory conduit flume", *J. Hydraul. Eng.* **148** (2022), no. 1, article no. 04021055.
[214] A. H. Vakili, M. Salimi, İ. Keskin, M. Jamalimoghadam, "A systematic review of strategies for identifying and stabilizing dispersive clay soils for sustainable infrastructure", *Soil Tillage Res.* **239** (2024), article no. 106036.
[215] F. Mercier, S. Bonelli, P. Pinettes, F. Golay, F. Anselmet, P. Philippe, "Comparison of computational fluid dynamic simulations with experimental jet erosion tests results", *J. Hydraul. Eng.* **140** (2014), no. 5, article no. 04014006.
[216] F. Mercier, S. Bonelli, F. Golay, F. Anselmet, P. Philippe, R. Borghi, "Numerical modelling of concentrated leak erosion during Hole Erosion Tests", *Acta Geotech.* **10** (2015), no. 3, p. 319-332.
[217] P. Philippe, P. Cuéllar, F. Brunier-Coulin, L.-H. Luu, N. Benahmed, S. Bonelli, J.-Y. Delenne, "Physics of soil erosion at the microscale", *EPJ Web Conf.* **140** (2017), article no. 08014.
[218] D. K. Tran, N. Prime, F. Froiio, C. Callari, E. Vincens, "Numerical modelling of backward front propagation in piping erosion by DEM-LBM coupling", *Eur. J. Environ. Civil Eng.* **21** (2017), no. 7–8, p. 960-987.
[219] Z. Benseghier, P. Cuellar, L.-H. Luu, S. Bonelli, P. Philippe, "A parallel GPU-based computational framework for the micromechanical analysis of geotechnical and erosion problems", *Comput. Geotech.* **120** (2020), article no. 103404.
[220] Z. Benseghier, L.-H. Luu, P. Cuellar, S. Bonelli, P. Philippe, "On the erosion of cohesive granular soils by a submerged jet: a numerical approach", *Granul. Matt.* **25** (2023), no. 1, article no. 8.
[221] J.-L. Briaud, H.-C. Chen, A. V. Govindasamy, R. Storesund, "Levee erosion by overtopping in new Orleans during the Katrina Hurricane", *J. Geotech. Geoenviron. Eng.* **134** (2008), no. 5, p. 618-632.

ACADÉMIE DES SCIENCES
INSTITUT DE FRANCE

Comptes Rendus. Physique
2024, Vol. 25, Special issue S3, p. 333-377
https://doi.org/10.5802/crphys.227

Review article / *Article de synthèse*

Geophysical and astrophysical fluid dynamics in the laboratory / *Dynamique des fluides géophysiques et astrophysiques au laboratoire*

Fluid dynamics of planetary differentiation

La différenciation des planètes telluriques vue par la mécanique des fluides

Renaud Deguen [*, a], Ludovic Huguet [a], Maylis Landeau [b], Victor Lherm [c], Augustin Maller [b] and Jean-Baptiste Wacheul [d]

[a] ISTerre, Université Grenoble Alpes, Université Savoie Mont Blanc, CNRS, IRD, Université Gustave Eiffel, 38000 Grenoble, France

[b] Université Paris Cité, Institut de Physique du Globe de Paris, CNRS, 75005 Paris, France

[c] Université Paris-Saclay, CNRS, FAST, 91405, Orsay, France

[d] Univ Lyon, ENSL, UCBL, UJM, CNRS, LGL-TPE, F-69007 Lyon, France

E-mails: renaud.deguen@univ-grenoble-alpes.fr (R. Deguen), ludovic.huguet@univ-grenoble-alpes.fr (L. Huguet), landeau@ipgp.fr (M. Landeau), victor.lherm@cnrs.fr (V. Lherm), maller@ipgp.fr (A. Maller), jb.wacheul@orange.fr (J.-B. Wacheul)

Abstract. The basic structure of the terrestrial planets—an iron-rich metallic core surrounded by a silicate mantle—was established during their accretion, when widespread melting allowed the metal and silicate phases to separate. The transfer of chemical elements and heat between the metal and silicate that occurred during this period is critical for the composition and initial temperature of the core and mantle, and has important implications for the long-term evolution and dynamics of the planets. After having summarised the main observational constraints on core-mantle differentiation, the article follows the sequence of processes that led to the formation of planetary cores, focusing on the contributions of laboratory fluid dynamics experiments to our understanding of these processes, and discussing the relevance and limitations of this approach to this problem. We first focus on the dynamics of planetary impacts, using laboratory experiments to illustrate and quantify the impact and cratering processes and the resulting metal phase dispersion. We then consider the two-phase flow that follows an impact, when a molten impactor core falls by buoyancy in a magma ocean. The model of miscible turbulent thermal, which we argue is a good reference model for the post-impact flow, is presented. We then discuss how additional factors—immiscibility and fragmentation, inertia inherited from the impact, Coriolis force, sedimentation—affect the predictions of this model, and discuss the extent of chemical equilibration. Finally, a last part of the article is devoted to the migration of the metal phase through a solid part of the mantle.

Résumé. La structure des planètes terrestres — un noyau métallique riche en fer entouré d'un manteau silicaté — a été établie pendant leur accrétion, lorsque la fusion généralisée a permis la séparation des phases métalliques et silicatées. Le transfert d'éléments chimiques et de chaleur entre métal et silicates qui s'est

* Corresponding author

produit pendant cette période est déterminant pour la composition et la température initiale du noyau et du manteau, et a des implications importantes pour l'évolution et la dynamique à long terme des planètes. Après avoir résumé les principales contraintes observationnelles sur la différenciation noyau-manteau, l'article suit la séquence des processus qui ont conduit à la formation des noyaux planétaires, en se concentrant sur les contributions de l'approche de dynamique des fluides expérimentale à notre compréhension de ces processus, et en discutant de la pertinence et des limites de cette approche. Nous nous concentrons d'abord sur la dynamique des impacts planétaires, en utilisant des expériences de laboratoire pour illustrer et quantifier les processus d'impact et de cratérisation, et la dispersion de la phase métallique qui en résulte. Nous examinons ensuite l'écoulement diphasique qui suit un impact, lorsque le noyau d'un impacteur chute dans un océan de magma. Nous introduisons le modèle de thermique turbulent, qui constitue selon nous un bon modèle de référence pour l'écoulement post-impact. Nous discutons ensuite des facteurs additionnels — immiscibilité et fragmentation, inertie héritée de l'impact, force de Coriolis, sédimentation — pouvant affecter les prédictions de ce modèle. Enfin, la dernière partie de l'article est consacrée à la migration de la phase métallique à travers une partie solide du manteau.

Keywords. Early earth, Core formation, Fluid dynamics experiments.

Mots-clés. Terre primitive, formation du noyau, dynamique des fluides expérimentale.

Funding. French Academy of Science, Electricité de France, European Research Council (ERC) (grant number 716429), Labex OSUG@2020 (ANR10 LABX56), Programme National de Planétologie (PNP) of CNRS-INSU co-funded by CNES, Center for Matter at Atomic Pressure (CMAP), National Science Foundation (NSF) Physics Frontier Center under award PHY-2020249.

Manuscript received 7 September 2024, revised and accepted 17 December 2024.

1. Introduction

1.1. *Geological context*

The terrestrial, or "Earth-like", planetary bodies all share the same internal structure: an iron-rich metallic core surrounded by a silicate (rocky) mantle. This is an expected outcome of planetary formation: the metal and silicate phases being immiscible and of different densities, they separated under the action of gravity to form the core and mantle. Efficient gravitational separation requires that at least one of the two phases is molten, a condition likely met during the accretion of the terrestrial planets, about 4.56 Gy ago. Planetary accretion models indeed strongly suggest that the Earth started hot [1]. Following the accretion of dust from the solar nebula into planetesimals with diameters ranging from several tenths of km to a few hundred km [2,3], the next 10 to 100 million years of the Solar System are thought to have been dominated by increasingly energetic collisions between massive planetary bodies several thousand km in diameter [3]. The dissipation into heat of the kinetic energy of these collisions likely resulted in widespread melting, leading to the formation of magma oceans in which the metal and silicate phases separated. A significant fraction of these collisions likely involved bodies that were already differentiated into a core and mantle, as a result of previous impact heating and radioactive heating from short-lived isotopes such as ^{26}Al and ^{60}Fe [4].

Importantly, the metal and silicate gradually added to the Earth were generally not in thermodynamic equilibrium with the silicate mantle of the growing Earth. Indeed, the temperature and composition of the bodies impacting the Earth very likely showed significant variability, and were therefore in general different from Earth's. In addition, the metal-silicate partition coefficients (the ratio of the concentrations of a given chemical element in metal and silicate phases at equilibrium with each other) depend on pressure, temperature, and composition, which makes the conditions of thermodynamic equilibrium time-dependent and spatially variable. This disequilibrium must have driven fluxes of heat and chemical elements between the metal and silicate phases, which set the initial compositions and heat content of the core and mantle. Once

the core has formed and the mantle has crystallised, the flux of chemical elements between the core and the mantle becomes small (it is limited by the slow solid state convective motions of the mantle) and its effect on the average compositions of the core and mantle is insignificant. This implies that the present-day composition of the core and mantle can in principle inform us about the differentiation process [5]. The chemical fractionation between the core and the mantle has been used to constrain the timing of differentiation, with radio-chronometers like the Hafnium–Tungsten (Hf–W) system [6–8], and the physical conditions under which it occurred, by comparing the estimated core/mantle chemical partitioning with the thermodynamic metal-silicate partition coefficients, which depend on the conditions of pressure P, temperature T, and oxygen fugacity fO_2 [5, 9, 10]. This chemical fractionation also has major geodynamical implications. In particular, the nature and abundance in the core of radioactive elements [11–13], magnesium [14, 15], or light elements (e.g. O, S, Si) depend on the pressure P, temperature T, and redox conditions under which metal and silicates equilibrated [16–18]. Like the chemical elements, the heat released during accretion was partitioned between the mantle and the core in a way that depended on the physical mechanisms of phase separation [19, 20]. The distribution of this heat defined the value of the temperature contrast between the mantle and the core at the end of accretion, a key parameter for the dynamics of the planet, and in particular for the existence of a basal magma ocean [21], the existence of an early dynamo [22, 23], and more generally for the thermal and magnetic evolution of the planet.

How long did it take to form the terrestrial planets? How were chemical elements and heat partitioned between the mantle and core? What was the state of the Earth at the end of accretion? Geochemistry provides critical data to address these questions, but their interpretation is not unique and depends on a number of assumptions. In particular, one key parameter is the *efficiency of metal-silicate equilibration*—a measure of how efficiently metal and silicates have been able to exchange chemical elements during core formation—which depends on the details of the physical mechanisms of metal-silicate segregation. This is of particular importance for the interpretation of core formation chronometers. There is an inverse trade-off between the estimated differentiation timescale and the efficiency of equilibration. Figure 1a shows the estimated core formation time according to Hf–W systematics, as a function of the assumed equilibration efficiency $\mathscr{E}_i$, here defined as the total mass of element i exchanged between metal and silicates normalized by their maximum possible value, had all the metal equilibrated with an infinitely larger silicate reservoir. As shown in Figure 1, the accretion time estimated from Hf/W is about 10 My if perfect equilibration is assumed [6–8], but can be much larger if equilibration is imperfect [8, 24, 25]. There is a limit where Hf–W systematics does not constrain the timing of core-formation anymore, but instead give constraints on the efficiency of metal-silicate chemical equilibration, which must be larger than $\simeq$40% [8, 24–26]. This implies a significant flux of chemical elements between metal and silicate during differentiation.

The abundance of siderophile elements (e.g. Ni, Co) in Earth's mantle provides further evidence of metal-silicate chemical equilibration, at rather high temperature and pressure [28]. The concentration of most siderophile elements is much greater in the silicate Earth than expected from their low-temperature and low-pressure partitioning behaviour, a situation known as the *excess siderophile problem* [29]. This can be seen in Figure 1b which compares the apparent core/mantle concentration ratio $D_{c/m}$ of several chemical elements (as estimated from geochemical models of mantle and core compositions) to the corresponding equilibrium partition coefficient D at low pressure (as measured in the laboratory). The estimated core/mantle concentration ratio is lower than expected from low-pressure data for siderophile elements ($D > 1$, e.g. Co and Ni), which means that these elements are more abundant than expected in the mantle. The opposite observation holds for lithophile elements ($D < 1$, e.g. Mn and V). The most plausible explanation for this discrepancy is chemical equilibration of the metal and silicate at

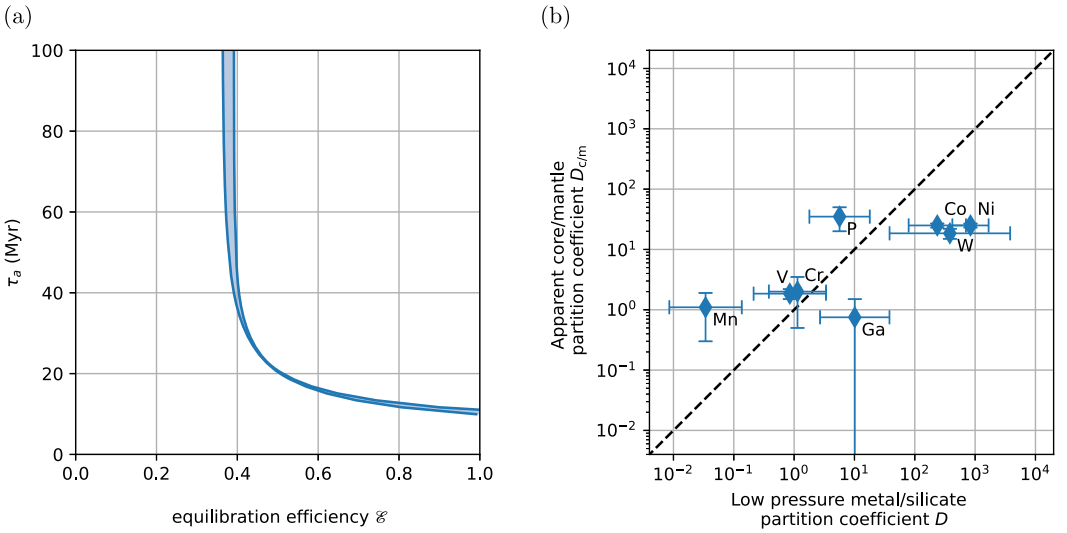


Figure 1. Geochemical constraints on core/mantle differentiation: (a) Accretion time τ_a as a function of the equilibration efficiency, assuming an exponentially decreasing accretion rate (modified from [8]). (b) Estimated core/mantle partitioning vs. low pressure, high temperature partition coefficient for a few low volatility elements, according to core and mantle model composition of [27] and partitioning parameterization of [10] for a range of oxygen fugacity (IW−1.5 to IW−3.5).

conditions of high temperature and high pressure (>2000 K and 30–60 GPa), under which the partitioning of these elements is more consistent with the silicate Earth composition [30–32]. Though the basic implications are clear—significant metal-silicate equilibration at high temperature and pressure—, a more precise interpretation of these data in terms of physical conditions during accretion is difficult. It must often rely on many assumptions, including on the degree of equilibration, starting compositions of primitive bodies, and evolution of the oxidation conditions in Earth's mantle [5, 8, 33–36].

Geochemical (as summarised above) and physical arguments have led to the scenario of planetary cores formation sketched in Figure 2. Radioactive and impact heating led to widespread melting of the growing terrestrial planets, providing favourable conditions for metal-silicate separation [38–40]. The extent of mantle melting is likely to have varied during accretion, possibly in a non-monotonic way, but the tendency was probably towards increasingly deep melting (due to increasingly energetic impacts), possibly down to the core-mantle boundary [41]. The metal delivered by each impact is thought to have fragmented into droplets that eventually settled at the base of the magma ocean [42–44]. The estimated size of these droplets (mm to cm) is small enough to have allowed them to equilibrate efficiently with the surrounding magma ocean [42–44]. These droplets either coalesced with the core if the molten mantle region extended down to the core-mantle boundary, or otherwise accumulated at the bottom of the magma ocean to form an iron pool [38]. In the latter case, a Rayleigh–Taylor instability at the boundary between the iron pool and the underlying mantle would have produced metal diapirs that could have migrated down to the core [39, 43, 45, 46]. Diking (fracturation) or percolation are also possible mechanisms [38]. In this scenario, metal-silicate chemical exchange was likely negligible during the migration through the solid portions of the mantle. Geochemical models of core-formation therefore usually assume that the metal last equilibrated with the silicate at the base of the magma ocean, with its composition set by the equilibrium partitioning coefficient at

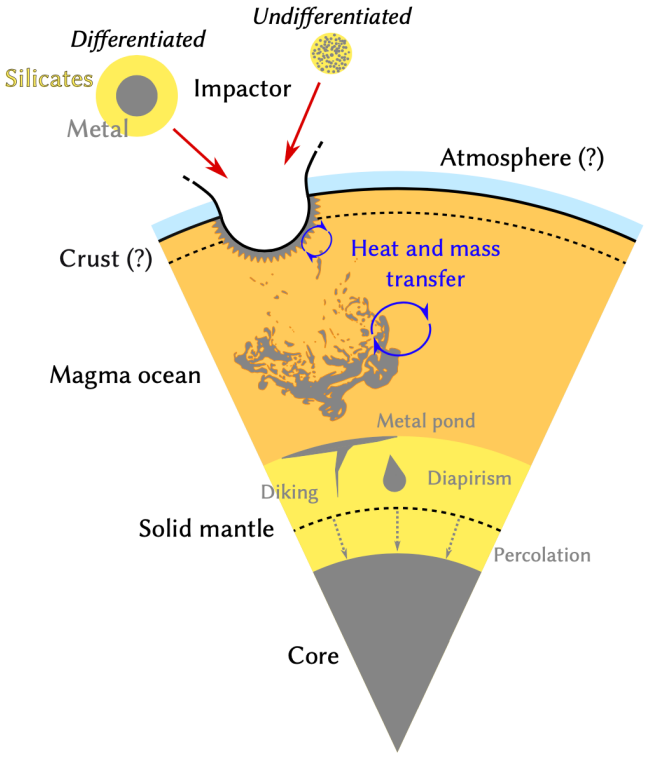


Figure 2. Sketch illustrating the various metal-silicate segregation processes that can occur during the differentiation of terrestrial planets. From [37], adapted from [4].

these conditions [30–32,47]. Each metal addition to the core would therefore have a composition reflecting the conditions of pressure, temperature, and oxygen fugacity at the base of the magma ocean.

Although this scenario is in qualitative agreement with the geochemical data, some of the assumptions are questionable. For example, a significant proportion of the impactors were probably differentiated [48, 49], and it is far from obvious that volumes of molten iron of size ~100 km or more delivered by differentiated impactors could indeed fully fragment into cm-sized droplets. Furthermore, and as discussed above, the interpretation of geochemical data in terms of chronological constraints and physical conditions during Earth formation depends critically on assumptions on the efficiency of chemical transfer between metal and silicate [8, 24–26]. The equilibration efficiency is constrained by Hf–W systematics (Figure 1a), but the range of permissible values allows for a number of different accretion and differentiation scenarios [8]. It is therefore desirable to develop physical models of metal-silicate chemical exchange that could supplement geochemical data and possibly improve the geochemically based constraints, or at least help interpret the geochemical constraints in terms of physical processes. Heat transfer between metal and silicates has received comparatively less attention, but, as explained above, is important for the thermal state and evolution of the planets.

1.2. *A fluid dynamicist's point of view*

From a fluid dynamics point of view, studying the differentiation of terrestrial planets comes down to investigating gravity-induced phase separation, and heat and mass transfer between the

two immiscible phases. In practice, this also requires considering the question of the possible *fragmentation* of the metal phase, as well as *stirring* and *mixing* processes. Phase separation, fragmentation, and mixing are of importance in many industrial and natural contexts, and have received significant interest from various communities [50,51]. However, phase separation in the context of planetary differentiation has some important specificities, as will be shown below, that warrant dedicated studies.

Consider a two-phase flow with characteristic length and velocity scales L and U. The separation of the two phases is induced by the gravity g. The two fluids have different densities and kinematic viscosities, which we denote by ρ_m, ρ_s and ν_m, ν_s, respectively (where the subscripts m and s denote metal and silicates). We denote by $\Delta\rho = \rho_m - \rho_s$ the density contrast. The fluids being immiscible, their boundary has a surface tension σ. The time and length scales at stake can be such that the rotation of the planet may affect the flow; the rotation rate Ω of the planet is therefore a possibly relevant parameter. In addition, most of the planetary collisions that deliver the two phases are supersonic, and the sound velocity c is yet another parameter to consider. Finally, we will be interested in heat or mass exchange between the two phases, and therefore at least one diffusivity κ needs to be included in the set of relevant parameters (κ is either a thermal diffusivity or compositional diffusivity). Overall, this forms a set of 11 parameters with 3 independent units (kg, m, s). Applying the Vaschy–Buckingham theorem, one finds that 8 independent dimensionless numbers can be formed from these parameters, one possible set being

$$Re = \frac{UL}{\nu_s}, \quad We = \frac{\rho_s U^2 L}{\sigma}, \quad Fr = \frac{U^2}{gL}, \quad Ro = \frac{U}{\Omega L}, \quad Pe = \frac{UL}{\kappa}, \quad M = \frac{U}{c}, \quad \frac{\Delta\rho}{\rho_s}, \quad \frac{\nu_m}{\nu_s}. \tag{1}$$

The Reynolds number *Re*, Weber number *We*, Froude number *Fr*, and Rossby number *Ro* compare inertia to viscous forces, surface tension, gravity forces, and Coriolis force, respectively. The Péclet number *Pe* compares the advection of a scalar field (here either heat or concentration) to diffusion. The Mach number M is the ratio of the velocity scale to the sound velocity, and informs us about the possible importance of compression effects. The two last parameters are density and viscosity ratios.

We end up with a eight-dimension parameter space to explore. Only parts of this parameter space are relevant to planetary differentiation, depending on the state (solid or molten) and degree of dispersion of the phases (representative ranges of values for relevant physical properties and parameters are given in Table 1):

(i) Metal-silicate separation in a magma ocean. During the migration of the metal phase in a magma ocean (i.e. when the metal and silicates are both molten), the possibly very large length and velocity scales involved ensure that *Re*, *We*, and *Pe* are all very large. For example, an iron volume 100 km in diameter falling in a magma ocean with an initial velocity of 1 km·s^{-1} has $Re \sim We \sim 10^{14}$ and $Pe \sim 10^{14}$ for heat exchange or $\gtrsim 10^{16}$ for a chemical species. In the impact stage, the Froude number based on impact velocity is ∼1 for large impacts and $\gg 1$ for small-sized impactors (see discussion in Section 2.1). Later, when the metal falls under its own weight, the typical velocity is set by a balance between inertia and buoyancy, and the Froude number is set by the dynamics. The Mach number is in general larger than 1 during the impact (and thus compressibility effects can be important) but then decreases quickly below 1 (see discussion in Section 2.3.1). The Rossby number is large during the impact (and thus rotational effects can be neglected) but can later decrease below 1, depending on the sizes of the impactor and magma ocean (Section 3.4.2).

The huge values of *Re* and *We* imply highly turbulent conditions, with viscosity and surface tension playing a role only at the smallest scales [65, 66]. Post-impact flows must have involved a wide range of length scales, from the size of the impactor to less than ∼mm scale at which

Table 1. Representative values of relevant physical parameters

Impactor radius		R_i	50–3000 km	[2, 3]
Impact velocity		v_i	5–40 km·s^{-1}	[52]
Earth rotation rate		Ω	2–5 present-day rate	
Earth's gravity		g	≤ 10 m·s^{-2}	
Density	Metal	ρ_m	5000–10 000 kg·m^{-3}	[53]
	Silicate	ρ_s	3000–5000 kg·m^{-3}	[54]
Dynamic viscosity	Molten metal	η_m	10^{-3}–10^{-2} Pa·s	[55, 56]
	Molten silicate	η_s	3×10^{-3}–10^{-1} Pa·s	[57, 58]
	Solid silicate	η_s	10^{12}–10^{21} Pa·s	[59, 60]
Thermal conductivity	Metal	k_m	30–100 W·m^{-1}·K^{-1}	[61]
	Silicate	k_s	1–2 W·m^{-1}·K^{-1}	[62]
Compositional diffusivity	Metal	$\kappa_{c,m}$	10^{-12}–10^{-8} m^2·s^{-1}	[44]
	Silicate	$\kappa_{c,s}$	10^{-12}–10^{-8} m^2·s^{-1}	[44, 62]
Interfacial tension	Metal-silicate	σ	0.1–1 J·m^{-2}	[63]
Heat capacity	Metal	$c_{p,m}$	500–1000 J·kg^{-1}·K^{-1}	
	Silicate	$c_{p,s}$	500–1000 J·kg^{-1}·K^{-1}	[64]
Sound velocity	Silicates	c	3–10 km·s^{-1}	[54]

The ranges given here take into account the pressure and temperature ranges that are representative of the Earth's mantle and magma oceans, and also take into account the effect of the composition of the metal and/or silicate phases. The range given for the viscosity of solid silicates accounts for the effect of temperature, melt fraction, and grain size.

surface tension and viscosity eventually come into play. Numerical simulations of planetary-scale impacts [67–70] can include relevant effects such as compressibility, phase change, self-gravity, and spherical geometry, that cannot be investigated with fluid dynamics experiments. However, they have spatial resolutions (~14 km in [71]) which are usually too rough to model the small turbulent scales at which chemical equilibration can occur (though useful information can be extracted, for example by calculating the Lagrangian stretching of advected structures [72]). Direct numerical simulations of the fragmentation of the metal phase in a magma ocean [73, 74] have been limited so far to laminar conditions. In contrast, fluid dynamics laboratory experiments can more easily reach turbulent conditions, and provide insight on the effect of turbulence on fragmentation and mass and heat transfer between the two phases.

(ii) Metal-silicate separation in a solid mantle. When the silicate phase is solid, the migration of the metal phase can occur either through diapirism, percolation, or diking. Diking, whose importance is not well understood in the context of core formation, will be discussed in mostly qualitative terms in Section 4.1.2. We will focus our discussion on the diapirism and percolation scenarios. In these cases the Reynolds number *Re* is small, either because the flow intensity is controlled by the deformation of the very viscous silicate phase (diapirism), or because of the small scale of the flow (percolation). Since the typical velocity is set by a balance between buoyancy and viscous forces, buoyancy forces also dominates over inertia ($Fr \ll 1$). Because of the negligible importance of inertia, the importance of surface tension and Coriolis force is better measured by comparing them to either buoyancy or viscous forces rather than inertia. Instead of *We* and *Ro*, it is therefore more relevant to use the Bond number *Bo* and the Ekman number *Ek*

defined as

$$Bo = \frac{\Delta\rho g L^2}{\sigma} = \frac{\Delta\rho}{\rho_s}\frac{We}{Fr}, \quad Ek = \frac{\nu_s}{\Omega L^2} = \frac{Ro}{Re}. \tag{2}$$

The Bond number is large in the case of metal diapirs, but possibly as small as ~1 in the case of percolation. The Coriolis force is negligible compared to the viscous forces ($Ek \gg 1$) in all of these cases. Typical velocities are much smaller than the speed of sound ($M \ll 1$) and thus dynamic compressibility effects (shock waves) are unimportant. However compression heating can be of importance for the thermal evolution of the metal phase, due to the large pressure variations experienced by the metal as it travels through the mantle (Section 4.1.1). The Péclet number *Pe* is large in the case of diapirism because of the large length scale involved (Section 4.1.1), indicating that transport of heat toward the core is faster than diffusion toward the surrounding mantle. In contrast diffusion is more important in percolation flow, due to the smallest scale of the flow (i.e. grain size of the silicate matrix).

1.3. *A note on metal-silicate chemical equilibration efficiency*

A particular focus of the experiments that will be discussed is the question of chemical equilibration between the metal and silicate phases. As discussed in Section 1.1, this is of primary importance for the interpretation of geochemical data in terms of core formation timing and conditions. The equilibration efficiency $\mathscr{E}_i$ can be defined as the total mass of a given element i exchanged between metal and silicates, normalized by its maximum possible value, had all the metal re-equilibrated with an infinitely larger silicate reservoir [75]. Assuming that the mass of metal fully equilibrates with a mass of silicate Δ times larger, one finds that

$$\mathscr{E}_i = \frac{1}{1 + D_i/\Delta}, \tag{3}$$

where D_i is the metal/silicate partitioning coefficient of element i. Equation (3) highlights the importance of the parameter Δ, which has been termed *metal dilution*. This is a convenient parameter for geochemical models because it appears quite naturally in the conservation equations on which geochemical models of core formation are based, but it is not straightforward to estimate in an experiment. Rather, what has typically been measured is the volume of "silicate" liquid in which the "metal" is dispersed [75–78]. In the following sections we will refer to this type of measurement as *metal dispersion*. Equating the volume of equilibrated silicates to the volume in which the metal is dispersed gives an upper bound on the mass transfer between metal and silicates, and therefore an upper bound on the equilibration efficiency $\mathscr{E}_i$. A better estimate of the mass transfer would require quantifying the variations of composition in both phases, possibly through their Probability Density Functions (Sections 3.2.3 and 3.5).

1.4. *Content*

The structure of the article follows the sequence of processes that led to the formation of planetary cores. Section 2 is devoted to the dynamics of planetary impacts. We present the governing dimensionless numbers and discuss the relevance and limitations of fluid dynamics laboratory experiments to the understanding of planetary impacts. Laboratory experiments are used to illustrate and quantify the impact and cratering processes and the resulting metal phase dispersion. Section 3 focuses on the two-phase flow that follows an impact, when a molten impactor core falls by buoyancy in a magma ocean. We start by presenting the model of miscible turbulent thermal, which we argue to be a good reference model for the post-impact flow. We then discuss how additional factors—immiscibility and fragmentation, inertia inherited from

the impact, Coriolis force, sedimentation—affect the predictions of this model, and discuss the extent of chemical equilibration. Finally, Section 4 is devoted to the migration of the metal phase through a solid part of the mantle, focusing on diapirism and percolation. Given the topic of this special issue on *Geophysical and Astrophysical Fluid Dynamics in the lab*, the paper is biased toward the experimental fluid dynamics contributions to the understanding of planetary differentiation. Results from numerical simulations and experimental petrology will be mentioned, but the review is by no means intended to be comprehensive on these approaches.

2. Planetary impacts

2.1. *Rationale*

Planetary impacts have been classified as being either in the so-called *strength regime* or *gravity regime*, depending on the importance of the resistance to deformation of the target material [79]. This can be evaluated by comparing the level of impact-induced stresses to either the yield stress for a solid target, or viscous stresses in the case of an impact onto a magma ocean. On Earth, impact-induced stresses exceed the yield stress for impactors that are larger than a few tens of meters [79, 80]. Given the expected range of sizes of planetesimals ($\gtrsim$100 km in diameter) and embryos ($\gtrsim$1000 km in diameter), most of the impacts that formed the Earth were thus likely in the gravity regime in which the level of induced stresses is significantly larger than the yield stress [79, 80]. In the case of an impactor striking a pre-existing magma ocean, the impact-induced stress is much larger than viscous stress i.e. $Re \gg 1$. The resistance to deformation is thus usually of negligible importance in this context. During an impact, *We*, *Pe*, and *Ro* are all much larger than unity. The Mach number M based on the impact velocity is usually larger than 1, and possibly up to ~10.

In this limit, the dominant forces are inertia, pressure forces, and gravity, and the non-dimensional numbers of most relevance are Fr, M, and the density ratio, with Fr and M defined in Equation (1) using the impactor radius and impact velocity. An additional parameter of importance is the impact angle, i.e. the angle between the impact velocity vector and the horizontal.

It will be useful to also introduce a modified Froude number defined as

$$Fr^* = \frac{\rho_i}{\rho_t}\frac{U_i^2}{g R_i}, \tag{4}$$

where R_i is the diameter of the impactor, U_i its velocity at impact, and ρ_i and ρ_t are the densities of the impactor and target material, which may be mixtures of metal and silicate (which is why we do not use the notations ρ_m and ρ_s in this section). With this definition, Fr^* is the ratio of the kinetic energy of the impacting body ($\sim\rho_i U_i^2 R_i^3$) to the gravitational potential energy ($\sim\rho_t g R_i^4$) released by displacing a volume $\sim R_i^3$ of target material over a height $\sim R_i$. Assuming that the impact velocity scales as the escape velocity, $U_i \simeq \sqrt{g D_p}$, where D_p is the diameter of the growing planet and g the acceleration of gravity at its surface, we find that

$$Fr^* \simeq \frac{\rho_i}{\rho_t}\frac{D_p}{R_i}. \tag{5}$$

Since ρ_i/ρ_t varies within a limited range, the Froude number Fr^* depends primarily on the impactor-to-target size ratio. Fr^* ranges from ~1 in the case of a giant impact to several hundreds in the case of ~100 km-diameter planetesimals impacting the Earth. Recent meteorite impacts have much larger Froude numbers. As an example, Meteor Crater (Arizona) is thought to have been formed by the impact of an iron mass about 50 m in diameter with a velocity of more than 10 km·s^{-1}, which gives a Froude number $\sim 2\times 10^5$.

The full range of Fr^* values relevant to the formation of terrestrial planets can be explored with impact experiments involving millimetre- to centimetre-sized drops released from different heights above a bath of a less dense liquid. This approach differs from experiments involving supersonic impacts of solid projectiles onto a solid target, more typically carried out in a planetological context [81, 82]. Both approaches have their advantages and limitations: the possibility of reaching supersonic impact speeds comes at the expense of the value of Fr^*, which is typically on the order of 10^9 in this type of experiments, i.e. seven orders of magnitude larger than during the impact of a 100 km-diameter body; in contrast, fluid dynamics laboratory experiments as discussed below allow to explore the relevant range of Froude number, but ignore any possible effects of compressibility.

To be relevant to the context of planetary impacts, experiments need to be done at high *Re* (to be in the "gravity" regime) and high *We* (if involving two immiscible liquids). In an experiment in which the impactor is produced by letting a volume of liquid fall under its own weight toward the target, the impact velocity U_i is controlled by the drop height. It can be varied between near zero and the terminal velocity $U_i^t \sim \sqrt{(\rho_i - \rho_{\text{air}})/\rho_{\text{air}} g R_i} \sim \mathscr{B}^{1/2}/R_i$ of a drop falling into air, where ρ_{air} is the density of air and $\mathscr{B} = (\rho_i - \rho_{\text{air}})/\rho_{\text{air}} g (4\pi/3) R_i^3$ is the buoyancy of the drop. The Reynolds, Weber, and Froude numbers based on the impactor radius R_i and velocity U_i can then be written and bounded as follows

$$Re = \frac{\mathscr{B}^{1/2}}{\nu} \frac{U_i}{U_i^t} \lesssim \frac{\mathscr{B}^{1/2}}{\nu}, \tag{6}$$

$$We = \frac{\rho_i - \rho_{\text{air}}}{\rho_{\text{air}}} Bo \left(\frac{U_i}{U_i^t} \right)^2 \lesssim \frac{\rho_i - \rho_{\text{air}}}{\rho_{\text{air}}} Bo, \tag{7}$$

$$Fr = \frac{\rho_i - \rho_{\text{air}}}{\rho_{\text{air}}} \left(\frac{U_i}{U_i^t} \right)^2 \lesssim \frac{\rho_i - \rho_{\text{air}}}{\rho_{\text{air}}}, \tag{8}$$

where the Bond number is defined as

$$Bo = \frac{\rho_i g R_i^2}{\sigma} \tag{9}$$

(where here σ is the interfacial tension between the two immiscible liquids, not between the drop and air). From this, it is found that Reynolds number values $\gtrsim 10^4$ and Weber number values $\gtrsim 10^3$ can easily be reached with drops of a few mm in diameters, at relatively large values of *Fr* [77, 83, 84]. However, reaching high values of *Re* and *We* at moderate values of *Fr* requires larger impactors. We can indeed notice that $We = BoFr$, which implies that reaching a high value of *We* while maintaining a moderate value of *Fr* requires a high value of *Bo*, and therefore a larger impactor, typically of a few cm in diameter at least. Drops with a diameter up to ~5 mm can be easily formed by dripping liquid from the tip of a syringe or capillar [77, 84, 85]. At this size, the drop is kept coherent by surface tension as it falls (though its shape starts to deviate from spherical, and can oscillate). Laboratory experiments with drops produced this way reach Froude numbers in the range [10^2–10^3] [77, 84]. Producing liquid impactors of a few centimeters with moderate deformation is more complicated, but necessary to explore smaller values of *Fr* while still keeping $Re, We \gg 1$ [76, 86]. One method consists in enclosing the impactor liquid in a balloon which is pierced just before impact [76, 86–88].

2.2. *Phenomenology and scaling laws*

The impact of a drop on a deep pool has been studied extensively [83, 84, 89–97] since the pioneering work of Worthington at the turn of the 19th and 20th centuries [89–91]. Although the analogy with planetary impacts and its limitations were not fully formalised, the idea of using

drop impacts as models for meteorite impacts was already explicit in Engel's 1966 paper [83]. Most studies focused on the impact of a drop on a pool of the same liquid. The effect of a difference of density between the drop and pool [76, 77, 98] and of immiscibility [85, 86, 99, 100] have been the subject of fewer studies, and not always in regimes relevant to planetary differentiation. Experiments on oblique impacts are scarce as well [101].

The main results from these studies will be discussed in the following subsections, and illustrated with the experiments shown in Figure 3. Figure 3a shows successive snapshots from an experiment in which a drop of Caesium Chloride ($\rho_i = 1789$ kg·m^{-3}) strikes a pool of water [77]. The drop has a radius $R_i = 2.36$ mm and its velocity at impact is $U_i = 3.54$ m·s^{-1}, which results in $Fr = 540$ and $\rho_i/\rho_t = 1.789$. Figure 3b shows snapshots from an experiment in which a volume of Perfluorodecalin ($\rho_i = 1940$ kg·m^{-3}) strikes a pool of water [86], with $R_i = 2$ cm and $U_i = 4.3$ m·s^{-1}, which results in $Fr = 94$, $\rho_i/\rho_t = 1.94$. Perfluorodecalin and water are immiscible and have an interfacial tension $\sigma = 50$ mJ·m^{-2}, giving $We = 1.4 \times 10^4$. Figures 3c and 3d are composite images from the experiment shown in Figure 3a (left part of the images) and similar experiments in which velocity field (PIV) and concentration (PLIF) measurements have been done [84]. Figure 3e shows a close-up of image iv of Figure 3b.

We will discuss the three main stages of the impact and cratering process that can be identified from these experiments at large *Re* and *We*: (i) the opening and growth of the crater (Section 2.2.1), with a particular focus on instabilities and fragmentation that are observed during this stage; (ii) the collapse of the crater and formation of a central peak (Section 2.2.2); and (iii) the collapse of the central peak (Section 2.2.3).

2.2.1. *The opening phase: Rayleigh–Taylor instability and fragmentation*

When it strikes the surface of the pool, the drop is abruptly decelerated, and flattens onto the surface of the pool. Part of the momentum of the drop is imparted to the pool, which induces an outward flow that opens a cavity—the crater (Figures 3ai and 3bi). The crater then expands and quickly becomes near spherical, until reaching a maximum in size. The liquid ejected from the crater forms a crown (images i and ii of Figures 3a and 3b) which expands concomitantly with the crater.

Evolution of crater size. The evolution of the crater mean radius $R_c(t)$ has been modelled by considering the energy balance of the system [77, 83, 92, 94]. Neglecting viscous dissipation (the flow around the crater is close to potential [84]), one can assume that the sum of kinetic energy of the flow, potential energy, and surface tension energy is constant. This can be written as

$$\xi \pi \rho_t R_c^3 \dot{R}_c^2 + \pi \sigma R_c^2 + \frac{\pi}{4} \rho_t g R_c^4 = \phi \frac{2\pi}{3} \rho_i R_i^3 U_i^2. \tag{10}$$

The first term on the LHS is the kinetic energy of the flow around the crater, with ξ a correction parameter accounting for the unknown spatial variations of the flow. $\xi = 1$ if the flow is radially outward and incompressible [77, 94]. PIV velocity measurements [84] have shown that this is actually a poor approximation (as shown in Figure 3c): the effective value is smaller than 1 and time-dependent. The second and third terms account for changes of surface energy and potential energy associated with the opening of the crater (here neglecting for simplicity the contributions of the crown). The term on the RHS is the kinetic energy of the impact, corrected by a factor ϕ which accounts for possible energy loss. Fitting the solution of (10) to experimental data requires $\xi \simeq 0.34$ and $\phi \simeq 0.4$ [77]. Surface tension does not affect much the shape of the crater during the opening phase if *We* is large enough ($We \gtrsim 54 Fr^{0.25}$ according to [94]), and its only effect is to slow down the opening.

Despite its simplicity, the energy approach gives the correct scaling relationships for the maximum size of the crater and the time at which this maximum is reached. The maximum crater

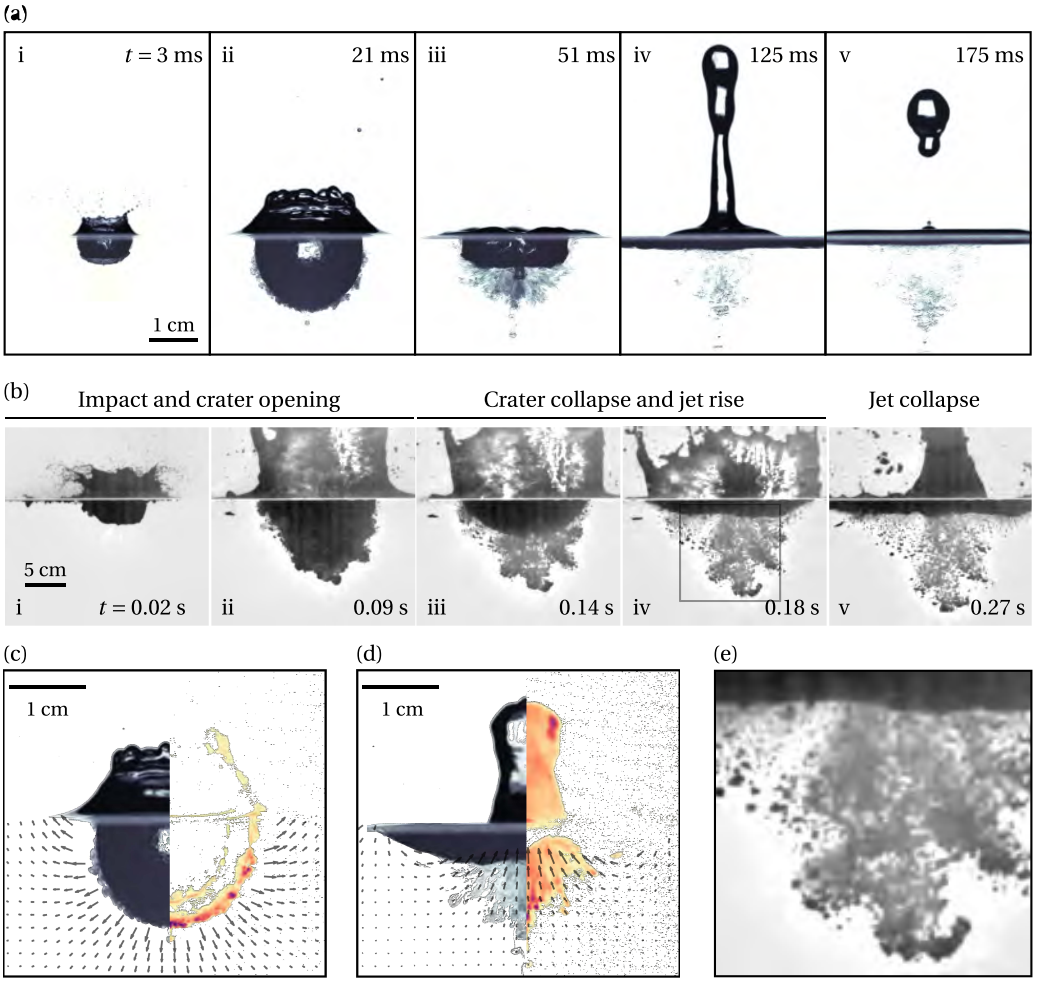


Figure 3. (a) Time sequence from a liquid impact experiment at $Fr = 540$ and $Re = 8.3 \times 10^3$ with miscible drop and target liquids (using a CsCl aqueous solution with $\rho_i = 1789$ kg·m^{-3} for the drop, water as the target liquid, $R_i = 2.36$ mm, and $U_i = 3.54$ m·s^{-1}). The CsCl solution appears blue on the pictures. (b) Time sequence from a liquid impact experiment at $Fr = 94$, $We = 1.4 \times 10^4$, and $Re = 8.6 \times 10^4$ with immiscible drop and target liquids (using Perfluorodecalin with $\rho_i = 1940$ kg·m^{-3} for the drop, water as the target liquid, $R_i = 2$ cm, and $U_i = 4.3$ m·s^{-1}) [86]. (c) and (d) Composite images with pictures from the experiments shown on subfigure (a) on the left, concentration fields obtained using Planar Laser Induced Fluorescence on the right, and the velocity field obtained from Particle Image Velocinetry shown with black arrows. The concentration measurements have been performed in an experiment with parameter values similar but slightly different from (a) ($Fr = 572$, $\rho_i/\rho_t = 1.754$); the velocity measurements have been performed in an experiment involving a water drop (to avoid strong variations in optical index) and has $\rho_i/\rho_t = 1$ and $Fr = 446$. (e) Close-up on image (b)iv.

size can easily be obtained by setting $\dot{R}_c = 0$ in Equation (10). Neglecting the surface tension term for simplicity, this yields,

$$R_{c,\max} = R_i \left(\frac{8}{3}\phi\right)^{1/4} Fr^{*1/4}, \tag{11}$$

which is in good agreement with drop impact experiments [77]. Importantly, this scaling law is also in good agreement with numerical simulations of planetary impacts until relatively large values of the Mach number (see Section 2.3.1).

The time $\tau_{\max}$ at which the crater reaches its maximum size can be predicted by integrating in time equation (10). This predicts

$$\tau_{\max} \sim \frac{R_i}{U_i}\left(\frac{\rho_i}{\rho_t}\right)^{-1/2} Fr^{*5/8}, \tag{12}$$

which again is consistent with experimental observations (see [77] for an analytical expression and extension to include the effect of surface tension). For a planetary impact with $R_i = 100$ km and $U_i = 10$ km·s^{-1}, Equation (12) predicts a crater opening time of ~3 min.

Instabilities. Inspection of Figures 3a,b,c shows that the liquid carried by the impactor forms a layer around the opening crater, on which small-scale corrugations and plumes quickly develop (see snapshots i and ii of Figures 3a and b, and 3a). In addition, measurements of the thickness of the layer show that it increases with time, while conservation of mass predicts a decrease of thickness in the absence of incorporation of ambient liquid, as a result of the spreading of the liquid around the growing crater [77].

This is interpreted as being the result of a Rayleigh–Taylor instability triggered by the deceleration of the crater boundary [76, 77, 98]. In the opening phase, the crater radius R_c is an increasing function of time and $\dot{R}_c = \mathrm{d}R_c/\mathrm{d}t$ is a positive but decreasing function of time (it is equal to 0 when the crater reaches its maximum size). The acceleration of the crater boundary $\ddot{R}_c = \mathrm{d}^2R_c/\mathrm{d}t^2$ is therefore negative: the boundary decelerates. In a reference frame moving with the boundary, this is equivalent to an outward apparent gravity of magnitude $-\ddot{R}_c$. If the impactor is denser than the ambient, the situation is analogous to having a dense layer above a less dense liquid, a situation which is known to be unstable against the Rayleigh–Taylor instability. In practice, $\ddot{R}_c$ can be significantly larger than the acceleration of gravity g. For a significant fraction of the crater opening phase, the kinetic energy of the flow surrounding the crater dominates over the contributions of the potential and surface energies. Neglecting these two terms in Equation (10), taking the derivative with respect to time and re-arranging gives $\ddot{R}_c/g \sim Fr^*(R_i/R_c)^4$. When $Fr^* \gg 1$, the magnitude of the deceleration is therefore initially much larger than g. $\ddot{R}_c$ becomes $\sim g$ when the crater approaches its maximum size.

The total increase of volume of the mixing layer depends on the magnitude of $\Delta\rho/\rho_t|\ddot{R}|$, but depends also on the time interval in which the mixing layer can grow, which is close to the opening time $\tau_{\max}$. Lherm et al. [77] found that the volume of the mixing layer, normalized by the impactor's volume, is $\simeq 0.07(\rho_i/\rho_t)^{2.8} Fr^{0.67}$.

Fragmentation. Maller et al. [86] recently investigated the impact of a large, centimetre-sized, spherical liquid volume onto a pool of a lighter immiscible liquid. When the impact speed is large enough, they observed that the impacting liquid fragments into millimetric drops (last two images in Figure 3b, and Figure 3e). Varying systematically the impactor size and speed, the authors quantified the degree of fragmentation of the impacting liquid by measuring the number of fragments prior to the collapse of the central peak. They found that the entire impacting volume fragments into drops when the Froude number *Fr* exceeds 40, regardless of the value of the Weber number *We*, and hence the strength of surface tension. This result is unexpected as surface tension, through the Weber number, often controls the fragmentation of a liquid.

To explain this observation, the authors assumed that, during the opening of the crater, the Rayleigh–Taylor instabilities described above stretch the impacting liquid into ligaments, which then break into drops by capillary instabilities. The timescale of capillary instabilities is much smaller than the cratering time in these experiments. This means that, as soon as a ligament forms, surface tension breaks it into drops almost instantaneously. The breakup of ligaments is therefore not the limiting process here.

In contrast, the timescale of nonlinear Rayleigh–Taylor instabilities is on the same order of magnitude as the cratering time. This suggests that fragmentation is possible only when Rayleigh–Taylor instabilities have time to grow and stretch the impacting liquid into ligaments. Because $We > 300$ in these experiments, Rayleigh–Taylor instabilities and impact cratering do not depend on surface tension, which explains why the degree of fragmentation is independent of We.

During the formation of planets, most impactors are differentiated into a metallic core and a silicate mantle. Maller et al. [86] also conducted experiments with two-phase impactors using a balloon enclosed into another. They found that the impact Froude number still controls the fragmentation, which again occurs when $Fr > 40$.

Applied to planetary impacts, the above results predict that the larger the impact speed, the larger the Froude number Fr, and hence the more fragmented the impactor core. As discussed in Section 2.1, the Froude number of a planetary impact scales as the ratio of the planet to impactor diameters (Equation (5)). This leads to the following result: the larger the impactor size, the smaller the Froude number, and hence the degree of fragmentation. For impacts onto Earth at the escape speed, Maller et al. [86] predict that the cores of impactors with a radius $R_i < 300$ km fully fragment into drops during the impact process, while the cores of giant impactors with $R_i > 1600$ km remain unbroken. For impact velocities higher than 1.5 times the escape speed, a significant fraction of the impactor core fragments for any impactor size.

2.2.2. *Crater closing and formation of a central peak*

The crater reaches its maximum radius when all the kinetic energy of the impact has been consumed by the change in gravitational potential energy associated with the opening of the crater. This potential energy is then converted back into kinetic energy when the crater closes. Qualitative [83] and quantitative [84] velocity measurements show that the flow is convergent toward the axis of symmetry of the crater (Figure 3d). This convergence leads to the formation of an upward-growing central peak, or jet (Figures 3aiv and 3biv and v), which is made of a mixture of drop and pool liquids [77]. In millimetre drop impact experiments (Figures 3aiv and v), the central peak is often observed to fragment due to the development of a capillary instability [89], a mechanism that is irrelevant in the case of a planetary impact. The central peak always remains coherent (no fragmentation) in experiments with multi-centimetre drops [76,86]. The flow associated with the closure of the crater and the formation of the central peak strongly stretches the mixing zone formed by the Rayleigh–Taylor instability [76].

2.2.3. *Collapse of the central peak and further mixing*

The central peak reaches a maximum height before collapsing, thus re-injecting into the pool the drop/pool liquid mixture it carries. At moderate values of Fr^*, this mixture forms a well-defined compact cloud with little residual velocity [76], as can be seen for example on image v of Figure 3a. The dispersion of the drop liquid at this stage has been quantified experimentally by estimating the volume over which the drop liquid is spread [76]. This volume has been found to scale as $\sim R_i^3((\rho_i - \rho_t)/\rho_t)^{-0.57} Fr^{1.2}$ [76]: it is an increasing function of Fr but, perhaps surprisingly, a decreasing function of the buoyancy ratio $(\rho_i - \rho_t)/\rho_t$. These experiments have

been performed with density ratios ρ_i/ρ_t larger than but close to 1; it remains to be checked that the above scaling law still applies at density ratios approaching the metal-silicate value of ≃2.

2.3. *Limitations and future work*

2.3.1. *On the effect of compressibility*

An obvious limitation of fluid mechanics experiments applied to planetary differentiation is their low Mach numbers M, and therefore absence of compressibility effects. This seems unavoidable; the effect of compressibility needs to be investigated with numerical models.

One well-identified effect of compressibility is the formation, when $M > 1$, of a shock wave which propagates away from the impact, followed and eventually caught up by a rarefaction wave (or pressure relief wave). The compression/decompression cycle associated with the shock and rarefaction waves is an irreversible process that results in melting, and possibly vaporisation, of the shocked material [79]. The impact crater opens in the decompressed, molten region behind the rarefaction wave (see for example Figure 4 from [102] showing snapshots from a numerical model of an impact at $M = 5$, or Figure 2 from [72]). This, in fact, justifies to some extent the use of liquids in laboratory experiments to model planetary impacts on solid targets [102]. However, compressibility does affect the maximum size of the crater, as shown by the systematic investigation of the effect of Fr and M on the maximum crater depth [102]. The effect of the Mach number on the maximum crater depth is moderate up to $M \sim 4$ (less than ~20%), but becomes more significant for $M \gtrsim 4$, a limit that is also relevant to planetary formation [102]. At large M, the maximum crater depth becomes independent of the impact velocity and depends on a Froude number defined from the speed of sound rather than the impact velocity [102], with the maximum crater depth scaling as $\sim R_i(FrM^{-2})^{1/4} = R_i(c^2/gR_i)^{1/4}$.

Compressibility can also affect the smaller scales of the flow around the crater, and therefore the dispersion and fragmentation of the metal. It is indeed know that compressibility can affect the coherence of large scale turbulent eddies in turbulent flows, which can be understood as follows. In a fluid, the pressure field adjusts to time variations of the flow through pressure waves (i.e. sound waves). At low Mach number, pressure waves travel much faster than the flow and the pressure field adjusts almost instantaneously, thus allowing long-range interactions between different parts of the flow. When the sound velocity is on the same order of magnitude or larger than the flow velocity, the finite speed of sound introduces a time delay in the transmission of pressure signals from one point to another, which can disrupt the coherence of large turbulent eddies [103–105]. This has been observed experimentally to have a significant effect on dispersion and mixing in jets and mixing layers when $M \gtrsim 1$ [104, 106].

However, there are reasons to believe that the effect of compressibility may not be as important as the value of the Mach number at impact would suggest, because the velocity of the flow after the impact is smaller than the impact velocity. The maximum velocity is abruptly decreased when the impactor comes into contact with the target because part of the momentum is transmitted to the target material. This results in a decrease of the maximum velocity, and therefore of the instantaneous Mach number, by roughly a factor of 2 [79]. In addition, the velocity is further decreased during crater opening because: (i) the flow around the crater occupies a volume significantly larger than the volume of the impactor, which means that the kinetic energy is distributed over an increasingly large volume; (ii) the total kinetic energy decreases in proportion to the increase of the potential energy associated with the excavation of the crater, as suggested by the energy balance (Equation (10)). This reasoning suggests that the effect of compressibility may be limited to a short interval of time after contact between the impactor and the target. This is supported by the analysis of snapshots from numerical simulations of planetary impacts,

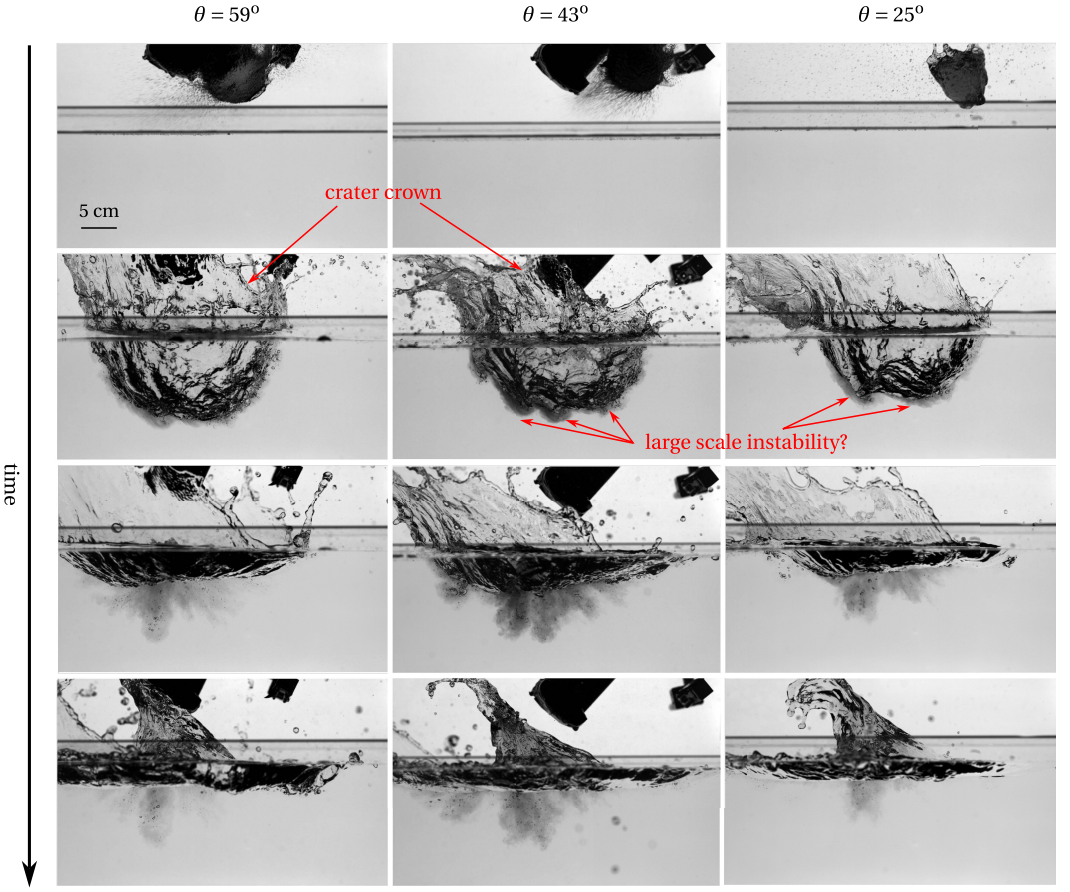


Figure 4. Time sequences from three oblique impact experiments with impact angles θ (with respect to the horizontal) equal to 59° (left column), 43° (middle column), and 25° (right column). In all three experiments, the impactor is made of 290 mL of dyed water (R_i = 4.1 cm) and is released from a height 70 cm above the surface of the tank, which is filled with fresh water. The impacting liquid is initially enclosed in a balloon which is allowed to slide with respect to a tilted guiding rail, giving it an oblique trajectory. The balloon falls under its own weight and is ruptured by a scalpel blade just before impact (first images of the time sequences). On these images, the two dark horizontal lines correspond to the contact lines of the free surface with the container. Two lines rather than one appear because the free surface is seen slightly from above.

which shows that the flow around the crater is subsonic for a significant part of the crater opening phase [72, 102].

2.3.2. *Oblique impacts*

The experiments discussed in Section 2.2 focused on vertical impacts. This is an important limitation: planetary impacts are more likely to be oblique, with the most probable impact angle being 45° [107]. This is known from numerical simulations and hyper-velocity or drop impact experiments to strongly affect the shape of the crater and the dispersion of the impactor [72, 101, 107–111].

Figure 4 shows snapshots from yet unpublished experiments [112] in which a volume of dyed water with radius $R_i = 4.1$ cm strikes a water bath with an impact angle of either 59°, 43°, or 25°. In contrast with vertical impacts, the crater, crown, and central peak are asymmetric, which is consistent with numerical models [72, 107] and fluid dynamics experiments using mm-sized drops [101, 110, 111]. The snapshots shown on the second line of Figure 4 show that a large-scale instability develops at the boundary between the impactor and pool liquid, in particular at the lowest impact angles of 43° and 25°. The shape of the observed structures is reminiscent of Kelvin–Helmoltz billows, which suggests that they originate from the shear associated with the anisotropic growth of the crater. Qualitatively, this instability appears to increase the amount of dispersion of the impactor material, but this remains to be quantified in detail. The effect of the impact angle on the dispersion and mixing of the impactor material remains to be quantified and modelled.

3. Metal-silicate separation in a magma ocean

3.1. *Rationale*

The experiments discussed in Section 2 show that the impact leaves the impactor material as a coherent mass without much momentum, distributed over a volume V_0 larger than the impactor's. This volume V_0 is a mixture of the impactor and target mantle material, which may or may not be fragmented. It is negatively buoyant and therefore falls under its own weight. Given its expected size (say a radius R_0 equal to 10 to 1000 km) and the low viscosity of the magma ocean ($\sim 10^{-2}$ Pa·s), its velocity initially scales as $\sqrt{(\Delta\rho_0/\rho_s)gR_0}$, where $\Delta\rho_0$ is the effective density difference between the impactor/magma mixture and surrounding magma. Using this scaling to estimate *Re* and *We* gives

$$Re \sim \frac{\mathscr{B}_0^{1/2}}{\nu_s}, \tag{13}$$

$$We \sim \frac{\Delta\rho_0 g R_0^2}{\sigma} = Bo, \tag{14}$$

where $\mathscr{B}_0 = (\Delta\rho_0/\rho_s)gV_0$ is the total buoyancy of the metal volume. For falling impactors, very large values are expected for these two dimensionless numbers. For example, taking $R_0 = 10$ km (a relatively small impact) and $\Delta\rho_0 = 1000$ kg.m^3 (which corresponds to a significant dispersion upon impact) gives $Re \sim We \sim 10^{12}$ (taking $\sigma \sim 1$ J·m^2 for the metal-silicate surface tension, $g = 10$ m·s^{-2}, $\rho_s = 4000$ kg·m^{-3}, $\nu_s = 10^{-6}$ m^2·s^{-1}). The large value of *We* suggests that surface tension is unimportant for large-scale dynamics. As a first step, the effect of surface tension can be ignored (i.e. taking the limit $We \to \infty$), which can be done experimentally by using *miscible* liquids instead of immiscible liquids. At large Reynolds numbers, a buoyant mass of fluid forms what is known as a *turbulent thermal*. This is discussed in Section 3.2, and provides a useful reference on which additional physical effects can be added incrementally. The effects of immiscibility, rotation, and impact-induced dispersion, which are all relevant to planetary formation, are discussed in the following subsections. We will also discuss experimental measurement of the evolution of the concentration field within a miscible thermal.

3.2. *The infinite We limit: miscible turbulent thermals*

Figure 5a shows snapshots from an experiment in which a negatively buoyant volume of an aqueous solution of sodium iodide (NaI) is released into fresh water. The volume of dyed liquid increases as it falls, which indicates that it entrains and incorporates ambient liquid, resulting

in its gradual dilution. Measurements on many similar experiments and numerical simulations have shown that the mean radius of the negatively buoyant mixture increases linearly with the distance from the point of release [113–118]. PIV measurements on similar experiments and numerical simulations show that the velocity field has a vortex ring structure, with most of the entrainment of ambient liquid occurring from the rear of the cloud [37, 118]. This is what is known as a *turbulent thermal* in the fluid mechanics and atmospheric science communities [113, 115–117], a name inherited from the usage of glider pilots, for whom a thermal is an isolated mass of warm air rising through the lower atmosphere. Though the buoyancy in atmospheric thermals is due to temperature differences, the nature of the source of buoyancy (thermal or compositional) happens to be of secondary importance and introduces no qualitative difference. The term thermal has since been used to denote an isolated buoyant mass of fluid rising or falling, regardless of the nature of the source of buoyancy. In the following, we will interchangeably use the terms *turbulent thermal*, *buoyant cloud*, *metal-silicate cloud*, or simply *cloud*.

3.2.1. *Large-scale asymptotic behaviour*

A *miscible* turbulent thermal falling in an ambient liquid of density ρ_s under the the action of a gravity field g is fully defined by its initial volume V_0 (or equivalent radius R_0) and shape, solute concentration c_0 (here measured in kilogram of solute per unit of volume), and its kinematic viscosity ν and solute diffusivity κ (the two latter properties being here assumed independent of composition). Experiments such as shown in Figure 5 show that ambient fluid is continuously entrained in the thermal as it moves, such that the volume V of the thermal increases with time, while its average concentration $\langle c \rangle$ decreases, together with the mean density difference $\Delta\rho$ between the thermal and surrounding [113, 114]. Assuming that the loss of material from the thermal (by "detrainment") is small [120] implies that the mass of solute within the thermal, which we denote by $\mathscr{M} = \langle c \rangle V$, is conserved and equal to its initial value

$$\mathscr{M}_0 = c_0 V_0. \tag{15}$$

This implies that the total buoyancy $\mathscr{B} = (\Delta\rho/\rho_s) g V$ of the thermal is constant as well, and equal to

$$\mathscr{B}_0 = \frac{\Delta\rho_0}{\rho_s} g V_0, \tag{16}$$

where $\Delta\rho_0$ is the density difference at release between the dense and ambient liquids.

The asymptotic time evolution of the bulk properties of the thermal in the Boussinesq limit can be predicted using dimensional analysis [113, 115, 117]. Far from the source, the state of the thermal is expected to be independent of the details of its release: it should depend on the conserved quantities $\mathscr{M}_0$ and $\mathscr{B}_0$, but not on its initial radius or shape. If in addition we assume that the large-scale properties are independent of the momentum and solute diffusivity, on account of the turbulent nature of the flow [113], then dimensional analysis predicts that the size R of the thermal, vertical velocity u_z, and average concentration $\langle c \rangle$ evolve with time or distance from the source according to

$$R \sim \mathscr{B}_0^{1/4} t^{1/2} \sim z, \tag{17}$$

$$u_z \sim \mathscr{B}_0^{1/4} t^{-1/2} \sim \mathscr{B}_0^{1/2} z^{-1}, \tag{18}$$

$$\langle c \rangle \sim \mathscr{M}_0 \mathscr{B}_0^{-\frac{3}{4}} t^{-\frac{3}{2}} \sim \mathscr{M}_0 z^{-3}, \tag{19}$$

when far from the release point. The proportionality between r and z predicted by Equation (17) is often written as

$$R = \alpha z, \tag{20}$$

where the factor α is the so-called *entrainment coefficient*. α is found to be typically in the range 0.1–0.3, and seems to be independent of the viscosity and diffusivity as long as the flow

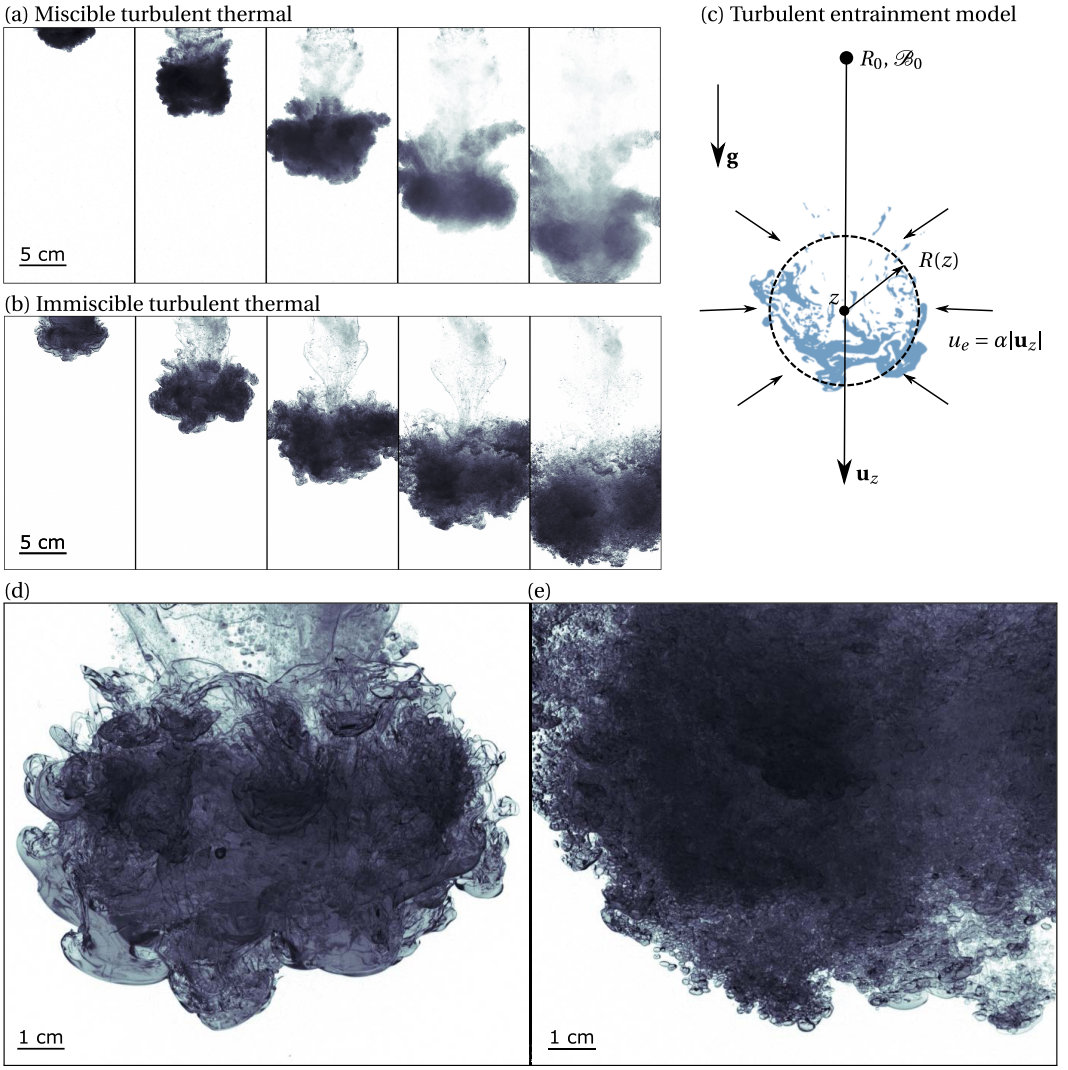


Figure 5. (a) A 169 mL volume of an aqueous solution of NaI (ρ_m = 1502 kg·m^{-3}) falling into fresh water, at $Re = 2.9 \times 10^4$ (as defined by Equation (21)). The time interval between each image is 0.3 s. (b) A 169 mL volume of an aqueous solution of NaI (ρ_m = 1601 kg·m^{-3}) falling into a low viscosity silicon oil (ρ_s = 821 kg·m^{-3}, $\eta = 8.2 \times 10^{-4}$ Pa·s), at $Bo = 9.3 \times 10^3$ and $Re = 4.0 \times 10^4$. The time interval between each image is 0.2 s. (c) The *turbulent thermal* model: a volume of fluid with initial radius R_0 and excess density $\Delta\rho$ is released at $z = 0$ in an initially motionless fluid. The thermal has a mean vertical velocity u_z. Its mean radius R increases with the distance z from the source due to the entrainment of ambient fluid at a rate $u_e = \alpha u_z$. (d) and (e) Close-ups on the second and forth images of subfigure (b). Figures (a), (b), and (c) are modified from [119].

is turbulent [117] . One of the main factors affecting the value of α appears to be the initial aspect ratio of the thermal, with α being higher in oblate thermals than in prolate thermals [121, 122]. Note also that the value of α depends on how the boundary of the thermal is defined, so care should be taken when comparing estimates from different studies. Equations (17) to (19) have

been extensively verified in experiments [115, 117, 123] and numerical simulations [120, 122]. Close to the source, the time evolution of the thermal radius is well described by a relation of the form $R = R_0 + \alpha z$ as soon as $z \gtrsim R_0$ [124]. The asymptotic expression 20 is therefore valid for $z \gtrsim R_0/\alpha$.

Interestingly, one can note that the Reynolds and Péclet numbers estimated using the above predictions for $R(t)$ and $u_z(t)$ are independent of time, since $R \propto t^{1/2}$ and $u_z \propto t^{-1/2}$. Ignoring any unnecessary dimensionless coefficients, this offers a convenient way to define the Reynolds and Péclet number of a turbulent thermal as

$$Re = \frac{\mathscr{B}_0^{1/2}}{\nu}, \tag{21}$$

$$Pe_c = \frac{\mathscr{B}_0^{1/2}}{\kappa_c}. \tag{22}$$

This will be further discussed in Section 3.2.4.

3.2.2. *Turbulent entrainment model*

Alternatively, models for the time evolution of thermals have been built from the conservation of mass and momentum by assuming that the ambient liquid is entrained in the thermal at a rate that is proportional to the mean velocity of the thermal [114]. This assumption implies that the time derivative of the volume of the thermal is given by

$$\frac{\mathrm{d}}{\mathrm{d}t}\left(\frac{4\pi}{3}R^3\right) = 4\pi R^2 \alpha u_z, \tag{23}$$

where α is the *entrainment coefficient*. Since $\mathrm{d}/\mathrm{d}t = u_z \mathrm{d}/\mathrm{d}z$, integration of Equation (23) gives $R = R_0 + \alpha z$, which shows that the coefficient introduced in Equation (20) to relate the size of the thermal to the distance it has travelled is in fact the entrainment coefficient. Conservation of momentum gives a prognostic equation for the vertical velocity u_z of the centre of mass of the cloud. Ignoring fluid drag on the thermal and a possible loss of buoyancy in the wake, conservation of momentum simply states that

$$\frac{\mathrm{d}}{\mathrm{d}t}\left(\frac{4\pi}{3}R^3\bar{\rho}u_z\right) = \frac{4\pi}{3}R_0^3\Delta\rho_0 g, \tag{24}$$

where $\bar{\rho}(t)$ is the mean density of the thermal. Conservation of mass implies that

$$\frac{\mathrm{d}}{\mathrm{d}t}\left(\frac{4\pi}{3}R^3\bar{\rho}\right) = 4\pi\rho_s R^2 \alpha u_z. \tag{25}$$

This set of equations, in general, requires to be solved numerically from initial conditions. It can be shown that the solution has an asymptotic limit consistent with the prediction of dimensional analysis (Equations (17) to (19)). The asymptotic laws are valid at times large compared to the timescale

$$t_g = \frac{R_0^2}{\mathscr{B}_0^{1/2}} \sim \sqrt{\frac{\rho_s}{\Delta\rho_0}\frac{R_0}{g}} \tag{26}$$

characteristic of the acceleration phase which follows the release from rest of the thermal (t_g is the time needed to reach from rest the free fall velocity $\sqrt{(\Delta\rho_0/\rho_s)gR_0}$ with an acceleration $(\Delta\rho_0/\rho_s)g$).

3.2.3. *Statistics of the concentration field*

Measurements of the concentration field within turbulent miscible thermals have been carried out by [37] using Planar Laser Induced Fluorescence, and further analysed by [125]. Figure 6(a) shows a snapshot of the concentration field in a vertical plane within a thermal having $Re = 4175$ and $Pe_c = 1.0\times10^7$. The red line is an isocontour of the concentration field which is used

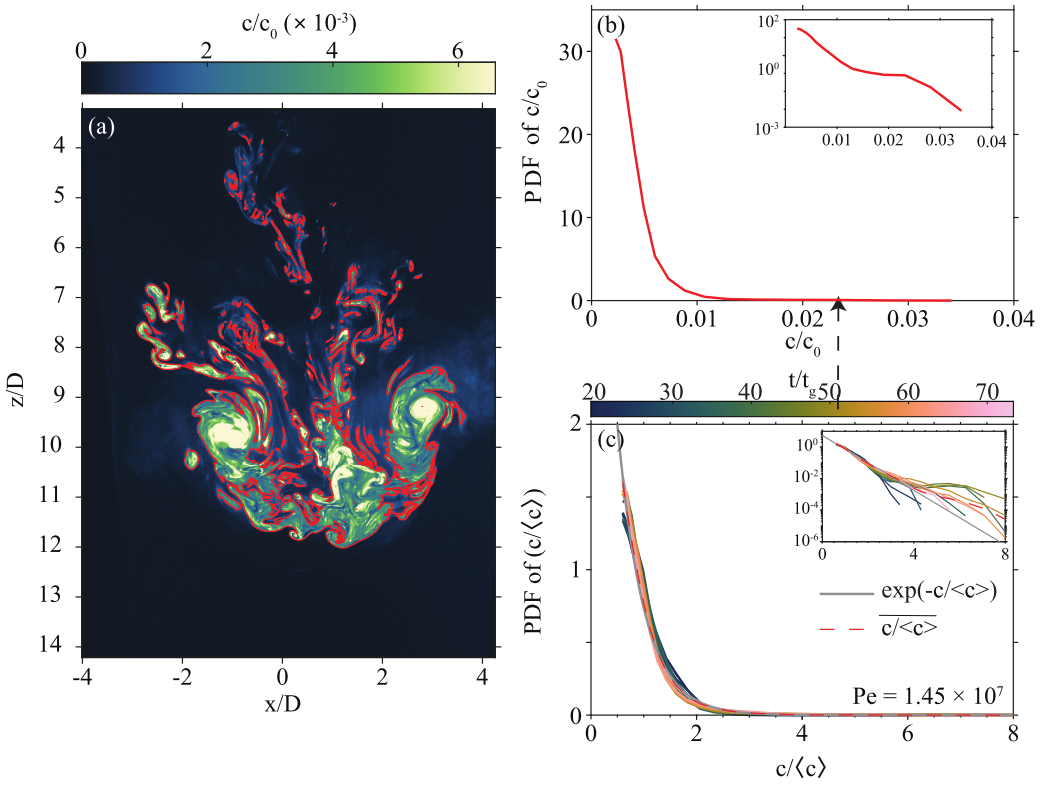


Figure 6. (a) Negatively buoyant mass (sodium chloride aqueous solution with rhodamine B) falling in an unstratified environment (pure water) and forming a turbulent thermal with a Reynolds number of $Re = 4175$ and a Péclet number of $Pe_c = 1.0 \times 10^7$. The red line denotes the contour of the thermal with a threshold equal to $c/\langle c\rangle = 0.5$, with $\langle c\rangle$ the mean of the concentration inside the contour. (b) Probability density function (PDF) of the concentration c/c_0 as a function of the concentration c/c_0 for the snapshot (a) at $t/t_g = 51$. (c) PDF of concentration normalized by the mean of the concentration $c/\langle c\rangle$ as a function of $c/\langle c\rangle$ for different times between $t/t_g = 20$ and $t/t_g = 75$. Here, red dashed lines show the temporal mean of the $c/\langle c\rangle$. Inserts in (b) and (c) are the semi-log version of the PDF. Panel (a) adapted with permission from Lherm (2021) [37].

to define the boundary of the thermal. Figure 6(a) shows that the concentration within the thermal is far from being homogeneous, the concentration field exhibiting small-scale, highly corrugated elongated structures. The standard deviation of the concentration field ($\simeq 2.5 \times 10^{-3} c_0$ for this particular snapshot) is about half of the concentration average ($\simeq 4.2 \times 10^{-3} c_0$), which shows that the concentration has a relatively wide distribution. Concentration variations can be further quantified by calculating the probability density function (PDF) of the concentration within the thermal, as shown in Figure 6(b). The probability density function is a strongly decreasing function of c, with a distribution dominated by the small concentrations.

Dimensional analysis predicts that far from the source the moment of order k of the concentration is of the form

$$\langle c^k \rangle = \left(\mathscr{M}_0 \mathscr{B}_0^{-\frac{3}{4}} t^{-\frac{3}{2}} \right)^k f_{c,k}(Re, Pe_c), \tag{27}$$

where Re and Pe_c are defined according to Equations (21) and (22), and $f_{c,k}$ non-dimensional factors which may be functions of Re and Pe_c [125]. It follows that the moments of $c/\langle c\rangle$,

$$\langle (c/\langle c\rangle)^k\rangle = \frac{\langle c^k\rangle}{\langle c\rangle^k} = \frac{f_{c,k}(Re,Pe_c)}{f_{c,1}^k(Re,Pe_c)}, \tag{28}$$

are predicted to be independent of time, which implies that the probability density function of $c/\langle c\rangle$ is independent of time as well. Figure 6(c) shows that the PDF of $c/\langle c\rangle$ calculated at different times in the asymptotic regime collapse on a well-defined master curve, thereby validating the above prediction. The PDFs of $c/\langle c\rangle$ are well modelled by a decreasing exponential given by

$$p(c/\langle c\rangle) = \exp\left(-\frac{c}{\langle c\rangle}\right) \tag{29}$$

with $\langle c\rangle$ given by Equation (19) (with a dimensionless prefactor adjusted to measurements of $\langle c\rangle$). The time average of the PDFs (dashed red line) indeed lies very close to the prediction of Equation (29) (grey line). Qualitatively, the stationary nature of the distribution of $c/\langle c\rangle$ can be understood as resulting from the competing effects of homogenization within the thermal and continuous addition of ambient liquid through entrainment. This is well illustrated by the fact that the standard deviation is always commensurate with the average concentration, $\sqrt{\langle c^2\rangle - \langle c\rangle^2} \sim \langle c\rangle$. The details of the mechanisms by which the stationary distribution is maintained, and the reasons why the resulting distribution is exponential, have yet to be understood and modelled.

3.2.4. *A note on self-similarity*

The state at time t of a miscible thermal can be characterised by its Reynolds and Péclet numbers. As noted at the end of Section 3.2.1, it so happens that the instantaneous values of Re and Pe_c estimated with the asymptotic predictions for $R(t)$ and $u_z(t)$ are independent of time. It can be argued that the self-similar behaviour of turbulent thermals is in fact linked with the time invariance of the instantaneous Re and Pe_c. This allows the velocity and composition fields to be self-similar in time, in the sense that, when normalised by their spatial average u_z and $\langle c\rangle$, the statistical distribution of the velocity and concentration can be constant in time.

Adding ingredients like surface tension or rotation might impede self-similarity. One can note that the Weber number based on the instantaneous size and velocity in the asymptotic regime (Equations (17) and (18)) is a decreasing function of time and distance given by

$$We \sim \frac{\rho_s \mathscr{B}_0}{\sigma R_0}\left(\frac{t}{t_g}\right)^{-1/2} \sim Bo\left(\frac{t}{t_g}\right)^{-1/2} \sim \alpha Bo\frac{R_0}{z}, \tag{30}$$

where here the Bond number is defined as

$$Bo = \frac{\Delta\rho_0 g R_0^2}{\sigma} \sim \frac{\rho_0 \mathscr{B}_0}{\sigma R_0}. \tag{31}$$

The proportionality between We and Bo reflects the force balance (inertia ~ buoyancy) which controls the velocity of the thermal.

Similarly, the Rossby number, which measures the relative importance of inertia and Coriolis force, writes

$$Ro = \frac{u_z(t)}{2\Omega R(t)} \sim \frac{1/\Omega}{t} \sim \left(\frac{\mathscr{B}_0^{1/4}\Omega^{-1/2}}{z}\right)^2 \tag{32}$$

when estimated with the asymptotic expressions for $R(t)$ and $u_z(t)$. This predicts that the Coriolis force becomes comparable to inertia after a time interval ~1 day, or, equivalently, when the distance travelled by the thermal is larger than $\sim\mathscr{B}_0^{1/4}\Omega^{-1/2}$ [126–128].

Finally, if the thermal is made of buoyant droplets or particles, then an additional relevant number is the Rouse number $\mathscr{R}$ defined as the ratio of the sedimentation velocity of the droplets

or particles, $u_{\rm sed}$, to a characteristic velocity scale of the surrounding fluid. Taking for this velocity scale the asymptotic scaling of u_z, the Rouse number writes

$$\mathscr{R} = \frac{u_{\rm sed}}{u_z} \sim \frac{u_{\rm sed}}{\mathscr{B}_0^{1/4}} t^{1/2} \sim \frac{u_{\rm sed}}{\mathscr{B}_0^{1/2}} z, \tag{33}$$

which is again time-dependent.

The fact that some of the relevant dimensionless parameters are time-dependent must prevent true self-similarity. The implications are further discussed in the following subsections.

3.3. *Immiscible turbulent thermals*

Section 2 suggests two possible scenarios for the fate of the impactor core. For projectiles smaller than 300 km in radius, or falling faster than twice the escape speed, the core fragments at the top of the magma ocean during the cratering process [86]. In this case, the metal drops behave collectively and generate a turbulent cloud of metal drops and entrained silicates that fall in the magma ocean [129]. Such particle-laden clouds behave as the miscible thermals described in the previous section [78, 128, 130]. In contrast, the cores of larger impactors coming onto Earth at the escape speed may not fragment during the impact [86]. In this scenario, the impactor core, still intact after the cratering stage, falls by buoyancy in an immiscible pool of liquid silicates under extremely large Reynolds and Weber numbers, as discussed in Section 3.1.

3.3.1. *Experimental test of the turbulent entrainment model*

Figure 5b shows snapshots from an experiment in which a negatively buoyant volume of sodium iodide is released into a low-viscosity silicon oil, under conditions otherwise similar to the experiment shown on Figure 5a. The NaI solution and the silicon oil are *immiscible*, so this experiment is one important step closer to the core-mantle differentiation configuration. The experimental fluids and configuration have been chosen so as to maximize the values of the Bond and Reynolds numbers, which are $Bo = 9.3 \times 10^3$ and $Re = 4.0 \times 10^4$ (with Bo and Re as defined by Equations (31) and (21)). We use here a Bond number rather than a Weber number, which is time-dependent in these experiments; as shown by Equation (30), Bo offers a convenient measure of the order of magnitude of $We(t)$. The density ratio is $\rho_m/\rho_s = 1.95$ (close to metal-silicate), and the viscosity ratio is $\eta_m/\eta_s = 1.2$. The large-scale evolution of the negatively buoyant volume is strikingly similar to what has been observed in the *miscible* experiment: the volume of the negatively buoyant fluid increases with distance, which indicates that it entrains and incorporates silicon oil. The analogy with miscible thermals also holds quantitatively: the evolution of the vertical position, size, and velocity of immiscible thermals are well predicted by the turbulent entrainment model. This has been verified in experiments similar to those shown in Figure 5b [75, 124] as well as in experiments in which a volume of galinstan ($\rho = 6440$ kg·m^{-3}) is released in a pool of UCON oil ($\rho = 1050$ kg·m^{-3}) of different viscosities [87, 88, 131]: when $Bo \gtrsim 100$, the entrainment coefficient $\alpha = 0.25 \pm 0.1$ is indistinguishable from that of miscible thermals.

3.3.2. *Fragmentation*

Immiscible thermals strongly differ from miscible thermals when looking at the small scales: in the former, the released liquid eventually breaks into drops. In the limit of large Weber numbers, the interface between the released and ambient liquids is stretched by the turbulence until it becomes fractal [75]. As this fractal interface builds up, ligaments emerge everywhere inside the thermal. All the ligaments break up almost simultaneously, leading to the sudden formation of droplets everywhere in the thermal (Figure 5b) [75, 124]. This sudden and global

fragmentation strikingly contrasts with the fragmentation of a liquid in air, which is often gradual and localised at a well-defined interface [51, 132].

At the very large values of *We* or *Bo* estimated in Section 3.1, the immiscible thermal is expected to be in this asymptotic regime, in which the impactor core forms a turbulent immiscible thermal and suddenly breaks up into drops. In experiments, the breakup into drops occurs at a constant depth of 4 to 8 initial radii when $Bo \gtrsim 100$ in the explored range of Bo ($\lesssim 10^4$) [124]. Coupling this result with the disruption caused by the impact stage, [86] predicts the depth of breakup as a function of the impactor size and velocity. They found that, on Earth, only impactors larger than about 2000 km in radius, and coming slowly at the escape speed, reach the bottom of the magma ocean unbroken. Any smaller or faster impactor is fragmented at the bottom of the ocean.

Once fragmented, the degree of chemical equilibration of the impactor core may depends in part on the drop size. In an isotropic and homogeneous turbulent flow with typical Weber number *We*, the drop size d is comparable to the Hinze scale [133], which is obtained assuming a Kolmogorov cascade such that the speed at scale l is $u_l \sim (l/L)^{1/3} U$, where L and U are the typical length and velocity at the largest scales. Then, at scale l, the local Weber number is

$$We_l = \frac{\rho_s u_l^2 l}{\sigma} \sim We \left(\frac{l}{L}\right)^{5/3}. \tag{34}$$

The Hinze scale is such that inertia balances surface tension, i.e. $We_l \sim 1$. From Equation (34), one obtains

$$l_H \sim L We^{-3/5}. \tag{35}$$

Assuming that the thermal speed arises from the buoyancy force only, we can take $L = R(t)$ and use Equation (30) for *We* to find

$$l_H \sim R_0 (\alpha^2 Bo)^{-3/5} \left(\frac{R}{R_0}\right)^{8/5} \sim \left(\frac{\alpha^2 \Delta\rho_0 g}{\sigma}\right)^{-3/5} \left(\frac{R}{R_0}\right)^{8/5} R_0^{-1/5}, \tag{36}$$

which is only weakly dependent on the initial size R_0 of the metal cloud. Estimated at R/R_0 between 4 and 8 (the fragmentation distance experimentally observed) with R_0 between 10 km and 1000 km, the Hinze scale is between a few millimeters and a few centimeters. Drops of this size are small enough to fully equilibrate with the surrounding silicates [44, 73, 134].

However, scaling (35) remains to be tested experimentally for immiscible thermals. The relevance of the Kolmogorov cascade to turbulent thermals is questionable (turbulence is likely affected by buoyancy forces and by the shear associated with the vortex ring structure of thermals). In addition, when fragmentation occurs during the cratering stage (Section 2), multiple choices are possible for the length scale L and the typical velocity U in the Weber number and the Hinze scale (35).

Experiments using galinstan and UCON oil have been used to investigate the effect of the viscosity contrast on the fragmentation behaviour [87, 88, 131, 135], though at smaller values of the Bond number ($Bo < 100$). Fragmentation has been observed to happen in a single global event, as described above for a viscosity ratio ~1, in experiments with a viscosity ratio η_s/η_m equal to 0.383, 8.37, and 72.5 (where η denotes the dynamics viscosity). The distribution of drop sizes does not seem to be affected by the viscosity ratio in this range, and the average drop size seems to be in agreement with Hinze scaling (Equation (35)) [88]. At the highest viscosity ratio investigated ($\eta_s/\eta_m = 691$), fragmentation has been observed to result from a different regime, the *Rayleigh–Taylor regime* [135], in which the initial deformation of the dense liquid results from large scale Rayleigh–Taylor instabilities. However, the Reynolds number of these experiments at $\eta_s/\eta_m = 691$ is moderate ($Re < 80$)[1], and it is not clear whether this regime persists at higher

[1]The Reynolds number given here is calculated using Equation (21), which gives a value twice larger than quoted in [88, 135].

values of *Re*. In fact *Re* is inversely correlated with the viscosity ratio in this suite of experiments (because the viscosity ratio can only be increased by increasing the ambient liquid viscosity), and it is therefore not straightforward to discriminate between the effects of the viscosity ratio and Reynolds number.

3.3.3. *Post-fragmentation dynamics*

If the metal phase does fragment before reaching the base of the magma ocean, then the dynamics of the resulting cloud of droplets depends on whether the droplets have a collective behaviour or fall without significant interaction between them. This is controlled by the Rouse number $\mathscr{R}$ defined as the ratio of the settling velocity of individual drops to the magnitude of the flow and, to a lesser extent, by the drop particle number Re_d (based on drop size and settling velocity) which affects the flow around each drop and the interactions between drops.

In experiments on immiscible turbulent thermals such as shown in Figure 5 or described by [75, 124], the size of the droplets resulting from fragmentation was such that, given the height of the tank, the cloud velocity remained larger than the settling velocity for most of the duration of the experiments, except when the cloud was approaching the base of the tank. There it was observed that the largest drops separated from the bulk of the thermal while smaller drops were still carried by the vortex ring flow, but the limited observations available did not allow any quantitative and systematic characterisation of the transition. This observation is consistent with the fact that the Rouse number estimated using the asymptotic scaling law for the turbulent thermal velocity (Equation (18)) is a decreasing function of time, as shown by Equation (33).

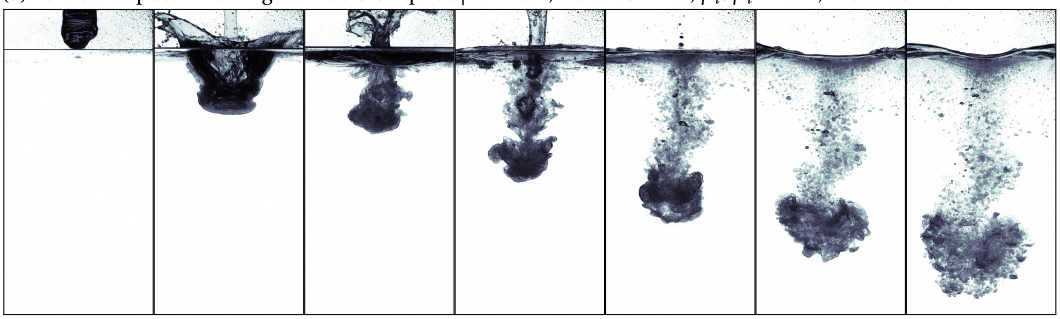
Using clouds made of solid particles rather than drops allows to characterize the effect of the settling velocity of the suspended phase in a much simpler and systematic way. Experiments have shown that particle clouds behave as turbulent thermals when $\mathscr{R} \lesssim 1$ but form bowl-shaped *particle swarms* when $\mathscr{R} \gtrsim 1$, falling at a velocity near the settling velocity of individual particles [128–130]. When estimated using the asymptotic scaling law for the turbulent thermal velocity (Equation (18)), the Rouse number is given by Equation (33). It is a decreasing function of time, due to the decrease of the cloud velocity resulting from the gradual entrainment of ambient liquid with no momentum. It is found from Equation (33) that $\mathscr{R}$ reaches the value of 1 when the cloud has travelled a distance of the order of $\mathscr{B}_0^{1/2}/u_{\text{sed}}$. [130] found experimentally that the fallout distance z_{fall} at which particle-ladden turbulent thermals transition to particle swarms indeed scale as $\mathscr{B}_0^{1/2}/u_{\text{sed}}$, with a prefactor $\simeq 9 \pm 2$, when the particle Reynolds number is larger than $\simeq 4.4$.

When the drop Reynolds number is large, then the settling velocity is $u_s \sim \sqrt{\Delta\rho/\rho_s g a}$ where a is the particule or drop radius. Using this scaling, [130] found experimentally that the ratio of the fallout distance to particle radius is only a function of the number of particles N_p, $z_{\text{fall}}/a \simeq (9 \pm 2) N_p^{1/2}$. Re-arranging, and denoting by ϕ_0 the initial metal fraction in the cloud, we can write the fallout distance as a function of the initial radius R_0 of the metal and of the drop size as

$$\frac{z_{\text{fall}}}{R_0} \simeq (9 \pm 2) \left(\phi_0 \frac{R_0}{a} \right)^{1/2}, \tag{37}$$

which is more convenient for application to metal-silicate separation in a magma ocean. Taking $a \sim 1$ cm, z_{fall} would only be smaller than ~3000 km (the thickness of the mantle) if R_0 is smaller than ~1 km. The critical value of R_0 decreases to ~500 m if we rather assume $a \sim 1$ mm. This suggests that fallout of drops from a metal-silicate thermal was unimportant, except for very small metal volumes.

(a) Vertical impact involving immiscible liquids | $Fr = 5.2$, $Re = 2.5 \times 10^4$, $\rho_i/\rho_t = 1.22$, $We = 7.5 \times 10^3$



(b) Oblique impact involving miscible liquids | $Fr = 7.1$, $Re = 5.8 \times 10^4$, $\rho_i/\rho_t = 1.088$, $\theta = 52.5^o$

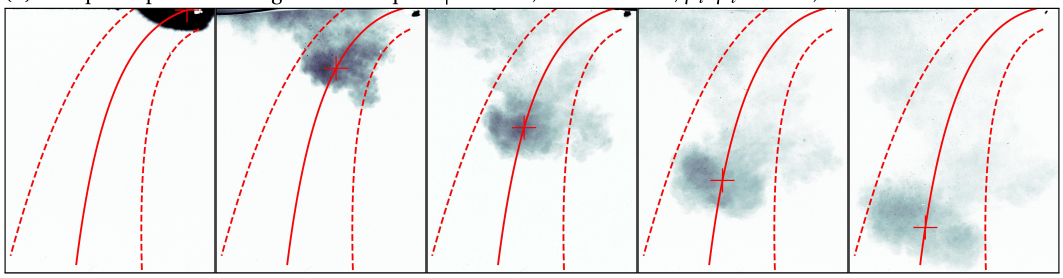


Figure 7. (a) Time sequence from an experiment in which a volume of water ($R_i = 2.3$ cm, $\nu = 10^{-6}$ m^2·s^{-1}, $\rho_i = 1000$ kg·m^{-3}) strikes a bath of low-viscosity silicon oil ($\nu = 1.2 \times 10^{-6}$ m^2·s^{-1}, $\rho_t = 821$ kg·m^{-3}) at a velocity $U_i = 1.1$ m·s^{-1}. The time step is 0.1 s between the three first images, and then 0.3 s. (b) Time sequence from an experiment in which a volume of NaCl solution ($R_i = 3.6$ cm, $\nu = 10^{-6}$ m^2·s^{-1}, $\rho_i = 1088$ kg·m^{-3}) strikes a bath of water at a velocity $U_i = 1.6$ m·s^{-1} with an angle $\theta = 52.5°$ with respect to the horizontal.

3.4. *Additional effects*

3.4.1. *Impact-generated thermals*

The experiments discussed in Sections 3.2 to 3.4.2 have been performed by releasing volumes of dense liquid *within* the host liquid, without accounting for the impact and cratering phase described in Section 2. As discussed above, the assumption is that the impact leaves the impactor material as a coherent and localized mass which then evolves as a turbulent thermal.

Experiments using both miscible liquid pairs [76] and immiscible liquid pairs (Figure 7a) show that after the collapse of the crater the liquid released by the impact does indeed evolve as a turbulent thermal, at least as long as the Froude number is not too large. This was the case for all experiments studied by [76], with $Fr \in [4, 100]$. Landeau et al. [76] quantified the amount of dispersion following the cratering phase, and found that the evolution of the equivalent radius of the dense liquid cloud evolves as

$$R = R_0 + \alpha z, \tag{38}$$

as predicted by the turbulent entrainment model, if the radius R_0 of the cloud at $z = 0$ is taken to be

$$R_0 = 0.29 R_i \left(\frac{\rho_m - \rho_s}{\rho_s} \right)^{-0.19} Fr^{0.4} \tag{39}$$

instead of the impactor radius R_i. This accounts for the dispersion induced by the impact which is, as expected, an increasing function of Fr.

Figure 7(b) shows snapshots from an experiment in which a volume of NaCl solution (R_i = 3.6 cm, ρ_i = 1088 kg·m^{-3}, appearing blue) strikes the surface of a water pool with an impact angle $\theta = 52.5°$, at $Fr = 7.1$ and $Re = 5.8 \times 10^4$. In contrast with the snapshots shown in Figure 4, which focused on the cratering dynamics, we focus here on the longer term evolution of the liquid delivered by the impact. Superimposed on the images are predictions from a turbulent entrainment model allowing for a non-vertical trajectory of the dense liquid (an extension of the model described in Section 3.2.2), with the initial conditions (size of the cloud and velocity of its center of mass) fitted to match the observations. The solid red line shows the model prediction for the trajectory of the center of mass of the cloud, the position of which is shown with a red cross at the times of the snapshots; the dashed red lines show the positions of the left and right edges of the cloud according to the turbulent entrainment model. The evolution of the dense liquid cloud is well described by the turbulent entrainment model, though one can notice that a significant amount of impactor liquid is dispersed at impact and left behind the leading cloud. Preliminary investigations shows that the initial conditions to be given to the turbulent entrainment model are functions of θ and Fr. A parameterization of these initial conditions, coupled to the turbulent entrainment model, will allow to build a predictive model for the dispersion following an oblique impact.

3.4.2. *Effect of planetary rotation*

As discussed in Section 3.2.4, the Rossby number based on the instantaneous size and velocity predicted in the asymptotic regime is a decreasing function of time or, equivalently, distance travelled by the cloud. Rotation starts to have a significant effect when the thermal reaches a depth $z_\Omega = \mathscr{B}_0^{1/4}\Omega^{-1/2} \propto R_0^{3/4}\Omega^{-1/2}$ [126–128]. This critical depth can also be written as

$$z_\Omega \sim \left(\frac{1\ \text{day}}{t_g}\right)^{1/2} R_0, \tag{40}$$

where t_g is the acceleration time scale defined in Equation (26). The prefactor in Equation (40) can be estimated from the asymptotic solutions of the turbulent entrainment model (e.g. [75, 136]), and is found to be close to 1, depending on the parameters, including α, of the entrainment model.

During core formation, the rotation of the Earth was likely faster than it is today. Taking R_0 between 10 km and 1000 km and a rotation rate twice as fast as today gives z_Ω between ~400 km and ~12 000 km, which needs to be compared to the thickness of the magma ocean, which is at most ~3000 km. z_Ω is equal to the thickness H of the magma ocean for $R_0 \sim H^{4/3}\Omega^{2/3}(\rho_s/(g\Delta\rho))^{1/3}$. Taking H = 2800 km and Ω twice the present day value gives $R_0 \sim 500$ km, in agreement with a more complete calculation made by [78]: impactors with a core radius larger than 500 km will not be affected much by rotation; smaller impactors can be affected, depending on the thickness of the magma ocean. Taking a rotation rate 5 times larger than today increases z_Ω by a factor $\sqrt{5/2} \simeq 1.6$, while increasing by a factor $(5/2)^{2/3} \simeq 1.85$ the maximum radius at which rotation can affect the flow. In contrast, assuming a magma ocean thickness of 1400 km instead of 2800 km reduces the critical radius to ≃200 km.

Experiments on miscible turbulent thermals [126, 127] and cloud particles [78, 128] with a rotation axis parallel to the gravity have shown that the thermal stops expanding laterally after reaching the critical depth z_Ω, and then grows as a column which keeps a constant radius $\sim\alpha z_\Omega$ but expands in the vertical direction. The amount of dispersion in this regime has been quantified and modelled by [78]. For small impactors falling in deep magma oceans, the amount of dispersion is significantly lowered compared to the prediction of the turbulent thermal model. In details, the results depends on the initial conditions. Assuming that the impactor is left with no vertical momentum at the end of the impact phase, and taking into account the dispersion

produced by the impact [76], Kriaa et al. [78] found that in a 2800 km thick magma ocean with a planetary rotation rate twice that of the Earth today, the evolution of all impactors with a radius less than 450 km is affected by rotation. For these impactors, rotation reduces the mass of silicate that is entrained and equilibrated with the impactor core. However, because dilution of the impactor core is very efficient for such small impactors, the degree of equilibration is already close to one and the effect of rotation on equilibration is quite moderate. It only becomes significant for highly siderophile elements with a metal/silicate partition coefficient $D \gtrsim 10^3$, for which the degree of equilibration is reduced by a factor of up to 3 when rotation is included. The effect of rotation is stronger at faster rotation rates: the evolution of all impactors is affected by rotation if the rotation rate was 5 times that of Earth today, again with a significant effect on the degree of equilibration for elements with a metal/silicate partition coefficient $D \gtrsim 10^3$ [78]. In contrast, the effect of rotation is less important in a shallower magma ocean: the critical impactor radius is reduced to 250 km in a 1400 km thick magma ocean [78].

The experiments discussed above [78, 126–128] have been done with a rotation axis parallel to the gravity. When transposed to planetary settings, this corresponds to impacts in the polar regions, which probably account for only a moderate fraction of the total mass accreted. Experiments with a rotation axis tilted with respect to the gravity field will be more challenging. In principle, this could be done in experiments with a rotation rate high enough to give a centrifuge acceleration close to or greater than g.

3.5. *Chemical equilibration within the cloud*

Published models of metal-silicate equilibration assume that the metal phase fully equilibrates with the entrained silicates [75, 76], in proportions predicted by the turbulent entrainment and impact mixing models. This allows to build simple models of mass transfer but ignores the concentration heterogeneities that must be continuously produced by the entrainment of fresh, unequilibrated material. For a chemical element that does not partition between metal and silicates (metal/silicate partition coefficient $D = 1$), the assumption of full equilibration amounts to assuming that the concentration within the thermal is homogeneous. This is inconsistent with the probability density function of the concentration field discussed in Section 3.2.3. This is also inconsistent with measurements made by [88] on the temperature of the metal phase in experiments in which a volume of galinstan falls as a turbulent immiscible thermal in a pool of UCON oil. It is indeed found in these experiments that the temperature of the galinstan is higher than predicted by full equilibration, which corresponds to less efficient heat transfer [88].

The implications for the degree of equilibration of the concentration density function given in Equation (29) need to be further quantified and generalized to two-phase flows and chemical elements with a partition coefficient $D \neq 1$. We can already note that the median of the distribution of c corresponding to Equation (29) is equal to $(\ln 2)\langle c\rangle \simeq 0.69\langle c\rangle$, which means that half of the thermal volume has concentration levels smaller than 69% of the value $\langle c\rangle$ assumed in perfect equilibration models. Taking into account the distribution of c within the thermal will therefore result in a decrease in the efficiency of equilibration.

3.6. *Reaching the bottom of the magma ocean*

The metal cloud may still have a velocity up to several hundreds of $\mathrm{m{\cdot}s^{-1}}$ when it reaches the bottom of the magma ocean, depending on the size of the impactor and depth of the magma ocean. This could cause a "secondary impact" which, while subsonic, can be energetic enough to result in significant additional dispersion [66]. Depending on the extent of mantle melting, several scenarios can be envisaged [75]. If the magma ocean extends down to the core, the metal

cloud can entrain mantle silicates into the core, leading to further chemical exchange at high pressure and temperature [137]. If instead a solid portion of mantle subsists, the metal-silicate mixture may spread laterally at the base of the magma ocean as a turbulent gravity current if the bottom of the magma ocean is flat, or may possibly be driven back upward by inertia and re-suspended if the magma ocean has an hemispherical shape [66]. If this is the case, then one may wonder how long the metal drops can be kept in suspension, given that typical convective velocity in a magma ocean are estimated to be $\sim$10 m·s^{-1} [64], significantly larger than the settling velocity v_s of a mm-to-cm sized drops, which is around 0.3–0.5 m·s^{-1} [44, 74].

Laboratory experiments have shown that sedimentation from a convective layer happens on a timescale $\sim H/v_s$, where H is the thickness of the convecting layer, even if the settling velocity is much smaller than the convective velocity [138–140]. This results from the presence of a boundary layer at the bottom of the convective layer in which the vertical velocity of the convecting liquid goes to zero, thus allowing the particles to sediment in spite of vigorous convection in the bulk [138]. With $v_s \sim$ 0.3–0.5 m·s^{-1} [44, 74], the sedimentation time from a 2000 km deep magma ocean would be $H/v_s \sim 2$ months. This is small compared to the lifetime of a magma ocean ($\gtrsim$1000 years [64]).

Laboratory experiments using solid particles have also shown that the volumetric fraction of suspended particles reach a non-zero equilibrium value, set by a balance between particle sedimentation and re-entrainment of particles from the layer of deposited particles [140, 141]. The processes behind entrainment from a dense liquid layer likely differs from those behind particles entrainment, because of the necessity to first produce new drops that could then be entrained by the convection. It is likely to be less efficient as it requires the convective stresses to overcome the surface tension in addition to the gravitational forces. As an illustration, we can however use the model developed for solid particles [140, 141] to estimate an upper bound on the equilibrium metal volume fraction in a convecting magma ocean. Using Equation (12) from [140] with a magma ocean thickness of 2000 km and a Rayleigh number in the range 10^{28}–10^{32}, we find the predicted equilibrium metal volume fraction to be in the range 10^{-10}–10^{-5}, suggesting that only a very small fraction of metal could have remained in the mantle.

Planetary rotation may affect the settling and dispersion of the metal phase, in particular through its effect on the regime and strength of magma ocean convection. This has not been investigated experimentally, but numerical simulations of the gravitational settling of particles in a vigorously convecting layer suggest that the effect of rotation can be strong if convection is strongly influenced by the Coriolis force, which depends on the state of the magma ocean [142]. In this case, Maas et al. [143] found that the degree of dispersion of the metal depends on the latitude of the impact: the degree of dispersion is rather limited in the case of impacts in the polar regions, and much higher in the case of impacts in the equatorial band. In these simulations, this is due to the presence of a strong zonal flow that transports and disperses the metal throughout the equatorial band [143].

4. Metal-silicate separation in a solid mantle

4.1. *Rayleigh–Taylor instability and diapirism*

4.1.1. *A simple reference model*

Let us consider a situation in which a global magma ocean or a more localized magma pond is separated from the core by an at least partially crystallised silicate layer. As discussed in Section 3.6, most of the metal is expected to sediment from the magma ocean in a timescale of a few months. This is small compared to the time needed to crystallise the magma ocean ($\gtrsim$1000 years [64]). A layer of metal would therefore accumulate at the base of the magma ocean [38].

Molten iron being denser than the underlying silicates, this situation is gravitationally unstable and gives rise to Rayleigh–Taylor instabilities [38, 42, 144–146].

In the relevant limit in which the lower layer is much more viscous than the thin upper layer, linear stability analysis shows that the most unstable mode has a wavelength λ that is commensurate with the thickness H of the lower viscous layer if it can be approximated as isoviscous [149]. The timescale of instability growth is

$$\tau_{RT} \sim \frac{\eta_s}{\Delta\rho g \lambda} \sim \left(\frac{\eta_s}{10^{18}\ \text{Pa·s}}\right)\left(\frac{10^3\ \text{km}}{\lambda}\right) \times 1\ \text{year}, \tag{41}$$

where η_s is here the effective viscosity of the solid mantle layer, and $\Delta\rho$ the density difference between the metal and silicate layers. With a viscosity of 10^{18} Pa·s, which corresponds to the estimate by [43] just below the solidus, and a wavelength of $\sim 10^3$ km, τ_{RT} is on the order of 1 year. A viscosity of 10^{18} Pa·s corresponds to the estimate by [43] just below the solidus. The viscosity may be orders of magnitude smaller if the mantle is partially molten. τ_{RT} is small enough compared to the lifetime of a magma ocean ($\gtrsim$1000 years [64]) to allow the development of the instability before magma ocean crystallisation.

The non-linear development of the Rayleigh–Taylor instability at the interface between a thin low viscosity layer and much thicker and more viscous layer has been investigated experimentally as a model for mantle plume [147, 150]. Figure 8a shows snapshots from one such experiment, in which a thin layer of glycerin with a density $\rho_m = 1250\ \text{kg·m}^{-3}$ (appearing black on the image) is placed at the top of a deep layer of a 32 times more viscous silicon oil of density $\rho_s = 920\ \text{kg·m}^{-3}$ [147]. Figure 8a shows that the interface between the two layers develops protrusions of low viscosity fluid that subsequently separate into several nearly spherical pockets of low-viscosity fluid, or diapirs [147]. These diapirs can be modelled as spherical inviscid spheres falling into a viscous liquid. A reasonable prediction for the velocity of a metal diapir of radius R migrating through solid silicate is therefore provided by the Stokes velocity (for an inviscid sphere)

$$u_z = \frac{\Delta\rho g R^2}{3\eta_s}, \tag{42}$$

which gives a transit time

$$\tau_{tr} = \frac{3\eta_s H}{\Delta\rho g R^2} \simeq \left(\frac{\eta_s}{10^{18}\ \text{Pa·s}}\right)\left(\frac{R}{100\ \text{km}}\right)^2\left(\frac{H}{1000\ \text{km}}\right) \times 250\ \text{year}. \tag{43}$$

Of particular interest is the thermal evolution of such a diapir and the amount of heat it exchanges with the surrounding mantle before reaching the core. The calculation detailed in Appendix A suggests that the amplitude of temperature variations within the diapir is small compared to the temperature contrast with the surrounding mantle. We therefore assume that the temperature within the diapir is uniform. Accounting for the compression of the diapir, the heat flow $Q_{m\to s}$ from the metal diapir to the surrounding, and the dissipation ψ_m in the metal, the energy balance of a diapir writes

$$M c_{p,m}\frac{\mathrm{d}T}{\mathrm{d}t} = M\frac{\alpha_m T}{\rho_m}\frac{\mathrm{d}P}{\mathrm{d}t} - Q_{m\to s} + \psi_m \tag{44}$$

where M is the diapir mass, T and P its average temperature and pressure, and $c_{p,m}$ and α_m the specific heat capacity and thermal expansion coefficient of the metal. This can be rewritten, using the transformation $\mathrm{d}(\cdots)/\mathrm{d}t = u_z \mathrm{d}(\cdots)/\mathrm{d}z$, as

$$\frac{\mathrm{d}T}{\mathrm{d}z} = \frac{\alpha_m g T}{c_{p,m}} - \frac{Q_{m\to s}}{M c_{p,m} u_z} + \frac{\psi_m}{M c_{p,m} u_z}. \tag{45}$$

The first term on the RHS is the isentropic gradient, which gives the rate of change of the temperature of the diapir if it evolves in an adiabatic ($Q_{m\to s} = 0$) and reversible ($\psi_m = 0$) way.

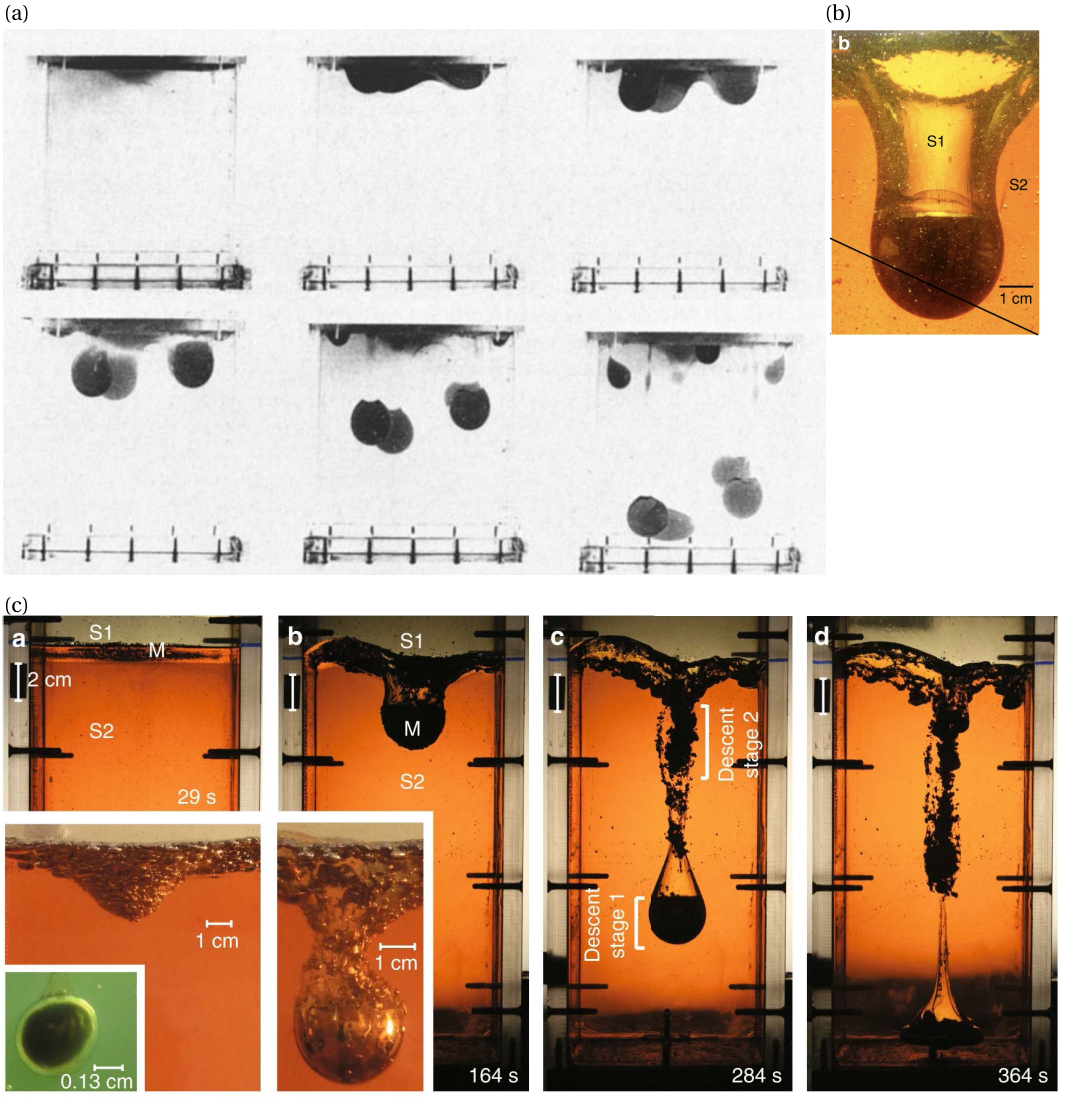


Figure 8. (a) Snapshots extracted and modified from Figure 2 of [147], with permission from Wiley (CCC license number 5781330644178). The dark liquid is glycerin ($\eta = 175$ Pa·s, $\rho = 1250$ kg·m^{-3}) and the ambient liquid (transparent) is silicon oil ($\eta = 5520$ Pa·s, $\rho = 920$ kg·m^{-3}). Note that in the original paper the images were flipped upside-down to be consistent with the problem studied (plume formation from a thin layer at the base of the mantle). Here the images have been put back to their original orientation. (b) A diapir formed in a three-layer experiment with initial conditions consisting of a layer of gallium (appearing dark) sandwiched between two layers of glucose solutions with different viscosities and densities, the lower layer (s2) being denser and more viscous than the upper layer (s1). (c) Similar to (b) except that the intermediate layer is a mixture of gallium and liquid from the upper layer. The density and viscosity of the working liquids are $\rho = 5910$ kg·m^{-3}, $\eta_m = 10^{-3}$ Pa·s for gallium, and $\rho = 1256$ kg·m^{-3}, $\eta_s = 0.1$ Pa·s and $\rho = 1417$ kg·m^{-3}, $\eta_s = 11.75$ Pa·s for the s1 and s2 glucose solutions. (b) and (c) are parts of Figures 1 and 2 of [148], under the CC BY 4.0 license (http://creativecommons.org/licenses/by/4.0/).

Assuming the diapir keeps a nearly spherical shape, the heat flux from the diapir to its surroundings is

$$Q_{m\to s} = a4\pi R^2 k_s \frac{T - T_s}{R} Pe^{1/2}, \tag{46}$$

with $a \simeq 0.46$ [151, 152], T_s the temperature of the surrounding mantle, and k_s the thermal conductivity of the silicate mantle. The Péclet number Pe is here defined with the diapir velocity and mantle thermal diffusivity. Assuming the diapir falls at the Stokes velocity,

$$Pe = \frac{Ru_z}{\kappa_s} = \frac{\Delta\rho g R^3}{3\kappa_s\eta_s} \sim \frac{\mathscr{B}}{\kappa_s\nu_s}, \tag{47}$$

where $\mathscr{B} = (4\pi/3)R^3\Delta\rho/\rho_s g$ is the total buoyancy of the diapir, and $\nu_s = \eta_s/\rho_s$ and κ_s the kinematic viscosity and thermal diffusivity of the silicate. As defined here, Pe is akin to a Rayleigh number. Using Equation (46), Equation (45) can be recast as

$$\frac{\mathrm{d}T}{\mathrm{d}z} + \left(\frac{1}{\ell_\kappa} - \frac{1}{\ell_c}\right) T = \frac{T_s}{\ell_\kappa} + \frac{\psi_m}{Mc_{p,m}}. \tag{48}$$

where

$$\ell_c = \frac{c_{p,m}}{\alpha_m g}, \tag{49}$$

$$\ell_\kappa = \frac{Pe^{1/2}}{3a} \frac{\rho_m c_{p,m}}{\rho_s c_{p,s}} R, \tag{50}$$

are the characteristic length scales for compression heating and heat exchange with the surrounding, respectively.

The length scale ℓ_κ can be interpreted as a *thermal equilibration distance* with the surrounding mantle. Replacing Pe with its expression (47), we find that ℓ_κ is larger than the solid mantle thickness H when the diapir radius is larger than

$$R_{\mathrm{eq},1} = H27^{1/5}\left(a\frac{\rho_s c_{p,s}}{\rho_m c_{p,m}}\right)^{2/5}\left(\frac{\Delta\rho g H^3}{\kappa_s\eta_s}\right)^{-1/5} \simeq \left(\frac{\eta_s}{10^{18}\ \mathrm{Pa{\cdot}s}}\right)^{1/5}\left(\frac{H}{10^3\ \mathrm{km}}\right)^{2/5} \times 10\ \mathrm{km}. \tag{51}$$

Note that $R_{\mathrm{eq},1}$ is weakly dependent on the mantle viscosity and solid mantle thickness. Only diapirs smaller than about 10 km could have been affected by heat transfer to the mantle, a prediction which is in agreement with numerical models [46, 153].

The ratio of the compression and heat exchange terms (1st and 2nd terms on the RHS of (45)) is given by the ratio of ℓ_κ and ℓ_c. It is larger than 1 if the diapir radius is larger than a critical radius $R_{\mathrm{eq},2}$ given by

$$R_{\mathrm{eq},2} = \left(3a\frac{c_{p,m}}{\alpha_m g}\frac{\rho_s c_{p,s}}{\rho_m c_{p,m}}\right)^{2/5}\left(\frac{3\kappa_s\eta_s}{\Delta\rho g}\right)^{1/5} \sim \left(\frac{\eta_s}{10^{18}\ \mathrm{Pa{\cdot}s}}\right)^{1/5} \times 20\ \mathrm{km}. \tag{52}$$

The ratio $\ell_\kappa/\ell_c = (R/R_{\mathrm{eq},2})^{5/2}$ strongly increases with R, which implies that heat exchange quickly becomes negligible compared to compression heating when R exceeds $R_{\mathrm{eq},2}$.

The total viscous dissipation ψ associated with the motion of the diapir is equal to the rate of change of gravitational energy. Of this, only a small part ψ_m is expected to be dissipated in the diapir, the remaining part ψ_s being dissipated in the surrounding mantle. The ratio ψ_m/ψ_s is indeed $\sim\eta_m/\eta_s$ if the flow within the diapir is laminar (consistent with [46]), and $\sim(\rho_m/\rho_s)(\Delta\rho g R^3/\eta_s^2)$ if the flow within the diapir is turbulent [20]. Because of the very large viscosity of the solid silicate, the contribution to the thermal evolution of the diapir is negligible in both cases, and dissipative heating can be safely neglected in the diapir energy balance.

Overall, the above simple calculations suggest that: (i) migration by diapirism of the metal through a solid mantle is fast (it happens on a timescale which is short compared to the duration of accretion); (ii) heat exchange between the diapir and surrounding mantle is negligible if the

diapir radius is $\gtrsim$10 km; (iii) dissipation of the potential energy released during the motion of the diapir is localized in the mantle, and has a negligible effect on the thermal evolution of the metal diapir. Together, points (ii) and (iii) suggest that the diapir temperature evolves along an isentrope.

4.1.2. *Additional complexities*

Several factors can alter the simple picture we have just described:

Three-layer systems. The experiments shown in Figure 8 have been done in a two-layer system: a thin dense liquid layer above a thicker, less dense but much more viscous layer. A more realistic set-up would include three layers with a dense layer representing the metal pond sandwiched between two layers representing the (partially) solidified mantle and magma ocean. This configuration has been investigated using gallium for the metal layer, and glucose solutions with different viscosities and densities to model the solid mantle and magma ocean [148, 154]. Like in the two-layer system, the interface between the dense metal layer and the underlying viscous liquid destabilizes through a Rayleigh–Taylor instability. Figure 8b shows a diapir that developed from this instability [148]. The structure differs markedly from the diapirs obtained in two-layer experiments (Figure 8a). The diapir has a shape close to hemispherical, with a flat trailing edge, and is followed by a trailing conduit filled with liquid from the upper layer (liquid s1 on the figure) corresponding to the magma ocean [148, 154]. The persistence of the trailing conduit is allowed by the slow viscous relaxation of the surrounding viscous liquid (s2). Compared to a spherical diapir, these "half diapirs" are faster. The drag is indeed reduced by the presence of the low viscosity trailing conduit on the trailing side of the half diapir [148].

Previous studies [148, 154] have also investigated the gravitational instability of metal emulsions, under the hypothesis that the metal droplets resulting from the fragmentation of impactor cores did not fully coalesce before migrating through the solid part of the mantle (either because coalescence is slow, or because the residence time of droplets in the magma ocean is larger than τ_{RT}). Figure 8c shows snapshots from an experiment of this type. The metal migrates as a two-phase plume consisting of a coalesced half-diapir followed by a trailing conduit made of metal droplets and low-viscosity liquid. Previous investigations [19, 148, 154] argue that dissipation heating in such metal-silicate plume could heat up both phases and increase the temperature of the metal by ~1000 K. This contrasts with the reference model of Section 4.1.1 which predicts negligible viscous heating of the metal. During a single differentiation event, the diapir transit time is much larger than the sedimentation time of metal droplets, at least with the nominal parameter values that we used. In this limit, the amount of metal droplets in suspension in the trailing conduit and therefore dissipation heating are likely small. However, [148, 154] argue that the conduit can be kept open for a significant time if additional metal is added before the conduit closure by viscous relaxation.

Temperature-dependent viscosity. The effective viscosity of the (partially) solidified mantle depends strongly on temperature and melt fraction. This can have at least two effects:

(i) A vertical stratification in viscosity can affect the wavelength of the most unstable mode of the Rayleigh–Taylor instability [38]. The wavelength λ can be smaller if the effective viscosity increases with depth, though likely not to the degree ($\lambda \sim$ a few km) proposed in 1981 by Stevenson [38], who considered the Rayleigh–Taylor instability of a molten metal layer above a cold and highly viscous non-differentiated layer.

(ii) If the diapir is hotter than the mantle, then the silicate would have a reduced viscosity in the thermal boundary layer surrounding the diapir, which can decrease the drag on the diapir and allow it to fall more rapidly than predicted by Stokes law (42). This has been investigated theoretically [155–157] and experimentally [157, 158] in the context of magma intrusions (plutons)

in Earth's crust. It is found that the drag is a function of *Pe* and of the ratio between the viscosity $\eta_{s,0}$ of the silicate in contact with the diapir and the viscosity $\eta_{s,\infty}$ far from it. Qualitatively, two end-members have been identified: (i) the *Stokes* limit as described in Section 4.1.1, in which the drag is controlled by the viscosity far from the diapir; and (ii) the *lubrication* limit, in which deformation is localized in a thin low viscosity layer coating the forward side of the diapir [157]. Using the prediction of [157] for the boundary between the lubrication and Stokes regimes (and equating the drag force with the buoyancy), we find that a diapir is in the Stokes regime if

$$\frac{\Delta\rho g R^3}{\eta_{s,\infty}\kappa_s}\left(\frac{\eta_{s,0}}{\eta_{s,\infty}}\right)^{1/3}\ln\left(\frac{\eta_{s,\infty}}{\eta_{s,0}}\right)\gtrsim 1. \tag{53}$$

Taking for example $R = 10$ km and $\eta_{s,\infty} = 10^{18}$ Pa·s, this would be verified if $\eta_{s,0} \gtrsim 1$ Pa·s. Any realistic viscosity value for partially molten silicates above the rheological transition brings the diapir well within the Stokes regime. The model described in Section 4.1.1 then gives a good approximation of the diapir dynamics. The low sensitivity of the diapir velocity to the temperature effect on viscosity results from the large *Pe* value of metal diapirs: since the boundary layer thickness is $\sim RPe^{-1/2}$, only a small volume around the diapir would have a reduced viscosity when $Pe \gg 1$. This could only be compensated if $\eta_{s,\infty}/\eta_{s,0} \gg 1$.

Dissipation heating is negligible in laboratory scale experiment, but could possibly affect the diapir velocity by softening a volume of silicates extending outside the thermal boundary layer. As discussed in Section 4.1.1, dissipative heating is expected to be localized in the adjacent mantle, in agreement with numerical simulations having $\eta_s/\eta_m \gg 1$ [46,153]. In addition to be of importance for the thermal evolution of the mantle, this can in principle also affect the velocity of diapirs by softening the surrounding silicates, thus decreasing the transit time. Numerical modelling [45] suggests that the effect on the diapir velocity is relatively weak in the parameters range investigated (a 1.7-fold increase for $\eta_{s,\infty}/\eta_{s,0} = 10^4$). This can be qualitatively understood along the same lines as in the case without dissipation (previous paragraph). In the Stokes regime, the volumetric dissipation rate $\tau : \nabla\mathbf{u}$ (where τ is the deviatoric stress tensor) evolves with distance r from the diapir center as $\sim r^{-4}$ (since the velocity around the diapir decreases as $1/r$). Dissipative heating is therefore localized in the close vicinity of the diapir, and the volume of softened silicate is moderate, and at least not sufficiently large to allow the diapir to be in the lubrication regime.

Diapirism vs. diking. The possibility that the metal migrated through the solid mantle as dikes has been proposed by [38]. In the 1981's paper in which this mechanism was proposed [38], the inner part of the planet was hypothesized to be cold and undifferentiated, with an effective viscosity possibly in excess of 10^{26} Pa·s [43]. In this limit the migration of metal diapirs would have been very slow [38], while the brittle nature of cold mantle rocks would have allowed the propagation of iron-filled cracks (analog to magma dikes in the present-day crust), in a possibly very efficient way [159]. However, whether this mechanism was operative in a hot and soft mantle near or above the solidus is not clear.

The competition between diapirism and diking has been a central question in the context of magma transport in the Earth's crust. Rubin [160] has developed a model of dike propagation in a viscoelastic rock, which predicts that the shape of dikes is not significantly affected by viscous deformation of the host rock if the viscosity of the melt is smaller than some fraction of the viscosity of the host rock. This fraction depends on the ratio of excess pressure in the dike to elastic stiffness of the host rock. Applied to an iron-filled crack, the model predicts negligible effect of viscous deformation on the shape of the dike if the mantle viscosity exceeds $\sim 10^{11}$–10^{14} Pa·s [4]. However, the model is "dike-oriented": by construction, it is a model of dike propagation in which the host rock has a viscoelastic rheology, focusing on how viscosity of

the host rock affects the shape of a volume of magma propagating along a pre-existing crack. It does not consider in a quantitative way the initiation of the crack. Application of the model therefore does not provide a definitive answer to the diapir vs. dike question. Experiments on buoyancy driven crack propagation in a viscoelastic material have been performed by Sumita and Ota [161] around the brittle–ductile transition, using a low concentration agar as the host material and aqueous solutions for the dike. They found that near the transition, the liquid migrates as a hybrid of diapir and dike, with a diapir-like head and a dike-like tail. Whether these diapir-dike hybrids can be of relevance for core/mantle differentiation remains to be explored.

4.2. *Percolation*

When the silicate phase is solid, phase separation may also result from the percolation of molten metal through solid or partially molten silicate. This is possible if the metal forms an interconnected network within the crystalline silicate matrix, which depends on the metal volume fraction and on the capacity of the metal to wet silicate grains. Phase separation through percolation may also be relevant to the separation of liquid metal and silicate at the base of magma oceans during the sedimentation of metal drops, as suggested by [148, 154, 162].

Most of the laboratory work relevant to metal-silicate separation by percolation has been focused on describing the wetting properties and mobility of iron-rich melts in mixtures of silicate crystals and iron alloys at various temperatures and pressures, using an experimental petrology approach [163–167]. As this falls somewhat outside of the scope of this paper, we will not give much details about this approach (a relatively recent review can be found in Section 2.3.1 of [4]), and only list a few salient points. Iron-rich melts with geologically relevant compositions do not wet silicates, except at low pressure ($\lesssim$3 GPa) at high O and S content and perhaps in the lower mantle, though this is debated [4]. As a result, the percolation of iron-rich melt is usually only possible if its volume fraction exceeds a threshold volume fraction (~5 vol%) above which it is interconnected. The threshold melt fraction may be smaller (~1 vol%) if the material undergoes shear deformation [168], though this is also debated [4]. Partial melting of the silicates further complicates the picture, with experiments suggesting the formation of aggregates of silicate crystals and molten iron [169].

In most situations familiar to fluid dynamicists, percolation occurs through a solid, undeformable porous medium, and is described by Darcy's law. In the context of core formation, percolation requires in addition that the porous medium—here the solid silicate matrix—can deform. Indeed, conservation of mass implies that any net radial flux of metal within a planetary body must be accompanied by changes of silicate volume fraction corresponding to either compaction of the silicate matrix (where metal is removed) or decompaction (where metal is added). In other words, the migration of the metal toward the center is only possible if the silicate matrix deforms to make room for the metal at the center of the planet. Models of core formation by percolation must therefore account for the deformation of the matrix.

Consider a two-phase medium made of a silicate matrix with effective dynamic viscosity η_s through which a liquid metal of viscosity η_m is percolating. We denote by k_0 a representative value of the matrix permeability, and by $\Delta\rho$ the density difference between the metal and silicate. We assume that melt fraction, and therefore the melt and matrix velocities, vary spatially over a length scale ℓ. Focusing on the relevant limit of gravity-driven phase separation, one can introduce two velocity scales characteristic of Darcy flow and matrix deformation (or compaction) (see also [170]): the Darcy velocity

$$V_D = \frac{\Delta\rho g k_0}{\eta_m}, \tag{54}$$

which is independent of ℓ, and the compaction velocity

$$V_C = \frac{\Delta\rho g \ell^2}{\eta_s}. \tag{55}$$

The ratio of these two velocity scales is

$$\frac{V_D}{V_C} = \frac{\eta_s}{\eta_m}\frac{k_0}{\ell^2} = \left(\frac{\delta}{\ell}\right)^2, \tag{56}$$

where

$$\delta = \sqrt{\frac{\eta_s}{\eta_m} k_0} \tag{57}$$

is the so-called *compaction length*. This name can be somewhat misleading and care must be taken when interpreting the value of δ. As shown by Equation (56), δ gives the length scale at which Darcy friction and viscous stress associated with matrix deformation affect phase separation to a similar extent. Phase separation is rate-limited by Darcy friction if $\ell \gg \delta$, and by matrix deformation if $\ell \ll \delta$. Both limits are relevant to the core formation problem, depending on the size and state of the planetary body [170].

The rich dynamics coming from the interplay between matrix deformation and Darcy flow is difficult to study experimentally, and has so far been almost exclusively studied from theoretical and numerical point of views [170–173]. To our knowledge the only fluid dynamics experiments devoted to gravity-driven percolation in the context of core formation are the experiments of Sato and Sumita [162], in which two immiscible liquids separate under the action of gravity after having been dispersed by mechanical stirring. Their purpose was to model the separation of molten silicate and metal following the sedimentation of the metal at the base of a magma ocean. They therefore focused on moderate viscosity ratios η_s/η_m (smaller than $\simeq$600), using silicon oil and hydroxyethylcellulose (HEC) solutions as working fluids. Figure 9 shows a snapshot of an experiment using a silicon oil with viscosity 12.1 Pa·s (appearing yellow on the pictures) and a HEC solution with viscosity 0.023 Pa·s (appearing blue). Mixtures of silicon oil and HEC appear green. Interestingly, it was found in these experiments that the most viscous phase forms drops, while the less viscous forms a continuous phase between the drops (Figure 9). Applied to metal-silicate separation at the base of a magma ocean, this would predict that the silicate phase would form drops surrounded by the metal, which is opposite to the standard view of an iron rain. It contrasts with the gallium-glucose mixtures of the experiments discussed in Section 4.1.2 and shown in Figure 8 in which the less viscous phase (gallium) was observed to form drops [148,154].

These experiments can be used to illustrate the difficulty of designing fluid dynamics experiments able to reach regimes in which matrix deformation is of importance for the separation dynamics. The compaction length in these experiments can be estimated from the viscosity values of the two liquids as given by [162] and the permeability law they used to model the experiment, namely the Blake–Kozeny–Carman permeability law

$$k = \frac{a^2}{K_0}\frac{\phi^3}{(1-\phi)^2}, \tag{58}$$

where a is the droplet size and $K_0 \simeq 15$ is an empirical constant. With $a \sim 0.1$ mm as estimated in the paper and a maximum viscosity ratio of $\simeq$600, one finds that δ is at most $\simeq$0.5 mm, which is not much larger than the droplets size. Given the thickness of the tank ($H = 14$ cm $\gg \delta$), phase separation is therefore expected to be controlled by Darcy flow, which is consistent with the measured separation times which are of the order of $\sim H/V_D$ in this set of experiments [162]. Increasing the importance of matrix deformation necessitates to increase the ratio of the compaction length to tank thickness, which can be done by either decreasing the tank thickness or increasing δ. To make sure the mixture can be modelled as a continuum, the tank size has to be much

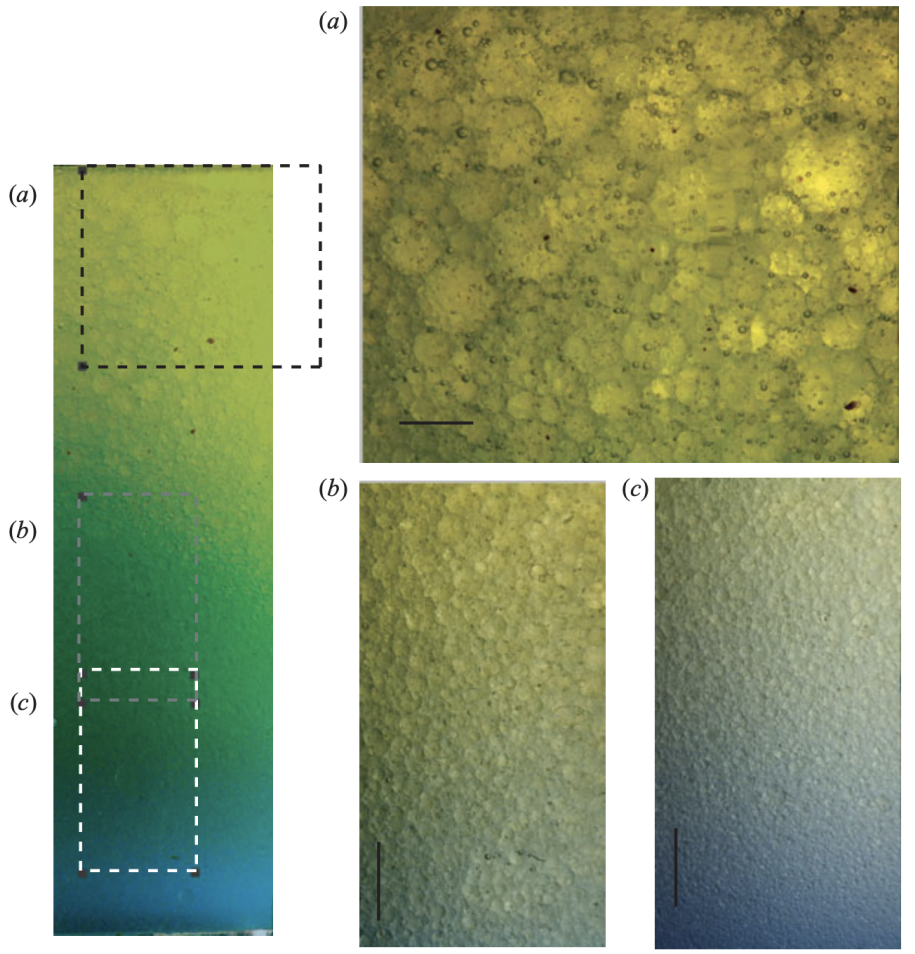


Figure 9. Snapshot from an experiment in which a mixture of silicon oil with viscosity 12.1 Pa·s (appearing yellow on the pictures) and hydroxyethylcellulose (HEC) solution with viscosity 0.023 Pa·s (appearing blue) separate under the action of gravity. The density difference between the HEC solution and the silicon oil is 31 kg·m^{-3}. On the left is shown a vertical section (with a height of 12.8 cm) of the fluid mixture. Subfigures (a), (b), and (c) are close-ups corresponding to the boxes shown on the left figure. The scale bar in (a) is 1 cm. Details on the experiment can be found in [162] Reproduced from Figure 9 of [162], 2007 © Cambridge University Press, reproduced with permission (Licence number 5797030122437).

larger than the drop size, which suggests a tank size of at least a few centimeters as in the experiments of Sato & Sumita. To increase the value of δ, one could use a pair of liquids with a higher viscosity ratio. One may for example use a silicon oil with viscosity 10^3 Pa·s and water (10^{-3} Pa·s) to reach a viscosity ratio of $\sim 10^6$. With a drop size $a \sim 0.1$ mm and assuming the permeability law (58), this would give $\delta \sim 2$ cm. It is therefore in principle possible to design a fluid dynamics experimental set-up that could allow to study gravity-driven separation in a regime in which the matrix deformation velocity and Darcy velocity are of similar magnitudes. However, a number of practical difficulties are to be expected. Among others, one could note that producing emulsions

with small drop size may be an issue with highly viscous liquids, or that longer separation times may increase the importance of drops coalescence, thus complicating the interpretation of the experiments.

5. Conclusion

The experimental fluid mechanics approach has proved relevant to the study of the differentiation of terrestrial planets, complementing the more established numerical modelling approach to the subject. Its main interest lies in its ability to incorporate physical effects and processes that are difficult to account for in numerical simulations, such as turbulence, surface tension and fragmentation, heat and mass transfer at large Péclet numbers, or large viscosity contrasts. Perhaps unexpectedly, experiments using common working fluids at ambient conditions can achieve dynamical conditions that are closer to early Earth conditions than current numerical simulations in terms of several (but not all) of the key governing non-dimensional parameters. In particular, laboratory experiments have allowed to model metal-silicate separation and fragmentation in turbulent conditions, at *Re* and *We* values around 10^4 that are still difficult to reach with numerical simulations.

However, the experimental approach also has important limitations. A number of important effects cannot be investigated easily in fluid dynamics experiments. The effects of compressibility (including shock waves propagation), phase change (melting and vaporisation), or self-gravitation on planetary impacts and differentiation are best studied using numerical models. Even when ignoring these effects, the results of the experiments still must be used with caution, because of the wild extrapolations required to apply them to the early Earth. For example, the metal-silicate equilibration model built from experiments such as described in Section 3 has been incorporated in several geochemical models of core-mantle formations with some success [15, 36, 174]. Yet, the model is incomplete and needs to be refined and further tested. The mechanisms leading to fragmentation and homogenisation in turbulent thermals or during crater opening are not fully elucidated yet, and additional experiments and analysis are needed. A better understanding of fragmentation and mixing in turbulent thermals is essential to give more weight to the extrapolation of experimental results.

Declaration of interests

The authors do not work for, advise, own shares in, or receive funds from any organization that could benefit from this article, and have declared no affiliations other than their research organizations.

Acknowledgments

The authors thank M. Le Bars and S. Fauve for offering them the opportunity to write this review article, and two anonymous reviewers for their very detailed and constructive comments. RD thanks the French Academy of Science and Electricité de France for granting their “Ampère Prize” to the Geodynamo team at ISTerre. This work was supported by the European Research Council (ERC) under the European Unions Horizon 2020 research and innovation programme (grant number 716429). ISTerre is part of Labex OSUG@2020 (ANR10 LABX56). This work was supported by the Programme National de Planétologie (PNP) of CNRS-INSU co-funded by CNES. Funding for this research was supported by the Center for Matter at Atomic Pressure (CMAP), a National Science Foundation (NSF) Physics Frontier Center, under award PHY-2020249. Any opinions, findings, conclusions or recommendations expressed in this material are those of the author(s) and do not necessarily reflect those of the National Science Foundation.

Appendix A. Temperature inside a metal diapir

The model of diapir thermal evolution presented in Section 4.1.1 assumes that the temperature in the diapir is uniform. This assumes that convection within the diapir is strong enough to ensure that temperature variations within the diapir are small compared to the temperature contrast between the diapir and the surrounding mantle. The magnitude of temperature variations within a diapir can be estimated by equating the heat flux associated with convection within the diapir with the mantle-side heat flux controlled by the slow viscous flow around the diapir. We denote by ΔT the temperature difference between the centre of the diapir and the surrounding mantle, and by ΔT_d the difference between the temperature at the centre of the diapir and the mean boundary temperature. The heat flux from the diapir to the mantle, when estimated from the diapir side, can be related to ΔT_d using a scaling law derived from experimental and numerical studies of natural convection in a sphere cooled from its boundary in a uniform (non-radial) gravity field [175–177]. According to these studies, the heat flux associated with internal convection is given by

$$q = a_d k_m \frac{\Delta T_d}{R} Ra_d^{\beta} = a_d k_m \frac{\Delta T}{R} \left(\frac{\Delta T_d}{\Delta T}\right)^{1+\beta} Ra_{\Delta T}^{\beta} \tag{59}$$

where $a_d = 0.553$ and $\beta = 0.2521$ [177], and

$$Ra_d = \frac{\alpha_m g R^3 \Delta T_d}{\nu_m \kappa_m}, \quad Ra_{\Delta T} = \frac{\alpha_m g R^3 \Delta T}{\nu_m \kappa_m}. \tag{60}$$

When estimated on the mantle side, the heat flux is given by

$$q = a k_s \frac{\Delta T - \Delta T_d}{R} Pe^{1/2}. \tag{61}$$

Equating the two expressions for q and re-arranging, we find that

$$\frac{(\Delta T_d/\Delta T)^{1+\beta}}{1-\Delta T_d/\Delta T} = \frac{a_o}{a_d}\frac{k_s}{k_m} Pe^{1/2} Ra_{\Delta T}^{-\beta} \propto R^{0.74}\Delta T^{-0.25} \tag{62}$$

Taking $R = 100$ km and $\Delta T = 100$ K gives $\Delta T_d/\Delta T \simeq 1.3\%$. Taking $R = 500$ km instead gives $\Delta T_d/\Delta T \simeq 3.5\%$. The ratio is smaller when ΔT is greater. This shows that the amplitude of temperature variations within the diapir is small compared to the temperature difference with the surrounding mantle, justifying the assumption of a uniform temperature within the diapir.

References

[1] D. J. Stevenson, "Evolution of the Earth: An introduction and overview", in *Treatise on Geophysics* (G. Schubert, ed.), vol. 9, Elsevier, Oxford, second ed., 2015, ISBN 978-0-444-53803-1, p. 1-9.

[2] A. Morbidelli, W. F. Bottke, D. Nesvornỳ, H. F. Levison, "Asteroids were born big", *Icarus* **204** (2009), no. 2, p. 558-573.

[3] J. I. Lunine, D. P. O'brien, S. N. Raymond, A. Morbidelli, T. Quinn, A. L. Graps, "Dynamical models of terrestrial planet formation", *Adv. Sci. Lett.* **4** (2011), no. 2, p. 325-338.

[4] D. C. Rubie, F. Nimmo, H. J. Melosh, "Formation of the Earth's core", in *Treatise on Geophysics* (G. Schubert, ed.), vol. 9, Elsevier, Oxford, second ed., 2015, ISBN 978-0-444-53803-1, p. 43-79.

[5] B. Wood, M. Walter, J. Wade, "Accretion of the Earth and segregation of its core", *Nature* **441** (2006), no. 7095, p. 825-833.

[6] Q. Yin, S. B. Jacobsen, K. Yamashita, J. Blichert-Toft, P. Telouk, F. Albarede, "A short timescale for terrestrial planet formation from Hf/W chronometry of meteorites", *Nature* **418** (2002), no. 6901, p. 949-952.

[7] T. Kleine, C. Münker, K. Mezger, H. Palme, "Rapid accretion and early core formation on asteroids and the terrestrial planets from Hf-W chronometry", *Nature* **418** (2002), p. 952-955.

[8] J. F. Rudge, T. Kleine, B. Bourdon, "Broad bounds on Earth's accretion and core formation constrained by geochemical models", *Nat. Geosci.* **3** (2010), p. 439-443.

[9] A. Corgne, S. Keshav, B. J. Wood, W. F. McDonough, Y. Fei, "Metal silicate partitioning and constraints on core composition and oxygen fugacity during Earth accretion", *Geochim. Cosmochim. Acta* **72** (2008), p. 574-589.

[10] J. Siebert, A. Corgne, F. J. Ryerson, "Systematics of metal–silicate partitioning for many siderophile elements applied to Earth's core formation", *Geochim. Cosmochim. Acta* **75** (2011), no. 6, p. 1451-1489.
[11] C. K. Gessmann, B. J. Wood, "Potassium in the Earth's core?", *Earth Planet. Sci. Lett.* **200** (2002), p. 63-78.
[12] A. Corgne, S. Keshav, Y. Fei, W. F. McDonough, "How much potassium is in the Earth's core? New insights from partitioning experiments", *Earth Planet. Sci. Lett.* **256** (2007), p. 567-576.
[13] M. A. Bouhifd, L. Gautron, N. Bolfan-Casanova, V. Malavergne, T. Hammouda, D. Andrault, A. P. Jephcoat, "Potassium partitioning into molten iron alloys at high-pressure: Implications for Earth's core", *Phys. Earth Planet. Inter.* **160** (2007), p. 22-33.
[14] J. G. O'Rourke, D. J. Stevenson, "Powering Earth's dynamo with magnesium precipitation from the core", *Nature* **529** (2016), no. 7586, p. 387-389.
[15] J. Badro, J. Siebert, F. Nimmo, "An early geodynamo driven by exsolution of mantle components from Earth's core", *Nature* **536** (2016), no. 7616, p. 326-328.
[16] J. Siebert, J. Badro, D. Antonangeli, F. J. Ryerson, "Metal–silicate partitioning of Ni and Co in a deep magma ocean", *Earth Planet. Sci. Lett.* **321** (2012), p. 189-197.
[17] J. Badro, J. P. Brodholt, H. Piet, J. Siebert, F. J. Ryerson, "Core formation and core composition from coupled geochemical and geophysical constraints", *Proc. Natl. Acad. Sci.* **112** (2015), no. 40, p. 12310-12314.
[18] R. A. Fischer, Y. Nakajima, A. J. Campbell *et al.*, "High pressure metal-silicate partitioning of Ni, Co, V, Cr, Si, and O", *Geochim. Cosmochim. Acta* **167** (2015), p. 177-194.
[19] C. King, P. Olson, "Heat partitioning in metal-silicate plumes during Earth differentiation", *Earth Planet. Sci. Lett.* **304** (2011), no. 3-4, p. 577-586.
[20] V. Clesi, R. Deguen, "Linking the core heat content to Earth's accretion history", *Geochem. Geophys. Geosyst.* **24** (2023), no. 5, article no. e2022GC010661.
[21] S. Labrosse, C. Jaupart, "Thermal evolution of the Earth: Secular changes and fluctuations of plate characteristics", *Earth Planet. Sci. Lett.* **260** (2007), p. 465-481.
[22] J.-P. Williams, F. Nimmo, "Thermal evolution of the Martian core: Implications for an early dynamo", *Geology* **32** (2004), p. 97-100.
[23] J. Monteux, A. M. Jellinek, C. L. Johnson, "Why might planets and moons have early dynamos?", *Earth Planet. Sci. Lett.* **310** (2011), no. 3, p. 349-359.
[24] A. Halliday, "Mixing, volatile loss and compositional change during impact-driven accretion of the Earth", *Nature* **427** (2004), no. 6974, p. 505-509.
[25] T. Kleine, K. Mezger, H. Palme, C. Münker, "The W isotope evolution of the bulk silicate Earth: Constraints on the timing and mechanisms of core formation and accretion", *Earth Planet. Sci. Lett.* **228** (2004), p. 109-123.
[26] F. Nimmo, D. P. O'Brien, T. Kleine, "Tungsten isotopic evolution during late-stage accretion: Constraints on Earth–Moon equilibration", *Earth Planet. Sci. Lett.* **292** (2010), no. 3-4, p. 363-370.
[27] A. N. Halliday, B. J. Wood, "The composition and major reservoirs of the earth around the time of the moon-forming giant impact", in *Treatise on Geophysics* (G. Schubert, ed.), vol. 9, Elsevier, Oxford, second ed., 2015, ISBN 978-0-444-53803-1, p. 11-42.
[28] V. R. Murthy, "Early differentiation of the earth and the problem of mantle siderophile elements: A new approach", *Science* **253** (1991), no. 5017, p. 303-306.
[29] A. Ringwood, "Chemical evolution of the terrestrial planets", *Geochim. Cosmochim. Acta* **30** (1966), no. 1, p. 41-104.
[30] J. Li, C. Agee, "Geochemistry of mantle–core differentiation at high pressure", *Nature* **381** (1996), no. 6584, p. 686-689.
[31] N. Chabot, D. Draper, C. Agee, "Conditions of core formation in the Earth: Constraints from Nickel and Cobalt partitioning", *Geochim. Cosmochim. Acta* **69** (2005), no. 8, p. 2141-2151.
[32] J. Siebert, J. Badro, D. Antonangeli, F. J. Ryerson, "Terrestrial accretion under oxidizing conditions", *Science* **339** (2013), no. 6124, p. 1194-1197.
[33] J. Wade, B. J. Wood, "Core formation and the oxidation state of the Earth", *Earth Planet. Sci. Lett.* **236** (2005), p. 78-95.
[34] B. J. Wood, "Accretion and core formation: Constraints from metal–silicate partitioning", *Philos. Trans. R. Soc. A: Math. Phys. Eng. Sci.* **366** (2008), no. 1883, p. 4339-4355.
[35] D. C. Rubie, D. J. Frost, U. Mann, "Heterogeneous accretion, composition and core–mantle differentiation of the Earth", *Earth Planet. Sci. Lett.* **301** (2011), no. 1, p. 31-42.
[36] D. C. Rubie, S. A. Jacobson, D. P. O'Brien, E. D. Young, J. de Vries, F. Nimmo, H. Palme, D. J. Frost, "Accretion and differentiation of the terrestrial planets with implications for the compositions of early-formed Solar System bodies and accretion of water", *Icarus* **248** (2015), p. 89-108.
[37] V. Lherm, *Dynamique du fractionnement thermique et chimique lors de la différenciation des planètes telluriques*, Phd thesis, Université de Lyon, 2021, https://theses.hal.science/tel-03377150.
[38] D. J. Stevenson, "Models of the Earth's core", *Science* **214** (1981), no. 4521, p. 611-619.
[39] W. B. Tonks, H. J. Melosh, "Core formation by giant impacts", *Icarus* **100** (1992), no. 2, p. 326-346.

[40] W. B. Tonks, H. J. Melosh, "Magma ocean formation due to giant impacts", *J. Geophys. Res.* **98** (1993), p. 5319-5333.
[41] J. T. Gu, R. A. Fischer, M. C. Brennan, M. S. Clement, S. A. Jacobson, N. A. Kaib, D. P. O'Brien, S. N. Raymond, "Comparisons of the core and mantle compositions of earth analogs from different terrestrial planet formation scenarios", *Icarus* **394** (2023), article no. 115425.
[42] D. J. Stevenson, "Fluid dynamics of core formation", in *Origin of the Earth* (H. E. Newsom, J. H. Jones, eds.), Oxford University Press, New York, 1990, p. 231-249.
[43] S.-i. Karato, V. R. Murthy, "Core formation and chemical equilibrium in the Earth—I. Physical considerations", *Phys. Earth Planet. Inter.* **100** (1997), no. 1-4, p. 61-79.
[44] D. C. Rubie, H. J. Melsoh, J. E. Reid, C. Liebske, K. Righter, "Mechanisms of metal-silicate equilibration in the terrestrial magma ocean", *Earth Planet. Sci. Lett.* **205** (2003), no. 3-4, p. 239-255.
[45] H. Samuel, P. J. Tackley, "Dynamics of core formation and equilibration by negative diapirism", *Geochem. Geophys. Geosyst.* **9** (2008), no. 6, article no. Q06011.
[46] J. Monteux, Y. Ricard, N. Coltice, F. Dubuffet, M. Ulvrova, "A model of metal–silicate separation on growing planets", *Earth Planet. Sci. Lett.* **287** (2009), no. 3-4, p. 353-362.
[47] Y. Thibault, M. J. Walter, "The influence of pressure and temperature on the metal-silicate partition coefficients of nickel and cobalt in a model C1 chondrite and implications for metal segregation in a deep magma ocean", *Geochim. Cosmochim. Acta* **59** (1995), no. 5, p. 991-1002.
[48] S. R. Taylor, M. D. Norman, "Accretion of differentiated planetesimals to the Earth", in *Origin of the Earth* (H. E. Newsom, J. H. Jones, eds.), 1990, p. 29-43.
[49] R. C. Greenwood, I. A. Franchi, A. Jambon, P. C. Buchanan, "Widespread magma oceans on asteroidal bodies in the early solar system", *Nature* **435** (2005), no. 7044, p. 916-918.
[50] E. Villermaux, "Mixing versus stirring", *Annu. Rev. Fluid Mech.* **51** (2019), p. 245-273.
[51] E. Villermaux, "Fragmentation versus Cohesion", *J. Fluid Mech.* **898** (2020), article no. P1.
[52] S. N. Raymond, D. P. OBrien, A. Morbidelli, N. A. Kaib, "Building the terrestrial planets: Constrained accretion in the inner solar system", *Icarus* **203** (2009), no. 2, p. 644-662.
[53] G. Morard, J. Siebert, D. Andrault, N. Guignot, G. Garbarino, F. Guyot, D. Antonangeli, "The Earth's core composition from high pressure density measurements of liquid iron alloys", *Earth Planet. Sci. Lett.* **373** (2013), p. 169-178.
[54] F. J. Spera, M. S. Ghiorso, D. Nevins, "Structure, thermodynamic and transport properties of liquid MgSiO3: Comparison of molecular models and laboratory results", *Geochim. Cosmochim. Acta* **75** (2010), p. 1272-1296.
[55] J. P. Poirier, "Transport properties of liquid metals and viscosity of the Earth's core", *Geophys. J. Int.* **92** (1988), no. 1, p. 99-105.
[56] G. A. De Wijs, G. Kresse, L. Vovcadlo, D. Dobson, D. Alfe, M. J. Gillan, G. D. Price, "The viscosity of liquid iron at the physical conditions of the Earth's core", *Nature* **392** (1998), no. 6678, p. 805-807.
[57] B. B. Karki, L. P. Stixrude, "Viscosity of MgSiO3 liquid at Earths mantle conditions: Implications for an early magma ocean", *Science* **328** (2010), no. 5979, p. 740-742.
[58] L. Xie, A. Yoneda, T. Katsura, D. Andrault, Y. Tange, Y. Higo, "Direct viscosity measurement of peridotite melt to lower-mantle conditions: A further support for a fractional magma-ocean solidification at the top of the lower mantle", *Geophys. Res. Lett.* **48** (2021), no. 19, article no. e2021GL094507.
[59] T. Scott, D. L. Kohlstedt, "The effect of large melt fraction on the deformation behavior of peridotite", *Earth Planet. Sci. Lett.* **246** (2006), no. 3-4, p. 177-187.
[60] L. Hansen, D. L. Kohlstedt, "2.18 constitutive equations, rheological behavior, and viscosity of rocks", *Treatise Geophys.* **2** (2015), p. 441-472.
[61] Q. Williams, "The thermal conductivity of Earth's core: A key geophysical parameter's constraints and uncertainties", *Annu. Rev. Earth Planet. Sci.* **46** (2018), no. 1, p. 47-66.
[62] H. Ni, H. Hui, G. Steinle-Neumann, "Transport properties of silicate melts", *Rev. Geophys.* **53** (2015), no. 3, p. 715-744.
[63] H. Terasaki, S. Urakawa, D. C. Rubie, K.-i. Funakoshi, T. Sakamaki, Y. Shibazaki, S. Ozawa, E. Ohtani, "Interfacial tension of Fe–Si liquid at high pressure: Implications for liquid Fe-alloy droplet size in magma oceans", *Phys. Earth Planet. Inter.* **202** (2012), p. 1-6.
[64] V. Solomatov, "Magma oceans and primordial mantle differentiation", in *Treatise on Geophysics* (G. Schubert, ed.), vol. 9, Elsevier, Oxford, second ed., 2015, ISBN 978-0-444-53803-1, p. 81-104.
[65] T. W. Dahl, D. J. Stevenson, "Turbulent mixing of metal and silicate during planet accretion — And interpretation of the Hf–W chronometer", *Earth Planet. Sci. Lett.* **295** (2010), p. 177-186.
[66] R. Deguen, P. Olson, P. Cardin, "Experiments on turbulent metal-silicate mixing in a magma ocean", *Earth Planet. Sci. Lett.* **310** (2011), p. 303-313.
[67] W. Benz, W. L. Slattery, A. G. W. Cameron, "Collisional stripping of Mercury's mantle", *Icarus* **74** (1988), p. 516-528.
[68] R. M. Canup, C. B. Agnor, "Accretion of the terrestrial planets and the Earth–Moon system", in *Origin of the Earth and Moon* (R. M. Canup, K. Righter, eds.), University of Arizona Press, Tucson, AZ, 2000, p. 113-129.

[69] M. Ćuk, S. T. Stewart, "Making the Moon from a fast-spinning Earth: A giant impact followed by resonant despinning", *Science* **338** (2012), no. 6110, p. 1047-1052.
[70] M. Nakajima, D. J. Stevenson, "Melting and mixing states of the Earth's mantle after the Moon-forming impact", *Earth Planet. Sci. Lett.* **427** (2015), p. 286-295.
[71] J. A. Kegerreis, S. Ruiz-Bonilla, V. R. Eke, R. J. Massey, T. D. Sandnes, L. F. Teodoro, "Immediate origin of the moon as a post-impact satellite", *Astrophys. J. Lett.* **937** (2022), no. 2, article no. L40.
[72] J. D. Kendall, H. J. Melosh, "Differentiated planetesimal impacts into a terrestrial magma ocean: fate of the iron core", *Earth Planet. Sci. Lett.* **448** (2016), p. 24-33.
[73] H. Ichikawa, S. Labrosse, K. Kurita, "Direct numerical simulation of an iron rain in the magma ocean", *J. Geophys. Res.* **115** (2010), article no. B01404.
[74] H. Samuel, "A re-evaluation of metal diapir breakup and equilibration in terrestrial magma oceans", *Earth Planet. Sci. Lett.* **313** (2012), p. 105-114.
[75] R. Deguen, M. Landeau, P. Olson, "Turbulent metal-silicate mixing, fragmentation, and equilibration in magma oceans", *Earth Planet. Sci. Lett.* **391** (2014), p. 274-287.
[76] M. Landeau, R. Deguen, D. Phillips, J. A. Neufeld, V. Lherm, S. B. Dalziel, "Metal-silicate mixing by large Earth-forming impacts", *Earth Planet. Sci. Lett.* **564** (2021), article no. 116888.
[77] V. Lherm, R. Deguen, T. Alboussière, M. Landeau, "Rayleigh–Taylor instability in impact cratering experiments", *J. Fluid Mech.* **937** (2022), article no. A20.
[78] Q. Kriaa, M. Landeau, M. Le Bars, "Influence of planetary rotation on metal-silicate mixing and equilibration in a magma ocean", *Phys. Earth Planet. Inter.* **352** (2024), article no. 107168.
[79] H. J. Melosh, in *Impact Cratering: A Geologic Process* (H. J. Melosh, ed.), Oxford Monographs on Geology and Geophysics, No. 11, Oxford University Press, New York, 1989, p. 253.
[80] K. A. Holsapple, "The scaling of impact processes in planetary sciences", *Annu. Rev. Earth Planet. Sci.* **21** (1993), p. 333-373.
[81] E. Pierazzo, N. Artemieva, E. Asphaug *et al.*, "Validation of numerical codes for impact and explosion cratering: Impacts on strengthless and metal targets", *Meteorit. Planet. Sci.* **43** (2008), no. 12, p. 1917-1938.
[82] H. Nagaoka, S. Takasawa, A. M. Nakamura, K. Sangen, "Degree of impactor fragmentation under collision with a regolith surface–Laboratory impact experiments of rock projectiles", *Meteorit. Planet. Sci.* **49** (2014), no. 1, p. 69-79.
[83] O. G. Engel, "Crater depth in fluid impacts", *J. Appl. Phys.* **37** (1966), no. 4, p. 1798-1808.
[84] V. Lherm, R. Deguen, "Velocity field and cavity dynamics in drop impact experiments", *J. Fluid Mech.* **962** (2023), article no. A21.
[85] H. Lhuissier, C. Sun, D. Lhose, "Drop fragmentation at impact onto a bath of an immiscible liquid", *Phys. Rev. Lett.* **110** (2013), no. 26, article no. 264503.
[86] A. Maller, M. Landeau, L. Allibert, S. Charnoz, "Condition for metal fragmentation during Earth-forming collisions", *Phys. Earth Planet. Inter.* **352** (2024), article no. 107199.
[87] J. B. Wacheul, M. Le Bars, J. Monteux, J. M. Aurnou, "Laboratory experiments on the breakup of liquid metal diapirs", *Earth Planet. Sci. Lett.* **403** (2014), p. 236-245.
[88] J.-B. Wacheul, M. Le Bars, "Experiments on fragmentation and thermo-chemical exchanges during planetary core formation", *Phys. Earth Planet. Inter.* **276** (2018), p. 134-144.
[89] A. M. Worthington, "On impact with a liquid surface", *Proc. R. Soc. Lond.* **34** (1883), no. 220-223, p. 217-230.
[90] A. M. Worthington, R. S. Cole, "V. Impact with a liquid surface, studied by the aid of instantaneous photography", *Philos. Trans. R. Soc. Lond. Ser. A-Contain. Pap. Math. Phys. Character.* **189** (1897), p. 137-148.
[91] A. M. Worthington, R. S. Cole, "IV. Impact with a liquid surface studied by the aid of instantaneous photography. Paper II", *Philos. Trans. R. Soc. Lond. Ser. A-Contain. Pap. Math. Phys. Character.* **194** (1900), no. 252-261, p. 175-199.
[92] O. G. Engel, "Initial pressure, initial flow velocity, and the time dependence of crater depth in fluid impacts", *J. Appl. Phys.* **38** (1967), no. 10, p. 3935-3940.
[93] A. Prosperetti, H. N. Oguz, "The impact of drops on liquid surfaces and the underwater noise of rain", *Annu. Rev. Fluid Mech.* **25** (1993), no. 1, p. 577-602.
[94] J.-L. Liow, "Splash formation by spherical drops", *J. Fluid Mech.* **427** (2001), p. 73-105.
[95] A. I. Fedorchenko, A.-B. Wang, "On some common features of drop impact on liquid surfaces", *Phys. Fluids* **16** (2004), no. 5, p. 1349-1365.
[96] A. Bisighini, G. E. Cossali, C. Tropea, I. V. Roisman, "Crater evolution after the impact of a drop onto a semi-infinite liquid target", *Phys. Rev. E* **82** (2010), no. 3, article no. 036319.
[97] B. Ray, G. Biswas, A. Sharma, "Regimes during liquid drop impact on a liquid pool", *J. Fluid Mech.* **768** (2015), p. 492-523.
[98] V. Lherm, R. Deguen, T. Alboussière, M. Landeau, "Rayleigh–Taylor instability in drop impact experiments", *Phys. Rev. Fluids* **6** (2021), no. 11, article no. 110501.
[99] U. Jain, M. Jalaal, D. Lohse, D. van der Meer, "Deep pool water-impacts of viscous oil droplets", *Soft Matter* **15** (2019), no. 23, p. 4629-4638.

[100] M. Hadj-Achour, N. Rimbert, M. Gradeck, R. Meignen, "Fragmentation of a liquid metal droplet falling in a water pool", *Phys. Fluids* **33** (2021), no. 10, article no. 103315.
[101] M. V. Gielen, P. Sleutel, J. Benschop *et al.*, "Oblique drop impact onto a deep liquid pool", *Phys. Rev. Fluids* **2** (2017), no. 8, article no. 083602.
[102] L. Allibert, M. Landeau, R. Röhlen, A. Maller, M. Nakajima, K. Wünnemann, "Planetary impacts: Scaling of crater depth from subsonic to supersonic conditions", *J. Geophys. Res.: Planets* **128** (2023), no. 8, article no. e2023JE007823.
[103] R. E. Breidenthal, "Sonic eddy-a model for compressible turbulence", *AIAA J.* **30** (1992), no. 1, p. 101-104.
[104] J. B. Freund, S. K. Lele, P. Moin, "Compressibility effects in a turbulent annular mixing layer. Part 1. Turbulence and growth rate", *J. Fluid Mech.* **421** (2000), p. 229-267.
[105] C. Pantano, S. Sarkar, "A study of compressibility effects in the high-speed turbulent shear layer using direct simulation", *J. Fluid Mech.* **451** (2002), no. 1, p. 329-371.
[106] G. L. Brown, A. Roshko, "On density effects and large structure in turbulent mixing layers", *J. Fluid Mech.* **64** (1974), p. 775-816.
[107] E. Pierazzo, H. J. Melosh, "Understanding oblique impacts from experiments, observations, and modeling", *Annu. Rev. Earth Planet. Sci.* **28** (2000), no. 1, p. 141-167.
[108] D. E. Gault, J. A. Wedekind, "Experimental studies of oblique impact", in *Lunar and Planetary Science Conference, 9th, Houston, Tex., March 13–17, 1978, Proceedings. Volume 3. (A79-39253 16-91) New York*, vol. 9, Pergamon Press, Inc., 1978, p. 3843-3875.
[109] E. Pierazzo, H. J. Melosh, "Melt production in oblique impacts", *Icarus* **145** (2000), no. 1, p. 252-261.
[110] G. Leneweit, R. Koehler, K. G. Roesner, G. Schäfer, "Regimes of drop morphology in oblique impact on deep fluids", *J. Fluid Mech.* **543** (2005), p. 303-331.
[111] T. Okawa, T. Shiraishi, T. Mori, "Effect of impingement angle on the outcome of single water drop impact onto a plane water surface", *Exp. Fluids* **44** (2008), p. 331-339.
[112] J.-B. Wacheul, R. Deguen, "A laboratory model for oblique planetary impacts" (in preparation).
[113] G. K. Batchelor, "Heat convection and buoyancy effects in fluids", *Q. J. R. Met. Soc.* **80** (1954), p. 339-358.
[114] B. R. Morton, G. Taylor, J. S. Turner, "Turbulent gravitational convection from maintained and instantaneous sources", *Proc. R. Soc. Lond. Ser. A, Math. Phys. Sci.* **234** (1956), p. 1-23.
[115] R. S. Scorer, "Experiments on convection of isolated masses of buoyant fluid", *J. Fluid Mech. Dig. Arch.* **2** (1957), no. 06, p. 583-594.
[116] B. Woodward, "The motion in and around isolated thermals", *Q. J. R. Meteorol. Soc.* **85** (1959), no. 364, p. 144-151.
[117] J. S. Turner, "Buoyant plumes and thermals", *Annu. Rev. Fluid Mech.* **1** (1969), no. 1, p. 29-44.
[118] D. Lecoanet, N. Jeevanjee, "Entrainment in resolved, dry thermals", *J. Atmosph. Sci.* **76** (2019), no. 12, p. 3785-3801.
[119] R. Deguen, M. Lasbleis, "Fluid dynamics of Earth's core: geodynamo, inner core dynamics, core formation", in *Fluid Mechanics of Planets and Stars* (M. Le Bars, D. Lecoanet, eds.), Springer, 2020, p. 129-212.
[120] D. Lecoanet, N. Jeevanjee, "Entrainment in resolved, dry thermals", *J. Atmosph. Sci.* **76** (2019), no. 12, p. 3785-3801.
[121] A. C. Lai, B. Zhao, A. W.-K. Law, E. E. Adams, "A numerical and analytical study of the effect of aspect ratio on the behavior of a round thermal", *Environ. Fluid Mech.* **15** (2015), p. 85-108.
[122] H. Morrison, N. Jeevanjee, D. Lecoanet, J. M. Peters, "What controls the entrainment rate of dry buoyant thermals with varying initial aspect ratio?", *J. Atmos. Sci.* **80** (2023), no. 11, p. 2711-2728.
[123] B. Zhao, A. W. K. Law, A. C. H. Lai, E. E. Adams, "On the internal vorticity and density structures of miscible thermals", *J. Fluid Mech.* **722** (2013), article no. R5.
[124] M. Landeau, R. Deguen, P. Olson, "Experiments on the fragmentation of a buoyant liquid volume in another liquid", *J. Fluid Mech.* **749** (2014), p. 478-518.
[125] L. Huguet, V. Lherm, R. Deguen, T. Le Borgne, J. Heyman, "On the self-similarity of turbulent thermals", *J. Fluid Mech.* (in preparation).
[126] B. A. Ayotte, H. J. Fernando, "The motion of a turbulent thermal in the presence of background rotation", *J. Atmos. Sci.* **51** (1994), no. 13, p. 1989-1994.
[127] K. R. Helfrich, "Thermals with background rotation and stratification", *J. Fluid Mech.* **259** (1994), p. 265-280.
[128] Q. Kriaa, E. Subra, B. Favier, M. Le Bars, "Effects of particle size and background rotation on the settling of particle clouds", *Phys. Rev. Fluids* **7** (2022), no. 12, article no. 124302.
[129] R. Deguen, P. Olson, P. Cardin, "Experiments on turbulent metal-slicate mixing in a magma ocean", *Earth Planet. Sci. Lett.* **310** (2011), no. 3-4, p. 303-313.
[130] J. W. M. Bush, B. A. Thurber, F. Blanchette, "Particle clouds in homogeneous and stratified environments", *J. Fluid Mech.* **489** (2003), p. 29-54.
[131] J.-B. Wacheul, M. Le Bars, "Fall and fragmentation of liquid metal in a viscous fluid", *Phys. Rev. Fluids* **2** (2017), no. 9, article no. 090507.
[132] P. Marmottant, E. Villermaux, "On spray formation", *J. Fluid Mech.* **498** (2004), p. 73-111.

[133] J. O. Hinze, "Fundamentals of the hydrodynamic mechanism of splitting in dispersion processes", *AIChE. J.* **1** (1955), no. 3, p. 289-295.
[134] B. Qaddah, J. Monteux, V. Clesi, M. A. Bouhifd, M. Le Bars, "Dynamics and stability of an iron drop falling in a magma ocean", *Phys. Earth Planet. Inter.* **289** (2019), p. 75-89.
[135] J.-B. Wacheul, *Étude de la fragmentation de métal liquide en chute libre dans un environnement visqueux: application à la formation des planètes— Theses. fr.*, Phd thesis, Aix-Marseille, 2019.
[136] M. P. Escudier, T. Maxworthy, "On the motion of turbulent thermals", *J. Fluid Mech.* **61** (1973), no. 03, p. 541-552.
[137] M. Landeau, P. Olson, R. Deguen, B. H. Hirsh, "Core merging and stratification following giant impact", *Nat. Geosci.* **9** (2016), no. 10, p. 786-789.
[138] D. Martin, R. Nokes, "Crystal settling in a vigorously convecting magma chamber", *Nature* **332** (1988), no. 6164, p. 534-536.
[139] D. Martin, R. Nokes, "A fluid-dynamical study of crystal settling in convecting magmas", *J. Petrol.* **30** (1989), no. 6, p. 1471-1500.
[140] G. Lavorel, M. Le Bars, "Sedimentation of particles in a vigorously convecting fluid", *Phys. Rev. E* **80** (2009), no. 4, article no. 046324.
[141] V. S. Solomatov, P. Olson, D. J. Stevenson, "Entrainment from a bed of particles by thermal convection", *Earth Planet. Sci. Lett.* **120** (1993), no. 3-4, p. 387-393.
[142] C. Maas, U. Hansen, "Dynamics of a terrestrial magma ocean under planetary rotation: A study in spherical geometry", *Earth Planet. Sci. Lett.* **513** (2019), p. 81-94.
[143] C. Maas, L. Manske, K. Wünnemann, U. Hansen, "On the fate of impact-delivered metal in a terrestrial magma ocean", *Earth Planet. Sci. Lett.* **554** (2021), article no. 116680.
[144] W. M. Elsasser, "Early history of the Earth", in *Earth Science and Meteorites* (J. Geiss, E. D. Goldberg, eds.), North-Holland Pub. Co., Amsterdam, 1963, p. 113-129.
[145] S. Sasaki, K. Nakazawa, "Metal-silicate fractionation in the growing Earth: Energy source for the terrestrial magma ocean", *J. Geophys. Res.: Solid Earth* **91** (1986), no. B9, p. 9231-9238.
[146] S. Ida, Y. Nakagawa, K. Nakazawa, "The Earth's core formation due to the Rayleigh–Taylor instability", *Icarus* **69** (1987), no. 2, p. 239-248.
[147] J. A. Whitehead Jr, D. S. Luther, "Dynamics of laboratory diapir and plume models", *J. Geophys. Res.* **80** (1975), no. 5, p. 705-717.
[148] J. R. Fleck, C. L. Rains, D. S. Weeraratne *et al.*, "Iron diapirs entrain silicates to the core and initiate thermochemical plumes", *Nat. Commun.* **9** (2018), no. 1, article no. 71.
[149] S. Chandrasekhar, *Hydrodynamic and Hydromagnetic Stability*, Dover Publications, Inc., Mineola, New York, 2013.
[150] D. Bercovici, A. Kelly, "The non-linear initiation of diapirs and plume heads", *Phys. Earth Planet. Inter.* **101** (1997), p. 119-130.
[151] R. Clift, J. R. Grace, M. E. Weber, *Bubbles, Drops, and Particles*, Dover Publications, Inc., Mineola, New York, 2005.
[152] M. Ulvrová, N. Coltice, Y. Ricard, S. Labrosse, F. Dubuffet, J. Velímskỳ, O. Šrámek, "Compositional and thermal equilibration of particles, drops, and diapirs in geophysical flows", *Geochem. Geophys. Geosyst.* **12** (2011), no. 10, article no. Q10014.
[153] H. Samuel, P. J. Tackley, M. Evonuk, "Heat partitioning in terrestrial planets during core formation by negative diapirism", *Earth Planet. Sci. Lett.* **290** (2010), no. 1-2, p. 13-19.
[154] P. Olson, D. Weeraratne, "Experiments on metal–silicate plumes and core formation", *Philos. Trans. R. Soc. A: Math. Phys. Eng. Sci.* **366** (2008), no. 1883, p. 4253-4271.
[155] B. D. Marsh, "On the mechanics of igneous diapirism, stoping, and zone melting", *Am. J. Sci.* **282** (1982), no. 6, p. 808-855.
[156] S. Morris, "The effects of a strongly temperature-dependent viscosity on slow flow past a hot sphere", *J. Fluid Mech.* **124** (1982), p. 1-26.
[157] A. Ansari, S. Morris, "The effects of a strongly temperature-dependent viscosity on Stokes's drag law: Experiments and theory", *J. Fluid Mech.* **159** (1985), p. 459-476.
[158] N. M. Ribe, "Diapirism in the Earth's mantle: experiments on the motion of a hot sphere in a fluid with temperature dependent viscosity", *J. Volcanol. Geotherm. Res.* **16** (1983), p. 221-245.
[159] D. J. Stevenson, "Mission to Earth's core—a modest proposal", *Nature* **423** (2003), no. 6937, p. 239-240.
[160] A. M. Rubin, "Dikes vs. diapirs in viscoelastic rock", *Earth Planet. Sci. Lett.* **117** (1993), no. 3-4, p. 653-670.
[161] I. Sumita, Y. Ota, "Experiments on buoyancy-driven crack around the brittle–ductile transition", *Earth Planet. Sci. Lett.* **304** (2011), no. 3-4, p. 337-346.
[162] M. Sato, I. Sumita, "Experiments on gravitational phase separation of binary immiscible fluids", *J. Fluid Mech.* **591** (2007), p. 289-319.
[163] M. C. Shannon, C. B. Agee, "Percolation of core melts at lower mantle conditions", *Science* **280** (1998), no. 5366, p. 1059-1061.

[164] T. Yoshino, M. J. Walter, T. Katsura, "Core formation in planetesimals triggered by permeable flow", *Nature* **422** (2003), no. 6928, p. 154-157.
[165] H. Terasaki, D. J. Frost, D. C. Rubie, F. Langenhorst, "Interconnectivity of Fe–O–S liquid in polycrystalline silicate perovskite at lower mantle conditions", *Phys. Earth Planet. Inter.* **161** (2007), no. 3-4, p. 170-176.
[166] H. Terasaki, D. J. Frost, D. C. Rubie, F. Langenhorst, "Percolative core formation in planetesimals", *Earth Planet. Sci. Lett.* **273** (2008), no. 1-2, p. 132-137.
[167] A. Néri, J. Guignard, M. Monnereau, M. J. Toplis, G. Quitté, "Metal segregation in planetesimals: Constraints from experimentally determined interfacial energies", *Earth Planet. Sci. Lett.* **518** (2019), p. 40-52.
[168] J. W. Hustoft, D. L. Kohlstedt, "Metal-silicate segregation in deforming dunitic rocks", *Geochem. Geophys. Geosyst.* **7** (2006), no. 2, article no. Q02001.
[169] A. Néri, M. Monnereau, J. Guignard, M. Bystricky, C. Tenailleau, B. Duployer, M. J. Toplis, G. Quitté, "Textural evolution of metallic phases in a convecting magma ocean: A 3D microtomography study", *Phys. Earth Planet. Inter.* **319** (2021), article no. 106771.
[170] M. Monnereau, J. Guignard, A. Néri, M. J. Toplis, G. Quitté, "Differentiation time scales of small rocky bodies", *Icarus* **390** (2023), article no. 115294.
[171] O. Šrámek, Y. Ricard, F. Dubuffet, "A multiphase model of core formation", *Geophys. J. Int.* **181** (2010), no. 1, p. 198-220.
[172] O. Šrámek, L. Milelli, Y. Ricard, S. Labrosse, "Thermal evolution and differentiation of planetesimals and planetary embryos", *Icarus* **217** (2012), no. 1, p. 339-354.
[173] T. Lichtenberg, T. Keller, R. F. Katz, G. J. Golabek, T. V. Gerya, "Magma ascent in planetesimals: Control by grain size", *Earth Planet. Sci. Lett.* **507** (2019), p. 154-165.
[174] S. A. Jacobson, D. C. Rubie, J. Hernlund, A. Morbidelli, M. Nakajima, "Formation, stratification, and mixing of the cores of Earth and Venus", *Earth Planet. Sci. Lett.* **174** (2017), p. 375-386.
[175] E. Schmidt, "Versuche zum Wärmeübergang bei natürlicher Konvektion", *Chemie Ingenieur Technik* **28** (1956), no. 3, p. 175-180.
[176] M. Y. Chow, R. G. Akins, "Pseudosteady-state natural convection inside spheres", *J. Heat Transfer* **97** (1975), no. 1, p. 54-59.
[177] J. Hutchins, E. Marschall, "Pseudosteady-state natural convection heat transfer inside spheres", *Int. J. Heat Mass Transfer* **32** (1989), no. 11, p. 2047-2053.

ACADÉMIE DES SCIENCES
INSTITUT DE FRANCE

Comptes Rendus. Physique
2024, Vol. 25, Special issue S3, p. 379-426
https://doi.org/10.5802/crphys.198

Review article / *Article de synthèse*

Geophysical and astrophysical fluid dynamics in the laboratory / *Dynamique des fluides géophysiques et astrophysiques au laboratoire*

Baroclinic instability from an experimental perspective

L'instabilité barocline d'un point de vue expérimental

Uwe Harlander [*, a], **Michael V. Kurgansky** [b], **Kevin Speer** [c] **and Miklos Vincze** [d]

[a] BTU Cottbus-Senftenberg, Dept. Aerodynamics and Fluid Mechanics, Siemens-Halske-Ring 15a, 03046 Cottbus, Germany

[b] A.M. Obukhov Institute of Atmospheric Physics, Russian Academy of Sciences, Pyzhevsky 3, 119017 Moscow, Russia

[c] Geophysical Fluid Dynamics Institute and Department of Scientific Computing, Florida State University, Tallahassee, 32306, FL USA

[d] Eötvös Loránd University Department of Materials Physics and HUN-REN-ELTE Theoretical Physics Research Group, Theoretical Physics Research Group, Budapest, H-1117, Hungary; Institute of Earth Physics and Space Science (HUN-REN EPSS), Sopron, H-9400, Hungary

E-mails: uwe.harlander@b-tu.de (U. Harlander), kurgansk@ifaran.ru (M. V. Kurgansky), kspeer@fsu.edu (K. Speer), mvincze@general.elte.hu (M. Vincze)

Abstract. In the mid-latitude atmosphere, synoptic eddies carry heat *and* momentum towards the poles and are hence a major element shaping weather and climate. The eddies are due to baroclinic instability caused by a supercritical vertical wind shear, which in turn is due to a supercritical meridional temperature gradient. Since the 1950s this crucial instability has systematically been studied with the thermally driven rotating annulus laboratory experiment. In this review, we summarize the research on baroclinic instability from the experimenter's perspective covering a period of about three quarters of a century. The fact that it was possible to tie in with the field of atmospheric dynamics, right from the start in the 1950s, makes the experiment unique compared to other experiments representing geophysical flow phenomena. The applications span a wide range of topics, e.g., regime transitions and the route to turbulence in the presence of rotation, or geostrophic turbulence, internal wave generation at baroclinic fronts, tests of operational weather forecasting methods, extreme value distributions with regard to climate, and more. In view of new measurement methods and data processing techniques, the baroclinic instability experiment will continue to be an important complement to numerical methods in the future.

Résumé. Dans l'atmosphère des latitudes moyennes, les tourbillons synoptiques transportent la chaleur et élan vers les pôles et constituent donc un élément majeur du temps et du climat. Les tourbillons sont dus

* Corresponding author

à l'instabilité barocline provoquée par un cisaillement vertical du vent supercritique, lui-même dû à un gradient de température méridien supercritique. Depuis les années 1950, cette instabilité cruciale a été systématiquement étudiée à l'aide de l'expérience de laboratoire de l'anneau rotatif à entraînement thermique. Dans cette revue, nous résumons les recherches sur l'instabilité barocline du point de vue de l'expérimentateur, sur une période d'environ trois quarts de siècle. Le fait qu'il ait été possible d'établir un lien avec le domaine de la dynamique atmosphérique, dès le début dans les années 1950, rend l'expérience unique par rapport à d'autres expériences utilisées pour examiner les phénomènes d'écoulements géophysiques. Les applications couvrent un large éventail de sujets, par exemple les transitions de régime et la voie vers la turbulence géostrophique, la génération d'ondes internes sur les fronts baroclines, les tests de méthodes opérationnelles de prévision météorologique, les distributions de valeurs extrêmes en ce qui concerne le climat, etc. Compte tenu des nouvelles méthodes de mesure et des techniques de traitement des données, l'expérience sur l'instabilité barocline restera à l'avenir un complément important des méthodes numériques.

Keywords. Baroclinic instability, jet streams, Eady waves, Rossby waves.

Mots-clés. Instabilité barocline, courant-jets, ondes de Eady, ondes de Rossby.

Funding. HA 2932/8-1&2 (DFG); HA 2932/17-4 (DFG); PROCOPE (DAAD); State Assignment no. FMWR-2022-0011; Office of Polar Programs no. 1643679; Office of Polar Programs no. 1644172; Office of Polar Programs no. 2148517; OCE 1658479 (Ocean Science).

Manuscript received 9 April 2024, revised 25 July 2024, accepted 5 August 2024.

1. Introduction

Laboratory experiments in baroclinic instability are at least a century old now, and have been reviewed numerous times over the years, beginning perhaps with Fultz's [1] discussion of laboratory experiments as analogues of atmospheric motion. At the time, Fultz's experiments were stirring up ideas concerning the role of eddies in the thermal equilibrium of the planet [2] and Hide had embarked on a series of studies in the laboratory, first meant to reveal circulation related to Earth's dynamo, but soon applied to atmospheric motion [3]. These studies were to become the backbone of rotating annulus experimentation on baroclinic instability. Together with [4], the appearance of Fultz's [2] work and Eady's contemporaneous paper [5], providing an analytical result for the transition from axisymmetric flow to waves, where, in the context of the annulus, the Rossby radius of deformation is similar to the size of the tank, hints at the explosion of scientific effort on baroclinic instability in this postwar period.

While Hide's experiments drove quantitative investigation of the transition between regimes forward, from symmetric to steady or regular waves, quasi-periodic waves, vacillation and more chaotic regimes, Fultz's experiments appear to have helped convince the community of scientists studying weather and dynamics early on of the fundamental role of eddies. Judging from the language of the debate [6] the question of the relative role of the symmetric circulation versus waves in the transfer of heat from equator to pole was still an ongoing and acrimonious debate at the time. Fultz's description of some of his experiments were evidently directed to laboratory analogues of the Polar Jet, leaving open the more global question of multiple jets and eddy-driven cells, but in any case the function of baroclinic wave development and the associated meandering jet carrying heat "poleward" were deep insights to the thermodynamic systems operating in both the lab and atmosphere. The annulus experiment illuminated the notion of a dynamic, detached thermal boundary carrying heat meridionally in a dramatic fashion.

Later, by the time of Hide and Mason's [7] review, extensive previous work had, in their words, already occurred to map out the various regimes of baroclinic instability in the differentially heated rotating annulus. This mapping took place on the Taylor–Rossby number diagram (see Figure 1 and (2), (3) where the Taylor number is modified taking into account the aspect ratio.).

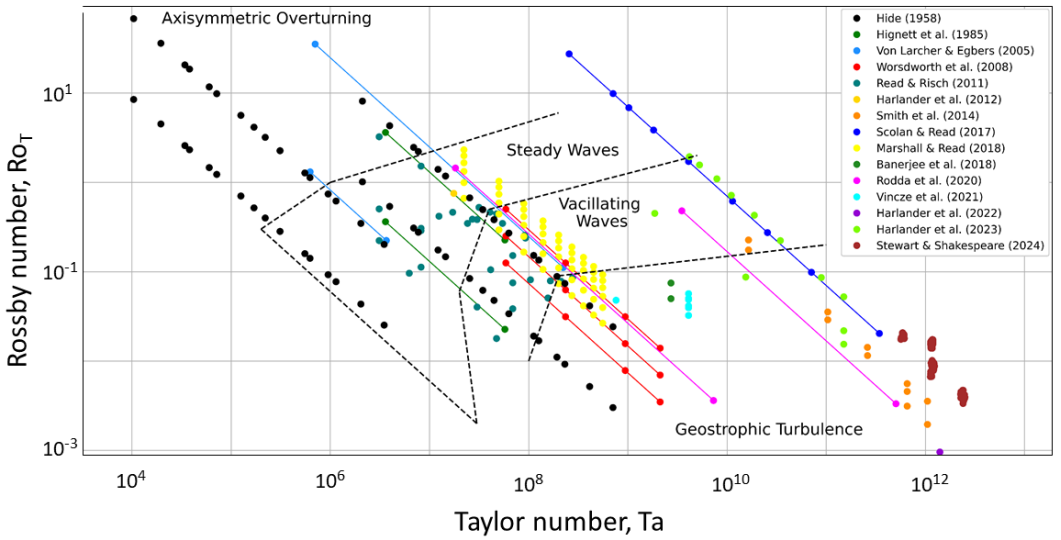


Figure 1. Regime diagram spanned by Ta and Ro_T. Data from different Hide experiments are shown (colored dots). Different flow regimes are indicated: axissymmetric (overturning) flow, steady waves, vacillating waves, and geostrophic turbulence. The Figure is an updated version of [9, Figure 2a].

Although it is important to note that variations in the exact definition of these parameters occur in the literature according to the laboratory configuration or the incorporation of related parameters, both of these parameters represent bulk properties of the system. Gent and Leach [8], on the other hand, performed experiments in an eccentric annulus with variable gap width and found azimuthally-dependent regimes. They made the observation that the parameters are locally important - that the flow structure is determined by local values of these parameters within the system.

In the time frame of the 1970 review [7], the Geophysical Fluid Dynamics Institute (GFDI) at Florida State University (FSU) was formed and devoted, in these early years, to the careful measurement of the time-dependent motion in the large rotating annulus, a new facility set up expressly for this purpose. GFDI publication number 1 by Pfeffer and Fowlis [10] described wave dispersion induced by beating waves of nearby wavenumber and placed this evolution of the circulation onto the regime diagram. Some of the pioneers in the field of laboratory experimentation on baroclinic currents are pictured in Figure 2.

Interestingly, new work still refers back to these early experiments [11] in wave dispersion and vacillation. Subsequent efforts were made especially to quantify amplitude vacillation [12] and the role of topographic forcing [13] neglected in earlier experiments. Later work showed progress in the transition to turbulence [14] and led to the inference that that internal potential vorticity gradients – difficult to measure initially – needed to be more realistic [15]. The notion of an organized transition to turbulence took hold across many fields at the time and the annulus played an important role as a more geophysical representation of such phenomena.

This exciting new subject [16] literally brought chaos to the regime diagram and sharply redefined the role of irregular, quasi-periodic, and other notions under the heading of geostrophic turbulence. The area of transition to turbulence grew to dominate some efforts, for which the baroclinically unstable annulus was an attractive system to explore, more relevant to large-scale geophysical systems than say, Couette flow experiments. At GFDI, the modification of the annu-

lus to include 98 thermistors [17], and, following that, the additional technical achievements to produce an array of 2016 thermistors for a "synoptic network" in the large annulus allowed for a deeper analysis of internal structure and stratification through the transitions among regimes and toward geostrophic turbulence. Details of the vertical structure of waves and eddies, and wavenumber spectra evolution revealed time-dependent characteristics of both amplitude and structural vacillation and better defined turbulent, uncorrelated behavior at highly resolved detail. Früh's [18] excellent review of these and related studies shows the richness of possible states found in the baroclinic annulus experiments, and foundational ideas about the feedback between internal flow and boundary layer structures.

Through these years of laboratory experiments with the rotating annulus, the application of the results was focused mainly on the atmosphere: the role of eddies, and the irregular, unpredictable nature of weather. With north-south continental boundaries that nearly span the globe the role of eddies and waves in the meridional circulation and transport of heat in the ocean was thought to be of a more secondary role. Moreover, the observational record from the ocean with respect to eddy motion lagged that of the atmosphere due largely to the difficulty making measurements from relatively slow-moving ships. But the circumpolar laboratory experiments with flow around Antarctica and the "dishpan" geometry of the Arctic Ocean make laboratory experiments with the baroclinic annulus-type configurations close analogies to these systems as well. Crucially, the deformation radius is so much smaller in the ocean relative to the size of the ocean basins that whole distinct regimes can "fit" into ocean basins, bringing back the notion of local parameters and local regime diagrams for individual oceans rather than a single planetary oceanic regime.

The record of ocean measurement expanded greatly in the 60's and 70's, partly as a result of the use of lagrangian techniques along with standard fixed point moorings. In parallel, laboratory experiments in baroclinic instability were also being carried out with the ocean in mind, to help explain observations that demonstrated the presence of Rossby waves (e.g. [19]) and turbulent mesoscale eddy motions in the ocean (The MODE Group, 1978; see also the review by [20]). Such efforts grew over time to help to comprehend instabilities associated with a vast range of conditions and ocean depths, and both convective and mean flow energy sources.

An early idealized experiment of lasting influence in the oceanographic community was that of Saunders [21], known as the cylinder collapse experiment, in which a volume of dense fluid was allowed to relax in a rotating container of slightly less dense fluid. This simple configuration, both relevant to the ocean and straitforward to model, generated vortices around the edge due to baroclinic instability. Maxworthy and Narimousa [22] carried out a series of experiments with a surface density or buoyancy flux and produced scaling arguments to demonstrate the evolution of these and related instabilities under forced conditions. A natural or "convective" Rossby number-like parameter R^* in these systems is based on a rotation length scale l_{rot}

$$R^* = \frac{l_{rot}}{H}, \quad \text{where} \quad l_{rot} = \left(\frac{B_0}{f^3}\right)^{1/2}, \tag{1}$$

with the fluid depth H, B_0 the buoyancy flux, and $f = 2\Omega$, making apparent the notion of "slope" in sloping convection. While the traditional Rossby number is of order one in the initial state of these convective flows or plumes, the system rapidly evolves toward a dominantly geostrophic balance. Marshall and Schott [23] provide a comprehensive review of laboratory, field, and numerical work in this area of "open-ocean" convection and instability far from lateral boundaries.

While the advent of more effective and powerful numerical modeling techniques in the years following the heyday of annulus experiments dampened to some extent laboratory efforts, at least in the US as funding became more difficult to obtain for the larger technical groups needed

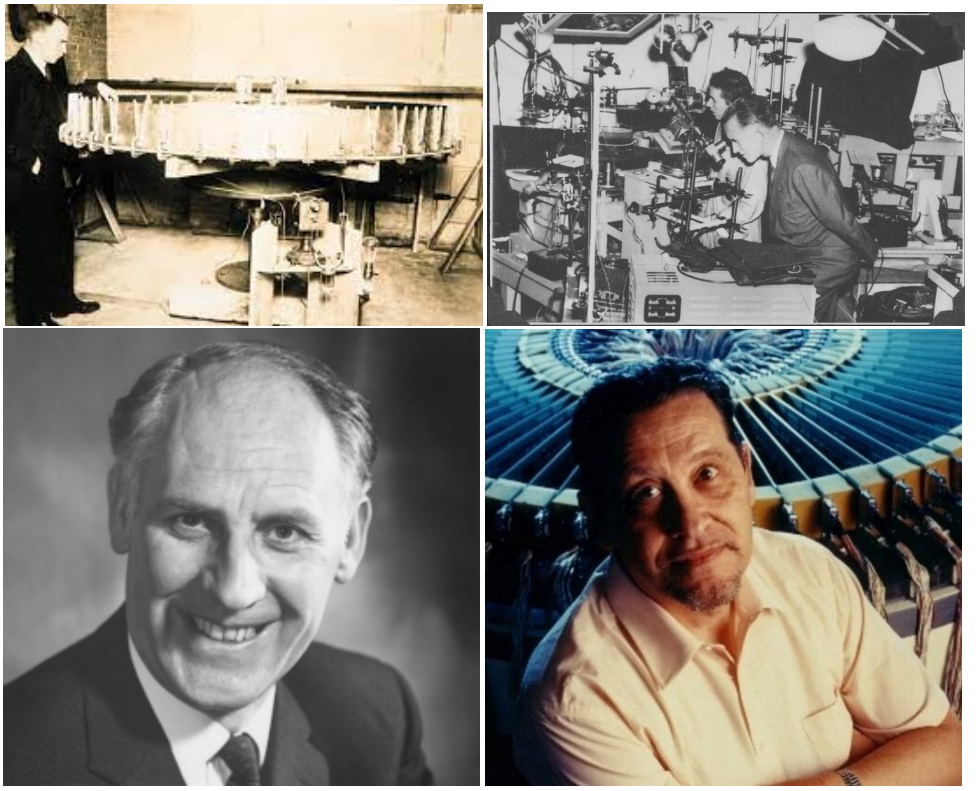


Figure 2. The pioneers (clockwise): Carl-Gustaf Arvid Rossby (Chicago), in front Dave Fultz (Chicago), Richard L. Pfeffer (Florida), and bottom left Raymond Hide (Oxford).

to maintain laboratory facilities, dedicated groups around the world remained very active. These and other later efforts are described in an exhaustive series of reviews by Read and associates [24–27], spanning the extension of laboratory experiments into detailed dynamical descriptions and analyses of the evolving time-dependent flow under various boundary conditions. The body of literature we can only touch upon here provide a broadly framed background to the history of the rotating baroclinic annulus and the vastness of the subject matter available in the laboratory. We are aware of shear-driven experiments (see the early experiments by J.E. Hart, e.g. [28] or the more recent studies by Lovegrove et al. [29] and Williams et al. [30]). Like the thermally driven rotating annulus systems, the mechanically driven open cylinder/annulus systems successfully reproduce the full range of flow regimes, and might allow for more direct verification of theoretical predictions in the laboratory. However, a two-layer density stratification is a very crude approximation to the structure of the atmosphere or ocean, and neglects the feedback of the flow on the stratification. Taking all this into account we focus here almost exclusively on the thermally driven variant. A thorough discussion of shear-driven experiments is well beyond the scope of this review.

New experiments are pointing to the continued relevance of the annulus experiment to climate change, and, for example, to extreme events in climate that may also have analogies in the laboratory [31], just as the early investigations were motivated by the idea of eddy fluxes in the atmosphere. The value of laboratory experiments as idealized testbeds for theory, parameterizations of complex heat, mass, and chemical property fluxes, and as inspiration and for the insight

they provide in and of themselves has not decreased over the years.

1.1. *Governing Nondimensional Parameters*

Returning to the earlier period, Fowlis and Hide [32] listed as many as 18 nondimensional parameters for the rotating differentially heated annulus, some of them not independent, and in the end only a small subset of the total number turned out to be important. To find the *relevant* dimensionless parameters it is perhaps easiest to start with the underlying equations suitable for studying baroclinic waves in the Hide experiment. Considering the Boussinesq equations in a rotating frame of reference and nondimensionalizing the equations by scaling $(\vec{x}, t, \vec{u}, p, T)$ with the factors $(1/L, \nu/L^2, L/\nu, L^2/\rho\nu^2, \kappa/\nu\Delta T)$, where $L = b - a$ is the gap-width, $a(b)$ the inner (outer) radius, ν the kinematic viscosity, ΔT the radial temparature difference, and κ the thermal conductivity, three nondimensional parameters appear in the dimensionless equations, the Rayleigh number Ra, the Taylor number Ta_L, and the Prandtl number Pr

$$Ra = \frac{g\alpha\Delta T L^3}{\nu\kappa}, \quad Ta_L = \frac{4\Omega^2 L^4}{\nu^2}, \quad Pr = \frac{\nu}{\kappa}, \tag{2}$$

where g is the constant of gravity, α the thermal expansion coefficient, and Ω the angular velocity of the cavity rotation. Note that the Ekman number Ek can be written as $Ek = 1/Ta_L^{1/2}$. Hide and Fowlis [32] modified Ta_L respecting different scales for the horizontal and axial direction, $Ta = Ta_L L/d$, where d is the fluid depth. In the literature on the baroclinic wave tank experiment it is common not to use the Rayleigh number but the so called thermal Rossby number, defined as

$$Ro_T = 4\frac{Ra}{Pr\,Ta} = \frac{gd\alpha\Delta T}{\Omega^2 L^2}. \tag{3}$$

The latter corresponds to the classical Rossby number $Ro = U/(\Omega L) = Ro_T$ when U is replaced by the thermal wind

$$U_T = \frac{gd\alpha\Delta T}{\Omega L}. \tag{4}$$

From the boundary conditions of the Boussinesq model two further geometrical parameters result, the radius ratio η_r and the aspect ratio Γ_d

$$\eta_r = \frac{a}{b}, \quad \Gamma_d = \frac{d}{L}. \tag{5}$$

Note that the four parameters, Ta, Ro_T, Pr, Γ_d correspond with $\Pi_5, \Pi_4, \Pi_6, \Pi_2$ in [32] and these parameters turned out to be most relevant in characterizing and comparing flows resulting from different annulus experiments. In fact, usually just Ta and Ro_T are taken to define the parameter space of the experiments. An recent example from [9] summarizing the parameters of Hide experiments covering a period from 1958 to 2024 is shown in Figure 1.

As discussed by [26], there are other nondimensional parameters that are relevant from a more physical point of view. One is the Burger number

$$Bu = \left(\frac{N}{2\Omega}\right)^2 \Gamma_d^2 = \frac{g\alpha\Delta T_v}{(2\Omega)^2 d}\left(\frac{d}{L}\right)^2, \tag{6}$$

a square of the product of the ratio between the buoyancy frequency N and the tank rotation frequency Ω and the aspect ratio. Here ΔT_v denotes the vertical temperature difference. According to the Eady model, this number needs to be small enough for baroclinic instability (see section 2.2 and 3.7.2). Read [26] calls this an "internal parameter" since it cannot be directly set by the experimenter. Note that the Froude number Fr is connected to the Rossby and Burger number via $Fr = U/(Nd) = (Ro_T/2)/Bu^{1/2}$. Assuming that $\Delta T_v \approx \Delta T$ we find $Fr \approx Ro_T^{1/2}$, i.e. $Bu = Ro_T/4$.

For similarity between the experiment and planetary circulations, Ro_T, Γ_d need to be very small, Pr needs to be order one, and Ta needs to be very large. From figure 1 it is obvious that the

conditions are fulfilled for Ro_T and Ta; however, in experiments with fluids like water or silicon oil, Pr is too large. This has an impact on the transition to instability and the complexity of the flow [33], but is not too essential for the process of baroclinic instability.

Figure 1 not only sorts experiments into the $Ta - Ro_T$-parameter space, it is also a regime diagram. Four different flow regimes are indicated: an axisymmetric regime without waves, a steady wave regime, a regime with vacillating waves, and a geostrophic turbulent regime. These regimes and the transitions between them have been discussed in detail, see e.g. [34]. There are further subdivisions into an upper and lower axisymmetric regime, into regimes with amplitude and structural vacillations, and a rich dynamics at the transition to geostrophic turbulence [24]. With the similarity parameters at hand, Read [26] and other authors connected these flow regimes to planetary circulation regimes.

1.2. *The baroclinic wave experimental setup*

The basic layout of the rotating annulus configuration and some of its variations are sketched in figure 3. Raymond Hide began his career using the annulus experiment at Cambridge in the 1950s, working on what was actually planned to be a simple laboratory model to study convection in the rapidly rotating fluid core of the Earth. The geometry of this experiment is shown in Figure 3, upper left picture [35]. The typical "Hide" tank is mounted on a turntable revolving around its axis of symmetry at angular velocity Ω counterclockwise ($\Omega > 0$) or clockwise ($\Omega < 0$) and is divided into three sections by heat conductive co-axial cylindrical walls. The innermost cylinder (radius $r = a$) is referred to as the "cold bath", where water of constant temperature usually below room temperature is circulated through a cooling thermostat (chiller). A separate regulated outer annular water circuit (radius $r = b$) keeps the "warm bath" at a temperature larger than the one in the inner cold cylinder. The inner annular cavity of gap width $L = b - a$ forms the experimental domain, and is filled up with the working fluid (air, water or oil) up to a certain height level. The fluid surface can be closed or is free, and the flow is driven by the

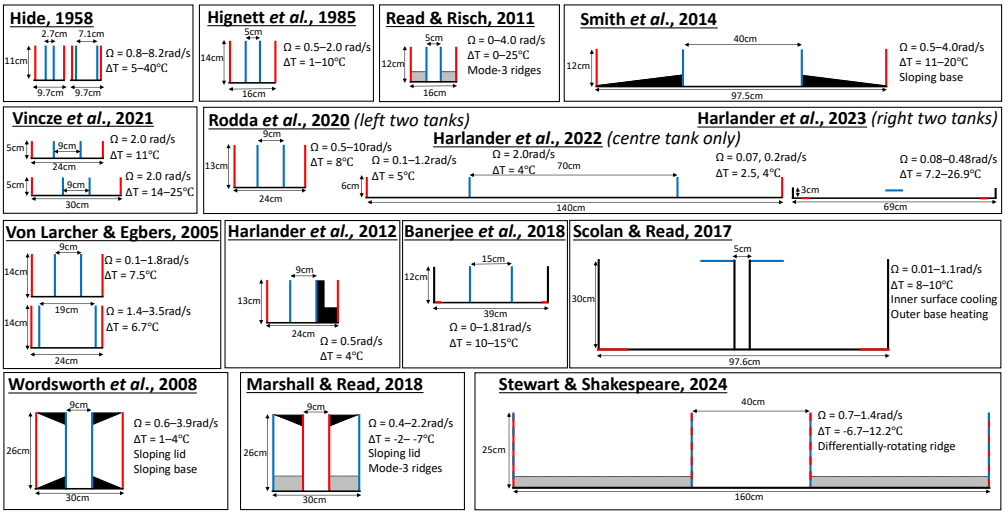


Figure 3. Geometries and setups for heating and cooling of baroclinic wave tanks from the period 1958 to 2024. The Figure is an updated version of [9, Figure 1].

buoyancy flux maintained by the temperature contrast $\Delta T = T_b - T_a$ between the cylindrical walls. This configuration is a barebone representation of the atmosphere at the mid-latitudes of the Northern ($\Omega > 0$) or Southern ($\Omega < 0$) Hemisphere with the inner "cold" cylinder modeling the cold polar regions and the "warm" outer rim the subtropics.

As can be seen in Figure 3, there are several variations of the original Hide setup. Most notable is the use of a topographic β-plane [36,37] allowing Rossby waves and the evolution of multiple jets or local topography [9,37,38] which partially blocks the flow or leads to interactions between stationary topographic waves and Rossby waves. The wide range of different geometries with a tendency towards larger tanks in more recent publications is also striking (compare the size of [35] and [9]). The aspect ratio Γ_d is $\ll 1$ for tanks with a larger gap is hence somewhat closer to atmospheric conditions. Finally we mention variations with respect to the way the cavity is heated/cooled. Scolan and Read [39] did not cool and heat the walls but, in contrast, placed heat sources and sinks at the bottom and top such that Rayleigh–Bénard convection could take place close to the inner and outer wall. Hence local vigorous convection was possible in the "tropical" and "polar" regions of the annulus mimicking the situation of the atmosphere. In such a setup, in between the convective regions, stably-stratified baroclinic motion can still develop in analogy to the mid-latitudes of the Earth's atmosphere. It was observed that, in contrast to the classical configuration, this alternative forcing typically exhibit more spatio-temporal complexity. This was confirmed by later studies [31,40,41].

As with the development towards more complex experiments and more complex questions to be answered with the experiments, the measurement methods used in the experiments also developed. In the early days, the focus was on flow visualisation. This was done, for example, with aluminium flakes floating on the surface [35]. Later, ink, Kalliroscope, Uranine and other substances were added as tracers, which, when illuminated with laser light, produced a fairly complete but only qualitative image of the flow (see Figure 8). Over the years, local flow measurements were done by using Laser Doppler Velocimetry and flow field measurements have been tackled by Particle Image Velocimetry (PIV), e.g. [11].

Temperature has been measured locally by temperature sensors or by arrays of thermocouple probes, e.g. [17,42]. Surface temperature was measured using infrared cameras [43]. The lateral heat transport is an important variable to obtain insight into the eddy dynamics. The total heat transport was determined in the laboratory by real-time calorimetry of the regular baroclinic wave regime accessible in the rotating annulus up to the transition to geostrophic turbulence [44] and in some studies PIV and infrared thermography has been combined to measure the heat transport, e.g, [38].

Before reviewing applications of the annulus experiments in more detail in section 3, we start with a section on the theory of baroclinic instability.

2. Theory of baroclinic instability

At the beginning of the 20$^{\text{th}}$ century, in connection with the problems of applying fluid dynamics to natural environments, such as the atmosphere and ocean (now called geophysical fluids), it became necessary to consider models when the density ρ depends not only on the pressure p, but also on a second independent thermodynamic variable (in the case of two independent thermodynamic functions of state): either temperature T (in Kelvin) or specific (per unit mass) entropy s. In this more complex, but more realistic, model of a baroclinic fluid, the isobaric surfaces $p = const$ and isopycnal surfaces $\rho = const$, generally speaking, no longer coincide with each other, but form an angle or "wedge". In the presence of gravity and in the absence of general fluid rotation, the overturning circulation induced will tend to reduce this angle to zero. However, the presence of the Coriolis force inhibits this overturning motion (cf. [34]), and a

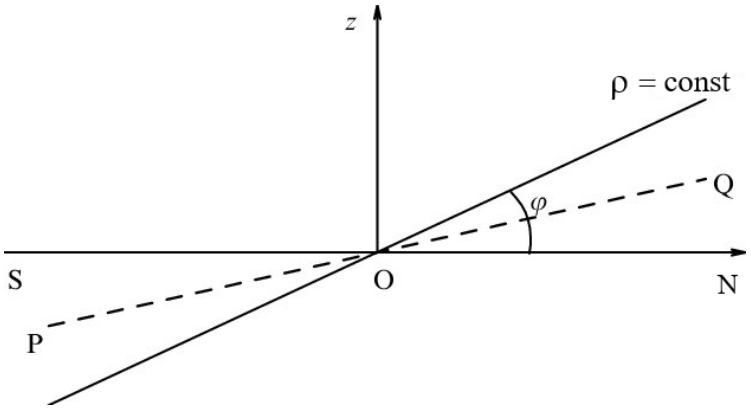


Figure 4. Disposition of isopycnal surfaces accompanying the baroclinic instability, φ is the angle of slope of surfaces $\rho = const$ with respect to the horizontal.

non-zero angle is established between these surfaces in a rotating baroclinic fluid, promoting non-axisymmetric flows ("baroclinic waves") of a general type sometimes called "sloping" or "slantwise" convection (ibid). According to the thermal wind equation, written here for a density-stratified, incompressible fluid

$$\left(2\vec{\Omega}\cdot\nabla\right)\vec{v} \approx \vec{g}\times\nabla\frac{\rho'}{\bar{\rho}}, \tag{7}$$

where $\vec{\Omega}$ is the angular velocity of general fluid rotation, $\vec{v}$ the velocity in a rotating reference frame, $\vec{g}$ the acceleration due to gravity, ρ' the density deviation from the hydrostatically balanced value $\bar{\rho}$, this generally small angle is sustained by the effects of both background fluid rotation and vertical wind shear. Therefore, the baroclinic instability that arises in such a system and is reviewed in this article is equally characterized by the inhomogeneity of the density field on isobaric surfaces and by vertical shear of velocity. An important integral characteristic of the first of these factors is the available potential energy [45–47], which, stored in the basic flow, is used to supply the energy of disturbances during the development of baroclinic instability.

In fact, only trajectories of fluid parcels with slopes between the horizontal and the slope of the mean isopycnal surface can release the available potential energy and lead to generation of baroclinic waves. This is the classic "wedge of instability" argument (see [45]; and Figure 4).

Indeed, when a fluid parcel makes an excursion from point O to either point P or point Q, it will find itself in the ambience of fluid parcels with either smaller (in point P) or, respectively, larger (in point Q) density values. A appearing buoyancy force $\vec{b} \approx \vec{g}(\rho'/\bar{\rho})$ will tend to move the fluid parcel at a greater distance from its initial position. Therefore, baroclinic instability is a specific form of thermal convection and is determined by the mutual configuration of the isopycnal and horizontal surfaces.

A major success of geophysical fluid dynamics in the 20$^{\text{th}}$ century was a rational explanation of why synoptic-scale atmospheric motions, particularly cyclones and anticyclones, have a dominant spatial scale of a few thousand kilometers, i.e., approximately an order of magnitude smaller than the scale at which energy is supplied from the Sun. This was a principal result of the theory of baroclinic instability pioneered by Charney and Eady [4,5]. The main prediction was that the spatial scale of the fastest growing baroclinic disturbances (waves) is limited from below by the characteristic length given by the ratio between the buoyancy frequency times the vertical

length scale and the rotation frequency,

$$L_R = \frac{Nd}{\Omega} = \left(\frac{g\alpha\Delta T_v}{d}\right)^{1/2}\frac{d}{\Omega}, \tag{8}$$

known as the Rossby (internal or baroclinic) radius of deformation. Identifying the vertical temperature contrast ΔT_v with the horizontal ΔT, we find

$$Ro_T = \frac{L_R^2}{L^2} \quad \text{or} \quad Bu = \frac{Ro_T}{4} = \frac{1}{4}\frac{L_R^2}{L^2}, \tag{9}$$

with L the characteristic length-scale. Note that in laboratory experiments with mechanically driven baroclinic instability in a rotating tank (an open cylinder/annulus) filled with a two-layer fluid [28–30], an inverse parameter $F = L^2/L_R^2$ is used, called the internal (rotational) Froude number. For a two-layer fluid $L_R = (gd(\Delta\rho/\rho))^{1/2}/2\Omega$, where $\Delta\rho/\rho$ is the relative density difference between the layers.

For typical atmospheric conditions and a geographical latitude of 45°, the Rossby radius is slightly less than 10^3 kilometers. In the case of the ocean, this radius is (much) smaller and in high latitude regions it is even less than 10 kilometers.

2.1. *Baroclinic instability and nonlinear stability analysis*

In order to unify the presentation and keeping in mind applications to most geophysical fluid media, as well as to the laboratory experiment, we will proceed from the equations of motion of a density-stratified, incompressible fluid in a Coriolis force field in (a) the Boussinesq approximation and (b) the so-called traditional approximation, when the axis of general rotation coincides with the direction of gravity (vertical)

$$\frac{du}{dt} - fv = -\frac{\partial\Phi}{\partial x}, \qquad \frac{dv}{dt} + fu = -\frac{\partial\Phi}{\partial y}, \qquad \frac{dw}{dt} = -\frac{\partial\Phi}{\partial z} + b, \tag{10}$$

and

$$\frac{db}{dt} = 0, \qquad \frac{\partial u}{\partial x} + \frac{\partial v}{\partial y} + \frac{\partial w}{\partial z} = 0. \tag{11}$$

A right-handed Cartesian coordinate system (x, y, z) is used, where in the case of geophysical media (such as the atmosphere and ocean) the x-axis is typically eastward, the y-axis northward, and the z-axis upward (opposite to the direction of gravity); (u, v, w) are the corresponding components of the fluid velocity. The Coriolis parameter, equal to twice the angular velocity of the general rotation, is presented as a linear function of the coordinate y: $f = f_0 + \beta y$, where f_0 and β are constants. Let us recall that $\Phi = \tilde{p}/\rho_0$, where ρ_0 is the constant (reference) value of density and $\tilde{p} = p - p_0(z)$, where $p_0(z) = const - g\rho_0 z$ is the hydrostatic pressure corresponding to the reference state; the variable $b = -g(\rho - \rho_0)/\rho_0$ is called buoyancy; here g is the acceleration due to gravity. In fact, this is the total buoyancy, which is further conveniently presented as the sum of the buoyancy corresponding to the average state of fluid stratification, $\bar{b} = -g\bar{\rho}/\rho_0$, and the deviation from it, $b' = -g\rho'/\rho_0$, assuming that $\rho - \rho_0 = \bar{\rho}(z) + \rho'(x, y, z, t)$. Similarly, $\tilde{p} = \bar{p}(z) + p'(x, y, z, t)$, where $\bar{p}(z)$ and $\bar{\rho}(z)$ are related by the hydrostatic relation, and we rewrite (1), explicitly highlighting the average stable state of the fluid

$$\frac{du}{dt} - fv = -\frac{\partial\Phi'}{\partial x}, \qquad \frac{dv}{dt} + fu = -\frac{\partial\Phi'}{\partial y}, \qquad \frac{dw}{dt} = -\frac{\partial\Phi'}{\partial z} + b', \tag{12}$$

and

$$\frac{db'}{dt} + N^2 w = 0, \qquad \frac{\partial u}{\partial x} + \frac{\partial v}{\partial y} + \frac{\partial w}{\partial z} = 0. \tag{13}$$

In (12) $\Phi' = p'/\rho_0$ and the square of the buoyancy frequency (Brunt–Väisälä frequency) $N^2(z) = -g(d\bar{\rho}/dz)/\rho_0$ is considered a given function. For the atmosphere, $N^2 = const$ is a good approximation away from the lower boundary, but in the ocean the profile $N^2(z)$ is very inhomogeneous: the N^2-value takes on large values in the surface layer and the mid-depth pycnocline region and is small in the deeper layers of the ocean. In a laboratory experiment, when a continuous density profile is concerned, most often a linear decrease in density with height is reproduced, so that $N^2 \approx$ constant.

The motions associated with baroclinic instability, to which this chapter is devoted, are characterized by the fact that hydrostatic and geostrophic relationships are satisfied to a good approximation. We represent the horizontal velocity field in the form $(u, v) = (-\partial\Psi/\partial y, \partial\Psi/\partial x)$, where $\Psi = \Phi'/f_0$ is the geostrophic stream function, and in the quasi-static approximation $b' = f_0(\partial\Psi/\partial z)$. Since in the continuity equation the terms $\partial u/\partial x$ and $\partial v/\partial y$ cancel each other with asymptotic accuracy, the vertical velocity is very small and to a good approximation

$$\frac{d}{dt} = \frac{\partial}{\partial t} - \frac{\partial\Psi}{\partial y}\frac{\partial}{\partial x} + \frac{\partial\Psi}{\partial x}\frac{\partial}{\partial y}. \tag{14}$$

Therefore, eliminating Φ' between the equations of the horizontal motion, we arrive at a system of two equations:

$$\frac{\partial}{\partial t}\nabla^2\Psi + J(\psi, \nabla^2\Psi + \beta y) = f_0\frac{\partial w}{\partial z}, \tag{15}$$

$$\frac{\partial}{\partial t}\frac{\partial\Psi}{\partial z} + J\left(\psi, \frac{\partial\Psi}{\partial z}\right) = -\frac{N^2}{f_0}w. \tag{16}$$

Here, ∇^2 is the two-dimensional Laplacian in the (x, y)-plane and $J(a, b) = (\partial_x a)(\partial_y b) - (\partial_y a)(\partial_x b)$ is the Jacobian. Eliminating the vertical velocity w between equations (15) and (16), we arrive at the equation for the conservation of quasi-geostrophic potential vorticity (in the case of fast annulus rotation and accordingly small Rossby numbers)

$$\frac{\partial q}{\partial t} + J(\psi, q) = 0, \qquad q = \nabla^2\Psi + \frac{\partial}{\partial z}\left(\frac{f_0^2}{N^2}\frac{\partial\Psi}{\partial z}\right) + f_0 + \beta y. \tag{17}$$

Equation (17) is solved with the boundary conditions of impermeability of the lower $z = z_-$ and upper $z = z_+$ boundaries of the fluid layer

$$\frac{\partial b}{\partial t} + J(\Psi, b) = 0, \qquad b = f_0\frac{\partial\Psi}{\partial z}, \qquad z = z_\pm. \tag{18}$$

In the atmosphere, the earth's surface is chosen as the lower boundary $z = z_- = 0$, and the tropopause (where N^2 experiences an upward jump) is taken as the upper boundary, $z = z_+ = H$. In the ocean, it is natural to take its surface $z = z_+ = 0$ as the upper boundary, and the ocean floor as the lower boundary $z = z_- = -D$. In the atmosphere, the buoyancy can be considered proportional to the deviation of the potential temperature from the average value. In liquid media, including the typical laboratory experiment, we take the corresponding temperature deviation.

The general problem of nonlinear Lyapunov stability of a zonal (axially symmetric) flow may be considered under the β-plane approximation. If, initially, we consider a problem with axial symmetry, for example, about a laboratory experiment with a rotating cylindrical annulus, then an approximate theoretical analysis can be carried out in Cartesian coordinates, neglecting the effects of curvature of coordinate lines. This can be done when the corresponding centrifugal forces are much smaller than the Coriolis force (cf. [48]). The flow is assumed to be periodic in the zonal (azimuthal) direction, with a spatial period equal to the average circumference of the channel. The flow is limited laterally by vertical walls. We consider these walls impermeable to

fluid $\partial_x \Psi = 0$, $y = y_*, y^*$, and the velocity circulation on them being preserved for each altitudinal level, $\int (\partial_y \Psi) dx = const$, $y = y_*, y^*$.

We follow Arnold's [49] method, first applied by Blumen [50] for a nonlinear stability study of rotating and stratified Boussinesq fluid flows and use the existence in the problem of constants of motion: (a) energy

$$E = \frac{1}{2} \int\int\int \left((\nabla \Psi)^2 + \frac{f_0^2}{N^2} \left(\frac{\partial \Psi}{\partial z} \right)^2 \right) dx dy dz, \tag{19}$$

as the sum of kinetic and available potential energy; (b) zonal (azimuthal) momentum

$$P = -\int\int\int \frac{\partial \Psi}{\partial y} dx dy dz, \tag{20}$$

and (c) Casimirs, whose conservation follows from (17) and (18):

$$F = \int\int\int \Phi(q,z) dx dy dz, \qquad G = \int_{\Sigma_-} \int \Gamma(b) dx dy, \qquad H = \int_{\Sigma_+} \int H(b) dx dy. \tag{21}$$

Here, Φ, Γ, and H are arbitrary continuously differentiable functions, and $\Sigma_\pm$ are the lower/upper end-walls at $z = z_\pm$, respectively. In the presentation, we follow [50–53].

Now a linear combination of constants of motion $I = E - UP + F + G + H$ is formed, where an arbitrary constant U has the dimension of velocity. Let $\bar{\Psi}(y,z)$ be a stationary zonal flow, the stability of which is being studied. Assuming the deviation $\delta\Psi = \Psi - \bar{\Psi}$ to be small, let us expand $I[\Psi] - I[\bar{\Psi}]$ into a series according to variations of successive orders: $I[\Psi] - I[\bar{\Psi}] = \delta I + (1/2)\delta^2 I^2 + \cdots$. By properly choosing arbitrary functions Φ, Γ, and H it is possible to arrange the series so that for a given $\bar{\Psi}(y,z)$ at any value U the first variation δI becomes zero:

$$\begin{gathered} \Phi'_q \,|_{q=\bar{q}} = \bar{\Psi} + Uy, \quad z_- < z < z_+, \\ \Gamma' \,|_{b=\bar{b}} = \frac{f_0}{N^2} \left(\bar{\Psi} + Uy \right), \quad z = z_-, \quad , H' \,|_{b=\bar{b}} = -\frac{f_0}{N^2} \left(\bar{\Psi} + Uy \right), \quad z = z_+, \end{gathered} \tag{22}$$

The prime at the top denotes differentiation and the subscript q means partial differentiation with respect to that variable. If we assume monotonicity of $\bar{q}$ with the coordinate y for each z, and monotonicity of $\bar{b}$ for $z = z_\pm$, respectively, then these conditions can always be satisfied. Calculating the second variation, we have

$$\begin{aligned} \delta^2 I = & \underbrace{\int\int\int \left((\nabla \delta\Psi)^2 + \frac{f_0^2}{N^2} \left(\frac{\partial \delta\Psi}{\partial z} \right)^2 + \frac{(\partial \bar{\Psi}/\partial y) + U}{\partial \bar{q}/\partial y} (\delta q)^2 \right) dx dy dz}_{\mathrm{A}} \\ & + \underbrace{\int_{\Sigma_-} \int \frac{f_0}{N^2} \frac{(\partial \bar{\Psi}/\partial y) + U}{\partial \bar{b}/\partial y} (\delta b)^2 dx dy}_{\mathrm{B}} - \underbrace{\int_{\Sigma_+} \int \frac{f_0}{N^2} \frac{(\partial \bar{\Psi}/\partial y) + U}{\partial \bar{b}/\partial y} (\delta b)^2 dx dy}_{\mathrm{C}}. \end{aligned} \tag{23}$$

If all coefficients of the squared field variables are positive, then the zonal flow $\bar{\Psi}$ is stable in the Lyapunov sense. This quadratic form is an exact conservation law (constant of motion) for equations linearized with respect to disturbances imposed on the basic flow, and represents a linear combination of pseudo-energy and pseudo-momentum.

What basic flows satisfy this stability criterion? To satisfy the necessary condition $\delta I = 0$, we assumed that $\bar{q}$ is a monotonic function of y. The most natural step is to assume that this is a monotonically increasing function, similar to the Coriolis parameter f. Zonal winds in the atmosphere of mid-latitudes are predominantly westerly, i.e. $\partial \bar{\Psi}/\partial y < 0$. By choosing a constant U greater than the maximum velocity of the basic flow, we find that the volume integral in the first line of (23), the term denoted by A, is positive. This is formally analogous to the transition to a reference frame in which the zonal wind is easterly and the condition for positive definiteness of the volume integral is satisfied (cf. [49]). In the subtropical ocean, zonal currents are directed

to the east and the condition for positive definiteness of the volume integral is satisfied at $U = 0$. The problem is caused by the surface integrals in the second line of (23), the terms denoted by B and C. The potential temperature on the earth's surface decreases monotonically towards the poles, and the integral over the earth's surface, that is, the first term in the second line of (23), term B, is negative, so the second variation is indefinite in sign. The situation is aggravated by the integral taken over the upper boundary, that is, term C in the second line of (23). It is positive if the potential temperature decreases towards the poles, and negative in the opposite case. In any case, the quadratic form (23) is indefinite in sign, and the necessary condition for baroclinic instability is satisfied. If the potential temperature (buoyancy) changes very little at the lower and upper boundaries, then the surface integrals (term B and C) of (23) can be omitted. All that remains is the volume integral A of (23), and we arrive at the Charney–Stern criterion [54], originally derived using the normal mode approach for linearized quasi-geostrophic equations. This criterion states that a basic flow with a monotonically increasing potential vorticity is always stable. The important effects of the lower boundary were incorporated by Pedlosky [55] also using the normal mode approach; see [46]. This gives the Charney-Stern-Pedlosky necessary criterion for linear instability (see [47]).

An interesting case is when the potential vorticity can be considered constant at each height. This is a special idealization, acceptable when considering fairly narrow channels, when the Coriolis parameter can be considered approximately constant and this constancy can be extended to the entire quasi-geostrophic potential vorticity. Now, in (23), the last term in the integrand in the volume integral in the first line, term A, disappears and if the buoyancy has the same sign of growth at the upper and lower boundaries, then baroclinic instability is possible in the problem. Linear instability analysis in the Eady model [5] confirms this situation.

2.2. *Linear stability analysis. Eady Model*

The Eady Model is the most famous model in the theory of baroclinic instability, and it naturally fits the conditions of a laboratory experiment. A vast literature is devoted to it, including whole monographs. We will therefore limit ourselves to a brief formulation of the problem and a presentation of the key results. We assume the constancy of the Coriolis parameter, $f = const$, and of the buoyancy frequency, $N^2 = const$. For mathematical simplicity, we place the origin of coordinates in the middle between the rigid end-walls; then $z_\pm = \pm H/2$, cf. (18). The stream function of the basic flow, whose linear stability is being studied, is chosen, up to an insignificant additive constant, in the form $\bar{\Psi} = -\Lambda yz$. It corresponds to a flow with the velocity profile linear in height $\bar{u} = -\partial\bar{\Psi}/\partial y = \Lambda z$ and the buoyancy field $\bar{b} = f\partial\bar{\Psi}/\partial z = -f\Lambda y$. The flow is considered within a channel with side walls at $y = \pm L/2$, on which the condition $\Psi = 0$ is set.

Let us impose small disturbances on this basic flow and linearize equations (17), (18) with respect to them

$$\left(\frac{\partial}{\partial t} + \Lambda z\frac{\partial}{\partial t}\right)\left(\nabla^2\Psi' + \frac{f^2}{N^2}\frac{\partial^2\Psi'}{\partial z^2}\right) = 0, \tag{24}$$

and the boundary condition

$$\left(\frac{\partial}{\partial t} + \Lambda z\frac{\partial}{\partial x}\right)\frac{\partial\Psi'}{\partial z} - \Lambda\frac{\partial\Psi'}{\partial x} = 0 \quad \text{at} \quad z = \pm H/2. \tag{25}$$

A class of disturbances of the normal mode type, $\Psi' = \hat{\Psi}(z)\exp(ik(x - ct))\sin ly$, is considered. The wave number k is real; $l = n\pi/L$, where n is an integer; the parameter c, generally speaking, is complex and is a proper, spectral parameter of the problem. The basic flow is unstable if c has a positive imaginary part. Discarding the continuous spectrum of the problem, which does

not lead to instability, we arrive from (24) to the equation $d^2\widehat{\Psi}/dz^2 - (k^2/n^2)\widehat{\Psi} = 0$. Its general solution has the form

$$\widehat{\Psi} = A\cosh\lambda z + B\sinh\lambda z, \qquad \lambda^2 = \frac{N^2}{f^2}\left(k^2 + l^2\right). \tag{26}$$

Taking into account the boundary conditions, we have a system of two homogeneous equations with two unknowns A and B, which can be considered real. Equating the determinant of this system to zero, we obtain the characteristic equation for determining the eigenvalue c

$$c^2 = \frac{\Lambda^2}{\lambda^2}\left(\frac{\lambda H}{2} - \coth\frac{\lambda H}{2}\right)\left(\frac{\lambda H}{2} - \tanh\frac{\lambda H}{2}\right). \tag{27}$$

Since $\lambda H/2 > \tanh(\lambda H/2)$, the value $\alpha = \lambda H$ critical for instability is found from the equation $\alpha_c = \coth(\alpha_c/2)$, which has an approximate solution $\alpha_c \approx 2.4$. When $\alpha > \alpha_c$ then the solution to the problem is a superposition of two neutral modes. For $\alpha < \alpha_c$, there are two complex conjugate imaginary roots, i.e. instability is long-wave in nature. The maximum growth rate of the unstable mode kc_i is achieved at $n = 1$, and moreover, we can further consider a wide channel so that $l^2 \ll k^2$ and $\alpha_{max} = \lambda_{max}H \approx 1.61$.

The wavelength of the fastest growing disturbances is given by $L_{max} = (2\pi/1.61)L_R$. Here $L_R = NH/f$ is the baroclinic Rossby deformation radius. The growth rate of this fastest growing mode is equal to (cf. [47]) $(kc_i)_{max} \approx 0.31\Lambda H/L_R = 0.31\Lambda f/N$. This formula is widely used for estimations. Baroclinic instability is also referred to as sloping, or slantwise, convection in a Coriolis force field [34,45,47]. If the fluid motion is to release available potential energy, which is stored in a main zonal flow, and convert it into the perturbation kinetic energy, then fluid particle paths must have a slope between that of the surfaces $z = const$ and $b = N^2 z - f\Lambda y = const$. For the Eady model the maximum rate of such a release is accompanied by the fluid particle path along the bisectrix of an angle $\phi \approx \tan\phi = f\Lambda/N^2 \ll 1$ between the surfaces.

In Eady's model the horizontal spatial scale of the baroclinic instability L_* is set by the vertical scale H of the domain, unlike the Charney's [4] baroclinic approach for a semi-infinite domain with account for the beta-effect (cf. [47]). In Charney's model the vertical scale is defined by $d^{-1} = d_\beta^{-1} + H_0^{-1}$, where $d_\beta = (f_0^2/N^2)(\Lambda/\beta)$ and H_0 is the density scale height [45]. Here, f_0 is a representative value of the Coriolis parameter. This means that if $d_\beta \ll H_0$ then $L_* = Nd_\beta/f_0$; if the inequality is reversed then $L_* = NH_0/f_0$. In Charney's model the maximal growth rate of unstable disturbances σ is of order $\Lambda f_0/N$, regardless of which vertical scale, either d_β or H_0, is used. It is also exactly the scale for the growth rate in Eady's model.

Above, the normal mode method was used for analysis. An alternative is the approach based on consideration of Eady edge waves, proposed in [56] and developed in [57,58] (see also [53]). Baroclinic instability is interpreted as a result of the interaction of these edge waves. The results coincide with those obtained by the normal mode method, but some additional useful results are obtained. Thus, this approach allows us to estimate the phase shift between waves concentrated at the lower and upper boundaries, respectively. For maximally rapidly growing disturbances with $\alpha_{max} \approx 1.61$, this angle is $\approx 47.8°$ [53]. In addition, this approach allows us to determine the characteristics of optimal (fastest growing) disturbances. This refers to nonmodal transient disturbances with instantaneous growth rate which, in virtue of the nonnormality of the linearized dynamical operator, can on finite timescales exceed the growth rate of normal modes, and these transients can stay growing beyond the Eady cutoff scale [56,59]. Unlike the normal mode method, the results significantly depend on the metric used: total energy, kinetic energy, potential energy on end-walls, etc. For two-dimensional disturbances (in the case of no dependence on y) maximization of $\gamma = E^{-1}(dE/dt)$, where E is the total energy, cf. (19), shows that the maximum of $\gamma_{opt}(\alpha)$ is achieved in the limit of long waves $\alpha \to 0$ and $\gamma_{opt}(\alpha)$ monotonically decreases along with an increase in α. The line $\gamma_{opt}(\alpha)$ touches the Eady normal

mode growth rate curve $(kc_i)(\alpha)$ in a point $\alpha \approx 1.915$, which means that the normal mode is an optimal disturbance only for $\alpha \approx 1.915$, which exceeds $\alpha_{max} \approx 1.61$. In this case, the phase shift between the edge Eady waves is $\approx 73.22^\circ$ [53]. In a more general approach, for a fixed point in time (optimization time), an initial disturbance is sought that maximizes the ratio $F = E(t)/E(0)$, where $E(0)$ is the initial energy. In particular, for the optimization time $t = 5(N/\Lambda f)$, the wave number corresponding to the maximum energy ratio is equal to $\alpha_{opt} \approx 1.2$. Details are given in the review [53].

Taking into account Ekman friction at the lower and upper rigid end-walls is reduced to replacing the impermeability condition $w' = 0$ with the condition $w' = w_E = \pm(h_E/2)\nabla^2\Psi'$ at the end-walls at $z = \mp H/2$. Here $h_E = (2\nu/f)^{1/2}$ is the thickness of the Ekman boundary layer, and ν is the kinematic viscosity of the fluid. It is assumed that $h_E \ll H/2$. In this case, the characteristic equation for determining the eigenvalues is replaced by [34]

$$c^2 - 2ic\frac{\Lambda}{\lambda}F\coth(\lambda H) - \frac{\Lambda^2}{\lambda^2}\left[\left(\frac{\lambda H}{2} - \coth\frac{\lambda H}{2}\right)\left(\frac{\lambda H}{2} - \tanh\frac{\lambda H}{2}\right) + F^2\right] = 0. \tag{28}$$

Here,

$$F = \frac{1}{2}\frac{h_E N^2\left(k^2 + l^2\right)}{k\Lambda f} \tag{29}$$

is the frictional parameter. When taking into account Ekman dissipation for the total energy E in the Eady model, cf. (19), we get the equation

$$\frac{d}{dt}\int\int\int \frac{1}{2}\left((\nabla\Psi)^2 + \frac{f^2}{N^2}\left(\frac{\partial\Psi}{\partial z}\right)^2\right)dxdydz = -\int\int_{\Sigma_-} f\frac{h_E}{2}(\nabla\Psi)^2 dxdy - \int\int_{\Sigma_+} f\frac{h_E}{2}(\nabla\Psi)^2 dxdy \tag{30}$$

with a positive definite dissipative function; here, the levels $\Sigma_\pm$ correspond to $z = \pm H/2$, respectively. As follows from this equation, for sufficiently deep annular containers, which are typically used in laboratory experiments, the influence of Ekman friction is relatively small [34].

At $c \to 0$, i.e. on the neutral stability curve if the principle of exchange of stabilities [60] is accepted, equation (28) reduces to the equality to zero of the expression in square brackets in (28). The minimum of the first term in these brackets is -0.09 [61]. When $F^2 < 0.09$, there are two roots of this equation with respect to $\alpha = \lambda H$, which, according to [61], define the boundaries between the lower (upper) symmetric regimes and the wave regime, which are observed in the laboratory experiment.

When $F^2 = 0.09$ then these roots merge and the critical value of the Ekman friction is given by

$$\frac{h_E}{H} = 0.3\frac{\Lambda f L}{\pi N^2 H}. \tag{31}$$

In intermediate calculations, the most favorable value for instability $l = \pi/L$ was used and it was also assumed that $k = \pi/L$, which maximizes the right side of (31). If following [61] we take $(\Lambda f L)/(N^2 H) = 0.4$, which is a reasonable choice for a laboratory experiment where this expression describes the ratio of the interior horizontal to the interior vertical temperature contrast, then the right side of (31) is equal to $0.12/\pi \approx 0.04$. It then follows from (31) that the baroclinic instability of an interior zonal flow is impossible if $h_E/H > 0.04$ in the considered experimental setup.

In the above, we considered the analytically simplest symmetric case of two identical Ekman layers at the lower and upper end-walls. However, the asymmetric case of only one Ekman layer on the lower rigid end-wall and its absence on the upper free end-wall corresponds better to the conditions of the laboratory experiment. This more complex case was analyzed in [62]. In the same work, a model account was taken of the possible variation of the squared frequency of buoyancy $N^2(z)$ in the Eady problem.

Rejecting the assumption $f = const$ and accounting for the β-effect introduces significant mathematical difficulties into the problem, related with necessity to account for critical levels that correspond to $\Lambda z - c = 0$. This leads to the appearance of a countable set of weakly unstable normal modes. However, a numerical analysis shows that the growth rate of the fastest growing two-dimensional deep mode ($l = 0, \alpha = O(1)$) is very insensitive to variations in the beta-effect. For example, $(kc_i)_{max} = 0.31\Lambda f/N$ at $\gamma = 0$ and $(kc_i)_{max} = 0.286\Lambda f/N$ at $\gamma = 10$ [63]. Here, $\gamma = \beta HN^2/\Lambda f_0^2$ is the Charney–Green number [4,63]. More details can also be found in [47] and [53].

Note that the surface quasi-geostrophic (SQG) model is conceptually close to the Eady model [64,65]. For constant N and f, the analysis of instability within the framework of the Eady model can in fact be carried out starting from equation

$$\nabla^2\Psi + \frac{f^2}{N^2}\frac{\partial^2\Psi}{\partial z^2} = 0, \tag{32}$$

as was shown by [53].

2.3. *Two-layer model*

The simplest way to account for the β-effect in the problem of baroclinic instability is within the framework of the two-level Phillips model [66]. Here, we will consider a quasi-geostrophic model, consisting also of two layers of immiscible liquids but which may be a slightly closer analogue with respect to conditions of a laboratory experiment. The top layer has a thickness H_1, and the liquid in it has a density ρ_1. For the lower layer, such characteristics will be H_2 and ρ_2, where $\rho_2 > \rho_1$. A reduced acceleration due to gravity $g' = g(\rho_2 - \rho_1)/\rho_1$ is introduced. The equations of the quasi-geostrophic two-layer model are reduced to conservation laws ([47, p. 213])

$$\frac{\partial}{\partial t}q_i + J(\Psi_i, q_i) = 0, \quad i = 1,2, \tag{33}$$

where

$$q_1 = \nabla^2\Psi_1 - m_1^2(\Psi_1 - \Psi_2) + f_0 + \beta y \tag{34}$$

$$q_2 = \nabla^2\Psi_2 + m_2^2(\Psi_1 - \Psi_2) + f_0 + \beta y + f_0\frac{\eta_b}{H_2}, \tag{35}$$

with $m_i^2 = f_0^2/(g'H_i)$. Indices $i = 1,2$ refer to the upper and lower layers, respectively. In this case, in (34) the condition is used that the vertical velocity at the top of the upper layer vanishes (the "rigid lid" approximation); in (35) the function η_b describes the bottom topography. A systematic slope of the bottom, such that the effective thickness of the lower layer linearly decreases with increasing coordinate y, is mathematically equivalent to the beta effect. This is the basis for a practical way to model the beta effect in rotating containers.

For the basic flow that does not depend on the horizontal coordinates, the necessary condition for instability at $\bar{u}_1 - \bar{u}_2 > 0$ has the form

$$m_2^2(\bar{u}_1 - \bar{u}_2) > \left(\beta + \frac{f_0}{H_2}\frac{d\eta_b}{dy}\right), \tag{36}$$

where it is assumed that η_b linearly depends on the coordinate y. In the case when $H_1 = H_2 = H/2$ and $d\eta_b/dy = 0$, condition (36) coincides with what occurs for a two-level model if $g' = HN^2/2$. When $\bar{u}_1 - \bar{u}_2 < 0$ the instability condition takes the form

$$m_1^2(\bar{u}_2 - \bar{u}_1) > \beta. \tag{37}$$

In both cases, instability requires vanishing either $d\bar{q}_1/dy$, cf. (34), or $d\bar{q}_2/dy$, cf. (35); see also [45]. The marginal stability curve at $d\eta_b/dy = 0$ is given (in our notation) by the equation (see [45, p. 562])

$$\beta^2\left(m_1^2+m_2^2\right)^2+2\beta(\bar{u}_1-\bar{u}_2)k^4\left(m_1^2-m_2^2\right)-k^4(\bar{u}_1-\bar{u}_2)^2\left(4m_1^2m_2^2-k^4\right)=0. \tag{38}$$

If we substitute $\bar{u}_1-\bar{u}_2=\beta/m_2^2$, cf. (37) at $d\eta_b/dy=0$, then the wave number at the minimum critical shear is equal to $k_+=(m_2^2(m_1^2+m_2^2))^{1/4}$; at $\bar{u}_1-\bar{u}_2=-\beta/m_1^2$, cf. (14), it will be $k_-=(m_1^2(m_1^2+m_2^2))^{1/4}$ (ibid.). When $m_1^2=m_2^2=m^2$ these formulas transform into the formula $k=2^{1/4}m$.

A two-layer model targeted at the interpretation of laboratory experiment results was proposed in Lorenz [67]; see also [68, p. 222]). In this model, the stream function of the horizontal flow in the upper and lower layers of equal thickness $H/2$ is $\Psi+\tau$ and $\Psi-\tau$; the buoyancy in these layers is $\theta+\sigma$ and $\theta-\sigma$; the velocity potential of the irrotational part of the horizontal flow in these layers is $-\chi$ and χ. If the Coriolis parameter f is constant and the static stability σ varies only with time, the equations of the model take the form

$$\frac{\partial}{\partial t}\nabla^2\Psi+J\left(\Psi,\nabla^2\Psi\right)+J\left(\tau,\nabla^2\tau\right)=0, \tag{39}$$

$$\frac{\partial}{\partial t}\nabla^2\tau+J\left(\Psi,\nabla^2\tau\right)+J\left(\tau,\nabla^2\Psi\right)=f\nabla^2\chi, \tag{40}$$

$$\frac{\partial}{\partial t}\theta+J(\Psi,\theta)=\bar{\sigma}\nabla^2\chi,\qquad \frac{\partial}{\partial t}\bar{\sigma}=\overline{-\theta\nabla^2\chi}. \tag{41}$$

Here, a bar denotes a horizontal average. This system of equations is rendered closed by the thermal wind equation $\nabla^2\tau=(1/4)(H/f)\nabla^2\theta$. With neglect of the time variations of $\bar{\sigma}$, the system reduces to the two-layer Phillips model. An exact match is obtained by setting $\theta=f(\Psi_1-\Psi_2)/(H/2)$ and $\bar{\sigma}=N^2H/2$.

Baroclinic instability has also been discussed for mean flows that depend on z and y, relative to disturbances that do not depend on the coordinate x along the flow, called symmetric baroclinic instability. A model with constant N and f has been discussed for an ideal fluid by [69]. Viscous and thermally conductive fluids have been studied by [48] and [70].

Finally we note that all the models discussed above were formulated in Cartesian coordinates. For application to the annulus the theoretical analysis has to be carried out in cylindrical coordinates. No surprises are to be expected with regard to the basic processes. However, due to the curvature of the streamlines in the cylindrical system, certain new effects may occur. It should also be mentioned that boundary layers, i.e. Ekman layers at the top and bottom boundaries and Stewartson layers at the vertical walls, influence the flow in the experimental cavity and might have an effect on the stability as well (see Section 3.7.1). In these regions quasi-geostrophic theory is not valid. Nevertheless, quasi-geostrophic numerical models have been rather successful capturing the essential features of experimental annulus data [71].

There may not be a direct comparison in the literature of all the theoretical results on baroclinic instability, which are discussed in this section, with experimental results on rotating annuli and their applications discussed in this review. However, fundamental theoretical results constitute the ideological basis of laboratory modeling, and theory and laboratory experiment complement and enrich each other. The third major player on this scene is the numerical modeling, which often helps establish a link between theory and laboratory experiment. For instance, numerical simulations of baroclinic wave flows in a rotating cylindrical annulus based on the Boussinesq Navier–Stokes equations, which form the basis of the quasi-geostrophic theory described in this section, have been successfully compared with laboratory measurement data (e.g., [72]).

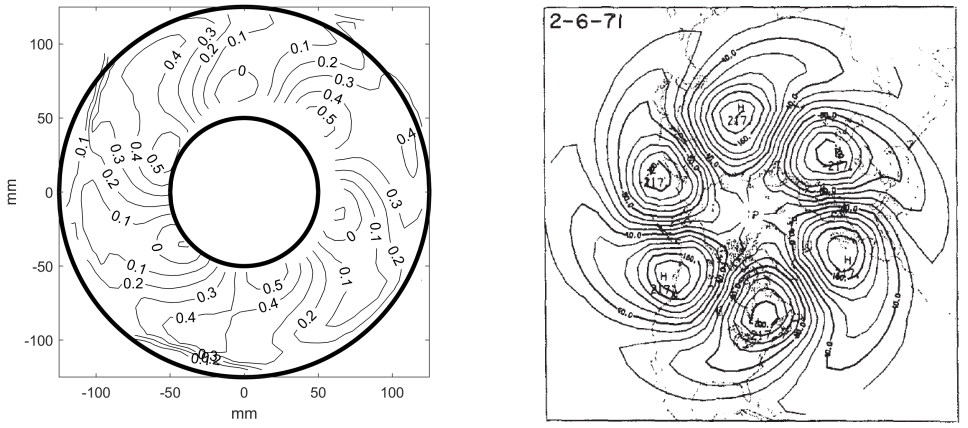


Figure 5. Fourier-analyzed 500hPa synoptic pattern of a state with maximum available eddy energy for wavenumber 3 (right), figure taken from [73] (with permission). Surface temperature anomaly (EOF1) measured at the BTU lab for $\Delta T = 4$ K, $\Omega = 4.8$ rpm, $d = 13.5$ cm (left). The southwest-northeast ridge line tilt imlies a northward/inward momentum transport.

3. Applications

3.1. *Flow regimes and heat flux*

3.1.1. *Unblocked flow*

A theory for the atmospheric general circulation should have at its center a theory for the eddy heat transport, $\overline{v'T'}$, where overbar means a zonal average, prime means a departure from the zonal average, v is the meridional velocity and T the temperature. Usually this transport is parameterized via $\overline{v'T'} = -D\overline{T}_y$, where the index y means a meridional derivative. D is a constant transport coefficient and it connects the transport with the meridional temperature gradient. D is, on the other hand, determined by characteristic length and velocity scales; however, it is not so obvious what these scales should be [74]. Moreover, the static stability is usually considered as a part of the background state but in fact it is a dynamic variable that varies strongly in space and time. The eddies in Earth's midlatitude atmosphere are part of the atmospheric *macro-turbulence* and at the end understanding this turbulence is essential for a theory of poleward heat transport.

The differentially heated rotating annulus is an experiment well suited to study and test ideas on the heat transport for different flow regimes and under different boundary conditions. As mentioned above, the experimental flow can be seen as an analog for atmospheric eddies and is therefore a good testbed for theoretical considerations on atmospheric flows. To illustrate this, Figure 5 shows an example of an atmospheric wavenumber 3 pattern of the 500hPa pressure level and a corresponding surface temperature pattern (EOF1) from an annulus experiment. The tilt of the patterns implies a northward/inward flux of momentum.

The heat transport in the annulus has been measured by [75], later by [44] and [76]. Without rotation but differential heating, the flow is resticted to boundary layers and a Hadley-type circulation can be observed. In the center of the cavity almost no motion can be seen and, in equilibrium, a stable vertical stratification is established. According to the experiments by [44] and [76], in this regime, the Nusselt number Nu, measuring the ratio between the total heat transport and the one by conduction alone, is about 13. When rotation is started, the thermal

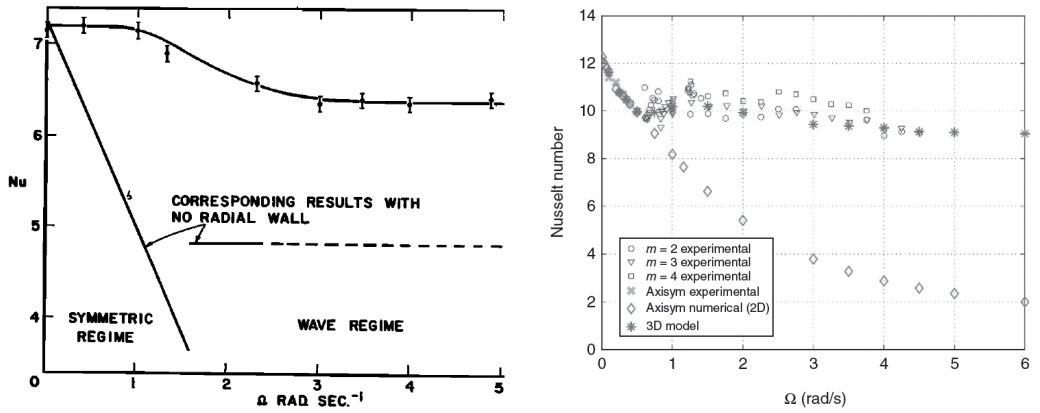


Figure 6. Left: A comparison of the variation of Nu with Ω for the cases of a bounded and free annulus. Figure taken from [78] (with permission). Right: Experimental and numerical total heat transport. Figure taken from [25] (with permission).

wind (4) produces azimuthal flow components with a vertical shear. However, as long as the flow is axisymmetric (no baroclinic instability) the radial component needs to be ageostrophic since, due to azimuthal symmetry, there is no azimuthal pressure gradient. Hence, radial flow is mainly in the Ekman layers and in fact the meridional streamfunction looks similar as in the nonrotating case. However, the isotherms in the center of the cavity are sloping and the radial temperature gradient is enhanced there compared to the nonrotating case. In the experiments by [44,76], for the axisymmetric regime with $\Omega \neq 0$, Nu goes down to about 10 following a power law $Nu \propto \Omega^{-3/2}$ (see Figure 6 (right)).

When rotation is further increased, the slope of the isotherms and the vertical shear in the bulk of the cavity increases and the azimuthal flow becomes baroclinically unstable (see the first transition in Figure 1). In the wave regime, Nu remains rather constant at about 10, no matter whether the azimuthal wavenumber is 2,3 or 4. Compared with the decline of $Nu \propto \Omega^{-3/2}$ for the hypothetic case of no baroclinic instability this is an amazing difference in the inward heat transport which is not fully understood from a theoretical viewpoint. Note that [44] suggested that the paper by [77] showed better agreement with the experimental results.

3.1.2. *Blocked flow*

There have been a number of experimental studies implementing a barrier in the annulus that fully or partly blocked the flow in the azimuthal direction [38,78,79]. For a complete blocking, as in the oceans, Bowden and Eden [78] pointed out that an azimuthal pressure gradient can exist and heat can then be advected due to a geostrophic boundary current along the barrier. In contrast to the free axisymmetric regime with a decline of Nu as $\Omega^{-3/2}$, no decline can be seen for the blocked flow (see Figure 6 (left)). For the latter, no regular wave regime exists and for larger Ω, Nu becomes somewhat smaller but remains constant when Ω is further increased. Nu is larger for the blocked flow over the full range of Ω considered. Similar results have later be found by [79].

The Antarctic Circumpolar Current is not blocked but has a prominent bottleneck, the Drake Passage. With a view on this situation, Harlander et al. [38] used a barrier that partially blocked the flow at the bottom and the inner wall. They measured the surface heat flux using velocity and temperature data for a single set of parameters in the wave regime. In that case baroclinic instability was present. However, the waves were not steady but showed a life cycle: downstream of the barrier the waves vanished but further downstream the waves recovered and reached

a steady state at the entrance of the narrows. The surface heat flux was computed from the combined PIV and surface temperature data with and without the barrier. The authors noticed that at the surface, Nu was almost an order of magnitude smaller with the barrier. Moreover, in the region where the baroclinic wave amplitude weakened, the radial heat flux was reversed and pointed from the inner to the outer wall. More recently, in a paleoclimate context, Vincze et al. [80] studied the effect of closing and opening the Drake Passage combining numerical modeling and lab experiments. This work is discussed in more detail in Section 3.6.

We note that experiments measuring the flow in the meridional plane of the baroclinic cavity are few in number (see Section 3.4 for Lagrangian data). However, numerical models suggest [31,41,81] that in the wave regime the meridional streamfunction can show a multi-cell structure depending on the aspect ratio Γ_d of the annulus. This will also alter the part of the heat flux related to the advection in the boundary layers.

3.1.3. *Flux parameterization*

The thermally driven rotating annulus is well suited to test parametrization schemes. Perez et al. [76] tested the mentioned closure for baroclinic eddy transport, $\overline{v'T'} = -D\overline{T_y}$ numerically, but surprisingly found only a weak correlation between $\overline{v'T'}$ and $\overline{T_y}$. A much better correlation was found between the potential vorticity flux $\overline{q'T'}$ and $\overline{q_y}$. On the basis of the numerical data they were able to deduce the eddy diffusivity D_q using linear regression. In a further step, [76] implemented eddy parametrizations into numerical annulus models to check whether the models can reproduce data from DNS simulations. A more detailed review of these activities is described in [25].

Quite recently, using a two-layer quasi-geostrophic model, Gallet and Ferrari [82] developed a predictive scaling theory for the eddy kinetic energy, temperature fluctuations and the meridional heat flux of baroclinic turbulence. Later, this so called vortex-gas scaling regime was tested by applying a Boussinesq Eady model of baroclinic instability [83]. The authors showed that their predictions could be carried over from the quasi-geostrophic to the fully three-dimensional Boussinesq model. It would certainly be of great interest to test the scaling experimentally by using the annulus experiment, but this is a task for future research. We finally note that ideas for testing parameterizations for internal gravity waves using annulus experiments have been considered in [84].

3.2. *Wave interactions, vacillations and turbulence*

Linear stability theory describes well the onset of instability and it was successfully applied for explaining the typical $Ta - Ro_T$-stability diagram as shown in Figure 1, see also [34, Fig. 15]. However, after a short period of growth consistent with linear instability, the waves in a baroclinic cavity do not grow anymore but are saturated by nonlinear processes. This saturation does not necessarily result in a steady wave state. In fact, a regime of regular nonlinear oscillations strictly periodic in time, called vacillations, was discovered by [85] and [35], modeling baroclinic instability in a rotating differentially heated annulus. Hide [85] initially discovered what is now known as structural vacillation, or what was at one time called tilted-trough vacillation, e.g. [86], or wave shape (or form) vacillation [87]. Pfeffer and Chiang [86] and also Fowlis and Pfeffer [88] made important advances in discovering amplitude vacillations, that is, vacillations in the amplitudes of eddies and not in the orientation of troughs and ridges (see [89] for an earlier and [18] for a later review). In the time that followed, attempts were made to detect a periodic, or quasi-periodic, regime in the analysis of real atmospheric data, which bears some resemblance to the zonal index cycle in the atmosphere (e.g. [90]). The observed oscillations of energy parameters in the atmosphere with a period of about 24 days and their connection with

baroclinic instability are described in [73]. Figure 5 (right) shows the wavenumber 3 geopotential height field at a state of maximum available potetial energy and this state is in fact part of an atmospheric vacillation cycle. The minimum state occurred three weeks earlier and shows a similar pattern than the one displayed but with smaller amplitude and with maxima and minima that are shifted further towards the pole.

The occurrence of vacillations is an important feature of the nonlinear dynamics of perturbations of a basic baroclinic flow. This characteristic reflects the fulfillment of the energy conservation law in the adiabatic and inviscid case and is not related to the specific structure of the flow, cf. [53]. In this regard, the nonlinear oscillatory regime of flow instability in a two-layer quasi-geostrophic model was studied in [91], where the mechanism of occurrence of oscillations is described in terms of a time-periodic energy exchange between an unstable baroclinic wave and the background flow. For the two-level, quasi-geostrophic model of [67], which was assumed to be adiabatic and frictionless, Merelees [92] obtained an exact formula for the oscillation period (in terms of the complete elliptic integral of the first kind); this period, however, depends sensitively on the initial conditions. In a slightly dissipative case, the direct effect of dissipation on linear baroclinic instability is negligible, but dissipation can affect nonlinear oscillations in the long run (cf. [93]). Alternatively, on the attractor of a dissipative system, a kind of compensation of the effects of nonlinear instability and dissipation may occur, resulting in (almost) periodic oscillations (orbits), and nonlinear oscillations (vacillations) in a conservative system could serve as approximations for these orbits.

Here, we mention also the pioneering results of [94] on the existence of a limit cycle for small (but non-zero) viscosity in a quasi-geostrophic two-layer model at small deviations of the parameters from critical values. This type of oscillation has the desirable property that the ultimate oscillation is independent (in detail) of the initial conditions. Such vacillations are indeed observed in such (slightly) dissipative systems as the laboratory analogues of the atmosphere [12], although in laboratory experiments we are inevitably faced with a dissipative/forced fluid system. Nevertheless, the results obtained are qualitatively very similar to those obtained in the framework of conservative systems. If we consider that the occurrence of nonlinear oscillations (vacillations) is a consequence of the conservation of energy, then this similarity is explained by the exact conservation of energy for a conservative system and the energy conservation on average over the period of oscillation for a dissipative/forced system.

The line of research initiated by Pedlosky [91,94] was further developed e.g. in [95] and in [96]. Pedlosky and Thomson [97] developed a weakly nonlinear theory of baroclinic instability of time-dependent flows, which exhibits finite-amplitude periodic oscillations of the limit cycle type when studying the nonlinear dynamics of parametrically unstable perturbations. Früh [18] reviews the amplitude vacillation in baroclinic flows based on experimental data, computational fluid dynamics, and low-order numerical models. The vacillation phenomenon, which occurs in various geophysical contexts, is addressed, e.g., in [98–101] and [102].

The above discussion mainly focused on amplitude vacillations, but for the route to irregular flows and geostrophic turbulence at higher rotation rates, structural vacillations are also important. Such vacillations have been described as an interaction between a small number of wave modes [67]. However, although mathematically elegant, this picture might not be complete. Ukajil and Tamaki [87] performed numerical simulation of structural vacillations in a rotating fluid annulus and revealed that the vacillations can be interpreted as the behavior of baroclinic waves affected by a weak barotropic instability. In view of the more irregular features observed in experiments with structural vacillations small-scale instabilities might also play a role (see also the discussion at the end of Section 3.7.4). The onset of structural vacillations is usually rather aprupt as was discussed by [103].

For higher rotation rates, the onset of structural vacillations is often a harbinger of the irregular flow state or geostrophic turbulence [14]. For the latter, energy power spectra show a slope between -3 and -4. The shallower spectrum can be explained following the theory by [104], a steeper spectrum might be due to sharp fronts and filaments [105] that frequently occur in geostrophic turbulence. On the basis of data from annulus experiments, [106] studied spectral energy transfers and recently Rodda and Harlander [107] detected a power spectrum with slopes of -3 for the large and $-5/3$ for the small scales in an experiment with a small aspect ratio. However, the latter case was not in a turbulent regime. Read [25] stated in his review nine years ago that highly resolved experimental data on temperature and velocity are really needed to better understand energy exchanges in the turbulent regime and that is still true today.

3.3. *Jet streams*

Earth's atmospheric Polar Jet was an early motivation for laboratory experiments, as noted in the Introduction. The Subtropical Jet, and various oceanic interior jets, distinct from lateral boundary currents, raised further questions about their origins, relation to the general symmetric or "overturning" circulation in the oceanic context, and the relation to eddy forcing. From the early periods of experimentation to the present, interest in the banded structure of giant planets has also brought the concept of zonal jets into the foreground of research with the annulus.

Waves, eddies, and jet-like currents or streams are often present together in planetary atmospheres, oceans, and in the laboratory annulus experiments themselves. Sometimes the separation or distinction between these various circulation elements is not clear, or is confounded by variability, or depends on the interpretation of flow regime. The flow in wave regimes of the annulus, for example, recognized for connecting the inner and outer boundaries and for carrying heat meridionally (from an outer heat source to an inner heat sink for example), is analogous to jet streams in a portion of Earth's atmosphere. But this regime is not representative of jets in Earth's ocean, with its much smaller deformation radius L_R compared to basin size. The situation can be described by the basic thermal Rossby parameter of the system, $Ro_T = L_R^2/L^2$, see (8) with L the characteristic length scale, where the oceanic regime is represented by a smaller value of Ro_T. Note that the Taylor number in the ocean is far larger than that in the laboratory, but laboratory results suggest that after transition to the geostrophic turbulence beyond a value of about 10^8, the regime is relatively independent of Ta.

The organization of the turbulent regime into quasi-zonal jets relies on the β-effect. The sloping surface of rotating tanks, either free or with a lid, provides a topographic beta-effect, investigated early on by [108], and more thoroughly by [106] into the stronger nonlinear flow regimes. While there is skepticism concerning the representation of β by a sloping upper or lower boundary, since it does not produce a true interior mean vorticity gradient, experimental results clearly imply an important effect. That small-scale convective motion, generated by either cooling at the surface or heating from below, can also lead to larger scale baroclinic flow structure including jets was developed in experiments by, for example, [109]. Their experiment used a parabolic bowl to produce a net thickness gradient, or potential vorticity gradient, and gave rise to azimuthal jets. Experiments on the large table at Grenoble, also forced with small-scale convection, showed that jets were produced consistent with a generation mechanism by Reynolds stresses [110].

The recognition of the role of jets in the ocean arising from baroclinic instability was slower to develop. Eventually, observations showed deep zonal jet structures with several candidate mechanisms, including the baroclinic instability of the meridional flow [111]. Modeling efforts also suggested alternate explanations not involving baroclinic instability via the arrested decay of long Rossby waves [112]. Similar to the case of small-scale forcing of larger scale flow structures

in the laboratory, interior mixing in the presence of topography has been implicated as well in the development of zonal jets [113].

In experimental configurations with a beta-effect, the introduction of a Rhines length scale, $L_\beta = (U/\beta)^{1/2}$, U being a characteristic eddy velocity, produces another parameter, L_β^2/L^2, where L is the annulus' gap width, that becomes useful for distinguishing the regimes for which jets appear in the baroclinic annulus. In the laboratory setting, [36] showed multiple jet structure in an annulus in a regimes with small values of this parameter, thought to be relevant to the largest and broadest zonal flow in the ocean, the Antarctic Circumpolar Current, present in the circumpolar open channel between Antarctica and the southern continents. This current system is known to be composed of multiple zonal jets, as many as ten or so, typically with one or two dominant at any particular time and place. Intermitency and meridional jet migration characterize the longer time evolution of this system [36]. We note finally that multiple jet formation has also been studied experimentally using a mechanical forcing [114].

Multiple jets in baroclinic flow resolved in the annulus have become profoundly relevant paradigms for circulation in Earth's ocean and atmosphere, and on other planets as well. For additional background and newer developments see the review on jets in this collection.

3.4. *Chaotic transport*

Lagrangian or chaotic transport is of interest in any branch of geophysical fluid dynamics in which the transport and mixing of fluid, fluid properties, and material moving in the fluid is relevant. The theory was developed as part of dynamical system theory and later applied to different fields in physics including fluid mechanics. In our context, transport properties in a meandering jet are in the center of attention. The Gulf Stream and the intense flow connected to the polar vortex are examples of meandering jets that show many features in common with the flow in the baroclinic wave experiment.

The motion of passive particles, not affecting the flow, follow the equation

$$\frac{d\vec{x}}{dt} = \vec{v}(\vec{x}, t), \tag{42}$$

where $\vec{x} = (x, y, z)$ is the particle position in the 3D space and $\vec{v} = (u, v, w)$ is the velocity vector in this space. For a given velocity, solutions of (42) are the trajectories of the particles. Note that invariants of adiabatic flows like potential vorticity or potential temperature (or temperature in Boussinesq models) can be considered as tracers as well, however, they are not passive since they affect the flow.

In the bulk of the fluid within a baroclinic wave tank the flow is nearly 2D. Then we can introduce a streamfunction $\psi(x, y, t)$ and write

$$\frac{dx}{dt} = u(x, y, t) = -\frac{\partial\psi}{\partial y}, \quad \frac{dy}{dt} = v(x, y, t) = \frac{\partial\psi}{\partial x}, \tag{43}$$

where ψ is a Hamiltonian and x and y the canonically conjugated variables [115]. In this case, chaotic transport can be studied by the methods from Hamiltonian dynamics.

To illustrate particle transport within a 2D meandering jet we consider the following streamfunctions

$$\psi\left(x', y, t\right) = cy + \psi_0\left(1 - \tanh\left(\frac{y - y_c}{\lambda/\cos\alpha}\right)\right) + \epsilon\psi_1\left(x', y, t\right), \tag{44}$$

with $y_c = A\sin kx'$, $\alpha = \tan^{-1}(Ak\cos kx')$, $0 < \epsilon < 1$, and

$$\psi\left(x', y, t\right) = cy + \psi_0 y_c \sin y + \epsilon\psi_1\left(x', y, t\right), \tag{45}$$

where x' is in a reference frame that moves with the constant speed c, i.e. $x' = x - ct$ and k is a zonal wave number. The amplitudes are constant and are denoted by ψ_0 and A. Here ψ_1

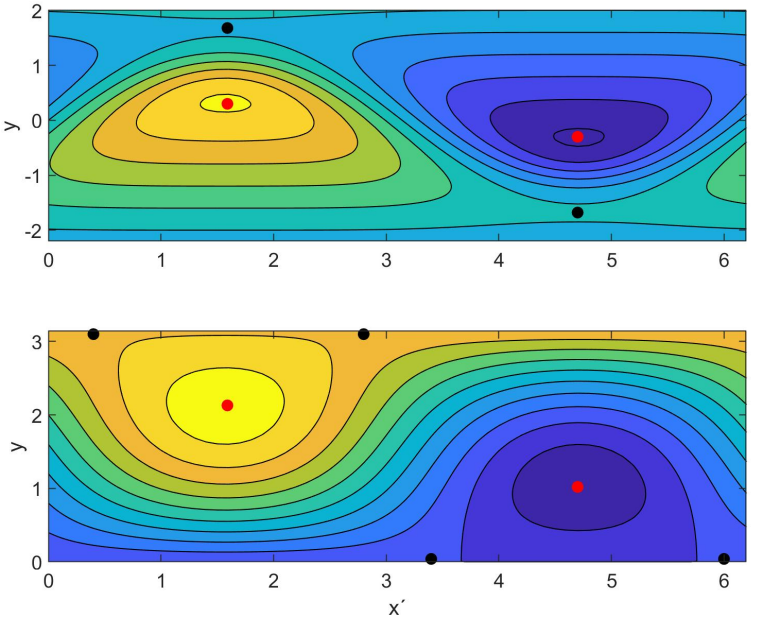
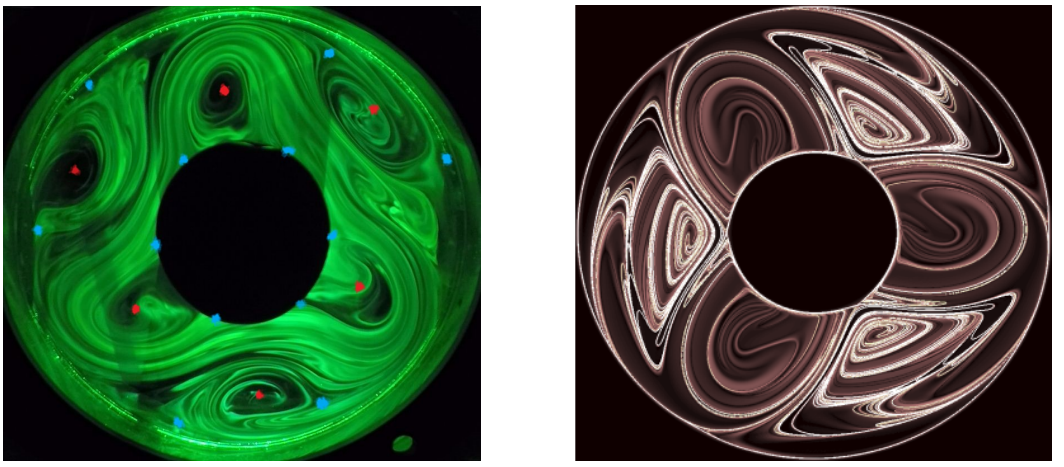


Figure 7. Two meandering jets, one localized in an open shear flow (top) (44), and one in a channel with walls oriented in the zonal direction (45). The black dots are hyperbolic (saddle) fixpoints, the red dots elliptic (oscillatory center) fixpoints. We used $k = A = \psi_0 = 1$, $c = 1/2$, $\lambda = \pi/6$, and $\epsilon = 0$.

is a time dependent perturbation of the primary wave. The former jet (44) corresponds to a localized meandering jet in an open shear flow [116] (see Figure 7, top), the latter one (45) to a meandering channel flow with walls oriented in the zonal direction [117] (see Figure 7, bottom). These examples are in a sense "clinical" versions of realistic jets for which a mathematical analysis is simpler than for its real counterparts.

The dots in Figure 7 mark fixpoints, i.e. points at which the left hand side of (43) vanishs. The red dots denote elliptic center points, surrounded by closed streamlines. In contrast, the black dots stand for hyperbolic saddle points located on streamlines that separate regions of meandering and circulating flows. In the reference frame in which the flow is displayed in Figure 7, the streamlines correspond with trajectories. Streamlines separating meandering and circulating flows are hence *transport barriers* for the flow: fluid exchange between the two regions is impossible since no trajectories can cross the transport barrier that itself is formed by a flow trajectory.

Transport barriers play a fundamental role in atmospheric as well as oceanic sciences. For example, mixing events at the edge of the Antarctic polar vortex play a key role for the transport of ozone and heat in this region [119,120] and thus have an impact on the southern hemisphere weather and climate [121]. In such large-scale vortices potential vorticity (PV) can be used as a tracer [122]. Transport barriers for PV are related to steep PV gradients found at the edge of the polar vortex. The same steep gradients occur in mid-latitude jets making meridional PV exchanges difficult. Spreading of pollutants play an important role in the global ocean. Forecasting the motion of polluted water, e.g. following an oil spill is essential to keep environmental damage within limits and in this context transport barriers are very relevant [123]. A recent extensive review on transport barriers is given by [124].



(a) (b)

Figure 8. a) Uranine visualization of a wavenumber 3 baroclinic wave at depth 1 cm from the surface. For this visualization experiment, the tank revolution was $\Omega = 5$ rpm, and the temperature difference was $\Delta T = 4$ K. Center points are given in red, saddle points in light blue. b) Contour lines of $\|\nabla M^{(b)}\|$ showing attracting material curves computed at initial time $t_0 = 0$s and $\tau = 6600$s. The calculations are based on the kinematic model developed by [118] using PIV velocity and temperature data from the experiment shown in a). A perturbation has been applied to the kinematic model that leads to a break up of the transport barriers. Figure taken from [118] (with permission).

Mixing events can be triggered by adding time dependence in the streamfunctions (44), (45), i.e. by using $\epsilon \neq 0$. For mixing, the saddle points marked as black dots in Figure 7 have a very significant meaning. The reason is that streamlines intersecting with saddle points are either so called stable or unstable material manifolds (also called hyperbolic manifolds). These hyperbolic manifolds mark regime boundaries. In the case sketched in Figure 7 we see either a meandering jet regime or vortex regime with closed streamlines. The hyperbolic manifods break up when ϵ is nonzero and the streamfunction becomes time dependent. Then mixing takes place along the hyperbolic manifolds close to the saddle points.

The mixing and its connection to saddle points can be observed in the baroclinic wave tank. Figure 8 (a) shows an example of a baroclinic wave with azimuthal wave number 3. Center points are given in red and saddle points in light blue. The two flow regimes, vortex flow and meandering jet, can clearly be distinguished. However, fluid mixing has obviously taking place and this is due to (a weak) time dependency and a breakup of hyperbolic manifolds close to the blue points. It is easy to recognize that the flow shown as an example corresponds to the streamfunction (45), displayed in Figure 7 (bottom). The straight channel displayed has wave number 1 (4 saddle points) in contrast to the wave with wave number 3 (3×4 saddle points) in the annular channel of Figure 8 (a).

Apart from these rather theoretical considerations, mixing in jet streams has also been the subject of intensive experimental research. Sommeria et al. [125] studied the transport of particles in a barotropic jet. The jet was produced in a rotating annulus with sources and sinks at the bottom. The bottom had conical shape to mimic a β-plane. The jet results from an instability due to the radial shear of the flow. The initially unstable jet profile is first broadened due to barotropic instability until it is stabilized by the beta effect. The sources and sinks in the annulus create a steep PV gradient in the jet's center forming a transport barrier for tracers. Using the

same experimental apparatus, Behringer et al. [126] heuristically fitted a kinematic model to the experimental data. Then they studied how transport barriers depend on the number of waves included in the model, and found that the addition of a third wave can break the transport barrier if the wave amplitudes exceed the width of the jet.

In addition to the consideration of jets caused by barotropic instability, three-dimensional jet streams formed by baroclinic instability have been studied using a differentially heated rotating annulus (see Figure 3). Saguta and Yoden [127] numerically studied Lagrangian motion in a steady baroclinic annulus wave. They subdivided the Lagrangian flow into different regions: the upper-level and lower-level jets, the cyclonically and anticyclonically trapped regions, and the inner, outer and lower boundary layers. Although the particle paths always showed some chaotic behaviour, the particles usually visit these regions in an organized way. However, inside the cyclonic and anticyclonic vortices particles were usually not found implying that these regions were separated from the flow by transport barriers. Interesting also is the Lagrangian view of the heat transport. The fluid particles absorb heat at the heated outer boundary layer and release it at the inner cooled boundary layer. In between, they carry the heat without much loss.

Later, Tajima et al. [128] tried to reproduce the numerical findings by experiments inserting ink at different positions in a steady baroclinic wave field. They found that the structure of the cyclonic and anti-cyclonic vortices are composed of a well-isolated core region but split into separate upper and lower layers. Next to the core a transition zone was found where fluid particles can travel towards and from a vortex' outside but usually not to its core region. A more quatitative view on chaotic trajectories in the 3D baroclinic wave flow was taken by [129]. Many features observed by [127] could be experimentally confirmed. However, from the tracking data alone it was not possible to derive measures for transport and mixing on the basis of the chaotic particle motions.

Keane et al. [130] showed that finite scale Lyapunov exponents (FSLEs) are useful to find boundaries between different regions of the differentially heated rotating annulus flow identified earlier by [127]. Keane et al. further considered Eulerian symmetry measures (ESMs) as an alternative or supplement to FSLEs. Very recently, Agaoglou et al. [118] quantitatively constructed a kinematic model (43) from simultaneous measurements of the temperature and the horizontal flow of a baroclinic wave experiment. In time-dependent dynamical systems stable and unstable manifolds as well as the structures around elliptic center points can be visualized by using Lagrangian Descriptors (LDs). This diagnostics has been introduced by [131] and was first applied in ocean dynamics. The LD that was used in [118] was the M-function defined as

$$M(\mathbf{x}_0, t_0, \tau) = \int_{t_0-\tau}^{t_0+\tau} \|\mathbf{v}(\mathbf{x}(t), t)\| \, dt, \tag{46}$$

where the norm $\|\cdot\|$ measures the length of the velocity vector and τ denotes the integration time. At a given initial time t_0, the function $M(\mathbf{x}_0, t_0, \tau)$ measures the arclength that is traced by the trajectory starting at $\mathbf{x}_0 = \mathbf{x}(t_0)$. The M function is powerful tool to disentangle a complex dynamics and this approach has many applications in oceanic and atmospheric sciences. A review can be found in [132]. The integral in (46) can be divided into two parts, $M = M^{(f)} + M^{(b)}$. The first term integrates from t_0 to $t_0 + \tau$ and the second from $t_0 - \tau$ to t_0. The forward component, $M^{(f)}$, elaborates structures of stable manifolds, and $M^{(b)}$, can find structures of unstable manifolds. In [118] the interest was on attracting material curves and the analysis was restricted to $M^{(b)}$.

Figure 8 (b) highlights singular features in $\|\nabla M_b\|$, the modulus of the gradient emphasizing singularities in $M^{(b)}$ even more clearly. Singular features in M are associated with the existence of invariant unstable manifolds. In Figure 8 (b), Agaoglou et al. [118] used $\tau = 600$ s and applied

a perturbation to the kinematic model. This perturbation allows for mixing across the jet by destroying invariant tori.

Dye dispersion processes in geostrophic turbulence were studied using rotating annulus experiments by Jánosi et al. [133], in the thermal Rossby number range of Ro_T = 0.01–0.1. In each run a 1 ml drop of standard fluorescent dye was injected at the water surface, and its dispersion was evaluated from video recordings taken from above, by determining the total area covered by the dye cloud, and its azimuthal extent as a function of time. The results were compared with passive tracer propagation simulations driven by global reanalysis wind fields (i.e. semi-empirical wind fields, based on measured data but interpolated to achive uniform global coverage). They found that in this irregular wave regime the horizontal extent of the tracer cloud increases linearly in time (Batchelor scaling) for intermediate timescales ("weeks") in the atmosphere and in the experiment as well.

3.5. *Blocking*

In meteorology, the term "atmospheric blocking" describes the formation and development of large-scale high pressure patterns in the midlatitude troposphere that are nearly stationary, highly persistent and block or redirect migratory cyclones. This causes long-term weather anomalies, heat waves and draughts in summer and cold spells in winter, and has profound impact on midlatitude weather and climate conditions, not only over the region in which the blocking occurs but over upstream and downstream areas as well.

The axis of blocking highs (blocks) usually has a slight tilt with height, i.e. blocking highs are, to a good first approximation, barotropic structures. However, the existing small tilt provides feeding of blocking highs not only due to migratory eddies (cyclones and anticyclones) [134], but also at the expense of the available potential energy stored in the main zonal flow [135], i.e. due to the action of baroclinic instability.

In Charney and Straus [136], by generalizing the work [137] to the case of a baroclinic atmosphere, a two-layer atmospheric model was considered taking into account the orography of the Earth. The highly truncated solution of the governing quasi-geostrophic equations, by using the Galerkin method, was shown to allow multiple equilibria, associated with resonantly forced Rossby waves, one of which corresponds to the atmospheric blocking. Maintaining this blocking state requires large values of the equator-pole temperature difference ΔT and is associated with both the so-called orographic (form-drag) instability, which is already present in the barotropic atmosphere [137], and with the baroclinic instability of the main zonal flow.

A competing point of view on the mechanism for the forcing and supporting a blocking high treats it as a regional phenomenon forced by migratory cyclones and baroclinic energy conversion [138]. To the major extent this corresponds to dipole-type [139] and omega-type blocking [140]. A conceptual model of these two types of blocking in terms of correspondingly a pair (dipole) and a system of three (tripole) Kirchhoff point vortices was introduced in [141] and further developed in [142] and [143]. There is a point of view that orography is not necessary for the blocking occurrence but does support its development (see [144]; and references therein).

With an increase in ΔT and a corresponding increase in the available potential energy stored in the main flow, the degree of its baroclinic instability increases. As a consequence, the Lorenz energy cycle of the atmosphere [145] intensifies. This leads to intensification of westerlies and of large-scale jet streams in the atmosphere and, as a reverse reaction, to an increase in the frequency of atmospheric blocking. The latter is Rossby's [146] famous scenario for the emergence of atmospheric blocking; see also [139]. A key ingredient of Rossby's theoretical scheme is accounting for the beta-effect. The observed increase in the frequency of blocking

in the winter season compared to the summer season, as well as an increase in the frequency of blocking during global cooling (e.g., [147,148]), are highly consistent with this scenario.

Meanwhile, the last two decades have demonstrated an increase in blocking frequency accompanying general warming at high-latitudes (Arctic Amplification), the mechanism of which is not entirely clear. A widely accepted paradigm in the climate community is that the shift to a less zonal type of circulation facilitates meridional excursions of air masses and, in particular, provokes blocking action [149]. Various aspects of reproducing future trends in blocking activity by climate models are discussed in [150] and in [151].

Kurgansky [152] attempted to unify the above paradigm with Rossby's ideas using a two-zone atmospheric circulation model over a hemisphere. The surface area of the proportion of extratropical zone occupied by migratory eddies (cyclones and anticyclones) was accepted as a measure of baroclinic instability (baroclinic chaos) over the hemisphere. The principle of maximum of the (informational) entropy of this eddy regime was applied to determine the climate equilibrium latitude of the boundary between the two zones. The model inference was obtained that the area occupied by blocking highs, which is formally included in the extratropical zone but free of eddies, increases with both global cooling (increase in ΔT) and global warming (decrease in ΔT). At the same time, modern conditions (more precisely, the conditions of the end of the 20$^{\text{th}}$ century) correspond to the minimum of blocking action.

An interesting attempt was made in [153] to reveal the dynamic mechanism explaining the increase in blocking frequency along with a decrease in ΔT. These authors proceeded from the fact that, unlike the classical mechanism of baroclinic instability, the decisive role here is played by motions on a planetary scale, the so-called geostrophic motions of the second type [154]. Therefore, the momentum equations reduce to the Sverdrup relation, which describes the balance of the meridional advection of the planetary vorticity and the vertical stretching of the vortex tubes. The subtle point is that in this case the Boussinesq approximation is abandoned and the average (standard) density of the atmosphere is assumed to decrease exponentially with scale height H. Basically, an anelastic approximation is used. In this case, the Sverdrup relation takes the form

$$\beta v = \frac{\partial w}{\partial z} - \frac{w}{H}. \tag{47}$$

For specific calculations, a two-layer atmospheric model is used. The atmospheric layer under consideration of thickness H is divided into two sublayers: lower $0 \le z \le H/2$ and upper $H/2 \le z \le H$. Relation (47) and the buoyancy equation, both differentiated with respect to z, are written at the levels $z = H/4, 3H/4$. The thermal wind equation is used in the differentiated equation (47), and the vertical velocity field is eliminated between the equations obtained. For the parabolic vertical velocity profile

$$w = w_m \frac{z}{H}\left(1 - \frac{z}{H}\right) \tag{48}$$

adopted in the cited work, due to the second term on the right-hand side of (47), the asymmetry necessary for baroclinic instability to occur arises between the equations of the upper and lower layers. According to [153], this instability is possible if the following inequalities are satisfied (in our notation)

$$0 \le \Delta U \le \frac{1}{2}\beta L_R^2, \tag{49}$$

where ΔU is the velocity shear of the main flow between the upper and lower levels and $L_R = NH/f_0$ is the Rossby deformation radius. Unlike the classical criterion of baroclinic instability in the two-level Phillips model, here the instability is favored by small values of the vertical velocity shear ΔU, that is by small values of ΔT, while the beta effect is a destabilizing factor. More details about the problem statement and its solution can be found in the cited work. An interesting question, especially in terms of possible applications to laboratory experiments,

is whether such instability can manifest itself in some baroclinic fluid model, but within the Boussinesq approximation? In other words, to what extent is it necessary to abandon Boussinesq approximation?

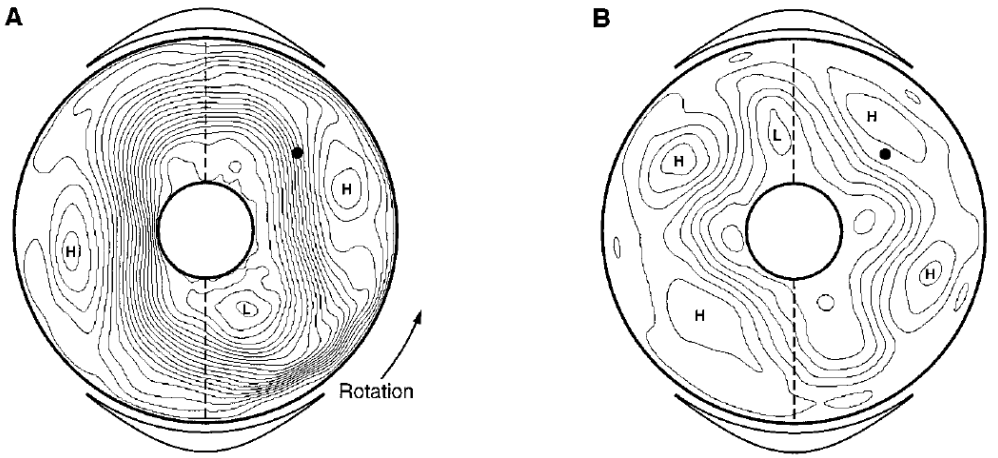


Figure 9. Time-averaged stream function contours derived from experimental data for (A) zonal and (B) blocked flow. The Rossby numbers for the zonal and blocked flows are 0.33 ± 0.02 and 0.22 ± 0.02, respectively. The tops of the ridges are indicated by dashed lines, and the profile of each ridge is shown by black curves outside the rim of the round panels. The black dots indicate the horizontal location of a hot-film probe. Figure has been taken from [155] (with permission).

We have described the state of research into the blocking phenomenon in more detail here because we believe that the baroclinic experiment in conjunction with numerical modelling is well suited to clarifying fundamental processes mentioned above. Most experimental studies on blocking focus on the aspect of flow/topography interactions. Weeks et al. [155] used the barotropic experimental setup by [125] to understand transitions between blocked and zonal flows in an rotating annulus with large-scale topography. An example of a block and a zonal flow situation is displayed in Figure 9. When the flow is blocked a much larger variability of the wave could be observed. Weeks et al. [155] conjectured that the two states correspond to two basins of attraction, connected by a heteroclinic orbit. For the observed multiple equilibria the wave/topography interactions are essential. However, note that even in the absence of topography, switches between different baroclinic regimes have been observed for the flat bottom thermally driven annulus [34] as well as for a two-layer setup using water for the upper and a dilute sugar solution for the bottom layer [156].

More recently, in a series of papers, wave/topography interactions and blocking have been investigated in more detail with the Hide setup of the differentially heated rotating annulus. The authors of [100,157] and [158] studied topographic resonance and multiple flow regimes. In particular, Marshall and Read [158] found a "stationary-transition" regime where oscillations between a stationary wavenumber-3 flow and axisymmetric or chaotic flows could be found. Wave-zonal-flow and wave-wave interactions (triads) were part of detected nonlinear instabilities. In a follow-up study, the same authors [37] replaced the wavenumber-3 topography by an isolated ridge that partially blocked the flow. Using this configuration, the occurrence of multiple baroclinic flow states have been studied. Again wave triads could be found, this time two triads have been noted sharing a wavenumber-1 mode. Finally, Marshall and Read [159] demonstrated that blocking can

also be induced by a local thermal forcing. Analogies with the atmospheric Walker circulation have been drawn and it was suggested that for the Martian atmosphere it is the thermal forcing that leads to its dominant low-wavenumber flow structures.

The β-effect plays an important role for baroclinic instability and also for the special characteristics of multiple flow regimes. The studies [34,156,157], and [100] considered an f-plane, [37,125,155,158], and [159] used a β-plane, by mounting a sloping bottom or slanted top lid.

As has become clear with the above the occurrence and the frequency of blocking depends on the meridional (radial) temperature gradient. This gradient shows natural fluctuations but also changes due to climate change. Blocking will hence be influenced by these changes [150]. In the following section, findings on changes in the frequency of extreme events from baroclinic wave tank experiments will be discussed.

3.6. *Climate and extreme values*

Earth's atmospheric circulation at mid-latitudes and the propagation of Rossby waves is driven by the large-scale meridional gradient of the air temperature. Therefore, as the change of the characteristic "Equator-to-pole" temperature contrast parameter ΔT impacts the thermal Rossby number Ro_T, it may also affect the general character of the flow. In the Earth system ΔT exhibits periodic (seasonal) changes through a year, superimposed onto a decreasing trend which has been observed in the weather stations and satellite data throughout the past decades, in parallel with the ongoing global warming. Temperature increase in the Arctic since 1979 has been reported to be more than four times larger than the increase of the global average, a process referred to as Arctic amplification [160].

The decreasing Ro_T influences the "waviness" of the polar jet stream separating the colder polar domain from the warmer mid-latitudes, as well as the typical extent of its North-to-South detours and the wind speeds in it. The conceptual baroclinic annulus model of the mid-latitude circulation provides a remarkable test bed for investigating Rossby waves in a system whose dynamics are driven by a temperature contrast ΔT prescribed by the thermal boundary conditions at the cylindrical sidewalls, and Coriolis force. Experiments in this configuration can help disentangle the complex causal connections of processes which cannot be studied separately in the real Earth system, and provide useful input to the problem of whether or not the wavier jets emerging due to Arctic amplification are also associated with stronger temperature extremes.

A convincing demonstration of the fact that nonlinear statistical features of daily mid-latitude temperature fluctuation time series from the atmospheric boundary layer can generally be reproduced in a rotating annulus experiment was performed by Gyüre et al. in 2007 [161]. Their seminal paper contrasted the time-reversal asymmetry of daily temperature time series from meteorological station data of the Global Daily Climatology Network (GDCN, compiled by the National Climatic Data Center), considering one day temperature differences. They found that the number of subsequent warming steps (i.e. consecutive days where the temperature is higher than on the previous day) is significantly larger than the number of cooling steps in the mid-latitudes, regardless of the length of the investigated records. In other words: large abrupt cooling events are typically followed by slower gradual warming. This strong asymmetry fades away if not consecutive days but larger time differences are compared, as the "memory" (persistence) of weather phenomena is known to have a timescale of a few days, after which the correlation – and the nonlinear, time-asymmetric behavior – vanishes.

In the rotating annulus of the Budapest von Kármán Laboratory (with $Ro_T = 0.01$–0.075 and $Ta = 4.47 \cdot 10^9$–$2.8 \cdot 10^{10}$, well within the irregular Rossby wave regime) Gyüre et al. implemented analogous measurements with temperature sensors placed in the vicinity of the bottom plate

of the tank, which recorded "daily" temperatures for approx. $5-6000$ revolutions. In these experiments the same marked asymmetries (with the quantitative agreement of the evaluated time-reversal asymmetry parameters) were observed as in the station data, underlying the physical analogy between the quasi-geostrophic turbulence of the troposphere and the differentially heated rotating annulus.

The above experiment featured constant thermal boundary conditions. In the dynamics of a changing climate a fundamental theoretical problem lies in the very definition of "climate": the Earth system is a nonstationary one, yet, the empirically obtainable measures of the climate state are time averages of certain observables (e.g., global mean temperature). *Changing* climate implies that on the decadal timescale the "average" behavior itself is also evolving, making the statistical interpretation of the results problematic, mostly in situations where the climate change is abrupt. Theoretically, as introduced by Rameiras et al. [162] for nonlinear systems subject to time-dependent driving and specifically in climatology by Ghil et al. [163], a consistent definition of climatic averages (and other statistics) in such systems could only be achieved via ensemble- (and not time-) averaging. The statistics over a multitude of "parallel histories" has to be considered, each subjected to the very same time-dependent external driving. Then, one can obtain "ensemble statistics" for each time instant t of the changing climate, a distribution with respect to which, for instance, the extremity of a given measured data point (e.g. daily temperature value) can be evaluated.

Obviously, since only a single realization of the actual Earth system exists, such empirical measures cannot be obtained for the real climate. However, experimental (and numerical) models can be repeated many times under identical pre-defined time-dependent forcing scenarios. Then the comparison of the obtained ensemble statistics with the traditional temporal statistics from a single experiment can teach us important lessons about the nature of such systems.

Results from a climate-change-inspired baroclinic annulus experiment featuring an ensemble of nine experiments with identical time-dependent $\Delta T(t)$ temperature contrast forcing were reported in [164]. The runs were conducted in the small rotating annulus of the Brandenburg University of Technology (BTU) shown in Figure 3 with parameters $Ta = 9.18 \cdot 10^8$ and $Ro_T = 0.013$–0.041. From each ensemble member pointwise temperature time series throughout 3300 revolutions ("days") were evaluated, with the onset of 'climate change' occurring exactly at half time: before that ΔT, which was then followed by an exponential decay $\Delta T \sim e^{-t/\tau}$ with $\tau \approx 360$ revolutions.

In the experiments, traditional single-realization statistics – e.g. standard deviations – and their ensemble-based counterparts were compared. It was found that based on the traditional methods (calculating temporal standard deviations of different time intervals) the change in the characteristic amplitude of the irregular temperature fluctuations was often not detectable, whereas in terms of the ensemble statistics the onset of the ΔT decrease clearly resulted in a marked increase of the ensemble standard deviation. This observation implies that a changing climate in a certain sense is more "sensitive" to the small perturbations than a quasi-stationary one, but the size distribution of temperature fluctuations obtained from an individual realization does not necessarily reveal this property. Even in a stationary climate model, however, the effect of the equator-to-pole ΔT on the extreme temperatures in the mid-latitude weather is far from being trivial. A series of experimental works conducted in baroclinic annuli were dedicated to explore jet stream variability and the character of temperature distributions as a function of ΔT. Rodda et al. [165] performed series of runs in the BTU small annulus (see Figure 3), where various values of (constatnt) ΔT were set, and the temperature statistics were obtained via infrared thermographic imaging of the free water surface. The results confirmed that a smaller ΔT yields slower eastward propagation of the jet along the boundary of the Rossby wave, and also indicated that (with decreasing ΔT) the variability of temperatures *decreases* – the histogram

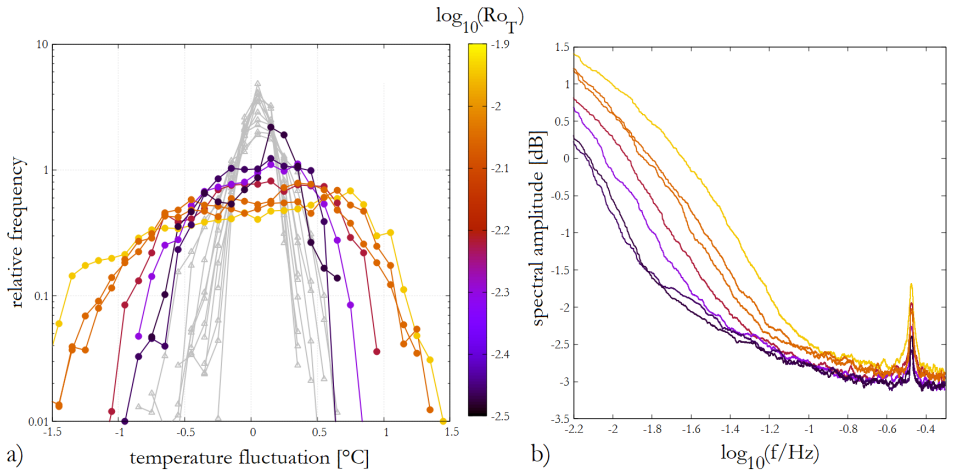


Figure 10. Histograms (a) and Fourier spectra (b) of fluctuations in temperature time series from rotating annulus experiments (BTU small tank). The coloring follows the logarithm of the thermal Rossby number Ro_T for each experiment. Apparently, with decreasing Ro_T – proportional to temperature contrast ΔT – the histograms become narrower, but the "small-slope" spectral domain (indicating less correlated behavior) widens, implying decreasing persistence. Figure taken from [167] (with permission).

of temperature fluctuations becomes narrower – at the "polar" and mid-radius domains of the tank, but *increases* at the "subtropical" region, closer to the outer rim, with decreasing ΔT. This finding was also in qualitative agreement with the NCEP reanalysis data based on actual weather station observations. The study showed that extreme events (defined as temperature values out of the 2-StDev interval around the mean) become more frequent if ΔT is set lower, even if these extremes are milder.

Similar conclusions were reported recently in the numerical minimal modeling of Rossby waves by Geen et al. [166], and in the experimental work of Vincze et al. [167], where the scaling of the width of the temperature fluctuation histograms, and the spectral properties of the time series were analyzed in a broader range of Ro_T, combining experiments from the large annulus at the Geophysical Fluid Dynamics Institute (GFDI) of the Florida State University, and the small tank at BTU. The authors found that the width of temperature fluctuation histograms in the vicinity of the bottom of the tank at mid-radius scales linearly with Ro_T, and also reported that the persistence (correlation timescale) of the "weather" in the tank decreases with ΔT, hence in the sense of greater unpredictability, the weather indeed becomes more extreme with the decreased ΔT, but this is not associated with the widening of the range of temperature anomalies (Figure 10).

Harlander et al. [168] conducted an extremely long (24-hour) rotating annulus experiment – at fixed stationary values of Ro_T and Ta – where "daily" surface temperature fields were analyzed, and the largest spatial mean temperatrue within each "month" (30-revolution interval) was logged. The so-called shape, scale, and location parameters of the generalized extreme value (GEV) distribution function were fitted to the empirical histogram of these monthly maximum values, and the resulting values were compared to those obtained via an identical procedure from 8-year series of daily atmospheric data. The comparison showed a good agreement, indicating that this laboratory model be a useful tool for investigating extreme event distributions of the climate system.

In the oceanic system, the only region of the planet where a dominantly zonal flow – analogous to the atmospheric jet stream – in the ocean can make a full circle around the globe without getting deflected by a meridional continental boundary is the Southern Ocean, where the strongest near-surface ocean current, the Antarctic Circumpolar Circulation (ACC) is to be found. This current is thought to be largely, but not entirely, wind-driven. The ACC has a particularly important climatic effect: it blocks warm tropical meridional ocean currents from reaching Antarctica, thus helping to maintain the continent's permanent ice cover. It is known from paleoclimate records that the glaciation of Antarctica happened roughly about the same geological epoch as the opening of the Drake Passage, where earlier the circumpolar flow had been interrupted by a continental bridge connecting the tip of South America and the Antarctic Peninsula. Both events took place at the Eocene-Oligocene transition (EOT) 34 million years ago, but their causal connections are still matter of debate. Bozóki et al. [169], and Vincze et al. [170] performed experiments in baroclinic annuli with the standard configuration, and a closed Drake Passage-like version where the azimuthal flow was blocked with a full-depth radial ("meridional"), thermally insulating wall.

They found that in the "closed" case a persistent azimuthal temperature gradient emerged whose magnitude scales linearly with the "meridional" temperature contrast. Furthermore, seemingly contradicting paleoclimatic data, the presence of the radial barrier yielded lower values of the surface temperature in the tank than those in the "open" experiments. This difference can be explained by the importance of the role ice-albedo feedback plays in an EOT-like transition, an aspect that is not captured in the laboratory setting. This idea was confirmed by numerical simulations conducted in a numerical global climate model, where the comparison of "closed" and "open" configurations could be made both with and without sea ice feedback. These runs indeed yielded opposite effects on sea-surface temperature and are therefore consistent with both the laboratory experiment and the paleoclimate data.

3.7. *Internal waves and small-scale instabilities*

At least for shallow atmospheres like the one of the Earth, the apect ratio $\Gamma_d = d/L$ of the experiment is too large for parameter similarity. As long as Bu is small enough, this does not have a fundamental effect for the large-scale dynamics under consideration. On the other hand, it is a problem when the generation of small-scale waves is considered. The differentially heated rotating annulus is a stratified rotating fluid that not only supports long Eady and Rossby waves but also short inertia-gravity waves (IGWs). For strongly (weakly) stratified rotating fluids such waves occur in the frequency band $f < \omega < N$ ($N < \omega < f$). The atmosphere of the Earth and the upper ocean are strongly stratified ($N/f \approx 10^2$) (whereas the deep ocean is weakly stratified only). It is therefore of interest to look for the occurrence of IGWs in the baroclinic wave tank.

3.7.1. *Boundary layer instabilities*

In the atmosphere, there are different main source mechanisms for IGWs: flow over mountains, convection, and jets and fronts [84]. For the baroclinic wave experiment, there is another source and this is boundary layer instability. Jacoby et al. [171] observed short period waves in the vicinity of the inner cooled cylinder of their differentially heated rotating annulus experiment and corresponding numerical simulations. Analysing their data they were able to prove that the waves fall nicely into the inertia-gravity wave band. Using the dispersion relation

$$\omega = \left(\frac{f^2 m^2 + N^2 \left(k^2 + l^2\right)}{k^2 + l^2 + m^2} \right)^{1/2} + Uk, \tag{50}$$

with $f = 2\Omega$ the Coriolis parameter, N the buoyancy frequency, U the azimuthal mean flow, and (k, l, m) the wave vector, one finds from their experiment with $f = 4.06$ rad/s, $N = 0.5$ rad/s,

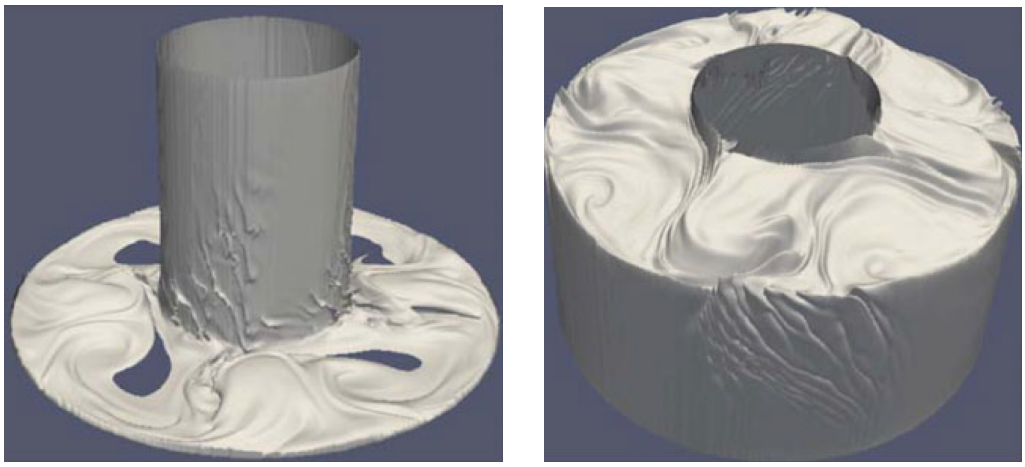
$U = 0.066$ mm/s and a wave vector $(k, l, m) = (2\pi/0.1, 2\pi/0.2, 2\pi/1.1)$ cm^{-1} an intrinsic frequency of $\omega = 1.01$ rad/s. We see that, in contrast to atmospheric conditions, the experiment in [171] was in the weakly stratified regime with $N < \omega < f$. As we will see later, this situation is rather typical for baroclinic wave experiments with an aspect ratio (comparing fluid depth, d, and gap width, L) of order one.

To explain the excitation of these waves, Jacoby at al. [171] applied the convective boundary layer model from [172]. In this model a viscous fluid with kinematic viscosity ν is bouded by an infinite vertical wall. The wall has a constant vertical temperature gradient. Moreover, between the wall and the fluid there is a fixed horizontal temperature difference with respect to the fluid far in the interior. Along the wall, a thermal boundary layer of constant thickness δ_B is considered in which the amplitude of the vertical velocity W is large. Gill and Davey [172] plotted $Pr^{1/2}Re$ against the vertical wave number where Pr is the Prandtl and $Re = \sqrt{2}W\delta_B/\nu$ is the Reynolds number. Numerically, Jacoby at al. [171] found that for their experimental parameters the critical Reynolds number is exceeded in the boundary layer of the cooled inner vertical wall of the annulus.

Based on direct numerical simulations with high-resolution pseudospectral methods a detailed study on small-scale instabilities occurring in a baroclinic cavity has been carried out [173]. In an experiment with a Prandtl number of 16 and $\Omega = 0.5125$ rad/s these authors observed small-scale fluctuations connected to baroclinic waves. These small-scale fluctuations occur for vacillating baroclinic waves studied with $\Omega = 0.5125$ rad/s, but also for steady baroclinic waves that could be found for smaller Ω. Using similar arguments as given in [171] they showed that the fluctuations correspond with inertia-gravity waves, occurring again in the regime of small frequency ratio $N/f = 0.17$. In contrast to [171], the authors emphasized that the IGWs are attached to the baroclinic waves and they develop a somewhat more sophisticated theory beyond the model by [172] that does not include rotational effects. However, the inner cold wall of the annulus plays an important role in [173], too. The latter authors showed that the small-scale fluctuations propagate vertically along the inner cold wall over three "ridges" following their baroclinic wave-3 flow. Towards the upper part of the cavity the characteristics of the IGWs developed to almost inertial waves with vertical propagation only. This latter feature might be due to the fact that in the whole cavity $N < f$ with a particular small N in the upper region of the annulus.

According to [173], the instability in the lower part of the downward flow along the inner wall is ultimately caused by Kelvin-Helmholtz instability. These authors find numerically that the local Richardson number, $Ri = N^2/U_z^2$, falls below the critical value of 1/4, signaling shear instability. This instability invokes resonant over-reflection, that is, a density overturn was observed close to the inner wall along the bottom boundary layer, associated with the presence of a reversal flow and a stagnation point. The scenario described is strongly reminiscent of the one which has already been described by [174]. It should be noted that critical Ri values cannot be found everywhere along the inner edge but only where the cold baroclinic vortices are in contact with the inner wall. Therefore, the instability exciting IGWs is intimately linked to the large-scale baroclinic wave field.

In a further study, von Larcher et al. [43] took a close look on the small-scale features at the cooled inner and heated outer wall by using two different numerical models and experimental data. In Figure 11 isosurface snapshots of the small-scale instabilities in the vertical sidewall regions are displayed. It could be shown that only the structures at the inner wall (Figure 11 (a)) correspond to IGWs able to radiate into the bulk of the baroclinic cavity. In contrast, the ripples at the outer wall (Figure 11 (b)) are not IGWs and they are due to inertial instability rather than the thermal boundary layer instability. These features remain trapped to the boundary layer of the outer wall and cannot propagate inward, in contrast to the IGWs generated at the inner wall that propagate outward.



(a) (b)

Figure 11. Isosurface snapshots of the small-scale instabilities in the vertical sidewall regions simulated with the EULAG model. a) $T = 296.15$ K, and b) $T = 291.15$ K. It should be noted that the holes in a) are due to the fact that the specific value of the isosurface is not given there at the time increment shown. Figure from [43] (with permission).

A necessary condition for inertial instability in an ideal fluid was discovered by [175], taking into account the general rotation of the fluid, it reads $d(U(r)r + \Omega r^2)^2/dr \leq 0$, where $U(r)$ is the azimuthal flow. For the differentially heated rotating annulus this criterion is insufficient since there is not only an azimuthal velocity but also a vertical velocity, W, at the outer wall. The criterion found by Hart and Kittelman [176] is more appropriate and it reads

$$2\Omega\cos\gamma\left(2\Omega\cos\gamma + \frac{d\,|\,\widetilde{U}\,|}{dr}\right) < 0, \tag{51}$$

where $\widetilde{U}$ is the velocity tangent to the wall at angle γ with $\tan\gamma = W/U$. This criterion is fulfilled in regions where the ripples in the outer boundary layer can be found. However, stratification has been neglected in the stability criterion (51).

3.7.2. *Imbalance*

It is compelling to use the differentially heated rotating annulus to study another IGW generation mechanism, spontaneous imbalance at baroclinic jets and fronts, which is an important source for the occurrence of IGWs in the atmosphere [177]. For the large-scale atmospheric flows, Froude number, $Fr = U/NH$, (also the centrifugal Froude number $Fr_c = \Omega^2 L/g$), Rossby number $Ro = U/2\Omega L$, and the aspect ratio H/L are much smaller than one. To reach similarity between the experiment and natural flows, these nondimensional parameters need to be small in the experiment as well. Using a suitable differential heating and rotation this is possible; however, compared to the atmosphere, the aspect ratio is typically too large in the experiment.

This situation is of particular relevance here, because the aspect ratio determines not only the instability of the baroclinic waves but also the special characteristics of IGWs. Put simply, keeping the radial temperature difference ΔT constant but reducing the depth H leads to larger N. The reason is that the temperature difference between the inner and outer wall also determines the difference between the surface and the bottom. This implies that for the standard setup of the baroclinic wave tank with $H/L \approx 1$, the ratio $N/f < 1$ and not $\sim 10^2$ like in the atmosphere. In

contrast to the atmosphere, small-scale IGWs will be strongly affected by rotation (see [178,179] for more details).

The importance of the aspect and frequency ratio for baroclinic instability can be seen from the Burger number given in equation (6) where $L = b - a$ is the annulus' gap width and d the annulus' fluid depth. For baroclinic instability, according to [5], a critical value of Bu depends on the horizontal wave numbers. For experiments with the baroclinic cavity we usually see a radial wave number of one (i.e. a structure $\sim \sin \pi y$, $0 \le y \le 1$, where y is the radial direction). For baroclinic instability, Bu needs to be smaller than $0.58/(1 + k^2/\pi^2)$ where k is the azimuthal wave number. Hide and Mason [34] found that for baroclinic wave experiments the azimuthal wave number depends on the geometry of the annulus,

$$\frac{\pi}{4}\frac{(b+a)}{(b-a)} \le k \le \frac{3\pi}{4}\frac{(b+a)}{(b-a)}. \tag{52}$$

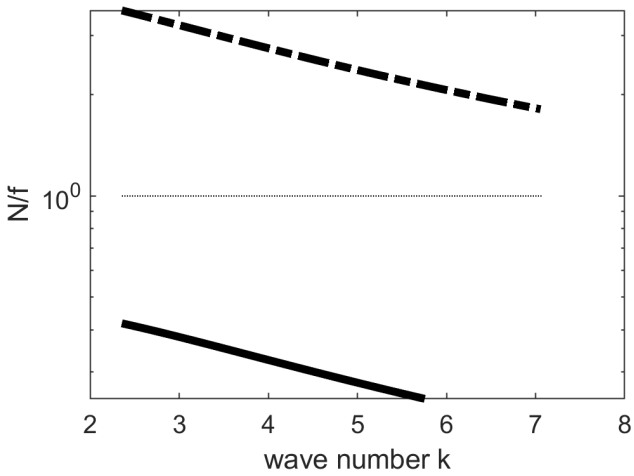


Figure 12. The critical ratio N/f in logarithmic scale over the wave number k for the small BTU tank ($d/L = 1.60$, solid line) and the large BTU tank ($d/L = 0.17$, dashed-dotted line). $N/f = 1$ is shown by the thin dotted line. The figure should be compared with [178, Figures 3c and 5c].

Figure 12 shows the wave number range and N/f at the critical value for Bu for the small ($(a,b) = (4.5,12)$cm) and the large ($(a,b) = (30.0,70.0)$cm) baroclinic cavity at the Brandenburg University of Technology (BTU). Obviously, the frequency ratio is larger (smaller) than 1 for the large (small) tank experiments. Therefore, for conducting IGW-related experiments with regard to atmospheric conditions, experimental setups with a small aspect ratio are more suitable.

To our knowledge, the first systematic study of the interaction between the large-scale nearly balanced flow and ageostrophic IGWs in a baroclinic wave tank was done by Lovegrove et al. [29]. These authors used a two layer setup with two immiscible fluids of different density, and baroclinic instability was not due to differential heating but a mechanical forcing. The upper lid of the experiment rotated slightly faster than the bottom driving the necessary vertical shear in the horizontal velocity. The aim was to find interactions between the balanced baroclinic waves that have basically no horizontal divergence, and the unbalanced or ageostrophic IGWs. Verified via (50), IGWs were found in flow regimes with amplitude vacillations and they were located mainly along the baroclinic fronts. Since the waves could be found during certain phases of the amplitude vacillation cycle, Lovegrove et al. [29] assumed that imbalance of the large-scale flow

generates the IGWs. This work was continued by [180] and they could show that for parameters that determine a baroclinic wave transition region, the IGWs play a role in terms of azimuthal wave number selection.

Somewhat later, Williams et al. [30] investigated the source mechanism for the IGW wave generation in more detail. The two possible mechanisms considered were spontaneous adjustment of the large-scale flow, and Kelvin–Helmholtz shear instability. The authors found that for stable baroclinic waves, the small scale waves can be found only for subcritical bulk two-layer Richardson numbers, defined as $Ri = 2g'\delta_E/r^2\Delta\Omega^2$, where g' is reduced gravity, $\delta_E = (\nu/\Omega)^{1/2}$ is the upper/lower Ekman layer thickness, ν kinematic viscosity, and r the radius. For unstable baroclinic waves, they found agreement between the spatial locations of IGW emission and regions in which the model Lighthill/Ford IGW source term is large, implying that the short waves in the baroclinically unstable case are freely propagating IGWs generated by spontaneous adjustment of the large-scale flow [181].

In a later work Williams et al. [182] confirmed the existence of spontaneous emission in their experiment, which implied an inevitable emission of IGWs for Rossby numbers of the same order as in the ocean and the atmosphere. They speculated that the emission of IGWs by mesoscale eddies may be a relevant process providing energy for mixing in the deep ocean. However, Flór et al. [183] questioned spontaneous emission as the dominant source mechanism for the experimentally observed IGWs. With their own experiments, they proposed that a special shear instability called *Hölmböe instability* is responsible for the IGWs. Note that this instability occurs in a two-layer fluid with a sharp interface by a resonance between an IGW and a wavelike background disturbance where the background shear varies vertically. Flór et al. [183] argued that for the generation of IGW radiation in a two-layer baroclinic cavity, Hölmböe instability could also be a candidate in addition to spontaneous emission.

For a closer connection to atmospheric conditions, Borchert et al. [178] did numerical simulations for a classical differentially heated rotating annulus with a heated outer and a cooled inner wall. For such a setup, a continuous thermal stratification develops. They considered two different geometries, similar to the two baroclinic wave experiments available at the BTU lab (see Figure 12). In their simulations they found IGWs generated at the inner vertical boundary layer as in [171] as well as at the frontal zone of the baroclinic waves. The latter have been attributed to spontaneous emission, however, these IGWs look very different from the one shown by [29]. That the patterns actually correspond to IGWs has been tested by a modal decomposition, based on linear IGW theory. In the solutions by [178] the scale-separation between the IGWs and the baroclinic waves was not so clear as in [29]. However, the IGWs in the large and small annulus configurations resemble, in their spatial structure, those observed in simulations of an idealized life cycle of an unstable baroclinic wave in the atmosphere (see e.g. [184]).

The numerical findings by [178] have been studied experimentally by [179] and [107]. The first evidence of IGWs in the continuously stratified annulus was reported but it became clear, that in spite of a good agreement with respect to the baroclinic waves, the experimentally derived buoyancy frequency N deviated from the one found numerically. The largest values of N occurred along the baroclinic jet axis and, in contrast to the numerical data, the IGWs in the experiment seemed to be trapped in the jet region.

Using data from the large BTU annulus configuration (see Figure 12), following [185] and separating the spectra into vortex and a wave components, Rodda and Harlander [107] could reproduce atmospheric spectra showing a -3 slope for the baroclinic waves but a $-5/3$ slope for the "meso-scale" part in which the IGWs occur. By computing the ratio between the divergent and the rotational component of the kinetic energy and checking the local Rossby number $Ro_l = |\zeta_z|/f$, where ζ_z is the vertical vorticity and f is the Coriolis parameter, [107] concluded that linear IGWs are responsible for the shallow part of the spectrum. This conclusion was drawn

from the fact that the energy ratio was larger than one in regions where $Ro_l < 1$ [186].

We mention finally baroclinic wave tank experiments that deviate from the classical setup by adding a continuous salt stratification to the thermal stratification [187]. The reason for this setup was a better control of the N/f ratio. The experiments were done with a small tank setup and, as we discussed above, this usually implies a small frequency ratio. However, adding a linear salt stratification gives additional freedom in adjusting N/f. This experiment was, in fact, the first to prove the existence of IGWs on fronts for a case with continuous stratification.

3.7.3. *Topography*

Remarkably, the best investigated IGW source in the atmosphere is not well studied in the context of baroclinic tank experiments. Interactions between topography and baroclinic waves of similar length scales have been studied mainly with regard to blocking (see Section 3.5). On the other hand there is a large literature on channel experiments on IGW geneneration by topography and the wave radiation into the flow (for a review see e.g. [188]). However, for the classical baroclinic cavity setup, for which the zonal flow is determined by the thermal wind relation (4), experiments have been conducted with topography having a characteristic length larger than the Rossby deformation radius, $L_R = (U_T(b-a)/(\Omega))^{1/2}$ and the focus was on the interaction between topography and planetary Rossby waves.

Recently, however, Stewart et al. [9] modified the setup by differentially rotating a small-scale topography with respect to the tank (and also to U_T). In this case, the experiments are closer to the IGW experiments reviewed in [188] and the interaction between the topographically excited IGWs with baroclinic eddies could be studied. For the excitation of IGWs, the topographic Froude number $Fr_B = U/Nh_B$, with h_B the height of the topography, should be one or larger. This can be reached by using the mentioned differentially moving ridge. (Note that Stewart et al. [9] defined a lee wave Froude number as Fr_B^{-1}.) The authors found that standing features, in particular upstream internal bores play an important role for steering the flow. Such features occurred over a wide range of flow speeds but only when the internal Froude number, $Fr_i = n\pi Fr$, where n is the vertical mode number, is smaller than one.

3.7.4. *Convection*

Convection can trigger IGWs in the atmosphere e.g. when deep convection deforms the tropopause which in turn emitts IGWs into the strongly stratified stratosphere [84]. Such proceses have been studied experimentally and we just give two recent references for an overview, [189] and [190]. In the context of baroclinic wave experiments this has, with one exception, not been investigated. Recently, Abide et al. [191] studied numerically surface effects in a large free-surface differentially heated rotating annulus. Knowing that small aspect ratio setups are more suitable for generating atmosphere-like IGWs, one must on the other hand take into account that there is a significant heat exchange at the free surface. It was found in [191] that the onset of baroclinic instability can be suppressed if the ambient temperature is higher than the mean temperature at the surface. Moreover, if the temperature of the environment is lower than the surface mean temperature, small-scale IGW-like features can be seen at the surface which are almost certainly caused by convective instability. These findings have not been confirmed experimentally. In the experiments, evaporation and the corresponding cooling can also affect the stability of the surface layer.

To round off the section, we can finally ask what role IGWs might play for the transition from the regular baroclinic wave regime to geostrophic turbulence. Using direct numerical simulation to investigate the flow in an air-filled baroclinic cavity, Read et al. [42] showed that small-scale fluctuations gradually break the regularity of the baroclinic waves, leading to structural wave vacillations before the transition to geostrophic turbulence. However, for an air-filled annulus with Prandtl numbers smaller than one, the small-scale features did not correspond with IGWs. Later, Randriamampianina and Crespo del Arco [173] speculated that IGW generation and not only small-scale fluctuations might be a relevant process for the transition. However, to our knowledge, this question on the role of IGWs for the transition process could not be conclusively answered yet.

3.8. *Benchmarks*

Experimental minimal models provide superb test-beds for the fine-tuning and validation of complex circulation models of the ocean and the atmosphere. Systematic tests of numerical codes operational in weather forcasting are especially hard to perform, as it is challenging to separate the inaccuracies arising from erroneous numerical implementation and those originating from our incomplete understanding of the processes of Earth's weather system. In the laboratory-based systems, however, all governing equations and boundary conditions are fairly well known and can be adjusted or controlled. Hence, if one uses the weather forcasting codes and numerical methods to simulate the experiment's model flow, the discrepancies cannot be blamed on the complexity of climate, but must be attributed to improper implementation.

In the framework of the MetStröm collaboration (2008–2014) the rotating annulus served as a reference experiment and the model flow was simulated by five different working groups and GCMs, using various numerical approaches, solvers and subgrid-scale parametrization methods [192].

The regular-type Rossby waves on the free water surface of the BTU small annulus have been analyzed in benchmark experiments covering a wide range of rotation rates (and fixed ΔT), also applying different initial conditions (spin-up and spin-down). Five groups of the collaboration have conducted numerical simulations in the same parameter regime using different approaches and solvers trying to reproduce the laboratory results. The experimentally and numerically obtained baroclinic wave patterns have then been contrasted in terms of various parameters, most notably their dominant wave numbers and drift rates. The study found that although most of the numerical codes were rather successful in predicting the waveform of the Rossby waves, almost all of them consistently underestimated their drift rates.

A similar approach – testing operational weather forecasting methods in the rotating annulus – has been followed by Young and Read [193]. They built a forecasting system for the annulus based on the same principles and techniques which are regularly applied by the British MetOffice for atmospheric predictions. Their results showed that a range of flow regimes could be accurately predicted, and forecasts in the regular wave flow regime performed well. Forecasts in the amplitude and structural vacillation flow regimes, however were found to be less accurate in terms of predicting wave drift rates and wavenumber transitions.

4. Conclusions

In the struggle to understand the atmospheric general circulation [145,194], the differentially heated rotating annulus has certainly made a contribution in spite of the fact that boundary layers have a more significant effect on the flow in the annulus compared to the flow of Earth's atmosphere. It is also true that laboratory analogues such as the thermally driven rotating annuli

are not exact experimental simulation models, however, they do contain important elements of a complex dynamics that enable a deeper understanding of fundamental aspects and relationships and are hence fully complementary to numerical simulations. The same could be said for the other two basic experiments used also in the context of geophysical flows: the Rayleigh–Bénard (RB) and the Taylor–Couette (TC) experiment. In a sense, the Hide–Fultz experiment reviewed here, combines RB-convection and TC-shear and adds (background) rotation and is hence, with a view on geophysical fluid dynamics, the most "complete" of the trio.

Last year, the Royal Society celebrated the 100 year anniversary of Taylor's fundamental 1923 paper [195] by a two volume special issue [196,197]. It is quite a remarkable coincidence that in the same year, Exner [198] did the first experiments on baroclinic instability. More precisely, he operated his experiment in a baroclinically unstable irregular regime where other experimenters before him considered the stable azimuthal regime only [199]. Although of course Taylor's work had a far greater impact on the development of fluid mechanics than Exner's article, we can humbly celebrate the 100 year anniversary of the first Hide-Fultz-type experiment with baroclinic instability with this review.

Environmental flows remain challeging [200] and the thermally driven rotating annulus will continue to play a role in the development of theories for convective rotating flows and further as a reference experiment to test numerical models and parameterizations. Numerical models have certainly developed to a level of greater performance, but direct numerical simulations are hardly possible, especially for the large experiments shown in Figure 3. The larger experiments have a free surface and surface effects like surface heat flux or evaporation become more important. These additional boundary conditions make numerical calculations even more time consuming. However, over the last years codes that allow for massively parallel computations have been developed for rotating stratified fluids [201]. Recently one such code was applied to stratified Taylor-Couette flows [202] and it seems possible in the near future to do direct numerical simulations also for large experimental setups. Finally, we note that even for smaller tanks, long simulations, which are necessary, e.g. to answer questions about extreme values, can currently be done only with great effort.

We pointed out that apart from baroclinic instability other types of instability generating small-scale inertia gravity waves are also an inherent part of the annulus fluid dynamics. In the atmosphere, such waves play a fundamental role for the large-scale atmospheric circulation [84]. Hence it is certainly a future task to understand better the interactions of these very different flow scales in the annulus and to uncover the role that the small-scale waves play for the transition to turbulence. Also, nonmodal instability might be worth considering in this context and first attempts have been made to estimate such modes from annulus data [203,204]. An extensive review on nonmodal instability can be found in [205]. Transient growth is possible only when the linearized Navier-Stokes operator is non-normal and this is usually the case in shear flows. At this point it seems appropriate to refer again to the remarkable similarity in the mathematics of barotropic (shear) and baroclinic instability [194].

Additionally, as pointed out by [206] and recently cited by [9], "modern technologies and analysis techniques have spawned a renaissance in laboratory experiments as these new approaches can provide new insights into processes, like rotating stratified turbulence, that remain challenging and/or infeasible to explore via numerical simulations." Two of the modern technologies we would like to mention here. One is combining laser induced fluoresence (LIF) with particle image velocimetry (PIV). Caudwell et al. [207] have shown that this technique is well suited for convective flows with a reasonable accuracy of 0.2° C with respect to temperature. A simultaneous measurement of the velocity field allows for a calculation of key parameters like the Richardson number or the heat flux in the interior of the fluid. LIF used a temperature sensitive dye like Rhodamine B. When this substance is excited with a green laser (532 nm), it emits light in the range

from 565 nm to 585 nm, depending on the temperature of the Rhodamine particles. Since PIV works with light sources of, for example, 532 nm, a wavelength outside the sensitivity of Rhodamine, these two methods can be used simultaneously if suitable filters are used.

The other method we wish to mention is 3D Lagrangian particle tracking [208]. This method allows for the detection of the position, speed, and acceleration of particles in 3D and gives hence a 3D view on a large number of particle tracks. Apart from the attempts described in Section 3.4, the 3D structure of the flow in the baroclinic annulus has not been studied. Many problems related to transport and mixing in geophysical flows are still open and could be attacked by particle tracking. Also, diagnostic tools that have been developed (see, e.g. [209]) to predict the spreading of pollutants could be used in annulus experiments together with 3D particle tracking. As described above for PIV, particle tracking could be combined with LIF to obtain the temperature along particle tracks. Of course, another condition is that all of these experimental techniques need a good optical access to the fluid chamber.

Acknowledgements

We thank Kial D. Stewart and C. J. Shakespeare for providing updated versions of Figures 1 and 3. U.H. thanks L.R.M. Maas and P. Szabo for helpful discussions and R. Stöbel, S. Rohark, and S. Misera for constant support in the laboratory. M.V. thanks T. Tel, M. Herein, and Z. Trocsanyi for the fruitful discussions. K.S. thanks J. Marshall and J. Whitehead for conversations concerning some of the historical context.

U. Harlander thanks DFG for financial support (HA 2932/8-1&2, HA 2932/17-4), DAAD for funding a series of french-german exchange projects within PROCOPE, and the BTU Graduate Research School (BTU-GRS) for constant support. M.V. Kurgansky was partly supported by funding from the State Assignment (No. FMWR-2022-0011) “Fundamental research into the dynamics of vortex structures and turbulence in geophysical flows”. K. Speer acknowledges the support of NSF Office of Polar Programs (OPP 1643679, OPP 1644172, and OPP 2148517) and Ocean Science (OCE 1658479).

Declaration of interests

The authors do not work for, advise, own shares in, or receive funds from any organization that could benefit from this article, and have declared no affiliations other than their research organizations.

References

[1] D. Fultz, “Experimental analogies to atmospheric motions”, in *Compendium of meteorology* (T. F. Malone, ed.), American Meteorological Society, Boston, MA, 1951, pp. 1235–1248.

[2] D. Fultz, “A preliminary report on experiments with thermally reproduced lateral mixing in a rotating hemispherical shell of liquid”, *J. Atmos. Sci.* **6** (1949), pp. 17–33.

[3] M. Ghil, P. L. Read and L. Smith, “Geophysical flows as dynamical systems: the influence of Hide’s experiments”, *Astron. Geophys.* **51** (2010), no. 4, pp. 4.28–4.35.

[4] J. G. Charney, “The dynamics of long waves in a baroclinic westerly current”, *J. Atmos. Sci.* **4** (1947), pp. 136–162.

[5] E. T. Eady, “Long waves and cyclone waves”, *Tellus* **1** (1949), no. 3, pp. 33–52.

[6] V. P. Starr, “Commentaries Concerning Research on the General Circulation”, *Tellus* **6** (1954), no. 3, pp. 268–272.

[7] R. Hide and P. J. Mason, “Baroclinic waves in a rotating fluid subject to internal heating”, *Philos. Trans. R. Soc. Lond., Ser. A* **268** (1970), no. 1186, pp. 201–232.

[8] P. R. Gent and H. Leach, “Baroclinic instability in an eccentric annulus”, *J. Fluid Mech.* **77** (1976), no. 4, pp. 769–788.

[9] K. D. Stewart and C. J. Shakespeare, "On stratified flow over a topographic ridge in a rotating annulus", *Geophys. Astrophys. Fluid Dyn.* **118** (2024), no. 1, pp. 25–70.

[10] R. L. Pfeffer and W. W. Fowlis, "Wave Dispersion in a Rotating, Differentially Heated Cylindrical Annulus Of Fluid", *J. Atmos. Sci.* **25** (1968), no. 3, pp. 361–371.

[11] U. Harlander, T. von Larcher, Y. Wang and C. Egbers, "PIV- and LDV-measurements of baroclinic wave interactions in a thermally driven rotating annulus", *Exp. Fluids* **51** (2011), pp. 37–49.

[12] G. Buzyna, R. L. Pfeffer and R. Kung, "Kinematic Properties of Wave Amplitude Vacillation in a Thermally Driven Rotating Fluid", *J. Atmos. Sci.* **46** (1989), no. 17, pp. 2716–2730.

[13] G.-Q. Li, R. Kung and R. L. Pfeffer, "An Experimental Study of Baroclinic Flows with and without Two-Wave Bottom Topography", *J. Atmos. Sci.* **43** (1986), no. 22, pp. 2585–2599.

[14] G. Buzyna, R. L. Pfeffer and R. Kung, "Transition to geostrophic turbulence in a rotating differentially heated annulus of fluid", *J. Fluid Mech.* **145** (1984), pp. 377–403.

[15] R. L. Pfeffer, S. Applequist, R. Kung, et al., "Progress in Characterizing the Route to Geostrophic Turbulence and Redesigning Thermally Driven Rotating Annulus Experiments", *Theor. Comput. Fluid Dyn.* **9** (1997), pp. 253–267.

[16] W.-G. Früh and P. L. Read, "Wave interactions and the transition to chaos of baroclinic waves in a thermally driven rotating annulus", *Philos. Trans. R. Soc. Lond., Ser. A* **355** (1997), no. 1722, pp. 101–153.

[17] R. L. Pfeffer, G. Buzyna and W. W. Fowlis, "Synoptic Features and Energetics of Wave-Amplitude Vacillation in a Rotating, Differentially-Heated Fluid", *J. Atmos. Sci.* **31** (1974), no. 3, pp. 622–645.

[18] W.-G. Früh, "Amplitude vacillation in baroclinic flows", in *Modelling Atmospheric and Oceanic Flows: Insights from Laboratory Experiments and Numerical Simulations* (T. von Larcher and P. D. Williams, eds.), Geophysical Monograph Series, American Geophysical Union, 2014, pp. 61–81.

[19] J. F. Price and H. T. Rossby, "Observations of a barotropic planetary wave in the western North Atlantic", *J. Mar. Res.* **40** (1982), pp. 543–558.

[20] P. L. Read, "From mixing to geostrophy: Geostrophic turbulence in atmospheres, oceans and the laboratory", in *Marine Turbulence: Theories, Observations, and Models* (H. Z. Baumert, J. Simpson and J. Sündermann, eds.), Cambridge University Press, 2005, pp. 406–422.

[21] P. M. Saunders, "The Instability of a Baroclinic Vortex", *J. Phys. Oceanogr.* **3** (1973), no. 1, pp. 61–65.

[22] T. Maxworthy and S. Narimousa, "Unsteady, Turbulent Convection into a Homogeneous, Rotating Fluid,with Oceanographic Applications", *J. Phys. Oceanogr.* **24** (1994), no. 5, pp. 865–887.

[23] J. Marshall and F. Schott, "Open-ocean convection: Observations, theory, and models", *Rev. Geophys.* **37** (1999), no. 1, pp. 1–64.

[24] P. L. Read, "Transition To Geostrophic Turbulence In The Laboratory, And As A Paradigm In Atmospheres And Oceans", *Surv. Geophys.* **22** (2001), pp. 265–317.

[25] P. L. Read, E. P. Pérez, I. M. Moroz and R. M. B. Young, "General circulation of planetary atmospheres: Insights from rotating annulus and related experiments", in *Modelling Atmospheric and Oceanic Flows: Insights from Laboratory Experiments and Numerical Simulations* (T. v. Larcher and P. D. Williams, eds.), American Geophysical Union, 2014, pp. 9–44.

[26] P. L. Read, "Dynamics and circulation regimes of terrestrial planets", *Planet. Space Sci.* **59** (2011), pp. 900–914.

[27] P. Read, D. Kennedy, N. Lewis, et al., "Baroclinic and barotropic instabilities in planetary atmospheres: energetics, equilibration and adjustment", *Nonlinear Process. Geophys.* **27** (2020), no. 2, pp. 147–173.

[28] J. E. Hart, "A Laboratory Study of Baroclinic Instability", *Geophys. Fluid Dyn.* **3** (1972), pp. 181–209.

[29] A. F. Lovegrove, P. L. Read and C. J. Richards, "Generation of inertia-gravity waves in a baroclinically unstable fluid", *Q. J. R. Meteorol. Soc.* **126** (2000), no. 570, pp. 3233–3254.

[30] P. D. Williams, T. W. N. Haine and P. L. Read, "On the generation mechanisms of short-scale unbalanced modes in rotating two-layer flows with vertical shear", *J. Fluid Mech.* **528** (2005), pp. 1–22.

[31] U. Harlander, A. Sukhanovskii, S. Abide, et al., "New Laboratory Experiments to Study the Large-Scale Circulation and Climate Dynamics", *Atmosphere* **14** (2023), article no. 836.

[32] R. Hide and W. W. Fowlis, "Thermal convection in a rotating annulus of liquid: effect of viscosity on the transition between axisymmetric and non-axisymmetric flow regimes", *J. Atmos. Sci.* **22** (1965), pp. 541–558.

[33] J. S. Fein and R. L. Pfeffer, "An experimental study of the effects of Prandtl number on thermal convection in a rotating, differentially heated cylindrical annulus of fluid", *J. Fluid Mech.* **75** (1976), no. 1, pp. 81–112.

[34] R. Hide and P. J. Mason, "Sloping convection in a rotating fluid", *Adv. Phys.* **24** (1975), no. 1, pp. 47–100.

[35] R. Hide and R. Stoneley, "An experimental study of thermal convection in a rotating liquid", *Philos. Trans. R. Soc. Lond., Ser. A* **250** (1958), no. 983, pp. 441–478.

[36] C. A. Smith, K. G. Speer and R. W. Griffiths, "Multiple Zonal Jets in a Differentially Heated Rotating Annulus", *J. Phys. Oceanogr.* **44** (2014), no. 9, pp. 2273–2291.

[37] S. D. Marshall and P. L. Read, "An experimental investigation of blocking by partial barriers in a rotating baroclinic annulus", *Geophys. Astrophys. Fluid Dyn.* **112** (2018), no. 2, pp. 97–129.

[38] U. Harlander, J. Wenzel, K. Alexandrov, Y. Y. Wang and C. Egbers, "Simultaneous PIV and thermography measurements of partially blocked flow in a differentially heated rotating annulus", *Exp. Fluids* **52** (2012), pp. 1077–1087.
[39] H. Scolan and P. L. Read, "A rotating annulus driven by localized convective forcing: a new atmosphere-like experiment", *Exp. Fluids* **58** (2017), no. 75, article no. 75.
[40] A. K. Banerjee, A. Bhattacharya and S. Balasubramanian, "Experimental study of rotating convection in the presence of bi-directional thermal gradients with localized heating", *AIP Adv.* **8** (2018), no. 11, article no. 115324.
[41] A. Sukhanovskii, E. Popova and A. Vasiliev, "A shallow layer laboratory model of large-scale atmospheric circulation", *Geophys. Astrophys. Fluid Dyn.* **117** (2023), no. 3, pp. 155–176.
[42] P. L. Read, P. Maubert, A. Randriamampianina and W.-G. Früh, "Direct numerical simulation of transitions towards structural vacillation in an air-filled, rotating, baroclinic annulus", *Phys. Fluids* **20** (2008), no. 4, article no. 044107.
[43] T. von Larcher, S. Viazzo, U. Harlander, M. Vincze and A. Randriamampianina, "Instabilities and small-scale waves within the Stewartson layers of a thermally driven rotating annulus", *J. Fluid Mech.* **841** (2018), pp. 380–407.
[44] P. L. Read, "A combined laboratory and numerical study of heat transport by baroclinic eddies and axisymmetric flows", *J. Fluid Mech.* **489** (2003), pp. 301–323.
[45] J. Pedlosky, *Geophysical Fluid Dynamics*, second edition, Springer, 1987.
[46] R. T. Pierrehumbert and K. L. Swanson, "Baroclinic Instability", *Ann. Rev. Fluid Mech.* **27** (1995), pp. 419–467.
[47] G. K. Vallis, *Atmospheric and Oceanic Fluid Dynamics. Fundamentals and Large-scale Circulation*, Cambridge University Press, 2006.
[48] M. E. McIntyre, "Diffusive destabilization of the baroclinic circular vortex", *Geophys. Fluid Dyn.* **1** (1970), pp. 19–58.
[49] V. I. Arnol'd, "On the conditions of nonlinear stability of plane stationary curvilinear currents of ideal fluids", *Dokl. Akad. Nauk SSSR* **162** (1965), no. 5, pp. 975–978.
[50] W. Blumen, "On the stability of quasi-geostrophic flow", *J. Atmos. Sci.* **25** (1968), no. 5, pp. 929–931.
[51] L. A. Diky and M. V. Kurgansky, "Integral conservation law for perturbations of zonal flow, and its applications to stability studies", *Izv. - Atmos. Ocean. Phys.* **7** (1971), no. 9, pp. 623–626.
[52] M. V. Kurgansky, *Adiabatic invariants in large-scale atmospheric dynamics*, Taylor & Francis, 2002, p. 222.
[53] M. V. Kalashnik, M. V. Kurgansky and O. G. Chkhetiani, "Baroclinic instability in geophysical fluid dynamics", *Physics - Uspekhi.* **65** (2022), no. 10, pp. 1039–1070.
[54] J. G. Charney and M. E. Stern, "On the stability of internal baroclinic jets in a rotating atmosphere", *J. Atmos. Sci.* **19** (1962), pp. 159–172.
[55] J. Pedlosky, "The Stability of Currents in the Atmosphere and the Ocean: Part I", *J. Atmos. Sci.* **21** (1964), no. 2, pp. 201–219.
[56] H. C. Davies and C. H. Bishop, "Eady edge waves and rapid development", *J. Atmos. Sci.* **51** (1994), no. 13, pp. 1930–1946.
[57] E. Heifetz, C. H. Bishop, B. J. Hoskins and J. Methven, "The counter-propagating Rossby-wave perspective on baroclinic instability. I: Mathematical basis", *Q. J. R. Meteorol. Soc.* **130** (2004), no. 596, pp. 211–231.
[58] E. Heifetz and J. Methven, "Relating optimal growth to counterpropagating Rossby waves in shear instability", *Phys. Fluids* **17** (2005), article no. 064107.
[59] B. F. Farrell and P. J. Ioannou, "Generalized Stability Theory. Part I: Autonomous Operators", *J. Atmos. Sci.* **53** (1996), no. 14, pp. 2025–2040.
[60] S. Chandrasekhar, *Hydrodynamic and Hydromagnetic Stability*, Oxford University Press, 1961.
[61] V. Barcilon, "Role of the Ekman friction in the stability of the symmetric regime obtained in a rotating annulus", *J. Atmos. Sci.* **21** (1964), pp. 291–299.
[62] G. P. Williams and J. B. Robinson, "Generalized Eady waves and Ekman pumping", *J. Atmos. Sci.* **31** (1974), pp. 1768–1776.
[63] J. S. A. Green, "A problem in baroclinic stability", *Q. J. R. Meteorol. Soc.* **86** (1960), no. 368, pp. 237–251.
[64] W. Blumen, "Uniform potential vorticity flow: Part I—Theory of wave interactions and two-dimensional turbulence", *J. Atmos. Sci.* **35** (1978), pp. 774–783.
[65] M. Held, R. T. Pierrehumbert, S. T. Garner and K. L. Swanson, "Surface quasi-geostrophic dynamics", *J. Fluid Mech.* **282** (1995), pp. 1–20.
[66] N. A. Phillips, "A simple three-dimensional model for the study of large-scale flow patterns", *J. Atmos. Sci.* **8** (1951), pp. 381–394.
[67] E. N. Lorenz, "The mechanics of vacillation", *J. Atmos. Sci.* **20** (1963), no. 3, pp. 448–465.
[68] B. M. Boubnov and G. S. Golitsyn, *Convection in Rotating Fluids*, Kluwer Academic Publishers, 1995.
[69] B. J. Hoskins, "The role of potential vorticity in symmetric stability and instability", *Q. J. R. Meteorol. Soc.* **100** (1974), pp. 480–482.

[70] T. J. Dunkerton, "On the inertial stability of the equatorial middle atmosphere", *J. Atmos. Sci.* **38** (1981), pp. 2354–2364.
[71] P. D. Williams, P. L. Read and T. W. N. Haine, "Testing the limits of quasi-geostrophic theory: application to observed laboratory flows outside the quasi-geostrophic regime", *J. Fluid Mech.* **649** (2010), pp. 187–203.
[72] B. P. Hignett, A. A. White, R. D. Carter, W. D. N. Jackson and R. M. Small, "A comparison of laboratory measurements and numerical simulations of baroclinic wave flows in a rotating cylindrical annulus", *Q. J. R. Meteorol. Soc.* **111** (1985), no. 467, pp. 131–154.
[73] J. P. McGuirk and E. R. Reiter, "A vacillation in atmospheric energy parameters", *J. Atmos. Sci.* **33** (1976), no. 11, pp. 2079–2093.
[74] L. Barry, G. Craig and J. Thuburn, "Poleward heat transport by the atmospheric heat engine", *Nature* **415** (2002), pp. 774–777.
[75] M. Bowden and H. F. Eden, "Thermal Convection in a Rotating Fluids Annulus: Temperature, Heat Flow and Flow Field Observations in the Upper Symmetric Regime", *J. Atmos. Sci.* **22** (1965), no. 2, pp. 185–195.
[76] E. Pérez-Pérez, P. L. Read and I. M. Moroz, "Assessing eddy parameterization schemes in a differentially heated rotating annulus experiment", *Ocean Model.* **32** (2010), no. 3, pp. 118–131. The magic of modelling: A special volume commemorating the contributions of Peter D. Killworth – Part 2.
[77] R. L. Pfeffer, G. Buzyna and R. Kung, "Time-Dependent Modes of Behavior of Thermally Driven Rotating Fluids", *J. Atmos. Sci.* **37** (1980), no. 10, pp. 2129–2149.
[78] M. Bowden and H. F. Eden, "Effect of a radial barrier on the convective flow in a rotating fluid annulus", *J. Geophys. Res. (1896-1977)* **73** (1968), no. 22, pp. 6887–6895.
[79] Q. G. Rayer, D. W. Johnson and R. Hide, "Thermal convection in a rotating fluid annulus blocked by a radial barrier", *Geophys. Astrophys. Fluid Dyn.* **87** (1998), no. 3-4, pp. 215–252.
[80] M. Vincze, T. Bozóki, M. Herein, et al., "The Drake Passage opening from an experimental fluid dynamics point of view", *Sci. Rep.* **11** (2021), article no. 19951.
[81] G. P. Williams, "Baroclinic annulus waves", *J. Fluid Mech.* **49** (1971), no. 3, pp. 417–449.
[82] B. Gallet and R. Ferrari, "The vortex gas scaling regime of baroclinic turbulence", *Proc. Natl. Acad. Sci. USA* **117** (2020), no. 9, pp. 4491–4497.
[83] B. Gallet, B. Miquel, G. Hadjerci, K. J. Burns, G. R. Flierl and R. Ferrari, "Transport and emergent stratification in the equilibrated Eady model: the vortex-gas scaling regime", *J. Fluid Mech.* **948** (2022), article no. A31.
[84] U. Achatz, M. J. Alexander, E. Becker, et al., "Atmospheric Gravity Waves: Processes and Parameterization", *J. Atmos. Sci.* **81** (2024), no. 2, pp. 237–262.
[85] R. Hide, "Some experiments on thermal convection in a rotating liquid", *Q. J. R. Meteorol. Soc.* **79** (1953), no. 339, pp. 161–161.
[86] R. L. Pfeffer and Y. Chiang, "Two kinds of vacillation in rotating laboratory experiments", *Mon. Wea. Rev.* **95** (1967), no. 2, pp. 75–82.
[87] K. Ukajil and K. Tamaki, "A Numerical Study of Tilted-Trough Vacillation Observed in a Differentially Heated Rotating Fluid Annulus", *J. Meteorol. Soc. Jpn. Ser. II* **68** (1990), no. 4, pp. 447–460.
[88] W. W. Fowlis and R. L. Pfeffer, "Characteristics of Amplitude Vacillation in a Rotating, Differentially Heated Fluid Determined by a Multi-Probe Technique", *J. Atmos. Sci.* **26** (1969), no. 1, pp. 100–108.
[89] J. E. Hart, "Finite Amplitude Baroclinic Instability", *Ann. Rev. Fluid Mech.* **11** (1979), no. 1, pp. 147–172.
[90] B. G. Hunt, "Atmospheric Vacillations in a General Circulation Model I: The Large-Scale Energy Cycle", *J. Atmos. Sci.* **35** (1978), no. 7, pp. 1133–1143.
[91] J. Pedlosky, "Finite-Amplitude Baroclinic Waves", *J. Atmos. Sci.* **27** (1970), no. 1, pp. 15–30.
[92] P. E. Merelees, "On the periods of amplitude vacillations", *J. Meteorol. Soc. Jpn. Ser. II* **50** (1972), pp. 214–225.
[93] K. Ohkitani and T. Sakajo, "Oscillatory damping in long-time evolution of the surface quasi-geostrophic equations with generalized viscosity: a numerical study", *Nonlinearity* **23** (2010), no. 12, article no. 3029.
[94] J. Pedlosky, "Finite-Amplitude Baroclinic Waves with Small Dissipation", *J. Atmos. Sci.* **28** (1971), no. 4, pp. 587–597.
[95] A. Barcilon and P. G. Drazin, "A Weakly Nonlinear Theory of Amplitude Vacillation and Baroclinic Waves", *J. Atmos. Sci.* **41** (1984), no. 22, pp. 3314–3330.
[96] B. Wang and A. Barcilon, "The Weakly Nonlinear Dynamics of a Planetary Green Mode and Atmospheric Vacillation", *J. Atmos. Sci.* **43** (1986), no. 12, pp. 1275–1287.
[97] J. Pedlosky and J. Thomson, "Baroclinic instability of time-dependent currents", *J. Fluid Mech.* **490** (2003), pp. 189–215.
[98] M. C. Nguyen, M. J. Reeder, N. E. Davidson, R. K. Smith and M. T. Montgomery, "Inner-core vacillation cycles during the intensification of Hurricane *Katrina*", *Q. J. R. Meteorol. Soc.* **137** (2011), no. 657, pp. 829–844.
[99] M. Vincze, U. Harlander, T. von Larcher and C. Egbers, "An experimental study of regime transitions in a differentially heated baroclinic annulus with flat and sloping bottom topographies", *Nonlinear Process. Geophys.* **21** (2014), no. 1, pp. 237–250.

[100] S. H. Risch and P. L. Read, "A laboratory study of global-scale wave interactions in baroclinic flow with topography II: vacillations and low-frequency variability", *Geophys. Astrophys. Fluid Dyn.* **109** (2015), no. 4, pp. 359–390.
[101] R. M. B. Young and P. L. Read, "Predictability of the thermally driven laboratory rotating annulus", *Q. J. R. Meteorol. Soc.* **142** (2016), no. 695, pp. 911–927.
[102] S. C. Hardiman, A. A. Scaife, N. J. Dunstone and L. Wang, "Subseasonal Vacillations in the Winter Stratosphere", *Geophys. Res. Lett.* **47** (2020), no. 9, article no. e2020GL087766.
[103] P. L. Read, "Rotating Annulus Flows and Baroclinic Waves", in *Rotating fluids in Geophysical and Industrial Applications* (E. J. Hopfinger, ed.), Springer, 1992, pp. 185–214.
[104] R. H. Kraichnan, "Inertial ranges in two-dimensional turbulence", *Phys. Fluids* **10** (1967), pp. 1417–1423.
[105] P. G. Saffman, "On the spectrum and decay of random two-dimensional vorticity distributions at large reynolds number", *Stud. Appl. Math.* **50** (1971), no. 4, pp. 377–383.
[106] R. D. Wordsworth, P. L. Read and Y. H. Yamazaki, "Turbulence, waves, and jets in a differentially heated rotating annulus experiment", *Phys. Fluids* **20** (2008), no. 12, article no. 126602.
[107] C. Rodda and U. Harlander, "Transition from Geostrophic Flows to Inertia–Gravity Waves in the Spectrum of a Differentially Heated Rotating Annulus Experiment", *J. Atmos. Sci.* **77** (2020), no. 8, pp. 2793–2806.
[108] P. J. Mason, "Baroclinic waves in a container with sloping end walls", *Philos. Trans. R. Soc. Lond., Ser. A* **278** (1975), no. 1284, pp. 397–445.
[109] S. Condie and P. Rhines, "A convective model for the zonal jets in the atmospheres of Jupiter and Saturn", *Nature* **367** (1994), pp. 711–713.
[110] P. L. Read, T. N. L. Jacoby, P. H. T. Rogberg, et al., "An experimental study of multiple zonal jet formation in rotating, thermally driven convective flows on a topographic beta-plane", *Phys. Fluids* **27** (2015), no. 8, article no. 085111.
[111] A. M. Treguier, N. G. Hogg, M. Maltrud, K. Speer and V. Thierry, "The Origin of Deep Zonal Flows in the Brazil Basin", *J. Phys. Oceanogr.* **33** (2003), no. 3, pp. 580–599.
[112] H. Nakano and N. Suginohara, "Importance of the eastern Indian Ocean for the abyssal Pacific", *J. Geophys. Res. Oceans* **107** (2002), no. C12, pp. 12-1–12-14.
[113] R. Herbei, I. W. McKeague and K. G. Speer, "Gyres and Jets: Inversion of Tracer Data for Ocean Circulation Structure", *J. Phys. Oceanogr.* **38** (2008), no. 6, pp. 1180–1202.
[114] D. Lemasquerier, B. Favier and M. M. Le Bars, "Zonal jets at the laboratory scale: hysteresis and Rossby waves resonance", *J. Fluid Mech.* **910** (2021), article no. A18.
[115] H. Aref, "The development of chaotic advection", *Phys. Fluids* **14** (2002), no. 4, pp. 1315–1325.
[116] A. S. Bower, "A Simple Kinematic Mechanism for Mixing Fluid Parcels across a Meandering Jet", *J. Phys. Oceanogr.* **21** (1991), no. 1, pp. 173–180.
[117] R. M. Samelson and S. Wiggins, *Lagrangian Transport in Geophysical Jets and Waves*, Interdisciplinary Applied Mathematics, Springer, 2006.
[118] M. Agaoglou, V. J. García-Garrido, U. Harlander and A. M. Mancho, "Building transport models from baroclinic wave experimental data", *Phys. Fluids* **36** (2024), no. 1, article no. 016611.
[119] R. Mizuta and S. Yoden, "Chaotic Mixing and Transport Barriers in an Idealized Stratospheric Polar Vortex", *J. Atmos. Sci.* **58** (2001), no. 17, pp. 2616–2629.
[120] A. de la Cámara, C. R. Mechoso, A. M. Mancho, E. Serrano and K. Ide, "Isentropic Transport within the Antarctic Polar-Night Vortex: Rossby Wave Breaking Evidence and Lagrangian Structures", *J. Atmos. Sci.* **70** (2013), no. 9, pp. 2982–3001.
[121] M. Abalos and A. de la Cámara, "Twenty-First Century Trends in Mixing Barriers and Eddy Transport in the Lower Stratosphere", *Geophys. Res. Lett.* **47** (2020), no. 21, article no. e2020GL089548.
[122] M. E. McIntyre, "On the Antarctic ozone hole", *J. Atmos. Sol.-Terr. Phys.* **51** (1989), no. 1, pp. 29–43. Cedar Science-Part II.
[123] G. García-Sánchez, A. M. Mancho, A. G. Ramos, J. Coca and S. Wiggins, "Structured pathways in the turbulence organizing recent oil spill events in the Eastern Mediterranean", *Sci. Rep.* **12** (2022), no. 1, article no. 3662.
[124] G. Haller, *Transport Barriers and Coherent Structures in Flow Data*, Cambridge University Press, 2023.
[125] J. Sommeria, S. Mayers and H. L. Swinney, "Laboratory model of a planetary eastward jet", *Nature* **337** (1989), pp. 58–61.
[126] R. P. Behringer, S. D. Meyers and H. L. Swinney, "Chaos and mixing in a geostrophic flow", *Phys. Fluids, A* **3** (1991), no. 5, pp. 1243–1249.
[127] S. Sugata and S. Yoden, "Chaotic Lagrangian Motion and Heat Transport in a Steady, Baroclinic Annulus Wave", *J. Meteorol. Soc. Jpn. Ser. II* **72** (1994), no. 4, pp. 569–587.
[128] T. Tajima, T. Nakamura and T. Kuroda, "Laboratory Experiments of Lagrangian Motions in a Steady Baroclinic Wave -Internal Structures of Vortices-", *J. Meteorol. Soc. Jpn.* **73** (1995), no. 1, pp. 37–46.

[129] T. Tajima and T. Nakamura, "Meridional Flow Field of Axisymmetric Flows in a Rotating Annulus", *J. Atmos. Sci.* **57** (2000), no. 18, pp. 3109–3121.
[130] R. J. Keane, P. L. Read and G. P. King, "On the stirring properties of the thermally-driven rotating annulus", *Phys. D: Nonlinear Phenom.* **268** (2014), pp. 50–58.
[131] C. Mendoza and A. M. Mancho, "Hidden Geometry of Ocean Flows", *Phys. Rev. Lett.* **105** (2010), no. 3, article no. 038501.
[132] A. M. Mancho, S. Wiggins, J. Curbelo and C. Mendoza, "Lagrangian descriptors: A method for revealing phase space structures of general time dependent dynamical systems", *Commun. Nonlinear Sci. Numer. Simul.* **18** (2013), no. 12, pp. 3530–3557.
[133] I. M. Jánosi, P. Kiss, V. Homonnai, et al., "Dynamics of passive tracers in the atmosphere: Laboratory experiments and numerical tests with reanalysis wind fields", *Phys. Rev. E* **82** (2010), no. 4, article no. 046308.
[134] G. J. Shutts, "The propagation of eddies in diffluent jetstreams: Eddy vorticity forcing of 'blocking' flow fields", *Q. J. R. Meteorol. Soc.* **109** (1983), no. 462, pp. 737–761.
[135] P. Martineau, H. Nakamura, A. Yamamoto and Y. Kosaka, "Baroclinic blocking", *Geophys. Res. Lett.* **49** (2022), article no. e2022GL097791.
[136] J. G. Charney and D. M. Straus, "Form-drag instability, multiple equilibria and propagating planetary waves in baroclinic, orographically forced, planetary wave systems", *J. Atmos. Sci.* **37** (1980), no. 6, pp. 1157–1176.
[137] J. G. Charney and J. G. DeVore, "Multiple flow equilibria in the atmosphere and blocking", *J. Atmos. Sci.* **36** (1979), no. 7, pp. 1205–1216.
[138] A. R. Hansen and T.-C. Chen, "A Spectral Energetics Analysis of Atmospheric Blocking", *Mon. Wea. Rev.* **110** (1982), no. 9, pp. 1146–1165.
[139] D. F. Rex, "Blocking action in the middle troposphere and its effect upon regional climate. I An aerological study of blocking action", *Tellus* **2** (1950), no. 3, pp. 196–211.
[140] P. M. Sousa, D. Barriopedro, R. García-Herrera, T. Woollings and R. M. Trigo, "A new combined detection algorithm for blocking and subtropical ridges", *J. Climate* **34** (2021), no. 18, pp. 7735–7758.
[141] A. M. Obukhov, M. V. Kurgansky and M. S. Tatarskaya, "Dynamic conditions for the origin of droughts and other large-scale weather anomalies", *Meteorol. Gidrol. (in Russian)* **10** (1984), pp. 5–13.
[142] T. Kuhlbrodt and P. Névir, "Low-order point vortex models of atmospheric blocking", *Meteorol. Atmos. Phys.* **73** (2000), pp. 127–138.
[143] A. Müller, P. Nevir, L. Schielicke, M. Hirt, J. Pueltz and I. Sonntag, "Applications of point vortex equilibria: blocking events and the stability of the polar vortex", *Tellus A* **67** (2015), article no. 29184.
[144] G. Gottwald and R. Grimshaw, "The formation of coherent structures in the context of blocking", *J. Atmos. Sci.* **56** (1999), pp. 3640–3662.
[145] E. N. Lorenz, *The Nature and Theory of the General Circulation of the Atmosphere*, World Meteorological Organization, 1967, p. 161.
[146] C.-G. Rossby, "On the dynamics of certain types of blocking waves", *J. Chin. Geophys. Soc.* **2** (1950), pp. 1–13.
[147] M. Kageyama, F. D'Andrea, G. Ramstein, P. J. Valdes and R. Vautard, "Weather regimes in past climate atmospheric general circulation model simulations", *Clim. Dyn.* **15** (1999), pp. 773–793.
[148] E. Moreno-Chamarro, D. Zanchettin, K. Lohmann, J. Luterbacher and J. H. Jungclaus, "Winter amplification of the European Little Ice Age cooling by the subpolar gyre", *Sci. Rep.* **7** (2017), article no. 9981.
[149] J. A. Francis and S. J. Vavrus, "Evidence for a wavier jet stream in response to rapid Arctic warming", *Environ. Res. Lett.* **10** (2015), article no. 014005.
[150] T. Woollings, D. Barriopedro, J. Methven, et al., "Blocking and its response to climate change", *Curr. Clim. Change Rep.* **4** (2018), pp. 287–300.
[151] I. I. Mokhov and A. V. Timazhev, "Atmospheric blocking and changes in its frequency in the 21st century simulated with the ensemble of climate models", *Russ. Meteorol. Hydrol.* **44** (2019), no. 6, pp. 369–377.
[152] M. V. Kurgansky, "A simple model of blocking action over a hemisphere", *Theor. Appl. Climatol.* **147** (2022), pp. 65–71.
[153] W. Moon, G. E. Manucharyan and H. A. Dijkstra, "Baroclinic instability and large-scale wave propagation in a planetary-scale atmosphere", *Q. J. R. Meteorol. Soc.* **148** (2022), pp. 809–825.
[154] N. A. Phillips, "Geostrophic motion", *Rev. Geophys.* **1** (1963), no. 2, pp. 123–176.
[155] E. R. Weeks, Y. Tian, J. S. Urbach, K. Ide, H. L. Swinney and M. Ghil, "Transitions Between Blocked and Zonal Flows in a Rotating Annulus with Topography", *Science* **278** (1997), no. 5343, pp. 1598–1601.
[156] R. W. Griffiths and P. F. Linden, "Intermittent baroclinic instability and fluctuations in geophysical circulations", *Nature* **316** (1985), no. 2, pp. 801–803.
[157] P. L. Read and S. H. Risch, "A laboratory study of global-scale wave interactions in baroclinic flow with topography I: multiple flow regimes", *Geophys. Astrophys. Fluid Dyn.* **105** (2011), no. 2-3, pp. 128–160.
[158] S. D. Marshall and P. L. Read, "An experimental investigation into topographic resonance in a baroclinic rotating annulus", *Geophys. Astrophys. Fluid Dyn.* **109** (2015), no. 4, pp. 391–421.

[159] S. D. Marshall and P. L. Read, "Thermal versus mechanical topography: an experimental investigation in a rotating baroclinic annulus", *Geophys. Astrophys. Fluid Dyn.* **114** (2020), no. 6, pp. 763–797.

[160] M. Rantanen, A. Y. Karpechko, A. Lipponen, et al., "The Arctic has warmed nearly four times faster than the globe since 1979", *Commun. Earth Environ.* **3** (2022), no. 1, article no. 168.

[161] B. Gyüre, I. Bartos and I. M. Jánosi, "Nonlinear statistics of daily temperature fluctuations reproduced in a laboratory experiment", *Phys. Rev. E* **76** (2007), no. 3, article no. 037301.

[162] F. J. Romeiras, C. Grebogi and E. Ott, "Multifractal properties of snapshot attractors of random maps", *Phys. Rev. A* **41** (1990), no. 2, pp. 784–799.

[163] M. Ghil, M. D. Chekroun and E. Simonnet, "Climate dynamics and fluid mechanics: Natural variability and related uncertainties", *Phys. D: Nonlinear Phenom.* **237** (2008), no. 14-17, pp. 2111–2126.

[164] M. Vincze, I. D. Borcia and U. Harlander, "Temperature fluctuations in a changing climate: an ensemble-based experimental approach", *Sci. Rep.* **7** (2017), no. 1, p. 254.

[165] C. Rodda, U. Harlander and M. Vincze, "Jet stream variability in a polar warming scenario – a laboratory perspective", *Weather Clim. Dynam.* **3** (2022), pp. 937–950.

[166] R. Geen, S. I. Thomson, J. A. Screen, et al., "An Explanation for the Metric Dependence of the Midlatitude Jet-Waviness Change in Response to Polar Warming", *Geophys. Res. Lett.* **50** (2023), no. 21, article no. e2023GL105132.

[167] M. Vincze, C. Hancock, U. Harlander, C. Rodda and K. Speer, "Extreme temperature fluctuations in laboratory models of the mid-latitude atmospheric circulation", *Sci. Rep.* **13** (2023), no. 1, article no. 20904.

[168] U. Harlander, I. D. Borcia, M. Vincze and C. Rodda, "Probability distribution of extreme events in a baroclinic wave laboratory experiment", *Fluids* **7** (2022), no. 8, article no. 274.

[169] T. Bozóki, L. Czelnai, A. Horicsányi, A. Nyerges, A. Pál, J. Pálfy and M. Vincze, "Large-scale ocean circulation in the Southern Hemisphere with closed and open Drake Passage–A laboratory minimal model approach", *Deep-Sea Res. II: Top. Stud. Oceanogr.* **160** (2019), pp. 16–24.

[170] M. Vincze, T. Bozóki, M. Herein, et al., "The Drake Passage opening from an experimental fluid dynamics point of view", *Sci. Rep.* **11** (2021), no. 1, article no. 19951.

[171] T. N. L. Jacoby, P. L. Read, P. D. Williams and R. M. B. Young, "Generation of inertia–gravity waves in the rotating thermal annulus by a localised boundary layer instability", *Geophys. Astrophys. Fluid Dyn.* **105** (2011), no. 2-3, pp. 161–181.

[172] A. E. Gill and A. Davey, "Instabilities of a buoyancy-driven system", *J. Fluid Mech.* **35** (1969), no. 4, pp. 775–798.

[173] A. Randriamampianina and E. Crespo del Arco, "Inertia–gravity waves in a liquid-filled, differentially heated, rotating annulus", *J. Fluid Mech.* **782** (2015), pp. 144–177.

[174] F. Lott, H. Kelder and H. Teitelbaum, "A transition from Kelvin–Helmholtz instabilities to propagating wave instabilities", *Phys. Fluids, A* **4** (1992), no. 9, pp. 1990–1997.

[175] L. Rayleigh, "On the dynamics of revolving fluids", *Proc. R. Soc. Lond., Ser. A* **93, (648)** (1917), pp. 148–154. http://rspa.royalsocietypublishing.org/content/93/648/148.full.pdf.

[176] J. E. Hart and S. Kittelman, "Instabilities of the sidewall boundary layer in a differentially driven rotating cylinder", *Phys. Fluids* **8** (1996), no. 3, pp. 692–696.

[177] B. R. Sutherland, U. Achatz, C. P. Caulfield and J. M. Klymak, "Recent progress in modeling imbalance in the atmosphere and ocean", *Phys. Rev. Fluids* **4** (2019), no. 1, article no. 010501.

[178] S. Borchert, U. Achatz and M. D. Fruman, "Gravity wave emission in an atmosphere-like configuration of the differentially heated rotating annulus experiment", *J. Fluid Mech.* **758** (2014), pp. 287–311.

[179] C. Rodda, S. Hien, U. Achatz and U. Harlander, "A new atmospheric-like differentially heated rotating annulus configuration to study gravity wave emission from jets and fronts", *Exp. Fluids* **61** (2020), article no. 2.

[180] P. D. Williams, P. L. Read and T. W. N. Haine, "Spontaneous generation and impact of inertia-gravity waves in a stratified, two-layer shear flow", *Geophys. Res. Lett.* **30** (2003), no. 24, article no. 2255.

[181] R. Ford, "Gravity wave radiation from vortex trains in rotating shallow water", *J. Fluid Mech.* **281** (1994), pp. 81–118.

[182] P. D. Williams, T. W. N. Haine and P. L. Read, "Inertia–Gravity Waves Emitted from Balanced Flow: Observations, Properties, and Consequences", *J. Atmos. Sci.* **65** (2008), no. 11, pp. 3543–3556.

[183] J.-B. Flór, H. Scolan and J. Gula, "Frontal instabilities and waves in a differentially rotating fluid", *J. Fluid Mech.* **685** (2011), pp. 532–542.

[184] D. O'sullivan and T. J. Dunkerton, "Generation of Inertia–Gravity Waves in a Simulated Life Cycle of Baroclinic Instability", *J. Atmos. Sci.* **52** (1995), no. 21, pp. 3695–3716.

[185] O. Bühler, J. Callies and R. Ferrari, "Wave–vortex decomposition of one-dimensional ship-track data", *J. Fluid Mech.* **756** (2014), pp. 1007–1026.

[186] Q. Li and E. Lindborg, "Weakly or Strongly Nonlinear Mesoscale Dynamics Close to the Tropopause?", *J. Atmos. Sci.* **75** (2018), no. 4, pp. 1215–1229.

[187] C. Rodda, I. D. Borcia, P. L. Gal, M. Vincze and U. Harlander, "Baroclinic, Kelvin and inertia-gravity waves in the barostrat instability experiment", *Geophys. Astrophys. Fluid Dyn.* **112** (2018), no. 3, pp. 175–206.

[188] P. G. Baines, *Topographic Effects in Stratified Flows*, second edition, Cambridge University Press, 2022.

[189] P. Léard, B. Favier, P. Le Gal and M. Le Bars, "Coupled convection and internal gravity waves excited in water around its density maximum at 4°C", *Phys. Rev. Fluids* **5** (2020), no. 2, article no. 024801.

[190] V. Dorel, P. Le Gal and M. Le Bars, "Experimental study of the penetrative convection in gases", *Phys. Rev. Fluids* **8** (2023), no. 10, article no. 103501.

[191] S. Abide, S. Viazzo, U. Harlander, G. Meletti, I. Raspo and A. Randriamampianina, "On the influence of the heat transfer at the free surface of a thermally-driven rotating annulus", 2024.

[192] M. Vincze, S. Borcert, U. Achatz, et al., "Benchmarking in a rotating annulus: a comparative experimental and numerical study of baroclinic wave dynamics", *Meteorol. Z.* **23** (2014), no. 6, pp. 611–635.

[193] R. M. B. Young and P. L. Read, "Predictability of the thermally driven laboratory rotating annulus", *Q. J. R. Meteorol. Soc.* **142** (2016), no. 695, pp. 911–927.

[194] I. M. Held, "100 Years of Progress in Understanding the General Circulation of the Atmosphere", *Meteor. Monogr.* **59** (2019), pp. 6.1–6.23.

[195] G. I. Taylor, "VIII. Stability of a viscous liquid contained between two rotating cylinders", *Philos. Trans. R. Soc. Lond., Ser. A* **223** (1923), no. 605-615, pp. 289–343.

[196] R. M. Lueptow, R. Hollerbach and E. Serre, "Taylor–Couette and related flows on the centennial of Taylor's Philosophical Transactions paper: part 1", *Philos. Trans. R. Soc. Lond., Ser. A* **381** (2023), no. 2243, article no. 20220140.

[197] R. Hollerbach, R. M. Lueptow and E. Serre, "Taylor-Couette and related flows on the centennial of Taylor's seminal Philosophical Transactions paper: part 2", *Philos. Trans. R. Soc. Lond., Ser. A* **381** (2023), no. 2246, article no. 20220359.

[198] F. Exner, "Über die Bildung von Windhosen und Zyklonen", *Sitzungs Ber. Akad. Wiss. Wien, Abt. IIa* **132** (1923), pp. 1–16.

[199] D. Fultz, R. R. Long, G. V. Owens, W. Bohan, R. Kaylor and J. Weil, *Studies of thermal convection in a rotating cylinder with some implications for large-scale atmospheric motions*, Meteorological Monographs, Springer, 1959.

[200] T. Dauxois, T. Peacock, P. Bauer, C. P. Caulfield, C. Cenedese, et al., "Confronting Grand Challenges in environmental fluid mechanics", *Phys. Rev. Fluids* **6** (2021), no. 2, article no. 020501.

[201] S. Abide, S. Viazzo, I. Raspo and A. Randriamampianina, "Higher-order compact scheme for high-performance computing of stratified rotating flows", *Comput. Fluids* **174** (2018), pp. 300–310.

[202] G. Meletti, S. Abide, S. Viazzo and U. Harlander, "A parameter study of strato-rotational low-frequency modulations: impacts on momentum transfer and energy distribution", *Philos. Trans. R. Soc. Lond., Ser. A* **381** (2023), no. 2246, article no. 20220297.

[203] T. Seelig, U. Harlander, R. Faulwetter and C. Egbers, "Irregularity and singular vector growth of the differentially heated rotating annulus flow", *Theor. Comput. Fluid Dyn.* **27** (2013), no. 3, pp. 415–432.

[204] M. Hoff, U. Harlander and C. Egbers, "Empirical singular vectors of baroclinic flows deduced from experimental data of a differentially heated rotating annulus", *Meteorol. Z.* **23** (2015), no. 6, pp. 581–597.

[205] P. J. Schmid, "Nonmodal Stability Theory", *Ann. Rev. Fluid Mech.* **39** (2007), pp. 129–162.

[206] B. R. Sutherland, T. Dauxois and T. Peacock, "Internal waves in laboratory experiments", in *Modelling Atmospheric and Oceanic Flows: Insights from Laboratory Experiments and Numerical Simulations* (T. v. Larcher and P. D. Williams, eds.), American Geophysical Union, 2015, pp. 193–212.

[207] T. Caudwell, J.-B. Flór and M. E. Negretti, "Convection at an isothermal wall in an enclosure and establishment of stratification", *J. Fluid Mech.* **799** (2016), pp. 448–475.

[208] A. Schröder and D. Schanz, "3D Lagrangian Particle Tracking in Fluid Mechanics", *Ann. Rev. Fluid Mech.* **55** (2023), no. 1, pp. 511–540.

[209] B. R. Sutherland, M. DiBenedetto, A. Kaminski and T. van den Bremer, "Fluid dynamics challenges in predicting plastic pollution transport in the ocean: A perspective", *Phys. Rev. Fluids* **8** (2023), no. 7, article no. 070701.

ACADÉMIE DES SCIENCES
INSTITUT DE FRANCE

Comptes Rendus. Physique
2024, Vol. 25, Special issue S3, p. 427-477
https://doi.org/10.5802/crphys.213

Review article / *Article de synthèse*

Geophysical and astrophysical fluid dynamics in the laboratory / *Dynamique des fluides géophysiques et astrophysiques au laboratoire*

Eddy-driven Zonal Jet Flows in the Laboratory

Jets zonaux en expériences de laboratoire

Peter Read [*,a], **Yakov Afanasyev** [b], **Jonathan Aurnou** [c] **and Daphné Lemasquerier** [d]

[a] Department of Physics, University of Oxford, UK

[b] Department of Physics and Physical Oceanography, Memorial University of Newfoundland, Canada

[c] Department of Earth, Planetary and Space Sciences, University of California, Los Angeles, USA

[d] School of Mathematics and Statistics, University of St Andrews, UK

E-mails: peter.read@physics.ox.ac.uk (P. Read), afanai@mun.ca (Y. Afanasyev), jona@epss.ucla.edu (J. Aurnou), d.lemasquerier@st-andrews.ac.uk (D. Lemasquerier)

Abstract. Zonal jets are a ubiquitous feature of the circulation of planetary atmospheres, oceans and interiors. Many of the dynamical mechanisms that lead to the formation and evolution of such jets can be reproduced and studied in laboratory experiments, which have proved to be important sources of insight for understanding the nature of planetary jets. Here we introduce some of the key concepts underlying the production and maintenance of patterns of zonal jets in rotating and/or stratified flows. We then review a broad range of laboratory experiments that have helped to test and verify many of the dynamical mechanisms proposed to interpret geophysical jets involving the interaction of eddies and zonal flows. Laboratory experiments continue to have an important role to play in elucidating a quantitative understanding of zonal jets and their interactions with other aspects of planetary circulation systems.

Résumé. Les courants ou jets zonaux sont des éléments clés de la dynamique des enveloppes fluides planétaires, depuis les atmosphères et océans jusqu'aux intérieurs liquides profonds. Les expériences de laboratoires permettent de reproduire plusieurs mécanismes à l'origine des jets zonaux dans un environnement contrôlé, et ont ainsi joué un rôle déterminant dans notre compréhension de la physique des jets. Après avoir introduit les concepts fondamentaux à l'émergence et la persistance de jets zonaux dans des écoulements tournants et/ou stratifiés, nous faisons une synthèse des dispositifs expérimentaux ayant permis de tester ou valider certains mécanismes à l'origine des jets dans les écoulements géophysiques, en particulier du point de vue des interactions entre fluctuations (ondes, tourbillons) et écoulement moyen (jets). Les expériences de mécanique des fluides ont un rôle central à jouer afin de tendre vers une compréhension quantitative de la dynamique jets zonaux au sein des systèmes fluides planétaires, et de leur interaction avec les autres composantes de la circulation.

Keywords. jets, eddies, Reynolds stress, wave-zonal flow interaction, Rossby waves.

Mots-clés. jets, tourbillons, tensions de Reynolds, interaction onde-écoulement zonal, ondes de Rossby.

* Corresponding author

Funding. JA thanks the NSF Geophysics Program for support via award EAR #2143939. DL acknowledges support from The Carnegie Trust via Research Incentive Grant RIG012674, and the Royal Society via Research Grant RG/R1/241426. YA is supported by the NSERC grant RGPIN 2019-04957 and PLR acknowledges support from UKRI/EPSRC grant EP/W022087/1.

Manuscript received 17 May 2024, revised and accepted 3 October 2024.

1. Introduction

Jet streams and other intense currents are common features of the circulation of planetary atmospheres, oceans and other geophysical contexts. Such jet-like flows in rotating and/or homogeneous or stratified fluids are phenomena that are well suited for demonstration and quantitative investigation in fluid dynamics laboratories. The topic has a long and distinguished history going back more than 60 years, and a variety of different experimental approaches and dynamical mechanisms have been studied, ranging from directly forced jets, using mechanical or buoyancy forcing, to complex eddy-driven zonal flows. Here we focus on the latter as representing the most interesting and challenging to understand.

As noted by Rhines [1], "it is not easy to give a precise definition of a jet of fluid motion, but most of us know one when we see it". Such a statement is clearly unsatisfactory from a theoretical standpoint but the concept of a jet can be applied to a variety of phenomena where flows are elongated along a particular direction and are energetic and persistent in time. For the present purpose, we adopt a set of criteria for jet-like flows that largely follows that of [2]. These criteria can be summarised as characterising a flow with the following properties:

(1) *Anisotropy* – length scale along the direction of the current is much longer than the width of the current;
(2) *Transport* – fluid near the centre of the current is transported along the current a distance much larger than the current width;
(3) *Connectivity* – the separation distance in the direction of the jet of nearby fluid elements near the centre of the jet diverges only slowly;
(4) *Longevity* – the jet pattern persists much longer than the advective timescale.

Zonal flows wrap around a system's rotation axis, traditionally oriented in $\widehat{z}$. Thus, they are oriented in the azimuthal $\widehat{\phi}$-direction in spherical $(r,\ \theta,\ \phi)$ or cylindrical $(s,\ z,\ \phi)$ coordinate systems. These flows travel along lines of latitude in planetary fluid layers. Geophysical zonal jets are relatively thin, coherent, azimuthal flows that form latitudinal stripes painted across the face, and potentially interior, of a given planetary body. Famous examples include zonal winds in the atmospheres of Earth and Jupiter and zonal currents such as the Antarctic Circumpolar Current in Earth's Southern Ocean. For a comprehensive description of zonal jets in nature, the reader is referred to [3, Part II].

The ability to capture such phenomena under conditions and on scales that share significant dynamical similarity with those of large-scale systems in geophysics and astrophysics is potentially powerful, though should not be taken for granted. As discussed in the next section, it follows for rapidly rotating fluids from the dominance of the geostrophic balance in the horizontal momentum equations, in which Coriolis accelerations are balanced mainly by specific pressure gradient forces and other effects, such as due to viscous dissipation or inertial accelerations, are relatively much weaker. This allows the detailed investigation and measurement of geophysically and astrophysically relevant dynamical processes in well controlled and repeatable experiments that are not subject to limitations and uncertainties associated either with simplifying approximations, necessary for progress in analytical and numerical models, or incomplete and sparse observations and lack of repeatability when measuring flow systems in nature.

Of course, laboratory investigations are subject to other kinds of limitation, associated e.g. with the practical requirements to impose boundary conditions or geometrical constraints that have no counterpart in geophysics or astrophysics, or the use of viscous, thermally-conducting liquids in place of nearly inviscid gases or plasmas. But the ability to produce and study fully developed and highly nonlinear flows *in real fluids* under controlled conditions provides opportunities to gain insights that strongly complement other approaches based on mathematical analysis, numerical simulation or direct observations of natural systems.

Here we focus on some key questions that relate to our general understanding of zonal jets and their occurrence and behaviour in geophysical and astrophysical contexts. In particular, we consider the following specific questions and the ways in which laboratory experiments have offered in the past, and continue to offer, useful insights into the processes that create and maintain zonal jets in the atmospheres, oceans and interiors of planetary bodies.

- How are jets driven by eddies and waves?
- What determines the amplitude of the rectified flow?
- What determines the shape and width of the induced jets?
- What is the nature of the scale to scale interactions that produce jets?

Section 2 introduces some of the basic scales and parameters that are relevant to determining the origin and properties of zonal jets, and which link phenomena on laboratory and geophysical scales. Section 3 reviews the basic theory underlying the formation of zonal flows by the action of nonlinear eddies that is useful when interpreting experimental results, while Section 4 outlines some of the main experimental techniques used to investigate jet formation phenomena in the laboratory. Sections 5 and 6 review a wide range of experiments and results on zonal jet formation, distinguishing between forcings that are either localised or global in space. Finally, some concluding remarks are presented in Section 7.

2. Basic parameters, scales and flow regimes

One of the most fundamental pre-requisites for laboratory experiments to provide insights which may be useful in the context of large-scale geophysical or astrophysical circulations is that of *dynamical similarity*. This essentially determines whether laboratory flows may serve as analogues of large-scale geophysical or astrophysical flow systems and have the same primary balance of forces acting as in their atmospheric or oceanic counterparts. This is generally verified by various forms of *Scale analysis*. Ideally, also, there should be some similarity of boundary conditions, at least in so far as they affect the way in which motions are driven and/or contained within both systems.

2.1. *Scales and dimensionless parameters*

The main balances and dominant terms in the governing equations are typically estimated with reference to sets of dimensionless parameters which are commonly designed to indicate the ratios of terms in those governing equations or ratios of characteristic length or timescales. Table 1 summarizes the dimensionless numbers discussed throughout this review, along with their definitions, while Table 2 provides estimates of many of these parameters for both natural flows and laboratory experiments, as discussed in Section 2.4. In Table 1 and elsewhere, U is a typical (horizontal) velocity, $\mathbf{\Omega}$ is the angular velocity of the rotating frame and $f_0 = 2\Omega \sin\phi_0$ the Coriolis parameter at reference latitude ϕ_0, $\mathbf{g}$ the acceleration due to gravity, $\Delta_{\rho(v,h)} = \Delta\rho/\rho$ the fractional density perturbation (in the Boussinesq approximation), where ρ is density, ν is the kinematic viscosity and κ the thermal diffusivity [4]. The subscript v or h in $\Delta_{\rho(v,h)}$ represents

the fractional density perturbation in either the vertical or horizontal respectively. The strength of the stratification is measured by the buoyancy frequency N, typically defined by

$$N^2 = -g\frac{\partial \ln \rho}{\partial z}. \tag{1}$$

From these physical parameters, several dimensionless parameters can be introduced to characterize the dynamical regimes of planetary flows [4] and the extent to which dynamical similarity can be obtained experimentally (Section 2.4). The importance of the Coriolis acceleration relatively to inertial forces in the Navier–Stokes equations is represented by the Rossby number Ro. When $\mathrm{Ro} \ll 1$, the flow is strongly affected by rotation. The relative strength of viscous forces to Coriolis accelerations is measured by the Ekman number. $\mathrm{E} \ll 1$ for sufficiently rapidly rotating systems and is related to the Rossby number by $\mathrm{Ro} = \mathrm{E} \times \mathrm{Re}$, where Re is the Reynolds number measuring the relative strength of inertial to viscous forces ($\mathrm{Re} \gg 1$ for turbulent flows).

The Burger number Bu measures the relative strength of stratification to rotation effects. It is approximately equivalent to the inverse of the Rotational Froude number), which is typically O(1) for energetically favoured scales of motion in a stably-stratified, rotating flow. For thermally-driven flows, we introduce the Rayleigh number Ra, an important parameter in many convection problems, which measures the relative importance of buoyancy forces to the effects of viscous and thermal diffusion, and the Prandtl number which compares viscous to thermal diffusion. The Rayleigh number is sometimes more conveniently defined with respect to the buoyancy flux, F_B, as the Flux Rayleigh number $\mathrm{Ra_F}$, where F_B is defined with respect to the heat flux F_H as

$$F_B = \frac{g\Delta_{\rho(v,h)}F_H}{\rho c_p}, \tag{2}$$

where c_p is the specific heat capacity.

2.2. *β-effects in planetary settings and in the laboratory*

A further factor which sometimes leads to misconceptions regarding the extent to which dynamical similarity between laboratory flows and atmospheric or oceanic circulations can be achieved concerns the β-effect of dynamical meteorology and oceanography. This is traditionally interpreted as the effect of the spherical curvature of the planet on Coriolis forces, though actually manifests itself in the balance of vorticity transport. In the former interpretation (often cited by

Table 1. Definition of the dimensionless parameters provided in Table 2. L and D are typical horizontal and vertical length scales, respectively.

	Definition	Expression
η	Vertical/Horizontal aspect ratio	D/L
Ro	Rossby number (inertia/Coriolis)	$U/(f_0 L)$
E	Ekman number (viscous effects/Coriolis)	$\nu/\left(f_0 D^2\right)$
Re	Reynolds number (inertia/viscous effects)	UL/ν
Bu	Burger number (stratification/rotation)	$\left(ND/\left(f_0 L\right)\right)^2$
Ra	Rayleigh number (buoyancy/diffusion)	$g\Delta_{\rho(v)}D^3/(\kappa\nu)$ or $g\Delta_{\rho(h)}L^3/(\kappa\nu)$
$\mathrm{Ra_F}$	Flux Rayleigh number (buoyancy/diffusion)	$F_B D^4/(\nu^2\kappa)$
Pr	Prandtl number (viscous/thermal diffusivity)	ν/κ
β_1	β-planarity (linearity of planetary vorticity gradients)	$\beta L/f_0$
β_2	planetary vorticity/relative vorticity gradients	$\beta L^2/U$
R_β	Zonostrophy (Rhines/transitional scales)	$\left(\beta U^5/\epsilon^2\right)^{1/10}$

meteorologists and oceanographers), the Coriolis parameter f is considered to be the projection of the planetary angular velocity vector onto the local vertical, so that

$$f = 2\Omega \sin\phi \tag{3}$$

where ϕ is the latitude. The β term then represents the latitudinal gradient of f:

$$\beta = \frac{1}{R}\frac{\partial f}{\partial \phi} = \frac{2\Omega\cos\phi}{R}, \tag{4}$$

where R is the radius of the planet. More generally, however, the β-effect may be regarded as resulting from the conservation of a barotropic *Potential vorticity*

$$q = \frac{(2\Omega + \zeta)}{h}, \tag{5}$$

where ζ and h are respectively the components of relative axial vorticity and distance between the upper and lower boundaries along the rotation axis $\mathbf{\Omega}\hat{\mathbf{z}}$. For the case of a *very thin* spherical shell of uniform thickness $D \ll R$,

$$h \simeq \frac{D}{\sin\phi} \tag{6}$$

inside the tangent cylinder (i.e. the cylinder just enclosing the inner sphere [5–7]), and the "planetary vorticity" component of q in (5) takes the form $q \simeq (2\Omega\sin\phi)/D$, thereby emulating the dependence of f on latitude commonly assumed in terrestrial meteorology.

Space missions have revealed the existence of deep zonal jets on the gas planets, in which the depth of the zonal jet flows can extend thousands of kilometers below the planet's observable surface [8–10]. Subsurface oceans have been detected as well within our solar system's icy moons [11,12], and may reasonably harbor strong deep jet flows [13,14]. These subsurface oceans may be 100's of kilometer deep on planets with radii far smaller than that of Earth. In these layers, the traditional shallow layer β formulation, which applies accurately to Earth's ocean and to planetary tropospheric layers, becomes progressively less accurate (with a fractional error $O(D/2R)$) as D/R increases and/or the tangent cylinder latitude is approached. In this case, it is best to consider β_T,the topographic β formulation,

$$\beta_T = \frac{2\Omega}{h}\frac{\partial h}{\partial s}, \tag{7}$$

where s denotes cylindrical radius (from the rotation axis) and it is assumed that axial fluid layer height variations h arise only due to the shape of the axisymmetric, spherical shell boundaries (e.g., [15,16]). Non-axisymmetric topographic features are not considered (cf. [17–20]).

The β_T approach leads to different formulations for a thick shell especially close to the equator outside the tangent cylinder (e.g. see [16,21]. Such a topographic β-effect is thus equivalent to the meteorological "planetary vorticity gradient" for barotropic flows, and also for two-layer baroclinic flows where the lower *and upper* boundaries slope in equal and opposite senses. For more general rotating, stratified flows, however, the β-effect associated with topographic slopes is no longer formally equivalent to the "planetary vorticity gradient" in a spherical shell, though it is empirically observed to lead to *qualitatively* similar effects (Rossby-like wave dispersion etc. – e.g. see [22]).

The vast majority of laboratory zonal jets experiments are carried out in geometrically thick fluid layers in which D is not orders of magnitude less than L. This is because it is difficult in laboratory settings to generate extremely thin fluid layers that are strongly turbulent and strongly influenced by rotation (cf. [23]). Thus, the topographic β approach is employed ubiquitously in laboratory jets studies (e.g., [15,24]). The essential effect of β is to describe how the planetary vorticity varies spatially, regardless of formulation.

Two dimensionless terms can be defined involving β,

$$\beta_1 \sim \frac{\beta L}{f} \tag{8}$$

and

$$\beta_2 \sim \frac{\beta L^2}{U}. \tag{9}$$

If β_1 is much less than unity, then f effectively changes little across the domain of interest, suggesting that the full spherical geometry can be replaced (at least conceptually) by a tangent plane centred at a particular latitude ϕ_0 such that $f = f_0 + \beta y$, where $f_0 = 2\Omega \sin\phi_0$ and y is a Cartesian lateral coordinate. The parameter β_2, on the other hand, represents a ratio of "planetary vorticity gradient" (denoted by β itself) to that of relative vorticity ($\sim U/L^2$), and provides a measure of the relative importance of planetary vorticity gradients in the dynamics to that of relative vorticity advection.

In experiments with a free surface and fast rotation, one can take an advantage of the parabolic shape of the surface when in solid-body rotation. The depth of the fluid layer in a cylindrical tank of radius R is given by

$$h(s) = H + \frac{\Omega^2}{2g}\left(s^2 - \frac{R^2}{2}\right), \tag{10}$$

where s is the distance from the axis of rotation as before, H is the depth of the layer in the absence of rotation, Ω is the rotation rate of the tank and g is the gravitational acceleration. Using the background potential vorticity (PV), $q = 2\Omega/h$, one can show that the quadratic depth variation is dynamically equivalent to the Coriolis parameter varying quadratically with radius, $f = 2\Omega - \gamma s^2$ where $\gamma = \Omega^3/(gH)$. The laboratory flows can be related to those on a rotating planet where

$$f = 2\Omega\cos\varphi \approx 2\Omega\left(1 - \frac{\varphi^2}{2}\right) = 2\Omega - \frac{\Omega}{R^2} r_s^2. \tag{11}$$

Here φ is the colatitude, R is the radius of the planet, and r_s is the spherical distance from the pole. This approximation is called the polar beta-plane or, alternatively, the gamma-plane. It is well suited for regional domains which include the pole.

2.3. *Zonostrophic and friction-dominated regimes*

In the context of eddy-driven zonal jets in forced-dissipative flows, the formation of strong, well delineated jets is a particular characteristic of the "zonostrophic" regime [25,26]. This regime is defined in terms of the ratio of scales between the Rhines scale, or Rhines wavenumber

$$k_R = \left(\frac{\beta}{U}\right)^{1/2}, \tag{12}$$

(where U is usually taken to imply the rms eddy velocity scale) and the eddy anisotropy scale, or eddy anisotropy wavenumber

$$k_\beta = \left(\frac{\beta^3}{\epsilon}\right)^{1/5}, \tag{13}$$

where ϵ represents the rate of upscale energy transfer within the turbulent energy cascade. The Rhines scale ($\propto k_R^{-1}$) estimates the halting scale at beyond which jets and eddies cease to grow on the β-plane [27,28]. The eddy anisotropy scale ($\propto k_\beta^{-1}$) defines the scale at which the eddy overturning timescale is equal to that due to Rossby wave propagation and represents the scale

at which the character of the flow changes from being roughly isotropic (at smaller scales) to being highly anisotropic (at larger scales) [25]. The ratio of these two wave numbers (or scales),

$$R_\beta = \frac{k_\beta}{k_R} = \beta^{1/10} U^{1/2} \epsilon^{-1/5}, \tag{14}$$

is known as the *Zonostrophy parameter* [25]. If we estimate ϵ in dynamic equilibrium by equating it to the rate of energy loss due to dissipation, so that $\epsilon \sim U^2/\tau_E$, where $\tau_E = H/\sqrt{\nu\Omega} \simeq E^{-1}\Omega^{-1}$ is the Ekman spin-down timescale (e.g., [29,30]), we can approximate R_β by

$$R_\beta \simeq \left(\beta U \tau_E^2\right)^{1/10} = \left(2Ro^2 \beta_2 E^{-1}\right)^{1/10}, \tag{15}$$

from which it is evident that large values for R_β are favored by strong β-effects, strong flows and weak Ekman dissipation (with large τ_E). Flows with small R_β are therefore known as *friction-dominated* to distinguish it from its *zonostrophic* counterpart, and are characterized by relatively weak flows, weak β-effects and/or strong Ekman dissipation. Since the zonostrophic regime is the one typified by strong, rectified zonal jet flows compared with the non-zonal flow components, we anticipate that strong eddy-driven jets will be most likely to occur in flows with strong β-effects and weak Ekman friction (small Ekman number).

It was first argued by Sukoriansky et al. (2007) [26], based upon the analysis of 2D simulations, that the zonostrophic regime is observed when $R_\beta^s \gtrsim 2.5$, where

$$R_\beta^s = \left(\frac{C_Z}{C_K}\right)^{3/10} \left(\frac{2^5 \beta U^5}{\epsilon^2}\right)^{1/10} = \left(\frac{C_Z}{C_K}\right)^{3/10} 2^{1/2} R_\beta. \tag{16}$$

Here, C_Z and C_K are supposedly universal constants determined from spectral analysis, with $(C_Z/C_K)^{3/10} \approx 0.5$ [26,31] such that $R_\beta^s \approx 0.7 R_\beta$. In contrast, the regime is friction-dominated when $R_\beta^s \lesssim 1.5$. These approximate regime boundaries are represented in Figure 1. The intermediate case around $R_\beta^s \sim 1.5 - 2.5$ is known as transitional flow, and is often found to share many qualitative properties (though not all) with fully zonostrophic flows.

2.4. *Dynamical similarity in experiments*

Table 2 shows a comparison of the approximate sizes of various dimensionless groups which provide an indication of the likelihood of dynamical similarity between phenomena in the large-scale atmosphere, the oceans and typical laboratory conditions. This shows clearly that the Rossby and Burger numbers appropriate to the atmosphere and oceans (at least on the eddy-scale) are readily accessible under laboratory conditions, and this form of similarity is an important basis upon which laboratory analogues of large-scale atmospheric and oceanic phenomena are designed. The atmospheric and oceanic β-parameters, too, would seem to be accessible in the laboratory, at least using boundary topography to simulate some of the effects of planetary vorticity gradients.

The degree of similarity is not perfect, however, as revealed in significant differences between the aspect ratio D/L and parameters related to viscous and thermal diffusion (E, Re, etc.). Planetary flows, particularly on gas giants, are characterized by a very large Reynolds number, a vanishing Ekman number and a small Rossby number, i.e., flows are both turbulent and rotationally constrained. Reaching $\mathrm{E} \ll 1$ or $\mathrm{Re} \gg 1$ in experiments is notoriously difficult. Doing so simultaneously is an even greater challenge, as increasing Re requires to increase the rotation rate to keep Ro small. Based on molecular viscosity and diffusivity, planetary parameters hence differ from those accessible in the laboratory by several orders of magnitude (see also Figure 1). However, it is important to note that, if approximate measures of *eddy*-diffusivity are used for the atmosphere and oceans, based on small-scale mixing processes (e.g. see [32, Chapter 9]), the values of E and (to a lesser extent) Re become more closely similar to those in the laboratory

Table 2. Comparison of the scale of various dimensionless parameters for the large-scale atmosphere of the Earth, eddy-scale and gyre-scale phenomena in the Earth's oceans, and in a typical laboratory. The topographic β-effect, β_T, is calculated for a spherical shell at midlatitudes (45°). Details on planetary estimates of R^s_β are provided in the Supplementary Information. Starred items denote those estimated assuming a notional eddy diffusivity of 10^{-2} m^2 s^{-1} in place of molecular quantities.

	Atmosphere (Earth)	Oceans (eddy)	Oceans (gyre)	Deep Atmospheres	Exo-oceans (e.g. Europa)	Laboratory
L (m)	$\sim 10^6$	$\sim 10^5$	$\sim 10^7$	$\sim 10^7$	$\sim 10^6$	0.1 - 10
D (m)	$\sim 10^4 - 10^5$	$\sim 10^3$	$\sim 10^3$	$\sim 10^6 - 10^7$	$\sim 10^5$	0.1 - 1
$\beta\,(\mathrm{m^{-1}s^{-1}})$	1.6×10^{-11}	1.6×10^{-11}	1.6×10^{-11}	–	–	–
$\beta_T\,(\mathrm{m^{-1}s^{-1}})$	–	–	–	1×10^{-11}	4×10^{-11}	0 - 10^2
η	10^{-2}	10^{-2}	10^{-4}	O(0.1-1)	O(0.1-1)	O(1)
Ro	0.1	0.1	10^{-4}	10^{-3} - O(10)	10^{-3} - O(10)	$10^{-4} - \infty$
E	10^{-10}	10^{-8}	10^{-8}	10^{-14} - 10^{-12}	$10^{-14} - 10^{-9}$	$10^{-7} - \infty$
E*	$\sim 10^{-6}$*	$\sim 10^{-4}$*	$\sim 10^{-4}$*	10^{-9}	10^{-5}	–
Bu	0.1	10^{-2}	10^{-6}	$10^{-8} - 10^{-2}$	O(1) - 10^6	$10^{-2} - \infty$
β_1	0.2	10^{-2}	O(1)	10^{-2}	10^{-2} - 10^{-1}	0 - O(1)
β_2	O(1)	O(1)	10^2	10^{-3}	0.1 - 10	0 - O(10)
Pr	~ 1*	~ 1*	~ 1*	~ 1*	~ 1*	0.025 - 10^2
Ra	$\sim 10^{21}$	$\sim 10^{20}$	$\sim 10^{20}$	0 - 10^{30}	10^{26}	0 - 10^{11}
$\mathrm{Ra_F}$	$\sim 10^{29}$	$\sim 10^{24}$	$\sim 10^{24}$	$\sim 10^{40}$	$\sim 10^{31}$	0 - 10^{13}
Re	$\sim 10^{12}$	$\sim 10^{11}$	$\sim 10^{12}$	$\sim 10^{13}$	$\sim 10^{12}$	$\leq 10^5$
Re*	$\sim 10^{9}$*	$\sim 10^{7}$*	$\sim 10^{8}$*	$\sim 10^{10}$*	$\sim 10^{6}$*	–
$\mathrm{R^s_\beta}$	~ 1.4	~ 1.2	~ 1.2	$\sim 4-5$	$\gtrsim 2-4$	$0-3$

based on *molecular* diffusivities. Table 2 illustrates examples of the corresponding values of E and Re if a diffusivity of 10^{-2} m^2 s^{-1} is used in place of the molecular values (shown as starred values), which lie significantly closer to the laboratory values. However, the concept of an eddy diffusivity is a controversial one in general and the effective value may be strongly dependent upon the details of the dynamics it represents and is quite uncertain.

In addition to $\mathrm{E} \ll 1$, $\mathrm{Re} \gg 1$, and $\mathrm{Ro} \leq 1$, simulating zonal jets require a large zonostrophy index, particularly for applications to the strongly zonated flows of gas giants. As represented in Figure 1, mid-latitude jets on gas giants are expected to be in the regime of zonostrophic turbulence with $R^s_\beta \sim 4-5$. In contrast, Earth's oceans and atmosphere exhibit more moderate regimes with $R^s_\beta \sim 1.2-1.4$, corresponding to weak and meandering jets. For exo-oceans, estimating R_β is challenging given that no direct measurements of their flow is available and flow speeds are not constrained. Using flow speeds estimates from Jansen et al. [37] on one hand (based on a drag coefficient) and Cabanes et al. [14] on the other hand (based on Ekman friction) leads to zonostrophic index ranging from transitional to largely zonostrophic (see Supplementary Information). This leaves open the question of the relevant regime for icy moon oceans, although the friction-dominated regime seems irrelevant.

Reaching a large zonostrophic index experimentally is a further challenge: as noted in [33], because of the power 1/10 in the definition of the zonostrophy index (15), if all the other parameters are unchanged, increasing the typical velocity (and hence the Reynolds number) by

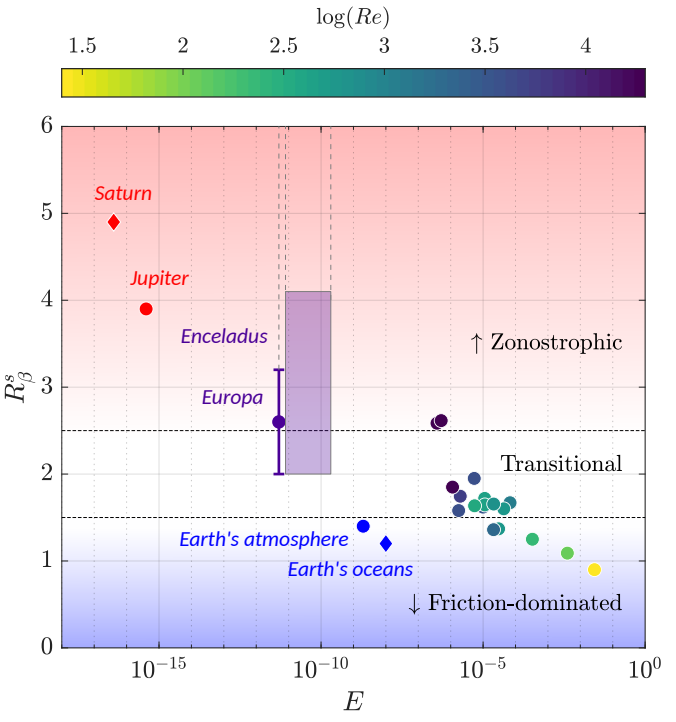


Figure 1. Zonal jets laboratory experiments in the non-dimensional parameter space Zonostrophy index R^s_β versus Ekman number E. The color of the symbols shows the Reynolds number. For the sake of comparison, we used similar definitions for all the experimental studies and planetary estimates (equation (16)). For all experimental studies, ϵ is estimated by $\epsilon \sim U^2\sqrt{\nu\Omega}/(2H)$. Details on planetary estimates are provided in the Supplementary Information. The vertical dashed lines for icy moon oceans indicate that the represented zonostrophy index is a lower bound due to the lack of constraints on their flow speed (see Supplementary Information). Figure adapted from [33, Figure 1], with the addition of experimental data from [34–36].

ten only increases the zonostrophy index by a factor $10^{1/10} \sim 1.26$! Most experiments to date lie in the transitional or friction-dominated regimes, as represented on Figure 1. More strongly-zonated regimes were recently reached by [33,38,39], as discussed in Section 6.3.

For thermally-driven flows, a further important dimensionless parameter is the Prandtl number. This is often large in the laboratory, because of the fluids in common use (based typically around water (Pr $\simeq$ 7) [40] or silicone oils (Pr $\sim$ 10-100 or greater) [41], cf. [42,43]). For geophysical flows, however, the appropriate value for Pr is less clear. This is because it is common to parametrize small-scale mixing in the atmosphere or oceans as a form of diffusive process via "eddy viscosities" and other coefficients. However, the relative efficiency of such processes for heat and momentum is often dependent on the problem, with effective Prandtl numbers ranging from significantly less than unity to much larger values (e.g. see [44]).

3. Basic theories and properties of jet flows

Jet-like flows can be driven via the rectified effect of generalised Reynolds stresses associated with eddies. This is an inherently nonlinear process that entails eddies adopting a particular

flow structure that results in systematic correlations between different velocity and buoyancy components in such a way as to result in transfer of linear (or angular) momentum.

3.1. *How are rectified zonal flows generated?*

For simplicity we use the Boussinesq equations on the beta-plane ([4, Chapter 2]). We hence work in a plane tangent to a reference latitude, with local Cartesian coordinates (x, y, z) representing the East-West, North-South, and local vertical coordinates, respectively. We denote $\mathbf{u} = (u, v, w)$ the corresponding velocity. Let us decompose the fields into a zonal ($x-$) mean (to be denoted with an overbar) plus a perturbation (denoted with a prime). Following e.g. [45] and [4], the equation governing the zonal mean velocity $\overline{u}$ can be written in the Transformed Eulerian form

$$\frac{\partial \overline{u}}{\partial t} - \overline{v^\star}\left(f - \frac{\partial \overline{u}}{\partial y}\right) + \overline{w^\star}\frac{\partial \overline{u}}{\partial z} = -\nabla.\mathbf{F} + \overline{\mathscr{F}_u}, \tag{17}$$

where $f = 2\Omega$ is the Coriolis parameter, $\overline{\mathscr{F}_u}$ represents direct body forces and dissipation, primed quantities denote departures from a zonal ($x-$) mean and $\mathbf{F} = (0, F^{(y)}, F^{(z)})$ is the Eliassen–Palm flux (effectively anti-parallel to the generalised Reynolds stress and flux of zonal momentum), defined as

$$F^{(y)} = \left(\frac{\partial \overline{u}}{\partial z}\frac{\overline{v'b'}}{\left(\partial \overline{b}/\partial z\right)} - \overline{u'v'}\right), \tag{18}$$

$$F^{(z)} = \left(\left[f - \frac{\partial \overline{u}}{\partial y}\right]\frac{\overline{v'b'}}{\left(\partial \overline{b}/\partial z\right)} - \overline{w'u'}\right). \tag{19}$$

Here b is the buoyancy, defined as $b = -g\delta\rho/\rho_0$ where ρ is density with reference value ρ_0, $\delta\rho = \rho - \rho_0$ and g the acceleration due to gravity. $\mathbf{u^\star} = (0, \overline{v^\star}, \overline{w^\star})$ represents the Transformed Eulerian Mean (TEM) meridional circulation, which approximates to a Lagrangian mean circulation that more cleanly separates the effects of eddies from a more conventional zonal mean circulation, and is defined by

$$\overline{v^\star} = \overline{v} - \frac{\partial}{\partial z}\left(\frac{\overline{v'b'}}{\left(\partial \overline{b}/\partial z\right)}\right), \tag{20}$$

$$\overline{w^\star} = \overline{w} + \frac{\partial}{\partial y}\left(\frac{\overline{v'b'}}{\left(\partial \overline{b}/\partial z)\right)}\right). \tag{21}$$

The TEM circulation $\overline{\mathbf{u}^\star}$ takes account of the partial cancellation of the Eulerian zonal mean circulation and the meridional overturning circulation induced by the eddies, and is typically dominated by a balance of zonal mean advection and diabatic heating or cooling. The Eliassen–Palm flux plays the role of a generalised Reynolds stress, whose divergence represents the effective stress acting on the zonal mean velocity due to the action of eddies. The resulting generalised Reynolds stress covariance may be divergent where waves or eddies are transiently growing or decaying in amplitude with time, and/or are being actively generated or dissipated. Such divergences lead to the net deposition of momentum, which can ultimately manifest itself as a rectified zonal flow or jet (e.g. [4,45,46]).

3.2. *Jet strength and direction?*

The direction and strength of the rectified zonal flow may depend upon the wave-like properties of the eddies (e.g. see [4]). The sign of $\nabla.\mathbf{F}$ in steady, forced or dissipated eddy flows, for example, depends on whether the waves or eddies are actually being locally forced or dissipated. For waves with a well defined phase velocity, $\mathbf{c}$, the theory suggests that dissipating waves will tend to deposit rectified (pseudo-)momentum in the same sense as $\mathbf{c}$ in the zonal mean, especially in the vicinity of critical layers where the flow velocity $\overline{\mathbf{u}}$ approaches $\mathbf{c}$. At latitudes or radii where waves are being energised by local forcing, however, zonally-averaged wave (pseudo-)momentum is being radiated away meridionally from the forcing region in the direction of the group velocity, leading to the generation of an eddy-induced zonal flow which is of opposite sign to $\mathbf{c}$; e.g. see [4,45,46] for further details.

For weakly nonlinear flows, the rectified zonal flow effectively results from the quadratic nonlinear self-interaction of the eddies or waves. So this would suggest that the magnitude of $|\overline{u}|$ should scale roughly as $O(\alpha^2)$. For dissipating waves, however, the dissipation may be enhanced as a critical line (where $\overline{u} \sim c$) is approached and the wavelength normal to the critical line decreases. This would indicate that $|\overline{u}| \lesssim |\mathbf{c}|$ for dissipating waves (e.g. see [4,45,46] and references therein.

3.3. *Jet structure and width?*

It is also of interest to understand what determines the vertical and lateral structure of eddy-induced zonal jets and the length scales associated with the variations of $\overline{u}$ in height and the direction transverse to the jet. The spatial structure of the forcing likely plays an important role, while for stratified flows the form of the dissipation and the vertical location of any critical layers affect the vertical structure of $\overline{u}$. For rapidly rotating flows, eddy forcing would be expected to favour the generation of barotropic structure of $\overline{u}$ in the vertical. In the horizontal, however, Rossby wave steepness (effectively measured by β_2, cf Eq. (9) is likely to be important, suggesting the possible significance of the Rhines scale $L_R \sim 1/k_R$ (see Eq. (12)) within the flow. This may depend on various factors but is likely to be significant in flows where multiple, persistent, parallel zonal jets emerge.

Such effects are observed in atmospheres and oceans, for example, where eddies generate substantial jet-like currents such as certain features of the tropospheric jet stream on Earth and the equatorial undercurrent in the oceans, as well as the multiple zonal jet streams on Jupiter and Saturn, and has also been suggested as contributing to the strong equatorial super-rotating flows on Venus and Jupiter. The process has been studied on a laboratory scale for many years, initially in relation to discussions on the effects of "negative viscosity" as a representation of the effects of nonlinear interactions between turbulent eddies and zonal flows (e.g. [47]).

3.4. *Potential Vorticity Mixing*

Potential vorticity (PV) is likely to be a conserved quantity in low Ro, low E planetary and stellar fluid settings [4]. Strong turbulent mixing in a latitudinal band may then act to homogenize $2\Omega/h$, the planetary potential vorticity, yielding some mixed value $\overline{q}$ everywhere in the band. The relative axial vorticity is then predicted to vary as

$$\zeta = \overline{q}\, h(s) - 2\Omega. \tag{22}$$

If it is further assumed that ζ is comprised of azimuthal axisymmetric zonal jet flows, then (22) provides upper bounding estimates on the strength of zonal jet flows in which all the planetary

PV reservoir in the mixed latitudinal band is converted into zonal jet motion [48]. See for example the experimental study of [49] for discussion of laboratory zonal flows potentially generated by potential vorticity mixing in low Rossby number turbulence.

4. Experimental Techniques: Metrology

Zonal jet experiments have been carried out for the past 50 years (e.g., [15,50,51]). In the majority of these, the turbulence is mechanically-driven (e.g., [15,36,38,49,52]), with a smaller subset driven by buoyancy (e.g., [53–55]) or Lorentz forces (e.g., [56]). Fewer still are driven by waves and wave turbulence (e.g., [51,57,58]). Irregardless of the forcing, zonal flows can be found to emerge in these differing laboratory systems, as detailed in Sections 5 and 6. However, relatively few to date have generated jets in the zonostrophic regime due to the difficulty in generating large R_β values, per Eq. (15).

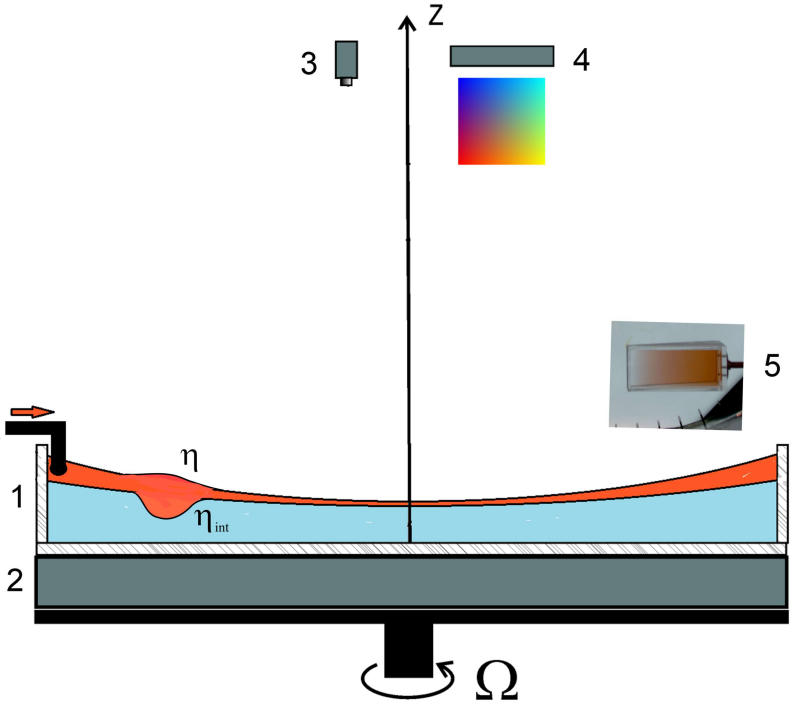


Figure 2. Schematic diagram of the experimental arrangement using Altimetric Imaging Velocimetry and Optical Thickness Velocimetry in rotating baroclinic two-layer flows: (1) rotating tank, (2) light panel for the optical thickness measurements, (3) video camera, (4) light source with color mask, and (5) wedge-shaped cuvette used for the calibration of the optical thickness.

Developments of new measuring techniques and digital video and data processing equipment have allowed laboratory experiments to progress from mostly qualitative and observational to quantitative; with resolutions comparable to those of numerical simulations (at least in 2D). It is often desirable to resolve all significant scales, from the viscous scale of an order of 1 mm up to the scale of the experimental tank (typically 1-2 m).

Particle image velocimetry (PIV) is a very popular technique for non-intrusive, quantitative and qualitative flow visualization, and has been widely used in experiments with fluids [59] including GFD rotating fluids for decades. Small reflective particles of neutral density are seeded in the water. For two-dimensional PIV (mostly used in rotating flows) the particles are visualized in a plane illuminated by a laser. Owing to the Taylor–Proudman theorem, motions in rapidly-rotating fluids are indeed expected to be almost invariant along the rotation axis, visualising them on a plane orthogonal to the rotation axis should hence be representative. A camera – usually attached to the rotating frame – records particle motion on the laser sheet, and particle displacement is calculated by subdividing the images into sub-regions called interrogation areas, so that it is actually the displacement of groups of particles that is calculated. This is done using cross-correlation of two consecutive images. The displacement per time gives a space-resolved, Eulerian velocity field, from which gradient-based quantities (e.g., vertical vorticity) can be calculated (see Figure 12 (b)). Both commercial and open-source PIV software are now widely available to perform post-processing of images (see [60] and references therein).

By design, the size of interrogation areas ultimately determines the spatial resolution, or rather the range of scales that PIV can resolve. In terms of temporal resolution, the typical flow velocities determine the maximum time step Δt_1 between images of a given pair for the cross-correlation to be successful. But the time between two pairs, Δt_2 can be chosen independently. For instance, Δt_2 can be chosen small (equal to Δt_1) if the goal is obtain time-resolved velocity fields of a turbulent flow. If on the other hand the goal is to follow the very slow evolution of the zonal flow, then one can choose $\Delta t_2 \gg \Delta t_1$. Of course, what limits the possibility of recording images with small time steps over very long times is the available memory of the system and its data streaming capabilities. Note that typical flow velocities in zonal jets experiments (mm s^{-1} to few cm s^{-1}) require only moderate temporal resolution (moderate Δt_1), hence CCD and CMOS based digital cameras are commonly employed for PIV measurements.

In meter-scale GFD experiments, particles consisting of hollow coated glass spheres of approximately 10-100 μm work very well. To obtain images of the highest possible quality, it is also possible to use fluorescent particles in combination with a band-pass filter on the camera to image only the light emitted by the particles (see [39, Supplementary Movie 1]). To improve measurements, the most common technique is to pre-process images before the actual cross-correlation (e.g., removing the background by subtracting a time-averaged image), however, the images have to be of the highest possible quality beforehand. Note also that if the laser sheet is visualised through a paraboloidal free-surface, images need to be corrected from the optical distortion induced by the paraboloidal free-surface [61].

An alternative technique developed specifically for rotating fluids with free surface is the Altimetric Imaging Velocimetry (AIV). It takes advantage of a parabolic shape of the surface when in equilibrium and measures the perturbations of this shape due to the flows. The AIV has evolved from the gray-scale optical altimetry [62] by incorporating color coding of the surface slope components [63,64]. The hardware for AIV includes a video camera and a light source with color mask located above the surface of water on the rotating table. The camera records reflection of multi-color light by the surface of water. Two components of the gradient $\nabla\eta = (\partial\eta/\partial x, \partial\eta/\partial y)$ of the surface elevation η are measured in the horizontal plane (x, y). This is unlike satellite altimetry which measures the surface elevation rather than its slope. However, the velocity computation is similar in both cases. Velocity of the flow is computed using the quasi-geostrophic (QG) approximation:

$$\mathbf{u} = \frac{g}{f_0}\widehat{\mathbf{z}} \times \nabla\eta - \frac{g}{f_0^2}\nabla\eta_t - \frac{g^2}{f_0^3} J\left(\eta, \nabla\eta\right), \tag{23}$$

where $\hat{\mathbf{z}}$ is the vertical unit vector, $f_0 = 2\Omega$ is the Coriolis parameter, Ω is the rotation rate of the tank and $J(A,B)$ is the Jacobian operator. The first term in the rhs of (23) is the geostrophic velocity, the second and third are higher order terms due to time tendency and advection. Thus, the AIV technique visualizes the surface, measures its slope and allows one to compute the barotropic QG velocity in virtually every pixel of the image.

A baroclinic two-layer fluid is often used in the experiments. In this case, AIV can be used in combination with the optical thickness velocimetry (OTV). The OTV is based on the absorption of light by dye dissolved in water. The upper (or lower) layer is dyed by a red (or green) food dye and illuminated by uniform white light provided by a light panel under the tank. The variations of thickness of the dyed layer due to the flow are visible to the camera above; color saturation in each pixel of the image can then be related to the thickness of the layer, h_1. Baroclinic geostrophic velocity is computed using thermal wind equation:

$$\mathbf{u}_{bc} = -\frac{g'}{f_0}\hat{\mathbf{z}} \times \nabla h_1, \tag{24}$$

where $g' = g(\rho_2 - \rho_1)/\rho_2$ is the reduced gravity, ρ_1 and ρ_2 are the densities of the upper and lower layer, respectively. Baroclinic velocity in the QG approximation can be obtained from (23) replacing η by $-h_1$. OTV and AIV can be used almost concurrently when the upper and lower lights are alternated [65]. Thus, the baroclinic two-layer system is fully resolved with the upper layer velocity $\mathbf{u_1} = \mathbf{u}$ and lower layer velocity $\mathbf{u_2} = \mathbf{u} + \mathbf{u}_{bc}$.

In the experiments (e.g., [40]) where density gradients are created by heating or cooling, thermal radiometry proved to be useful. Infra-red camera can provide snapshots of the temperature field at the surface; the temperature is converted into density using the equation of state for water. Density gradient, in say, the radial direction can then be related to the vertical shear of the zonal velocity using the thermal wind equation (see also [66]).

In the next section we review a range of experiments that have demonstrated and explored the applicability of many of the theoretical concepts and issues introduced in the previous Section 3. Experiments may be distinguished in their approach towards generating and maintaining eddies, with or without the presence of background rotation or stratification, and have explored in both qualitative and quantitative terms some of the mechanisms that lead to the generation of zonal jet flows. Different configurations of experiments have investigated both the structure of eddy-driven jet flows subject to very different forcing processes and the dependence of their strength, direction and width on various scaling parameters.

5. Zonal Jets Experiments: localized forcing

5.1. *"Moving flame" experiments*

Some of the earliest experiments to demonstrate nonlinear rectification effects in a fluid excited by waves were those intended to demonstrate the "moving flame" effect [67]. In these experiments, a localized heat source (such as a bunsen burner) was rotated underneath a cylindrical vessel containing a fluid that was initially stationary. The heat source would excite a thermal (buoyancy) wave that would translate in the direction of the moving heat source. For various reasons (such as due to the inertia associated with thermal diffusion), the thermal wave could develop a phase shift with height, so that the associated vertical and zonal velocity field would acquire a tilt, and hence a significant $\overline{u'w'}$ Reynolds stress. As the thermal wave propagates with height above the heat source, it dissipates and leads to a rectified acceleration of the zonal mean state of the fluid which develops a significant streaming flow in the opposite direction to the motion of the heat source.

Several versions of this kind of experiment were investigated during the 1960s and 1970s as possible analogues of the thermal tide on Venus, which was then thought to be the main driver of the strong super-rotation of its atmosphere [68–70]. The results did, indeed, demonstrate various forms of zonal streaming in fluids of widely varying Prandtl number, associated with the zonal tilt and phase shift of thermally driven gravity waves and convective cells excited by different forms of heat source (including both boundary and internal heat sources), though a convincing quantitative theory to account for the observed flows was slow to emerge. The simplest theories relied on diffusive inertia to produce the required tilt of the thermally excited waves with height and resulting Reynolds stresses, which were then expected to lead to zonal flows comparable in magnitude to the phase speed of the heat source. In a few cases, however, much stronger flows were observed [69], as would be necessary to account for the observed super-rotation of Venus's atmosphere, which is at least 30 times faster than the motion of its semi-diurnal thermal tide [71,72]. In practice, however, this turned out to be at least partly driven by temperature variations in surface tension at the free surface of the fluid, so was of less interest as an analogue of planetary flows. Even those flows for which surface tension effects were not significant relied on molecular heat diffusion to provide the thermal inertia needed to created vertical phase shifts, which limits the degree to which they can emulate planetary-scale phenomena. But nevertheless these experiments played an important historical role, serving to excite interest in exploring more general mechanisms for driving zonal streaming effects due to eddies.

5.2. *Barotropic jet flows with Rossby wave forcing*

Another important class of experiments excited eddy-driven jets in homogeneous, barotropic flows by directly forcing eddying motions but mostly without explicit zonally-symmetric forcing. In a prescient series of experiments, [51] was able to demonstrate the formation of barotropic, eddy-driven zonal flows in a cylindrical water tank with a flat bottom and centrifugally-deformed, parabolic free surface to induce a topographic β-effect. By using relatively simple localized stirring, either via oscillating mechanical plates or streams of air bubbles, a train of Rossby waves were generated that spontaneously formed a rectified zonal streaming flow. [51] noted that the induced zonal flow was prograde at the radius where the forcing was introduced and weakly retrograde on either side of the forcing.

In subsequent studies [15,73], a rotating, cylindrical tank of water or a silicone oil was used with a centrifugally deformed free surface (to create a polar β-plane) and an ingenious method of exciting topographic Rossby waves of a fixed wavenumber ($m = 6$), frequency and phase speed c via a source-sink technique developed by A. McEwan (see Figure 3). This was used to demonstrate the development of an eddy-driven jet, aligned along the (azimuthal) geostrophic contours. The experiments were able to show how the $m = 6$ forcing would excite a zonally propagating Rossby wave that would radiate away from the region of source-sink forcing, producing a zonal flow at the forcing radius that was in the opposite sense to c for the forced travelling wave. This rectified flow was flanked on either side by weaker zonal jets that were in the same sense as the motion of the forced wave (see Figure 4). The mean zonal flow $\overline{u}(r)$ was anticorrelated with the divergence of the Reynolds stress $\overline{u'v'}$, as expected from the discussion above.

They also investigated the scaling of the induced zonal velocity with the strength of the forced eddies and showed that the forcing pattern needed to propagate zonally at the same rate as the corresponding Rossby wave pattern in order to produce a strong response. The resulting rectified zonal flow scaled roughly quadratically in amplitude with the amplitude of the wave forcing and was interpreted in terms of a modulational instability of Rossby wave packets. In addition, the behavior of potential vorticity mixing was also investigated and shown to be consistent with the eddy driving mechanism.

However, these experiments did not investigate the formation of multiple zonal jet patterns and the associated length scales and their dependence on experimental parameters.

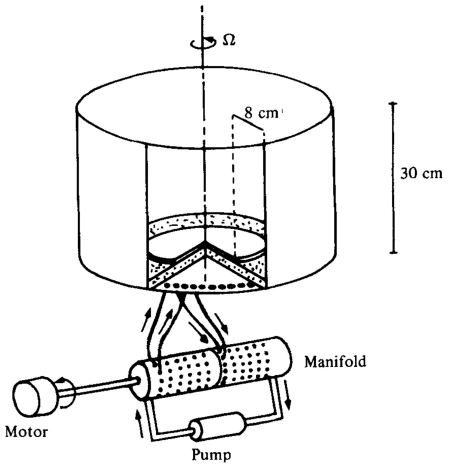


Figure 3. Schematic diagram of the experimental arrangement to create trains of travelling wave-like eddies to force zonal flows using mass sources and sinks in the bottom of the tank at a fixed radius towards the outer boundary of a cylindrical tank (taken from [15] and [73] with permission).

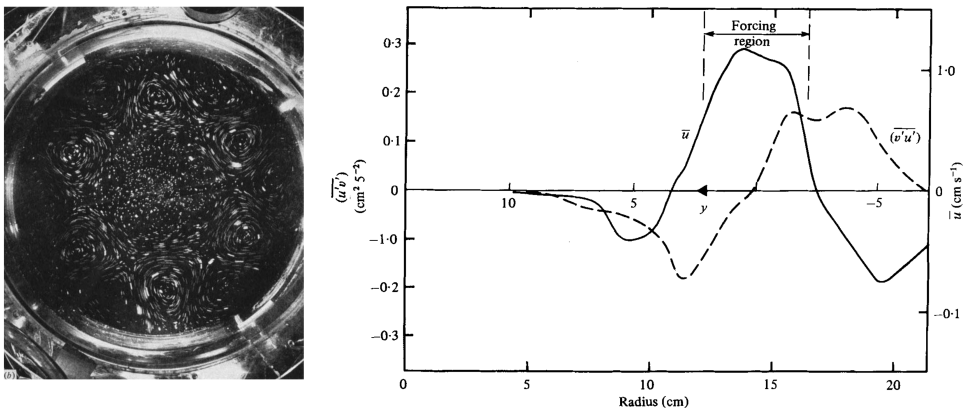


Figure 4. (a) Surface streak photograph of a typical equilibrated flow in the experiments of [73] forced by a wavenumber $m = 6$ travelling wave pattern. (b) Profiles of $\overline{u}$ and $\overline{u'v'}$ for a similar equilibrated flow. Experiment (a) corresponds to $f = 9.74\ \mathrm{s}^{-1}$, $\gamma = ck^2/\beta = -0.36$; (b) corresponds to $f = 8.46\ \mathrm{s}^{-1}$, $\gamma = -0.36$. Reproduced from [73] with permission.

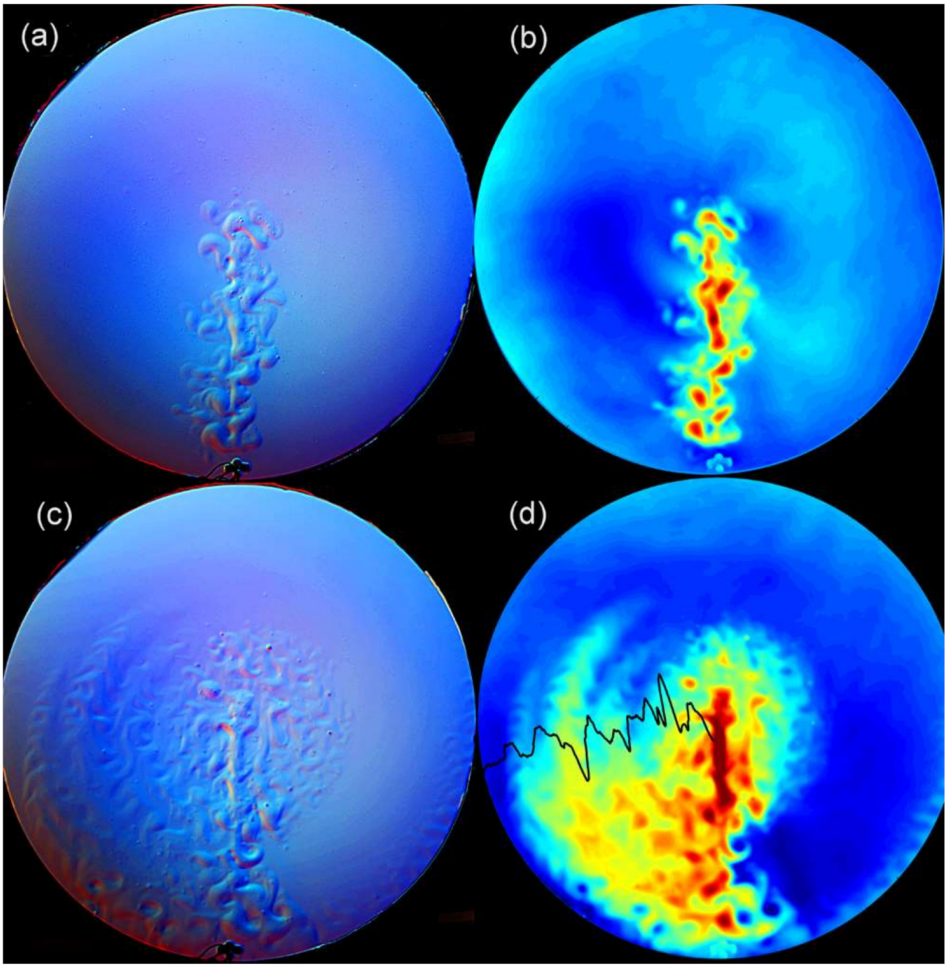


Figure 5. Flow on the polar β-plane generated by a linear heater: altimetric color images (a, c) and surface elevation derived from altimetry (b, d). Insert in (d) shows a radial profile of the azimuthal velocity (black line).

5.3. *Zonal flows excited by Rossby wave radiation from localized buoyancy sources and boundary currents*

To get an insight into dynamics of jets and especially the interplay between jets, eddies and Rossby waves, it is often desirable to observe the evolution of flows created by localized forcing from rest. Typically, we don't have this opportunity in the ocean or in the experiments where jets are created by multiple eddies/Reynolds stresses in the entire domain (Section 6).

An initial response of fluid to a spatially localized source is described by a linear theory of Rossby waves (e.g. [54,74–76]). This response is called the β-plume and is a gyre-like circulation consisting of two zonal jets flowing in opposite directions which are reconnected in the area of the source as well as at the front of the plume. The β-plume extends westward of the source area where longer waves propagate while to the east of the source, shorter waves create a periodic wavy pattern. The two jets in the the β-plume are flowing along the slopes of the ridge on the surface; the ridge being an extension of the elevated surface above the source. While initial

dynamics is linear, the finite amplitude circulation is soon established. Thus Rossby waves provide a path for creation of the zonal flows. It is difficult to observe Rossby waves in the laboratory with any techniques other than altimetry. The illustrations of the barotropic and baroclinic β-plumes generated by sources or sinks on the polar β-plane are given in [54,76,77]. Oceanographic examples of localized forcing include local mixing, surface cooling/heating, outflows, eddies, and meanders of coastal currents.

A series of papers by [35,54,78] investigates baroclinically unstable flows where multiple β-plumes were observed. The experiments were designed to model coastal currents flowing along the eastern shores of oceans. These currents form meanders due to a baroclinic/frontal instabilities which, in turn, emit Rossby waves and shed eddies. The perturbations then propagate westward and create alternating zonal jets. The laboratory flows were created using two different methods. In the first method, a source placed at the wall of the tank continuously delivered fresh water on top of a thick layer of saline water. A radial barrier was used to model an eastern coast. Fresh water flows as a coastal current along the wall, turns to the north, toward the pole, along the barrier, then turns around the tip of the barrier and flows back to the South along the other side of the barrier and eventually continues flowing along the wall of the tank. In the second method, a heater placed along the radius of the tank near the bottom was used. The heater creates an upwelling of warm water which becomes unstable; the flow then evolves very similarly to that generated by a coastal current.

Figure 5 shows altimetric images of the flow in the beginning (top row) and at the end (bottom row) of the experiment. Warm water from the heater rises to the surface and creates elevated surface topography. Note the current above the heater flows according to geostrophy, northward and then southward following the outline of the heater just like the coastal current flows around a barrier. Eventually, multiple plumes, ridges on surface, each consisting of counter-flowing jets on their slopes, form westward of the heater. We can also see some interesting details of the Rossby wave propagation. Warm anticyclonic eddies are characterized by an elevated surface (yellow-red color); the baroclinic flow comprised of the eddies can be easily identified. However, if we look closely at the fluid westward or eastward of the baroclinic area we can also see the larger –scale perturbations there. These perturbations are barotropic Rossby waves propagating in the homogeneous fluid. The difference between the wave patterns westward and eastward of the heater reveals the east-west asymmetry of the Rossby waves. The perturbations to the west of the front of the baroclinic area are in the form of annular modes with small zonal wavenumber; in contrast, the perturbations to the east of the baroclinic area are of relatively high zonal wavenumber. This can be easily understood from the textbook theory of Rossby waves which demonstrates that only short wavelength waves are capable of propagating to the east. These observations illustrate the mechanism of β-plume formation where fast long Rossby waves emitted by (quasi) stationary perturbations propagate to the west and establish an almost zonal plume circulation. This circulation provides an initial deformation field which, in turn, affects the distribution of the baroclinic eddies which results in their chain-like arrangements. Note that there is no transport of eddies to the east (except perhaps along the wall of the tank where a coastal currents develops later in the experiment.

Finally, paper [35] investigates β-plume generated jets in the system where β changes sign thus creating critical latitudes. The experiments were designed to model Jovian jets in the weather layer lying on top of dynamic topography created by deeper flows in the convecting interior. In the experiments, β due to the parabolic surface was modified by a bottom topography which had a tent-shaped radial cross section. This created a negative β zone in the midlatitudes of the tank. The flows were forced by a submerged source pipe injecting fluid along one radius. In the negative β zone, long Rossby waves propagate eastward, "upwind" against westward current. This flow is characterised by a hydraulic-like control such that the analogue of the Mach number for Rossby

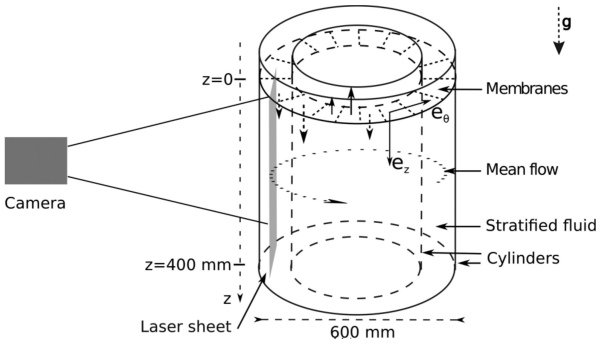


Figure 6. Schematic layout of the internal gravity wave experiment of [80]. ©American Physical Society. Used with permission.

waves, $M_R = u/(-c_x) = 1$, where u is the zonal velocity and c_x is the intrinsic zonal phase speed of the waves (before Doppler shifting). This parameter occurs in a range of theories including those of jet spacing [27], hydraulic control [24], and shear instability [79]. A similar result was obtained in the experiments by [39] where M_R goes to unity for their forced Rossby waves.

6. Zonal Jets Experiments: global forcing

Section 5 focuses on experiments where the forcing, regardless of its nature, is localised in space. In the present section, we turn to experiments where the forcing is global, and waves and eddies are excited in the entire domain. This configuration is arguably more relevant to some planetary applications (e.g., fully convective interiors).

6.1. *Wave forcing in stably stratified flows*

One of the conceptually simplest contexts in which zonal mean flow acceleration may arise via the interaction of waves or eddies relates to the generation, propagation and dissipation of internal gravity waves in a stratified fluid. The observations of strong zonal flows in the Earth's stratosphere that oscillate on a roughly 2 year period (e.g. [81]) led to some early pioneering theoretical work on mechanisms to drive zonal flows through the forcing and dissipation of vertically propagating internal waves (e.g. [82–85]). In particular, the effect of competing eastward and westward propagating waves, driven upwards from the tropical troposphere, was suggested to lead to an alternating dominance of wave streaming effects successively driving eastward and westward zonal flows as the zonal flow structure would successively promote and inhibit the upward propagation of westward and eastward propagating waves in turn.

Our understanding of such complex oscillatory flows and the development of theoretical models of the QBO is based on assumptions of how individual, weakly nonlinear, vertically propagating internal waves interact and energise a zonally symmetric zonal flow. It is somewhat surprising, therefore, that until recently, experimental investigations of this kind of phenomenon have tended to explore rather complicated configurations of wave forcing that are spatially inhomogeneous and/or complex in time [57,86,87] The reasons for this are partly historical in that experiments were typically motivated by a desire to reproduce an analogue of a complex geophysical phenomenon, such as the QBO itself (see also [88,89]). But one of the particular strengths of an experimental approach is the possibility of isolating particular fundamental processes in a real fluid and exploring their sensitivity to and dependence upon different experimental conditions.

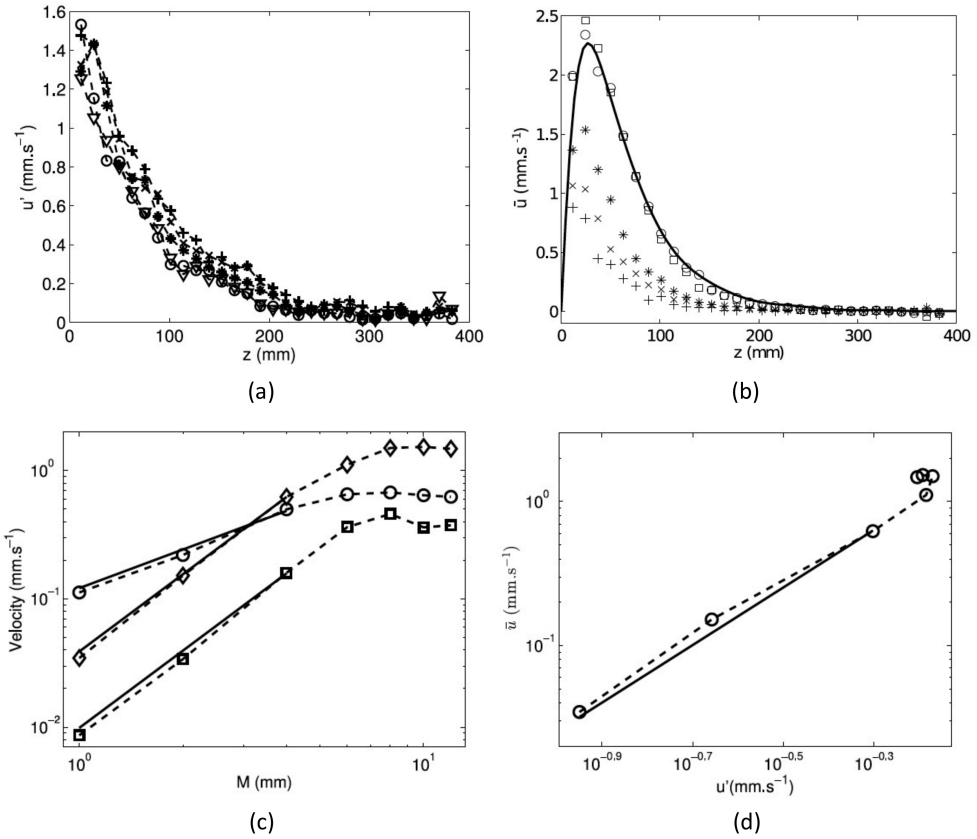


Figure 7. Vertical profiles of (a) horizontal wave amplitude u' and (b) mean flow $\overline{u}$ at various times, showing convergence towards a fit to a theoretical model based on [83] (solid line in (b)); (c) dependence of the amplitude of the mean flow $\overline{u}$ (diamonds), dominant wave mode $u'(k_x)$ (circles) and its first harmonic $u'(2k_x)$ (squares) of the internal wave at a depth of z = 64 mm below the top surface as a function of the forcing amplitude M; (d) dependence of the amplitude of the mean flow $\overline{u}$ on the amplitude u' of the internal wave at a depth of z = 64 mm below the top surface. Solid line indicates a quadratic fit to $\overline{u}(u')$. ©American Physical Society. Used with permission.

In a recent study [80], almost the simplest possible configuration of a vertically propagating, quasi-two-dimensional internal gravity wave was investigated to explore the validity of some of the assumptions underlying wave-zonal flow interactions in simple (and not so simple) models. The experiment was inspired by the ingenious and influential set of experiments by [57] in a form similar to that used by [86], in which an annular channel was filled with water that was stably stratified with a salt concentration that varied linearly with height. A single, monochromatic travelling wave of a given zonal wavenumber k_x, frequency ω and displacement amplitude M was imposed at the top boundary by the use of a series of segmented chambers covered with a rubber membrane, each of which could be elevated or depressed by a set of actuators. A schematic of the apparatus is shown in Figure 6. The flexible top boundary was able to launch a monochromatic, downward-propagating internal gravity wave that would then decay with depth as it was dissipated by the fluid viscosity.

The impact of this downward propagating and dissipating wave in generating a zonal flow was then explored as a function of depth and parameters such as the forcing amplitude M at the top boundary and the local internal wave amplitude u'. Some examples are illustrated in Figure 7, which show (a) how the wave amplitude varies with depth, (b) the corresponding vertical profile of mean zonal flow, (c) how the strength of the mean zonal flow, the fundamental and the second harmonic of the forced wave varies with M at a fixed depth and (d) how the strength of the rectified zonal flow $\overline{u}$ varies with local internal wave amplitude u'. Viscous damping evidently causes the wave to decay with depth below the forcing over a typical length scale of 10-20 cm. This leads to an eddy-driven zonal flow which peaks in strength just below the forcing and decays with depth further down. Figure 7 (c) shows how the amplitude of the directly forced wave $u'(k)$ scales linearly with forcing amplitude M until it saturates at large M, while $\overline{u}$ and the second wave harmonic $u'(2k)$ scale quadratically with M, as expected for nonlinear interactions. This quadratic dependence of $\overline{u}$ on wave amplitude u' is seen also to hold locally, as evident in Figure 7 (d).

6.2. *Orbitally-forced flows*

Banded azimuthal flows can also be excited by way of mechanically-imposed "orbital" forcings that generate inertial waves and container-scale modes [58,90]. In planetary settings, these arise in association with an externally-imposed body force, such as the effect of gravitational forces on a planetary or stellar interior due to an orbiting moon or planet. The excited inertial waves and oscillations can resonate and reach large amplitude within a confined cavity if the forcing frequency matches that of an inertial eigenmode. The existence of such tidal resonances and the consequent interactions with viscous boundary layers (essentially modified Ekman and Stewartson layers at the surface of spheroidal cavities) can lead to the formation of internal shear layers and nonlinear interactions that can non-locally transfer kinetic energy into zonally-symmetric flows, even though the forcing may be strongly nonaxisymmetric. In theory, the strength of zonal flows driven by strongly nonlinear inertial waves can reach large amplitudes as viscous dissipation tends towards zero (e.g., [91]).

Orbital forcings investigated via laboratory experimentation include precession of the rotation axis, libration and tidal deformation. In precession and latitudinal libration experiments the container's rotation vector is fixed in place. Instead, it precesses [92–94] or latitudinally nods in space [95]. In the case of longitudinal libration, the purely axial angular velocity oscillates sinusoidally in time around its mean value [96–99]. In tidally driven experiments, the fluid shell is sinusoidally deformed as it passes through a simulated tidally-distorted gravity field [100,101].

Figure 8 shows shear layers in (a, b) librating [99], (b) tidally-deforming, and (c, d) precessing [92,100] laboratory experiments. In all three cases, nonlinear inertial wave dynamics drive the development of strong zonal shear layers. In panel (a), the predicted inertial shear layers are demarcated in white dot-dashed lines, and the locations of the critical layers on the inner boundary are denoted by the dot-dashed maroon lines. Panel (b) shows the same image sans the guiding lines. These experimental libration images show that the predicted geostrophic zonal shear structures correspond well with the locations of the critical latitudes, and the inclined shear structures map out the predicted structure of oscillating inertial mode shear layers.

Figure 8 (c) shows shear structures from the tidal deformation experiments of [100] in which $m = 2$ inertial waves were excited by deforming a water-filled, rotating, spherical cavity between a pair of rollers that could be independently rotated at a controllable rate. The resulting flow patterns were visualized using kalliroscope particles and velocity fields in the equatorial

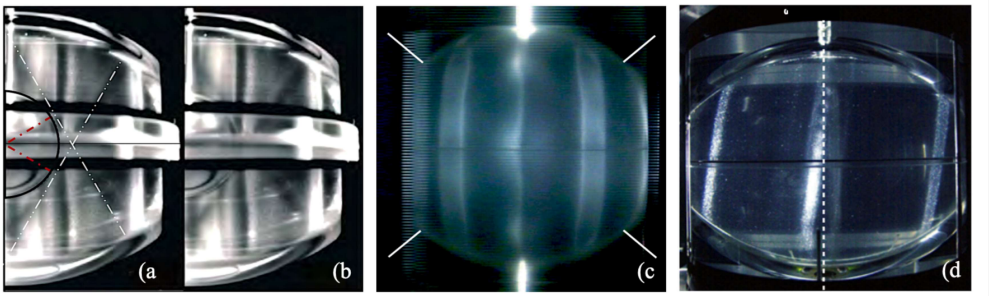


Figure 8. Kalliroscope images of zonal shear flows in orbitally-forced (a, b) libration [99], (b) tidal deformation [100] and (c) precession experiments [92]. (a, b) Reproduced from [99] with permission from Wiley ©2017 American Geophysical Union. (c) Reprinted with permission from [100] ©2010 American Physical Society. (d) Reproduced from [92] with permission from Wiley ©2001 American Geophysical Union.

plane measured using PIV. The shear pattern in Figure 8 (c) shows the formation of axisymmetric geostrophic flows, aligned along cylinders coaxial with the rotation axis, when the forcing frequency came into resonance with inertial eigenmodes. Strong shear layers occur near critical latitudes where the group velocity of the reflected inertial waves becomes tangential to the bounding surface of the cavity. This leads to a local thickening of the Ekman boundary layer and the generation of zonal flow, similarly to the librationally-driven flows shown in Figure 8 (a, b). These critical latitudes are indicated by short white lines in Figure 8 (c). The location of the shear layers moves with the critical latitudes, which depends on the forcing frequency. The strength and width of the shear layers depend strongly on the Ekman number, which in turn is reflected in the dependence of maximum azimuthal flow as $\sim \epsilon_a^2 E^{-\zeta}$, where ϵ_a^2 scales the forcing amplitude and the exponent ζ ranges from 1/10 to 3/10 in recent studies [100,102].

Figure 8 (d) shows that strong axially-aligned zonal shear structures also form in precessionally-driven flows [92]. The two bright banded structures situated away from the rotation axis form where the inertial modes' conical shear layers are tangent to the surface of the ellipsoidal cavity. These shear layers are aligned with the total rotation vector, that includes the rotation of the container as well as the angular rotation around the precession axis.

The Figure 8 flows demonstrate that orbitally-forced flows can generate banded zonal flows. However, it has yet to be shown unambiguously that these orbitally-driven zonal flows develop robustly in the strongly turbulent, zonostrophic regime.

6.3. *Barotropic jet flows with random forcing*

The previous two subsections focus on zonal flows emergence due to global scale wave forcing. Another method, which allows a somewhat better control of the location, scale and intensity of the forcing, consists in applying a mechanical forcing, provided that it does not directly force the mean flow. Electromagnetic forcing was used to study barotropic jet formation. The working fluid is a homogeneous electrolyte through which an electric current is passed in the presence of arrays of permanent magnets, leading to the formation of vortex-like flow structures resulting from the pattern of Lorentz forces. For a recent review, the reader is referred to [103]. Another approach consists in performing an eddy-forcing using sinks and sources of fluid [15,36,49,52,104] (see also the review by [105]). In this section, we focus on updating recent progress made towards reaching a zonostrophic regime experimentally. Two experiments were recently built in Marseille in which

zonal jets spontaneously emerge from a mechanically-forced turbulent flow in a rapidly rotating water tank [33,38,39]. In these experiments, the fast rotation (75 revolutions per minute) of a 1 m-diameter tank with a deep water height allows to reach higher zonostrophy index, lower Ekman number and higher Reynolds number than previous experiments (see also Figure 1).

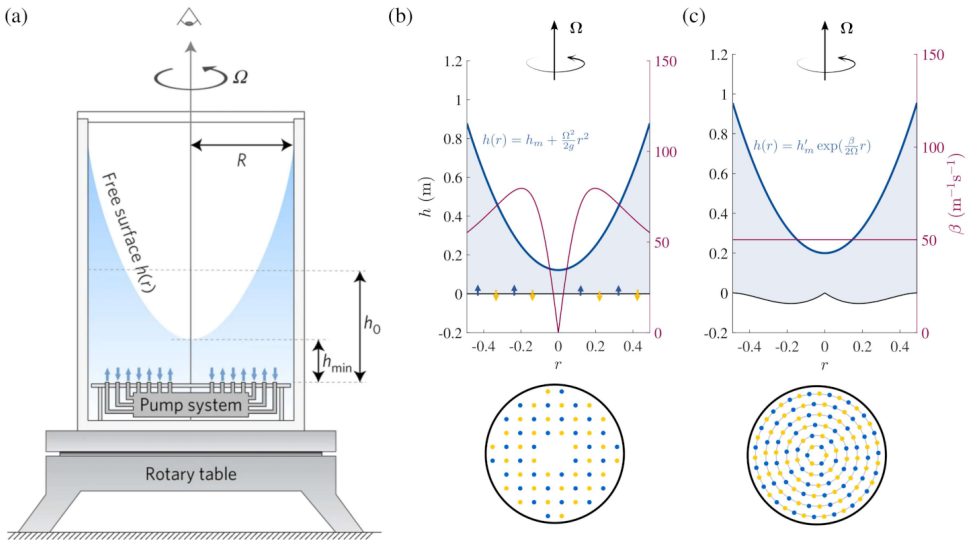


Figure 9. (a) Schematic section through the apparatus used by [33,38,39] to obtain a zonostrophic multiple-jet flow in a rapidly rotating, homogeneous fluid. The tank has a radius $R = 0.5$ m and is rotated at $\Omega = 7.85$ rad s^{-1} with a free surface which becomes strongly distorted into a paraboloid by centrifugal forces. Relative motions were driven by a network of inlet and outlet tubes to drive a turbulent flow. Material from [38], Macmillan Publishers Ltd: © 2017. (b,c) Free surface height (blue curve), topographic β-effect (purple curve) and forcing pattern in the experiments of [38] (b) and [39] (c).

Figure 9 (a) shows a sideview schematic of the experimental set up used in [38,39]. Fast rotation led to a very strong centrifugal distortion of the upper free surface into an extreme paraboloid, with the depth varying from 20 cm on the rotation axis to ~ 90 cm near the periphery. This greatly curved (e.g., $\beta_1 \approx 3.3$), free-surface paraboloidal fluid layer geometry is a necessary design requirement in order to reach the zonostrophic regime in which $R_\beta^s \gtrsim 2.5$. The large deflection of the free surface leads to large values of $\beta_T \simeq 70$ (m.s)$^{-1}$, due both to the high values of Ω and due to the large value of the topographic stretching ($h^{-1}\partial h/\partial s$). The free surface also greatly lowers the effects of Ekman drag which is then only present due to Ekman pumping at the bottom no-slip boundary. This is in addition to the rapid rotation rate that generates a low Ekman number, $E \simeq 10^{-7}$. For an approximately fixed value of the forced flows, these high β_T and E^{-1} values are what allow for large R_β per (15).

As sketched in Figure 9 (b), in the first version of the experiment [38], the forcing consisted in 64 sources and sinks distributed on a Cartesian array, and the bottom of the tank was flat, resulting in a spatially varying β-effect. The container employed in [38] was made of polyethylene, which is not transparent. This disallowed for the passage of a horizontal light sheet through the fluid layer, as required for standard particle image velocimetry techniques. Instead, [38] put small floating

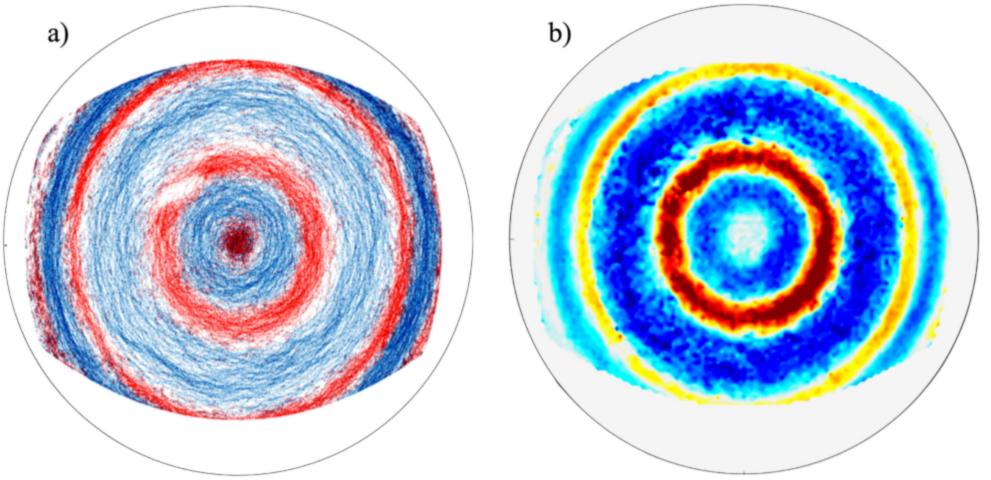


Figure 10. Surface floater velocity measurements from the free surface paraboloidal experiment of [38] in the zonostrophic regime. (a) Lagrangian particle tracks with path coloration given by prograde (red) and retrograde (blue) azimuthal velocity. (b) Eulerian mean azimuthal velocities, $u_\phi(s,\phi)$. Both panels reveal the existence of strongly coherent zonal jet flows in the zonostrophic turbulence regime ($R^s_\beta \gtrsim 2.5$). Material from [38], Macmillan Publishers Ltd: © 2017.

particles atop the free surface and employed Lagrangian tracking freeware [106] to generate 4900 particle tracks over the course of 5350 rotations of the tank at 75 rpm experiment.

Figure 10 (a) shows these particle tracks with their local color denoting prograde particle motions in red and retrograde particle motions in blue. The formation of long period, coherent, strongly anisotropic jets is observed in the coloration pattern of the tracks.

Figure 10 (b) shows the Eulerian mean azimuthal velocities, acquired by binning the Lagrangian particle tracking data that passes through a given areal region. The data shows that these flows are in the geostrophic turbulence regime, with high characteristic Reynolds numbers of order $Re \simeq 3\times10^4$ and low Rossby numbers of order $Ro \simeq 7\times10^{-3}$. Further, the velocity data shows that the radial extent of the jets is well approximated by the Rhines scale, k_R^{-1}.

The particle tracking data of Cabanes et al. [38], in combination with a three-dimensional direct numerical simulation, showed that the turbulent flow exhibited kinetic energy spectra in agreement with theoretical predictions [25,26,107] and Jupiter observations [56]. The Rhines and transitional wavenumbers in the numerical simulation appeared to be well separated with $R^s_\beta \approx 3.7$ calculated using using their spectral prefactor $(C_Z/C_K)^{3/10} \sim 0.7$ in (16). If, for the sake of comparison, we use the prefactor $(C_Z/C_K)^{3/10} \approx 0.5$ used in Figure 1, this leads to $R^s_\beta \approx 2.6$, which is still above the zonostrophy threshold estimated in [26,31]. However, the sensitivity of the calculated values of C_Z and C_K calls into question the robustness of any regime boundaries defined solely in terms of R^s_β value. Irregardless, the agreement found in [38] between lab, computation and theory confirms the zonostrophic character of the flow in the single experiment investigated.

The primary goal of the first experimental study [38] was to generate unambiguous, multiple zonostrophic jet flows in a laboratory setting. The aim of the second study was to delve further into the generation mechanism and the long-term zonostrophic dynamics of these jet flows [33,39].To achieve this, an optically-clear acrylic tank was employed in [39] to allow for time-resolved particle image velocimetry (PIV) measurements (see Figure 11(a)). Further, the bottom

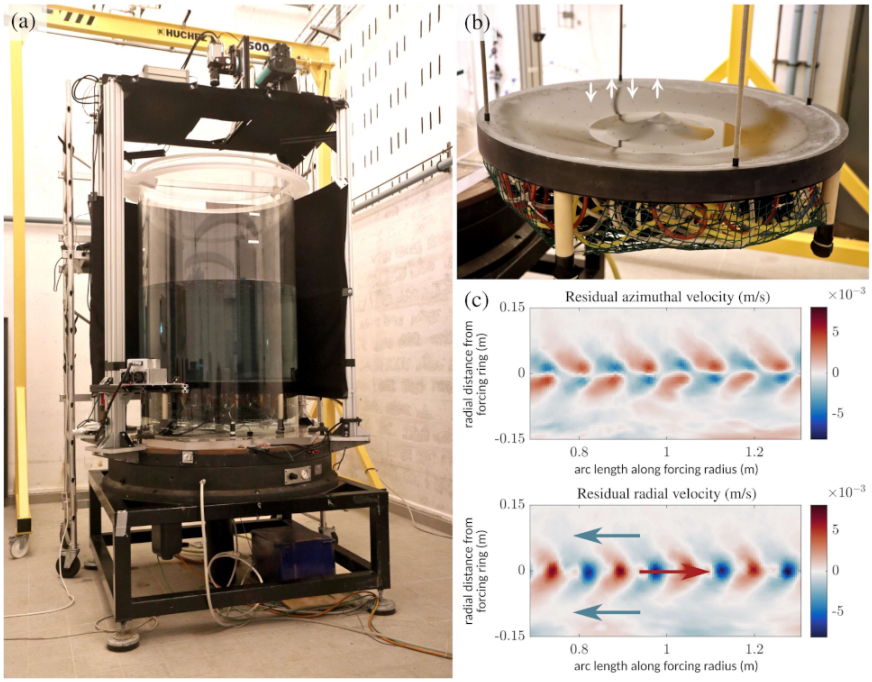


Figure 11. (a) Global view of the experimental setup of [39]. A laser attached on the side is used to illuminate the fluid on a horizontal sheet and perform PIV. (b) Bottom plate used to perform the source/sink forcing. Submersible pumps and tubes are attached below the plates. (c) Azimuthal and radial components of the residual velocity measured at the very beginning of an experiment. We show here an unwrapped section (from polar to cartesian) of the field of view, zoomed onto 8 sources and sinks of a forcing ring. The chevron-like pattern is indicative of Rossby waves radiated by the forcing. The red/blue arrows indicate the direction in which the zonal flow is accelerated (prograde/retrograde). Figure adapted from [39] (2021) with permission from © Cambridge University Press.

of the tank was curved to achieve a uniform topographic β-effect over the whole domain (see Figure 9 (c) and a picture of the bottom plate on Figure 11 (b)). This was done to allow a more straightforward comparison with theories developed in the β-plane framework. To achieve a better scale separation between the forcing and the jets, the forcing scale was reduced by a factor two by increasing the number of inlets/outlets from 64 to 128. Further, the inlets/outlets were distributed on a polar array and 6 submersible pumps controlled independently each one of the 6 forcing rings, allowing a precise control of the forcing amplitude with radius (Figures 9 (c) and 11 (b)). In these experiments, the – homogeneous – topographic β-effect is of about 50 $m^{-1}s^{-1}$, the Ekman number $E \sim 3 \times 10^{-7}$ and the root-mean-squared velocities could reached a few cm s^{-1}, leading to Reynolds numbers from 5×10^3 to 2×10^4 [33].

This second experimental set-up demonstrated that despite the strongly turbulent nature of the experiments, zonal jets emergence and non-linear equilibration are controlled by the transport and deposition of momentum by Rossby waves [39]. At low forcing amplitude, prograde jets were observed to emerge above each forcing ring, with retrograde flows in between (Figure 12), even though there were as many inlets as outlets along a given forcing ring. A careful analysis of the PIV velocity fields revealed that each forcing ring radiates Rossby waves (at the forcing scale),

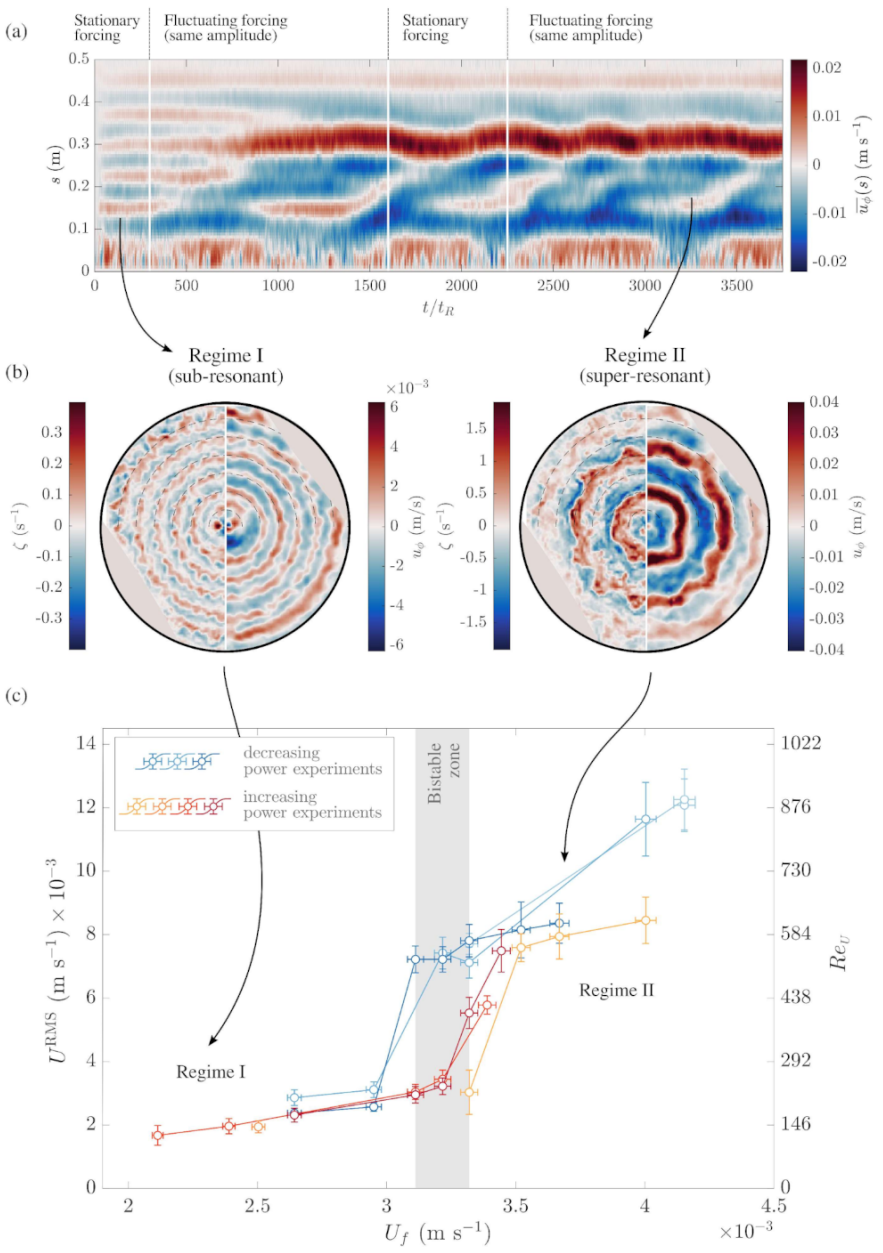


Figure 12. Instantaneous zonal flow in the source-sink driven experiments of [39]. (a) Space-time diagram of the zonal flow profile. The forcing amplitude is in the bistable range of panel (c), hence a transition from Regime I to Regime II is observed when "noise" is added to the forcing. (b) Instantaneous vorticity (ζ) and azimuthal velocity (u_ϕ) measured in an experiment at low forcing amplitude (Regime I) and at high forcing amplitude (Regime II). In the sub(super)-resonant Regime I (II), the Doppler-shifted Rossby waves phase speed is negative (positive), as resonant Rossby waves are stationary. (c) Hysteresis diagram showing the transition between the two regimes of turbulent zonal jets and associated bistability. U_f quantifies the forcing amplitude, $\overline{u}^{\mathrm{RMS}}$ is the root-mean-squared amplitude of the time averaged (mean) flow once in steady state, and $\overline{Re}$ the Reynolds number of the mean flow. Figure adapted from [39] (2021) with permission from © Cambridge University Press.

as seen in the chevron-like patterns of Figure 11 (c). The corresponding divergence of Reynolds stresses is positive at the radius of wave emission, and negative on the flanks of the forcing region, resulting in the observed zonal flow pattern. In this first regime (called Regime I), the jets are individual and locally forced (Figure 12 (a, b)).

As the forcing amplitude was increased, a transition was observed during which the jets were seen to merge and form a set of fewer but stronger jets whose location was not correlated with the location of the mass sources and sinks, called Regime II hereafter (Figure 12 (a, b)). As demonstrated by the hysteresis diagram of Figure 12 (c), the transition comes with bistability: in some range of the forcing amplitude, both Regime I and Regime II could be obtained for the same forcing amplitude depending on the history of the system. Figure 12 (a) shows for instance an experiment at a fixed forcing amplitude in the bistable range, where adding "noise" to the forcing was enough to transition from Regime I to II. It was shown that the transition arises from a linear Rossby waves resonance due to their advection by the background zonal flow: given that Rossby waves have a retrograde phase speed, a prograde flow can make them stationary, i.e., phase-locked with the forcing, leading to their resonant amplification. This mechanism also quantitatively explains the bistability [39].

In both Regime I and II, the zonal flow profile is well correlated with the Reynolds stresses in the turbulent flow [33,39], i.e. the zonal flow is the indirect result of correlations in the fluctuating velocities, and is never directly forced. However, while Regime I, where the jets are individual and locally forced, may be relevant for jets in the terrestrial oceans, Regime II is arguably the regime relevant for gas giants. In a follow-up study [33], the saturated turbulent and statistically steady state obtained in Regime II was analysed. Experimental PIV measurements could be used to compute kinetic energy spectra. In agreement with [38], it was shown that the measured turbulent flow shares the properties of zonostrophic turbulence relevant to the gas giants, in which the zonal flow alone contains more kinetic energy than the remaining of the flow. Spectral slopes consistent with an inverse cascade of energy were nevertheless hardly retrieved experimentally. Using two-dimensional quasi-geostrophic simulations of the experiments, [33] showed that this is due to the lack of scale separation between the forcing scale and the transitional scale. Interestingly, decreasing numerically the forcing scale allows to retrieve the theoretical slope, without influencing the final zonal flow profile. This suggests that even if the "large" experimental forcing scale prevents the development of an isotropic inverse cascade of energy, it does not limit the emergence of strong turbulent zonal jets.

Potential vorticity (PV) mixing was also investigated in strongly turbulent experiments of Regime II [33]. Despite the strength of the zonation, potential vorticity mixing is only moderate in these experiments because of the moderate zonostrophy index relatively to cases leading to strong staircaising [108]. That being said, experimental data was used to confirm that turbulent upscale energy transfer rates can be estimated by measuring a local PV mixing length, as proposed by [56] by analogy with measuring the Thorpe scale in stratified turbulence.

While these experiments were successful in indirectly forcing jets in extreme regimes, several limitations should be underlined to better understand the challenges of making more progress in this direction (see [61] for a more in-depth discussion). First, reaching a good enough scale separation between the forcing and the jets, and the jets and the experimental domain is a great challenge. Forcing the flow stronger to reach more extreme regimes means that the jets width will be larger, requiring a larger tank radius so multiple jets can fit within the fluid volume. That being said, these experiments are a clear example of the added value of the laboratory approach: a single three-dimensional direct numerical simulation at an Ekman number three times higher (e.g., [38]) requires 13 days of computation on 2048 CPU cores (650,000 CPU hours) in order to simulate 13 minutes of an experiment (1000 rotation periods). It is thus clear that numerical systematic studies in these regimes are currently inconceivable, whereas multiple experiments

can be performed, as well as experiments over very long times, allowing to study in detail the processes of jets emergence as well as their long-term nonlinear dynamics.

For instance, experiments could have a crucial role to play in investigating critical transitions between attractors. Multistability and transitions have been described in simulations of stochastically forced barotropic jets on the β-plane [109,110]. For identical external parameters, several turbulent steady states with a different number or position of jets are possible and "reversals" between different jets configurations can occur. Simonnet et al. [110] observed transitions over time scales of about 10^5 or even 10^6 turnover times. Although multistability was reported in the experiments of Lemasquerier et al. [33], spontaneous transitions were not observed despite running experiments over 8 hours, corresponding to 40,000 rotation periods (see [61, Chapter 5]). Note that this corresponds to about 10^4 turnover times. Hence, experiments designed to run much longer and/or with a shorter turnover time would be necessary to observe rare transition events. Note also that the forcing in [33] is idealised, performed at a unique scale and spatially fixed. This could prevent long-term dynamics such as drifting zonal jets or spontaneous transitions.

6.4. *Zonal jets in convection*

Experiments that drive eddies using devices fixed with respect to the apparatus have some advantages in allowing close experimental control on the location, scale and intensity of the applied forcing and/or initialization of turbulent motions, from which zonal flows could emerge. However, they also impose a number of geometric constraints by construction on the flow which are not typically found in systems that occur in nature on geophysical or astrophysical scales.

Free convection at high Rayleigh number in an unstably stratified fluid provides alternative and geophysically plausible means of energizing relatively unconstrained turbulent motions, albeit initially to form complex, three-dimensional circulation patterns of a form that may be hard to predict or control in detail. Even without background rotation to induce departures from

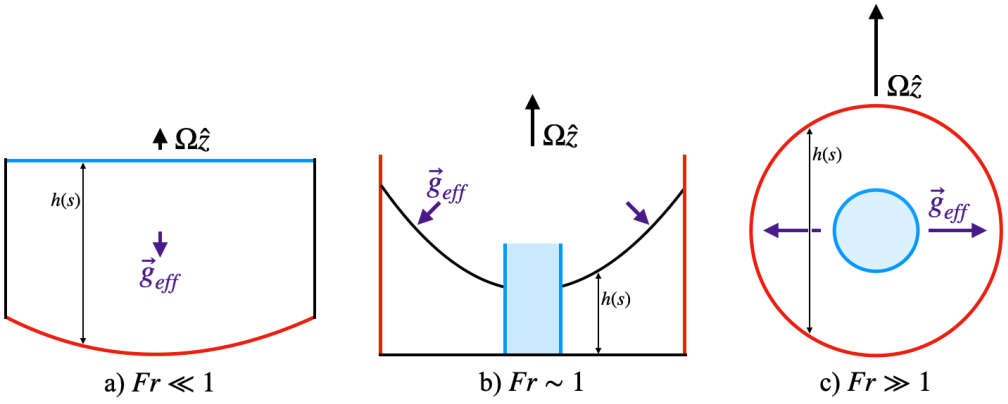


Figure 13. Schematic cross-sections of different experimental schemes for generating convectively-driven zonal flows. Red (blue) surfaces are actively heated (cooled). (a) Low external Froude number set-up, with axial gravity shown antiparallel to the rotation vector. b) Moderate Fr set up, in which the free-surface equipotentials are deflected into a paraboloid. c) Large Froude number set up in which centrifugal gravity is dominant. In cases with $Fr \gg 1$, such experiments must be carried out in close tanks, such as spherical shells, in order that the working fluid remain contained. In each schematic, h denotes the axial height of the fluid layer, which figures into calculations of $\beta_T = (2\Omega/h)(\partial h/\partial s)$.

isotropy, laboratory experiments have demonstrated that free convection under some circumstances can spontaneously form a rectified mean flow (e.g. [111–113]). This is associated with a spontaneous symmetry breaking of patterns of convective plumes, which become tilted in a preferred direction to result in an upward flux of horizontal momentum in a manner somewhat similar to the "moving flame" mechanism discussed above. The influence of background rotation, however, can help to organize the convection into quasi-two dimensional, vortical plume structures of a characteristic form and scale (e.g. [7,114–124] which can seed turbulent processes that can ultimately lead to the formation of zonal flows (e.g., [43,125]).

Differing styles of convectively-driven zonal flow experiments are carried out based on the effective gravitational acceleration, as shown in Figure 13. In laboratory settings, the effective gravity,

$$\mathbf{g_{eff}} = -g_o\widehat{\mathbf{z}} + \Omega^2\mathbf{s}, \tag{25}$$

is always an admixture of vertically downward lab gravity, $-g_o\widehat{\mathbf{z}}$ (where $g_o \simeq 9.8$ m/s^2), and cylindrically-radial centrifugal acceleration, $\Omega^2\vec{s}$. The ratio of these two terms is estimated by the external Froude number, $Fr = \Omega^2 S/g_o$ with the system's maximum cylindrical radius S employed as the characteristic length scale.

The left-hand cartoon in Figure 13 (a) shows the low Froude number limit in which lab gravity is dominant. These $Fr \ll 1$ experiments are based on "standard" upright convection. The bottom boundary here is depicted with curvature in order that $\beta_T \neq 0$, as is argued to be required for the formation of coherent laboratory zonal jet structures.

Figure 13 (b) shows a moderate Froude, annular convection set up. In this $Fr \sim 1$ regime, effectively gravity becomes increasingly canted away from the axial direction with increasing s. This casuses the fluid's free surface to deflected into a paraboloid, as in to [38,39]. The density gradients are primarily radial, being set by the thermal boundary conditions on the annular sidewalls. For a 1 m diameter tank, $Fr = 1$ when $\Omega = 4.4$ rad/s $\simeq 40$ rpm.

Figure 13 (c) show the rapidly rotating $Fr \gg 1$ limit. In this end-member case, centrifugal acceleration greatly exceed g_o, and $\mathbf{g_{eff}} \simeq \Omega^2\mathbf{s}$. The cylindrically radial increase in outward effective gravity is qualitatively similar to the radially increasing inward spherical gravity that exists in self-gravitating uniform density spheres, $\mathbf{g} = -(4\pi\rho G/3)\mathbf{r}$, as adequately describes gravity in terrestrial liquid metal cores [126] and where ρ is the mass density and G is the universal gravitational constant. However, opposite to planetary gravity, the outward centrifugal acceleration requires that the inner spherical shell boundary be cooled in order to generate a convectively-unstable density profile. Note that the boundaries, which we are taking to be nearly isothermal here, are not perpendicular to $\mathbf{g_{eff}}$ in all three systems shown in Figure 13. Thus, these convection experiments all have a nonzero component of baroclinic driving. Thermal winds will therefore always need to be deconvolved from any barotropic zonal flows that develop.

6.4.1. $Fr \ll 1$ *Convection Experiments*

Condie and Rhines [129,130] carried out elegant $Fr \ll 1$ laboratory experiments that combined thermal convective forcing with background rotation and a topographic β-effect. In their experiments, a circular, bowl-shaped tank was filled with hot water and allowed to cool from above, inducing free convection from the upper free surface. The tank was placed on a rotating table and fluid motions near the top surface visualised and measured relative to the rotating tank. After a while, the convective motions were seen to organize themselves spontaneously into a pattern of concentric meandering jets, interspersed with closed vortices and other eddying structures. The jets were interpreted by [130] as being associated with meridionally overturning circulations arising from buoyancy forcing related to a radial gradient in depth-averaged density $\sigma(r)$. The jet separation distance was shown to be consistent with a scale of the order of a "deformation radius" $L_d \sim (g[\Delta\sigma/\sigma]\overline{D})^{1/2}/f$ (where $\overline{D}$ is the mean depth of the fluid), defined

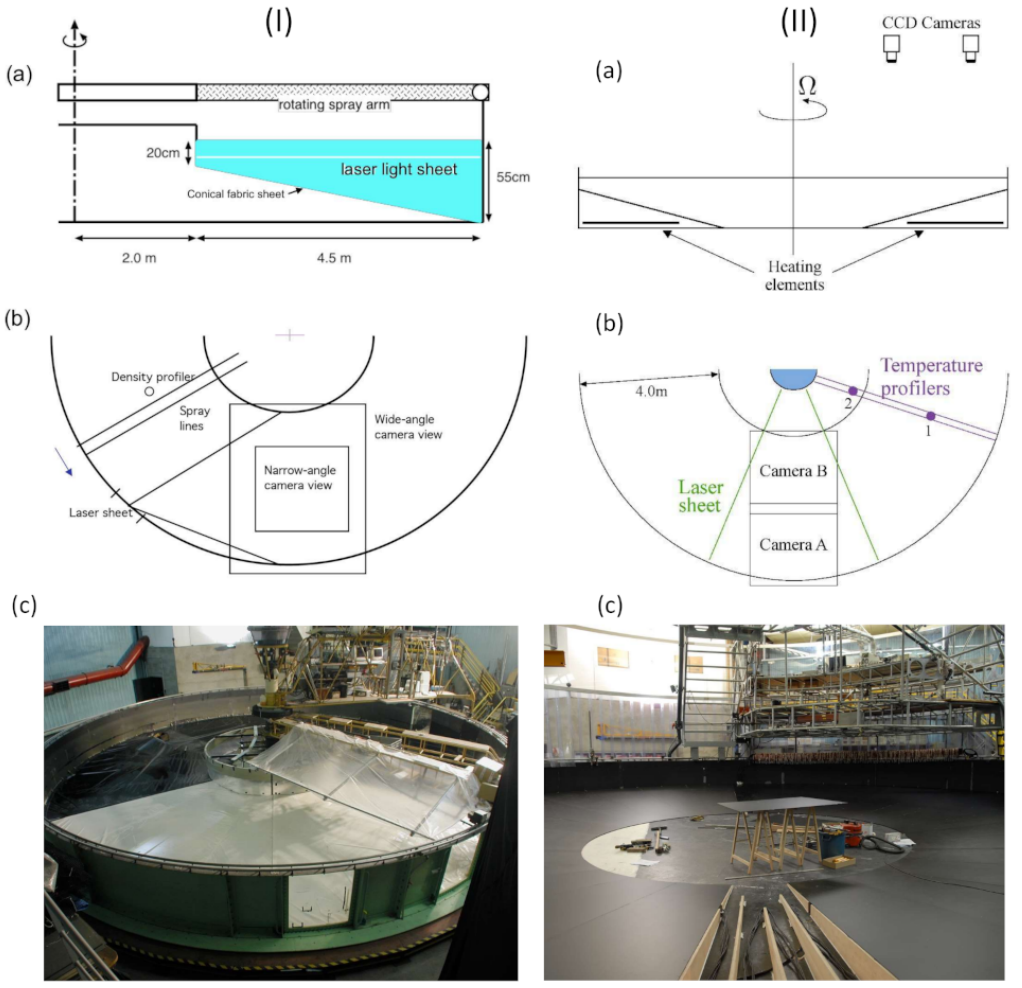


Figure 14. Schematic configurations of the 13 m diameter Coriolis Platform in Grenoble, France, as used for jet formation experiments in rotating convection [53,127,128]. I(a-b) Configuration I, in which convection was driven from above using a distributed spray of salt water [53]; II(a-b) Configuration II, in which thermal convection was driven from below using electrical heating beneath the sloping base [127]. I(c) and II(c) show photographic views of the Coriolis platform (I) set up for configuration I and (II) under construction for configuration II showing the network of heating cables under the sloping base.

with respect to a difference in σ over the radial distance L_d, while the jet amplitude appeared to be of order $U \sim fL_d$. Such a dependence is perhaps suggestive of angular momentum conserving, or possibly a potential vorticity mixing, flow over a distance L_d (provided $L_d \ll$ the radius R of the tank).

The mechanism considered by [129,130] did not directly attribute the formation of the zonal jets observed to eddy processes, and likely were dominated by baroclinic, thermal wind dynamics. It was noted, however, that eddies were aligned with the zonal flows and could "contribute significantly to the zonally averaged flow at certain latitudes". The horizontal Reynolds stresses

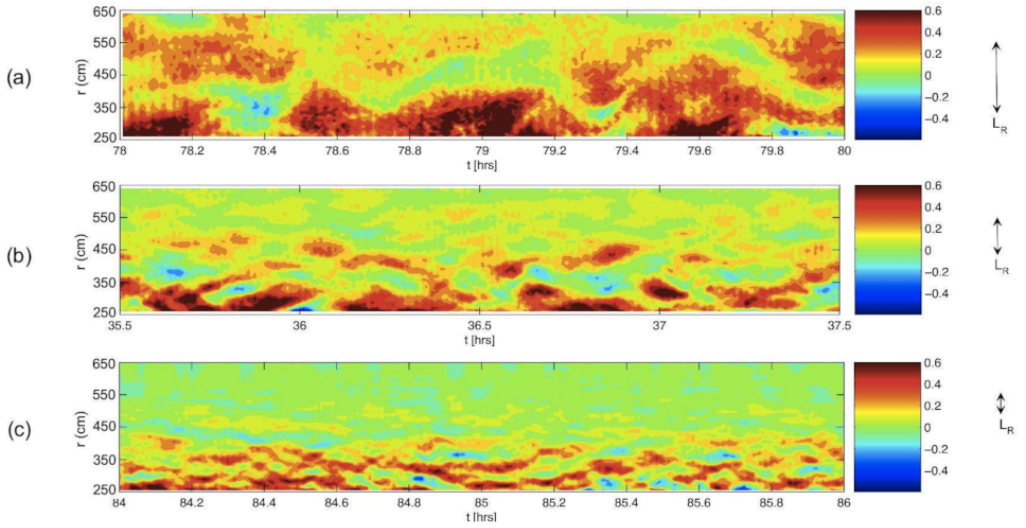


Figure 15. Time series of the radial structure of the azimuthal flow velocity in experiments using Configuration II of the Coriolis convection experiments [127], averaged in azimuth across the combined field of view of two overhead Cameras (see Figure 14 (II)). Results are shown for various values of rotation period τ_R and water depth. Parameters correspond to (a) τ_R = 320 s, D = 0.8 m (β^* = 43), (b) τ_R = 80 s, D = 0.8 m (β^* = 180) and (c) τ_R = 40 s, D = 0.8 m (β^* = 395). Colour bars indicate the azimuthal flow velocity in cm s^{-1} and arrows indicate the Rhines lengthscale L_R.

due to the wave-like meanders and vortex-like eddies were not measured directly, though appear tilted in the visualization presented in their figure 3. So it might also be the case that the zonal jets found in this experiment were also at least partially driven by eddy stresses, with the eddies themselves redistributing momentum and producing concentrated zonal jet structures fueled by convective eddies.

The role of eddies in driving the formation of zonal jets in the presence of convection was much clearer in large scale experiments carried on the 13 m diameter Coriolis platform by Read et al. [53,127,128]. Experiments on such a large scale enabled access to fairly extreme parameters such as the flux Rayleigh number Ra_F ($1.5 \times 10^{10} - 6 \times 10^{13}$), convective Rossby number Ro^* ($1.7 \times 10^{-3} - 4 \times 10^{-2}$) and Ekman number E ($5.2 \times 10^{-6} - 5 \times 10^{-5}$) while keeping the Froude number quite small. The experimental configurations are shown schematically in Figure 14 as cross-sections and plan views. Two configurations were used (I and II) which both used a free surface and conically sloping lower boundary. In configuration I, convection was initiated from above by gently spraying dense, salty water onto the top surface using nozzles mounted on a radial arm [53]. For configuration II, however, convection was maintained by electrical heaters embedded under the bottom sloping boundary while the upper surface cooled to the laboratory environment [127]. In both configurations, the horizontal flow was measured using PIV with particles illuminated from one side by a powerful horizontal laser sheet.

One disadvantage of operating experiments on such a large scale was that it was impractical to view or measure the flow across the entire tank. Small arrays of cameras were therefore used to sample the flow across the full range of radii across the annular channel. This approach only enabled around 10% of the domain to be measured, but the spatial resolution was sufficient to

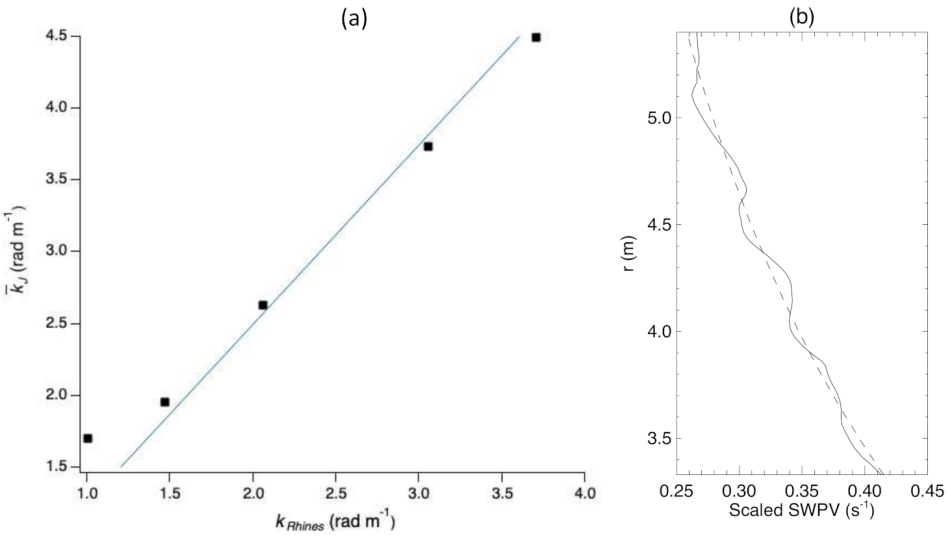


Figure 16. (a) Graph showing the variation of the dominant time-mean radial wavenumber $\overline{k}_J$ of zonal jets vs estimates of the Rhines wavenumber k_{Rhines} for the thermally driven experiments illustrated in Figure 15 [127]. Straight line represents a fit to the data passing through the origin with slope 1.25 ±0.04. (b) Radial profile of shallow water PV from 5 min time averages of zonal velocity in the salt-driven convection experiments on the Coriolis platform [53]. Solid line represents the total PV while the dashed line represents the background "planetary" component (see [53,128] for further details).

resolve most of the energetic scales of motion.

As found by Condie & Rhines, the resulting convective flow was found to develop patterns of zonal jets meandering among vortices of either sign that equilibrated after a few hours of operation. Such jets were most prominent in the presence of the topographic β-effect due to the sloping lower boundary and the radial scale and separation of the jets was found to depend strongly on the rotation speed Ω. Figure 15 illustrates this trend clearly for three cases in the configuration II [127], showing radius-time maps of the zonally-averaged zonal velocity at different values of Ω. Also shown on the right of Figure 15 are estimates of the Rhines scale L_R for each case, derived using the rms horizontal eddy velocity, indicating a clear correlation between the radial wavelength of the jets and L_R.

This correlation was shown to hold over at least a factor of 4 in L_R (see Figure 16). The experiments covered a range in $\beta_2 = \beta_T L^2/u_{rms}$ from around 40 to 580, covering a range of jet scales from the width of the annular channel to much narrower jets with up to 5 jet pairs at the highest value of β_2. The strength of the jets, however, was relatively weak and scarcely different in magnitude from the non-axisymmetric eddies. This was consistent with estimates of the zonostrophy parameter R_β^s of between 1.5 and 1.6 which suggests all of the flows in both configurations were only marginally zonostrophic. Nevertheless, the jets were sufficiently strong to perturb the zonal mean PV profile to produce some clear staircasing, even in short-term (5 min) time averages (see Figure 16 (b)).

Detailed analysis also confirmed a strong anti-correlation between the divergence of the horizontal Reynolds stress and the observed acceleration of the zonal jet flow, indicating a clear role for the eddies in generating and maintaining the latter. The analysis of Read et al. [53] went even further to compute the nonlinear spectral transfer function in 2D, $\mathcal{T}_E(\mathbf{k}|k_c)$ as a function

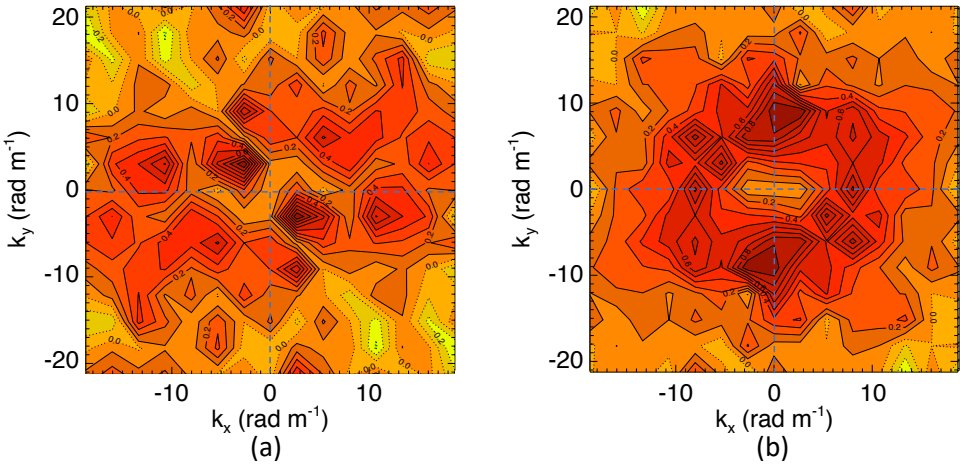


Figure 17. Normalized spectral energy transfer functions for two cases of salt-driven convection on the Coriolis Platform [53,128]: (a) flat bottom (weak β-effect) and (b) sloping bottom with full β-effect, both at rotation periods of 40s. Functions were computed from sequences of vorticity fields obtained from narrow angle camera images, and integrated over triads in wavenumber that include at least one component with $|k| \geq$ cut-off wavenumber $k_c \simeq 20$ rad m^{-1}, averaging in time over approximately 40-50 rotation periods. Each field is normalized by the maximum value and contours are shown with interval 0.1 and with contours below 0.5 dashed.

of both radial and zonal wavenumbers. This measures the average rate of change of KE at vector wavenumber **k** due to nonlinear, resonant wave triad interactions involving at least one component with $|\mathbf{k}| \geq k_c$ [131]. The results (reproduced in Figure 17) show a clear tendency for KE to accumulate in modes close to $k_x = 0$, corresponding to zonal jets, for cases with a significant topographic β-effect. Without such a β-effect, however, this tendency is much less clear.

6.4.2. $Fr \gg 1$ *Convection Experiments*

Busse and colleagues carried out the first $Fr \gtrsim 1$ centrifugal convection experiments in simulating rotating convection and zonal flows in planetary settings [50]. Based on these experiments, it was argued that convection in the interior of a spherical planet could give rise to the generation of eddies and zonal flows that were coherent along axes parallel to the axis of rotation of the planet itself [132,133]. The zonal flows were suggested to arise in association with Reynolds stresses that resulted from β_T-induced radial tilts in the convective vortices, leading to momentum fluxes that could drive zonal motions (e.g., [134]). This hypothesis was further investigated in a number of laboratory experiments using either hemispheric shells or a cylindrical annulus with conical end walls, all in rapid rotation [135–137]. Weakly nonlinear convection was induced in each case by maintaining the inner and outer spheres or cylinders at different temperatures in order to produce statically unstable stratification. These experiments were able to demonstrate the formation of fields of axially-aligned convective eddies, all roughly parallel with the rotation axis, accompanied by zonal motions, although the experiments used mostly qualitative visualisations.

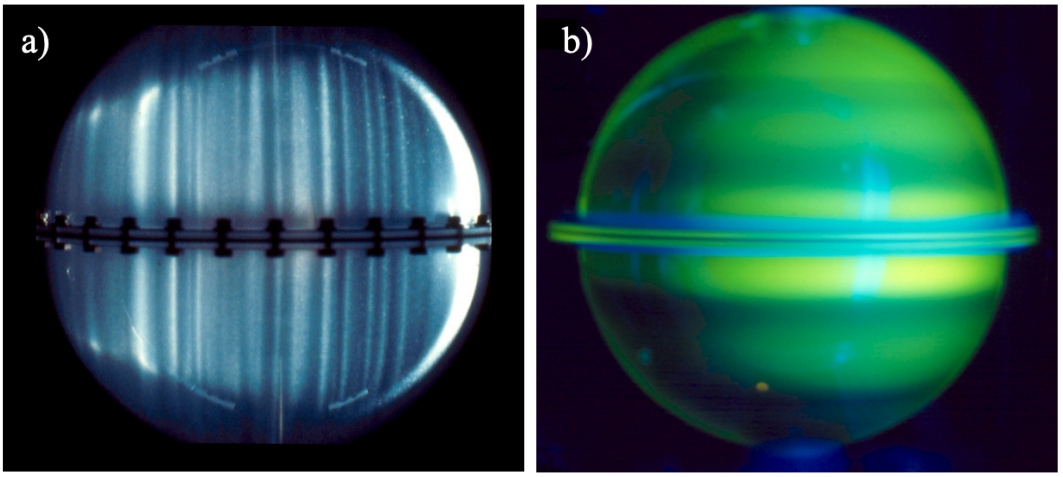


Figure 18. (a) Kalliroscope snapshot visualization of axially-aligned $Ro \ll 1$ convective flow structures in a water-filled, rotating, spherical shell between spheres of radius 5 cm and 15 cm respectively at $Ra \simeq 50\ Ra_c$, $E = 2.5 \times 10^{-6}$ and $Fr = 5.4$ (b) Time-lapsed dye visualization of outer boundary zonally banded flow in a rapidly rotating spherical shell containing water with differential heating between the inner and outer sphere. Images: Peter L. Olson.

Fully nonlinear centrifugally-driven spherical shell visualization experiments were extended by Olson and colleagues [138,139]. Figure 18 (a) shows a Kalliroscope visualization on a light sheet crossing the fluid bulk of a rapidly rotating spherical shell with inner and outer radii, respectively, of 5 cm and 15 cm in radius, and water as the working fluid [138]. The Kalliroscope flakes reveals axially-aligned shear structures in the convecting fluid. The control parameters for this experiment were $Ra \sim 50 Ra_c$ (where Ra_c is the critical Rayleigh number for the onset of convection) and $E = 2.5 \times 10^{-6}$, with corresponding Froude number of $Fr \simeq 5.4$ (180 rpm).

Figure 18 (b) shows a time-lapsed image of flourescein dye trapped below the outer boundary in the most rapidly rotating experiment of [139]. This case was carried out at $Ra \gtrsim 10^2$) and $E = 7 \times 10^{-7}$ (760 rpm), such that $Fr \simeq 9.6$. The inner shell boundary is 76% the radius of the outer shell boundary. Clear zonal banding is seen in the time-lapsed dye pattern, with as many as nine detectable zonal bands. This suggests that if similar experiments were carried out with state-of-the-art velocimetry capabilities, zonostrophic jets would form under the most extreme conditions investigated in the $Fr \gg 1$ spherical shell experiments of [139].

Quantitative ultrasonic Doppler velocimetry measurements in spherical shell experiments made in Grenoble, using either water (with Prandtl number 7) or gallium (with Prandtl number 0.025) as the working fluid, have since been acquired by [140,141]. The jets form consistently on a radial length scale of order $(\overline{U}/\beta_T)^{1/2}$ in [141], where $\overline{U}$ is the amplitude of the mean zonal flow. From the velocimetry data, it emerged that two kinds of flow regime could be identified; one (at relatively small supercritical Rayleigh numbers Ra_c) with rather weak, meandering zonal jets and another (with $Ra/Ra_c > 40$) in which the kinetic energy of the zonal flow was dominant over the non-axisymmetric flow, in a manner that seems to anticipate the Rossby resonance effects associated with the transition to "Regime II" observed by Lemasquerier et al. [39]. The amplitude of the volume-averaged zonal flow $\overline{U}$ was found to scale with the non-axisymmetric radial flow V' as $\overline{U} \sim V'^{4/3}$.

6.4.3. $Fr \sim 1$ *Convection Experiments*

A number of recent experiments have investigated zonal flows using rotating cylindrical experiments in the $Fr \sim 1$ regime, where β_T is set by the paraboloidal deflection of the fluid's upper free surface (e.g., [34,40,55,65,142–144]). (The fact that the baroclinic annulus jets experiments of Smith et al. [55] are referenced in this section illuminates the diaphanous, and possibly false, curtain that separates $Fr \sim 1$ convective flows from the baroclinically-driven annular flows discussed in the following section.)

The low R_β, $Fr \sim 1$ study of [40] simulated deep ocean convection dynamics via rotating thermal convection experiments on the topographic polar β-plane. Their zonostrophy index of $R_\beta \approx 1.3$ was close to oceanic values, placing these experiments within Figure 1's transitional regime. Thus, zonal jets were not a dominant feature of the flows and were only revealed after averaging. The spacing between the jets was in good agreement with the Rhines scale.

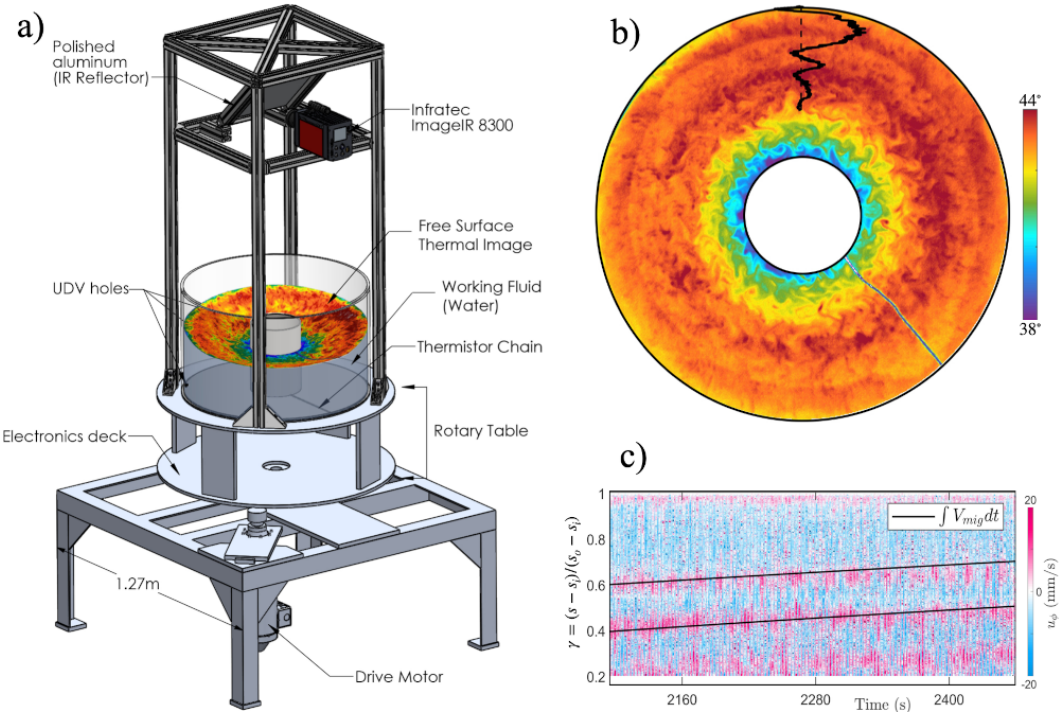


Figure 19. a) Schematic rendering of the "Coreaboloid" apparatus used by [34] to obtain a zonostrophic multiple-jet flow in a rapidly rotating buoyany-driven flow. The fluid annulus has an outer (inner) radius $R_o = 0.37$ m ($R_i = 0.10$ m) and a free surface that becomes strongly distorted into a paraboloid by centrifugal acceleration. Thermographic free-surface overlay is from the $\Omega = 5.24$ rad/s case (50 rpm, $Fr = 1.0$). b) Thermographic top down image from the $\Omega = 2\pi$ rad/s case (60 rpm; $Fr = 1.5$). The solid black curve denotes the zonal velocity profile averaged over the last 10 minutes of the ultrasonic Doppler velocimetry data. The vertical black dashed line demarcates zero zonal velocity (aka, solid body rotation). c) Hovmuller diagram displaying ultrasonic Doppler velocimetry zonal velocity data as a function of time, t, and nondimensional cylindrical radius, $\gamma = (s - R_i)/(R_o - R_i)$. Solid black lines denote empirical jet migration rate predictions of Cope [145]. Figure adapted from [34]; Wiley ©2022 American Geophysical Union.

The higher R_β, $Fr \sim 1$ paraboloidal annular convection experiments of Lonner et al. [34] were carried out in similar spirit to that of Cabanes et al. [38], with the goal of generating zonostrophic laboratory jets driven by thermal buoyancy forces. Figure 19 (a) shows a rendering of their "Coreaboloid" device. The tank's inner and outer cylindrical radii are $S_i = 10$ cm and $S_o = 37$ cm, respectively. A thermographic snapshot of the surface temperature field from a 50 rpm experiment is overlain atop the paraboloidal free surface. The thermal buoyancy is provided by an ice bath situated within the inner cylinder. The outer wall and base are both acrylic, and thus thermally insulating. To increase the strength of the thermally-driven flows, the fluid bulk is warmed up to approximately 50° Celsius before each experiment. This increases the effective temperature drop across the fluid, but also necessitates the Coreaboloidal flows to be a complex mix of centrifugal and upright convective motions.

Rotating at 60 rpm yielded an Ekman number values of order $E \approx 4 \times 10^{-7}$, using the outer radius as the characteristic length scale, a peak topographic β value of order 1 $(\mathrm{m.s})^{-1}$, and an estimated zonostrophy index of $R_\beta \simeq 2.7$, corresponding to $R_\beta^s \approx 2.67$ using the $(C_Z/C_K)^{3/10} = 0.7$ value of [38] and $R_\beta^s \approx 1.90$ using the $(C_Z/C_K)^{3/10} = 0.5$ value of [26]. The zonostrophy index is smaller than the values attained in the larger volume, higher rotation rate, mechanically-driven experiments carried out in Marseilles [33,38,39]. The broadband buoyancy forcing in these experiments, which accurately replicates the turbulent flows that exist in natural settings, generates coherent, robust Rhines-scale jets that, agnostic to how one defines the zonostrophic regime boundaries, appear to exist in the zonostrophic regime.

Figure 19 (b) shows a thermographic top view image of the free surface temperature field in the 60 rpm case from [34]. Centrifugal convective instabilities form at the inner boundary and propagate out into the bulk. The convective structures also drift in azimuth in the form of thermal Rossby waves [146]. The black solid curve denotes the time-mean azimuthal flow averaged over the last 10 minutes of the 60 rpm experiment, measured using ultrasonic Doppler velocimetry. This azimuthal velocity profile contains multiple alternating jet flows, which are in adequate agreement with Rhines length scale predictions. There is also a net retrograde flow in the Doppler data, which may be due to baroclinic thermal wind flows. Figure 19 (c) displays a Hovmuller diagram of Doppler velocimetry data as a function of time and nondimensional cylindrical radius, $\gamma = (s - S_i)/(S_o - S_i)$. Coherent, alternating jets migrate in time, traveling outwards in radius over the range $0.2 \lesssim \gamma \lesssim 0.7$. The jet migration rates agree well with the empirically-derived predictions of Cope [145], based on her broad suite of two-dimensional simulations of β-plane turbulence.

The buoyancy-driven multiple jet flows reported in [34] imply that moderately small ($S_o \approx$ 30 cm), moderately slowly rotating ($\Omega \approx 5$ rad/s) laboratory devices can be fabricated to study zonostrophic jet dynamics. Further, the free upper fluid surface allows for the existence of large β_T, Re, and τ_E turbulence, while simultaneously providing relatively easy access for thermographic, PIV, Lagrangian surface tracking and altimetric diagnostic methods. Significant advances in our understanding of zonostrophic fluid physics may result from well-diagnosed, broad experimental surveys of zonal jet flows in such strongly curved ($\beta_1 \gtrsim 1$), free surface paraboloidal devices.

6.5. *Zonal jets in baroclinic eddy flows*

The previous Subsections 6.4.2 and 6.4.3 were mainly concerned with flows confined in rotating, annular channels with sidewall differential heating and cooling, for which the effective stratification was statically unstable, either because heating or cooling was applied at horizontal boundaries or via centrifugal accelerations modifying the direction of effective gravity. But another class of convective flows that can exhibit multiple zonal jet formation via eddy-zonal flow interactions

is represented by baroclinically unstable configurations, in which the basic flow is statically *stable* but with buoyancy sources and sinks displaced in the horizontal direction, such that isopycnal surfaces are sloped with respect to the local horizontal. The "classical" rotating annulus [147] is a type of experiment, typically with $Fr \lesssim 1$, which has been extensively used to investigate this configuration in the laboratory as a dynamical analogue of the baroclinically unstable, meandering jet stream in the Earth's troposphere and in the atmospheres of other terrestrial planets. In the absence of a "planetary vorticity gradient" e.g. due to a radial gradient of depth, the basic azimuthally-symmetric flow can become baroclinically unstable at high enough values of rotation rate Ω to traveling wave perturbations that fill the annular channel and efficiently transport heat both laterally across the channel and upwards, releasing potential energy stored in the sloping isopycnal surfaces. The resulting equilibrated flows take the form of azimuthally-traveling waves that may be either spatially symmetrical and coherent or irregular and chaotic, depending upon the values of Ω and other control parameters. The principal dimensionless parameters that determine the flow regime observed are the Thermal Rossby number

$$\Theta = \frac{g\Delta_{\rho h} D}{\Omega^2 L^2}, \tag{26}$$

and the Taylor number

$$\mathcal{T} = \frac{4\Omega^2 L^5}{\nu^2 D}, \tag{27}$$

where ν is the kinematic viscosity of the fluid. Θ and $\mathcal{T}$ are related to Ra, E, η and Pr from Table 1 by

$$\Theta = \frac{4\mathrm{RaE}^2\eta^2}{\mathrm{Pr}} = \frac{4\mathrm{Ra}}{\mathcal{T}\,\mathrm{Pr}\eta^3}, \tag{28}$$

$$\mathcal{T} = \mathrm{E}^2\eta^{-5}. \tag{29}$$

The Thermal Rossby number was originally defined as a proxy for the Burger number (see Section 2.1) based on the externally imposed *horizontal* boundary temperature contrast rather than the internally determined static stability. But it also provides an external measure of the mean Rossby number (see Table 1) provided $\Theta \sim \mathrm{Ro} < 1$. The Taylor number is an alternative measure of viscous effects to the Ekman number, but also takes into account dependencies on aspect ratio η. The Prandtl number also plays a role, though is rather less significant than the other two (e.g. [147,148].

In its "classical" configuration with a flat, horizontal base and either free upper surface or flat, horizontal lid in contact with the fluid, this system has been extensively investigated in the laboratory (see [147,148] for reviews). The dominant baroclinically unstable wave flows are found to occur with a wavelength comparable to the internal Rossby deformation radius

$$L_d^{\mathrm{int}} = ND/f, \tag{30}$$

where N is the buoyancy frequency, D the depth of the system and $f = 2\Omega$, so that shorter wavelength disturbances are favored at higher values of Ω. Without a "planetary vorticity gradient" e.g. due to a topographic gradient in either or both of the horizontal boundaries, however, the baroclinic wave flows tend to fill the annular domain in the radial direction. Amongst other things, this leads to a maximum zonal wavenumber that can remain stable and coherent, since higher wave numbers then correspond to a wave shape that has a horizontal aspect ratio (zonal:radial length scale) that is too small to be stable to Rossby wave perturbations of other wave numbers (e.g. [149,150], so the corresponding flow breaks up into an irregular, chaotic flow. The nonlinear interaction between the equilibrating baroclinic wave and the background zonal flow, however, will modify the latter, reducing the strength of the baroclinic jet near the centre of the channel

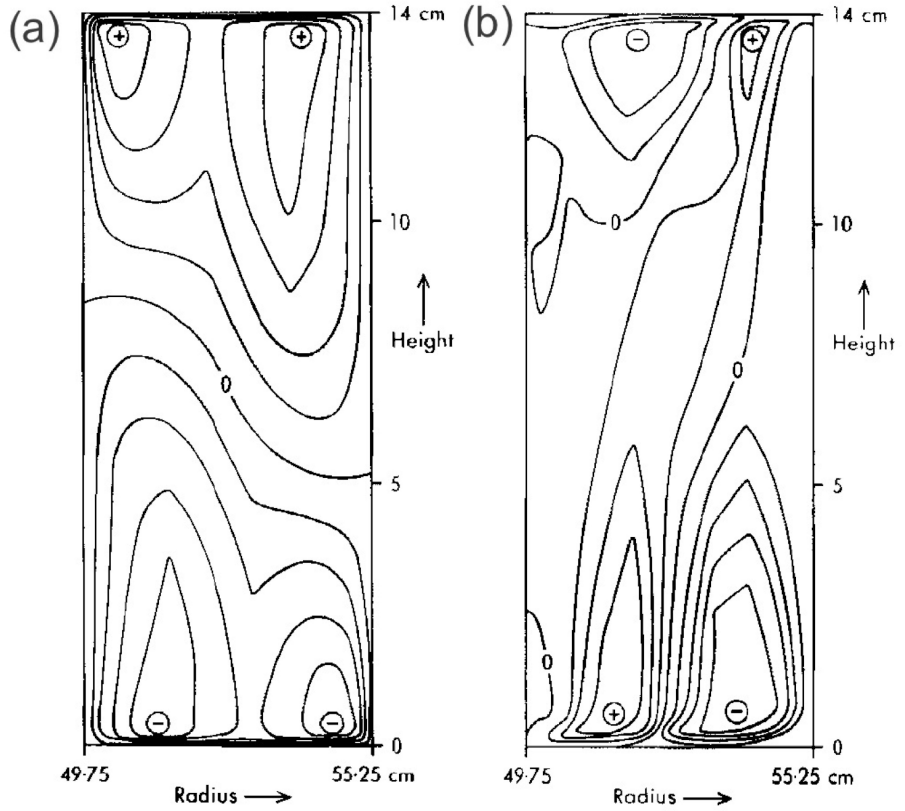


Figure 20. Contour maps of (a) zonal (azimuthal) flow and (b) horizontal Reynolds stress or momentum flux $\overline{u'v'}$ in a rotating, sidewall heated/cooled annulus experiment. Fields were computed in a Boussinesq Navier–Stokes model simulation by [152] [reproduced with permission; Copyright ©1986 Royal Meteorological Society].

and effectively turning it into a baroclinic "double-jet" structure [151,152] with azimuthal velocity maxima close to each sidewall and a local minimum of azimuthal velocity in mid-channel.

An example is illustrated in Figure 20(a) for an equilibrated steady wave flow [152]. Also shown in Figure 20(b) is the corresponding horizontal Reynolds stress field $\overline{u'v'}$ which show the baroclinic wave acting to transfer zonal momentum into each corner jet of the appropriate sign. This indicates a strongly nonlinear interaction between the wave and its parent zonal flow, sufficient to modify the structure of the latter substantially from its form before the baroclinic wave developed.

The presence of an externally imposed "planetary vorticity gradient", however, such as may be produced by sloping the upper and/or lower boundary to produce a radial gradient of depth across the channel, introduces a number of changes to the baroclinic wave behavior. Consistent with its effect on a barotropic wave flow, such a radial depth gradient causes the zonal propagation of baroclinic waves to become dispersive, in a manner that closely emulates the behavior of Rossby waves in the presence of a β-effect with a value of topographic $\beta = \beta_T$ approximated by

$$\beta_T \simeq \frac{2\Omega}{D}\frac{\partial D}{\partial r} \tag{31}$$

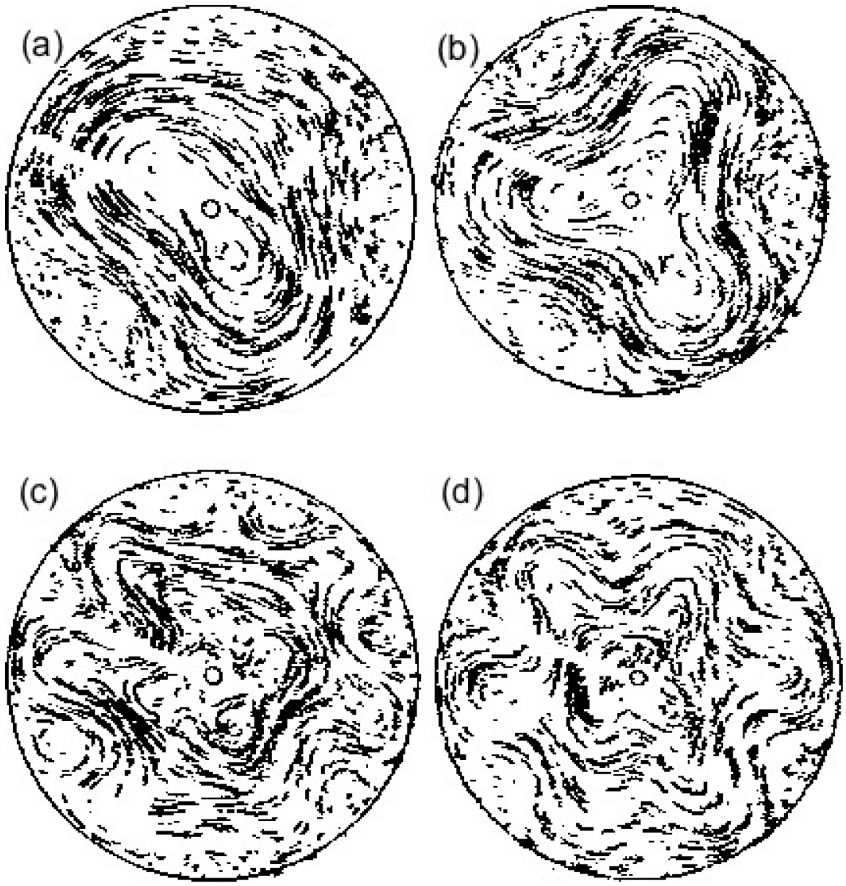


Figure 21. Streak images of tracer particle tracks at an upper horizontal level for baroclinic wave flows in a rotating fluid subject to internal heating and cooling at the outer sidewall, for constant heating rate and different rotation speeds Ω (from the polar β-plane experiments of [154]). Low rotation rate cases (a) and (b) illustrate regular, coherent wave flows that fill the domain, but higher rotation rate cases (c) and (d) show a transition to multiple parallel wave trains and weak zonal jets.

(cf. (5) and (7) above). In addition, for large enough values of β_T it was found (e.g. [22] that baroclinic waves would no longer span the entire annular channel but became confined, at least initially, to a range of radii close to the inner cylinder. Further experimental investigations (e.g. [22,153–155] have shown that this trend continues at even higher values of Ω and β_T until two or more independent baroclinic wave trains are discernible at different radii, associated with the baroclinic zone within the annular channel breaking up into a banded structure.

Some clear examples of this trend are illustrated in Figure 21, which shows streak images at an upper level from a sequence of equilibrated baroclinic wave flows in an open cylinder subject to internal heating and sidewall cooling, taken from the experiments of [154]. The electrical internal heating was concentrated close to the centre of the cylinder, leading to a broad baroclinic zone spanning the entire radius of the tank (see [154] for more details). The four examples in Figure 21 illustrate changes in flow structure as Ω was increased while keeping the heating rate constant. Relatively low rotation rate cases (a) and (b) are dominated by large, domain-filling baroclinic waves that propagate steadily around the apparatus. At a higher rotation speed, however, as in (c),

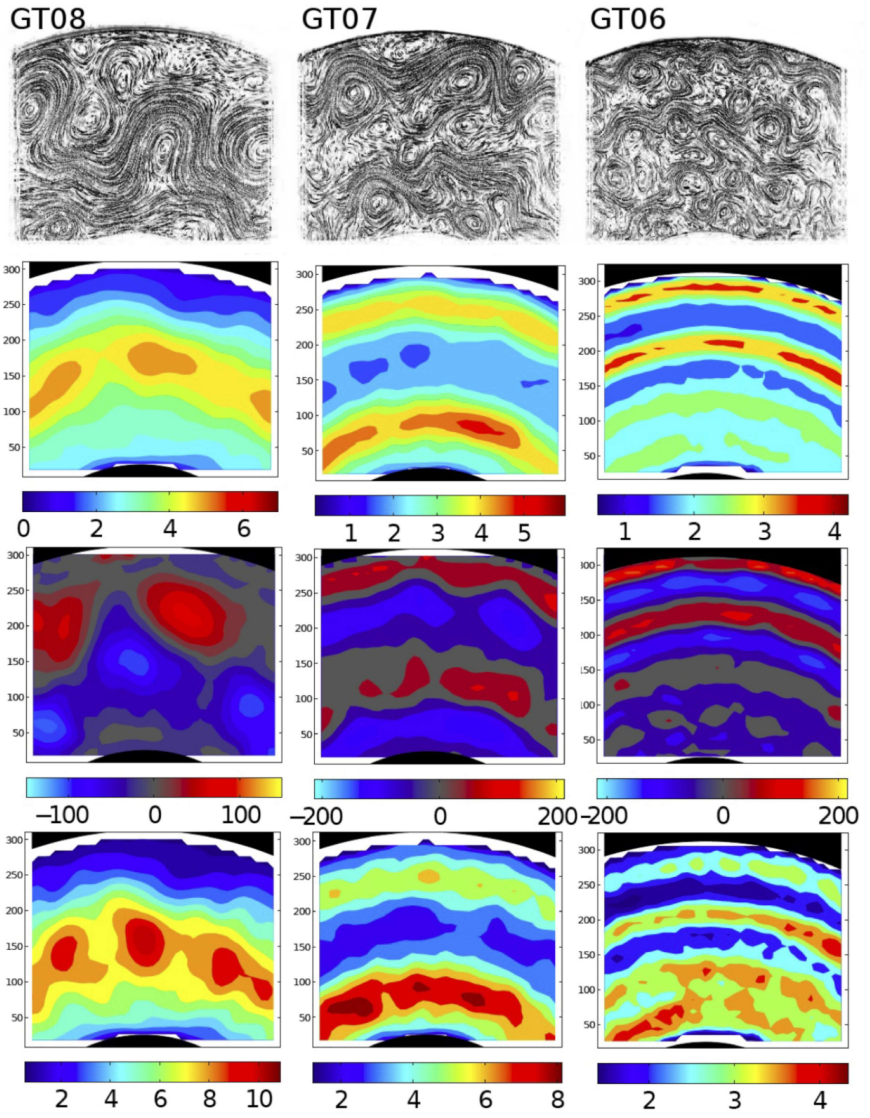


Figure 22. Various fields and streak images for baroclinic wave flows in a rotating fluid subject to sidewall heating and cooling, for three different rotation speeds Ω (from the topographic β-plane experiments of [55]). Experiments correspond to $(\mathcal{T},\Theta,\beta_2)$ values of $(9.6\times10^{10},0.061,11.75)$ [GT08], $(2.4\times10^{11},0.024,43.1)$ [GT07] and $(6.1\times10^{11},0.01,200)$ [GT06]. Top row shows streak images of tracer particle tracks at an upper horizontal level, the second row shows time-averaged fluid speeds (in mm s^{-1}), the third row time-averaged vorticity fields (in s^{-1}) and the fourth time-averaged eddy kinetic energy (in mm^2 s^{-2}). Figures reproduced from [55]; © American Meteorological Society. Used with permission.

show a higher wavenumber wave train that no longer fills the tank but is confined to a narrower band of radii, with the hint of a second wave train with a wavenumber $m\simeq 4$ nearer the centre of the tank. This becomes more clearly apparent in (d), which is taken at an even higher rotation speed experiment, within which $m\simeq 6$ is apparent near the outer cylinder but $m\simeq 3-4$ is evident

nearer the centre of the tank. This trend was found by [154] to continue to even higher rotation speeds (and weaker heating rates), such that up to three separate wave trains were discernible at three different radii. The results of [153] were broadly consistent with a Rhines scaling for the width of the baroclinic zones in their multiple wave-train regimes, and they also showed some evidence of eddies appearing at scales larger than the Rhines scale, L_R, consistent with upscale energy transfers penetrating to scales larger than L_R. In the presence of a topographic β-effect, spectral transfers of kinetic energy were found [155] to strengthen the azimuthally-symmetric jet-like flows, whereas with flat topography the transfers of kinetic energy were simply upscale to lower azimuthal wavenumbers. This indicates the importance of β-effects in favouring spectrally non-local transfers of kinetic energy into zonal jets.

More recently, Smith et al. [55] have run a series of experiments in a relatively large thermally-driven annulus experiment at the Australian National University of nearly 1 m in diameter and with a channel width of 28.75 cm. A conically-sloping bottom was used, together with a free upper surface, a mean fluid depth of 12 cm, and a range of experiments were run that explored well into the multiple wave-train regime. The results of carrying out experiments on a larger scale than hitherto were to produce flows in which the effects of viscous dissipation were significantly reduced, since horizontal wavelengths even within the multiple wave-train regime were of order 10 cm or longer, although Ekman numbers were not substantially smaller than in the smaller tanks used in the earlier studies referenced above.

Their results, however, do show some interesting advances on some of the previous studies in terms of illustrating banded jet-like features. Figure 22 shows some representative examples from their experiments in the form of streak images of upper level flows and time-averaged fields of zonal flow speeds, vorticity and eddy kinetic energy at three different rotation rates, keeping the temperature contrast across the annular channel fixed at $\Delta T \simeq 20$ K. Around a quarter of the tank could be visualized and measured at a time and the fields in Figure 22 shows such a section stretching from the inner cylinder (at the bottom of each frame) to the outer cylinder (at the top). Although instantaneous snapshots indicated highly chaotic and meandering zonal flows, the first column presents a flow with just one or two independent baroclinic jets, the second shows at least two substantial prograde jets and wave trains and the third column illustrates a flow with 3-4 separate wave trains and prograde jets. As Ω is increased, the intensity of the meandering jets weakens as the number of jets increases, but the banded nature of the flow becomes steadily more apparent.

Figure 23 shows an example of the clear anti-correlation between the zonal mean multiple jet flow and the pattern of horizontal Reynolds stress divergence. This clearly indicates that the banded pattern of zonal flows arises in association with a strong eddy-zonal flow interaction on similar scales, with eddies tending to reinforce the multiple jet pattern and sustain it (in the zonal mean) against dissipation and other effects. The resulting jet separation was also found to scale fairly clearly with a Rhines scale, based either on the rms horizontal velocity or on the zonal mean thermal wind scale, such that $L_{jet} \sim 5 - 8 L_R$.

A series of works by [65,142,143] explored a somewhat different baroclinic forcing in a domain including the pole, on a polar β-plane in a tank of 1.1 m in diameter. The flow is created by a coastal current of fresh water which flows along the wall of the tank on top of the layer of saline water. While the upper layer coastal current flows in the cyclonic (prograde) direction, the lower layer acquires anticyclonic (retrograde) rotation. The vertical shear in combination with the density difference is the recipe for a baroclinic instability. Baroclinic instability continuously creates meanders and filaments which protrude in a meridional direction and eventually fill the entire domain (Figure 24). The velocity in both layers was measured by a combination of altimetric, AIV, and thickness measurements, OTV. Apart from the coastal jet at the wall, at least two zonal jets can be easily identified in the interior of the domain, the direction of the flow of the

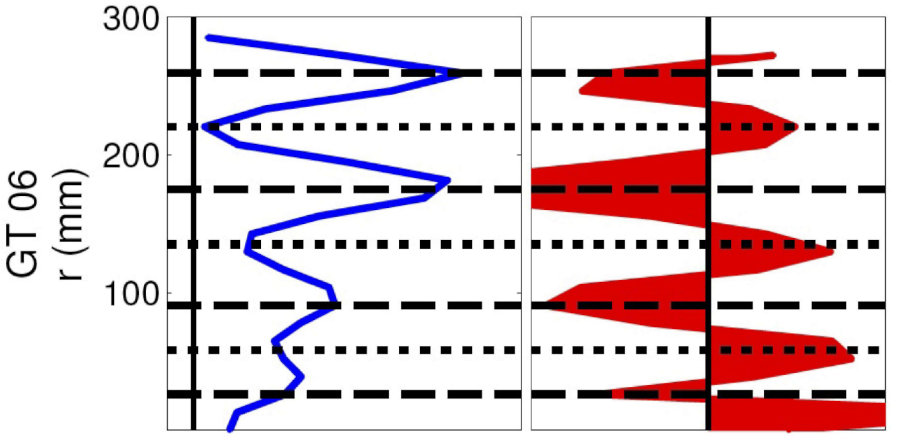


Figure 23. Radial profiles of azimuthal flow velocity (blue line) and Reynolds stress divergence $1/r\partial/\partial r(r\overline{u'v'})$ (red shaded profile) for experiment GT06 $[(\mathscr{T},\Theta,\beta_2) = (6.1 \times 10^{11}, 0.01, 200)]$, reproduced from [55]; ©American Meteorological Society. Used with permission.

barotropic component being opposite to that of the baroclinic component. The computations of the Reynolds stress forcing shows that the jets are clearly eddy-driven.

Measurements of the meridional wavelength, L_{jet} showed its linear dependence on the baroclinic radius of deformation, $L_{jet} = 4.4L_d$ and, at the same time, on the Rhines scale, $L_{jet} = 0.5L_R$. This indicates an interesting relationship between the rms velocity and the main control parameters of the flow, $U_{rms} \propto \beta L_d^2$.

7. Discussion

In the foregoing sections we have surveyed a wide range of laboratory investigations that have explored different aspects of how zonal jets can form through the action of nonlinear waves and eddies. The results of all the experiments are largely consistent with the general theory summarised in Section 3 but each experiment emphasises different components of the generalised Reynolds stress or Eliassen–Palm flux, depending upon the basic background state and experimental conditions. The range of experiments reviewed seem to indicate the following as requirements for generating substantial zonal motions from initial eddy fields in a forced-dissipative fluid flow:

- A process to generate intense eddying motions to provide a means of stirring and mixing on a scale comparable to or smaller than that of the resulting zonal motion;
- The presence of a "planetary vorticity gradient" and/or stratification to ensure that any eddies generated may be adequately wave-like and dispersive;
- A source of dissipation or "friction" on both large- and small scales, necessary to allow the flow to reach a stable equilibrium.

The first requirement is common to all of the experiments discussed. Furthermore, rotating flows that form significant eddy-driven jets generally require large, rapidly rotating domains with a strong β-effect, regardless of how eddies are generated. The β-effect is generally imposed by radially-varying topography which may be achieved either through a sloping bottom or lid or

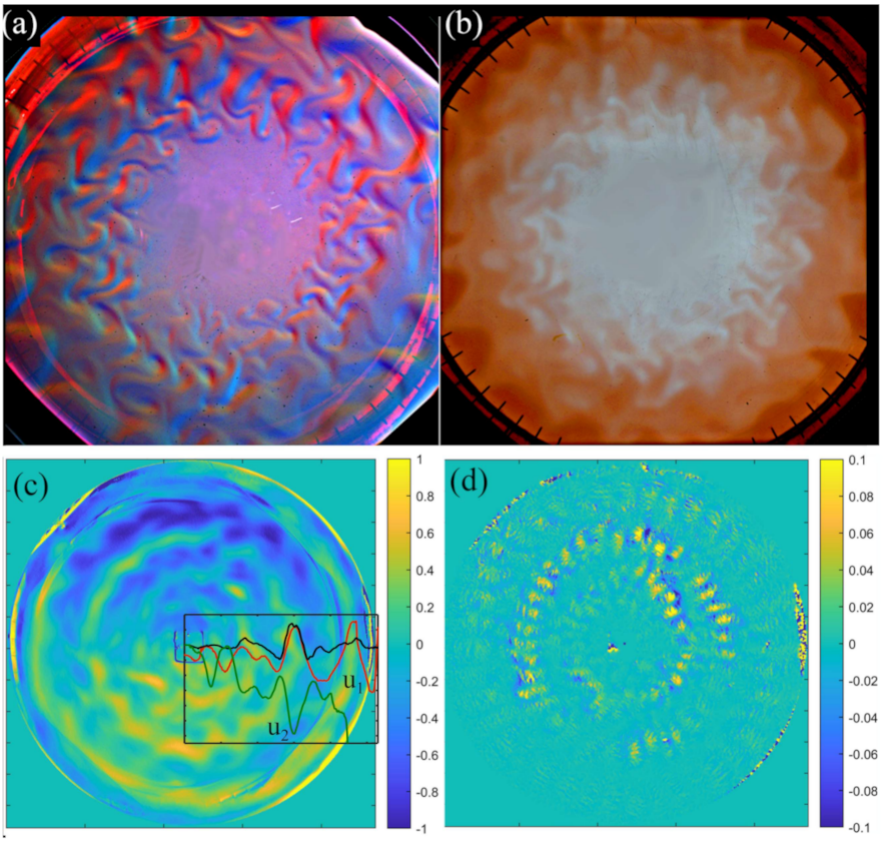


Figure 24. Baroclinically unstable flow on the polar β-plane: (a, b) Typical images of the flow obtained by AIV and OTV, respectively; (c) Barotropic azimuthal velocity measured by AIV (upper layer velocity); (d) Azimuthal component of the Reynolds stress forcing in the upper layer. Color scales show the velocity in cm s^{-1} and the forcing in cm s^{-2}. Insert in (c) shows radial profiles of the upper and lower layer velocity, u_1 and u_2, and the azimuthal component of the Reynolds stress in the upper layer (black line, in arbitrary units). Figure adapted from [65].

through a centrifugally-deformed free surface. What distinguishes different types of experiment are mainly (a) in the respective roles of background rotation and stratification in determining the basic state and (b) in the way eddies or waves are generated and maintained, as discussed in next section.

7.1. *Diversity of experiments*

Much of the diversity in the experiments reported in the literature, however, derives from the eddy forcing mechanism used to energise the flow. The choice in each case largely comes from the various different planetary applications that motivate each study and, as discussed in Sections 5 and 6, may use either spatially localised or uniformly global forcing. Localised forcing is of particular interest when investigating natural flows, where the turbulence intensity is far from homogeneous in space. This can be especially significant for understanding circulation on a planetary scale which is typically non-homogeneous and anisotropic. On the other hand,

global forcing aims at studying how non-homogeneity and anisotropy may *spontaneously* emerge from homogeneous, isotropic forcing, a situation likely relevant to globally convecting planetary interiors and atmospheres.

Experiments also differ in their approach to the excitation of waves and eddies, and typically fall into one of two categories, either using fixed mechanical forcing e.g. with arrays of mass sources and sinks, or by forming basic states that spontaneously develop eddies through natural instabilities. Both approaches have both advantages and disadvantages. Natural instability forcing is in many respects more realistic when compared with processes in atmospheres, oceans or planetary interiors. But such instabilities are difficult to control experimentally and the results are consequently often difficult to interpret. Fixed mechanical forcing on the other hand is easier to control and maintain in terms of amplitude, scale and location, which can facilitate the quantitative interpretation of experimental results. But this approach is arguably less realistic compared with natural systems. So in practice both approaches have a role to play in advancing our understanding of zonal jet formation.

7.2. *Applications*

Experimental studies have been motivated by a variety of different applications to jet-like phenomena in planetary atmospheres, oceans and interiors. In many cases, experiments have enabled the elucidation of how various flow properties depend on particular parameters of the system. In stratified flows, for example, experiments have been able to verify the dependence of the strength of rectified zonal flow on wave amplitude and propagation velocity, and demonstrate the validity of a wave forcing mechanism to explain the quasi-biennial oscillation (QBO), corresponding to a nearly periodic reversal of Earth's equatorial stratospheric winds between easterlies and westerlies [80,89].

In rotating flows, experiments have been able to demonstratethe key role of Rossby waves in the emergence and nonlinear saturation of jets, how the length scale of zonal jets is associated with the Rhines scale, at least under some conditions, and have confirmed many of the properties of the zonostrophic regime previously identified only in idealised models. Here, applications are focused towards Earth's oceans and gas giants' atmospheres and different application-driven questions motivated different experimental set-ups. For instance, localised forcing along the wall of the tank is relevant to coastal currents in the ocean (Sections 5.3), but not to the atmospheres of gas giants, where global scale forcing, unperturbed by topography, is more realistic (Sections 6.3, 6.4 and 6.5).

The distinction between deep and shallow jets has been controversial for many years in the context of the atmospheres and interiors of the gas giant planets. By exploring different experimental configurations, experiments have played an important role in clarifying the similarities and differences between such shallow and deep flows, confirming the rotational constraints that cause jet flows to align themselves along the direction parallel to the rotation axis; a property that has recently received observational support in the gravity field measurements from the Juno mission [10].

7.3. *Key outstanding challenges*

Advances in the capabilities of metrology techniques in the laboratory have ensured that experimental analogues continue to provide new insights and discoveries concerning the nature of zonal jets in turbulent flows. But while experiments have proved their worth as an avenue for such discoveries and insights which complements more traditional approaches to studying natural phenomena on geophysical scales, many challenges and outstanding questions remain for future investigation. Key challenges that deserve further attention include the following.

- The nature of, and distinction between, the friction-dominated and zonostrophic regimes of rotating, geostrophic turbulence continues to pose challenges for both models and experiments alike. Access in experiments to zonostrophic conditions has been demonstrated for values of the zonostrophic index up to around $R_\beta^s \simeq 3$. But accessing more extreme conditions, similar to those on the gas giant planets, is very difficult, as discussed in Section 6.3. It would be desirable, for example, to achieve a greater separation of scales between the eddy forcing and the zonal jets, but this would probably require fast rotating experiments on a much bigger scale than hitherto.
- Exploring the nature of the energy cascades that result in zonated flows also poses both theoretical and experimental challenges. Upscale energy transfer appears to be a necessary feature of zonal flow generation. But whether a more conventional homogeneous, isotropic, inverse energy cascade is necessary to the process is not yet clear. Exploration of this issue experimentally would again require maximising the scale separation between forcing and zonated scales, but expanding this substantially is difficult in practice.
- A key issue for planetary scale patterns of multiple zonal jets is how they may evolve over long timescales. Numerical simulations of planetary configurations suggest that jets may drift in latitude and the possibility of transitions and bifurcations between different kinds of jet regime may also be possible. But such investigations require very long duration experiments which will remain out of reach for high resolution numerical simulations for the foreseeable future. Experiments have an important role to play here but running experiments for a sufficiently long time relative to internal dynamical timescales is very challenging if very large experimental setups are needed to access extreme parameter regimes. Larger experimental setups with a significant scale separation between zonal jets and the size of the experimental domain also need to be developed.
- Feedback from large scales onto the small scale eddy processes can now be studied in detail, thanks to improvements in measurement techniques and the ability of some experimental configurations to run for long periods. But measurements may need to be able to keep track of the time evolution of both large scale features (evolving slowly) and very small scale waves and turbulence (evolving rapidly) to address some of the key issues.
- Interactions between highly three-dimensional eddies and deep zonal flows are still incompletely understood, though such interactions may underlie some of the complexities observed in gas giant planet atmospheres. The role of different kinds of dissipative process is another related issue where a knowledge of complex 3D structures may be required. Exploring these issues in experiments will require some ingenuity in the design of suitable configurations.
- A further open issue is the extent to which the range of rotating turbulent regimes between friction dominated and zonostrophic flows is sufficient to account for the range of circulation regimes encountered in planetary atmospheres and oceans. The Earth's atmosphere, for example, does not seem to fit comfortably into either category and exhibits an energy spectrum with some characteristic features (cf [156]) that seem anomalous compared with regimes identified from barotropic model simulations. A novel regime of rotationally controlled turbulence has been proposed [157], based on idealised model calculations, which appears to account for some of these anomalous characteristics. But this regime is yet to receive confirmation from any experimental study and its properties need further investigation.

In conclusion, therefore, the past 50 years have shown that laboratory experiments have played a clear and important role in evaluating theories and models of zonal jet formation by interactions with waves and eddies, as well as their long-term, nonlinear evolution. Further advances in measurement techniques seem likely to ensure that laboratory experiments will continue to play an important role alongside other approaches, particularly since they naturally resolve all necessary time and length scales and can be run in a systematic way over long timescales. But certain flow properties will continue to remain beyond the capabilities of direct or indirect experimental measurements, making complementary numerical simulations a highly desirable component of such investigations. For instance, modelling tools enable researchers to test the sensitivity of experimental results to some technical limitations such as the boundary conditions, e.g. to spherical geometry in place of cylindrical, as well as to variations in the nature and amplitude of forcing and dissipation.

Acknowledgements

The authors are grateful for the constructive reviews provided by two anonymous reviewers.

Declaration of interests

The authors do not work for, advise, own shares in, or receive funds from any organization that could benefit from this article, and have declared no affiliations other than their research organizations.

References

[1] P. B. Rhines, "Jets", *Chaos* **4** (1994), pp. 313–339.
[2] P. C. Cornillon, E. Firing, A. F. Thompson, L. M. Ivanov, I. Kamenkovich, C. E. Buckingham and Y. D. Afanasyev, "Oceans", in *Zonal Jets* (B. Galperin and P. L. Read, eds.), Cambridge University Press, 2019, pp. 46–71.
[3] B. Galperin and P. L. Read, *Zonal jets: Phenomenology, genesis, and physics*, Cambridge University Press, 2019.
[4] G. K. Vallis, *Atmospheric and Oceanic Fluid Dynamics - Fundamentals and Large-Scale Circulation*, 2nd edition, Cambridge University Press, 2017.
[5] Y. D. Afanasyev, "High-Latitude Westward Jets in the Earth's Outer Core Due to Small-Scale Convection", *Geophys. Res. Lett.* **45** (2018), no. 15, pp. 7454–7461.
[6] K. Aujogue, A. Pothérat, B. Sreenivasan and F. Debray, "Experimental study of the convection in a rotating tangent cylinder", *J. Fluid Mech.* **843** (2018), pp. 355–381.
[7] J. Aurnou, S. Andreadis, L. Zhu and P. Olson, "Experiments on convection in Earth's core tangent cylinder", *Earth Planet. Sci. Lett.* **212** (2003), no. 1-2, pp. 119–134.
[8] E. Galanti, Y. Kaspi, Y. Miguel, T. Guillot, D. Durante, P. Racioppa and L. Iess, "Saturn's deep atmospheric flows revealed by the Cassini grand finale gravity measurements", *Geophys. Res. Lett.* **46** (2019), no. 2, pp. 616–624.
[9] H. Cao, J. Bloxham, R. S. Park, B. Militzer, R. K. Yadav, L. Kulowski, D. J. Stevenson and S. J. Bolton, "Strong resemblance between surface and deep zonal winds inside Jupiter revealed by high-degree gravity moments", *Astrophys. J.* **959** (2023), no. 2, p. 78.
[10] Y. Kaspi, E. Galanti, R. S. Park, et al., "Observational evidence for cylindrically oriented zonal flows on Jupiter", *Nat. Astron.* **7** (2023), no. 12, pp. 1463–1472.
[11] C. Zimmer, K. K. Khurana and M. G. Kivelson, "Subsurface oceans on Europa and Callisto: Constraints from Galileo magnetometer observations", *Icarus* **147** (2000), no. 2, pp. 329–347.
[12] K. M. Soderlund, "Ocean dynamics of outer solar system satellites", *Geophys. Res. Lett.* **46** (2019), no. 15, pp. 8700–8710.
[13] S. Bire, W. Kang, A. Ramadhan, J.-M. Campin and J. Marshall, "Exploring ocean circulation on icy moons heated from below", *J. Geophys. Res. Planets* **127** (2022), no. 3, article no. e2021JE007025.
[14] S. Cabanes, T. Gastine and A. Fournier, "Zonostrophic turbulence in the subsurface oceans of the Jovian and Saturnian moons", *Icarus* **415** (2024), article no. 116047.
[15] A. Colin de Verdiere, "Mean flow generation by topographic Rossby waves", *J. Fluid Mech.* **94** (1979), no. 1, pp. 39–64.

[16] M. Heimpel and J. Aurnou, "Turbulent convection in rapidly rotating spherical shells: A model for equatorial and high latitude jets on Jupiter and Saturn", *Icarus* **187** (2007), pp. 540–557.

[17] E. R. Weeks, Y. Tian, J. S. Urbach, K. Ide, H. L. Swinney and M. Ghil, "Transitions between blocked and zonal flows in a rotating annulus with topography", *Science* **278** (1997), no. 5343, pp. 1598–1601.

[18] J. Herrmann and F. H. Busse, "Stationary and time dependent convection in the rotating cylindrical annulus with modulated height", *Phys. Fluids* **10** (1998), no. 7, pp. 1611–1620.

[19] M. A. Calkins, J. Noir, J. D. Eldredge and J. M. Aurnou, "The effects of boundary topography on convection in Earth's core", *Geophys. J. Int.* **189** (2012), no. 2, pp. 799–814.

[20] U. Harlander, J. Wenzel, K. Alexandrov, Y. Wang and C. Egbers, "Simultaneous PIV and thermography measurements of partially blocked flow in a differentially heated rotating annulus", *Exp. Fluids* **52** (2012), pp. 1077–1087.

[21] A. P. Ingersoll and D. Pollard, "Motion in the atmospheres and interiors of Jupiter and Saturn: scale analysis, anelastic equations, barotropic stability criterion", *Icarus* **52** (1982), pp. 62–80.

[22] P. J. Mason, "Baroclinic waves in a container with sloping endwalls", *Philos. Trans. R. Soc. Lond., Ser. A* **A278** (1975), pp. 397–445.

[23] X. Q. He, A. D. Bragg, Y. L. Xiong and P. Fischer, "Turbulence and heat transfer on a rotating, heated half soap bubble", *J. Fluid Mech.* **924** (2021), article no. A19.

[24] L. Armi, "Hydraulic control of zonal currents on a β-plane", *J. Fluid Mech.* **201** (1989), pp. 357–377.

[25] B. Galperin, S. Sukoriansky, N. Dikovskaya, P. L. Read, Y. H. Yamazaki and R. Wordsworth, "Anisotropic turbulence and zonal jets in rotating flows with a β-effect", *Nonlinear Process. Geophys.* **13** (2006), no. 1, pp. 83–98.

[26] S. Sukoriansky, N. Dikovskaya and B. Galperin, "On the Arrest of Inverse Energy Cascade and the Rhines Scale", *J. Atmos. Sci.* **64** (2007), pp. 3312–3327.

[27] P. B. Rhines, "Waves and turbulence on a beta-plane", *J. Fluid Mech.* **69** (1975), pp. 417–443.

[28] G. K. Vallis and M. E. Maltrud, "Generation of Mean Flows and Jets on a Beta Plane and over Topography", *J. Phys. Oceanogr.* **23** (1993), no. 7, pp. 1346–1362.

[29] J. O'Donnell and P. F. Linden, "Free-surface effects on the spin-up of fluid in a rotating cylinder", *J. Fluid Mech.* **232** (1991), pp. 439–453.

[30] J. M. Aurnou, V. Bertin, A. M. Grannan, S. Horn and T. Vogt, "Rotating thermal convection in liquid gallium: multi-modal flow, absent steady columns", *J. Fluid Mech.* **846** (2018), pp. 846–876.

[31] B. Galperin, S. Sukoriansky and N. Dikovskaya, "Geophysical flows with anisotropic turbulence and dispersive waves: flows with a β-effect", *Ocean Dynamics* **60** (2010), pp. 427–441.

[32] A. E. Gill, *Atmosphere-Ocean Dynamics*, Academic Press Inc., 1982.

[33] D. Lemasquerier, B. Favier and M. Le Bars, "Zonal jets experiments in the gas giants' zonostrophic regime", *Icarus* **390** (2023), article no. 115292.

[34] T. L. Lonner, A. Aggarwal and J. M. Aurnou, "Planetary core-style rotating convective flows in paraboloidal laboratory experiments", *J. Geophys. Res. Planets* **127** (2022), no. 10, article no. e2022JE007356.

[35] Y. D. Afanasyev and T. E. Dowling, "Evolution of Jupiter-Style Critical Latitudes: Initial Laboratory Altimetry Results", *J. Geophys. Res. Planets* **127** (2022), no. 5, article no. e2021JE007048.

[36] J. Sommeria, S. D. Meyers and H. L. Swinney, "Laboratory model of a planetary eastward jet", *Nature* **337** (1989), pp. 58–61.

[37] M. F. Jansen, W. Kang, E. S. Kite and Y. Zeng, "Energetic constraints on ocean circulations of icy ocean worlds", *Planet. Sci. J.* **4** (2023), no. 6, article no. 117.

[38] S. Cabanes, J. Aurnou, B. Favier and M. Le Bars, "A laboratory model for deep-seated jets on the gas giants", *Nat. Phys.* **13** (2017), no. 4, pp. 387–390.

[39] D. Lemasquerier, B. Favier and M. Le Bars, "Zonal jets at the laboratory scale: hysteresis and Rossby waves resonance", *J. Fluid Mech.* **910** (2021), article no. A18.

[40] Y. Zhang and Y. Afanasyev, "Rotating thermal convection: surface turbulence observed with altimetry and thermal radiometry", *Geophys. Astrophys. Fluid Dyn.* **115** (2021), no. 5-6, pp. 499–522.

[41] J. A. Abbate and J. M. Aurnou, "Rotating convective turbulence in moderate to high Prandtl number fluids", *Geophys. Astrophys. Fluid Dyn.* **117** (2023), pp. 397–436.

[42] S. Su, D. Cébron, H.-C. Nataf, P. Cardin, J. Vidal, M. Solazzo and Y. Do, "Acoustic spectra of a gas-filled rotating spheroid", *Eur. J. Mech. B Fluids* **84** (2020), pp. 302–310.

[43] T. Vogt, S. Horn and J. M. Aurnou, "Oscillatory thermal–inertial flows in liquid metal rotating convection", *J. Fluid Mech.* **911** (2021), A5.

[44] M. Lesieur, *Turbulence in Fluids*, 3rd edition, Kluwer Academic Publishers, 1997.

[45] D. G. Andrews and M. McIntyre, "Planetary waves in horizontal and vertical shear: the generalized Eliassen–Palm relation and the mean zonal acceleration", *J. Atmos. Sci.* **33** (1976), pp. 2031–2048.

[46] D. G. Andrews and M. McIntyre, "Generalized Eliassen–Palm and Charney–Drazin Theorems for Waves on Axisymmetric Mean Flows in Compressible Atmospheres", *J. Atmos. Sci.* **35** (1978), pp. 175–185.

[47] V. P. Starr, *Physics of Negative Viscosity Phenomena*, McGraw Hill: New York, 1968.

[48] P. S. Marcus and C. Lee, "A model for eastward and westward jets in laboratory experiments and planetary atmospheres", *Phys. Fluids* **10** (1998), no. 6, pp. 1474–1489.
[49] J. Aubert, S. Jung and H. L. Swinney, "Observations of zonal flow created by potential vorticity mixing in a rotating fluid", *Geophys. Res. Lett.* **29** (2002), no. 18, pp. 23-1–23-4.
[50] F. H. Busse and C. R. Carrigan, "Laboratory simulation of thermal convection in rotating planets and stars", *Science* **191** (1976), no. 4222, pp. 81–83.
[51] J. A. Whitehead, "Mean flow generated by circulation on a β-plane: An analogy with the moving flame experiment", *Tellus* **27** (1975), pp. 358–364.
[52] M. J. Burin, K. J. Caspary, E. M. Edlund, et al., "Turbulence and jet-driven zonal flows: Secondary circulation in rotating fluids due to asymmetric forcing", *Phys. Rev. E* **99** (2019), no. 2, article no. 023108.
[53] P. L. Read, Y. H. Yamazaki, S. R. Lewis, et al., "Dynamics of convectively driven banded jets in the laboratory", *J. Atmos. Sci.* **64** (2007), pp. 4035–4056.
[54] Y. D. Afanasyev, S. O'Leary, P. B. Rhines and E. G. Lindahl, "On the origin of jets in the ocean", *Geophys. Astrophys. Fluid Dyn.* **106** (2012), pp. 113–137.
[55] C. A. Smith, K. G. Speer and R. W. Griffiths, "Multiple Zonal Jets in a Differentially Heated Rotating Annulus", *J. Phys. Oceanogr.* **44** (2014), pp. 2273–2291.
[56] B. Galperin, J. Hoemann, S. Espa and G. Di Nitto, "Anisotropic turbulence and Rossby waves in an easterly jet: An experimental study", *Geophys. Res. Lett.* **41** (2014), no. 17, pp. 6237–6243.
[57] R. A. Plumb and A. D. McEwan, "The instability of a forced standing wave in a viscous stratified fluid: A laboratory analogue of the quasi-biennial oscillation", *J. Atmos. Sci.* **35** (1978), pp. 1827–1839.
[58] M. Le Bars, D. Cébron and P. Le Gal, "Flows driven by libration, precession, and tides", *Ann. Rev. Fluid Mech.* **47** (2015), pp. 163–193.
[59] M. Raffel, C. E. Willert, F. Scarano, C. J. Kähler, S. T. Wereley and J. Kompenhans, *Particle image velocimetry: A practical guide*, Springer, 2018.
[60] W. Thielicke and R. Sonntag, "Particle Image Velocimetry for MATLAB: Accuracy and enhanced algorithms in PIVlab", *J. Open Res. Softw.* **9** (2021), no. 1, article no. 12.
[61] D. Lemasquerier, *Experimental and numerical study of Jupiter's dynamics: jets, vortices and zonostrophic turbulence*, PhD thesis, Aix-Marseille Université, Marseille, France, 2021.
[62] P. B. Rhines, E. G. Lindahl and A. J. Mendez, "Optical altimetry: A new method for observing rotating fluids with application to Rossby waves on a polar beta-plane", *J. Fluid Mech.* **572** (2007), pp. 389–412.
[63] Y. D. Afanasyev, P. B. Rhines and E. G. Lindahl, "Velocity and potential vorticity fields measured by altimetric imaging velocimetry in the rotating fluid", *Exp. Fluids* **47** (2009), pp. 913–926.
[64] Y. D. Afanasyev, "Altimetry in a GFD laboratory and flows on the polar β-plane", in *Modelling Atmospheric and Oceanic Flows: Insights from Laboratory Experiments and Numerical Simulations* (T. von Larcher and P. Williams, eds.), American Geophysical Union, 2014, pp. 101–117.
[65] A. M. Matulka and Y. D. Afanasyev, "Zonal jets in equilibrating baroclinic instability on the polar beta-plane: Experiments with altimetry", *J. Geophys. Res. Oceans* **120** (2015), no. 9, pp. 6130–6144.
[66] J. E. Moscoso et al., "Low-cost table-top experiments for teaching multi-scale geophysical fluid dynamics", *Front. Mar. Sci.* **10** (2023), article no. 1192056.
[67] M. Stern, "The Moving Flame experiment", *Tellus* **11** (1959), no. 2, pp. 175–179.
[68] G. Schubert and J. A. Whitehead, "Moving Flame Experiment with Liquid Mercury : Possible Implications for the Venus Atmosphere", *Science* **163** (1969), no. 3862, pp. 71–72.
[69] J. A. Whitehead, "Observations of rapid mean flow produced in mercury by a moving heater", *Geophys. Astrophys. Fluid Dyn.* **3** (1972), no. 1, pp. 161–180.
[70] H. A. Douglas, P. J. Mason and E. J. Hinch, "Motion due to a moving internal heat source", *J. Fluid Mech.* **54** (1972), no. 3, pp. 469–480.
[71] P. J. Gierasch, R. M. Goody, R. E. Young, et al., "The general circulation of the Venus atmosphere: an assessment", in *Venus II: Geology, Geophysics, Atmosphere and Solar Wind Environment* (S. W. Bougher, D. M. Hunten and R. J. Philips, eds.), University of Arizona Press, 1997, pp. 459–502.
[72] S. S. Limaye and M. Rengel, "Atmospheric circulation and dynamics", in *Towards Understanding the Climate of Venus: Applications of Terrestrial Models to Our Sister Planet* (L. Bengtsson, R.-M. Bonnet, D. Grinspoon, S. Koumoutsaris, S. Lebonnois and D. Titov, eds.), Springer, 2013, pp. 55–70.
[73] A. D. McEwan, R. O. R. Y. Thompson and R. A. Plumb, "Mean flows driven by weak eddies in rotating systems", *J. Fluid Mech.* **99** (1980), no. 3, pp. 656–672.
[74] H. M. Stommel, "Is the South Pacific helium-3 plume dynamically active?", *Earth Planet. Sci. Lett.* **61** (1982), pp. 63–67.
[75] M. K. Davey and P. D. Killworth, "Flows produced by discrete sources of buoyancy", *J. Phys. Oceanogr.* **19** (1989), pp. 1279–1290.

[76] Y. D. Afanasyev and L. M. Ivanov, "β-Plume mechanism of zonal jet creation by a spatially localized forcing", in *Zonal jets: Phenomenology, genesis, and physics* (B. Galperin and P. L. Read, eds.), Cambridge University Press, 2019, pp. 266–283.

[77] Y. Sui and Y. D. Afanasyev, "Buoyancy storms in a zonal stream on the polar beta-plane: experiments with altimetry", *Phys. Fluids* **25** (2013), article no. 066604.

[78] A. G. Slavin and Y. D. Afanasyev, "Multiple zonal jets on the polar beta plane", *Phys. Fluids* **24** (2012), pp. 113–137.

[79] T. E. Dowling, "Jets in planetary atmospheres", *Oxford Research Encyclopedia of Planetary Science* (2019).

[80] B. Semin, G. Facchini, F. Pétrélis and S. Fauve, "Generation of a mean flow by an internal wave", *Phys. Fluids* **28** (2016), article no. 096601.

[81] M. P. Baldwin, L. J. Gray, T. J. Dunkerton, et al., "The Quasi-Biennial Oscillation", *Rev. Geophys.* **39** (2001), pp. 179–229.

[82] R. S. Lindzen and J. R. Holton, "A theory of the quasi-biennial oscillation", *J. Atmos. Sci.* **25** (1968), pp. 1095–1107.

[83] J. R. Holton and R. S. Lindzen, "An updated theory for the quasi-biennial cycle of the tropical stratosphere", *J. Atmos. Sci.* **29** (1972), pp. 1076–1080.

[84] S. B. Fels and R. Lindzen, "The interaction of thermally excited gravity waves with mean flows", *Geophys. Fluid Dyn.* **6** (1974), pp. 149–191.

[85] R. A. Plumb, "The interaction of two internal waves with the mean flow: Implications for the theory of the quasi-biennial oscillation", *J. Atmos. Sci.* **34** (1977), pp. 1847–1858.

[86] N. Otobe, S. Sakai, S. Yoden and M. Shiotani, "Visualization and WKB analysis of the internal gravity wave in the QBO experiment", *Nagare: Japan Soc. Fluid Mech.* **17** (1998), no. 3.

[87] G. Bordes, A. Venaille, S. Joubaud, P. Odier and T. Dauxois, "Experimental observation of a strong mean flow induced by internal gravity waves", *Phys. Fluids* **24** (2012), article no. 086602.

[88] B. Semin, N. Garroum, F. Pétrélis and S. Fauve, "Nonlinear saturation of the large scale flow in a laboratory model of the quasibiennial oscillation", *Phys. Rev. Lett.* **121** (2018), p. 134502.

[89] B. Semin and F. Pétrélis, "Quasi-biennial oscillation: laboratory experiments", *Comptes Rendus. Phys.* (2024), pp. 1–25.

[90] M. Le Bars, A. Barik, F. Burmann, D. P. Lathrop, J. Noir, N. Schaeffer and S. A. Triana, "Fluid dynamics experiments for planetary interiors", *Surv. Geophys.* **43** (2022), no. 1, pp. 229–261.

[91] A. Tilgner, "Zonal Wind Driven by Inertial Modes", *Phys. Rev. Lett.* **99** (2007), no. 19, article no. 194501.

[92] J. Noir, D. Brito, K. Aldridge and P. Cardin, "Experimental evidence of inertial waves in a precessing spheroidal cavity", *Geophys. Res. Lett.* **28** (2001), pp. 3785–3788.

[93] J. Noir, P. Cardin, D. Jault and J.-P. Masson, "Experimental evidence of non-linear resonance effects between retrograde precession and the tilt-over mode within a spheroid", *Geophys. J. Int.* **154** (2003), no. 2, pp. 407–416.

[94] F. Burmann and J. Noir, "Experimental study of the flows in a non-axisymmetric ellipsoid under precession", *J. Fluid Mech.* **932** (2022), article no. A24.

[95] Y. Charles, *Flows driven by librations in latitude in triaxial ellipsoids*, PhD thesis, ETH Zurich, Switzerland, 2018.

[96] A. Sauret, D. Cébron, C. Morize and M. Le Bars, "Experimental and numerical study of mean zonal flows generated by librations of a rotating spherical cavity", *J. Fluid Mech.* **662** (2010), pp. 260–268.

[97] J. Noir, M. A. Calkins, M. Lasbleis, J. Cantwell and J. M. Aurnou, "Experimental study of libration-driven zonal flows in a straight cylinder", *Phys. Earth Planet. Inter.* **182** (2010), no. 1-2, pp. 98–106.

[98] A. M. Grannan, M. Le Bars, D. Cébron and J. M. Aurnou, "Experimental study of global-scale turbulence in a librating ellipsoid", *Phys. Fluids* **26** (2014), no. 12, article no. 126601.

[99] D. Lemasquerier, A. M. Grannan, J. Vidal, D. Cébron, B. Favier, M. Le Bars and J. M. Aurnou, "Libration-driven flows in ellipsoidal shells", *J. Geophys. Res. Planets* **122** (2017), no. 9, pp. 1926–1950.

[100] C. Morize, M. Le Bars, P. Le Gal and A. Tilgner, "Experimental Determination of Zonal Winds Driven by Tides", *Phys. Rev. Lett.* **104** (2010), no. 21, p. 214501.

[101] A. M. Grannan, B. Favier, M. Le Bars and J. M. Aurnou, "Tidally forced turbulence in planetary interiors", *Geophys. J. Int.* **208** (2017), no. 3, pp. 1690–1703.

[102] Y. Lin and J. Noir, "Libration-driven inertial waves and mean zonal flows in spherical shells", *Geophys. Astrophys. Fluid Dyn.* **115** (2021), no. 3, pp. 258–279.

[103] S. Espa, G. Di Nitto, B. Galperin, J. Hoemann, G. Lacorata, et al., "Zonal Jets in the Laboratory. Experiments with Electromagnetically Forced Flows", in *Zonal Jets. Phenomenology, Genesis, and Physics*, Cambridge University Press, 2019, pp. 167–177.

[104] J. Sommeria, S. D. Meyers and H. L. Swinney, "Experiments on vortices and Rossby waves in eastward and westward jets", in *Nonlinear Topics in Ocean Physics* (A. R. Osborne, ed.), North-Holland: Amsterdam, 1991, pp. 227–269.

[105] P. L. Read, "Zonal Jet Flows in the Laboratory: An Introduction", in *Zonal Jets: Phenomenology, Genesis, and Physics* (B. Galperin and P. L. Read, eds.), Cambridge University Press, 2019, pp. 119–134.

[106] D. H. Kelley and N. T. Ouellette, "Using particle tracking to measure flow instabilities in an undergraduate laboratory experiment", *Am. J. Phys.* **79** (2011), no. 3, pp. 267–273.
[107] S. Sukoriansky, B. Galperin and N. Dikovskaya, "Universal spectrum of two-dimensional turbulence on a rotating sphere and some basic features of atmospheric circulation on giant planets", *Phys. Rev. Lett.* **89** (2002), no. 12), article no. 124501.
[108] R. K. Scott and D. G. Dritschel, "The structure of zonal jets in geostrophic turbulence", *J. Fluid Mech.* **711** (2012), pp. 576–598.
[109] F. Bouchet, J. Rolland and E. Simonnet, "Rare event algorithm links transitions in turbulent flows with activated nucleations", *Phys. Rev. Lett.* **122** (2019), no. 7, article no. 074502.
[110] E. Simonnet, J. Rolland and F. Bouchet, "Multistability and rare spontaneous transitions in barotropic β-plane turbulence", *J. Atmos. Sci.* **78** (2021), no. 6, pp. 1889–1911.
[111] R. Krishnamurti and L. N. Howard, "Large-scale flow generation in turbulent convection", *Proc. Natl. Acad. Sci. USA* **78** (1981), no. 4, pp. 1981–1985.
[112] E. Brown and G. Ahlers, "Rotations and cessations of the large-scale circulation in turbulent Rayleigh–Bénard convection", *J. Fluid Mech.* **568** (2006), pp. 351–386.
[113] T. Vogt, S. Horn, A. M. Grannan and J. M. Aurnou, "Jump rope vortex in liquid metal convection", *Proc. Natl. Acad. Sci. USA* **115** (2018), no. 50, pp. 12674–12679.
[114] Y. Nakagawa and P. Frenzen, "A theoretical and experimental study of cellular convection in rotating fluids", *Tellus* **7** (1955), no. 1, pp. 2–21.
[115] B. M. Boubnov and G. S. Golitsyn, "Experimental study of convective structures in rotating fluids", *J. Fluid Mech.* **167** (1986), pp. 503–531.
[116] H. J. S. Fernando, R.-R. Chen and D. A. Boyer, "Effects of rotation on convective turbulence", *J. Fluid Mech.* **228** (1991), pp. 513–547.
[117] F. Zhong, R. E. Ecke and V. Steinberg, "Rotating Rayleigh–Bénard convection : asymmetric modes and vortex states", *J. Fluid Mech.* **249** (1993), pp. 135–159.
[118] T. Maxworthy and S. Narimousa, "Unsteady deep convection in a homogeneous rotating fluid, with Oceanographic Applications", *J. Phys. Oceanogr.* **24** (1994), pp. 865–887.
[119] M. J. Coates and G. N. Ivey, "On convective turbulence and the influence of rotation", *Dyn. Atmos. Oceans* **25** (1997), pp. 217–232.
[120] S. Sakai, "The horizontal scale of rotating convection in the geostrophic regime", *J. Fluid Mech.* **333** (1997), pp. 85–95.
[121] J. M. Aurnou, M. A. Calkins, J. S. Cheng, et al., "Rotating convective turbulence in Earth and planetary cores", *Phys. Earth Planet. Inter.* **246** (2015), pp. 52–71.
[122] J. S. Cheng, S. Stellmach, A. Ribeiro, A. Grannan, E. M. King and J. M. Aurnou, "Laboratory-numerical models of rapidly rotating convection in planetary cores", *Geophys. J. Int.* **201** (2015), no. 1, pp. 1–17.
[123] S. Horn and J. M. Aurnou, "Regimes of Coriolis-centrifugal convection", *Phys. Rev. Lett.* **120** (2018), no. 20, article no. 204502.
[124] J. S. Cheng, M. Madonia, A. J. A. Guzmán and R. P. J. Kunnen, "Laboratory exploration of heat transfer regimes in rapidly rotating turbulent convection", *Phys. Rev. Fluids* **5** (2020), no. 11, article no. 113501.
[125] M. Wedi, V. M. Moturi, D. Funfschilling and S. Weiss, "Experimental evidence for the boundary zonal flow in rotating Rayleigh–Bénard convection", *J. Fluid Mech.* **939** (2022), article no. A14.
[126] B. L. N. Kennett, "Radial Earth models revisited", *Geophys. J. Int.* **222** (2020), no. 3, pp. 2189–2204.
[127] P. L. Read, T. N. L. Jacoby, P. H. T. Rogberg, et al., "An experimental study of multiple zonal jet formation in rotating, thermally driven convective flows on a topographic beta-plane", *Phys. Fluids* **27** (2015), article no. 085111.
[128] P. L. Read, J. Sommeria and R. M. B. Young, "Convectively Driven Turbulence, Rossby Waves and Zonal Jets: Experiments on the Coriolis Platform", in *Zonal jets: Phenomenology, genesis, and physics* (B. Galperin and P. L. Read, eds.), Cambridge University Press, 2019, pp. 135–151.
[129] S. A. Condie and P. B. Rhines, "A convective model for the zonal jets in the atmospheres of Jupiter and Saturn", *Nature* **367** (1994), pp. 711–713.
[130] S. A. Condie and P. B. Rhines, "Topographic Hadley cells", *J. Fluid Mech.* **280** (1994), pp. 349–368.
[131] A. Chekhlov, S. A. Orszag, S. Sukoriansky, B. Galperin and I. Staroselsky, "The effect of small-scale forcing on large-scale structures in two-dimensional flows", *Phys. D: Nonlinear Phenom.* **98** (1996), pp. 321–334.
[132] F. H. Busse, "A simple model of convection in the Jovian atmosphere", *Icarus* **29** (1976), no. 2, pp. 255–260.
[133] F. H. Busse, "A model of mean zonal flows in the major planets", *Geophys. Astrophys. Fluid Dyn.* **23** (1983), pp. 153–174.
[134] K. Zhang, "Spiralling columnar convection in rapidly rotating spherical fluid shells", *J. Fluid Mech.* **236** (1992), pp. 535–556.

[135] F. H. Busse and L. L. Hood, "Differential rotation driven by convection in a rapidly rotating annulus", *Geophys. Astrophys. Fluid Dyn.* **21** (1982), no. 1-2, pp. 59–74.

[136] C. R. Carrigan, "An experimental and theoretical investigation of the onset of convection in rotating spherical shells", *J. Fluid Mech.* **126** (1983), pp. 287–305.

[137] F. H. Busse, G. Hartung, M. Jaletzky and G. Sommermann, "Experiments on thermal convection in rotating systems motivated by planetary problems", *Dyn. Atmos. Oceans* **27** (1997), pp. 161–174.

[138] P. Cardin and P. Olson, "Chaotic thermal convection in a rapidly rotating spherical shell: Consequences for flow in the outer core", *Phys. Earth Planet. Inter.* **82** (1994), pp. 235–259.

[139] J.-B. Manneville and P. Olson, "Banded Convection in Rotating Fluid Spheres and the Circulation of the Jovian Atmosphere", *Icarus* **250** (1996), pp. 242–250.

[140] J. Aubert, D. Brito, H.-C. Nataf, P. Cardin and J.-P. Masson, "A systematic experimental study of rapidly rotating spherical convection in water and liquid gallium", *Phys. Earth Planet. Inter.* **128** (2001), no. 1-4, pp. 51–74.

[141] N. Gillet, D. Brito, D. Jault and H.-C. Nataf, "Experimental and numerical studies of convection in a rapidly rotating spherical shell", *J. Fluid Mech.* **580** (2007), pp. 83–121.

[142] A. M. Matulka, Y. Zhang and Y. D. Afanasyev, "Complex environmental β-plane turbulence: laboratory experiments with altimetric imaging velocimetry", *Nonlinear Process. Geophys.* **23** (2016), no. 1, pp. 21–29.

[143] Y. Zhang and Y. D. Afanasyev, "Baroclinic turbulence on the polar beta-plane in the rotating tank: Down to submesoscale", *Ocean Model.* **107** (2016), pp. 151–160.

[144] Y. D. Afanasyev and T. E. Dowling, "Evolution of Jupiter-Style Critical Latitudes: Initial Laboratory Altimetry Results", *J. Geophys. Res. Planets* **127** (2022), no. 5, article no. e2021JE007048.

[145] L. Cope, *The Dynamics of Geophysical and Astrophysical Turbulence*, PhD thesis, University of Cambridge, Cambridge, United Kingdom, 2020.

[146] F. H. Busse and A. C. Or, "Convection in a rotating cylindrical annulus: thermal Rossby waves", *J. Fluid Mech.* **166** (1986), pp. 173–187.

[147] R. Hide and P. J. Mason, "Sloping convection in a rotating fluid", *Adv. Phys.* **24** (1975), pp. 47–99.

[148] P. L. Read, E. P. Pérez, I. M. Moroz and R. M. B. Young, "General circulation of planetary atmospheres: Insights from the rotating annulus and related experiments", in *Modelling Atmospheric and Oceanic flows: insights from laboratory experiments and numerical simulations* (T. v. Larcher and P. D. Williams, eds.), American Geophysical Union, 2014, pp. 7–44.

[149] B. J. Hoskins, "Stability of the Rossby–Haurwitz wave", *Q. J. R. Meteorol. Soc.* **99** (1973), pp. 723–745.

[150] P. G. Baines, "The stability of planetary waves on a sphere", *J. Fluid Mech.* **73** (1976), pp. 193–213.

[151] P. Hignett, A. A. White, R. D. Carter, W. D. N. Jackson and R. M. Small, "A comparison of laboratory measurements and numerical simulations of baroclinic wave flows in a rotating cylindrical annulus", *Q. J. R. Meteorol. Soc.* **111** (1985), pp. 131–154.

[152] A. A. White, "Finite amplitude, steady Rossby waves and mean flows: analytical illustrations of the Charney-Drazin non-acceleration theorem", *Q. J. R. Meteorol. Soc.* **112** (1986), pp. 749–773.

[153] M. E. Bastin and P. L. Read, "A laboratory study of baroclinic waves and turbulence in an internally heated rotating fluid annulus with sloping endwalls", *J. Fluid Mech.* **339** (1997), pp. 173–198.

[154] M. E. Bastin and P. L. Read, "Experiments on the structure of baroclinic waves and zonal jets in an internally heated rotating cylinder of fluid", *Phys. Fluids* **10** (1998), pp. 374–389.

[155] R. D. Wordsworth, P. L. Read and Y. H. Yamazaki, "Turbulence, waves and jets in a differentially heated rotating annulus experiment", *Phys. Fluids* **20** (2008), article no. 126602.

[156] G. D. Nastrom and K. S. Gage, "A climatology of atmospheric wave number spectra of wind and temperature observed by commercial aircraft", *J. Atmos. Sci.* **42** (1985), pp. 950–960.

[157] B. Galperin and S. Sukoriansky, "Quasinormal scale elimination theory of the anisotropic energy spectra of atmospheric and oceanic turbulence", *Phys. Rev. Fluids* **5** (2020), article no. 063803.

ACADÉMIE DES SCIENCES
INSTITUT DE FRANCE

Comptes Rendus. Physique
2024, Vol. 25, Special issue S3, p. 479-507
https://doi.org/10.5802/crphys.196

Review article / *Article de synthèse*

Geophysical and astrophysical fluid dynamics in the laboratory / *Dynamique des fluides géophysiques et astrophysiques au laboratoire*

Geophysical stratified turbulence and mixing in the laboratory

Turbulence et mélange stratifiés géophysiques en laboratoire

Adrien Lefauve [a]

[a] Department of Applied Mathematics and Theoretical Physics, University of Cambridge, United Kingdom
E-mail: lefauve@damtp.cam.ac.uk

Abstract. Geophysical fluid flows that are stably-stratified in density, like most of the ocean, can be strongly turbulent at small scales as a result of shear instabilities. The resulting mixing controls the vertical transport of heat and tracers that are key to large-scale layering and circulation patterns, including those crucial to Earth's climate. However, the physics of sheared stratified turbulence remain poorly understood due to their extraordinary range of scales and spatio-temporal intermittency. This paper reviews a laboratory model, the stratified inclined duct (SID), which encapsulates these fundamental physics and complexity while permitting precise control and measurements, a sweet spot to stimulate fruitful research. We explain how this exchange flow down a modest slope sustains high levels of energy dissipation and mixing while remaining strongly-stratified, thereby accessing the relevant geophysical parameter regime. Emphasising the role of detailed measurements, we highlight key discoveries and unsolved questions around the transition to turbulence, intermittent dynamics and parameterisations of mixing. Dimensional design guidelines show how the optical measurements of the full three-dimensional flow field could be perfected to extrapolate laboratory results to the tantalisingly close regime of the most intense geophysical stratified turbulence.

Résumé. Les écoulements géophysiques de fluides qui sont stablement stratifiés en densité, comme la plupart de l'océan, peuvent être fortement turbulents à petite échelle en raison d'instabilités de cisaillement. Le mélange qui en résulte contrôle le transport vertical de la chaleur et des traceurs qui sont essentiels pour la stratification et la circulation à grande échelle, et donc pour notre climat. Cependant, la physique de la turbulence stratifiée cisaillée reste mal comprise en raison de sa gamme d'échelles extraordinaire et de son intermittence spatio-temporelle. Cet article passe en revue un modèle de laboratoire, le conduit incliné stratifié (SID), qui capture les fondamentaux de cette physique et sa complexité tout en permettant un contrôle et des mesures précis, une combinaison optimale pour stimuler des recherches fructueuses. Nous expliquons comment cet écoulement d'échange le long d'une pente modeste maintient une dissipation turbulente et un mélange élevés tout en restant fortement stratifié, accédant ainsi au régime géophysique pertinent. En mettant l'accent sur le rôle de mesures détaillées, nous soulignons les découvertes clés et les nombreuses questions non résolues autour de la transition vers la turbulence, des dynamiques intermittentes et des paramétrisations du mélange. Le dimensionnement expérimental montre comment perfectionner les mesures optiques tridimensionnel de l'écoulement pour extrapoler ces résultats au régime le plus intense de la turbulence stratifiée géophysique, qui est enfin à portée de main.

Keywords. turbulence, mixing, geophysical, shear, instability, intermittency, ocean, parameterisation.

Mots-clés. turbulence, mélange, géophysique, cisaillement, instabilité, intermittence, océan, paramétrage.

Funding. The author is supported by a NERC Independent Research Fellowship NE/W008971/1. The experimental facilities were funded by an EPSRC Programme Grant EP/K034529/1 (2013-2018) and an ERC Horizon 2020 Grant No 742480 (2018-2023).

Manuscript received 3 May 2024, revised 19 July 2024, accepted 5 August 2024.

1. Introduction

Turbulence in density-stratified environments plays a central role in geophysical and astrophysical fluid dynamics (GAFD) because it enhances the transport of heat, mass and momentum several orders of magnitude above molecular values. This turbulent transport shapes the bulk properties, spatial structure and temporal evolution of stars, planetary cores, atmospheres, oceans and freshwater bodies, which are often physically and/or chemically heterogeneous, and thus layered in density.

This paper focuses on stably-stratified turbulence generated by a large-scale free shear, a canonical GAFD problem alongside, for example, boundary layer turbulence (affected by the presence of a solid boundary) or thermal convection (driven by an unstable stratification). Stably-stratified shear-driven turbulence (hereafter simply "stratified turbulence") is responsible for most of the mixing in Earth's ocean interiors and coastal waters, as it mediates the transfer of energy between large-scale currents or internal waves and small-scale mixing by molecular diffusion [1]. The irreversible homogeneisation of temperature, salinity and passive tracers, and the efficiency of this process, are crucial to our environment and climate. This is because mixing not only controls regional-scale water composition but also the global circulation of our oceans, the rate at which they draw and sequester atmospheric heat and carbon, upwell nutrients, and thereby shape the biogeochemical cycles on which life depends [2].

Over a century of research in the physics of turbulent mixing revealed that this nonlinear transfer of energy is highly sensitive to the details of the flow – not only to the overall geometry and bulk dimensionless parameters, but also to details in the boundary conditions, the source of energy feeding the turbulence, the instabilities causing the transition to turbulence, the flow history, etc. As a result, it is frustratingly difficult to say anything generic about stratified turbulence and mixing, a theoretical hurdle which limits practical parameterisations of mixing in general circulation models [3,4]. An improved physical understanding of small-scale stratified turbulent mixing is thus necessary to improve the scientific credibility and interpretation of models. It is also important to reduce the uncertainty and increase the public confidence in climate predictions and mitigation measures [5].

A few generic statements can nevertheless be made about stratified turbulence in order to contrast it to classical turbulence. The restoring buoyancy force in the momentum equation and the potential energy cost associated with vertical motions have at least three far-reaching consequences. First, stratified turbulence is distinctively intermittent, and connected with internal gravity waves and their associated temporal scales [6]. Second, it is more anisotropic and prone to the formation of vertical well-mixed layers separated by sharp interfaces – a pattern that produces vertical velocity and density gradients higher than horizontal ones [7]. Third, it has a wider and richer spectrum of dynamically important length scales [8]. The Ozmidov scale, below which stratification ceases to be felt by eddies, is located between the integral (production) scale of the largest eddies and the dissipation (or Kolmogorov) scale. The Batchelor scale, signalling where molecular diffusion occurs, is typically located below the dissipation scale. These three generic

properties make the direct numerical simulations of sustained, stratified turbulence in the parameter regime relevant to GAFD very challenging [9–11]. Physicists, therefore, need relatively simple laboratory experiments in which stratified turbulence can be generated, carefully controlled and accurately measured. Simple, canonical laboratory models such as pipe flow [12], Rayleigh–Bénard flow [13] and Taylor–Couette flow [14] have long been vital playgrounds to develop and test new theories of turbulence, and as such they are the "drosophilas" of turbulence research [15]. A "drosophila" flow should capture the essence of the "real-world" problem of ultimate interest while retaining enough realism and complexity to be a stimulating and fruitful long-term research challenge attracting a diverse group of researchers. This experimental tradition in fluid dynamics draws its power from dimensional analysis, which enables us to extrapolate the turbulent properties from the laboratory scale to the geophysical scale of interest. However, devising such extrapolation models necessitates a deep understanding of the complex physics at play in a realistic flow, of the peculiarities of its boundary conditions and scaling laws, and of the practical setup and measurements techniques – an understanding that can only be gained from a sustained community effort requiring a critical mass.

This paper surveys a relatively recent "drosophila" for stratified turbulence research, the stratified inclined duct (SID) experiment, introduced 10 years ago by Meyer and Linden [16]. This paper has three objectives. First, to explain why SID represents an effective and versatile laboratory model to improve the GAFD community understanding of stratified turbulence. Second, to convey the substantial physical understanding gained in the last 10 years, with an emphasis on the measurements that contributed to it. Third, to exhibit the wealth of open questions raised in the process, and to guide researchers in the design of further experiments to answer them.

With these objectives in mind, we introduce SID in Sec. 2, with its historical roots and dimensionless framework. In Sec. 3, we focus on the three types of measurements that shaped our "first-order" physical understanding, before touching on more advanced "second-order" findings and open questions in Sec. 4. In Sec. 5, we leverage this understanding to explain how SID should be scaled up for stronger geophysical turbulence, translating dimensionless scaling laws to physical units and practical design guidelines. Finally, we conclude in Sec. 6.

2. The Stratified Inclined Duct (SID)

2.1. *History: from a transient to a sustained flow*

An early attempt to study the transition to turbulence in a stably-stratified flow dates back to Reynolds's seminal paper in 1883 [17] on turbulence in pipe flow. In the lesser known § 12, he contrasted the instability in unidirectional pipe flow to that observed in a stratified counterflow generated between two immiscible liquid layers upon tilting the pipe (see Figure 1 (a)). In the late 1960s, Thorpe [18] studied the Kelvin–Helmholtz instability of a shear layer and its breakdown to turbulence by tilting a rectangular tank initially filled with salt solutions at different densities (Figure 1 (b)). Both of these experiments are by nature transient and short-lived because of the limited longitudinal extent of the apparatus.

The Stratified Inclined Duct (SID) proposed by Meyer and Linden in 2014 [16] overcomes this limitation by adding large reservoirs on either side of a long rectangular duct to sustain a long-lived exchange flow (Figure 1 (c)). (Note that a similar setup was described by Macagno and Rouse in 1961 [19] but their paper was not widely disseminated.) Importantly, the apparatus can be tilted at a small angle θ to force the denser layer to accelerate as it flows downslope and vice versa. Whether the apparatus is tilted or not, SID creates a virtually pure ("baroclinic") exchange flow with no net ("barotropic") component; in other words, the reservoirs exchange buoyancy but keep a constant volume. As we shall see, the originality of SID is that the simple, natural

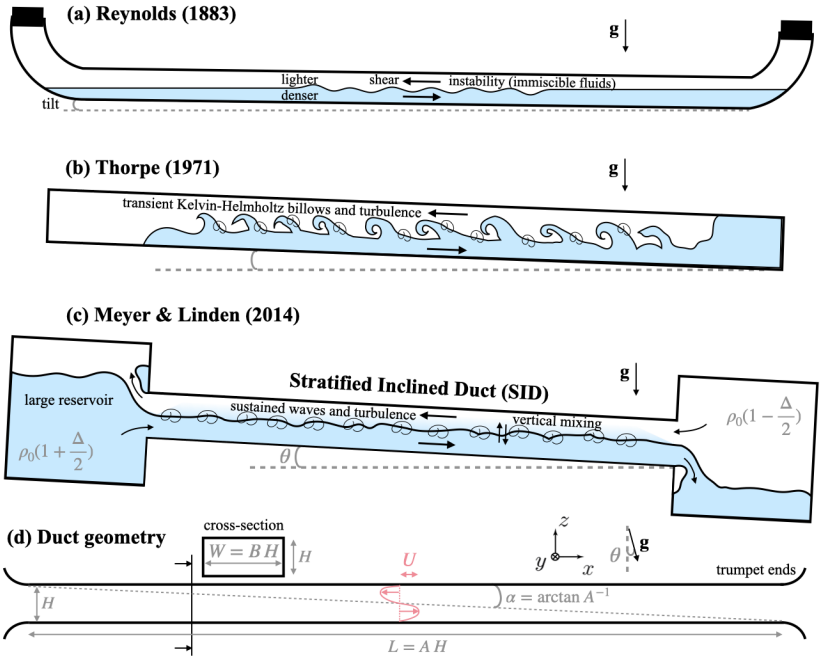


Figure 1. Early experiments on stratified turbulence compared to the more recent Stratified Inclined Duct (SID) discussed in this paper. The reservoirs on either side of a long rectangular duct sustain an exchange flow for long times, forced by a tilt θ.

forcing of gravity through θ sustains for very long times statistically stationary and vigorous interfacial stratified turbulence that long seemed out of reach of either laboratory or numerical experiments [7].

Following the classification of Turner [20, § 4.3.1], SID turbulence is an example of "internal mixing process" [20, § 4.1.4., § 10] because it is fed by the mean shear, which is itself a consequence of the stratification. This leads to a self-sustaining local equilibrium between turbulence, shear, stratification and mixing, typical of geophysical flows. Other laboratory experiments studied turbulent entrainment by relying either on pumps to generate the shear, resulting in a different kind of equilibrium [21–23], or by relying on "external mixing processes" using oscillating grids, rakes or a surface stress (see [20, § 9.1], [4, § 7]).

2.2. *Dimensionless numbers*

The first parameter driving SID flow is the reduced gravity $g' = g\Delta$ where Δ is the dimensionless density difference. By convention the left reservoir has density $\rho_0(1+\Delta/2)$ and the right reservoir has density $\rho_0(1-\Delta/2)$ (where $0 < \Delta \ll 1$), noting that $\Delta/2$ is sometimes called the Atwood number. The second obvious parameter is the tilt angle θ, usually kept below ≈ 0.2 rad (corresponding to $\approx 11^\circ$) to remain in the "stably-stratified" realm (in which we assume $\cos\theta \approx 1$ and $\sin\theta \approx \tan\theta \approx \theta$). The duct geometry (Figure 1 (d)) also plays an important role. In order of decreasing dynamical importance, we define the duct height H, length $L = AH$ and width $W = BH$ and impose that the streamwise aspect ratio be very large $A > 10$, while the spanwise aspect ratio

tends to be $B = O(1)$ (say between 1/4 and 4). At times, it will prove useful to interpret the aspect ratio A as a slope $\alpha = \arctan(A^{-1}) \approx A^{-1} \ll 1$ radian (see dashed line in Figure 1 (d)). These parameters are summarised in Table 1.

In the last 10 years, three generations of apparatus have been used in the G. K. Batchelor Laboratory in Cambridge, as well as multiple duct geometries, with heights H between 45 mm and 100 mm, $A = 15, 30, 40$ and $B = 1/4, 1$ and 2. (See [16] for the first generation, see [24] for the second generation, see [25] for a summary of the data in both, and see [26] for the third generation.) The ends of the duct can either be sharp or trumpet-shaped without greatly affecting the flow in the duct away from the ends.

Importantly, SID does not have an intrinsic velocity scale. The flow is driven by the reduced gravity $g\Delta$. The observed velocity scale, which we can take as the peak exchange velocity U (figure 1d) must be set by a dominant balance between the terms in the along-duct (x) momentum equation [25]; these are the inertia $\sim U^2/L$, the hydrostatic pressure gradient driving the exchange $\sim g\Delta H/L = g\Delta\alpha$ (an acceleration down the slope α), the additional downslope acceleration $g\Delta\theta$, and the viscosity $\nu U/H^2$, where ν is the kinematic viscosity. As we are interested in turbulent flows, the dominant balance must include the inertial rather than the viscous term, but it is not a priori clear whether it should be balanced by the hydrostatic term, giving $U \sim (g\Delta H)^{1/2}$, or by the gravitational term, giving $U \sim (g\Delta L\theta)^{1/2}$. As we shall see, experiments revealed early on that it was the former, i.e. an inertial-hydrostatic scaling, with the tilt θ and viscosity ν playing a more minor role in regulating the exchange. In SID, the along-duct velocity scale is $U = (g\Delta H)^{1/2}$, corresponding to a "free fall" from the duct height H rather than from the duct elevation $L\theta$.

Table 1. Summary of the parameters and scales used to make the analysis dimensionless, such that the vertical coordinate $\tilde{z}$, the streamwise velocity $\tilde{u}$ and the density $\tilde{\rho}$ are all bounded by ± 1.

Input parameters	
Dimensional	
$g' = g\Delta$	Reduced gravity (Δ is the dimensionless density difference)
H, L, W	Duct height, length and width
ν, κ	Kinematic viscosity and scalar diffusivity
Dimensionless	
θ	Duct tilt set by the experimenter
$Re = \left(g\Delta H^3\right)^{1/2}/(2\nu)$	Reynolds number
$Pr = \nu/\kappa$	Prandtl number
$A \approx \alpha^{-1}$	Streamwise aspect ratio (α is the duct geometric slope)
B	Spanwise aspect ratio
Scales for normalisation	
$H/2$	Length scale: thickness of each layer and of the shear layer
$U = (g\Delta H)^{1/2}$	Velocity scale: maximum velocity expected in each layer
$H/(2U) = \left[H/(g\Delta)\right]^{1/2}/2$	Time scale: inverse of the bulk shear
$g'/2 = g\Delta/2$	Buoyancy scale : half of the maximum difference (leading to a bulk buoyancy time scale of $[H/(g\Delta)]^{1/2}$ and a bulk Richardson number $Ri = 1/4$)

We can now add to our existing set of dimensionless parameters (θ, A or α, and B), the Reynolds number Re based on U and the typical layer thickness $H/2$ as well as the Prandtl number Pr:

$$Re = \frac{UH}{2\nu} = \frac{\left(g\Delta H^3\right)^{1/2}}{2\nu}, \qquad Pr = \frac{\nu}{\kappa}. \tag{1}$$

For practical reasons, SID has traditionally been run with salt, having very low diffusivity κ, in which case $Pr = 700$, but it has also been run with temperature stratification, in which case $Pr = 7$ (note that we take a reference value of $\nu = 1.05 \times 10^{-6}$ m^2 s^{-1} for water at a room temperature of 20°C). Scaling all the flow variables accordingly (see Table 1), we create dimensionless "tilde" variables for the spatial coordinates $\mathbf{x} = (x, y, z) = (H/2)\widetilde{\mathbf{x}}$, velocity $\mathbf{u} = (u, v, w) = U\widetilde{\mathbf{u}}$, time $t = U/(H/2)\widetilde{t}$ and density variations around the neutral density $\rho = \rho_0[1 + (\Delta/2)\widetilde{\rho}]$ (i.e., $-\widetilde{\rho}$ is a buoyancy). The dimensionless equations of motion are:

$$\widetilde{\nabla}\cdot\widetilde{\mathbf{u}} = 0, \qquad \frac{\partial\widetilde{\mathbf{u}}}{\partial\widetilde{t}} + \widetilde{\mathbf{u}}\cdot\widetilde{\nabla}\mathbf{u} = -\widetilde{\nabla}\widetilde{p} + \frac{1}{Re}\nabla^2\widetilde{\mathbf{u}} + Ri\,\widetilde{\rho}(\theta\mathbf{e}_x - \mathbf{e}_z), \qquad \frac{\partial\widetilde{\rho}}{\partial\widetilde{t}} + \widetilde{\mathbf{u}}\cdot\widetilde{\nabla}\widetilde{\rho} = \frac{1}{Re\,Pr}\widetilde{\nabla}^2\widetilde{\rho}, \tag{2}$$

expressing incompressibility, conservation of momentum (Navier–Stokes) and the coupled buoyancy transport, under the Boussinesq approximation that $0 < \Delta \ll 1$ (recall that in the gravity forcing, we assume $\cos\theta \approx 1$ and $\sin\theta \approx \theta$, in radians). The buoyancy is coupled to the momentum through the bulk Richardson number $Ri = g(\Delta/2)(H/2)/U^2$. In SID, it is essentially fixed at $Ri = 1/4$ by the scaling $U = (g\Delta H)^{1/2}$. Another interpretation is that the bulk buoyancy frequency $U/H = (g\,\Delta\,H^{-1})^{1/2}$ is half the mean shear used to make time dimensionless.

Importantly, the Reynolds number in (1) is a prognostic parameter set by the experimenter, assuming $U = (g\Delta H)^{1/2}$, rather than a diagnostic parameter using measured values. This choice has the advantage of simplicity, but when it was desirable to compare the evolution of detailed flow properties with Re across a range of experiments, and when detailed velocity measurements were available, we have also used a carefully defined, diagnostic "shear layer" Reynolds number [27]. Drawing a parallel with vertical convection [28], it is possible to approximate SID as a closed duct having Dirichlet boundary conditions $\widetilde{\rho} = \pm 1$ on the left and right boundaries $\widetilde{x} = \mp A$ sustaining the exchange. This problem is well defined by the (prognostic) Rayleigh number $Ra = g\,\Delta\,H^3/(\nu\kappa)$, and our Reynolds number (1) is equivalent to the scaling $Re = Ra^{1/2}\,Pr^{-1/2}$.

Compared to a lock exchange gravity current down a slope [29,30], SID differs in that its large reservoirs allow it to access the stationary stratified shear flow established after the initial gravity currents have exited the duct. The gravity current dynamics last a time $L/U = (L/H)(H/U)$ i.e. only A shear time scales and are sensitive to the behaviour of the head of the current and to initial conditions. These initial transients are discarded in SID experiments to focus on the long-time dynamics of the ensuing shear flow. These dynamics are insensitive to the initial conditions and to the plume dynamics in the reservoirs, as we will see next.

3. Experimental methods and first-order findings

3.1. *Shadowgraphs: flow regimes and interfacial mixing*

The simplicity of SID allowed Meyer and Linden [16] to explore the parameter space (Re, θ) (in their original paper (Δ, θ)), where they discovered various flow regimes. To visualise the flow, they used the simple shadowgraph technique (see Figure 2 (a)), in which the experimenter illuminates a central section of the duct with nearly parallel light, and records with a camera the pattern of shadows resulting from density-related refractive index variations inside the duct. Shadowgraphs are well-suited for the dair detection of sharp density contrasts within the flow, caused by interfacial waves, turbulence and mixing. (Shadowgraphs from many of their experiments, and more recent ones, are shared in the repository [33].)

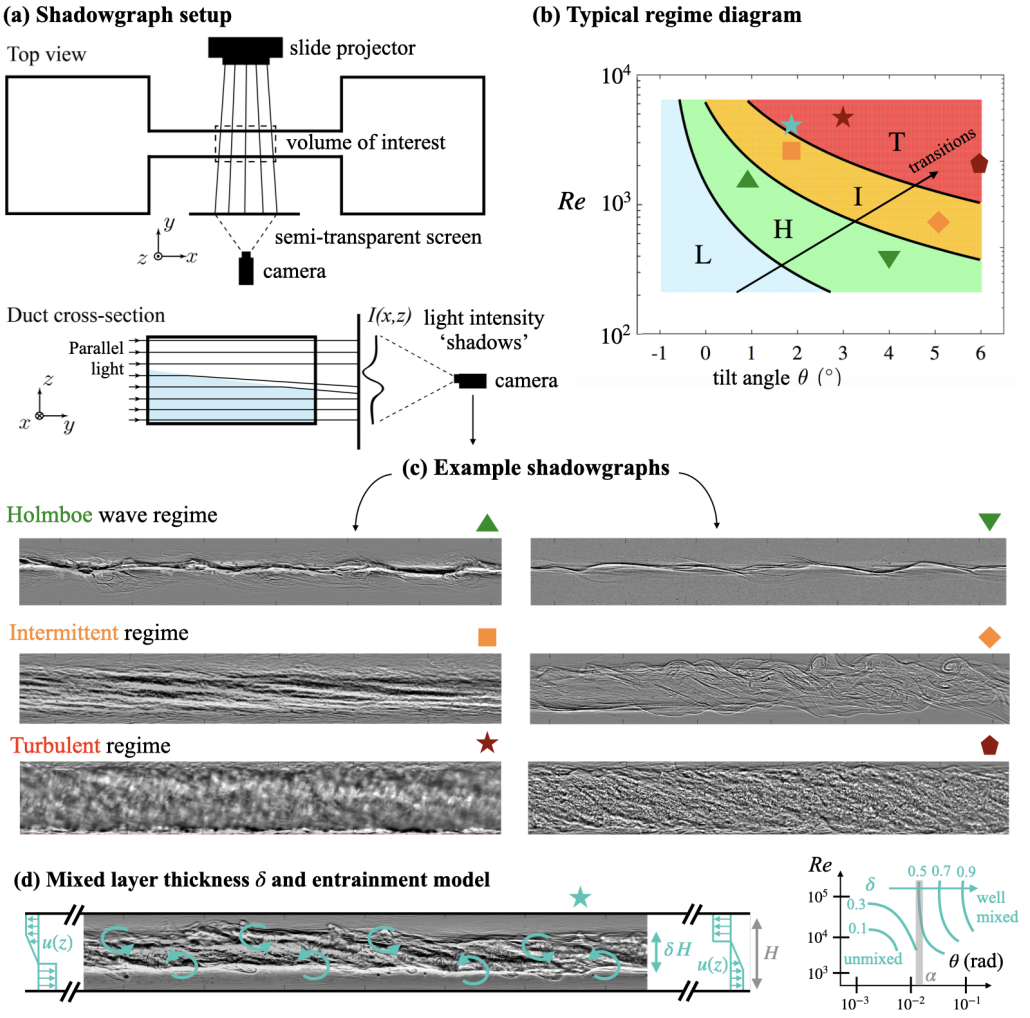


Figure 2. (a) Shadowgraphy exploit the refraction of initially parallel light to visualise density contrasts within the flow [31]. (b) This technique was instrumental in mapping the multiple flow regimes in parameter space: Laminar, Holmboe waves, Intermittently turbulent, Turbulent (originals in [25]). (c) Visualisations in different regions of parameter space (see matching symbols in (b)) highlight the diversity of SID dynamics idealised regime diagram (data in [32]). (d) Shadowgraph also helped model the thickness of the interfacial mixed layer (see Sec. 3.1 and [25]).

The regimes they identified are mapped in a typical (Re,θ) "regime diagram" in Figure 2(b) and are illustrated by representative snapshots in Figure 2(c). These regimes, are, by order of increasing Re and θ: laminar two-layer flow with a sharp, stable interface (snapshot not shown); wavy flow with an unstable but still sharp interface featuring travelling "Holmboe" waves ("H" regime); wave breaking and intermittent bursts of interfacial turbulence with complex spatio-temporal patterns ("I"); fully-developed and sustained interfacial turbulence with a thick, partially mixed layer ("T"). The discovery and qualitative description of these regimes were influential as they showed that SID harbours a wealth of flow behaviours – internal waves,

intermittency and anisotropic layering – that are the hallmark of stratified turbulence. Moreover, comparing the snapshots in the left and right columns of Figure 2 (c) reveals that even within the broad H, I and T "territories", flow in different subregions can be very different, thus begging for a finer classification of regimes.

To this end, an automated, data-driven classification was performed in [26] using a newer, curated dataset of 113 long shadowgraph movies covering the parameter space (shared in the repository [32]). The method was applied frame by frame and combined edge detection to extract fine-scale density interfaces, physically-interpretable dimensionality reduction based on the morphology of these interfaces, and unsupervised clustering to identify dense regions in the reduced space. Subtly different turbulent states were revealed and interpreted, with gradual shifts in their distribution across parameter space, as well as different temporal routes between them in the intermittent regime. These results further highlighted the richness of the dynamics present in SID and the potential of machine learning techniques to assist the human eye in extracting physical insights from large laboratory datasets.

Shadowgraphs were also used in [25] to systematically estimate the thickness of the partially mixed layer, which we define as a dimensionless ratio $\delta \in [0,1]$ of the duct height (Figure 2 (d)). A simple entrainment model (see cyan profiles) was developed to explain empirical scaling laws for the scaling of $\delta(Re,\theta)$ in the dataset [33], as well as earlier data at very large $Re > 10^5$ in an earlier SID-like experiment [34]. The layer δ was assumed to be linearly stratified, and each counterflowing layer was assumed to enter the duct unmixed with a "plug", irrotational velocity and to leave the duct by carrying the mixed fluid out with a linear velocity. The balance between the turbulent entrainment of unmixed fluid, its mixing with an efficiency $\Gamma \in [0,1]$, and its outflow yields a steady-state thickness

$$\delta \approx [(3/2)\,\theta\, A\, \Gamma]^{1/3} \approx 0.5(\theta/\alpha)^{1/3} \;\text{ for }\; Re > 10^5, \tag{3}$$

assuming $\Gamma(Re) \to 0.1$ for $Re > 10^5$, a 10 % efficiency consistent with data from lock-release gravity currents [35]. To first order, the mixed layer thickness therefore depends only on the ratio of the duct's tilt θ to its geometrical slope α, as long as Re is large enough (Figure 1 (d)). As a rule of thumb, the mixed layer thus fills half the duct height ($\delta \approx 0.5$) when $\theta \approx \alpha$.

3.2. *Mass flux: hydraulic control and transition*

The observed distribution of flow regime "territories" in (Re,θ) space raised the question: what controls the transitions, shown by black curves in Figure 2 (b)? An important clue to answer this question was the behaviour of the dimensionless mass flux Q_m, which quantifies the average amount of mass (more specifically, buoyancy) exchanged along the duct:

$$Q_m = \left\langle \widetilde{\rho}\,\widetilde{u} \right\rangle_{x,y,z,t}, \tag{4}$$

where $\langle\cdot\rangle_{x,y,z,t}$ denotes averaging over the duct volume and over a sufficiently long time. We bear in mind that this baroclinic exchange has a zero net barotropic exchange $\langle \widetilde{u} \rangle_{x,y,z,t} = 0$. This mass flux is a key diagnostic parameter in SID, akin to the Nusselt number in convection.

Measurements of Q_m were performed as sketched in Figure 3 (a). Initially, the reservoirs were filled with salt solutions having an initial density difference $\Delta\rho^i$. The duct was typically filled with fluid at intermediate density, but initial conditions were soon forgotten after the initial transients and thus unimportant for the long-time evolution of the flow. The gates on either side of the duct were then opened, the exchange flow of interest allowed to run for a time τ, before the gates were closed and the reservoirs were mixed. The difference between the initial and final density in both reservoirs $\Delta\rho^f$ (which should be equal) was then measured with a high-precision density meter to compute the mass exchanged Δm and the dimensionless Q_m (details in Figure 3 (a) and

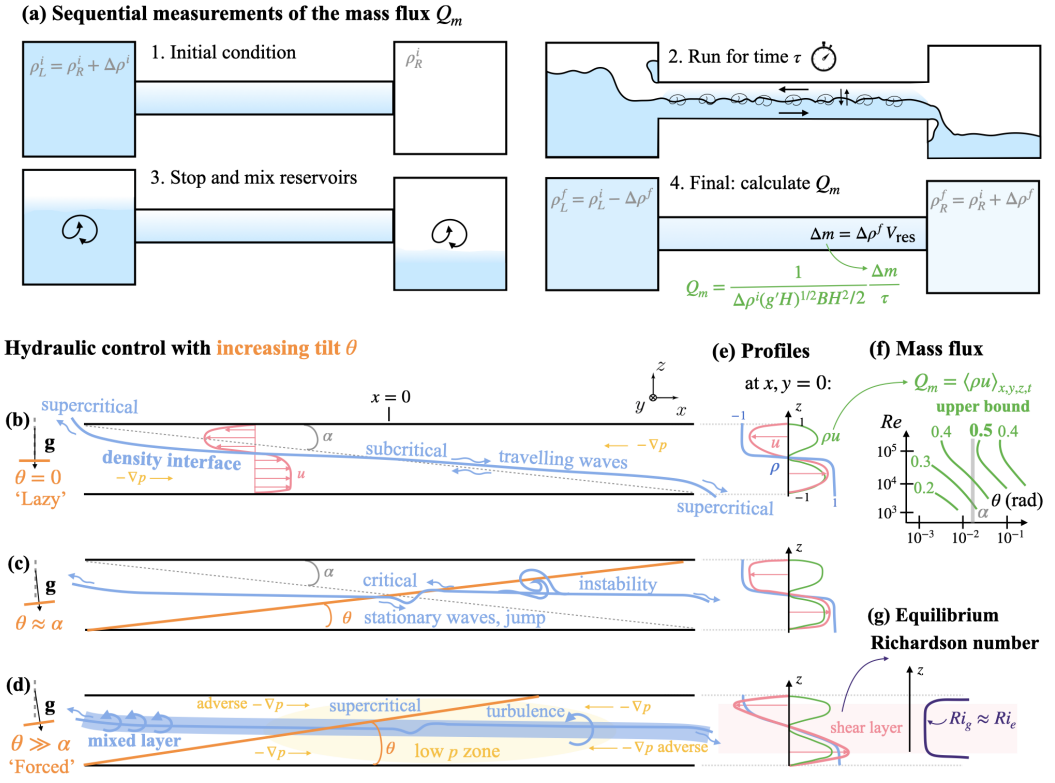


Figure 3. The mass flux Q_m quantifies the net exchange of buoyancy (salt) between reservoirs, a key variable in SID flow. (a) Mass flux data relies on density measurements in the reservoirs before and after an experimental run, and shaped our understanding of the two-layer hydraulics behind the transitions to turbulence (see Sec. 3.2). (b-d) Put simply, the forcing by the tilt θ opposes the frictional slope of the interface and causes an internal hydraulic jump at a peak $Q_m = 0.5$. Increasing θ above α sustains intense turbulent mixing, affecting the velocity and density profiles (e) thereby reducing Q_m (f) and Ri_e (g).

in [25]). Conveniently, the next experiment could then be run at a lower initial density difference, allowing for sequential measurements of Q_m at decreasing values of Re for a fixed θ, and an efficient coverage of parameter space.

The results of Meyer and Linden [16] showed that Q_m was of order 1 for all $Re = O(10^3 - 10^4)$. More specifically, $Q_m \approx 0.5$ in the range $\theta \approx (0.5-1)\alpha \approx 1-2°$, and dropped below 0.5 for lower or higher θ (see sketch in figure 3f). This meant that, assuming weak mixing, the (dimensional) layer-averaged velocity could be estimated as $\langle|u|\rangle_{x,y,z,t} \approx Q_m(g'H)^{1/2} \approx 0.5(g'H)^{1/2}$. This substantiated the scaling for the peak velocity $U \approx (g'H)^{1/2}$ introduced above (in fact, [16] interpreted Q_m as a Froude number). It also meant that pre-turbulent flows at lower tilts $\theta \ll \alpha$ and strongly turbulent flows at higher tilts $\theta \gg \alpha$ were robustly below the peak $Q_m = 0.5$.

How are the physics behind these observations related to the approximate scaling of regime transitions with the product $Re\,\theta$ sketched in Figure 2 (b)? To understand this, consider gravity waves propagating on the density interface sketched in blue in Figure 2 (b) at the shallow-water phase speed $\propto (g'H)^{1/2}$ [36]. When $\theta = 0$, the interface slopes downwards, with a slope $\propto Re^{-1}$, as a result of viscous friction at the interface and duct walls. Importantly, its mean

slope must always remain shallower than α as it is bounded by the duct walls. In this "lazy flow", the convective acceleration of each layer along the duct results in a maximum layer-averaged velocity and interfacial offset at the outlets, where the geometry expands rapidly. This results in a locally supercritical flow, against which the waves cannot travel. (Technically, supercritical flow is flagged by a "composite" (two-layer) Froude number > 1 [37,38], akin to the sound waves in a supersonic flow at Mach number > 1.) The flow is said to be in a state of hydraulic control because the supercritical outlet regions control the duct by isolating it from external information or disturbances (waves) coming from the reservoirs. Hydraulic control leads to a "maximal exchange" Froude number condition which translates to $Q_m = 0.5$ in an inviscid laminar flow, but is reduced slightly by viscous friction at intermediate Re [39].

As θ is increased above 0, hydrostatic balance (see orange lines in Figure 3(c)) tends to make the density interface slope upwards, partially countering the downward frictional slope, thereby forcing an increase in Q_m towards the hydraulic limit of 0.5. When $\theta \approx \alpha$, the upward forcing slope θ dominates over the maximum possible downward friction slope α [25]. This "forced flow" is then confronted to an inadmissible mid-duct ($x = 0$) upward slope (which would decelerate each layer along the duct), giving rise to an internal hydraulic jump, akin to a shock wave in supersonic flow. Recent direct numerical simulations (DNS) of the flow along the duct [40] and their analysis in the framework of two-layer hydraulics [41] revealed that this forced flow is then mildly supercritical all along the duct. This leads to the unstable growth of stationary, long (hydrostatic) waves, followed by travelling, short (non-hydrostatic) waves that break, overturn and dissipate just enough energy to keep a zero mean interfacial slope.

As θ is increased well above α (Figure 3(d), turbulence intensifies in order for the viscous dissipation $\propto Re^{-1}$ to keep up with and "regularise" the "inadmissible" upward tilt θ. This balance leads to turbulence levels $\propto Re\,\theta$ consistent with the regime transitions. The mean interface is thus always approximately parallel to the duct walls, i.e. the mean isopycnals (in blue) are always tilted by θ relative to gravity (orange lines). This robust relative tilt sustains the baroclinic generation of spanwise vorticity, primarily shear $\partial\widetilde{u}/\partial\widetilde{z}$, which in turn sustains the turbulence and the mixed layer. DNS revealed that turbulence creates a zone of low pressure in the central half of the duct length (see yellow shade) [40]. This zone creates, for each layer, a large-scale adverse pressure gradient over the second half of their transit along the duct (see yellow arrows). This gradient balances the acceleration of the flow along the slope θ with a matching deceleration, which prevents the "free fall" scaling from height $L\theta$ (which would give $U = (g\,\Delta\,L\theta)^{1/2} \Leftrightarrow Q_m = 0.5(\theta/\alpha)^{1/2}$) and enforces the maximal exchange condition $Q_m \leq 0.5$ when $\theta > \alpha$. Increasingly intense turbulence for $\theta \gg \alpha$ then decreases Q_m below 0.5, because turbulence transports salt from the right-flowing, dense bottom layer upwards into the left-flowing, light upper layer. Some of this vertical buoyancy flux translates to irreversible mixing by small-scale diffusion; thus some of the fluid ends up being advected back to the reservoir where it originates, decreasing the net longitudinal buoyancy flux Q_m. In fact, assuming self-similar, linear profiles for $\widetilde{u}, \widetilde{\rho}$ in the mixed layer yields a Q_m decreasing linearly with δ. This completes the "hydraulics" interpretation of regime transitions and mass flux data.

The resulting turbulent equilibrium across the shear layer (Figure 3(e)), in pink) can be characterised by a gradient Richardson number profile $Ri_g(\widetilde{z}) = N^2/S^2$ along the duct z-direction (Figure 3(g), in purple), the ratio of the squared buoyancy frequency $N^2 = -(g'/H)\partial\langle\widetilde{\rho}\rangle_{x,y,t}/\partial\widetilde{z}$ (stabilising the flow) to the squared shear $S^2 = (4g'/H)(\partial\langle\widetilde{u}\rangle_{x,y,t}/\partial\widetilde{z})^2$ (destabilising the flow). The linearly stratified mixed layer must have a mean $-\partial\widetilde{\rho}/\partial\widetilde{z} \approx 1/\delta$, while velocity measurements (detailed in the next section) show that the turbulent shear layer has a typical dimensionless thickness $\approx \sqrt{2}$ and peak-to-peak velocity jump $\approx \sqrt{5}$, resulting in a mean $(\partial\widetilde{u}/\partial\widetilde{z})^2 \approx 5/2$. This

suggests an approximately uniform "equilibrium" Richardson number:

$$Ri_g(\widetilde{z}) = \frac{N^2}{S^2} \approx Ri_e = \frac{1}{4}\frac{\left(-\partial\widetilde{\rho}/\partial\widetilde{z}\right)}{\left(\partial\widetilde{u}/\partial\widetilde{z}\right)^2} \approx \frac{1}{4}\frac{1/\delta}{5/2} \approx \frac{1}{10\delta}. \tag{5}$$

We thus expect $Ri_e \approx 1/4 = 0.25$ when $\delta \approx 0.4$ (i.e. when $\theta \approx \alpha/2$ according to (3)), noting that sustaining turbulence with such weak forcing requires $Re > 10^4$. However, we expect a lower $Ri_e \approx 1/7 \approx 0.15$ when the mixed layer is thicker $\delta \approx 0.7$ (i.e. when $\theta \approx 3\alpha$). Sustaining turbulence with this strong forcing is possible at $Re = O(10^3)$, as shown next.

3.3. *Volumetric velocimetry and density: energy budgets and dissipation*

The last piece of the puzzle to complete our "first-order" understanding of the physics of SID came from analysing the kinetic and potential energy pathways of the flow. This analysis was made possible by a major technological advance, sketched in Figure 4 (a) and detailed in [42], which provided the time-resolved velocity and density fields simultaneously in three dimensions, at a high enough spatial resolution for the dynamically active scales to be captured.

These measurements are entirely optical and non-intrusive, relying on a dual-cavity Nd:YAG pulsed laser to illuminate a thin sheet of the flow in a central section of the duct. Microscopic, neutrally-buoyant reflective particles are seeded in the flow and imaged to determine the two-dimensional velocity field through Particle Image Velocimetry, or PIV (see "Raw PIV-B image"). Two images taken a short time interval apart are divided into small, partially overlapping, interrogation windows and compared window by window. The shift in the pattern of particles between successive frames yields a local velocity vector in each window. In order for particle images to remain sharp, the refractive indices are carefully matched by achieving the density difference with a pure sodium nitrate ($NaNO_3$) solution in the dense reservoir and a pure sodium chloride (NaCl) solution in the light reservoir [31]. (Note that matching refractive indices is not possible if the experiment is run with temperature stratification only.) To obtain the y-component of velocity (across the laser sheet), two cameras (PIV-A and PIV-B) are positioned at a angle to the plane of interest. Any motion along y appears to each camera as an apparent left or right motion, and v is calculated with suitable coordinate transformations. The result is a three-component, two-dimensional velocity field whose resolution depends on the size of the interrogation windows. Using video cameras with a resolution of 8 Mpixels and speed of 200 frames per second (to match the laser frequency), $x-z$ planes containing 400×100 three-dimensional vectors were output at a frequency of 100 Hz [42].

The density field is measured simultaneously in the same plane with Laser Induced Fluorescence (LIF), which relies on mixing the rhodamine 6G dye in one of the reservoirs (here on the right). The dye tagging the upper layer (see "Raw LIF" image) absorbs the 532 nm laser light and emits it back with a minor redshift, allowing optical filters to separate the dye and the particle signals. The fluid density is then calculated using an appropriate calibration and assuming that the passive dye concentration faithfully tags the active salinity field, since both have a very high $Pr = O(10^3)$. (This assumption would be questionable if the active scalar were temperature.)

The technological leap to obtain three-dimensional data was to continuously scan this laser sheet back and forth along y and combine PIV and LIF planes captured in quick succession into volumes. This scanning approach is advantageous in SID due to the requirement of measuring velocity and density simultaneously at high-resolution, which is impractical with other volumetric approaches [42]. A smooth, continuous scanning motion is necessary considering the speed and the inertia of the traverse-mounted carriage carrying the light sheet optics, and the sensitivity of these measurements to vibrations. But how can a fast and continuous scanning yield two overlapping laser sheets required to perform PIV? This challenge was overcome by introducing

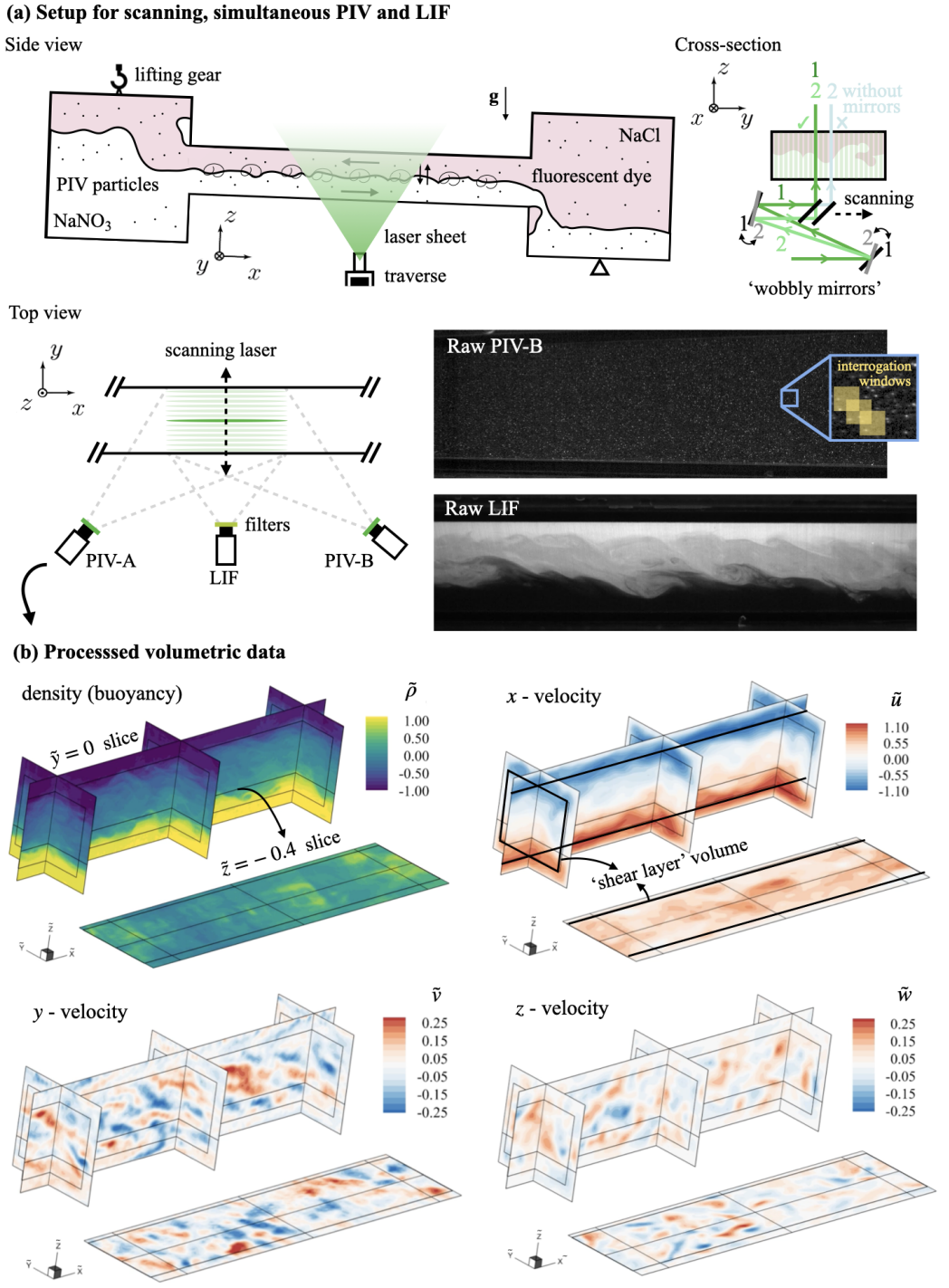


Figure 4. (a) Scanning technique combining simultaneous planar Particle Image Velocimetry (PIV) and Laser Induced Fluorescence (LIF) to measure the time-resolved, volumetric velocity and density fields. (b) Here we show a snapshot at $Re = 1256$, $\theta = 6° \approx 3\alpha$ (datasets available at [43]). These data provide full access to the detailed flow energetics sketched in Figure 5, which were decisive to complete the first-order physical understanding of SID in Sec. 3.3.

a pair of rapidly oscillating mirrors mounted on galvanometers ("wobbly mirrors" in the cross-section view of Figure 4 (a)) that correct the position of the laser sheet to recover overlapping pairs of images [42]. The DigiFlow software [44] handled the hardware control, synchronisation of the laser pulses, traverse, wobbly mirrors, cameras, as well as the processing of PIV and LIF data.

The processed volumetric data in world coordinates are illustrated in Figure 4 (b) by a single "snaphsot" of $(\widetilde{\rho},\widetilde{u},\widetilde{v},\widetilde{w})(\widetilde{x},\widetilde{y},\widetilde{z})$ in a turbulent dataset called "T2" at $Re = 1256$, $\theta = 6^\circ \approx 3\alpha$ which shows considerable three-dimensionality. We notice that the along-duct flow $\widetilde{u}$ is about four times as strong as the other two components, except in the middle of the shear layer where turbulent fluctuations exceed the mean flow. Also, $\widetilde{v}$ is more energetic than $\widetilde{w}$, which is typical of stratified turbulence because of the potential energy cost associated with vertical motions. We must keep in mind that the volume is not truly instantanenous as it is made of a sequence of ≈ 40 planes captured along $\widetilde{y}$ over a typical dimensionless time of $O(1)$. Hundreds of such volumes were typically captured by continuous back-and-forth scanning, providing time-resolved data over long times of $O(10^2 - 10^3)$, yielding ≈ 150 GB of raw data and ≈ 3 GB of processed data per experiment [43,45].

A total of 16 such volumetric datasets spanning all flow regimes were used to build the energetics picture in Figure 5. To grasp how energy flows through the measured sub-volume (sketched in yellow), let us first consider the whole (closed) system composed of the duct (in red) and reservoirs (in grey). Initially, the presence of dense fluid on one side sitting above light fluid on the other side provides a large reservoir of "available" potential energy (Figure 5 (b)). An open duct allows this potential energy to be steadily converted into kinetic energy. Eventually, the fluids have been exchanged, the kinetic energy has been dissipated, some mixing has occurred in the process, and the system comes to rest. In the final state, the "available" potential energy has been transferred to internal energy, i.e. heat and "background" potential energy, that cannot drive any further motion [46]. We are interested in the energy fluxes (bottom sketch) during the statistically-steady state where potential energy is converted to kinetic energy and to heat. The GAFD community is particularly interested in the mixing efficiency Γ, the ratio of irreversible mixing to viscous dissipation, in other words the "tax" imposed by stratification on turbulence [3].

The measured sub-volume is bounded by four walls, but remains open and exchanges energy with the in-flow and out-flow along x (see yellow energy reservoir in Figure 5 (c)). When the flow is forced ($\theta > \alpha$), the interface is approximately horizontal, the flow is approximately periodic in x, and these fluxes simplify as sketched, with a single external forcing F [47]. Essentially, the dimensionless kinetic energy reservoir $\langle|\widetilde{\mathbf{u}}|^2/2\rangle_{x,y,z,t}$ is fed with an average flux $\widetilde{F} \approx 0.5\,Ri_e\,Q_m\,\theta \approx 0.5\times 0.15\times 0.5\times\theta \approx 0.04\,\theta$ (in radians). (Note that this and the following relations were derived for the turbulent "shear layer volume" highlighted by black lines in Figure 4 (b)), excluding laminar flow in the vicinity of the four walls [27,48]). This flux feeds the mean kinetic energy (defined with respect to the $x-t$ averaged velocity) and is balanced by the mean dissipation D. The key observation, supported by the experimental data [47,48], is that the "hydraulic control" plateau in $Q_m = 0.5$ enforces a plateau on the mean-flow dissipation D. The increase in F beyond this plateau in D opens another pathway, the production of turbulent kinetic energy (TKE) P, in order to close the kinetic energy budget. This production term is balanced by the TKE dissipation ε, and by a (weaker) buoyancy flux B, an inevitable consequence of vertical motions in a stratified flow (the potential energy cost). The budget of potential energy, approximately equal to the scalar variance $(1/2)Ri_e\langle\widetilde{\rho}^2\rangle$, is simple: the net production B is balanced by dissipation χ, such that the average mixing efficiency is $\Gamma = B/\varepsilon \approx \chi/\varepsilon$. The limited experimental data suggest a modest tax of $\Gamma \approx 0.05-0.1$ [48] (we return to it in Sec. 4.3). In a very turbulent flow where $\varepsilon \gg D$, the TKE dissipation is thus in direct balance with the forcing. In dimensionless units:

$$\widetilde{\varepsilon} \approx \widetilde{P} - \widetilde{B} \approx \widetilde{P}(1-\Gamma) \approx \widetilde{F}(1-\Gamma) \approx 0.5\,Q_m\,Ri_e\,\theta(1-\Gamma) \approx 0.035\,\theta \ \text{ (in radians).} \tag{6}$$

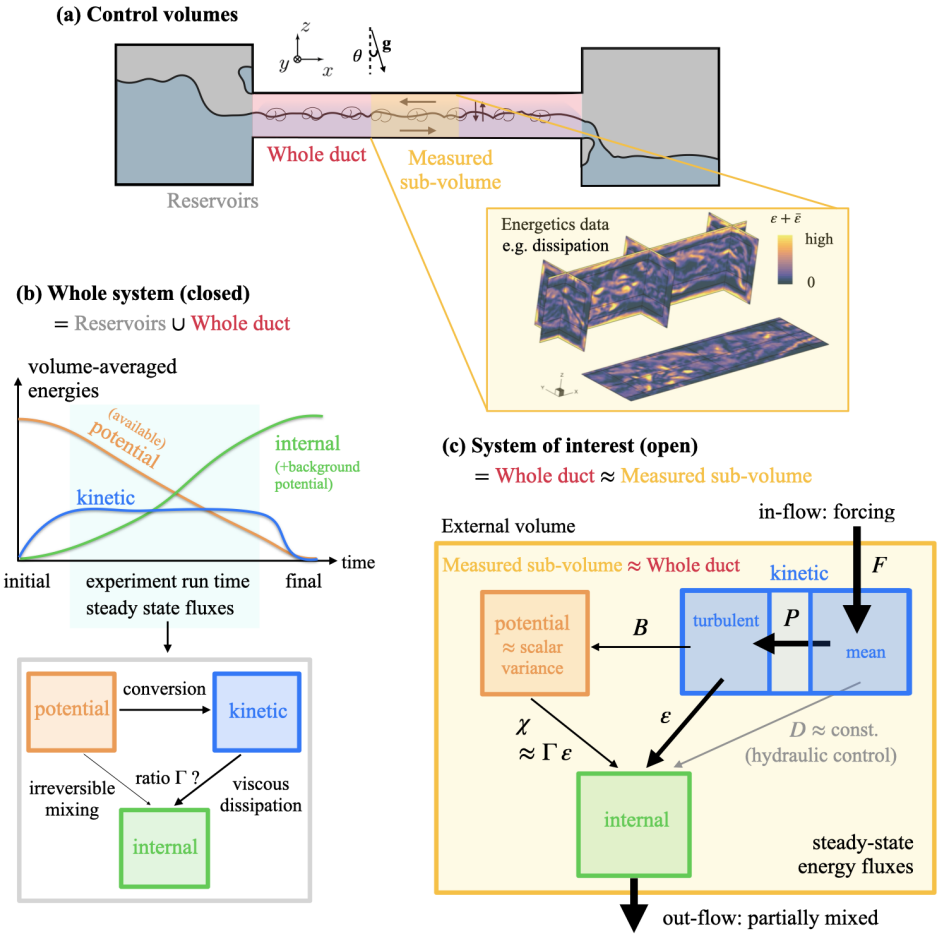


Figure 5. Energetics of SID, considering (a) control volumes, (b) the closed system (reservoir and duct) to provide background, and (c) the open system of interest (measured sub-volume of the duct, as in Figure 4). The out-of-equilibrium, statistically steady turbulence is forced by a flux F proportional to the tilt θ. Under hydraulic control when $\theta > \alpha$ (see Figure 3), [47,48] showed that this flux is almost entirely dissipated turbulently by ε, leading to the keystone of SID turbulence (6).

This equation is the keystone of SID turbulence, and is firmly rooted in the data averaged over the turbulent shear layer volume. The second approximation assumes $B/P \approx B/\varepsilon = \Gamma$ based on the observation that $\Gamma \ll 1$. The third approximation assumes $\varepsilon \gg D$ which is expected by hydraulic control and supported by our moderately turbulent data The last two approximations use our measured values for the key diagnostic flow parameters Q_m, Ri_e, Γ. Note that these values are expected to vary a little under a wider range of flow conditions Re, θ, Pr than investigated so far, effectively modulating the prefactor in (6). The keystone equation $\widetilde{\varepsilon} \approx 0.035\theta$ is the quantitative energetic translation of the hydraulic arguments of Sec. 3.2. Beyond the state of hydraulic control, the baroclinic production of shear by the tilt θ is balanced by interfacial dissipation $\widetilde{\varepsilon}$ (plus a modest mixing "tax"), keeping the interface in a marginal state of zero slope along the duct.

To wrap up this section on "first-order" findings, how does this keystone equation quantitatively explain the scaling of regime transitions with $Re\,\theta$? Recalling that the TKE dissipation is

defined by the square norm of the turbulent strain rate tensor $\widetilde{\varepsilon} = (2/Re)\|\widetilde{\mathbb{s}}'\|^2$, we deduce that $\|\widetilde{\mathbb{s}}'\|^2 \approx 0.02\,Re\theta$ [47,48]. In other words, the product $Re\theta$ controls turbulence levels because an increase in the volume-averaged dimensionless turbulent strain rate must be achieved by vortex stretching and a cascade of energy to increasingly finer scales.

4. Second-order findings and open questions

4.1. *Instability, waves, coherent structures and transitions to turbulence*

How exactly does the stable, laminar exchange flow in SID become turbulent? Instability theory seeks to predict the onset of instability, the physical mechanism at play, and the resulting spatio-temporal flow structures. As a dimensionless parameter is varied, say Re, we know that the transition to turbulence can be either of "supercritical" or "subcritical" nature. The supercritical scenario, for example in Rayleigh–Bénard convection or Taylor–Couette flow dominated by inner-cylinder rotation, starts with a linear instability triggered by virtually any infinitesimal disturbance, followed by secondary instabilities in a gradual cascade leading to chaos and turbulence [49]. This scenario is fundamentally different to the subcritical scenario, for example in unidirectional pipe flow or plane Couette flow, which are linearly stable and thus require particular finite-amplitude disturbances. (Note that "supercritical" and "subcritical" have a different meaning here compared to the discussion on interfacial waves in Sec. 3.2). Turbulence, then, is akin to an abrupt phase transition, where turbulent regions compete with laminar regions and proliferate with a lifetime increasing with Re [50]. In SID, the repeatable onset of a Holmboe wave regime for a threshold in Re and θ, the robustness of this regime in a wide region of (Re,θ), and the gradual increase in disorder at higher Re, are strong evidence of a supercritical scenario. Reynolds already understood in 1883 [17] that the transition to regular waves and turbulence in the exchange flow of Figure 1 (a) had, unlike in unidirectional flow, a critical velocity and was insensitive to the magnitude of perturbations, in other words, that it is supercritcal.

What is causing the primary instability in SID? A necessary condition for the linear instability of an idealised stratified parallel shear flow is that the gradient Richardson number $Ri_g(z) = N^2/S^2$ drops below the Miles–Howard criterion of 1/4 for some z [51]. In SID, because $Pr \gg 1$, a sharp density interface at $z \approx 0$ is embedded within a more diffuse shear layer. This produces two local minima of Ri_g on either side of the interface, and thus the potential for an instability depending on the value of Ri_g. As $Re\,\theta$ increases, the mass flux Q_m and thus the interfacial shear S increase while N remains unchanged, leading to a decrease of these Ri_g minima below 1/4 consistent with the observed onset of instability. This picture was confirmed with a stability analysis on the experimentally measured mean flow profiles, predicting growth at the correct wavelength and phase speeds [24]. As the density interface is sharp (recall $Pr = 700$ with salt) and the stratification is significant (recall the bulk $Ri = 1/4$) the instability in SID is not of Kelvin–Helmholtz type (which is stabilised by stratification) but instead of Holmboe type (which is destabilised by stratification), caused by the resonance of an internal gravity wave with the vorticity waves sandwiching it [52]. In this supercritical Holmboe transition (a pitchfork bifurcation), nonlinearities have a stabilising effect and eventually saturate the exponentially-growing instability [53] to a finite, observable amplitude as shown in Figure 2 (c)). Excellent agreement was indeed found between the measured three-dimensional Holmboe waves structure and the most unstable eigenfunctions predicted by the stability analysis performed on the two-dimensional $(y-z)$ mean flow [24]. This not only proved that the Holmboe waves in SID were saturated Holmboe instabilities, but also that they were distinctively three-dimensional because of confinement by the duct walls, most notably the side walls [54].

How do primary Holmboe waves eventually become turbulent? At $Re = O(10^2)$ Holmboe waves travel as two modes of counter-rotating vortices on either side of a cusped density interface

(see Figure 2 (c)), downward pointing triangle). Around $Re = O(10^3)$, secondary instabilities develop (see Figure 2 (c)), upward pointing triangle). The occasional ejection of whisps creates only minimal mixing; instead it "scours" the the density interface and keeps it sharp [55]. This leads to a long-lived state of coherent Holmboe wave "turbulence", which can be found up to $Re = O(10^4)$ for zero or even slightly negative θ [25]. Holmboe wave turbulence has been proposed to interpret field data in the deep ocean [56], surface ocean [57], and in an estuary [58] either through direct observation of its distinctive cusps or more indirect scouring behaviour. This turbulence differs markedly from the transient, rapidly overturning and less coherent turbulence resulting from the Kelvin–Helmholtz (K-H) transition found at lower Ri [59]. (Note that this K-H transition has also been achieved in SID by impulsively tilting the apparatus to a higher θ, as in Thorpe's experiment sketched in figure 1b. This allows to transiently exceeds the maximal exchange condition, thereby decreasing Ri below the hydraulic constraint of "steady SID".)

How does SID flow become intermittently turbulent? Eventually, the Holmboe regime is replaced by the intermittent regime at $Re = O(10^4)$ or at much lower Re if the tilt is $0 < \theta < \alpha$. What is the role of θ in this further transition, which is defined by stronger interfacial overturning and mixing distinct from the spatio-temporal Holmboe coherence? In Sec. 3.2, we saw that turbulence levels were $\propto Re\theta$ following an internal hydraulic jump, i.e., the instability of a shallow water wave of length comparable to the duct length (equivalently, the long-wave cousin of K-H, bounded by top and botttom walls [41]). This long-wave instability distorts the mean flow and leads to secondary, overturning instabilities of shorter wavelength comparable to the duct height, reminiscent of K-H billows. This hydraulic transition primarily caused by the ratio θ/α is clearly distinct from the Holmboe transition, but it is also of supercritical nature. Moreover, this hydraulic transition does not rely on the Holmboe transition, as was confirmed by mapping the (Re,θ) regime diagram at $Pr = 7$ (rather than 700) using temperature stratification. Indeed, shadowgraphs [31] and DNS [40] revealed that the more diffuse density interface supported transient internal waves but not Holmboe waves, without affecting the robust hydraulic transition associated with long waves. The two key control parameters Re and θ in SID thus give rise to at least two fundamentally different and co-existing supercritical transitions, and Pr further complicates the picture. The addition of θ to the classic linear stability problem has been recently shown to add multiple new families of long-wave instabilites, some of which do not even rely on shear or are only expected in extremely long systems ($A = O(10^2 - 10^3)$) [60]. Their relevance to SID – and generally to the route to stratified turbulence – remains to be assessed. Many insightful discoveries likely await those interested in completing the picture of the transition to turbulence in SID in the space spanned by Re, θ, Pr as well as the aspect ratios A, B (without mentioning the bulk Ri, which, as we touched upon, can be transiently lowered by impulsively tilting the duct, leading to yet another supercritical transition).

Finally, is the fully turbulent regime "aware" of these turbulent transitions? In other words, do transitions still "matter" even in distant regions of parameter space? According to dynamical systems theory, the answer is yes. Turbulence is viewed as underpinned by a relatively low-dimensional attractor, with phase-space trajectories spending significant time near a relatively small "skeleton" of exact (but unstable) solutions of the Navier–Stokes equations [61,62]. Periodic orbit theory seeks to predict turbulent coherence and statistics using a weighted average over these simple solutions [63], some of which are likely connected to linear instabilities [64]. The search for such a skeleton in three-dimensional, stratified turbulence at $Re = O(10^3 - 10^4)$ would be a formidable computational task. To stimulate such future endeavours, tantalising experimental evidence for this skeleton is accumulating in the form of coherent structures. In [65], their morphology has been tracked in SID across increasingly turbulent volumetric datasets, showing how hairpin-like vortical structures are born around the strong three-dimensional shearing structures of confined Holmboe waves. These hairpins gradually strengthen with $Re\,\theta$ and morph

into pairs of upward- and downward-pointing hairpins propagating in opposite directions on either side of the partially mixed layer. Their arched-up heads entrain and engulf unmixed blobs of fluid into the mixed layer, while their legs further stir the fluid laterally and vertically causing mixing. In [26], the data-driven mining of shadowgraphs revealed further complexity across the two-dimensional space (Re,θ). At equal values of "turbulent intensity" $Re\theta$ (and thus of the turbulent strain rate tensor $\|\widetilde{\mathsf{s}}'\|^2$) the dynamics at higher Re and lower θ organises around distinctively different structures than vice versa (compare the star and pentagon symbols in Figure 2 (c)). Investigation of the intermittent regime therefore appears key to flesh out the dynamical systems picture of SID turbulence, as we discuss next.

4.2. *Temporal intermittency and self-organisation*

Do the multiple primary instabilities in SID lead to multiple types of intermittency? The intermittent dynamics in the reduced-order space of [26] indeed revealed at least two different routes to turbulence at equal $Re\theta$. At higher Re and lower θ the flow cycles quasi-periodically between three clusters labelled "laminarising" (decaying) turbulence, "braided" turbulence and "granular" (strongly three-dimensional and incoherent) turbulence. At lower Re and higher θ the cycles are just as regular but the "granular" turbulence phase is replaced by an "overturning" turbulence phase, having steep, two-dimensionally coherent billows. Intermittency thus appears to organise around at least two distinct "slow manifolds' [66] in different regions of (Re,θ), but further progress on such data-driven reduced-order modelling is needed. At high θ, the cycles to "overturning" turbulence are consistent with repeated hydraulic transitions (long wave instability giving rise to short overturning waves), but the "laminarising" phase has a partially mixed layer which begs for a more complex three-layer hydraulics model. At low θ, the cycles to "granular" turbulence also remain to be explained, especially as the persistent third layer precludes the Holmboe instability but allows others, including Taylor–Caulfield [67]. The role of the boundary layers on the top, bottom and side walls should also be investigated. Although SID data suggest the boundary layers are laminar until $Re \approx 10^3$ they likely become turbulent before $Re = O(10^4)$ (depending on the duct length A), another transition which may complicate the analysis further.

How do the intermittent dynamics evolve between the wave and turbulent regime? Spatio-temporal $z-t$ diagrams generated from shadowgraphs (Figure 6 (a)) show that regular Holmboe waves are present at $Re = 706$ with a temporal spectrum peaking at a dimensionless period of ≈ 25 (Figure 6 (b)). The Holmboe coherence gradually disappears at $Re = 993$ and 1356 with growing mixing shown by darker shades of grey in the shadowgraph variance. The quasi-periodic cycles between laminarising and intense granular turbulence become recognisable at $Re = 1853$ and remarkably clear at $Re = 2294$ and 2828, with a temporal spectrum peaking at ≈ 100. This coherence gradually fades at $Re = 3426$, and disappears entirely just above this value (not shown here). The emergence of turbulent patches and their subsequent evolution into a complex spatio-temporal pattern with increasingly long-lived turbulent events is reminiscent of the competition between bistable laminar and turbulent phases characteristic of the subcritical bifurcation in pipe flow [50]. Could the fully-developed "ultimate" turbulent regime in SID be reached subcritically, like in other initally supercritical systems such as boundary layers and Rayleigh–Bénard [13]? Alternatively, could it be reached supercritically by a homoclinic bifurcation? Recognising that the turbulent bursts may be caused by a repeated linear shear instability, could we interpret them as noisy homoclinic pulses [68], i.e., near-periodic visits in phase space in the vicinity of the laminar unstable saddle point, followed by large turbulent excursions away from it?

What sets the period of these cycles also remains an open question (here ≈ 100 dimensionless time units). One candidate timescale is the average duct transit time $\approx 2A = 80$ shear time scales,

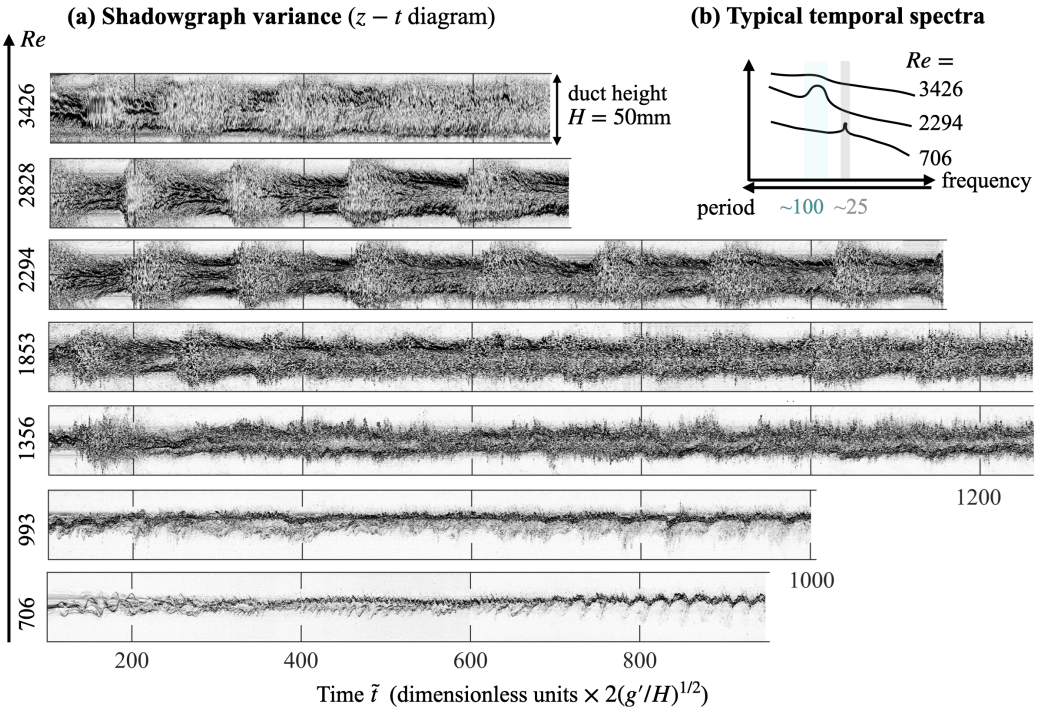


Figure 6. Intermittent turbulence evolving between the Holmboe wave regime at $Re < 1000$ and the fully turbulent regime at $Re > 3500$ (here $\theta = 2° \approx 1.4\alpha$). (a) Each spatio-temporal diagram show the temporal evolution of shadowgraph variance in a vertical slice across the full duct height. Darker shades indicate high shadowgraph variance caused by interfacial waves or turbulence. (Note we only show $\widetilde{t} > 100$ after the start of an experiment to discard initial gravity current transients.) The striking quasi-periodicity at intermediate Re, highlighted by idealised temporal spectra in (b), raises many open questions concerning the nature of the transitions to turbulence in SID (see Sec. 4.1-4.2).

taken by a fluid parcel travelling half the duct length at the layer-averaged speed $\widetilde{u} \approx Q_m \approx 0.5$. Another candidate is the turbulent dissipation timescale (the ratio of TKE to ε), which is an enigmatic ≈ 10 in the available turbulent data [48] (recall that the dimensionless shear timescale is 1 and the buoyancy timescale is 2). Cycles between turbulent de-stratification and quiescent re-stratification are common in geophysical applications, including in estuaries [69] and marginal seas [70] (controlled by tidal timescales) as well as the Pacific equatorial undercurrent [71] (controlled by diurnal solar heating). The "deep cycle" of equatorial ocean turbulence was explained by a low-dimensional interaction between mean shear and turbulence relying on the threshold $Ri_g = 1/4$ [72], which may inspire a similar model for SID.

Finally, is intermittency the signature of an underlying universal turbulent equilibrium? Why does the flow dissipate a required flux in periodic turbulent bursts instead of in a continuous, but weaker turbulent equilibrium? This connects with the previous observation that fully-developed SID turbulence has a nearly uniform equilibrium gradient Richardson number $Ri_g \approx Ri_e$ across the shear layer (see (5)). The idea of forced stratified turbulence being attracted to a constant $Ri_e = O(0.1)$ was already clear to Turner in 1973 in his discussion of internal mixing processes [20, § 10.2] and connects to Monin–Obukhov similarity theory [73]. It was also was interpreted in Holmboe wave turbulence [74] as a manifestation of self-organised criticality [75]. Self-organisation around $Ri_e = 1/4$ is now central to the "marginal instability" paradigm for ocean turbulence [76,77].

4.3. *Turbulent parameterisations, length scales and spectra*

A key objective in the GAFD community is to predict from a known ambient flow the unknown turbulent buoyancy flux $B = \langle w'b' \rangle$ (previously sketched in Figure 5(c)), where $b' = -g(\rho' - \rho_0)/\rho_0 = -(g'/2)\widetilde{\rho}'$). The simplest and most widely used parameterisation is the "flux-gradient" model, $B = \kappa_T N^2$, which posits that an unknown eddy diffusivity κ_T acts against the large-scale, stable gradient $N^2 = \partial\langle b \rangle/\partial z = -(g'/H)\partial\langle\widetilde{\rho}\rangle/\partial\widetilde{z}$, by analogy with the molecular flux κN^2. The turbulent enhancement of buoyancy transport orders of magnitude above molecular values is quantified by the ratio

$$\frac{\kappa_T}{\kappa} = \frac{B}{\kappa N^2} = \frac{\nu}{\kappa}\frac{B}{\varepsilon}\frac{\varepsilon}{\nu N^2} = Pr\,\Gamma\,Re_b. \tag{7}$$

This key ratio is expressed as the product of three dimensionless parameters: the known Prandtl number Pr and the unknown (diagnostic) mixing efficiency $\Gamma = B/\varepsilon$ introduced earlier, and the "buoyancy Reynolds number"

$$Re_b = \frac{\varepsilon}{\nu N^2} = Re\frac{\widetilde{\varepsilon}}{\widetilde{N}^2} \approx Ri_e^{-1}\,Re\,\widetilde{\varepsilon} \approx 0.2\,Re\,\theta. \tag{8}$$

In the above we used the observation that $\widetilde{N}^2 \approx Ri_e \approx 0.15$ (though Ri_e is expected to vary slightly with δ, see (5)), and the keystone of SID turbulence for $\widetilde{\varepsilon}$ (see (6)). This key result connects the diagnostic Re_b in the shear layer to the prognostic $Re\,\theta$. In other words, $\kappa_T/\kappa \approx 0.2\,\Gamma\,Pr\,Re\,\theta$, meaning that the key to unravel this mysterious ratio in SID lies in Γ.

What is the value of the mixing efficiency Γ? This question has long been and remains debated [4,78] given the leading role of Γ on the meridional overturning circulation of the ocean, and thus, on upwelling and downwelling rates [79]. More work is needed to understand why the canonical $\Gamma = 0.2$ used by oceanographers appears robust in observations [4,80,81] despite theoretical arguments that Γ should vary substantially with the nature of the turbulence, including with Re_b and Pr. In SID, the experimental data at $Re_b \approx 20$ and $Pr = 700$ suggest $\Gamma \approx 0.05 - 0.1$ [48] while the DNS data at $Pr = 7$ suggest $\Gamma = 0.1$ [40]. These values are two to three times below the value expected from parameterisations of $\Gamma(Re_b)$ developed using transient K-H turbulence at $Pr = 1$ [82]. Could these lower values of Γ in SID turbulence be due to the sustained forcing and much higher Pr [83]?

What does the important buoyancy Reynolds number Re_b represent? A scaling analysis of the Navier–Stokes equations reveals that in a stratified, anisotropic flow with a horizontal length scale L_h much larger than its vertical length scale, the vertical diffusion term is controlled not by Re but by $Re_b = Re\,F_h^2$, where $F_h = U/(L_h N)$ is the horizontal Froude number [84]. Stratified turbulence requires not only a large Re and $Re_b \gg 20$ but also a small $F_h \ll 1$ to ensure the scalar remains active. This interpretation is consistent with the definition (8), i.e. $Re_b = \varepsilon/(\nu N^2) \approx Re\,F_h^2$, if we accept the inertial (unstratified) scaling $\varepsilon \approx U^3/L_h$. The requirement $F_h \ll 1$ then ensures that a high Re_b is not achieved by a vanishing N^2. While this regime is notoriously difficult to achieve and sustain in DNS, (8) shows that it is surprisingly easy in SID. This is because stratification is always strong as $F_h \approx (0.2\theta)^{1/2} \leq 0.2$ using our self-imposed bound $\theta \leq 0.2$ rad $\approx 11°$. The sustained production and dissipation of turbulence by θ can thus access intense stratified turbulence $Re_b = O(10^2 - 10^3)$ even at the modest laboratory scale of $Re = O(10^4)$. Furthermore, the community's interpretation of Re_b as a turbulent intensity is fully consistent with the regimes transitions in SID, which are controlled by the volume-averaged turbulent strain rate tensor $\|\widetilde{\mathsf{s}}'\|^2 \approx 0.02\,Re\theta \approx 0.1\,Re_b$.

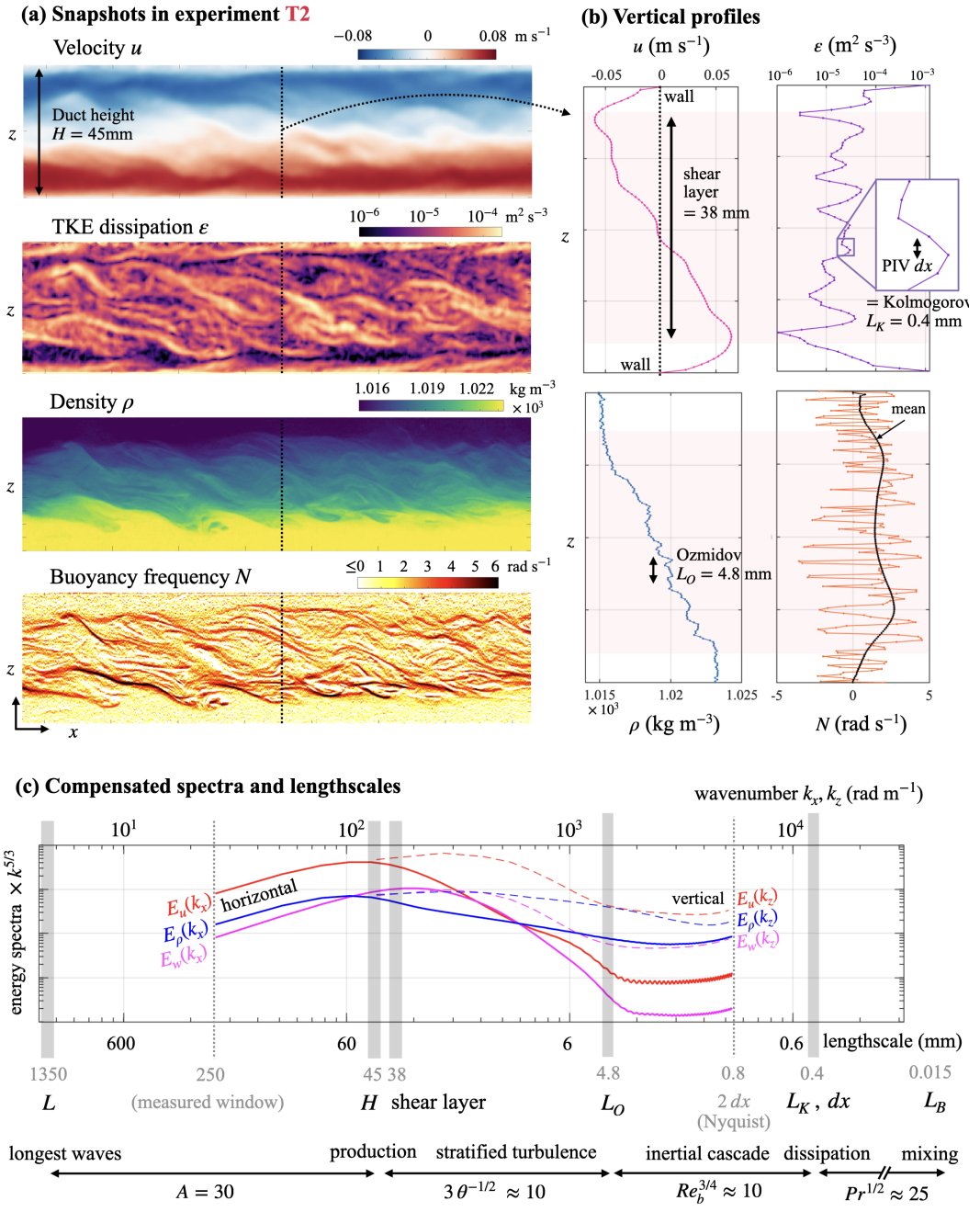


Figure 7. Fully-developed turbulence visualised by (a) two-dimensional snapshots, (b) one-dimensional profiles, and (c) energy spectra of u', w', ρ' demonstrating the hierarchy of length scales in dimensional units (see Sec. 4.3). We show the same T2 data as in Figure 4 at $Re_b = 20$. The data are shown without filtering, except ρ, which requires the raw LIF image to be filtered, and thus, down-sampled. Although the resolution of ρ still exceeds that of **u**, energetics and spectra are computed here after collocating both on a grid of resolution dx, set by the PIV. The challenge of measuring turbulence at higher dynamic range Re_b is addressed in Sec. 5 and Figure 8.

What are the length scales of SID turbulence? It is useful to interpret Re_b as the ratio of the Ozmidov scale L_O to the Kolmogorov scale L_K:

$$Re_b = \left(\frac{L_O}{L_K}\right)^{4/3} \text{ where } L_O = \left(\frac{\varepsilon}{N^3}\right)^{1/2} \text{ and } L_K = \left(\frac{\nu^3}{\varepsilon}\right)^{1/4}, \tag{9}$$

Thus, Re_b is the dynamic range of scales that are neither affected by stratification ($< L_O$) nor by viscous dissipation ($> L_K$). To illustrate these scales in SID, Figure 7 (a) shows a snapshot of $(u, \varepsilon, \rho, N)(x, z)$ in dimensional units and Figure 7 (b) shows corresponding vertical profiles using the T2 data at $Re_b = 20$ (as previously shown in Figure 4). Black arrows indicate the important length scales in SID turbulence: the duct height $H = 45$ mm, shear layer height 38 mm, the Ozmidov scale $L_O = 4.8$ mm, and the Kolmogorov scale $L_K = 0.4$ mm, which is here equal to the resolution of the PIV data dx.

The energy spectra in Figure 7 (c) help illustrate the separation between these scales (large to small from left to right). The compensated horizontal spectra of u (solid red), w (solid pink), ρ (solid blue) peak near the production scale H, before decaying in the stratified turbulence range until L_O, and plateauing in the inertia range towards L_K (the vertical spectra in dashed lines follow a similar trend). The plateau between L_O and L_K corresponds to a $k^{-5/3}$ decay consistent with the classical Kolmogorov cascade expected in this range. However, this may be fortuitous, keeping in mind that spectra can suffer distortions at high wavenumbers due to the nature of PIV and the computation of Fourier transforms on non-periodic grided data [48]. Furthermore, the dynamical interpretation of scales defined in (8) should consider numerical prefactors which may be significant [85]. The dissipation range may in fact start at $10L_K$ or above, in which case the T2 data shown in Figure 7 would be too viscous to even have an inertial range. These spectra also highlight the challenges of resolving scales below L_K, where at high Pr a broad viscous-convective subrange exists down to $L_B = L_K\, Pr^{-1/2} = 15\,\mu$m here [86]. How do these microscopic scales feed back on the large scale flow and control layering and mixing efficiency [83]? We have shown in this section that SID is well suited to tackle stratified turbulence at high Re_b and Pr. In the next section, we explain how this could be achieved in the laboratory by future researchers.

5. The future: measuring geophysical stratified turbulence in the laboratory

5.1. *Scaling up SID*

Faced with the challenge of increasing the dynamic range Re_b, the SID experimenter must decide on three main parameters: the physical height of the duct H (units: m), the dimensionless density difference driving the flow Δ, and the tilt of the apparatus θ. Table 2 summarises how these three parameters control the scaling of the key SID variables. The peak flow speed in each layer is approximately $U \approx (g'H)^{1/2} \approx 3.1\, H^{1/2}\, \Delta^{1/2}$ m s^{-1} (assuming a maximum mass flux $Q_m \approx 0.5$). The dimensional translation of the keystone of SID turbulence for the time- and volume-averaged TKE dissipation within the shear layer (6) is $\varepsilon \approx 0.035\theta\, U^3/(H/2) \approx 2.2\ H^{1/2}\, \Delta^{3/2}\theta$ m^2 s^{-3} (or W kg^{-1}). The buoyancy frequency scales with $(g'/H)^{1/2}$ and we find an average $N \approx 2.6\, H^{-1/2}\, \Delta^{1/2}$ (the pre-factor varies across the shear layer between $1.0 - 4.5$). The expressions for Re, Re_b, L_O and L_K follow from (1), (8) and (9). The separation of scale between the shear layer height H, the Ozmidov scale L_O and the Kolmogorov scale L_K are deduced as

$$\frac{H}{L_O} \approx 3\,\theta^{-1/2}, \qquad \frac{H}{L_K} \approx 3.8\times 10^4\ H^{9/8}\Delta^{3/8}\theta^{1/4}, \qquad \frac{L_O}{L_K} \approx 1.3\times 10^4\ H^{9/8}\Delta^{3/8}\theta^{3/4}, \tag{10}$$

as sketched in Figure 8 (a). Comparing with results from the previous section, we note that $L_O/H \approx 0.7F_h$, which is consistent with $Re_b \approx 0.2\, Re\, \theta \approx Re\, F_h^2$ and $L_h \approx 0.7L_O$.

Table 2. Key estimates for SID turbulence as functions of duct height H (in m), dimensionless density difference Δ, and θ (in radians). The flow speed U is the peak in each layer (used for Re), while $\varepsilon, N, Re_b, L_k$ and L_O are shear-layer averages.

Flow speed (layer peak)	U	$\approx$	$3.1\ H^{1/2}\Delta^{1/2}$	m s^{-1}
TKE dissipation	ε	$\approx$	$2.2\ H^{1/2}\Delta^{3/2}\theta$	m^2 s^{-3}
Buoyancy frequency	N	$\approx$	$2.6\ H^{-1/2}\Delta^{1/2}$	rad s^{-1}
Reynolds number	Re	$\approx$	$1.6\times10^6\ H^{3/2}\Delta^{1/2}$	–
Buoyancy Reynolds	Re_b	$\approx$	$3.1\times10^5\ H^{3/2}\Delta^{1/2}\theta$	–
Ozmidov scale	L_O	$\approx$	$0.34\ H\,\theta^{1/2}$	m
Kolmogorov scale	L_K	$\approx$	$2.6\times10^{-5}\ H^{-1/8}\Delta^{-3/8}\theta^{-1/4}$	m

The expressions for $(\varepsilon, N)(H, \Delta, \theta)$ allow us to compare in Figure 8 (b) the "practical" SID region (in yellow) to geophysical stratified turbulence (in purple) [87,88]. The yellow region is the two-dimensional projection of a cuboid whose sides are spanned by H, Δ, θ (see black arrows). The overlap in this diagram is remarkable as it shows that by varying these three simple parameters, SID can reproduce the low ε and N found, for example, in the deep ocean as well as the high ε and N found, for example, in the upper ocean and estuaries. Overlap in this dimensional space is, however, not necessary to tackle geophysical stratified turbulence; it is sufficient to achieve similitude in the dimensionless Re_b. By spanning nearly three orders of magnitude $Re_b = O(10-10^4)$, SID can be dynamically similar – and thus simulate – the vast majority of geophysical conditions. In fact, it remains to be seen if exploration well above $Re_b = O(10^2)$ is necessary, as DNS suggest that an asymptotic state may be reached around $Re_b = 300$ [89].

What values of Re and Re_b can the experimenter achieve? Figure 8 (c-d) illustrates their scaling in the (H, Δ) plane, noting that we assumed for Re_b a modest tilt $\theta = 0.1 \approx 6^\circ$ (as in the T2 data, shown by a red star). What determines the limits of the "practical SID region" in yellow? Practical considerations suggest that we keep the duct height 0.05 m $\leq H \leq$ 0.5 m, while the Boussinesq approximation and matching the refractive indices for PIV and LIF with $NaCl/NaNO_3$ salts suggest $\Delta \leq 0.05$. Using these maximum values, one can reach $Re \approx 10^5$ and $Re_b \approx 2000$. Since $Re_b \propto \theta$, this value (and all Re_b contour values in Figure 8 (d)) would be doubled for $\theta = 0.2$ rad $\approx 11^\circ$, a suggested maximum for turbulence to remain nearly horizontal and thus stably stratified. Next, the choice of θ is connected to the duct aspect ratio A, or equivalently, its geometrical slope $\alpha \approx A^{-1}$. Forced flow conditions with dissipation obeying (6) require a forcing parameter $\theta/\alpha \geq 1$, but keeping the mixed layer below 70 % of the duct height to avoid boundary effects requires $\theta/\alpha \leq 3$ according to (3). These bounds suggest $0.016 \leq \theta \leq 0.2$, the minimum being achieved for $\theta = \alpha = 1/60 \approx 1^\circ$ (for $A = 60$) and the maximum $\theta = 3\alpha = 3/15 \approx 11^\circ$ (for $A = 15$). This effectively suggests that the duct should be long enough ($A \geq 15$) but not too long ($A \leq 60$) for the setup to remain practical and for θ to remain measurable. Figure 8 (e) shows how the $(\theta/\alpha, A)$ space influences the separation of scale H/L_O. As $H/L_O \approx 1.4F_h^{-1}$ the top left corner the yellow region ($F_h \approx 0.2$) harbours less strongly stratified turbulence, and thus more large-scale density overturns [26,27], than the bottom right corner ($F_h \approx 0.06$).

In summary, geophysical values up to $Re_b = O(10^3)$ can be reached in SID. Limiting ourselves for now to the goal of reaching $Re_b = 300$ to test the hypothesis of an asymptotic behaviour [89], the green regions in Figure 8 (c-d) show that such values have already been achieved. Shadowgraph data exists up to $Re = 200,000$ and $Re_b = 300$ was achieved with $H = 0.1$ m [16,25,33], while more recently $Re_b = 100$ was achieved with a more modest $H = 0.05$ m [26,32]. Velocity measurements, however, do not yet exist at these high Re_b, not least because of the very large separation

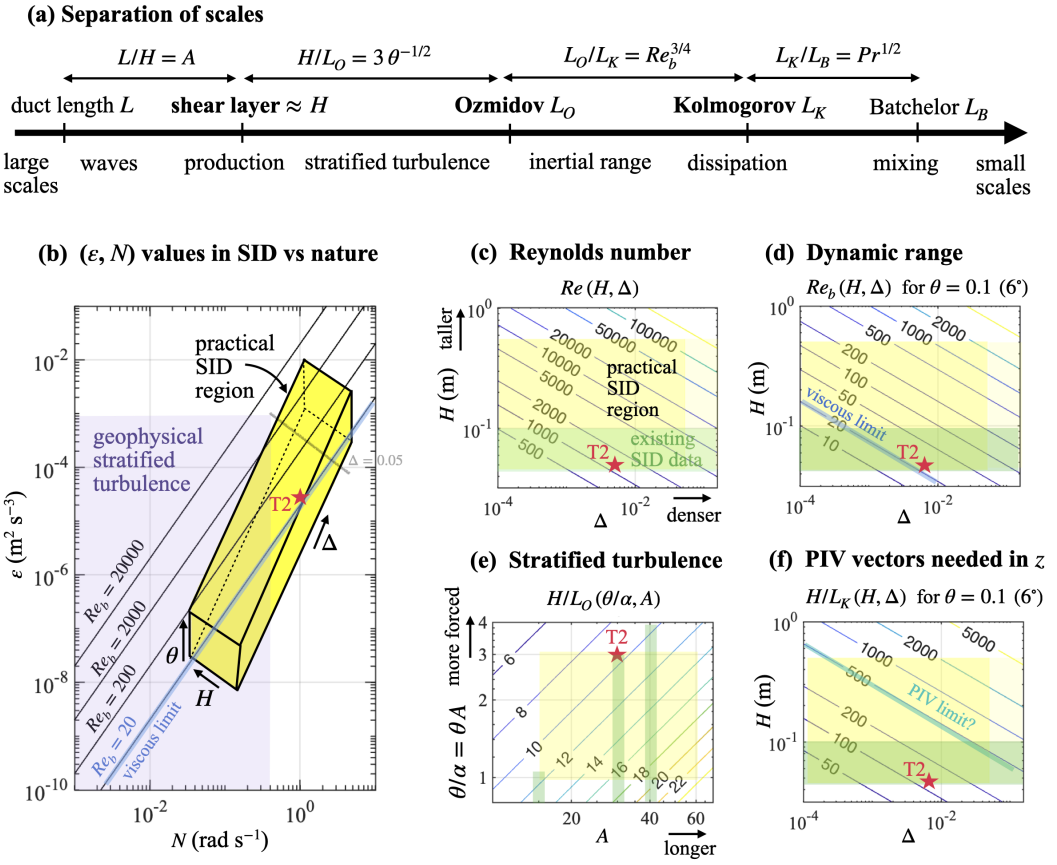


Figure 8. Geophysical stratified turbulence in the laboratory using SID (see Sec. 5). (a) The separation between scales is controlled by the dynamic range $Re_b \approx 0.2\,Re\theta$, as well as A, θ, and Pr. (b) SID can access $Re_b = O(10^3 - 10^4)$ (in yellow), with significant overlap in dimensional (ε, N) in strongly stratified (high N) geophysical flows. The arrows on the sides of the yellow "practical SID region" cuboid show the effect of increasing the duct height H, density difference Δ and tilt θ within the practical bounds discussed in the main text $H \in [0.05\,\mathrm{m}, 0.5\,\mathrm{m}]$, $\Delta \in [0.0001, 0.15]$ (or 0.05, annotated in grey, to satisfy Boussinesq and match refractive indices), and $\theta \in [1^\circ, 11^\circ]$. The scaling of (c) Re, (d) Re_b with H and Δ show that $Re_b = O(10^3)$ may be obtained at relatively modest laboratory values of $Re = O(10^5)$ thanks to θ, according to (8). The scaling of (e) $H/L_O(\theta/\alpha, A)$ shows how the tilt θ and the duct aspect ratio A influence the nature of stratified turbulence, while (f) $H/L_K(\Delta, H)$ shows the required resolution of PIV measurements, which controls the design of future experiments.

of scale H/L_K and the required PIV resolution (see Figure 8 (f)). Next, we discuss how to make them a reality.

5.2. *Experimental design and technological challenges*

What makes accurate PIV and LIF measurements so challenging at high Re_b? How should future SID experiments be designed to achieve a new milestone at $Re_b = 300$? (This would be over an order of magnitude above the T2 data at $Re_b = 20$ shown in Figures 4 and 7.)

First, we need to choose the duct height, which, according to table 2, is $H \approx 2.2 \times 10^{-4}\, Re_b^{2/3}\, \Delta^{-1/3}\, \theta^{-2/3}$ (in m). Achieving $Re_b = 300$ under the constraints $\Delta \leq 0.05$ and $\theta \leq 0.2$ requires a minimum height $H \geq 80$ mm, as well as $Re \approx 5\, Re_b\, \theta^{-1} \geq 8000$ and $H/L_K \approx 2.9\, Re_b^{3/4}\, \theta^{-1/2} \geq 500$. These minimum values assume the maximum $\theta = 0.2 = 3\alpha$ with the minimum aspect ratio $A = 15$, and they would all increase for a lower θ or higher A. Can we select the minimum height of $H = 80$ mm to keep the apparatus as compact as possible? Unfortunately not, because it would be too small for PIV. The reason is that a distinct pattern of particles in each interrogation window suggests a minimum vector spacing of $dx \geq 500\,\mu$m, considering that particles should have a diameter $\geq 30\,\mu$m due to limits on the particle seeding density and the diffraction of visible light. Furthermore, we wish to resolve the Kolmogorov scale, i.e. $dx = L_K$, to obtain velocity spectra accurate down to a scale no smaller than $\approx 5L_K$ (because of the Nyquist cut-off and high-wavenumber filtering artefacts inherent to PIV and Fourier transforms [48]). As a result, the duct height must be scaled up to a minimum height of $H = 500\, L_K = 500\, dx = 250$ mm and length of $L = A\, H = 3.75$ m. Conveniently, this larger scale allows us to achieve our target $Re_b = 300$ and $Re = 8000$ with a lower $\Delta \approx 0.0015$ (which is more forgiving for matching refractive indices) and slower velocity U (and thus a better "freezing" of the flow by scanning).

Does the camera hardware impose further constraints? Not substantially. Using PIV interrogation windows that are a minimum of 20 pixels wide and a vector spacing of 10 pixels (50 % overlap between windows), resolving the separation of scale $H/L_K = H/dx = 500$ along z requires 5000 pixels, which around the current limit of high-speed cameras (note that the aspect ratio of the image would limit the extent of the domain along x). Even in an ideal world where LIF would output a meaningful density data point per pixel, we will likely never resolve the separation of scales $H/L_B \approx 500\, Pr^{1/2} \approx 13{,}000$. In reality, the LIF signal is not expected to be at a much higher usable resolution than the PIV signal because filtering is almost always required to eliminate various sources of high-frequency noise in the dye intensity signal, which is why it is often collocated on the PIV grid. Numerical data assimilation is a promising direction to super-resolve the flow between $L_K = 500\,\mu$m and $L_B = 20\,\mu$m. Physics-informed neural networks can achieve this without having to simulate the flow (which would be prohibitively expensive) as was shown in SID [90]. However, strongly turbulent flows pose convergence and implementation challenges which future research will hopefully resolve.

Next, what scanning and laser frequencies are required to reconstruct quasi-instantaneous three-dimensional volumes? To scan the duct width in an ambitious dimensionless time of 0.4, the traversing speed should be $5BU \approx 300\,\text{mm s}^{-1}$ assuming a square duct $B = 1$. To ensure that at least 90% of the time is spent scanning the volume at constant speed, each ramp-up and ramp-down phases on either end of the volume should have an acceleration of at least $\approx 500\, B\, g' \approx 0.75g$ with adequate vibration control. To fit $n_y = 200$ planes across y (with a spacing of 2.5 mm typical of the thickness of a laser sheet), the frequency of the dual-cavity pulsed laser should be $5n_y(g'/H)^{1/2} = 250$ Hz (note the scaling with the buoyancy frequency). As far as video recording is concerned, this setup would output a typical 250 pairs of $5 \times 5 = 25$ MPixels raw images per second per camera (assuming a square image). Assuming an 8-bit depth suitable for PIV (but limiting for LIF) this would require a bandwidth of 100 Gbit s^{-1} = 12.5 GB s^{-1} per camera. This precisely matches the best 100 Gigabit Ethernet networking technology, but it exceeds the current speed of solid state drives. Progress on computing hardware is thus needed to match the desired scanning speed. Parallelised PIV post-processing is also required (now standard in the DigiFlow software [44]), and would output volumes of $500 \times 200 \times 500 = 5 \times 10^8$ vectors in (x, y, z).

What reservoirs are needed on either side of the duct? Here a generous rule of thumb is to sustain a layer-averaged exchange flow rate of $(U/2)BH^2/2$ during five duct transit times $5AH/(U/2) \approx 625$ s for the turbulent dynamics to be in quasi-equilibrium (corresponding to $20A = 300$ shear time scales). Each reservoir should therefore have a volume $5ABH^3 \approx 1.2\,\text{m}^3$,

i.e., twice the exchanged volume, assuming the duct connects at mid-level in both reservoirs and neglecting mixing. (Note this volume will increase if the experimenter chooses $B > 1$ to reduce the influence of side walls.) Finally, how much salt should be dissolved in each reservoir? Achieving the density difference Δ at a matched refractive index would require concentrations of ≈ 0.8 wt % $NaNO_3$ and ≈ 0.5 wt % NaCl corresponding to a modest ≈ 10 kg and ≈ 6 kg of dry salt, respectively.

Other challenges are worth highlighting. First, this experiment would generate at least $\approx 3 \times 12.5$ GB/s $\times 625$ s ≈ 23 TB of raw data. Although the processed data would be more compact, data transfer, storage and back up resources become a key issue. Post-processing times are also expected to increase, perhaps from a few days to a few weeks per experiment. Second, the time needed for the preparation and acquisition of experiments, often by a pair of experimentalists, depends on the size of the reservoirs and other design details. This time ranged from one or two days per experiment with the "second generation" apparatus (see Sec. 2.2) having reservoirs of volume ~ 0.08 m^3 each and an easily-accessible 1.35 m-long duct thanks to open-lid reservoirs, to several days with the "third generation" apparatus having reservoirs of volume ~ 0.4 m^3 each and a less accessible 2 m-long duct because of closed lids. The advanced nature of the imaging also requires much trial and error; not all experiments yield usable data.

In summary, these guidelines illustrate how PIV imaging at the small Kolmogorov scales at high Re_b imposes a minimum duct height H controlling the overall design of SID experiments. The greatest challenge lies in the acquisition of near-instantaneous volumetric data, particularly because of the required scanning and recording speed. Relaxation of a few specifications, ingenious workarounds and technological progress will allow future researchers to get very valuable data at $Re_b = O(10^2)$.

6. Conclusions

In conclusion, the Stratified Inclined Duct (SID, see Sec. 2) is a conceptually simple laboratory experiment that allows us to control and measure shear-driven, stably-stratified turbulence with the necessary and sufficient realism and complexity needed to drive substantial progress in geophysical and astrophysical fluid dynamics (GAFD). This paper focused on transition and mixing, which are two theoretical and practical questions central to GAFD.

When turbulence sets in, the transition is often mediated by internal or interfacial waves and shear instabilities, which control where and when turbulence grows, persists, or decays. In SID, the multi-dimensional parameter space spanned by the Reynolds number Re, the tilt angle θ and the Prandtl number Pr gives rise to a variety of flow regimes and transitional states between them. Successive generations of measurements, including shadowgraph data (Sec. 3.1), mass flux data (Sec. 3.2), and fully-resolved three-dimensional velocity and density data (Sec. 3.3), recently assisted by direct numerical simulations (DNS), discovered multiple supercritical bifurcations, but also raised a multitude of questions, in particular on the ultimate route to chaos (Sec. 4.1). The dynamical systems "skeleton" of high-Re and high Pr turbulence, both in geophysics and in SID, is intimately connected to spatio-temporal intermittency, layering and self-organising equilibria, on which much remains to be discovered (Sec. 4.2).

When turbulence intensifies, small-scale mixing vastly enhances the transport of the buoyancy (heat, salt) and other scalars, with leading-order feedbacks and implications on the large-scale flows such as those controlling Earth's climate. The effects of mixing are captured by parameterisations, typically using the eddy diffusivity in (7). A key challenge lies in understanding how the mixing efficiency Γ scales with Pr and with the turbulent intensity called the buoyancy Reynolds number Re_b, which is also a key separation of scales (Sec. 4.3). In SID, the continuous baroclinic generation of sheared turbulence by a sufficiently large tilt of the duct is balanced by the dissipation, in an equilibrium distilled in the "keystone" equation (6). SID thus offers the rare

ability to control and sweep through Re_b with the simple product $Re\theta$ (see (8)), thereby accessing values of $Re_b = O(10-10^3)$ relevant to most geophysical turbulence and allowing us to extrapolate laboratory results. Practical design guidelines should assist future efforts to scale SID up (Sec. 5.1) and overcome spatial resolution challenges (Sec. 5.2) to measure the full flow field at $Re_b = 300$. This is an order of magnitude above current values and would be a new decisive milestone for the community.

Experimental data outputs are now converging with what would be expected from DNS, which remain extremely costly and challenging in this parameter regime. Data assimilation offers exciting prospects to accelerate this convergence. DNS of sufficiently real and complex flows inspired and validated by laboratory experiments have been and will remain powerful and complementary tools. We hope this paper may inspire future combined experimental and numerical investigations of SID, and mobilise the collective expertise of the community needed to unravel the intricacies of geophysical stratified turbulence.

Acknowledgements

I am deeply grateful to P. F. Linden for the opportunity to work on this fascinating problem and for his invaluable mentorship. I am also indebted to S. B. Dalziel, who conceived the volumetric scanning technique, and to J. L. Partridge, X. Jiang, G. Kong and the technicians of the G. K. Batchelor Laboratory for their precious experimental expertise and support. This paper is enriched by the collaborations and discussions I have been fortunate to have over the years, particularly with the stratified turbulence group in DAMTP. Finally, I acknowledge support from the 2023 GFD program at the Woods Hole Oceanographic Institution and discussions that contributed to this paper, including with S. M. de Bruyn Kops, C. P. Caulfield, T. S. Eaves, W. R. Geyer, D. Lohse, J. J. Riley and B. R. Sutherland.

Declaration of interests

The author does not work for, advise, own shares in, or receive funds from any organisation that could benefit from this article, and have declared no affiliation other than their research organisations

References

[1] E. A. D'Asaro, "How do Internal Waves Create Turbulence and Mixing in the Ocean?", 2022. Preprint, ESS Open Archive.

[2] A. V. Melet, R. Hallberg and D. P. Marshall, "The role of ocean mixing in the climate system", in *Ocean Mixing. Drivers, Mechanisms and Impacts*, Elsevier, 2022, pp. 5–34.

[3] C. P. Caulfield, "Open questions in turbulent stratified mixing: Do we even know what we do not know?", *Phys. Rev. Fluids* **5** (2020), article no. 110518.

[4] M. C. Gregg, E. A. D'Asaro, J. J. Riley and E. Kunze, "Mixing efficiency in the ocean", *Ann. Rev. Mar. Sci.* **10** (2018), pp. 443–473.

[5] T. Dauxois et al., "Confronting Grand Challenges in environmental fluid mechanics", *Phys. Rev. Fluids* **6** (2021), no. 2, article no. 020501.

[6] B. R. Sutherland, *Internal Gravity Waves*, Cambridge University Press, 2010.

[7] C. P. Caulfield, "Layering, instabilities, and mixing in turbulent stratified flows", *Ann. Rev. Fluid Mech.* **53** (2021), pp. 113–145.

[8] W. D. Smyth and J. N. Moum, "Length scales of turbulence in stably stratified mixing layers", *Phys. Fluids* **12** (2000), no. 6, pp. 1327–1342.

[9] P. Bartello and S. M. Tobias, "Sensitivity of stratified turbulence to the buoyancy Reynolds number", *J. Fluid Mech.* **725** (2013), pp. 1–22.

[10] S. Almalkie and S. M. De Bruyn Kops, "Kinetic energy dynamics in forced, homogeneous, and axisymmetric stably stratified turbulence", *J. Turbul.* **13** (2012), article no. N29.

[11] M. M. P. Couchman, S. M. de Bruyn Kops and C. P. Caulfield, "Mixing across stable density interfaces in forced stratified turbulence", *J. Fluid Mech.* **961** (2023), article no. A20.

[12] M. Avila, D. Barkley and B. Hof, "Transition to Turbulence in Pipe Flow", *Ann. Rev. Fluid Mech.* **55** (2023), pp. 575–602.

[13] D. Lohse and O. Shishkina, "Ultimate turbulent thermal convection", *Phys. Today* **76** (2023), no. 11, pp. 26–32.

[14] D. Feldmann, D. Borrero-Echeverry, M. J. J. Burin, K. Avila and M. Avila, "Routes to turbulence in Taylor–Couette flow", *Philos. Trans. R. Soc. Lond., Ser. A* **381** (2023), no. 2246, article no. 20220114.

[15] D. Lohse, "Causality in Rayleigh–Bénard and Taylor-–Couette turbulence", in *Caust Workshop on Causality in Turbulence and Transition*, 2022.

[16] C. R. Meyer and P. F. Linden, "Stratified shear flow: experiments in an inclined duct", *J. Fluid Mech.* **753** (2014), pp. 242–253.

[17] O. Reynolds, "An experimental investigation of the circumstances which determine whether the motion of water shall be direct or sinuous, and of the law of resistance in parallel channels", *Philos. Trans. R. Soc. Lond.* **174** (1883), pp. 935–982.

[18] S. A. Thorpe, "Experiments on the instability of stratified shear flows: miscible fluids", *J. Fluid Mech.* **46** (1971), no. 02, pp. 299–319.

[19] E. O. Macagno and H. Rouse, "Interfacial mixing in stratified flow", *J. Eng. Mech.* **87** (1961), no. 5, pp. 55–81.

[20] J. S. Turner, *Buoyancy effects in fluids*, Cambridge University Press, 1973.

[21] G. I. Taylor, "An Experiment on the Stability of Superposed Streams of Fluid", *Math. Proc. Camb. Philos. Soc.* **23** (1927), no. 6, pp. 730–731.

[22] E. J. Strang and H. J. S. Fernando, "Entrainment and mixing in stratified shear flows", *J. Fluid Mech.* **428** (2001), pp. 349–386.

[23] P. Odier, J. Chen and R. E. Ecke, "Entrainment and mixing in a laboratory model of oceanic overflow", *J. Fluid Mech.* **746** (2014), pp. 498–535.

[24] A. Lefauve, J. L. Partridge, Q. Zhou, C. P. Caulfield, S. B. Dalziel and P. F. Linden, "The structure and origin of confined Holmboe waves", *J. Fluid Mech.* **848** (2018), pp. 508–544.

[25] A. Lefauve and P. F. Linden, "Buoyancy-driven exchange flows in inclined ducts", *J. Fluid Mech.* **893** (2020), article no. A2.

[26] A. Lefauve and M. M. P. Couchman, "Data-driven classification of sheared stratified turbulence from experimental shadowgraphs", *Phys. Rev. Fluids* **9** (2024), article no. 034603.

[27] A. Lefauve and P. F. Linden, "Experimental properties of continuously forced, shear-driven, stratified turbulence. Part 1. Mean flows, self-organisation, turbulent fractions", *J. Fluid Mech.* **937** (2022), article no. A34.

[28] C. S. Ng, A. Ooi, D. Lohse and D. Chung, "Bulk scaling in wall-bounded and homogeneous vertical natural convection", *J. Fluid Mech.* **841** (2018), pp. 825–850.

[29] T. Maxworthy, "Experiments on gravity currents propagating down slopes. Part 2. The evolution of a fixed volume of fluid released from closed locks into a long, open channel", *J. Fluid Mech.* **647** (2010), pp. 27–51.

[30] Y. Tanino, F. Moisy and J.-P. Hulin, "Laminar-turbulent cycles in inclined lock-exchange flows", *Phys. Rev. E* **85** (2012), no. 6, article no. 066308.

[31] A. Lefauve, *Waves and turbulence in sustained stratified shear flows*, PhD thesis, University of Cambridge, Cambridge, United Kingdom, 2018.

[32] X. Jiang, G. Kong and A. Lefauve, *Shadowgraph visualisations of salt-stratified turbulence obtained in a stratified inclined duct (SID) laboratory experiment*, dataset, Apollo - University of Cambridge Repository (December 14, 2023). https://doi.org/10.17863/CAM.104471, 2023.

[33] A. Lefauve and P. F. Linden, *Research data supporting "Buoyancy-driven exchange flows in inclined ducts"*, dataset, Apollo - University of Cambridge Repository (April 17, 2020). https://doi.org/10.17863/CAM.48821, 2020.

[34] D. E. Kiel, *Buoyancy driven counterflow and interfacial mixing*, PhD thesis, University of Cambridge, Cambridge, United Kingdom, 1991.

[35] G. O. Hughes and P. F. Linden, "Mixing efficiency in run-down gravity currents", *J. Fluid Mech.* **809** (2016), pp. 691–704.

[36] J. B. Schijf and J. C. Schönfled, "Theoretical considerations on the motion of salt and fresh water", in *Proceedings Minnesota International Hydraulic Convention*, IAHR, 1953, pp. 321–333.

[37] L. Armi, "The hydraulics of two flowing layers with different densities", *J. Fluid Mech.* **163** (1986), pp. 27–58.

[38] D. Z. Zhu and G. A. Lawrence, "Hydraulics of exchange flows", *J. Hydraul. Eng.* **126** (2000), no. 12, pp. 921–928.

[39] L. Gu and G. A. Lawrence, "Analytical solution for maximal frictional two-layer exchange flow", *J. Fluid Mech.* **543** (2005), pp. 1–17.

[40] L. Zhu, A. Atoufi, A. Lefauve, J. R. Taylor, G. A. Lawrence, S. B. Dalziel, R. R. Kerswell and P. F. Linden, "Stratified inclined duct: direct numerical simulations", *J. Fluid Mech.* **969** (2023), article no. A20.

[41] A. Atoufi, L. Zhu, A. Lefauve, et al., "Stratified inclined duct: two-layers hydraulics and instabilities", *J. Fluid Mech.* **977** (2023), article no. A25.

[42] J. L. Partridge, A. Lefauve and S. B. Dalziel, "A versatile scanning method for volumetric measurements of velocity and density fields", *Meas. Sci. Tech.* **30** (2019), article no. 055203.

[43] A. Lefauve and P. F. Linden, *Research data supporting "Experimental properties of continuously-forced, shear-driven, stratified turbulence"*, dataset, Apollo - University of Cambridge Repository (February 7, 2022). https://doi.org/10.17863/CAM.75370, 2022.

[44] S. B. Dalziel, M. Carr, J. K. Sveen and P. A. Davies, "Simultaneous synthetic schlieren and PIV measurements for internal solitary waves", *Meas. Sci. Tech.* **18** (2007), no. 3, pp. 533–547.

[45] A. Lefauve, J. L. Partridge and P. F. Linden, *Research data supporting "Regime transitions and energetics of sustained stratified shear flows"*, dataset, Apollo - University of Cambridge Repository (July 22, 2019). https://doi.org/10.17863/CAM.41410, 2019.

[46] K. B. Winters, P. N. Lombard, J. J. Riley and E. A. D'Asaro, "Available potential energy and mixing in density-stratified fluids", *J. Fluid Mech.* **289** (1995), pp. 115–128.

[47] A. Lefauve, J. L. Partridge and P. F. Linden, "Regime transitions and energetics of sustained stratified shear flows", *J. Fluid Mech.* **875** (2019), pp. 657–698.

[48] A. Lefauve and P. F. Linden, "Experimental properties of continuously forced, shear-driven, stratified turbulence. Part 2. Energetics, anisotropy, parameterisation", *J. Fluid Mech.* **937** (2022), article no. A35.

[49] M. C. Cross and P. C. Hohenberg, "Pattern formation outside of equilibrium", *Rev. Mod. Phys.* **65** (1993), no. 3, pp. 851–1112.

[50] D. Barkley, "Theoretical perspective on the route to turbulence in a pipe", *J. Fluid Mech.* **803** (2016), article no. P1.

[51] W. D. Smyth and J. R. Carpenter, *Instability in Geophysical Flows*, Cambridge University Press, 2019.

[52] J. R. Carpenter, E. W. Tedford, E. Heifetz and G. A. Lawrence, "Instability in stratified shear flow: Review of a physical interpretation based on interacting waves", *Appl. Mech. Rev.* **64** (2011), no. 6, article no. 060801.

[53] J. Cudby and A. Lefauve, "Weakly nonlinear Holmboe waves", *Phys. Rev. Fluids* **6** (2021), no. 2, article no. 024803.

[54] Y.-M. Ducimetière, F. Gallaire, A. Lefauve and C. P. Caulfield, "The effects of spanwise confinement on stratified shear instabilities", *Phys. Rev. Fluids* **6** (2021), article no. 103901.

[55] H. Salehipour, C. P. Caulfield and W. R. Peltier, "Turbulent mixing due to the Holmboe wave instability at high Reynolds number", *J. Fluid Mech.* **803** (2016), pp. 591–621.

[56] H. Van Haren, "Stratified turbulence and small-scale internal waves above deep-ocean topography", *Phys. Fluids* **25** (2013), no. 10, article no. 106604.

[57] A. Kaminski, E. A. D'Asaro, A. Y. Shcherbina and R. R. Harcourt, "High-Resolution Observations of the North Pacific Transition Layer from a Lagrangian Float", *J. Phys. Oceanogr.* **51** (2021), no. 10, pp. 3163–3181.

[58] P. Held, K. Bartholomä-Schrottke and A. Bartholomä, "Indications for the transition of Kelvin-Helmholtz instabilities into propagating internal waves in a high turbid estuary and their effect on the stratification stability", *Geo-Mar. Lett.* **39** (2019), no. 2, pp. 149–159.

[59] A. Mashayek and W. R. Peltier, "The 'zoo' of secondary instabilities precursory to stratified shear flow transition. Part 1: Shear aligned convection, pairing, and braid instabilities", *J. Fluid Mech.* **708** (2012), pp. 5–44.

[60] L. Zhu, A. Atoufi, A. Lefauve, R. R. Kerswell and P. F. Linden, "Long-wave instabilities of sloping stratified exchange flows", *J. Fluid Mech.* **983** (2024), article no. A12.

[61] G. Kawahara, M. Uhlmann and L. van Veen, "The Significance of Simple Invariant Solutions in Turbulent Flows", *Ann. Rev. Fluid Mech.* **44** (2012), no. 1, pp. 203–225.

[62] M. D. Graham and D. Floryan, "Exact Coherent States and the Nonlinear Dynamics of Wall-Bounded Turbulent Flows", *Ann. Rev. Fluid Mech.* **53** (2021), pp. 227–253.

[63] P. Cvitanović, "Recurrent flows: the clockwork behind turbulence", *J. Fluid Mech.* **726** (2013), pp. 1–4.

[64] D. Lucas, C. P. Caulfield and R. R. Kerswell, "Layer formation in horizontally forced stratified turbulence: connecting exact coherent structures to linear instabilities", *J. Fluid Mech.* **832** (2017), pp. 409–437.

[65] X. Jiang, A. Lefauve, S. B. Dalziel and P. F. Linden, "The evolution of coherent vortical structures in increasingly turbulent stratified shear layers", *J. Fluid Mech.* **937** (2022), A30.

[66] P. J. Schmid, "Data-driven and operator-based tools for the analysis of turbulent flows", in *Advanced Approaches in Turbulence*, Elsevier, 2021, pp. 243–305.

[67] C. P. Caulfield, W. R. Peltier, S. Yoshida and M. Ohtani, "An experimental investigation of the instability of a shear flow with multilayered density stratification", *Phys. Fluids* **7** (1995), no. 12, pp. 3028–3041.

[68] T. S. Eaves and N. J. Balmforth, "Noisy homoclinic pulse dynamics", *Chaos* **26** (2016), no. 4, article no. 043104.

[69] W. R. Geyer and P. MacCready, "The Estuarine Circulation", *Ann. Rev. Fluid Mech.* **46** (2014), no. 1, pp. 175–197.

[70] F. Chegini et al., "Processes of Stratification and Destratification During An Extreme River Discharge Event in the German Bight ROFI", *J. Geophys. Res. Oceans* **125** (2020), no. 8, article no. e2019JC015987.

[71] W. D. Smyth, J. N. Moum, L. Li and S. A. Thorpe, "Diurnal shear instability, the descent of the surface shear layer, and the deep cycle of equatorial turbulence", *J. Phys. Oceanogr.* **43** (2013), no. 11, pp. 2432–2455.

[72] W. D. Smyth, H. T. Pham, J. N. Moum and S. Sarkar, "Pulsating turbulence in a marginally unstable stratified shear flow", *J. Fluid Mech.* **822** (2017), pp. 327–341.
[73] L. Mahrt, "Stably Stratified Atmospheric Boundary Layers", *Ann. Rev. Fluid Mech.* **46** (2014), no. 1, pp. 23–45.
[74] H. Salehipour, W. R. Peltier and C. P. Caulfield, "Self-organized criticality of turbulence in strongly stratified mixing layers", *J. Fluid Mech.* **856** (2018), pp. 228–256.
[75] P. Bak, C. Tang and K. Wiesenfeld, "Self-organized criticality", *Phys. Rev. A* **38** (1988), no. 1, pp. 364–374.
[76] W. D. Smyth, "Marginal Instability and the Efficiency of Ocean Mixing", *J. Phys. Oceanogr.* **50** (2020), no. 8, pp. 2141–2150.
[77] A. Mashayek, L. E. Baker, B. B. Cael and C. P. Caulfield, "A Marginal Stability Paradigm for Shear-Induced Diapycnal Turbulent Mixing in the Ocean", *Geophys. Res. Lett.* **49** (2022), no. 2, article no. e2021GL095715.
[78] D. Bouffard and L. Boegman, "A diapycnal diffusivity model for stratified environmental flows", *Dyn. Atmos. Oceans* **61-62** (2013), pp. 14–34.
[79] L. Cimoli, C. P. Caulfield, H. K. Johnson, D. P. Marshall, A. Mashayek, A. C. Naveira Garabato and C. Vic, "Sensitivity of Deep Ocean Mixing to Local Internal Tide Breaking and Mixing Efficiency", *Geophys. Res. Lett.* **14** (2019), pp. 14622–14633.
[80] R. C. Holleman, W. R. Geyer and D. K. Ralston, "Stratified Turbulence and Mixing Efficiency in a Salt Wedge Estuary", *J. Phys. Oceanogr.* **46** (2016), no. 6, pp. 1769–1783.
[81] M. Meredith and A. C. Naveira Garabato, *Ocean Mixing: Drivers, Mechanisms and Impacts*, Elsevier, 2021.
[82] A. Mashayek, H. Salehipour, D. Bouffard, C. P. Caulfield, R. Ferrari, M. Nikurashin, W. R. Peltier and W. D. Smyth, "Efficiency of turbulent mixing in the abyssal ocean circulation", *Geophys. Res. Lett.* **44** (2017), no. 12, pp. 6296–6306.
[83] N. Petropoulos, M. M. P. Couchman, A. Mashayek, S. M. De Bruyn Kops and C. P. Caulfield, "Prandtl number effects on extreme mixing events in forced stratified turbulence", *J. Fluid Mech.* **983** (2024), article no. R1.
[84] G. Brethouwer, P. Billant, E. Lindborg and J.-M. Chomaz, "Scaling analysis and simulation of strongly stratified turbulent flows", *J. Fluid Mech.* **585** (2007), pp. 343–368.
[85] S. M. de Bruyn Kops, "Classical scaling and intermittency in strongly stratified Boussinesq turbulence", *J. Fluid Mech.* **775** (2015), pp. 436–463.
[86] G. K. Batchelor, "Small-scale variation of convected quantities like temperature in turbulent fluid Part 1. General discussion and the case of small conductivity", *J. Fluid Mech.* **5** (1959), no. 01, pp. 113–133.
[87] W. R. Geyer, M. E. Scully and D. K. Ralston, "Quantifying vertical mixing in estuaries", *Environ. Fluid Mech.* **8** (2008), no. 5-6, pp. 495–509.
[88] P. R. Jackson and C. R. Rehmann, "Experiments on Differential Scalar Mixing in Turbulence in a Sheared, Stratified Flow", *J. Phys. Oceanogr.* **44** (2014), no. 10, pp. 2661–2680.
[89] G. D. Portwood, S. M. de Bruyn Kops and C. P. Caulfield, "Asymptotic dynamics of high dynamic range stratified turbulence", *Phys. Rev. Lett.* **122** (2019), article no. 194504.
[90] L. Zhu, X. Jiang, A. Lefauve, R. R. Kerswell and P. F. Linden, "New insights into experimental stratified flows obtained through physics-informed neural networks", *J. Fluid Mech.* **981** (2024), article no. R1.

ACADÉMIE DES SCIENCES
INSTITUT DE FRANCE

Comptes Rendus. Physique
2024, Vol. 25, Special issue S3, p. 509-535
https://doi.org/10.5802/crphys.197

Review article / *Article de synthèse*

Geophysical and astrophysical fluid dynamics in the laboratory / *Dynamique des fluides géophysiques et astrophysiques au laboratoire*

Internal gravity waves versus inertial waves in the laboratory

Ondes internes de gravité versus ondes inertielles au laboratoire

Sylvain Joubaud [*,a], **Samuel Boury** [b] **and Philippe Odier** [a]

[a] Ens de Lyon, CNRS, Laboratoire de Physique, Lyon, France

[b] Université Paris-Saclay, CNRS, FAST, 91405 Orsay, France

E-mails: sylvain.joubaud@ens-lyon.fr (S. Joubaud), samuel.boury@universite-paris-saclay.fr (S. Boury), philippe.odier@ens-lyon.fr (P. Odier)

Abstract. Density-stratified and/or rotating fluids are very common in geophysical and astrophysical flows and enable the propagation of respectively internal gravity waves and inertial waves. Their peculiar dispersion relation has the same mathematical form for both classes of waves and can lead to unexpected outcomes through amplification, resonance or non-linearities. Even though their dispersion relation is very similar, internal gravity waves and inertial waves have different structural characteristics and arise from distinct physical mechanisms. Understanding the analogies and the differences in their behaviors is crucial for studying their respective roles. In this review, we will describe laboratory experiments that have studied either inertial waves in rotating homogeneous fluids or internal gravity waves in non-rotating density stratified fluids to highlight both the similarities and the differences between these two types of waves. We will focus on linear and non-linear phenomena occurring for three different configurations: wave beams in 2D and in 3D geometry, axisymmetric waves, as well as wave attractors, a specific feature for these waves. In particular, we will describe the influence of these various configurations on the Triadic Resonant Instability (TRI).

Résumé. Les fluides stratifiés en densité et/ou tournants sont très courants dans les écoulements géophysiques et astrophysiques et permettent respectivement la propagation d'ondes internes de gravité et d'ondes inertielles. Mathématiquement, la relation de dispersion particulière a la même forme pour les deux classes d'ondes et peut conduire à des résultats inattendus via amplification, résonance ou non-linéarités. Même si leur relation de dispersion est très similaire, les ondes internes de gravité et les ondes d'inertie ont des caractéristiques structurelles différentes et résultent de mécanismes physiques distincts. Comprendre les analogies et les différences dans leurs dynamiques est crucial pour étudier leurs rôles respectifs. Dans cette revue, nous décrirons des expériences en laboratoire qui ont étudié soit les ondes d'inertie dans un fluide homogène en rotation, soit les ondes internes de gravité dans un fluide stratifié en densité non tournant, afin de mettre en évidence à la fois les similitudes et les divergences entre ces deux types d'ondes. Nous nous concentrerons sur les phénomènes linéaires et non linéaires se produisant pour trois configurations différentes : les

* Corresponding author

faisceaux d'ondes en géométrie 2D et 3D, les ondes axisymétriques, ainsi que les attracteurs d'ondes, spécificité de ces ondes. En particulier, nous décrirons l'influence de ces différentes configurations sur l'instabilité triadique résonante (TRI).

Keywords. Internal gravity waves, Inertial waves, Stratified fluid, Rotating fluid, Triadic Resonant Instability, wave attractors.

Mots-clés. Ondes internes de gravité, Ondes inertielles, Fluides stratifiés, Fluides en rotation, Instabilité par résonance triadique, attracteurs d'ondes.

Funding. The authors acknowledge support from the Simons Foundation through Grant No. 651475. S. Joubaud acknowledge the support from Institut Universitaire de France.

Manuscript received 19 April 2024, revised 23 July 2024, accepted 5 August 2024.

1. Introduction

Internal gravity waves and inertial waves are two distinct classes of waves that commonly occur in fluid dynamics, respectively for density stratified fluids and rotating fluids [1]. On the one hand, internal gravity waves correspond to disturbances in the density structure of the fluid, which leads to buoyancy forces acting as a restoring force. In a non-rotating density stratified fluid, the energy flux of pure monochromatic internal gravity waves propagates in a direction tilted by an angle β with the horizontal, given by the dispersion relation [2,3]

$$\omega = N \sin\beta, \tag{1}$$

with N the buoyancy frequency, which characterizes the stratification of the fluid.
On the other hand, pure inertial waves result from the action of the Coriolis force leading to an energy flux for monochromatic waves also inclined by an angle β with the horizontal defined by the dispersion relation [4]

$$\omega = 2\Omega \cos\beta, \tag{2}$$

with Ω the solid rotation rate of the fluid. As a comparison to the vertical density stratification, Coriolis force in rotating flows leads to a horizontal stratification in angular momentum.

In various geophysical and astrophysical phenomena, the dynamics is often based on a coupling between rotation and gravity. Such flows are therefore dominated by inertia-gravity waves, which is a combination of internal gravity waves and inertial waves. This type of waves share similar properties since their dispersion relation explicitly involves a coupling between the two characteristic frequencies N and $f = 2\Omega$

$$\omega^2 = N^2 \sin^2\beta + f^2 \cos^2\beta\,. \tag{3}$$

Internal gravity waves and inertial waves are fundamental phenomena observed in various fluid systems, including the ocean, atmosphere, and astrophysical environments. In the oceans, these waves play a crucial role in mixing water masses, redistributing nutrients and heat, and influencing oceanic currents and circulation patterns [5–10]. Atmospheric internal waves often arise in stably stratified layers, such as within the troposphere or the bottom boundary layer, and contribute to turbulence, cloud formation, and the propagation of weather systems [10–14]. Gravity and inertial waves are also observed in astrophysical environments, such as stars, where they influence stellar dynamics, energy transport, and magnetic field generation [15–19].

The large scale of fluids in geophysical and astrophysical bodies induces for the waves a cascade of mechanical energy resulting from wave-wave, wave-vortex, wave-topography and/or wave-mean flow interactions. In particular, Triadic Resonant Instability (TRI) is an important type of wave-wave interaction that plays a major role in various geophysical contexts, and that has been extensively studied in the literature [20]. TRI is characterized by the non-linear

generation of two subharmonic secondary waves from a monochromatic primary wave, forming a triad of temporally and spatially resonant waves. We will come back throughout this article on various features of this instability. In general, these interactions result in an energy transfer from large scale to small scale structures so that waves can break and lead to turbulence and mixing or are dissipated through viscosity and diffusivity [21].

Understanding these waves is therefore crucial for modeling and predicting the behavior of fluid systems across various scales. Interestingly, the dispersion relations for gravity waves (1), inertial waves (2), and inertia-gravity waves (3) share similar properties. In particular, the phase and group velocities are orthogonal for plane waves and no characteristic length is prescribed. This mathematical analogy between rotating and stratified fluids has been well-known for more than 75 years. In his review, Veronis [22] describes this parallel and shows in different examples how results from one system can be analyzed and understood in terms of the behavior in the analogous system. More recently, the similarities among models for rotating fluids, stratified flows and even flows in magnetohydrodynamics have been used to understand in a unified manner the problem of weak turbulence of, respectively, inertial, gravity, and Alfvèn waves [23]. Differences, however, still exist and have to be taken into account. The major one is the motion of the fluid particles in a wave. Indeed, for a plane wave, the wave is made of rectilinear oscillations for internal gravity waves while it is made of anticyclonic circular oscillations for inertial waves, implying a 3D motion in the latter case, contrary to the former (see in Maurer [24, Fig. I.3]). Since the first experimental validation of the dispersion relation for internal gravity waves [25] and for inertial waves [26], they have been the object of many theoretical, numerical, and experimental studies in the last decades. In this review, we discuss recent experimental studies on either inertial waves or gravity waves in different setups using either non-rotating stratified fluids or rotating homogeneous (unstratified) fluids; a few cases of rotating-stratified configurations are also discussed. We focus on three main setups: wave beams, axisymmetric waves, and, finally, wave attractors. We will pay particular attention to studies involving Triadic Resonant Instability (TRI).

1.1. *Governing equations*

In this article, we consider a linearly stratified incompressible fluid subject to a global rotation at a rate $\Omega = f/2$ around the vertical axis, defined by the unit vector $\mathbf{e}_z$. We consider the case in which the background stratification is constant and parallel to the axis of rotation, i.e. the background density $\bar{\rho}$ is a linear function of z, characterized by the constant buoyancy frequency $N = \sqrt{-\frac{g}{\rho_0}\frac{\partial \bar{\rho}}{\partial z}}$ with ρ_0 the mean density. In the rotating frame of reference, the dynamics of such flow is described by the Navier–Stokes and mass conversation equation under the Boussinesq approximation

$$\rho_0\left(\frac{\partial \mathbf{v}}{\partial t} + (\mathbf{v}\cdot\nabla)\,\mathbf{v}\right) = -\rho_0 f\,\mathbf{e}_z \times \mathbf{v} - \nabla p' - \rho' g\,\mathbf{e}_z + \rho_0 \nu \Delta \mathbf{v}, \tag{4}$$

$$\frac{\partial \rho'}{\partial t} - \frac{\rho_0}{g} N^2 \mathbf{v}\cdot\mathbf{e}_z + \mathbf{v}\cdot\nabla\rho' = \kappa\Delta\rho', \tag{5}$$

$$\nabla\cdot\mathbf{v} = 0. \tag{6}$$

In these equations, $\mathbf{v}(\mathbf{x}, t)$ stands for the velocity field, ν the kinematic viscosity, κ the diffusivity of the stratifying agent. The pressure field p' is the pressure perturbation to the hydrostatic pressure incorporating the centrifugal acceleration. The density field ρ' is the difference between the total density field ρ and the density background stratification $\rho'(\mathbf{x}, t) = \rho(\mathbf{x}, t) - \bar{\rho}(z)$. As a result, the system forms a set of five equations with five unknown quantities: the velocity field $\mathbf{v}$, the

pressure perturbation p' and the density perturbation ρ'. In a given problem, ($\mathbf{v}$, ρ', p') are the solutions of equations (4)-(6) completed with boundary conditions.

Introducing U a characteristic velocity amplitude and L a characteristic length, the previous equations exhibit various dimensionless numbers, which are important to characterize the flows. In what follows, we will consider waves and therefore, the characteristic length will be related in most cases to the wave length, $2\pi/|\mathbf{k}|$, with $\mathbf{k}$ the wave vector. Due to the anisotropy of rotating and/or stratified flows, it is important to consider separately the components that are perpendicular and parallel to the direction of the stratification/axis of rotation. We denote $k_\perp = 2\pi/\lambda_\perp$ (respectively $k_z = 2\pi/\lambda_z$) the perpendicular component (respectively parallel component) to $\mathbf{e}_z$. For each dimensionless number described below, two can be defined using the horizontal or the vertical wavelength, the subscript $_j$ standing for $_\perp$ and $_z$. Note that, in most stratified turbulence theories, the anisotropic limit $\lambda_z \ll \lambda_\perp$ is considered [27]. This limit is indeed relevant for geophysical flow. On the contrary, in experiments, $\lambda_\perp \sim \lambda_z$.

- The Froude number, $\mathrm{Fr}_j = \frac{U}{\lambda_j N}$, represents the ratio between the buoyancy time scale and the inertial time scale. The regime where internal gravity wave propagation takes place is the small Froude number regime.
- The Rossby number, $\mathrm{Ro}_j = \frac{U}{2\Omega\lambda_j}$, compares the advection term to the Coriolis term. The regime where inertial wave propagation takes place is the small Rossby number regime.
- The ratio $N/2\Omega$ compares the importance of stratification with rotation.
- The Reynolds number, $\mathrm{Re}_j = \frac{U\lambda_j}{\nu}$, characterizes the separation between laminar and turbulent flow.
- The Schmidt number, $\mathrm{Sc} = \nu/\kappa$, compares the viscous effects with the diffusive ones. In the ocean, for salt water, $\mathrm{Sc} \approx 700$.
- The Ekman number is defined as $\mathrm{Ek} = \frac{\nu}{2\Omega L^2} = \frac{\mathrm{Ro}}{\mathrm{Re}_j}\frac{\lambda_j^2}{L^2}$ with L a characteristic global scale of the flow. It characterizes the importance of viscous forces compared with Coriolis forces. It is associated to phenomena emerging from boundary layers.
- The Richardson number, $\mathrm{Ri} = \frac{g}{\rho_0}\frac{|\partial_z\rho'|}{(\partial_z U)^2}$, compares the potential energy due to buoyancy with eddy kinetic energy. Small Richardson numbers are associated to overturning and mixing [28,29].

An interesting regime is the one for which $\mathrm{Re} \gg 1$ while $\mathrm{Fr} \ll 1$, with low-frequency waves $\omega/N \ll 1$. This regime corresponds to stratified turbulence. For forcing frequencies ω/N comparable to the Froude number, the dynamics falls in the strongly stratified turbulence regime, relevant notably for the atmosphere. If ω/N is large compared to the Froude number, i.e. if $\mathrm{Fr} \ll \omega/N \ll 1$, the dynamics is dominated by weakly interacting non-linear internal gravity waves and corresponds to a weak wave turbulence regime. These regimes are the object of the review [30].

In the linear inviscid limit, this set of equations has wave solutions with the following dispersion relation

$$\omega^2 = N^2 \sin^2\beta + f^2\cos^2\beta = f^2\frac{k_z^2}{k^2} + N^2\frac{k_\perp^2}{k^2}, \tag{7}$$

The angle β is the angle between the vertical and the wave vector. This dispersion relation is illustrated in Figure 1 using (ω, β) polar plane. The angle β is associated to a single value ω while a value of ω is almost always associated to 4 values of the angle β corresponding to the 4 quadrants of the oft-cited Saint Andrews cross. In the special case $f = N$, only a single value $\omega = N = f$ is allowed and valid for all angles. This schematic illustrates the symmetry between N and f.

The dispersion relation (7) leads to different features. First of all, it limits the accessible values of the frequency ω to either $f < \omega < N$ or $N < \omega < f$. Outside these ranges, internal waves are evanescent. The low frequency domain can however be populated by other types of waves, such

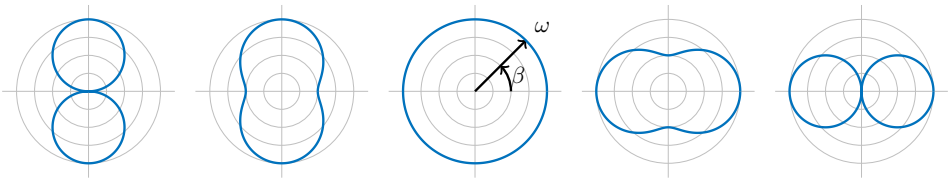


Figure 1. Dispersion relation (7) plotted in the (ω, β) polar plane, for dimensionless parameters N and f: to each angle β corresponds a unique frequency ω given by the blue curve (extracted from [31]).

as Rossby waves which exist in the presence of a zonal mean flow. Another feature of these types of waves, the phase velocity $\mathbf{c}_\varphi$, aligned with the wave vector, and the group velocity $\mathbf{c}_g$ are orthogonal. Importantly, as already mentionned in the introduction, the value of ω does not determine the wave length, which depends on many phenomena such as boundary effects or non-linear effects. This final remark implies that a particular attention must be paid to the choice of the wave maker to generate controlled gravity or inertial wave beams, as will be discussed in Section 1.2.

An important feature in the comparison between internal gravity and inertial waves is the wave structure itself. To explain this difference, let us first consider a plane wave characterized by a single wave vector $\mathbf{k}_0$. The fluid motion for internal gravity waves is rectilinear, perpendicular to $\mathbf{k}_0$, and contained in the $(\mathbf{k}_0, \mathbf{e}_z)$ plane. In contrast, due to the Coriolis term, the inertial wave field is characterized by anticyclonic oscillations in the plane perpendicular to $\mathbf{k}_0$ and is therefore inherently three dimensional. In the following, for both inertial and internal gravity waves, we will call 2D wave any superposition of plane waves for which all the wave vectors are localized in a single plane containing $\mathbf{e}_z$. The velocity field will therefore be uniform in the direction normal to this plane. Note that, with this definition, an inertial wave will be considered as a 2D wave even if the three components of the velocity field are non zero. Such differences could lead to different behaviors as we will describe in the rest of this article.

Dissipation effects take place through viscosity or salt/temperature diffusion. In almost all experiments, this influence of viscosity has a negligible effect on the relation between ω and the direction of the wave vector. However, as the waves propagate, viscosity results in energy dissipation and attenuation of the wave. This dissipation has a characteristic time scale $1/(\nu k^2)$ and is therefore large for short wave lengths. It explains why viscosity has to be taken into account in laboratory experiments compared to geophysical and astrophysical flows. A self-similar solution describing the propagation of a viscous wave beam was found independently for rotating fluids [32] and for density-stratified fluids [33]. Near boundaries, such as the ocean floor or a container wall, viscosity plays a significant role in modifying gravity/inertial wave behavior. The dissipation near topographies clearly matters in the global energy budget [34]. Both inertial waves and gravity waves can be affected by the presence of a viscous boundary layers, which in turn can be modified due to the presence of gravity/inertial waves, leading to intricate patterns of motion and transport within these fluid systems [35–39]. For internal gravity waves, a strong mean flow will modify the wave field and may in turn be generated due to non-linearities of internal gravity waves in 3D [20,40] or due to streaming in the viscous boundary layer as predicted theoretically [41] and observed experimentally [38]. The equivalent feature for rotating flows is the existence of zonal flows, a characteristic phenomenom of forced rotating flows. They are generated by different mechanisms such as non-linearities in the Ekman

boundary layer [42] or non-linear inertial waves [43]. Such axisymmetric mean flows have been observed experimentally [44].

Finally, an important phenomenon that needs to be considered in stratified fluids is internal-wave driven mixing [45]. When the wave amplitude is large enough, the shear associated with it can be characterized by a small Richardson number ($Ri < 0.25$), inducing overturns that can lead to mixing. This can be particularly true if TRI is present, contributing to energy transfers to smaller scales, resulting in a more efficient mixing. This mixing can be seen as a problem in experiments since the linear stratification cannot be conserved contrary to numerical simulations. However, mixing is critical for climate models [46]. In numerical models, mixing and associated turbulence are usually linked to subgrid scale internal wave processes. It is therefore crucial to understand the mixing caused by internal waves and to properly parameterise the mixing efficiency. To that extent, various experiments have been performed at ENS de Lyon to study the influence of TRI on mixing [47,48].

1.2. *Experimental techniques*

Internal gravity waves in the laboratory require a stratified medium, which is generally achieved using salt as the stratifying agent, easier to manipulate than temperature. The filling of the tank is performed via the so called two-bucket method [49,50], which in its initial version produces a linearly stratified medium in a tank whose horizontal section is vertically uniform, but which can actually be generalized, using computer-controlled pumps, to create non-linear density profiles, or to produce a linear profile in a tank of vertically varying section [51]. Stewart et al. [52] have recently developed a derivation of this method, allowing to use temperature stratification.

As to rotating fluids, one "simply" needs to place a tank on top of a rotating table, which of course implies a number of technical challenges, including dealing with spin-up processes, non horizontal isobars, mechanically restraining the tank and all the measuring devices and allowing proper communication of power and data between the non-rotating and the rotating frame. The spin-up process, in particular, is rendered more complex when the fluid is also stratified [24], since the stratification prevents Ekman pumping motion, which is the major driving motion to attain solid body rotation during a spin-up.

Once the supporting medium is ready, a device is necessary to create the perturbation to this medium that will generate the wave. Almost 60 years ago, Mowbray and Rarity [2] were the first to produce internal waves in a laboratory experiment, using a sphere oscillating vertically in a linearly stratified fluid. Since then, experimentalists have been very creative in improving the design of the wave generators. Table 1 is an attempt to summarize and classify these various types of wave generators.

In laboratory experiments, internal waves can be observed thanks to the following techniques:

- Dye lines, showing the motion of iso-density lines (or isopycnals), mainly qualitative;
- Particle Image Velocimetry (PIV), based on following in time the motion of patterns of tracer particles, giving access to the velocity field;
- Synthetic Schlieren, based on the apparent displacement of a pattern placed behind the experimental tank, linked to the change in refraction index of the fluid, associated with the density perturbation accompanying the wave propagation. It gives access to the density gradient field [53] or to the whole density field [54] (only possible for gravity waves);
- Planar Laser Induced Fluorescence (PLIF), using a laser-excited fluorescent dye as tracer for density, allowing to measure directly the density field. It can be coupled to PIV, using the same laser plane, to get access to density-velocity correlations and therefore density fluxes, important for studies of mixing [47] (only possible for gravity waves).

Table 1. List of experimental gravity and/or inertial wave generators, organised by type of wave form generation.

	Category	Description	Type of wave	Example reference
I	Whole tank oscillation	Up and down motion	Global mode or self-similar wave beam	[55]
		Libration		[56]
II	Global boundary motion	Oscillating rigid wall	Guided wave	[37,57]
		Oscillating rigid lid		[58]
III	Oscillating object	Oscillating cylinder	Self-similar wave beam	[25,59]
		Oscillating sphere		[60]
		Oscillating torus		[61]
		Multiple oscillating objects		[62]
		Tidal motion on a fixed obstacle		
				[63]
IV	Towed object	Towed object	Wave beam	[64]
V	Oscillating plates	Linear device	Versatile wave form	[65]
		Independent oscillating plates		[66–68]
		Axisymmetric oscillating plates		
				[69]
VI	Local boundary deformation	Deformable tank	Specific purpose	[70,71]
VII	Liquid interface motion	Turbulent underlayer	Uncontrolled	[72]
		Convective underlayer		[73]

The two most common techniques, PIV and Schlieren, allow quite easily for an extraction of wave frequency content and spatial structure, using respectively Fourier transform (or time frequency analysis [74] when time-dependence is relevant) and Hilbert transform [75]. Many experiments require to estimate or to measure quantitatively the amplitude of the primary wave. One cannot rely on the amplitude of the wave generator motion, since there is an efficiency factor that comes into play and that depends strongly on frequency, wave form and experimental conditions. For the Schlieren technique, such measurement requires integration of the mass conservation equation, which in general cases with multiple waves is not a simple task. In the same way, for PIV measurements, a direct estimate of the kinetic energy of the whole velocity field can easily be computed. However, quantifying the amplitude of a specific wave among other waves in interaction can be difficult.

Among the various methods used to extract a wave amplitude, Mathur et al. [76] studied transmission and reflection of internal wave beams across a transmission region and took a Fourier transform of the reflected and transmitted wave fields along appropriately chosen transects. Maurer [24] measured wave amplitudes by looking at the maximum of the velocity over a given spatial area, and Supekar et al. [77] utilized the distribution of maxima of amplitudes for a velocity field in a widespread two-dimensional beam. Boury et al. [78] first performed a fit of the wave form to the expected spatial profile as a function of time, thus extracting a wave amplitude as a function of time, before averaging in time the obtained amplitude, choosing a time window where the process was as stationary as possible. When the amplitude of two different waves of same frequency must be estimated (in the case of wave reflection for example), a method based

on the signal processing technique called Variable Mode Decomposition has been adapted successfully [79]. In the case where time stationarity is not achieved in the observed experiment, Boury et al. [80] developed a method based on using Hilbert transform times series and root-mean-square averaging to obtain a time dependent amplitude of the waves. Finally, in the case where synthetic Schlieren is used to observe the waves, Grayson et al. [81], based on previous developments [64,82], used integrated components of the density gradient field, to which they apply a root-mean-square and spatial average.

2. Internal Wave Beams in a Square Geometry and its Instability

During the years 2010-2015, a series of studies [40,83,84] was undertaken by a group at ENS de Lyon, jointly with a group at Université d'Orsay (now Université Paris-Saclay), where the generation of plane beams of internal gravity waves (in Lyon) and inertial waves (in Orsay) was obtained using the same wave generator (linear oscillating plates, type V of Table 1), allowing for interesting comparisons between both types of generated waves, and in particular regarding the Triadic Resonant Instability of the corresponding wave beams.

2.1. *Generation of Gravity Versus Inertial Waves*

In both cases, the generation of the waves was very similar, using the wave generator described in [65], placed in a tank, either non-rotating but linearly salt stratified (in Lyon) or non stratified but lying on top of a platform rotating at rotation rate Ω (in Orsay). It was actually the same device, which travelled from Lyon to Orsay. In both cases, the generator configuration was set to excite a plane wave beam, with 3 to 4 wave lengths of about 7 cm each along the whole height of the generator, with a tapering amplitude at each end to avoid spurious emission of internal waves.

However, a main difference lies in the generation process, since the fluid motion in the case of internal gravity waves is a simple oscillating translation in the direction of the group velocity, whereas fluid particles describe anticyclonic circular translation in the case of inertial waves. As a consequence, for inertial waves, the oscillating plates of the wave maker only force the longitudinal component of their circular motion, while the lateral component is let to freely adjust according to the spatial structure of the wave solution. This makes the generator less efficient in producing inertial waves, compared to gravity waves. A detailed description of the added difficulty when producing inertial waves with this generator, with an efficiency depending strongly on generator amplitude and wave length can be found in the appendix of [85, Chapter 3].

In order to make up for that difficulty, the generator angle was adapted to the oscillating frequency ω, so that the plate motion would actually be in the exact direction of the longitudinal component of the wave motion. Note that this solution is not applicable to the case of gravity waves, since reclining the generator, with a change of inclination for each frequency studied, would be complicated and would also rapidly destroy the stratification.

In the case of inertial waves, it turned out that in order to vary the wave angle, set by the ratio $\omega/f = \omega/2\Omega$, it was easier to change the global rotation of the table, rather than changing the generator frequency. For gravity waves, of course, changing the stratification was not an option and it is the wave frequency ω that was varied.

One last point of comparison: in both cases, the generator was parallelepippedic. While for gravity waves, which have a perfect 2D behaviour, this is not a problem, it becomes more tricky with inertial waves, which have inherent 3D motion and the tank shape is not really adapted, with lateral walls restraining the transverse motion. For this reason, while the tank used for gravity

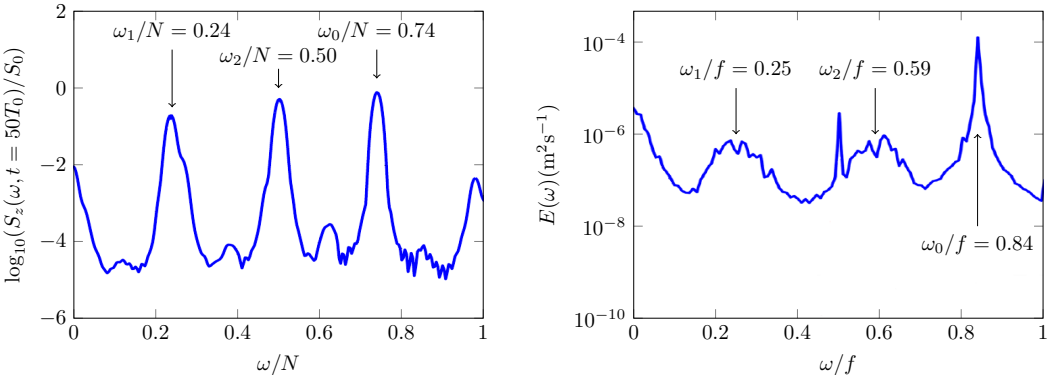


Figure 2. Examples of frequency spectra showing TRI. (Left) Frequency spectrum for internal gravity waves ($N \neq 0, f = 0$), from [83]. (Right) Frequency spectrum for inertial waves ($N = 0, f \neq 0$), from [40]. In the latter case, a narrow peak corresponding to the rotation frequency of the table (thus at $\omega/f = 0.5$) is visible, linked to mechanical noise of the table.

waves was narrow (2 wave lengths), in the case of inertial waves, the tank was much wider, with a width of about 10 wave lengths.

As we will show later, in spite of these differences, the production of the waves and the characteristics of the instability via resonant interaction are very similar.

2.2. *Instability of the Wave Beams*

Already in 1967, Davis and Acrivos [86] showed experimentally and theoretically that, due to the non-linear terms of the wave equations, internal waves are unstable to infinitesimal perturbations, which grow to form temporally and spatially resonant triads between the primary wave (indicated in what follows by index 0), and two secondary waves (indicated by indices 1 and 2). These resonant conditions write respectively

$$\omega_0 = \omega_1 + \omega_2, \tag{8}$$

$$\mathbf{k}_0 = \mathbf{k}_1 + \mathbf{k}_2. \tag{9}$$

This instability is now referred to as *Triadic Resonant Instability* (TRI). The analytical derivation for the plane wave solutions of the non-linear wave equations can be found in Dauxois et al. [20]. For a given primary wave vector of components (ℓ_0, m_0), combining the dispersion relation of the waves with the temporal resonance condition (and eliminating one of the two secondary wave vectors using the spatial resonance condition), one obtains the following equation for the components (ℓ_1, m_1) of the remaining secondary wave vector

$$\frac{|\ell_0|}{\sqrt{\ell_0^2 + m_0^2}} = \frac{|\ell_1|}{\sqrt{\ell_1^2 + m_1^2}} + \frac{|\ell_0 - \ell_1|}{\sqrt{(\ell_0 - \ell_1)^2 + (m_0 - m_1)^2}}. \tag{10}$$

The set of solutions of this equation can be represented by a resonance locus ([20, Figure 2.a]) defined as the possible locations in wave vector space of the tip of vector $\mathbf{k}_1$. We recall the typical shape of this locus, with examples of the vector triads $\mathbf{k}_0$, $\mathbf{k}_1$, and $\mathbf{k}_2$ in the insets of Figure 3 (left).

The TRI instability was observed in several laboratory experiments [87–89] with increasing details thanks to progresses in fluid motion imaging, using in particular PIV and synthetic Schlieren in the last decade. This instability was shown to play a role in oceanic energy transport and vertical mixing [90,91].

Here again, the joined study performed by the Lyon and Orsay groups using the same wave generator provides an interesting view on the TRI instability in the respective case of internal gravity waves and inertial waves. In both cases, with a large enough amplitude – typical wave velocity of the order of 2 to 3 mm.s^{-1}, or in other words dimensionless quantity ψ_0/ν (equivalent to a typical Reynolds number of the flow), of the order of a few tens, where ψ_0 is the stream function amplitude of the wave – the instability starts after 20 to 40 generator periods.

Figure 2 shows the frequency spectra of the wave system after the onset of instability, on the left for the gravity waves and on the right for the inertial waves. Three main peaks are observed, corresponding to the primary and two secondary waves. In both cases, the temporal resonance condition is verified. However, the secondary peaks are much broader for the inertial wave case than for gravity waves. A possible explanation for this observation is given in Section 4.4.

One of the interesting features of TRI, in the oceanic mixing context, is that it allows for a transfer of energy to smaller scales, without the necessity of a turbulent energy cascade. That happens in particular when both secondary waves have larger wave vectors, compared to the primary wave: $\kappa_{1,2} > \kappa_0$, where κ is the modulus of the wave vector. This is the case, in general, when the solutions belong to the external branches of the resonance locus (see example in top inset of Figure 3 (left)). In contrast, when the solutions are on the central part of the locus, the transfer goes both directions, with $\kappa_1 > \kappa_0 > \kappa_2$, or vice-versa (see example in bottom inset of Figure 3 (left)).

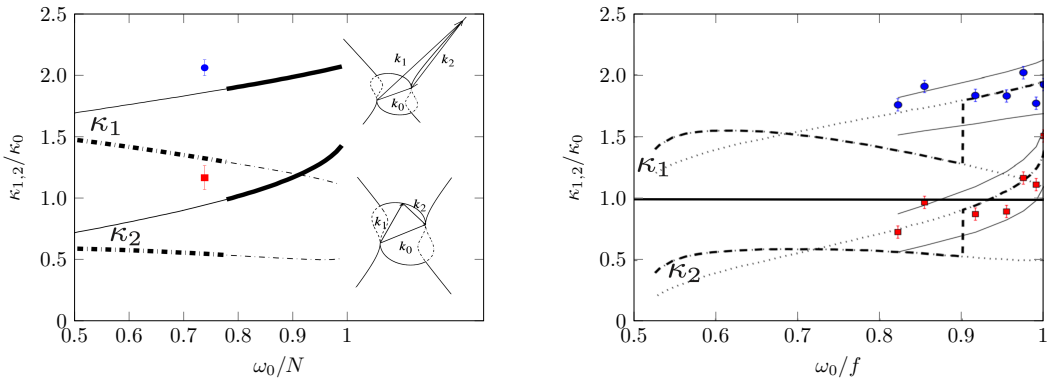


Figure 3. Normalized wave numbers $\kappa_{1,2}/\kappa_0$ of the secondary waves, as a function of the primary wave frequency ω_0. (Left) Gravity waves, adapted from[83]. (Right) Inertial waves [40]. The lines represent theoretical predictions, computed for the wave dimensionless amplitude $\psi_0/\nu = 28$ (left) and $\psi_0/\nu = 37$ (right). The insets on the left plot show two typical examples of the resonance locus. As illustrated in this inset, the solid lines on the left plot (upward going dotted lines on right plot) represent the case where the secondary wave vectors are on the external branches of the resonance locus, while the dashed lines on the left plot (mostly downward going dotted lines on the right plot) represent the case where the secondary wave vectors are on the central part of the locus. Between these two types of solutions, the one that has the largest growth rate is represented by a thicker line. Filled circles and squares with error bars correspond to experimental measurements. The two solid thin lines on the right plot show the allowed range around the dotted curves, determined by considering an uncertainty of ±50% on the wave amplitude.

Both studies mentioned earlier delved into this issue. For a given wave amplitude and for each normalised frequency ω/N of the primary wave, the relative magnitudes $\kappa_{1,2}/\kappa_0$ of the secondary wave vectors that correspond to the largest growth rate of the instability were computed, both in

the case of the external and central branches of the resonance locus. The result is presented in Figure 3, on the left plot for internal gravity waves [83] and on the right plot for inertial waves [40]. In addition, a thickening of the lines highlights the case (between central and external branches) with highest growth rate. There is a transition from the central to the external branch, at a frequency around $\omega/N = 0.77$ for gravity waves and $\omega/f = 0.79$ for inertial waves. Experimental points are also shown, with colored symbols. Interestingly, in both cases, even below the transition frequencies mentioned above, the experimental solutions seem to stay on the external branch, with, mostly, an energy transfer towards smaller scales, except at the lowest frequencies where TRI was observed in the case of inertial waves. Note that for gravity waves, were only one experimental point is shown, the magnitude of the wave vectors is slightly larger than predicted.

In a laboratory experiment of typical sub-meter size, the viscosity of water is such that small scale waves are damped quickly and secondary waves with wave vector magnitude above a few times the primary wave vector magnitude are never the most unstable solution (see [20, Figure 2.c]) and are therefore never observed. However, the opposite trend can be observed in Figure 3, where wave vectors longer than expected were measured and the solution on the central branch of the resonance locus, where wave vectors are shorter, was never observed.

This could be explained by a finite-size effect. This effect was described in Bourget et al. [84] and relates to the fact that in finite-size beams with a width equal to only a few wave lengths, the secondary waves, which have a group velocity with a different direction than the primary wave, leave the interaction region, located within the primary wave beam width, before the instability has time to grow. This effect is of course enhanced when the waves have a large group velocity, which is the case of waves of small wave vectors, since group velocity increases when wave vector amplitude decreases. For this reason, one can understand that the solutions on the central branches of the resonance locus, which, for infinitely wide beams, have a larger growth rate below the transition frequency, are not observed in the experiments, since the actual growth rate, taking into account the finite size effect, is reduced (see equation 3.7 in [84]).

2.3. *Variability of the Triadic Resonant Instability*

A recent study by Grayson et al. [81] focused on the long-term fate of TRI in the case of narrow beams of internal gravity waves. The authors used a large scale tank (11 m wide) to prevent interactions between the beam and its reflections and they took advantage of the very versatile "magic carpet" wave generator built in Cambridge (type V of Table 1, [66]). By doing a refined analysis of the characteristics of the secondary waves of the TRI, they showed that there exists an important variability in amplitude, frequency and wave vector of these secondary waves. This variability takes place both in time and space.

This is illustrated in Figure 4, showing the power spectral density at the function of time and frequency (left plot) and as a function of the secondary wave vector horizontal components and of the height in the tank (right plots). On the left plot, one can observe that while the primary wave frequency maintains a constant value at the forcing frequency Ω_0/N=0.62, both secondary frequencies fluctuate in time, while conserving the resonance property $\omega_1 + \omega_2 = \omega_0$. Note that frequencies around 0.0, 0.8, and 1.0 come from higher order interactions. In order to better understand the underlying modal structure of the observed beams, Grayson et al. decomposed the flow field using Dynamic Mode Decomposition (DMD, white line superimposed in the time-frequency plot), confirming the observed variability. A similar variation in frequency has been witnessed by both Bourget et al. [83] and Brouzet et al. [92] in their experimental studies. One can also observe at certain times (in particular between 100 and 200 T_0, as well as between 200 and 300 T_0), other pairs of secondary beams appearing and then merging with the continuous mode,

in the form of convergent "wisps" on the ω_1/N and ω_2/N bands. The authors have checked that in such cases, the triadic resonance in frequency persists across all the spectrum.

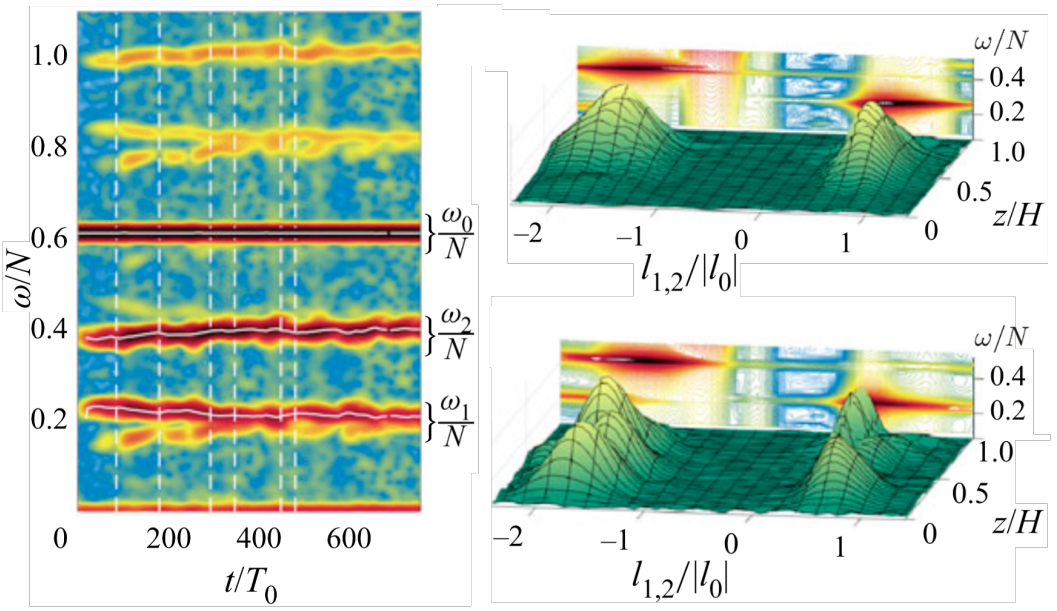


Figure 4. (Left) Time-frequency spectra (log scale of normalised spectral density) for a long term experiment. The dominant frequencies obtained from the DMD frequency decomposition are overlaid in white. (Right) For the same experiment, distribution of energy in the ℓ/ℓ_0 space and over the non-dimensional height in the domain z/H. (top) $t/T_0 = 83$, (bottom) $t/T_0 = 481$. Both the surface plot colour and the height of the peaks show the power spectral density. The left (right) "bump" corresponds to ℓ_2 (ℓ_1). The background plot shows the power spectral density at the same instant in time in the Fourier plane of horizontal wave number component and frequency. Adapted from [81].

The right plot shows, at two different times, the distribution of energy along the horizontal component of the wave vector and across the height of the tank. One can observe that at the earlier time (top figure), the TRI is mostly localised in the upper part of the tank, with the ℓ_2 component at a value around $-2\ell_0$ and the ℓ_1 component at a value around $0.8\ell_0$. Note that the two secondary waves can be identified on this plot thanks to the background plot, showing the distribution of energy in the (ℓ,ω) plane, the wave with largest frequency being identified with index 2 ($\omega_2 > \omega_1$, see left plot). At a much later time (bottom figure), towards the end of the experiment (which lasted $682T_0$), one can see that the distribution of energy over ℓ and z have evolved, with in particular different values of ℓ_1 and ℓ_2 depending on z/H, as well as a central region (around $z/H = 0.5$), where no secondary waves are present.

Grayson et al. [81] interpret these observations by a finite-size effect, using a model quite similar to the one presented in Bourget et al. [84], taking into account how the secondary waves exit their interaction region with the primary wave due to their group velocity. However, the main difference with the model of Bourget et al. [84] is that the instability is allowed to be a function of space, and not only time as was the case in the previous model. The authors show that including this feature in the model actually results in the observed variability. In addition, they show that with the parameters of the experimental study, the ratio between the residence time of the secondary waves in the interaction region and the development time of the instability is close

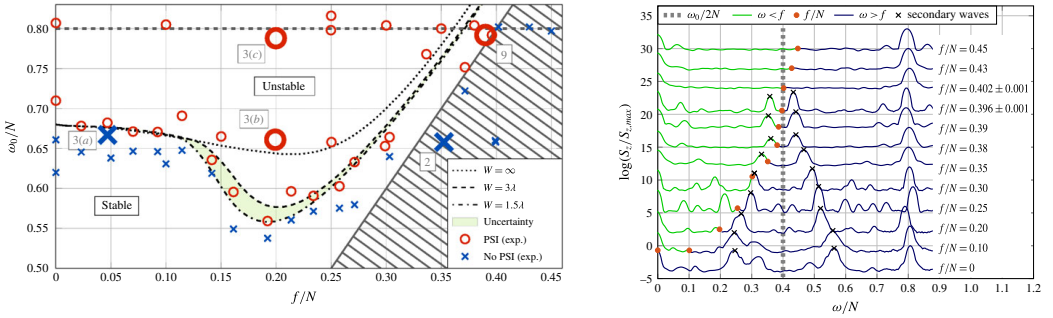


Figure 5. (Left) Experimental observations showing the triadic resonance stability or instability of a primary wave of dimensionless frequency ω_0/N at Coriolis parameter f/N. The instability threshold in this $(f/N, \omega_0/N)$ phase space is shown by various curves, depending on the beam width. The hatched zone corresponds to a forbidden zone for TRI (see text). (Right) Renormalized amplitude of the Fast Fourier Transform of the vertical gradient of density for various values of f/N. For the sake of clarity, the spectra were shifted vertically. The vertical dashed line indicates $\omega/N = 0.4 \simeq \frac{1}{2}\omega_0/N$. On each spectrum the peak on the right represents the primary wave, daughter waves correspond to the other peaks. Extracted from [93].

to one, so that the TRI is actually very sensitive to the actual properties of the secondary beams. As a result, preferential selection of triads is locally determined. As one triadic interaction decays, another forms, but this time at a different physical location and with new secondary beam properties. This explains why, experimentally, modulations are observed not only in physical space but also in Fourier space.

2.4. *What Happens with TRI when Combining Stratification and Rotation ?*

An extensive comparison of the characteristics of TRI between gravity and inertial waves has been presented in Section 2.2, mainly based on the joined studies of the Lyon and Orsay groups. A question remains: how is, for example, the TRI for gravity waves modified when rotation is added? This study has been performed in [93], where the same experiment used in [83,84] was placed on a rotating table, which was rotated at values of f/N between 0 and 0.45.

The main results are summarised in Figure 5. The left plot represents the phase space (f/N, ω_0/N), where the instability threshold, computed including the effect of rotation in the finite-width analysis of Bourget et al. [84], is represented by several lines, depending on the beam width (infinite, 3 wave lengths and 1.5 wave length). One can observe that - as expected since the group velocity, at the heart of the finite-width effect, decreases with the rotation rate - the instability threshold lowers when rotation increases, all the more when beams are narrow. This effect only takes place on a limited range of rotation rates, since in this phase space there is an exclusion region for TRI (hatched). This is due to the fact that, as rotation rate increases above $\omega_0/2$, with secondary wave frequencies that have to be larger than f, it implies $\omega_0 > 2f$, which is not possible for propagating waves. As a result, there is a value of f/N for which the threshold is minimum, reminiscent of the critical latitude phenomenon described in MacKinnon et al. [90]. Experimental data points are shown, with symbols indicating if TRI was observed or not, and they are in very good agreement with the analytical predictions given by the smooth curves.

On the right plot of Figure 5, the frequency spectra for all values of rotation rates are shown, allowing to observe the evolution of the secondary frequencies with f/N. As rotation increases,

the frequencies of the two secondary waves get closer (and therefore closer to $\omega_0/2$). As the rotation rate gets very close to the limit of the forbidden region ($\omega_0/2$), the secondary wave of lowest frequency surprisingly falls below f. An explanation of this result could be the existence of a non-zero out-of-plane component of the wave vector. This has been discussed in Mora et al. [94], who show that when rotation is present, the maximum growth rate is obtained with a non-zero component of the wave vectors in a direction perpendicular to the primary wave beam. This result is attributed to the 3D structure of inertial waves. Indeed, while theoretical analysis have shown that coplanar triads always display the highest growth rates for TRI of internal gravity waves [95], in contrast, for inertial waves the possibility of an out-of-plane component of the secondary wave vectors is still an open question both theoretically and experimentally.

3. Axisymmetric Waves

Beyond two-dimensional (2D) wave beams, various recent studies have delved into three-dimensional (3D) internal waves assuming that they would exhibit peculiar dynamics. The drive to study such wave fields is, interestingly, both experimental and theoretical to investigate whether purely 3D effects may exist, either in the linear or in the non-linear regime. Besides in-situ measurements of axisymmetric wave fields [96,97], it is interesting to note that various laboratory systems generate such wave fields, e.g. vertically oscillating spheres [98,99] or impacting plumes [100].

In what follows, we will use the distinction made in [101] between axisymmetric waves that are invariant by rotation (θ-independent, where θ is the orthoradial angle in the horizontal plane) and cylindrical waves that allow for an orthoradial dependence (θ-dependent). Axisymmetric waves are a particular class of cylindrical waves, easier to generate and study experimentally.

Axisymmetric wave fields have traditionally been experimentally excited using a vertically oscillating sphere and exploring the shape of the wave beams [2,98,99,102–104]. The radially decreasing amplitude and the viscous decay of the conical wave beam emitted by an oscillating sphere has been explored in laboratory experiments by Flynn et al. [99] showing good agreement with theoretical predictions. More sophisticated axisymmetric experimental geometries have later been investigated using a vertically [61] and a horizontally [105] oscillating torus, in which case a highly non-linear process occurs due to the three-dimensional geometric focusing, able to transport momentum and break into turbulence. None of these experimental configurations, however, readily permitted a change in the form nor the wave number of the wave field being excited. Versatile configurations have been obtained thanks to a cam-based axisymmetric wave [69] generator, derived from the planar wave generator developed by Gostiaux et al. [65] (see Table 1).

The experimental study of axisymmetric waves presents several difficulties. First, the fundamentally 3D geometry of the waves means that a complete characterisation requires visualizations both in the vertical and in the horizontal planes. A way to obtain this imaging is to elevate the tank and use an mirror inclined at 45 degrees below it (e.g. [69]). Second, to match boundary conditions with the axisymmetry of the wave field, it is more appropriate to use a cylindrical tank with the same geometry; to prevent optical distorsions, this cylindrical tank should then be enclosed in a larger tank of square cross section.

3.1. *Linear Dynamics*

Axisymmetric waves can be described in natural cylindrical coordinates (r,θ,z) by decomposing the velocity field into two horizontal (radial and orthoradial) and one vertical velocity compo-

nents, (v_r, v_θ, v_z). For practical reasons, it is instructive to introduce the stream function under a symmetric formalism

$$v_r = -\frac{1}{r}\frac{\partial(r\psi)}{\partial z} \qquad \text{and} \qquad v_z = \frac{1}{r}\frac{\partial(r\psi)}{\partial r}. \tag{11}$$

Neglecting non-linear and dissipative terms, the axisymmetric stream function satisfies a collapsed equation

$$\frac{\partial^2 \Delta\psi}{\partial t^2} + f^2\frac{\partial^2\psi}{\partial z^2} + \frac{N^2}{r}\frac{\partial^2(r\psi)}{\partial r^2} = 0, \tag{12}$$

whose solutions can be found analytically under the form of either a product of a radial Bessel function and a vertical exponential, or a product of a radial Hankel function and a vertical exponential. These are the counterparts of sine-cosine and exponentials for Cartesian modes and plane waves, respectively. Bessel-shaped wave fields describe modes; Hankel-shaped ones are more appropriate to describe converging or diverging conical wave fields.

The dispersion relation can be obtained thanks to a Hankel–Fourier transform on equation (12), yielding

$$\omega^2(\ell^2 + m^2) = f^2 m^2 + N^2\ell^2, \tag{13}$$

with ω the wave frequency, and ℓ and m the radial and vertical wave numbers.

Cylindrical wave fields satisfy a system of equations similar to equation (12), but with non-zero θ-derivatives. Solutions to these equations are called Kelvin modes [101,106,107]. They involve rotating and counter-rotating waves, and preserve the 2π orthoradial periodicity through a dimensionless, integer, orthoradial wave number p. The axisymmetric dynamics is recovered by setting $p = 0$. Interestingly, p does not appear in the dispersion relation (13) which thus remains the same for both axisymmetric and cylindrical waves. A thorough description of these Kelvin modes can be found in [101].

Horizontal axisymmetric modal wave fields, propagating vertically, are the easiest to study and characterize experimentally as the radial structure can be described under the simple analytical form of a single Bessel function. Similarly to Cartesian studies, axisymmetric modes can be obtained experimentally by enforcing appropriate boundary conditions with a tank of the same radial size as the wave generator. Such modes have been described in [78].

3.2. *Non-Linear Dynamics*

While the linear dynamics of axisymmetric waves remains fairly similar to the linear dynamics of Cartesian plane waves, strong differences have been evidenced in the non-linear regime both in stratified and in rotating experiments [24,56,101,108,109]. The analytical justification is two-fold: first, contrary to the plane wave case, the cylindrical Jacobians giving the non-linear terms are no longer anti-symmetric, due to the r-derivatives, preventing some terms to mutually cancel out; second, while the product of two exponentials (plane waves) or sine-cosines (Cartesian modes) can be expressed under the form of another exponential or sine-cosine, the product of two Bessel functions does not usually have a similar simple expression but rather yields a sum of Bessel functions. This is further complexified for waves with a non-zero orthoradial velocity v_θ (notably inertial waves), as the horizontal Laplacian introduces additional non-linear terms coupling the horizontal velocities $(v_r,\ v_\theta)$ [101]. These different terms bring several questions regarding the non-linear dynamics of axisymmetric and cylindrical waves, whether it be the subsistance of the triadic resonant instability in a similar formalism as with plane waves, or the possibility for other non-linear behaviors to arise due to the modification of the Jacobian structure.

3.2.1. *Triadic Resonant Instability*

Axisymmetric Triadic Resonant Instability (TRI) has been proposed as a natural extension of TRI, extensively studied in 2D for plane waves. Various experimental studies in axisymmetric geometry led to the observation of localized TRI whose resonant conditions, both temporal and spatial, are the same as for plane waves [101,109]. This is due to the assimilation, locally, of the axisymmetric wave field with a Cartesian wave field when disregarding the overall geometry of the system imposed by the forcing or by the boundary conditions. As such, it does not provide clear indications on a totally cylindrical, fully developed, TRI that would preserve the imposed geometry of the system. In axisymmetric focusing experiments performed with an oscillating torus in a stratified fluid, [109] have shown that a primary wave field can lead to resonant subhmarmonics in agreement with the 2D TRI theory. However, other experiments led by Maurer et al. [24] in a stratified and rotating fluid suggested that the axisymmetry could be broken for the subharmonics and that they may not fully satisfy the spatial resonance conditions.

An analytical derivation of the resonance conditions involving three cylindrical wave fields (Kelvin modes) performed by [101] showed that a fully 3D TRI could exist, preserving the cylindrical geometry of the system, although with some modifications compared to the Cartesian case. First, the three waves have resonant frequencies ω and two exact spatial resonances, along the vertical (m) and orthoradial (p) directions. The p resonance along θ is particular insofar as the wave fields also have to satisfy a 2π periodicity, which necessarily leads to a discretized resonance. Second, the situation gets more complex along the radial direction, as exact resonances have been shown to exist only for sufficiently large wave fields whereas in configurations of small extent or in confined geometries quasi-resonances are more likely to appear. Lastly, due to an asymptotic divergence at the center of the domain, it is unclear whether waves are locally spatially resonant at $r = 0$.

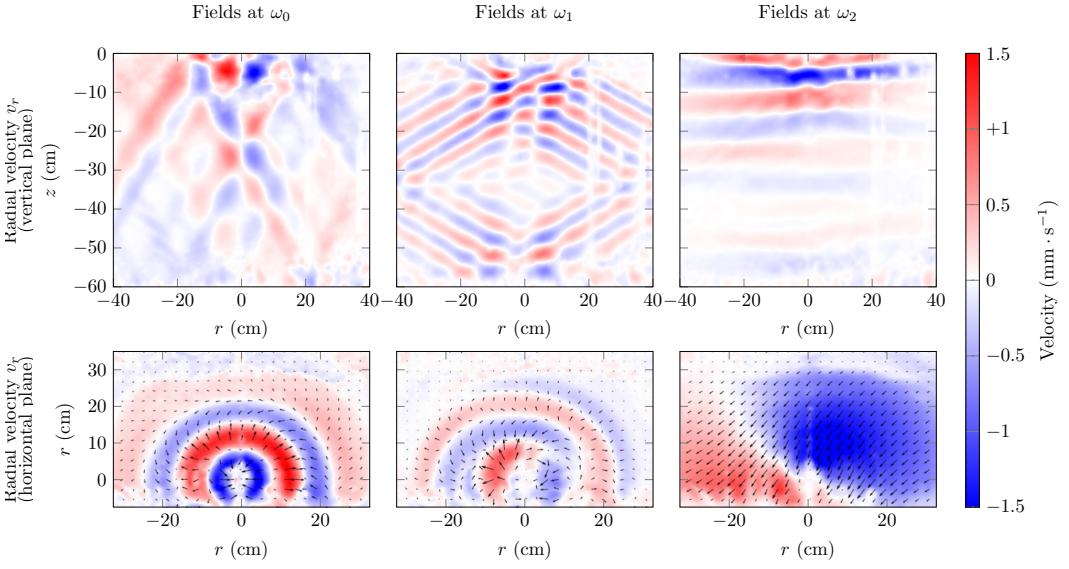


Figure 6. Experimental visualization of TRI for cylindrical wave fields. The top row shows the radial velocity field v_r in the vertical plane; the bottom row shows the same radial velocity field in the horizontal plane. From left to right: forcing wave field, at $\omega_0 = 0.80\ \mathrm{rad\cdot s^{-1}}$; first and second subharmonics at $\omega_1 = 0.50\ \mathrm{rad\cdot s^{-1}}$ and $\omega_2 = 0.30\ \mathrm{rad\cdot s^{-1}}$. Experiments conducted at $f = 0.29\ \mathrm{rad\cdot s^{-1}}$ and $N = 0.97\ \mathrm{rad\cdot s^{-1}}$ (adapted from [101]).

These results have been confirmed experimentally both in confined and in unconfined geometries [101]. Figure 6 shows an example of TRI obtained in an unconfined stratified-rotating experiment ($f = 0.29\,\mathrm{rad}\cdot\mathrm{s}^{-1}$ and $N = 0.97\,\mathrm{rad}\cdot\mathrm{s}^{-1}$), in which the forcing wave (shown in the first column) generates two resonant subharmonics (second and third columns). The velocity field in the horizontal plane shows that the two subharmonics are not axisymmetric. In addition, their time behavior shows that they have opposite orthoradial wave numbers. Interestingly, the axisymmetric forcing seems to lead to axisymmetric subharmonics if the fluid is stratified only; however, if the fluid is also rotating (as in the example shown in Figure 6), cylindrical subharmonics with a non-zero orthoradial wave number have been observed with the emergence of two contra-rotating subharmonic waves. Similar experiments performed in a confined domain have shown that TRI is slightly modified, as the radial wave numbers of the waves forming the triad can be quasi-resonant and not exactly resonant[101]. This result is consistent with the fact that boundary conditions are known to have a significant impact on the characteristics of TRI, as discussed in the case, for instance, of surface waves [110].

3.2.2. *Super-Harmonic Generation*

While for a single monochromatic plane wave, the self-interaction term $(\mathbf{u}\cdot\nabla)\mathbf{u}$ vanishes, this is no longer the case for axisymmetric wave fields. A direct consequence is that axisymmetric waves can self-interact and transfer energy to waves at higher frequencies, contrary to Cartesian plane waves (self-interaction is only possible for plane waves if the stratification is non-linear [111]). This process generates super-harmonics, i.e. waves at frequencies 2ω, 3ω, ... from an axisymmetric wave field initially forced at ω. These super-harmonics are propagating if the primary forcing occurs at sufficiently small frequency so that the harmonic frequencies remain smaller than the cut-off frequency imposed either by f or N. Evidenced for the first time in the experimental study of [108], these harmonics remain axisymmetric if the fluid is stratified and non-rotating. The energy is then distributed onto several waves (cavity modes in the aforementioned study), that satisfy temporal resonance conditions but not necessarily spatial ones. As for TRI, this could be due to the enforcement of boundary conditions that prevail over the resonances.

4. Internal Gravity Wave/Inertial Wave Attractor

4.1. 2*D and* 3*D Reflection*

As underlined in the introduction, internal waves propagate along a double cone with a half top angle equal to β which is given by the dispersion relation (7). Such a property leads to a peculiar reflection law of these waves on a slope. Snell's reflection law, applicable e.g. for light waves and surface waves, prescribes that the reflected and the incident waves have the same angle with respect to the normal to the slope. This is not the case for internal waves (either gravity or inertial waves). The first conservation law in this case is given by the non penetrability condition, written as

$$(\mathbf{v}_r + \mathbf{v}_i)\cdot\mathbf{n} = 0. \tag{14}$$

This leads to the conservation of frequency and of the projection of the wave vector along the direction of the slope. As a consequence, the reflected and incident waves propagate along the same double cone.

In 2D geometry, this means that the reflected wave propagates in a different quadrant of the Saint Andrews cross. In addition, the reflection on a slope inclined with an angle α with the horizontal leads to focusing or defocusing, depending on the relative values of α and β and on

the direction of propagation of the incident wave. When focusing occurs, the wave length of the wave beam decreases by a factor

$$\gamma = \left| \frac{\sin(\alpha + \beta)}{\sin(\alpha - \beta)} \right| . \tag{15}$$

Assuming conservation of energy, the energy flux density is increased by a factor γ^2 and the reflected wave is therefore more prone to instability. Note that the case $\beta = \alpha$ is a singularity ($\gamma \to \infty$), the so-called critical reflection. It has been the focus of theoretical analysis [112] and experiments [79].

In three dimensions, the orthoradial angle is not imposed by the dispersion relation and is therefore not conserved. The derivation of the reflection law in this case has been performed for internal gravity and inertial waves following slightly different approaches [113–117]. The different derivations use three ingredients: non penetrability; propagation of the incident and reflected waves on the same cone and conservation of the horizontal component of the velocity normal to the slope. They have shown that the rays of waves change direction upon reflection and have the tendency to converge toward the upslope gradient.

4.2. *Wave Attractor*

In a closed domain with a particular geometry and for a specific range of frequencies, successive reflections of wave rays in the domain have been shown to converge on the same limit cycle, which is a geometric pattern, called wave attractor [118]. Theoretical predictions can be made using ray-tracing methods, in which the wave beam is assumed to be localized enough so that its propagation along the group velocity can be described by a geometrical ray path. The phenomenon of concentration of the energy on attractors in 2D geometries has been the subject of different mathematical studies [35,119–121]. In the past years, different geometries leading to the possible existence of wave attractors have been investigated. These works have been summarized in a recent review [122].

In astrophysics, the link between wave attractors and trapped wave in the equatorial regions of rotating planets has been first considered [123–125]. Rotating spherical shells have been shown to be a generic geometry for inertial wave attractors [126,127], which appear in numerical simulations [16]. The role of different features such as the behavior of the waves in the vicinity of the axis of rotation, the critical latitude phenomenon, and non-linearities have then been analyzed [128–131].

Even if different works have considered the possible existence of internal wave attractors in real stratifications and topographies using different geometries [82,132–134], no field observations of attractors has been reported so far.

In the following, we will focus on the main experimental results obtained in 2D trapezoidal geometries and in an axisymmetric frustrum to show the difference and similarities between gravity and inertial wave attractors.

4.3. *Experiments in Quasi-2D Trapezoidal Domains*

Following his seminal theoretical study [118], Maas has collaborated in different experimental studies to visualize internal gravity wave and inertial wave attractors. There were first observed in a density stratified fluid using an oscillating tank [135]. Even though the structure of an inertial wave is three-dimensional, a linear attractor was also observed in the case of inertial waves, using as well an oscillating tank as generator [35,115,136]. Without dissipation, the energy density along the attractor tends to infinity due to multiple focusings. In a more realistic scenario, the energy is dissipated through viscous dissipation or non-linear phenomena. The balance between

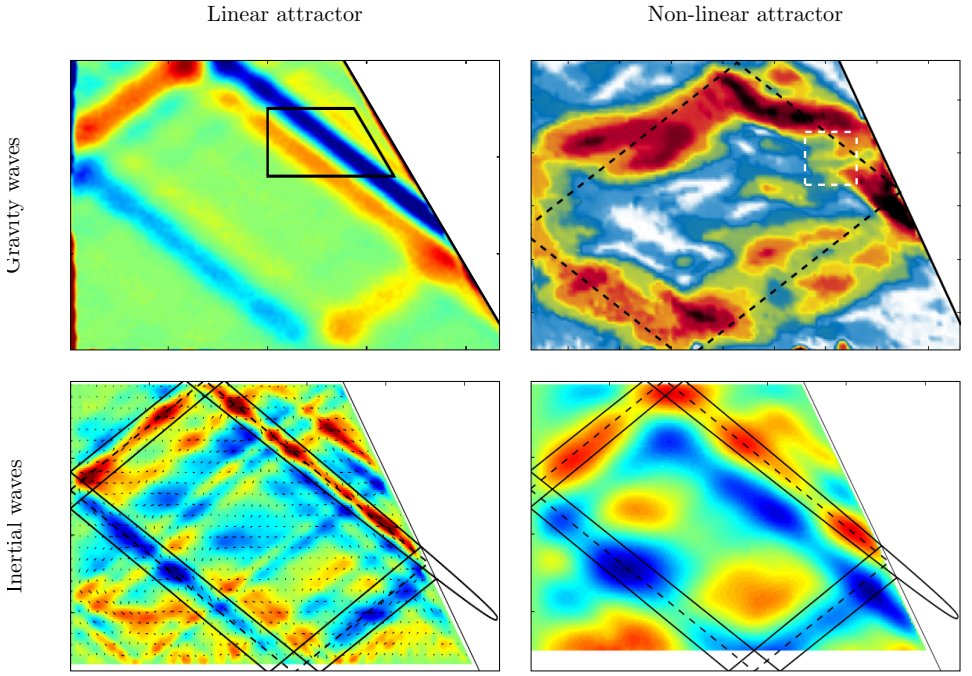


Figure 7. Examples of experimental realization of internal wave attractors. (Top left) Synthetic Schlieren visualization of a linear gravity wave attractor (adapted from [141]). (Top right) Kinetic energy for a non-linear gravity wave attractor (adapted from [92]). (Bottom left) Horizontal velocity field for a linear inertial wave attractor (adapted from [67]). (Bottom right) Horizontal velocity field for a non-linear inertial wave attractor (adapted from [67]).

focusing at the slope and viscous effects can be used to predict the width of the branches of the attractor. Based on experimental results for gravity internal waves [137], this width was predicted to scale as $(\nu/L^2N)^{1/3}$ with L the perimeter of the attractor. This result was checked numerically by Grisouard et al. [138]. For inertial waves, the equivalent scaling factor is $\mathrm{Ek}^{1/3} = (\nu/L^2 f)^{1/3}$, as verified numerically [139,140].

To illustrate this discussion, a typical linear wave field for both types of attractors is displayed in Figure 7(left). The scaling proposed above was satisfied in the case of a linear inertial wave attractor [67]. For the linear gravity wave attractor, the agreement was less clear [141]. An explanation was further proposed in [142] and validated in [37]. It is related to boundary dissipation effects, whose magnitude is different between the two configurations, due to the size of the tanks. The different tanks were chosen to be adapted to the structure of the waves. For internal gravity waves, the tank had a small thickness compared to the other dimensions and the velocity profiles were measured to be two-dimensional except in the viscous boundary layer near the lateral walls. This layer induces a strong dissipation which is at least ten times larger than the bulk dissipation. This effect is reduced in the case of inertial waves, since the tank is much wider, relatively to the other typical dimensions, and as a consequence, the bulk dissipation dominates. A new scaling law for the size of the branches of the internal wave attractors was then proposed and is in better agreement with experiments [142].

The three-dimensional effects on a wave attractor were then studied for internal gravity waves by Pillet et al. [143] using an extension in the third direction of the quasi-2D experiments performed at ENS de Lyon. These experiments show a trapping of the waves in different 2D planes.

Due to the accumulation of energy in the branches of the attractor, gravity wave attractors and inertial wave attractors are prone to instabilities and in particular triadic resonance instability. Snapshots of the non-linear gravity wave attractor obtained at ENS de Lyon [92,141,144] and of the non-linear inertial wave attractor obtained at Paris-Saclay [67] are reproduced in Figure 7. One can still see the geometrical structure, on top of which several other waves have formed. Both studies have shown that the attractor amplitude was reduced and the attractor typical length increased.

Such results were attributed to an energy transfer due to the instability and can be quantified by replacing, in the model for linear attractors, the kinematic viscosity by a turbulent viscosity based on the features of the forced waves [67]. In the non-linear case, strong differences between gravity wave attractors and inertial wave attractors have been observed. An important one is the selectivity of the secondary waves. The feature already mentioned for wave beams (Section 2.2 and Figure 2) is also observed here: indeed, for inertial waves the frequency peaks for the secondary waves are very wide compared to the ones for gravity waves. In addition, there is a clear discrepancy between experimental results for rotating fluids and the 2D numerical simulations [139], while the agreement between experiments and simulations is very good for gravity wave attractors [141]. This weak selectivity in the case of inertial waves can be attributed to the three-dimensional structure of these waves interacting with physical walls, which was clearly neither the case for internal gravity waves [141], nor in the numerical simulations of inertial waves using proper boundary conditions [139]. The second difference concerns the possibility of secondary inertial waves with a non-zero component in the direction perpendicular to the plane of the attractor. This observation, specific to inertial waves and already mentioned for wave beams, could explain the dependence of the secondary waves on Reynolds number, which displays an opposite behavior compared to 2D numerical simulations. Indeed, in the latter case the frequencies ω_1 and ω_2 of the subharmonic waves tend toward $\omega_0/2$ for larger Reynolds number while for experiments they depart from $\omega_0/2$.

4.4. *Axisymmetric Domain: Frustrum*

A second geometry has been widely used to study 3D effects for gravity or inertial wave attractors: the frustrum, i.e. an annulus whose inner cylinder is replaced by a truncated cone. This geometry has been investigated for inertial waves both numerically and experimentally [145–148]. These studies show a wide variety of dynamical systems including linear wave attractors, triadic instability, and emergence of mean flows.

We would like to focus on a similar geometry without the inner cylinder, used in experiments conducted at ENS de Lyon [58]. Using exactly the same experimental setup, rotating fluids and stratified fluids were studied. If the formation of a linear internal wave axisymmetric attractor is similar for both inertial and gravity waves, a major difference is visible for the nonlinear dynamics. Here again, the secondary waves are associated with discrete frequencies for gravity waves contrary to inertial waves for which the frequency range is large, as can be seen in Figure 8 (top, respectively left and right). To explain this behavior, the authors of this study [58] show that the secondary internal waves are the global resonant modes of the tank while the secondary inertial waves are only localized near the center of the tank, as can be seen in the bottom row of Figure 8, left and right respectively. It is explained by the fact that for rotating fluids, standing modes are associated with frequencies larger than the forcing frequency and therefore

not accessible through TRI, resulting only in a local appearance of these secondary waves. The important role of the boundaries is therefore highlighted in the respective non-linear dynamics of gravity and inertial waves. At Paris-Saclay, an experiment to study internal wave turbulence has been designed with inclined panels at the bottom of the tank to inhibit the emergence of wave eigenmodes [149]. In such a configuration, the frequency peaks of the secondary waves excited through TRI are much broader. The frequency spectrum for internal gravity waves becomes therefore closer to the frequency spectrum observed for weakly non-linear inertial waves (Figure 2 right).

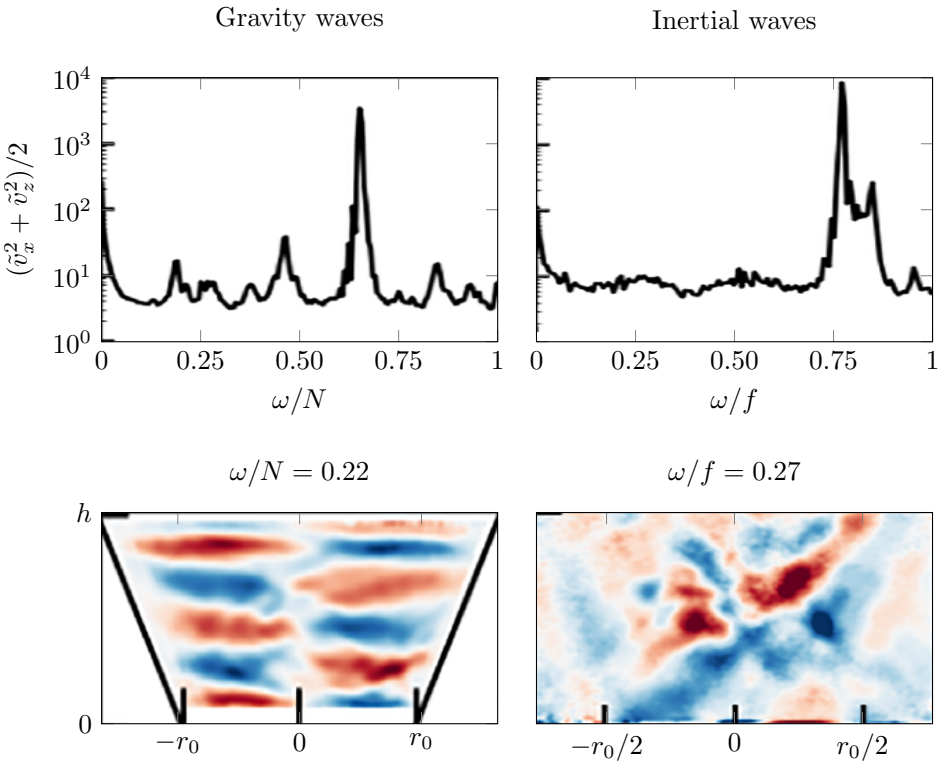


Figure 8. Non-linear behavior of an axisymmetric wave attractor in a frustrum, for gravity waves (left) and inertial waves (right). (Top row) Frequency spectrum. (Bottom row) Snapshots of one of the secondary waves filtered at a given frequency. (Figure adapted from [58]).

Finally, breaking the axisymmetry could induce the trapping of a wave attractor in a particular plane in 3D. This has been recently predicted theoretically and verified numerically [117].

5. Conclusions and Future Directions

In this article, we have discussed several examples of experiments investigating both the linear and non-linear behaviors of internal gravity waves in stratified fluids and of inertial waves in rotating fluids. More specifically, we have focused on the Triadic Resonant Instability (TRI) in various configurations. All these experiments show that, although these waves have a similar dispersion relation, their spatial structure is very important and must be taken into account in

order to accurately predict their linear and non-linear dynamics. In particular, clear differences have been noted in the weakly non-linear regime for different geometries. The main difference is the attraction of energy by discrete frequencies associated to resonances and standing modes in the stratified case. This process seems not to be at play in the rotating case, probably because of the 3D structure of wave field. This observation is of great interest to guide future developments in the study of internal waves.

Recently, efforts have been made to observe, in laboratory experiments, both a weakly non-linear regime of internal gravity wave turbulence in a density stratified fluid [30], and a regime of inertial wave turbulence in a rotating flow [150]. It will be interesting as well to study the similarities and differences in these wave turbulence regimes between gravity and inertial waves.

As mentioned in the introduction, rotating-stratified fluids are ubiquitous in geophysical and astrophysical systems. Laboratory experimental studies combined with theoretical developments and numerical simulations help complement the fundamental understanding of the non-linear behavior of both internal gravity and inertial waves, and therefore help improve the parametrization of (stratified) mixing and other small scale phenomena in climate models. To further assess the role of these waves in atmospheric and oceanic processes, additional features have recently been the focus of a more sustained attention such as the generation of inertial or internal gravity waves due to moving obstacles, the combination of rotation and stratification, the role of a non-linear stratification in density stratified fluids, ice-melting and double diffusive mechanisms, wave-turbulence interaction, wave-mean flow interaction, and the coupling between internal gravity/inertial waves with other type of waves (Lee waves, Kelvin waves, surface waves…). These are important processes that need to be further understood.

Declaration of interests

The authors do not work for, advise, own shares in, or receive funds from any organization that could benefit from this article, and have declared no affiliations other than their research organizations.

References

[1] J. Lighthill, *Waves in fluids*, 3rd edition, Cambridge University Press, 1978.
[2] D. E. Mowbray and B. S. H. Rarity, "The internal wave pattern produced by a sphere moving vertically in a density stratified liquid", *J. Fluid Mech.* **30** (1967), pp. 489–495.
[3] B. R. Sutherland, *Internal gravity waves*, Cambridge University Press, 2010.
[4] H. P. Greenspan, *The Theory of Rotating Fluids*, Cambridge University Press, 1968.
[5] C. Garrett, "Internal Tides and Ocean Mixing", *Science* **301** (2003), no. 5641, pp. 1858–1859.
[6] C. Wunsch and R. Ferrari, "Vertical mixing, energy and the general circulation of the oceans", *Annu. Rev. Fluid Mech.* **36** (2004), pp. 281–314.
[7] J. A. MacKinnon, Z. Zhao, C. B. Whalen, et al., "Climate Process Team on Internal Wave–Driven Ocean Mixing", *Bull. Am. Meteorol. Soc.* **98** (2017), no. 11, pp. 2429–2454.
[8] C. de Lavergne, S. Falahat, G. Madec, F. Roquet, J. Nycander and C. Vic, "Toward global maps of internal tide energy sinks", *Ocean Model.* **137** (2019), pp. 52–75.
[9] F. Pollmann, "Global Characterization of the Ocean's Internal Wave Spectrum", *J. Phys. Oceanogr.* **50** (2020), no. 7, pp. 1871–1891.
[10] U. Achatz, O. Bühler, C. Staquet and W. R. Young, "Multiscale Wave-Turbulence Dynamics in the Atmosphere and Ocean", *Oberwolfach Rep.* **19** (2022), no. 3, pp. 2467–2510.
[11] E. Becker and G. Schmitz, "Climatological Effects of Orography and Land–Sea Heating Contrasts on the Gravity Wave–Driven Circulation of the Mesosphere", *J. Atmos. Sci.* **60** (2003), no. 1, pp. 103–118.
[12] Y.-J. Kim, S. D. Eckermann and H.-Y. Chun, "An overview of the past, present and future of gravity-wave drag parametrization for numerical climate and weather prediction models", *Atmosphere-Ocean* **41** (2003), no. 1, pp. 65–98.

[13] A. de la Cámara, F. Lott and M. Abalos, "Climatology of the middle atmosphere in LMDz: Impact of source-related parameterizations of gravity wave drag", *Journal of Advances in Modeling Earth Systems* **8** (2016), no. 4, pp. 1507–1525.
[14] L. A. Holt, F. Lott, R. R. Garcia, et al., "An evaluation of tropical waves and wave forcing of the QBO in the QBOi models", *Q. J. R. Meteorol. Soc.* **148** (2022), no. 744, pp. 1541–1567.
[15] R. R. Kerswell and W. V. R. Malkus, "Tidal instability as the source for Io's magnetic signature", *Geophys. Res. Lett.* **25** (1998), no. 5, pp. 603–606.
[16] G. I. Ogilvie and D. N. C. Lin, "Tidal Dissipation in Rotating Giant Planets", *Astrophys. J.* **610** (2004), no. 1, pp. 477–509.
[17] T. Sidery, N. Andersson and G. L. Comer, "Waves and instabilities in dissipative rotating superfluid neutron stars", *Mon. Not. Roy. Astron. Soc.* **385** (2008), no. 1, pp. 335–348.
[18] M. Le Bars, D. Cébron and P. Le Gal, "Flows Driven by Libration, Precession, and Tides", *Ann. Rev. Fluid Mech.* **47** (2015), pp. 163–193.
[19] M. Bouffard, B. Favier, D. Lecoanet and M. Le Bars, "Internal gravity waves in a stratified layer atop a convecting liquid core in a non-rotating spherical shell", *Geophys. J. Int.* **228** (2021), no. 1, pp. 337–354.
[20] S. Dauxois T. rand Joubaud, P. Odier and A. Venaille, "Instabilities of Internal Gravity Wave Beams", *Ann. Rev. of Fluid Mech.* **50** (2018), pp. 131–156.
[21] C. Staquet and J. Sommeria, "Internal gravity waves: From instabilities to turbulence", *Annu. Rev. Fluid Mech.* **34** (2002), pp. 559–593.
[22] G. Veronis, "The analogy between rotating and stratified fluids", *Ann. Rev. Fluid Mech.* **2** (1970), pp. 36–67.
[23] S. Medvedev and V. Zeitlin, "Parallels between stratification and rotation in hydrodynamics, and between both of them and external magnetic field in magnetohydrodynamics, with applications to nonlinear waves", in *IUTAM Symposium on Turbulence in the Atmosphere and Oceans* (D. Dritschel, ed.), IUTAM Bookseries, Springer, 2010, pp. 27–37.
[24] P. Maurer, *Approche expérimentale de la dynamique non-linéaire d'ondes internes en rotation*, PhD thesis, Université de Lyon, France, 2017.
[25] D. E. Mowbray and B. S. H. Rarity, "A theoretical and experimental investigation of the phase configuration of internal waves of small amplitude in a density stratified liquid", *J. Fluid Mech.* **28** (1967), no. 1, pp. 1–16.
[26] T. Peacock and A. Tabaei, "Visualization of nonlinear effects in reflecting internal wave beams", *Phys. Fluids* **17** (2005), no. 6, article no. 061702.
[27] G. Brethouwer, P. Billant, E. Lindborg and J.-M. Chomaz, "Scaling analysis and simulation of strongly stratified turbulent flows", *J. Fluid Mech.* **585** (2007), pp. 343–368.
[28] G. N. Ivey, K. B. Winters and J. R. Koseff, "Density stratification, turbulence, but how much mixing?", *Annu. Rev. Fluid Mech.* **40** (2008), pp. 169–184.
[29] C. P. Caulfield, "Layering, Instabilities, and Mixing in Turbulent Stratified Flows", *Ann. Rev. Fluid Mech.* **53** (2021), no. 1, pp. 113–145.
[30] P.-P. Cortet and L. Lanchon, "Turbulence of internal gravity waves in the laboratory", *C. R. Phys.* **25** (2024), no. S3, pp. 537–556.
[31] S. Boury, *Energy and Buoyancy Transport by Inertia-Gravity Waves in Non-Linear Stratifications. Application to the Ocean*, PhD thesis, Université de Lyon, Lyon, France, 2020.
[32] D. W. Moore and P. G. Saffman, "The structure of free vertical shear layers in a rotating fluid and the motion produced by a slowly rising body", *Philos. Trans. R. Soc. Lond., Ser. A* **264** (1969), no. 1156, pp. 597–634.
[33] N. H. Thomas and T. N. Stevenson, "A similarity solution for viscous internal waves", *J. Fluid Mech.* **54** (1972), no. 3, pp. 495–506.
[34] M. Nikurashin and R. Ferrari, "Radiation and Dissipation of Internal Waves Generated by Geostrophic Motions Impinging on Small-Scale Topography: Theory", *J. Phys. Oceanogr.* **40** (2010), no. 5, pp. 1055–1074.
[35] A. M. M. Manders, J. J. Duistermaat and L. R. M. Maas, "Wave attractors in a smooth convex enclosed geometry", *Phys. D: Nonlinear Phenom.* **186** (2003), no. 3-4, pp. 109–132.
[36] P.-Y. Passaggia, P. Meunier and S. Le Dizès, "Response of a stratified boundary layer on a tilted wall to surface undulations", *J. Fluid Mech.* **751** (2014), pp. 663–684.
[37] G. Davis, T. Dauxois, T. Jamin and S. Joubaud, "Energy budget in internal wave attractor experiments", *J. Fluid Mech.* **880** (2019), pp. 743–763.
[38] E. Horne, F. Beckebanze, D. Micard, P. Odier, L. R. M. Maas and S. Joubaud, "Particle transport induced by internal wave beam streaming in lateral boundary layers", *J. Fluid Mech.* **870** (2019), pp. 848–869.
[39] S. Le Dizès, "Reflection of oscillating internal shear layers: nonlinear corrections", *J. Fluid Mech.* **899** (2020), article no. A21.
[40] G. Bordes, F. Moisy, T. Dauxois and P.-P. Cortet, "Experimental evidence of a triadic resonance of plane inertial waves in a rotating fluid", *Phys. Fluids* **24** (2012), no. 1, article no. 014105.
[41] A. Renaud and A. Venaille, "Boundary streaming by internal waves", *J. Fluid Mech.* **858** (2019), pp. 71–90.

[42] M. A. Calkins, J. Noir, J. D. Eldredge and J. M. Aurnou, "Axisymmetric simulations of libration-driven fluid dynamics in a spherical shell geometry", *Phys. Fluids* **22** (2010), no. 8, article no. 086602.
[43] A. Tilgner, "Kinematic dynamos with precession driven flow in a sphere", *Geophys. Astro. Fluid* **101** (2007), no. 1, pp. 1–9.
[44] C. Morize, M. Le Bars, P. Le Gal and A. Tilgner, "Experimental Determination of Zonal Winds Driven by Tides", *Phys. Rev. Lett.* **104** (2010), no. 21, article no. 214501.
[45] Y. Onuki, S. Joubaud and T. Dauxois, "Simulating turbulent mixing caused by local instability of internal gravity waves", *J. Fluid Mech.* **915** (2021), article no. A77.
[46] C. B. Whalen, C. de Lavergne, A. C. Naveira Garabato, J. M. Klymak, J. A. MacKinnon and K. L. Sheen, "Internal wave-driven mixing: governing processes and consequences for climate", *Nat. Rev. Earth Environ.* **1** (2020), no. 11, pp. 606–621.
[47] Y. Dossmann, B. Bourget, C. Brouzet, T. Dauxois, S. Joubaud and P. Odier, "Mixing by internal waves quantified using combined PIV/PLIF technique", *Exp. Fluids* **57** (2016), no. 8, article no. 132.
[48] Y. Dossmann, F. Pollet, P. Odier and T. Dauxois, "Mixing and Formation of Layers by Internal Wave Forcing", *J. Geophys. Res. Oceans* **122** (2017), no. 12, pp. 9906–9917.
[49] J. M. H. Fortuin, "Theory and application of two supplementary methods of constructing density gradient columns", *J. Polym. Sci.* **44** (1960), no. 144, pp. 505–515.
[50] G. Oster and M. Yamamoto, "Density Gradient Techniques", *Chem. Rev.* **63** (1963), no. 3, pp. 257–268.
[51] D. F. Hill, "General density gradients in general domains: the "two-tank" method revisited", *Exp. Fluids* **32** (2002), no. 4, pp. 434–440.
[52] K. D. Stewart, C. J. Shakespeare, Y. Dossmann and A. M. Hogg, "A simple technique for developing and visualising stratified fluid dynamics: the hot double-bucket", *Exp. Fluids* **62** (2021), no. 5, article no. 103.
[53] S. B. Dalziel, G. O. Hughes and B. R. Sutherland, "Whole-field density measurements by 'synthetic schlieren'", *Exp. Fluids* **28** (2000), no. 4, pp. 322–335.
[54] A. M. van Oers, R. de Kat and L. R. M. Maas, "Whole-field density measurements by digital image correlation", *Exp. Fluids* **64** (2023), no. 11, p. 175.
[55] D. Benielli and J. Sommeria, "Excitation of internal waves and stratified turbulence by parametric instability", *Dynam. Atmos. Oceans* **23** (1996), no. 1-4, pp. 335–343. 4th International Symposium on Stratified Flows, Grenoble, France, Jun 29 - Jul 02, 1994.
[56] J. Noir, D. Cébron, M. Le Bars, A. Sauret and J. M. Aurnou, "Experimental study of libration-driven zonal flows in non-axisymmetric containers", *Phys. Earth Planet. Inter.* **204** (2012), pp. 1–10.
[57] C. Savaro, A. Campagne, M. C. Linares, et al., "Generation of weakly nonlinear turbulence of internal gravity waves in the Coriolis facility", *Phys. Rev. Fluids* **5** (2020), no. 7, article no. 073801.
[58] C. Pacary, T. Dauxois, E. Ermanyuk, P. Metz, M. Moulin and S. Joubaud, "Observation of inertia-gravity wave attractors in an axisymmetric enclosed basin", *Phys. Rev. Fluids* **8** (2023), no. 10, article no. 104802.
[59] T. Dauxois, A. Didier and E. Falcon, "Observation of near-critical reflection of internal waves in a stably stratified fluid", *Phys. Fluids* **16** (2004), no. 6, pp. 1936–1941.
[60] B. Voisin, E. V. Ermanyuk and J.-B. Flór, "Internal wave generation by oscillation of a sphere, with application to internal tides", *J. Fluid Mech.* **666** (2011), pp. 308–357.
[61] M. Duran-Matute, J.-B. Flór, F. S. Godeferd and C. Jause-Labert, "Turbulence and columnar vortex formation through inertial-wave focusing", *Phys. Rev. E* **87** (2013), no. 4, article no. 041001.
[62] E. Monsalve, M. Brunet, B. Gallet and P.-P. Cortet, "Quantitative experimental observation of weak inertial-wave turbulence", *Phys. Rev. Lett.* **125** (2020), no. 25, article no. 254502.
[63] L. Gostiaux and T. Dauxois, "Laboratory experiments on the generation of internal tidal beams over steep slopes", *Phys. Fluids* **19** (2007), no. 2, article no. 028102.
[64] M. M. Scase and S. B. Dalziel, "Internal wave fields generated by a translating body in a stratified fluid: an experimental comparison", *J. Fluid Mech.* **564** (2006), pp. 305–331.
[65] L. Gostiaux, H. Didelle, S. Mercier and T. Dauxois, "A novel internal waves generator", *Exp. Fluids* **42** (2007), no. 1, pp. 123–130.
[66] T. E. Dobra, A. G. W. Lawrie and S. B. Dalziel, "The magic carpet: an arbitrary spectrum wave maker for internal waves", *Exp. Fluids* **60** (2019), pp. 1–14.
[67] M. Brunet, T. Dauxois and P.-P. Cortet, "Linear and nonlinear regimes of an inertial wave attractor", *Phys. Rev. Fluids* **4** (2019), no. 3, article no. 034801.
[68] P. Husseini, D. Varma, T. Dauxois, S. Joubaud, P. Odier and M. Mathur, "Experimental study on superharmonic wave generation by resonant interaction between internal wave modes", *Phys. Rev. Fluids* **5** (2020), no. 7, article no. 074804.
[69] P. Maurer, S. J. Ghaemsaidi, S. Joubaud, T. Peacock and P. Odier, "An axisymmetric inertia-gravity wave generator", *Exp. Fluids* **58** (2017), no. 10, article no. 143.

[70] W. V. R. Malkus, "An experimental study of global instabilities due to the tidal (elliptical) distortion of a rotating elastic cylinder", *Geophys. Astrophys. Fluid Dyn.* **48** (1989), no. 1-3, pp. 123–134.
[71] B. Favier, A. Grannan, T. Le Reun, J. Aurnou and M. Le Bars, "The turbulent response to tidal and libration forcing", in *Astro Fluid: An International Conference in Memory of Professor Jean-Paul Zahn's Great Scientific Achievements*, EAS Publications Series, EDP Sciences, 2019, pp. 51–58.
[72] J. R. Munroe and B. R. Sutherland, "Generation of internal waves by sheared turbulence: experiments", *Environ. Fluid Mech.* **8** (2008), pp. 527–534.
[73] V. Dorel, P. Le Gal and M. Le Bars, "Experimental study of the penetrative convection in gases", *Phys. Rev. Fluids* **8** (2023), article no. 103501.
[74] P. Flandrin, *Time-Frequency/Time-Scale Analysis, Time-Frequency Toolbox for Matlab©*, Wavelet Analysis and Its Applications, Academic Press, San Diego, 1999.
[75] M. J. Mercier, N. B. Garnier and T. Dauxois, "Reflection and diffraction of internal waves analyzed with the Hilbert transform", *Phys. Fluids* **20** (2008), no. 8, article no. 086601.
[76] M. Mathur and T. Peacock, "Internal wave interferometry", *Phys. Rev. Lett.* **104** (2010), no. 11, article no. 118501.
[77] R. Supekar and T. Peacock, "Interference and transmission of spatiotemporally locally forced internal waves in non-uniform stratifications", *J. Fluid Mech.* **866** (2019), pp. 350–368.
[78] S. Boury, T. Peacock and P. Odier, "Excitation and resonant enhancement of axisymmetric internal wave modes", *Phys. Rev. Fluids* **4** (2019), no. 3, article no. 034802.
[79] E. Horne, J. Schmitt, N. Pustelnik, S. Joubaud and P. Odier, "Variational Mode Decomposition for estimating critical reflected internal wave in stratified fluid", *Exp. Fluids* **62** (2021), article no. 110.
[80] S. Boury, B. R. Sutherland, S. Joubaud, T. Peacock and P. Odier, "Axisymmetric internal wave tunneling", 2024.
[81] K. M. Grayson, S. B. Dalziel and A. G. W. Lawrie, "The long view of triadic resonance instability in finite-width internal gravity wave beams", *J. Fluid Mech.* **953** (2022), article no. A22.
[82] J. Hazewinkel, S. B. Dalziel, A. Doelman and L. R. M. Maas, "Tracer transport by internal wave beams", 2010.
[83] B. Bourget, T. Dauxois, S. Joubaud and P. Odier, "Experimental study of parametric subharmonic instability for internal plane waves", *J. Fluid Mech.* **723** (2013), pp. 1–20.
[84] B. Bourget, H. Scolan, T. Dauxois, M. Le Bars, P. Odier and S. Joubaud, "Finite-size effects in parametric subharmonic instability", *J. Fluid Mech.* **759** (2014), pp. 739–750.
[85] G. Bordes, *Interactions non-linéaires d'ondes et tourbillons en milieu stratifié ou tournant*, PhD thesis, Université de Lyon, Lyon, France, 2012.
[86] R. E. Davis and A. Acrivos, "The stability of oscillatory internal waves", *J. Fluid Mech.* **30** (1967), no. 4, pp. 723–736.
[87] A. D. McEwan and R. M. Robinson, "Parametric-Instability of Internal Gravity-Waves", *J. Fluid Mech.* **67** (1975), no. FEB25, pp. 667–687.
[88] D. Benielli and J. Sommeria, "Excitation and breaking of internal gravity waves by parametric instability", *J. Fluid Mech.* **374** (1998), pp. 117–144.
[89] S. Joubaud, J. Munroe, P. Odier and T. Dauxois, "Experimental parametric subharmonic instability in stratified fluids", *Phys. Fluids* **24** (2012), no. 4, article no. 041703.
[90] J. A. MacKinnon, M. H. Alford, O. Sun, R. Pinkel, Z. Zhao and J. Klymak, "Parametric subharmonic instability of the internal tide at 29 N", *J. Phys. Oceanogr.* **43** (2013), no. 1, pp. 17–28.
[91] Q. Hu et al., "Parametric Subharmonic Instability of Diurnal Internal Tides in the Abyssal South China Sea", *J. Phys. Oceanogr.* **53** (2023), no. 1, pp. 195–213.
[92] C. Brouzet, E. V. Ermanyuk, S. Joubaud, I. Sibgatullin and T. Dauxois, "Energy cascade in internal-wave attractors", *Europhysics Letters* **113** (2016), no. 4, article no. 44001.
[93] P. Maurer, S. Joubaud and P. Odier, "Generation and stability of inertia-gravity waves", *J. Fluid Mech.* **808** (2016), pp. 539–561.
[94] D. O. Mora, E. Monsalve, M. Brunet, T. Dauxois and P.-P. Cortet, "Three-dimensionality of the triadic resonance instability of a plane inertial wave", *Phys. Rev. Fluids* **6** (2021), no. 7, article no. 074801.
[95] S. J. Ghaemsaidi and M. Mathur, "Three-dimensional small-scale instabilities of plane internal gravity waves", *J. Fluid Mech.* **863** (2019), pp. 702–729.
[96] K. N. Kumar, T. K. Ramkumar and M. Krishnaiah, "MST radar observation of inertia-gravity waves generated from tropical cyclones", *J. Atmos. Sol.-Terr. Phys.* **73** (2011), pp. 1890–1906.
[97] W. H. Schubert, J. J. Hack, P. L. Silva Dias and S. R. Fulton, "Geostrophic adjustment in an axisymmetric vortex", *J. Atmos. Sol.-Terr. Phys.* **37** (1980), pp. 1464–1484.
[98] T. N. Stevenson, "Axisymmetric Internal Waves Generated by a Travelling Oscillating Body", *J. Fluid Mech.* **35** (1969), pp. 219–224.
[99] M. R. Flynn, K. Onu and B. R. Sutherland, "Internal wave excitation by a vertically oscillating sphere", *J. Fluid Mech.* **494** (2003), pp. 65–93.

[100] J. K. Ansong and B. R. Sutherland, "Internal gravity waves generated by convective plumes", *J. Fluid Mech.* **648** (2010), pp. 405–434.
[101] S. Boury, P. Maurer, S. Joubaud, T. Peacock and P. Odier, "Triadic resonant instability in confined and unconfined axisymmetric geometries", *J. Fluid Mech.* **957** (2023), article no. A20.
[102] E. V. Ermanyuk, J.-B. Flór and B. Voisin, "Spatial Structure of First and Higher Harmonic Internal Waves from a Horizontally Oscillating Sphere", *J. Fluid Mech.* **671** (2011), pp. 364–383.
[103] S. J. Ghaemsaidi, H. V. Dosser, L. Rainville and T. Peacock, "The impact of multiple layering on internal wave transmission", *J. Fluid Mech.* **789** (2016), pp. 617–629.
[104] T. Peacock and P. Weidman, "The Effect of Rotation on Conical Wave Beams in a Stratified Fluid", *Exp. Fluids* **39** (2005), pp. 32–37.
[105] E. V. Ermanyuk, N. D. Shmakova and J.-B. Flór, "Internal Wave Focusing by a Horizontally Oscillating Torus", *J. Fluid Mech.* **813** (2017), pp. 695–715.
[106] D. Guimbard, *L'instabilité elliptique en milieu stratifié tournant*, PhD thesis, Université du Sud Toulon Var, France, 2008.
[107] D. Guimbard, S. Le Dizès, M. Le Bars, P. Le Gal and S. Leblanc, "Elliptic instability of a stratified fluid in a rotating cylinder", *J. Fluid Mech.* **660** (2010), pp. 240–257.
[108] S. Boury, T. Peacock and P. Odier, "Experimental generation of axisymmetric internal wave super-harmonics", *Phys. Rev. Fluids* **6** (2021), no. 6, article no. 064801.
[109] N. D. Shmakova and J.-B. Flór, "Nonlinear aspects of focusing internal waves", *J. Fluid Mech.* **862** (2019), article no. R4.
[110] G. Michel, "Three-wave interactions among surface gravity waves in a cylindrical container", *Phys. Rev. Fluids* **4** (2019), article no. 012801.
[111] L. E. Baker and B. R. Sutherland, "The evolution of superharmonics excited by internal tides in non-uniform stratification", *J. Fluid Mech.* **891** (2020), article no. R1.
[112] T. Dauxois and W. R. Young, "Near-critical reflection of internal waves", *J. Fluid Mech.* **390** (1999), pp. 271–295.
[113] O. M. Phillips, "Energy Transfer in Rotating Fluids by Reflection of Inertial Waves", *The Physics of Fluids* **6** (1963), no. 4, pp. 513–520.
[114] C. C. Eriksen, "Observations of internal wave reflection off sloping bottoms", *J. Geophys. Res. Oceans* **87** (1982), no. C1, pp. 525–538.
[115] A. M. M. Manders and L. R. M. Maas, "On the three-dimensional structure of the inertial wave field in a rectangular basin with one sloping boundary", *Fluid Dyn. Res.* **35** (2004), no. 1, pp. 1–21.
[116] G. Pillet, L. R. M. Maas and T. Dauxois, "Internal wave attractors in 3D geometries : A dynamical systems approach", *Eur. J. Mech. B Fluids* **77** (2019), pp. 1–16.
[117] B. Favier and S. Le Dizès, "Inertial wave super-attractor in a truncated elliptic cone", *J. Fluid Mech.* **980** (2024), article no. A6.
[118] L. R. M. Maas and F. P. A. Lam, "Geometric focusing of internal waves", *J. Fluid Mech.* **300** (1995), pp. 1–41.
[119] J. Bajars, J. Frank and L. R. M. Maas, "On the appearance of internal wave attractors due to an initial or parametrically excited disturbance", *J. Fluid Mech.* **714** (2013), pp. 283–311.
[120] Y. Colin de Verdière and L. Saint-Raymond, "Attractors for Two-Dimensional Waves with Homogeneous Hamiltonians of Degree 0", *Commun. Pure Appl. Math.* **73** (2020), no. 2, pp. 421–462.
[121] Z. V. Makridin, A. K. Khe, I. N. Sibgatullin and E. V. Ermanyuk, "Forced internal wave attractors: Linear inviscid theory", *Phys. Rev. Fluids* **8** (2023), no. 8, article no. 084801.
[122] I. N. Sibgatullin and E. V. Ermanyuk, "Internal and Inertial Wave Attractors: A Review", *J. Appl. Mech. Tech. Phys.* **60** (2019), no. 2, pp. 284–302.
[123] M. E. Stern, "Trapping of low frequency oscillations in an equatorial boundary layer", *Tellus* **15** (1963), pp. 246–250.
[124] F. P. Bretherton, "Low frequency oscillations trapped near the equator", *Tellus* **16** (1964), no. 2, pp. 181–185.
[125] K. Stewartson, "On trapped oscillations of a rotating fluid in a thin spherical shell II", *Tellus* **24** (1972), pp. 283–287.
[126] M. Rieutord and L. Valdettaro, "Inertial waves in a rotating spherical shell", *J. Fluid Mech.* **341** (1997), pp. 77–99.
[127] M. Rieutord, B. Georgeot and L. Valdettaro, "Wave attractors in rotating fluids: a paradigm for ill-posed Cauchy problems", *Phys. Rev. Lett.* **435** (2001), pp. 103–144.
[128] M. Rieutord and L. Valdettaro, "Viscous dissipation by tidally forced inertial modes in a rotating spherical shell", *J. Fluid Mech.* **643** (2010), pp. 363–394.
[129] A. Rabitti and L. R. M. Maas, "Equatorial wave attractors and inertial oscillations", *J. Fluid Mech.* **729** (2013), pp. 445–470.
[130] B. Favier, A. J. Barker, C. Baruteau and G. I. Ogilvie, "Non-linear evolution of tidally forced inertial waves in rotating fluid bodies", *Mon. Not. R. Astron. Soc.* **439** (2014), pp. 845–860.

[131] J. He, B. Favier, M. Rieutord and S. Le Dizès, "Internal shear layers in librating spherical shells: the case of attractors", *J. Fluid Mech.* **974** (2023), article no. A3.
[132] A. M. M. Manders, L. R. M. Maas and T. Gerkema, "Observations of internal tides in the Mozambique Channel", *J. Geophys. Res. Oceans* **109** (2004), no. C12.
[133] W. Tang and T. Peacock, "Lagrangian coherent structures and internal wave attractors", *Chaos* **20** (2010), no. 1, article no. 017508.
[134] G. Wang, Q. Zheng, M. Lin, D. Dai and F. Qiao, "Three dimensional simulation of internal wave attractors in the Luzon Strait", *Acta Oceanologica Sinica* **34** (2015), no. 11, pp. 14–21.
[135] L. R. M. Maas, D. Benielli, J. Sommeria and F. P. A. Lam, "Observations of an internal wave attractor in a confined stably stratified fluid", *Nature* **388** (1997), pp. 557–561.
[136] L. R. M. Maas, "Wave focusing and ensuing mean flow due to symmetry breaking in rotating fluids", *J. Fluid Mech.* **437** (2001), pp. 13–28.
[137] J. Hazewinkel, P. van Breevoort, S. Dalziel and L. R. M. Maas, "Observations on the wavenumber spectrum and evolution of an internal wave attractor", *J. Fluid Mech.* **598** (2008), pp. 373–382.
[138] N. Grisouard, C. Staquet and I. Pairaud, "Numerical simulation of a two-dimensional internal wave attractor", *J. Fluid Mech.* **614** (2008), pp. 1–14.
[139] L. Jouve and G. I. Ogilvie, "Direct numerical simulations of an inertial wave attractor in linear and nonlinear regime", *J. Fluid Mech.* **745** (2014), pp. 223–250.
[140] K. Wu, B. D. Welfert and J. M. Lopez, "Inertial wave attractors in librating cuboids", *J. Fluid Mech.* **973** (2023), article no. A20.
[141] C. Brouzet, I. N. Sibgatullin, H. Scolan, E. V. Ermanyuk and T. Dauxois, "Internal wave attractors examined using laboratory experiments and 3D numerical simulations", *J. Fluid Mech.* **793** (2016), pp. 109–131.
[142] F. Beckebanze, C. Brouzet, I. N. Sibgatullin and L. R. M. Maas, "Damping of quasi-two-dimensional internal wave attractors by rigid-wall friction", *J. Fluid Mech.* **841** (2018), pp. 614–635.
[143] G. Pillet, E. V. Ermanyuk, L. R. M. Maas, I. N. Sibgatullin and T. Dauxois, "Internal wave attractors in three-dimensional geometries: trapping by oblique reflection", *J. Fluid Mech.* **845** (2018), pp. 203–225.
[144] C. Brouzet, E. Ermanyuk, S. Joubaud, G. Pillet and T. Dauxois, "Internal wave attractors: different scenarios of instability", *J. Fluid Mech.* **811** (2017), pp. 544–568.
[145] A. Swart, A. Manders, U. Harlander and L. R. M. Maas, "Experimental observation of strong mixing due to internal wave focusing over sloping terrain", *Dynam. Atmos. Oceans* **50** (2010), no. 1, pp. 16–34.
[146] M. Klein, T. Seelig, M. V. Kurgansky, et al., "Inertial wave excitation and focusing in a liquid bounded by a frustum and a cylinder", *J. Fluid Mech.* **751** (2014), pp. 255–297.
[147] I. Sibgatullin, X. Xu, A. Tretyakov and E. Ermanyuk, "Influence of geometry on energy flow and instability in inertial wave attractors for rotating annular frustum", *AIP Conf. Proc.* **2116** (2019), no. 1, article no. 030034.
[148] S. Boury, I. Sibgatullin, E. Ermanyuk, et al., "Vortex cluster arising from an axisymmetric inertial wave attractor", *J. Fluid Mech.* **926** (2021), article no. A12.
[149] N. Lanchon, D. O. Mora, E. Monsalve and P.-P. Cortet, "Internal wave turbulence in a stratified fluid with and without eigenmodes of the experimental domain", *Phys. Rev. Fluids* **8** (2023), no. 5, article no. 054802.
[150] S. Galtier, "Inertial Wave Turbulence", in *Physics of Wave Turbulence*, Cambridge University Press, 2022, pp. 155–178.

ACADÉMIE DES SCIENCES
INSTITUT DE FRANCE

Comptes Rendus. Physique
2024, Vol. 25, Special issue S3, p. 537-556
https://doi.org/10.5802/crphys.192

Review article / *Article de synthèse*

Geophysical and astrophysical fluid dynamics in the laboratory / *Dynamique des fluides géophysiques et astrophysiques au laboratoire*

Turbulence of internal gravity waves in the laboratory

La turbulence d'ondes internes de gravité au laboratoire

Pierre-Philippe Cortet [*, a] **and Nicolas Lanchon** [a]

[a] Université Paris-Saclay, CNRS, FAST, 91405 Orsay, France

E-mails: pierre-philippe.cortet@universite-paris-saclay.fr (P.-P. Cortet), nicolas.lanchon@universite-paris-saclay.fr (N. Lanchon)

Abstract. In this article, we review the recent efforts of several teams that aimed at observing in the laboratory a turbulence of internal gravity waves in a density stratified fluid in the weakly non-linear regime. The common feature to these studies is that they adopted the same strategy of injecting energy in weakly non-linear waves before increasing the forcing amplitude in order to trigger a transition to a wave turbulence regime. The motivation to these works is twofold. On the one hand, it has long been proposed that the dynamics of small oceanic scales is driven by a regime of weakly non-linear internal wave turbulence, without however a definitive confirmation so far. A better understanding of the weakly non-linear internal wave turbulence thus appears as an important lever for improving the parameterization of small oceanic scales in climate models. On the other hand, the identification of valid solutions to the theory of internal gravity wave turbulence is still an open problem, and the experimental observation of this regime is therefore of great interest to guide future theoretical developments. We conclude that two features should be improved in the experiments in order to access to a genuine weakly non-linear wave turbulence in the laboratory. First, one should mitigate the finite size effects and especially prevent the concentration of the energy in wave eigenmodes of the fluid domain. Second, one should implement a significant increase of the wavelength at which the energy is injected in order to access to larger Reynolds numbers and lower flow Froude numbers and build a turbulence with well developed power law spectra while remaining in the weakly non-linear regime.

Résumé. Dans cet article, nous passons en revue les efforts récents de plusieurs équipes visant à observer au laboratoire une turbulence d'ondes internes de gravité dans un fluide stratifié en densité dans le régime faiblement non-linéaire. Ces études ont en commun d'adopter la même stratégie consistant à injecter l'énergie dans des ondes faiblement non-linéaires avant d'augmenter l'amplitude du forçage afin de déclencher une transition vers un régime de turbulence d'ondes. La motivation à ces travaux est double. D'une part, il est depuis longtemps proposé que la dynamique des petites échelles océaniques soit pilotée par le régime de turbulence d'ondes internes faiblement non-linéaire, sans toutefois qu'une confirmation définitive n'ait pour l'instant pu être apportée. Une meilleure compréhension de la turbulence d'ondes internes faiblement non-linéaire apparaît ainsi comme un levier important pour améliorer la paramétrisation des petites échelles océaniques dans les modèles climatiques. D'autre part, l'identification de solutions valides à la théorie de la turbulence d'ondes internes de gravité reste un problème ouvert et l'observation expérimentale de ce régime

* Corresponding author

apparaît donc d'un grand intérêt pour guider les développements théoriques. Nous concluons que deux caractéristiques doivent être améliorées dans les expériences afin d'accéder à un véritable régime de turbulence d'ondes faiblement non-linéaire au laboratoire. Il faut d'une part contrôler les effets de taille finie et en particulier empêcher la concentration de l'énergie dans les modes propres d'ondes du domaine fluide. Il convient d'autre part d'augmenter sensiblement la longueur d'onde à laquelle l'énergie est injectée afin d'accéder à des nombres de Reynolds plus élevés et des nombres de Froude plus faibles pour construire une turbulence avec des spectres en loi de puissance développés tout en restant dans un régime faiblement non linéaire.

Keywords. Internal gravity waves, Stratified fluids, Turbulence, Oceans.

Mots-clés. Ondes internes de gravité, Fluides stratifiés, Turbulence, Océans.

Funding. This work was supported by a grant from the Simons Foundation (651461, PPC).

Manuscript received 5 March 2024, revised 14 June 2024, accepted 25 June 2024.

1. Introduction to internal waves and "stratified" turbulence

The most remarkable feature of fluids that are stably stratified in density is that they support the propagation of a specific class of waves in their bulk [1–3]. These waves are called internal gravity waves and result from the restoring action of the buoyancy force. They are dispersive and anisotropic and possess peculiar features: group and phase velocities normal to each other and a direction of propagation set by the wave frequency. Also, their wavelength is independent of their frequency and is set by boundary conditions, viscous dissipation and non-linearities [4,5]. In the case of a uniform vertical gradient of density that is generally considered, the inviscid dispersion relation writes [1–3]

$$\omega = \pm N \frac{k_\perp}{\sqrt{k_\perp^2 + k_z^2}} \tag{1}$$

where ω is the wave angular frequency, and $k_\perp$ and k_z are the norm of the components of the wavevector $\mathbf{k}$ normal and parallel to gravity, respectively. The buoyancy frequency $N = \sqrt{-g/\rho_0\, d\bar{\rho}/dz}$ is defined by the amplitude of the density gradient at rest, $d\bar{\rho}/dz < 0$, and the acceleration of gravity g (with the vertical coordinate z oriented opposite to gravity). Equation (1) is obtained from the Euler equation under the approximation of weak density variations (both static and dynamic) with respect to the reference density ρ_0 [2,3].

It is worth to note that a global rotation at a rate Ω also allows for a specific class of waves to propagate in the volume of a fluid, this time as a result of the Coriolis force [6,7]. These waves, called inertial waves, possess features similar to those of internal gravity waves but also differ from them in several other respects. Plane inertial waves have for example three non-zero velocity components whereas plane internal gravity waves have only two, which importantly differentiates their behavior regarding solid boundaries [5,8], resonances in finite size domains [9,10] and non-linear interactions [11,12]. When rotation and stratification are both present, the two types of waves merge into gravity-inertia internal waves of dispersion relation

$$\omega = \pm \frac{1}{k} \sqrt{(2\Omega k_z)^2 + (N k_\perp)^2}\,, \tag{2}$$

with $k = \sqrt{k_\perp^2 + k_z^2}$ the norm of the wavevector (we consider a rotation vector along z).

With the rotation of the Earth, the stratification in density of the oceans and the atmosphere is a key and ubiquitous ingredient of the turbulent dynamics of geophysical flows [13–16]. In this context, an important feature of global oceanic and atmospheric models is the use of parameterizations accounting for the "fine scales" [16–20], which are generally strongly affected by the fluid stratification and the associated internal wave dynamics, and often (but to a lesser extent) by the Earth rotation (N being generally significantly larger than Ω). Progress in the modeling of these

small scale dynamics constitutes an important lever to improve oceanic and atmospheric simulations [20] which has long motivated the search for a fundamental understanding of "stratified turbulence".

Turbulence in a stably stratified fluid can develop in several different regimes [21–24], which all are anisotropic and which can coexist over different ranges of scales. To avoid any ambiguity, we specify that in this article we do not consider the effects of the diffusion of mass. Strictly speaking, this amounts to consider fluids with Prandtl number much larger than 1, i.e. with a buoyancy diffusivity negligible with respect to the kinematic viscosity. In practice, when focusing on turbulent dynamics at large Reynolds numbers, having a Prandtl number not lower than 1 is generally enough to ignore the effects of buoyancy diffusion. In this framework, the richness of stratified turbulence is related to the fact that *weakly non-linear* internal waves can coexist and interact with *strongly non-linear* vortex structures. In order to anticipate which regime will be at play, one should consider three independent non-dimensional numbers: the Reynolds number $Re = \tau_\nu/\tau_{\rm nl}$, the Froude number $Fr = 1/\tau_{\rm nl}N$ and the non-dimensional frequency $\omega^* = \omega/N$, where $\tau_{\rm nl}$ and τ_ν are the characteristic non-linear and viscous timescales of the flow structures at scale ℓ, respectively, and $1/\omega$ is their linear timescale, which might be different from $\tau_{\rm nl}$ (with $\omega\tau_{\rm nl} \geq 1$) since we consider a system in which waves can propagate. Moreover, since stratified turbulence is anisotropic, in order to characterize the flow structures "at scale ℓ", one might have to introduce different characteristic values for the horizontal $u_\perp$ and vertical u_z velocity components and for the horizontal $\ell_\perp$ and vertical ℓ_z length scales. In practice, a cautious analysis of the equations of the dynamics is necessary in order to explicit the scaling of the non-linear and viscous times, the result depending on the considered regime of the flow. In this context, theoreticians often consider the strongly anisotropic limit $\ell_z \ll \ell_\perp$ in order to simplify the problem. In this limit, the non-linear timescale follows the scaling $\tau_{\rm nl} \sim \ell_\perp/u_\perp$ [25,26] and the viscous timescale $\tau_\nu \sim \ell_z^2/\nu$. Besides, the linear timescale simplifies to $1/\omega \simeq k_z/(Nk_\perp) \sim \ell_\perp/(N\ell_z)$ according to the dispersion relation (1). This scaling reveals that this regime, often called "hydrostatic", corresponds to slow dynamics.

Coming back to the general case, two main classes of turbulence can be expected for stratified turbulence depending on the value of the ratio Fr/ω^* of the Froude number and the non-dimensional frequency (see Figure 1). This ratio, also equal to $1/\omega\tau_{\rm nl}$, compares the linear timescale to the non-linear one. When it is of order 1, we expect a regime of strongly-nonlinear turbulence with an energy cascade carried by flow modes with comparable linear and non-linear timescales. This class of stratified turbulence includes the phenomenologies called "saturated wave" turbulence [27], "critical balance" turbulence [28] and "strongly stratified turbulence" [25,29] which have been introduced to describe the strongly non-linear regime in the "hydrostatic" limit where $Fr \simeq \omega^* \ll 1$.

The other limit case is expected when, at scale ℓ, the Reynolds number Re is large whereas the Froude number Fr is low compared to the non-dimensional frequency ω^* and therefore $\omega\tau_{nl} \gg 1$. This is the "weak turbulence" regime also called "wave turbulence" [30,31]. In this regime, an energy cascade is expected to result from triadic resonant interactions within a statistical ensemble of weakly non-linear internal gravity waves which exchange energy a rate much slower than their frequency [20,32]. This framework has often been suggested as a potential explanation for the oceanic dynamics at small scales [20,33,34], without however a direct confirmation so far. This question is of great interest in view of the advance that a validation of the weak turbulence theory could bring for the parameterization of the oceanic small scales in climate models [16–20].

In this context, even if significant progresses have been achieved during the last two decades regarding the internal wave turbulence theoretical problem [26,32,35–39] and its comparison with oceanic data [20,32], analytical solutions are still out of reach in the general case [38,39], in particular, without using the hydrostatic hypothesis. As a consequence, conducting experiments

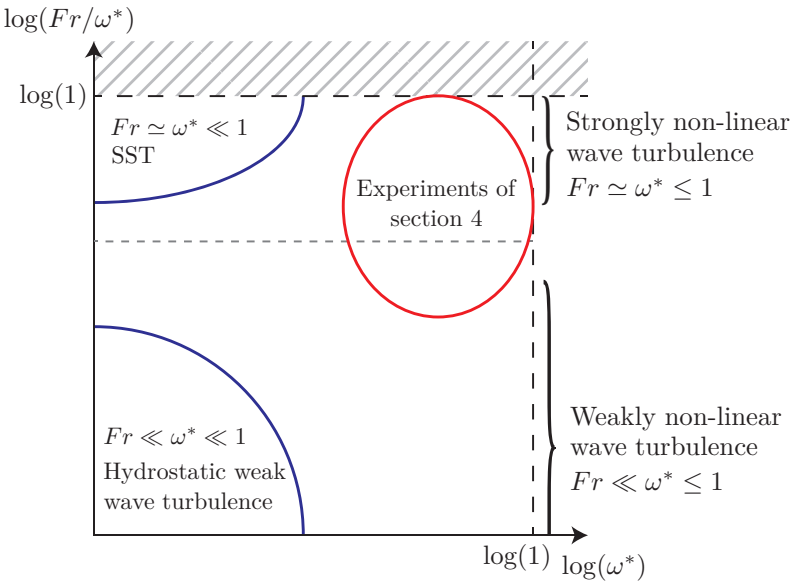


Figure 1. Diagram of the expected regimes of internal gravity wave turbulence as a function of the non-dimensional frequency $\omega^* = \omega/N$ and the ratio Fr/ω^* between the Froude number $Fr = 1/\tau_{\rm nl}N$ and ω^*. We recall that $Fr/\omega^* = 1/\omega\tau_{\rm nl} \leq 1$ identifies to the ratio between the flow linear $1/\omega$ and non-linear $\tau_{\rm nl}$ timescales and thus assesses its degree of non-linearity. The Reynolds number $Re = \tau_\nu/\tau_{\rm nl}$ is assumed infinitely large. The location in this diagram of the experiments described in Section 4 is also indicated even if the corresponding Reynolds numbers are not always very large.

to identify empirically what is(are) the fundamental solution(s) to the internal wave turbulence problem is of great interest.

This article focuses on experimental studies that have recently been carried out in order to access to the regime of weakly non-linear internal gravity wave turbulence in the laboratory. Before we present these experimental works in Section 4, we introduce in more detail the theoretical framework of the "strongly stratified turbulence" in Section 2 and of the "internal wave turbulence" in Section 3.

2. The "strongly stratified turbulence" phenomenology

The "strongly stratified turbulence" phenomenology (SST) have been developed to describe stratified turbulence in its strongly non-linear and low-frequency limit $Fr \simeq \omega^* \ll 1$ [21,23,25,29]. This regime is thought to be relevant for the atmospheric dynamics at small and intermediate scales [40]. In this regime, the flow consists in an ensemble of horizontally elongated "pancake" eddies (with $\ell_z \ll \ell_\perp$ and $u_z \ll u_\perp$) which are shearing each other in the vertical direction producing a cascade of energy from large to small scales. Phenomenological predictions have been put forward for the 1D spatial kinetic energy spectra of SST [25,27–29]. One expects a Kolmogorov scaling for the spectrum as a function of the horizontal wavevector component, $E(k_\perp) \sim \epsilon^{2/3} k_\perp^{-5/3}$, where ϵ is the mean rate of kinetic energy dissipation per unit mass, and a scaling involving the buoyancy frequency N for the spectrum as a function of the vertical wavevector component, $E(k_z) \sim N^2 k_z^{-3}$. This vertical spectrum is often referred to as the "saturation spectrum" [41,42] in relation with the concept of waves which saturate because of

strong non-linearities [27]. This scaling for the vertical spectrum can also be found from the "critical balance" phenomenology [28] (based on the assumption that $\omega\tau_{nl} \simeq 1$) which is close to the concept of turbulence of "saturated waves". A more demonstrative and complete justification of the SST phenomenology has been proposed during the 2000's on the basis of a self-similarity of the system of dynamical equations [25,29,43].

Adopting the usual non-dimensional numbers used in the SST literature [25], the SST regime is expected for large "horizontal" Reynolds numbers $Re_\perp = u_\perp \ell_\perp / \nu \gg 1$ and low "horizontal" Froude numbers $Fr_\perp = u_\perp / N\ell_\perp \ll 1$ on the condition that the parameter $\mathscr{R} = Re_\perp Fr_\perp^2$ (sometimes called buoyancy Reynolds number) is large [25]. Besides, it is expected that the largest vertical thickness of the "pancake eddies", i.e. the vertical integral scale of the turbulence, adjusts dynamically to the so-called buoyancy scale $u_\perp / N$ [21,25,43,44]. This process can result for instance from the zig-zag instability [45,46]. This vertical scale selection eventually leads the "vertical" Froude number $Fr_z = u_\perp / N\ell_z$ to be of order 1 at the integral scale, this result being also true on a scale-by-scale basis. It is important to highlight that the conditions under which the SST regime is expected are actually simpler when expressed in terms of the non-dimensional numbers we introduced in the previous section: these conditions simply are $Re = \tau_\nu / \tau_{\rm nl} \gg 1$ and $Fr = 1/N\tau_{\rm nl} \simeq \omega^* \ll 1$. This can be shown from the fact, in the strongly anisotropic limit $\ell_z \ll \ell_\perp$, one has $\tau_{\rm nl} \sim \ell_\perp / u_\perp$ and $\tau_\nu \sim \ell_z^2 / \nu$ such that (in the strongly anisotropic limit) $\mathscr{R}$ is nothing more than the Reynolds number Re, $Fr_\perp$ the Froude number Fr, and Fr_z the ratio Fr/ω^* of the Froude number to the non-dimensional frequency.

To conclude this section, it is important to mention that the predictions of the "strongly stratified turbulence" phenomenology are in line with the results of several direct numerical simulations [25,29,42,47,48]. These predictions for the 1D spatial energy spectra, i.e. $E(k_\perp) \sim k_\perp^{-5/3}$ and $E(k_z) \sim k_z^{-3}$, also remarkably seem to agree with observations at small and intermediate scales in the atmosphere [25,27,40,49–51] as well as at (very) small scales in the oceans [40].

3. The internal wave turbulence theory

In this section, we still consider flows with large Reynolds numbers $Re = \tau_\nu / \tau_{\rm nl} \gg 1$ and small Froude numbers $Fr = 1/N\tau_{\rm nl} \ll 1$. However, they will be weakly non-linear: This implies a separation between the linear timescale $1/\omega$ and the non-linear timescale $\tau_{\rm nl} \gg 1/\omega$ which is the primary characteristic of a "wave turbulence" [30,31]. This timescale separation is equivalent to having a Froude number $Fr = 1/\tau_{\rm nl} N$ much smaller than the non-dimensional frequency ω^* which is itself bounded by 1 for internal waves. Since the strongly anisotropic limit, corresponding to $\ell_\perp \gg \ell_z$, is often considered in the theoretical literature, it is worth to mention that in this limit the weak non-linearity condition is equivalent to having a very small vertical Froude number $Fr_z = u_\perp / N\ell_z$ (remembering that in the hydrostatic limit $\tau_{\rm nl} \sim \ell_\perp / u_\perp$). Coming back to the general case, the wave turbulence regime is expected when the condition $Fr = 1/\tau_{\rm nl} N \ll \omega^*$ is fulfilled [30]. In this regime, the energy, carried by an ensemble of weakly non-linear internal waves, is expected to be transferred on statistical average from large to small scales at a rate much lower than the wave frequencies. Also, because of the quadratic non-linearity of the Navier-Stokes equation, this energy cascade is expected to result from triadic resonant interactions between internal waves [26,30,32].

The theoretical study of the weakly non-linear wave turbulence regime in stratified fluids is a very active area [26,32,33,35–39,52]. An underlying motivation is the understanding of the oceanic dynamics and energy spectra at small scales [20,34,53]. To be more specific, oceanic data classically reveal one-dimensional (1D) energy spectra, in frequency ω and in vertical wavenumber k_z, following power laws with an exponent of the order of -2 [34]. These scaling laws are proposed to result from a cascade of energy from low to high frequencies (periods

typically in the range from the tides period, of about 12 h, to a few tens of minutes) and from large to small vertical scales (typically from a few hundred meters to a few meters). This fine-scale oceanic behavior is often summarized by the two-dimensional (2D) energy spectrum $E(k_z,\omega) \sim k_z^{-2}\omega^{-2}$ introduced by Garrett and Munk (GM) in the 1970s [53–55]. It should be noticed that this extrapolation of a 2D energy spectrum from two 1D effectively measured energy spectra is based on the strong assumption of a decorrelation between ω and k_z which is not necessarily valid for internal wave turbulence [26]. These oceanic spectra have nevertheless long been thought to result from the non-linear dynamics of internal gravity waves [20,34] producing a forward energy cascade. Oceanic data also suggest that this small-scale internal wave turbulence eventually feeds, at even smaller oceanic scales, a cascade of energy of the "saturated wave/critical balance" type (see, e.g., [40, Fig. 1] and [34, Fig. 21] which illustrate the transition between the two regimes).

From a more fundamental perspective, the Wave Turbulence Theory (WTT) is also attractive because of its analytical nature [30,31] and because it has already been successfully applied to other wave systems, such as capillary surface waves[1] [56] and inertial waves in rotating fluids [57]. Similarly to the SST regime, we still expect in the wave turbulence regime a direct and anisotropic energy cascade from large to small scales but with different scaling laws for the rate of energy transfer and for the energy spectra [26,30,35,38].

The classical derivation of the wave turbulence theory in stratified fluids leads to an analytical prediction for the 2D (axisymmetric) spatial energy spectrum scaling as $E(k_\perp,k_z) \sim \sqrt{\varepsilon N}\, k_\perp^{-3/2} k_z^{-3/2}$ [35,36,52]. This steady solution of the kinetic equation –the central equation in the wave turbulence theory– has been derived in the limit $k_\perp \ll k_z$ corresponding to low frequency internal waves ($\omega^* \simeq k_\perp/k_z$). It also results from the assumption that the non-linear interactions are local in the wavenumber and frequency spaces. Nevertheless, the derivation of this spectrum $E(k_\perp,k_z) \sim \sqrt{\varepsilon N}\, k_\perp^{-3/2} k_z^{-3/2}$ is achieved by ignoring a divergence of the so-called "collision integral" which, at the end, makes this spectrum irrelevant [26,35,38]. This divergence suggests that non-local triadic interactions between internal gravity waves of very different frequencies and/or wavenumbers are important in the turbulent dynamics and cannot be ignored.

In practice, the implementation of the WTT in the case of stratified fluids is still an open subject which involves delicate analytical questions regarding the convergence of the collision integral [38]. Over the past 20 years, several theoretical works have been carried out in an attempt to solve this issue by taking into account non-local interactions [26,32,38]. These works, all derived in the hydrostatic limit, first suggested that a whole family of stationary solutions with a constant energy flux exists [32,37] before identifying that the spectrum $E(k_\perp,k_z) \sim k_\perp^{2-a} k_z^{-1}$ with $a \simeq 3.69$ is a remarkable solution because it leads to an exact compensation of two diverging parts of the collision integral [32,38]. Remarkably, this prediction is relatively close to the Garrett-and-Munk spectrum (which corresponds to the case $a = 4$). This spectrum is nevertheless suspected to be a non-realizable singular stationary state of the kinetic equation in reference [39].

In this context, a stationary solution of a simplified kinetic equation describing the small scales of the internal wave turbulence problem in the hydrostatic limit has recently been derived analytically in reference [26]. This derivation is based on the assumption that energy transfers are driven only by a subset of the non-local resonant triads, the so-called "induced diffusion" triads, which leads to a scale separation in the kinetic equation. Despite it ignores the other types of resonant triads (the so-called "elastic scattering" triads, "parametric subharmonic instability" triads and local triads [58]), it appears that this solution is consistent with the -2 exponents typically observed in the ocean interior for the 1D energy spectra in ω and k_z [34]. In this

[1] It is worth mentioning that the anisotropic nature of the dynamics of stratified fluids makes the implementation of WTT more complex from the outset for internal waves than for isotropic waves with a power-law dispersion relation between their frequency and the norm of their wavevector [30,31].

theoretical framework, the phenomenology of the "induced diffusion" triads leads to a wave frequency ω proportional to the vertical wavenumber k_z along the turbulent cascade.

In parallel, Dematteis et al. [20] recently succeeded to quantitatively compute the actual small-scale energy dissipation in the ocean interior by injecting oceanic intermediate-scale data as an input in the equations of wave turbulence theory in the hydrostatic limit which are analyzed numerically. This work seems to demonstrate that the internal wave turbulence framework can quantitatively account for the oceanic processes at very small scales from the knowledge of the mesoscale properties of the flow (putting aside regions where internal waves interact with strong mesoscale currents). Considering realistic values for the oceanic buoyancy frequency and the Earth rotation which is here included in the model, Dematteis et al. [20] also propose that both local and non-local triadic interactions are important in oceanic internal wave turbulence. It should nevertheless be highlighted that, in this work, 2D energy spectra are extrapolated from *in situ* measurements of 1D energy spectra using the assumption of the decorrelation of k_z and ω.

It is finally worth to note the recent theoretical work by Labarre et al. [39] in which the kinetic equation of internal wave turbulence (without rotation) is for the first time shown to have a canonical structure, typical of Hamiltonian systems, even in the general non-hydrostatic case. This work paves the way for searching (at least numerically) for solutions of the internal wave turbulence problem in the general case (not restricted to the low-frequency limit).

In this complex theoretical framework, where no definitive solution(s) has(have) been identified to the internal wave turbulence theoretical problem, experiments (possibly numerical) promoting the emergence of a turbulent flow in the regime of weakly non-linear internal wave turbulence are of strong interest to guide and test theoretical developments.

4. Internal wave turbulence experiments

In the following, we review several experiments [59–70], most of which conducted over the last decade, in which the authors aimed at forcing a turbulent flow in a linearly stratified fluid by injecting energy in internal gravity waves. Turbulence experiments in stratified fluids were previously most often carried out with a preferential energy injection in vortical structures. These works consisted in practice in studies of decaying turbulence triggered by a translated grid [71,72] or a grid in a wind tunnel [73,74] and of statistically steady turbulence forced by an oscillating grid [75] or vortex dipole generators [76]. In any case, these kinds of forcing naturally lead, if the Reynolds number is large enough, to flows dominated by vortical structures or "saturated waves" in a strongly-non-linear regime of the type of the SST regime described earlier.

4.1. *Preliminary remarks*

Despite a strong interest discussed in the previous section, weakly non-linear stratified turbulence obtained from energy injection in internal gravity waves has only recently been approached in experiments and numerical simulations. This is most probably due to the fact it requires large facilities in the experimental case in order to simultaneously reach large Reynolds numbers and small Froude numbers and large computational resources in the numerical case, especially because of the linear/non-linear timescale separation, characteristic of wave turbulence, which imposes an integration of the dynamics over particularly long durations.

In order to succeed producing a weakly-non-linear internal wave turbulence regime in the lab, the primary condition is indeed to impose distinct linear and non-linear timescales. To do so, one must enforce independently an oscillation period $T = 2\pi/\omega$ and a velocity u to the fluid motion such that the weak non-linearity condition $T \ll \tau_{\mathrm{nl}}$ is fulfilled. We already noticed in the previous

Table 1. Parameters of several experiments presented in this article. $Fr = u/N\ell$ and $Re = u\ell/\nu$ are the Froude and Reynolds numbers based on the flow parameters. u is the typical velocity of the turbulent flows in the considered study (for the experiment at the largest forcing amplitude) and ℓ is the typical wavelength of the forced internal waves (u and ℓ are just orders of magnitude). $\omega_0^* = \omega_0/N$ is the forcing frequency non-dimensionalized by the buoyancy frequency N. In the cases of Benielli & Sommeria [59,60] and Le Reun et al. [65], ω_0 is half the forcing frequency since the primary waves are forced through a parametric instability. We take $\nu = 10^{-6}$ m^2/s for the kinematic viscosity of the fluid. H is the height of the stratified fluid.

	N (rad/s)	ω_0^*	ℓ (cm)	u (cm/s)	Fr	Re	H (m)
Oscillating water tank							
(Benielli et al. [59,60])	1.9	0.7	26	15	0.30	39 000	0.25
Tidal forcing simulations		0.25			0.012	720	
(Le Reun et al. [65])		0.67			0.035	3 700	
Attractor experiments							
(Davis et al. [66])	0.7	0.6	30	1.5	0.07	4 500	0.92
Oscillating wall experiments							
(Savaro et al. [67])	0.6	0.7	100	1.5	0.03	15 000	1
Oscillating wall experiments	0.4	0.16	100	0.6	0.014	6 000	1
(Rodda et al. [68])	0.4	0.38	100	1.5	0.03	15 000	1
Self-similar							
wave beam experiments	1.0	0.94	15	0.5	0.03	700	0.62
(Lanchon et al. [70])							

section that in the low-frequency limit, the actual non-linear time driving the triadic interactions is set by the ratio between the wave horizontal scale and the horizontal velocity, $\tau_{\rm nl} \sim \ell_\perp/u_\perp$, despite the alternative time built with the vertical scale, $\ell_z/u_\perp$, would be much smaller. This illustrates the fact this is not trivial to choose the relevant timescale in the anisotropic context of stratified turbulence. Nevertheless, since in the experimental works we will discuss, mainly waves at finite frequencies are considered (i.e. with $\omega^* = \omega/N$ neither too close to 0 nor too close to 1) we will simplify in the following the weak non-linearity condition to $T \ll \tau_{\rm nl} = \ell/u$, with ℓ the wavelength. We recall that the wavelength of internal waves ℓ is independent of their frequency which provides an additional degree of freedom to the experimentalist. The weak non-linearity condition, essential to wave turbulence, is equivalent to having a Froude number $Fr = u/N\ell$ small compared to the non-dimensional wave frequency $\omega^* = \omega/N$. At the same time, the Reynolds number $Re = \tau_\nu/\tau_{\rm nl} = u\ell/\nu$ should be large in order for a turbulent cascade over large ranges of scales to develop.

Experimentally, stably stratified fluids are made of salt-water mixtures with a decreasing concentration of salt as a function of the vertical coordinate z (opposite to gravity). They are fabricated by means of the so-called *double-bucket* method [77,78]. Some experimentalists alternatively use water-salt-ethanol mixture to fabricate the stratified fluid [79,80]. The advantage is that this makes it possible to obtain a fluid stratified in density with a uniform optical index, which becomes important for particle image velocimetry measurements when the fluid displacements do not remain weak [69]. In both cases, the typical largest buoyancy frequencies N that can be reached are of the order of 1 rad/s. One therefore realizes that the only mean to progress toward the limit under which internal wave turbulence is expected (low Froude number $Fr = u/N\ell$ and large Reynolds number $Re = u\ell/\nu$) is to access to large wavelength ℓ of the forced waves and therefore necessarily to build large experiments.

Another interesting point is the frequency ω_0^* at which the energy should be injected in the wave frequency domain $0 \leq \omega_0^* \leq 1$. The canonical solution to the theoretical internal wave turbulence problem $E(k_\perp, k_z) \sim \sqrt{\varepsilon N}\, k_\perp^{-3/2} k_z^{-3/2}$ [35,36,52] (which leads to a divergent collision integral) is associated to an energy cascade from large to low frequencies. In parallel, this is not necessarily the case in the alternative theoretical approaches that have later been developed for the internal wave turbulence problem [20,26,32,37–39]. The non-local low-frequency solution proposed in reference [26] is for example associated to an energy flux toward large frequencies. We should also mention that typical fine-scale oceanic spectra [20,34] involve dominant energy sources at low frequencies of the order of $0.01\,N$ to $0.1\,N$ (due to near-inertial waves and tidal forcing) and an energy spreading up to the buoyancy frequency N (and often even beyond), consistent with an energy cascade from small to large frequencies. In this context, the authors of the experimental studies discussed in the following, not sure about in which frequency direction an energy cascade might emerge, have tried to trigger wave turbulence by forcing waves at frequencies either of the order of N but also at significantly lower frequencies.

In the following, we will not present the measurement techniques specifically used for each of the described experimental works. We just specify here that the studied flows are characterized by measurements of 2D cross sections of the velocity field by particle image velocimetry, vertical profiles and time-series of the fluid density derived from conductivity measurements and/or dye motion visualizations.

4.2. *Internal waves forced by a parametric instability*

4.2.1. *Vertically oscillating water tank experiments*

We start our review by describing the work of Benielli and Sommeria [59,60] who conducted experiments in which a parallelepipedic tank filled with a stratified fluid is submitted to vertical oscillations. These experiments are not fully in line with the ones described in the sequel in which weakly non-linear waves are forced directly. However, since in this work internal waves eventually lead to a turbulent state, it is worth to present these experiments.

In references [59,60], the tank horizontal dimensions are of about 10 cm × 26 cm, the fluid height is of 25 cm and the buoyancy frequency of $N \simeq 1.9$ rad/s. The fluid container is oscillated at a frequency lower than $2N$ (several values are studied). No internal gravity waves directly resulting from the forcing are reported. This follows primarily from the fact the forcing consists in an oscillating vertical translation which is equivalent to an apparent oscillating uniform gravity. This is even more natural for the forcing frequency which is discussed the most since it is about $1.4\,N$, i.e. a frequency at which internal waves cannot propagate. Internal waves nevertheless emerge in the fluid for discrete resonance frequencies by a mechanism of parametric instability: above a threshold in the forcing amplitude, internal waves develop at half the forcing frequency, as standing internal wave eigenmodes of the fluid domain [9]. As the forcing amplitude is increased above this threshold, the standing wave eigenmodes rapidly become unstable themselves through the mechanism of the triadic resonance instability also known under the name of parametric subharmonic instability in the inviscid limit [3]. This secondary instability feeds localized propagative internal waves at smaller scales and at frequencies of the order of half the primary wave frequency. After a transient growth, these secondary internal waves rapidly experience wave breaking resulting in three-dimensional instabilities and local overturning of the density field. The flow eventually reaches a turbulent regime with an energy cascade toward small scales.

In these experiments, Benielli and Sommeria [59] report temporal potential energy spectra with a clear power law of exponent -3 over more than a decade of frequencies above the

buoyancy frequency N. They interpret it as the consequence of a k_z^{-3} 1D vertical energy spectrum that is transposed in time by an intense vertical advection of the small-scale turbulent structures by the largest scales of the flow, a phenomenon known as the sweeping effect [81]. As discussed for example by Staquet [82] and by Nazarenko and Schekochihin [28], 1D vertical energy spectra scaling as $N^2 k_z^{-3}$ are expected from phenomenological arguments for a turbulent cascade driven by strongly non-linear internal waves, which phenomenology is consistent, in the low frequency limit, with the more complete scenario of the strongly stratified turbulence presented earlier in Section 2. We should nevertheless mention that the experiments of Benielli and Sommeria [59], like those described in the following, are not involving low-frequency strongly-anisotropic waves but modes with $k_\perp$ and k_z of the same order of magnitude. In any case, the observation by Benielli and Sommeria of spectra in line with a strongly non-linear internal wave turbulence is compatible with the values of their flow Froude numbers which tend to be of order 1 whereas their Reynolds numbers are relatively high (see Table 1).

4.2.2. *Simulations driven by the tidal excitation of internal waves*

In this section dedicated to studies in which internal waves are indirectly forced by a parametric instability, it is worth to also discuss the direct numerical simulations of the Boussinesq equations by Le Reun et al. [65]. In this study, the flow forcing mimics a periodic tidal deformation which indirectly injects energy in internal waves at half the forcing frequency through a parametric instability. The flow finally reaches a turbulent state which can be, depending on the simulation parameters, statistically steady or made of cycles between turbulent phases and relaminarisation phases, a situation which is actually also reported in the experiments of Benielli and Sommeria [59,60].

Le Reun and coworkers [65] show that the energy of the turbulence they observe for their largest Reynolds numbers is carried almost only by internal waves verifying the wave dispersion relation. For these simulations, they report 1D spatial energy spectra compatible with scaling laws in $k_\perp^{-3}$ and k_z^{-3} and a dominant transfer of energy toward frequencies smaller than the primary wave frequency ω_0^*. Such scaling laws are typical of the phenomenology of the "saturated wave" turbulence, in which the internal waves are strongly non-linear, here applied in the case where $k_\perp$ and k_z are comparable in order of magnitude (which is the case in all the experiments presented in this review). Indeed, assuming a "critical balance" between the linear and non-linear timescales of the form $N \sim uk$ dimensionally leads to spatial energy spectra in $N^2 k^{-3}$ where k is the considered wavenumber (either vertical or horizontal) and u the typical velocity at wavenumber k [82]. In addition to these features and at variance with the results of Benielli and Sommeria [59,60], a power-law behavior of the temporal energy spectrum, compatible with an exponent -2, is observed at frequencies larger than the primary wave frequency ω_0^*, when it is significantly smaller than 1 (the limit frequency for internal waves). This scaling can also be seen as compatible with a "saturated wave/critical balance" type of turbulence of internal waves (through nevertheless modifying the critical balance criterion to $\omega \sim uk$).

To conclude this section, even if the parametric instabilities that feed the primary internal waves in the flow are different, the results of the simulations of Le Reun et al. [65] are similar from many points of view to the ones of the experiments of Benielli and Sommeria [59,60]: Once the forcing has overcome the threshold of the primary parametric instability, the flow rapidly saturates to a turbulent state which seems compatible with a turbulence of "saturated" internal waves in a "critical balance" regime.

4.3. *Internal wave attractor experiments*

We start now the description of recent efforts to access a weakly non-linear internal wave turbulence regime in the laboratory by discussing a series of experiments conducted at ENS de Lyon [61–64,66] in which an attractor of internal waves is used as a base flow. In these works, the authors use a wave maker to force a large-scale internal gravity wave at a specific frequency $\omega_0 \sim 0.6\,N$ in the wave frequency domain. These experiments have been conducted in trapezoidal containers which are nearly 2D, i.e. thin in the horizontal direction normal to the vertical trapeze. The water tanks that have been used, with a height of either 42.5 cm or 92 cm, are filled with a water solution of salt, linearly stratified in density. The resulting buoyancy frequencies are of the order of 1 rad/s.

Internal gravity waves follow anomalous reflection laws on inclined solid boundaries and their wavelength is modified during reflection [83,84]. This is a consequence of their peculiar dispersion relation $\omega^* = \sin\theta$, which relates the wave non-dimensional frequency $\omega^* = \omega/N$ to the angle θ between the wave group velocity, along which the energy propagates, and the horizontal. As a consequence, for certain geometries of the fluid domain (and certain ranges of frequencies depending on the geometry), waves at a given frequency tend to focus on a closed limit cycle called "wave attractor" [85–87]. In particular, it is the case in trapezoidal domains in which the obtained base flow consists in a mono-frequency self-similar internal wave beam resulting from an equilibrium between viscous dissipation and wave focusing at reflection on the tilted surface [5,87,88]. The great advantage of this method of forcing internal waves is that, thanks to the wave focusing processes during reflections on the inclined wall, it produces a base flow with relatively high fluid velocities (~cm/s), which would lead to significant mixing of the stratification close to the wave maker if they were directly imposed by the wave maker motion. This system has nevertheless two drawbacks. First, the typical wavelength of the forced wave mode is reduced by the focusing processes building the attractor. Second, the fact that the water tank is thin in one of the horizontal directions results in an enhanced contribution of the viscous dissipation on the vertical walls.

In the experiments of ENS de Lyon, as the forcing amplitude is increased, non-linear effects emerge first through a triadic resonance instability of the primary wave beam (i.e. the attractor) [3,61,89]. This instability produces new internal waves at two subharmonic frequencies ω_1 and ω_2 in spatial ($\mathbf{k}_0 \pm \mathbf{k}_1 \pm \mathbf{k}_2 = 0$) and temporal ($\omega_0 = \omega_1 + \omega_2$) resonances with the primary wave beam [61,63,64] ($\mathbf{k}_i$ and ω_i are the typical wavenumber and frequency of the wave mode i, respectively). Then, as the forcing amplitude is further increased, secondary triadic resonant interactions between the first three wave modes lead to the emergence, in the temporal energy spectrum, of a series of additional peaks at discrete frequencies in the wave domain [such as $\omega_2 - \omega_1$, $\omega_0 - (\omega_2 - \omega_1)\ldots$] [62,66]. A whole hierarchy of peaks finally emerges through the triadic resonant interactions between the wave modes. Brouzet et al. [64] further show that some of the energy peaks in these temporal spectra are associated to quasi-standing modes and quasi-resonance frequencies of the experimental vessel (trapezoidal domains do not possess exact standing modes theoretically). Even if not all the peaks in this discrete temporal energy spectrum are associated to standing modes, it is tempting to think that the attraction of the energy by resonance frequencies associated with standing modes of the experimental vessel plays a major role here in the construction of the discrete nature of the energy spectrum.

Increasing further the forcing amplitude, a continuum of energy over the wave frequency domain progressively emerges in addition to the discrete temporal energy spectrum [62,66]. These large amplitude experiments however seem to start involving some mixing of the stratification in density associated to the presence of vortices [62,64]: the flow seems to approach a strongly non-linear regime. For these experiments at large forcing amplitude, Davis et al. [66] report a be-

havior compatible with $E(k) \sim k^{-3}$ for the 1D spatial kinetic energy spectrum averaged over all directions in the vertical plane, a scaling which is again reminiscent of "critical balance/saturated wave" turbulence regimes. We should nevertheless notice that this power-law behavior is not observed over more than half-a-decade of wavenumber k, revealing that the turbulent cascade is still not well developed at the Reynolds numbers reached in these experiments.

4.4. *Experiments forced by oscillating walls*

A second series of experiments aiming at producing a weakly non-linear internal wave turbulence by forcing a periodic flow in a stratified fluid has been conducted recently on the Coriolis Platform in Grenoble [67–69]. This platform consists in a 13-m-diameter water tank which can be driven in rotation (a feature not used in the studies we will discuss) but also filled with a stratified water solution of salt.

In a first article by Savaro et al. [67], the authors report experiments in a stratified fluid (with $N \simeq 0.6$ rad/s), where energy is injected in large-scale internal waves at frequency $\omega_0^* \simeq 0.7$. The effective fluid domain is a parallelepiped of 6 m-side square base filled with 1 m of stratified salt-water mixture. Two of the four vertical walls of the square domain can oscillate around a horizontal axis at mid-depth of the fluid, acting as generators of internal waves of characteristic vertical length of 1 m.

Despite the forced base flow is significantly different from the one of the attractor experiments, the scenario of the emergence of nonlinearities in the flow is very similar when increasing the forcing amplitude. At moderate forcing, the authors indeed report the growth of a set of discrete peaks distributed over the wave frequency domain ($0 \leq \omega^* \leq 1$) in the temporal kinetic energy spectrum of the flow. The authors further show that these energy peaks (at least several of them) correspond to an ensemble of internal wave eigenmodes of the fluid domain. These wave modes moreover seem to verify temporal and spatial triadic resonance conditions ($\omega_i = \omega_j \pm \omega_p$ and $\mathbf{k}_i = \pm\mathbf{k}_j \pm \mathbf{k}_p$) within themselves and/or with the forced wave mode. The only fundamental difference with the attractor experiments is that parallelepipedic domains theoretically possess exact standing eigenmodes of internal gravity waves [9,67]. Nevertheless, from a practical viewpoint, this does not seem to significantly modify the observed scenario of the transition to turbulence.

Then, as the forcing amplitude is increased, a continuum of energy at subharmonic frequencies (i.e., below the forcing frequency ω_0) grows and tends to progressively engulf the eigenmode peaks (which are not increasing in amplitude) in the temporal energy spectrum. By computing several physical observables, the authors show that this continuum of energy is compatible with an ensemble of propagating internal waves verifying the wave dispersion relation. The wavelengths of these subharmonic waves are spreading from the scale of the forced mode ($\ell \simeq 1$ m) down to values typically ten times smaller. A remarkable feature is that, among these "turbulent" experiments, the smallest length scales present in the flow are increasing with the forcing amplitude, which might seem counter-intuitive. The authors interpret this feature as the result of the emergence of strong nonlinearities such as overturning and breaking of the subharmonic internal waves, which processes are indeed expected to affect the smallest scales in an internal wave turbulence [26].

In a following paper, Rodda et al. [68] report experiments with a modified version of the setup of Savaro et al. [67] where the shape of the water tank has been changed from square to pentagonal. A second difference is that the forcing injects now the energy in internal waves at a lower non-dimensional frequency ω_0^*, in the range $0.16 \leq \omega_0^* \leq 0.38$ (and also at $\omega_0^* \simeq 0.7$ for the sake of comparison with the previous work). These experiments led, in the nonlinear regime, to a temporal kinetic energy spectrum dominated by a series of discrete peaks at

harmonic frequencies ($2\omega_0^*$, $3\omega_0^*$, $4\omega_0^*\ldots$) of the forcing frequency. Remarkably, when the forcing Froude number is increased, this discrete spectrum superimposes with a continuum of energy at frequencies larger than the forcing frequency which is compatible with a power law ω^{-2}, an observation reminiscent of the results of Le Reun et al. [65]. This emerging power-law behavior extends here beyond the limit frequency of internal waves, typically up to $\omega \simeq 2N$ (whereas it clearly stops at $\omega = N$ in reference [65]). This extension at frequencies at which internal waves cannot propagate might indicate that the flow is evolving toward a strongly nonlinear regime. It is important also to note the difference with the experiments of Benielli and Sommeria [59,60] where a ω^{-3} power-law is observed and proposed to result from the conversion of a k_z^{-3} spatial energy spectrum by a turbulent sweeping.

Another remarkable result of Rodda et al. [68] is the presence of so-called *bound waves* revealed by the spatio-temporal scale analysis of the flow energy in the experiments at $\omega_0^* \simeq 0.7$. These wave modes are not verifying the internal wave dispersion relation and are directly forced by the non-linear interaction of two other modes, which can be genuine internal waves, the three modes forming a resonant triad in time and space, i.e., verifying $\omega_{\text{bw}} = \omega_1 \pm \omega_2$ and $\mathbf{k}_{\text{bw}} = \pm\mathbf{k}_1 \pm \mathbf{k}_2$. In a weakly non-linear regime, such bound waves are expected to be of second order compared to triadic resonances between internal gravity waves. Their presence is therefore another sign that strong non-linearity is emerging in the flow as the forcing amplitude is increased. We can note that such bound waves have also been detected in the attractor experiments where traces of a ω^{-2} power-law have also been reported in the temporal energy spectrum (see [90, Chapter 4], in french). Rodda et al. [68] finally suggest that these bound waves might have a role in the ω^{-2} power-law they observed above ω_0^* in their temporal energy spectrum (for the experiments at $\omega_0^* \simeq 0.7$ but also the ones at lower forcing frequency). This interpretation is motivated by the fact the ω^{-2} power-law extends beyond the frequency limit $\omega = N$ of internal waves. It is nevertheless worth to recall that a temporal energy spectrum in ω^{-2} is also not incompatible with "critical balance/saturated wave" regimes for which the condition $\omega \sim ku$ coupled to the conservation of the energy flux $\epsilon \sim u^3 k$ suggests that $E(\omega) \sim u^2/\omega \sim \epsilon\,\omega^{-2}$ (here, we consider the case of waves with $k_\perp \sim k_z$).

In a subsequent paper by Rodda et al. [69], the team of Grenoble studied the flow at even larger Reynolds number (with $\omega_0^* \simeq 0.7$) for which a turbulent cascade develops over a wide range of scales from the injection scale of about 1 m down to few millimeters. The authors first evidence, through dye visualizations, the intermittent occurrence of intense wave overturning events. They also show that a strong sweeping effect [81] induced by the large-scale wave modes of the flow affects almost all other modes at smaller scales, spreading their frequencies up to values much larger than N (in a way similar to Benielli and Sommeria [59,60]). The final result of this work is the observation of power laws of exponent -3 for the 1D kinetic energy spectra as a function both of the horizontal $k_\perp$ and the vertical k_z wavenumbers. These power laws are observed from the scale of the forced waves towards smaller scales over typically half-a-decade, which is consistent with the spectral behavior reported in the attractor experiments of Davis et al. [66]. The spectra further show a transition to a second behavior at smaller scales which is interpreted as a small-scale isotropic turbulence driven by the classical Kolmogorov phenomenology. A remarkable result here is the fact the vertical potential energy spectrum (which has been measured in this work) closely follows the vertical kinetic energy spectrum over the half-decade over which the k_z^{-3} behavior is observed. This equipartition between the potential and kinetic energies strongly suggests that the physics of internal waves is at play here (because the kinetic and potential energies in an internal wave are equal) whereas a wealth of strongly non-linear processes are also involved at the same time. Such behavior is (once again) typical of turbulence in a "critical balance" regime [30] driven by strongly non-linear waves.

4.5. *Experiments forced by multiple self-similar wave beams*

In this section, we describe a more recent attempt to observe a weakly non-linear internal wave turbulence in the laboratory, which has been conducted by Lanchon and coworkers at Université Paris-Saclay [70]. These experiments were carried in a glass tank of 105 cm side square-base filled up to a height of 62 cm with a linearly stratified salt water of buoyancy frequency $N \simeq 1$ rad/s. The forcing device consists in twenty-four horizontal cylinders oscillating vertically at frequency $\omega_0 = 0.94\,N$. The cylinders are evenly organized on an 80-cm-diameter virtual sphere centered in the tank. In the linear regime, each oscillating cylinder produces self-similar internal wave beams, which propagate in the four directions normal to the cylinder axis and which make an angle $\cos^{-1}(\omega_0/N) \simeq 20°$ with respect to the vertical. The forcing device eventually produces, in the central region of the experiment, a flow made of an ensemble of internal waves which approaches statistical homogeneity and axisymmetry around the vertical axis (axisymmetry in the Fourier space), which are two central hypotheses under which wave turbulence calculations are conducted [26,35]. The typical wavelength of the forced mode is $\ell = 15 \pm 5$ cm.

When the forcing amplitude is increased, the flow non-linearities produce, in the statistically steady state, a set of internal wave modes at discrete subharmonic frequencies (i.e. lower than ω_0). These modes, the most energetic of which are shown to be eigenmodes of the fluid domain, are in temporal triadic resonances with the forced waves and/or between themselves. This scenario is very similar to the one observed in the experiments conducted in Lyon and Grenoble and described earlier. The discretization of the energy in frequency and in wavenumber that is observed in all these experiments prevents the flow from approaching the regime described in the wave turbulence theories [26,32,33,35,37,38] in which the turbulent cascade is carried by an ensemble of weakly non-linear and propagating waves in an infinite domain which builds an energy continuum in the frequency and wavenumber spaces.

In Lanchon et al. [70], a study of the transient regime of the flow from the start of the wavemakers is also reported. During a first stage after the start of the wavemakers which lasts several hundreds of forcing periods, the time-frequency spectra reveal the growth of two wide subharmonic bumps in temporal resonance with the forced waves. The emergence of these bumps is in line with the classical scenario of the triadic resonance instability observed for inertial waves in rotating fluids [11,91], a system similar to stratified fluids to some extent but in which eigenmodes of the fluid domain are much less prone to develop compared to stratified fluids [9] (due to differences in the wave interactions with solid boundaries). In a second stage of the experiments of Lanchon et al. [70], the subharmonic wide bumps in the temporal energy spectrum progressively vanish while the eigenmodes associated to the steady state energy peaks slowly establish: the subharmonic energy seems to be slowly drained from the propagating waves produced by the triadic resonance instability towards the eigenmode resonance frequencies.

Again in a way similar to the attractor and oscillating wall experiments, in the steady state of the Paris-Saclay experiments, the eigenmodes coexist with a weakly energetic background which is continuous in frequency and the level of this continuum grows more rapidly than that of the eigenmodes when the forcing amplitude is increased. A natural way forward to try to observe a weakly non-linear wave turbulence is therefore to explore larger forcing amplitudes. However, doing so results, again similarly to the Lyon and Grenoble experiments, in the onset of significant irreversible mixing of the fluid stratification and the emergence of strong non-linearities.

The only way to avoid this transition to a strongly non-linear regime while still promoting the emergence of a turbulent cascade is to increase the flow Reynolds number $Re = u\ell/\nu$ while keeping the Froude number $Fr = u/N\ell$ low. We have seen that one cannot "simply" increase the flow velocity u since this leads to leaving the weakly non-linear regime. Besides, for practical reasons, one cannot increase the buoyancy frequency N significantly above 1 rad/s with usual

salt-water(-ethanol) mixtures (the fluid needs to be transparent to allow image velocimetry measurements). The only way forward is therefore to increase the wavelength ℓ at which energy is injected and consequently also the size (and especially the height) of the experiment. At the same time, it is also crucial to inhibit the finite size effects and the associated concentration of the wave energy in eigenmodes of the fluid domain.

Regarding this point, Lanchon et al. [70] identified a slight but crucial modification of their experimental setup which allows to efficiently inhibit the emergence of the wave eigenmodes. It consists in introducing slightly tilted panels in the fluid domain, one at the top and one at the bottom with a 4° tilt in the present case. The change in wavelength induced by these inclined planes when the waves are reflecting on them is small to moderate for most frequencies in the internal wave range ($\omega \leq N$) but sufficient to prevent the formation of standing modes in the experimental cavity. With this modified setup, the first non-linear state of the turbulent flow composed of subharmonic propagating internal waves distributed over wide ranges of frequency, which is only transient in the experiments without tilted planes, seems to become the statistically steady state (at least to the time horizon explored experimentally, of 600 forcing periods). For the largest forcing amplitude studied by Lanchon et al. [70], a continuum of energy over typically one decade in the wave frequency range is observed together with a disappearance of the energy peaks associated to eigenmodes of the fluid domain. Moreover, the authors show that this energy continuum is mainly carried by internal gravity waves verifying the wave dispersion relation.

In this configuration, Lanchon et al. [70] report 1D spatial energy spectra, as a function of the horizontal and vertical wavenumbers, which both tend to show a power law with an exponent -3 at the largest explored Reynolds number. Despite the fact wave eigenmodes have been suppressed here, the spatial energy spectra are reproducing the recent observations of Le Reun et al. [65], Davis et al. [66] and Rodda et al. [69]. Here too, the power-law behaviors remain questionable since they are observed over no more than half-a-decade of wavenumbers. Also in line with the previously discussed experiments, the scaling laws with an exponent -3 emerge in the experiments of Lanchon et al. [70] while mixing of the stratification starts to become significant which might reveal a system of internal waves becoming strongly non-linear.

5. Conclusion

In this article, we reviewed recent experimental works that aimed at observing a turbulence of internal gravity waves in a stratified fluid in the weakly non-linear regime. The common feature of these works is that they adopted the same strategy of injecting energy in weakly non-linear waves before increasing the forcing amplitude in order to trigger a transition to a wave turbulence regime.

The motivation to achieve this regime in the laboratory is twofold. On the one hand, it has long been proposed that the dynamics of small oceanic scales is driven by a regime of weakly non-linear internal wave turbulence, without however a definitive confirmation so far. Besides, this dynamics is not resolved in global oceanic models and better understanding the weak internal wave turbulence is a promising lever to improve the parameterization of small oceanic scales in climate models. On the other hand, the identification of valid solutions to the theory of weakly non-linear internal gravity wave turbulence is still not completed and providing experimental data in this regime is of great interest to guide future theoretical developments.

Adopting a synthetic (and probably oversimplifying) point of view, we can say that most of the works described in this review led to comparable scenarios [61–64,66,67,70]. Above a threshold in the forcing amplitude, the waves directly forced by the wave generators at a specific frequency ω_0 (in the range between $0.6\,N$ and the buoyancy frequency N) transfer energy to a couple of subharmonic wave modes (at frequencies $\omega_1 < \omega_0$ and $\omega_2 < \omega_0$) through the mechanism of

the triadic resonance instability. Secondary triadic resonant interactions between these wave modes and/or the forced waves then give birth to additional wave modes at other frequencies and wavenumbers. As time goes on and/or as the forcing amplitude is increased, one observes the progressive concentration of the energy of these modes on a set of discrete frequencies in triadic resonance between themselves and/or with the forced wave mode. Many of these discrete modes are actually shown to be internal wave eigenmodes of the experimental water tank. The discretization of the energy on specific frequencies and wavenumbers therefore results from finite size effects and a strong energy attraction toward the tank eigenmodes. In this regime, the flow produced in the experiments reviewed in this article is in some way close to a weakly non-linear wave turbulence. Nevertheless, the energy discretization critically prevents the flow from approaching the regime described by the wave turbulence theory, in which a turbulent cascade forms an energy continuum in the frequency and wavenumber spaces.

We should also highlight the experiments of Rodda et al. [68] in which the frequency ω_0 at which internal waves are forced is significantly lower (in the range between $0.16\,N$ and $0.38\,N$). In this case, the scenario is different but still leading to a discrete energy spectrum in frequency. Non-linearities indeed emerge through the growth of wave modes at harmonic frequencies of the forcing frequency ($2\omega_0, 3\omega_0, \ldots$).

In all these experiments, continuing to increase the forcing amplitude leads to the gradual emergence of an energy continuum in the wave frequency domain that tends to ultimately take over the wave eigenmodes (or the harmonic modes in the case of reference [68]). In this regime, finite size effects seem to progressively lose their influence. However, the flow seems in parallel to transition to a strongly non-linear wave turbulence regime of the "critical balance/saturated wave" type. Indeed, different experimental analyses report that the flow is still composed of internal waves verifying the dispersion relation whereas strongly non-linear features (including mixing of the density, wave breaking leading to vortices) seem to emerge at the same time. Also, many of these studies [59,60,66,69,70] report 1D spatial energy spectra tending to follow power laws with an exponent close to -3 as a function of the vertical and/or the horizontal wavenumber. Such scaling is typical of "saturated wave" turbulence for which a "critical balance" between the linear and non-linear timescales of the form $N \sim uk$ dimensionally leads to spatial energy spectra in $N^2 k^{-3}$ where k is the considered wavenumber and u the typical velocity at k [82]. On the contrary, several power laws are reported for the temporal energy spectrum, with an exponent -3 in reference [59] and an exponent -2 in references [65,69]. But, both exponents are actually not incompatible with a "critical balance" regime. Indeed, a power law in ω^{-3} for the temporal energy spectrum can result from the conversion of a k^{-3} spatial energy spectrum when a turbulent sweeping induced by energetic large scale modes is dominant [59], whereas a temporal energy spectrum in $\epsilon\,\omega^{-2}$ might be expected when a "critical balance" of the type $\omega \sim uk$ is at play.

To conclude, we can say that two features should be modified in the experiments in order to access to a genuine weakly non-linear wave turbulence regime in the laboratory. First, one should prevent the concentration of the energy in wave eigenmodes of the fluid domain. In this respect, the work of Lanchon et al. [70] proposed a practical solution consisting in introducing slightly tilted panels at the top and/or at the bottom of the stratified fluid. By slightly modifying the wavelength of the reflected waves, the panels prevented the emergence of standing waves in the flow of Lanchon et al. which was shown to be composed of a continuum of propagating internal waves distributed over nearly one decade of frequencies. The second change that should be implemented is "simply" a significant increase in the wavelength ℓ at which the energy is injected together with an increase in the water tank size. The objective is to access to large Reynolds numbers $Re = u\ell/\nu$, to observe turbulent spectra with developed power laws, while remaining in the weakly non-linear regime which implies to reduce the flow Froude number $Fr = u/N\ell$. In the experiments (and the numerical simulations) discussed in this review, the amplitude of

the non-linearities, which are measured by the ratio Fr/ω^* of the Froude number Fr to the non-dimensional wave angular frequency ω^*, is typically of the order of 0.1 for the experiments at the largest Reynolds numbers. This value seems not to be small enough to avoid the transition of the flow to a strongly non-linear regime. It therefore appears crucial to increase the wavelength of the forced waves in order to reduce significantly the non-linearity parameter Fr/ω^*. Regarding this point, we can recall the especially large size of the experiments on the Coriolis platform in Grenoble (6 m in the horizontal direction)[67–69]. Nevertheless, it is also crucial to have a large vertical size of the experimental water tank in order to be able to access vertical scales as large as the horizontal ones. This is especially important if one does not want to focus only on low frequency waves. In conclusion, future experiments aiming at weak internal wave turbulence should be much larger and especially much taller if we want them to fully succeed. This is a real challenge, especially regarding the fabrication of stratified fluids over large heights.

An alternative strategy to access to an internal wave turbulence in the weakly non-linear regime experimentally could be to work in a cryostat filled with liquid helium warming up at liquid-vapor equilibrium, in which system a stable gradient of density can establish. The low viscosity of liquid helium coupled to its important density variations as it approaches its critical point, can lead one to expect higher Reynolds numbers and lower Froude numbers than in most salt water experiments. However, in addition to the intrinsic difficulty of designing a cryogenic experiment, the challenge will be here to perform spatio-temporally resolved measurements of the velocity fields [92] as well as to assess that the Boussinesq approximation is valid.

Acknowledgements

We would like to thank Paul Billant and Frédéric Moisy for their precious comments.

Declaration of interests

The authors do not work for, advise, own shares in, or receive funds from any organization that could benefit from this article, and have declared no affiliations other than their research organizations.

References

[1] C. Staquet and J. Sommeria, "Internal gravity waves: From instabilities to turbulence", *Annu. Rev. Fluid Mech.* **34** (2002), pp. 559–593.
[2] B. R. Sutherland, *Internal Gravity Waves*, Cambridge University Press, 2010.
[3] T. Dauxois, S. Joubaud, P. Odier and A. Venaille, "Instabilities of internal wave beams", *Annu. Rev. Fluid Mech.* **50** (2018), pp. 131–156.
[4] C. Brouzet, I. N. Sibgatullin, E. V. Ermanyuk, S. Joubaud and T. Dauxois, "Scale effects in internal wave attractors", *Phys. Rev. Fluids* **2** (2017), article no. 114803.
[5] M. Brunet, T. Dauxois and P.-P. Cortet, "Linear and non linear regimes of an inertial wave attractor", *Phys. Rev. Fluids* **4** (2019), article no. 034801.
[6] H. P. Greenspan, *The Theory of Rotating Fluids*, Cambridge University Press, 1968.
[7] J. Lighthill, *Waves in Fluids*, Cambridge University Press, 1978.
[8] F. Beckebanze, C. Brouzet, I. N. Sibgatullin and L. R. M. Maas, "Damping of quasi-two-dimensional internal wave attractors by rigid-wall friction", *J. Fluid Mech.* **841** (2018), pp. 614–635.
[9] L. R. M. Maas, "On the amphidromic structure of inertial waves in a rectangular parallelepiped", *Fluid Dyn. Res.* **33** (2003), p. 373.
[10] C. Pacary, T. Dauxois, E. Ermanyuk, P. Metz, M. Moulin and S. Joubaud, "Observation of inertia-gravity wave attractors in an axisymmetric enclosed basin", *Phys. Rev. Fluids* **8** (2023), article no. 104802.
[11] D. O. Mora, E. Monsalve, M. Brunet, T. Dauxois and P.-P. Cortet, "Three-dimensionality of the triadic resonance instability of a plane inertial wave", *Phys. Rev. Fluids* **6** (2021), article no. 074801.

[12] M. Remmel, J. Sukhatme and L. M. Smith, "Nonlinear gravity-wave interactions in stratified turbulence", *Theor. Comput. Fluid Dyn.* **28** (2014), pp. 131–145.
[13] J. Pedlosky, *Geophysical Fluid Dynamics*, Springer, 1987.
[14] G. K. Vallis, *Atmospheric and Oceanic Fluid Dynamics*, Cambridge University Press, 2006.
[15] C. Wunsch and R. Ferrari, "Vertical mixing, energy and the general circulation of the oceans", *Annu. Rev. Fluid Mech.* **36** (2004), pp. 281–314.
[16] J. A. MacKinnon, Z. Zhao, C. B. Whalen, et al., "Climate Process Team on Internal Wave-Driven Ocean Mixing", *Bull. Am. Meteorol. Soc.* **98** (2017), pp. 2429–2454.
[17] D. J. Stensrud, *Parametrization schemes: Keys to Understanding Numerical Weather Prediction Models*, Cambridge University Press, 2007.
[18] K. L. Polzin, A. C. N. Garabato, T. N. Huussen, B. M. Sloyan and S. Waterman, "Finescale parameterizations of turbulent dissipation", *J. Geophys. Res.* **119** (2014), pp. 1383–1419.
[19] M. C. Gregg, E. A. D'Asaro, J. Riley and E. Kunze, "Mixing efficiency in the ocean", *Ann. Rev. Mar. Sci.* **10** (2018), pp. 443–473.
[20] G. Dematteis, A. Le Boyer, F. Pollmann, K. L. Polzin, M. H. Alford, C. B. Whalen and Y. V. Lvov, "Interacting internal waves explain global patterns of interior ocean mixing", 2023. *preprint*, arXiv:2310.19980.
[21] P. A. Davidson, *Turbulence in Rotating, Stratified and Electrically Conducting Fluids*, Cambridge University Press, 2013.
[22] J. Riley and E. Lindborg, "Recent Progress in Stratified Turbulence", in *Ten Chapters in Turbulence* (P. Davidson, Y. Kaneda and K. Sreenivasan, eds.), Cambridge University Press, Cambdrige, UK, 2012, pp. 269–317.
[23] C. P. Caulfield, "Layering, Instabilities, and Mixing in Turbulent Stratified Flows", *Annu. Rev. Fluid Mech.* **53** (2021), pp. 113–145.
[24] K. Shah, G. P. Chini, C.-C. P. Caulfield and P. Garaud, "Regimes of stratified turbulence at low Prandtl number", 2023. *preprint*, arXiv:2311.06424.
[25] G. Brethouwer, P. Billant, E. Lindborg and J.-M. Chomaz, "Scaling analysis and simulation of strongly stratified turbulent flows", *J. Fluid Mech.* **585** (2007), pp. 343–368.
[26] N. Lanchon and P.-P. Cortet, "Energy Spectra of Nonlocal Internal Gravity Wave Turbulence", *Phys. Rev. Lett.* **131** (2023), article no. 264001.
[27] E. Dewan, "Saturated-cascade similitude theory of gravity wave spectra", *J. Geophys. Res.* **102** (1997), pp. 29799–29817.
[28] S. V. Nazarenko and A. A. Chekochihin, "Critical balance in magnetohydrodynamic, rotating and stratified turbulence: towards a universal scaling conjecture", *J. Fluid Mech.* **677** (2011), pp. 134–153.
[29] E. Lindborg, "The energy cascade in a strongly stratified fluid", *J. Fluid Mech.* **550** (2006), pp. 207–242.
[30] S. Nazarenko, *Wave Turbulence*, Springer, 2011.
[31] S. Galtier, *Physics of Wave Turbulence*, Cambridge University Press, 2022.
[32] Y. V. Lvov, K. L. Polzin, E. G. Tabak and N. Yokoyama, "Oceanic internal-wave field: Theory of scale-invariant spectra", *J. Phys. Oceanogr.* **40** (2010), pp. 2605–2623.
[33] C. H. McComas and P. Müller, "The dynamic balance of internal waves", *J. Phys. Oceanogr.* **11** (1981), pp. 970–986.
[34] K. L. Polzin and Y. V. Lvov, "Toward regional characterizations of the oceanic internal wavefield", *Rev. Geophys.* **49** (2011), article no. RG4003.
[35] P. Caillol and V. Zeitlin, "Kinetic equations and stationary energy spectra of weakly nonlinear internal gravity waves", *Dyn. Atmos. Oceans* **32** (2000), pp. 81–112.
[36] Y. V. Lvov and E. G. Tabak, "Hamiltonian Formalism and the Garrett–Munk Spectrum of Internal Waves in the Ocean", *Phys. Rev. Lett.* **87** (2001), article no. 168501.
[37] Y. V. Lvov, K. L. Polzin and E. G. Tabak, "Energy Spectra of the Ocean's Internal Wave Field: Theory and Observations", *Phys. Rev. Lett.* **92** (2004), article no. 128501.
[38] G. Dematteis and Y. V. Lvov, "Downscale energy fluxes in scale-invariant oceanic internal wave turbulence", *J. Fluid Mech.* **915** (2021), article no. A129.
[39] V. Labarre, N. Lanchon, P.-P. Cortet, G. Krstulovic and S. Nazarenko, "Kinetics of internal gravity waves beyond hydrostatic regime", 2023. *preprint*, arXiv:2311.14370.
[40] J. J. Riley and E. Lindborg, "Stratified Turbulence: A Possible Interpretation of Some Geophysical Turbulence Measurements", *J. Atmos. Sci.* (2008).
[41] M. L. Waite and P. Bartello, "Stratified turbulence generated by internal gravity waves", *J. Fluid Mech.* **546** (2006), pp. 313–339.
[42] C. Rorai, P. D. Mininni and A. Pouquet, "Stably stratified turbulence in the presence of largescale forcing", *Phys. Rev. E* **92** (2015), article no. 013003.
[43] P. Billant and J.-M. Chomaz, "Self-similarity of strongly stratified inviscid flows", *Phys. Fluids* **13** (2001), pp. 1645–1651.

[44] J. J. Riley and S. M. de Bruyn Kops, "Dynamics of turbulence strongly influenced by buoyancy", *Phys. Fluids* **15** (2003), pp. 2047–2059.
[45] P. Billant and J.-M. Chomaz, "Experimental evidence for a new instability of a vertical columnar vortex pair in a strongly stratified fluid", *J. Fluid Mech.* **418** (2000), pp. 167–188.
[46] P. Billant and J.-M. Chomaz, "Theoretical analysis of the zigzag instability of a vertical columnar vortex pair in a strongly stratified fluid", *J. Fluid Mech.* **419** (2000), pp. 29–63.
[47] P. Augier, P. Billant and J.-M. Chomaz, "Stratified turbulence forced with columnar dipoles: numerical study", *J. Fluid Mech.* **769** (2015), pp. 403–443.
[48] A. Maffioli, "Vertical spectra of stratified turbulence at large horizontal scales", *Phys. Rev. Fluids* **2** (2017), article no. 104802.
[49] G. D. Nastrom and K. S. Gage, "A climatology of atmospheric wavenumber spectra of wind and temperature observed by commercial aircraft", *J. Atmos. Sci.* **42** (1985), pp. 950–960.
[50] E. M. Dewan and R. E. Good, "Saturation and the 'Universal' spectrum for vertical profiles of horizontal scalar winds in the atmosphere", *J. Geophys. Res.* **91** (1986), pp. 2742–2748.
[51] C. Cot, "Equatorial mesoscale wind and temperature fluctuations in the lower atmosphere", *J. Geophys. Res.* **106** (2001), pp. 1523–1532.
[52] E. N. Pelinovsky and M. A. Raevsky, "Weak turbulence of the internal waves in the ocean", *Izv. Acad. Sci. USSR Atmos. Oceanic Phys.* **13** (1977), pp. 187–193.
[53] C. Garrett and W. Munk, "Internal waves in the ocean", *Annu. Rev. Fluid Mech.* **11** (1979), pp. 339–369.
[54] C. Garrett and W. Munk, "Space-Time Scales of Internal Waves", *Geophys. Fluid Dyn.* **2** (1972), pp. 225–264.
[55] C. Garrett and W. Munk, "Space-Time Scales of Internal Waves: A Progress report", *J. Geophys. Res.* **80** (1975), pp. 291–297.
[56] E. Falcon and N. Mordant, "Experiments in Surface Gravity-Capillary Wave Turbulence", *Annu. Rev. Fluid Mech.* **54** (2022), pp. 1–25.
[57] E. Monsalve, M. Brunet, B. Gallet and P.-P. Cortet, "Quantitative Experimental Observation of Weak Inertial-Wave Turbulence", *Phys. Rev. Lett.* **125** (2020), article no. 254502.
[58] C. H. McComas and F. P. Bretherton, "Resonant Interaction of Oceanic Internal Waves", *J. Geophys. Res.* **82** (1977), pp. 1397–1412.
[59] D. Benielli and J. Sommeria, "Excitation of internal waves and stratified turbulence by parametric instability", *Dyn. Atmos. Oceans* **23** (1996), pp. 335–343.
[60] D. Benielli and J. Sommeria, "Excitation and breaking of internal gravity waves by parametric instability", *J. Fluid Mech.* **374** (1998), pp. 117–144.
[61] H. Scolan, E. Ermanyuk and T. Dauxois, "Nonlinear Fate of Internal Wave Attractors", *Phys. Rev. Lett.* **110** (2013), article no. 234501.
[62] C. Brouzet, E. V. Ermanyuk, S. Joubaud, I. N. Sibgatullin and T. Dauxois, "Energy cascade in internal-wave attractors", *Eur. Phys. Lett.* **113** (2016), article no. 44001.
[63] C. Brouzet, I. N. Sibgatullin, H. Scolan, E. V. Ermanyuk and T. Dauxois, "Internal wave attractors examined using laboratory experiments and 3D numerical simulations", *J. Fluid Mech.* **793** (2016), pp. 109–131.
[64] C. Brouzet, E. Ermanyuk, S. Joubaud, G. Pillet and T. Dauxois, "Internal wave attractors: Different scenarios of instability", *J. Fluid Mech.* **811** (2017), pp. 544–568.
[65] T. Le Reun, B. Favier and M. Le Bars, "Parametric instability and wave turbulence driven by tidal excitation of internal waves", *J. Fluid Mech.* **840** (2018), pp. 498–529.
[66] G. Davis, T. Jamin, J. Deleuze, S. Joubaud and T. Dauxois, "Succession of Resonances to Achieve Internal Wave Turbulence", *Phys. Rev. Lett.* **124** (2020), article no. 204502.
[67] C. Savaro, A. Campagne, M. Calpe Linares, P. Augier, J. Sommeria, T. Valran, S. Viboud and N. Mordant, "Generation of weakly nonlinear turbulence of internal gravity waves in the Coriolis facility", *Phys. Rev. Fluids* **5** (2020), article no. 073801.
[68] C. Rodda et al., "Experimental observations of internal wave turbulence transition in a stratified fluid", *Phys. Rev. Fluids* **7** (2022), article no. 094802.
[69] C. Rodda, C. Savaro, V. Bouillaut, P. Augier, J. Sommeria, T. Valran, S. Viboud and N. Mordant, "From Internal Waves to Turbulence in a Stably Stratified Fluid", *Phys. Rev. Lett.* **131** (2023), article no. 264101.
[70] N. Lanchon, D. O. Mora, E. Monsalve and P.-P. Cortet, "Internal wave turbulence in a stratified fluid with and without eigenmodes of the experimental domain", *Phys. Rev. Fluids* **8** (2023), article no. 054802.
[71] A. M. Fincham, T. Maxworthy and G. R. Spedding, "Energy dissipation and vortex structure in freely decaying, stratified grid turbulence", *Dyn. Atmos. Oceans* **23** (1996), pp. 155–169.
[72] O. Praud, A. M. Fincham and J. Sommeria, "Decaying grid turbulence in a strongly stratified fluid", *J. Fluid Mech.* **522** (2005), pp. 1–33.
[73] V. J. H. Lienhard and C. W. Van Atta, "The decay of turbulence in thermally stratified flow", *J. Fluid Mech.* **210** (1990), pp. 57–112.

[74] K. Yoon and Z. Warhaft, "The evolution of grid-generated turbulence under conditions of stable thermal stratification", *J. Fluid Mech.* **215** (1990), pp. 601–638.
[75] S. A. Thorpe, "On the layers produced by rapidly oscillating a vertical grid in a uniformly stratified fluid", *J. Fluid Mech.* **124** (1982), pp. 391–409.
[76] P. Augier, P. Billant, M. E. Negretti and J.-M. Chomaz, "Experimental study of stratified turbulence forced with columnar dipoles", *Phys. Fluids* **26** (2014), article no. 046603.
[77] G. Oster and M. Yamamoto, "Density gradient techniques", *Chem. Rev.* **63** (1963), pp. 257–268.
[78] D. F. Hill, "General density gradients in general domains: the 'two-tank' method revisited", *Exp. Fluids* **32** (2002), pp. 434–440.
[79] G. J. Daviero, P. J. W. Roberts and K. Maile, "Refractive index matching in largescale stratified experiments", *Exp. Fluids* **31** (2001), pp. 119–126.
[80] Y. Dossmann, B. Bourget, C. Brouzet, T. Dauxois, S. Joubaud and P. Odier, "Mixing by internal waves quantified using combined PIV/PLIF technique", *Exp. Fluids* **57** (2016), article no. 132.
[81] A. Campagne, B. Gallet, F. Moisy and P.-P. Cortet, "Disentangling inertial waves from eddy turbulence in a forced rotating-turbulence experiment", *Phys. Rev. E* **91** (2015), article no. 043016.
[82] C. Staquet, "Internal gravity waves: parametric instability and deep ocean mixing", *C. R. Mécanique* **335** (2007), pp. 665–678.
[83] O. M. Phillips, *The Dynamics of the Upper Ocean*, Cambridge University Press, 1966.
[84] T. Dauxois and W. R. Young, "Near-critical reflection of internal waves", *J. Fluid Mech.* **390** (1999), pp. 271–295.
[85] L. R. M. Maas and F.-P. A. Lam, "Geometric focusing of internal waves", *J. Fluid Mech.* **300** (1995), pp. 1–41.
[86] L. R. M. Maas, D. Benielli, J. Sommeria and F.-P. A. Lam, "Observation of an internal wave attractor in a confined stably stratified fluid", *Nature* **388** (1997), pp. 557–561.
[87] N. Grisouard, C. Staquet and I. Pairaud, "Numerical simulation of a two-dimensional internal wave attractor", *J. Fluid Mech.* **614** (2008), pp. 1–14.
[88] J. Hazewinkel, P. van Breevoort, S. Dalziel and L. R. M. Maas, "Observations on the wavenumber spectrum and evolution of an internal wave attractor", *J. Fluid Mech.* **598** (2008), pp. 373–382.
[89] S. Joubaud, J. Munroe, P. Odier and T. Dauxois, "Experimental parametric subharmonic instability in stratified fluids", *Phys. Fluids* **24** (2012), article no. 041703.
[90] G. Davis, *Attracteurs d'ondes internes de gravité : des résonances en cascade : une approche expérimentale des régimes linéaire et non linéaire*, PhD thesis, Université de Lyon, Lyon, France, 2019.
[91] G. Bordes, F. Moisy, T. Dauxois and P.-P. Cortet, "Experimental evidence of a triadic resonance of plane inertial waves in a rotating fluid", *Phys. Fluids* **24** (2012), article no. 014105.
[92] C. Peretti, J. Vessaire, E. Durozoy and M. Gibert, "Direct visualization of the quantum vortex lattice structure, oscillations, and destabilization in rotating ^{4}He", *Sci. adv.* **9** (2023), article no. eadh2899.

ACADÉMIE DES SCIENCES
INSTITUT DE FRANCE

Comptes Rendus. Physique
2024, Vol. 25, Special issue S3, p. 557-581
https://doi.org/10.5802/crphys.195

Review article / *Article de synthèse*

Geophysical and astrophysical fluid dynamics in the laboratory / *Dynamique des fluides géophysiques et astrophysiques au laboratoire*

Quasi-biennial oscillation: laboratory experiments

Oscillation quasi-biennale : expériences de laboratoire

Benoît Semin [*,a] **and François Pétrelis** [b]

[a] PMMH, CNRS, ESPCI Paris, PSL University, Sorbonne Université, Université Paris-Cité, F-75005, Paris, France

[b] LPENS, CNRS, ENS Paris, PSL University, Sorbonne Université, Université Paris-Cité, F-75005, Paris, France

E-mails: benoit.semin@espci.fr (B. Semin), petrelis@lps.ens.fr (F. Petrelis)

Abstract. The quasi-biennial oscillation (QBO) is an oscillation of the wind in the equatorial stratosphere. This wind is a mean flow induced by atmospheric waves, including internal gravity waves, which explain that the period (28 month) is not linked to any astrophysical forcing. This oscillation has only been reproduced in 3 laboratory experiments, which share a similar geometry. We present the details of our experimental set-up, and we explain which improvements allowed us to obtain quantitative measurements during long times. We show experimentally the feedback of the mean flow on the waves, which is one of the key ingredient of the oscillation. The details of the analytical resolution of the 1D model of Plumb and McEwan are given. We compare experimental results to analytical and numerical results, and found a qualitative agreement. The period decreases when the forcing increases, and the amplitude of the mean flow is not monotonic with respect to height and displays two local maxima as a function of height close to the threshold. The bifurcation is always a Hopf one, but can be subcritical or supercritical depending on the dominant dissipation mechanism of the mean flow which can be tuned experimentally by changing the Brunt–Väisälä frequency. We argue that an investigation of the bifurcation in general circulation models (GCM) is of interest to better understand the evolution of the QBO due to climate change.

Résumé. L'oscillation quasi-biennale (QBO) est une oscillation du vent dans la stratosphère équatoriale. Ce vent est un écoulement moyen engendré par des ondes atmosphériques, notamment des ondes internes de gravité, ce qui explique que la période (28 mois) n'est liée à aucun forçage astrophysique. Cette oscillation n'a été reproduite qu'à 3 reprises par des expériences analogues de laboratoire, et ces 3 expériences ont été réalisées dans la même géométrie. Nous présentons en détail notre dispositif expérimental, et en particulier les améliorations qui nous ont permis d'obtenir des mesures quantitatives sur de longues durées. Nous montrons expérimentalement la rétroaction du l'écoulement moyen sur les ondes, qui est l'un des ingrédients clés de la QBO. Nous donnons les détails de la résolution analytique du modèle 1D de Plumb et McEwan. Nous comparons les résultats expérimentaux à ceux obtenus analytiquement et numériquement, et nous

* Corresponding author

montrons qu'ils sont en accord qualitatif. La période de l'écoulement moyen diminue lorsque le forçage augmente, et l'amplitude d'écoulement moyen en fonction de la hauteur n'est pas monotone et présente au voisinage du seuil deux maxima locaux. La bifurcation est toujours une bifurcation de Hopf, mais elle peut être sous-critique ou supercritique en fonction du mécanisme dominant de dissipation de l'écoulement moyen, qui peut être changé expérimentalement en modifiant la fréquence de Brunt-Väisälä. Nous concluons en expliquant qu'une étude de la bifurcation dans les modèles de circulation générale (GCM) serait intéressante pour mieux comprendre l'évolution de la QBO liée au changement climatique.

Keywords. Fluid mechanics, internal gravity waves, wave-mean flow interaction, instability, non-linear physics.

Mots-clés. Mécanique des fluides, ondes internes de gravité, interaction ondes-écoulement moyen, instabilité, physique non-linéaire.

Manuscript received 27 March 2024, revised 15 July 2024, accepted 5 August 2024.

1. Introduction

The quasi-biennial oscillation (QBO) is the periodic reversal of the wind in the equatorial stratosphere [1] (the stratosphere is the second layer of the atmosphere, between 16 km to 50 km at the equator). The period of the oscillation is 28 months on average, and is not directly linked to any astrophysical forcing. This wind is known to be generated by a broad spectrum of atmospheric waves, including small scale internal gravity waves and planetary waves like Kelvin waves, Rossby-gravity waves and inertia-gravity waves [1]. The interaction between the wind and the waves leads to the periodic reversal of the wind.

A key feature of the QBO is its downward propagation without loss of amplitude [1]. The position where the mean flow changes sign drifts towards the location from where the waves are emitted, i.e. the troposphere (the troposphere is the bottom layer of the atmosphere, between 0 km to 16 km at the equator).

The QBO has been mainly studied through observations on Earth, but similar wind oscillations exist on other planets like Saturn [2] or Jupiter [3,4]. Internal waves can also be sustained in stably stratified layers in stars [5], and models of the Sun tachocline also observe periodic reversals of a mean flow similarly to the QBO mechanism [6]. Overall this mechanism is robust and generic.

The QBO used to be one of the most predictable fluctuations of the large-scale circulation of the Earth's atmosphere [7]. However, two disruptions of the QBO have been observed recently in 2015/16 and 2019/20, after more than 50 years without observed disruption [8]. These disruptions are thought to be due to strong extra-equatorial waves forcing.

A key interest of the QBO is the correlation between phenomena outside the tropical stratosphere, the so-called teleconnections [7,9]. The QBO influences the convection in the troposphere close to the equator [10] and modulates the mixing and the transport of chemical constituents in the atmosphere, including ozone among others [11]. Even if this wind oscillation is located close to the equator, it has some influence in the extratropics. This wind oscillation is correlated with hurricanes in North America [1] and affects winter conditions in Europe [12]. It also influences the Madden-Julian oscillation [13,14], an eastward propagation of large regions of both enhanced and suppressed tropical rainfall, observed over the Indian and Pacific oceans.

The QBO has been simulated using general circulation models (GCM) for more than 20 years now [15]. It used to be difficult for the models used for climate change forecast to produce a QBO. For instance, most of the models included in CMIP5 (Coupled Model Intercomparison Project Phase 5) do not reproduce the QBO [16]. Now, many climate models simulate QBO-like oscillations, but often with an amplitude weaker than the observed one in the lower stratosphere [7]. Moreover, these models rely on the parametrization of small-scale tropical waves which cannot

be resolved [7,17], and the uncertainty on the response of the QBO to climate change is at least partly due to uncertainties on internal gravity waves [18].

Simple 1D models have been developed when the basics mechanisms of the QBO have been understood [19,20]. These models have inspired the analog experiments of the QBO (see [21] and discussion below), and reciprocally the experiments have shown the relevance of the physical ingredients used in these simple models. We will discuss this aspect later in the present article. These simple models are still useful to extract some basics mechanisms, as for example in [22] where the successive bifurcations of the Plumb and McEwan model are investigated and where the existence of a second bifurcation is shown, leading to quasi-periodic trajectories. In [23] the effect of the boundary condition is investigated. The excitation with a spectrum of waves has been studied in [24], where the authors show that the spreading of the wave energy across a wide frequency range leads to more regular oscillations.

Couston et al. 2018 [25] have shown that an oscillating flow can emerge from internal gravity waves generated by turbulent convective motion, using direct numerical simulations (DNS), i.e. without parametrization. A 2D model coupling the troposphere and the stratosphere and taking into account the phase change of water has been used to investigate the effect of the QBO on precipitations [26]. A comparison between 2D and 3D direct numerical simulations reproducing the experiments has been performed for different forcing parameters [27].

Three analog experiments of the QBO have been performed: the first has been performed by Plumb and McEwan in 1978 [21], the second by Otobe et al. in 1998 [28] and the third by Semin et al. in 2018 [29]. These 3 experiments share a similar geometry: a linearly stratified aqueous solution is placed between two concentric vertical cylinders, of size about 0.5 m. The forcing is achieved using 16 membranes placed at the bottom [21] or top [28,29] of the fluid. Each membrane oscillates in opposite phase with its two neighbors, so that the forcing is a pattern of azimuthal standing waves, which is equivalent to two counter-propagating waves. The choice of the geometry, size and number of membranes has thus been done by Plumb and McEwan in 1978 [21].

In the first experiment by Plumb and McEwan [21], the flow was measured using tracers. Since this study dates back before particle image velocimetry (PIV) became widely available, the particles were tracked manually from “Cine film”. The average velocity on a cycle was measured. Tracers generated by electrolysis on a vertical wire were also used. This first experiment has validated the wave/mean flow theory, the instability of mean flow, the reversal of the mean flow and the origin of the downward propagation. This was an essential validation of a mechanism which is far from being obvious. A stability diagram is displayed in this article, which shows a very qualitative agreement with the theory. Only measurements over one period are presented.

The second experiment by Otobe et al. [28] has confirmed the results of Plumb and McEwan [21]. The mean flow is measured with particles, and the waves with a Moiré technique. The distortion of the waves by the mean flow is presented. The difficulty to obtain reproducible results is emphasized: the authors state for example “The period of the oscillation is 1 to 2 hours, but there is no apparent correlation with the experimental parameters”.

The third experiment has been done by Semin et al. [29]. We will present this experiment in more detail in the present article. This is a quantitative experiment, where both the waves and the mean flow are measured using PIV. Continuous slow injection of new (and heavier) fluid at the bottom of the tank and slow withdrawal of fluid at the top prevented the weakening of the stratification at the top where the membranes move, and thus allows very long measurements. We have determined the nature of the bifurcation. The bifurcation is always a Hopf bifurcation, but can be supercritical or subcritical depending on the main dissipation of the mean flow.

An experiment close to the analog QBO experiments has been performed by Léard et al. [30] (see also [31]). The authors take advantage of the non-monotonic change of the density of water

around 4 °C to excite directly the waves in a stratified layer by the convection in the lower layer. A mean flow appears in the upper stratified layer, but with a dynamics different from the QBO, explained by the authors by the difference in Prandtl numbers between water and air. Another experiment has been reported by Léard et al. 2021 [32]. The waves in a stratified fluid are forced by 12 jets in a upper unstratified layer. A mean flow of very low intensity is obtained in this set-up where the forcing is turbulent and statistically symmetric, contrary to the previously reported experiments of mean flow generation by internal waves [33,34]. However, no reversal has been obtained, probably due at least partly to the mixing at the interface between the two layers. These experiments justify a posteriori the use of membranes to force the fluid in the analog QBO experiments.

In this article, we present in Section 2 the details of our experimental set-up, including many tricks not discussed in our previous articles in [29,35]. The details of the analytical resolution of the Plumb and McEwan model is given in Section 3 and in Appendix B. Numerical simulations are also discussed. The experimental results are presented in Section 4.

2. Experimental set-up

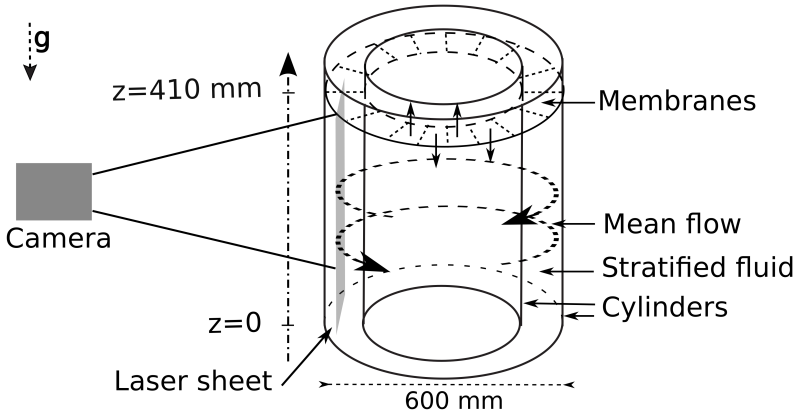


Figure 1. Schematic view of the experimental set-up.

A schematic view of the experimental set-up is shown in Figure 1 and a picture in Figure 2 left. It has been already described in [35]. It is made of two transparent concentric vertical cylinders. The outer diameter of the inner cylinder is 365 mm, the inner diameter of the outer cylinder is 600 mm, and the height is $H = 410$ mm.

The gap h between these two cylinders is filled with a linearly density-stratified solution of NaCl or $MgCl_2$ in water, obtained using the double-bucket method [28]. We use NaCl for water softener (Laugil) and magnesium chloride ice melt (France Déneigement). For NaCl, we use 62 L of tap water in bucket 1, and 48.5 L of tap water and 15 kg of NaCl in bucket 2. For $MgCl_2$, we use 55.9 L of tap water in bucket 1, and 19.5 L of tap water and 36.4 kg of $MgCl_2$ in bucket 2 ($MgCl_2$ is already partially hydrated when we buy it). Moreover 40 mL of chlorine bleach is added in each bucket to avoid algea proliferation. During the injection, bucket 1 is constantly mixed using a VWR VOS overhead stirrer, as required by the double-bucket method. The density profile is obtained from conductivity, measured using a conductivity probe (Mettler-Toledo SevenGo Pro) positioned at different heights using a linear manual translation stage. We have used a pycnometer to measure the density of solution that we used to calibrate the conductivity.

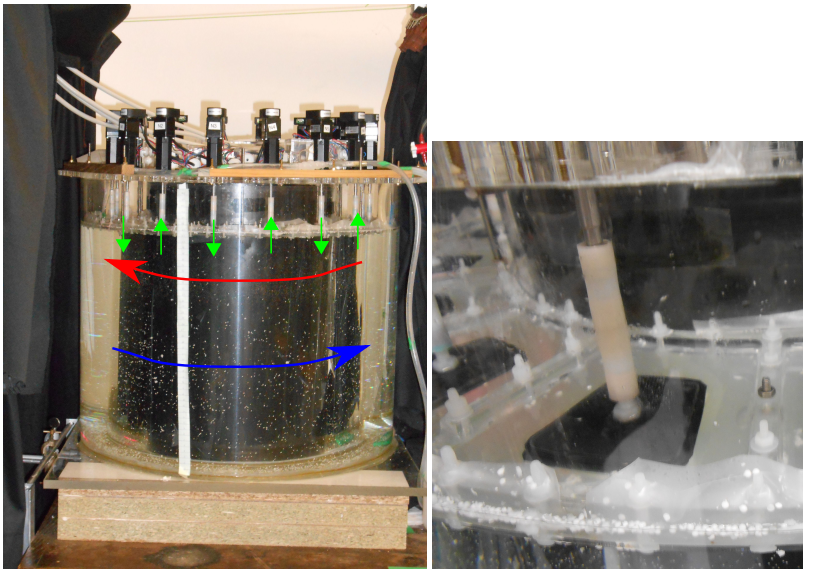


Figure 2. Left: picture of the experimental set-up. The green arrows indicate the motion of the membranes, and the red and blue arrow the direction of the mean flow. Right: picture of a membrane.

Note that the conductivity of $MgCl_2$ is not monotonic with respect to density: a given value of conductivity may correspond to two values of density. We use the stably stratified property of the fluid to select the right value. The stratification is quantified by the Brunt–Väisälä frequency, $N = \sqrt{-(g/\rho_0)\,\mathrm{d}\rho_0/\mathrm{d}z}$, where g is the acceleration of gravity, ρ_0 is the background density at the top and z is the vertical axis. The typical value of N is $1.5-2.2\,\mathrm{rad\cdot s^{-1}}$, the highest values are obtained using $MgCl_2$.

The fluid motion is forced using 16 silicone membranes (Profiles Market, thickness 0.3 mm). The membranes are in contact with the top of the fluid and are fixed using nylon and stainless steel screws on a laser-cut PMMA annulus (see Figure 2 right). We used Boehm hollow punches to make the fixation holes in the membranes. However, it happened several times that a membrane broke due to tearing, which then induced mixing at the top and unreliable experimental results, which were then discarded. The silicone membranes do not degrade in salty water. A gap of a few millimeters is located between the annulus and the cylinders, so that air can be removed from the membrane by pushing gently with a plastic stick.

Each membrane can be individually moved up and down by a linear stepper motor (Nanotec L2818-OV15601 with SMCI36 controller), which is computer controlled using Labview. The membranes are fixed to the motor stick using two rubber plates (typical dimensions 45 mm, in black in Figure 2 right) which are sandwiched between two transparent and rigid PMMA plates. The motion of each motor is a sine function, and two neighboring membranes are driven by motors in opposition of phase so that the forcing is a standing wave whose azimuthal wavelength $\lambda_x \simeq 200$ mm is twice the curvilinear distance between 2 motors. We note M the amplitude of the motion of the membranes and we report here on measurements performed with a forcing period $T_f = 15$ s. The length of the stick of the motor number m is:

$$h(t) = M\sin(\omega t + m\pi) + h_{0,m} \tag{1}$$

where $\omega = 2\pi/T_f$ and $h_{0,m}$ is the initial value of the stick length.

The fluid velocity is measured using particle image velocimetry (PIV). Since the velocities are slow, we use a low-cost laser sheet (Apinex, 5 mW) and an industrial camera (Allied Vision Stingray) at 10 or 12 frames per second. The particles are imaged in the whole height on a width of about 30 mm. Movies of 900 images are acquired every 100 s or 1500 images every 250 s. We made the seeding particles using wax and alumina powder, to obtain particles with a range of average densities similar to the range of densities in the fluid. The protocol to make the beads is detailed in Appendix A. The beads are mixed with hand washing liquid and water (50%) before being gently poured at the top of the fluid, to avoid air bubble accumulation at their surface. We use OpenPiV [36] on Matlab to determine the velocity field from two successive images. To take into account the small lens effect due to the cylinder, a different calibration length is used on the vertical and horizontal axis. The relaxation time of the particle is $t_b = \rho_b (2r_b)^2/(18\eta)$, where ρ_b is the density of the particle (slightly above that of water), $r_b \sim 0.5$ mm is the radius of the particle and η the dynamic viscosity of water. An estimate of this time is thus $t_b \sim 0.06\,\mathrm{s} \ll T_f$: despite their large size, the particles are expected to follow the flow. The typical interrogation windows has a width of 64 pixels and a height of 32 pixels (corresponding to 11 mm), and the overlap between the interrogation windows is 50%. In each interrogation window, the velocity as a function of time is fitted using a sine function to obtain the amplitude and the phase of the wave (oscillation at the forcing angular frequency ω) and the mean flow. We have checked that the mean flow is azimuthal and only depends on the height z, except very close to the boundaries.

One of the main improvements between our set-up and the previous ones is the continuous injection of fluid at the bottom and removal at the top using a peristaltic pump (Ismatec Reglo ICC 4 channels). Even if the membrane motion at the top tends to slowly mix the fluid, this ensures that the stratification remains linear (see Figure 3). No measurement of mean flow lasting more than 2 periods had been reported before our experiments. In the first experiments that we performed, without pump, we also observed only 1 or 2 oscillations of the mean flow, and the measured stratification at the top was very weak at the end of the experiment. Since the stratification affects the emission and propagation of waves in the system, the weakening of the stratification is consistent with the impossibility to generate a mean flow any more. To avoid such a weakening of the stratification due to mixing, salty fluid is continuously injected at the bottom (around $9\,\mathrm{mL\cdot min^{-1}}$) and removed at the top of the experiment in 3 points: between the annulus of membranes and the cylinder (around $21\,\mathrm{mL\cdot min^{-1}}$) and on top of two membranes (around $14\,\mathrm{mL\cdot min^{-1}}$). This configuration ensures that no liquid accumulates at the top. The typical vertical velocity associated with this flow is $1\,\mu\mathrm{m\cdot s^{-1}}$, which is significantly smaller than the other velocities involved in the experiment. This modification allows us to perform quantitative measurements in a nearly steady state (variation of N less than $0.1\,\mathrm{rad\cdot s^{-1}}$ during a run of 90 000 s, see Figure 3). However, since the saturated concentration of the salt is finite, this system imposes a limit on the duration of the experiment. When the saturated fluid is injected, the experiment has to be stopped.

3. Theoretical approach

3.1. *Description of the model*

The aim of this section is to present the model of [21,35], which is a minimal model of the QBO. In the next section, we present several analytical results obtained on this model. Some of them were mentioned in the supplementary material of [29]

In this model, a mean flow is generated by two counter-propagating internal gravity waves. These two waves propagate through a linearly stratified fluid, characterized by a Brunt–Väisälä frequency, $N = \sqrt{-(g/\rho_0)\,\mathrm{d}\rho_0/\mathrm{d}z}$, where g is the acceleration of gravity, ρ_0 is the background

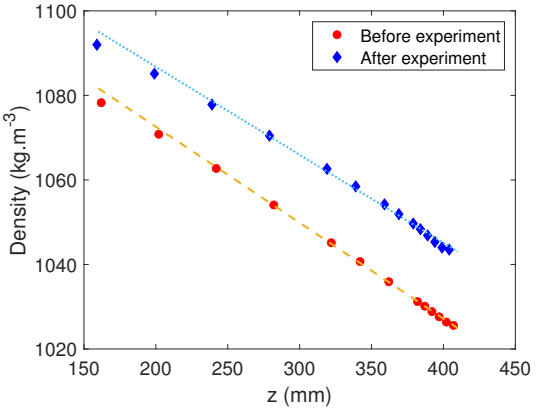


Figure 3. Stratification before (red dots) and after (blue diamonds) a 90 000 s long experiment. The orange dashed line is a linear fit of the red dots, and the cyan dotted line is a linear fit of the blue diamonds. Stratification using NaCl, $T = 15$ s, $M = 13.5$ mm. The Brunt–Väisälä frequency computed from the linear fits is $N = 1.48\,\mathrm{rad\cdot s^{-1}}$ before the experiment, and $N = 1.40\,\mathrm{rad\cdot s^{-1}}$ after.

density and z is the upwards vertical axis. The angular frequency of the waves is ω, one of the wave is propagating in the azimuthal direction $+x$, and the other in the direction $-x$; the horizontal wavevector is written k_x. These waves verify the linear dispersion relation for internal gravity waves:

$$\omega^2 = N^2(\sin(\theta))^2, \tag{2}$$

where θ is the angle between the wavevector $\boldsymbol{k}$ and the vertical. Due to the structure of the internal gravity waves, the horizontal wave component u' and the vertical component v' verify:

$$v' = u' \tan(\theta), \tag{3}$$

The equation of the model are obtained using the Navier–Stokes equation, the Boussinesq approximation and the Wentzel–Kramers–Brillouin approximation. As in the original work of Plumb and McEwan [21], we consider upward propagating waves in the calculation. The following dimensionless equation is obtained for the mean flow u:

$$\frac{\partial u}{\partial t} = -\frac{\partial D}{\partial z} + \Lambda_1 \frac{\partial^2 u}{\partial z^2} - \Lambda_2 u, \tag{4}$$

where:

$$D = F\left(c_1 \exp\left[-\int_0^z \left(\frac{\alpha_1}{(u-c_1)^2} + \frac{\alpha_2}{(u-c_1)^4}\right) \mathrm{d}z'\right] + c_2 \exp\left[-\int_0^z \left(\frac{\alpha_1}{(u-c_2)^2} + \frac{\alpha_2}{(u-c_2)^4}\right) \mathrm{d}z'\right]\right), \tag{5}$$

traces back to the forcing of the mean flow by the waves. ν is the kinematic viscosity, $c_1 = 1$ and $c_2 = -1$, Λ_1, Λ_2, α_1, α_2 are positive, $\alpha_1 + \alpha_2 = 1$ and F is the control parameter. An experiment is characterised entirely by 3 dimensionless parameters, for instance Λ_1, Λ_2, and α_1. However, we keep F as a free parameter here because we will expand F close to the threshold to apply the perturbation method. The boundary conditions are:

$$u(0) = 0, \tag{6}$$

$$u(+\infty) = 0, \tag{7}$$

and corresponds to a no slip boundary condition at $z = 0$ like in [21] and a vanishing velocity at infinity. We chose the latter condition to simplify the analysis and because the mean flow is actually localised close to the forcing boundary.

To make the link between the dimensionless variables and the physical variables, we note in the following set of equation and only in this set the dimensional variables with a $\sim$:

$$\begin{aligned}
\widetilde{F} &= \langle \widetilde{u}'\,\widetilde{v}' \rangle\,, \\
\widetilde{c} &= \frac{\widetilde{\omega}}{\widetilde{k}_x}, \\
\widetilde{d} &= \left(\frac{\widetilde{N}\widetilde{\gamma}}{\widetilde{k}_x \widetilde{c}^2} + \frac{\widetilde{N}^3 \widetilde{\nu}}{\widetilde{k}_x \widetilde{c}^4} \right)^{-1}, \\
z &= \frac{\widetilde{z}}{\widetilde{d}}, \\
u &= \frac{\widetilde{u}}{\widetilde{c}}, \\
\alpha_2 &= \frac{\widetilde{N}^3 \widetilde{\nu} \widetilde{d}}{\widetilde{k}_x \widetilde{c}^4}, \\
\Lambda_1 &= \frac{\widetilde{\nu}\widetilde{c}}{\widetilde{F}(0)\widetilde{d}}, \\
\Lambda_2 &= \frac{\widetilde{\gamma}\widetilde{c}\widetilde{d}}{\widetilde{F}(0)},
\end{aligned}$$

where $\widetilde{F}$ the momentum flux, $\widetilde{c}$ the horizontal phase velocity, $\widetilde{d}$ the vertical dissipation length, $\widetilde{\nu}$ is the kinematic viscosity, $\widetilde{\gamma}$ the dissipation due to the walls, $\widetilde{F}(0)$ the momentum flux at $\widetilde{z} = 0$.

From the dimensionless solution of equation (4), it is possible to obtain the dimensional variables: the dimensionless lengths should be multiplied by $\widetilde{d}$ to obtain the dimensional lengths, the dimensionless times should be multiplied by $\widetilde{c}\widetilde{d}/\widetilde{F}(0)$ and the dimensionless mean flow by $\widetilde{c}$.

3.2. *Linear and weakly non-linear solutions of the equations*

For the dimensionless system of equations (4) and (5), with the boundary conditions (6) and (7), we have obtained an explicit solution of the linear problem from which an equation for the threshold is obtained. We have also derived the amplitude equation in the vicinity of the threshold. Details of the calculation are given in Appendix B and we sum up the results here.

We introduce the stream function ψ

$$\psi = \int_0^z u \, \mathrm{d}z \tag{8}$$

so that

$$u = \frac{\partial \psi}{\partial z} \tag{9}$$

We are considering eigenmodes such that:

$$\frac{\partial \psi}{\partial t} = \mu \psi \tag{10}$$

with $\mu \in \mathbb{C}$.

We define the parameters

$$a = \frac{F \times 2(2\alpha_1 + 4\alpha_2)}{\Lambda_1}, \tag{11}$$

$$b = \frac{\mu + \Lambda_2}{\Lambda_1}, \tag{12}$$

that appear in the expression of ψ

$$\psi(z) = \psi_0(z)\left(1 + K f(z)\right). \tag{13}$$

ψ_0, K and f are given by

$$\psi_0 = J\left(2\sqrt{b}, 2\sqrt{a}\exp(-z/2)\right), \tag{14}$$

$$K = \frac{-1}{f(0)} = \frac{-1}{\int_{z_0}^{0} \frac{\int_{+\infty}^{z} \psi_0(z')\,\mathrm{d}z'}{(\psi_0(z))^2}\,\mathrm{d}z}. \tag{15}$$

$$f(z) = \int_{z_0}^{z} \frac{\mathrm{d}z' \int_{+\infty}^{z'} \psi_0(z'')\,\mathrm{d}z''}{(\psi_0(z'))^2}, \tag{16}$$

where J is the Bessel function of the first kind, of order $2\sqrt{b}$, and of argument $2\sqrt{a}\exp(-z/2)$. z_0 is an arbitrary positive constant ; the final solution does not depend on the value chosen for z_0.

Using the boundary conditions and properties of the Bessel functions, we obtain an integral equation that relates the parameters of the problem and the growth rate

$$\int_0^1 \left[J\left(2\sqrt{b}-1, 2\sqrt{a}v\right) + J\left(2\sqrt{b}+1, 2\sqrt{a}v\right)\right]\mathrm{d}v = 0. \tag{17}$$

We have solved equation (17) numerically using a Matlab minimization routine and Bessel functions of complex order and argument [37]. We fix the value of α_1 (and thus $\alpha_2 = 1-\alpha_1$). We set $F = 1$ which amounts to changing Λ_i into $\widetilde{\Lambda}_i = \Lambda_i/F$ and dropping the $\widetilde{.}$ to ease notation. We then compute a from equation (11). Using equation (17), we obtain the corresponding value for b at the threshold. Since μ is imaginary at the threshold and Λ_2 is real, we obtain from equation (12) the value of $\Lambda_2 = \Lambda_1 \Re(b)$ and $\mu = \Lambda_1 \Im(b)$. The eigenmodes are obtained using equation (13) with equations (16), (15) and (14), and their time evolution are given by multiplying the eigenmodes by $\exp(\mu t)$.

We have also derived the amplitude equation for the unstable mode in the vicinity of its onset of instability. We note

$$F = F_0 + \varepsilon F_1 \tag{18}$$

where F_0 is the value at the instability threshold (Λ_1 and Λ_2 being fixed) and ε a small parameter (dimensionless distance to the threshold).

We introduce a slow timescale $T = \varepsilon t$ and write u as:

$$u = \sqrt{\varepsilon}\left(u_0 + \varepsilon u_1 + \varepsilon^2 u_2 + \ldots\right) \tag{19}$$

At order $\varepsilon^{1/2}$, we recover the linear problem so that u_0 is the product of the eigenmode of the linear problem u with a slowly varying amplitude:

$$u_0(t,T,z) = \frac{1}{2}\left(A(T)u(t,z) + A^*(T)u^*(t,z)\right), \tag{20}$$

where u is given by equation (9) and (13).

At order $\varepsilon^{3/2}$, using the solvability condition, we obtain the amplitude equation for A

$$\frac{\partial A}{\partial T} = \alpha A F_1 + \beta |A|^2 A, \tag{21}$$

where explicit expressions for α and β are given in the annex.

This is the amplitude equation of a pitchfork Hopf bifurcation. Indeed, this is constrained by the oscillatory nature of the unstable mode that breaks invariance under shift in the origin of time.

The coefficients can be calculated numerically using the expressions given in Appendix B. In particular, we have calculated the following expression using a Matlab routine

$$S = \frac{\Re(\beta)}{\Re(\alpha)}, \tag{22}$$

where $\Re$ denotes the real part. The nature of the bifurcation is determined by the sign of S: if $S > 0$, the bifurcation is subcritical, and it is supercritical if $S < 0$.

The value of S is determined by a and b through equation (14) and the equations mentioned after. Since $\mu \in i\mathbb{R}$ at the threshold, the value of b at the threshold only depends on the mean flow dissipation through Λ_1 and Λ_2 (see equation (12)). The wave dissipation, i.e. the values of α_1 and α_2, only changes the value at the threshold of F. The nature of the bifurcation thus depends on the dissipation of the mean flow, whereas the nature of the dissipation of the waves only changes a prefactor which has always the same sign.

3.3. *Numerical simulations*

We have solved numerically the system of equations (4) and (5) using a centered second-order finite difference method with grid size $\delta z = 10^{-2}$ (or $\delta z = 4 \times 10^{-3}$ for the stability diagram). The total length is 4 in dimensionless unit, i.e. $4d$ in physical units: this is sufficient to mimic an infinite domain, since the waves are almost entirely damped for $z = 4$. Since the optimization of the numerical simulations is not the core of the present article, we have used an explicit Euler method in time with $\delta t = 10^{-4}$ (or $\delta t = 10^{-5}$ for the stability diagram), which is simpler than the schemes used by [38] and [25]. The boundary conditions are no-slip at both the bottom and upper boundary, according to equations (6) and (7). This numerical scheme is implemented in Matlab. The equations and the boundary conditions are not exactly the same as thee ones in the works of [38] and [25], who only consider bulk dissipation of the mean flow an a stress-free boundary condition at the upper boundary.

The numerical system can be solved using explicit Euler method, is numerically rather stable, and rapid to solve using a laptop (a few minutes with a 2 GHz processor laptop, using a Matlab script). We point out that this system can be used as a non-trivial example of numerical resolution at the undergraduate level.

4. Experimental results

4.1. *Interaction between wave and mean flow*

The mechanism of the QBO is based on the interaction between the waves and the mean flow. We investigate this interaction in this section.

The characteristic of the waves and the mean flow 2 min after the beginning of the forcing at $M = 14.5$ mm is shown in Figures 4 (a,b,c). The waves are established, but the mean flow is still zero. This is in agreement with the study of a single wave in the same set-up [35], and confirms that the characteristic time-scale of the mean flow is much larger than the one of the waves.

The initial phase of the wave is shown in Figures 4 (b). This phase corresponds to the expected stationary wave in the x direction. The measured vertical wavelength $\lambda_z = 46$ mm is in reasonable agreement with the expected value $\lambda_z = \lambda_x \tan(\theta) \simeq 40$ mm. The local amplitude of the wave is given by Figure 4 (a). The amplitude of the wave is not constant in the x direction, as expected for the sum of two counter-propagative waves. The wave amplitude does not vanish, which is linked to the choice of the position of the field of view, and to the fact that it is shorter than half the wavelength in the x direction $\lambda_x/2 = 100$ mm. By averaging the amplitude in the x direction, we obtain Figure 5. The amplitude of the wave decreases with height. This is due to the dissipation of the wave, mainly due to the dissipation by viscosity in the bulk: $\alpha_2 = 0.965$ where α_2 is the dimensionless quantification of the bulk dissipation whereas $\alpha_1 = 0.035$ is the dissipation due to the wall. We can fit the curve with the function:

$$u = \mu_0 \exp\left(-z/(2d_e)\right) \tag{23}$$

where d_e is the experimental decay length and μ_0 is related to the amplitude of the wave at the top through $u_0 = \mu_0/q$, where $q = 1.6$ in our experiment takes into account that the measured

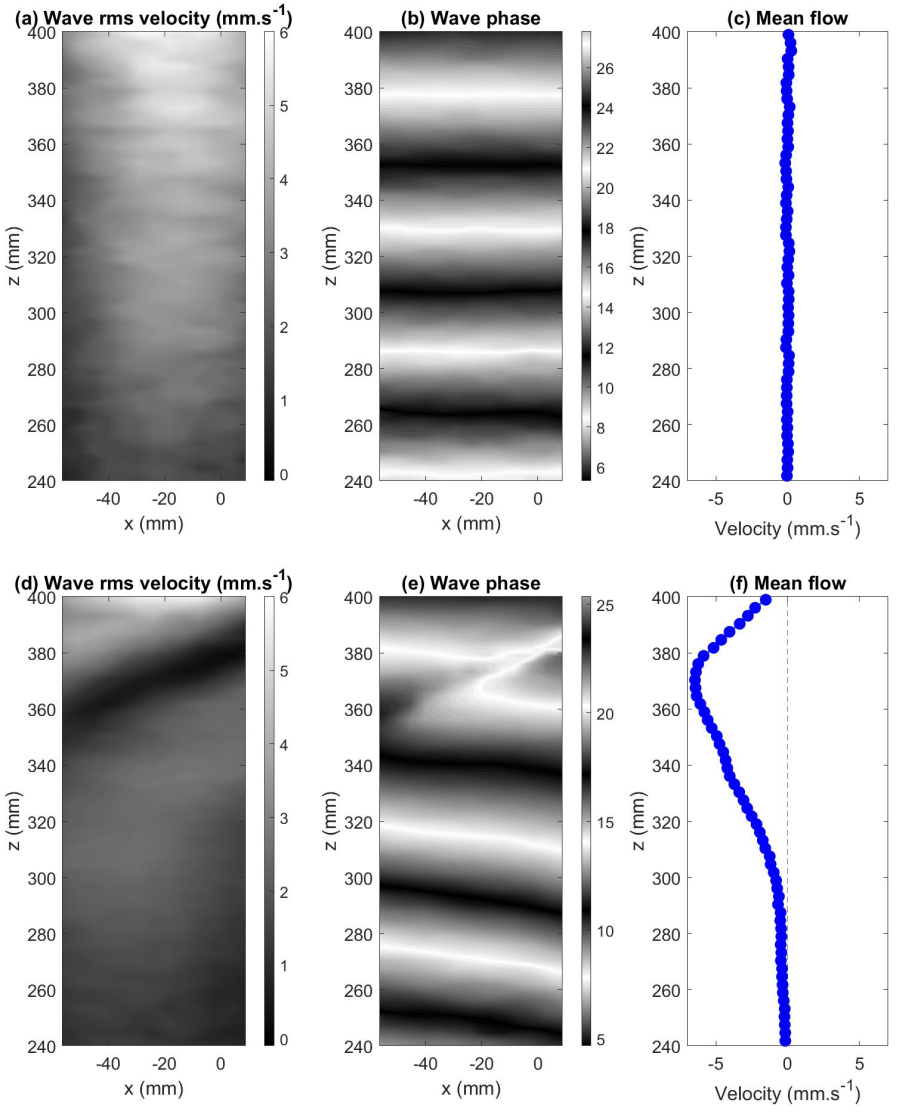


Figure 4. Measurements of the wave and mean flow for an experiment with $M = 14.5$ mm with $MgCl_2$ ($N = 2.16\,\mathrm{rad\cdot s^{-1}}$). The first row of the figure corresponds to the beginning of the forcing, when the mean flow is still small (sub-figures a,b,c). The second row corresponds to a time at which the mean flow is established. We chose a time at which the mean flow is negative everywhere for the simplicity of the interpretation (sub-figures d,e,f). The first column corresponds to the root-mean square value of the horizontal wave velocity $\langle\sqrt{(u')^2}\rangle$ (sub-figures a,d). The second column corresponds to the wave phase, obtained from the horizontal wave velocity u' (sub-figures b,e). The third column corresponds to the mean flow (sub-figures c,f).

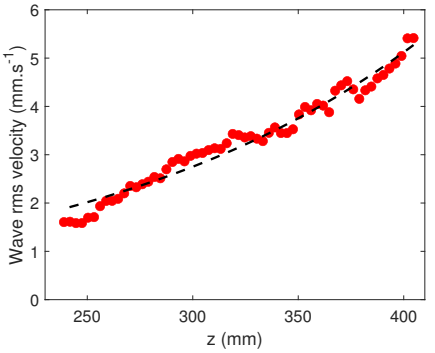


Figure 5. Red dots: wave root-mean-square value averaged in the x direction, from Figure 4 (a), i.e. $M = 14.5$ mm with $MgCl_2$, no mean flow. Dashed line: exponential fit, with $\mu_0 = 5.45\ \mathrm{mm\cdot s^{-1}}$, $d_e = 81$ mm.

amplitude is linked to the sum of two counter-propagating waves, measured in a finite field of view. The fit is good, indicating that the model is satisfactory. The value of d_e from the fit is $d_e = 81$ mm, is in rather good agreement with the theoretical value $d = 95$ mm, obtained using $\gamma = 10^{-3}$ s (see [35]), $\nu = 10^{-6}\ \mathrm{m^2\cdot s^{-1}}$ and the measured value of N. The small discrepancy is probably due to the difference in viscosity, the solution of $MgCl_2$ being more viscous than water or NaCl solution. We did not perform a quantitative analysis because the concentration and thus the viscosity is not homogeneous in the solution.

We now consider the same forcing parameters but after 75 min in Figures 4 (d,e,f). The mean flow is well established at that time. We have chosen a snapshot at which the mean flow has the same sign everywhere so that the qualitative explanations are easier. The phase displayed in Figure 4 (d) is different from the one when there is no mean flow (Figure 4 (b): there is a kink in the phase at the top. At the bottom, the phase is tilted with an angle 10°, where the theoretical angle for a single wave is $\theta = \arcsin(\omega/N) = 11°$. This figure shows that there is a feedback of the mean flow on the wave, and that one of the wave is dominant at the bottom, the other being of much smaller amplitude. The wave at the bottom has a positive horizontal wave velocity (see for instance [39] for the basic geometry of internal gravity waves). This feedback is consistent with the denominator in equation (5), and consistent with the qualitative explanation of the QBO [1] for which the wave which has a horizontal phase velocity of the same sign as the mean flow accelerates the mean flow more efficiently than the wave which has a horizontal phase velocity of the opposite sign, and is thus more attenuated. The modification of the waves by the mean flow has been shown in [28] using the Moiré technique and numerically in [27], but our method is more direct because we extract the wave phase. The feedback of the mean flow on the wave is also seen by comparing the amplitude of the wave without and with a mean flow in Figures 4 (a) and (d). In the latter case, the amplitude is lower everywhere but very close to the membrane. This is consistent with an increased attenuation of one of the waves due to the mean flow. The feedback of the mean flow on the waves for a single wave has been already shown experimentally in the geometry of a dipole and a wave beam in [40] and in a similar geometry in our previous work [35]. It has also been shown with two waves in [28], but with a more qualitative measurement of the waves.

4.2. *Characteristics of the mean flow*

An example of a space-time diagram of the mean flow, known as Hovmöller diagram in the atmospheric sciences, is shown in Figure 6. In this example, the mean flow is zero during a very long time and then suddenly appears without any apparent cause. This is consistent with

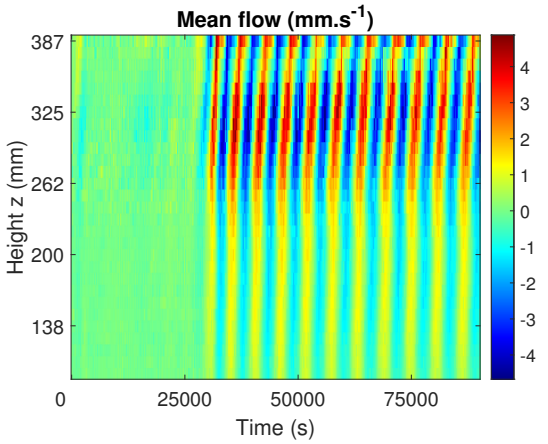


Figure 6. Example of mean flow as a function of time for a forcing amplitude $M = 13.5$ mm, a period $T_f = 15$ s and $N = 1.5\,\mathrm{rad}\cdot\mathrm{s}^{-1}$, stratification using NaCl.

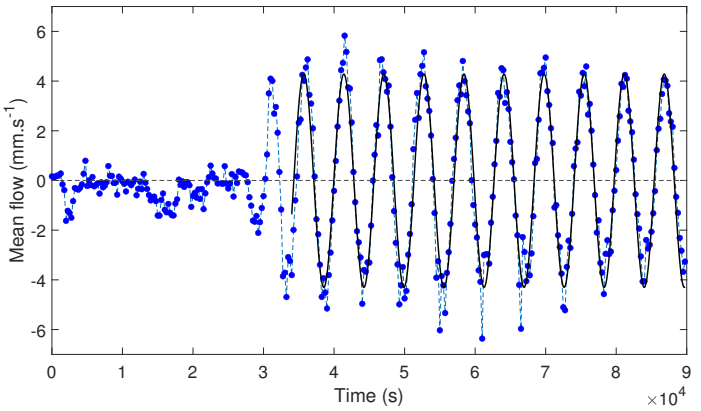


Figure 7. Mean flow as a function of time at $z = 320$ mm for the same experiment as the one shown in Figure 6: $M = 13.5$ mm, $T_f = 15$ s, $N = 1.5\,\mathrm{rad}\cdot\mathrm{s}^{-1}$, NaCl. Blue points: experimental data, blue dashed line: curve linking the experimental points, black line: sine fit.

a subcritical transition to the QBO for this value of N, as discussed in [29] and in Section 4.3. More than 9 periods of the mean flow are observed in this example, which is much higher than in any previous experiments [21,28]. As mentioned in Section 2, this has been achieved by the continuous injection of fluid at a very small velocity using an peristaltic pump.

The value of the mean flow at a given height for the same experiment is shown in Figure 7. This figure shows that the mean flow is actually quite regular, and can be fitted at a given height by a sine function during more than 9 periods. This sinusoidal behaviour of the mean flow is consistent with the weakly nonlinear methods used in the theoretical approach of Section 3.

Since the mean flow is sinusoidal in time, it is possible to plot the relative phase of the mean flow as a function of height, as done in Figure 8 left. The phase difference between the top and the bottom is close to π in the field of view. This is consistent with the usual view of the QBO and the theoretical calculations where the mean flow at the top and at the bottom are in opposition of phase.

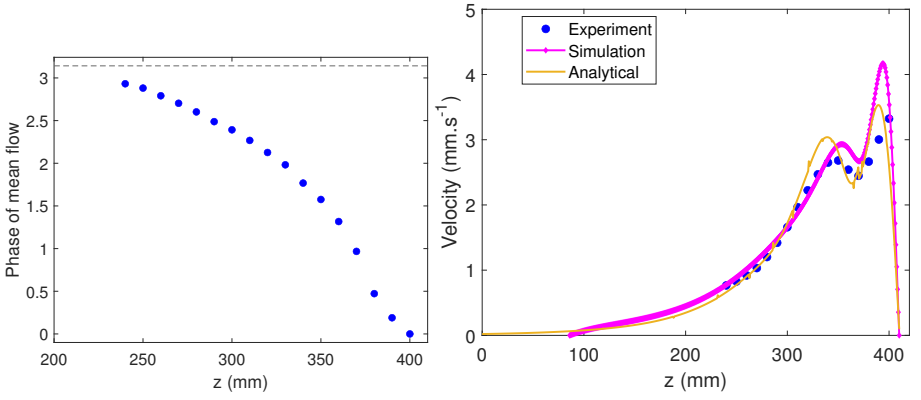


Figure 8. Left: relative phase of the mean flow, $M = 12$ mm, $MgCl_2$. The horizontal dashed line corresponds to π. Right: amplitude of the mean flow as a function of height z. Blue dots: experiment, $M = 12$ mm (threshold at $M = 11.3$ mm), $MgCl_2$; magenta line and diamond symbols: numerical resolution of the 1D model, $M = 10.0$ mm (threshold at $M = 9.1$ mm), orange line: analytical linear profile, height coefficient chosen to match the data.

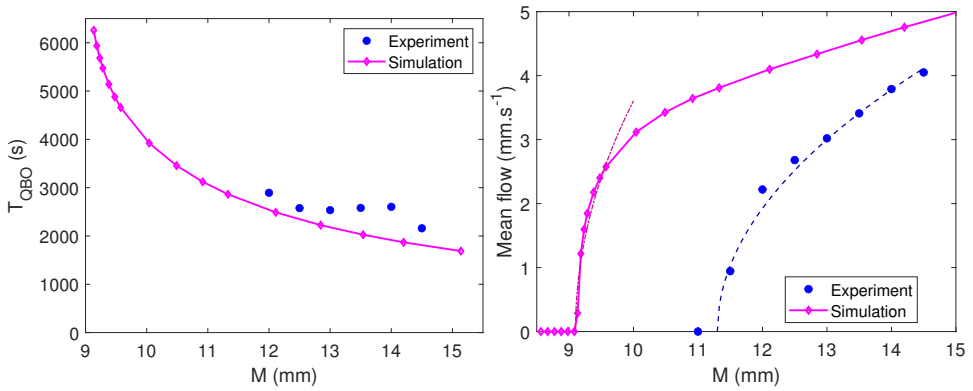


Figure 9. Left: period of the mean flow as a function of the forcing amplitude M, for $MgCl_2$. Blue points: experiment, the forcing is changed every 8 000 s to reach a quasi-steady state, and the period is measured in the last 4 000 s. See [29] for the space-time diagram. Magenta line and diamond symbols: numerical simulation. Right: amplitude as a function of M. Same color code. Height $z = 320$ mm for the experimental data, i.e. about d_e from the forcing, and distance d for the simulations. The blue dashed line and the violet dashed dotted line are of the form $\propto \sqrt{M - M_t}$, where M_t is the threshold, which is different for the experiments and the simulations.

The amplitude of the mean flow as a function of height is displayed in Figure 8 right. Experimental results, numerical and analytical results are shown in this figure. The chosen parameters are slightly different, due to the difference in the thresholds between the experiment and the numerical simulation. The value of d for scaling the simulation is taken from Figure 5, and the value of F is extrapolated from the value of μ_0 obtained from this figure, and by using the fact that F is quadratic in M. Since the wave velocity varies by about 20% across the width [35], and that the previous hypotheses may not be perfectly valid, we cannot expect a perfect quantitative

agreement. However, Figure 8 right shows that the values of the velocities and the shape of the mean flow profile are in qualitative agreement. In particular, the variation of the mean flow with height is not monotonic, leading to a local minimum in the amplitude. Experimentally, this effect is robust and has been observed irrespective of the stratification. Numerically, it is observed provided that the distance to the threshold is not too large. This shape is also observed in the linear analytical shape.

The period as a function of the forcing M is shown in Figure 9 left. The set of experiments used includes the one used in Figure 8, and the numerical simulations are performed using the same parameters. The period is finite at the threshold and decreases when M increases. The experiments and the simulations are in qualitative agreement. The period of the mean flow, about $T_{\mathrm{QBO}} = 2\,500\,\mathrm{s}$ is much larger than the wave period $T_f = 15\,\mathrm{s}$ as expected. Note that obtaining a reasonable value of the mean flow period is not easy experimentally. It is achieved successfully here thanks to the continuous injection of new fluid, as shown by the failure of [28] to obtain meaningful values for this period.

The mean flow amplitude as a function of the forcing M is shown in Figure 9 right. The value of the thresholds between experiment and theory are different but close. In both cases, the transition is continuous and the first point can be fitted by a form $\propto \sqrt{M - M_t}$. This behavior and the finite value of the period at the threshold shows that the bifurcation is a supercritical Hopf bifurcation in that experiment. The nature of the bifurcation will be investigated in more details in the next section.

4.3. *Stability diagram*

The stability diagram is shown in Figure 10. The bifurcation is subcritical at small values of Λ_1, and supercritical for large values of Λ_1. The tricritical point is at about $\Lambda_1 = 0.12$ and $\Lambda_2 = 1.88$. The values of the thresholds are in agreement to within 3% between the numerical and analytical solutions. The nature of the bifurcation is roughly in agreement. The behaviour of the bifurcation for the two different salts depends on the ratio $\Lambda_2/\Lambda_1 = \gamma d^2/\nu$. This ratio depends on N, and in our experiments of the salt because we use the more soluble and more expensive $MgCl_2$ only to achieve high values of N. The two lines displayed in Figure 10 correspond to two experiments, one with NaCl and a low value of N and one with $MgCl_2$ and a larger value of N. During an experiment with $MgCl_2$ where the amplitude of the forcing is changed, the ratio Λ_2/Λ_1 changed slightly due to the change in the stratification (see Section 2) and to the fact that the kinematic viscosity of a $MgCl_2$ solution depends on its density. The ratio γ/ν is independent of the viscosity, but d decreases when the viscosity is increased. More precisely, it is possible to evaluate the value of Λ_i for the point where there is no mean flow, because the wave amplitude can be fitted by an exponential (see an example in Figure 5). This is the case for the largest forcing amplitude (plain diamonds), for which the mean flow is initially zero. It is also possible for the points at which there is no more mean flow (empty diamonds). In between, it is possible to interpolate the values of Λ_i for the other values of the forcing for which there is a mean flow, assuming that $F(0)$ is quadratic in the forcing amplitude and that the viscosity increases linearly with time (the latter hypothesis is reasonable because the change is small). The dashed lines in Figure 10 correspond to a guide to the eye of where the experimental points should be without viscosity effects.

For $MgCl_2$, we have a rather good agreement between the experimental threshold and the theoretical one, without any adjustable parameter. This is not the case with NaCl. The reason is not clear, but we can note that the decay length d for NaCl is different from the calculated one.

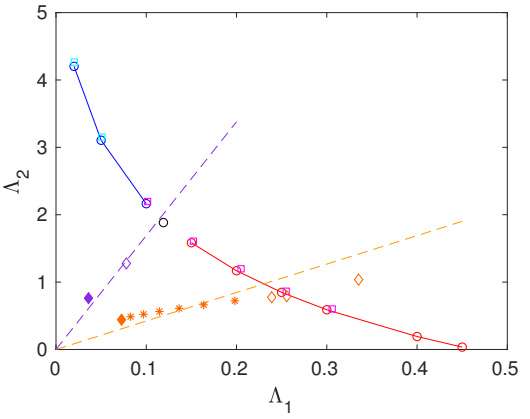


Figure 10. Stability diagram, from analytical solutions ($\alpha_2 = 1$), simulations, with experimental values. The solution is stable (i.e. no mean flow) for large values of Λ_1 and Λ_2, and unstable (oscillating mean flow) for small values of Λ_1 and Λ_2. Red line and red circles: analytical values for the threshold, supercritical bifurcation; black circle: analytical value of the tricritical point; blue line and blue circles: analytical values for the linear threshold, subcritical bifurcation. Red squares: threshold from numerical simulations, case where the bifurcation is supercritical; blue squares: threshold from numerical simulations, case where the bifurcation is subcritical. Dashed orange line: line corresponding approximately to $MgCl_2$ during an experiment where the wave flux is changed; dashed violet line: same for NaCl. Plain orange diamond: experimental values where a mean flow is observed for $MgCl_2$; empty orange diamonds: same but without mean flow; orange asterisk: experimental values for which a mean flow is observed, with value of forcing interpolated. Violet diamonds: same as orange diamonds, but for NaCl.

5. Conclusion

The quasi-biennial oscillation (QBO) is a the periodic reversal of the wind in the equatorial stratosphere, due to the forcing by atmospheric waves. The period, of about 28 months, is not linked to any external astrophysical forcing, which is a remarkable feature [41].

Three analog experiments have been performed in 1978 by Plumb and McEwan [21], in 1998 by Otobe et al. [28] and in 2018 by Semin et al. [29]. The geometry is similar in all three experiments: a linearly stratified aqueous solution between two cylinders is forced using 16 membranes. Simple 1D model [20] and a careful consideration of the dimensionless numbers of the problem have lead to the choice of this particular set-up.

The first experiment [21] has provided a proof of the concept of the wave induced mean flow oscillation. The last experiment [29] has shown that the bifurcation between a state without mean flow and a state with a mean flow depends experimentally on the value of the Brunt–Väisälä frequency. The model shows that the nature of the bifurcation depends on the main dissipation mechanism of the mean flow, i.e. in the bulk or in the boundary layer close to the wall of the cylinders. This main dissipation mechanism changes in our experiments when the Brunt–Väisälä frequency changes.

In this article, we have presented the details of the experimental set-up discussed in [29,35], including many experimental tricks.

We also give the details of the analytical resolution of the 1D model of Plumb and McEwan [21]. This model describe the generation of a mean flow by two counter-propagating internal gravity waves. We have presented an analytical solution of this model up to the third order, in order

to determine the threshold, the eigenvectors and the nature of the bifurcation. Two dissipation mechanisms are taken into account for the waves and the mean flow: one linked to the effect of viscosity in the bulk, described by the dimensionless coefficient Λ_1 for the mean flow and α_2 for the waves, and one for the dissipation at the lateral walls, described by the dimensionless coefficient Λ_2 for the mean flow and α_1 for the waves. We have solved analytically this model, and we have obtained the value of the threshold as a function of the dimensionless parameters. The nature of the dissipation of the waves changes only quantitatively the threshold. In contrast, the nature of the dissipation of the mean flow plays a major role in the bifurcation: the bifurcation is supercritical for large values of Λ_1 and subcritical for small values of Λ_1.

It is remarkable that the model of Plumb and McEwan can be solved analytically. However, as shown in this article, the resolution is long. On the other hand, the numerical resolution of this model is simple and rapid: we think that it would be a good example for advanced undergraduate students.

We have measured simultaneously the waves and the mean flow using PIV. We have shown an example of feedback of the mean flow on the waves. The experimental results are consistent with the mechanism of the QBO: the attenuation of a wave (and its momentum transfer to the mean flow) depends on the relative sign of the mean flow and the horizontal phase velocity of the wave. In particular, at the special time where the mean flow has the same sign everywhere, one of the waves is filtered out and only the other wave is measured at the bottom.

We have also shown an example of a mean flow as a function of time for a fixed forcing. The example we have chosen correspond to a subcritical bifurcation: there is no mean flow during a very long time, and then it appears due to an unknown perturbation. The space-time diagram also shows that the oscillation of the mean flow is very stable, and last more that 9 periods. This is significantly more than the duration of the oscillation of the mean flow reported in previous works [21,28]. This is due to the use of a pump to continuously inject fluid at the bottom and remove fluid at the top, which keep the stratification linear even close to the membranes and the injection of waves efficient.

The experimental mean flow at a given height can be well fitted by a sinusoidal fit. This is consistent with the weakly nonlinear approach used in the analytical model and is used to obtain the relative phase and the amplitude of the mean flow as a function of height z. The amplitude profile of the mean flow is qualitatively similar for the experimental, analytical and numerical results. In both cases, the amplitude is non-monotonous. We recover the main characteristics of the mean flow profile: a phase difference of π between the top and the bottom, consistent with the usual qualitative description of the QBO [1]. The variation of the amplitude of the mean flow with height is not monotonic, displaying a local minimum in theory, simulations and experiments.

We have shown a set of values of the period of the mean flow as a function of the forcing. The experiments and the simulations are in good qualitative agreement and show that this period decreases when the amplitude of the forcing increases.

We also discuss in detail one of the main result of [29]: the bifurcation is always a Hopf one: when a mean flow is generated, it is always oscillating at a finite frequency, but the transition can be subcritical (sudden, possible hysteresis) or supercritical (continuous). The experimental results for the bifurcation are in agreement with the analytical results, and we have been able to find two different configurations for which the bifurcation is subcritical (small value of N, NaCl) or supercritical (large value of N, $MgCl_2$).

One of the perspective for the analog experiments is to study the effect of the ratio of the dissipation length to the height of water, and to force the membrane with two frequencies. The goal is to reproduce experimentally the numerical results of [42] about the robustness of the periodic behavior of the QBO.

Another perspective for the analog experiments is to investigate a less regular forcing. It is surely feasible to use a similar set-up with membrane, and apply an irregular forcing, or at least use only a fraction of the motors. Obtaining a QBO without membrane is very difficult and has not been achieved yet. No oscillation has been observed in numerical simulations of the experiments for random forcing in the case of perfectly smooth membrane [27]. Even with a very careful optimisation of the forcing and of the stratification it is not clear that such an experiment will work.

The geophysics perspective is the use of the tools of nonlinear physics, in particular bifurcation theory, for the QBO in GCM (general circulation model). Theses tools are becoming (again) very popular in atmospheric science to study the effects of climate change, and the bifurcations are one of the types of the so-called "tipping points" [43–45]. The QBO is expected to decrease in amplitude due to climate change [7]. The experiments have shown that the bifurcation can be subcritical or supercritical, depending mainly on the effective dissipation form of the mean flow. A first question in GCM will be to identify the dissipation of the main flow, which is neither molecular viscosity nor friction on the wall like in the experiment, but probably involves turbulence and maybe the coupling of the velocity field with other fields. An even more relevant question that can be addressed using GCM is the nature of the bifurcation: will the QBO disappear, and if yes continuously or suddenly? A first approach would be to plot the amplitude and period as a function of the CO_2 concentration or the wave forcing and search for the variations of the mean flow close to the onset of instability.

Appendix A. Fabrication of the seeding beads

To make the seeding beads, we use the following ingredients:

- *Paraffin wax:* We used paraffin wax with a solidification point at $52-54\,^{\circ}C$, supplier VWR, reference 26157.291
- Aluminum oxide (alumina) 3 μm powder. Supplier Lam Plan reference A003 P105K
- *Hand washing liquid:* We use Green Lime Hand Washing Liquid 500 ml from the brand "Arbre Vert"

It is very probably not necessary to use exactly the same ingredients to obtain beads, we just mention the ones that we use. We are not even sure that the hand washing liquid is necessary.

The protocol that we use is given below.

We mix 31 g of paraffin, 6 g of alumina and one droplet of washing-up liquid in a borosilicate glass beaker with a teflon stirring bar. Due to the size of alumina particles, we use a FFP2 mask for safety.

The beaker should be placed in a boiling water bath ("bain-marie") and stirred. To do this, we put a crystallizing dish with water on a magnetic hotplate stirrer. The beaker with wax was placed inside the water, close enough to the surface of the hotplate so that the bar can stir the mixture.

When the wax is liquid, we poured the mixture in a plastic weighing boat to cool it down. It is possible to use a spoon to take the alumina which remains at the bottom of the beaker.

Then we let the alumina particles sediment. We started to stir again when the wax is very viscous but not yet solid.

When the wax is cold but still malleable by hand, we made a sphere with the mixture. We waited then one night so that the mixture is hard.

Then we used a chopper to make the particles (Moulinette Mini Chopper from the brand Moulinex).

It is important to stop after a few seconds (5-20) to avoid any melting of the wax.

The last step is to sieve the particles. The amount of beads around 1 mm is about $5-10$ g.

Appendix B. Linear and weakly nonlinear solution

Equations (4) and (5) are investigated analytically close to the threshold in the following.

We will determine the linear threshold, the eigenmodes and where the bifurcation is super-critical or sub-critical in the parameter space.

This will be achieved using a weakly non-linear expansion up to the third order in the amplitude of the mean flow u.

At this order, the operator $-\partial D/\partial z$ writes (see equation (5)) :

$$-\frac{\partial D}{\partial z} = F(Lu + \Phi(u)) \tag{24}$$

where L is the linear operator:

$$Lu = -\frac{\partial}{\partial z}\left(\exp(-z)\ell(u)\right) = \frac{\partial}{\partial z}\left(2(2\alpha_1 + 4\alpha_2)\exp(-z)\int_0^z u\,\mathrm{d}z\right) \tag{25}$$

$\ell(u)$ is defined by

$$\ell(u) = -2(2\alpha_1 + 4\alpha_2)\int_0^z u\,\mathrm{d}z' \tag{26}$$

Φ is the non-linear operator.

$$\Phi(u) = -\frac{\partial}{\partial z}\left(\exp(-z)\xi(u)\right) \tag{27}$$

and $\xi(u)$ is given by

$$\begin{aligned}\xi(u) = &-2(4\alpha_1 + 20\alpha_2)\int_0^z u^3\,\mathrm{d}z' \\ &+ 2(2\alpha_1 + 4\alpha_2)(3\alpha_1 + 10\alpha_2)\left(\int_0^z u\,\mathrm{d}z'\right)\left(\int_0^z u^2\,\mathrm{d}z'\right) - \frac{1}{3}(2\alpha_1 + 4\alpha_2)^3\left(\int_0^z u\,\mathrm{d}z'\right)^3\end{aligned} \tag{28}$$

B.1. *Linear order*

At linear order, the model (4) reduces to:

$$\frac{\partial u}{\partial t} = F\frac{\partial}{\partial z}\left(2(2\alpha_1 + 4\alpha_2)\exp(-z)\int_0^z u\,\mathrm{d}z\right) + \Lambda_1\frac{\partial^2 u}{\partial z^2} - \Lambda_2 u \tag{29}$$

We introduce the variable ψ like in [20]:

$$\psi = \int_0^z u\,\mathrm{d}z \tag{30}$$

Then (29) becomes:

$$\frac{\partial^2\psi}{\partial t\partial z} = F\frac{\partial}{\partial z}\left(2(2\alpha_1 + 4\alpha_2)\exp(-z)\psi\right) + \Lambda_1\frac{\partial^3\psi}{\partial z^3} - \Lambda_2\frac{\partial\psi}{\partial z} \tag{31}$$

Using the linearity of the equations, we use complex variables, so that the solution is the real part of the corresponding complex variable. To simplify the notations, we use the same variable for the complex and real variables. We are considering eigenmodes of (31) so that:

$$\frac{\partial\psi}{\partial t} = \mu\psi \tag{32}$$

$\mu \in \mathbb{C}$. At the threshold, the real part of the growth rate vanishes and thus $\mu \in i\mathbb{R}$.

We then integrate (31):

$$\mu\psi = F \times 2(2\alpha_1 + 4\alpha_2)\exp(-z)\psi + \Lambda_1\frac{\partial^2\psi}{\partial z^2} - \Lambda_2\psi + K_1 \tag{33}$$

where K_1 is an unknown complex number. This equation can be rewritten:

$$\frac{\partial^2\psi}{\partial z^2} + (a\exp(-z) - b)\psi = K, \tag{34}$$

with:

$$a = \frac{F \times 2(2\alpha_1 + 4\alpha_2)}{\Lambda_1}, \tag{35}$$

$$b = \frac{\mu + \Lambda_2}{\Lambda_1}, \tag{36}$$

and K is unknown.

We first solve the homogeneous equation:

$$\frac{\partial^2 \psi}{\partial z^2} + (a\exp(-z) - b)\psi = 0. \tag{37}$$

The solutions are:

$$\psi = J\left(\pm 2\sqrt{b}, 2\sqrt{a}\exp(-z/2)\right), \tag{38}$$

where J is the Bessel function of the first kind, of order $\pm 2\sqrt{b}$ and of argument $2\sqrt{a}\exp(-z/2)$.

The function $J(-2\sqrt{b}, 2\sqrt{a}\exp(-z/2))$ does not have a finite limit when $z \to +\infty$, and we disregard this solution due to the boundary condition (see equation (7)).

The solution of (37) is thus:

$$\psi_0 = J\left(2\sqrt{b}, 2\sqrt{a}\exp(-z/2)\right), \tag{39}$$

up to a multiplicative constant, which is irrelevant for the linear problem.

We then solve (34), and we search a particular solution using the method of the variation of parameter:

$$\psi(z) = f_1(z)\psi_0(z). \tag{40}$$

Using equation (34) and that ψ_0 is solution of the homogeneous equation, we obtain:

$$2\frac{\mathrm{d}f_1}{\mathrm{d}z}\frac{\mathrm{d}\psi_0}{\mathrm{d}z} + f_1\frac{\mathrm{d}^2\psi_0}{\mathrm{d}z^2} = K. \tag{41}$$

We multiply the previous equation by ψ_0:

$$\frac{\mathrm{d}}{\mathrm{d}z}\left(\psi_0^2\frac{\mathrm{d}f_1}{\mathrm{d}z}\right) = K\psi_0, \tag{42}$$

which gives:

$$\psi_0^2\frac{\mathrm{d}f_1}{\mathrm{d}z} = \int_{+\infty}^{z} K\psi_0(z')\,\mathrm{d}z', \tag{43}$$

assuming that f_1, $\frac{\mathrm{d}f_1}{\mathrm{d}z}$ vanish when $z \to +\infty$ and using that ψ_0 vanishes when $z \to +\infty$.

We write $f_1 = Kf$, so that we have:

$$f(z) = \int_{z_0}^{z} \frac{\mathrm{d}z' \int_{+\infty}^{z'} \psi_0(z'')\,\mathrm{d}z''}{\left(\psi_0(z')\right)^2}, \tag{44}$$

where z_0 is an arbitrary positive constant ; the final solution does not depend on the value chosen for z_0.

So the solution of (34) is thus:

$$\psi(z) = \psi_0(z)\left(1 + Kf(z)\right), \tag{45}$$

where ψ_0 is given by (39) and f by (44).

We can also write the solution for u:

$$u = \frac{\partial}{\partial z}\left(\psi_0(z)\left(1 + Kf(z)\right)\right), \tag{46}$$

Using (7), (30), we have the following boundary conditions:

$$\psi(0) = 0, \tag{47}$$

$$\frac{\mathrm{d}\psi}{\mathrm{d}z}(0) = 0, \tag{48}$$

$$\frac{\mathrm{d}\psi}{\mathrm{d}z}(+\infty) = 0, \tag{49}$$

Using (47) in (45) gives:

$$0 = \psi_0(0)(1 + Kf(0)). \tag{50}$$

So that:

$$K = \frac{-1}{f(0)} = \frac{-1}{\int_{z_0}^{0} \frac{\int_{+\infty}^{z} \psi_0(z')\,\mathrm{d}z'}{(\psi_0(z))^2}\,\mathrm{d}z}. \tag{51}$$

Using (48) in (45) gives:

$$0 = \psi_0'(0)\left(1 + Kf(0)\right) + \psi_0(0)\left(Kf'(0)\right) = \psi_0(0)\left(Kf'(0)\right). \tag{52}$$

We thus have $f'(0) = 0$, i.e.:

$$\int_0^{+\infty} \psi_0(z)\,\mathrm{d}z = 0 \tag{53}$$

i.e.:

$$\int_0^{+\infty} J\left(2\sqrt{b}, 2\sqrt{a}\exp(-z/2)\right)\mathrm{d}z = 0 \tag{54}$$

This equation allows us to compute the threshold of the instability.

Using the new variable

$$v = \exp(-z/2), \tag{55}$$

equation (54) gives:

$$\int_0^1 \frac{J\left(2\sqrt{b}, 2\sqrt{a}v\right)}{v}\,\mathrm{d}v = 0. \tag{56}$$

Using the following property of Bessel functions:

$$\frac{2\alpha}{y} J(\alpha, y) = J(\alpha - 1, y) + J(\alpha + 1, y), \tag{57}$$

we finally obtain equation (17).

B.2. *Non-linear order*

Using equation (24), equation (4) is considered up to the third order in the amplitude of u:

$$\frac{\partial u}{\partial t} = F(Lu + \Phi(u)) + \Lambda_1 \frac{\partial^2 u}{\partial z^2} - \Lambda_2 u \tag{58}$$

More precisely, we note

$$F = F_0 + \varepsilon F_1 \tag{59}$$

where F_0 is the value at the instability threshold (Λ_1 and Λ_2 being fixed) and ε a small parameter (dimensionless distance to the threshold).

We introduce a slow timescale $T = \varepsilon t$ which correspond to the slow variation of the amplitude of the oscillation. Using the multiple scale expansion, $\frac{\partial u}{\partial t}$ should be replaced by :

$$\frac{\partial u}{\partial t} + \frac{\partial u}{\partial T}\frac{\partial T}{\partial t} = \frac{\partial u}{\partial t} + \varepsilon \frac{\partial u}{\partial T} \tag{60}$$

We choose the expansion for u:

$$u = \sqrt{\varepsilon}\left(u_0 + \varepsilon u_1 + \varepsilon^2 u_2 + \ldots\right) \tag{61}$$

At order $\varepsilon^{1/2}$, equation (58) gives:

$$\frac{\partial u_0}{\partial t} = F_0 L u_0 + \Lambda_1 \frac{\partial^2 u_0}{\partial z^2} - \Lambda_2 u_0 \tag{62}$$

This is the linear order (see equation (29)), which has already been solved. The solution is proportional to

$$u = \frac{\partial \psi}{\partial z} \tag{63}$$

where ψ is given by equations (45), (51), (44), and (39).

We write u_0 as a product of the eigenmode of the linear problem u with a slowly varying amplitude:

$$u_0(t,T,z) = \frac{1}{2}\left(A(T)u(t,z) + A^*(T)u^*(t,z)\right), \tag{64}$$

where u is given by equation (63)

At order $\varepsilon^{3/2}$, equation (58) gives:

$$\frac{\partial u_1}{\partial t} + \frac{\partial u_0}{\partial T} = F_0 L u_1 + F_1 L u_0 + \Phi(u_0) + \Lambda_1 \frac{\partial^2 u_1}{\partial z^2} - \Lambda_2 u_1 \tag{65}$$

which can be rewritten:

$$\underbrace{\frac{\partial u_1}{\partial t} - F_0 L u_1 - \Lambda_1 \frac{\partial^2 u_1}{\partial z^2} + \Lambda_2 u_1}_{\mathscr{L} u_1} = \underbrace{-\frac{\partial u_0}{\partial T} + F_1 L u_0 + \Phi(u_0)}_{\mathscr{H} u_0} \tag{66}$$

The next step is to calculate the adjoint operator of $\mathscr{L}$. We introduce the (hermitian) scalar product:

$$\langle a|b\rangle = \lim_{T\to+\infty} \frac{2}{T}\int_{-T}^{T}\int_{0}^{+\infty} a^* b \,\mathrm{d}t\,\mathrm{d}z' \tag{67}$$

where a^* is the complex conjugate of a.

The fields verify the following properties: they do not diverge when $t \to \pm\infty$ and they vanish when $x = 0$ or $+\infty$.

After integration by parts we obtain for the adjoint operator:

$$\mathscr{L}^\dagger c = +\frac{\partial c}{\partial t} + F_0 \times 2\,(2\alpha_1 + 4\alpha_2)\int_0^z \exp(-z')\frac{\partial c}{\partial z}\,\mathrm{d}z' + \Lambda_1 \frac{\partial^2 c}{\partial z^2} - \Lambda_2 c \tag{68}$$

We now search a vector q in the kernel of $\mathscr{L}^\dagger$:

$$\mathscr{L}^\dagger q = 0 \tag{69}$$

We thus have:

$$\frac{\partial}{\partial z}\left(\mathscr{L}^\dagger q\right) = 0 \tag{70}$$

We define φ by:

$$\varphi = \frac{\partial q}{\partial z} \tag{71}$$

We search modes proportional to $\exp(\kappa t)$ so that

$$\frac{\partial \varphi}{\partial t} = \kappa \varphi \tag{72}$$

We thus obtain:

$$\frac{\partial^2 \varphi}{\partial z^2} + \left(a\exp(-z) - B\right)\varphi = 0 \tag{73}$$

with:

$$\begin{aligned} a &= \frac{F_0 \times 2\,(2\alpha_1 + 4\alpha_2)}{\Lambda_1} \\ B &= \frac{-\kappa + \Lambda_2}{\Lambda_1} \end{aligned} \tag{74}$$

This equation is nearly identical to the one solved for the direct problem (equation (34)). We thus have:

$$\varphi = J\left(2\sqrt{B}, 2\sqrt{a}\exp(-z/2)\right) \tag{75}$$

so that we have finally obtained an expression of an element of the kernel of the adjoint of the linear operator:

$$q = \int_0^z J\left(2\sqrt{B}, 2\sqrt{a}\exp\left(-z'/2\right)\right) \mathrm{d}z' \tag{76}$$

From equation (66), the solvability condition then writes:

$$\langle q \,|\, \mathscr{L} u_1 \rangle = \left\langle q \left| -\frac{\partial u_0}{\partial T} + F_1 L u_0 + \Phi(u_0) \right. \right\rangle = 0 \tag{77}$$

Using the expression of u_0, see eq. (64), we obtain the amplitude equation:

$$\frac{\partial A}{\partial T} = A F_1 \frac{\langle q \,|\, Lu \rangle}{\langle q \,|\, u \rangle} + |A|^2 A \frac{\left\langle q \left| \Phi\left(\frac{1}{2}\left(u(t,z) + u^*(t,z)\right)\right) \right.\right\rangle}{\langle q \,|\, u \rangle}, \tag{78}$$

from which we obtain the expression of the coefficients α and β as defined in Eq. (21):

$$\alpha = \frac{\langle q \,|\, Lu \rangle}{\langle q \,|\, u \rangle}, \tag{79}$$

$$\beta = \frac{\left\langle q \left| \Phi\left(\frac{1}{2}\left(u(t,z) + u^*(t,z)\right)\right) \right.\right\rangle}{\langle q \,|\, u \rangle}. \tag{80}$$

The different coefficients are given by

$$\begin{aligned} \langle q \,|\, u \rangle &= \int_0^{+\infty} \left(\int_0^z J\left(2\sqrt{B}, 2\sqrt{a}\exp\left(-z'/2\right)\right) \mathrm{d}z' \right)^* \left(\frac{1}{2} \frac{\partial \psi}{\partial z} \right) \mathrm{d}z, \\ &= -\frac{1}{2} \int_0^{+\infty} J\left(2\sqrt{B}, 2\sqrt{a}\exp\left(-z'/2\right)\right)^* \psi \, \mathrm{d}z. \end{aligned} \tag{81}$$

where ψ is given by eq (45), and

$$\begin{aligned} \frac{1}{2(2\alpha_1 + 4\alpha_2)} \langle q \,|\, Lu \rangle &= \int_0^{+\infty} \left(\int_0^z J\left(2\sqrt{B}, 2\sqrt{a}\exp\left(-z'/2\right)\right) \mathrm{d}z' \right)^* \left(\frac{1}{2} \frac{\partial}{\partial z} \left(\exp(-z)\psi(z)\right) \right) \mathrm{d}z \\ &= -\frac{1}{2} \int_0^{+\infty} J\left(2\sqrt{B}, 2\sqrt{a}\exp\left(-z'/2\right)\right)^* \exp(-z)\psi \, \mathrm{d}z \end{aligned} \tag{82}$$

and for the non-linear term by

$$\left\langle q \left| \Phi\left(\frac{1}{2}\left(u(t,z) + u^*(t,z)\right)\right) \right.\right\rangle = \left\langle q \left| \frac{\partial}{\partial} \left(\exp(-z)\xi(u)\right) \right.\right\rangle = Q_1 + Q_2 + Q_3, \tag{83}$$

with:

$$Q_1 = 2(4\alpha_1 + 20\alpha_2) \int_0^{+\infty} \mathrm{d}z J\left(2\sqrt{B}, 2\sqrt{a}\exp(-z/2)\right)^* \exp(-z) \int_0^z \frac{3}{8} \left|u(z')\right|^2 u(z') \, \mathrm{d}z',$$

$$\begin{aligned} Q_2 = -2(2\alpha_1 + 4\alpha_2)(3\alpha_1 + 10\alpha_2) \int_0^{+\infty} \mathrm{d}z J\left(2\sqrt{B}, 2\sqrt{a}\exp(-z/2)\right)^* \exp(-z) \\ \frac{1}{8}\left(\left(\int_0^z u(z')^* \, \mathrm{d}z' \right) \left(\int_0^z u(z')^2 \, \mathrm{d}z' \right) + 2 \left(\int_0^z u(z') \, \mathrm{d}z' \right) \left(\int_0^z |u(z')|^2 \, \mathrm{d}z' \right) \right), \end{aligned}$$

$$Q_3 = \frac{1}{3}(2\alpha_1 + 4\alpha_2)^3 \int_0^{+\infty} \mathrm{d}z J\left(2\sqrt{B}, 2\sqrt{a}\exp(-z/2)\right)^* \exp(-z) \frac{3}{8} |\psi(z)|^2 \psi(z).$$

Acknowledgements

We gratefully acknowledge J. da Silva Quintas, C. Goncalves, E. Nicolau, C. Herrmann, and L. Bonnet for their technical support. We thank our collaborators S. Fauve, N. Garroum and G. Facchini for discussions and with whom [29] or [35] were written.

Declaration of interests

The authors do not work for, advise, own shares in, or receive funds from any organization that could benefit from this article, and have declared no affiliations other than their research organizations.

References

[1] M. P. Baldwin, L. J. Gray, T. J. Dunkerton, et al., "The quasi-biennial oscillation", *Rev. Geophys.* **39** (2001), pp. 179–229.

[2] T. Fouchet, S. Guerlet, D. F. Strobel, A. A. Simon-Miller, B. Bézard and F. M. Flasar, "An equatorial oscillation in Saturn's middle atmosphere", *Nature* **453** (2008), pp. 200–202.

[3] X. Li and P. L. Read, "A mechanistic model of the quasi-quadrennial oscillation in Jupiter's stratosphere", *Planet. Space Sci.* **48** (2000), no. 7-8, pp. 637–669.

[4] A. P. Showman, X. Tan and X. Zhang, "Atmospheric Circulation of Brown Dwarfs and Jupiter- and Saturn-like Planets: Zonal Jets, Long-term Variability, and QBO-type Oscillations", *Astrophys. J.* **883** (2019), no. 1, article no. 4.

[5] E.-J. Kim and K. B. MacGregor, "Gravity Wave-driven Flows in the Solar Tachocline", *Astrophys. J.* **556** (2001), no. 2, pp. L117–L120.

[6] C. Pinçon, K. Belkacem and M.-J. Goupil, "Implications of the generation of internal gravity waves by penetrative convection for the internal rotation evolution of low-mass stars", *EPJ Web Conf.* **160** (2017), article no. 02002.

[7] J. A. Anstey, S. M. Osprey, J. Alexander, et al., "Impacts, processes and projections of the quasi-biennial oscillation", *Nat. Rev. Earth Environ.* **3** (2022), no. 9, pp. 588–603.

[8] Y. Wang, J. Rao, Y. Lu, Z. Ju, J. Yang and J. Luo, "A revisit and comparison of the quasi-biennial oscillation (QBO) disruption events in 2015/16 and 2019/20", *Atmos. Res.* **294** (2023), article no. 106970.

[9] N. Butchart, "The stratosphere: a review of the dynamics and variability", *Weather Clim. Dynam.* **3** (2022), no. 4, pp. 1237–1272.

[10] C. C. Collimore, D. W. Martin, M. H. Hitchman, A. Huesmann and D. E. Waliser, "On The Relationship between the QBO and Tropical Deep Convection", *J. Climate* **16** (2003), no. 15, pp. 2552–2568.

[11] K. P. Bowman, "Global Patterns of the Quasi-biennial Oscillation in Total Ozone", *J. Atmos. Sci.* **46** (1989), no. 21, pp. 3328–3343.

[12] A. G. Marshall and A. A. Scaife, "Impact of the QBO on surface winter climate", *J. Geophys. Res.* **114** (2009), article no. D18110.

[13] Z. Martin, S.-W. Son, A. Butler, H. Hendon, H. Kim, A. Sobel, S. Yoden and C. Zhang, "The influence of the quasi-biennial oscillation on the Madden–Julian oscillation", *Nat. Rev. Earth Environ.* **2** (2021), no. 7, pp. 477–489.

[14] L. L. Hood and C. A. Hoopes, "Arctic Sea Ice Loss, Long-Term Trends in Extratropical Wave Forcing, and the Observed Strengthening of the QBO-MJO Connection", *J. Geophys. Res. Atmos.* **128** (2023), no. 24, article no. e2023JD039501.

[15] M. Takahashi, "Simulation of the Quasi-Biennial Oscillation in a general circulation model", *Geophys. Res. Lett.* **26** (1999), no. 9, pp. 1307–1310.

[16] N. Butchart, J. A. Anstey, K. Hamilton, et al., "Overview of experiment design and comparison of models participating in phase 1 of the SPARC Quasi-Biennial Oscillation initiative (QBOi)", *Geosci. Model Dev.* **11** (2018), no. 3, pp. 1009–1032.

[17] F. Lott and L. Guez, "A stochastic parameterization of the gravity waves due to convection and its impact on the equatorial stratosphere", *J. Geophys. Res. Atmos.* **118** (2013), pp. 8897–8909.

[18] U. Achatz, M. J. Alexander, E. Becker, et al., "Atmospheric Gravity Waves: Processes and Parameterization", *J. Atmos. Sci.* **81** (2024), no. 2, pp. 237–262.

[19] R. S. Lindzen and J. R. Holton, "A theory of the Quasi-biennial Oscillation", *J. Atmos. Sci.* **25** (1968), pp. 1095–1107.

[20] R. A. Plumb, "The interaction of two internal waves with the mean flow: implications for the theory of the quasi-biennial oscillations", *J. Atmos. Sci.* **34** (1977), pp. 1847–1858.

[21] R. A. Plumb and A. D. McEwan, "The instability of a Forced Standing Wave in a Viscous Stratified Fluid : A Laboratory Analogue of the Quasi-Biennial Oscillation", *J. Atmos. Sci.* **35** (1978), pp. 1827–1839.

[22] A. Renaud, L.-P. Nadeau and A. Venaille, "Periodicity Disruption of a Model Quasibiennial Oscillation of Equatorial Winds", *Phys. Rev. Lett.* **122** (2019), no. 21, article no. 214504.

[23] A. Renaud and A. Venaille, "On the Holton—Lindzen—Plumb model for mean flow reversals in stratified fluids", *Q. J. R. Meteorol. Soc.* **146** (2020), no. 732, pp. 2981–2997.

[24] P. Léard, D. Lecoanet and M. Le Bars, "Multimodal Excitation to Model the Quasibiennial Oscillation", *Phys. Rev. Lett.* **125** (2020), no. 23, article no. 234501.

[25] L.-A. Couston, D. Lecoanet, B. Favier and M. Le Bars, "Order Out of Chaos: Slowly Reversing Mean Flows Emerge from Turbulently Generated Internal Waves", *Phys. Rev. Lett.* **120** (2018), no. 24, article no. 244505.

[26] H.-H. Bui, E. Nishimoto and S. Yoden, "Downward Influence of QBO-Like Oscillation on Moist Convection in a Two-Dimensional Minimal Model Framework", *J. Atmos. Sci.* **74** (2017), no. 11, pp. 3635–3655.

[27] N. P. Wedi and P. K. Smolarkiewicz, "Direct numerical simulations of the Plumb-McEwan laboratory analog of the QBO", *J. Atmos. Sci.* **63** (2006), pp. 3226–3252.

[28] N. Otobe, S. Sakai, S. Yoden and M. Shiotani, "Visualization and WKB analysis of the internal gravity wave in the QBO experiment", *Nagare multimedia* **17** (1998). *preprint*, https://www2.nagare.or.jp/mm/98/otobe/index.htm.

[29] B. Semin, N. Garroum, F. Pétrélis and S. Fauve, "Nonlinear saturation of the large scale flow in a laboratory model of the quasibiennial oscillation", *Phys. Rev. Lett.* **121** (2018), no. 13, article no. 134502.

[30] P. Léard, B. Favier, P. Le Gal and M. Le Bars, "Coupled convection and internal gravity waves excited in water around its density maximum at 4C", *Phys. Rev. Fluids* **5** (2020), article no. 024801.

[31] M. Le Bars, L.-A. Couston, B. Favier, P. Léard, D. Lecoanet and P. Le Gal, "Fluid dynamics of a mixed convective/stably stratified system—A review of some recent works", *Comptes Rendus. Physique* **21** (2020), no. 2, pp. 151–164.

[32] P. Léard, L. Margaillan, T. Raymond, M. Rouby and M. Le Bars, "Large-scale flow driven by turbulently generated internal gravity waves", *Phys. Rev. Fluids* **6** (2021), no. 8, article no. 084801.

[33] B. King, H. P. Zhang and H. L. Swinney, "Tidal flow over three-dimensional topography in a stratified fluid", *Phys. Fluids* **21** (2009), article no. 116601.

[34] G. Bordes, A. Venaille, S. Joubaud, P. Odier and T. Dauxois, "Experimental observation of a strong mean flow induced by internal gravity waves", *Phys. Fluids* **24** (2012), article no. 086602.

[35] B. Semin, G. Facchini, F. Pétrélis and S. Fauve, "Generation of a mean flow by an internal wave", *Phys. Fluids* **28** (2016), article no. 096601.

[36] H. Ben-Gida, R. Gurka and A. Liberzon, "OpenPIV-MATLAB – An open-source software for particle image velocimetry; test case: Birds' aerodynamics", *SoftwareX* **12** (2020), article no. 100585.

[37] H. Cai, *Bessel Function of Complex Order and Argument*. MATLAB Central File Exchange, accessed: 2024-02-26, https://math.stackexchange.com/questions/585240/bessel-function-with-complex-argument.

[38] S. Yoden and J. Holton, "A new look at equatorial quasi-biennial oscillation Models", *J. Atmos. Sci.* **45** (1988), pp. 2703–2717.

[39] T. Dauxois, S. Joubaud, P. Odier and A. Venaille, "Instabilities of Internal Gravity Wave Beams", *Ann. Rev. Fluid Mech.* **50** (2018), no. 1, pp. 131–156.

[40] R. Godoy-Diana, J.-M. Chomaz and C. Donnadieu, "Internal gravity waves in a dipolar wind: a wave–vortex interaction experiment in a stratified fluid", *J. Fluid Mech.* **548** (2006), pp. 281–308.

[41] K. Hamilton, "Dynamics of the Tropical Middle Atmosphere: A Tutorial Review", *Atmosphere-Ocean* **36** (1998), no. 4, pp. 319–354.

[42] X. Chartrand, L.-P. Nadeau and A. Venaille, "Recovering Quasi-Biennial Oscillations from Chaos", *J. Atmos. Sci.* **81** (2024), pp. 1213–1224.

[43] S. Bathiany, M. Scheffer, E. H. Van Nes, M. S. Williamson and T. M. Lenton, "Abrupt climate change in an oscillating world", *Sci. Rep.* **8** (2018), no. 1, article no. 5040.

[44] N. Wunderling, A. von der Heydt, Y. Aksenov, et al., "Climate tipping point interactions and cascades: A review", *Earth Syst. Dyn.* **15** (2024), pp. 41–74.

[45] Intergovernmental Panel on Climate Change (IPCC), *Climate Change 2021 – The Physical Science Basis: Working Group I Contribution to the Sixth Assessment Report of the Intergovernmental Panel on Climate Change*, Cambridge University Press, 2023.

ACADÉMIE DES SCIENCES
INSTITUT DE FRANCE

Comptes Rendus. Physique
2024, Vol. 25, Special issue S3, p. 583-610
https://doi.org/10.5802/crphys.204

Review article / *Article de synthèse*

Geophysical and astrophysical fluid dynamics in the laboratory / *Dynamique des fluides géophysiques et astrophysiques au laboratoire*

Laboratory modeling of MHD accretion disks

Modèles expérimentaux des disques d'accrétion MHD

Christophe Gissinger [a]

[a] LPENS, Ecole Normale Superieure, Paris, France. IUF
E-mail: gissinger@ens.fr (C. Gissinger)

Abstract. This review article summarizes two decades of laboratory research aimed at understanding the dynamics of accretion disks, with particular emphasis on magnetohydrodynamic experiments involving liquid metals and plasmas. First, the Taylor–Couette experiments demonstrated the generation of magnetorotational instability (MRI) in liquid metals, and highlighted how this instability is critically influenced by boundary conditions and the geometry of the applied magnetic field. These experiments also highlight the nonlinear transition to turbulence in accretion disks, and their link with other MHD instabilities in centrifugally-stable flows. A complementary approach, involving laboratory experiments with volumetric fluid driving rather than rotating boundaries, enables a quantitative study of angular momentum transport by Keplerian turbulence. Collectively, these various laboratory studies offer new constraints on the theoretical models designed to explain the dynamics of accretion disks. This is particularly true with regard to the role of Keplerian turbulence in protoplanetary disks, where recent observations from the ALMA telescope have considerably revised previously expected values of the magnitude of the turbulent fluctuations. Finally, the paper discusses outstanding questions and future prospects in laboratory modeling of accretion disks.

Résumé. Cet article de revue résume deux décennies de recherche en laboratoire visant à comprendre la dynamique des disques astrophysiques, en mettant particulièrement l'accent sur les expériences magnétohydrodynamiques impliquant des métaux liquides et des plasmas. Tout d'abord, les expériences de Taylor–Couette ont démontré la génération de l'instabilité magnétorotationnelle (MRI) dans les métaux liquides, et ont mis en évidence la façon dont cette instabilité est influencée de manière critique par les conditions aux limites et la géométrie du champ magnétique appliqué. Ces expériences permettent également de mieux comprendre la transition non linéaire vers la turbulence dans les disques d'accrétion et leur lien avec d'autres instabilités dans les écoulements centrifuges stables. Une approche complémentaire, impliquant des expériences de laboratoire avec un entraînement volumique du fluide plutôt qu'avec un dispositif en rotation, permet une étude quantitative du transport du moment cinétique par la turbulence Képlèrienne. Collectivement, ces diverses études de laboratoire offrent de nouvelles contraintes sur les modèles théoriques visant à expliquer la dynamique des disques d'accrétion. Ceci est particulièrement vrai en ce qui concerne le rôle de la turbulence Képlèrienne dans les disques proto-planétaires, dont les récentes observations du télescope ALMA ont considérablement révisé les valeurs précédemment attendues pour l'amplitude des fluctuations turbulentes. Enfin, l'article aborde les questions en suspens et les perspectives futures dans la modélisation en laboratoire des disques d'accrétion.

Keywords. Accretion disks, magnetohydrodynamics (MHD), instabilities, turbulence, rotating flow, MRI.

Mots-clés. Disques d'accrétion, magnétohydrodynamique (MHD), instabilités, turbulence, écoulements, MRI.

Funding. ANR "JCJC" grant no. ANR 19-CE30-0025-01 and Institut Universitaire de France.
Manuscript received 17 April 2024, revised 29 August 2024, accepted 4 September 2024.

1. Introduction

Astrophysical disks are present in a myriad of cosmic systems, from protoplanetary disks surrounding young stars (the most common) to accretion disks surrounding compact celestial bodies such as white dwarfs, neutron stars and black holes [1–3]. These structures are formed by the gravitational collapse of rotating clouds of gas and dust. In binary star systems, for example, accretion disks form when a star captures material from its companion, creating a rapidly rotating gaseous disk. In the most extreme cases, accretion onto black holes fuels the intense luminosity observed in active galactic nuclei and quasars, and can power gamma-ray bursts [4]. Given the diversity of these origins, accretion disks displays a wide range of properties, well beyond the scope of this review. But despite this variety, we will see in this review that astrophysical disks share defining characteristics that allow for their study in a generalized manner within idealized laboratory models. The purpose of these experimental studies, though simplified, is to encapsulate the complex interactions of gravitation, hydrodynamics, and magnetic fields that govern most of the dynamics of accretion disks.

Addressing such complex phenomena undeniably calls for a cross-disciplinary approach, with laboratory experiments playing a pivotal role. Nonlinear dynamics and the role of turbulence in accretion disks are probably among the most important outstanding questions: the process by which turbulence arises and whether fully developed turbulence can account for the substantial amounts of gas and matter typically accreted onto the central object are still unclear. A key component in understanding this process is magnetohydrodynamics (MHD), which describes the behavior of electrically conducting fluids under the influence of magnetic fields, such as the ionized gas of accretion disks. MHD laboratory experiments, by providing large Reynolds numbers, highly nonlinear regimes, and a strong coupling between the flow and the magnetic field, have offered a valuable opportunity to investigate these two questions under conditions relevant to these disks.

In this review, I will first discuss the main constraints derived from observations and theory, as well as the technical limitations that guide the development of laboratory facilities. I will then describe the extent to which MHD experiments conducted over the last two decades have improved our understanding of accretion disks. In particular, we will see how these studies have focused mainly on the primary instabilities of Keplerian disks and their nonlinear characteristics, the mechanisms responsible for turbulence generation, the transport properties of turbulence, angular momentum dynamics and the role of boundary conditions. In the last part, I will discuss some possible perspectives for the next decade in modeling the magnetohydrodynamics of accretion disks.

2. Observational constraints, theoretical considerations, and experimental strategies

Studying accretion disks is challenging due to their vast diversity. Among the simplest are protoplanetary disks, where a dense molecular cloud collapses to form a proto-star surrounded by a protoplanetary disk. In contrast, more exotic configurations include cataclysmic variable stars, a binary pair that involves a white dwarf accreting matter from a companion (usually a classical star), and which exhibits dramatic brightness variations due to limit-cycle instabilities [5]. Active galactic nuclei (AGNs) present another intriguing case, featuring accretion disks surrounded by

moving gas clouds and encircled by a torus of gas and dust, with powerful jets often emerging. Several complex challenges arise in the physics of accretion disks. Radiative transfer within these disks requires a correct understanding of opacity and energy transport to model cooling and illumination accurately [6]. Chemical processes and dust dynamics play a critical role in thermal stability and opacity, and are not yet fully understood. Disk-planet interactions, such as planet migration and gap formation, further complicate disk dynamics and planetary system architecture. Modeling accretion disks in the laboratory therefore presents significant challenges, requiring substantial simplifications, compromises, and unavoidable choices in the specific physics processes to be investigated. Many characteristics of astrophysical disks cannot be directly replicated in laboratory setups, which are then guided by observational data and theoretical constraints. The following subsections discuss these observational and theoretical constraints relevant to the specific laboratory modelling of the astrophysical fluid dynamics of accretion disks.

2.1. *Hydrodynamical models*

As this review focuses on the hydrodynamic aspects of accretion disks, it is essential to first address how these disks are modeled using hydrodynamic equations. Accretion disks primarily consist of hydrogen, helium, and trace amounts of heavier elements, with dust contributing only a small fraction of the mass (a few %). Even if the interaction between dust and gas remains significant, initial approximations often concentrate solely on gas dynamics. This single-fluid approach can hinder the investigation of important accretion mechanisms, with the streaming instability being the most well-known example [7]. In a typical protoplanetary disk, the mean free path λ is of the order of a few centimeters, which is much smaller than the typical macroscopic size L of the disk. Consequently, the Knudsen number $Kn = \lambda/L$ is extremely small, indicating that the continuum mechanics described by the Navier–Stokes equations are generally applicable for modeling disk dynamics. The specific hydrodynamic approximation used can vary depending on the type of disk. For example, in accretion disks around white dwarfs, compressibility effects and supersonic shocks are significant and must be considered [8]. Conversely, in some protoplanetary disks, such effects may be negligible. Regarding magnetohydrodynamics, the ionization state of the disk varies with distance from the central object. The innermost regions or outer parts of the disk are often highly ionized and dominated by plasma, while cosmic rays and stellar X-rays, which ionize only the surface layers, create a non-ionized central region known as the "dead zone" [9]. This review emphasizes MHD aspects of accretion disks but acknowledges that cold disks or dead zones in classical disks would require consideration of non-MHD dynamics.

2.2. *Disk Geometry and Keplerian rotation*

A first crucial observation concerns the geometry of accretion disks: whether they are spiral galaxies, protoplanetary disks imaged by the Atacama Large Millimeter Array (ALMA) [10] or disks around compact objects, all observations show that accretion disks take the form of relatively thin disks of gas and dust orbiting rapidly around the central object. This a clear consequence of the force balance. Contrary to a star in which the gravitational pull is in balance with tremendous radial pressure forces, the gravitation in a accretion disk, mainly due to the mass of the central object, is rather supported by the centrifugal force, resulting in the formation of a disk-like structure. Balancing this centrifugal force U_φ^2/r with the gravitational pull GM/r^2 immediately leads to the velocity profile of an accretion disk, $\Omega \sim r^{-3/2}$, where cylindrical coordinates are used here and $\Omega(r) = rU_\varphi$ is the angular rotation of the fluid. This balance is especially accurate for dust, while the pressure gradient produces a slightly sub-Keplerian velocity profile in the gas, a

small correction which is often neglected. However, any rotation profile in which the specific angular momentum $r^2\Omega$ increases outward – as it does in Keplerian disks – is known to be stable against Rayleigh's centrifugal instability (Rayleigh, 1917 [11]). This stability poses a significant challenge in identifying a plausible process that could destabilize a Keplerian disk and eventually induce turbulence.

As we will see, reproducing a thin-disk geometry and a Keplerian rotation in the lab is a challenge and is rarely achieved, but it is essential to capture at least the role of the centrifugal force and the main stability properties of this rotation profile. For this reason, most experiments reviewed here are Taylor–Couette devices, consisting of two concentric cylinders that rotate independently and are bounded vertically by two endcaps (rotating or not). For infinitely tall cylinders, the background flow between these cylinders follows the well known Couette profile:

$$\Omega = A + \frac{B}{r^2} \tag{1}$$

where the constants are given by $A = (\Omega_2 r_2^2 - \Omega_1 r_1^2)/(r_2^2 - r_1^2)$ and $B = r_1^2 r_2^2(\Omega_1 - \Omega_2)/(r_2^2 - r_1^2)$ and depends on the rotation rates of the inner and outer cylinders, Ω_1 and Ω_2, respectively, as well as the radii of the inner and outer cylinders, r_1 and r_2. Although achieving a Keplerian rotation rate $\Omega \propto r^{-3/2}$ is not feasible in Taylor–Couette devices, such experiments can still operate under conditions below the Rayleigh stability line. If a centrifugally stable flow ($\Omega_1 r_1^2 < \Omega_2 r_2^2$) is maintained but exhibits an outwardly decreasing angular rotation ($\Omega_1 > \Omega_2$), the flow is termed "quasi-Keplerian". it is believed that quasi-Keplerian flows have characteristics quite similar to keplerian disks, particularly with regard to the stability to magnetohydrodynamic instabilities, which are the focus of most MHD experiments.

2.3. *The problem of accretion*

In addition to the azimuthal flow, observations also indicate that Keplerian disks experience significant accretion, meaning there is a substantial radial influx of gas and matter towards the central object. Naturally, such radial accretion is always expected in a gas, because of the presence of angular momentum dissipation due to the molecular viscosity of the gas. The main issue – and one of the most fascinating aspects of accretion disks – is that accretion rates are generally extremely large, corresponding to a tremendous transport which is virtually impossible to explain with viscous dissipation alone. According to median values known from observations, a typical protoplanetary disk of size $L \sim 10$ Astronomical Units (1 A.U. $\sim$ 150 millions kilometers) accretes matter at an astonishing rate of $\dot{M} \sim 10^{-8} M_\odot.\mathrm{yr}^{-1}$. But with a mean free path of $\lambda \sim 10$ cm and a thermal velocity $V_T \sim 10^3 \mathrm{m}.s^{-1}$, the typical molecular viscosity of such a disk can be estimated to $\nu \sim 10^2 \mathrm{m}^2.\mathrm{s}^{-1}$, leading to the accretion timescale $t_\nu \sim 10^{15}$ yr. This timescale, vastly longer than the lifetime of a protostellar accretion disk, implies that almost no accretion would occur in a disk governed solely by molecular viscosity. To explain the observed accretion rates, an additional mechanism, such as instabilities or turbulence, must be invoked. A very useful approach was proposed by Shakura and Sunyaev in 1973 [12], where molecular viscosity is conveniently replaced by an effective viscosity induced by small scale turbulent fluctuations:

$$\nu_t = \alpha_{SS} \frac{c_s^2}{\Omega} \tag{2}$$

where c_s is the isothermal sound speed, and $\alpha_{SS} < 1$ is an adjustable dimensionless parameter, whose precise value depends on the specific mechanism driving the turbulence. As stated above, centrifugal instability is not possible for Rayleigh-stable Keplerian disks, and finding a credible explanation for generating turbulence and large values of α_{SS} in disks has been a central focus of vigorous theoretical investigation over the past few decades.

From an experimental perspective, replicating the strong gravitational field that drives the inward accretion in astrophysical disks is a very complex and challenging task. This might initially seem like a discouraging argument against laboratory experiments. However, fortunately, the conservation of angular momentum dictates that the inward spiraling of matter corresponds to a global outward transfer of angular momentum within the disk: as material moves closer to the central object, it transfers some of its angular momentum to the outer parts of the disk. With appropriately designed rotating experiments (typically Taylor–Couette devices) and precise flow measurements, this flux of angular momentum can be accurately reproduced and studied in laboratory setups, without any need for gravitational infall. We will see that in some cases, some aspects of the gravity field can even be replaced by a similar effect, such as electrostatic [13] or magnetic forces [14,15].

2.4. *Turbulence and angular momentum transport*

In recent years, the advent of state-of-the-art telescopes, such as the Atacama Large Millimeter/submillimeter Array (ALMA) has revealed astonishing substructures in protoplanetary disks and largely reshaped our understanding of turbulence in astrophysical disks [10]. For instance, it is now believed [16] that the α_{SS} parameter could be substantially lower than earlier predictions, implying that the expected level of turbulent viscosity might be reduced by several orders of magnitude. This calls into question the relevance of several earlier theories concerning the origin of turbulence and its ability to produce efficient angular momentum transport, such as the MRI discussed in Section 3.2.

Indeed, the theoretical landscape is complex: first, one must identify a sufficiently robust mechanism capable of triggering instability within a centrifugally stable Keplerian flow. Second, the nonlinear development of this instability must lead to turbulence under conditions that are sufficiently universal to accommodate the diversity of observed accretion disks and match constraints of these recent observations. Finally, this turbulent state must align with the observed accretion rates – a theoretical challenge, as the angular momentum transport in rotating flows may depends critically on the type of turbulence generated.

A variety of theories have been proposed in this perspective. Notable among these are several compelling mechanisms, including gravitational instability [17], baroclinic instabilities [18], vertical shear instability [19], to name a few.

Magnetic fields offer another interesting possibility for generating turbulence, but require an electrically conducting plasma. Observations consistently show significant ionization across most accretion disks, albeit localized to specific regions excluding the dead zones previously discussed. This favors theories on powerful but local MHD mechanisms stemming from the interplay between magnetic fields and fluid dynamics in some restricted areas of disks (inner and/or outer parts).

Reproducing these MHD effects in experiments requires careful consideration of several key dimensionless numbers. Besides the conventional Reynolds number $Re = UL/\nu$ (where U and L are respectively the typical azimuthal velocity and size of the disk, and ν is the molecular viscosity), MHD effects are gauged by the magnetic Reynolds number $R_m = UL/\eta$, where $\eta = 1/(\mu_0\sigma)$ is the magnetic diffusivity, μ_0 the vacuum magnetic permeability and σ the electrical conductivity. This magnetic Reynolds number simply compares induction effects to the magnetic diffusion. The magnetic Prandtl number $P_m = R_m/Re = \nu/\eta$ compares the two diffusivities. In accretion disks, both Reynolds numbers are typically very high, except in regions with weak ionization where induction is negligible and R_m becomes small. To model MHD effects in laboratory experiments, there are essentially three possible types of fluid : plasmas, liquid metals, or electrolytes. The low electrical conductivity of most electrolytes makes them a less favorable

Table 1. Physical properties and typical dimensionless numbers for the liquid metal experiments used in modeling astrophysical disks.

	Princeton	Promise	Maryland	Kepler
Kinematic viscosity ν $[m^2.s^{-1}]$	$3,7\times10^{-7}$	$3,7\times10^{-7}$	$7,3\times10^{-7}$	$3,7\times10^{-7}$
Electrical conductivity σ $[\mathrm{S.m^{-1}}]$	$3,3\times10^{6}$	$3,3\times10^{6}$	10^{7}	$3,3\times10^{6}$
Density ρ $[\mathrm{kg.m^{-3}}]$	$6,4\times10^{3}$	$6,4\times10^{3}$	$0,93\times10^{3}$	$6,4\times10^{3}$
Maximum flow velocities U $[\mathrm{m.s^{-1}}]$	15	2×10^{-2}	20	2
Applied magnetic field B_0 [mT]	500	10	200	100
Typical radius L [m]	0,1	6×10^{-2}	0,1	0,1
Reynolds number $Re = UL/\nu$	4×10^{6}	3000	3×10^{6}	5×10^{5}
Magnetic Reynolds number $Rm = \mu_0\sigma UL$	6	5×10^{-3}	20	0.8
Lundquist number $S = \mu_0\sigma B_0 L/\sqrt{\mu_0\rho}$	2,3	$2,8\times10^{-2}$	8	0.5

choice, as they only allow for small magnetic Reynolds numbers ($R_m < 1$). Given the technical challenges associated with driving a rotating plasma, most MHD experiments have opted for liquid metals, typically liquid gallium or one of its alloys, due to the feasibility of the experiments and usability of liquid gallium at room temperature. Table 1 summarizes the physical properties and typical dimensionless numbers for the liquid metal laboratory experiments described in the present article. But in liquid metals, achieving large R_m requires large power. For instance, reaching $R_m > 10$ in a 20 cm experiment using liquid gallium ($\sigma \sim 3\times10^6\mathrm{S.m^{-1}}$) requires large rotation speeds, typically in the range $30-50$ Hz, translating to hundreds of kW in power given the large density of gallium ($\rho \sim 6100\mathrm{kg.m^{-3}}$). In addition, because $P_m \sim 10^{-5}$ in liquid metals, large R_m can only be achieved in extremely turbulent flows. Plasma experiments might offer alternatives at much higher P_m, but they introduce their own technical challenges such as plasma confinement, high temperatures, and measurement difficulties, as detailed in Section 5.2.

A certain diversity in experimental setups is therefore crucial for addressing the complex problem of accretion disks, as will be shown throughout this review. In the next sections, I will focus on various experimental studies aimed at understanding the magnetohydrodynamics within accretion disks. Given that laboratory experiments can realistically achieve fully turbulent flows and provide accurate long-term statistical data, recent observational breakthroughs have highlighted the critical importance of experimental modeling of accretion disks.

3. Laboratory studies

3.1. *Stability of Keplerian flows*

The linear stability of Keplerian rotation with respect to the centrifugal instability is a strong argument for seeking alternative mechanisms for destabilizing a disk. It should be noted, however, that Rayleigh's criterion only provides a criterion for linear stability. At the considerable Reynolds numbers reached in accretion disks, it is quite conceivable that linearly stable accretion disks could be subject to a nonlinear transition to turbulence (Lesur, 2005 [20]). This question was investigated by several experimental teams in the early 2010s [21–23] that reported the presence of turbulent fluctuations even in the quasi-Keplerian stable regime.

Naturally, it is very tempting to interpret these results as a consequence of boundary effects. Indeed, the viscous friction at the top and bottom endcaps in finite-sized Taylor–Couette devices

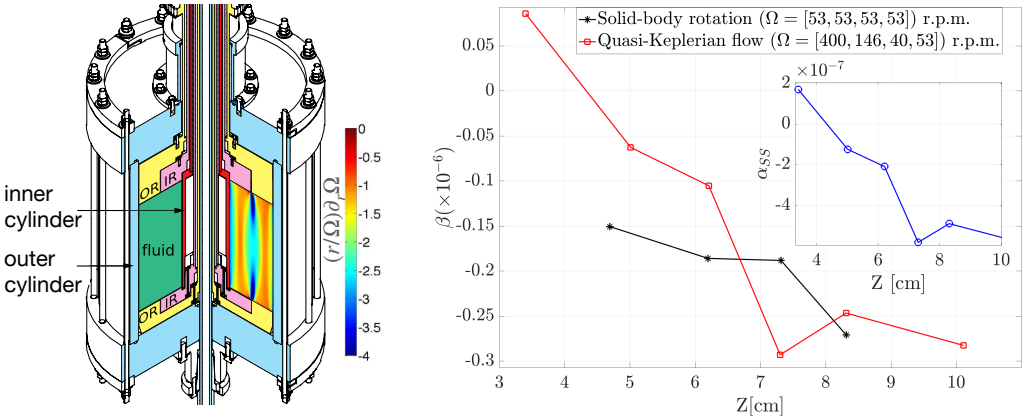


Figure 1. Left: Experimental setup used in (Ji et al., 2006 [25]). A rotating fluid (water or a water/glycerol mixture) is confined between two concentric cylinders with a height of 27.86 cm and radii of 7.06 cm and 20.30 cm, which rotate at rates Ω_1 and Ω_2. Each endcap is divided into two independently driven rings with angular velocity Ω_3 (inner rings) and Ω_4 (outer rings). For appropriate rotations, the secondary circulation is minimized, and ideal Couette profiles are obtained. Right: dimensionless turbulent viscosity $\beta = \overline{u'_\varphi u'_r}/(r^2\partial\overline{\Omega}/\partial r)^2$ measured from velocity fluctuations, for solid-body rotation and quasi-Keplerian flows, showing no sign of transition to turbulence, even at large Re [adapted from [25, Figure 3]]. The inset shows the corresponding value of α_{SS} computed for the quasi-Keplerian regime.

produces secondary recirculations associated with a strong transport of angular momentum. The velocity profile can deviate from Couette's ideal solution and become unstable, even in the absence of a magnetic field [24]. Figure 1 shows the setup developed at Princeton University to address this issue. The Princeton experiment is a Taylor–Couette device in which the space between two co-axial cylinders is filled with either water or a liquid metal. The two differentially rotating cylinders are confined in the axial direction by two endcaps which, in conventional Taylor–Couette experiments, rotate simultaneously with the inner or the outer cylinder and can drive undesired circulation, as mentioned above. In the Princeton experiment, this issue is solved by dividing each axial endcap into two rings whose rotations can be controlled independently, thus leading to 4 different rotational speeds: the speed of the inner cylinder Ω_1, that of the outer cylinder Ω_2, of the inner rings (upper and lower) Ω_3 and of the outer rings Ω_4. The rotation of the rings can be judiciously chosen to reduce the influence of the system's axial boundaries and get closer to Couette's ideal solution for infinite cylinders. It was shown in [25,26] that this approach enables hydrodynamically stable flow to be achieved in this geometry at very high Reynolds numbers ($Re > 10^6$). Naturally, this experiment does not definitively eliminate the possibility of a subcritical transition to turbulence in Keplerian flows. However, it demonstrates that Rayleigh-stable Taylor–Couette flows tend to remain stable even at extremely high Reynolds numbers, strongly suggesting the need to identify a more powerful instability to explain the occurrence of turbulence in linearly stable flows.

3.2. *Magnetohydrodynamics and MRI instability*

One of the best explanations for the transition to turbulence in such stable flows is to consider the magnetic field. In this case, the traditional framework of hydrodynamics must be replaced

by magnetohydrodynamics [27], accounting for the behavior of the disk's ionized gas, which now acts as an electrically conducting medium. In its simplest form, addressing a dense, incompressible, and homogeneous plasma, the governing equations of MHD are:

$$\rho\left(\partial_t \boldsymbol{u} + (\boldsymbol{u}.\boldsymbol{\nabla})\,\boldsymbol{u}\right) = -\boldsymbol{\nabla} p + \rho\nu\boldsymbol{\nabla}^2\boldsymbol{u} + \boldsymbol{j}\times\boldsymbol{B} \tag{3}$$

$$\partial_t \boldsymbol{B} = \boldsymbol{\nabla}\times(\boldsymbol{u}\times\boldsymbol{B}) + \frac{1}{\mu_0\sigma}\boldsymbol{\nabla}^2\boldsymbol{B} \tag{4}$$

where $\boldsymbol{u}$, $\boldsymbol{B}$ and $\boldsymbol{j} = \boldsymbol{\nabla}\times\boldsymbol{B}/\mu_0$ are respectively the velocity, the magnetic field and the electrical current of the fluid, and μ_0 the vacuum magnetic permeability. The first equation is the classical Navier–Stokes equation including a Lorentz force which describes the action of the magnetic field on the fluid. For simplicity in this discussion, we assume incompressibility, as most laboratory experiments are conducted at extremely low Mach numbers. However, as mentioned in the introduction and briefly discussed in the conclusion, compressibility effects are expected to play a significant role in some accretion disks. The second equation is called the induction equation and simply corresponds to a combination of Maxwell's equations and the Ohm's law. It describes how the evolution of the magnetic field results from the interplay between induction processes and magnetic diffusion.

A first naive explanation to the accretion of astrophysical disks is that the presence of a magnetic field will produce a torque on the plasma, that can efficiently transport angular momentum. Perhaps the first laboratory experiment aligning with this idea was proposed by [28], in a Taylor–Couette experiment filled with mercury. It was shown, in agreement with theoretical predictions, that when applied to a rotating flow in a centrifugally unstable regime, a magnetic field sharply increases the onset of centrifugal instability, actually stabilizing the flow. This stabilizing role of the magnetic field, known since the work of Chandrasekhar [29], probably explains the lack of interest for MHD processes in accretion disks.

At least, this was the case until 1991, when a more subtle mechanism was proposed by Balbus and Hawley [30], in which the magnetic field can instead destabilize a centrifugally-stable flow. This is the magnetorotational instability (MRI), which has since become the paradigm for explaining the transition to turbulence in accretion disks. The basic mechanism was initially discovered by Velikhov (1959) [31] and Chandrasekhar (1960) [32] for Taylor–Couette geometries in a non-astrophysical context, and was later rediscovered as a powerful source of turbulence within accretion disks. The underlying process is elegantly straightforward : the Lorentz force exerted on the fluid divides into two components, $\boldsymbol{j}\times\boldsymbol{B} = (\boldsymbol{\nabla}B^2 + (\boldsymbol{B}.\boldsymbol{\nabla})\boldsymbol{B})/\mu_0$, with the latter often referred to as magnetic tension. This tension acts like an invisible spring, providing a force that binds fluid elements within the disk together. Analogous to how a spring connecting two masses can facilitate the transfer of angular momentum, the magnetic tension generated by the Lorentz force can similarly induce instability in a conducting fluid. This concept is illustrated in Figure 2. This spring-mass analogy for MRI was also reproduced in a clever laboratory experiment that validated many features of the MRI, providing a clear understanding of the physical mechanism behind this MHD instability [33].

An important point of the theory is that the instability criterion is remarkably simple and easy to satisfy: any rotation profile where the rotation rate Ω decreases with increasing distance - as observed in Keplerian disks - will be prone to MRI, even for a weak magnetic field.

It has been shown that this mechanism not only produces a powerful linear destabilization of centrifugally-stable flows, but also that its nonlinear development easily leads to a fully turbulent flow [34]. For example, applied to astrophysical conditions, MRI can lead to $\alpha_{SS} \sim [10^{-2} - 10^{-1}]$, a value large enough to easily explain the highest accretion rates observed [34]. Given these

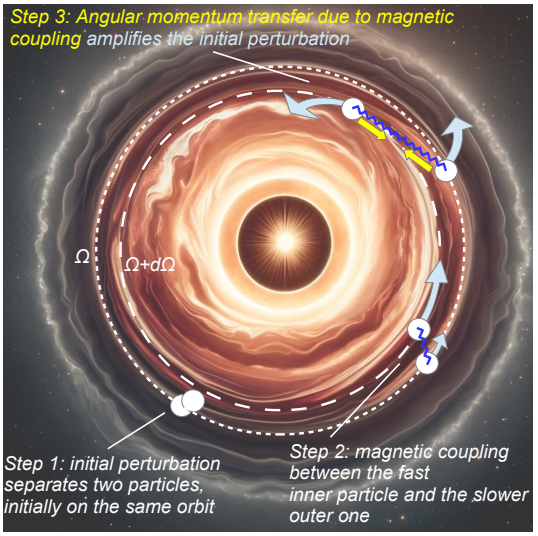


Figure 2. Simple sketch of the mechanism for MRI, using the spring model. An initial disturbance separates two fluid particles, initially in the same orbit. The inner particle ends up on a faster orbit as the velocity decreases outwards in a Keplerian flow. The presence of the magnetic field acts like a spring connecting the particles, slowing down the inner particle and accelerating the outer one. This net transfer of angular momentum causes the inner particle to fall a little further inwards, while the other gains angular momentum and moves outwards. The initial disturbance is thus amplified, yielding the flow instability.

considerations, the detection of MRI in large-Re laboratory experiments emerged as an essential undertaking, almost as important as its theoretical demonstration.

In 2001, Goodman and Ji therefore proposed a strategy to detect MRI in a laboratory experiment [35,36],which led to the experimental setup described in Figure 1. In order to trigger MRI, the device is filled with Galinstan, a room-temperature liquid alloy of gallium, tin, and indium, and subjected to a vertical magnetic field generated by external Helmholtz coils [37]. The experiment can then be operated under quasi-Keplerian rotation, i.e., a flow that is Rayleigh-stable yet potentially MRI-unstable, closely mimicking the dynamics of actual Keplerian disks. Instability within the flow can be detected through various measurements: magnetic perturbations via Hall probes and velocity profiles using ultrasound Doppler velocimetry for instance.

This approach proved to be very challenging, as the onset for MRI is difficult to reach in liquid metals. To understand what controls this onset, one can linearize MHD equations around a magnetized Couette solution, and look for infinitesimal perturbations of the form $\exp(\gamma t - ik_z z - ik_r r)$, leading to the classical dispersion relation [35] for the growth rate γ:

$$\left[(\gamma+P_m)(\gamma+1)+S^2\right]^2\left(1+\varepsilon^2\right)+2\zeta R_m^2(\gamma+1)^2-2(2-\zeta)R_m^2S^2=0 \tag{5}$$

where $\zeta = 2+\partial\ln\Omega/\partial\ln r$ characterizes the flow's vorticity and the Rayleigh stability criterion (Rayleigh-stable flows for $\zeta \geq 0$), R_m is the magnetic Reynolds number, $\varepsilon = k_r/k_z$, P_m the magnetic Prandtl number and $S = BL/(\mu_0\rho\eta)$ the Lundquist number, a dimensionless measure of the magnetic field. Although highly simplified, this local approach nevertheless captures the essence of the linear aspects of the MRI instability, as shown by the numerical integration of dispersion relation (5) in Figure 3. As R_m increases from zero (where rotation effects are negligible and only damped Alfvén waves exist due to magnetic tension), the Alfven solutions split into Magneto–Coriolis (MC) waves (or magneto-inertial waves). These are termed "slow" and "fast"

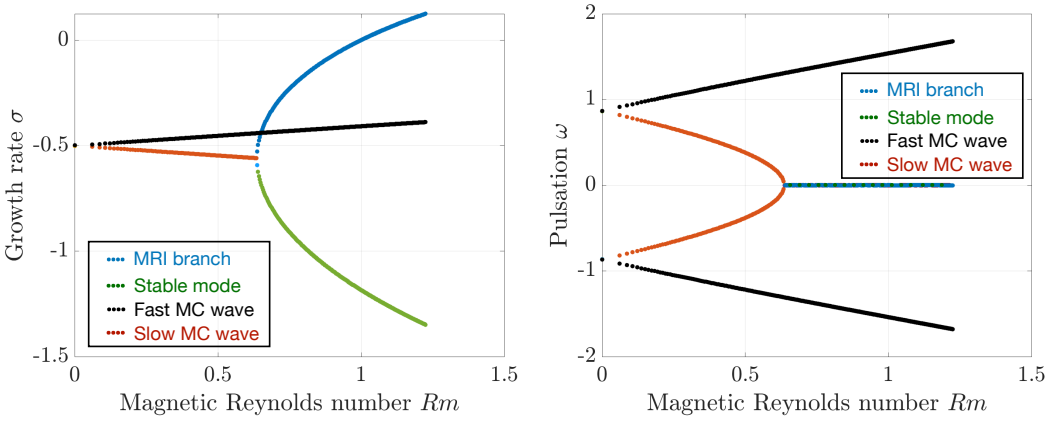


Figure 3. Numerical integration of the dispersion relation (5) showing on the left the real part (growth rate) and on the right the imaginary part (pulsation) of the roots of the equation, as a function of R_m, for $\varepsilon = 1$, $S = 1$, $\zeta = 0.5$ and $Pm = 10^{-5}$. At small R_m, only damped magneto-coriolis waves are present (red and black curves). But there is a critical value of R_m for which the two slow MC waves coalesce, producing two real eigenvalues from two complex conjugates (blue and green curves). At $Rm = 1$ (for the parameter used here), one of these purely real eigenvalues (the blue one) becomes positive, corresponding to the emergence of MRI.

based on their frequencies and are due to the combined action of magnetic tension and Coriolis force. At a critical R_m, complex conjugate slow MC waves merge and form two real eigenvalues (a so-called exceptional point [38]). One of these two branches eventually becomes unstable at high R_m: this is the MRI instability, which in this framework, can be simply regarded as a destabilization of magneto-Coriolis waves! This unstable branch also traces back to centrifugal instability if followed into the non-magnetized, Rayleigh-unstable regime.

It is noteworthy that Nornberg et al., 2001 [37] reported the first observation of slow magneto-rotational (MC) waves in a Taylor–Couette apparatus designed to detect the magnetorotational instability. The identification of such a precursor to MRI significantly enhances our understanding of how MRI can emerge in laboratory setups.

3.3. *Helical MagnetoRotational Instability and the PROMISE experiment*

In fact, the difficulty of observing MRI in laboratories mainly arises from the high magnetic Reynolds number required, because standard MRI (hereafter called SMRI) necessitates a robust induction process. This led to the clever concept of Helical MRI (HMRI) [39], where the azimuthal magnetic field, typically induced by diffential rotation at large R_m in SMRI, is now directly applied as part of the experimental setup. In theory, this approach allows for the observation of MRI at much lower rotation rate and magnetic field strengths compared to Standard MRI (SMRI), because this by-passes the requirement of very large rotation rate to induce an azimuthal field.

The first experimental evidence for HMRI was obtained in 2006 at the PROMISE (Potsdam ROssendorf Magnetic InStability Experiment) facility by F. Stefani and collaborators [41]. The setup is essentially identical to the Princeton experiment, with the exception of an applied azimuthal field in addition to the traditional vertical field. An interesting destabilization of the otherwise centrifugally-stable flow was reported, taking the form of axisymmetric traveling waves

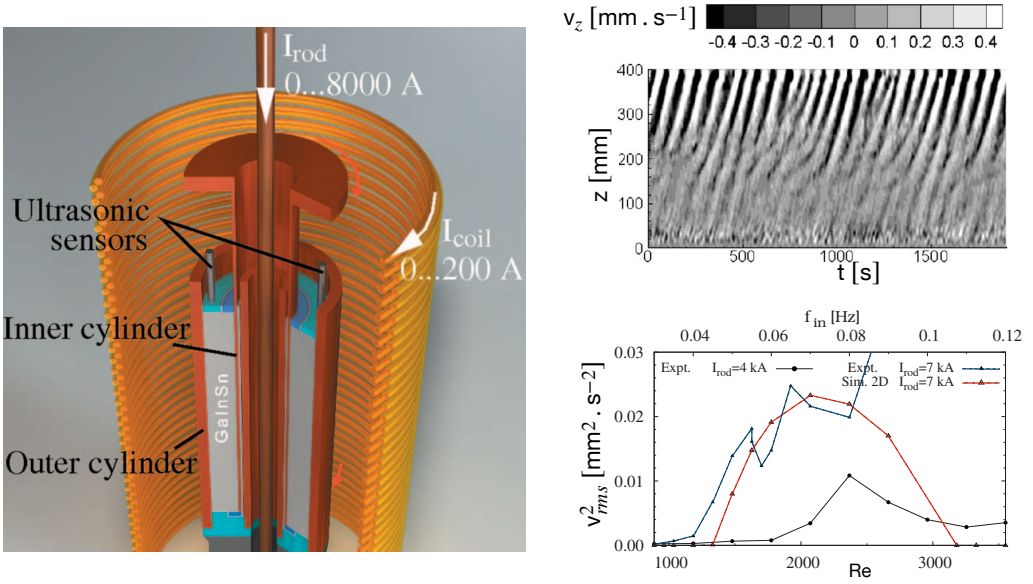


Figure 4. Results obtained in the Promise experiment for the Helical MRI [40]. Left: experimental setup, with a gap width of 40 mm and height 400 mm, showing that the azimuthal field is generated using a very large current passing through a central rod in the inner cylinder. Right, top: spatio-temporal map in the (z,t) plane of the measured axial velocity perturbation v_z obtained from UDV sensors for $Re = 3000$, $\Omega_1/\Omega_2 = 0.27$, $I_{rod} = 7000$ A and $I_{coil} = 76$ A. The HMRI takes the form of axisymmetric travelling waves. Right, bottom: bifurcation diagram of the MRI obtained from measurements of the rms value of $|\mathbf{v}|^2$, displaying an onset close to $Re \sim 1000$ and a good agreement with simulations.

(see Figure 4). HMRI is undoubtedly a new type of magnetorotational instability, but it also fundamentally differs from SMRI: if dispersion relation (5) is modified to incorporate the azimuthal field, it shows that HMRI is a magnetic destabilization of pure inertial waves rather than a destabilization of Magneto–Coriolis waves. Consequently, magnetic induction is almost unimportant [42], a dynamical regime sometimes referred as inductionless: the induction term $u \times B$ does not need to be significantly larger that magnetic diffusion, and the relevant control parameters is now the Reynolds number Re rather than R_m, making the instability onset much easier to reach. Despite this difference, the two instabilities remain connected, as there is a continuous and monotonic transition from HMRI to SMRI when rotation and the magnetic field strength are increased simultaneously [38]. Note that centrifugally-stable Taylor–Couette flows can also undergo a similar instability if the vertical magnetic field is completely suppressed, an instability known as the Azimuthal MRI (AMRI) that was observed a few years later [43] and may play an important role in stellar interiors.

The application of HMRI to real accretion disks is highly debated. Similar to SMRI, HMRI is expected to produce a fully turbulent flow when operating sufficiently far from the linear onset, particularly at very large Reynolds numbers. Its inductionless nature is extremely appealing, because it provides a simple explanation to turbulence in cold, non-conducting regions of disk, where SMRI cannot operate. On the other hand, it is clear from linear calculations that it only works for relatively steep rotation profiles (i.e., slightly above the Rayleigh line) and disappears in the Keplerian regime [44]. However, further studies have shown that HMRI can still be relevant in Keplerian flows if at least one radial boundary is highly conducting [45], a requirement that could

be supported by the fact that hot inner part of the disks could be regarded as such conducting boundaries for the colder outer part of accretion disks [46]. This is one of many examples of a recurrent pattern in the laboratory modeling of accretion disks: much of the physics is influenced by the boundaries of the system, as we will see in the next section.

3.4. *Boundary effects in Taylor–Couette devices*

It is obvious that the no-slip boundary conditions in experimental setups differ significantly from those in real accretion disks, which, due to their vast extent and lack of clear boundaries, are relatively immune to boundary effects. In this section, we will see how this issue with boundary conditions poses a substantial challenge in modeling laboratory disks, but has also led to some interesting discoveries.

The problem of boundary conditions in experimental setups is perfectly illustrated by the role of differentially rotating rings in the Promise and Princeton experiments. This configuration minimizes Ekman recirculation, a necessary condition for efficient detection of the MRI instability. But it was shown in 2012 in the Princeton experiment [47] that this is also the source of a new class of MHD instability, very close to the MRI but based on a different physical mechanism. Figure 5 summarizes the results obtained in [47]: above some critical values of both the magnetic field and the rotation of the cylinders, the flow is destabilized through a supercritical bifurcation of non-axisymmetric modes (azimuthal wavenumbers $m = 1$ and $m = 2$) which produce a net outward transport of angular momentum. These results are therefore identical to those expected in the case of non-axisymmetric MRI instability. The scaling law is however different. Whereas MRI instability is expected at high R_m, flow destabilization in the Princeton experiment occurs systematically for $\Lambda > 1$, where $\Lambda = B^2/(4\pi\rho\eta\Delta\Omega)$ is the Elsasser number, and $\Delta\Omega$ is the difference between the inner- and outer-ring rotation rates. This expression interestingly implies that destabilization is possible at very low R_m.

Direct numerical simulations (Gissinger et al., 2006 [48]) based on this experimental configuration help understanding these confusing results. They show that the difference in velocity between the inner and outer rings generates a flow discontinuity in the middle, which remain localized close to the endcaps as long as the magnetic field is weak. Under a sufficiently strong magnetic field, a Shercliff layer forms, which is distinct from Hartmann layers that are perpendicular to the magnetic field. Classically, Shercliff layers occur near boundaries that are tangential to the magnetic field lines. They result from a local balance between the Lorentz force and viscous friction as the fluid velocity approaches zero. Here however, the Shercliff layer forms due to the velocity discontinuity between the two endcaps' rings, resulting in a free shear layer. Specifically, this layer emerges when magnetic tension stretches the velocity discontinuities into the bulk flow, generating a shear layer characterized by a strong $\partial_r u_\phi$ (see Figure 5, bottom-right). When this free Shercliff layer extends into the bulk, a Kelvin–Helmholtz destabilization of the layer in the azimuthal direction leads to the non-axisymmetric modes reported in the experiment.

Figure 6 illustrates the many similarities between this Shercliff layer instability, and the MRI instability initially sought: in both cases, the instability produces outward transport of angular momentum, requires both a critical magnetic field and a critical rotation rate, and displays a restabilization at high field strength. However, like HMRI, non-axisymmetric Shercliff modes are inductionless, and the relevant dimensionless numbers are different: Rm and S for the MRI, versus Λ and Re for this Shercliff layer instability. As with HMRI, the domain of existence of this instability extends to very small R_m (as long as the hydrodynamic Reynolds number Re is sufficiently large).

3.5. *The Maryland experiment*

Of course, it is highly unlikely that such free shear layers play a role in real astrophysical disks. But it is interesting to note that a simple boundary layer instability can produce most of the diagnostics expected for MRI. In fact, it is believed that this scenario is general enough to be observed in other systems, and could explain results obtained in at least one other experimental setup, quite different from the one describe above.

In 2004, the team of Dan Lathrop at the University of Maryland observed an MHD instability in a Couette flow subjected to an intense magnetic field, but this time in spherical geometry [49].

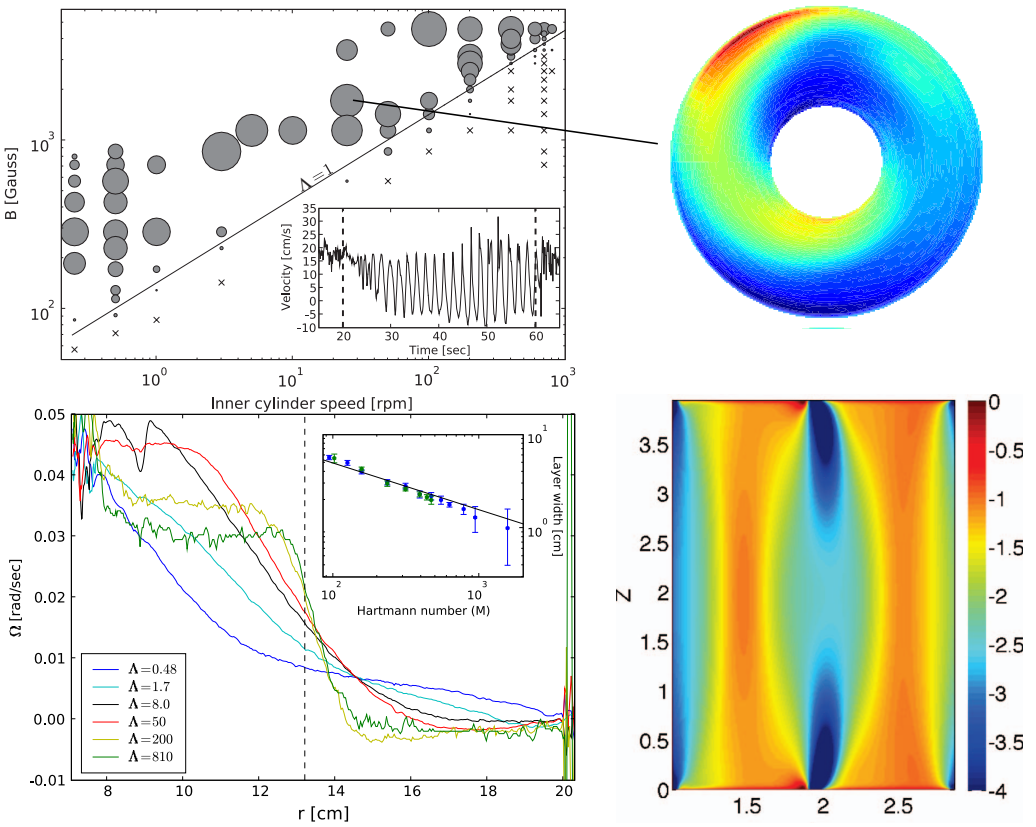


Figure 5. Top-left: Stability diagram obtained in [47] in the (B,Ω_1) plane. The area of the circles is proportional to the power in the dominant Fourier harmonic mode of the instability, while "x"s indicate stability. The line corresponds to $\Lambda = 1$. The inset plot shows a typical time series of the velocity. Top-right: Structure of the unstable mode, reconstructed from Ultrasonic Doppler velocimetry of the azimuthal velocity component (a few cm/s). The spiraling pattern corresponds to an outward transport of angular momentum. Bottom-left: radial profile of the angular rotation $\Omega(r)$ close to the top endcap, for different values of the applied magnetic field (measured by the Elsasser number Λ). The magnetic field tends to homogenize the flow in the vertical z direction. The velocity jump between the two rings at the endcaps extends into the bulk flow, generating a free shear layer at mid-radius. Bottom-right: snapshot of the unstable eigenmode obtained in the simulations reported in [48], showing the shear parameter $q(r,z) = r\partial_r\Omega/\Omega$ in the (r,z) plane and illustrating the Kelvin–Helmholtz destabilization of the Shercliff layer.

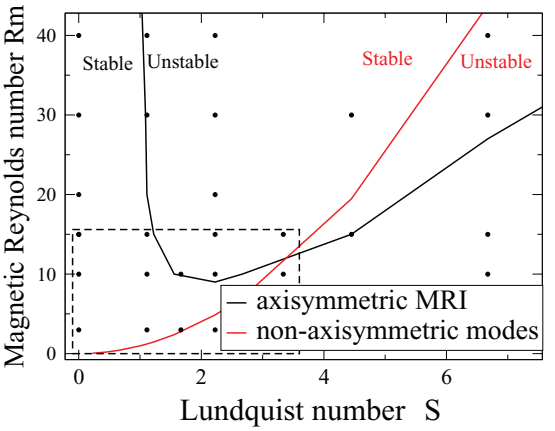


Figure 6. Marginal stability curves in the (R_m, S) plane computed in numerical simulations of magnetized Taylor–Couette setups [48]. The black curve indicates the stability line of the axisymmetric SMRI. The red curve is the marginal stability for non-axisymmetric Kelvin–Helmholtz instability of the free Shercliff shear layer, obtained from 3D simulations (black dots). The dotted square indicates the parameter space accessible to the Princeton experiment.

In this spherical Couette experiment, where the outer sphere is held at rest and an axial external magnetic field is imposed parallel to the axis of rotation, non-axisymmetric oscillations of the induced magnetic field and velocity were observed, on top of a highly turbulent background flow. These oscillations are associated with a marked increase in torque on the inner sphere, a definitive signature of outward angular momentum transport. A this time, these results were interpreted as an observation of the MRI instability. But numerical simulations of the Maryland experiment [50] have clearly called for a different interpretation in terms of an instability of free shear layers, a priori unrelated to MRI. Indeed, a similar Shercliff layer instability has been numerically predicted in magnetized spherical Couette flows similar to the Maryland experiment, showing striking similarities with the experiment (see Figure 7). In this case, instability results from differential rotation between the inner and outer spheres, with the shear layer localized along the tangent cylinder. As in the cylindrical case, the Shercliff layer instability exhibits all the features of MRI, including a considerable increase of angular momentum transport, as shown by the excess torque on the outer sphere. The excellent agreement between these numerical results and those reported by the Maryland group in 2006 [49] led to a reinterpretation of their experiment as a Shercliff layer instability rather than a detection of the magnetorotational instability.

3.6. *Nonlinear aspects of the MRI*

A general statement must be made here, which applies beyond the physics of accretion disks. In most fluid dynamics experiments, experimental constraints often force researchers to use geometries and boundary conditions that do not match the idealized boundaries considered in theoretical models or the actual boundary conditions found in astrophysical and geophysical systems. It is generally well accepted that boundaries will influence the linear properties of the studied instability, such as wavenumber and threshold. However, in many cases, these boundary modifications can also significantly impact the nonlinear dynamics of the system. This section illustrates this aspect with two examples: first, how boundary-driven recirculation can alter the nature of the flow bifurcation; and second, how it affects the mechanism for the saturation of the

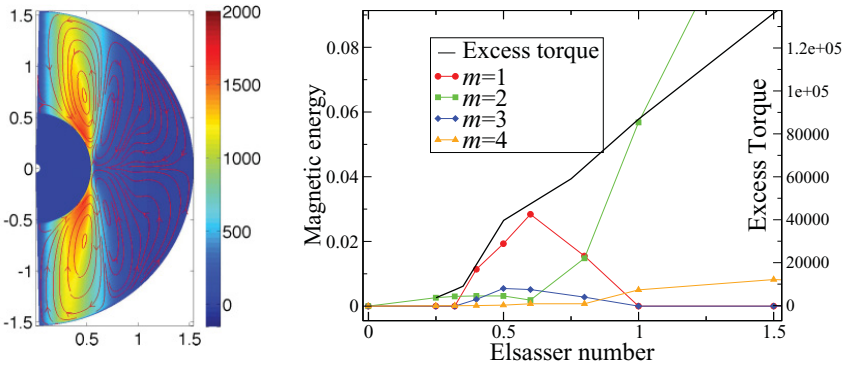


Figure 7. Left: structure of the spherical Couette flow when the outer sphere is at rest in a numerical modeling using the same parameters as in the Maryland experiment [50]. Colors indicate azimuthal flow u_φ displaying a Shercliff layer surrounding the tangent cylinder. Poloidal field lines of the velocity averaged in the azimuthal direction are also shown. Right: bifurcation diagram of the magnetic energy (contained in different azimuthal wavenumbers m) when Λ is increased. A good agreement with the Maryland experiment is obtained, including the generation of an $m = 1$ mode and increase of the torque on the inner sphere (to be compared with [49, Figure 4]).

underlying instability. Both examples highlight the important and sometimes underestimated connection between the nonlinear dynamics of fluid systems and boundary conditions.

Numerical simulations of MRI Taylor–Couette experiments predict that the eigenmode for the MRI consists of two large poloidal recirculation cells (see Figure 8, top-left), associated with an outward jet near the endcaps. It is therefore similar to the usual recirculation pattern generated by the presence of vertical boundaries in rotating Taylor–Couette flows. Under these conditions, how to distinguish MRI from the background flow? The answer is not easy.

To understand the difference, Figure 8-bottom shows the bifurcation diagram of the MRI mode, for two typical simulations: when periodic boundary conditions in the axial direction are used (red curve), a perfect supercritical pitchfork bifurcation is observed. But with cylinders of finite size, there is always a non-zero poloidal recirculation generated by the endcaps, and the bifurcation is modified to a gradual transition, which does not allow to define a clear onset. This imperfect pitchork bifurcation can be modeled [48] by:

$$\dot{A} = \mu A - A^3 + h \tag{6}$$

where h represents a symmetry-breaking parameter reflecting the solution's lack of axial periodicity, and which therefore prohibits the $A \to -A$ symmetry obtained in the case of periodic or infinite cylinders. Figure 8 (top-right) shows a schematic diagram of these two types of bifurcation and provides a number of predictions: Under experimental conditions, MRI emerges continuously from magnetized Ekman recirculation, and angular momentum increases progressively, well below the linear onset. On the other hand, the critical exponent 1/2 typical for supercritical bifurcation is only measurable well above the onset predicted by linear theory. Also, different MRI structures are expected depending on the hydrodynamic background state. For instance, in the Princeton experiment, the rotation of the endcaps determines the direction of rotation of the poloidal background flow, which will select a similar structure for the MRI mode. This change in the experiment's boundary conditions corresponds to the change $h \to -h$ in equation (6), which selects mode $-A$. Finally, in the case of an imperfect bifurcation, the branch that is not connected

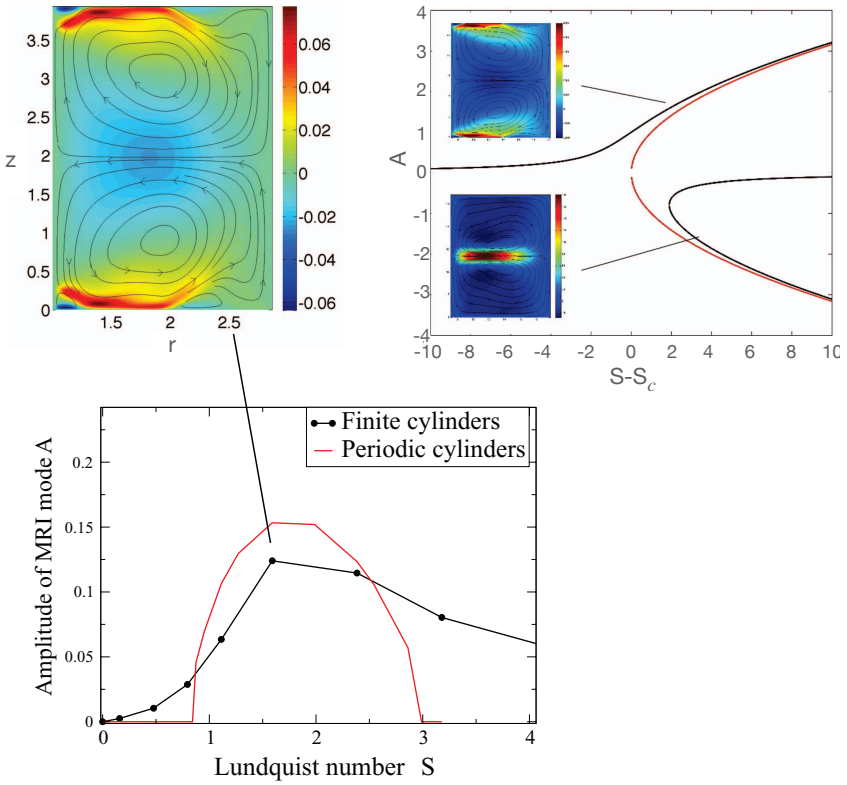


Figure 8. Top-Left: structure of the MRI mode for $R_m = 15$ and $S = 2.3$ in numerical simulations [48] showing the radial velocity u_r in the (r,z) plane and streamlines of the poloidal flow. Bottom: bifurcation diagram of the MRI amplitude as a function of S for $R_m = 15$. Red curve correspond to periodic boundary conditions in z, whereas the black one shows results obtained with no-slip rotating rings at the endcaps. In the latter case, the bifurcation is an imperfect supercritical pitchfork bifurcation due to the poloidal flow. Top-Right: Schematic representation of theoretical perfect (red) and imperfect (black) pitchfork bifurcations $A(S-S_c)$ of the MRI, where S_C is the critical onset for MRI in the perfect case. Each branch corresponds to a different structure of the MRI mode.

to the background state is replaced by a saddle-node bifurcation, which leads to a bistability between two MRI modes with very different structures. This predicts the existence of a subcritical bifurcation towards the MRI, much easier to observe than the continuous transition generally sought [48]. Interestingly, although these nonlinear aspects primarily concern experimental setups, some could also apply to astrophysical disks. Any strong perturbation to the Keplerian background rotation (such as gravitational perturbation from the central object or radial suction [51] for instance) may lead to similar behavior. The existence of a subcritical transition to turbulence triggered by boundary effects is particularly appealing.

A second important nonlinear aspect involves predicting the saturated amplitude of the MRI in experimental setups. Various mechanisms have been proposed for the saturation of the MRI. In the astrophysical context, where the background shear is maintained by the gravitational field and remains unperturbed by turbulent fluctuations, a straightforward scenario suggests that MRI-driven turbulence generates sufficient turbulent dissipation to quench the MRI back to its onset. In laboratory experiments, the simplest explanation is that the instability saturates

by modifying the shear responsible for its occurrence (Knobloch and Julien, 2005 [52]). More precisely, the altered shear profile produced in the bulk by the growing MRI can be balanced by an appropriate radial pressure gradient. In Taylor–Couette flows, this pressure gradient is inherently linked to the meridional recirculation induced by axial boundary conditions, thus depending on both viscous and Ohmic dissipation. Consequently, saturation in laboratory setups is closely tied to boundary effects.

Numerical modeling of magnetized Taylor–Couette flows show that in the linear phase, the growth rate is independent of the Reynolds number, underscoring the relevance of non-viscous linear theory. In contrast, the saturation phase is highly dependent on Re. The saturated amplitude of the magnetic perturbation B follows a scaling law $S \propto Re^{-1/4}$ (where $S = BL/(\mu_0 \rho \eta)$ is the Lundquist number previously introduced) [48], that can be traced back to the weak viscous coupling between the boundaries and the liquid metal: this scaling law can be roughly recovered by dimensional analysis as a balance between Ekman pumping ($\propto Re^{-1/2}$) and the Maxwell stress tensor in the bulk ($\propto B^2$), in agreement with the saturation mechanism proposed by Knobloch and Julien. Although such a scaling law does not directly apply to astrophysical disks, it highlights the challenge of observing MRI in the laboratory, where Re typically reaches several tens of millions at the critical onset. A naive interpolation of this scaling law thus suggests an extremely low saturation amplitude for laboratory MRI. Note that a similar scaling law applies to Helical MRI, but the oscillatory nature of this instability simplifies its detection compared to the stationary standard MRI.

4. Detection of the MRI by the Princeton experiment

Experimental modeling of accretion disks recently took a new turn when the Princeton experiment was updated to take into account some of the remarks made above. This led the group to report convincing evidence of the experimental detection of MRI (Wang et al., 2022 [53]). The primary change involved implementing electrically-conducting segmented endcaps made of copper. One of the motivations was to enhance the coupling between these endcaps and the liquid metal [54] thereby achieving a more powerful driving of the flow. Additionally, it appears that the modification of induced currents in the boundary layers due to the presence of these conducting endcaps alters the adverse pressure gradient. Fortunately, this change affects the scaling law $S \sim Re^{1/4}$ and increases the saturation level discussed in the previous section. This clearly increases the detectability of the standard MRI, particularly through magnetic measurements using Hall probes. But these conducting boundaries also increase the vertical extension of Shercliff layers, which significantly perturb the background flow and magnetic field. Adjustments were therefore made in the detection techniques to account for the imperfect nature of the bifurcation described in [48].

More precisely, a radial field B_r is naturally induced as soon as the vertical magnetic field B_z is applied to the flow. This is represented by the parameter h in equation (6). As expected for this type of induction process due to the residual Ekman circulation, B_r was reported to evolve linearly with Rm. However, beyond a critical onset Rm_c, a nonlinear increase in B_r is observed and interpreted as a signature of the MRI, as predicted by equation (6). The instability thus exhibits all the characteristics of an imperfect pitchfork bifurcation typical of MRI (see Figure 9): it is unstable only beyond a specific magnetic Reynolds number R_m (well above the onset of inductionless instabilities), it transitions gradually from residual Ekman recirculation, and restabilizes if the magnetic field becomes too strong, all while presenting an axisymmetric eigenmode consistent with numerical predictions. Moreover, the experiment confirmed a weak but clear outward transport of angular momentum, attributed to both velocity fluctuations and the magnetic torque induced by the MRI instability, corroborating theoretical expectations of

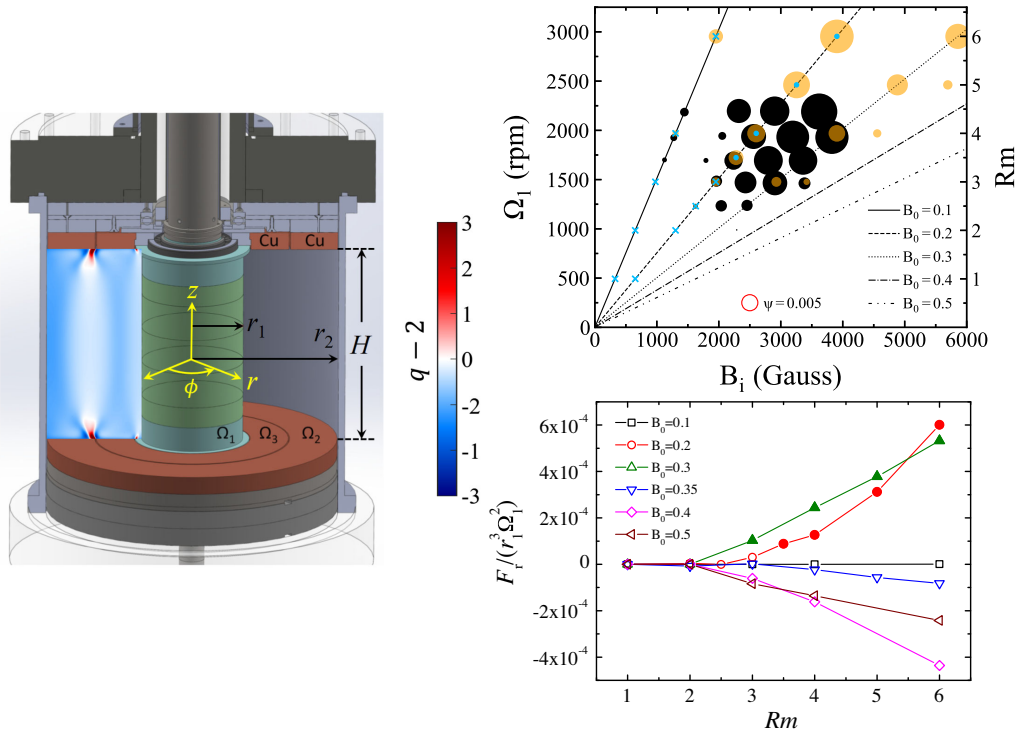


Figure 9. Results obtained with the new version of the Princeton experiment (schematic view given on the left) for the Standard MRI [53]. Top-right: Stability diagram in the (Ω_1, B) plane obtained in [53]. The area of the circles is proportional to the magnitude of the instability and the diagram is in good agreement with the theoretical predictions of an imperfect supercritical bifurcation. Right, bottom: Evolution of the angular momentum flux with R_m, showing a net outward transport of angular momentum above the instability onset.

MRI in accretion disks. It has also been checked that this instability is not related to the Shercliff layer instabilities reported previously.

An unexpected observation is the detection of non-axisymmetric MRI modes alongside the $m = 0$ mode, suggesting a complex interplay of MRI modes with different symmetries [55]. This complexity warrants further investigation, as it may provide insights into how MRI could lead to fully developed turbulence through nonlinear interactions between multiple modes.

5. Beyond Taylor–Couette MRI: angular momentum transport

5.1. *Limitations inherent to Taylor–Couette devices*

The recent success of the Princeton MRI experiment, along with the alternative scenarios proposed by the PROMISE experiment, has significantly advanced our understanding of accretion disks. These developments now provide a viable scenario for Keplerian flows to become unstable and conclusively demonstrate that the magnetorotational instability can be generated in a real system. This represents a substantial progress in unraveling the destabilization of astrophysical disks, a puzzle that has persisted for at least five decades. To draw definitive conclusions,

however, a complementary approach beyond the Taylor–Couette geometry is necessary. Taylor–couette devices present at least three significant limitations for accurately modeling accretion disks:

- Firstly, the velocity profile in these experiments, while quasi-Keplerian, differs from a true Keplerian rotation rate. In other words, the radial stratification of angular momentum is different, leading to turbulent transport properties that can be different from those of accretion disks.
- Secondly, even when quasi-Keplerian flows become unstable to MRI, the resulting turbulence remains very weak. The reason is that it is exceedingly difficult to increase the magnetic Reynolds number beyond the instability threshold, resulting in only minimal angular momentum transport. This necessity of observing Keplerian turbulence in the laboratory is important, especially since recent observations have suggested that the level of turbulence in Keplerian disks may be much smaller than expected before [16].
- Thirdly, and perhaps most critically, Taylor–Couette devices rely on rotating boundaries, which corresponds to a surface injection of angular momentum: it is produced on the rotating vessel walls, then diffuse through the viscous boundary layers located on the cylinders, to finally produce transport in the turbulent bulk. This is a scenario far removed from that of astrophysical disks, which are essentially immune to boundary effects, especially for angular momentum transport.

5.2. *Plasma experiments*

In this perspective, alternative approaches are necessary. One possibility is the use of plasma. An active research effort is currently underway to develop Taylor–Couette equivalents in plasmas, where the flow is instead generated by a series of electrodes injecting currents through the plasma [56,57].

Two experiments of this type are currently being developed at the Wisconsin Plasma Physics Laboratory: the 1-meter-wide cylindrical Plasma Couette Experiment (PCX) and the 3-meter-wide spherical Big Red Ball (BRB). In the PCX experiment, an argon plasma is generated at approximately 10,000 K by a hot lanthanum hexaboride (LaB6) cathode located at the top of the cylindrical axis and collected by cold molybdenum anodes positioned near the outer equatorial edge. A radial current flows through an externally applied vertical magnetic field, creating a torque that drives the plasma in the toroidal direction, producing a Couette velocity profile. While an array of permanent magnets on the boundary helps confine the plasma, the bulk magnetic field remains weak (typically ≤ 10 G). The BRB experiment operates on a similar principle but with reversed electrode positions—the molybdenum anodes are placed at the top axis. The plasma in these experiments operates in a flow regime quite distinct from the classical MHD framework relevant to liquid metals. Here, the ratio β between kinetic and magnetic pressures is large, and plasma dynamics occur on scales smaller than the ion inertial length (≈ 1 m here) but larger than the electron inertial length. At these scales, ions and electrons are decoupled, requiring a two-fluid description. Electrons remain tied to the magnetic field, while the ion fluid decouples from it. This decoupling is accounted for by adding the Hall term to Ohm's law which now becomes:

$$\mathbf{J} = \sigma \left(\mathbf{E} + \mathbf{v} \times B - \frac{1}{n_e e} (\mathbf{J} \times B) \right) \tag{7}$$

where n_e is the electron number density, e is the elementary charge, and the last term is the Hall term. The plasma is therefore described by what is known as the collisionless Hall regime. In [57], it has been shown that a significant amplification of the magnetic field (by a factor of 20) occurs when the electrons flow radially inwards, while an almost total expulsion of the field is

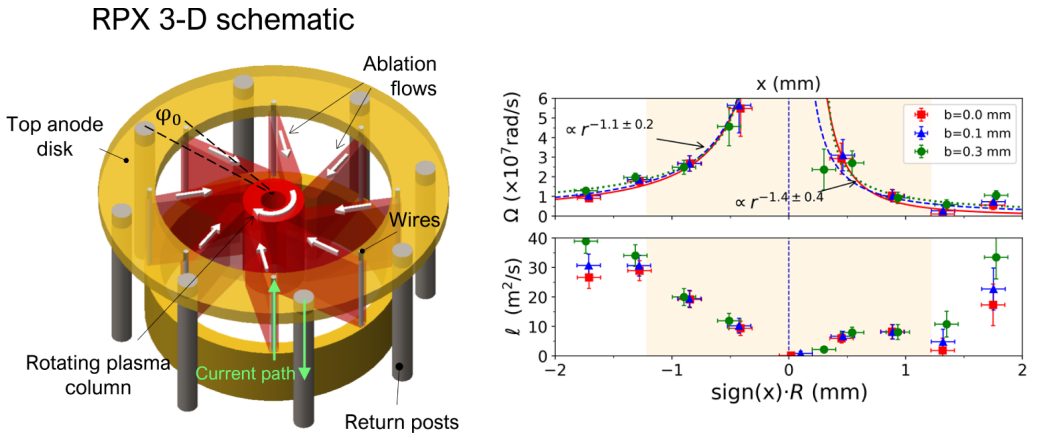


Figure 10. Left: Schematic diagram of the experiment using an inertially driven rotating plasma reported in [61]. The setup uses the oblique collision of multiple plasma jets, resulting from the ablation flows from a cylindrical aluminum wire array (eight 40μm wires, 16 mm diameter, 10 mm high), to inject both mass and angular momentum into the rotating plasma. Right: radial profile of both the angular roation Ω (top) and the angular momentum distribution (bottom), showing quasi-Keplerian flows.

observed when the flow is reversed - behaviour that is well explained by the Hall effect. Plasma Couette flow experiments are crucial as they expand MRI research to include Hall effects and kinetic physics. These effects directly address key issues relevant to hot and dense disks, and partially magnetized protostellar accretion disks [58]. Beyond MRI, the Hall effect has significant applications, including turbulent reconnection in magnetospheres [59] and the evolution of magnetic fields in neutron star crusts [60].

Another recent laboratory study [61] was proposed in this direction by reporting on a pulsed-power driven differentially rotating plasma. In this setup, a strong current flows axially through a cylindrical array of aluminum wires (called a Z-pinch configuration in reference to the axial direction Z), causing the wires to heat up resistively and generate a low-density plasma by ablation. The central cathode directs the return current along the axis of the array, driving ablation flows radially. The ram pressure resulting from these ablation flows induces a rotating plasma column near the center, effectively injecting angular momentum without relying on boundary-driven methods (see Figure 10). The rotational speed profile is quasi-Keplerian, and the flow rotates subsonically, with an azimuthal velocity of 23 km.s^{-1}, a rotational speed in no way comparable to flows of a few m/s obtained in liquid metals. This translates into Reynolds numbers of the order of $Re \sim 10^4$ and $R_m \sim 30$. It should be noted, however, that it would not be so easy to reach the onset of MRI, as the fastest MRI growth mode would develop on timescales of the order of 100 ns and for a critical magnetic field of up to 5 Tesla depending on plasma density. These experiments nevertheless represent a key initial step in establishing a laboratory plasma framework for basic investigations of accretion disks physics.

5.3. *The Kepler experiment*

The Kepler experiment at ENS Paris is another approach, which avoids the measurements difficulties associated with laboratory plasmas. It was also designed specifically to address the

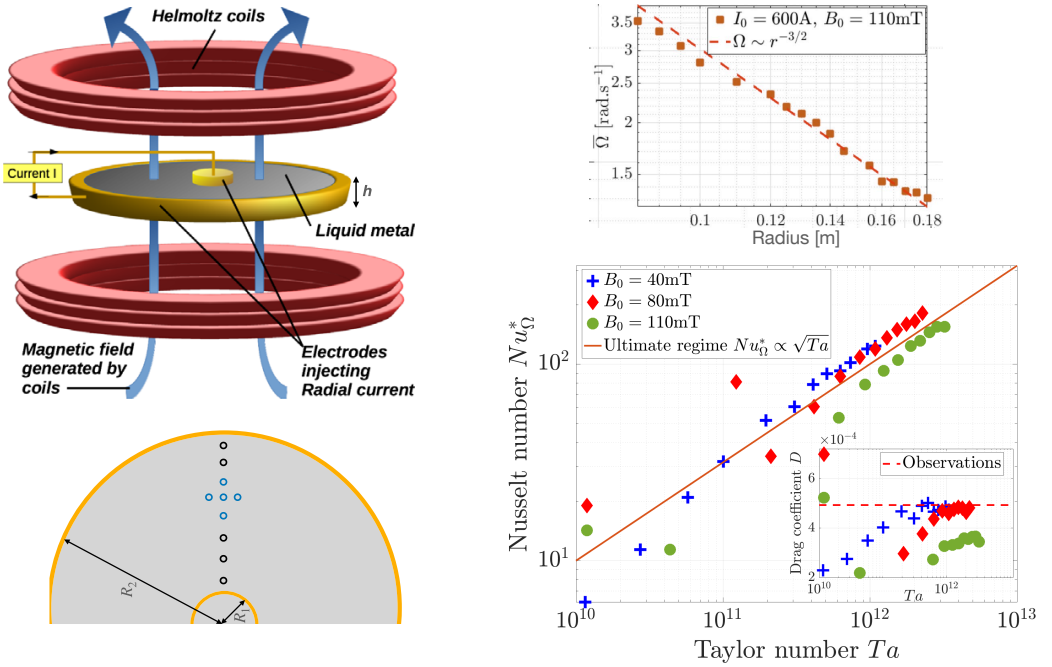


Figure 11. Left: Setup of the Kepler experiment [14,15]. A thin disk (height h = 15 mm, diameter D = 380mm) filled with liquid galinstan is placed between two Helmholtz coils applying a vertical magnetic field. To drive the flow, radial boundaries are not rotating, but acts as electrodes injecting a radial current through the liquid metal. A series of potential probes give access to radial and azimuthal velocity in the bulk. Right-top: Keplerian velocity profile $\Omega \sim r^{-3/2}$ measured in the bulk. Right-bottom: Scaling law Nu_Ω vs Ta reported in the Kepler experiment [15], showing good agreement with Kraichnan's prediction of an ultimate angular momentum transport by Keplerian turbulence. Inset: dimensionless drag coefficient compared to observations (see text).

three limitations discussed in Section 5.1, and to focus on the angular momentum transport observed in Keplerian turbulence (Vernet et al., 2021 [14],Vernet et al., 2022 [15]). The primary aim of this experiment is not to demonstrate MRI or any other mechanism for destabilizing accretion disks, but rather to study the transport properties of Keplerian turbulence in thin disks, independently of the exact mechanisms that generate this turbulence.

In this experiment, the magnetic Reynolds number is less than one, indicating that induced magnetic fluctuations are negligible compared to the applied magnetic field. In this Quasi-Static limit, neither the Magneto-Rotational Instability (MRI) nor dynamo instabilities are expected, a situation close to the dead zones found in real accretion disks. On the other hand, a very large turbulent angular momentum transport is obtained in a Keplerian flow. It is therefore an essential complementary approach to the Taylor–Couette MRI experiments.

The setup includes two concentric cylinders that mimic the thin geometry of a disk, measuring 380 mm in diameter and only 15 mm in height (see Figure 11). Insulating Plexiglass endcaps seal the system, which is filled with Gallinstan and placed between two large Helmholtz coils that generate a vertical magnetic field. Unlike previous Taylor–Couette experiments, the radial boundaries here do not rotate. Instead, the inner and outer cylinders are brass Nickel-plated electrodes through which a strong radial electrical current (approximately $I_0 \sim 3000$ Amps) is applied. This current, combined with the vertical magnetic field B_0 generated by the coils,

generates a volumetric Lorentz force that drives the liquid metal in the azimuthal direction. Velocity fields in both radial and azimuthal directions are measured through ultrasound Doppler velocimetry and a series of potential probes.

Figure 11 shows that a critical difference from previous experiments is the angular rotation generated in the bulk flow, much closer to that obtained in astrophysics. Except near the boundaries where the velocity must go to zero, the Lorentz force, which replaces gravitation in the force balance with fluid's inertia, imposes an exact Keplerian rotation profile $\Omega \sim r^{-3/2}$, for the first time observed in the laboratory.

The situation is not, however, comparable to the first phase of a Keplerian disk, before the MRI or another instability destabilizes the flow. On the contrary, this velocity profile is turbulent, and only appears at very high forcing, after a series of centrifugal and boundary layers instabilities [14] have occured. Consequently, the Kepler experiment models the final state of an accretion disk, which exhibits the same Keplerian turbulence once destabilized by MRI or any other instability. This approach has a clear advantage: by relying on a transition to turbulence easier to obtain than MRI, it allows us to reach a more turbulent state, and thus to study for the first time the transport properties of Keplerian turbulence in a thin disk.

The generation of Keplerian turbulence by the Lorentz force also provides a volume injection of angular momentum, a more satisfactory mechanism compared to the boundary injection achieved by rotating cylinders in Taylor–Couette geometries. Using local measurements of radial and azimuthal velocity fields, [15] reported the flux of angular momentum $J_\Omega = r^3(\overline{u_r\Omega} - \nu\partial_r\overline{\Omega})$, as a function of the fluid's rotation rate over several orders of magnitude. This transport can be quantified by two dimensionless numbers: the Nusselt number $Nu = J_\Omega/(2\nu\Omega r^2)$, which measures the efficiency of angular momentum transport relative to the laminar case, and the Taylor number $Ta = 4r^2 u_\varphi^2/\nu^2$, which quantifies the angular rotation of the fluid.

Two primary contributions to local angular momentum transport were identified: one from the poloidal recirculation induced by the boundaries, similar to the one observed in Taylor–Couette devices, and a contribution from turbulent fluctuations in the bulk flow. Figure 11 demonstrates that for sufficiently large Taylor numbers, the experimental data align well with the asymptotic scaling law:

$$Nu_\Omega^* \propto \sqrt{Ta} \tag{8}$$

where the star indicates that the contribution from poloidal circulation has been subtracted. The observation of this law is a significant achievement as it represents a scaling known for describing efficient angular momentum transport independent of the fluid's molecular viscosity. This scaling was predicted by Kraichnan 60 years ago in the context of heat transport by astrophysical turbulence, and represents the most efficient regime for angular momentum transport by a turbulent flow. This so-called "ultimate" regime of transport had not been reported in previous Taylor–Couette experiments: in those setups, as mentioned above, the angular momentum injected at the boundaries systematically diffuses through the thin viscous layer on the cylinders. This diffusion in the boundary layer dominates much of the transport, and it is impossible to avoid the effect of molecular viscosity, thus preventing the emergence of a diffusivity-free angular momentum regime. In contrast, the Kepler experiment circumvents this constraint by injecting angular momentum volumetrically via the Lorentz force and reaching a state in which the boundary layers are fully turbulent, thus suppressing the role of the molecular viscosity on the transport. This approach is remarkably similar to the method used by Bouillaut et al., 2019 [62] for thermal convection. In their experiment, turbulent thermal convection was generated by applying radiative forcing to the bulk rather than heating the boundaries. This technique produced highly efficient heat transport in the flow, bypassing the boundary layers and reaching the ultimate regime of turbulent convection. Although focused on different topics,

these two experiments echo each other as distinct manifestations of the non-molecular ultimate regime predicted by Kraichnan.

This asymptotic scaling law is particularly relevant for astrophysical systems characterized by low viscosity and negligible boundary layers, and is sometimes presented as a universal prediction for astrophysical transport. Indeed, it can be recovered for the Kepler experiment using just a few general arguments: firstly, the angular momentum flux J_Ω must be equal to the angular momentum rate injected locally by the Lorentz force, $J_\Omega \sim I_0 B_0 r^2/(2\pi\rho h)$ (which can be seen as a consequence of the Keplerian rotation produced by the magnetic forcing). Secondly, a simple energy balance dictates that the rate of energy dissipation ε must be balanced by the work of the Lorentz force driving fluid motion, i.e. $\varepsilon \sim \int_V (\boldsymbol{j} \times \boldsymbol{B}).\boldsymbol{u} \propto I_0 B_0 u_\varphi$. Combining these two results, we obtain $\varepsilon = \gamma J_\Omega u_\varphi$, with γ a geometric parameter of order one. Finally, Kraichnan's argument of an ultimate regime without molecular diffusivity leads to the expression $\varepsilon \sim u_\varphi^3/\ell$ where ℓ is the appropriate mixing length and we have assumed that radial boundary layers are fully turbulent. In the case where the mixing length ℓ is chosen to be the disc thickness h, the scaling law (8) is finally recovered, with the correct prefactor. This simple calculation also shows that the transport properties are relatively independent of the details of the instability driving the turbulence, an important point given recent doubts about the applicability of MRI to cold accretion disks. Here the only three important assumptions are a molecular-free transport, a Keplerien rotation and some specification of the mixing length.

Despite substantial differences between this experiment and real accretion disks, it thus enables predictive analysis. In [63,64] it was shown that a dimensionless drag D can be computed from observations – it is proportional to the accretion rate of protoplanetary disks and correlates directly with the α_{SS} parameter. Interestingly, this dissipation coefficient D can also be determined in laboratory experiments from the $Nu_\Omega^*(Ta)$ scaling law, and is given by $D = 4Nu_\Omega^*/\sqrt{Ta}$. The inset of Figure 11 shows that this dimensionless turbulent drag simply tends to a constant value of $D \sim 5\times10^{-4}$ in the Kepler experiment, as expected in the ultimate regime where $Nu_\Omega^*/\sqrt{Ta}$ = constant. This is an advantage compared to Taylor–Couette devices, where D varies with the Reynolds number and cannot be directly compared to real accretion disks operating at extremely high Re values. This constant value D closely matches the one measured in disks around T Tauri stars: the median value of the observational data reported by [64] is $4,9\times10^{-4}$, as indicated by the red dashed line in the inset of Figure 11).

This remarkable agreement warrants careful interpretation. While the median value of D from observations aligns with the Kepler experiment, calculating the mean value yields $D_{obs} \sim 2\times10^{-3}$, indicating that many accretion disks exhibit significantly higher values than those observed in the Kepler experiment. However, it is important to note that the Kepler experiment operates in a parameter regime quite distinct from real accretion disks, particularly with a magnetic Reynolds number below unity (compared to $Rm \sim 10$ in the Princeton experiment). Consequently, the transport observed in the Kepler experiment is purely due to hydrodynamical stress, without any contribution from Maxwell stress, which would be expected in the presence of MRI. The simple calculation above suggests that the experimental value of D is consistent with a scenario of pure hydrodynamical transport, characterized by non-molecular angular momentum transport, Keplerian turbulence, and a mixing length based on disk thickness. Deviations from these conditions will lead to different values of D. In other words, the Kepler experiment and its value $D \sim 5\times10^{-4}$ likely represents a minimal bound for ultimate turbulent transport in Keplerian disks, particularly in the absence of Maxwell stress, as expected in cold disks or dead zones. Any observational value exceeding this number could however be interpreted as an indication of MRI. This experimental study could thus be extremely useful for a quantitative analysis of observational data and their interpretation in terms of turbulence models.

6. Conclusion and perspectives

This article presents a comprehensive review of laboratory studies aimed at modelling the dynamics of accretion disks, focusing on magnetohydrodynamic experiments carried out over the last two decades. Taylor–Couette devices, such as the one developed at the Princeton University, have focused on the destabilization of Keplerian disks. It has been shown that even at high Reynolds numbers, Keplerian or quasi-Keplerian flows appear to remain stable without MHD effects. However, when an external magnetic field is applied and for sufficiently large inductive effects, a stable centrifugal flow can become unstable to MRI. It then follows a scenario relatively close to the one relevant to astrophysical disks, exhibiting outward angular momentum transport and complex turbulent fluctuations. This remarkable result was only possible after a long journey through the role of boundary conditions and nonlinearities in rotating flows.

Laboratory modeling of astrophysical disks also led to the discovery of other MHD instabilities such as the Shercliff layer instability, or the one reported by the group in Dresden: the Promise experiment have reported the discovery of a new type of MRI in which the presence of an azimuthal field strongly modifies the flow dynamics, producing a magnetorotational instability at very small R_m. This approach opens up interesting new avenues for the weakly ionized regions of disks for which SMRI could not operate.

Finally, these studies of the first stage of an accretion disk, focusing on the origin of turbulence, have recently been complemented by an experimental model of the final stage of the accretion disk, which reproduces the Keplerian turbulence of a thin disk in the laboratory. Providing a quantitative study of angular momentum transport by astrophysical turbulence, the Kepler experiment offers new constraints for turbulent transport in accretion disks, universal enough to be applied to a large range of proto-planetary disks, MRI-unstable or not.

Looking ahead, and building on the recent success of these experiments, we have a number of options open to us to address some outstanding questions on astrophysical disks.

An immediate improvement, currently ongoing in the Princeton experiment, is to make additional measurements in the MRI-unstable regime. Improved flow characterization, for example using multidimensional ultrasonic Doppler velocimetry and Hall probe arrays, will enable detailed measurements of the various components of velocity and magnetic fields. In particular, analysis of their correlations would greatly help to understand the transport of angular momentum by the instability.

In light of the discussions in previous sections, another question that emerges relates to the nonlinear dynamics of MRI. Currently, most results suggest that nonlinear effects appear to be system-dependent, influenced by factors such as geometry, materials, and boundary conditions, and a generic understanding of these aspects is still lacking [65]. In particular, a clear understanding of the mechanisms controlling the saturation of MRI and the corresponding route to fully developed turbulence in laboratory experiments would be of great interest, both for fundamental physics and accretion disk studies. To achieve this, future experiments need to explore the instability well beyond its onset, an exciting challenge due to the considerable power requirements.

In Dresden, several new MHD experiments are currently developed in order to extend the results obtained from the PROMISE experiment [66]. It includes a new version of the Taylor–Couette experiment using liquid sodium, which is a much better electrical conductor than gallium. This enhancement opens up new opportunities. One possibility is to test the MRI-driven dynamo scenario, in which flow perturbations generated by the MRI can produce their own magnetic field through dynamo action. This scenario is extremely popular in astrophysics because it provides a self-sustaining mechanism to explain both turbulence and the magnetic field that sustains the MRI in accretion disks.

We also mentioned several attempts to study this problem using plasma experiments, This is a very promising approach since many limiting factors associated with liquid metals disappear. The magnetic Prandtl number P_m influences various aspects of MRI such as the linear onset, the saturation and the level of fluctuations. In plasma, the viscosity can be varied independently of the conductivity, allowing P_m to range from values typical of liquid metals ($P_m \ll 1$) to those akin to interstellar plasmas ($Pm \gg 1$), an interesting tool for understanding the nature of plasma turbulence [56]. In addition, plasma experiments operating at $Pm \sim 1$ offer the possibility of reaching high magnetic Reynolds numbers while maintaining a kinetic Reynolds number that is not excessively large. This is a significant advantage for observing many MHD instabilities, which are generally known to exhibit a substantial increase of the onset with the level of turbulence.

Finally, by increasing both the size of the disk and the conductivity of the fluid in the Kepler experiment, the Keplerian flow may also become MRI-unstable. Interestingly, this possibility of studying MRI with an electromagnetically-driven flow of liquid sodium was proposed by Velikhov himself [67]. Analytical and numerical calculations support this [68,69], suggesting that the critical onset of the MRI could be reached with a larger version of the Kepler experiment, provided the aspect ratio h/R is increased. An ongoing modification of the experiment involves filling this larger setup with two non-miscible fluids, specifically a free-surface layer of liquid gallium atop a layer of mercury. This layered configuration offers two major advantages: first, it significantly reduces top and bottom friction, allowing the gallium layer to rotate at much faster rates while remaining centrifugally stable, a situation highly conducive to the detection of MRI. Second, by carefully selecting the thickness of these layers, the experiment can be conducted in the shallow water limit. Invoking the analogy between shallow water dynamics and compressible gas dynamics [70,71], this type of setup could provide the first laboratory study of an accretion disk incorporating compressible effects.

These different examples illustrate how a set of complementary approaches, with diverse experimental setups, can collectively improve our understanding of accretion disks. However, such advances will only be possible in close collaboration with observational data. At a time when observational techniques are undergoing revolutionary changes, we could not hope for a better opportunity to deepen our understanding of astrophysical disks.

Declaration of interests

The authors do not work for, advise, own shares in, or receive funds from any organization that could benefit from this article, and have declared no affiliations other than their research organizations.

References

[1] B. Zhao, K. Tomida, P. Hennebelle, et al., "Formation and evolution of disks around young stellar objects", *Space Sci. Rev.* **216** (2020), article no. 43.
[2] J. E. Pringle, "Accretion discs in astrophysics", *Annu. Rev. Astron. Astrophys.* **19** (1981), pp. 137–162.
[3] J. Frank, A. R. King and D. Raine, *Accretion power in astrophysics*, Cambridge University Press, 2002.
[4] A. C. Fabian, "Observational evidence of active galactic nuclei feedback", *Annu. Rev. Astron. Astrophys.* **50** (2012), no. 1, pp. 455–489.
[5] B. Warner, *Cataclysmic variable stars*, Cambridge University Press, 2003.
[6] F. H. Shu, *The physics of astrophysics. Volume 1: Radiation*, University Science Books: Mill Valley, CA (USA), 1991.
[7] A. N. Youdin and J. Goodman, "Streaming instabilities in protoplanetary disks", *Astrophys. J.* **620** (2005), no. 1, pp. 459–469.
[8] K. Wu, "Accretion onto magnetic white dwarfs", *Space Sci. Rev.* **93** (2000), no. 3, pp. 611–649.
[9] C. F. Gammie, "Layered accretion in T Tauri disks", *Astrophys. J.* **457** (1996), pp. 355–362.

[10] S. M. Andrews, J. Huang, L. M. Pérez, et al., "The Disk Substructures at High Angular Resolution Project (DSHARP). I. Motivation, Sample, Calibration, and Overview", *Astrophys. J. Lett.* **869** (2018), no. 2, p. L41.
[11] Lord Rayleigh, "On the dynamics of revolving fluids", *Proc. R. Soc. A: Math. Phys. Eng. Sci.* **93** (1917), no. 648, pp. 148–154.
[12] N. I. Shakura and R. A. Sunyaev, "Black holes in binary systems. Observational appearance", *Astron. Astrophys.* **24** (1973), pp. 337–355.
[13] J. E. Hart, G. A. Glatzmaier and J. Toomre, "Space-laboratory and numerical simulations of thermal convection in a rotating hemispherical shell with radial gravity", *J. Fluid Mech.* **173** (1986), pp. 519–544.
[14] M. Vernet, M. Pereira, S. Fauve and C. Gissinger, "Turbulence in electromagnetically-driven Keplerian flows", *J. Fluid Mech.* **924** (2021), article no. A29.
[15] M. Vernet, S. Fauve and C. Gissinger, "Angular momentum transport by Keplerian turbulence in liquid metals", *Phys. Rev. Lett.* **129** (2022), no. 7, article no. 074501.
[16] K. M. Flaherty, A. M. Hughes, K. A. Rosenfeld, et al., "Weak turbulence in the HD 163296 Protoplanetary disk revealed byALMA CO Observations", *Astrophys. J.* **813** (2015), article no. 99.
[17] D. N. C. Lin and J. E. Pringle, "The formation of the exponential disk in spiral galaxies", *Astrophys. J. Lett.* **320** (1987), pp. L87–L91.
[18] H. H. Klahr and P. Bodenheimer, "Turbulence in accretion disks: vorticity generation and angular momentum transport via the global baroclinic instability", *Astrophys. J.* **582** (2003), no. 2, pp. 869–892.
[19] V. Urpin and A. Brandenburg, "Magnetic and vertical shear instabilities in accretion discs", *Mon. Not. Roy. Astron. Soc.* **294** (1998), no. 3, pp. 399–406.
[20] G. Lesur and P. Y. Longaretti, "On the relevance of subcritical hydrodynamic turbulence to accretion disk transport", *Astron. Astrophys.* **444** (2005), no. 1, pp. 25–44.
[21] M. S. Paoletti, D. P. M. van Gils, B. Dubrulle, C. Sun, D. Lohse and D. P. Lathrop, "Angular momentum transport and turbulence in laboratory models of Keplerian flows", *Astron. Astrophys.* **547** (2012), article no. A64.
[22] B. Eckhardt, S. Grossmann and D. Lohse, "Torque scaling in turbulent Taylor-–Couette flow between independently rotating cylinders", *J. Fluid Mech.* **581** (2007), pp. 221–250.
[23] S. G. Huisman, D. P. M. van Gils, S. Grossmann, C. Sun and D. Lohse, "Ultimate Turbulent Taylor–Couette Flow", *Phys. Rev. Lett.* **108** (2012), article no. 024501.
[24] J. M. Lopez and M. Avila, "Boundary-layer turbulence in experiments on quasi-Keplerian flows", *J. Fluid Mech.* **817** (2017), pp. 21–34.
[25] H. Ji, M. Burin, E. Schartman and J. Goodman, "Hydrodynamic turbulence cannot transport angular momentum effectively in astrophysical disks", *Nature* **444** (2006), no. 7117, pp. 343–346.
[26] E. Schartman, H. Ji, M. J. Burin and J. Goodman, "Stability of quasi-Keplerian shear flow in a laboratory experiment", *Astron. Astrophys.* **543** (2012), article no. A94.
[27] H. K. Moffatt, *Magnetic Field generation in electrically conducting fluids*, Cambridge University Press, Cambridge, London, New York, Melbourne, 1978.
[28] R. J. Donnelly and M. Ozima, "Hydromagnetic stability of flow between rotating cylinders", *Phys. Rev. Lett.* **4** (1960), no. 10, pp. 497–498.
[29] S. Chandrasekhar, *Hydrodynamic and hydromagnetic stability*, Courier Corporation, 2013.
[30] S. A. Balbus and J. F. Hawley, "A powerful local shear instability in weakly magnetized disks. I – Linear analysis. II – Nonlinear evolution", *Astrophys. J.* **376** (1991), pp. 214–233.
[31] E. P. Velikhov, "Stability of an ideally conducting liquid flowing between cylinders rotating in a magnetic field", *Sov. Phys. JETP* **36** (1959), no. 9, pp. 995–998.
[32] S. Chandrasekhar, "The stability of non-dissipative Couette flow in hydromagnetics", *Proc. Natl. Acad. Sci. USA* **46** (1960), no. 2, pp. 253–257.
[33] D. M. H. Hung, E. G. Blackman, K. J. Caspary, E. P. Gilson and H. Ji, "Experimental confirmation of the standard magnetorotational instability mechanism with a spring-mass analogue", *Commun. Phys.* **2** (2019), no. 1, article no. 7.
[34] S. Fromang and R. P. Nelson, "Global MHD simulations of stratified and turbulent protoplanetary discs-I. Model properties", *Astron. Astrophys.* **457** (2006), no. 1, pp. 343–358.
[35] H. Ji, J. Goodman and A. Kageyama, "Magnetorotational instability in a rotating liquid metal annulus", *Mon. Not. Roy. Astron. Soc.* **325** (2001), no. 2, pp. L1–L5.
[36] J. Goodman and H. Ji, "Magnetorotational instability of dissipative Couette flow", *J. Fluid Mech.* **462** (2002), pp. 365–382.
[37] M. D. Nornberg, H. Ji, E. Schartman, A. H. Roach and J. Goodman, "Observation of magnetocoriolis waves in a liquid metal Taylor–Couette experiment", *Phys. Rev. Lett.* **104** (2010), no. 7, article no. 074501.
[38] O. N. Kirillov and F. Stefani, "On the relation of standard and helical magnetorotational instability", *Astrophys. J.* **712** (2010), no. 1, pp. 52–68.

[39] R. Hollerbach and G. Rüdiger, "New type of magnetorotational instability in cylindrical Taylor–Couette flow", *Phys. Rev. Lett.* **95** (2005), no. 12, article no. 124501.

[40] F. Stefani, G. Gerbeth, T. Gundrum, R. Hollerbach, J. Priede, G. Rüdiger and J. Szklarski, "Helical magnetorotational instability in a Taylor–Couette flow with strongly reduced Ekman pumping", *Phys. Rev. E* **80** (2009), no. 6, article no. 066303.

[41] F. Stefani, T. Gundrum, G. Gerbeth, et al., "Experimental Evidence for Magnetorotational Instability in a Taylor–Couette Flow under the Influence of a Helical Magnetic Field", *Phys. Rev. Lett.* **97** (2006), article no. 184502.

[42] J. Priede, I. Grants and G. Gerbeth, "Inductionless magnetorotational instability in a Taylor–Couette flow with a helical magnetic field", *Phys. Rev. E* **75** (2007), no. 4, article no. 047303.

[43] M. Seilmayer, V. Galindo, G. Gerbeth, et al., "Experimental evidence for nonaxisymmetric magnetorotational instability in a rotating liquid metal exposed to an azimuthal magnetic field", *Phys. Rev. Lett.* **113** (2014), no. 2, article no. 024505.

[44] W. Liu, J. Goodman, I. Herron and H. Ji, "Helical magnetorotational instability in magnetized Taylor–Couette flow", *Phys. Rev. E* **74** (2006), no. 5, article no. 056302.

[45] G. Rüdiger and R. Hollerbach, "Comment on "Helical magnetorotational instability in magnetized Taylor–Couette flow"", *Phys. Rev. E* **76** (2007), no. 6, article no. 068301.

[46] S. A. Balbus and P. Henri, "On the magnetic Prandtl number behavior of accretion disks", *Astrophys. J.* **674** (2008), no. 1, pp. 408–414.

[47] A. H. Roach, E. J. Spence, C. Gissinger, E. M. Edlund, P. Sloboda, J. Goodman and H. Ji, "Observation of a Free-Shercliff-Layer Instability in Cylindrical Geometry", *Phys. Rev. Lett.* **108** (2012), p. 154502.

[48] C. Gissinger, H. Ji and J. Goodman, "The role of boundaries in the Magnetorotational instability", *Phys. Fluids* **24** (2012), article no. 074109.

[49] D. R. Sisan, N. Mujica, W. A. Tillotson, W. D. Yi-Min Huang, A. B. Hassam, T. M. Antonsen and D. P. Lathrop, "Experimental Observation and Characterization of the Magnetorotational Instability", *Phys. Rev. Lett.* **93** (2004), article no. 114502.

[50] C. Gissinger, H. Ji and J. Goodman, "Instabilities in magnetized spherical Couette flow", *Phys. Rev. E* **84** (2011), no. 2, article no. 026308.

[51] B. Gallet, C. R. Doering and E. A. Spiegel, "Destabilizing Taylor–Couette flow with suction", *Phys. Fluids* **22** (2010), no. 3, article no. 034105.

[52] E. Knobloch and K. Julien, "Saturation of the magnetorotational instability", *Phys. Fluids* **17** (2005), no. 9, article no. 094106.

[53] Y. Wang, E. P. Gilson, F. Ebrahimi, J. Goodman and H. Ji, "Observation of axisymmetric standard magnetorotational instability in the laboratory", *Phys. Rev. Lett.* **129** (2022), no. 11, article no. 115001.

[54] X. Wei, H. Ji, J. Goodman, F. Ebrahimi, E. Gilson, F. Jenko and K. Lackner, "Numerical simulations of the Princeton magnetorotational instability experiment with conducting axial boundaries", *Phys. Rev. E* **94** (2016), no. 6, article no. 063107.

[55] Y. Wang, E. P. Gilson, F. Ebrahimi, et al., "Identification of a non-axisymmetric mode in laboratory experiments searching for standard magnetorotational instability", *Nat. Commun.* **13** (2022), no. 1, article no. 4679.

[56] C. Collins, N. Katz, J. Wallace, J. Jara-Almonte, I. Reese, E. Zweibel and C. B. Forest, "Stirring unmagnetized plasma", *Phys. Rev. Lett.* **108** (2012), no. 11, article no. 115001.

[57] K. Flanagan, J. Milhone, J. Egedal, et al., "Weakly magnetized, Hall dominated plasma Couette flow", *Phys. Rev. Lett.* **125** (2020), no. 13, article no. 135001.

[58] M. W. Kunz and G. Lesur, "Magnetic self-organization in Hall-dominated magnetorotational turbulence", *Mon. Not. R. Astron. Soc.* **434** (2013), no. 3, pp. 2295–2312.

[59] T. D. Phan, J. P. Eastwood, M. A. Shay, et al., "Electron magnetic reconnection without ion coupling in Earth's turbulent magnetosheath", *Nature* **557** (2018), no. 7704, pp. 202–206.

[60] A. Cumming, P. Arras and E. Zweibel, "Magnetic field evolution in neutron star crusts due to the Hall effect and ohmic decay", *Astrophys. J.* **609** (2004), no. 2, pp. 999–1017.

[61] V. Valenzuela-Villaseca, L. G. Suttle, F. Suzuki-Vidal, et al., "Characterization of quasi-Keplerian, differentially rotating, free-boundary laboratory plasmas", *Phys. Rev. Lett.* **130** (2023), no. 19, article no. 195101.

[62] V. Bouillaut, S. Lepot, S. Aumaître and B. Gallet, "Transition to the ultimate regime in a radiatively driven convection experiment", *J. Fluid Mech.* **861** (2019), R5.

[63] B. Dubrulle, O. Dauchot and F. Daviaud, "Stability and turbulent transport in Taylor–Couette flow from analysis of experimental data", *Phys. Fluids* **17** (2005), article no. 095103.

[64] F. Hersant, B. Dubrulle and J.-M. Huré, "Turbulence in circumstellar disks", *Astron. Astrophys.* **429** (2005), pp. 531–542.

[65] A. Mishra, G. Mamatsashvili and F. Stefani, "Nonlinear evolution of magnetorotational instability in a magnetized Taylor–Couette flow: Scaling properties and relation to upcoming DRESDYN-MRI experiment", *Phys. Rev. Fluids* **8** (2023), no. 8, article no. 083902.

[66] F. Stefani, A. Gailitis, G. Gerbeth, et al., "The DRESDYN project: liquid metal experiments on dynamo action and magnetorotational instability", *Geophys. Astrophys. Fluid Dyn.* **113** (2019), no. 1-2, pp. 51–70.

[67] E. P. Velikhov, A. A. Ivanov, S. V. Zakharov, V. S. Zakharov, A. O. Livadny and K. S. Serebrennikov, "Equilibrium of current driven rotating liquid metal", *Phys. Lett. A* **358** (2006), article no. 216221.

[68] I. Khal'zov and A. I. Smolyakov, "On the calculation of steady-state magnetohydrodynamic flows of liquid metals in circular ducts of a rectangular cross section", *Tech. Phys.* **51** (2006), pp. 26–33.

[69] I. Khal'zov, A. Smolyakov and V. Ilgisonis, "Equilibrium magnetohydrodynamic flows of liquid metals in magnetorotational instability experiments", *J. Fluid Mech.* **644** (2010), pp. 257–280.

[70] F. Günzkofer and P. Manz, "Outwards transport of angular momentum in a shallow water accretion disk experiment", *Phys. Rev. Fluids* **6** (2021), no. 5, article no. 054401.

[71] T. Foglizzo, F. Masset, J. Guilet and G. Durand, "Shallow Water Analogue of the Standing Accretion Shock Instability: Experimental Demonstration and a Two-Dimensional Model", *Phys. Rev. Lett.* **108** (2012), no. 5, article no. 051103.

ACADÉMIE DES SCIENCES
INSTITUT DE FRANCE

Comptes Rendus. Physique
2024, Vol. 25, Special issue S3, p. 611-627
https://doi.org/10.5802/crphys.205

Research article / *Article de recherche*

Geophysical and astrophysical fluid dynamics in the laboratory / *Dynamique des fluides géophysiques et astrophysiques au laboratoire*

Experimental dynamos: from models to applications to the geodynamo

Dynamos expérimentales : des modèles aux applications à la géodynamo

François Pétrélis [a]

[a] LPENS, CNRS, ENS Paris, PSL University, Sorbonne Université, Université de Paris, F-75005, Paris, France

Abstract. Larmor proposed in 1919 an explanation for the origin of the Sun's magnetic field. This phenomenon, known as the dynamo effect, is considered to be responsible for most of the magnetic fields of astrophysical objects, including that of the Earth. It took over 80 years after Larmor's explanation for the first laboratory experiments to demonstrate the dynamo instability. After a brief introduction to the three experiments that have managed to observe this effect, I will describe what they have taught us about the possible regimes of dynamos of planets and stars, especially regarding the geodynamo.

Résumé. Larmor a proposé en 1919 une explication pour l'origine du champ magnétique du soleil. Cette instabilité dite effet dynamo est considérée comme responsable de la plupart des champs magnétiques des objets astrophysiques dont celui de la Terre. Il a fallu plus de 80 ans après l'explication par Larmor pour que les premières expériences de laboratoire mettent en évidence l'instabilité dynamo. Après une brève présentation des trois expériences qui ont réussi à observer cet effet, je décris ce qu'elles nous ont appris sur les régimes possibles des dynamos des planètes et des étoiles et notamment sur la géodynamo.

Keywords. Magnetohydrodynamics, dynamo instability, reversals of the Earth's magnetic field.

Mots-clés. Magnétohydrodynamique, instabilité dynamo, inversions du champ magnétique terrestre.

Manuscript received 9 April 2024, revised 30 July 2024, accepted 4 September 2024.

1. Introduction

The Earth and the Sun both generate a magnetic field that can easily be measured at their surface. This is also true for most planets and stars.

It was Larmor in 1919 who first proposed that the origin of the Sun's magnetic field is a dynamo instability: in an electrically conductive fluid, part of the kinetic energy of the flow is converted into magnetic energy [1]. A similar effect was known for solid dynamos, consisting of electrical windings and magnetic structures. Modern investigations of solid dynamos are discussed in [2–4].

Planetary interiors, containing electrically conductive liquid zones, have led to the dynamo instability being commonly accepted as the mechanism generating the magnetic fields of planets, including that of Earth.

For a long time after Larmor's initial publication, most results obtained were theoretical and numerical in the more recent period, for reviews see [5,6].

It took more than 80 years before the first laboratory observations of the dynamo effect in conductive fluids were achieved. To date, there are three experiments that have demonstrated this effect. A dynamo based on a helical flow in Riga, Latvia [7], a dynamo based on an array of helical flows in Karlsruhe, Germany [8], and a dynamo based on a swirling flow between two counter-rotating coaxial disks in Cadarache, France [9]. We note that there had been other attempts that remained unsuccessful to observe the dynamo instability even though they were able to measure induction mechanisms [10–12].

In this article, we will briefly review what the three successful experiments have taught us, an in particular how they have contributed to the understanding of the magnetic fields of astrophysical objects. A more extensive review on the generation of magnetic field by experimental dynamos can be found in [13]. Here the focus is made on the dynamical features of the magnetic field generated in the experimental dynamos and we show that their understanding provides an explanation for the dynamical regimes of natural dynamos and in particular for the random reversals of the geodynamo.

2. Description of the three fluid dynamo experiments

2.1. *Generic features of experimental dynamos*

The three experiments share common properties. The electrically conductive fluid is liquid sodium maintained above its melting temperature, nearly 98°C.

As we will see in the description of each experiment, the order of magnitude of the experiments' size is the meter, and setting the fluid in motion requires mechanical powers greater than one hundred kilowatts.

These properties are actually required by the nature of the instability. As they are also responsible for the difficulty to perform such experiments, it is interesting to understand their origin. Let us consider an experiment with a liquid of electrical conductivity σ, density ρ, kinematic viscosity ν and magnetic permeability the one of vacuum μ_0. The fluid flows at characteristic speed V with a typical size L.

The dynamo instability takes place when the source of growth of the magnetic field overcomes the dissipative terms. More precisely, in the induction equation

$$\frac{\partial \mathbf{B}}{\partial t} = \nabla \times (\mathbf{v} \times \mathbf{B}) + \frac{1}{\mu_0 \sigma} \nabla^2 \mathbf{B}, \tag{1}$$

when the ratio of the first to the second term of the right hand side is large enough. Estimating these terms, we define their ratio by the magnetic Reynolds number $R_m = \mu_0 \sigma V L$. The dynamo instability onset is associated to a critical value of R_m which is of order $10 - 100$ in the flows used in the experiments.

A second dimensionless number controls the properties of such systems. It is convenient to use the magnetic Prandtl number $P_m = \mu_0 \sigma \nu$. Values of P_m are smaller than 10^{-5} for liquid metals. This is actually constrained by the physics of liquid metals. Indeed, ν measures the microscopic transport of momentum and $(\mu_0 \sigma)^{-1}$ the one of electricity. They take quite different values in liquid metals as electricity is carried by electrons and impulsion by the nucleus of the atoms. These quantities can be calculated using Drude's law for the electrical conductivity and standard estimates of the viscosity of fluids. This provides orders of magnitude built upon

microscopic quantities. Ultimately, we obtain an estimate of the magnetic Prandtl number, that can be written in a compact form as

$$P_m = \alpha^2 \sqrt{\frac{m_e}{m_p}}, \tag{2}$$

where $\alpha = q^2/(\hbar c) \simeq 137^{-1}$ is the fine structure constant and m_e and m_p are the masses of an electron and a proton. This leads to $P_m \simeq 10^{-6}$ which order of magnitude compares well with the values for liquid metals in the vicinity of their melting temperature. The small value of the magnetic Prandtl number thus results from the smallness of the mass ratio between electrons and protons, and from the smallness of the fine structure constant.

A consequence of this property is that, at onset of the dynamo instability, the kinematic Reynolds number $Re = VL/\nu = R_m/P_m$ reaches very large values, superior to 10^6. Dynamo unstable flow are thus highly turbulent.

We can then estimate the power P needed to drive the turbulent which is, in order of magnitude, $P = \rho R_m^3/(L\mu_0^3\sigma^3)$. This leads to an estimate of $100kW$ for a 1 meter flow of liquid sodium at R_m of order fifty [13]. Experimental dynamos thus require to operate large amounts of liquid metal at very large mechanical power which explains the difficulties in observing the dynamo effect.

Finally, we note that the three flows chosen for the experimental dynamos all have domains where the helicity is strong. Helicity is a measure of how the flow breaks mirror symmetry. It is associated to a local amplification mechanism, named α effect, see [5] for a description of the relation between helicity and the α effect.

2.2. *The Ponomarenko-type dynamo in Riga*

The experiment conducted by Gailitis et al. [7] is based on one of the simplest models of homogeneous dynamo, introduced by Ponomarenko in 1973 [14]. Ponomarenko's flow involves a conductive cylinder immersed in a static infinite environment of identical conductivity, with which it is in electrical contact, performing both a uniform rotation and a translation along its axis. When the flow speed reaches a sufficiently high value, so that R_m reaches the instability threshold, this flow generates a magnetic field in the form of a helical wave. The instability is oscillatory and the helical wave propagates in the direction of the flow.

The experiment set up by the Riga group is sketched in Figure 2. The flow is generated by a propeller, creating a helical flow in a central cylindrical cavity. The return flow occurs in a ring surrounding this central flow. This flow changes the nature of the instability from convective to absolute [15]. A layer of liquid at rest is located around these two first layers. The width of the experiment is $0.8m$ and its height $3m$.

The growth of the magnetic field is observed at a driving power close to $100kW$ [15]. The nature of the bifurcation as well as the growth rates of the dynamo were found to be in good agreement with kinematic theory [7]. The measured magnetic field is about $1mT \simeq 10G$ measured at the external boundary of the layer at rest and can reach around $100mT$ at the inner cylinder where the amplification processes are the largest [16].

2.3. *The Roberts-type dynamo in Karlsruhe*

The experiment in Karlsruhe, Germany, is inspired by a kinematic dynamo model developed by G.O. Roberts [17], which showed that various periodic flows can generate a magnetic field at large scale relative to the spatial periodicity of the flow, see [18] for a recent discussion of mean-field dynamos.

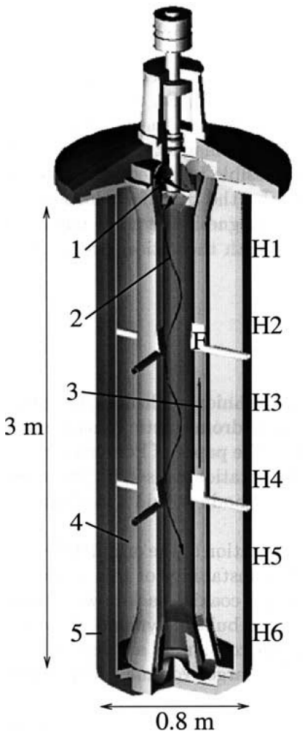


Figure 1. Sketch of Riga's experiment from [15]. A propeller (1) drives an helical flow of liquid sodium in the most inner cylindrical cavity (2). A return flow (3) is located in a second cavity and a layer of sodium at rest (4) is around these two layers. (5) is the thermal insulation. H and F indicate the positions of hall probes and of a fluxgate.

The experiment consists of 52 cells located in a cylinder with a width of $1.85m$, through which liquid sodium circulates [8]. The flow in each cell is helical, so that it generates an α-effect.

When the speed is sufficiently high, a magnetic field is generated by dynamo action. The structure of the generated field, a dipole with axis perpendicular to the z-direction, is in agreement with what is expected from a dynamo generated by the α-effect of the flow. The measured generated field is up to 350 G in the core of the experiment [19]. Estimating the power required to drive the flow from the pressure drop in the pumps that drive the flow multiplied by the flow rate, an order of magnitude slightly larger than 10 kW is obtained in the vicinity of the onset of instability. Measurements above the onset lead to an estimate of the Joules dissipation that is in agreement with a scaling law for the power dissipation derived from a set of numerical simulations. Assuming that this prediction holds for the Earth provides information on several aspects of the Earth dynamics, and in particular for the age of the inner core and for the absence of need for radioactive heating [20].

2.4. *The Von Karman Sodium dynamo*

The Von Karman Sodium (VKS) experiment is a collaboration between ENS Paris, ENS Lyon, and CEA, with the experiment being conducted at CEA-Cadarache.

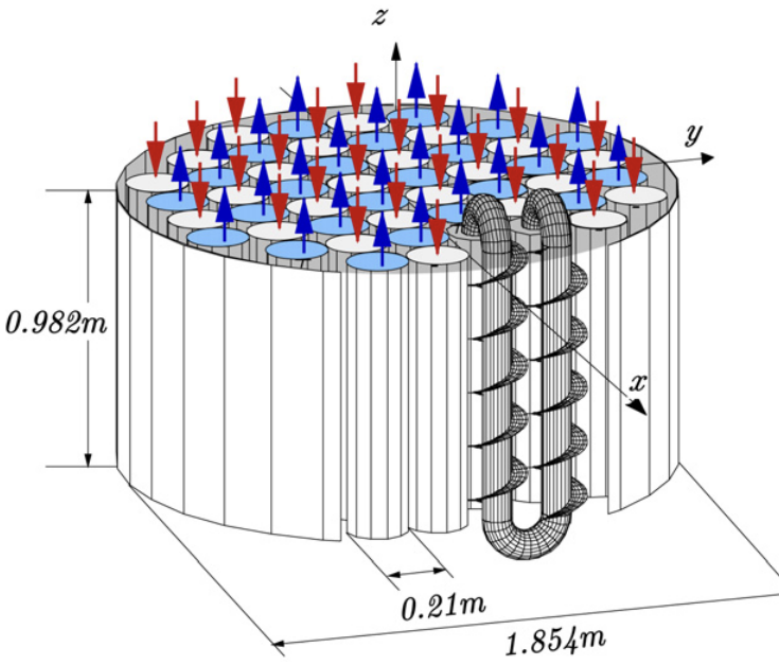


Figure 2. Sketch of Karlsruhe's experiment, figure from [19]. An array of 52 cells in which liquid sodium flows and generates an α-effect. The color arrows represent the axial direction of the flow.

The setup consists of a counter-rotating flow driven by the motion of two soft iron disks equipped with blades and located in a cylinder, see Figure 3. 150 liters of liquid sodium are set in motion by a mechanical power up to 300 kW [9].

For sufficient rotation of the disks with equal and opposite speeds, a magnetic field is observed whose large scales are dominated by an axial dipole. The dipole axis is parallel to the rotation axis of the disks. The fields fluctuates because of the turbulent fluctuations of the flow and yet the direction of the dipole remains fixed.

Unlike the two previous experiments, the time-averaged flow is not close to a known laminar flow that would generate a dynamo. Cowling's anti-dynamo theorem [5] implies that a dipolar field generated by the averaged flow should be a transverse field in order to break the azimuthal invariance of the averaged flow. Therefore, the non-axisymmetric velocity fluctuations are involved in the generation of the large-scale magnetic field.

The observations are consistent with an α-ω type mechanism, where the azimuthal shear is the source of the ω effect, while speed fluctuations due to the helical vortices near the blades are the source of the α effect [13]. Several numerical simulations have subsequently measured these effects and discussed the role of the soft iron disks [22–25]. An explanation for the role of soft iron is that it allows both the toroidal and the poloidal magnetic field component to be strong in the vicinity of the disk near the domain where the α effect is strong [26]. This lowers the instability threshold that can then be reached in the experiment. A magnetic field of amplitude up to $100-200$ G is measured in the bulk of the flow.

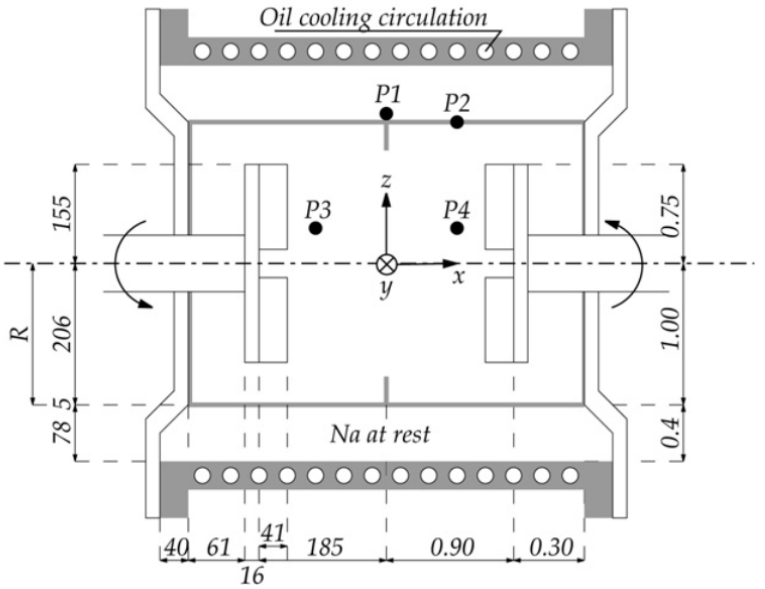


Figure 3. Sketch of VKS experiment, figure from [21]. Two soft iron discs put into motion 150 l of liquid sodium. A layer at rest is located around the swirling flow but has been removed without changing qualitatively the behavior. An oil cooling circulation maintains the temperature above the sodium melting point.

3. What the experiments taught us

3.1. *Generation mechanisms and saturation of the magnetic field*

The standard α and ω effects, enable the generation of a dynamo for flows close to laminar dynamos, but also for flows with turbulent fluctuations at all scales, as seen in the VKS experiment.

The observed magnetic field is approximately 10 to 100 G at 10% above the instability threshold. These observations are explained by the scaling law predicted for turbulent dynamos [27]. In particular, the saturation of the magnetic field results from a balance between the Laplace force and the inertial term of the Navier–Stokes equation acting on the modification of the velocity field.

A balance between the Laplace force and the viscous term of the Navier–Stokes equation can be captured analytically close to the onset of dynamo instability or numerically for a balance with the inertial term [28,29]. The order of magnitude of the generated magnetic field will not be relevant for an astrophysical object, as they are independent of the global rotation.

A similar argument can be used to take into account rotation [27], which is usually the dominant term in astrophysical objects. This leads to the order of magnitude estimate $B^2 = \frac{\rho\Omega}{\sigma}(R_m - R_{mc})$ with Ω the angular velocity. The prefactor $\sqrt{\rho\Omega/\sigma}$ is close to $10\,G$ which is not unrealistic for the Earth magnetic field. More details on the generation processes and on the saturation properties can be found in [13].

3.2. *Dynamical regimes*

An important symmetry property of the VKS experiment is that in exact counter-rotation, the forcing is symmetrical under rotation of π around any axis in the mid-plane. We denote such a

rotation by R_π. In that situation, we already mentioned that the direction of the dipolar unstable mode does not change.

When this symmetry is broken by rotating one disk faster than the other, dynamical regimes are observed such as periodic reversals as seen in the Sun, random reversals as produced by the Earth's dipole or bursting behaviors [30,31]. Examples of time series are displayed in Figure 4.

We note that a minute change of forcing parameters allows the field to transition from stationary to time periodic oscillation and to random reversals. A consequence is that the nature of the observed magnetic field is not predictive of the induction mechanism operating in the fluid. This has implications for astrophysical observations as one could be tempted to link magnetic field behavior with flow properties.

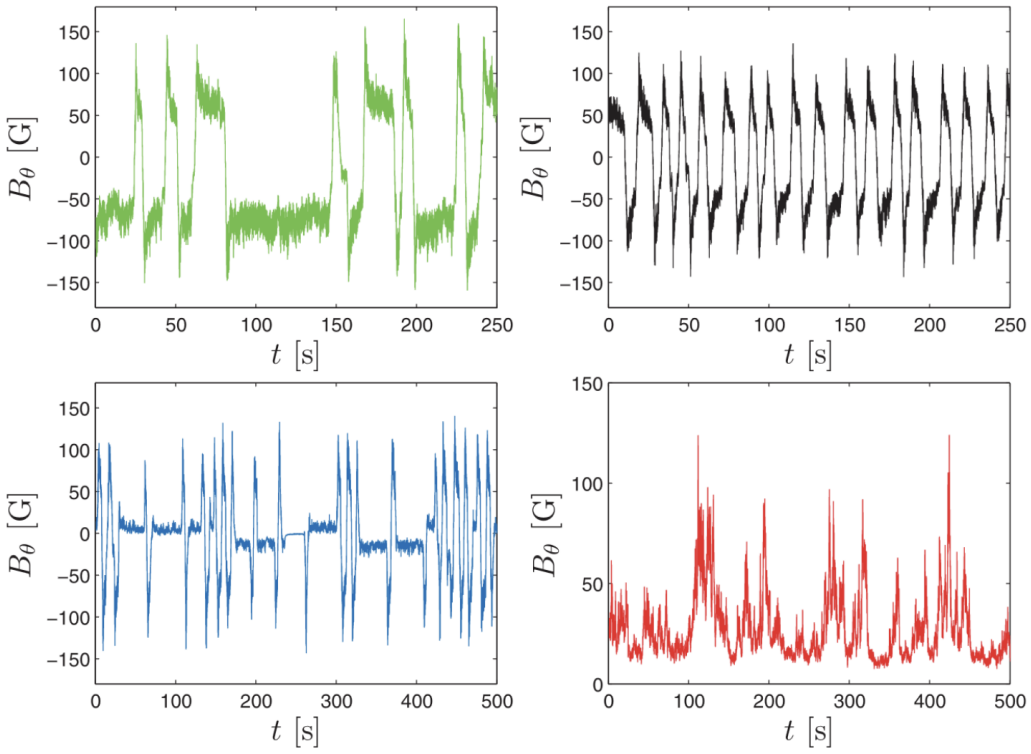


Figure 4. Time series of the azimuthal component of the magnetic field generated in the VKS experiment. One of the disks rotates faster than the other one. The different regimes are obtained by a change of temperature or a change of speed of one of the motors. These modifications result in a relative change of R_m or R_e that is smaller than 7%. See [31] for details.

The field behavior results from the competition between two modes: the dipolar mode as observed in exact counter-rotation and a second mode of quadrupolar symmetry [32]. The spatial structure of these modes is sketched in Figure 5.

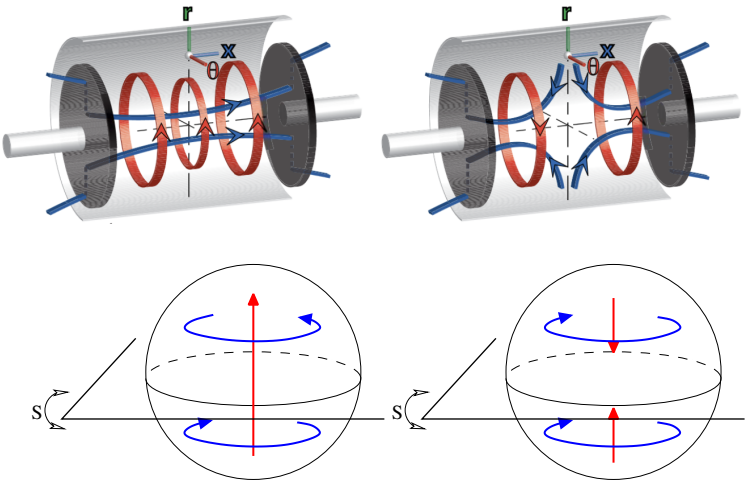


Figure 5. Schematic of the spatial structure of the large scales of the unstable modes. Left: dipolar field; right: quadrupolar field. Top: in the VKS experiment figure from [31]. Bottom: for the geodynamo. Note the different behavior of the poloidal and toroidal components of the different modes with respect to (top) the R_π symmetry around the axis noted r, (bottom) the planar reflection with respect to the equatorial plane.

4. A low-dimensional approach to the dynamics of the magnetic field

4.1. *Two competing magnetic modes*

The simplest model that describe the observations from the VKS experiment is based on the competition between two magnetic field modes [33,34]. A review and a comparison with other models is presented in [35]. The two modes involved in the dynamics have, at large scale, a dipolar structure and a quadrupolar one. The same model can be introduced to describe the dynamics of the Earth's magnetic field and the spatial structure of the modes is displayed in Figure 5 bottom. We note that these two modes transform differently with respect to the equatorial symmetry (in the case of the geodynamo) and with respect to R_π the rotation of angle π about any axis contained in the median plane (in the case of the VKS dynamo). These different symmetries notably explain the spatial structure of the toroidal field of each mode.

We assume that each mode is close to its instability threshold. We then write the total field as

$$\mathbf{B}(\mathbf{r},\mathbf{t}) = d(t)\mathbf{D}(\mathbf{r}) + q(t)\mathbf{Q}(\mathbf{r})\,, \tag{3}$$

where $\mathbf{D}(\mathbf{r})$ and $\mathbf{Q}(\mathbf{r})$ are the spatial structures as schematized in Figure 5 and $d(t)$ and $q(t)$ their amplitudes.

Let's note $A = d + iq$. Near their instability threshold, the evolution equation for A is

$$\dot{A} = \mu A + \nu \bar{A} + \mathrm{NL}(A)\,, \tag{4}$$

where $\mu = \mu_r + i\mu_i$, $\nu = \nu_r + i\nu_i$ are complex coefficient and NL(A) stands for non linear terms, of cubic order at least due to the invariance of the magnetohydrodynamic equations under change of sign of the magnetic field ($B \to -B$).

The difference in behavior of the two modes with respect to the equatorial symmetry (or the R_π rotation for VKS) implies the following property: if the flow has this symmetry, then the imaginary

parts of μ and ν are zero. The amplitude of these imaginary parts is thus a measure of how much the symmetry is broken by the flow.

It is possible to keep all the nonlinear term of cubic order [33] but for simplicity we assume that they will simply maintain fix the norm of A. In other words, we note $A = r \exp i\theta$ and assume that the effect of the nonlinear term in Eq. (4) is to enforce r to remain at a constant value. Then θ can be shown to satisfy

$$\dot{\theta} = \mu_i + \nu_i \cos(2\theta) - \nu_r \sin(2\theta) . \tag{5}$$

4.2. *Random or periodic reversals*

Let's first discuss the case where μ_i is significantly larger than ν_i and thus set $\nu_i = 0$. For small μ_i, Eq. (5) has 4 steady solutions, 2 of which are stable and 2 are unstable, see Figure 6. Note that the phase space remains invariant under central symmetry through the origin, as a consequence of the $B \to -B$ invariance of the MHD equations.

A weak breaking of the symmetry brings the stable fixed points closer to the unstable fixed points in the phase space but the solution remains stationary. When $\mu_i > \nu_r$, there is no longer any stationary solution, and the solution becomes a non-linear oscillation. In other words, at $\mu_i = \nu_r$ a saddle-node bifurcation transforms the pair of stable solutions into a limit cycle: the magnetic field becomes oscillatory. Its spatial structure evolves over time from a dipole to a quadrupole to the opposite of the initial dipole, the opposite of the initial quadrupole and back to the initial dipole.

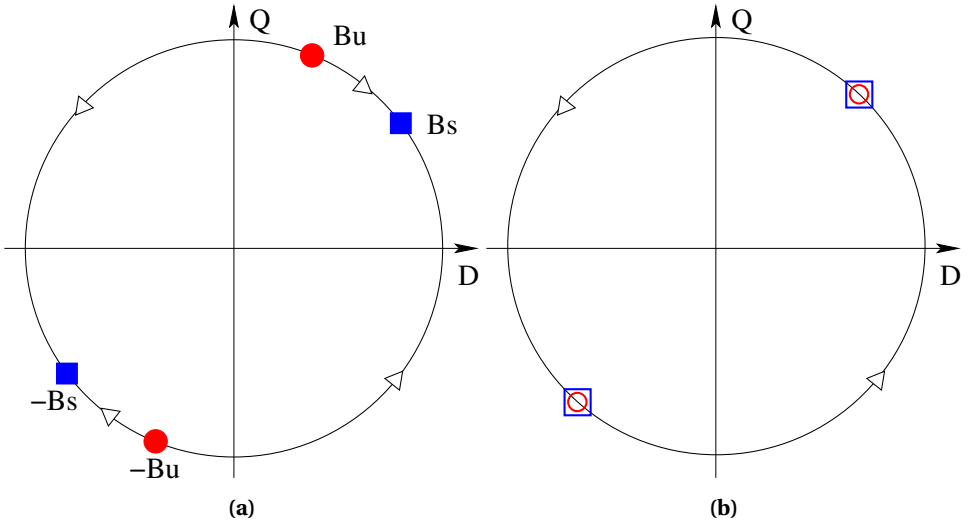


Figure 6. Phase space close to the saddle node bifurcation. Left: the two stable state B_s are at finite distance of the unstable ones B_u. Right: At the onset of the saddle node bifurcation, the steady states collide and disappear and a limit cycle appears. Figures from [34].

In addition to this periodic oscillation behavior, this system can easily generate random reversals. We assume that we are close to the threshold of the bifurcations as in Figure 6(a) and we model the effect of turbulent fluctuations by random perturbations that cause the system state to diffuse in the phase space.

If the solution is initially located close to one of the stable fixed points, say B_s, fluctuations can push the system away from B_s. If it goes beyond the unstable fixed point B_u, it is attracted by the

opposite fixed point $-B_s$, and thus achieves a polarity reversal. Several properties arise from this mechanism:

- A reversal is made of two successive phases. The first phase $B_s \to B_u$ in Figure 6(a) is the approach toward an unstable fixed point. The deterministic dynamics acts against the evolution, and this phase is slow. The second phase $B_u \to -B_s$, is fast since the deterministic dynamics favors the motion.
- At the end of the first phase, the system may return toward the initial stable fixed point (phase $B_u \to B_s$), which corresponds to an aborted reversal or an excursion. Notably, the Earth dipole has displayed several excursions in the past.
- At the end of a reversal, the dipolar amplitude $d(t)$ reaches large values before it tends towards the value of the dipolar part of B_s: this is an overshoot. In contrast, excursions do not display overshoots.

These prediction can be easily tested on Eq. (4) by adding a stochastic term that models the effect of the turbulent fluctuations. Time series are displayed in Figure 7. We also display time series of the Earth dipole and of the magnetic field measured in the VKS experiment. The aforementioned properties are clearly displayed by the three systems: existence of reversals and of excursions, the existence of a slow and a fast phase during the reversal, the overshoot at the end of the reversal and its absence for the excursions.

4.3. *Hemispherical dynamos*

The model of competition between dipole and quadrupole also allows for the description of another regime of interest: when the symmetry is broken but the dominant term in Eq. (5) is ν_i. Then the solution remains stationary and corresponds to $\theta = \pi/4, 5\pi/4$. This means that the dipole and quadrupole are of equal amplitudes as $d = r\cos\theta$ and $q = r\sin\theta$. On one side of the Earth's core or the VKS dynamo, the two modes add together, while on the other side, they subtract. Thus, we are in the presence of a hemispherical or localized dynamo [37]. This regime could possibly be that of Mars' field in the past and has also been observed in the VKS experiment [38].

It is quite remarkable that the same mechanism of competition between a dipolar mode and a quadrupolar mode allows for capturing such diverse regimes as random or periodic reversals, burst behaviors, or hemispheric modes.

4.4. *Role of symmetry breaking*

When the dynamics involve a dipolar mode and a quadrupolar mode, it is the breaking of symmetry that couples the two modes and allows for reversals of the field or for localized dynamos.

In the case where reversals are generated by the coupling, it can be shown that the frequency of the reversals increases with the amplitude of the symmetry breaking [34].

This breaking of symmetry is controlled in the VKS experiment by the difference in rotation between the two discs. On Earth, several origins of symmetry breaking can be thought of: spontaneous fluctuations in the large-scale structure of the flow in the liquid core, asymmetric forcings at the core-mantle boundary, or similar effects at the level of the solid core. In the following section, using what we have understood about the mechanism of magnetic field reversal, we will propose an explanation for the long-term variability in the frequency of the geodynamo reversals. It relies on the mantle dynamics and thus relates plate tectonics to the dynamo of the liquid core.

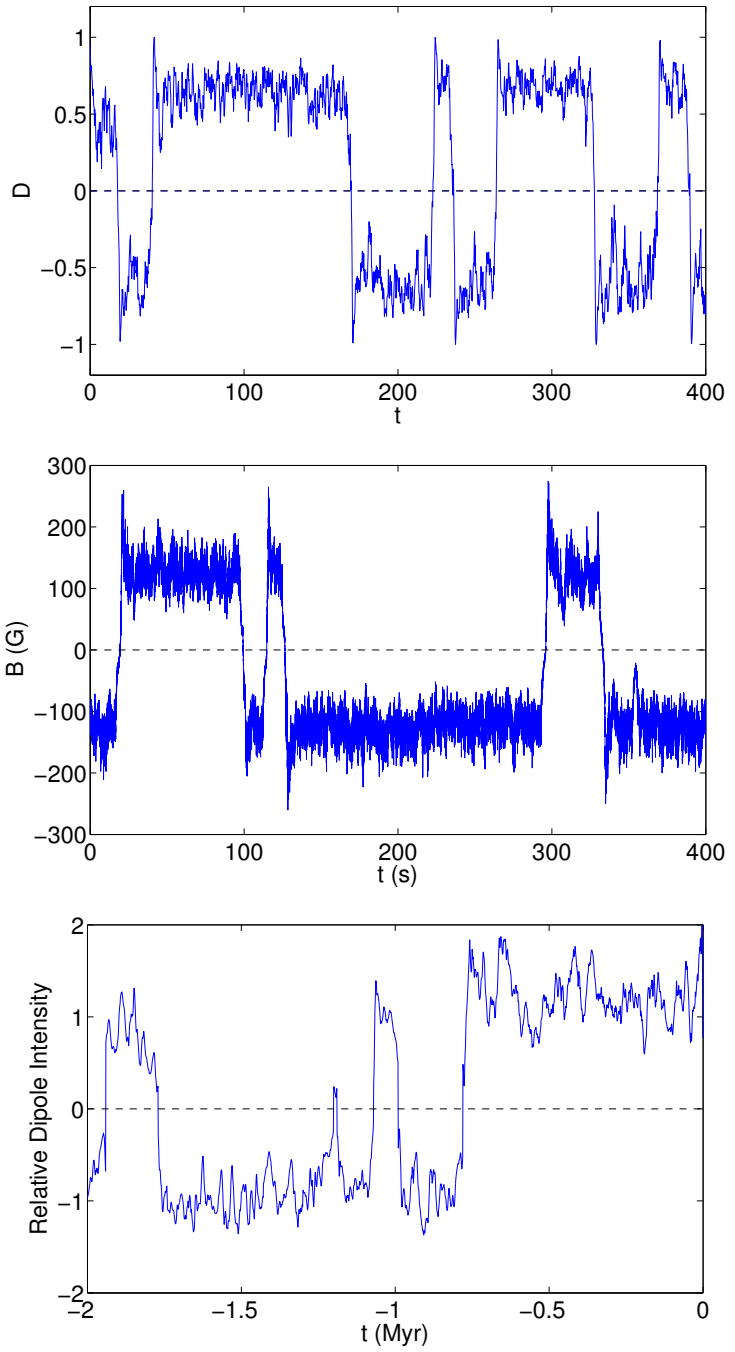


Figure 7. (Top) Time series of the dipole amplitude for a system below the threshold of the saddle-node bifurcation (Eq. (5)) subject to noise. (Middle) Time series of the magnetic field measured in the VKS experiment for the two impellers rotating with different frequencies in the regime of random reversals (data from [30]). (Bottom) Composite paleointensity curve for the past 2 millions years (data from [36]).

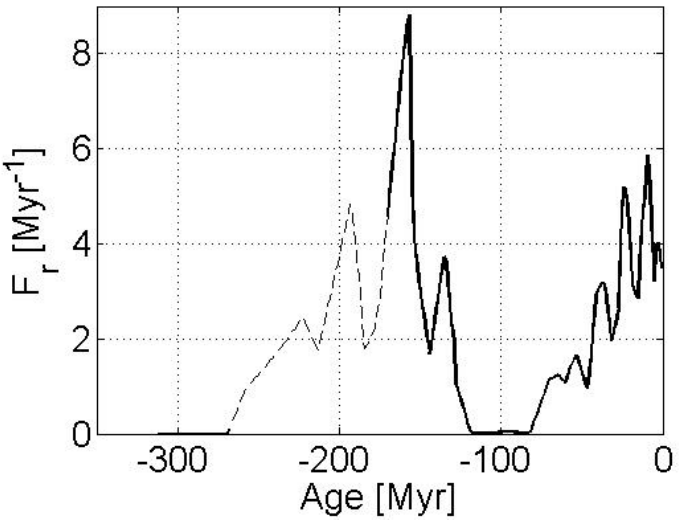


Figure 8. Reversal frequency as a function of age, data from [41].

5. Plate Tectonics and the Frequency of Reversals

The number of reversals of the Earth's magnetic field per unit of time has not remained constant over time. Over the last 80 million years, the average frequency, see Figure 8, has increased from zero reversals during the Cretaceous Normal Superchron (CNS) between 80 and 120 million years ago to about 4 per million years over the last 5 million years (Myr). Before this superchron, the frequency decreased over several tens of millions of years. We also note that older superchrons have been measured. Therefore, the frequency of reversals follows long-term variations over durations of several tens of millions of years, see discussions in [39] or [40].

Among the physical phenomena that determine the evolution of the Earth, few are associated with such a time scale. Ultimately, it is the convective movements in the mantle, and thus plate tectonics, that seems to be the most capable of explaining the variability in the frequency of reversals. Indeed, the characteristic time scale built upon the typical velocity of plates say 10cm/yr over the Earth radius 6000km is 60Myr and is of the correct order of magnitude.

Considering what we have learned from modeling the reversals of the magnetic field, as described in Section 4, a coupling between plate tectonics and properties of the dynamo in the liquid core is possible provided there exists a breaking of equatorial symmetry of the boundary conditions at the core mantle boundary (CMB).

Assuming that the properties at the CMB are correlated with the ones at the surface of the mantle, we have studied the arrangement of continents, which has been known for over 300 million years, as seen in Figure 9. We note that their arrangement in relation to the equator varies and alternates between globally symmetrical arrangements and arrangements preferentially in one hemisphere. In particular, the recent evolution between age 65 Myr and present time (figure b and a) and the one between age 260 and 200 Myr (figure d and c) are associated to a drift of the continent position away from an equatorially symmetric position towards a more northern one. During these periods, the reversal frequency increases.

To quantify this effect, we have determined the convex hull of the continents and then calculated $D = \int z dS/St$ where z is the distance to the equator, the sum is taken over the convex hull, and St is the total surface area of the Earth. This term thus measures how asymmetrical the distribution of continents is in relation to the equator.

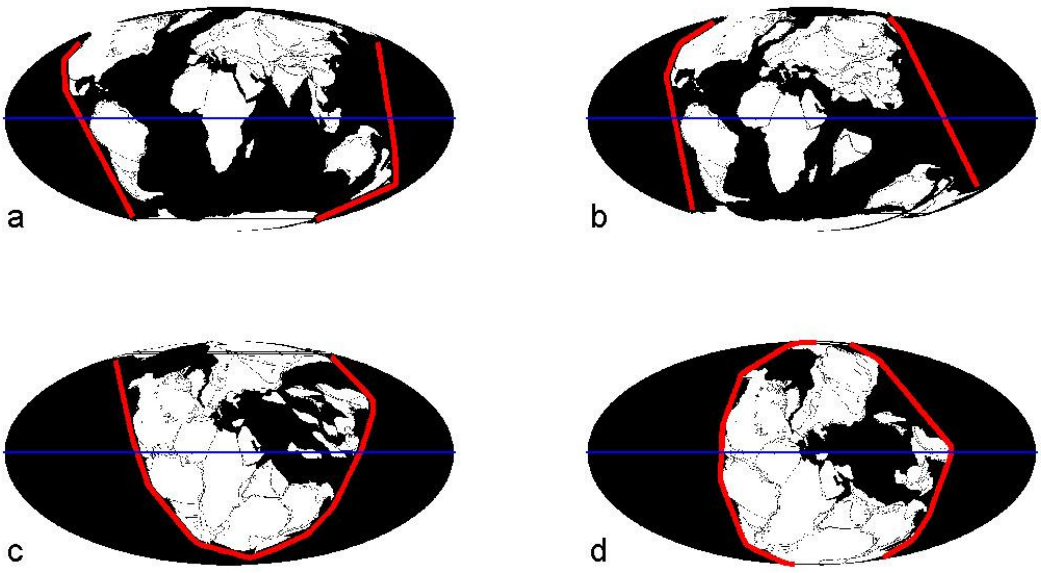


Figure 9. Position of the continents with their convex envelope (red line) at various periods of time: (a) present time, (b) 65 Myr ago, (c) 200 Myr ago, (d) 260 Myr ago. Figure from [39].

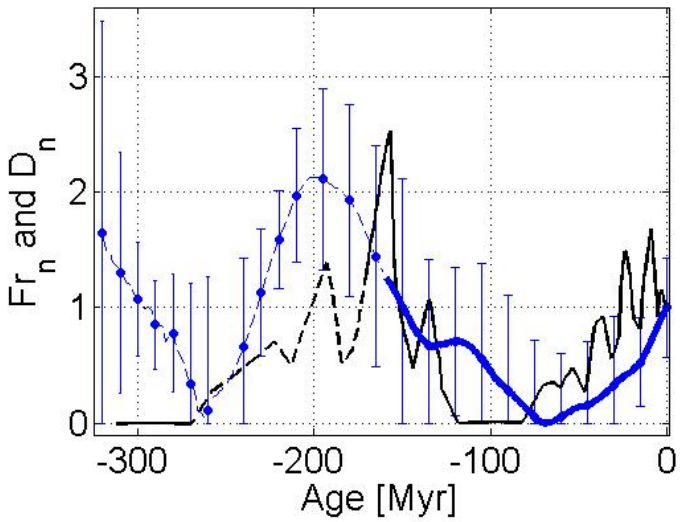


Figure 10. Comparison between changes in reversal frequency (black line) and the D parameter obtained after $D_n = |D - D(-65Myr)|$ (blue line). The bold line corresponds to the past 170 Ma documented by magnetic oceanic anomalies. Error bars represent uncertainties in continental reconstructions. Both curves have been normalized to their present value. Figure from [39].

The characteristic time of variation of D is similar to that of the frequency of reversals and we observe that D presents a minimum 65 million years ago. If we plot the deviation $|D-D(65Myr)|$ as a function of time, the curve is similar to that of F_r, see Figure 10.

We deduce that the position of the continents is correlated with the frequency of reversals and, based on our understanding of the origin of variability of the reversal frequency, this is coherent with a control of the reversal frequency by plate tectonics.

Let us now discuss a possible mechanisms at work. We know that it is the equatorial symmetry of the flow in the liquid core that is important and that this is therefore correlated with the position of the continents. The most direct explanation is as follows: the continents affect the large-scale temperature structure in the mantle, especially since they determine the areas where cold matter descends and where hot plumes rise. This has been verified numerically [42] who observe that supercontinents promote temperature anomalies on the largest scales. These spatial variations in temperature and composition propagate to the CMB (core-mantle boundary) where they affect the equatorial symmetry of the flow. This modifies the reversal frequency as explained in Section 4.

6. Conclusions

Dynamo experiments have notably demonstrated the validity of amplification mechanisms, their ability to generate a magnetic field at large scale, and their robustness for very turbulent flows.

Random or periodic reversals of the magnetic field as seen in astrophysical objects are generic behaviors. They result from the competition between a small number of modes, and a dynamical system approach allows us to identify their origin and to predict other behaviors, such as hemispherical dynamos, which have also been observed.

For the geodynamo, it is the equatorial symmetry of the flow that plays a role in the case of competition between a dipole and a quadrupole. In particular, this symmetry breaking determines the frequency of reversals. We have shown that variations of the reversal frequency on time scales of 100 million years are correlated with the position of the continents. This indicates a strong coupling between what is observed on the surface of the mantle and what happens at the core-mantle boundary and then in the liquid core.

To finish, we mention some related problems of interest.

Geodynamo simulations. Numerical simulations of the geodynamo do not clearly observe a dipole-quadrupole coupling, except for some specific parameter values such as [43] or [44]. Numerical simulations are bound to run with P_m not too small. P_m of order unity implies that the velocity modes and the magnetic ones have similar dissipative time scale. This is quite different from the realistic situation of a liquid metal for which $P_m < 10^{-5}$ so that the magnetic modes are heavily damped compared to the velocity ones. We expect that decreasing P_m in numerical simulations will simplify the dynamics of the magnetic field that will be less sensitive to the velocity turbulent fluctuations.

Low dimensional chaos. The coupling of two magnetic modes with a single hydrodynamic degree of freedom is sufficient to generate chaotic attractors for which the dipolar amplitude changes sign [45]. This regime might be observable in numerical simulations with order one P_m and at moderate forcing so that a small number of hydrodynamic and magnetic modes are dynamically coupled and evolve at similar timescales.

Properties of mantle convection. Numerical models of the mantle can be used to investigate further the relation between the surface (location of the continents, of the descending and ascending material, etc…) and the boudary condition enforced to the liquid core at the CMB, see for instance [46].

Earth magnetic field measurements. Some measurements of the magnetic field in the last 100 thousand years have a temporal resolution that could be precise enough to estimate the quadrupolar component of the magnetic field. It would be interesting to investigate its behavior, for instance during the more recent excursions.

Precession driven dynamos. Efforts are currently ongoing in the development of an experimental dynamo based on a precession driven flow, see the related article in this article collection. This forcing mimicks the effect of the precession of the rotating axis of astrophysical objects when tides are the dominant forcing. If a magnetic field is generated by the dynamo instability, it will be interesting to investigate whether dynamical regimes appear as a result from the competition between a small number of unstable modes.

Acknowledgments

I thank Stephan Fauve for many discussions and suggestions that drove our researches on this topic. I also thank Basile Gallet, Christophe Gissinger with whom I collaborated on part of the works reviewed in this article and also all the other members of the VKS collaborations with whom the data obtained in [9,21,30,31] were obtained. I also acknowledge Emmanuel Dormy, Jean-Pierre Valet and Jean Besse for discussions and collaborations on the geodynamo and on plate tectonics. I thank F. Stefani and the authors of [15] and A. Tilgner and the authors of [19] for providing figures or datas from their publications.

Declaration of interests

The authors do not work for, advise, own shares in, or receive funds from any organization that could benefit from this article, and have declared no affiliations other than their research organizations.

References

[1] J. Larmor, "How could a rotating body such as the sun become a magnet?", in *Rep. 87th Meeting Brit. Assoc. Adv. Sci., Bornemouth, Sept. 9–13*, John Murray: London, 1919, pp. 156–160.

[2] F. Lowes and I. Wilkinson, "Geomagnetic Dynamo: An Improved Laboratory Model", *Nature* **219** (1968), pp. 717–718.

[3] A. A.-Z. Raúl and P. Jānis, "Realization of Bullard's disc dynamo", *Proc. R. Soc. Lond., Ser. A* **479** (2023), article no. 20220740.

[4] F. Alboussière T. Plunian and M. Moulin, "Fury: an experimental dynamo with anisotropic electrical conductivity", *Proc. R. Soc. Lond., Ser. A* **478** (2022), article no. 20220374.

[5] H. K. Moffatt, *Magnetic Field Generation in Electrically Conducting Fluids*, Cambridge Monographs on Mechanics and Applied Mathematics, Cambridge University Press: Cambridge, 1978.

[6] Y. B. Zeldovich, A. A. Ruzmaikin and D. D. Sokoloff, *Magnetic Fields in Astrophysics*, The Fluid Mechanics of Astrophysics and Geophysics, Gordon and Breach Science Publishers: New York, 1983.

[7] A. Gailitis, O. Lielausis, E. Platacis, et al., "Magnetic field saturation in the Riga dynamo experiment", *Phys. Rev. Lett.* **86** (2001), pp. 3024–3027.

[8] R. Stieglitz and U. Müller, "Experimental demonstration of a homogeneous two-scale dynamo", *Phys. Fluids* **13** (2001), pp. 561–564.

[9] R. Monchaux, M. Berhanu, M. Bourgoin, et al., "Generation of magnetic field by dynamo action in a turbulent flow of liquid sodium", *Phys. Rev. Lett.* **98** (2007), article no. 044502.

[10] N. L. Peffley, A. B. Cawthorne and D. P. Lathrop, "Toward a self-generating magnetic dynamo: The role of turbulence", *Phys. Rev. E* **61** (2000), no. 5, pp. 5287–5294.

[11] M. D. Nornberg, E. J. Spence, R. D. Kendrick, C. M. Jacobson and C. B. Forest, "Measurements of the magnetic field induced by a turbulent flow of liquid metal", *Phys. Plasmas* **13** (2006), no. 5, article no. 055901.

[12] S. Cabanes, N. Schaeffer and H.-C. Nataf, "Magnetic induction and diffusion mechanisms in a liquid sodium spherical Couette experiment", *Phys. Rev. E* **90** (2014), article no. 043018.

[13] F. Pétrélis, N. Mordant and S. Fauve, "On the magnetic fields generated by experimental dynamos", *Geophys. Astrophys. Fluid Dyn.* **101** (2007), no. 3-4, pp. 289–323.
[14] Y. B. Ponomarenko, "Theory of the hydromagnetic generator", *J. Appl. Mech. Tech. Phys.* **14** (1973), pp. 775–778.
[15] A. Gailitis, O. Lielausis, E. Platacis, G. Gerbeth and F. Stefani, "The Riga Dynamo Experiment", *Surv. Geophys.* **24** (2003), pp. 247–267.
[16] A. Gailitis, G. Gerbeth, T. Gundrum, O. Lielausis, G. Lipsbergs, E. Platacis and F. Stefani, "Self-excitation in a helical liquid metal flow: the Riga dynamo experiments", *J. Plasma Phys.* **84** (2018), no. 3, article no. 735840301.
[17] G. O. Roberts, "Dynamo action of fluid motions with two- dimensional periodicity", *Philos. Trans. R. Soc. Lond., Ser. A* **271** (1972), pp. 411–454.
[18] A. Alexakis, S. Fauve, C. Gissinger and F. Pétrélis, "Effect of fluctuations on mean-field dynamos", *J. Plasma Phys.* **84** (2018), no. 4, article no. 735840401.
[19] U. Müller, R. Stieglitz, F. H. Busse and A. Tilgner, "The Karlsruhe two-scale dynamo experiment", *Comptes Rendus. Physique* **9** (2008), no. 7, pp. 729–740.
[20] U. Christensen and A. Tilgner, "Power requirement of the geodynamo from ohmic losses in numerical and laboratory dynamos", *Nature* **429** (2004), pp. 169–171.
[21] S. Aumaître, M. Berhanu, M. Bourgoin, et al., "The VKS experiment: turbulent dynamical dynamos", *Comptes Rendus. Physique* **9** (2008), no. 7, pp. 689–701.
[22] C. J. P. Gissinger, "A numerical model of the VKS experiment", *Eur. Phys. Lett.* **87** (2009), no. 3, article no. 39002.
[23] A. Giesecke, F. Stefani and G. Gerbeth, "Role of Soft-Iron Impellers on the Mode Selection in the von Kármán–Sodium Dynamo Experiment", *Phys. Rev. Lett.* **104** (2010), no. 4, article no. 044503.
[24] C. Nore, J. Léorat, J.-L. Guermond and A. Giesecke, "Mean-field model of the von Kármán sodium dynamo experiment using soft iron impellers", *Phys. Rev. E* **91** (2015), no. 1, article no. 013008.
[25] S. Kreuzahler, Y. Ponty, N. Plihon, H. Homann and R. Grauer, "Dynamo Enhancement and Mode Selection Triggered by High Magnetic Permeability", *Phys. Rev. Lett.* **119** (2017), no. 23, article no. 234501.
[26] J. Herault and F. Pétrélis, "Optimum reduction of the dynamo threshold by a ferromagnetic layer located in the flow", *Phys. Rev. E* **90** (2014), article no. 033015.
[27] F. Pétrélis and S. Fauve, "Saturation of the magnetic field above the dynamo threshold", *Eur. Phys. J. B, Condens. Matter Complex Syst.* **22** (2001), pp. 273–276.
[28] A. Tilgner and F. H. Busse, "Simulation of the bifurcation diagram of the Karlsruhe dynamo", *Magnetohydrodynamics* **38** (2002), pp. 35–40.
[29] A. Nunez, F. Petrelis and S. Fauve, "Saturation of a Ponomarenko type fluid dynamo", in *Dynamo and Dynamics, a Mathematical Challenge* (P. Chossat, D. Armbruster and I. Oprea, eds.), NATO Science Series, Kluwer Academic Publishers : Dordrecht, 2001, pp. 67–74.
[30] M. Berhanu, R. Monchaux, S. Fauve, et al., "Magnetic field reversals in an experimental turbulent dynamo", *Eur. Phys. Lett.* **77** (2007), no. 5, article no. 59001.
[31] F. Ravelet, M. Berhanu, R. Monchaux, et al., "Chaotic Dynamos Generated by a Turbulent Flow of Liquid Sodium", *Phys. Rev. Lett.* **101** (2008), no. 7, article no. 074502.
[32] C. Gissinger, "Dipole-quadrupole dynamics during magnetic field reversals", *Phys. Rev. E* **82** (2010), no. 5, article no. 056302.
[33] F. Pétrélis and S. Fauve, "Chaotic dynamics of the magnetic field generated by dynamo action in a turbulent flow", *J. Phys. Cond. Matt.* **20** (2008), no. 49, article no. 494203.
[34] F. Pétrélis, S. Fauve, E. Dormy and J.-P. Valet, "Simple Mechanism for Reversals of Earth's Magnetic Field", *Phys. Rev. Lett.* **102** (2009), article no. 144503.
[35] F. Pétrélis and S. Fauve, "Mechanisms for magnetic field reversals", *Philos. Trans. R. Soc. Lond., Ser. A* **368** (2010), no. 1916, pp. 1595–1605.
[36] J.-P. Valet, L. Meynadier and Y. Guyodo, "Geomagnetic dipole strength and reversal rate over the past two million years", *Nature* **435** (2005), pp. 802–805.
[37] B. Gallet and F. Pétrélis, "From reversing to hemispherical dynamos", *Phys. Rev. E* **80** (2009), no. 3, article no. 035302.
[38] B. Gallet, S. Aumaître, J. Boisson, et al., "Experimental Observation of Spatially Localized Dynamo Magnetic Fields", *Phys. Rev. Lett.* **108** (2012), no. 14, article no. 144501.
[39] F. Pétrélis, J. Besse and J.-P. Valet, "Plate tectonics may control geomagnetic reversal frequency", *Geophys. Res. Lett.* **38** (2011), no. 19, article no. L19303.
[40] V. Courtillot and P. Olson, "Mantle plumes link magnetic superchrons to phanerozoic mass depletion events", *Earth Planet. Sci. Lett.* **260** (2007), no. 3, pp. 495–504.
[41] S. C. Cande and D. V. Kent, "Revised calibration of the geomagnetic polarity timescale for the Late Cretaceous and Cenozoic", *J. Geophys. Res. Solid Earth* **100** (1995), no. B4, pp. 6093–6095.
[42] B. R. Phillips and H.-P. Bunge, "Heterogeneity and time dependence in 3D spherical mantle convection models with continental drift", *Earth Planet. Sci. Lett.* **233** (2005), no. 1, pp. 121–135.

[43] J. Li, T. Sato and A. Kageyama, "Repeated and Sudden Reversals of the Dipole Field Generated by a Spherical Dynamo Action", *Science* **295** (2002), no. 5561, pp. 1887–1890.

[44] J. Wicht and P. Olson, "A detailed study of the polarity reversal mechanism in a numerical dynamo model", *Geochemistry, Geophys. Geosystems* **5** (2004), no. 3, article no. Q03H10.

[45] C. Gissinger, "A new deterministic model for chaotic reversals", *Eur. Phys. J. B, Condens. Matter Complex Syst.* **85** (2012), article no. 137.

[46] T. Frasson, S. Labrosse, H.-C. Nataf, N. Coltice and N. Flament, "On the impact of true polar wander on heat flux patterns at the core-mantle boundary", *EGUsphere* **2023** (2023), pp. 1–24.

ACADÉMIE DES SCIENCES
INSTITUT DE FRANCE

Comptes Rendus. Physique
2024, Vol. 25, Special issue S3, p. 629-647
https://doi.org/10.5802/crphys.214

Research article / *Article de recherche*

Geophysical and astrophysical fluid dynamics in the laboratory / *Dynamique des fluides géophysiques et astrophysiques au laboratoire*

The DRESDYN precession experiment

L'expérience de précession DRESDYN

Frank Stefani [a,*], Sten Anders [a], Sven Eckert [a], Nico Freyer [a], Gunter Gerbeth [a], André Giesecke [a], Thomas Gundrum [a], Peter Kaever [a], Vivaswat Kumar [a], Federico Pizzi [b], Dirk Räbiger [a], Ján Šimkanin [c], Christian Steglich [a], Tobias Vogt [a], Nicole Wagner [a] and Gerald Wedel [a]

[a] Helmholtz-Zentrum Dresden-Rossendorf, Bautzner Landstr. 400, D-01328 Dresden, Germany

[b] Department of Fluid Mechanics, Universitat Politècnica de Catalunya-Barcelona Tech, Barcelona 08034, Spain

[c] Institute of Geophysics of the Czech Academy of Sciences, Boční II/1401, Praha 4-Spořilov 141 31, Czech Republic

E-mails: F.Stefani@hzdr.de (F. Stefani), S.Anders@hzdr.de (S. Anders), S.Eckert@hzdr.de (S. Eckert), N.Freyer@hzdr.de (N. Freyer), G.Gerbeth@hzdr.de (G. Gerbeth), A.Giesecke@hzdr.de (A. Giesecke), Th.Gundrum@hzdr.de (Th. Gundrum), P.Kaever@hzdr.de (P. Kaever), V.Kumar@hzdr.de (V. Kumar), federico.pizzi@upc.edu (F. Pizzi), D.Raebiger@hzdr.de (D. Räbiger), jano@ig.cas.cz (J. Šimkanin), csteglich@gmx.de (C. Steglich), T.Vogt@hzdr.de (T. Vogt), N.Wagner@hzdr.de (N. Wagner), G.Wedel@hzdr.de (G. Wedel)

Abstract. The most ambitious project within the DREsden Sodium facility for DYNamo and thermohydraulic studies (DRESDYN) at Helmholtz-Zentrum Dresden-Rossendorf (HZDR) is the set-up of a precession-driven dynamo experiment. After discussing the scientific background and some results of water pre-experiments and numerical predictions, we focus on the numerous structural and design problems of the machine. We also outline the progress of the construction work and give an outlook for the upcoming experimental campaigns.

Résumé. Le projet le plus ambitieux au sein de l'installation DREsden Sodium pour les études DYNamo et thermohydrauliques (DRESDYN) au Helmholtz-Zentrum Dresden-Rossendorf (HZDR) est la mise en place d'une expérience de dynamo entrainée par précession. Après avoir discuté du contexte scientifique, de quelques résultats d'expériences préliminaires en eau et de prédictions numériques, nous nous concentrons sur les nombreux problèmes structurels et de conception de la machine. Nous décrivons également l'avancement des travaux et donnons un aperçu des campagnes expérimentales prévues.

Keywords. precession, dynamo, sodium.

Mots-clés. précession, dynamo, sodium.

* Corresponding author

Funding. European Research Council (ERC) under the European Union's Horizon 2020 research and innovation program (Grant Agreement No. 787544), Deutsche Forschungsgemeinschaft (Grant No. GI 1405/1-1).

Manuscript received 1 March 2024, revised 29 July 2024, accepted 3 October 2024.

1. Introduction

Hydromagnetic dynamo action in moving electrically conducting fluids is at the root of planetary, stellar and galactic magnetic fields [1]. While dynamo *theory* is now a well-established cornerstone of magnetohydrodynamics [2,3], dynamo *experiments* have been rare due to the enormous technical effort that is required for their successful realization. Yet, the last decades have seen significant progress in this field [4–8], starting with the nearly concurrent successes of the single-scale, Ponomarenko-type dynamo in Riga [9–14] and the two-scale α^2-type dynamo in Karlsruhe [15–18], followed by the von-Kármán-sodium (VKS) experiment in Cadarache [19–23]. Despite, or better, because of the use of impellers with high magnetic permeability [24–26], the latter experiment has shown a wealth of most interesting dynamical effects, including field reversals and excursions, depending on the rotation rates of two impellers. With regard to comparable events the geomagnetic field is known to undergo, these results have spurred new theoretical efforts to understand the underlying physical mechanism(s) in a more generic sense [27–29].

It is here where astronomical, or harmonic, forcings of dynamos come into play [30]. As discussed by Consolini and De Michelis [31] (and later corroborated in a simple α^2-dynamo model [32]) the probability density of the intervals between reversals appears to be governed by a stochastic resonance with the 95-kyr periodicity of the ellipticity of the Earth's orbit. Further paleomagnetic data suggest complementary influences of the other two Milankovic cycles, viz., precession and nutation, on the geodynamo [33]. Tidal forces have also been invoked as possible sources of the (early) geodynamo, although a quantification of the effects of all these forces, and their interaction with more conventional convective dynamo drivers, is still under scrutiny [34]. The same applies to precession as a source of the ancient lunar dynamo [35,36], or of the magnetic field of the asteroid Vesta [37].

Going beyond planets, moons and asteroids, there is growing empirical evidence that the solar dynamo might also be influenced by astronomical forcings. First and foremost, it is the suspicious (though not undisputed, see [38,39]) synchronicity of the Schwabe cycle with the 11.07-yr periodicity of the envelope of the Venus-Earth-Jupiter alignments that points to a possible influence of tides on the dynamo [40–48]. The two-planet spring tides of those planets were recently shown [49,50] to be capable of exciting magneto-Rossby waves with typical periods between 100 and 300 days, whose joint quadratic action indeed comprises a 11.07-yr periodicity that may well be capable of entraining the solar dynamo by parametric resonance. Moreover, longer type-periodicities, such as the Suess–de Vries cycle, could arise as a 193-yr beat period of the primarily synchronized 22.14-yr Hale cycle with the 19.86-yr period of the rosette-shaped motion of the Sun around the barycenter of the solar system. First attempts to apply the underlying orbit-spin coupling [51] to the case of the Sun [52] point to an interesting parallelity with precession (for the specific influence of eccentric orbits on rotating ellipsoids, cp. [53]).

That said, this paper will exclusively concentrate on how to generate, in the lab, a precession driven flow that is prone to dynamo action. Our restriction to precession follows from two general considerations on how to progress from the pioneering experiments in Riga, Karlsruhe and Cadarache towards a more "natural", i.e. truly homogeneous, dynamo. First, we note that any realization of a convection driven dynamo in the lab would be extremely expensive, requiring an enormous heating power and/or vessel size (although this hurdle could possibly

be overcome by using centrifugal buoyancy [54]). Second, among the various candidates of astronomical forcings, precession represents a key paradigm with a relatively straightforward (although challenging) technical implementability. In this regard, the DRESDYN precession experiment may, hopefully, pave the way for later implementations of libration, nutation, tides or changes of the orbital ellipticity.

To get a glimpse on the advantages and limitations of dynamo experiments we compare, in Figure 1, some dimensionless numbers reachable at the DRESDYN machine with those that are accessible by present-day numerics, and those of the geodynamo. This is illustrated in two panels covering (a) the magnetic Reynolds number and the magnetic Prandtl number and (b) the Reynolds number and the Poincaré number. While, evidently, the experiment can go much farther than simulations, it is still way off the reality of the geodynamo.

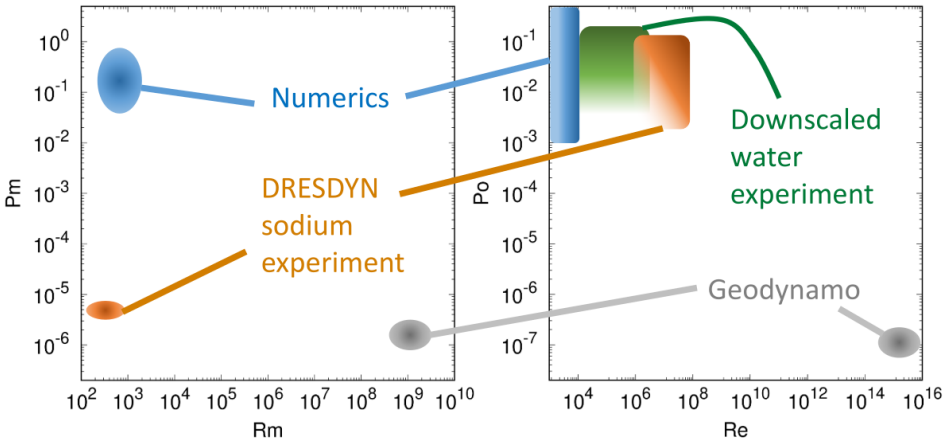


Figure 1. Comparison of various dimensionless numbers of the DRESDYN precession experiment, the 1 : 6 downscaled water experiment, the utilized numerics, and the geodynamo. Using the radius R, the angular frequencies of the rotation and precession, Ω_c and Ω_p, the viscosity ν and the electrical conductivity σ, (a) shows the magnetic Reynolds number $Rm = \mu_0 \sigma R^2 \Omega_c$ and the magnetic Prandtl number $Pm = \nu \mu_0 \sigma$, while (b) shows the (hydrodynamic) Reynolds number $Re = R^2 \Omega_c / \nu$ and the Poincaré number $Po = \Omega_p / \Omega_c$.

In the next section, we delineate the fundamental hydrodynamics behind precession-driven flows in cylindrical geometry, and discuss the dependence of the flow on the main parameters such as Reynolds number, precession ratio, and nutation angle. Then we explore the suitability of the emerging flows for dynamo action and indicate some optimum experimental parameters.

Section 3 is then devoted to the more technical aspects of the experiment, including the massive basement, the main parts of the platform and the design of the rotation vessel.

The paper will close with a summary and an outlook on the upcoming experimental campaigns.

2. Precession driven flows in cylindrical geometry, and their dynamo action

Precession-driven flows were first investigated for the case of an inviscid fluid in a spheroidal cavity [55,56] for which an analytical solution was obtained assuming uniform vorticity. This so-called Poincaré solution was later extended by Busse [57] to the weakly nonlinear regime, including the viscous effects in boundary layers. Meanwhile, the theory of precession-driven flows has

been extended to other geometries, and a couple of corresponding experiments were dedicated to understand particular features such as instabilities [58–60], large-scale vortex formation [61], the transition to turbulence and its hysteretic behaviour [62–67]. Dynamo action for precession-driven flows was numerically found in various geometries [68–75]. Most remarkably, a field amplification by a factor of three was reached in an early liquid-sodium experiment by Gans [76].

In this section, we will first present the mathematical and numerical basics of precession driven flows in cylindrical geometry and some details of a corresponding down-scaled water experiment. Then we will compare the obtained numerical and experimental results for different precession ratios and nutation angles. Based on those findings we will discuss some predictions for dynamo action in the large machine.

2.1. *Basic theory*

Assuming an incompressible fluid with constant density ρ, the Navier–Stokes equation in the doubly-rotating frame (henceforth called the *container frame*),

$$\frac{\partial \boldsymbol{u}}{\partial t} + \boldsymbol{u}\cdot\boldsymbol{\nabla}\boldsymbol{u} = -\frac{\boldsymbol{\nabla} P}{\rho} \underbrace{-2(\boldsymbol{\Omega_p} + \boldsymbol{\Omega_c}) \times \boldsymbol{u}}_{\text{Coriolis force } \boldsymbol{F_c}} \underbrace{-(\boldsymbol{\Omega}_\mathrm{p} \times \boldsymbol{\Omega_c}) \times \boldsymbol{r}}_{\text{Poincaré force } \boldsymbol{F_p}} + \nu\nabla^2\boldsymbol{u}. \tag{1}$$

comprises, as indicated, a Coriolis and a Poincaré force term. Here, $\boldsymbol{u}$ is the velocity field (supposed to be divergence-free), P a modified pressure (that includes also centrifugal terms), $\boldsymbol{\Omega}_p$ the precession angular frequency, $\boldsymbol{\Omega}_c$ the angular frequency of the container, and ν the kinematic viscosity of the fluid [77]. In the container frame, the boundary conditions at all walls are no-slip.

Denoting by α the nutation angle between the rotation and the precession axis (see Figure 2 (a)), $\boldsymbol{\Omega}_\mathrm{p}$ in the container frame reads

$$\boldsymbol{\Omega}_p(t) = \Omega_p\big[\sin\alpha\cos(\Omega_c t+\varphi)\widehat{\boldsymbol{r}} - \sin\alpha\sin(\Omega_c t+\varphi)\widehat{\boldsymbol{\varphi}} + \cos\alpha\widehat{\boldsymbol{z}}\big], \tag{2}$$

with $\widehat{\boldsymbol{r}}$, $\widehat{\boldsymbol{\varphi}}$, and $\widehat{\boldsymbol{z}}$ being the unit vectors in radial, azimuthal, and axial direction, respectively.

Then, the Poincaré force in equation (1), which results from the temporal change of the orientation of the rotation axis, acquires the form

$$\boldsymbol{F}_p = -\Omega_c\Omega_p r\sin\alpha\cos(\Omega_c t+\varphi)\widehat{\boldsymbol{z}}\,. \tag{3}$$

The spatial structure of this Poincaré force preordains the fundamental pattern of the directly driven flow which consists of a non-axisymmetric mode with azimuthal wave number $m = 1$ ($\propto \cos\varphi$) and axial wave number $k = 1$, representing a flow that is anti-symmetric with respect to the equatorial plane (Figure 2 (b), middle).

For a more general characterization of precession driven flows in cylinders with height H and radius R it is most appropriate to use the eigenfunctions (inertial waves), resulting from the linear inviscid approximation of rotating systems, which have the analytical form

$$\boldsymbol{U}_j(r,z,\varphi,t) = \boldsymbol{u}_j(r,z)e^{\mathrm{i}(\omega_j t+m\varphi)} + \text{c.c.}\,. \tag{4}$$

Here, the collective index j incorporates three integers m,k,n, comprising the azimuthal wave number m and the axial wave number k. A third (radial) number n counts the roots of the dispersion relation

$$\omega_j\zeta_j \mathrm{J}_{m-1}(\zeta_j) + m\big(2-\omega_j\big)\mathrm{J}_m(\zeta_j) = 0 \qquad \text{with} \qquad \omega_j = \pm 2\left[1+\left(\frac{\zeta_j}{\Gamma k\pi}\right)^2\right]^{-1/2}, \tag{5}$$

that determines the eigenfrequences of the inertial modes. In Equation (5), J_m denotes the Bessel function of order m, Γ the aspect ratio defined by $\Gamma := H/R$, and ζ_j a radial wave number with its position in the sequence of zeros of (5) corresponding to the number of half-cycles in the radial

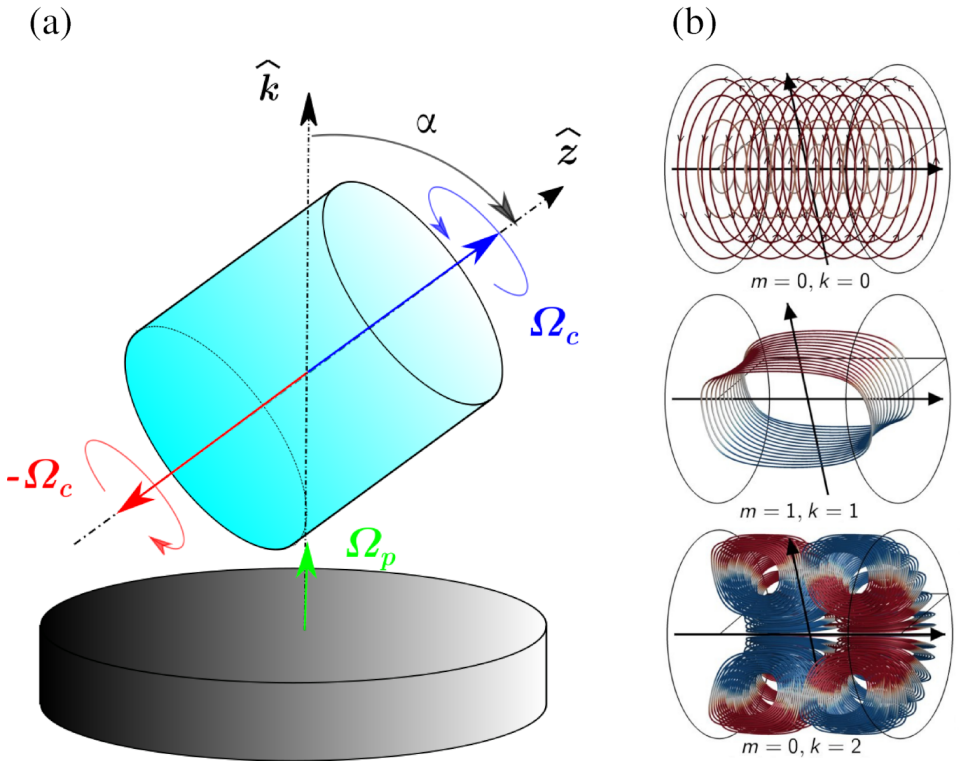


Figure 2. (a) Sketch of a precessing cylinder with the container's angular frequency $\Omega_c = 2\pi f_c$ and the precession angular frequency $\Omega_p = 2\pi f_p$. The nutation angle α between the axis of precession $\widehat{\boldsymbol{k}}$ and the axis of rotation $\widehat{\boldsymbol{z}}$ varies between 0 and 90°. Pro- and retrograde precession is indicated in blue and red, respectively. (b) The three most important flow modes are (from top to bottom): the geostrophic, axisymmetric mode with $(m = 0, k = 0)$; the forced mode with $(m = 1, k = 1)$, and the axisymmetric double-roll mode with $(m = 0, k = 2)$.

direction. For the following it is important that an inertial mode becomes resonant when the frequency of the precession matches the natural frequency of a corresponding eigenfunction. For the resonance of the simplest inertial (or Kelvin) mode with $m = 1$, $k = 1$ and $n = 1$, this condition applies to the aspect ratio $\Gamma = 1.9898$, which is indeed very close to the value $\Gamma = 2$ chosen for the DRESDYN experiment.

Going beyond the linear regime, for increasing forcing the nonlinear interactions of the forced mode with itself, and with its viscous modifications in the boundary layers, become relevant. The underlying nonlinear theory is a quite complex issue and allows for closed solutions only under special conditions in the weakly nonlinear regime [78–80]. One of the major flow contributions beyond the directly forced mode is connected with a considerable modification of the azimuthal circulation [59,81] that is always oriented opposite to the (initial) solid body rotation, giving rise to a "braking" of the flow in the bulk of the cylinder. A direct consequence of the reduced rotation is the observed detuning [82–85] of free inertial modes that emerge in form of triadic resonances [86,87]. For very strong forcing, the rotation profile even becomes Rayleigh-unstable, leading to an abrupt transition into a turbulent flow regime, which also shows a hysteretic behaviour [63].

2.2. *Numerics*

Having discussed the basic physics of precession-driven flows in the container frame, we turn now to the numerical simulations that were actually carried out in the so-called *turntable frame*. In this frame, the Poincaré force vanishes and the boundary conditions are governed by the cylinder walls rotating at Ω_c. We used the spectral element Fourier code *Semtex* [88], and meshed the domain with 300 quadrilateral elements in the meridional half plane and 128 Fourier modes in azimuthal direction.

As for the magnetic field, we focus on the kinematic dynamo problem and solve the corresponding induction equation in a fluid with conductivity σ

$$\frac{\partial \boldsymbol{B}}{\partial t} = \boldsymbol{\nabla} \times \left(\langle \boldsymbol{u} \rangle \times \boldsymbol{B} - \frac{\nabla \times \boldsymbol{B}}{\mu_0 \sigma} \right) \tag{6}$$

for the resulting time-averaged velocity field $\langle \boldsymbol{u} \rangle$ by means of a finite volume method with constraint transport which maintains the divergence-free condition $\nabla \cdot \boldsymbol{B} = 0$. While, in principle, the code developed in [89] allows a correct treatment of vacuum boundary conditions by employing an additional surface integral equation, for our quite comprehensive parameter studies we employed the simplified vertical-field conditions by demanding all tangential field components to vanish at the surface. Comparable studies, as previously applied to other dynamo experiments [90–92], showed that vertical-field conditions typically lead to somewhat lower thresholds for the occurrence of dynamo action when compared to more realistic vacuum boundary conditions. Corresponding comparisons for the DRESDYN experiment are ongoing and will be published elsewhere.

Specifically, the simulations were carried out as follows: at $t = 0$ we started with a pure solid body rotation, which in the turntable frame reads $\boldsymbol{u} = (\Omega_c r)\widehat{\boldsymbol{\varphi}}$. Then we imposed the precessional forcing, and waited until the flow had reached a statistically steady regime. After inserting the resulting time-averaged flow field $\langle \boldsymbol{u} \rangle$ into the induction equation (6), the kinematic dynamo simulations were run for more than one diffusion time, after which an exponential growth, or decay, is clearly established. As we will see later, dynamo action mainly occurs in the transition regime (between the laminar and the fully turbulent regime) which is governed by only a few large-scale modes. Here, the utilized time-averaged flow can be considered as a good representative of the total flow.

The typical parameter space investigated numerically for the kinematic dynamo problem covers Reynolds numbers $Re := R^2|\Omega_c + \Omega_p \cos\alpha|/\nu \in [1000, 10000]$ and precession ratios (or Poincaré numbers) $Po := \Omega_p/\Omega_c \in \pm [0.01, 0.20]$. Later on, we will focus on the results for nutation angles $\alpha = 75°$, both for prograde and retrograde precession, as well as for $\alpha = 90°$.

2.3. *The* 1 : 6 *down-scaled water experiment*

Complementary to the numerical simulations, we have set-up and utilized a water experiment, which is 1 : 6 down-scaled with respect to the big machine, to measure the flow structure and amplitude (Figure 3). This device consists of a cylindrical vessel with inner height $H = 326$ mm and inner radius of $R = 163$ mm. Just as the big one, the down-scaled vessel can rotate with a maximum rotation rate of 10 Hz around its axis, while the turntable can rotate with up to 1 Hz. One end wall of the vessel is equipped with 9 ultrasound transducers (TR0408SS, Signal Processing SA, Lausanne), six of which being arranged in a radial array ranging from $r/R = 0$ to 0.92. Four transducers are located at $r/R = 0.92$ (i.e., $r = 150$ mm), with 90° azimuthal spacing in order to estimate the azimuthal symmetry of the flow. All transducers are aligned parallel to the vessel axis and can capture the instantaneous axial velocity distribution between $z/H = 0$ and 1. The transducers are connected to an ultrasound Doppler velocimeter (DOP 3010, Signal

Processing SA, Savigny) that records the velocity profiles with a temporal resolution of about 10 Hz.

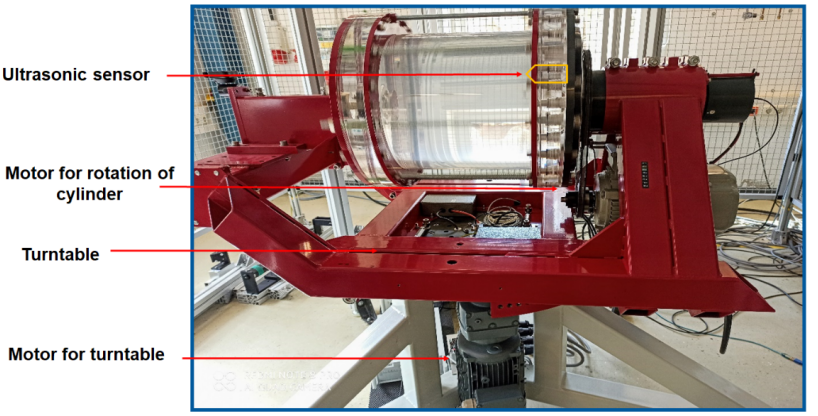


Figure 3. The 1 : 6 down-scaled water precession experiment with the central vessel of radius $R = 163$ mm and height $H = 326$ mm. The nutation angle can vary between 60° and 90°.

Later below, we will show measurements with one ultrasonic transducer at radius $r = 150$ mm. During the experiments, the room was air-conditioned in order to minimize any changes of the temperature-dependent viscosity of water (assumed as $\nu = 1 \times 10^{-6} \mathrm{m}^2\mathrm{s}^{-1}$).

2.4. *Comparison between numerical and experimental results*

In the following, we will summarize and compare some of the most important numerical and experimental results, with the main focus on the flow dependence on the precession ratio Po and the nutation angle α. As for the latter, we will concentrate on the exemplary cases 75° prograde, 90° and 75° retrograde (more results can be found in [93–95]). Figure 4 shows the temporal evolution of the depth dependence of the axial velocity profile u_z, as measured by one UDV sensor at $r = 150$ mm (the depth indicates the distance along the beam axis from the transducer). The three rows display results for $\alpha = 75°$ prograde, 90° and $\alpha = 75°$ retrograde. The visible oscillatory pattern of the velocity profile (governed by the rotational frequency Ω_c of the cylinder to which the sensor is attached) is representative of the directly forced $(m = 1, k = 1)$ mode which is stationary in the turntable frame.

With growing Po we observe, for all considered angles, an increasingly complex flow pattern. At lower values of Po (first column), the flow shows a stable structure which is mirrored by the regular pattern in form of vertical stripes in all cases. As Po exceeds a certain higher value, for $\alpha = 75°$ prograde and 90° the flow structure changes and exhibits a breaking of the equatorial symmetry, as evidenced by the emerging tilt of the stripes. By contrast, in the 75° retrograde case (third row) the occurrence of the tilt is shifted to larger values of Po.

This breaking of the equatorial symmetry indicates a flow state transition at a critical value of Po, where Kelvin modes with even axial wave numbers emerge [93]. This transition has considerable effects on the amplitudes of all flow modes, which we will quantify in the following.

The mode amplitudes are calculated by decomposing the axial velocity field $u_z = u_z(r, \varphi, z, t)$ into (m, k) modes (the details of the underlying discrete sine transformation can be found in [95]). Of the various observable modes, we mainly examined those which acquire substantial

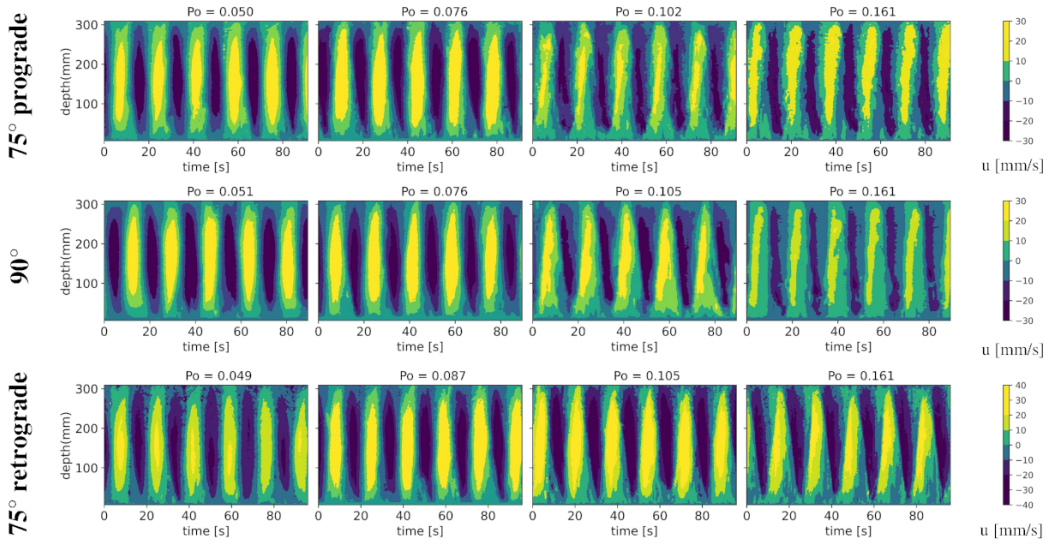


Figure 4. Axial velocity u_z, measured by one UDV sensor positioned at $r = 150$ mm, in dependence on time and depth, for three different nutation angles and four different Po. The Reynolds number in all cases was approximately 10^4. Adapted from reference [95].

amplitudes and are most relevant for dynamo action [74]. This applies, in particular, to the directly forced ($m = 1, k = 1$) mode and the torus-shaped ($m = 0, k = 2$) mode (see Figure 2 (b)).

Figure 5 shows the measured and simulated amplitudes of these prominent modes versus the precession ratio Po for the three angles 75° prograde, 90°, and 75° retrograde, respectively. Note that, since a comprehensive numerical parameter sweep at $Re \approx 10^4$ would have been forbiddingly expensive, the results of simulations carried out at $Re = 6500$ were linearly extrapolated to the higher experimental value $Re = 10^4$ (while, in this low Re regime, the scaling of the mode amplitudes might actually be a bit flatter then linear, any arising discrepancies remain rather small).

For 75° prograde and 90°, we observe that the directly forced ($m = 1, k = 1$) mode increases up to $Po \approx 0.08$, beyond which there is an abrupt transition of the flow state connected with a breakdown of this mode. Simultaneously, an axially symmetric mode ($m = 0, k = 2$) emerges in a narrow range of Po, which corresponds to the double-roll structure that was previously shown to be most relevant for dynamo action [93]. Obviously, the nutation angle influences the critical Po, such that as the angle increases (from 75° prograde to 90°), so does the critical Po (from 0.087 to 0.10).

By contrast, the data for 75° retrograde precession exhibit not such a clear breakdown of the directly forced ($m = 1, k = 1$) mode whose amplitude rather shows a gradual decrease with Po. At the same time, we observe a smoother increase of the axially symmetric ($m, = 0, k = 2$) mode within the considered range of Po. In comparison to the other cases, $\alpha = 75°$ retrograde exhibits the largest amplitude of the ($m = 0, k = 2$) mode, and the critical Po is shifted to larger values. In general, the results of the numerical simulations are in good agreement with the experimental values, with the exception of the ($m = 0, k = 2$) mode for the case 75° prograde when Po is large. The latter discrepancy is presently not well understood.

The right column of Figure 5 may help to explain the observed transitions. It shows, for the three nutation angles, the radial profile of the angular momentum $L(r) = r u_\varphi(r)$, averaged both in azimuthal and axial direction (excluding the boundary layers at the endcaps). For all α, with increasing Po the angular momentum deviates more and more from the original solid

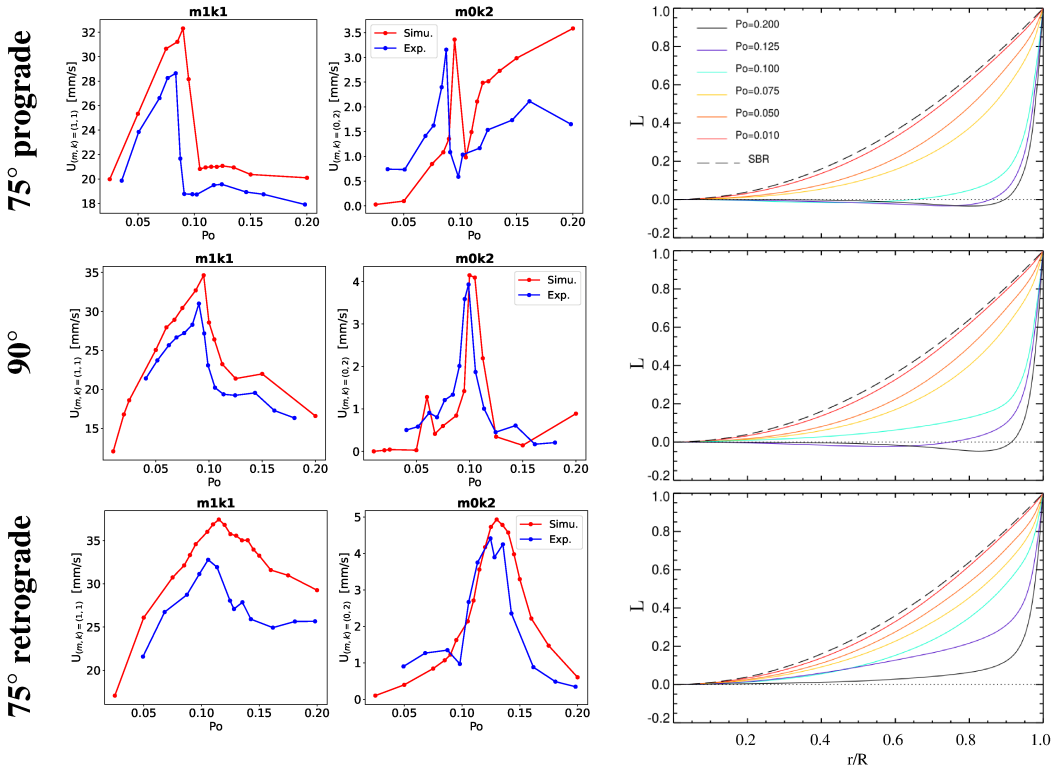


Figure 5. Left: Comparison of the amplitudes of the directly forced ($m = 1, k = 1$) mode and the axisymmetric ($m = 0, k = 2$) mode between numerically calculated (red) and experimentally measured flows (blue) for three representative nutation angles. Note that the numerical values were computed at $Re = 6500$ and then (linearly) extrapolated to the experimental value $Re = 10000$. Adapted from reference [95]. Right: Radial distribution of the (normalized) angular momentum, determined numerically at $Re = 6500$, for the three considered angles. Adapted from reference [94].

body rotation (SBR) and eventually becomes rather flat, at least until $r/R < 0.8$, say. Remarkably, though, for 75° prograde and 90°, L turns slightly negative, indicating a *counter-rotation* in this region, and a breaking of Rayleigh's stability criterion (radially increasing L^2). By contrast, this breaking of the Rayleigh criterion does not occur for 75° retrograde, which might explain the smoother transition in this case. However, the violation of the Rayleigh criterion occurs only (appr. 15 per cent) after the onset of instability, suggesting that a complete understanding of this connection would also require to consider the influence of large-scale radial and axial flow components (a quantitative improvement might also result when measuring the angular momentum in the frame of inertia rather than in the turntable frame as done here).

2.5. *Towards an optimized dynamo*

Based on the rather consistent experimental and numerical findings of the last subsection, we ask now what Poincaré number and nutation angle might be best suited for dynamo action. The relevant criterion is a minimum value of the critical magnetic Reynolds number $Rm = RePm$ (with the magnetic Prandtl number $Pm = \mu_0 \sigma \nu$). Self-excitation is characterized by an

exponential increase of the volume-averaged magnetic energy when time-stepping the induction equation (6). From the temporal evolution of the magnetic energy the growth rate γ is calculated.

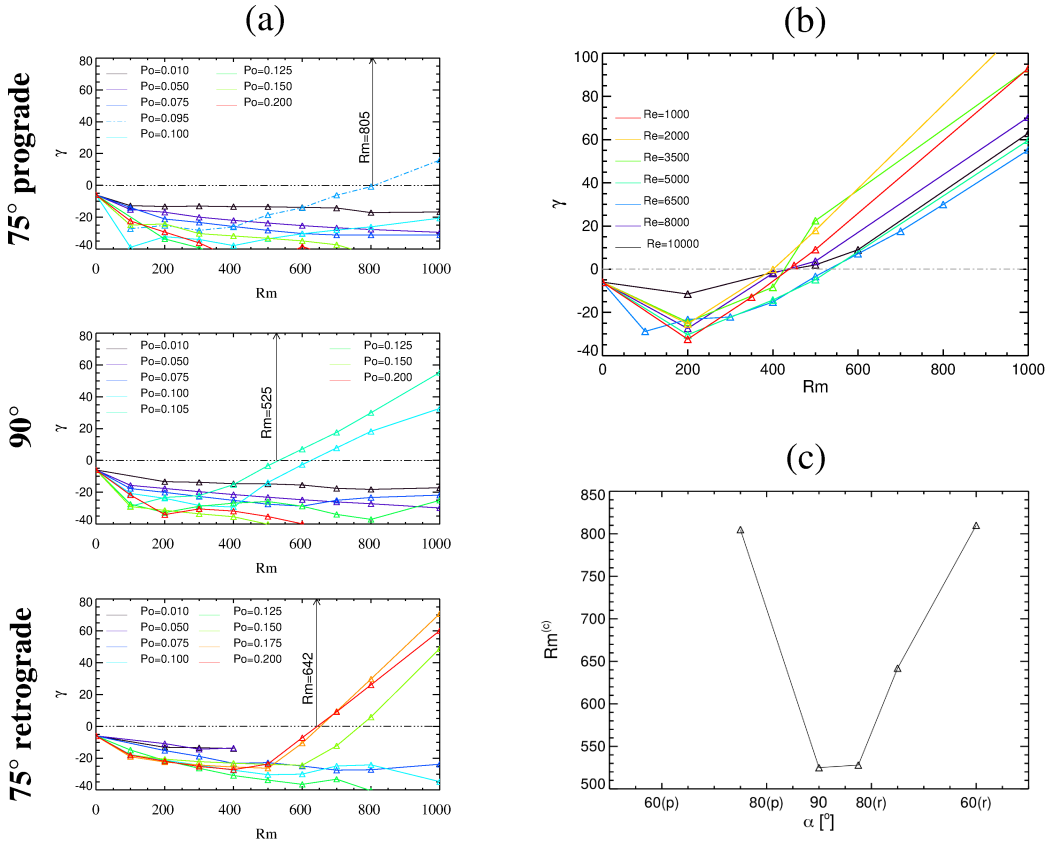


Figure 6. (a) Growth rate γ of the magnetic field energy as a function of the magnetic Reynolds number $Rm = RePm$ for three nutation angles α, computed at $Re = 6500$. The different curves represent different precession ratios, and the arrows mark the dynamo onset at the optimum Po characterized by the lowest critical Rm. (b) Dependence of the lowest critical Rm on Re for the special case $\alpha = 90°$. Note the decrease of the critical Rm from 525 (for $Re = 6500$) to 430 (for $Re = 10000$), in agreement with [74]. (c) Dependence of the optimized critical Rm on the nutation angle α, simulated for $Re = 6500$. The optimum α seems to lie somewhere between 90° and 82.5° retrograde. (a) and (b) are adapted from Reference [95]. (c) is adapted from [96].

In Figure 6 (a), we plot the Rm-dependence of γ for eight different precession ratios Po, and a fixed $Re = 6500$. The critical Rm achieves a minimum of 525 for $Po = 0.1$ and $\alpha = 90°$. For this particular angle, Figure 6 (b) specifies the Rm-dependence of γ when computed for different values of Re. We observe a sort of convergence to a critical Rm of 430, which had already been found in [74,93]. However, as shown in Figure 6 (c), the real optimum might still lie at slightly retrograde precession, somewhere between 90° and 82.5°. It is this range of nutation angles where we will start our hunt for dynamo action. As for Po, we will focus on the transition region with a strong contribution of the $(m = 0, k = 2)$ mode, which for high Re seems to converge to a Po value between 0.06 and 0.07 [63,93]. Note, however, that beyond the transition region, i.e. in the fully turbulent regime, the use of the time-averaged velocity field in the induction equation

becomes increasingly problematic. Dynamo simulations for the time-dependent flow fields in this regime are underway and will be published elsewhere.

3. The machine

Following up on the pioneering experiments in Riga, Karlsruhe and Cadarache, the DRESDYN precession experiment (Figure 7) is supposed to work as a truly homogeneous dynamo that does not use any impellers, guiding tubes, or magnetic materials (for the two other recent experimental efforts in Maryland and Madison with a similar ambition, see [97] and [98], respectively.) The central rotation vessel encases a cylindrical sodium volume of 2 m diameter and 2 m height (Figure 8). This size resulted as a sort of optimum from the two requirements to reach a magnetic Reynolds number of about 700 while keeping the necessary driving power (which scales, in the turbulent regime, as $\sim Rm^3/R$) in the technically affordable range of 1 MW. While the latter value can be roughly estimated from extrapolating the 10 W jump as measured in the downscaled water experiment at 4 Hz (see [63, Figure 4]) it certainly needs real confirmation in the "big one". For this vessel, we aim at reaching a rotation rate of 10 Hz to obtain $Rm = 700$, and a precession rate of 1 Hz to cover the laminar, the fully turbulent, and the transition state in between them which is the most "dynamo-prone" one. This motion of the vessel, which is driven by a motor with maximum electric power of 1.2×10^6 Watts, results in an acceleration of 500 g and a total gyroscopic torque of up to 8×10^6 Nm. The total budget of moving masses amounts to approximately 150 tons. From a mechanical perspective, the entire machine is in many respects at the edge of technical feasibility, so that a careful design and much optimization was required to ensure that the mechanical strain does not exceed the material limitations [99].

Due to the use of sodium (the best liquid conductor) and the high acceleration forces, critical components had to be developed and manufactured in-house. In addition to the mechanical challenges, this also included the design and implementation of both a personal safety system (PSS) and a machine interlock system. Here, the real-time extraction of internal states for machine-monitoring and an online camera inspection of the container surface had to be implemented. As this involves the use of FFT-transforms, a sampling rate of 6 kHz was selected for all sensors in the data acquisition system (DAQ). On the other side, this also ensures a high level of qualitative and quantitative data recording on both platform and vessel in order to answer the scientific questions posed to the experiment. To withstand the exceptional conditions (120°C, accelerations up to 500 g), commercially available DAQ-electronics were not qualified, so that a dedicated DAQ-system had to be developed and tested in-house. The communication between the sensor electronics on the vessel and the evaluation system is based on ethernet, providing sufficient bandwidth to transfer data via two signal rotary transmitters (for the container and the platform), in order to enable live processing and viewing of the measurement data.

The simultaneous rotation around two axes poses a couple of challenges for the filling and emptying procedures, heating and the handling of thermal expansion of sodium. To accommodate all resulting requirements, a decision was made in favor of a slightly enlarged vessel (Figure 8), comprising two conical volumes that serve, first, for a well-defined filling and emptying procedure at 43° vessel tilting, and, second, for hosting two bellows which will compensate the thermal expansion of the liquid sodium.

For the vessel material the austenitic steel 1.4571 was chosen which is well-known for its corrosion resistance against liquid sodium. A shell thickness of 3 cm makes it safe to withstand the centrifugal pressure of approximately 20 bar in case of pure rotation with 10 Hz. While for increasing precession ratio this total pressure decreases, it is complemented by an increasing pressure vacillation Δp of up to 10 bar, resulting from the gyroscopic forces (see [100, Figure 1]). In addition to those mechanical stresses, we also had to consider thermal stresses caused by

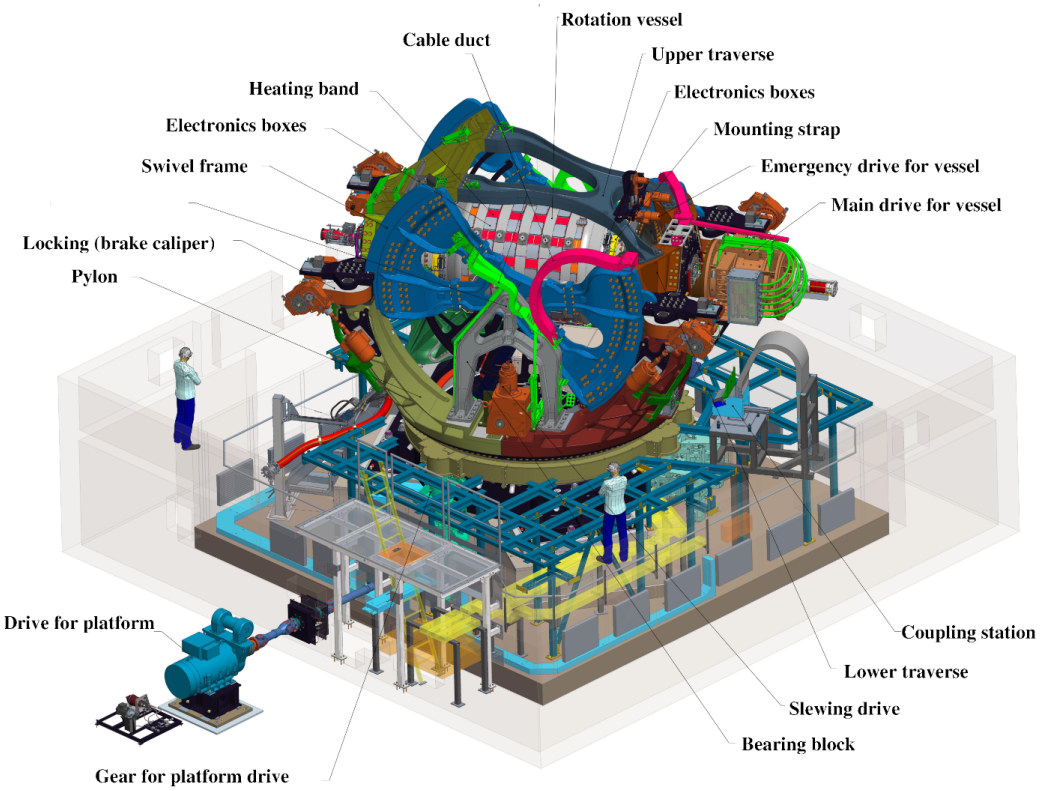


Figure 7. Drawing of the DRESDYN precession experiment with main parts indicated. The separate basement rests on 7 ferro-concrete pillars reaching 22 m deep into the bedrock. The machine is housed in a containment (the lower part of which being indicated in gray). The 540 kW drive for the platform is situated in a separate engine room, jointly with the two oil lubrication systems for the large slewing bearing and the two bearings for the rotation vessel.

the temperature difference over the shell when the rotating vessel is cooled by a strong flow of air [101].

Speaking of temperature: any attempt at perfectly controlling it, i.e. by using an oil jacket as in the Maryland experiment [97], would have required an enormous technical effort. Presently, cooling is realized by a strong air flow in the containment which provides (through the 3 cm stainless-steel wall of the vessel) a cooling power of around 50 kW. Heating before the experiment, and between the runs, is accomplished by heating foils with a total power of appr. 60 kW. In view of the vast thermal inertia of the sodium and the vessel, these cooling and heating processes would lead to temperature ramps of appr. 0.2 degree per minute which seem well manageable by a thorough protocol of the experimental campaign. The big player, though, is the expected hydrodynamic dissipation, going up to 1 MW in the fully turbulent regime, which indeed constrains the duration of individual runs.

Although the main goal of the experiment is to achieve dynamo action in a truly homogeneous volume, we have also provided some baffles at the end caps which can be inserted into the cylindrical volume. By increasing the penetration depth of the baffles, the flow transitions are shifted to larger Poincaré numbers [102]. This gives, on one hand, an additional handle to further optimize the dynamo conditions, but may, on the other hand, also help to elucidate the role of topographic roughness on the transport of angular momentum in rapidly rotating fluids [103].

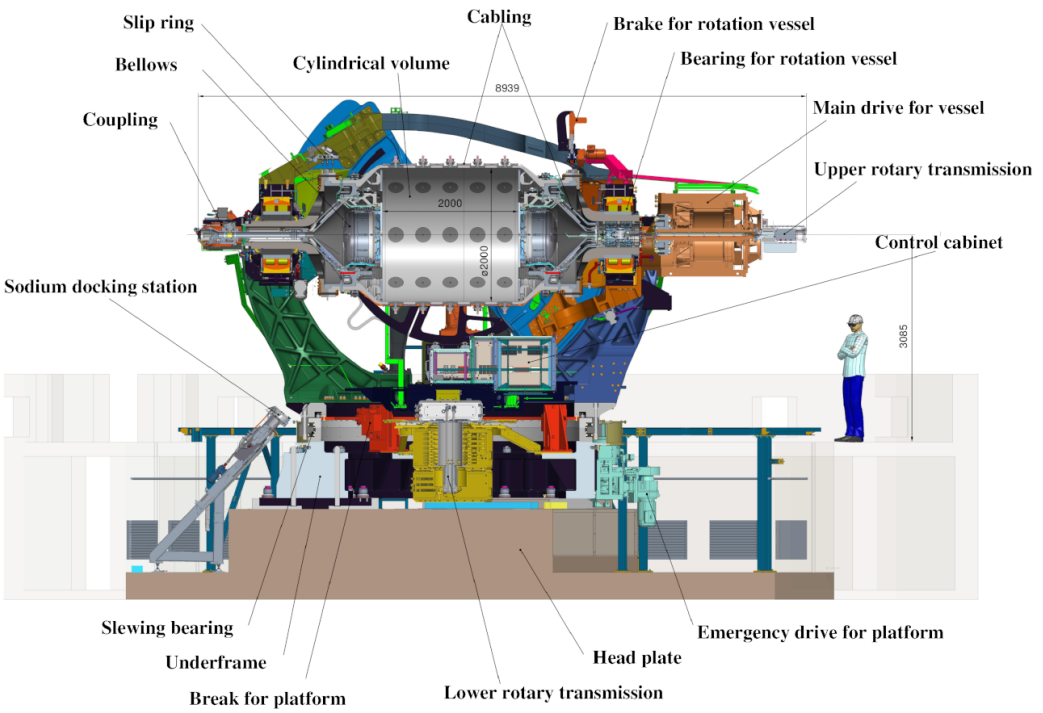


Figure 8. Sectional view of the DRESDYN precession experiment with the main dimensions indicated (in mm).

A particular challenge was the design of the tilting frame that allows to choose different angles between rotation and precession axis. Finding appropriate roller bearings for the vessel turned out to be quite demanding, mainly because of the huge gyroscopic torque. The same gyroscopic torque also requires a very stable basement, supported by seven pillars, each extending into the granite bedrock. For safety measures, the entire machine is housed in a containment. Since the double rotation cannot be stopped quickly in case of an accident, this containment is the only chance of preventing sodium jets (when spilling out of a potential leak) from covering all surrounding areas. For such accidents, the containment can be flooded with argon, which is stored in liquid form. A corresponding test has validated that by injecting 4 tons of argon the oxygen content in the containment can be reduced to 4 per cent which is low enough for extinguishing any sodium fire [104].

After many years of design and construction (see Figure 9 (a-c)), the “marriage” between the frame and the vessel was successfully carried out on 17 January 2024 (Figure 9 (d, e)). After accomplishing some remaining technical work, first precession experiments with water are scheduled for fall 2024. In these experiments, the flow diagnostics will mainly rely on the data of pressure sensors (situated in the flanges of the vessel) whose amplitudes and spatial structures can be matched to the typical flow modes discussed above. Some tests with UDV sensors are also foreseen, but will presumably be restricted to lower rotation rates when the velocities and the centrifugal accelerations are not too excessive. For the later sodium experiments, two rows of flanges will be equipped with Hall sensors to measure the magnetic field.



Figure 9. Some impressions from the construction, with relevant dates indicated. (a) Shell construction of the containment and the air duct (for cooling). (b) Insertion of the underframe. (c) Slewing bearing mounted on the underframe. (d) and (e) Insertion of the vessel into the frame. (f) The DRESDYN building.

4. Conclusion

Besides the 3 m diameter spherical Couette experiment in Maryland [97] and the 3 m diameter Madison plasma dynamo experiment (MPDX) [98], the DRESDYN precession experiment is another attempt to realize a truly homogeneous dynamo in the lab. Setting into motion a cylindrical volume of liquid sodium by two rotations, dynamo action is expected to start at a magnetic Reynolds number of around 430, a precession ratio of approximately 0.06, and a nutation axis close to 90°. For these parameters we expect a dynamo-prone flow state, governed by a combination of differential rotation, a remaining $(m = 1, k = 1)$ mode, and a double-roll mode of the $(m = 0, k = 2)$-type. Since this flow combination is not yet strongly turbulent, we do not expect any significant turbulence-enhanced resistivity which might have played (possibly) a detrimental role in previous dynamo experiments [105].

While we have little doubt that the flow state in the big machine will be quite similar to that extrapolated from numerical simulations and the results of the 1 : 6 down-scaled water experiment, there are some remaining caveats concerning the role of the magnetic boundary conditions on dynamo action. First water experiments, which are expected still for 2024, will be decisive in validating the mechanical integrity of the entire machine with respect to the huge mechanical loads resulting from the gyroscopic moment. Moreover, these water experiments will allow to validate the flow predictions based on previous numerical and experimental results, and to further constrain the optimal conditions for dynamo action. If everything runs smoothly, first sodium experiments may start in 2025, provided that the technical inspection of the rotation vessel after the water experiments does not reveal any structural failures. Apart from its specific goal to show self-excitation in a mechanically forced homogeneous fluid, we also hope that this experiment may act as a catalyst for further investigations into astronomical forcings of planetary and stellar dynamos.

Acknowledgments

We would like to thank Oliver Bähr, Martin Becker, Andre Büchner, Jürgen Claussner, Thomas Egeln, Hans-Olaf Engel, Johannes Feder, Tim Gitzel, Jonas Gorgis, Stefan Grunze, Jens Helbig, Frank Herbrand, Jakob Kaiser, Richard Kaubisch, Sebastian Köppen, Bert Lange, Markus Meyer, Benjamin Nebe, Pierre Ramm, Anett Schräger, Robert Stöckel, Thomas Süßmilch, Henrik Tietze, Thomas Wiesner, Bernd Wustmann, and Yvonne Zimmermann for technical support, and Johan Herault and Thomas Albrecht for early contributions to the project. The long-lasting cooperation with Georg Schnurr, Gunter Weigelt and Steffen Wohlrab from SBS Bühnentechnik Dresden, and with Michael Beitelschmidt and Stephan Rother from TU Dresden is gratefully acknowledged.

Declaration of interests

The authors do not work for, advise, own shares in, or receive funds from any organization that could benefit from this article, and have declared no affiliations other than their research organizations.

References

[1] H. K. Moffatt and E. Dormy, *Self-exciting fluid dynamos*, Cambridge Texts in Applied Mathematics, Cambridge University Press: Cambridge, 2019.
[2] F. Rincon, "Dynamo theories", *J. Plasma Phys.* **85** (2019), article no. 205850401.
[3] S. Tobias, "The turbulent dynamo", *J. Fluid Mech.* **912** (2021), article no. P1.
[4] A. Gailitis, O. Lielausis, E. Platacis, G. Gerbeth and F. Stefani, "*Colloquium:* Laboratory experiments on hydromagnetic dynamos", *Rev. Mod. Phys.* **74** (2002), pp. 973–990.
[5] F. Stefani, A. Gailitis and G. Gerbeth, "Magnetohydrodynamic experiments on cosmic magnetic fields", *Z. Angew. Math. Mech.* **88** (2008), pp. 930–954.
[6] G. Verhille, N. Plihon, M. Bourgoin, P. P. Odier and J.-F. Pinton, "Laboratory dynamo experiments", *Space Sci. Rev.* **152** (2010), pp. 543–564.
[7] D. P. Lathrop and C. B. Forest, "Magnetic dynamos in the lab", *Phys. Today* **64** (2011), pp. 40–45.
[8] F. Stefani, "Liquid metal experiments on geophysical and astrophysical phenomena", *Nat. Rev. Phys.* **6** (2024), pp. 409–425.
[9] Y. B. Ponomarenko, "On the theory of hydromagnetic dynamos", *Zh. Prikl. Mekh. & Tekh. Fiz. (USSR)* **6** (1973), pp. 47–51.
[10] A. Gailitis, O. Lielausis, S. Dement'ev, et al., "Detection of a flow induced magnetic field eigenmode in the Riga dynamo facility", *Phys. Rev. Lett.* **84** (2000), pp. 4365–4368.
[11] A. Gailitis, O. Lielausis, E. Platacis, et al., "Magnetic field saturation in the Riga dynamo experiment", *Phys. Rev. Lett.* **86** (2000), pp. 3024–3027.

[12] A. Gailitis, O. Lielausis, E. Platacis, G. Gerbeth and F. Stefani, "The Riga dynamo experiment", *Surv. Geophys.* **24** (2003), pp. 247–267.

[13] A. Gailitis, O. Lielausis, E. Platacis, G. Gerbeth and F. Stefani, "Riga dynamo experiment and its theoretical background", *Phys. Plasmas* **11** (2004), pp. 2838–2834.

[14] A. Gailitis, G. Gerbeth, T. Gundrum, O. Lielausis, G. Lipsbergs, E. Platacis and F. Stefani, "Self-excitation in a helical liquid metal flow: the Riga dynamo experiments", *J. Plasma Phys.* **84** (2018), article no. 73584030.

[15] U. Müller and R. Stieglitz, "The Karlsruhe dynamo experiment", *Nonl. Proc. Geophys.* **9** (2002), pp. 165–170.

[16] U. Müller, R. Stieglitz and S. Horanyi, "A two-scale hydromagnetic dynamo experiment", *J. Fluid Mech.* **498** (2004), pp. 31–71.

[17] U. Müller, R. Stieglitz and S. Horanyi, "Experiments at a two-scale dynamo test facility", *J. Fluid Mech.* **552** (2006), pp. 419–440.

[18] U. Müller and R. Stieglitz, "The response of a two-scale kinematic dynamo to periodic flow forcing", *Phys. Fluids* **21** (2009), article no. 034108.

[19] R. Monchaux, M. Berhanu, M. Bourgoin, et al., "Generation of a magnetic field by dynamo action in a turbulent flow of liquid sodium", *Phys. Rev. Lett.* **98** (2007), article no. 044502.

[20] M. Berhanu, R. Monchaux, S. Fauve, et al., "Magnetic field reversals in an experimental turbulent dynamo", *Eur. Phys. Lett.* **77** (2007), article no. 59001.

[21] F. Ravelet, M. Berhanu, R. Monchaux, et al., "Chaotic dynamos generated by a turbulent flow of liquid sodium", *Phys. Rev. Lett.* **101** (2008), article no. 074502.

[22] R. Monchaux, M. Berhanu, S. Aumaître, et al., "The von Kármán sodium experiment: Turbulent dynamical dynamos", *Phys. Fluids* **21** (2009), article no. 035108.

[23] B. Gallet, S. Aumaître, J. Boisson, et al., "Experimental observation of spatially localized dynamo magnetic fields", *Phys. Rev. Lett.* **108** (2012), article no. 144501.

[24] A. Giesecke, F. Stefani and G. Gerbeth, "Role of soft-iron impellers on the mode selection in the von-Kármán-sodium dynamo experiment", *Phys. Rev. Lett.* **104** (2010), article no. 044503.

[25] S. Kreuzahler, Y. Ponty, N. Plihon, H. Homann and R. Grauer, "Dynamo enhancement and mode selection triggered by high magnetic permeability", *Phys. Rev. Lett.* **119** (2017), article no. 234501.

[26] C. Nore, D. C. Quiroz, L. Cappanera and J.-L. Guermond, "Numerical simulation of the von-Kármán-sodium dynamo experiment", *J. Fluid Mech.* **854** (2018), pp. 164–195.

[27] F. Stefani, G. Gerbeth, U. Günther and M. Xu, "Why dynamos are prone to reversals", *Earth Planet. Sci. Lett.* **243** (2006), pp. 828–840.

[28] F. Pétrélis, S. Fauve, E. Dormy and J.-P. Valet, "Simple mechanism for reversals of Earth's magnetic field", *Phys. Rev. Lett.* **102** (2009), article no. 144503.

[29] R. Benzi and J.-F. Pinton, "Magnetic reversals in a simple model of magnetohydrodynamics", *Phys. Rev. Lett.* **105** (2010), article no. 024501.

[30] M. Le Bars, D. Cébron and P. Le Gal, "Flows driven by libration, precession, and tides", *Annu. Rev. Fluid Mech.* **147** (2015), pp. 163–193.

[31] G. Consolini and P. De Michelis, "Stochastic resonance in geomagnetic polarity reversals", *Phys. Rev. Lett.* **90** (2003), article no. 058501.

[32] M. Fischer, G. Gerbeth, A. Giesecke and F. Stefani, "Inferring basic parameters of the geodynamo from sequences of polarity reversals", *Inverse Probl.* **25** (2008), article no. 065011.

[33] L. Cappellotto, M. J. Orgeira, V. M. V. Herrera and R. G. Cionco, "Multivariable statistical analysis between geomagnetic field, climate, and orbital periodicities over the last 500 kyr, and their relationships during the last interglacial", *Global Planet. Change* **213** (2022), article no. 103836.

[34] M. Landeau, A. Fournier, H.-C. Nataf, D. Cebron and N. Schaeffer, "Sustaining Earth's magnetic dynamo", *Nat. Rev. Earth Environ.* **3** (2022), pp. 255–269.

[35] C. A. Dwyer, D. J. Stevenson and F. Nimmo, "A long-lived lunar dynamo driven by continuous mechanical stirring", *Nature* **479** (2011), pp. 212–214.

[36] S. M. Tikoo, B. P. Weiss, D. L. Shuster, C. Suavet, H. Wang and T. L. Grove, "A two-billion-year history for the lunar dynamo", *Sci. Adv.* **3** (2017), article no. e170020.

[37] R. R. Fu, B. P. Weiss, D. L. Shuster, et al., "An ancient core dynamo in asteroid Vesta", *Science* **338** (2012), pp. 238–241.

[38] H.-C. Nataf, "Tidally synchronized solar dynamo: A rebuttal", *Solar Phys.* **297** (2022), article no. 107.

[39] E. Weisshaar, R. H. Cameron and M. Schüssler, "No evidence for synchronization of the solar cycle by a "clock"", *Astron. Astrophys.* **671** (2023), article no. A87.

[40] C.-C. Hung, *Apparent relations between solar activity and solar tides caused by the planets*, tech. rep., NASA, 2007. no. NASA/TM-2007-214817.

[41] N. Scafetta, "Does the Sun work as a nuclear fusion amplifier of planetary tidal forcing? A proposal for a physical mechanism based on the mass-luminosity relation", *J. Atmos. Sol.-Terr. Phys.* **81-82** (2012), pp. 27–40.

[42] I. R. G. Wilson, "The Venus-Earth-Jupiter spin-orbit coupling model", *Pattern Recogn. Phys.* **1** (2013), pp. 147–158.

[43] V. P. Okhlopkov, "The gravitational influence of Venus, the Earth, and Jupiter on the 11-year cycle of solar activity", *Mosc. Univ. Phys. Bull.* **71** (2016), pp. 440–446.

[44] F. Stefani, A. Giesecke, N. Weber and T. Weier, "Synchronized helicity oscillations: a link between planetary tides and the solar cycle?", *Solar Phys.* **291** (2016), pp. 2197–2212.

[45] F. Stefani, A. Giesecke and T. Weier, "A model of a tidally synchronized solar dynamo", *Solar Phys.* **294** (2019), article no. 60.

[46] F. Stefani, R. Stepanov and T. Weier, "Shaken and Stirred: When Bond Meets Suess–de Vries and Gnevyshev–Ohl", *Solar Phys.* **296** (2021), article no. 88.

[47] P. Charbonneau, "External forcing of the solar dynamo", *Front. Astron. Space Sci.* **9** (2022), article no. 853676.

[48] M. Klevs, L. Jouve, F. Stefani and T. Weier, "A synchronized two-dimensional $\alpha - \Omega$ model of the solar dynamo", *Solar Phys.* **298** (2023), article no. 90.

[49] G. Horstmann, G. Mamatsashvili, A. Giesecke, T. Zaqarashvili and F. Stefani, "Tidally forced planetary waves in the tachocline of solar-like stars", *Astrophys. J.* **944** (2023), article no. 48.

[50] F. Stefani, G. Horstmann, G. Mamatsashvili and T. Weier, "Rieger, Schwabe, Suess–de Vries: The sunny beats of resonance", *Solar Phys.* **299** (2024), article no. 51.

[51] J. H. Shirley, "Orbit-spin coupling and the circulation of the Martian atmosphere", *Planet. Space Sci.* **141** (201), pp. 1–16.

[52] J. H. Shirley, "Orbit-spin coupling, the solar dynamo, and the planetary theory of sunspots", 2023. *preprint*, arXiv:2309.13076.

[53] J. Vidal and D. Cébron, "Inviscid instabilities in rotating ellipsoids on eccentric Kepler orbits", *J. Fluid Mech.* **833** (2017), pp. 469–511.

[54] S. Horn and J. M. Aurnou, "Rotating convection with centrifugal buoyancy: Numerical predictions for laboratory experiments", *Phys. Rev. Fluids* **4** (2019), article no. 073501.

[55] T. Sloudsky, "De la rotation de la terre supposée fluide à son intérieur", *Bull. Soc. Imp. Natur. Mosc.* **2** (1895), pp. 285–318.

[56] H. Poincaré, "Sur la précession des corps déformables", *Bull. Astron.* **27** (1910), pp. 321–356.

[57] F. Busse, "Steady fluid flow in a precessing spheroidal shell", *J. Fluid Mech.* **33** (1968), pp. 739–751.

[58] R. Manasseh, "Breakdown regimes of inertia waves in a precessing cylinder", *J. Fluid Mech.* **243** (1992), pp. 261–296.

[59] J. J. Kobine, "Azimuthal flow associated with inertial wave resonance in a precessing cylinder", *J. Fluid Mech.* **319** (1996), pp. 387–406.

[60] Y. Lin, J. Noir and A. Jackson, "Experimental study of fluid flows in a precessing cylindrical annulus", *Phys. Fluids* **26** (2014), article no. 046604.

[61] W. Mouhali, T. Lehner, J. Léorat and R. Vitry, "Evidence of a cyclonic regime in a precessing cylindrical container", *Exp. Fluids* **53** (2012), pp. 1693–1700.

[62] S. Goto, A. Matsunaga, M. Fujiwara, et al., "Turbulence driven by precession in spherical and slightly elongated spheroidal cavities", *Phys. Fluids* **26** (2014), article no. 055107.

[63] J. Herault, T. Gundrum, A. Giesecke and F. Stefani, "Subcritical transition to turbulence of a precessing flow in a cylindrical vessel", *Phys. Fluids* **27** (2015), article no. 124102.

[64] K. Komoda and S. Goto, "Three-dimensional flow structures of turbulence in precessing spheroids", *Phys. Rev. Fluids* **4** (2019), article no. 014603.

[65] C. Nobili, P. Meunier, B. Favier and M. Le Bars, "Hysteresis and instabilities in a spheroid in precession near the resonance with the tilt-over mode", *J. Fluid Mech.* **909** (2021), article no. A17.

[66] J. Noir and D. Cébron, "Precession-driven flows in non-axisymmetric ellipsoids", *J. Fluid Mech.* **737** (2013), pp. 412–439.

[67] F. Burmann and J. Noir, "Experimental study of the flows in a non-axisymmetric ellipsoid under precession", *J. Fluid Mech.* **923** (2022), article no. A24.

[68] A. Tilgner, "Precession driven dynamos", *Phys. Fluids* **17** (2005), article no. 034104.

[69] C.-C. Wu and P. H. Roberts, "On a dynamo driven by topographic precession", *Geophys. Astrophys. Fluid Dyn.* **103** (2009), pp. 467–501.

[70] A. Krauze, "Numerical modeling of the magnetic field generation in a precessing cube with a conducting melt", *Magnetohydrodynamics* **46** (2010), pp. 271–280.

[71] C. Nore, J. Léorat, J.-L. Guermond and F. Luddens, "Nonlinear dynamo action in a precessing cylindrical container", *Phys. Rev. E* **93** (2011), article no. 043113.

[72] Y. Lin, P. Marti, J. Noir and A. Jackson, "Precession-driven dynamos in a full sphere and the role of large scale cyclonic vortices", *Phys. Fluids* **28** (2016), article no. 066601.

[73] O. Goepfert and A. Tilgner, "Dynamos in precessing cubes", *New J. Phys.* **18** (2016), article no. 103019.

[74] A. Giesecke, T. Vogt, T. Gundrum and F. Stefani, "Nonlinear large scale flow in a precessing cylinder and its ability to drive dynamo action", *Phys. Rev. Lett.* **120** (2018), article no. 024502.

[75] J. Vidal and D. Cébron, "Kinematic dynamos in triaxial ellipsoids", *Proc. R. Soc. Lond., Ser. A* **A477** (2021), article no. 20210252.

[76] R. F. Gans, "On hydromagnetic precession in a cylinder", *J. Fluid Mech.* **45** (1971), pp. 111–130.

[77] A. Tilgner, "On models of precession driven core flow", *Stud. Geophys. Geod.* **42** (1998), pp. 232–238.

[78] P. Meunier, C. Eloy, R. Lagrange and F. Nadal, "A rotating fluid cylinder subject to weak precession", *J. Fluid Mech.* **599** (2008), pp. 405–440.

[79] R. Lagrange, P. Meunier, F. Nadal and C. Eloy, "Precessional instability of a fluid cylinder", *J. Fluid Mech.* **666** (2011), pp. 104–145.

[80] D. Gao, P. Meunier, S. L. Dizès and C. Eloy, "Zonal flow in a resonant precessing cylinder", *J. Fluid Mech.* **923** (2021), article no. A29.

[81] J. J. Kobine, "Inertial wave dynamics in a rotating and precessing cylinder", *J. Fluid Mech.* **303** (1995), pp. 233–252.

[82] A. Giesecke, T. Albrecht, T. Gundrum, J. Herault and F. Stefani, "Triadic resonances in nonlinear simulations of a fluid flow in a precessing cylinder", *New J. Phys.* **17** (2015), article no. 113044.

[83] J. M. Lopez and F. Marquez, "Nonlinear and detuning effects of the nutation angle in precessionally forced rotating cylinder flow", *Phys. Rev. Fluids* **1** (2016), article no. 023602.

[84] T. Albrecht, H. M. Blackburn, J. M. Lopez, R. Manasseh and P. Meunier, "On triadic resonance as an instability mechanism in precessing cylinder flow", *J. Fluid Mech.* **841** (2018), article no. R3.

[85] J. Herault, A. Giesecke, T. Gundrum and F. Stefani, "Instability of precession driven Kelvin modes: Evidence of a detuning effect", *Phys. Rev. Fluids* **4** (2019), article no. 033901.

[86] R. Lagrange, C. Eloy, F. Nadal and P. Meunier, "Instability of a fluid inside a precessing cylinder", *Phys. Fluids* **20** (2008), article no. 081701.

[87] P. Meunier, "Geoinspired soft mixers", *J. Fluid Mech.* **903** (2020), article no. A15.

[88] H. Blackburn, D. Lee, T. Albrecht and J. Singh, "Semtex: A spectral element–fourier solver for the incompressible Navier–Stokes equations in cylindrical or cartesian coordinates", *Comput. Phys. Commun.* **245** (2019), article no. 106804.

[89] A. Giesecke, F. Stefani and G. Gerbeth, "Kinematic simulation of dynamo action by a hybrid boundary-element/finite-volume method", *Magnetohydrodynamics* **44** (2008), pp. 237–252.

[90] F. Ravelet, A. Chiffaudel, F. Daviaud and J. Léorat, "Toward an experimental von Kármán dynamo: Numerical studies for an optimized design", *Phys. Fluids* **17** (2005), article no. 117104.

[91] F. Stefani, M. Xu, G. Gerbeth, et al., "Ambivalent effects of added layers on steady kinematic dynamos in cylindrical geometry: application to the VKS experiment", *Eur. J. Mech. B Fluids* **25** (2006), pp. 894–908.

[92] A. Giesecke, F. Stefani and G. Gerbeth, "Influence of high-permeability discs in an axisymmetric model of the Cadarache dynamo experiment", *New J. Phys.* **14** (2012), article no. 053005.

[93] A. Giesecke, T. Vogt, T. Gundrum and F. Stefani, "Kinematic dynamo action of a precession-driven flow based on the results of water experiments and hydrodynamic simulations", *Geophys. Astrophys. Fluid Dyn.* **113** (2019), pp. 235–255.

[94] F. Pizzi, A. Giesecke, J. Šimkanin and F. Stefani, "Prograde and retrograde precession of a fluid-filled cylinder", *New J. Phys.* **23** (2021), article no. 123016.

[95] V. Kumar, F. Pizzi, A. Giesecke, et al., "The effect of nutation angle on the flow inside a precessing cylinder and its dynamo action", *Phys. Fluids* **35** (2023), article no. 014114.

[96] F. Pizzi, A. Giesecke, J. Šimkanin, V. Kumar, T. Gundrum and F. Stefani, "Numerical and theoretical framework for the DRESDYN precession dynamo experiments", *Magnetohydrodynamics* **58** (2022), pp. 445–453.

[97] M. M. Adams, D. R. Stone, D. S. Zimmerman and D. P. Lathrop, "Liquid sodium models of the Earth's core", *Prog. in Earth and Planet. Sci.* **2** (2015), article no. 29.

[98] D. B. Weisberg, E. Peterson, J. Milhone, et al., "Driving large magnetic Reynolds number flow in highly ionized, unmagnetized plasmas", *Phys. Plasmas* **24** (2017), article no. 056502.

[99] S. Rother and M. Beitelschmidt, "Strength assessment of a precession driven dynamo", *Tech. Mech.* **37** (2017), pp. 120–128.

[100] F. Stefani, T. Albrecht, G. Gerbeth, et al., "Towards a precession driven dynamo experiment", *Magnetohydrodynamics* **51** (2015), pp. 275–284.

[101] S. Rother and M. Beitelschmidt, "Input reduction for nonlinear thermal surface loads", *Arch. Appl. Mech.* **93** (2023), pp. 1863–1878.

[102] M. Wilbert, A. Giesecke and R. Grauer, "Numerical investigation of the flow inside a precession driven cylindrical cavity with additional baffles using an immersed boundary method", *Phys. Fluids* **34** (2022), article no. 96607.

[103] F. Burmann and J. Noir, "Effects of bottom topography on the spin-up in a cylinder", *Phys. Fluids* **30** (2018), article no. 106601.

[104] N. Saito, C. Liao and T. Tsuruda, "Ignition and extinguishment of sodium fires in air diluted by nitrogen", in *Proceedings, 5th AOSFST, Newcastle, Australia, 2001* (M. A. Delichatsios, B. Z. Dlugogorski and E. M. Kennedy, eds.), International Association for Fire Safety Science, 2001, pp. 285–294.

[105] K. Rahbarnia, B. P. Brown, M. M. Clark, et al., "Direct observation of the turbulent emf and transport of magnetic field in a liquid sodium experiment", *Astrophys. J.* **759** (2012), article no. 80.

Comptes Rendus

Physique

Objectif de la revue

Les *Comptes Rendus Physique* sont une revue électronique évaluée par les pairs de niveau international, qui couvre l'ensemble des domaines de la physique et de l'astrophysique.

Ils publient des numéros thématiques, des articles originaux de recherche, des articles de synthèse, des mises en perspective historiques, des textes à visée pédagogique, ou encore des actes de colloque, en anglais ou en français, sans limite de longueur et dans un format aussi souple que possible (figures, données associées, etc.).

Depuis 2020, les *Comptes Rendus Physique* sont publiés avec le centre Mersenne pour l'édition scientifique ouverte, selon une politique vertueuse de libre accès diamant, gratuit pour les auteurs (pas de frais de publication) comme pour les lecteurs (accès libre, immédiat et pérenne).

Directeur de la publication : Étienne Ghys.

Rédacteurs en chef : Daniel Estève, Stephan Fauve.

Rédacteurs en chef invités : Stephan Fauve et Michael Le Bars

Comité éditorial : Jacqueline Bloch, Hélène Bouchiat, Alexandre Bouzdine, Yves Bréchet, Françoise Combes, Jean Dalibard, Michel Davier, Pierre Fayet, Frédérique de Fornel, Maurice Goldman, Denis Gratias, Guy Laval, Chaouqi Misbah, Jean-Yves Ollitrault, Nathalie Palanque-Delabrouille.

Secrétaire scientifique : Isabelle Vallet.

À propos de la revue

Les *Comptes Rendus Physique* sont exclusivement publiés au format électronique.

Toutes les informations sur la revue, ainsi que le texte intégral de l'ensemble des articles, sont disponibles sur son site internet, à l'adresse https://comptes-rendus.academie-sciences.fr/physique/.

Informations pour les auteurs

Pour toute question relative à la soumission d'un manuscrit, merci de consulter le site internet de la revue : https://comptes-rendus.academie-sciences.fr/physique/.

Contact

Académie des sciences
23 quai de Conti
75006 Paris (France)
cr-physique@academie-sciences.fr



Les articles de cette revue sont mis à disposition sous la licence Creative Commons Attribution 4.0 International (CC-BY 4.0) https://creativecommons.org/licenses/by/4.0/deed.fr

Comptes Rendus
de l'Académie des sciences

Physique

Volume 25, nº S3, 2024

Special issue / *Numéro spécial*

Geophysical and astrophysical fluid dynamics in the laboratory / *Dynamique des fluides géophysiques et astrophysiques au laboratoire*

Guest editors / *Rédacteurs en chef invités*

Stephan Fauve (Laboratoire de Physique de l'ENS, CNRS, PSL Research University, Sorbonne Université, Université Paris Cité, Paris, France) and Michael Le Bars (CNRS, Aix Marseille Univ, Centrale Marseille, IRPHE, Marseille, France)

Cover illustration / *Illustration de couverture*

Credits for cover illustration: Uwe Harlander (Brandenburg University of Technology (BTU), Cottbus-Senftenberg, Germany).

Contents / *Sommaire*

Michael Le Bars, Stephan Fauve
Foreword to the special issue: Geophysical and astrophysical fluid dynamics in the laboratory 1-4

Gabriel Hadjerci, Vincent Bouillaut, Benjamin Miquel, Sébastien Aumaître, Basile Gallet
Radiatively driven convection: diffusivity-free regimes of geophysical and astrophysical flows in the laboratory 5-20

Alban Pothérat, Susanne Horn
Seven decades of exploring planetary interiors with rotating convection experiments 21-75

A. Tilgner
Experiments on double diffusive convection 77-94

Sabrina Carpy, Michael Berhanu, Martin Chaigne, Sylvain Courrech du Pont
Fingerprints of surface flows on solid substrates ablated by phase change: from laboratory experiments to planetary landscapes 95-142

Ludovic Huguet, Quentin Kriaa, Thierry Alboussière, Michael Le Bars
Solid–liquid phase change in planetary cores 143-181

Jérémie Vidal, Jérôme Noir, David Cébron, Fabian Burmann, Rémy Monville, Vadim Giraud, Yoann Charles
Geophysical flows over topography, a playground for laboratory experiments 183-234

Marie Poulain-Zarcos, Nimish Pujara, Gautier Verhille, Matthieu J. Mercier
Laboratory experiments related to marine plastic pollution: a review of past work and future directions 235-266

Philippe Claudin, Sylvain Courrech du Pont, Clément Narteau
From lab to landscape-scale experiments for the morphodynamics of sand dunes 267-295

Pierre Philippe, Nadia Benahmed
Quantifying soil surface erosion 297-332

Renaud Deguen, Ludovic Huguet, Maylis Landeau, Victor Lherm, Augustin Maller, Jean-Baptiste Wacheul
Fluid dynamics of planetary differentiation 333-377

U. Harlander, M. V. Kurgansky, K. Speer, M. Vincze
Baroclinic instability from an experimental perspective 379-426

Peter Read, Yakov Afanasyev, Jonathan Aurnou, Daphné Lemasquerier
Eddy-driven Zonal Jet Flows in the Laboratory 427-477

Adrien Lefauve
Geophysical stratified turbulence and mixing in the laboratory 479-507

Sylvain Joubaud, Samuel Boury, Philippe Odier
Internal gravity waves versus inertial waves in the laboratory 509-535

Pierre-Philippe Cortet, Nicolas Lanchon
Turbulence of internal gravity waves in the laboratory 537-556

Benoît Semin, François Pétrelis
Quasi-biennial oscillation: laboratory experiments 557-581

Christophe Gissinger
Laboratory modeling of MHD accretion disks 583-610

François Pétrélis
Experimental dynamos: from models to applications to the geodynamo 611-627

F. Stefani, S. Anders, S. Eckert, N. Freyer, G. Gerbeth, A. Giesecke, T. Gundrum, P. Kaever, V. Kumar, F. Pizzi, D. Räbiger
The DRESDYN precession experiment 629-647

1878-1535 (electronic)

Académie des sciences — Paris

Comptes Rendus
de l'Académie des sciences

Physique

Volume 25, nº S3, 2024